CONF-820897
SLAC-259
(T/E)
UC-34d

PROCEEDINGS

OF

SUMMER INSTITUTE ON PARTICLE PHYSICS

August 16 - 27, 1982

PHYSICS AT VERY HIGH ENERGIES

Program Directors

Gary J. Feldman

Frederick J. Gilman

David W. G. S. Leith

Ed. by Anne Mosher

Sponsored by Stanford University and Stanford Linear Accelerator Center under contract with the U.S. Department of Energy. Contract DE-AC03-76SF00515

January 1983

Printed in the United States of America. Available from National Technical Information Service, U.S. Department of Commerce, 5285 Port Royal Road, Springfield, VA 22161. NTIS Price codes:
Printed copy, A24
Microfiche copy, A01

Table of Contents

PART I. Lectures page

R. N. CAHN
"Expectations for Old and New Physics at High Energy Colliders". 1

M. STROVINK
"Beyond the Standard Model in Lepton Scattering and Beta Decay". 47

H. H. WILLIAMS
"Grand Unification, Proton Decay, and Neutrino Oscillations". 73

J. DORFAN
"e^+e^- Interactions at Very High Energy: Searching Beyond the Standard Model" 137

L. SUSSKIND
"The Gauge Hierarchy Problem, Technicolor, Supersymmetry, and All That" 197

H. HARARI
"Composite Models for Quarks and Leptons" 211

B. H. WIIK
"Electron-Proton Colliding Beams: The Physics Programme and the Machine" 233

PART II. Seminars

M. ARENTON
"Evidence for Jets from a Transverse Energy Triggered Calorimeter Experiment at Fermilab". 313

W. H. SMITH
"A search for Neutrino Oscillations with $\Delta m^2 > 20\ eV^2$". 321

PART III. Topical Conference

D. DI BITONTO
"Results from Experiment UA1 at the CERN $p\bar{p}$ Collider". 337

T. HIMEL
"Results from the UA2 Experiment at the CERN SPS Collider". 357

R. H. SCHINDLER
"The Emergence of Jet Structure in Events Triggered on Large Transverse Energy at $\sqrt{s}$ = 63 GeV" .371

PART III. Topical Conference (continued) page

W. M. GEIST
"Quark and Gluon Jets from the Split Field Magnet Detector at the ISR" 389

A. H. MUELLER
"Soft Hadron Production in QCD Jets". 405

F. BOEHM
"Neutrino Mass Limits from Oscillation and Double Beta Decay Experiments" 411

S. CHILDRESS
"Production of Prompt Neutrinos in 400 GeV Proton Interactions" 429

C. ROSENFELD
"Recent Results from CLEO at CESR". 447

J. LEE-FRANZINI
"What have We Learned from the Upsilons?" 467

D. SCHLATTER
"Heavy Quark Fragmentation from e^+e^- Annihilation and νN Scattering Experiments" 489

A. BÖHM
"Weak Neutral Currents in e^+e^- Experiments" 505

D. CORDS
"Two-Photon Interactions" 533

S. L. WU
"QCD and Hadron Jets - New Results from PEP and PETRA" 555

J. A. JAROS
"c, b, and τ Lifetime Measurements" 595

K. H. LAU
"Particle Searches in e^+e^- Experiments at PEP and PETRA" 613

B. CABRERA
"Superconductive Monopole Detectors". 631

G. STEIGMAN
"The Early Universe - The Ultimate Accelerator" 651

List of Participants. 667

PREFACE

This year's SLAC Summer Institute on Particle Physics was held from August 15 to August 27, 1982, its 10th meeting. The celebration of this birthday was absorbed into a more general celebration of 5th, 10th, 15th, 20th, and 25th anniversaries of many significant events in the life of the laboratory. The title of this year's Institute was "Physics at Very High Energies," and in pursuing that theme we heard lectures on the Standard Model, and on what may lie beyond it, from varying degrees of heresy. We heard of the new tools being designed and built to probe the secrets to be found at higher energies than presently attainable, and reviewed the existing experimental data that shed light on the physics of very high energy.

The now traditional format for the Institute was followed, the first seven days being spent with the mornings given to pedagogic lectures on the experimental and theoretical foundations of the topic. In the afternoon we had seminars and (often) lively discussions of the morning's lectures. The "school" led into a three-day topical conference in which the most recent theoretical and experimental results were presented and discussed. We heard the first results from the CERN $\bar{p}p$ collider, and perhaps the first clear evidence of jets in hadronic collisions from the $p\bar{p}$ and new ISR experiments.

About 365 physicists participated in this, the 10th Institute, with representatives from 12 foreign countries. This year, 102 participants were from out of state. It was a lively, informative and stimulating meeting.

We would like to thank Anne Mosher for her efforts as Coordinator of the Institute and as Editor of the Proceedings. The success of this meeting is, in very large part, due to her careful preparation and thoughtful attention. We would also like to thank Anne and her staff for the smooth and effective running of the meeting.

Gary J. Feldman

Frederick J. Gilman

David W. G. S. Leith

Program Directors

Expectations for Old and New Physics at High Energy Colliders

R. N. Cahn

CERN, Geneva
and
Lawrence Berkeley Laboratory,
University of California, Berkeley CA 94720[*]

[*] Permanent address.

© R. Cahn 1982

PREFACE

During the past year, the first data from the SPS collider at CERN have become available. The initial results are only a glimpse at a new energy regime and we can reasonably expect an increase in the extent of the data by a factor of 10^4 to 10^5. Moreover, within a few years, the Fermilab Tevatron Collider will be in operation with a center of mass energy nearly four times as great as that at CERN. Beyond these machines are other possibilities: a high luminosity pp machine at Brookhaven with a center of mass energy of 0.8 TeV; a $p\bar{p}$ or pp machine in the LEP tunnel at CERN; a "desetron" in the southwestern United States with many TeV in the center of mass. The purpose of these lectures is to provide an orientation for the wealth of data that these machines will provide.

It is quite impossible to cover comprehensively the topic of high energy hadronic collisions in two lectures or ten. As a first step in reducing the scope of the subject I have omitted any discussion of multiparticle production at low momentum transfer. Since these events make up the bulk of the cross section, this is a serious omission indeed. Nevertheless, the remaining topics are so extensive that a complete review of them would probably require the entirety of the Summer School rather than the two lectures I have available.

To reduce the task even further I have relied on a particular advantage I bring to the assignment: I am not an expert on the topic of hadronic interactions. In deciding what material to include in the lectures, I simply asked myself what I would like to know about the subject, with the hope that this would correspond to the wishes of most of the participants in the Summer School. In this way I decided to restrict myself to two topics: very soft physics and very hard physics. The first lecture, then, is devoted to total cross sections, the ratio of the real to the imaginary part of the forward scattering amplitude, and the slope parameter. The second discusses, at the most elementary level, lepton pair production, Z^0 production, high transverse momentum, and heavy flavor production.

The first topic is so old that it has almost become new. Many younger physicists are unaware of the very beautiful work on analyticity, which once played such a central role in the concerns of high energy physics. Indeed, many who were once familiar with this topic may enjoy refreshing their memories. Moreover, the colliders are taking us a long way toward the elusive asymptopia where most of the rigorous theorems apply.

The second topic is by comparison new, but runs the risk of becoming worn out, so much has been said of high transverse momentum and the like. The intent here is to use the most direct means available for estimating the cross sections of interest while eschewing all considerations of theoretical refinements such as higher order corrections in QCD. This is dictated both by lack of space and time and by my lack of expertise; it is justified by the inherent uncertainties in the best of calculations.

How interesting are $p\bar{p}$ colliders? Aren't the Z^0 factories about to be built at SLAC and CERN much more interesting? My own bias is that if nothing unexpected happens, the results from the Z^0 factories will be cleaner and thus more susceptible to interpretation. But if nothing unexpected happens, we shall not have learned very much. We should hope for the unanticipated which may give us the new clues we need. In these lectures I show what we should expect, in the hope that it will provide a standard against which we can measure to find discrepancies that will lead to a better understanding.

These are truly lectures, not reviews. Consequently, I have not tried to give complete references to the original literature, but instead

have often chosen to cite reviews that I found useful. I apologize to the many authors whose contributions have thus been slighted.

I would like to thank CERN and the A. P. Sloan Foundation which provided support during the time the lectures were initially written. Also, I would like to thank Jacques Prentki for the hospitality of the Theory Group at CERN. Thanks are also due to Maurice Jacob and Andre Martin for their interest and assistance. Most especially, thanks are due to Marty Block with whom most of the material in the first lecture was prepared jointly. This work was also supported in part by the Director. Office of Energy Research, Office of High Energy and Nuclear Physics, Division of High Energy Physics of the U.S. Department of Energy under Contract DE-AC03-76SF00098.

I. Elastic Scattering

1.1 Geometrical Picture

We begin our study of elastic scattering at very high energies by recollecting some basic concepts from ordinary scattering theory [Schiff, 1968;Eden, 1967;Jackson, 1973]. We neglect spin even though we are interested primarily in pp and $p\bar{p}$ scattering. The intent here is to develop a geometrical picture of the scattering which will provide a suggestive language and some intuition for the subject.

The standard partial wave expansion for the scattering amplitude is

$$f(\theta,k)=\frac{1}{k}\sum_l(2l+1)P_l(\cos\theta)a_l(k), \tag{1}$$

where

$$a_l(k)=\frac{\exp(2i\delta_l)-1}{2i}, \tag{2}$$

and δ_l is the phase shift in the l^{th} partial wave. At very high energies, elastic scattering involves very many partial waves so it is convenient to convert the sum over l into an integral. Let k be the center of mass momentum, θ the center of mass scattering angle, and q the momentum transfer. Then $q^2=4k^2(\sin\theta/2)^2$. A classical description of the scattering would introduce the impact parameter, b, which is related to the angular momentum by

$$bk=l+\frac{1}{2} \tag{3}$$

The extra 1/2 is thrown in for convenience and in recognition of its appearance in the WKB approximation.

To convert Eq.(1) to an integral, we replace $\sum_l \to \int dl \to \int k\,db$ and $a_l(k)\to a(b,k)$. We need also to express $P_l(\cos\theta)$ in terms of b and q.

For large l, we have [Erdélyi,1953]

$$P_l(\cos\theta) \to J_0((2l+1)\sin\theta/2) \tag{4}$$

With these replacements, Eq.(1) becomes

$$f(\theta,k) = 2k\int_0^\infty bdbJ_0(qb)a(b,k) \tag{5}$$

or, using the integral representation of J_0 [Abramowitz and Stegun, 1964, p. 360]

$$J_0(z) = \frac{1}{2\pi}\int_0^{2\pi} d\phi \exp(iz\cos\phi) \tag{6}$$

it is simply

$$f(\theta,k) = \frac{k}{\pi}\int d^2b\, \exp(i\mathbf{q}\cdot\mathbf{b})a(b,k) \tag{7}$$

With the standard non-relativistic normalization, we have

$$\sigma_{el} = \int d\Omega|f|^2 = \int d^2q\frac{|f|^2}{k^2} = 4\int d^2b|a(b,k)|^2, \tag{8}$$

and

$$\sigma_{tot} = \frac{4\pi}{k}Im\, f(0,k) = 4\int d^2b\, Im\, a(b,k). \tag{9}$$

where the latter follows from the optical theorem [Schiff, 1968]. The amplitude in impact parameter space, $a(b,k)$ is still of the form of Eq. (2). Thus it lies in the usual Argand plot shown in Fig. 1a. Elastic scattering corresponds to δ being real. If there is inelastic scattering as well, then δ has a positive imaginary part and $a(b,k)$ lies inside the Argand circle.

Total absorption corresponds to $Im\,\delta = \infty$ or $a(b,k) = i/2$. Thus a black disc of radius R gives a total cross section (see Eq.(9)) $2\pi R^2$ and an elastic cross section of πR^2 (see Eq.(8)).

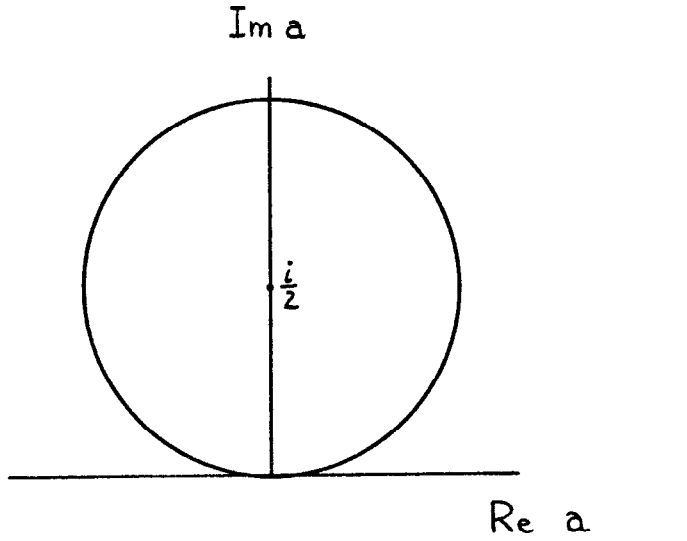


Fig. 1.a. The Argand circle inside which the partial wave amplitude, $a_l(k)$, Eq. (2), must lie.

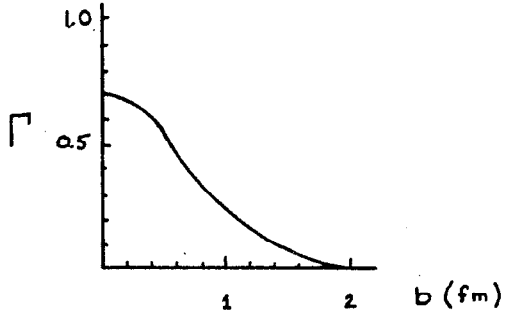


Fig. 1.b. The profile of the proton, $\Gamma = |\frac{2}{i}a(b,k)|$ vs. b , for a purely imaginary Gaussian elastic amplitude. See Eq. (13).

We can translate the scattering amplitude into an amplitude in impact parameter space by inverting the Fourier transform in Eq.(7). Thus we find

$$a(b,k) = \frac{1}{4\pi k}\int d^2q \exp(-i\mathbf{q}\cdot\mathbf{b}) f(\theta,k) \tag{10}$$

Let us apply this simple geometrical picture to elastic pp scattering using the parameters appropriate to ISR data. The amplitude will be taken to be purely imaginary (the ratio of the real to the imaginary part is less than 0.1 at these energies) with a dependence on q^2 of the form $\exp(-Bq^2/2)$. The value measured for B at the ISR is around 13 GeV^{-2} [Giacomelli and Jacob, 1979]. Using the optical theorem, Eq.(9), we find the amplitude

$$f = \frac{ik\sigma_{tot}}{4\pi}\exp(-Bq^2/2) \tag{11}$$

and the elastic cross section

$$\sigma_{el} = \int d\Omega |f|^2 = \int |f|^2 \frac{\pi dq^2}{k^2} = \frac{\sigma_{tot}^2}{16\pi B} \tag{12}$$

Moreover, we can calculate the profile of the proton in impact parameter space.

$$a(b,k) = \frac{i\sigma_{tot}}{16\pi^2}\int d^2q \exp(-Bq^2/2)\exp(-i\mathbf{b}\cdot\mathbf{q})$$

$$= \frac{i\sigma_{tot}}{16\pi}\frac{2}{B}\exp(-b^2/2B) \tag{13a}$$

$$= \frac{2i\sigma_{el}}{\sigma_{tot}}\exp(-b^2/2B) \tag{13b}$$

At zero impact parameter, $a(0,k) = i\sigma_{tot}/(8\pi B) = i\,43\,\mathrm{mb}\,(8\cdot\pi\cdot 13\mathrm{GeV}^{-2})^{-1}$. $(0.389\,\mathrm{mb\,GeV}^2)^{-1} = 0.34\,i$. This is 68% black. As the impact parameter increases, the proton becomes progressively more transparent. See Fig.1b.

1.2 Analyticity

Having begun with a very physical approach to the scattering of high energy particles, we reverse our direction completely to consider the most abstract techniques, those based on analyticity [Eden, 1967; Martin and Cheung, 1970; Jackson, 1973]. Analytic properties of the scattering amplitude seemed a central aspect of hadronic physics before the advent of QCD [Chew, 1966]. While dynamical calculations based on QCD seem more compelling than approaches based on analyticity, there remains a truly impressive edifice built by Gell-Mann, Goldberger, Lehmann, Martin, Mandelstam, and others which is part of the cultural heritage of particle physics. Here we shall treat the topic in a brutally simplistic way, striving only to reveal results of direct applicability to high energy scattering.

The forward scattering amplitude for pp scattering is a function of s, the square of the center of mass energy.[1] It is the boundary value of an analytic function. By this we mean that there is an analytic function of s, say $F(s)$, such that if we let s be just above the real axis, say $x + i\epsilon$, then $F(x+i\epsilon)$ is the scattering amplitude for center of mass energy squared x. The function $F(s)$ is analytic in the s-plane, except for cuts (and poles) along the real axis. See Fig. 2a. One cut begins at $4m_p^2$ and extends to infinity along the positive real axis. There is also a left hand cut. Below the left hand cut, $F(s)$ represents the scattering amplitude of $\mathrm{p\bar{p}}$ scattering. If the value of s is $-x - i\epsilon$, $F(s)$ represents the scattering amplitude for $\mathrm{p\bar{p}}$ scattering at a center of mass energy squared of $x+4m_p^2$. When s is just below the left hand cut, it corresponds to the value of u for the $\mathrm{p\bar{p}}$ scattering. It is often useful to use a variable $\nu = (s-u)/4m_p$ which has nicer symmetry than u or s, but at high energies and fixed t we can just as well use s itself.



Fig. 2.a. The complex s-plane with left and right hand cuts. The pp elastic amplitude is evaluated just above the right hand cut and the p$\bar{p}$ elastic amplitude is evaluated just below the left hand cut.

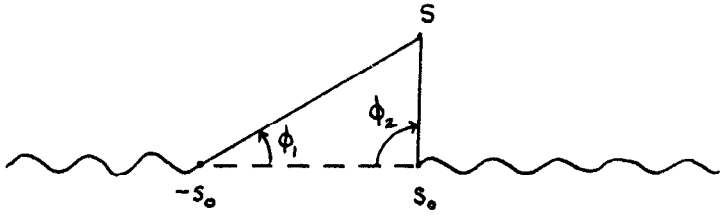


Fig. 2.b. The cut complex s-plane for the function g_+ of Eq.(16). The value of the function is

$$g_+(s) = |s_0 + s|^\alpha e^{i\alpha\phi_1} + |s_0 - s|^\alpha e^{-i\alpha\phi_2}.$$

We shall consider the Lorentz invariant amplitude M ,which for convenience we normalize so that the optical theorem reads

$$\sigma = -ImM/s \tag{14}$$

where we have ignored m_p^2 relative to s.[2] It is very useful to define two amplitudes which are combinations of the pp and p$\bar{p}$ elastic amplitudes:

$$M_\pm = \frac{1}{2}(M_{p\bar{p}} \pm M_{pp}). \tag{15}$$

The amplitude M_+ is even under $s \to -s$, while M_- is odd (again, we really should be using the variable ν). As a prototypical example, consider the function

$$g_+(s) = (s_0 - s)^\alpha + (s_0 + s)^\alpha, \tag{16}$$

This function has branch points at $\pm s_0$. We can take the branch cuts to extend from s_0 to infinity and from $-s_0$ to negative infinity along the real axis. We define the function so that it is real along the real axis between $-s_0$ and s_0. See Fig.2b.

Just above the right hand cut, for $s \gg s_0$,

$$g_+(s) \approx |s|^\alpha(1 + \exp(-i\pi\alpha)) = 2\cos(\pi\alpha/2)|s|^\alpha \exp(-i\pi\alpha/2), \tag{17}$$

while just below the left hand cut

$$g_+(s) \approx |s|^\alpha(\exp(-i\pi\alpha) + 1) = 2\cos(\pi\alpha/2)|s|^\alpha \exp(-i\pi\alpha/2), \tag{18}$$

This function is even and real analytic (that is, it is real on the real axis). Moreover, (since it is real analytic) its value just above the cut is just the complex conjugate of its value just below the cut, as one easily verifies. It has all the properties we want for the forward scattering amplitude. Its imaginary part would be related to the cross section. Just below threshold, it is purely real. From this example, we infer that even amplitudes which behave asymptotically as s^α have the phase $\exp(-i\pi\alpha/2)$. This inference can be made rigorous with the Phragmèn-Lindelöf theorem [Titchmarsh, 1939]. The corresponding analysis for odd amplitudes shows that their phase is $\exp(i\pi(1-\alpha)/2)$ if their power behavior is s^α.

Of course, not all amplitudes need have power law behavior. An example of an even function of a different sort is

$$\tilde{g}_+(s) = \frac{1}{2}[\ln((s_1+s)/s_0) + \ln((s_1-s)/s_0)], \tag{19}$$

which has the same sort of cut structure as before and which we can define so that it is real on the real axis between the two branch points. We then find that above the right hand cut (and below the left hand cut), for $s \gg s_0$

$$\tilde{g}_+(s) \approx \ln(s/s_0) - \frac{i\pi}{2}. \tag{20}$$

1.3 The Froissart Bound

Before the operation of the ISR , it appeared that all hadron-hadron total cross sections might become constant at high energies (this was believed inspite of the apparent rise in the K^+p cross section). It was known on fundamental grounds that the cross sections could not grow faster than $\ln^2 s$ - the Froissart bound [Froissart, 1961]- but this limit seemed quite irrelevant. Now the pp cross section appears to be growing as $\ln^2 s$, though that may not continue.

We present here a derivation of the Froissart bound based on two fundamental results which we take as given [Martin and Cheung, 1970]:

i. The scattering amplitude $M \sim \sqrt{s}f$ grows no faster than s^2.

ii. For fixed s (i.e. k^2), the amplitude is analytic in the region $|q|^2 < 4m_\pi^2$.

We use (2) and evaluate M at $q = 2im_\pi$ using Eq.(7).

$$\begin{aligned} M &\sim s\int d^2b \exp(i\mathbf{q}\cdot\mathbf{b})\, a(b,s) \\ &\sim s\int bdb\, d\phi\, \exp(-2m_\pi b\cos\phi)\, a(b,s) \\ &\sim s\int bdb \exp(2m_\pi b)\, a(b,s) \qquad < Cs^2. \end{aligned} \tag{21}$$

The third line is a rough approximation valid for $m_\pi b \gg 1$.

We seek to maximize the cross section, subject to this constraint. Clearly it is best to make $a(b,s)$ purely imaginary. Also, it is best to keep all the contributions at the lowest possible value of b in order to minimize the above integral. Thus we take $a(b,s) = i$ for $b < b_c$ and $a(b,s) = 0$ for $b > b_c$. A rough evaluation of the integral gives us a limit for b:

$$\exp(2m_\pi b_c) \approx Cs,$$

$$b_c \approx \frac{1}{2m_\pi}\ln(s/s_0), \tag{22}$$

where s_0 is an unknown scale.

Now using Eq.(9), we find

$$\sigma_{tot} = 4\int d^2b\, Im\, a(b,s) = 4\pi b_c^2$$
$$= \frac{\pi}{m_\pi^2}(\ln(s/s_0))^2 \quad \approx 60\text{mb}\cdot(\ln(s/s_0))^2. \tag{23}$$

Of course, all the hard work has been done for us by our friends like Martin who proved (i) and (ii).

1.4 Pomeranchuk Theorems

When the highest energy data available came from Serpukhov, it seemed that the pp total cross section was becoming constant. In such circumstances, the Pomeranchuk theorem would apply [Pomeranchuk, 1958]. This theorem states that if pp and $p\bar{p}$ (or more generally, ab and $a\bar{b}$) cross sections become constant asymptotically and if the ratio of the real to the imaginary part of the forward scattering amplitude increases less rapidly than $\ln s$, the two cross sections become equal asymptotically.

It is easy to understand this result by considering examples. If pp and $p\bar{p}$ cross sections become constant, then $M_+ \sim -is$. If M_- grows slower than this, then surely the difference cross section falls with s. Suppose then that M_- grows as $s(\ln(s/s_0) - i\pi/2)^\beta$. If $\beta = 1$ the difference cross section is asymptotically a non-zero constant, but the ratio of the real to the imaginary part grows as $\ln s$. If $\beta < 1$,the real part over the imaginary part grows as $(\ln s)^\beta$, that is, less rapidly than $\ln s$, but then the cross section difference goes as $(\ln s)^{\beta-1}$, that is, it falls to zero. Certainly β cannot be greater than one. Thus, we see that the Pomeranchuk theorem holds for amplitudes of this class.

This lovely theorem is of no use if the cross sections rise. There are useful theorems, however, that speak to this situation. Suppose the pp and $p\bar{p}$ cross sections grow as $(\ln s)^\gamma$. Then we can show that the difference of the cross sections cannot grow faster than $(\ln s)^{(\gamma/2)}$ [Eden, 1966; Kinoshita, 1966].

The proof goes as follows. Referring to Fig.1a, we see that since the amplitude $a(b)$ must lie in the Argand circle (we drop the indication of the energy at which the amplitude is evaluated),

$$|Re\, a(b)|^2 \leq Im\, a(b).$$

In the previous section, we showed that the impact parameters that contribute significantly to scattering must lie within some value b_c which grows as $\ln s$. Thus we can approximate the scattering amplitude, Eq. (7) as

$$f(q=0) = \frac{k}{\pi}\int d^2b\, a(b) \approx 2k\int_0^{b_c} bdb\, a(b). \tag{24}$$

It follows that

$$|Ref(0)| \approx 2k|\int_0^{b_c} bdb\, Re\, a(b)|$$
$$\leq 2k \int_0^{b_c} bdb|Re\, a(b)|$$
$$\leq 2k \int_0^{b_c} bdb[Im\, a(b)]^{1/2} \qquad (25)$$

Next we apply the Cauchy-Schwartz inequality

$$|Ref(0)| \leq 2k\left[\int_0^{b_c} bdb\, Im\, a(b)\right]^{1/2}\left[\int_0^{b_c} bdb\right]^{1/2}$$
$$\leq 2k\left(\frac{\sigma_{tot}}{8\pi}\right)^{1/2}\left(\frac{1}{2}b_c^2\right)^{1/2}$$
$$\leq \text{constant} \cdot k \cdot (\ln s/s_0)^{\gamma/2}(\ln s/s_0). \qquad (26)$$

Now the generic form for the odd amplitude is

$$f_- \sim k(\ln s/s_0 - i\pi/2)^{\gamma'}, \qquad (27)$$

so

$$\gamma' \leq \gamma/2 + 1. \qquad (28)$$

But the difference of the cross sections goes as

$$\Delta\sigma \sim (\ln s/s_0)^{\gamma'-1} \leq \text{constant}(\ln s/s_0)^{\gamma/2}, \qquad (29)$$

as we wished to show.

1.5 Testing Analyticity

An analytic function has real and imaginary parts which are intimately linked. The relation may be expressed by Cauchy's equations or by the vanishing of a contour integral around a region free of singularities. Traditionally, analyticity of scattering amplitudes has been tested using dispersion relations, that is to say, using the contour integral. In this way, the real part of the amplitude can be calculated from the imaginary part, which is known from the measured cross section. A behavior must be postulated for the cross section above the energies where it has been measured. Another problem occurs when the amplitude can have an imaginary part in an unphysical region. We shall use a simpler approach that is effective in the high energy domain where the cross section is relatively smooth.

The real part of the forward scattering amplitude is measured by observing the interference between the hadronic and Coulombic scattering. A naive analysis indicates that at small momentum transfer squared, t, the full amplitude is a sum

$$k^{-1}f(s,t) = \frac{i+\rho}{4\pi}\sigma_{tot}\, e^{bt/2} + \frac{2\alpha}{t} \qquad (30)$$

where the first term is hadronic and the second Coulombic. See Fig. 3. The ratio of the real to the imaginary part of the hadronic amplitude is indicated by ρ and $\alpha = 1/137$ is the fine structure constant. By fitting this form, the value of ρ can be deduced.

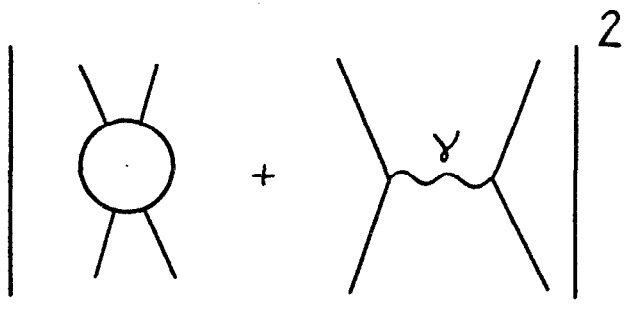


Fig. 3. The elastic pp amplitude as a sum of hadronic and Coulombic interactions. The interference is used to determine the phase of the hadronic amplitude.

In fact, this treatment is not really adequate. The Coulomb amplitude is not precisely as we have written it because there is in addition the mysterious Coulomb phase. In fact, the Coulomb amplitude is not well defined because the scattering wave function contains in the exponential a term $\ln kr$ as well as the standard kr term. This technical complication is well understood and the appropriate corrections established. [Bethe, 1958; West and Yennie, 1968; Cahn; 1982]

The recent use of the ISR to study $p\bar{p}$ interactions has provided a unique opportunity to measure ρ for this process, with a high intensity, monochromatic beam. Some data collected by the Louvain- Northwestern collaboration are shown in Fig. 4 [Louvain -Northwestern Collaboration, 1982].

Rather than using dispersion relations, we shall test analyticity by fitting the data directly with complex amplitudes with the proper behavior [Eden, 1967; Bourrelly and Fischer, 1973]. We parameterize the even amplitude in terms of real constants [Cahn, 1982a; Block and Cahn, 1982a]

$$M_+ = -is\left[A + \frac{B(\ln s/s_0 - i\pi/2)^2}{1 + a(\ln s/s_0 - i\pi/2)^2}\right] + C, \tag{31}$$

and first consider the case $a = 0$. Then, from Eqs.(30) and (31),

$$\sigma_+ = A + B(\ln^2 s/s_0 - \pi^2/4), \tag{32}$$

which saturates the form of the Froissart bound, and which has often been used in fitting the pp cross section data. Permitting the parameter a to take on small positive values allows for a deviation from this form.

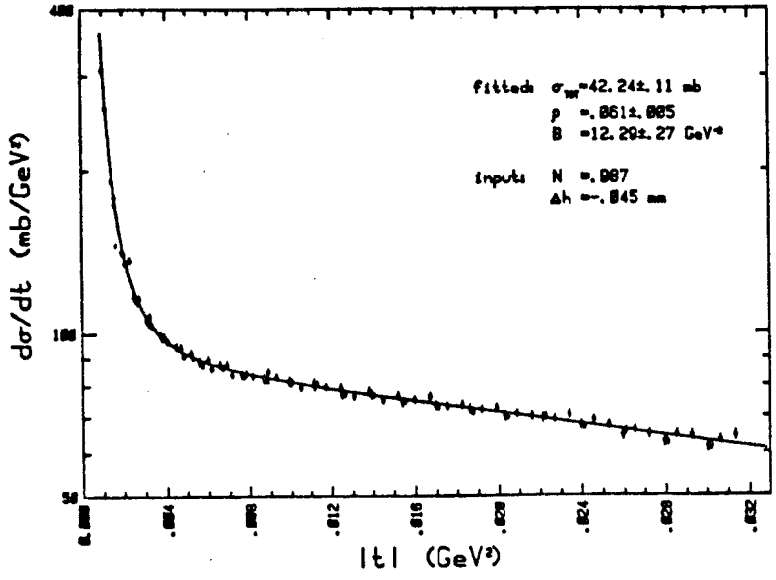


Fig. 4.a. Data on elastic pp scattering at the ISR taken by the Louvain-Northwestern Collaboration, 1982. Below $-t = 0.002\,\mathrm{GeV}^2$ the sharp Coulomb peak is visible. The gentle slope is due to hadronic scattering. Between these is the interference region. The data were taken at $\sqrt{s} = 52.8\,\mathrm{GeV}$.

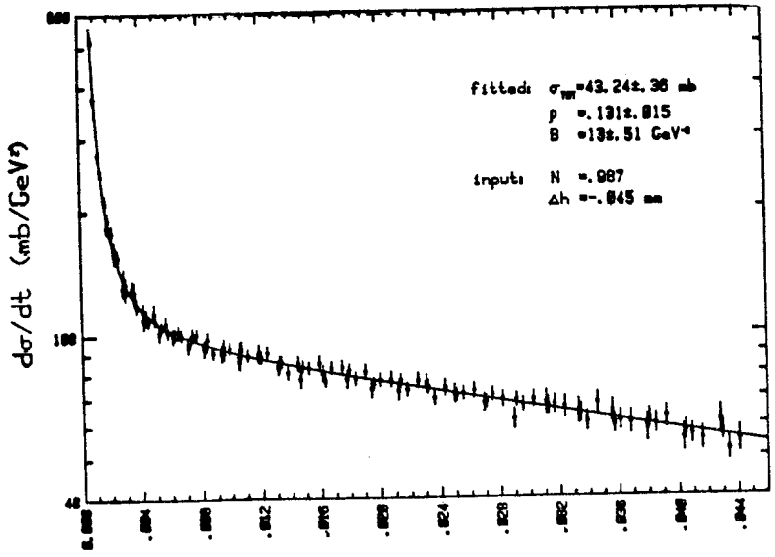


Fig. 4.b. Data for elastic $p\bar{p}$ scattering at the ISR. [Louvain-Northwestern Collaboration, 1982].

Indeed, asymptotically the form gives a constant cross section, $\sigma_+(\infty) = A + B/a$. The constant C is permitted by the requirements of analyticity for the even amplitude and corresponds to a subtraction constant in the usual dispersion relation treatment. We shall show that C is unimportant in the region of interest, as we might expect since it lacks the factor of s present in the dominant terms. We shall also see that very fine fits are obtained with $a = 0$. Thus, just three parameters, A (in mb), B (in mb), and s_0(in GeV^2), are needed to parameterize the even amplitude [3]. The parameter a is useful, however, for it will provide a means of estimating our uncertainty when we try to extrapolate our fit to higher energies.

The odd amplitude is known to be dominated by a piece with the approximate behaviour $s^{1/2}$ (that is, $\sigma_{p\bar{p}} - \sigma_{pp} \sim s^{-1/2}$). We take the power, α and the magnitude, D, of the amplitude as parameters and write

$$M_- = Ds^\alpha \exp[i\pi(1-\alpha)/2]. \tag{33}$$

Later, we shall consider odd amplitudes with unconventional asymptotic behaviour in an attempt to establish limits on the presence of such terms. For the purpose of finding an adequate fit to the present data, they are unnecessary.

The cross sections and ρ values may be obtained directly from Eqs.(31) and (33). If $a = 0$, the resulting forms are especially simple:

$$\begin{aligned}
\sigma_{pp} &= A + B(\ln^2 s/s_0 - \pi^2/4) + Ds^{\alpha-1}\cos(\pi\alpha/2), \\
\sigma_{p\bar{p}} &= A + B(\ln^2 s/s_0 - \pi^2/4) - Ds^{\alpha-1}\cos(\pi\alpha/2), \\
\rho_{pp} &= \frac{\pi B}{\sigma_{pp}}\ln s/s_0 + \frac{Ds^{\alpha-1}}{\sigma_{pp}}\sin(\pi\alpha/2), \\
\rho_{p\bar{p}} &= \frac{\pi B}{\sigma_{p\bar{p}}}\ln s/s_0 - \frac{Ds^{\alpha-1}}{\sigma_{p\bar{p}}}\sin(\pi\alpha/2).
\end{aligned} \tag{34}$$

In Fig. 5, we show the result of fitting Eqs.(31) and (33) to the available data above $s^{1/2} = 5$ GeV. It is clear that the fits are quite successful and there is no apparent violation of analyticity since our fits incorporate analyticity in their very form (at least far from the actual thresholds). In Table I are displayed the values found for the various parameters, together with those for some additional fits to be discussed shortly.

The simplest fit (#1 in Table I) gives an acceptable χ^2/d.f. and provides a reliable means of interpolating the available data for the cross section and ρ values. The second fit allows a non-zero value for a and the best fit is obtained for $a = 0.0050 \pm 0.0031$. We can say that the data do not require $a \neq 0$, but that a small value is permitted. The third fit allows for $C \neq 0$, but the result shows that little is gained by allowing this freedom.

Extrapolating the present fit to collider energies is a speculation, but it is more than just curve fitting because of the constraints imposed by analyticity. However, a bias is introduced by our choice of the $\ln^2 s$ parameterization of the existing data. The present rise in the cross section need not persist indefinitely. The introduction of the parameter $a > 0$ yields a cross section which has a $\ln^2 s$ dependence near the minimum of the cross section but which is asymptotically constant. Of course, that the data slightly prefer a small positive value for a is not necessarily an indication that the cross sections are going to become constant asymptoti-

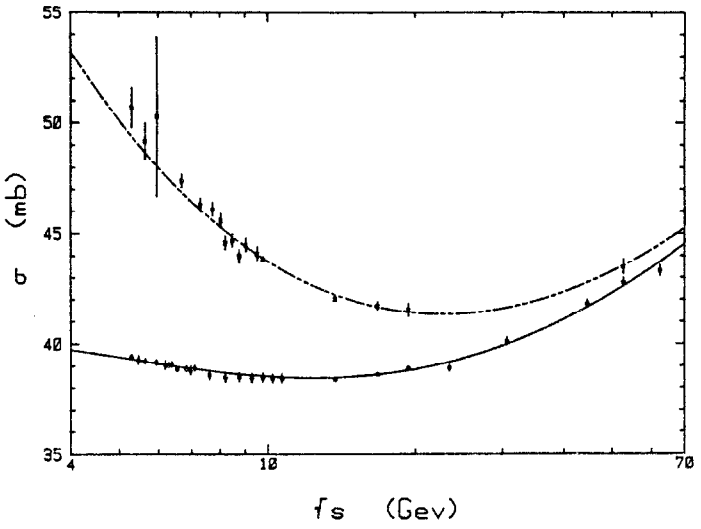


Fig. 5.a. Fit to pp (solid curve) and $p\bar{p}$ (dot-dash) total cross section data using the five parameter fit, #1 of Table I. See Eq. (34) [Block and Cahn, 1982a] .

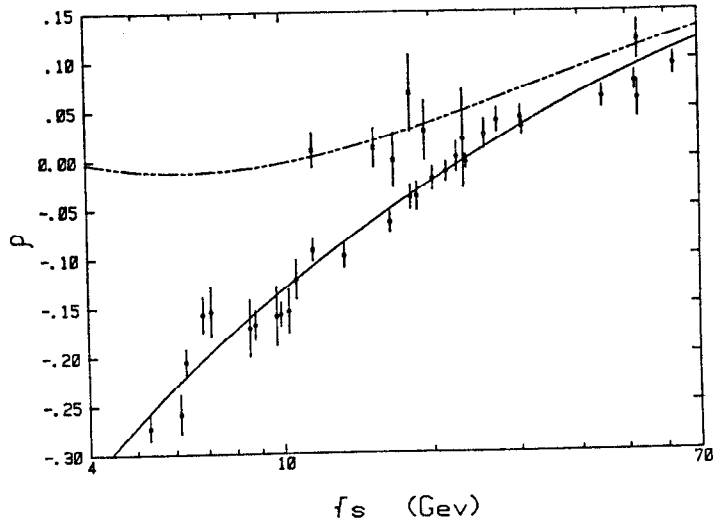


Fig. 5.b. Fit to ρ values for pp (solid curve) and $p\bar{p}$ (dot-dash) using Fit #1 of Table I. See Eq. (34). [Block and Cahn, 1982a]

Table I. Parameters for the best fits to the cross-section and ρ values for pp and $p\bar{p}$ data.The even amplitude is given in Eq.(31) . The parameters a and C are set equal to zero except in Fits #2 and #3. The odd amplitude for the first three fits is given by Eq.(33). For the last three fits, the odd amplitude is a sum of this term and one term from among the three Odderons, Eqs.(37a)-(37c). [Block and Cahn, 1982a]

	#1	#2	#3	#4	#5	#6
A(mb)	41.77 $\pm$0.04	41.74 $\pm$0.04	41.77 $\pm$0.04	41.77 $\pm$0.04	41.74 $\pm$0.04	41.70 $\pm$0.05
B(mb)	0.68 $\pm$0.01	0.66 $\pm$0.02	0.68 $\pm$0.01	0.69 $\pm$0.02	0.69 $\pm$0.01	0.66 $\pm$0.01
s_0(GeV^2)	343. $\pm$8.	338. $\pm$8.	344. $\pm$8.	345. $\pm$8.	350. $\pm$8.	356. $\pm$10.
D (mb GeV$^{2-2\alpha}$)	$-$39.0 $\pm$1.7	$-$38.7 $\pm$1.6	$-$39.2 $\pm$1.8	$-$41.7 $\pm$2.4	$-$40.8 $\pm$1.8	$-$35.2 $\pm$2.2
α	0.48 $\pm$0.01	0.49 $\pm$0.01	0.48 $\pm$0.01	0.46 $\pm$0.02	0.49 $\pm$0.01	0.50 $\pm$0.02
a		0.0050 $\pm$0.0031				
C(mb GeV^2)			5.0 $\pm$10.6			
E(mb)				$-$0.26 $\pm$0.13	$-$0.10 $\pm$0.04	$-$0.04 $\pm$0.02
$\chi^2/d.f.$	86.7/73	84.0/72	86.5/72	82.6/72	80.1/72	81.8/72

cally. We consider the difference between the $a = 0$ and $a \neq 0$ fits as providing an estimate of the uncertainty in our extrapolation.

In Fig.6 we show the five parameter fit ($a = 0, C = 0$) and the six parameter fit ($a = 0.0050, C = 0$) extrapolated to collider energies. These fits are simultaneously constrained by data for cross sections and ρ values, for both pp and $p\bar{p}$. In Table II we display some values obtained in these fits, including extrapolations to collider energies. The uncertainties quoted are just those due to the uncertainties for the parameters as determined by the fits. We note that the $a \neq 0$ fit predicts a cross section at $s^{1/2} =$ 540 GeV of 66.0 mb $\pm$ 2.8 mb, while the $a = 0$ fit gives 70.9 mb $\pm$ 0.6 mb. This difference is in rough accord with the result that the best fit for a differs from zero by a little less than two standard deviations: $a = 0.0050 \pm 0.0031$.

Preliminary data from the CERN SPS Collider are now available. The UA-4 Collaboration has reported that it finds, by extrapolating the differential cross section to the $t = 0$ point [UA4 Collaboration, 1982b]

$$(1 + \rho^2)\sigma_{tot} = 66 \pm 7\text{mb}. \tag{35}$$

Referring to Fig. 5, we see that at $s^{1/2} = 540\,\text{GeV}, \rho^2 \approx 0.02 - 0.03$, if the cross section is nearer to 65 mb than to 70 mb. Thus we interpret the UA-4 result as

$$\sigma_{tot} = 64 \pm 7\text{mb} \tag{36}$$

which is in agreement with either the $a = 0$ or $a = 0.0050$ fit. Clearly, higher precision measurements will be of great interest.

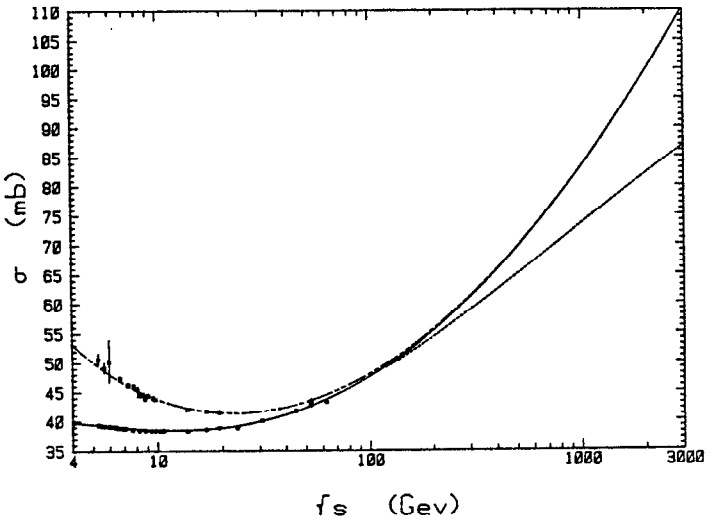


Fig. 6.a. Extrapolations of Fits #1 and #2 of Table I. At high energies, the upper curve is Fit #1 (a=0) and the lower curve is Fit #2 (a=0.0050). At lower energies, the fits are indistinguishable. At high energies, the pp and $p\bar{p}$ cross sections are nearly equal , but at lower energies the $p\bar{p}$ cross section exceeds that of pp. [Block and Cahn, 1982a]

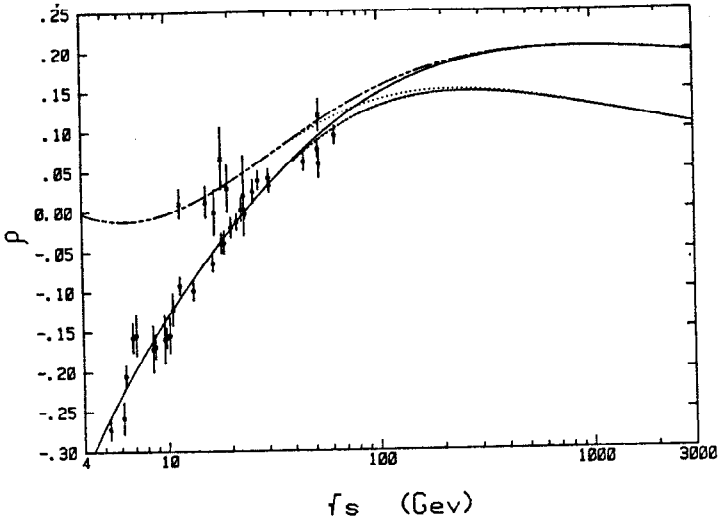


Fig. 6.b. Extrapolations of Fits #1 and #2 for the ρ values. At high energies, the upper curve is Fit #1 and the lower is Fit #2. At low energies, the fits coincide and the upper curve is for $p\bar{p}$. See Table II. [Block and Cahn,1982a]

Table II. Values of σ and ρ at selected energies. Fit #1 has $a = 0$. Fit #2 has $a = 0.0050$. See Table I for a complete listing of the parameters.[Block and Cahn, 1982a]

	σ_{pp}(mb)	$\sigma_{p\bar{p}}$(mb)	ρ_{pp}	$\rho_{p\bar{p}}$
$\sqrt{s} = 23.5$ GeV				
Fit #1	39.2±0.03	41.3±0.07	0.00±0.001	0.05±0.003
Fit #2	39.2±0.04	41.3±0.07	0.00±0.002	0.05±0.003
$\sqrt{s} = 62.5$ GeV				
Fit #1	43.7±0.1	44.5±0.1	0.11±0.003	0.12±0.002
Fit #2	43.8±0.1	44.6±0.1	0.10±0.005	0.12±0.005
$\sqrt{s} = 540$ GeV				
Fit #1	70.9±0.6	71.0±0.6	0.20±0.002	0.20±0.002
Fit #2	66.0±2.8	66.1±2.8	0.14±0.03	0.14±0.03
$\sqrt{s} = 2000$ GeV				
Fit #1	99.6±1.2	99.6±1.2	0.20±0.001	0.20±0.001
Fit #2	82.3±8.0	82.3±8.0	0.12±0.03	0.12±0.03

1.6 The Odd Amplitude

Even before the recent ISR running with antiprotons produced very high energy cross sections which could be compared with pp cross sections, there was impressive evidence that the difference cross section, $\sigma_{p\bar{p}} - \sigma_{pp}$, fell about as $s^{-1/2}$. The recent data confirm this. See. Fig. 7. This, however, does not rule out the possibility that the cross section difference might turn out to be asymptotically a small constant value, say a fraction of a millibarn. In fact, we have seen that in principle, if the cross section grows as $(\ln s)^2$, the difference cross section could grow as fast as $\ln s$. An even more subtle possibility is that the odd amplitude grows asymptotically as s, which according to our earlier discussion would be purely real (odd amplitudes go as $s^\alpha \exp[i\pi(1-\alpha)/2]$) and would thus not contribute to the total cross section, but would affect the ρ values.

To investigate such possibilities, we introduce [Łukaszuk and Nicolescu, 1973; Kang and Nicolescu, 1975; Joynson *et al.*,1975; Martin, 1982a]

$$\mathcal{M}^0_- = E^0_- s, \tag{37a}$$
$$\mathcal{M}^1_- = E^1_- s(\ln s/s_1 - i\pi/2), \tag{37b}$$
$$\mathcal{M}^2_- = E^2_- s(\ln s/s_1 - i\pi/2)^2, \tag{37c}$$

where the E's are real constants. We shall refer to the amplitudes in Eqs.(37) as Odderon-0, Odderon-1 and Odderon-2, respectively. The full odd amplitude is given by the sum, $\mathcal{M}^{tot}_-$ of $\mathcal{M}_-$ from Eq.(33), and one of the terms from Eq. (37). Odderon-0 affects the ρ values but not the cross sections, being entirely real. Odderon-1 gives a constant cross section difference, while Odderon-2 gives a cross section difference growing as $\ln s$.

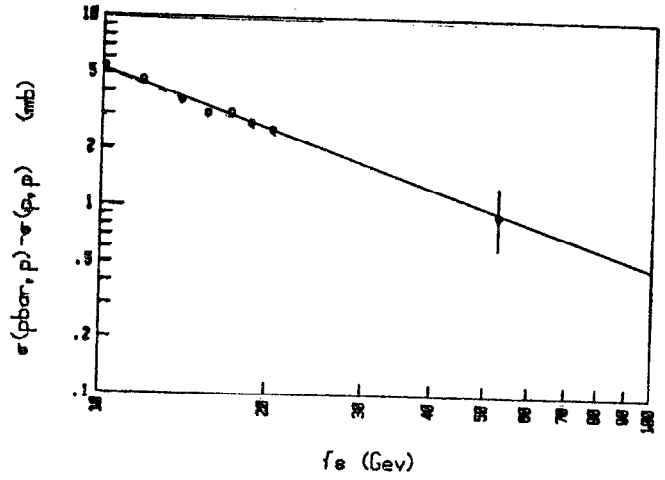


Fig. 7. The difference, $\sigma_{p\bar{p}} - \sigma_{pp}$ vs. $\sqrt{s}$. The curve is from Fit #3. See Eq. (34) and Table I. [Block and Cahn, 1982a]

If the scale, s_1, in Odderon-1 or Odderon-2 is too large, the magnitude of the amplitude may fall with increasing s, contrary to our intent in using this parameterization. To prevent this distortion, we constrain s_1 to be the same as s_0, the parameter in the even amplitude.

There is a theorem, due to Fischer and co-workers [Fischer *et al.*, 1978; Fischer, 1981] ,which states, in part, that if above some energy, the signs of $Im\mathcal{M}_{-}^{tot}$ and $Re\mathcal{M}_{-}^{tot}$ remain the same, then the difference of the cross sections tends to zero. Clearly this theorem is satisfied by the amplitude $\mathcal{M}_{-}$ of Eq. (33) for $0 < \alpha < 1$. The addition of an Odderon-1 or an Odderon-2 amplitude can be seen to lead to opposite signs for $Im\mathcal{M}_{-}^{tot}$ and $Re\mathcal{M}_{-}^{tot}$ in the limit of high s. This is of course in accord with the Fischer theorem, since these terms lead to non-vanishing cross section differences.

We have made three separate fits to the data using successively Odderon-0, Odderon-1, and Odderon-2. The results of these fits are shown in Table I. In all three cases, the value of E is about two standard deviations away from zero and there is thus no proven need for these amplitudes. It is of interest to examine quantitatively the limits that can be placed on their presence. For Odderon-0, an appropriate comparison is that between A and E, the coefficients of the purely imaginary odd amplitude and the purely real even amplitude with the same s-dependence. The magnitude of E is less than one percent of that of A. This is an impressive limit since this odd amplitude cannot contribute to the cross section. The limits on the other fits are comparable. Altogether, then, we conclude that these amplitudes which are allowed by analyticity, if present at all, are less than one percent as strong as the dominant portion of the forward scattering amplitude.

Using the values for Odderon-1 found in Table I, we note that

since D and E are both negative, $Re\mathcal{M}_{\pm}^{tot}$ is negative for $s > s_0$. On the other hand, $Im\mathcal{M}_{\pm}^{tot}$ is negative and dominated by $\mathcal{M}_-$ [Eq.(33)] at ISR energies. It does not change sign until $s^{1/2} = 200$GeV. Thus any attempt to invoke the Fischer theorem at present energies is premature. The corresponding sign change for the Odderon-2 would be at $s^{1/2} = 75$ GeV. Since these sign changes occur in $Im\mathcal{M}_{\pm}^{tot}$, they reflect a change in the sign of $\Delta\sigma = \sigma_{p\bar{p}} - \sigma_{pp}$. The existing data are thus compatible with such a sign change, and using Table I we extrapolate the Odderon-2 fit to $s^{1/2} = 540$ GeV, where we find $\sigma_{p\bar{p}} - \sigma_{pp} = -1.6 \pm 0.8$ mb. The unconventional sign of the difference is possible because the Odderon contributes oppositely to the amplitude $\mathcal{M}_-$, Eq. (33), which dominates the odd amplitude at lower energies. The magnitude of this difference and its uncertainty show clearly the desirability of making both pp and $p\bar{p}$ cross section measurements at collider energies. At the same time, these numbers provide a quantitative estimate of the required precision. The presence of Odderon-0 is especially difficult to detect experimentally. Data at very high energies would not particularly improve the situation. For example, using our values for Odderon-0 from Table I, we would predict $\Delta\rho = \rho_{pp} - \rho_{p\bar{p}}$ at $s^{1/2} = 540$ GeV to be 0.008 ± 0.003, whereas the fit without any Odderon gives $\Delta\rho = 0.0009 \pm 0.0002$ at the same s, a difference too small to be detected.

1.7 The Slope Parameter

In addition to the total cross section and ρ value, the nearly forward elastic scattering cross section has a third measurable feature, the slope parameter:

$$B(s,t) = \frac{d}{dt} \ln \frac{d\sigma}{dt}. \tag{38}$$

Frequently, it is the value at $t = 0$, $B(s) \equiv B(s, t = 0)$ which is of interest. For the simple amplitude of Eq.(11), $B(s)$ is the constant B. Back in the days when the total cross sections were believed to become constant asymptotically, the elastic scattering amplitude near the forward direction was parameterized as

$$\mathcal{M} \sim s^{\alpha(t)} e^{-i\pi\alpha(t)/2} e^{\beta t}, \tag{39}$$

where $\alpha(t) \approx 1 + \alpha'(0)t$ was the Pomeron trajectory, and β was a constant. In this model then

$$B(s) = 2\beta + 2\alpha'(0) \ln s. \tag{40}$$

Thus the canonical expectation was $B(s) \sim a \ln s + b$.

It is easy to see that this is not going to work if instead the cross section grows as $\ln^2 s$. If B is independent of t and the amplitude is purely imaginary, we can use Eq.(12):

$$\sigma_{el} = \frac{\sigma_{tot}^2}{16\pi B}, \tag{12}$$

We see that since σ_{el} cannot grow faster than $\ln^2 s$, certainly $B(s)$ must grow at least as fast as $\ln^2 s$ in the small t region.

Returning to our impact parameter representation

$$\mathcal{M} \sim s \int d^2b \exp(i\mathbf{q}\cdot\mathbf{b})\, a(b,s), \tag{41}$$

we expand about $q = 0$. Thus, if the phase of $a(b,s)$ is independent of b,

$$B(s) = \frac{\int db\, b^3 a(b,s)}{2\int db\, b a(b,s)}. \tag{42}$$

This again shows that $B(s)$ measures the size of the proton.

We know that $a(b,s)$ must drop off for $b > b_c \sim \ln s$. It is surprising to learn that a form like

$$a(b,s) \sim \exp[-(b/b_c)^2], \tag{43}$$

is not permissible. Remember that even for imaginary q (if $|q|$ is small enough) this amplitude must be bounded by s^2. However, setting $q = iQ$ we find from Eqs.(41) and (43)

$$\mathcal{M} \sim s b_c^2 \exp(Q^2 b_c^2/4). \tag{44}$$

This grows faster than any power of s. We conclude that we need $a(b,s)$ to cut off very sharply, essentially as $a(b,s) = 0$ for $b > b_c$.

We can model this by supposing that $a(b,s) = \bar{a}(b/b_c)$ where $b_c = C\ln s$ and $\bar{a}(x) = 0$ for $x > 1$. Then

$$\mathcal{M} \sim s b_c^2 \int_0^1 dx\, x\bar{a}(x) J_0(q b_c x). \tag{45}$$

The remaining integral is an entire function of qb_c, that is it has no singularities in the finite qb_c plane. This is a consequence of the integral being confined to a finite range. Moreover, as qb_c goes to infinity, the amplitude grows no faster than exp(constant $\times$ qb_c). This result is a general one for total cross sections growing as $\ln^2 s$. We can state the conclusion by writing for the amplitude [Auberson, Kinoshita, and Martin, 1971]

$$\mathcal{M} \sim -is \ln^2 s\, f(t\ln^2 s), \tag{46}$$

where $f(z)$ is an entire function of order one-half, that is, for large $|z|$, $|f(z)|$ is bounded by $C\exp(C'|z|^{1/2})$ where C and C' are constants. This form is correct as $s \to \infty$. If t is fixed, then we see that

$$\begin{aligned} B(s,t) &< \frac{d}{dt} C'|t|^{1/2} \ln s \\ &< C'' \ln s. \end{aligned} \tag{47}$$

On the other hand, if we want the slope parameter at $t = 0$, we can expand Eq. (46) in powers of $t\ln^2 s$

$$\mathcal{M} \sim -is \ln^2 s [a + bt \ln^2 s + \cdots], \tag{48}$$

so that

$$B(s,0) \sim \ln^2 s. \tag{49}$$

This non-uniform behavior was discovered recently by Martin [Martin, 1982b]. As a practical matter, it still seems reasonable to use the form for $B(s,0)$ even at non-zero values of t since the other form, Eq.(47) is derived on the assumption that $t \ln^2 s$, or equivalently $t\sigma_{tot}$ is large.

On the basis of the above discussion, we choose to parameterize the amplitudes near the forward direction as [Block and Cahn, 1982b]

$$M_+(s,t) = M_+(s,0)\exp(b_+ t/2), \tag{50a}$$
$$M_-(s,t) = M_-(s,0)\exp(b_- t/2), \tag{50b}$$

where

$$b_+ = c_+ + d_+ \ln s + e_+ \ln^2 s, \tag{51a}$$
$$b_- = c_- + d_- \ln s, \tag{51b}$$

The amplitudes at $t = 0$ are just those in Eqs.(31) and (33) with $a = 0$ and $C = 0$, and the remaining parameters at $t = 0$ are fixed to be those of the first fit in Table I. The five parameters left to describe the slope are then fitted using the available data. Unfortunately, the data are not mutually consistent. However, with a suitable choice of data sets, the results are sensible, as shown in Fig. 8. The value of the slope parameter at $-t = 0.02\,\mathrm{GeV}^2$ is predicted to be $16.7 \pm 0.7\,\mathrm{GeV}^{-2}$ at the SPS collider energy, $s^{1/2} = 540$ GeV. The result reported by UA-4 is $17.2 \pm 1.0\,\mathrm{GeV}^{-2}$ at $-t = 0.05\,\mathrm{GeV}^2$ [UA4 Collaboration, 1982a].

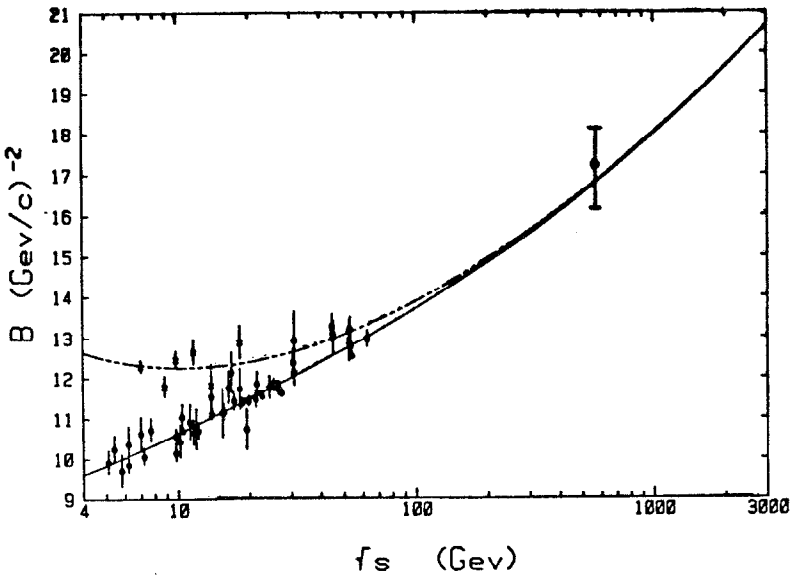


Fig. 8. The slope parameter, $B(s, t = -0.02\mathrm{GeV}^2)$ vs. $\sqrt{s}$. The upper curve and data are for $p\bar{p}$ and the lower are for pp. [Block and Cahn, 1982b]

2. Hard Scattering Processes

2.1 Perspective

Quantum chromodynamics provides a means of analyzing hard scattering processes including the production of high transverse momentum jets, high invariant mass dilepton pairs, and heavy quarks. These processes are imagined to proceed through the scattering of partons (quarks and gluons). If we look only at this scattering process, which takes place in a volume of about 1 fm^3, perturbative QCD should be reliable (see Bjorken's SLAC Summer School Lectures of 1979 on QCD). It is conventional to view the full scattering event as having three stages: the breakdown of the initial hadrons into partonic constituents, the scattering of the partons, and the transformation of the final state partons into hadrons.

We shall adopt this view in an extreme form. We shall use the term "beam" to mean the flux of partons arising from the physical beam. The "scattering" will refer just to the partonic scattering event.By the "detector" we shall mean not just the physical apparatus, but also the space outside the tiny region - the "femto-universe" - in which the "scattering" occurs. Thus, for example, the hadron cascade inside a calorimeter and the hadronization of a high momentum quark will both be regarded as characteristics of the "detector." This is a description in keeping with Bj's notion that a really good detector would be able to detect quarks and gluons. Our inability to make such measurements will simply be regarded as a flaw in our detector. Of course, we may hope to compensate for this by obtaining a very complete understanding of our "detector," meaning that we may hope to find signatures that will identify the outgoing parton type and its momentum. Such an understanding would naturally require great advances both theoretically and experimentally.

This separation may seem perverse. It pushes off the difficult problems into the experimental factors: the "beam" and the "detector." In fact, this separation is dictated by QCD . The concept of "factorization" tells us that the infrared singularities we encounter in calculating can be relegated either to the process by which the initial hadron turns into partons (the "beam") or to the process by which the final partons become hadrons(in the "detector").

2.2 The Beam

For colliding beam machines, the fundamental equation is

$$Rate = \mathcal{L}\sigma, \tag{52}$$

where $\mathcal{L}$ is the luminosity. If the two physical beams have "transverse" densities (i.e. particles/cm^2) of $\rho_1(\mathbf{r})$ and $\rho_2(\mathbf{r})$, and cross n times per second, the luminosity is

$$\mathcal{L} = n \int d^2r\, \rho_1(\mathbf{r})\rho_2(\mathbf{r}). \tag{53}$$

For the CERN SPS collider, the design values of $\int d^2r\, \rho_1$ and $\int d^2r\, \rho_2$ are about 10^{11} with an effective area of 3×10^{-3}cm^2. With six beam-beam collisions per cycle at each intersection point (that is, six bunches each of protons and anti-protons) and a machine radius of about 10^3 m, we have

$$n = \frac{6 \cdot 3 \cdot 10^8 \mathrm{m/s}}{2\pi \cdot 10^3 \mathrm{m}}, \tag{54}$$

and a design luminosity of $10^{30}\text{cm}^{-2}\text{sec}^{-1}$. The maximum luminosity achieved before July1, 1982 was about $1.8 \times 10^{28}\text{cm}^{-2}\text{sec}^{-1}$.

The "beams" we are concerned with are the beams of partons - quarks, anti-quarks, and gluons. These partons are not monochromatic of course. In fact, each proton carries a distribution of quarks and gluons which depends on x, the fraction of the proton's momentum carried by the parton: $f_i(x), (i = u, \overline{u}, \ldots g)$. This function is also weakly a function of the momentum transfer in the subprocess of interest (this dependence is called "scale breaking" or violation of " Bjorken scaling"). Ignoring this "Q^2" dependence for the moment, we ask what is the effective luminosity for, say, u-quarks on anti-u-quarks, per unit of center-of-mass energy squared (of the quark anti-quark system)? If we indicate the contributions from the two incident physical particles by the subscripts 1 and 2, we have

$$\frac{dL_{u\overline{u}}}{d\hat{s}} = \int dx_1\, dx_2 \delta(\hat{s} - s x_1 x_2)[f_{1u}(x_1) f_{2\overline{u}}(x_2) + f_{1\overline{u}}(x_1) f_{2u}(x_2)], \quad (55)$$

where $\hat{s}$ is the parton-parton center of mass energy squared. Let us call $\tau = \hat{s}/s$ so that

$$\frac{dL_{u\overline{u}}}{d\tau} = \int dx_1 dx_2 \delta(\tau - x_1 x_2)[f_{1u}(x_1) f_{2\overline{u}}(x_2) + f_{1\overline{u}}(x_1) f_{2u}(x_2)]. \quad (56)$$

The quantities $\frac{dL_{u\overline{u}}}{d\tau}, \frac{dL_{u\overline{d}}}{d\tau}, \ldots, \frac{dL_{uu}}{d\tau}, \ldots, \frac{dL_{gg}}{d\tau}$ are the fundamental characteristics of the "beam." The functions $f_u(x), f_d(x), \ldots, f_g(x)$ are determined by experiments including electroproduction and neutrinoproduction, and by theoretical considerations.

Some of these luminosity spectra have been calculated by Horgan and Jacob, 1981, and by Duke and Quigg, 1982. See Fig. 9. Their results

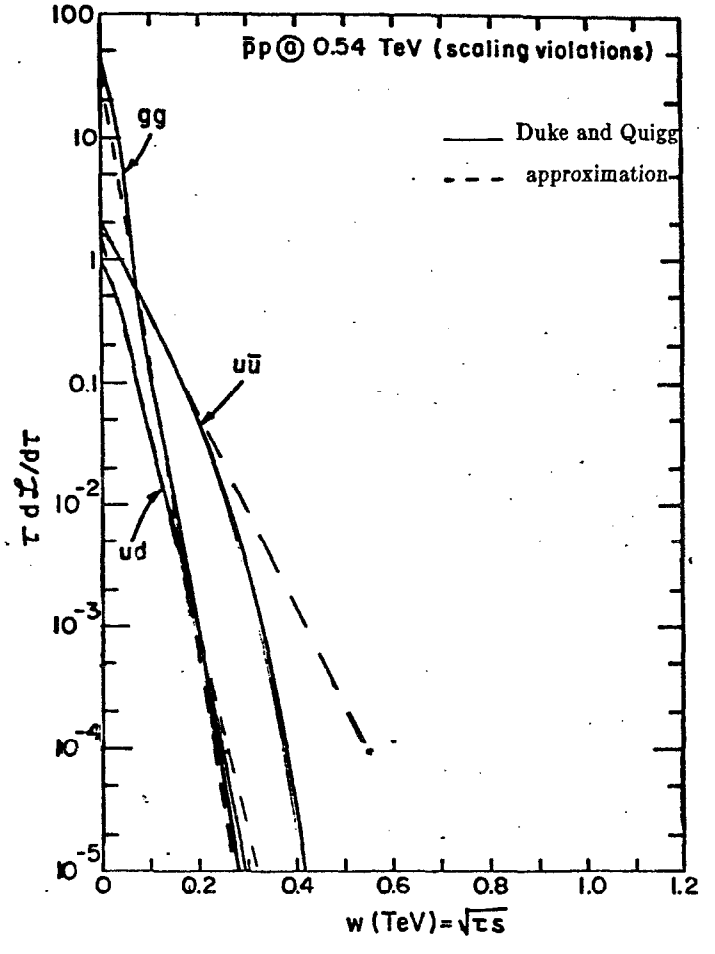


Fig. 9.a. The luminosity spectrum $\tau \frac{dL}{d\tau}$ vs. $W = \sqrt{\tau s}$ for $p\overline{p}$ collisions at $\sqrt{s} = 540\,\text{GeV}$. The dashed lines are the approximations Eq.(57). [after Duke and Quigg, 1982]

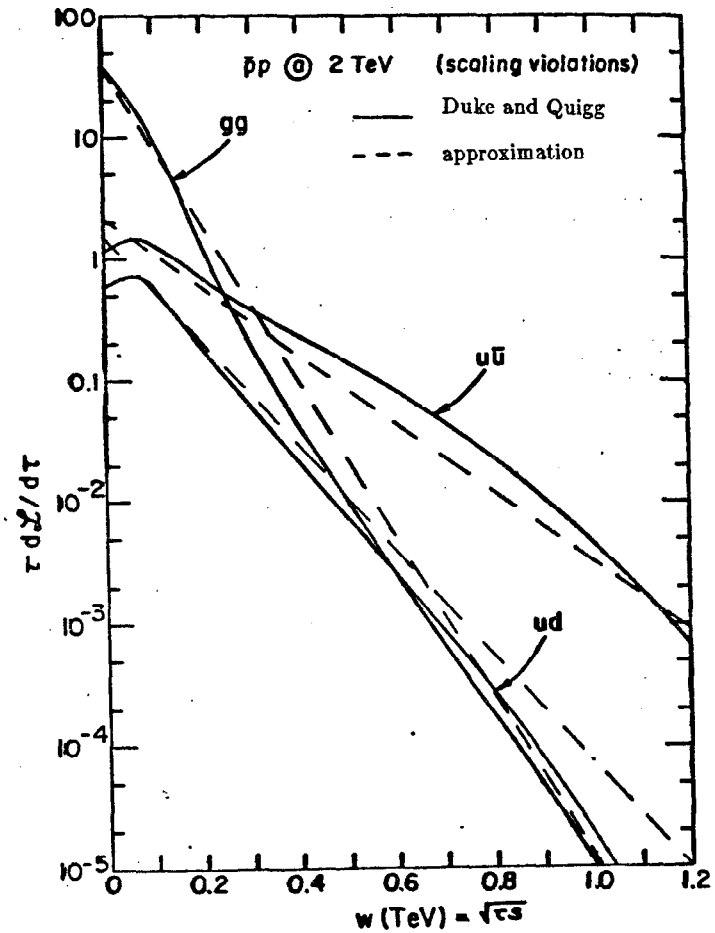


Fig. 9.b. The luminosity spectrum $\tau\frac{dL}{d\tau}$ vs. $W = \sqrt{\tau s}$ for $p\bar{p}$ collisions at $\sqrt{s} = 2000\,\text{GeV}$. The dashed lines are the approximations Eq.(57). [after Duke and Quigg,1982]

can be approximated by analytic forms. For $p\bar{p}$ collisions at $s^{1/2} = 540\,\text{GeV}$ we take

$$\begin{aligned}
\tau\frac{dL_{u\bar{u}}}{d\tau} &= 2e^{-10\sqrt{\tau}} \\
\tau\frac{dL_{uu}}{d\tau} &= 1.5e^{-20\sqrt{\tau}} \\
\tau\frac{dL_{gg}}{d\tau} &= 40e^{-30\sqrt{\tau}} \\
\tau\frac{dL_{ug}}{d\tau} &= 20e^{-20\sqrt{\tau}}
\end{aligned} \tag{57}$$

For simplicity, we have chosen forms with no scale breaking. It is apparent from Figs.(9.a) and (9.b) that this is an adequate approximation for the energy range between the CERN and Fermilab colliders.

When valence quarks are present (u and d in a proton, anti-u and anti-d in an antiproton), they dominate the distribution. Very roughly, in a proton, $f_u = 2f_d$. Thus for $p\bar{p}$ collisions, we take

$$\begin{aligned}
\frac{dL_{u\bar{d}}}{d\tau} &\approx \frac{1}{2}\frac{dL_{u\bar{u}}}{d\tau} \\
\frac{dL_{d\bar{d}}}{d\tau} &\approx \frac{1}{4}\frac{dL_{u\bar{u}}}{d\tau}
\end{aligned} \tag{58}$$

If we have a cross section $d\sigma$ for a partonic subprocess which depends on $\hat{s}$, we can find an effective cross section by integrating over τ:

$$d\sigma_{eff}(s) = \int d\tau \sum_{i,j} d\sigma_{ij}(\hat{s} = \tau s)\frac{dL_{ij}}{d\tau}. \tag{59}$$

Here the sum is over the various parton types, i and j. We shall use this basic formula to estimate the cross sections for the important hard scattering processes.

2.3 Cross Sections

We first consider the production of high mass dilepton pairs in hadronic collisions. The partonic cross section is simply related to the usual $e^+e^- \to \mu^+\mu^-$ cross section at center of mass energy squared s,

$$\sigma = \frac{4\pi\alpha^2}{3s}. \tag{60}$$

The only change required is that we must take into account the charge of the annihilating quarks and their color. A quark and an anti-quark can annihilate only if they have opposite colors. Thus we use

$$\sigma(q\bar{q} \to \mu^+\mu^-) = \frac{1}{3}e_Q^2\frac{4\pi\alpha^2}{3s}, \tag{61}$$

where e_Q is the quark charge. The effective cross section is given then by

$$\frac{d\sigma_{eff}}{d\tau} = \frac{4\pi\alpha^2}{3\hat{s}}\frac{1}{3}\left[\frac{4}{9}\frac{dL_{u\bar{u}}}{d\tau} + \frac{1}{9}\frac{dL_{d\bar{d}}}{d\tau}\right]. \tag{62}$$

Using our approximations for the luminosity spectra, Eq. (57), we find

$$s\frac{d\sigma_{eff}}{d\tau} = \frac{4\pi\alpha^2}{9\tau}\left[\frac{17}{36}\cdot\frac{2e^{-10\sqrt{\tau}}}{\tau}\right]. \tag{63}$$

This is displayed in Fig. 10. As an example,we calculate the Drell-Yan cross section (i.e. $\mu^+\mu^-$ production) for $M^2 = 100\,\mathrm{GeV}^2$ at $s^{1/2} = 540\,\mathrm{GeV}$. Thus $\sqrt{\tau} = 0.0185$. From Fig. 10, we find $sd\sigma/d\tau = 5\cdot 10^2$. Thus we estimate

$$\begin{aligned}\frac{d\sigma}{dM} &= 2M\frac{d\sigma}{s\,d\tau}\\ &= 20\ \mathrm{GeV}\cdot\frac{1}{(540\ \mathrm{GeV})^4}\cdot 5\cdot 10^2\cdot(0.389\,\mathrm{mb\ GeV}^2)\\ &= 0.5\cdot 10^{-34}\mathrm{cm}^2\,\mathrm{GeV}^{-1}.\end{aligned} \tag{64}$$

We can use our expression to compare the expected performance of the colliders at CERN ($s^{1/2} = 540\,\mathrm{GeV}$) and at Fermilab ($s^{1/2} = 2000\,\mathrm{GeV}$). Let us compare $d\sigma/dM$ at M=50 GeV. Referring back to Eqs.(63) and (64), we see that $d\sigma/dM \sim f(M)\exp(-10\sqrt{\tau})$ so that

$$\begin{aligned}\frac{(d\sigma/dM)_{FNAL}}{(d\sigma/dM)_{CERN}} &= e^{10(\sqrt{\tau}_{CERN}-\sqrt{\tau}_{FNAL})}\\ &= e^{10(0.093-0.025)}\\ &\approx 2.\end{aligned} \tag{65}$$

We can also make the comparison with CBA (née Isabelle) where $s^{1/2} = 800\,\mathrm{GeV}$, but where we must use the luminosity spectrum for uu in $p\bar{p}$ to represent the luminosity for $u\bar{u}$ in pp.

$$\frac{(d\sigma/dM)_{CBA}}{(d\sigma/dM)_{FNAL}} = \frac{1.5e^{-20\sqrt{\tau}}}{2e^{-10\sqrt{\tau}}} = \frac{1.5e^{-20\cdot\frac{50}{800}}}{2e^{-10\cdot\frac{50}{2000}}} = 0.3. \tag{66}$$

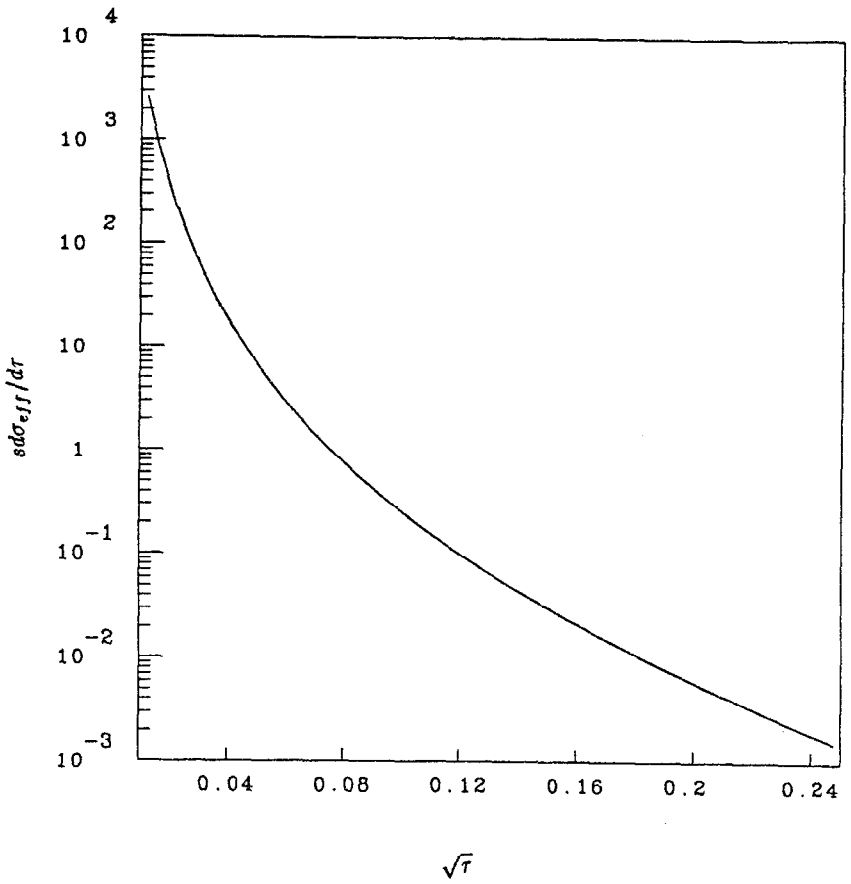


Fig. 10. The dimensionless Drell-Yan cross section, $sd\sigma_{eff}/d\tau$ vs. $\sqrt{\tau}$. See Eq. (63).

CBA is the clear winner if it has, as designs suggest, 10^3 times the luminosity of the Tevatron collider. At a sufficiently high invariant mass, the Fermilab cross section makes up for the three orders of magnitude difference in luminosity. That mass is M = 330 GeV. This is too late. There are no events at this mass.

Just how large an invariant mass can we expect to reach? The cross section to produce a dilepton pair with $m_{\mu\mu} > m_0 = \sqrt{\tau_0 s}$ is, for $p\overline{p}$ machines

$$\sigma(m_{\mu\mu} > \sqrt{\tau_0 s}) = \int d\tau \frac{d\sigma_{eff}}{d\tau}, \tag{67}$$

$$= \frac{4\pi\alpha^2}{9s}\frac{17\cdot 2}{36}\int d\tau \frac{e^{-10\sqrt{\tau}}}{\tau^2}, \tag{68}$$

$$= 0.94\cdot 10^{-37}\mathrm{cm}^2\left(\frac{540\,\mathrm{GeV}}{\sqrt{s}}\right)^2 g(\tau_0), \tag{69}$$

where the function $g(\tau)$ is given by

$$g(\tau) = \frac{2}{\tau}E_3(10\sqrt{\tau}). \tag{70}$$

where $E_3(z)$ is an exponential integral [Abramowitz and Stegun, 1964, p.228]. The function $g(\tau)$ is shown in Fig. 11.

In the domain of interest to us, a simple but adequate approximation is

$$E_3(z) \approx \frac{1}{2}2^{-2z}, \tag{71}$$

so

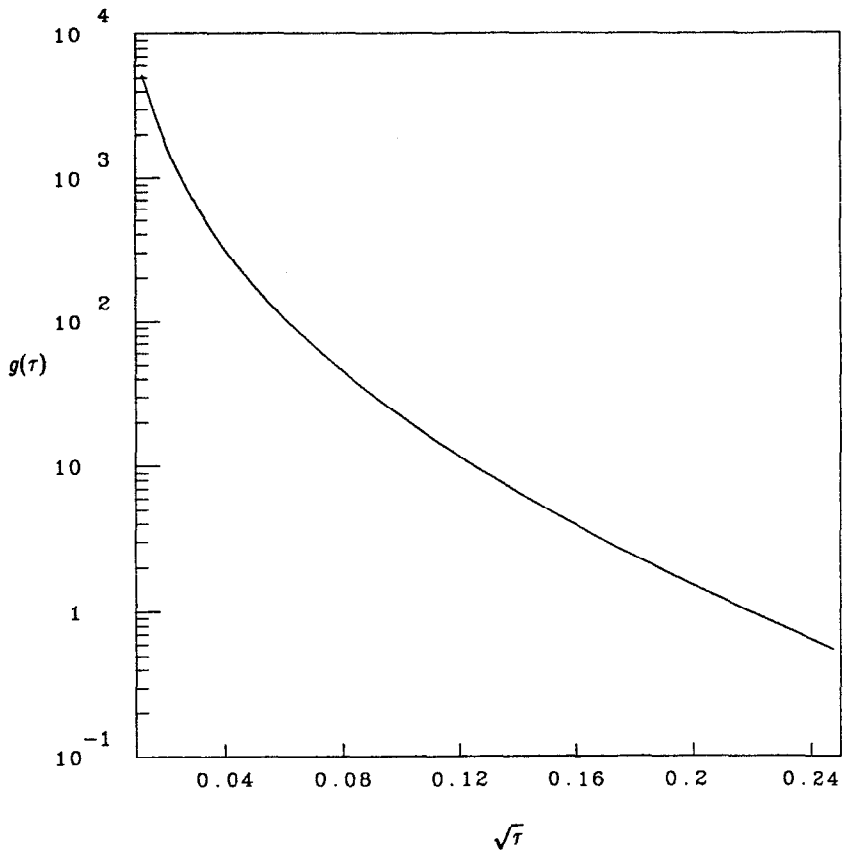


Fig. 11. The dimensionless function $g(\tau)$ vs. $\sqrt{\tau}$. See Eqs.(69), (70),and (72).

$$\sigma(m_{\mu\mu} > \sqrt{\tau_0 s}) \approx 10^{-37}\mathrm{cm}^2\left(\frac{540\ \mathrm{GeV}}{\sqrt{s}}\right)^2 \frac{1}{\tau_0} 2^{-20\sqrt{\tau_0}}. \qquad (72)$$

For $m_{\mu\mu} > 54$ GeV at the SPS collider, $\tau_0 = 0.01$ and $\sigma \approx 2.5 \cdot 10^{-36}\,\mathrm{cm}^2$. For $m_{\mu\mu} > 100$ GeV at the Fermilab collider, $\tau_0 = 0.0025$ and $\sigma = 1.5 \cdot 10^{-36}\,\mathrm{cm}^2$. These invariant masses are thus near the limit of what we may expect to see.

2.4 Resonance Production

We are especially interested in the production of W's and Z's, but without much extra effort we can find general expressions for the cross sections for production of any resonance in terms of its basic parameters. Naturally, we begin with the Breit-Wigner formula for the cross section for producing a resonance of mass M and width Γ. If the initial particles have spins S_1 and S_2, while the spin of the resonance is J, and if the branching ratio of the resonance into the initial channel is B, then

$$\sigma(\hat{s}) = \frac{\pi}{p_{cm}^2} \frac{2J+1}{(2S_1+1)(2S_2+1)} \frac{B\Gamma^2}{(\sqrt{\hat{s}} - M)^2 + (\Gamma/2)^2}. \qquad (73)$$

The factor $(2S_1 + 1)(2S_2 + 1)$ is just the total number of initial spin orientations, which is four for two spin one-half particles. Actually, we must also use the value four if the two initial particles are massless vectors since the longitudinal degrees of freedom are missing. If the resonance is narrow, we can approximate Eq.(73) as

$$\sigma(\hat{s}) = \frac{2\pi^2}{p_{cm}^2}\frac{2J+1}{(2S_1+1)(2S_2+1)}B\Gamma\,\delta(\sqrt{\hat{s}}-M). \qquad (74)$$

The effective cross section is obtained by integrating this cross section together with the luminosity spectrum:

$$\sigma_{eff} = \frac{4\pi^2}{M^2}(2J+1)B\frac{\Gamma}{M}\left(\tau\frac{dL}{d\tau}\right)_{\tau=M^2/s}, \qquad (75)$$

where we have taken the initial spin multiplicity to be four and assumed the incident particle (parton) masses are small compared to the resonance mass.

The expected properties of the Z and W are derived in Appendix A. The results are summarized in Table III. The branching ratio of the Z into a $u\bar{u}$ pair of a given color is 0.11/3 and into a $d\bar{d}$ pair is 0.13/3. In addition, we must multiply by a factor of 1/3 since only quarks with the proper color can annihilate. We can combine the $u\bar{u}$ and $d\bar{d}$ production if we assume the luminosity spectrum for $d\bar{d}$ is simply 1/4 of what it is for $u\bar{u}$. Putting all these factors together, we obtain an effective B:

$$B = \frac{1}{3}\left[\frac{0.11}{3}+\frac{1}{4}\cdot\frac{0.13}{3}\right] = 0.016. \qquad (76)$$

At the CERN collider, we have for Z production, $\sqrt{\tau} = 0.17$, while at the Tevatron collider it will be 0.046. Thus we have using Eq.(57) for $\tau\frac{dL_{u\bar{u}}}{d\tau}$

$$\sigma_{eff}(Z) = \frac{4\pi^2}{(92\text{GeV})^2}(0.389\,\text{mbGeV}^2)\cdot 3\cdot(0.016)\cdot\frac{2.8}{92}\begin{cases}0.37 & \text{CERN}\\ 1.3 & \text{FNAL}\end{cases}$$

Table III. Basic characteristics of the intermediate vector bosons according to the standard model with $\sin^2\theta_W = 0.21$.

	Z		W	
mass	92 GeV		81 GeV	
width	2.8 GeV		2.8 GeV	
branching ratios	e^+e^-	0.03	$e^+\nu_e$	0.08
	$\mu^+\mu^-$	0.03	$\mu^+\nu_\mu$	0.08
	$\tau^+\tau^-$	0.03	$\tau^+\nu_\tau$	0.08
	$\nu_e\bar{\nu}_e$	0.06		
	$\nu_\mu\bar{\nu}_\mu$	0.06		
	$\nu_\tau\bar{\nu}_\tau$	0.06		
	$u\bar{u}$	0.11	$u\bar{d}$	0.25
	$c\bar{c}$	0.11	$c\bar{s}$	0.25
	$t\bar{t}$	0.11	$t\bar{b}$	0.25
	$d\bar{d}$	0.13		
	$s\bar{s}$	0.13		
	$b\bar{b}$	0.13		

that is

$$\sigma_{eff}(Z) = 2.7 \cdot 10^{-33}\text{cm}^2 \times \begin{cases} 0.37 & \text{CERN} \\ 1.3 & \text{FNAL} \end{cases} \tag{77}$$

If we now include the sum of the branching ratios to e^+e^- and to $\mu^+\mu^-$ which is 0.06, we find cross sections into these modes of

$$\sigma_{eff}(p\overline{p} \to Z^0 + X \to \mu^+\mu^- \text{and} e^+e^- + X) = \begin{cases} 6 \cdot 10^{-35}\text{cm}^2 & \text{CERN} \\ 21 \cdot 10^{-35}\text{cm}^2 & \text{FNAL} \end{cases} \tag{78}$$

The cross section for W production is calculated analogously. The W^+ is produced by annihilation of a u and a $\overline{d}$.We take the luminosity for $u\overline{d}$ to be one-half the luminosity for $u\overline{u}$.The branching ratio of W^+ into $u\overline{d}$ of a single color is 1/12, which we again must divide by 3 to insure that the colliding quarks have the same color. Thus the effective value of B is 1/36. The value of $\sqrt{\tau}$ is 0.15 at CERN and 0.0405 at FNAL. We thus compute the cross section for W^+ production as

$$\sigma_{eff}(W^+) = \frac{4\pi^2}{(81\text{GeV})^2}(0.389\,\text{mbGeV}^2) \cdot 3 \cdot \frac{1}{36}\frac{2.8}{81}\begin{cases} 0.22 & \text{CERN} \\ 0.67 & \text{FNAL} \end{cases}$$

$$= 6.7 \cdot 10^{-33}\text{cm}^2 \times \begin{cases} 0.22 & \text{CERN} \\ 0.67 & \text{FNAL} \end{cases} \tag{79}$$

If we insist on a leptonic decay of the W^+, we must add a factor of $1/6 = 1/12 + 1/12$ for the $e^+\nu$ and $\mu^+\nu$ modes. The result is

$$\sigma_{eff}(p\overline{p} \to W^+ + X \to \mu^+\nu \text{ and } e^+\nu) = \begin{cases} 2.5 \cdot 10^{-34}\text{cm}^2 & \text{CERN} \\ 7.5 \cdot 10^{-34}\text{cm}^2 & \text{FNAL} \end{cases}. \tag{80}$$

Of course there is an equal cross section for W^- production. The sum of the two is about one order of magnitude greater than that for the production of Z^0 with a subsequent decay into e^+e^- or $\mu^+\mu^-$.

The formula for the cross section for the production of a resonance has much broader applicability. Let us consider the production of p-wave quarkium (i.e. $Q\overline{Q}$) states by the collision of two gluons. The factor B should be set equal to 1/64 if we presume that gg is the only important channel. This is the product of one factor of 1/8 for the branching ratio into a single gluonic color channel and one factor of 1/8 to insure that the gluons colliding have the right colors to annihilate. For the width of the state, let us take 5 MeV, a figure representative of the values for the charmonium system. The spin of the produced resonance should be zero or two since two truly massless gluons cannot make a spin one state (by Yang's theorem). Thus 2J+1 is either one or five. Altogether then, we have for a resonance with a mass of 5 GeV

$$\sigma_{eff}(p\overline{p} \to P - state) = \frac{4\pi^2}{(50\text{GeV})^2}(0.389\,\text{mbGeV}^2)\begin{Bmatrix} 1 \\ 5 \end{Bmatrix}$$

$$\times \frac{1}{64}\frac{5 \cdot 10^{-3}}{50}\begin{cases} 2.5 & \text{CERN} \\ 19 & \text{FNAL} \end{cases}$$

$$= 10^{-35}\text{cm}^2\begin{Bmatrix} 1 \\ 5 \end{Bmatrix}\begin{cases} 2.5 & \text{CERN} \\ 19 & \text{FNAL} \end{cases} \tag{81}$$

While at first, the production of 1000 such particles in a standard run at Fermilab might sound encouraging, we must remember that the

only useful signature would be a cascade into an s-wave state followed by a decay into e^+e^- or $\mu^+\mu^-$. For simplicity, let us take as a guide, the branching ratios in the $c\bar{c}$ system. The 1982 Particle Data Booklet lists $B(\chi_2 \to \psi\gamma) = 0.157 \pm 0.017$ and $B(\psi \to e^+e^-) + B(\psi \to \mu^+\mu^-) = 0.148 \pm 0.012$. Thus we would expect about $1000 \times 0.15 \times 0.16 \approx 25$ events with a good signature. This appears to be observable since we estimate only eight Drell-Yan pairs above 50 GeV for the same standard run using Eq. (72). Increasing the mass of the resonance to 60 GeV decreases the yield by about 0.5 , and increasing it again to 70 GeV decreases it by an additional factor of 0.25 . There is no hope of finding quarkium above the Z mass this way.

2.5 High Transverse Momentum

We wish to use our ubiquitous formula

$$d\sigma_{eff} = \int d\tau \frac{dL}{d\tau} d\sigma, \tag{82}$$

to estimate high transverse momentum jet cross sections. For the partonic cross sections we shall use the lowest order QCD results [Combridge, Kripfganz, and Ranft,1977; Cutler and Sivers, 1978; Owens, Reya, and Glück, 1978; Feynman, Field, and Fox, 1978]. This is not simply a consequence of laziness. As long as the problem of higher order QCD corrections to the Drell-Yan process is unresolved [Bodwin and Brodsky, 1981; Collins and Soper, 1982], it is pointless to take seriously QCD corrections for much more complicated processes. The lowest order differential cross sections for various partonic scattering processes are listed in Table IV and displayed in Fig. 12.

Table IV. Differential cross sections for partonic scattering. The differential cross section in the parton-parton center of mass is $d\sigma/d\Omega = (\alpha_s^2/4s)\Sigma$. The cross sections are color averaged and the expressions are derived from the results of Owens, Glück, and Reya, 1978 .

Process	Σ
$gg \to gg$	$18[(1-\cos\theta)^{-2} + (1+\cos\theta)^{-2}]$ $-9[(1-\cos\theta)^{-1} + (1+\cos\theta)^{-1}]$ $+99/8 + (9/8)(\cos\theta)^2$
$gg \to q\bar{q}$	$(1/3)[(1-\cos\theta)^{-1} + (1+\cos\theta)^{-1}]$ $-(25/48) - (3/16)(\cos\theta)^2$
$q\bar{q} \to gg$	$(64/27)[(1-\cos\theta)^{-1} + (1+\cos\theta)^{-1}]$ $-(100/27) - (4/3)(\cos\theta)^2$
$gq \to gq$	$8(1-\cos\theta)^{-2} - 4(1-\cos\theta)^{-1}$ $+(8/9)(1+\cos\theta)^{-1} + (11/9)$
$qq' \to qq'$	$(32/9)(1-\cos\theta)^{-2} - (16/9)(1-\cos\theta)^{-1}$ $+(4/9)$
$qq \to qq$	$(32/9)[(1-\cos\theta)^{-2} + (1+\cos\theta)^{-2}]$ $-(64/27)[(1-\cos\theta)^{-1} + (1+\cos\theta)^{-1}] + 16/9$
$q\bar{q} \to q\bar{q}$	$(32/9)(1-\cos\theta)^{-2} - (32/27)(1-\cos\theta)^{-1}$ $+(2/9)$
$q\bar{q} \to q'\bar{q}'$	$(2/9)(1+(\cos\theta)^2)$

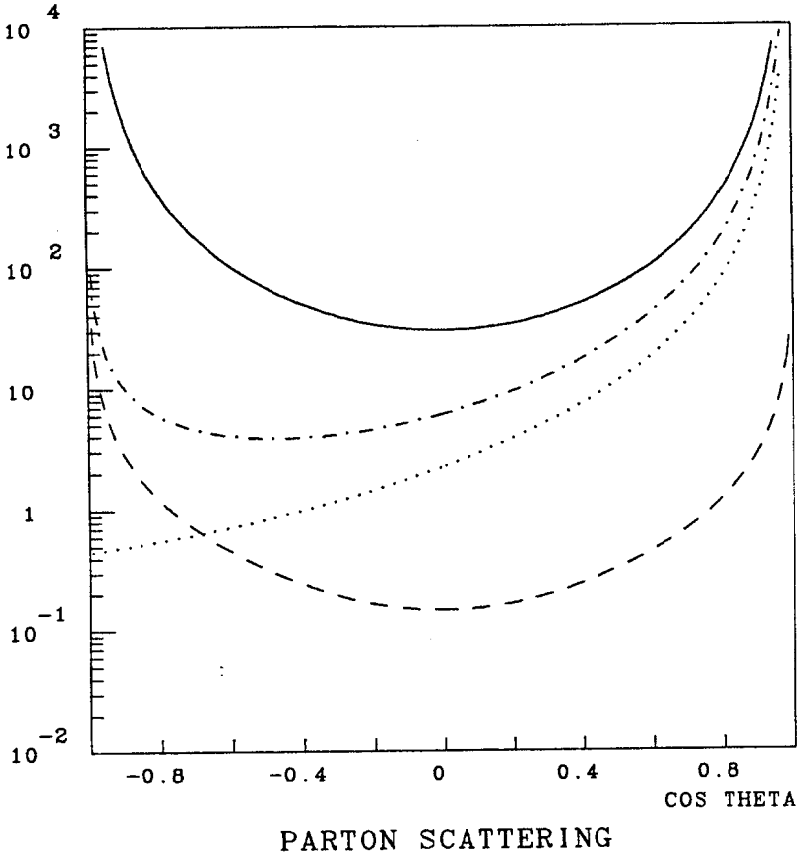


Fig. 12.a. The parton differential cross sections in the center of mass $(4s/\alpha_s^2)d\sigma/d\Omega$ vs. $\cos\theta$, $gg \to gg$(solid), $gg \to q\bar{q}$(dashed), $gq \to gq$(dot-dash), $qq' \to qq'$(dotted). Here q and q′ represent different flavors. The cross sections are color averaged.

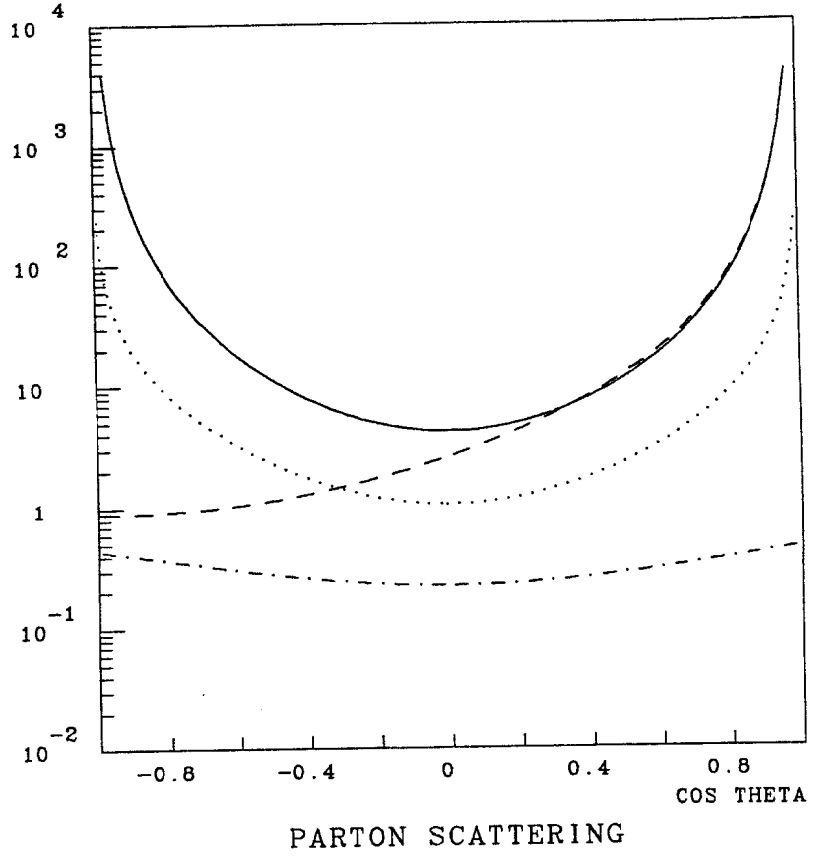


Fig. 12.b. The parton differential cross sections in the center of mass $(4s/\alpha_s^2)d\sigma/d\Omega$ vs. $\cos\theta$, $qq \to qq$(solid), $q\bar{q} \to q\bar{q}$(dashed), $q\bar{q} \to q'\bar{q}'$(dot-dash), $q\bar{q} \to gg$(dotted).

The quantity of physical interest is the differential cross section with respect to the transverse momentum of the jet, p_t. If the final state in the partonic scattering has unlike particles (i.e. all except $q\bar{q} \to gg, gg \to gg$ and $qq \to qq$), there are two contributions to consider: if a scattering angle θ gives a contribution, so does $\pi - \theta$. Thus we can add these two contributions and then restrict ourselves to scattering angles between 0 and $\pi/2$. We indicate this modified cross section by $d\bar{\sigma}/d\Omega$ and display it in Table V.

These differential cross sections are for the center of mass of the parton-parton system. The colliding partons have a momentum $\sqrt{\tau s}/2$ in this reference frame. Thus the center of mass scattering angle is related to the transverse momentum by

$$\sin\theta = \frac{2p_t}{\sqrt{\tau s}} = \frac{x_t}{\sqrt{\tau}}. \tag{83}$$

At fixed p_t, varying θ is equivalent to varying τ:

$$d\tau = \frac{2x_t^2 \cos\theta}{\sin^3\theta} d\theta. \tag{84}$$

On the other hand,

$$\frac{d\sigma}{dp_t} = \frac{2\pi}{p_t} \frac{\sin^2\theta}{\cos\theta} \frac{d\sigma}{d\Omega}, \tag{85}$$

so that

Table V. The differential cross section for partonic scattering with scattering angles between $\pi/2$ and π folded back to the region 0 to $\pi/2$. The differential cross section is given by $d\bar{\sigma}/d\Omega = (\alpha_s^2/4s)\overline{\Sigma}$.

Process	$\overline{\Sigma}$
$gg \to gg$	$18[(1-\cos\theta)^{-2} + (1+\cos\theta)^{-2}]$ $-9[(1-\cos\theta)^{-1} + (1+\cos\theta)^{-1}]$ $+99/8 + (9/8)(\cos\theta)^2$
$gg \to q\bar{q}$	$(2/3)[(1-\cos\theta)^{-1} + (1+\cos\theta)^{-1}]$ $-(25/24) - (3/8)(\cos\theta)^2$
$q\bar{q} \to gg$	$(64/27)[(1-\cos\theta)^{-1} + (1+\cos\theta)^{-1}]$ $-(100/27) - (4/3)(\cos\theta)^2$
$gq \to gq$	$8[(1-\cos\theta)^{-2} + (1+\cos\theta)^{-2}]$ $-(28/9)[(1-\cos\theta)^{-1} + (1+\cos\theta)^{-1}] + (22/9)$
$qq' \to qq'$	$(32/9)[(1-\cos\theta)^{-2} + (1+\cos\theta)^{-2}]$ $-(16/9)[(1-\cos\theta)^{-1} + (1+\cos\theta)^{-1}] + 8/9$
$qq \to qq$	$(32/9)[(1-\cos\theta)^{-2} + (1+\cos\theta)^{-2}]$ $-(64/27)[(1-\cos\theta)^{-1} + (1+\cos\theta)^{-1}] + 16/9$
$q\bar{q} \to q\bar{q}$	$(32/9)[(1-\cos\theta)^{-2} + (1+\cos\theta)^{-2}]$ $-(32/27)[(1-\cos\theta)^{-1} + (1+\cos\theta)^{-1}]$ $+(4/9) + (4/9)(\cos\theta)^2$
$q\bar{q} \to q'\bar{q}'$	$(4/9)(1+(\cos\theta)^2)$

$$\frac{d\sigma_{eff}}{dp_t} = \int d\tau \frac{dL}{d\tau}\frac{d\sigma}{dp_t}$$
$$= \frac{4\pi}{p_t}\int d\theta \sin\theta\left(\tau\frac{dL}{d\tau}\right)\frac{d\overline{\sigma}}{d\Omega}. \qquad (86)$$

In principle, this integral goes from $\pi/2$ from $\sin^{-1} x_t$ but it is not a bad approximation to let the lower limit be zero since this extends the range of τ to $\tau = 1$ where the luminosity spectrum is very small anyway.

To proceed further, we need to make some assumptions about the luminosity spectrum. Rather than use the particular values given in Eq.(6), let us simply assume a parameterization

$$\tau\frac{dL}{d\tau} = Ae^{-b\sqrt{\tau}}, \qquad (87)$$

so that our results will be useful even if we want to vary A or b to consider another parameterization of the parton distributions, as might be appropriate at very much higher energies, say. Our general formula is thus

$$\frac{d\sigma}{dp_t} = \frac{4\pi}{p_t}\int_0^{\pi/2} d\theta \sin\theta A e^{-bx_t/\sin\theta}\frac{\alpha_s^2}{16p_t^2}\sin^2\theta\,\overline{\Sigma}(\theta)$$
$$= \frac{\pi A}{4p_t^3}\alpha_s^2\int_0^{\pi/2} d\theta \sin^3\theta e^{-bx_t/\sin\theta}\,\overline{\Sigma}(\theta). \qquad (88)$$

The values of the functions $\overline{\Sigma}$ for the various fundamental partonic processes are given in Table V. It is useful to define the dimensionless integrals

$$g_{qq\to qq}(z) = \int_0^{\pi/2} d\theta \sin^3\theta e^{-z/\sin\theta}\,\overline{\Sigma}_{qq\to qq}(\theta), etc. \qquad (89)$$

which can, in fact, be done analytically in terms of modified Bessel functions and the like. Some representative values for these functions are given in Table VI and shown in Fig. 13.

In terms of these

$$\frac{d\sigma_{eff}}{dp_t} = \frac{\pi A}{4p_t^3}\alpha_s^2 g(bx_t). \qquad (90)$$

For example, consider jets with $p_t = 27\,\mathrm{GeV}$ at the SPS collider. The contribution from the subprocess $gg \to gg$ is determined by noting that $x_t = 0.1$ and inserting the values (see Eq.(6)) b=30, A=40, and the nominal value $\alpha_s = 0.2$ to find, using Table VI,

$$g_{gg\to gg}(3) = 1.3,$$

and

$$\frac{d\sigma_{eff}}{dp_t} = \frac{\pi\cdot 40}{4(27\mathrm{GeV})^3}\cdot(0.2)^2\cdot 1.3(0.389\mathrm{mbGeV}^2)$$
$$= 3.2\cdot 10^{-32}\mathrm{cm}^2\mathrm{GeV}^{-1}. \qquad (91)$$

For small x_t, $gg \to gg$ dominates jet production, but at high enough x_t, $q\bar{q} \to q\bar{q}$ dominates in $p\bar{p}$ collisions. We can estimate that value of x_t as follows: For large bx_t, from Eq.(89),

$$g(bx_t) \approx \overline{\Sigma}(90^o)\sqrt{\frac{\pi}{2bx_t}}e^{-bx_t}. \qquad (92)$$

Table VI. Values of the functions g(z) for $z = 0.1 - 4.$ used to determine $d\sigma/dp_t$ for hard scattering processes. See Eqs.(89)-(90).

z	0.1	0.2	0.4	1.	2.	4.
$gg \to gg$	140	90	50	18	4	0.4
$gg \to q\bar{q}$	0.5	0.4	0.3	0.1	0.04	0.004
$gq \to gq$	60	40	24	8	2	0.2
$qq' \to qq'$	26	17	10	3	0.8	0.07
$qq \to qq$	25	17	10	3	0.7	0.06
$q\bar{q} \to q\bar{q}$	27	18	11	4	0.8	0.07
$q\bar{q} \to q'\bar{q}'$	0.3	0.3	0.2	0.1	0.04	0.004
$q\bar{q} \to gg$	1.7	1.5	1.1	0.5	0.13	0.013

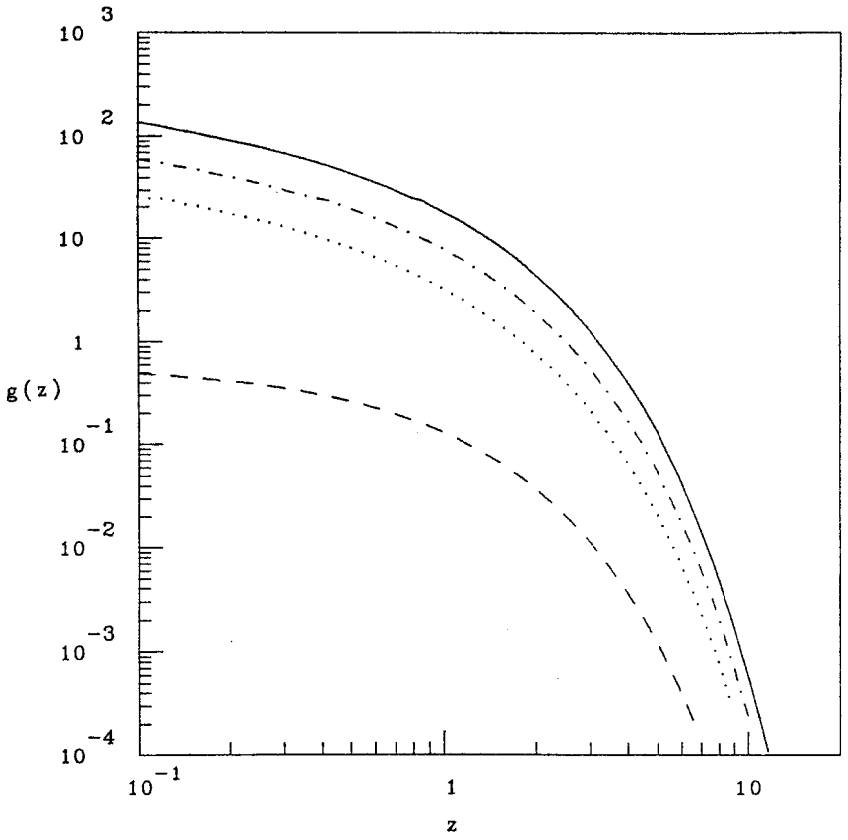


Fig. 13.a. The functions g(z), Eq. (89), vs. z for $gg \to gg$(solid), $gg \to q\bar{q}$(dashed), $gq \to gq$(dot-dash), and $qq' \to qq'$(dotted).

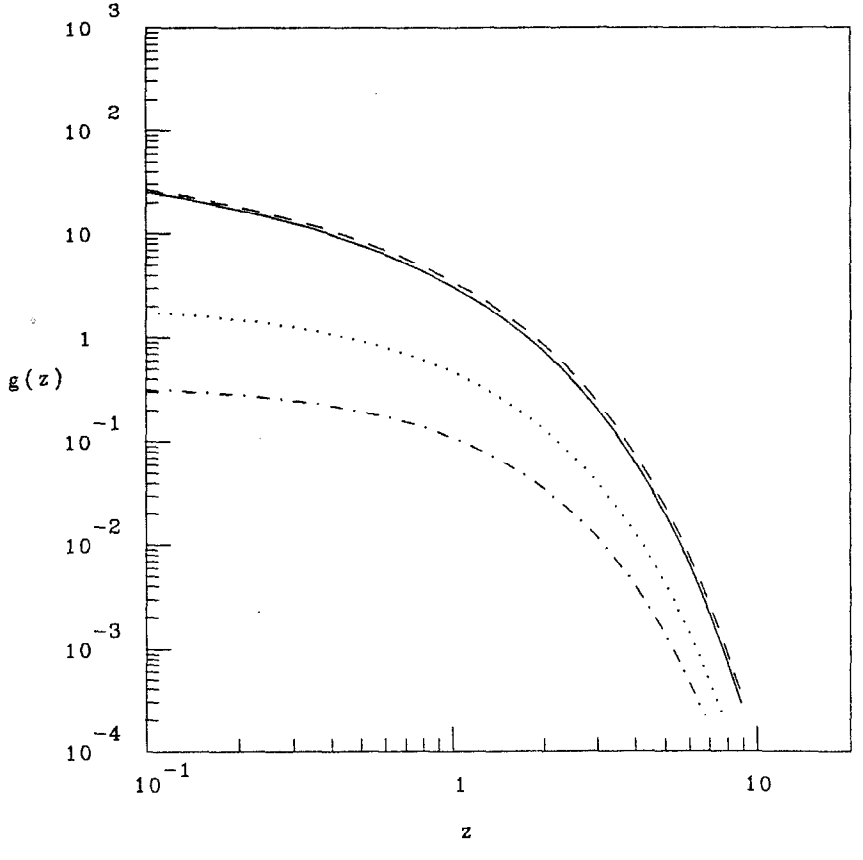


Fig. 13.b. The functions g(z), Eq. (89), vs. z for $qq \to qq$(solid), $q\overline{q} \to q\overline{q}$(dashed), $q\overline{q} \to q'\overline{q}'$(dot-dash), and $q\overline{q} \to gg$(dotted).

Now

$$\frac{d\sigma_{eff}}{dp_t} \sim Ag(bx_t), \tag{93}$$

so

$$\begin{aligned}\frac{(d\sigma_{eff}/dp_t)_{gg\to gg}}{(d\sigma_{eff}/dp_t)_{q\overline{q}\to q\overline{q}}} &= \frac{A_{gg\to gg}}{A_{q\overline{q}\to q\overline{q}}}\frac{\overline{\Sigma}_{gg\to gg}}{\overline{\Sigma}_{q\overline{q}\to q\overline{q}}}\sqrt{\frac{b_{q\overline{q}\to q\overline{q}}}{b_{gg\to gg}}}e^{(b_{q\overline{q}\to q\overline{q}}-b_{gg\to gg})x_t} \\ &\approx \frac{40}{2}\frac{30}{5}\sqrt{\frac{1}{3}}e^{-20x_t} \\ &\approx 70e^{-20x_t}\end{aligned} \tag{94}$$

This is unity if $x_t \approx 0.21$.

The cross section to produce a pair of jets, each with $x_t > x_{t0}$ is

$$\begin{aligned}\sigma(x_{t0}) &= \frac{\pi A\alpha_s^2}{s}\int_{x_{t0}}^{\infty} dx_t \frac{1}{x_t^3}g(bx_t) \\ &= \frac{\pi A\alpha_s^2 b^2}{s}\int_{bx_{t0}}^{\infty} du\frac{1}{u^3}g(u) \\ &\equiv \frac{\pi A\alpha_s^2 b^2}{s}h(bx_{t0})\end{aligned} \tag{95}$$

The functions h(z) for the various processes are displayed in Table VII and Fig. 14. For example, the cross sections for producing jets through $gg \to gg$, $gu \to gu$, and $u\overline{u} \to u\overline{u}$ at the Fermilab collider with $p_t >$ 100 GeV are calculated as follows:

Table VII. Selected values of the functions h(z) ,for $z = 0.1 - 4.$, used to determine the cross section to produce a jet with greater than a given value of the transverse momentum. See Eq.(95).

z	0.1	0.2	0.4	1.	2.	4.
$gg \to gg$	$3.4 \cdot 10^4$	$2.9 \cdot 10^3$	$2.2 \cdot 10^2$	6	$2.3 \cdot 10^{-1}$	$4 \cdot 10^{-3}$
$gg \to q\bar{q}$	$1.2 \cdot 10^3$	$1.3 \cdot 10^1$	1.2	$4 \cdot 10^{-2}$	$2 \cdot 10^{-3}$	$3 \cdot 10^{-5}$
$gq \to gq$	$1.5 \cdot 10^4$	$1.3 \cdot 10^3$	$1 \cdot 10^2$	2.5	0.1	$1.5 \cdot 10^{-3}$
$qq' \to qq'$	$6 \cdot 10^3$	$5 \cdot 10^2$	$4 \cdot 10^1$	1	$4 \cdot 10^{-2}$	$6 \cdot 10^{-4}$
$qq \to qq$	$6 \cdot 10^3$	$5 \cdot 10^2$	$4 \cdot 10^1$	1	$4 \cdot 10^{-2}$	$5 \cdot 10^{-4}$
$q\bar{q} \to q\bar{q}$	$7 \cdot 10^3$	$6 \cdot 10^2$	$4 \cdot 10^1$	1	$4 \cdot 10^{-2}$	$7 \cdot 10^{-4}$
$q\bar{q} \to q'\bar{q}'$	$8 \cdot 10^1$	9	0.9	$4 \cdot 10^{-2}$	$2 \cdot 10^{-3}$	$4 \cdot 10^{-5}$
$q\bar{q} \to gg$	$4 \cdot 10^2$	$5 \cdot 10^1$	4	0.2	$7 \cdot 10^{-3}$	$1 \cdot 10^{-4}$

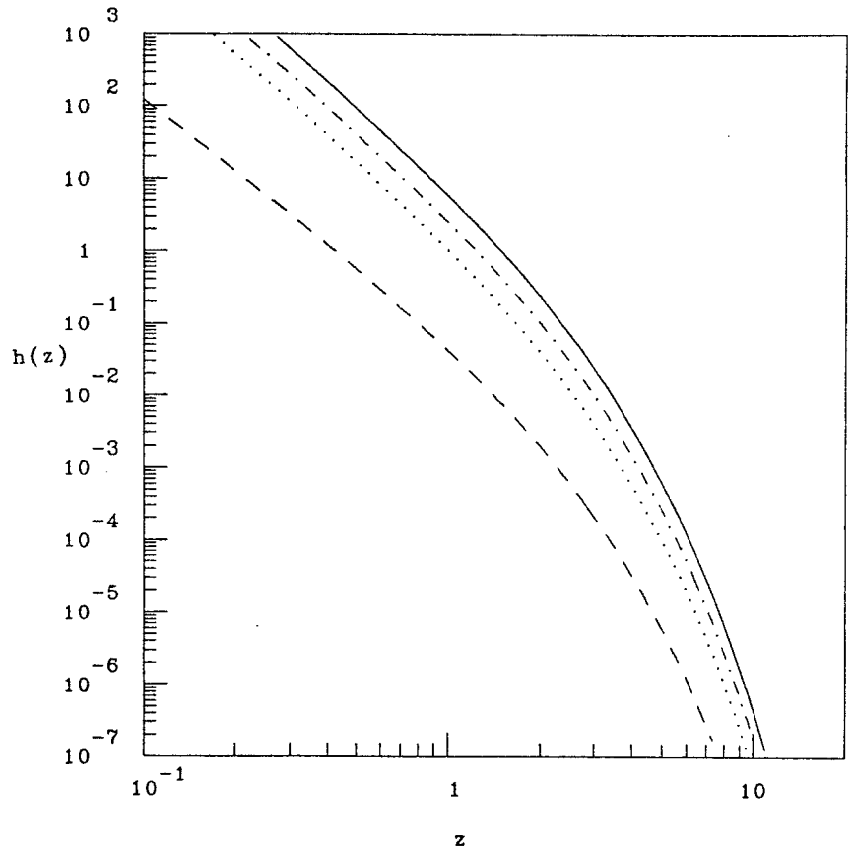


Fig. 14.a. The functions h(z), Eq. (89), vs. z for $gg \to gg$(solid), $gg \to q\bar{q}$(dashed), $gq \to gq$(dot-dash), and $qq' \to qq'$(dotted).

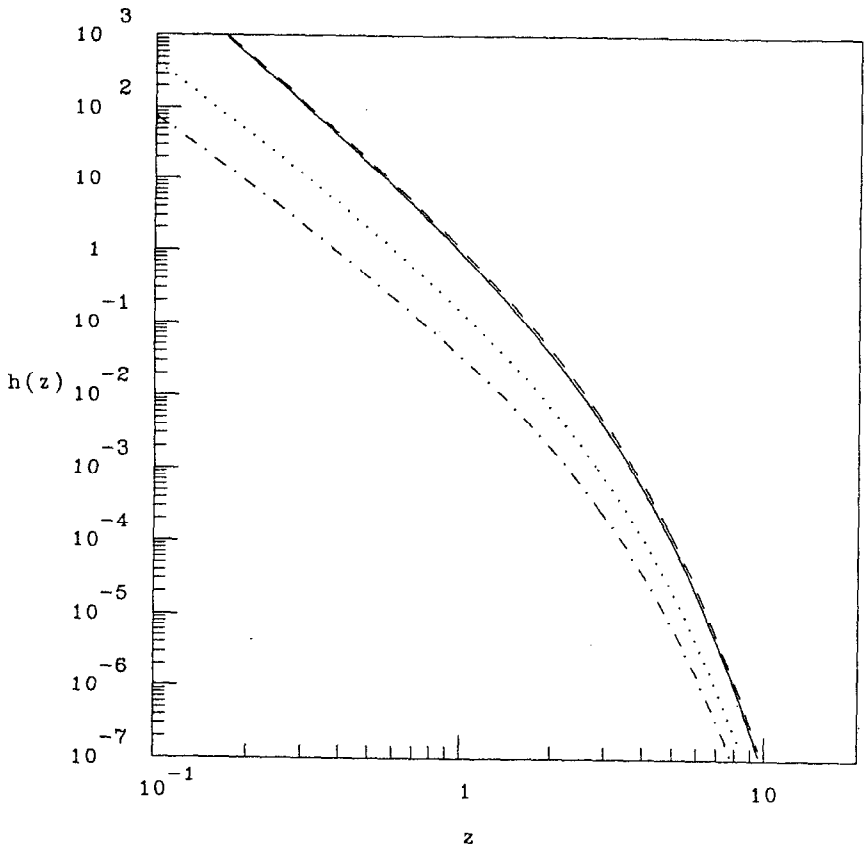


Fig. 14.b. The functions h(z), Eq. (89), vs. z for $qq \to qq$(solid), $q\overline{q} \to q\overline{q}$(dashed), $q\overline{q} \to q'\overline{q}'$(dot-dash), and $q\overline{q} \to gg$(dotted).

$$gg \to gg: \; A = 40, b = 30, x_t = 0.1, h_{gg\to gg}(3) = 4 \cdot 10^{-2}$$

$$\sigma = \frac{\pi \cdot 40 \cdot (0.2)^2 30^2}{(2000\,\mathrm{GeV})^2} 0.389\mathrm{mb\,GeV^2} \cdot 0.04 = 1.8 \cdot 10^{-32}\mathrm{cm}^2$$

$$gu \to gu: \; A = 20, b = 20, x_t = 0.1, h_{gq\to gq}(2) = 0.1$$

$$\sigma = \frac{\pi \cdot 20 \cdot (0.2)^2 20^2}{(2000\,\mathrm{GeV})^2} 0.389\mathrm{mb\,GeV^2} \cdot 0.1 = 1.0 \cdot 10^{-32}\mathrm{cm}^2$$

$$u\overline{u} \to u\overline{u}: A = 2, b = 10, x_t = 0.1, h_{q\overline{q}\to q\overline{q}}(1) = 1.$$

$$\sigma = \frac{\pi \cdot 2 \cdot (0.2)^2 10^2}{(2000\,\mathrm{GeV})^2} 0.389\,\mathrm{mb\,GeV^2} \cdot 1. = 0.25 \cdot 10^{-32}\,\mathrm{cm}^2$$

For large values of bx_t there is a simple approximation for h(z) based on Eq. (92):

$$\begin{aligned} h(z) &\approx \int_z^\infty du \overline{\Sigma}(90^o) \sqrt{\frac{\pi}{2u}} \frac{1}{u^3} e^{-u} \\ &\approx \overline{\Sigma}(90^o) \sqrt{\frac{\pi}{2}}\, z^{-7/2}\, e^{-z}. \end{aligned} \tag{96}$$

Inserting this into Eq. (95) we have

$$\sigma(x_t > x_{t0}) \approx \frac{\pi A \alpha_s^2 b^2}{s} \overline{\Sigma}(90^o) \sqrt{\frac{\pi}{2}} (bx_{t0})^{-7/2} e^{-bx_{t0}}. \tag{97}$$

For $u\bar{u}$ in $p\bar{p}$ colllisions or uu in pp collisions, $A = 2, b = 10, \overline{\Sigma}(90^\circ) \approx 5$, so

$$\sigma(x_t > x_{t0}) \approx 6.6 \cdot 10^{-35}\text{cm}^2\left(\frac{540\,\text{GeV}}{\sqrt{s}}\right)^2 x_{t0}^{-7/2} e^{-10x_{t0}}. \quad (98)$$

For example, the cross section at the Fermilab collider $p_t = 300$GeV or more from such $u\bar{u}$ collisions should be about $16 \cdot 10^{-36}\text{cm}^2$.

2.6 Heavy Flavor Production

A number of mechanisms have been suggested for heavy flavor production. One obvious possibility is $q\bar{q} \to Q\overline{Q}$. Another is $gg \to Q\overline{Q}$. Of course, at a minimum the effects of the heavy quark mass, m_Q, must be retained in our QCD analysis. Although the naive predictions based on these processes are not especially successful, we shall restrict ourselves to this approach since it fits with the unified presentation of hard processes given above. While the absolute cross section predictions may not be accurate (even by the lax standards we believe are appropriate for the predictions in the previous sections), the general dependence on the center of mass energy may not be too far from the truth.

We begin then with the cross sections calculated by Combridge(1979)

$$\sigma_{q\bar{q}\to Q\overline{Q}} = \frac{8\pi\alpha_s^2}{27\pi}\left(1+\frac{2m_Q^2}{s}\right)\sqrt{1-\frac{4m_Q^2}{s}},$$
$$\sigma_{gg\to Q\overline{Q}} = \frac{\pi\alpha_s^2}{3s}\left[\left(1+\frac{4m_Q^2}{s}+\frac{m_Q^4}{s^2}\right)\ln\frac{1+\chi}{1-\chi} - \frac{1}{4}\chi\left(7+\frac{31m_Q^2}{s}\right)\right], \quad (99)$$

where

$$\chi = \sqrt{1-\frac{4m_Q^2}{s}}. \quad (100)$$

Let us write

$$\sigma_{q\bar{q}\to Q\overline{Q}}(\hat{s}) = \frac{\pi\alpha_s^2}{3s}F_{q\bar{q}}(\frac{\hat{s}}{4m_Q^2}), \quad (101)$$

$$\sigma_{gg\to Q\overline{Q}}(\hat{s}) = \frac{\pi\alpha_s^2}{3s}F_{gg}(\frac{\hat{s}}{4m_Q^2}). \quad (102)$$

Then in this model, the total heavy flavor production is

$$\sigma_{Q\overline{Q}} = \frac{\pi\alpha_s^2}{3s}\int d\tau\left(\tau\frac{dL}{d\tau}\right)\frac{1}{\tau^2}\begin{cases}F_{q\bar{q}}(s\tau/4m_Q^2)\\ F_{gg}(s\tau/4m_Q^2)\end{cases}, \quad (103)$$

$$\sigma_{Q\overline{Q}} = \frac{\pi\alpha_s^2 A}{12m_Q^2}\int_1^\infty du\frac{1}{u^2}\exp(-b\sqrt{4m_Q^2u/s})\begin{cases}F_{q\bar{q}}(u)\\ F_{gg}(u)\end{cases}, \quad (104)$$

where

$$u = s\tau/4m_Q^2, \quad (105)$$

and where

$$F_{q\bar{q}}(u) = \frac{8}{9}\left(1+\frac{1}{2u}\right)\sqrt{1-\frac{1}{u}}, \tag{106}$$

$$F_{gg}(u) = \left(1+\frac{1}{u}+\frac{1}{16u^2}\right)\ln\frac{1+\chi}{1-\chi} - \frac{1}{4}\chi\left(7+\frac{31}{4u}\right), \tag{107}$$

$$\chi = \sqrt{1-\frac{1}{u}}. \tag{108}$$

Having reduced the problem to quadrature, we can simply do the integrals numerically to find

$$G_{q\bar{q}}(z) = \int_1^\infty du\, e^{-z\sqrt{u}}\frac{1}{u^2}F_{q\bar{q}}(u),$$
$$G_{gg}(z) = \int_1^\infty du\, e^{-z\sqrt{u}}\frac{1}{u^2}F_{gg}(u), \tag{109}$$

in terms of which

$$\sigma_{Q\bar{Q}}(s) = \frac{\pi\alpha_s^2 A}{12m_Q^2}\begin{cases} G_{q\bar{q}}\left(b\sqrt{4m_Q^2/s}\right) \\ G_{gg}(b\sqrt{4m_Q^2/s}) \end{cases} \tag{110}$$

The functions $F_{q\bar{q}}$ and F_{gg} are shown in Fig. 15. At high energy (i.e. large u), the gg mechanism is more effective since it is suppressed only by the t-channel exchange of the heavy quark, rather than the s-channel single gluon pole. The integrated functions, $G_{q\bar{q}}$ and G_{gg} , are shown in Fig. 16. As $z \to 0$, these functions approach constant values, so as

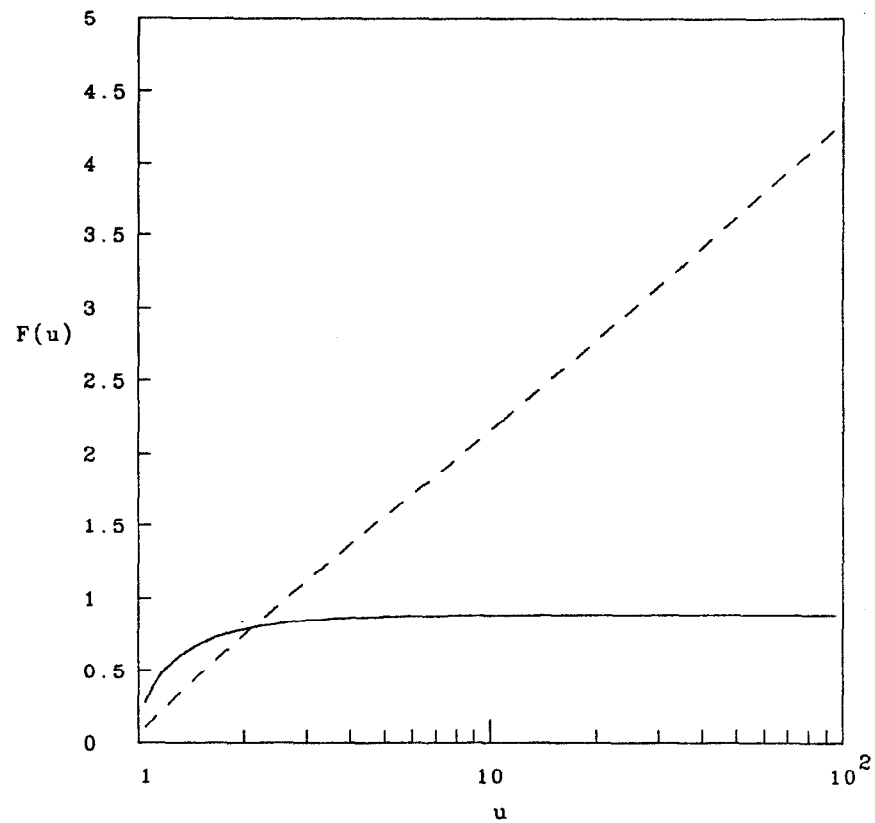


Fig. 15. The heavy quark production cross section function, $F_{q\bar{q}}$ (solid) and F_{gg} (dashed) vs. u. See. Eqs.(99) - (102).

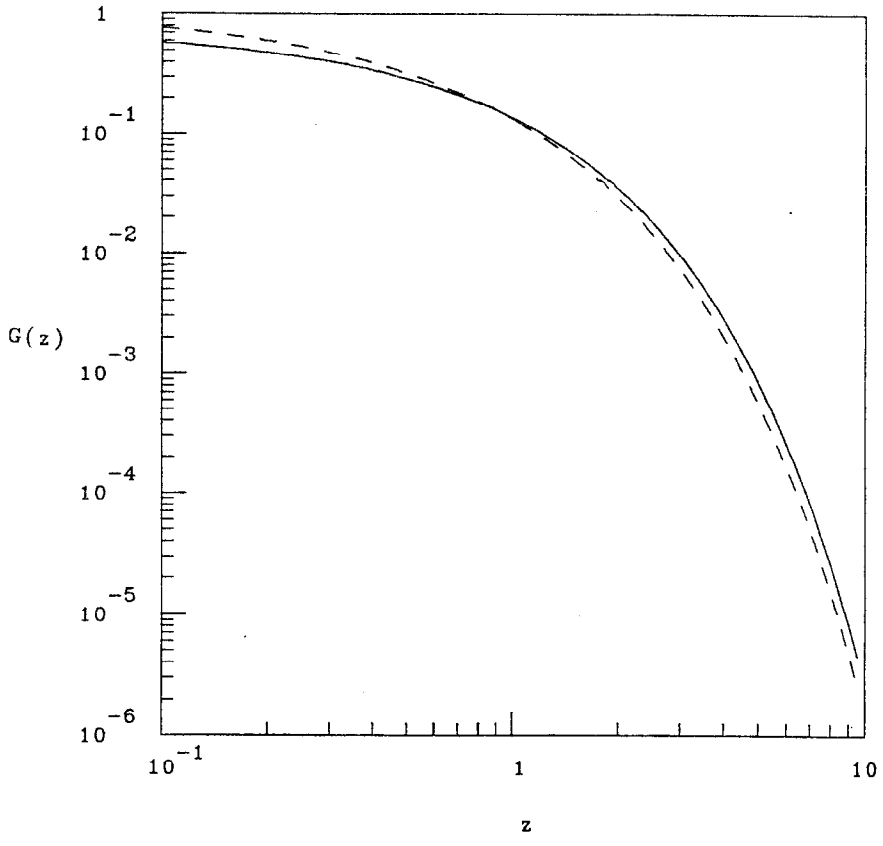


Fig. 16. The heavy quark production functions $G_{q\bar{q}}$ (solid) and G_{gg} (dashed) vs. z. See Eq. (109).

$s \to \infty$, $\sigma_{Q\bar{Q}}$ becomes a constant, dominated by the gg contribution. In Table VIII, we show predictions based on this simple model for c and b quarks with masses 1.5 GeV and 5 GeV and for hypothetical t-quarks with mass either 20 GeV or 40 GeV. We see that the predicted charm cross section is quite small, suggesting that these mechanisms are not the only ones contributing in the Fermilab and ISR range. Thus we regard these predictions as conservative estimates for the production of heavier quarks.

Table VIII. Heavy quark production in $p\bar{p}$ collisions through the mechanisms discussed in Section 2.7. See Eq.(110).

$\sqrt{s}$	$q\bar{q} \to Q\overline{Q}$	$gg \to Q\overline{Q}$
$c\bar{c}$:	$m = 1.5\text{GeV}$	
60GeV	$1 \cdot 10^{-30}\text{cm}^2$	$5 \cdot 10^{-30}\text{cm}^2$
540GeV	$3 \cdot 10^{-30}\text{cm}^2$	$40 \cdot 10^{-30}\text{cm}^2$
2000GeV	$4 \cdot 10^{-30}\text{cm}^2$	$50 \cdot 10^{-30}\text{cm}^2$
$b\bar{b}$:	$m = 5\text{GeV}$	
60GeV	$1.5 \cdot 10^{-32}\text{cm}^2$	$6 \cdot 10^{-33}\text{cm}^2$
540GeV	$2 \cdot 10^{-31}\text{cm}^2$	$2 \cdot 10^{-30}\text{cm}^2$
2000GeV	$3 \cdot 10^{-31}\text{cm}^2$	$3 \cdot 10^{-30}\text{cm}^2$
$t\bar{t}$:	$m = 20\text{GeV}$	
540GeV	$4 \cdot 10^{-33}\text{cm}^2$	$1 \cdot 10^{-32}\text{cm}^2$
2000GeV	$1 \cdot 10^{-32}\text{cm}^2$	$1 \cdot 10^{-31}\text{cm}^2$
$t\bar{t}$:	$m = 40\text{GeV}$	
540GeV	$3 \cdot 10^{-34}\text{cm}^2$	$2 \cdot 10^{-34}\text{cm}^2$
2000GeV	$2 \cdot 10^{-33}\text{cm}^2$	$1 \cdot 10^{-32}\text{cm}^2$

Appendix

Here we summarize the major points of the SU(2) x U(1) theory of electroweak interactions which are needed for deriving the fundamental properties of the W and Z bosons. The SU(2) x U(1) theory is a generalization of the usual theory of electromagnetism in which the coupling of fermions to the photon,

$$\overline{\psi}\, eQ\, A_\lambda \gamma^\lambda\, \psi, \tag{A1}$$

(where Q measures the charge of the fermion destroyed by ψ in units of e) is replaced by

$$\overline{\psi}[g\mathbf{T}\cdot\mathbf{W}_\lambda + g'\frac{Y}{2}B_\lambda]\gamma^\lambda\, \psi, \tag{A2}$$

where T represents weak isospin and contains implicitly a factor $(1-\gamma_5)/2$ to project out the left-handed piece of the fermion. The weak hypercharge is represented by Y which is related to the usual electric charge by

$$Q = T_3 + \frac{1}{2}Y. \tag{A3}$$

Assigning all left-handed fermions to doublets of weak isospin, and right-handed fermions to singlets, we derive the following table:

	e_L^-	e_R^-	ν_L	u_L	u_R	d_L	d_R
Q	-1	-1	0	$2/3$	$2/3$	$-1/3$	$-1/3$
T_3	$-1/2$	0	$1/2$	$1/2$	0	$-1/2$	0
Y	-1	-2	-1	$1/3$	$4/3$	$1/3$	$-2/3$

If we define

$$W^{\pm} = \frac{1}{\sqrt{2}}(W_1 \pm iW_2),\ T^{\pm} = T_1 \pm iT_2, \tag{A4}$$

we have the couplings

$$\overline{\psi}\left[g(T_3 W_3 + \frac{1}{\sqrt{2}}T^{+}W_{\lambda}^{-} + \frac{1}{\sqrt{2}}T^{-}W_{\lambda}^{+}) + g'\frac{Y}{2}B_{\lambda}\right]\gamma^{\lambda}\psi. \tag{A5}$$

The charged W couplings produce the usual charged current interactions. Consider, for example, $\mu^- \to e^-\,\overline{\nu}_e\,\nu_\mu$. The usual V-A theory interaction is

$$\frac{G_F}{\sqrt{2}}\overline{\nu}_\mu\gamma^{\lambda}(1-\gamma_5)\mu\,\overline{e}\,\gamma_{\lambda}(1-\gamma_5)\nu_e \tag{A6}$$

On the other hand, putting in $1/M_W^2$ for the W propagator, our model gives

$$\left(\frac{g}{\sqrt{2}}\right)^2\overline{\nu}_\mu\gamma^{\lambda}\frac{1}{2}(1-\gamma_5)\mu\frac{1}{M_W^2}\,\overline{e}\,\gamma_{\lambda}\frac{1}{2}(1-\gamma_5)\nu_e, \tag{A7}$$

so we can make the indentification

$$\frac{G_F}{\sqrt{2}} = \frac{g^2}{8M_W^2}. \tag{A8}$$

The gauge vector fields W and B are also coupled to scalars according to

$$\left|(g\mathbf{W}_\mu\cdot\mathbf{T} + g'B_\mu\frac{1}{2}Y)\phi\right|^2. \tag{A9}$$

Here ϕ is a multiplet with T=1/2 and Y=1:

$$\phi = \begin{pmatrix}\phi^+\\ \phi^0\end{pmatrix}, \tag{A10}$$

and the electrically neutral part has a vacuum expectation value:

$$<\phi> = \begin{pmatrix}0\\ v\end{pmatrix}. \tag{A11}$$

Thus

$$\left(g\mathbf{W}\cdot\mathbf{T} + g'\frac{1}{2}YB\right)<\phi> = \begin{pmatrix}\frac{g}{\sqrt{2}}W^-v\\ -\frac{1}{2}gW_3v + \frac{1}{2}g'Bv\end{pmatrix}. \tag{A12}$$

The scalar interaction, Eq. (A9), through this vacuum expectation value, produces masses for some of the vector bosons:

$$\frac{g^2}{2}W^-W^+v^2+\frac{1}{4}(gW_3-g'B)^2v^2. \qquad (A13)$$

This term gives equal masses to the W^+ and W^-:

$$M_W^2=\frac{g^2v^2}{4}. \qquad (A14)$$

The massive neutral vector field with proper normalization is seen from Eq.(A13) to be

$$Z=\frac{gW_3-g'B}{\sqrt{g^2+g'^2}}. \qquad (A15)$$

Thus the Z mass is given by

$$M_Z^2=\frac{g^2+g'^2}{4}v^2. \qquad (A16)$$

The orthogonal linear combination of neutral fields is massless:

$$A=\frac{g'W_3+gB}{\sqrt{g^2+g'^2}}. \qquad (A17)$$

Defining $\tan\theta=g'/g$, we have

$$\begin{aligned} A&=\sin\theta W_3+\cos\theta B \quad ; \quad W_3=\sin\theta A+\cos\theta Z \\ Z&=\cos\theta W_3-\sin\theta B \quad ; \quad B=\cos\theta A-\sin\theta Z \end{aligned} \qquad (A18)$$

and the relation between the W and Z masses

$$M_Z^2=M_W^2/\cos^2\theta. \qquad (A19)$$

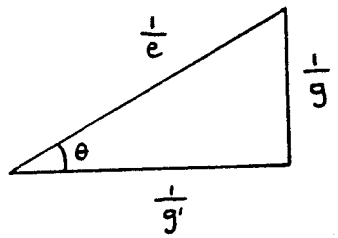
Now we can express the original gauge interaction in terms of the physical fields W^+, W^-, Z, and A . The term in square brackets in Eq.(A5) becomes

$$\frac{g}{\sqrt{2}}(T^+W^-+T^-W^+)+g\sin\theta QA+\frac{g}{\cos\theta}(T_3-\sin^2\theta Q)Z. \qquad (A20)$$

Thus we conclude

$$e=g\sin\theta, \qquad (A21)$$

which we can summarize with the mnemonic



Using the measured value for $\sin^2\theta=0.21$, we can find the W mass:

$$M_W^2=\frac{\sqrt{2}g^2}{8G_F}=\frac{\pi\alpha}{\sqrt{2}\sin^2\theta G_F}=(81\,\mathrm{GeV})^2. \qquad (A22)$$

We can calculate the partial widths of the Z and W. The W^+ decays into $e^+\,\nu_e$ with a matrix element (ϵ is the W polarization vector)

$$\mathcal{M} = \frac{g}{\sqrt{2}}\epsilon_\lambda \overline{\nu}_e \gamma^\lambda \frac{1}{2}(1-\gamma_5)e. \qquad (A23)$$

Quite generally, a vector of mass M decaying into two light fermions with a matrix element

$$\mathcal{M} = \frac{1}{2}\epsilon_\lambda \overline{f}\gamma^\lambda (g_V + g_A\gamma_5) f', \qquad (A24)$$

has a width

$$\Gamma = \frac{1}{48\pi}(g_V^2 + g_A^2)M. \qquad (A25)$$

Thus we find the partial width

$$\Gamma(W \to e\nu) = \frac{\alpha M_W}{12\sin^2\theta} = 240\text{MeV}. \qquad (A26)$$

For the full width of the W, we add three times this for the $u\bar{d}$ (to account for color) and multiply by three for the number of fermion generations, to obtain a full width

$$\Gamma(W) = \frac{\alpha M_W}{\sin^2\theta} = 2.8\,\text{GeV}. \qquad (A27)$$

For the Z, the appropriate couplings to a given fermion pair are, from Eq.(A20)

$$g_V = \frac{e}{\sin\theta\cos\theta}(T_3 - 2Q\sin^2\theta),$$
$$g_A = \frac{e}{\sin\theta\cos\theta}(-T_3). \qquad (A28)$$

Thus the partial width to $\nu_e\overline{\nu}_e$ is

$$\Gamma(Z \to \nu_e\overline{\nu}_e) = \frac{\alpha M_Z}{24\sin^2\theta\cos^2\theta} = 170\text{MeV}. \qquad (A29)$$

The partial widths to ν, e, u, and d are in the proportions

$$1 : 1 - 4\sin^2\theta + 8\sin^4\theta : 3(1 - \frac{8}{3}\sin^2\theta + \frac{32}{9}\sin^4\theta)$$
$$: 3(1 - \frac{4}{3}\sin^2\theta + \frac{8}{9}\sin^4\theta)$$
$$\approx 1 : 0.5 : 1.8 : 2.3 \qquad (A30)$$

Including a factor three for the number of generations, we find the branching ratio into e^+e^-

$$B(Z \to e^+e^-) = \frac{1 - 4\sin^2\theta + 8\sin^4\theta}{24(1 - 2\sin^2\theta + \frac{8}{3}\sin^4\theta)}$$
$$\approx 0.031 \qquad (A31)$$

and the total width of the Z

$$\Gamma(Z) = \frac{\alpha M_Z}{\sin^2\theta\cos^2\theta}(1 - 2\sin^2\theta + \frac{8}{3}\sin^4\theta)$$
$$\approx 2.8\,\text{GeV} \qquad (A32)$$

If the Z and W widths are equal, then $\sin^2\theta = 0.2196$.

Footnotes

1. For a two-body to two-body scattering process with initial momenta p_a and p_b and final momenta p_c and p_d, the standard Mandelstam variables are $s = (p_a + p_b)^2$, $t = (p_a - p_c)^2$, and $u = (p_a - p_d)^2$.

2. Really, we should have $p_{cm}\sqrt{s}$ in place of s. The difference is of order m_p^2/s.

3. The erudite and/or older reader may wonder why there is no f-trajectory, that is, an even amplitude with $s^{1/2}$ behavior. Its effect is simulated by the $\log^2 s/s_0$ piece when $s < s_0$. We found we could do without any additional even terms, so they were omitted.

References

1. Abramowitz, M. and I. A. Stegun, eds., 1964, *Handbook of Mathematical Functions* , National Bureau of Standards.

2. Amaldi, U., and K. R. Schubert, 1980, *Nucl. Phys.* **B166**, 301.

3. Auberson, F., T. Kinoshita, and A. Martin, 1971 , *Phys. Rev.* **D3**, 3185.

4. Bethe, H. A., 1958 , *Ann. Phys.* **3**, 190.

5. Bjorken, J. D., 1979, in *Proceedings of Summer Institute on Particle Physics, Quantum Chromodynamics.*

6. Block, M. M., and R. N. Cahn, 1982a, to be published in *Phys. Letters B.*

7. Block, M. M., and R. N. Cahn, 1982b, to be published in *Phys. Letters B.*

8. Bodwin, G. T. and S. J. Brodsky, *Phys. Rev. Lett.* **47**, 1799.

9. Bourrelly, C. and J. Fischer, 1973, *Nucl. Phys.* **B61**, 513.

10. Cahn, R. N.,1982a, in *Proceedings of the 17th Rencontre de Moriond on Elementary Particle Physics.*

11. Cahn, R. N., 1982b, *Zeit. Phys.* **C15**, 253.

12. Chew, G. F., 1966, *The Analytic S-Matrix* , W. A. Benjamin, New York.

13. Collins, J. C. and D. E. Soper, 1982, *Phys. Letters* **109B**, 388.

14. Combridge, B. L., J. Kripfganz, and J. Ranft, 1977, *Phys. Lett.* **70B**, 234.

15. Combridge, B. L., 1979, *Nucl. Phys.* **B151**, 429.

16. Cutler, R., and D. Sivers, 1978, *Phys. Rev.* **D17**, 196.

17. Duke, D. and C. Quigg, 1982, unpublished Fermilab note.

18. Eden, R. J., 1966, *Phys. Rev. Lett.* **16**, 39.

19. Eden, R. J., 1967, *High Energy Collisions of Elementary Particles* , Cambridge Univ. Press, 1967.

20. Erdély, A., 1953, *Higher Transcendental Functions, v. II* , McGraw-Hill, p.58.

21. Feynman, R. P., R. D. Field, and G. C. Fox, 1978, *Phys. Rev.* **D18**, 3320.

22. Fischer, J., 1981, *Physics Reports* **76**, 157.

23. Fischer, J. *et al.*, 1978, *Phys. Rev.* **D18**, 4271.

24. Froissart, M., 1961, *Phys. Rev.* **123**, 1053.

25. Giacomelli, G. and M. Jacob, 1979, *Physics Reports* **55**, 1.

26. Horgan, R., and M. Jacob, 1981, in the *Proceedings of the International School of Elementary Particle Physics, Kupari-Dubrovnik, 1981,* to be published.

27. Jackson, J. D.,1973, in the *Proceedings of the Fourteenth Scottish Universities Summer School in Physics, 1973,* R. L. Crawford and R. Jennings, eds., Academic Press, London, 1974.

28. Kang, K., and B. Nicolescu, 1975, *Phys. Rev.* **D11**, 2461.

29. Louvain-Northwestern Collaboration, private communication from M. M. Block, 1982.

30. Lukaszuk, L. and B. Nicolescu, 1973, *Nuovo Cim. Lett.* **8**, 405.

31. Kinoshita, T.,1966, in *Perspectives in Modern Physics,* R. E. Marshak Ed., Wiley and Sons, New York, 1966, p.211

32. Martin, A.,1965, *Nuovo Cimento* **39**, 704.

33. Martin, A. and F. Cheung, 1970, *Analytic Properties and Bounds of the Scattering Amplitudes* , Gordon and Breach.

34. Martin, A.,1982a, *Zeit. Phys.* **C15**, 185.

35. Martin, A., 1982b. Private communication.

36. Owens, J. F., E. Reya, and M. Glück, 1978, *Phys. Rev.* **D18**, 1501.

37. I. Ya. Pomeranchuk, 1958, *Soviet Physics JETP* **7**, 499.

38. Schiff, L. I., 1968, *Quantum Mechanics* , Third Edition, McGraw-Hill, 1968.

39. Titchmarsh, E. C., 1939, *The Theory of Functions* , Oxford University Press, p. 176.

40. UA4 Collaboration, 1982a, *Phys. Letters* **115B**, 333.

41. UA4 Collaboration, 1982b, *Phys. Letters* **117B**, 126.

42. West, G. B., and D. Yennie, 1968 , *Phys. Rev* **172**, 1413.

Beyond the Standard Model in Lepton Scattering and Beta Decay

Mark Strovink

Physics Department and Lawrence Berkeley Laboratory
University of California, Berkeley

Introduction

These two lectures are an experimental review of some aspects of lepton scattering and β decay, with emphasis on possible departures from the standard electroweak model. I shall focus upon areas of recent progress, and I hope to mention a few kinds of experimental activity which may not be wholly familiar to young researchers engaged in the more typical high-energy physics programs. In most cases, my intent is to impart some of the flavor of current activity, rather than to deliver an exhaustive review.

The topics are organized as follows:

I.1	Scalar Currents	$\pi \to e\nu$
I.2	Massive Neutrinos	$\pi,K \to e\nu,\mu\nu$; $\nu N,\bar{\nu}N$ scattering
I.3	Electron Nonconservation	$\beta\beta$ decay
II.	Heavy Gauge Bosons	
II.1	Z_2^0 Limits	eD, νN, $\nu_\mu e$ scattering
II.2	$W_2^\pm$ Limits:	
	Majorana ν	$\beta\beta$ decay
	Light ν_R	β, μ decay
	Any ν_R	Λ, K decay; νN scattering

© M. Strovink 1982

By "standard model" I mean the following:

Gauge group:	$SU(3)_C \times SU(2)_L \times U(1)$
Coupling constants:	g, g' ; $\sin^2\theta_W = g'^2/(g^2+g'^2)$
Fermions:	LH doublets, RH singlets (*no RH charged current*)
Gauge bosons:	$W^\pm$, Z^0, γ
Minimal physical Higgs:	H^0, mass $\gtrsim$300 GeV (strongly interacts if heavier)

Although color SU(3) is very much a part of the standard model, I shall not discuss its experimental tests here. The ubiquitous experimental conclusion "..our results agree with QCD" has turned out to be difficult even for experts to evaluate.

1.1 Scalar Currents

In general, the less minimal electroweak theories possess a richer Higgs structure, and motivate the search for charged as well as neutral Higgs. Two often-cited reviews of Higgs physics are those of Haber, Kane, and Sterling[1] and Li and McWilliams[2]. In the notation of the latter authors, charged Higgs exchange contributes to the Lagrangian a piece

$$2^{3/4}[G_F^{1/2}M_H^{\pm}]\ (\bar{\psi}_f[\alpha^R_{ff'}\tfrac{1}{2}(1+\gamma_5) + \alpha^L_{ff'}\tfrac{1}{2}(1-\gamma_5)]\psi_{f'}\bar{H}(x) + \text{h.c.}),$$

where f and f' are the fermions, and the right- and left-handed couplings $\alpha^{R,L}_{ff'}$ are related to the β's of Ref. 1 by

$$\beta_{Kane} = 2^{1/4}M_l/(M_H^{\pm}\,\alpha^L_{l\nu}) ,$$

where l is the charged lepton. As an alternative to producing on-shell Higgs at energies which are very difficult to achieve, one may search for the effects of the exchange of off-shell charged Higgs. In particular, it is attractive to study the decay $\pi \to e\nu$ because, when mediated by W exchange, it is suppressed by the usual spin argument[3]: Only a fraction $(1-\beta^2)^{1/2}$ of the electron amplitude is emitted with a spin which will cancel the (fully polarized) neutrino spin so as to conserve angular momentum about the decay axis. In lowest order, the calculated branching ratio is

$$R_{e\mu} = \frac{\Gamma(\pi \to e\nu)}{\Gamma(\pi \to \mu\nu)} = \left(\frac{m_e}{m_\mu}\right)^2 \left(\frac{m_\pi^2 - m_e^2}{m_\pi^2 - m_\mu^2}\right)^2 ,$$

or 1.287×10^{-4}. In an early (V,A) phenomenological calculation including radiative corrections, Kinoshita[4] obtained $R_{e\mu} = 1.233\times10^{-4}$ (assuming muon-electron universality). This result has been reaffirmed to the level ±0.5% in the context of the standard model by a theorem on radiative corrections proved by Marciano and Sirlin[5], and by model calculations by Goldman and Wilson[6]. On the other hand, with the exchange of a pseudoscalar current, for example using the appropriate combination of the $\alpha_{ff'}$'s above, the same ratio would be 5.49. Thus the experimental sensitivity to Higgs exchange is enhanced by an enormous factor.

What effect upon $R_{e\mu}$ is expected from charged Higgs exchange? In the standard model, $H^\pm$ are possible, but not minimal; Higgs coupling to leptons is proportional to lepton mass:

$$\alpha_{ff'} \propto (m_f + m_{f'})/m_H .$$

In this case, $R_{e\mu}$ from Higgs exchange also is of order m_e^2/m_μ^2, and the sensitivity is lost. The best remaining lower limits upon charged Higgs mass arise from searches for $e^+e^- \to H^+H^-$ at PETRA; limits in the neighborhood of 15 GeV are obtained[7] using various branching ratio assumptions. Conversely, in some nonstandard models (unfortunately not including $SU(2)_L \times SU(2)_R \times U(1)$),

$$\alpha_{ff'} \propto m_F/m_H ,$$

where F is the same heavy fermion independent of f and f'. In these models the sensitivity of $R_{e\mu}$ to charged Higgs exchange is preserved.

A new measurement[8,9] of $R_{e\mu}$ has been performed in a low-energy π^+ beam at the TRIUMF cyclotron (Vancouver, Canada). The beam was brought to rest within a stack of thin plastic scintillators, so that the decay μ^+ could not escape. A 41 cm dia x 51 cm NaI crystal preceded by MWPC's analyzed the decay positrons. These arose both from the decay $\pi^+ \to e^+\nu_e$ (total counts "$N_{\pi e}$") and from the decay chain $\pi^+ \to \mu^+\nu_\mu$, $\mu^+ \to e^+\nu_e\bar{\nu}_\mu$ (total counts "$N_{\pi\mu e}$"). Positron energy spectra (Fig. 1) were analyzed during the time intervals (A) 6-31 nsec, and (B) 180-205 nsec following the π^+ stop. The branching ratio was obtained from the relation

$$\frac{\Gamma(\pi\to e\nu)}{\Gamma(\pi\to\mu\nu)} = \frac{\tau_\mu^{-1}}{\tau_\pi^{-1}+\tau_\mu^{-1}} \frac{N^A_{\pi e}\{1-\exp[-(\tau_\pi^{-1}-\tau_\mu^{-1})(174\ \text{nsec})]\}}{N^B_{\pi\mu e}\exp[\tau_\mu^{-1}(174\ \text{nsec})] - N^A_{\pi\mu e}} ,$$

in principle independent of the absolute time gate width, the beginning of the first gate, the μ^+ fraction in the π^+ beam, and the $\Delta\Omega$ of the detector. A final value

$$R_{e\mu} = (1.218 \pm 0.014) \times 10^{-4}$$

was obtained. It provides a measure

$$f_p = (-0.0061 \pm 0.0057) f_\pi m_e$$

of the contribution of a pseudoscalar coupling to π_{l2} decay, and a precise test of μ - e universality in the ratio of pseudoscalar couplings:

$$f^e_\pi / f^\mu_\pi = 0.9939 \pm 0.0057 .$$

The corresponding lower limit on the charged Higgs mass, for the special case that its fermion coupling is proportional to heavy fermion masses, has been estimated[8,10] to be ≈350 GeV. Although such estimates are model-dependent, it is probably safe to conclude that any charged Higgs coupled in this way exceeds 100 GeV in mass.

It is a pity that the impressive Higgs mass limit which is obtained from these data applies only to a limited class of gauge models.

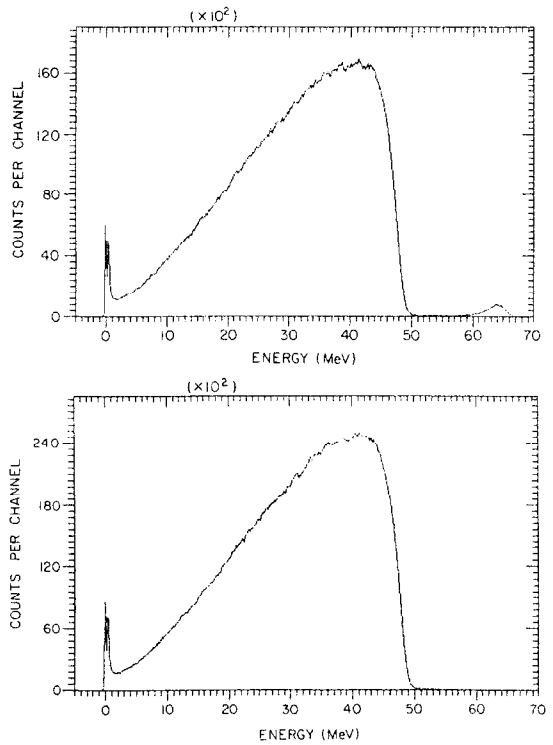


FIG. 1. Energy spectra of e^+ from μ^+ and π^+ decay in the TRIUMF - Victoria - NRC Canada - UBC - Queens NaI crystal, used to measure the $\pi \to e\nu$ branching ratio and to search for heavy neutrinos coupling to electrons (Refs. 8, 9). The top (bottom) spectrum is for decays between 6 and 31 (180 and 205) nsec after the beam π^+ stopping time. The small peak to the right of the top spectrum contains the $\pi \to e\nu$ signal, amounting to ≈20,000 events. Comparison of the two spectra makes the branching ratio determination insensitive to several sources of possible systematic uncertainty.

1.2 Massive Neutrinos

This section will be devoted to possible neutrino masses which are quite large by comparison to those often discussed -- larger than 5 MeV, to be specific. I have chosen not to review the very interesting subject of ν_e mass measurements in the range below $\approx$100 eV, because as yet little new data have appeared following publication[11] of the positive ITEP result. Many new experiments are in progress, but scant information about them and about the ITEP measurement do not permit firm conclusions. A brief review[12] by C.S. Wu is useful for criticism and further references on this topic.

The mass range above 5 MeV is the "incoherent limit" in neutrino mixing -- any oscillations would be too fast to detect. In what follows, and in the accompanying lectures by H.H. Williams which will discuss ν oscillations in detail, it will become evident that experimental methods other than detection of ν oscillations are more sensitive for searches in much of this mass region.

1.2.1 Massive Neutrinos in π,K $\to e\nu,\mu\nu$ Decay

Any neutrino from π or K decay must have a mass below $\approx$350 MeV. In most of that range, so that an excessive contribution to the mass of the universe can be avoided, a massive neutrino must be unstable.[13] Leptons in that mass range coupled with Fermi strength would be relatively long-lived; typical experiments would not be sensitive to their decay products. Irrespective of stability, neutrinos above $\approx$5 MeV are expected[13] to have "frozen out" at a temperature too high to affect strongly the primordial nucleosynthesis of light elements.

A minimal extension of the standard model can accommodate massive neutrinos. To avoid lepton nonconservation associated with a self (Majorana) mass term, the "minimal" massive neutrino can be a four-component Dirac spinor. Its right-handed part, like that of the charged lepton, need not interact. As in the quark sector, lepton flavor mixing may be introduced:[14]

$$\begin{bmatrix} \nu_e \\ \nu_\mu \\ \nu_\tau \\ \vdots \end{bmatrix} = \begin{bmatrix} U_{e1} & U_{e2} & U_{e3} & \cdots \\ U_{\mu 1} & U_{\mu 2} & U_{\mu 3} & \\ U_{\tau 1} & U_{\tau 2} & U_{\tau 3} & \\ \vdots & & & \end{bmatrix} \begin{bmatrix} \nu_1 \\ \nu_2 \\ \nu_3 \\ \vdots \end{bmatrix}$$

The mass eigenstates ν_1, ν_2, and ν_3, coupling mainly to electrons, muons, and tauons, respectively, are known to be less massive than 50 eV, 500 KeV, and 250 MeV. A sufficiently massive ν_3, for example, could be found in the decay $\pi^+ \to e^+\nu_e$, if the electron mixing ratio U_{e3} were large enough. The spectrum of positron momenta in this decay would show the usual spike corresponding to ν_1 emission, and a smaller spike at lower energy corresponding to ν_3 emission. An analogy is provided by the decomposition $\frac{1}{2}K^0 \approx K_L + K_S$ of the neutral kaon produced in association with a Λ^0. However, in the neutrino case, the mixing angles are $\ll 45^0$, the masses are highly nondegenerate, and, for the neutrino masses considered here, the two mass eigenstates are (observationally) incoherent.

It is clear that a second mass spike in π and K two-body leptonic decay would provide striking evidence of a heavy neutrino and immediate determination of its mass. With sufficient mixing, searches in these channels are sensitive to neutrinos of the appropriate mass in any lepton generation, including those which have defied discovery by other means. Especially in π_{e2} and K_{e2} decay, the spin argument mentioned in section I.1 enhances the relative probability of obtaining the heavy-neutrino final state. Relevant experiments in three-body decays also are possible, but the signatures are much less clean.

Many experiments contribute to the present limits on $|U_{\mu i}|^2$ and $|U_{ei}|^2$ in various neutrino mass ranges. Figure 2 displays the μ^+

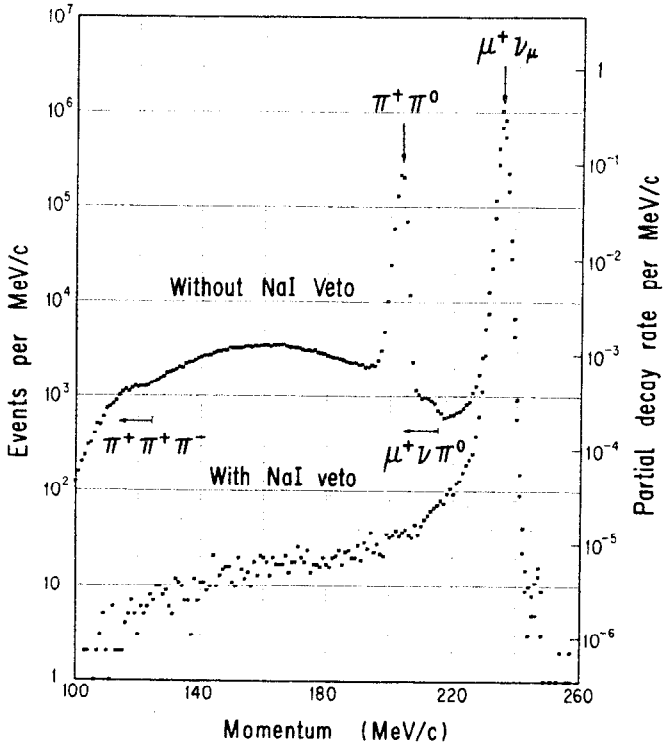


FIG. 2. Momentum spectra from K^+ decay in the Tokyo - KEK - Tsukuba magnetic spectrograph (Ref. 15). The top spectrum results from magnetic analysis of all charged particles; the bottom spectrum is the final distribution of decay muon momenta with use of photon veto and particle identification.

momentum spectrum from K^+ decay in the Tokyo - KEK - Tsukuba magnetic spectrograph.[15] Figure 3 exhibits the corresponding limits on $|U_{\mu i}|^2$ from these data and from earlier experiments.[16-19] The μ^+ energy spectrum from π^+ decay in a plastic scintillator at SIN[18] is depicted in Fig. 4. The corresponding limit on $|U_{\mu i}|^2$ appears in the top graph in Fig. 5, together with that of a previous compilation by R.E. Shrock.[14] The bottom graph in Fig. 5 displays the limits on $|U_{ei}|^2$ obtained from the search[9] for monoenergetic peaks and from the measurement[8] of the $\pi_{e\nu}$ branching ratio in the TRIUMF experiment discussed in section I.1.

Over most of the kinematic range accessible in π and K decay, the present experimental limits are already quite stringent. Roughly speaking, for $5 < m(\nu_i) < 120$ MeV, $|U_{ei}|^2 < 10^{-4}$; for $10 < m(\nu_i) < 320$ MeV, $|U_{\mu i}|^2 < 10^{-4}$. By way of comparison, in the quark sector, $|U_{ds}|^2 \approx 0.05$. The major area remaining to be explored is that of relatively light (<5 MeV) neutrinos coupled to muons.

I.2.2 Massive Neutrinos in νN and γN Scattering

Experimentally, it has been possible to search for heavy neutrinos of the muon type in the mass range below ≈10 GeV, in the reactions

$$\mu^+ N \to \bar{M}^0 X \quad \text{(via } W_R \text{ exchange)}$$
$$\nu_\mu N \to M^0 X \quad \text{(via } Z^0 \text{ exchange)} .$$

Right-handed coupling is assumed in the charged-current case, in order to provide the ν_R with a "natural" neutral partner, and to conform to the available muon beam helicity. The experimental sensitivities are such that detectable M^0 couplings must be $\tilde{>} G_{Fermi}$, i.e. $M(W_R) \approx M(W_L)$. Unfortunately, the simplest such "hybrid" gauge model predicts parity conservation as $y \to 0$ in e^-D scattering, which is not seen.[20] Figure 6 is an example of the search for $\bar{M}^0$ muoproduction[21] among 122,965 background events (mostly charm

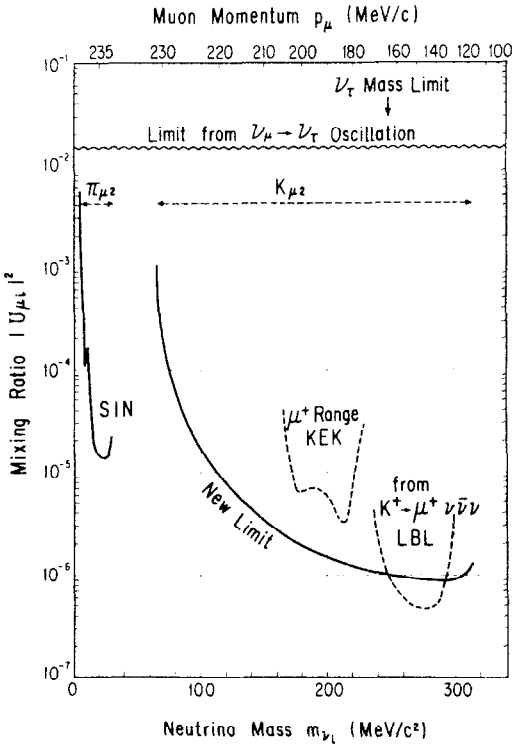


FIG. 3. Limits on muon mixing ratio $|U_{\mu i}|^2$ of hypothetical heavy neutrinos, vs. neutrino mass. The new limit from the Tokyo - KEK - Tsukuba magnetic spectrograph is indicated. Other bounds shown are: $K_{\mu 2}$ range measurement (Ref. 16); $K^+ \rightarrow \mu^+ \nu\bar{\nu}\nu$ decay experiment (Ref. 17); and recent $\pi_{\mu 2}$ heavy neutrino search (Ref. 18). The wavy line shows the limit from a neutrino-oscillation experiment (Ref. 19).

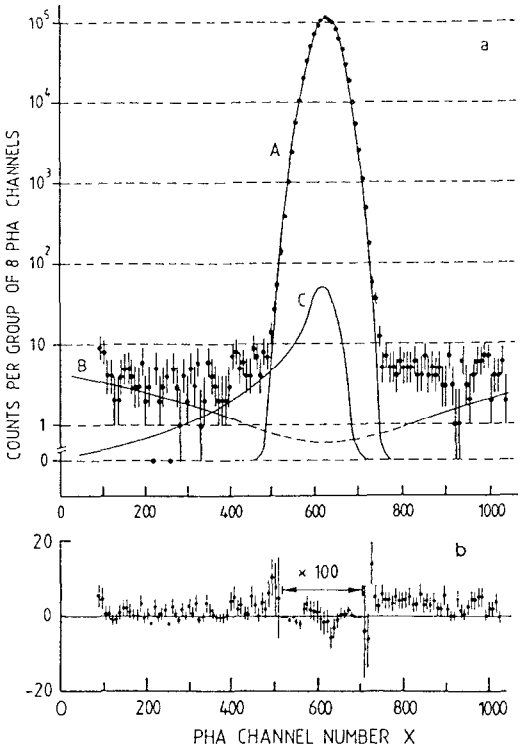


FIG. 4. Pulse height spectra of μ^+ from π^+ decay in the SIN plastic scintillator (Ref. 18). (a) Uncorrected spectrum of muon pulse heights for π^+ lifetimes from 65 to 85 nsec. The ordinate scale is linear below 1 and logarithmic above 1. Points with error bars are counts per group of 8 PHA channels. The curves are: (A) Poisson fit to the peak region, channels 522-690; (B) estimate of accidental background; (C) background due to radiative decay $\pi^+ \rightarrow \mu^+ \nu_\mu \gamma$. (b) Experimental points of (a) after subtraction of curves A, B, and C. The channel number is (muon kinetic energy/6.5 KeV) - 27.

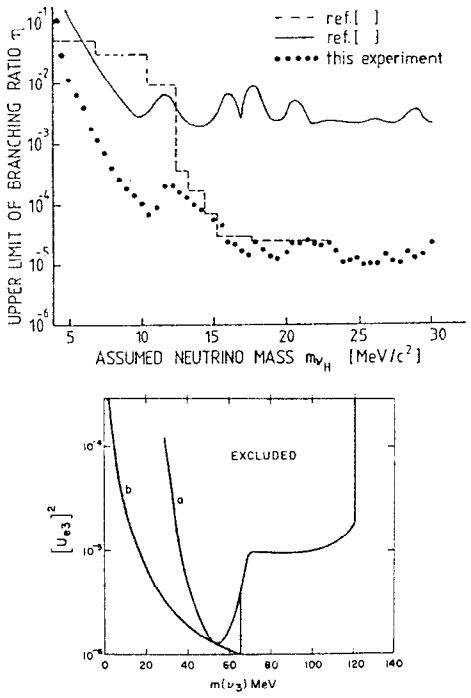


FIG. 5. The upper graph shows the upper limit (Ref. 18) on the branching ratio $\Gamma(\pi^+ \to \mu^+\nu_H)/\Gamma(\pi^+ \to \mu^+\nu_L)$, where ν_H (ν_L) is the heavy (light) neutrino emitted in the decay $\pi^+ \to \mu^+\nu_\mu$, vs. the assumed ν_H mass. This is the low-energy complement to Fig. 3. The dashed line is the previous upper limit, taken from the compilation by R.E. Shrock (Ref. 14). The lower graph shows the limits on the electron mixing ratio $|U_{ei}|^2$ of hypothetical heavy neutrinos, vs. neutrino mass. Curve (a) is the limit obtained from the search for monoenergetic peaks (Ref. 9); curve (b) is the limit obtained from the $\pi \to e\nu$ branching ratio (Ref. 8).

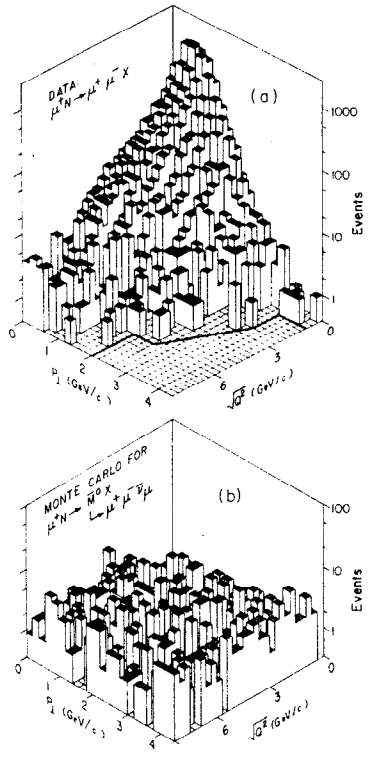


FIG. 6. Two-muon-final-state data from the Berkeley - Fermilab - Princeton muon scattering experiment at 209 GeV (Ref. 21). Events were analyzed as muon scattering with single extra muon production (for example, by charm pair production with one semileptonic decay). (Logarithmic) event populations are displayed in bins of (virtual photon) $\sqrt{Q^2}$ and produced muon momentum transverse to $\vec{Q}$. The Monte Carlo distribution (b), in contrast to the data (a), shows the large transverse momenta expected in production and $\mu^+\mu^-\bar{\nu}_\mu$ decay of a hypothetical heavy muon neutrino $\bar{M}^0$ of mass 6 GeV.

muoproduction with single semileptonic decay). For a right-handed $\mu^+ - \bar{M}^0$ coupling with Fermi strength, assuming typical leptonic branching ratios, that experiment obtained the mass limit

$$M(\bar{M}^0) < 9 \text{ GeV} \quad (90\% \text{ confidence}) .$$

Assuming a Fermi-strength M^0 - neutrino coupling, an analysis[22] of BEBC $\nu N \to \mu e$ and CDHS $\nu N \to \mu\mu$ data has found 90%-confidence upper limits upon $M(M^0)$ of 4 and 6 GeV, respectively.

I.3 Electron Nonconservation in Double β Decay

I have chosen not to review the lively field of lepton <u>flavor</u> nonconservation, primarily because the famous SIN $\mu - e$ conversion limit[23] is no longer a new result, but as yet has not been improved upon. Instead I shall discuss possible nonconservation of leptons themselves, in the context of $\beta\beta$ decay. At present, a surge of new interest is centered upon this old topic. However, the experiments and the phenomenology are difficult, and are outside the expertise of most particle physicists like myself. This Summer Institute will benefit from the more authoritative lecture of F. Boehm, who <u>is</u> an expert.

In the diagram in Fig. 7(a), lepton conservation would require that the two neutrino lines be external, corresponding to two-neutrino double β decay [$\beta\beta(2\nu)$]. Double β decay has been observed indirectly from geochemical measurements at something like the lifetime expected for $\beta\beta(2\nu)$ decay, i.e. 10^{20-21} y. In this mode, the energy sum of the two electrons is expected to be centered broadly at $\approx Q/3$, where Q, the total kinetic energy released, is typically 1 to 4 MeV, depending upon the nuclear masses involved.

If the two neutrino lines join to form one internal line, one has zero-neutrino double β decay [$\beta\beta(0\nu)$]. The electron energy sum is a

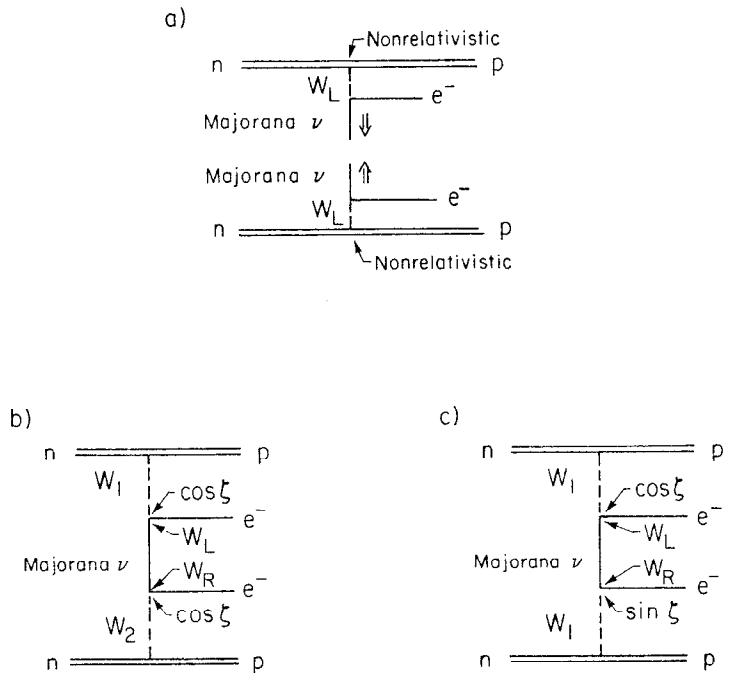


FIG. 7. Diagrams for (0ν) $\beta\beta$ decay (all baryons indicated are part of the same nucleus). Diagram (a) illustrates the suppression of (0ν) $\beta\beta$ decay by angular momentum conservation, even with lepton-nonconserving Majorana ν_e's, when both neutrinos have the helicity associated with W_L exchange. Diagrams (b) and (c) restore angular momentum conservation, at the expense of (b) the exchange of a (primarily right-handed) W_2, or of (c) the mixing of a (primarily left-handed) W_1 into a W_R, with finite mixing angle ζ.

δ-function at Q. Recalling that the Fermi integral for single β decay gives a lifetime $\tau \tilde{\propto} Q^{-4}$, one expects a substantial phase-space enhancement for this mode, because the limited Q is shared only by the two electrons. In fact, ββ decay is a process in which lepton nonconservation [ββ(0ν)] is enhanced typically by a factor of $\approx 10^6$ relative to lepton conservation [ββ(2ν)].

A "natural" mechanism for electron nonconservation is provided by Majorana neutrinos.[24] If one requires only left-handed currents in the weak Hamiltonian, the lepton-nonconserving term which is quadratic in the neutrino fields is formally equivalent to

$$H = \bar{\chi}_e M \chi_e + \cdots ,$$

where χ_e is a (2-component) Majorana field

$$\sqrt{2}\,\chi_e = \nu_{eL} + (\nu_{eL})^{\text{charge conjugated}} .$$

Thus the Majorana neutrino χ_e is its own antiparticle. In the zero-neutrino-mass limit, the physical consequences of this mechanism are precisely those of the Dirac left-handed neutrino picture. The well-known differences in the interactions of what we call "ν_e" and "$\bar{\nu}_e$" are ascribed entirely to the difference in neutrino helicity, which is complete in this limit. The conventional neutrino and antineutrino are reinterpreted as the left- and right-handed components of the Majorana χ_e.

For massless left-handed Majorana neutrinos, ββ(0ν) decay is still forbidden, no longer by lepton conservation, but by angular momentum conservation. Again in Fig. 7(a), if the leptonic vertices are left-handed and the χ_e line is internal, the χ_e spin must flip. This is impossible in the zero-neutrino-mass limit. However, the existence of a $\bar{\chi}_e \chi_e$ term in the Hamiltonian provides a mechanism for finite χ_e mass. In the latter case, the χ_e exchanged in ββ(0ν) decay is incompletely polarized, and the neutrinoless mode is allowed. Although not part of the standard model, finite-mass Majorana neutrinos are not incompatible with modified versions of that model. They are more natural in left-right symmetric gauge models, to which we shall return in the second lecture.

Two possible χ_e mass regions may be distinguished:
(1) Light χ_e (<<(1 MeV). The amplitude for χ_e exchange is suppressed by a helicity factor

$$(1 - \beta^2)^{1/2} \approx M(\chi_e)/M(e) .$$

A phase space enhancement factor of 10^5 for ββ(0ν) relative to ββ(2ν) implies

$$M(\chi_e) \tilde{<} 10^{-3} M(e) \quad \text{if} \quad \Gamma_{\beta\beta}(0\nu) \tilde{<} \Gamma_{\beta\beta}(2\nu) .$$

(2) Heavy χ_e (>>1 MeV). The amplitude for χ_e exchange is suppressed by a propagator term $\approx Q/M(\chi_e)$. The same phase-space enhancement factor implies a limit

$$M(\chi_e) \tilde{>} 10^8 Q \quad \text{if} \quad \Gamma_{\beta\beta}(0\nu) \tilde{<} \Gamma_{\beta\beta}(2\nu) .$$

Therefore, by observing (0ν + 2ν) ββ decay at the rate expected for (2ν) ββ decay, naively one would expect to be able to limit

$$M(\chi_e) \tilde{<} 500 \text{ eV} \quad \text{or} \quad M(\chi_e) \tilde{>} 2 \text{ GeV} .$$

In practice, the data are somewhat more restrictive, the calculations are more precise, and the experimental limits are more stringent. However, we shall see that conflicts exist both in the data and in the calculations.

The ββ decay experiments and their interpretation are reviewed by Rosen,[25] Haxton,[26] Primakoff and Rosen[27], and Bryman and Picciotto,[28] where references to the experiments[29-32] may be found. Frequently mentioned ββ decays are enumerated in Table 1. A ββ-decaying isotope must be protected by energy conservation from depletion by single β decay

$$(A,Z) \rightarrow (A,Z+1)\, e^- \bar{\nu}_e .$$

TABLE 1. Frequently mentioned $\beta\beta$ decays.

Reaction	Q (MeV)	Lower limit (y) $\log_{10}\tau_{1/2}(0\nu)$	Exp. method
$^{48}Ca \rightarrow {}^{48}Ti$	4.27	21.3 [a]	Tracking
$^{76}Ge \rightarrow {}^{76}Se$	2.05	21.7 [b]	Crystal
$^{82}Se \rightarrow {}^{82}Kr$	3.00	21.5 [c]	Geochemical
$^{128}Te \rightarrow {}^{128}Xe$	0.87	24.5 [d]	Geochemical
$^{130}Te \rightarrow {}^{130}Xe$	2.54	21.1 [d]	Geochemical
$^{136}Xe \rightarrow {}^{136}Ba$	2.72	--	Tracking

TABLE 2. Upper limits on $m(\chi_e)$ assuming that it is $<<$ 1 MeV.

$\beta\beta(0\nu)$ experimental input	Upper limit on $m(\chi_e)$
$\tau_{1/2}(^{76}Ge) > 5 \times 10^{21}$ y [b]	20 eV [e]
$\tau_{1/2}(^{82}Se) > 3 \times 10^{21}$ y [c]	15 eV [e]

[a] Bardin et al., Ref. 29
[b] Fiorini et al., Ref. 30
[c] Kirsten et al. and Srinivasan et al., Ref. 31
[d] Hennecke et al., Ref. 32
[e] Rosen, Ref. 25

The systematics of nuclear masses therefore require A and Z to be even. Most decays are $0^+ \rightarrow 0^+$; the $0^+ \rightarrow 2^+$ decay is also allowed for a few isotopes, for which additional information on the $\beta\beta(0\nu)$ decay mechanism in principle can be obtained. Double β decay can occur for 26 isotopes; $\beta^+\beta^+$ as well as $\beta^-\beta^-$ decays are possible.

Experimental methods fall into three categories. The geochemical experiments require the produced isotope to be a noble gas which is retained in the ore containing the decaying isotope. The degree of retention and the age of the ore are sources of uncertainty which can cause the lifetime to be overestimated, as opposed to the underestimates common for other systematic errors. The extent of the $(0\nu + 2\nu)$ $\beta\beta$ decay is inferred from mass-spectroscopic measurement of the abundances of the various noble-gas isotopes. The crystal experiments study decays of the 8% natural ^{76}Ge in a Ge detector, with or without an anticoincidence shield. With good energy resolution but no tracking, this method is sensitive primarily to $\beta\beta(0\nu)$ decay. Typical backgrounds are caused by Compton scattering and photoelectric absorption of ambient γ rays. The (existing and proposed) tracking experiments take on a variety of forms: a foil source with visual track detector and scintillators; a foil source with a Time Projection Chamber (TPC) track detector; a ^{136}Xe source doubling as a component of the TPC gas. Usually the energy resolution in tracking detectors is only fair. Among the backgrounds are γ Compton scattering together with a knock-on electron, and γ conversion with positron charge misidentification.

Table 2 exhibits two of the more stringent upper limits upon $m(\chi_e)$ (assuming that it is $<<$1 MeV) discussed in Rosen's review.[25] The primary uncertainties in these limits are the calculations of the nuclear matrix elements. As is evident in Table 3, the lower limit upon $m(\chi_e)$ (assuming that it is $>>$ 1 MeV) is enormously sensitive to the type of nuclear potential which is used in these evaluations.[33]

TABLE 3. Lower limits on $m(\chi_e)$ assuming that it is >> 1 MeV.

$\beta\beta(0\nu)$ experimental input	Lower limit on $m(\chi_e)$
^{48}Ca, ^{76}Ge, and ^{82}Se	≈3 GeV [a] (0.5 Fm radius hard core)
data corresponding to $m(\chi_e)<60$ eV (older analyses)	≈700 GeV [a] (no hard core)

TABLE 4. Example of the effect of various calculations of the Te $\beta\beta$ decay matrix elements upon the interpretation of a single experimental datum. (The ratio of experimental $\beta\beta$ decay rates of the two Te isotopes indicated below is in conflict with a more recent measurement[b], which is consistent with zero χ_e mass.)

Experimental input	Calculated $m(\chi_e)$
$\frac{\tau_{1/2}(^{130}Te;\ 0\nu+2\nu)}{\tau_{1/2}(^{128}Te;\ 0\nu+2\nu)} = (6.3\pm0.2)\times10^{-4}$ [d]	≈24 eV [c]
	≈10 eV [e]
	≈25±? eV [f]
	≈0.8-2.6 eV [g]

[a] Halprin, Minkowski, Primakoff, and Rosen, Ref. 33
[b] Kirsten et al., Ref. 34
[c] Rosen (Ref. 25) using Primakoff and Rosen matrix element (Ref. 35)
[d] Hennecke et al., Ref. 32
[e] Rosen (Ref. 25) using Haxton et al. matrix element (Ref. 36)
[f] Doi et al., Ref. 37
[g] Minkowski, Ref. 38

To emphasize the great importance of further progress in understanding these nuclear matrix elements, I have listed four calculations of the χ_e mass in Table 4. The common experimental input is the ratio of $\beta\beta(0\nu + 2\nu)$ half-lives in ^{130}Te and ^{128}Te. This ratio is sensitive to the relative amounts of 0ν and 2ν $\beta\beta$ decay because of the different Q-dependence of the 0ν and 2ν mechanisms, and the different Q of the $\beta\beta$ decays of the two isotopes. (A recent measurement,[34] consistent with no 0ν decay, is in conflict with the experimental ratio[32] which these calculations used.) The calculations by Rosen[25] using two different matrix elements[35-36] are in reasonable agreement with that of Doi et al.,[37] but the Majorana neutrino mass obtained by Minkowski[38] is one order of magnitude lower. Since the two nuclear wavefunctions should be quite similar, the $^{130}Te/^{128}Te$ ratio is regarded as a quantity which ought to be particulary amenable to reliable calculation.

Table 5 reproduces M. Witherell's compilation of some of the $\beta\beta$ decay experiments planned or in progress in early 1982. Many of them use the Ge crystal technique widely associated with the experiment of Fiorini et al.[30] Figure 8 reproduces portions of the energy spectra obtained in that measurement. The background level and its dependence upon the surrounding materials emphasize that the experiment was not rate-limited. Figure 9, taken from Avignone's proposal,[39] illustrates the care with which ambient radioactivity must be eliminated by careful choice of (active and passive) shielding materials.

The anticipated level of new experimental activity in this exciting field stimulates the following comments:

- Much of the expense and tedium in these experiments is associated with the construction of a low-activity counting environment with properly designed shielding and sufficient overburden. Such an environment would be useful for many other scientific purposes. It should be constructed and scheduled as part of a National Underground

TABLE 5. Compilation by M. Witherell (early 1982) of some new $\beta\beta$ decay experiments.

Institutions/participants	Detector properties
Caltech (F. Boehm)	100 cm^3 Ge detector; special cryostat (Cu) with no molecular sieve. Outer veto with surrounding plastic scintillators ready by March 1982; goal $\tau_{1/2}>5\times10^{22}$y.
Guelph (J.J. Simpson, J. L. Campbell, P. Jagam); Aptec, Toronto (H. Maim)	200 cm^3 → 500 cm^3 Ge; possibly with active shielding. First crystal has been purchased. Goal $\tau_{1/2}>3\times10^{22}$y (95% confidence).
Battelle Pacific (R. Brodzinski); Northwest (N. Wogman); South Carolina (F.T. Avignone)	250 cm^3 Ge; NaI shield. Now operating above ground. Present 0ν limits: $0^+\to0^+$ 4×10^{21}y; $0^+\to2^+$ 2×10^{21}y.[a]
Milano (E. Bellotti, E. Fiorini, C. Liquori, A. Pullia, Q. Sarracino, L. Zanotti)	135 cm^3 Ge(Li); passive shielding, Mt. Blanc tunnel. Present 0ν limits: $0^+\to0^+$ 3×10^{21}y; $0^+\to2^+$ 2×10^{21}y. Late in 82: test with NaI shield, intrinsic Ge detector.
U. C. Santa Barbara (D.O. Caldwell, R.M. Eisberg, M.S. Witherell); LBL (F. Goulding, N. Madden, R. Pehl)	1000 cm^3 Ge; NaI shield. Proposal pending; goal 2×10^{23}y.

TABLE 5 (continued)...

Brookhaven (B. Cleveland); CUNY (J. Ullman); Oak Ridge (S. Hurst, W. Chen)	10 kg Se; radiochemical experiment. Single atom counting of ^{82}Se.
U. C. Irvine (M. Moe, A. Hahn, F. Reines)	15 g ^{82}Se → 40g; using Time Projection Chamber. Goal: 0ν limit 3×10^{22}y; expect serious data in 8-12 months, first tracks in a few weeks.
U. C. Irvine (H.H. Chen, H.J. Mahler, P.J. Doe)	$^{136}Xe\to^{136}Ba$ liquid Xenon TPC. 1000 cm^3 Xe; complete feasibility study in about one year.

[a]Details may be found in Avignone, Ref. 39

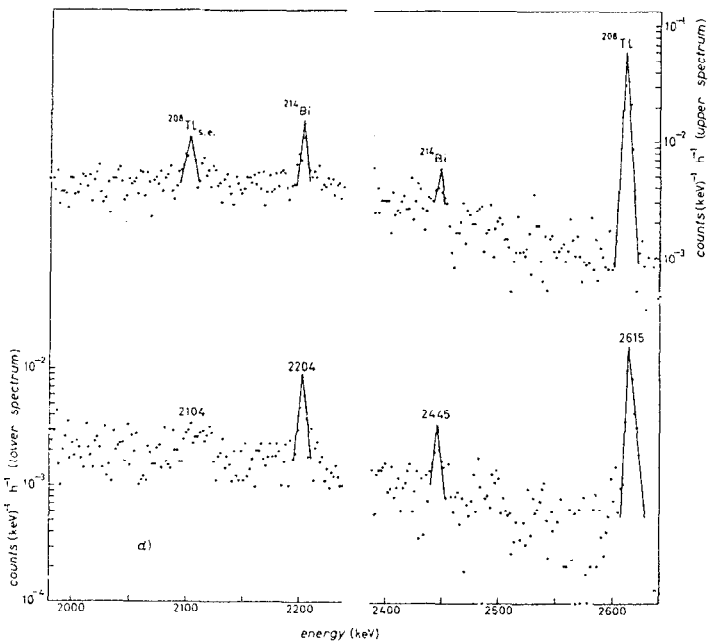


FIG. 8. Pulse spectra from the Milano-Ispra GeLi crystal in the classic $\beta\beta$ experiment operated under Mt. Blanc (Ref. 30). The detector for the upper spectrum (2100 h) used an 1100 Al support and a cryostat made of electrolytic Cu; the detector for the lower spectrum (2300 h) had a support and crystal cap made of OFHC Cu. The decay $^{76}Ge(0^+) \rightarrow {}^{76}Se(0^+)$ would have produced a peak in the region of 2045 KeV, where ≈70 counts were observed in the high-purity run. Therefore, the limit obtained was ≈5 times weaker than if the experiment had been rate-limited.

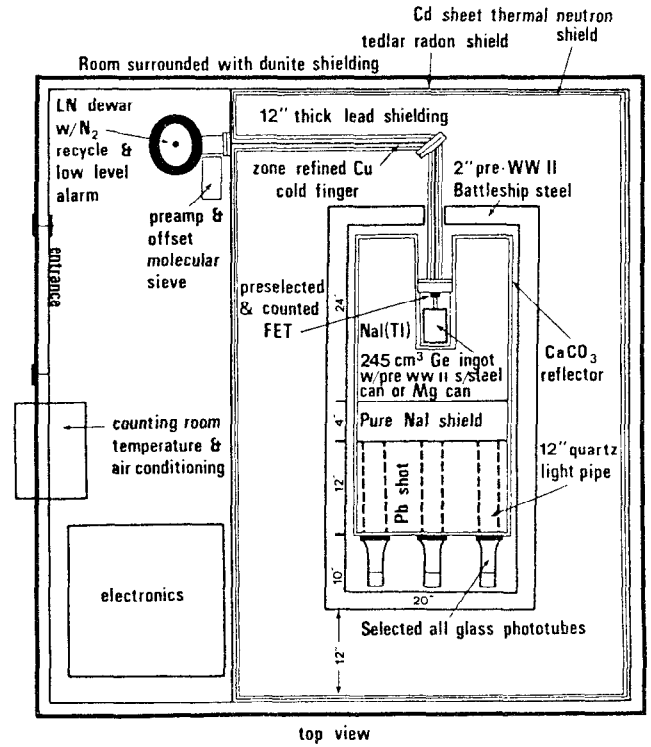


FIG. 9. Proposed experimental setup for the Battelle Pacific - Northwest - South Carolina $\beta\beta$ experiment using a Ge crystal. The counting system, to be located ≥1280 m underground in an Idaho silver mine, is to be constructed mainly of pre-WW II battleship steel, laboratory quality Pb, and sacked dunite (low U and Th). The layout emphasizes the importance of a properly shielded low-activity counting environment.

Laboratory (NUL) devoted to such measurements.

- The necessary Ge crystals may become so expensive that they should also be acquired and scheduled as part of the underground laboratory facilities.
- Caution must be exercised in scaling up the Fiorini et al. experiment.[30] Their limit was already ≈5 times weaker than if the experiment had been rate-limited. A new experiment merely scaled up by the factor F could produce a new limit stronger by less than $\sqrt{F}$, in view of the probable existence of backgrounds which increase more than linearly with the Ge volume.
- The crystal experiments reject background essentially by means of one precise cut on summed electron energies. Additional topological constraints may prove to be a particularly effective means of background rejection. Ability to identify $2\nu\beta\beta$ decay will continue to be especially important in providing additional constraints on the nuclear matrix elements.

II. Heavy Gauge Bosons

Beyond the standard electroweak model, it is possible that additional gauge bosons Z_2^0, Z_3^0,.. and $W_2^\pm$, $W_3^\pm$,.. exist at higher masses. Recently, a great deal of attention has been focussed upon the "left-right symmetric" gauge model based on the group

$$SU(2)_L \times SU(2)_R \times U(1)_{B-L} \qquad [\, Q = T_{3L}+T_{3R}+(B-L)/2 \,]$$

as an alternative to the standard group

$$SU(2)_L \times U(1)_Y \qquad [\, Q = T_3+Y/2 \,] \; .$$

Table 6 is a partial summary of the comparative properties of the two models. The left-right symmetric model has some aesthetic advantages:

- Parity invariance would be restored for four-momentum transfers above the masses of the two heavier gauge bosons W_2 and Z_2.
- Right-handed and left-handed fermions are assigned symmetrically to doublets.
- Right-handed neutrino interactions could suggest finite neutrino masses, which, for example, might close the universe.
- The U(1) quantum number corresponding to hypercharge in the standard model is B-L .

Boredom in the "desert" above the W_1 and Z_1 masses may be relieved if the W_2 or Z_2 is sufficiently light, which is an advantage at least for experimenters. Unfortunately, the $SU(2)_L \times SU(2)_R \times U(1)$ model will be with us for at least as long as the standard model, since the experimental consequences are the same in the infinite W_2 and Z_2 mass limit.

If there are right-handed charged currents, in general the W mass eigenstates W_1 and W_2 need not be the same as the left- and right-handed helicity eigenstates W_L and W_R:

$$\begin{bmatrix} W_1 \\ W_2 \end{bmatrix} = \begin{bmatrix} \cos\zeta & \sin\zeta \\ -\sin\zeta & \cos\zeta \end{bmatrix} \begin{bmatrix} W_L \\ W_R \end{bmatrix} \; .$$

TABLE 6. Comparative properties of $SU(2)_L \times U(1)$ and $SU(2)_L \times SU(2)_R \times U(1)$.

Properties	$SU(2)_L \times U(1)$	$SU(2)_L \times SU(2)_R \times U(1)$
Gauge bosons	$W^{\pm}$, Z^0, γ	$W_1^{\pm}$, $W_2^{\pm}$, Z_1^0, Z_2^0, γ
Higgs	$H^0(1)$ (mass of order $M(W)$)	$H^0(6)$, $H^{\pm}(4)$ (1 neutral mass of order $M(W_1)$, other 9 of order $M(W_2)$)
Fermions	LH doublets (W); RH singlets	LH doublets (W_1); RH doublets (W_2)
Mixing	$\sin^2\theta_W = \frac{g'^2}{g^2+g'^2}$	$\sin^2\theta = \frac{g'^2}{g^2+2g'^2}$
Masses	$\cos\theta_W = M(W)/M(Z)$	$\cos\theta = M(W_1)/M(Z_1)$; $(\frac{1}{2}\cos 2\theta)^{\frac{1}{2}}/\cos\theta = M(W_2)/M(Z_2)$

In particular, a finite mixing angle ξ could be manifested at presently accessible energies even if the ratio

$$\zeta = M^2(W_1) / M^2(W_2)$$

is zero. The parameters ξ and ζ generally are used[40] to provide a convenient, physical description of right-handed charged-current phenomenology. The weak mixing angle θ must be included for the neutral currents since it affects their chirality. Since θ relates the charged and neutral gauge boson masses (Table 6), we may use $M(W_1)$ as the mass parameter for both neutral and charged currents. It will be close to $M(W)$ in the standard model, as ζ and ξ are small.

11.1 Z_2^0 Limits

The major experimental inputs to the phenomenology of heavy neutral gauge bosons have been (i) polarized e^-D scattering at SLAC; (ii) $\nu_\mu N$ and $\bar{\nu}_\mu N$ scattering; and (iii) $\nu_\mu e^-$ and $\bar{\nu}_\mu e^-$ elastic scattering. In general, mixing between the three neutral gauge bosons can occur. To obtain Z_2^0 mass limits, it has been necessary to simplify the analysis by making assumptions about the Higgs structure. To a certain extent, progress in the phenomenology has been achieved by iteration. At present, the exhaustive analysis by Rizzo and Senjanovic[42] is widely cited. These authors discuss the experimental consequences of the $SU(2)_L \times SU(2)_R \times U(1)$ model in the context of "popular" choices for the Higgs multiplets. Essentially, the effective Hamiltonia for reactions (i), (ii), and (iii) get modified by the existence of Z_2^0 in various (complex!) ways. Inconsistencies then develop in different measurements of the parameters of the standard model, for example $\sin^2\theta_W$. The experimentally allowed subset of the ξ-ζ-$\sin^2\theta$ parameter space thereby can be mapped out.

The present conclusions are the following:

1. All neutral current data can be fitted with $SU(2)_L \times U(1)$ values:

$$\zeta = \xi = 0 \; ; \quad \sin^2\theta_w = 0.215 \pm 0.014 \; ^{42} \; ; \quad M(W_1) \approx 81 \text{ GeV} .$$

2. From neutral current data alone, the experimental constraints can be satisfied with (not all at once!)

$$0 \leq |\zeta| \leq 0.05 \; ; \quad 0 \leq \xi \leq 0.24 \; ; \quad 0.20 \lesssim \sin^2\theta \lesssim 0.28 .$$

The limit on ξ corresponds to $M(W_2) \geq 165$ GeV .

3. If SO(10) grand unification is imposed, relating $\sin^2\theta$ at low energy to its value 3/8 at the unification mass, two regimes survive:

$$\sin^2\theta \approx 0.27 \text{ and } M(W_2) \approx 150\text{-}250 \text{ GeV} \; ; \; \underline{\text{or}}$$
$$\sin^2\theta \approx 0.22 \text{ and } M(W_2) \gtrsim 10^9 \text{ GeV} .$$

A relevant experimental result which could be obtained at the SLAC Linear Collider has been discussed by Hollik.[48] First the Z_1^0 mass is measured and the parameters of the standard model adjusted to agree with it. (It is assumed that the low-energy measurements of $\sin^2\theta_w$ will not be so precise as to prevent that adjustment.) Then the helicity asymmetry of $e^+e^- \to \mu^+\mu^-$ near the Z_1^0 pole is compared with the standard model prediction. After one year of measurement at the Z_1^0, with 50% electron polarization, one may be able to reach the limit

$$M(Z_2^0) \gtrsim 350 \text{ GeV} .$$

To summarize, neutral-current limits on heavy gauge bosons are only moderately restrictive, and appear to be unlikely to improve radically in the short term. Their analysis is complex and model-dependent. On the bright side, much of the experimental input useful for setting these limits is independent of the mass of any right-handed neutrino, because that neutrino in many cases does not need to be produced.

II.2 $W_2^\pm$ Limits

I shall discuss phenomenological limits on the existence of a heavy charged gauge boson $W_2^\pm$ with predominantly right-handed coupling, in the context of three different possibilities concerning the right-handed neutrino ν_R to which it couples: (1) ν_R is a Majorana neutrino; (2) ν_R is light, for example compared to the muon mass; (3) no assumption is made with regard to ν_R. As usual, the parameters in which these limits will be expressed are the W_1-W_2 mass-square ratio ξ and mixing angle ζ.

II.2.1 $W_2^\pm$ Limits for Majorana ν_R

We have seen that the existence of Majorana neutrinos in a certain mass range would make zero-neutrino double beta decay [$\beta\beta(0\nu)$] observable. Irrespective of the existence of any right-handed W, non-observation of $\beta\beta(0\nu)$ decay excludes Majorana electron neutrinos (χ_e) with left-handed coupling over the range $\approx$20 eV - $\approx$3 GeV ; data at the endpoint of tritium single β-decay[11] restrict $M(\chi_e)$ $\lesssim$ 50 eV . If Majorana neutrinos exist well below this mass range, $\beta\beta(0\nu)$ decay at experimentally interesting levels still could occur if the right-handed W parameters ξ or ζ were large enough. Turning back to Fig. 7, diagram (b) illustrates $\beta\beta(0\nu)$ decay mediated by W_2 exchange (relative amplitude suppressed by ξ), and diagram (c) illustrates $\beta\beta(0\nu)$ decay made possible by mixing of an exchanged W_1 into a W_R (relative amplitude suppressed by ζ). Since the (nonrelativistic) hadron vertices have no strong helicity suppression, these two diagrams are expected to interfere.

In general, any null experimental result will take the form of a contour in ξ, ζ space within which these parameters are limited. I conclude from Fig. 7 that:

- A limit from $\beta\beta(0\nu)$ decay obtained on ξ (i.e. $M(W_2)$), assuming

that ζ is zero, is equivalent to a limit on ζ of the same order of magnitude, assuming that ξ is zero.

- Since diagrams 7(b) and 7(c) are expected to interfere, the corresponding contour in ξ, ζ space probably is skewed.
- Since the interference is not likely to be complete, the contour should be closed.

To the best of my knowledge, the correlated limits on ξ and ζ corresponding to $\beta\beta(0\nu)$ decays of experimental interest remain to be calculated. Assuming that $\zeta = 0$, Rosen[25] has quoted the following bounds on ξ, based on $\beta\beta(0\nu)$ limits:

$$^{82}\text{Se}: \quad \xi < 1.8 \times 10^{-5} \quad [\, M(W_2) > 19 \text{ TeV} \,]$$
$$^{76}\text{Ge}: \quad \xi < 3.5 \times 10^{-5} \quad [\, M(W_2) > 13.7 \text{ TeV} \,] \; .$$

He cautions that uncertainties in the nuclear matrix elements could make the limits on ξ two orders of magnitude weaker. If the more conservative limit $\xi \tilde{<} 10^{-3}$ were adopted, it would correspond to $M(W_2) \tilde{>} 2.6$ TeV. This is still a very impressive limit, compared to what is possible with other experimental techniques.

It is important to keep in mind <u>all</u> the assumptions which must be made in order to derive <u>any</u> information on right-handed W's from neutrinoless double β decay:

- Lepton flavors, leptons themselves, and B-L cannot be conserved.
- The participating Majorana neutrino must have appreciable coupling <u>both</u> to right-handed and to left-handed W's. This is a terribly restrictive requirement, satisfied by no gauge model of which I am aware. In typical models the neutrinos which couple to W_R and to W_L have vastly different masses, and mix by an angle only of the order of their mass ratio.
- The Majorana electron neutrino must be lighter than $\approx$20 eV -- otherwise, W_L-mediated $\beta\beta(0\nu)$ decay already would have been observed. Unfortunately, attempts[44] to calculate neutrino masses in the context of grand unified theories instead have obtained right-handed neutrino masses of the order of $M(W_2)$ or higher. This is a general criticism of any experiment searching for W_R effects in reactions requiring production of right-handed neutrinos.

II.2.2 $W_2^{\pm}$ Limits for Light ν_R

As we have seen, measurements of π and K decay into $e\nu$ and $\mu\nu$ rule out the existence of neutrinos having appreciable coupling to electrons and muons over much of the mass range $\approx$ 5-350 MeV. So, "light ν_R" will refer to neutrinos below $\approx$5 MeV in mass, of either the Dirac or Majorana type. In what follows, it will be assumed that the reaction discussed is not affected kinematically by any finite neutrino mass.

Figure 10 illustrates schematically a "general" first-order charged-current semileptonic or leptonic diagram and the modifications to that diagram which could arise from a right-handed W. In addition to the usual diagram (a), one may have (b) W_2 exchange, (c) W_L-W_R mixing at the neutrino (upper) vertex, and (d) W_L-W_R mixing opposite to the neutrino vertex. The distinction between (c) and (d) is present only for semileptonic processes, for which diagram (c) requires that a right-handed neutrino be produced, but diagram (d) does not. Because the vertices at the bottom of diagrams (b) and (c) have opposite helicity, those diagrams will interfere only for a semileptonic process with nonrelativistic hadrons. Diagrams (a) and (d) will interfere under the same conditions. When there is no interference, the relative rates are (a) 1, (b) ξ^2, (c) ζ^2, and (d) ξ^2. Interference between (b) and (c) produces a $\xi\zeta$ term. In principle, first-order sensitivity to ζ could arise from interference between (a) and (d), but there appears to be no obvious experimental signature for that interference. With typical choices for the Higgs sector in $SU(2)_L \times SU(2)_R \times U(1)$, ζ is of the same order as ξ. Therefore, relative effects of right-handed currents upon experimentally measured quantities are of the order of the square of the small parameter ξ, or the fourth power of the ratio

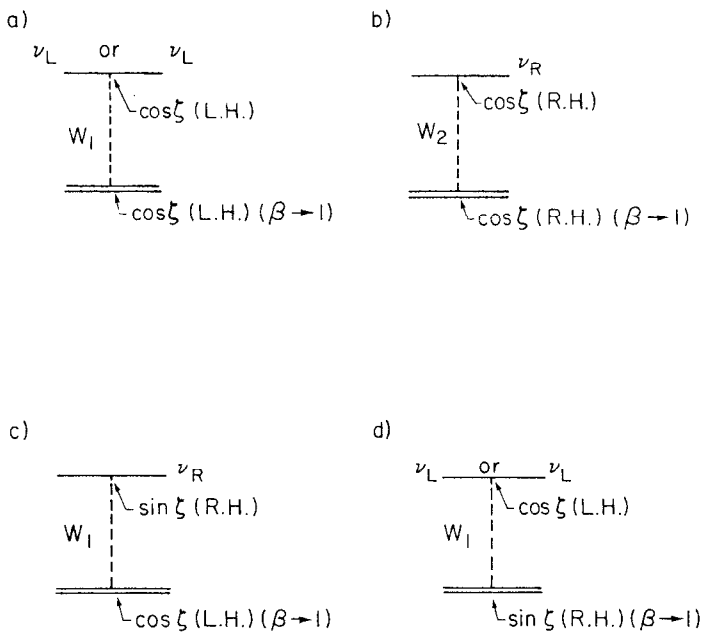


FIG. 10. Left- and right-handed charged-current vertices. Mass eigenstates $W_{1,2}$ transform to helicity eigenstates $W_{L,R}$ with mixing angle ζ. One neutrino is always at the top vertex; in a semileptonic process the quarks are at the bottom vertex. Diagram (a) is the dominant left-handed process, and diagram (b) is heavy W exchange. Diagrams (c) and (d) exhibit W_L- W_R mixing (c) at the neutrino vertex, and (d) opposite to the neutrino vertex. Diagrams (b) and (c) may interfere with each other, but not with (a) if ν_R is orthogonal to ν_L. If the process is semileptonic, diagram (d) is of special interest because ν_R need not be produced.

$M(W_L)/M(W_R)$.

Table 7 lists a number of experimentally measurable quantities and their sensitivity to ξ and ζ . With the exception of the last entry, these are "low-energy" or at most "medium-energy" measurements. The reason is simple enough: β or μ decay experiments usually can be performed with greater precision than is possible for processes at higher energy. The relative effects of W_R and W_L exchange are independent of q^2 below the mass-squared of the lightest W. By that standard, every experiment which can be performed today is a low-energy experiment.

The semileptonic decays (1)-(4) in Table 7 exhibit the cross terms in ξ and ζ characteristic of interference between diagrams (b) and (c). The interference is complete, resulting in limit contours on the ξ - ζ plane which are open. Summing over positron spin, the muon decay parameters (5) as usual are defined by

$$\frac{d\Gamma}{x^2\,dx\,d\cos\theta} \propto (3-2x) + (4\rho/3-1)(4x-3) + 12(m_e/m_\mu x)(1-x)\eta - \tilde{\alpha}\left[(2x-1) + (4\delta/3-1)(4x-3)\right]\xi P_\mu \cos\theta \ ,$$

where x is the reduced positron energy and θ is the angle between its direction of emission and a vector opposite to the muon spin direction. (This vector is the beam direction in many experiments.) The Michel parameters are the symmetric shape parameter ρ , the asymmetric shape parameter δ , the low-energy parameter η , and the polarization parameter ξ . Any weak-interaction model prescribes their values; in the standard model $\rho = \delta = 3/4$, $\eta = 0$, $\xi = 1$. The Michel parameters themselves have no particular theoretical significance, as they are at least two transformations removed from the Lagrangian. As it turns out, δ and η are insensitive to ζ and ζ , while ρ and ξ are sensitive to ζ^2 and ζ^2 but not to $\zeta\zeta$, as must be the case for a purely leptonic decay. Experiments determining ξ in fact always measure ξP_μ , where P_μ is the polarization of a μ^+ from π^+ decay at rest. The sensitivity of the

TABLE 7. Experimental sensitivity to the phenomenological parameters ζ ($= M^2(W_L)/M^2(W_R)$) and ξ (W_L-W_R mixing angle) which characterize possible right-handed charged weak currents.

Measurement	Diagrams (Fig. 10)	Sensitive to: (lowest order)
1. $P(\beta)/P(\beta)_{V-A}$ (Fermi)	b,c	$1 - 2(\zeta-\xi)^2$
2. $P(\beta)/P(\beta)_{V-A}$ (Gamow-Teller)	b,c	$1 - 2(\zeta+\xi)^2$
3. $\lvert(1. - 2.)\rvert$ above	b,c	$8\lvert\xi\xi\rvert$
4. P_μ in $\pi \to \mu\nu$	b,c	$1 - 2(\zeta+\xi)^2$
5. Muon decay parameters:		
ρ, η	---	---
$(4/3)\rho$	c,d	$1 - 2\xi^2$
ξ	b,c,d	$1 - 2(\zeta^2 + \xi^2)$
ξP_μ (from π decay)	b,c,d	$1 - 4(\zeta^2 + \xi\zeta + \xi^2)$
Rate at endpoint of μ^+ decay spectrum opposite to μ^+ spin	b,c,d	$4(1-x) + (1-\cos\theta) + + 4(\zeta^2 + \xi\zeta + \tfrac{1}{4}\xi^2)$
6. $\dfrac{d\sigma/dy(\bar{\nu}N) - (1-y)^2 d\sigma/dy(\nu N)}{d\sigma/dy(\nu N) - (1-y)^2 d\sigma/dy(\bar{\nu}N)}$	d	$\dfrac{q_R}{q_L} + \dfrac{\sigma_S(1-y)}{\sigma_T(1-\frac{1}{3}y)}$ $[q_R/q_L \geq \zeta^2]$

experiment both to ζ and to ξ thereby is nearly doubled. If instead the rate at ($x = 1$, $\cos\theta = 1$) is measured, the sensitivity to ζ and ξ is very similar.

Figure 11 exhibits the contours[40] which limit ζ and ξ. Measurements of ρ,[45] ξP_μ,[46] $P(\beta)/P(\beta)_{V-A}$ (Gamow-Teller),[47] and the asymmetry in ^{19}Ne β decay[48] provide the important limits. The closed contour corresponds to $\xi P_\mu > 0.946$, from the 1966 measurement of π^+ decay in emulsion at Dubna. The other measurements are of similar vintage.

As an example of one attempt to make new progress in this venerable field, I shall describe briefly the Berkeley - Northwestern - TRIUMF search[49] for right-handed currents at the endpoint of the muon decay spectrum. This is just an advertisement, since no result is available yet. We hope to measure a quantity very similar to ξP_μ with an accuracy approaching 0.1%. A null result then would restrict $M(W^2) \gtrsim$ 600 GeV assuming $\xi = 0$. The measurement exploits the nearly complete polarization in the TRIUMF beam of "surface" muons derived from π^+ decay at rest. The μ^+ are stopped in essentially non-depolarizing pure metal foils within a ≈12 Kgauss longitudinal field that preserves their spin alignment. Within 200 mrad of the beam direction and 10% of the endpoint energy, decay positrons are momentum-analyzed to 0.2%. In the ($x \to 1$, $\cos\theta \to 1$) limit, the standard model requires the muon decay rate to vanish. Near the same limit, any muon-decay component which is mediated by a right-handed current would have its maximum rate. When the ≈12 kgauss "holding" field is replaced by a ≈70 gauss transverse field, the stopped muon spin precesses, removing most of the longitudinal polarization. Data collected under the latter conditions are displayed in Fig. 12, which shows the characteristic sharp edge at $x = 1$. At this early stage of the experiment, the momentum resolution, statistical power, and consistency of the data between different target types have met our expectations, but more analysis remains to be done.

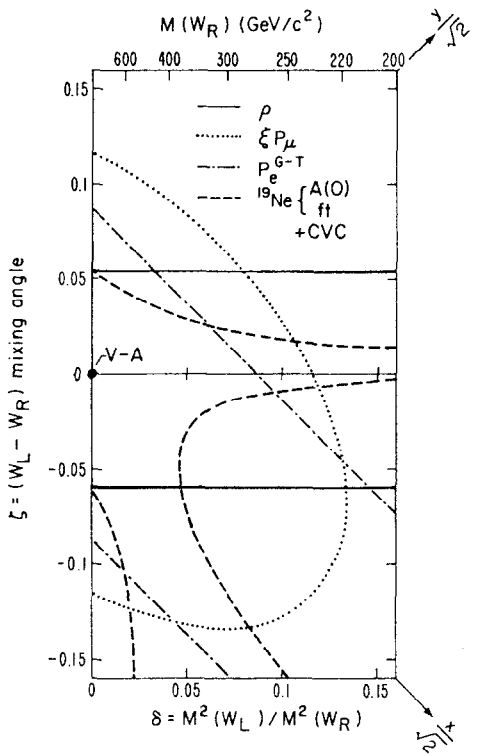


FIG. 11. Present two-standard-deviation limits on the $W_{L,R}$ mass-squared ratio δ and mixing angle ζ describing right-handed charged currents. The contours labelled ρ (Ref. 45) and ξP_μ (Ref. 46) are from measurement of those muon decay parameters; the contour labelled P_e^{G-T} (Ref. 47) is from measurement of β polarization in Gamow-Teller decay; and the dashed contour (Ref. 48) is from measurement of the asymmetry in ^{19}Ne β decay, with additional assumptions. Not shown is the limit from comparison of $d\sigma/dy(\bar{\nu}N)$ with $d\sigma/dy(\nu N)$, which lies $\approx$1.5x beyond that from ρ, but is independent of the ν_R mass.

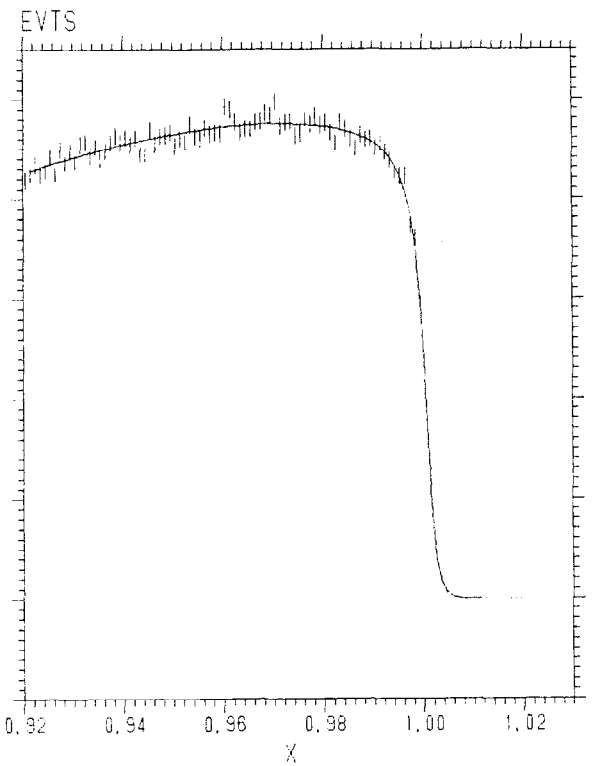


FIG. 12. Endpoint spectrum in reduced e^+ momentum X from decay of unpolarized μ^+ in the Berkeley - Northwestern - TRIUMF spectrometer designed to measure ξP_μ to very high accuracy (Ref. 49). Beam μ^+ (from π^+ decay at rest) stop in a thin metal foil within a region of weak perpendicular (as shown) or strong parallel magnetic field -- the latter to preserve their essentially complete polarization. The experiment consists of a precise comparison of the two endpoint spectra. As seen from the sharp edge, the gaussian part of the e^+ momentum resolution is less than 0.2% rms.

II.2.3 $W_2^{\pm}$ Limits for Any ν_R

If no assumption is made regarding the mass of the (Dirac or Majorana) right-handed neutrino, an interesting limit on right-handed currents has been provided by only one semileptonic reaction: comparison of $\bar{\nu}N$ and νN scattering. Additional strong but model-dependent limits have been calculated based on nonleptonic weak processes: the K_L-K_S mass difference, and the comparison of $K_{\pi 2}$ and $K_{\pi 3}$ decay amplitudes.

Comparison of $\bar{\nu}N$ and νN scattering. Again referring to Fig. 10, it is clear that diagrams (b) and (c) cannot contribute at a measurable level to antineutrino-quark scattering, because the beam is derived from π and K decays which are known to be predominantly left-handed. The limit $y \to 1$, where $y = \nu/E_\nu$, corresponds to backscattering in the center of mass. In this limit, the same argument which was used to explain the small ratio $\Gamma(\pi \to e\nu) / \Gamma(\pi \to \mu\nu)$ requires diagram (a) to be suppressed relative to diagram (d). That is, any finite rate for deep-inelastic $\bar{\nu}$-quark interactions at $y = 1$ would be a manifestation of W_L-W_R mixing.

Of course, experiments measure $\bar{\nu}$-N rather than $\bar{\nu}$-quark scattering; if the longitudinal/transverse ratio σ_S/σ_T is not exactly zero, the chirality of the deep-inelastic W-hadron vertex is not exactly the same as that of the W-lepton vertex. Using Llewellyn Smith's review[50] as a starting point, one can derive

$$\frac{d\sigma/dy(\bar{\nu}N) - (1-y)^2 d\sigma/dy(\nu N)}{d\sigma/dy(\nu N) - (1-y)^2 d\sigma/dy(\bar{\nu}N)} = \frac{q_R}{q_L} + \frac{\sigma_S(1-y)}{\sigma_T(1-\frac{1}{2}y)} \quad ,$$

where

$$q_L(x) = q(x) + \zeta^2 \bar{q}(x)$$
$$q_R(x) = \bar{q}(x) + \zeta^2 q(x) \quad .$$

I have neglected terms of order M(nucleon)/E_ν. Since ζ^2 is less than unity, it is less than q_R/q_L and therefore is bounded by the quotient on the left-hand side of the equation.

The CDHS data[51] were restricted to $x > 0.5$ and $y > 0.66$, in order to limit the systematic errors associated with the subtractions in that quotient (Fig. 13, top graph). In that range, the value 0.000 ± 0.005 was obtained for q_R/q_L when σ_S/σ_T was set to zero, leading to the 90%-confidence limit $|\zeta| \lesssim 0.095$. (The CDHS analysis was carried to higher order in ζ and in M(nucleon)/E_ν.) The bottom graph in Fig. 13 shows the extent to which the best fit $q_L/q_R = 0$ (solid line) is consistent with the experimental points. Bearing in mind that the horizontal bars indicate the width of the bins and not the errors in their mean y, the figure is not totally reassuring; a finer scale might help.

The limit on ζ derived from comparison of $\bar{\nu}N$ and νN scattering is $\approx$1.5x that obtained from measurement of the Michel ρ parameter[45] (Fig. 11). However, as emphasized earlier, the $\bar{\nu}N$ - νN comparison measures the contribution of diagram (d) in Fig. 10, which in a semileptonic process does not require the ν_R to be produced. Therefore the CDHS contribution is unique, and should be refined even further if at all possible.

Calculations of the K_L-K_S mass difference. In the K^0, $\bar{K}^0$ basis the mass matrix is

$$\begin{bmatrix} m & \Delta m/2 \\ \Delta m/2 & m \end{bmatrix} \quad ,$$

with the K_L-K_S mass difference $\Delta m = 2 \langle \bar{K}^0 | H_{eff} | K^0 \rangle$. In the standard model, this matrix element is calculated by means of box diagrams containing two W and two (up or charmed) quark propagators. Originally, the charmed-quark mass was predicted by that calculation.[52] In the $SU(2)_L \times SU(2)_R \times U(1)$ gauge model, there are many more diagrams. Each exchanged W_i can become a W_2 or a (Higgs) ϕ^+.

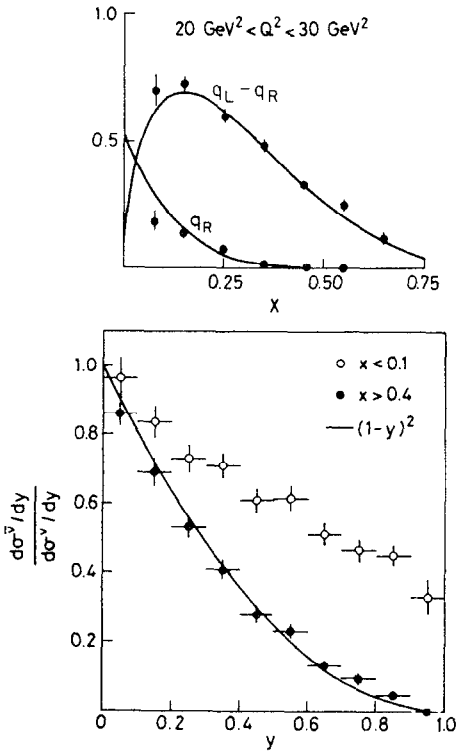


FIG. 13. Distributions from inclusive $\bar{\nu}N$ and νN scattering in the CERN - Dortmund - Heidelberg - Saclay - Peking spectrometer at the CERN SPS (Ref. 51). The top graph shows the distributions in x of q_R and $q_L - q_R$, where q_L (q_R) is the structure function of quarks with left- (right-) handed charged weak coupling (see text). It shows that q_R is negligible for $x > 0.4$. The bottom graph is the ratio of distributions in y for $\bar{\nu}N$ and νN scattering in two ranges of x. The solid line corresponds to $\zeta = 0$, where ζ is the W_L-W_R mixing angle.

Also, one of the W_1's can become a ϕ^0, providing the necessary flavor change; the other W_1 becomes a Z_1 or Z_2. Adding the crossed diagrams and the neutral-boson diagrams with interchanged quark helicity, and squaring, one has a mess.

The K_L-K_S mass difference is calculated to be larger in this left-right symmetric model. Part of the enhancement can be understood on an intuitive basis.[52] Inside the initial or final pseudoscalar, say a $\bar{K}^0$, the s and $\bar{d}$ must have opposite spins and therefore the same helicities. In the purely left-handed diagrams, one quark is forced into the wrong helicity, producing a suppression of order $[M(\text{quark})/M(K)]^2$. (This is a recurring theme in these lectures.) In diagrams with right-handed currents, no such suppression need take place.

Expressing the result for ΔM in terms of the W_1-W_2 mass-squared ratio ζ, deForcrand[54] obtained the general limit

$$\zeta \lesssim \frac{1.6 \times 10^{-2}}{[m_K/(m_s+m_d)]^2 + 1.6} + \frac{\rho^+ - \rho^0}{32} ,$$

where

$$\rho^+ = \frac{2 \log [M(\phi^+)/M(W_1)]}{[M(\phi^+)/M(W_1)]^2 - 1} ,$$

and

$$\rho^0 = \frac{2 \log [M(\phi^0)\cos\theta/M(W_1)]}{[M(\phi^0)\cos\theta/M(W_1)]^2} .$$

Previously, Beall, Bander and Soni[55] had published the special case in which all Higgs diagrams were neglected entirely, and fairly low current-quark masses ($m_s = 150$ MeV) were chosen. (Note that the limit on ζ is proportional to the square of the quark masses.) These authors obtained the limit $\zeta \lesssim 0.0023$ [$M(W_R) \gtrsim 1.6$ TeV] . More conservatively, deForcrand used $m_s + m_d \leq m_K$, and $|\rho^+ + \rho^0| \lesssim 1$.

He obtained the limit $\zeta < 0.047$ [$M(W_R) > 370$ GeV] . Despite the fact that both calculations were made in the context of a particular gauge model, one might view the ability to improve on these limits as an experimental figure of merit. In that case, the difference between the two calculations amounts to a factor of 400 in running time.

Comparison of $K_{\pi 2}$ and $K_{\pi 3}$ Decay Amplitudes. In the soft-pion limit, partially conserved axial-vector current algebra (PCAC) may be used to relate the amplitudes for $K \to 3\pi$ to those for $K \to 2\pi$. Donoghue and Holstein[56] observed that if there is no left-right interference (W_L at one vertex and W_R at the other, possible if $\zeta \neq 0$), the ($\Delta I=3/2$) $K_{\pi 3}$ amplitude is related only to the (small) $\Delta I=3/2$ part of the $K_{\pi 2}$ amplitude. On the other hand, if left-right interference were to exist, the ($\Delta I=3/2$) $K_{\pi 3}$ amplitude would receive a contribution from the $\Delta I=1/2$ part of the $K_{\pi 2}$ amplitude. This would spoil the $\Delta I=1/2$ rule predictions for the $K \to 3\pi$ amplitude and slope parameters, which these authors characterize[56] as being in agreement with experiment to "roughly 10%." On that basis, they obtain the limit $\zeta \lesssim 0.004$.

The calculation which led to this limit appears to have required many approximations: PCAC; the same Kobayashi-Maskawa matrix for left- and right-handed currents; the MIT bag; and others which in the present short preprint[56] have not yet been spelled out. Because cancellations did play a role in that calculation, potentially the limit is numerically controversial. Perhaps a less stringent limit ($\zeta < 0.02$?) would be easier to justify. If PCAC instead had been shown to fail in a 10%-level comparison with experiment, one wonders whether this could have been interpreted as evidence for right-handed weak currents.

Conclusions

I have discussed a number of efforts to probe departures from the standard electroweak model, but I have not been able to present any evidence for such departures. After all, it is the standard model. To my taste, some of the experiments are beautiful. When fundamental symmetries are pushed to new limits, the experiments are of great interest. Unfortunately, from the standpoint of specific alternatives to the standard model, the experiments too often are looking for high orders of improbability -- combinations of unconventional effects. I believe that we need fewer experiments and phenomenological analyses which are useful only in a lowest-order description -- e.g. $(1-\gamma_5) + \eta(1+\gamma_5)$ -- of electroweak processes. We need more interaction between experimenters and builders of particular alternative electroweak models which still are consistent with present data.

I would like to thank R. Cahn, H. Harari, and M. Suzuki for their patience in attempting to increase my understanding of some of the points that I have discussed. I am grateful to those who have contributed new results to this review, often in advance of publication. The preparation of these lectures was supported in part by the Director, Office of Energy Research, Office of Basic Energy Sciences, High Energy Physics Division of the U.S. Department of Energy under Contract No. W-7405-ENG-48.

References

[1] H.E. Haber, G.L. Kane, and T. Sterling, Nucl. Phys. B161, 493 (1979)

[2] B. McWilliams and L.F. Li, Nucl. Phys. B179, 62 (1981)

[3] See e.g. E.D. Commins, Weak Interactions (McGraw-Hill, New York, 1973), p. 81.

[4] T. Kinoshita, Phys. Rev. Lett. 2, 477 (1959)

[5] W. Marciano and A. Sirlin, Phys. Rev. Lett. 36, 1425 (1976)

[6] T. Goldman and W. Wilson, Phys. Rev. D15, 709 (1977)

[7] See e.g. Mark J Collaboration, MIT-LNS Report No. 125 (1982); Jade Collaboration, DESY 82-023 (1982)

[8] D. Bryman et al., Phys. Rev. Lett. 50, 7 (1983)

[9] D. Bryman et al., TRI-PP-82-XX, submitted to Phys. Rev. Lett.

[10] O. Shanker, Nucl. Phys. B204, 375 (1982)

[11] V.A. Lyubimov et al., Phys. Lett. 94B, 266 (1980); V.S. Kozik et al., Yad. Fiz. 32, 301 (1980) [Sov. J. Nucl. Phys. 32, 154 (1980)]; V.A. Lyubimov et al., Zh. Eksp. Teor. Fiz. 81, 1158 (1981) [Sov. Phys. JETP 54, 616 (1981)].

[12] C.S. Wu, in Weak Interactions as Probes of Unification, Virginia Polytechnic Institute, 1980, G.B. Collins, L.N. Chang, and J.R. Ficenec, eds. (AIP Conference Proceedings No. 72), p. 1.

[13] See e.g. G. Steigman, in Unification of Elementary Forces and Gauge Theories, Fermilab, Oct. 20-22, 1977, D.B. Cline and F.E. Mills, eds. (Harwood, London, 1978), p. 453.

[14] R.E. Shrock, Phys. Lett. 96B, 159 (1980); Phys. Rev. D24, 1232 (1981); Phys. Rev. D24, 1275 (1981)

[15] R.S. Hayano et al., Phys. Rev. Lett. 49, 1305 (1982)

[16] Y. Asano et al., Phys. Lett. 104B, 84 (1981)

[17] C.Y. Pang et al., Phys. Rev. D8, 1989 (1973)

[18] R. Abela et al., Phys. Lett. 105B, 263 (1981)

[19] N.J. Baker et al., Phys. Rev. Lett. 47, 1576 (1981)

[20] C.Y. Prescott et al., Phys. Lett. 77B, 347 (1978); Phys. Lett. 84B, 524 (1979)

[21] A.R. Clark et al., Phys. Rev. Lett. 46, 299 (1981); W.H. Smith et al., Phys. Rev. D25, 2762 (1982)

[22] D. Kirch, Aachen preprint PITHA-81/01 (1981)

[23] A. Badertscher et al., Phys. Rev. Lett. 39, 1385 (1977)

[24] See e.g. S.M. Bilenky and B. Pontecorvo, Phys. Lett. 41C, 226 (1978)

[25] S.P. Rosen, in Proceedings, Neutrino '81, Maui, Hawaii, July 1-8, 1981, p. 76

[26] W. Haxton, LASL Preprint LA-UR-82-1626, submitted to Comments on Nuclear and Particle Physics (1982)

[27] H. Primakoff and S.P. Rosen, Ann. Rev. Nuc. Part. Sci. 31, 145 (1981)

[28] D. Bryman and C. Picciotto, Rev. Mod. Phys. 50, 11 (1978)

[29] R. Bardin et al., Nucl. Phys. A158, 337 (1970)

[30] E. Fiorini et al., Nuovo Cimento 13A, 747 (1973)

[31] T. Kirsten and H. Muller, Earth and Plan. Sci. Lett. 6, 271 (1969); B. Srinivasan et al., Econ. Geol. 68, 252 (1973)

[32] E. Hennecke et al., Phys. Rev. C11, 1378 (1975), and references cited therein.

[33] A. Halprin, P. Minkowski, H. Primakoff, and S.P. Rosen, Phys. Rev. D13, 2567 (1976)

[34] T. Kirsten, cited in note added in proof to Ref. 38.

[35] H. Primakoff and S.P. Rosen, Phys. Rev. 184, 1925 (1969)

[36] W. Haxton, G. Stephenson, and D. Strottman, Phys. Rev. Lett. 47, 153 (1981)

[37] M.S Doi et al., Osaka preprints OS-GE-81-28, 81-29 (1981)

[38] P. Minkowski, Nucl. Phys. B201, 269 (1982)

[39] F.T. Avignone, in Weak Interactions as Probes of Unification, Virginia Polytechnic Institute, 1980, G.B. Collins, L.N. Chang, and J.R. Ficenec, eds. (AIP Conference Proceedings No. 72), p. 34.

[40] M. Strovink, in Weak Interactions as Probes of Unification, Virginia Polytechnic Institute, 1980, G.B. Collins, L.N. Chang, and J.R. Ficenec, eds. (AIP Conference Proceedings No. 72), p. 46. The variables ξ and ζ are related to the variables η_{AV} and η_{AA} of M.A.B. Beg et al., Phys. Rev. Lett. 38, 1252 (1977) by $\eta_{AV} \approx -1 + 2(\xi - \zeta + 4\xi\zeta - \zeta^2)$ and $\eta_{AA} \approx 1 + 4(\xi + \zeta^2 - 2\xi\zeta)$. The same variables are related to the variables x and y of B.R. Holstein and S.B. Treiman, Phys. Rev. D16, 2369 (1977) by $x \approx \xi - \zeta$ and $y \approx \xi + \zeta$.

[41] T.G. Rizzo and G. Senjanovic, Phys. Rev. Lett. 46, 1315 (1981); T.G. Rizzo and G. Senjanovic, Phys. Rev. D24, 704 (1981)

[42] Value quoted by A.K. Mann at the DPF Snowmass workshop (July 1982).

[43]W. Hollik, Physikalisches Institut der Universitat Wurzburg preprint (November 1980)

[44]See e.g. M. Gell-Mann, P. Ramond, and R. Slansky, unpublished.

[45]M. Bardon et al., Phys. Rev. Lett. 14, 449 (1965); J. Peoples, Ph.D Dissertation, Columbia University, Nevis Cyclotron Laboratory Report No. 147 (1966).

[46]V.V. Akhmanov et al., Yad. Fiz. 6, 316 (1967) [Sov. J. Nuc. Phys. 6, 230 (1968)]

[47]J. Van Klinken, Nucl. Phys. 75, 145 (1966)

[48]F.T. Calaprice et al., Phys. Rev. Lett. 35, 1566 (1975)

[49]J. Carr, G. Gidal, B. Gobbi, A. Jodidio, C.J. Oram, K.A. Shinsky, D. Stoker, H.M. Steiner, M. Strovink, and R.D. Tripp, "Search for the Effects of a Right-Handed Gauge Boson in Muon Decay: Precise Measurement of the Polarization Parameter ξ", TRIUMF Proposal No. 185 (1980), unpublished.

[50]C.H. Llewellyn Smith, Phys. Lett. 3C, 333 (1972)

[51]H. Abramowicz et al., CERN-EP/81-63 (1981)

[52]M.K. Gaillard and B.W. Lee, Phys. Rev. D10, 897 (1974)

[53]M.K. Gaillard and H. Harari, private communication.

[54]P. deForcrand, Ph.D. Dissertation, University of California, Berkeley, 1982 (to be published).

[55]G. Beall, M. Bander, and A. Soni, Phys. Rev. Lett. 48, 848 (1982)

[56]J.F. Donoghue and B.R. Holstein, University of Massachusetts preprint UMHEP-165 (1982)

GRAND UNIFICATION, PROTON DECAY, AND NEUTRINO OSCILLATIONS

H. H. Williams*
University of Pennsylvania
Philadelphia, PA 19104

I. Grand Unification and Proton Decay

(1) Local Gauge Invariance

Electromagnetic
Weak Isospin
General case

(2) Asymptotic Freedom

(3) Gauge Group & Particle Representation

(4) Proton Lifetime and Branching Ratios

(5) Proton Decay Experiments

Results from Present Experiments
New Experiments (near term)
Future Experiments

II. Neutrino Oscillations

(1) Introduction and Formalism

(2) Present Limits

(3) Future Experiments

© H.H. Williams 1982

I have the privilege of talking to you today about proton decay and neutrino oscillations, two very exciting topics which, although they concern mass scales different by at least twenty-three orders of magnitude, are both expected at some level within the framework of grand unified theories (GUTS). The former, while not absolutely necessary, appears naturally in most GUT models while the latter occurs naturally in some models (e.g., SO(10)) but not in others (SU(5)). I will try to ignore the large presence of experts in the audience and to give a reasonably pedagogical talk. Since time is limited, I will have to give a rather cursory discussion of some topics, but will try to emphasize the important concepts. I will say embarrassingly little about the Higgs sector, the excuse being that it is closely related to the subject of Prof. Susskind's lectures. While there exist many good reviews, I will rely particularly on those of Ellis[1], Langacker[2], and Quigg[3], each of which I consider to be outstanding.

The general concept of "local gauge invariance" is sufficiently important that it is probably useful to review it in some detail. I also find it quite interesting historically and will therefore spend 5-10 minutes reviewing (or at least refreshing in your memory) the concepts of local gauge invariance. I will try to explain some of the motivations for grand unification, including the significance of such questions as "Why is the charge of the electron equal to the charge of the proton?" We then discuss the choice of a gauge group: how arbitrary is it and what are the consequences? Finally, the theoretical introduction concludes with a discussion of the unification mass scale, and the uncertainties in the proton lifetime and branching ratios.

I will then go on to talk about experiments under way to search for proton decay, in particular those experiments which are beginning to present results. Following that I will say a little bit about new experiments to come on soon, (in particular, three large water Cherenkov detectors), and future experiments (what are their capabilities, what is the best design?).

Let us first recall the importance of symmetries of nature. Symmetries of nature are reflected in an invariance of the Lagrangian under symmetry transformations, and this invariance leads to certain conservation laws.

$$\text{symmetry of nature} \Longleftrightarrow \text{Invariance of Lagrangian} \Longleftrightarrow \text{Conservation Laws}$$

For example, for the space time symmetries (see the excellent review by Hill)[4], we have the following correspondences:

$$\text{invariance under space translation} \Longleftrightarrow \text{conservation of momentum}$$

$$\text{invariance under time translation} \Longleftrightarrow \text{conservation of energy}$$

$$\text{invariance under spatial rotation} \Longleftrightarrow \text{conservation of angular momentum}$$

We also know that elementary particles have internal symmetries. For example, the invariance of the Lagrangian under a phase transforma-

tion $\psi \to \psi' = e^{iq\theta}\psi$ implies that there exists a conserved current $\partial_\mu J_\mu = 0$; the existence of this conserved current leads to charge conservation. Similarly, we know that the strong interactions are approximately invariant under isospin rotations (up to effects of the quark masses). If, for example, ψ represents an isospin doublet, such as $\begin{pmatrix} p \\ n \end{pmatrix}$, and we rotate the isospin axes, the description of the state in terms of the new isospin coordinate system is given in general by $\psi' = e^{i\frac{\vec{\tau}}{2}\cdot\vec{\theta}}\psi$ where τ_1, τ_2, τ_3 are just the Pauli matrices. If the Lagrangian is invariant under this rotation, then there exists a conserved isospin current:

$$\vec{J}_\mu = \bar{\psi}\vec{\tau}\gamma_\mu\psi \tag{1}$$

for the case of free Lagrangian

$$\mathcal{L}_0 = \bar{\psi}(i\gamma_\mu\partial_\mu)\psi - m\bar{\psi}\psi \tag{2}$$

We also know now that there is an important and fundamental difference between what we call "global" symmetries and "local" symmetries. To take again a simple example, consider a case where we have two scalar fields ϕ_1 and ϕ_2 with "charged" fields defined in the usual way

$$\begin{aligned} \phi^+ &= (\phi_1 + i\phi_2)/\sqrt{2} \\ \phi^- &= (\phi_1 - i\phi_2)/\sqrt{2} \end{aligned} \tag{3}$$

If we perform the phase rotation, $\phi^+ \to \phi^{+\prime} = e^{iq\theta}\phi^+$, we are essentially changing our definition of what we call ϕ^+ and ϕ^-; the change is, however, the same at all points in space. If the Lagrangian is invariant under this change, we say that it possesses a "global" symmetry or is invariant under global phase transformations.

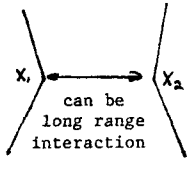
If we consider a long range force, it somehow seems contrary to our concepts of local fields and Lorentz invariance to be required to make the same definition for $\phi^+(\phi^-)$ at widely separated points in space. We can therefore consider requiring that the Lagrangian be invariant even if we perform a phase rotation by different amounts at different points in space.

$$\phi^+ \to \phi^{+\prime} = e^{iq\theta(x)}\phi$$

(equivalent to being allowed to pick different definitions of ϕ^+ and ϕ^- at different points in space). If the Lagrangian is invariant under such a transformation, we say that it possesses a "local symmetry" or is invariant under "local" phase transformations.

$\mathcal{L}$ invariant under independent change of phase at each point

$\Rightarrow$ Local Symmetry



We know in the case of electromagnetism that such a symmetry implies that the particles must be coupled to a field of spin one particles (gauge bosons), in this case the photon.

Local Gauge Invariance of QED

Let us review in more detail local gauge invariance for quantum electrodynamics (QED); it will be the model or "testing ground" which shows us how to proceed to the more general case. If we designate

the spin-1/2 free particle Lagrangian by

$$\mathcal{L}_{free} = i\bar{\psi}\gamma_\mu\partial_\mu\psi - m\bar{\psi}\psi \equiv \mathcal{L}_0 \tag{4}$$

then under the transformation

$$\psi(x) \rightarrow \psi'(x) = e^{iq\theta(x)}\psi(x) \tag{5}$$

we obtain

$$\mathcal{L}_{free} = \mathcal{L}_0 - q\bar{\psi}\gamma_\mu\frac{\partial\theta}{\partial_\mu}\psi \tag{6}$$

i.e., $\mathcal{L}_{free}$ is not invariant under (5). We know, however, that the correct Lagrangian for the fermions includes an interaction term

$$\mathcal{L}_{ferm} = i\bar{\psi}\gamma_\mu(\partial_\mu - iqA_\mu(x))\psi$$

and $\mathcal{L}_{ferm}$ is invariant under (5) if we require that $A_\mu(x)$ also changes according to

$$A_\mu(x) \rightarrow A_\mu'(x) = A_\mu(x) + \partial_\mu\theta(x) \tag{7}$$

We can demand that (7) be true since the additional term does not change any of the physical observables. The gauge field tensor

$$F_{\mu\nu} = \partial_\nu A_\mu - \partial_\mu A_\nu = \begin{pmatrix} 0 & -E_1 & -E_2 & -E_3 \\ E_1 & 0 & B_3 & -B_2 \\ E_2 & -B_3 & 0 & B_1 \\ E_3 & B_2 & -B_1 & 0 \end{pmatrix}$$

is also invariant under (7) so that the usual gauge field kinetic energy term

$$-\frac{1}{4}F_{\mu\nu}F_{\mu\nu}$$

is invariant.

It is useful to rewrite the transformations slightly more formally to facilitate comparison with the more general cases. We designate the phase rotation by $U(\theta)$, in which case the transformation becomes

$$\psi(x) \rightarrow \psi'(x) = U(\theta)\psi(x) \tag{9}$$

The $U(\theta)$ then form a unitary group

$$\begin{aligned} &U(\theta_1)\,U(\theta_2) = U(\theta_1 + \theta_2) \\ &U(0) = 1 \\ &U(-\theta_1)\,U(\theta_1) = 1 \end{aligned} \tag{10}$$

We say that the group is <u>Abelian</u> since the phase rotations commute.

$$U(\theta_1)U(\theta_2) = U(\theta_2)U(\theta_1) \tag{11}$$

This will not be the case for all of the other groups which we consider.

We can now formally write the transformation of the gauge group (7) as

$$A_\mu(x) \rightarrow A_\mu'(x) = A_\mu(x) - \frac{i}{q}(\partial_\mu U)U^{-1} \tag{12}$$

A very important property of QED (and other Abelian groups) is that particles of different charge can couple to the same photon (gauge

field) and the Lagrangian is still invariant under the local gauge transformations. This will not be true for symmetry transformations corresponding to non-Abelian groups.

Gauge Invariance Under Local Isospin Rotations

In 1954, Yang and Mills[5] presented in a very beautiful paper the application of the ideas of local gauge invariance to the case of isospin rotations. It is difficult to present the motivations and conclusions more clearly and succinctly than what they stated in their abstract:

> "It is pointed out that the usual principle of invariance under isotopic spin rotation is not consistent with the concept of localized fields. The possibility is explored of having invariance under local isotopic spin rotations. This leads to ...the existence of a b field which has the same relation to the isotopic spin that the electromagnetic field has to the electric charge....The quanta of the b field are particles with spin unity, isotopic spin unity, and electric charge, $e^{\pm}$ or zero."

Most of the current concepts of theories invariant under local gauge transformations, including the three-point and four-point "gauge-gauge" couplings are realized in this paper. They



3 point and 4 point gauge-gauge couplings

visualized, however, a field coupled to strong isospin multiplets such as (p,n) and (π^+, π^0, π^-). We now believe, of course, that there are gauge fields coupled to "weak-isospin" and to "color," but not to strong isospin.

In detail one proceeds in close analogy with QED. If we let ψ represent an isodoublet, e.g., (p,n), then the most general, local isospin rotation of ψ is given by

$$\psi(x) \rightarrow \psi'(x) = e^{\frac{i}{2}\vec{\tau}\cdot\vec{\omega}}\psi(x) = U(x)\psi(x) \tag{13}$$

As with QED, we find that the free Lagrangian

$$\mathcal{L}_{free} = \bar{\psi}(i\gamma_\mu\partial_\mu)\psi - m\bar{\psi}\psi \tag{14}$$

is not invariant under this transformation, but that a Lagrangian obtained by replacing

$$\partial_\mu \rightarrow I\partial_\mu - igB_\mu \tag{15}$$

is invariant if we demand

$$B_\mu \rightarrow B_\mu' = UB_\mu U^{-1} - \frac{i}{g}(\partial_\mu U)U^{-1} \tag{16}$$

Since ψ is a two component spinor, B_μ and of course the terms depending on U in eq. (16) are 2 x 2 matrices (simply linear combinations of τ_1, τ_2, τ_3). The first term in eq. (16) is simply the transformation of an isospin operator under an isospin rotation and hence should not be surprising; the second term is completely analagous to the corresponding term in eq. (12).

Again proceeding by analogy with QED, Yang and Mills constructed

a gauge field tensor given by

$$F_{\mu\nu} = \partial_\nu B_\mu - \partial_\mu B_\nu - ig[B_\nu, B_\mu] \tag{17}$$

The latter term is, if you like, also present for QED, but vanishes because the rotation operators $U(\theta)$ commute (as do the field operators A_μ). It is the latter term which, when the kinetic energy $F_{\mu\nu} F_{\mu\nu}$ is constructed, leads to the cubic and quartic terms corresponding to the three-point and four-point gauge couplings characteristic of all non-Abelian gauge theories.

Generalization of Yang-Mills Trick

There is just one more step in our discussion of local gauge theories, that is to understand what is required, and what the consequences are, for the general case; this was first realized in an elegant paper by Gell-Mann and Glashow (1961)[6] in which they discussed "generalizations of the Yang-Mills trick."

> "the description of all possible straightforward generalizations of the Yang-Mills trick. We are interested in such generalizations because we do not know for either the strong or the weak interactions, exactly how many intermediate vector fields may be involved (if any)."

They proceed by analogy with the Yang-Mills procedure in imagining multiplets of N fields $\begin{pmatrix} \psi_1 \\ \psi_2 \\ \vdots \\ \psi_N \end{pmatrix}$ analogous for example to

$$\begin{pmatrix} p \\ n \end{pmatrix} \quad \text{or} \quad \begin{pmatrix} \pi^+ \\ \pi^0 \\ \pi^- \end{pmatrix}$$

which transform among themselves under some symmetry operation:

$$\psi(x) \to \psi'(x) = \psi(x) - ig \sum_{i=1}^{n} M_i \Lambda_i(x) \psi(x) \tag{18}$$

The M_i are N x N matrices which will describe the transformation of the N fields belonging to $\psi(x)$. We don't know *a priori* how many such matrices will be required, so we assume that there are n of them. There will in general then be n gauge functions $\Lambda_i(x)$ required to represent the most general local transformation. Eq. (18) is for simplicity the infinitesimal transformation and it is exactly analagous to the infinitesimal form of eq. (13) for isospin.

$$\psi(x) \to \psi'(x) = \psi(x) - i/2g \tau_i \alpha_i(x) \psi(x)$$

Since there are n independent gauge functions, $\Lambda_i(x)$, one must introduce n gauge fields $A_{\mu i}(x)$. Again by analogy with the isospin case, they are assumed to transform according to

$$A_{\mu i} \to A'_{\mu i}(x) = A_{\mu i}(x) - \partial_\mu \Lambda_i(x) + g \sum_{j,k}^{n} c_{ijk} \Lambda_j(x) A_{\mu k}(x) \tag{19}$$

From the requirement that the Lagrangian be invariant under these transformations (see Ref. 6 for the details), one obtains a number of relatively simple, and very powerful conclusions:

$$(1)\ [M_i, M_j] = i c_{ijk} M_k \quad c_{ijk} \text{ antisymmetric and real} \tag{20}$$

$$[M_i, [M_j, M_k]] + [M_j, [M_k, M_i]] + [M_k, [M_i, M_j]] = 0$$

(the latter condition is just the Jacobi identity)

That is, the multiplets $\begin{pmatrix}\psi_1\\ \psi_2\\ \vdots\\ \psi_N\end{pmatrix}$ which we didn't know anything about before, transform according to the N-dimensional representation of a group S_i satisfying

$$[S_i, S_j] = ic_{ijk} S_k$$

and the Jacobi Identity. These are just the conditions which define a Lie Algebra.

(2) the n gauge fields $A_{\mu i}$ transform as a multiplet (the adjoint representation) of S.

(3) All the gauge fields, $A_{\mu i}$, couple to all particle multiplets with the same strength.

(4) The $A_{\mu i}$ couple to one another.

These results are particularly powerful since all the Lie Algebras have been categorized; e.g., one has the series

SU(2), SU(3)...SU(n)

O(7), O(8),

Sp(ν/2) ν = 4,6,8

Exceptional Groups

Hence, in trying to develop a local gauge theory one has a specific list of groups, and hence symmetries, to choose from. Point (3) implies that we are not allowed to tune, or turn off, any of the couplings between gauge bosons and particle multiplets; they are fixed by the requirement of gauge invariance.

In picking a particular group, it is important to know its "dimensionality" which corresponds to the number of gauge fields n, and its "rank" which is simply the number of simultaneously-commuting generators of the group, and hence the number of observable quantum numbers which describe the members of particle multiplets. For SU(ν), the dimensionality is $n = \nu^2 - 1$ and the rank is $\nu - 1$. Consider, for example, multiplets of strong isospin such as (p,n) and (π^+, π^0, π^-) which transform under isospin rotations as multiplets of SU(2). Since the rank of SU(2) is 1, we expect the members of any particle multiplet to be classified by a single quantum number, which is just the third component of isospin. Similarly, SU(3) flavor-multiplets such as the meson nonet, baryon decuplet, etc., should be classified by 3 - 1 = 2 quantum numbers which are usually taken to be hypercharge and the third component of isospin, I_3.

The Electroweak Interaction and Quantum Chromodynamics as Examples

(a) Electroweak

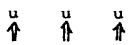
While it is clearly beyond the scope of this talk to discuss in detail the electroweak interaction or quantum chromodynamics, let us see how, armed with our new knowledge, one might proceed. Imagine we are trying in 1965 to apply the concept of local gauge invariance to the weak interaction. At this point it was of course known that leptons appeared to come in pairs or doublets

$$\begin{pmatrix}\nu_e\\ e^-\end{pmatrix}_L \qquad \begin{pmatrix}\nu_\mu\\ \mu^-\end{pmatrix}_L$$

where the L indicates that the charged current weak interaction couples only to left-handed leptons (or right-handed antileptons). This is very reminiscent of isospin, and if we assumed that the weak interaction were invariant under rotations in this "weak isospin" space, that would tend to imply a symmetry under SU(2). It was also known at this time (mostly by trial and error) that at least four fields are required if one wants to simultaneously explain both the weak and electromagnetic interactions. The two simplest group structures corresponding to four gauge fields are U(1) x U(1) x U(1) x U(1) or SU(2) x U(1). Hence the motivation to try the latter is quite strong.

(b) Quantum Chromodynamics

With regards to quantum chromodynamics, we recall first the motivation (or one of the strong motivations) for the introduction of color. The total wave function of a fermion state must be antisymmetric. But consider the simplest quark model wave function for the Δ^{++} which is expected to consist of three u-type quarks with their spins aligned and with relative angular momentum $\ell = 0$.



quark model wave function for Δ^{++}

In this case the isospin, spin, and angular momentum wave functions are all symmetric and hence the total wave function would be symmetric, contrary to the usual requirement for fermions. This problem was "solved" by assuming that there exist three different types or "colors" of quarks (e.g., red, blue and green). This additional degree of freedom then allows one to make the color part of the wave-function (and hence the total wave-function) anti-symmetric:

$$\Delta^{++} = \frac{1}{\sqrt{6}} (u^R u^G u^B + u^G u^B u^R + u^B u^R u^G - u^R u^B u^G - u^B u^G u^R - u^G u^R u^B) \qquad (22)$$

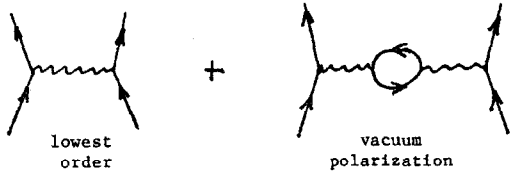
The existence of three colors of quarks also eliminated a discrepancy in the calculated and measured value of the π^0 lifetime, and of course, it is now known that three colors of quarks are required to explain the value of $R = \sigma(e^+e^- \rightarrow \text{hadrons})/(e^+e^- \rightarrow \mu^+\mu^-)$.

Given the existence of this color degree of freedom, it is reasonable to hypothesize that the strong interaction is invariant under local, color rotations. That would imply the existence of massless gauge fields coupled to color; if we furthermore assume that the three colors of quark transform among themselves as a fundamental triplet representation, we would be led to try SU(3) implying the existence of eight colored "gluons."

Asymptotic Freedom

There is one other theoretical development which is crucial for grand unification: that is the concept of asymptotic freedom. Again we proceed by analogy to quantum electrodynamics with which we are more familiar. If we consider electron-electron scattering we have, in addition to the lowest order diagram, higher order

diagrams such as vacuum polarization.



If we sum the higher order diagrams in a consistent fashion (keeping the leading logarithms), their effect can be expressed by writing the cross section in terms of an effective α which changes or "evolves" as a function of Q^2 according to

$$\frac{1}{\alpha(Q^2)} = \frac{1}{\alpha(Q_0^2)} - \frac{1}{3\pi}\ln\left(\frac{Q^2}{Q_0^2}\right) \qquad (23)$$

i.e., if we know the effective α at Q_0^2 then we can determine the effective value of α at Q^2 according to eq. (23). A similar analysis for QCD, and also for the SU(2) and U(1) couplings, leads to three evolution equations:

$$\frac{1}{\alpha_i(Q)} = \frac{1}{\alpha_i(Q_0)} + \frac{1}{12\pi}\left[-4N_G + 11i\right]\ln\left(\frac{Q^2}{Q_0^2}\right) \quad i=2,3$$
$$\frac{1}{\alpha_1(Q)} = \frac{1}{\alpha_1(Q_0)} + \frac{1}{12\pi}\left[-4N_G\right]\ln\left(\frac{Q^2}{Q_0^2}\right) \qquad (24)$$

where g_1, g_2, g_3 are the coupling constants for U(1), SU(2) and SU (3) respectively, $\alpha_i = g_i^2/4\pi$ and N_G is the number of generations or families. A significant point is that the couplings for SU(3) and SU(2), both of which are non-Abelian theories, decrease while the effective coupling for U(1), which is an Abelian theory, increases.

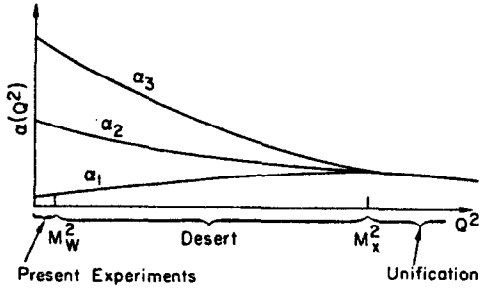


Fig. 1. Variation of the running fine structure constants α_3, α_2, and α_1 of the SU(3), SU(2), and U(1) subgroups of G. Above the scale M_X of spontaneous symmetry breaking they approach a common value. It is assumed that there are only two scales (M_W and M_X) of symmetry breaking and that there is a plateau or desert with no new thresholds in between.

The fact that the coupling constants evolve in such a way that at some value of Q^2 they may all have the same value is critical to the concept of grand unification.

Motivation for Grand Unification

We have then our Standard Model:

SU (3)	x	SU(2) x U(1)
octet of colored gluons		W^+, W^-, Z^0,
gauge symmetry under color rotations		symmetry broken by Higgs ⇒ W^+, W^-, Z^0 massive
unbroken ⇒ massless gluons		
coupling: g_3, strong		coupling: g_2, g_1 weak

In spite of the spectacular success of the Standard Model, there are a number of questions which have not been answered, questions which motivate one to search for a still "grander" theory that incorporates the Standard Model into a single framework.

(1) Are g_1, g_2, g_3 really unrelated? Is the value of $\sin^2\theta_W$ (which relates the g_1 and g_2 coupling) really arbitrary?

(2) Why is the electron charge equal to the proton charge (to a few parts in 10^{-20})?

We are now in a position to understand better the significance of this question. You recall that

$$e^2 = \frac{g^2 g'^2}{g^2+g'^2} \Rightarrow \frac{1}{e^2} = \frac{1}{g^2} + \frac{1}{g'^2}$$

where g and g' are the usual "electroweak" definitions of the SU(2) and U(1) coupling constants. The coupling constant g must be the same for quark and electron doublets since we saw that all non-Abelian gauge theories have universal couplings. In general, there is no reason for g' to be the same for quarks and leptons; however, if SU(2) and U(1) are imbedded in a larger group they would have to be the same.

(3) Can we understand why the weak coupling is left-handed, and why the ν is massless (if it is)?

(4) There exist a very large number of coupling constants to describe our standard model.

g_1, g_2, g_3

$m_d, m_u, m_c, m_s, m_t, m_b, m_e, m_\mu, m_\tau$

3 Cabibbo angles θ_{ci}

1 Kobayashi-Maskawa phase, δ

m_h, m_W

2 non-perturbative vacuum parameters

It seems unlikely (unaesthetic?) that a theory should have so many fundamental constants. The hope is that by imbedding SU(3) x SU(2) x U(1) into a larger "grand-unified" group one may obtain relations between many of these constants.

(5) Our "religion" doesn't allow global symmetries. Rigorous baryon number conservation (or lepton number conservation) would appear to imply a global symmetry since there doesn't seem to exist any long range gauge fields coupled to these quantities.

Gauge Group and Particle Representation

What are the clues to the gauge group? We now try in the same manner as we did for the electroweak and QCD to obtain clues as to the correct group structure for grand unification. If we wish to imbed SU(3) color which is rank two, and SU(2) and U(1), each of which is rank one, into a larger group, then we must have a group of at least rank four.

SU(3) rank 2 x SU(2) rank 1 weak T_3 x U(1) rank 1 weak hypercharge $\Rightarrow$ group of rank 4 minimum

We can then simply write down all the Lie groups of rank 4 and examine their suitability in the light of the knowledge we currently have.

Lie groups of rank 4

SU(2) x SU(2) x SU(2) x SU(2) O(5) x O(5)	do not contain SU(3)
SU(3) x SU(3)	would require u, d, s in triplet
G x G , O(8), O(9), Sp(8), F	have only real representations
SU(5)	just fine

The first two possibilities do not contain SU(3) as a sub-group. SU(3) x SU(3) would require the u, d and s quarks to be in a triplet which does not seem to be in accord with what we currently know. The next set of groups have only real representations. While some of these groups do contain SU(3) x SU(2) X U(1) as a sub-group, they lead to "vector-like" theories, which are parity conserving. While adjusting the masses of the quarks or intermediate vector bosons that couple in a left- or right-handed fashion can yield theories with parity violation at present energies, it may at least be said that these models do not naturally yield the maximal parity violation that is observed. Also the use of real representations allows additional mass terms in the Lagrangian which permit the masses of the fermions to be arbitrary. The final choice, SU(5), satisfies all of what we currently know as we see below.

Let us now consider the possible multiplet representations. Our basic family consists of 15 particles.

$$\overbrace{\begin{pmatrix} u \\ d \end{pmatrix}_L \quad u_R \downarrow \bar{u}_L \quad d_R \downarrow \bar{d}_L}^{\times 3 \text{ for color}} \; ; \quad \begin{pmatrix} \nu_e \\ e^- \end{pmatrix}_L \quad e^-_R \downarrow e^+_L$$

The left-handed up and down quark occurs as a weak isospin doublet while the right-handed up and down quark we assume in the usual electroweak model to be isospin singlets. We also know that we consider the left-handed component of the $\bar{u}$ and $\bar{d}$ quarks to be weak isospin singlets. Now since any gauge theory conserves helicity, we may consider all the left-handed helicity states together or all the right-handed helicity states. It will therefore prove convenient to work with the states $\bar{u}_L$ and $\bar{d}_L$ in place of u_R or d_R. Each of the quarks, of course, comes in three colors. In addition, we have a lepton doublet which contains the left-handed ν_e and e^-, and the right-handed component of the electron which we assume to be an isospin singlet. We will again work with the state e^+_L instead of e_R.

Now let us ask how these states are classified under SU(3) x SU(2) x U(1). We know that the up and down quarks are a color triplet and a weak doublet. Similarly, we know that the u and d anti-quarks transform as a color antitriplet and as a weak isospin singlet. Similarly, as we already noted, the $(\nu_e, e^-)_L$ transforms as a color singlet and a weak isospin doublet. Finally, the e^+_L is a singlet under both color and weak isospin.

$$(u,d)_L + \bar{u}_L + \bar{d}_L + (\nu_e, e^-)_L + e^+_L$$
$$(3,2) \quad 2(\bar{3},1) \quad (1,2) \quad (1,1)$$

color triplet; weak doublet; etc.

Now what are the possible representations of SU(5) and in particular, how are they classified under SU(3) x SU(2) x U(1)? That is, if we look at the elements of a particular representation one can ask what the classification of those elements is under SU(3) x SU(2) x U(1). I will not list all the possibilities, but two of them are of particular interest--the so-called $\bar{5}$ and the 10. The classification of these two multiplets under SU(3) x SU(2) x U(1) corresponds precisely with what occurs in reality.

$$5 = (\bar{3},1) + (1,2)$$
$$10 = (3,2) + (\bar{3},1) + (1,1)$$

color triplet; weak doublet

Specifically, the observed particle states can be placed in these representations in the following fashion:

$$\bar{5} = \begin{pmatrix} d^c_R \\ d^c_G \\ d^c_B \\ e^- \\ \nu_e \end{pmatrix}_L \qquad 10 = \left(\begin{array}{ccc|cc} 0 & u^c_B & -u^c_G & -u_R & -d_R \\ -u^c_B & 0 & u^c_R & -u_G & -d_G \\ u^c_G & -u^c_R & 0 & -u_B & -d_B \\ \hline u_R & u_G & u_B & 0 & -e^+ \\ d_R & d_G & d_B & e^+ & 0 \end{array}\right)$$

$$f = C\,\bar{f}^T$$

Now in SU(5) we expect to have 24 gauge bosons and we can again ask how these gauge bosons are classified according to SU(3) x SU(2) x U(1). We obtain

$$24 = (8,1) + (1,3) + (1,1) + (3,\bar{2}) + (\bar{3},2)$$

G^α_β $\quad W^\pm, W^0 \quad$ B $\quad \bar{X}_\alpha \quad X_\alpha$

octet colored gluons: $\bar{Y}_\alpha \quad Y_\alpha$

$\alpha = 1,2,3$

Hence we have an octet in color which transforms as a singlet in weak isospin that corresponds to our octet of color gluons. In addition, we have three bosons which transform as a singlet under color, but as a triplet in weak isospin, and a single gauge boson which transforms both as a singlet under color and under weak isospin. Clearly these four correspond to the $W^\pm, W^0$ and B bosons which we require for the standard electroweak model. In addition we obtain twelve additional bosons, six of which transform as a color triplet and a weak isospin isodoublet, and six of which transform as a color antitriplet and a weak doublet. These twelve bosons carry both color and flavor, and will connect quarks to antileptons and quarks to antiquarks. They will, therefore, mediate baryon number and lepton number violating processes. Recall that the fact that we have local gauge invariance prohibits us from tampering with these couplings. They must exist if our theory is to be invariant under local gauge transformations with SU(5) as the gauge group.

We may now go on to consider the possible groups of rank 5.

Groups of Rank 5

SU(2) SU(2) SU(2) SU(2) SU(2)	no SU(3) factor
SO(11), SP(10)	only real representations. Also no 15 or 16 dimensional representation
SU(6)	$15 = (3,2)+(3,1)+(\bar{3},1)+(1,2)+(1,1)$ Doesn't agree with observed breakdown
SO(10)	*Looks OK*

Analogous to our treatment of the group of rank 4 there is really only one group which appears completely satisfactory--that is SO(10). Depending on the Higgs structure, there are two possible ways in which SO(10) can break down. It may contain SU(5) directly as a subset or alternatively it may break down first to SU(4) x SU(2) x SU(2) and subsequently to SU(3) x U(1).

$$SO(10) \begin{cases} \nearrow SU(5) \rightarrow SU(3) \times SU(2) \times U(1) \searrow \\ \searrow SU(4) \times SU(2) \times SU(2) \nearrow \end{cases} SU(3) \times U(1)$$

While we will not discuss the SO(10) model in any detail, it is useful to note one or two things concerning the structure of the gauge bosons in the particle multiplets. In the simplest scheme one has at least 45 gauge bosons

$$45 = 24 + 10 + \overline{10} + 1$$

These include the ones discussed above in connection with SU(5) as well as more heavy bosons which can mediate proton decay. The simplest particle representation in this case is irreducible

$$16 = 10 + \bar{5} + 1$$

colorless isosinglet, $Q_{em} = 0$

$\Rightarrow$ ideal candidate for ν_R.

and includes in addition to the 10 and the $\bar{5}$ a state which is a singlet under both color and weak isospin, and which has charge equal to 0. This is then an ideal candidate for a right-handed neutrino. Thus a ν_R and hence massive neutrinos fit naturally into SO(10). In this case the simplest particle representation is also irreducible which, although perhaps not necessary, is at least aesthetically more satisfying.

Repercussions of Unification

Let us now go on to consider some of the repercussions of grand unification. Here we consider specifically the SU(5) model.

(a) The sum of the quantum numbers of the particles in a representation must be equal to 0. Thus, since Q_{em} is one of the generators of SU(5) the sum of the charges of the particles in any representation must be equal to 0. In particular this then implies

$$Q_{\bar{d}_R} + Q_{\bar{d}_B} + Q_{\bar{d}_G} + Q_{e^-} + 0 = 0$$

$$Q_{\bar{d}} = +1/3$$

where the charge is expressed in units of the electron charge. But

we also know that $Q_u = Q_d + 1$ since the same W boson couples to lepton doublets and to quark doublets (the W boson must have a charge equal to that of the electron). Thus it must be true that $Q_u = 2/3$ and

$$Q_p = 2Q_u + Q_d = 1$$

SU(5) then explains why the charge of the proton is identically equal to the charge of the electron.

(b) As we have already seen, there is no room in either the $\bar{5}$ or the 10 for ν_L^c (i.e., ν_R). Such a state could occur as a singlet. Thus the existence of a right-handed neutrino or similarly massive neutrinos is allowed in SU(5), though it does not occur as naturally as would seem to be the case for SO(10).

(c) There exist new heavy bosons usually denoted by X,Y which carry both color and flavor and consequently couple quarks to anti-quarks and quarks to anti-leptons. The interaction terms in the Lagrangian are of the form

$$\frac{1}{\sqrt{2}}\, g\, \bar{X}_{\alpha\mu}(+\bar{d}_{\alpha R}\gamma^{\mu} e_R^{+} + \epsilon_{\alpha\beta\gamma}\bar{u}^{c}_{\beta L}\gamma^{\mu}u_{\beta L} + \bar{q}_{\alpha L}\gamma^{\mu}e_L^{+}) + \text{H.C.}$$

$$\frac{1}{\sqrt{2}}\, g\, \bar{Y}_{\alpha\mu}(-\bar{d}_{\alpha R}\gamma^{\mu}\gamma_{eR}^{c} + \epsilon_{\alpha\beta\gamma}\bar{u}^{c}_{\beta L}\gamma^{\mu}d_{\beta L} - \bar{u}_{\alpha L}\gamma^{\mu}e_L^{+}) + \text{H.C.}$$

Here the indices α, β, γ are color indices and repeated indices are to be summed over. These interaction terms may be schematically represented as shown in Fig. 2.

(d) One of the most significant results from grand unification is the prediction for low energy couplings, and in particular for the value of $\sin^2\theta_w$. The two fundamental parameters of our grand

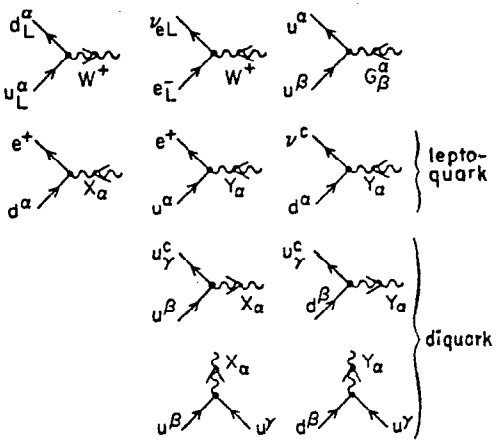


Fig. 2. Typical vertices of the gauge bosons. The W bosons carry flavor but no color, the gluons carry color but not flavor, and the X and Y carry both. The X and Y bosons are referred to as lepto-quark bosons because of the vertices on the second line and as diquark bosons because of the vertices on the third line.

unification model are the mass scale of the X and Y boson, M_X and the coupling constant $g(M_X)$. Grand unification of course implies that the coupling constants for the separate groups SU(3), SU(2), SU(1) must be the same when evaluated at momentum transfers corresponding to the mass scale M_X

$$\alpha_1(M_X) = \alpha_2(M_X) = \alpha_3(M_X) \qquad \alpha_i = g_i^2/4\pi$$

Using our definition of $\sin^2\theta_W$ within the electroweak model

$$\sin^2\theta_W = \frac{e^2}{g^2} = \frac{g'^2}{g^2+g'^2}$$

and the fact that correct normalization of the U(1) operator implies that

$$g' = \sqrt{\tfrac{3}{5}}\, g_1$$

we obtain

$$\sin^2\theta_W(M_X) = 3/8$$

Hence we expect $\sin^2\theta_W$ at momentum transfers corresponding to M_X to have a value of 3/8. In order to compare this prediction to our measurements at lower energies we must now evolve this prediction for $\sin^2\theta_W$ to lower Q^2. We do this using our expressions for evolution derived from the renormalization group equations (eq. 24). It is then a few line derivation to show that

$$\sin^2\theta_W(Q^2) = \frac{3}{8}\left[1-\frac{\alpha}{4\pi}\left(\frac{110}{9}\right)\ln\frac{M_X^2}{Q^2}\right] + \begin{matrix}\text{higher}\\ \text{order}\\ \text{corrections}\end{matrix}$$

$$\sin^2\theta_W(M_W) \approx 0.20 \pm .01$$

This result corresponds to using the one loop renormalization group equations and does not include the effect of thresholds. If we include higher order corrections and threshold effects (still assuming, however, that there are no new thresholds between M_W and M_X), we obtain

$$\sin^2\theta_W(M_W) = 0.208 + 0.004(\overbrace{N_H}^{\#\ \text{Higgs (light)}}-1) + 0.006\ \ln\left(\frac{400\ \text{MeV}}{\Lambda_{\overline{MS}}}\right)$$

where the uncertainty due to the number of light Higgs bosons, N_H, and the value of $\Lambda_{\overline{MS}}$ has been explicitly included. For the usual assumptions of $N_H = 1$ and $\Lambda_{\overline{MS}} = 100$–$200$ MeV we obtain

$$\sin^2\theta_W(M_W) = 0.214 \pm 0.002$$

This may be compared with the most recent experimental value obtained from an analysis of deep inelastic neutrino scattering and the measurement of parity violation in electron deuterium scattering where the effect of both weak and electromagnetic radiative effects has been included. The biggest effect is simply the radiation of a hard photon by the outgoing muon in deep inelastic charged current neutrino scattering. The value of $\sin^2\theta_W$ determined is correlated with the value of $\rho = M_W^2/M_Z^2\ \cos^2\theta_W$. Including an estimate of the statistical and systematic errors one obtains

$$\sin^2\theta_W(M_W) = 0.223 - 0.49(1-\rho^2) \pm 0.010 \pm .004$$

The value of ρ is expected to be 1.0 for any model in which the Higgs bosons are either weak isospin singlets or doublets. This naive

value of 1.0 is, however, renormalized to $\rho^2 = 0.983$ by the higher order corrections. Assuming this value one then has

$$\sin^2\theta_W(M_W) = 0.215 \pm 0.014$$

The agreement of the theoretical prediction with the experimental value is certainly excellent, and it is this agreement which really motivates the idea of the desert; that is, if there existed many new thresholds between M_W and M_X the prediction for $\sin^2\theta_W$ would be different.

Let us now consider baryon number violation and to begin with we consider several ideas to help break down our prejudices against baryon number violation.

(a) First of all, our new religion tells us that "The only exact symmetries are gauge symmetries." Since the long-range interactions which would be implied by a gauge field coupled to baryon number do not appear to exist, one can conclude that there is no reason for baryon number to be rigorously observed. (It should be noted, however, that the SU(5) theory yields exact B-L conservation, which one would have to object to also, if one is to be fully consistent.)

(b) Secondly, an argument is given by Hawking[8] that black holes conserve only quantum numbers associated with long-range gauge fields, in particular, the mass m, angular momentum J, and the charge Q. In the vicinity of a black hole one may then expect to get baryon number violation by the following process:

$$p + BH(m,J,Q) \rightarrow BH(m', J + \tfrac{1}{2}, Q + 1) \rightarrow BH(m,J,Q) + e^+$$

(c) There is an argument by Zeldovich[9] that one can obtain an effective $\Delta B \neq 0$ interaction from the existence of virtual black holes with mass $\approx$ Planck mass (10^{19} GeV). Such an interaction would yield a rather long proton lifetime

$$10^{45} - 10^{50} \text{ years}$$

but again gives an existence proof that baryon number may not be rigorously conserved.

The interaction for baryon decay (Fig. 3) becomes, for momentum transfers much less than M_X, an effective four fermion interaction in exactly the same way as the weak interaction becomes an effective four fermion interaction for momentum transfers much less than M_W

$$\frac{1}{4}\mathcal{L}_{GU} = \frac{1}{\sqrt{2}} G_{GU} (\epsilon_{\alpha\beta\gamma} \bar{u}^c_{\gamma L} \gamma_\mu u_{\beta L})(2e^+_L \gamma_\mu d_{\alpha L} + \bar{e}^+_R \gamma_\mu d_{\alpha R})$$
$$-(\epsilon_{\alpha\beta\gamma} \bar{u}^c_{\gamma L} \gamma_\mu d_{\beta L})(\bar{\nu}^c_e \gamma_\mu d_{\alpha R}) + \text{H.C.}$$

The effective grand unification coupling constant, G_{GU}, is related to the actual coupling constant g and to M_X

$$\frac{G_{GU}}{\sqrt{2}} = \frac{g^2}{8M_X^2} = \frac{g^2}{8M_Y^2}$$

in exactly the same way as G_F is related to the coupling constants g and M_W.

$$\frac{G_F}{\sqrt{2}} = \frac{g^2}{8M_W^2}$$

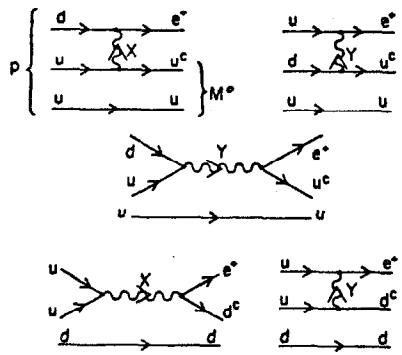


Fig. 3. Diagrams for $p \to e^+\bar{u}u$ or $e^+\bar{d}d$. The $\bar{q}q$ pair can form into neutral mesons such as π^0, ρ^0, ω, η, $\pi^+\pi^-$, etc. The first three diagrams also contribute to the decay of bound neutrons if the spectator u quark is replaced by a d.

The amplitude for proton decay will therefore be proportional to $1/M_X^4$ and the lifetime will therefore be proportional to M_X^4.

$$\tau_p = C \frac{M_X^4}{M_W^5}$$

Now how do we determine the unification mass M_X? Again we use the relation between the coupling constants

$$e^2 = \frac{g^2 g'^2}{g^2+g'^2} \Rightarrow \frac{1}{e^2} = \frac{1}{g^2} + \frac{1}{g'^2} \Rightarrow \frac{1}{\alpha} = \frac{1}{\alpha_2} + \frac{5}{3}\frac{1}{\alpha_1}$$

and the evolution equations (24) to show in a few lines that

$$\frac{8}{3}\frac{1}{\alpha_3(Q)} - \frac{1}{\alpha(Q)} = \frac{11}{2\pi} \ln \frac{Q^2}{M_X^2}$$

If we then plug in the values of $\alpha_3(Q)$, ($\alpha_s(Q)$) and $\alpha(Q)$ which we measure at low Q^2, we can determine M_X. Again there are a few subtleties; namely, we must include the threshold effects at M_W and M_X, we must evaluate α at M_W

$$\alpha(M_W^2) = 1/128.5$$

and we should obtain a somewhat more accurate prediction if we use the "two loop" renormalization equations. We then obtain

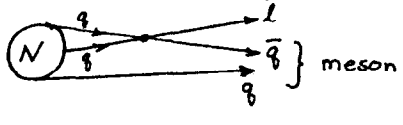
$$M_X(\text{GeV}) = 2.4 \times 10^{14} \times (1.5)^{\pm 1} \times \left[\frac{\Lambda_{\overline{MS}}}{.16\text{GeV}}\right] \times \left[\frac{1}{1.5}\right]^{N_H - 1} \times (1.2)^{F-3}$$

where the uncertainty due to higher order terms, the treatment of thresholds, existence of heavy Higgs, etc., is explicitly shown as

well as the dependence on $\Lambda_{\overline{MS}}$, the number of light Higgs N_H and the number of families of particles, F.

Given M_X and $g(M_X)$, what are the uncertainties in the proton lifetime? One of the largest uncertainties arises from the mixing between the different generations of fermions which is in general, relatively arbitrary and unknown. In the event that the light quarks which exist within the proton are strongly coupled to heavier quarks or leptons, the mass of which exceed the proton mass, the effective amplitude for proton decay would be strongly suppressed. In the case of minimal SU(5) (i.e., with the simplest Higgs schemes), however, this problem is enormously simplified; the only allowed mixings are expected to be of the same order as the Cabibbo angle.

The other large uncertainty in the proton lifetime has to do with estimates of the hadronic matrix elements. That is, given, for example, the fact that two quarks within the nucleon couple to an outgoing anti-quark and anti-lepton, we must know the probability that the outgoing anti-quark joins with the remaining quark in the



nucleon to form a meson. A number of different theoretical approaches have been used to estimate the hadronic matrix elements. If we make an estimate of the combined uncertainty arising from our lack of knowledge of the mixing angle, the hadronic matrix elements, and M_X, and if we assume

$$\Lambda_{\overline{MS}} = 0.16^{+.01}_{-0.08} \text{ GeV}$$

we then obtain for our estimate of the proton lifetime

$$\tau_p = 3.2 \times 10^{29^{+2.1}_{-2.5}} \text{ years}$$

The fact that this lifetime is substantially shorter than the values typically quoted a year or two ago results from the fact that currently the most popular value of $\Lambda_{\overline{MS}}$ is closer to 0.2 than to 0.5.

What can we say about the branching ratios expected for proton decay? These will again depend on the matrix elements, the mixings between light and heavy quarks, assumptions concerning phase space, and treatment of the pion recoil and the spin of the quark. Table 1 presents the results of calculations of the branching ratios by a number of different groups using a number of different techniques.[10] Of particular interest, perhaps, is the fact that the branching ratio into $e^+\pi^o$, which is a very important decay mode for the water Cherenkov experiments, is expected to be reasonably large in most calculations, though a large value is not guaranteed. Other points of interest are that the branching ratio to neutrinos is of the order of 10% and that the branching ratio to muon or kaon is expected to be of that order or smaller. Particularly important branching ratio measurements are the ratio of the decay probability to e^+ versus $\overline{\nu}_e$, to μ^+ versus e^+, and to final states which contain strange hadrons.

Table 1. Predictions for branching ratios for proton decay into the major two body modes in the SU(5) model. (a) - (f) correspond to different theoretical assumptions concerning the hadronic matrix elements, phase space, quark spins, etc. See reference 10 for a discussion and references to the original papers.

Mode	(a) REC	(b) NR	(c) R	(d) R	(e) R	(f) NR	(f) REC	(f) R
$e^+\pi^o$	31	37	9	13	31	36	40	38
$e^+\rho^o$	15	2	21	20	21	2	7	11
$e^+\eta$	11	7	3	.1	5	7	1.5	0
$e^+\omega$	18	18	56	46	19	21	25	26
$\nu_e^c\pi^+$	12	15	3	5	11	14	16	15
$\nu_e^c\rho^+$	6	1	8	7	8	1.0	2.6	4
μ^+K^o	1	19	--	7	.5	18	8	5
$\nu_\mu^cK^+$	2	0	--	.5	--	0	.2	.6

It is useful to say a few words concerning the general classification of models and selection rules. We may consider three rather broad categories of grand unification models.[11]

1. Standard GUTS. By "standard" grand unification models we mean those which are non-supersymmetric and which involve only one new mass scale, that is, the superheavy mass scale of the grand unification. It is interesting to note that all "standard GUTS" models predict the following selection rules and decay modes:

$$\Delta B = \Delta L \qquad N \to e^+X_{NS},\ e^+X_S$$
$$\Delta S/\Delta B = -1,0 \qquad \mu^+X_{NS},\ \mu^+X_S$$
$$\Delta I = \tfrac{1}{2} \text{ for } \Delta S = 0 \qquad \bar{\nu}X_{NS},\ \bar{\nu}X_S$$

where B, L, S are the total baryon number, lepton number and strangeness of the initial or final state and X_{NS} indicates that the hadrons in the final state have S = 0, and X_S is a final state with $S \neq 0$. Of particular interest is a subset of these standard models, those in which the grand unification group G breaks down to SU(3) x SU(2) x U(1) directly at a mass scale M_X.

$$G \to SU(3) \times SU(2) \times U(1)$$

All such theories include the prediction for $\sin^2\theta_W$ presented above and are referred to as the "3-2-1 desert theories."

2. Supersymmetric GUTS. For this class of theories the dominant decay modes are generally $K^+\bar{\nu}$ and $K^0\mu^+$. Predictions for $\sin^2\theta_W$, though not as unambiguous as in the 3-2-1 desert theories, are consistent with experimental data. Predictions of the proton

lifetime are much less certain, however, though values can be obtained which are consistent with the present lower limits.

3. Low Mass Scales. In this category one generally includes all models with more complicated interactions such as

$$qqql^c\phi, \quad qqql^c l^c l^c \phi$$
$$\text{Higgs} \qquad \text{Higgs}$$

Because the decay rate for these "higher dimensional" interactions is suppressed relative to the simpler interactions, for example in SU(5), these models can tolerate gauge bosons and Higgs bosons with lower masses than the scale of 10^{14} GeV. In general, these models have little predictive power for either $\sin^2\theta_W$ or for the proton lifetime.

Proton Decay Experiments

Now let us go on to look at the arsenal of experiments which are preparing to attack the question of whether protons decay or not. We will discuss these experiments in the order of those that are presently operating, those which will become operational in the near term, and those experiments which have been proposed for the future. In fact, the Irvine-Michigan-Brookhaven experiment has just recently become fully operational, and it should be noted that of the future experiments, only the Frejus experiment is approved and under construction.

Presently Operating

Homestake
Soudan I
Kolar Gold Fields
Mt. Blanc

Near Term

Irvine-Michigan-BNL (now operating)
Harvard-Purdue-Wisconsin
Kamioka, Japan

Future

Frejus Tunnel (approved)
Soudan II
Homestake upgrade
Pennsylvania
Gran Sasso

The first two experiments I will cover extremely briefly. The Pennsylvania-Brookhaven experiment,[12] which is located in the Homestake Mine, is the original water Cherenkov nucleon decay experiment. It comprises approximately 150 tons of water, doped with wave shifter, and the detector is composed of an array of 2 m x 2 m x 1.2 m modules (Fig. 4). The experiment is located at a depth of 4500 mwe (meters water equivalent) and is therefore quite deep. They have obtained three apparently-contained muon decays where the muon or pion yielding the decay was traveling either horizontally or upwards. It can not be excluded that these events come from background sources. From this observation they obtain a lower limit on the lifetime of $\tau_p > 1.5 \times 10^{30}$ yr.

A second small experiment[13] which has been operating for some time is a prototype for a baryon decay detector constructed and opera-

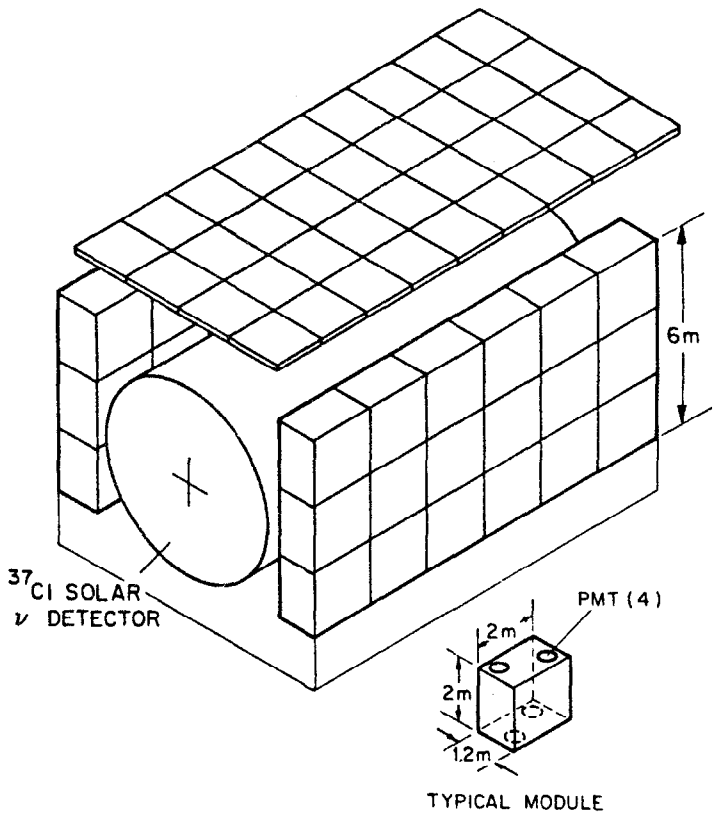


Fig. 4. Schematic of the Homestake proton decay experiment operated by a Brookhaven-University of Pennsylvania collaboration. Each module is filled with water doped with wave-shifter. The detector includes end walls which are not shown.

ted by a Minnesota-Argonne collaboration and located in the Soudan Mine (depth 1700 mwe). It consists of 35 tons of iron ore interlaced with proportional tubes as shown in Fig. 5. They have observed one neutrino event and no candidates for baryon decay leading to a lifetime limit of $\tau_p \geq 1 \times 10^{30}$ yr. In addition to studying the backgrounds relevant to a proposal for a larger experiment, they have made some nice measurements of events with multiple muons. It should be noted that they record the pulse height from each proportional tube as well as whether a hit occurred or not. A typical event from a single muon is shown in Fig. 6.

The two other operating experiments I want to talk about in some detail, because they have some rather interesting results. The first is the experiment in the Kolar Gold Fields, a collaboration of the Tata Institute, Osaka and Tokyo.[14] This detector (shown in Fig. 7) is 140 tons and consists of iron plates approximately 1.2 cm thick with 10 cm x 10 cm proportional tubes (effective thickness .5 cm Fe) between each plate. The detector is roughly 4 m x 4 m x 6 m and is located very deep, 7600 mwe, where only two muons per day are incident. It has been operating for approximately 500 days. The statistics for the events observed to date are shown in Table 2. Of particular interest is the fact that they attribute 11 events in the detector to neutrino interactions and 6 events are considered as nucleon decay candidates. Three of nucleon decay candidates are not fully contained, rendering them perhaps somewhat dubious. However, three of the candidates are fully contained, and it is interesting to examine these candidates. Fig. 8 provides an overview simply

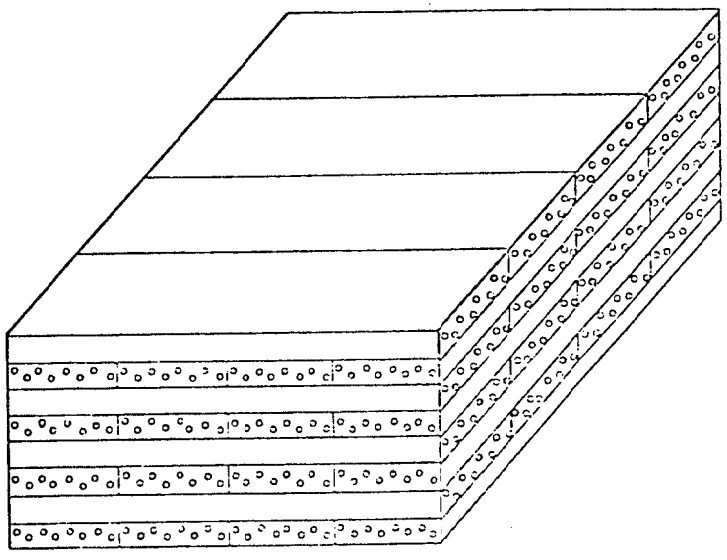


Fig. 5. Schematic of the 35 ton Minnesota-ANL prototype detector operating in the Soudan Mine. Proportional tubes, which record ionization information, are interspersed in an iron-ore media.

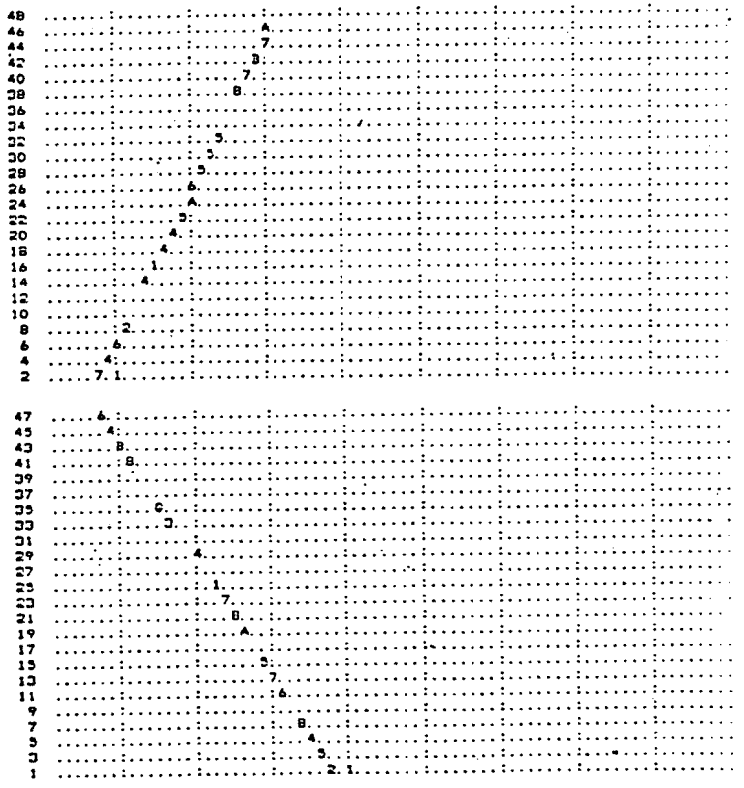


Fig. 6. A typical muon event recorded in the Minnesota-ANL detector.

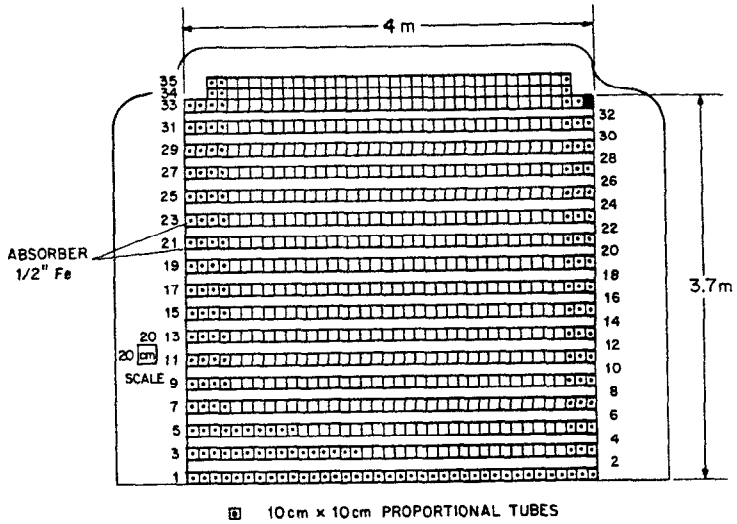


Fig. 7. Schematic of the 140 ton baryon decay detector operated by a Tokyo-Osaka-Tata Institute collaboration in the Kolar Gold Fields. The effective sampling thickness between each layer of proportional tubes in 1.7 cm Fe.

Table 2. Event statistics for the Tata, Osaka, Tokyo experiment in the Kolar Gold Field.

Atmospheric Muons	788
Parallel Muons	9
ν interactions in rock with tracks in detector ($\theta > 55^{o}$)	28
ν interactions in detector	11
Nucleon decay candidates (3 fully contained)	6

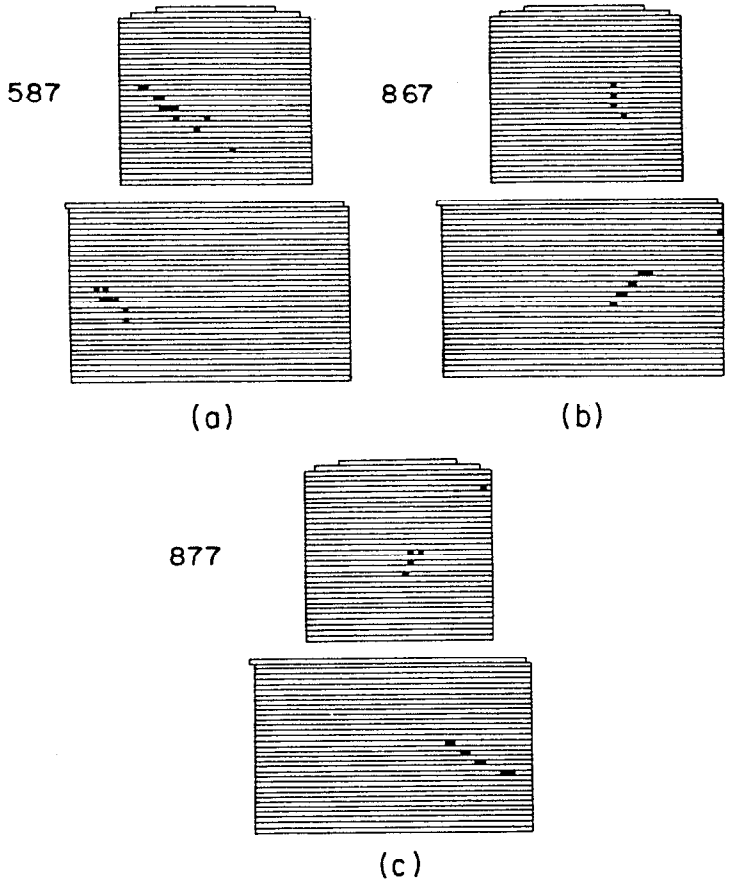


Fig. 8. Overall view of the three, confined baryon decay candidates observed in the Kolar gold field detector.

illustrating the nature of the confinement within the detector. Since a paper now exists describing these events and since time is limited, I will not describe each of them in detail. However, it is interesting to examine one of them to obtain a feeling for the quality of the event, the capabilities of the detector, and the extent to which the event can be excluded as having been produced by a neutrino interaction. I simply repeat the discussion as presented by the Japaese-Indian collaboration in their paper. Fig. 9 presents

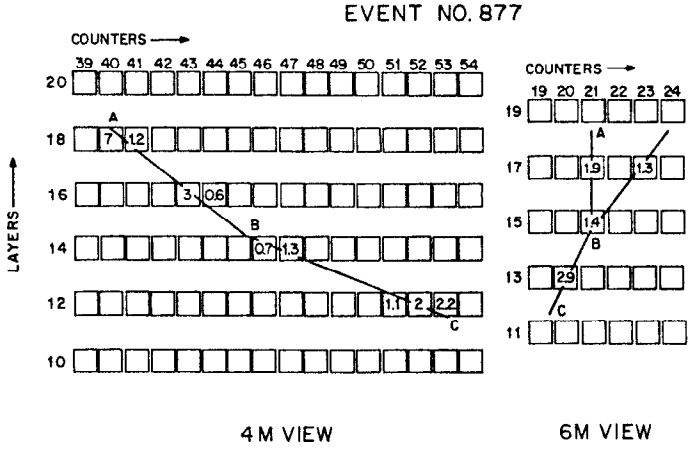


Fig. 9. Expanded view of a baryon decay candidate observed in the Kolar gold field detector. The numbers in each cell indicate the ionization energy loss in units of minimum ionizing tracks.

a blown-up view of event No. 877. The numbers in each box are the pulse height measured in units of minimum ionizing particles. The lines drawn show their interpretation of the trajectory of the particles. The trajectory B-C is interpreted as having been produced by a non-showering particle while that along BA is taken to be a shower-like configuration. The motivation for the latter interpretation is both the topology, which is not consistent with a single track, and also the existence of energy depositions much larger than minimum ionizing. (Recall that there does exist an additional hit shown in Fig. 8 that is not reproduced in Fig. 9.) The kink at point B (the angle between the two tracks is $\simeq 157^{\circ}$) is believed to be consistent with having been produced by the Fermi motion. The total energy of the event is estimated as $\simeq 1$ GeV, the energy of the shower having been estimated to be $\simeq 400$ MeV, and the energy of the non-showering track to be ≈ 450 MeV. The event is considered to be a strong candidate for $N \rightarrow e^{\pm} \pi^{\mp}$.

One may now consider the probability that the event was produced by a neutrino interaction. Possible interactions are

$$\overset{(-)}{\nu_{\mu}} + Z \rightarrow \mu^{\pm} \pi^{0} Z'$$

$$\overset{(-)}{\nu_{e}} + Z \rightarrow e^{\pm} \pi^{\mp} Z'$$

$$\overset{(-)}{\nu} + Z \rightarrow \overset{(-)}{\nu} \pi^{\pm} Z'$$

$\pi^{\pm}$ → CEX at B

The overall rate for the first two reactions assuming an energy interval of 1 ± 0.4 GeV is approximately 1/yr according to their estimation. Assuming the vertex to be at point B, it would be quite unlikely for a neutrino interaction to yield such a back-to-back configuration. The experimenters also consider a neutrino interacting at point A with a large angle back-scatter occurring at point B. This configuration is also deemed to be unlikely and the experimenters thus estimate a total rate from these sources of $< .05$ events/year. The other possibility considered is a single pion produced a point C which then charge exchanges at point B. However, the very low probability for charge exchange leads the experimenters to conclude that this background is essentially negligible.

A summary of the estimated energy, the expected background from neutrino interactions, and the interpretation of the three events as nucleon decay candidates are presented in Table 3. The experimenters consider these events to be completely inconsistent with having been produced by neutrinos and they are therefore tentatively considered as evidence for proton decay. If true, then these three events would correspond to a proton lifetime of $\approx 7 \times 10^{30}$ years. The general conclusion of Perkins[15], Fiorini[16] and others who have reviewed these results is that these are very intriguing events, that they are not easy to explain as background, but that the coarseness of the detector makes it difficult to conclusively exclude the neutrino interaction hypothesis.

We now go on to discuss a very nice experiment which has just recently become operational, the so-called Nusex experiment[16] which is operated by a Frascati-Milano-Torino-CERN collaboration and which is located in the Mt. Blanc Tunnel. This experiment has the advan-

Table 3. Summary of contained Nucleon Decay Candidates in the KGF experiment.

Event	Decay Mode	Energy Estimates	ν Background
		(MeV)	
587	$e^+\pi^o$	$E_e \approx 500$ $E_{\pi^o} \approx 500$	< 0.5
867	$\bar{\nu}\pi^+$	$E_\pi \approx 435$	< 0.5
877	$e^+\pi^-$	$E_e \approx 400$ $E_\pi \approx 450$	< 0.5

tage of being very fine-grained, quite deep, and extremely well-calibrated. It consists of 150 tons, has 1 cm iron plates, and uses conductive plastic tubes with cathode strip readout to obtain two coordinates per sampling as shown in Fig. 10. In total, the experiment has 90,000 channels of electronics which yield a spatial

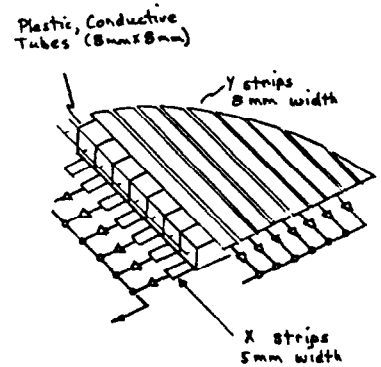


Fig. 10. Schematic of the track chamber construction utilized in the NUSEX experiment. Operated by a Frascati-Milano-Torino-CERN collaboration, the 140 ton fine-sampling iron plate calorimeter is located in the Mt. Blanc tunnel.

resolution of ≈ 1 cm. There is, however, no measurement of the ionization loss of the particles. The experiment is located at a depth of 5000 mwe which corresponds to a muon flux of ≈ 20 muons/day.

The experiment has been calibrated in a neutrino beam as well as in a pion beam and an electron beam. Fig. 11 presents the response of the detector to a 500 MeV/c pion, while Fig. 12 shows the signature corresponding to 500 MeV electron. Clearly the identification of pions and electrons in this detector is far superior to that of the Kolar Gold Fields detector which has much coarser sampling. Shown in

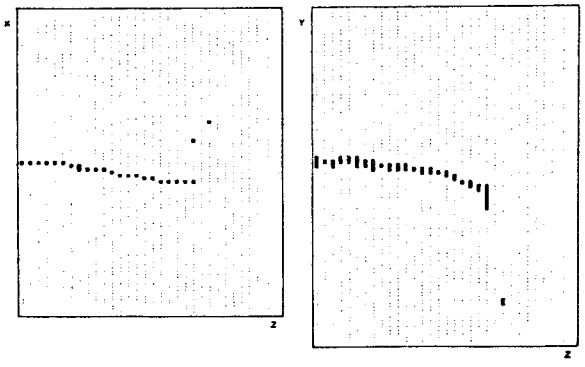


Fig. 11. Response of the NUSEX detector to a 500 MeV/c pion.

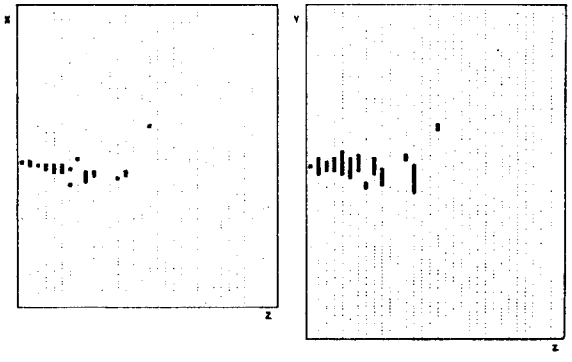


Fig. 12. A 500 MeV/c electron in the NUSEX detector.

Fig. 13 is a fairly typical neutrino interaction. In the calibration of the detector with neutrino interactions, the results of which I show you in more detail in a moment, the experimenters use a 10 GeV beam and a bare target to simulate as closely as possible the atmospheric neutrino flux. A comparison of the neutrino flux they used with that calculated for atmospheric neutrinos is presented in Fig. 14. The main uncertainty is that the PS beam has 99% ν_μ's while the atmospheric neutrino flux is expected to consist of approximately one-third ν_e's. The experiment has been running for several months and has observed numerous events of muon bundles and stopping muons. Fig. 15 presents what appears to be a rather well defined neutrino interaction, a very preliminary interpretation of which would be one of the following two possibilities:

$$\overset{(-)}{\nu}_e N \rightarrow e^{\pm} \pi^{\mp} N'$$

$$\overset{(-)}{\nu}_\mu N \rightarrow \mu^{\pm} \pi^{o} N'$$

The experiment also has another event obtained the Friday before the Paris conference which is by now quite famous since it does not resemble a typical neutrino interaction. This event is well-contained within the detector and is presented in Fig. 16. While a detailed interpretation of this event in terms of neutrino background has not been completed, the potential significance of the event is made clear by an examination of the topology of the neutrino events obtained when their prototype detector was exposed to the PS neutrino beam; 210 events were obtained with the plates of the detector orthogonal

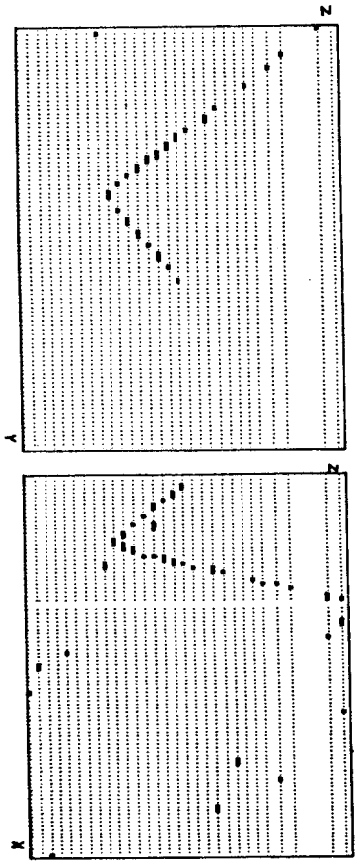


Fig. 13. Observation of a neutrino event in the NUSEX detector while exposed to a neutrino beam at CERN.

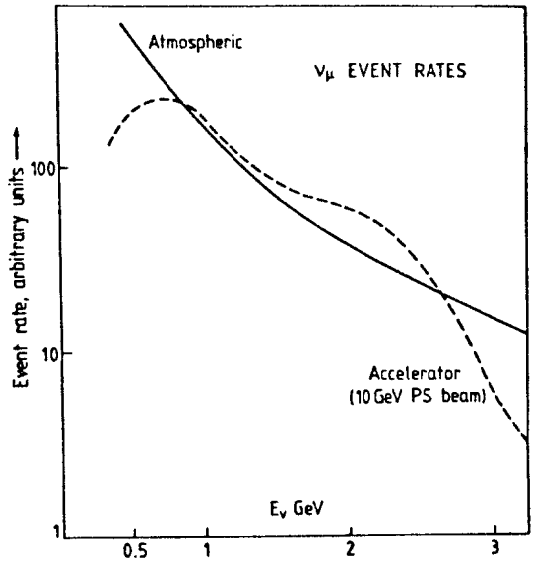


Fig. 14. Comparison of the calculated atmospheric flux (solid line) with that employed at a neutrino test beam at CERN (dashed line).

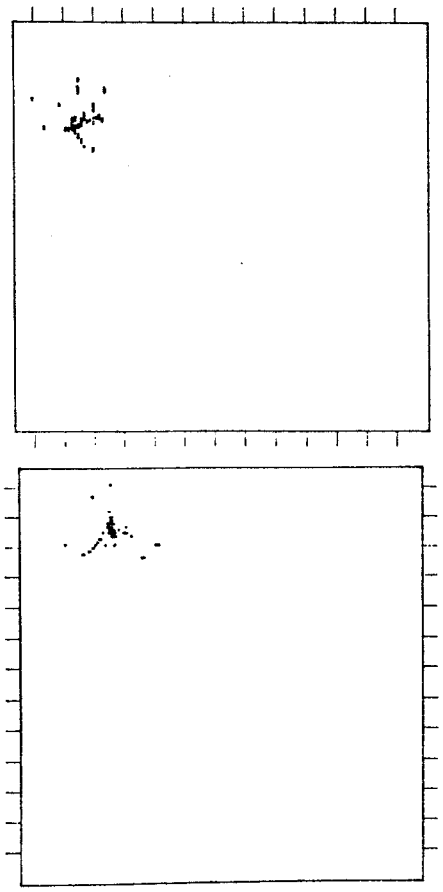


Fig. 15. An event recorded during operation of the NUSEX detector in the Mt. Blanc tunnel. The topology of the event is consistent with a neutrino interaction.

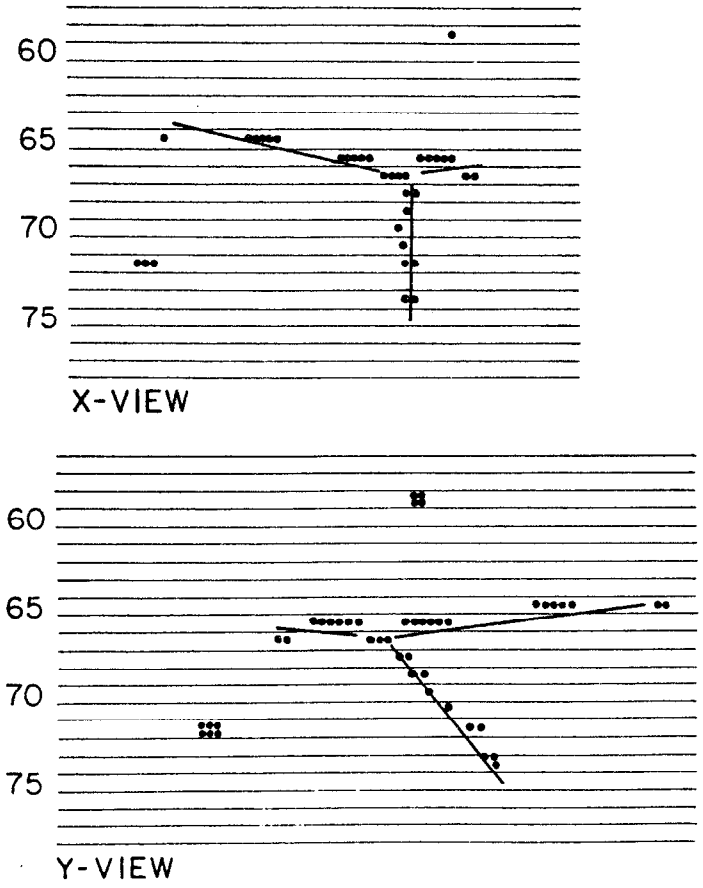
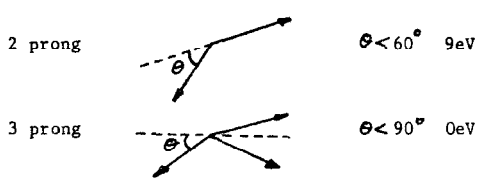


Fig. 16. A proton decay candidate observed in the NUSEX detector. It is not conclusively excluded that a neutrino interaction is the source of the event, though such a topology appears somewhat unlikely.

to the neutrino beam while an additional 184 events were obtained with the plates rotated by 45 . The event statistics in terms of 1 prong, 2 prong, and 3 prong events are:

1 prong	58%	209 + 19 with shower
2 prong	27%	98 + 6 with shower
3 prong	8%	32

The experimenters then define what one might call a nucleon decay topology in which 2 prong events must have an angle between the two tracks of $< 60^\circ$ (as defined below), and for 3 prong events one of the tracks must have an angle of $< 90^\circ$ with respect to the direction opposite the resultant momentum of the other two tracks



Only 3% of the total observed neutrino interactions in the test run satisfy these topological constraints. If, in addition, one demands that the observed energy lie within 20% of that of the proton mass, the experimenters estimate that only 0.5% of neutrino interactions will simulate nucleon decay (for their detector). Hence the event shown in Fig. 16 is very interesting and can not be readily interpreted as a neutrino interaction. Reasons for caution include the fact that, as noted above, there are only 1% ν_e's in the neutrino test beam and that while the calibration was performed with two different configurations of the iron plates, neutrino interactions in the actual detector will be almost isotropically distributed. The event shown in Fig. 16 is consistent according to a preliminary interpretation with either of the decays

$$p \rightarrow \bar{\nu} K^{*+} \hookrightarrow \pi^+ + \pi^+ + \pi^-$$

$$p \rightarrow e^+ \pi^+ \pi^-$$

$$p \rightarrow \mu^+ K^\circ$$

However, I repeat once again that the experimenters are not at this time making any claims for the observation of baryon decay. Clearly, their detector is sufficiently sophisticated that one may hope to learn a great deal in the near future.

New Experiments (Near Term)

The biggest of the water Cherenkov experiments is being built by the Irvine-Michigan-Brookhaven collaboration at the Morton Salt Mine in Ohio.[17] Its real strength is that it has a total of 9000 tons of water with a fiducial volume of $\simeq$ 4000 tons. A potential weakness is that it is located only 1700 mwe below the surface and therefore must contend with $\approx 10^8$ muons/year; one must, therefore, do an excellent job rejecting these muon events if one is to be sensitive to only a few proton decays per year. The accuracy to which the angle of a particle may be determined, based on the reconstruction of the Cherenkov ring, is $\approx 7^\circ$ for a non-showering track (limited by multiple scattering) and 12° for a shower; in addition the Fermi momentum smears the actual angle of the track by $\approx 20^\circ$. The posi-

tion resolution of the vertex is estimated to be 70 cm, and the energy resolution is estimated to be $\approx$ 20% per track (dominated again by the effects of Fermi momentum), though if one sums the energy of the two tracks, one expects an energy resolution of about 10%. The detector is particularly sensitive to decays to purely electromagnetic final states, such as $e^+\pi^0$. The detector is now completely filled, with all the photomultipliers installed and operating. A schematic of the detector is shown in Fig. 17. I now show you a few typical events

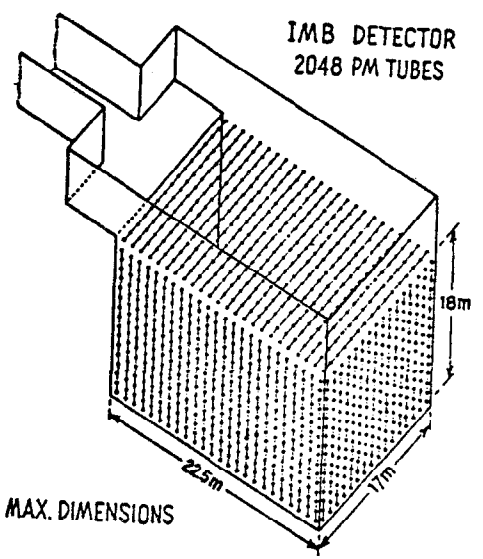


Fig. 17. Schematic of the Irvine-Michigan-Brookhaven (IMB) proton decay experiment located in a Morton salt mine. Approximately two thousand 5" photomultipliers mounted on the faces of the cube view Cherenkov light produced in the pure water.

obtained last spring when the detector was filled with 23 feet of water. At that time, only the bottom photomultipliers were installed. Figs. 18a and 18b show events in which two muons traverse the detector. Each dot corresponds to a photomultiplier which produced a signal, the size of the dot being proportional to the number of photoelectrons. In Fig. 18c is shown a stopping muon as evidenced by the fact that the circle of hits is not filled in the center. Shown in Fig. 19 is an event observed when the detector was filled with all photomultipliers installed. In this event, the muon traverses just a corner of the detector entering through one side and exiting through the other side just a short distance away. Each line represents a single photoelectron. Finally we show in Fig. 20 a Monte Carlo calculation of the expected pattern of hits for an $e^+\pi^0$ event. The sides of the detector have been unfolded onto a plane, and the Cherenkov rings corresponding to the e^+ and the $\gamma\gamma$ are visible. Both pulse height and timing information may be used to reconstruct the event topology.

A second large water Cherenkov experiment is being built by a Harvard-Purdue-Wisconsin collaboration to be located in a mine in Utah.[18] It will have 800 tons of water with the 800 five-inch photomultipliers uniformly distributed throughout the volume. In addition, the experiment has mirrors along the inside of the tank to increase the amount of light detected, and shielding and an active veto along the edge. A view of the detector is shown in Figs. 21 and 22. The combination of the volume distribution of the photomultipliers plus the active shielding is expected to yield a much better

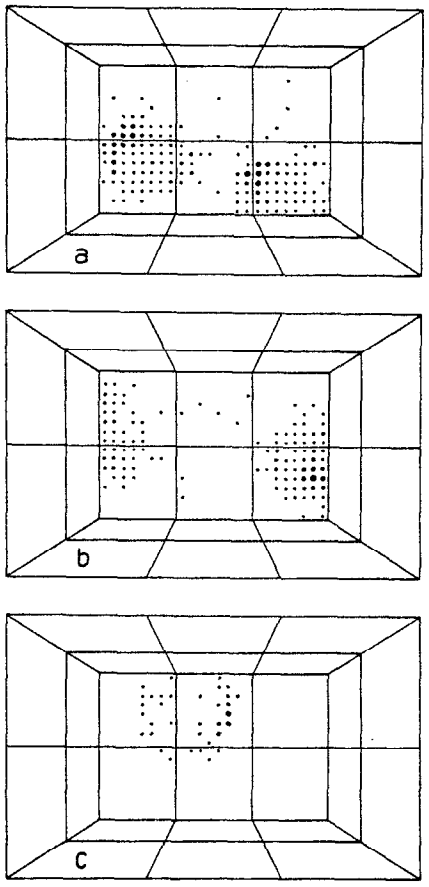


Fig. 18. Three events observed in the IMB experiment with 23 feet of water and only the bottom photomultipliers installed. Each dot indicates a photomultiplier with a signal above threshold, the size of the dot being proportional to the pulse height. (a) and (b) Events with two muons traversing the detector; (c) A stopping muon.

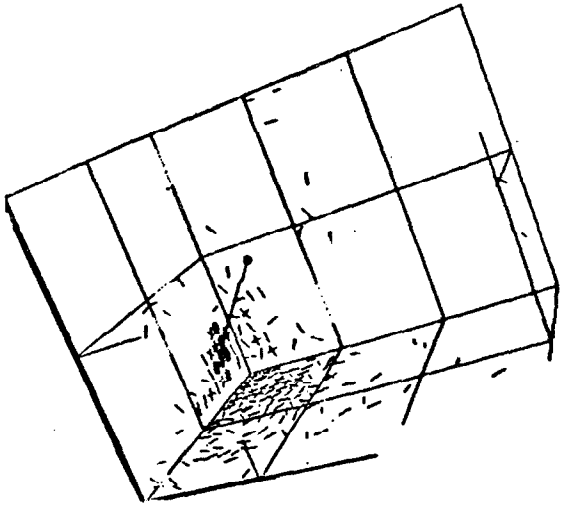


Fig. 19. An event observed in the IMB experiment with all photomultipliers installed. Each line represents a single photoelectron (approximately). A muon traverses a corner of the cube.

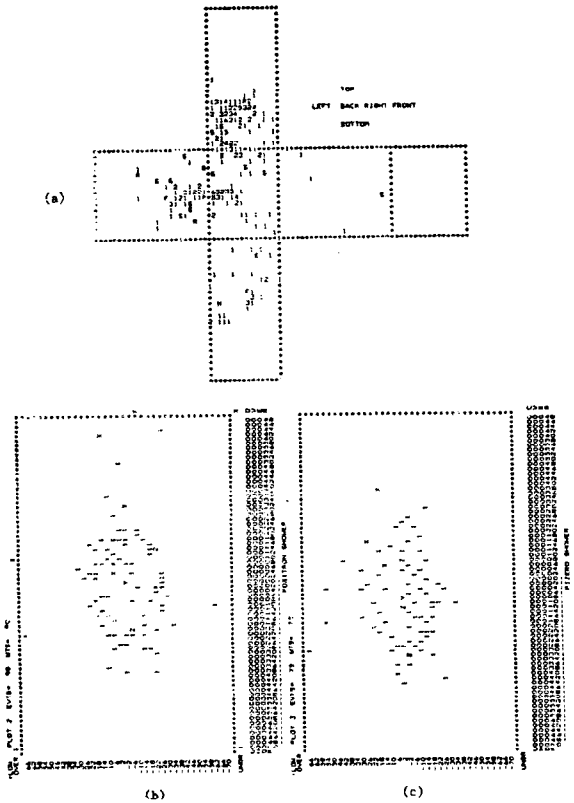


Fig. 20. A Monte Carlo representation of a $p \rightarrow e^{+}\pi^{o}$ decay in the IMB detector.

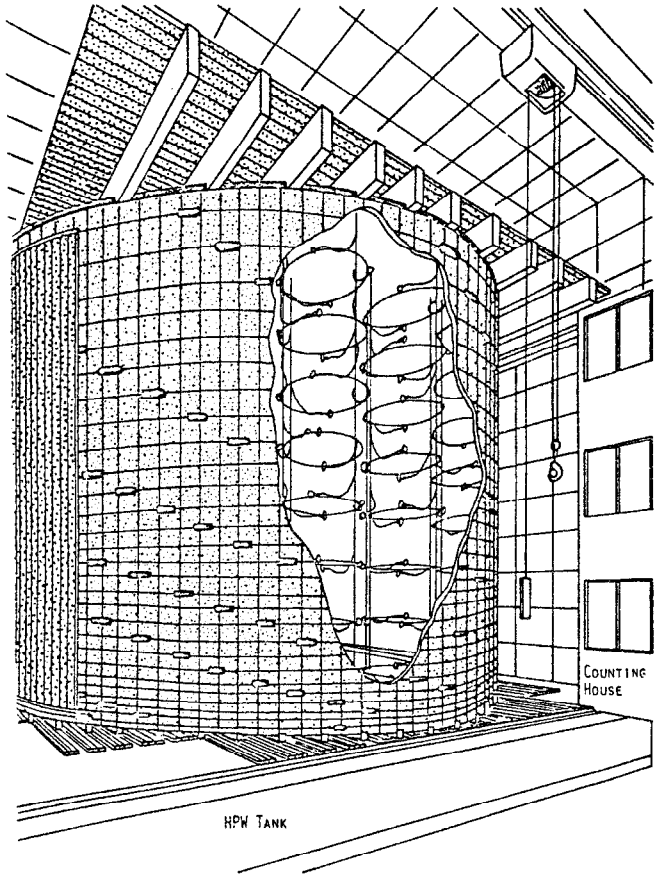


Fig. 21. Cutaway view from the side of the Harvard-Purdue-Wisconsin (HPW) water Cherenkov counter. Photomultipliers mounted on columns are distributed throughout the volume.

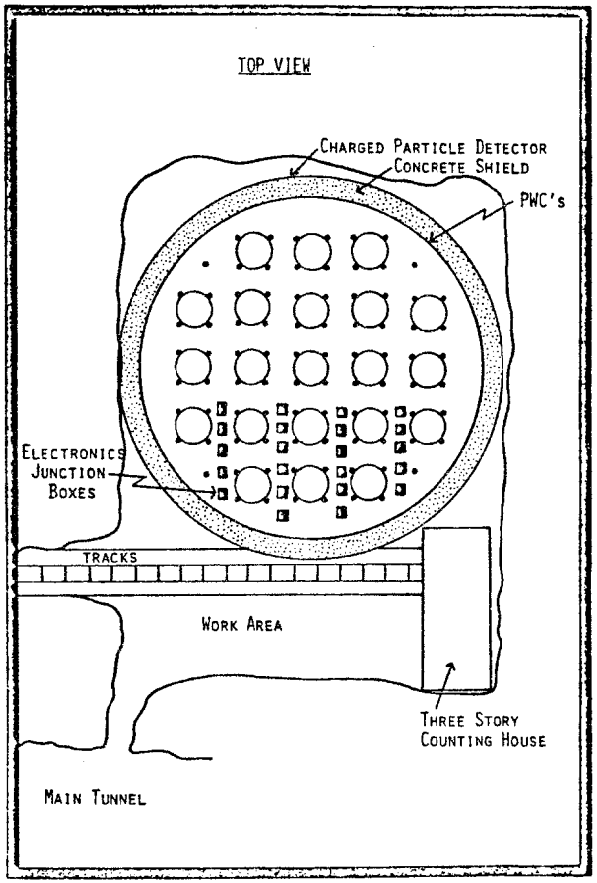


Fig. 22. Top view of the HPW detector indicates the passive and active shield and the layout of the photomultipliers.

rejection against particles entering from the side. Located also at a depth of 1700 mwe, the experiment has been designed with emphasis on rejecting the $\approx 10^8$ muon events/year.

A third experiment coming along which looks very nice is being constructed by a KEK-Tokyo-Tsukuba collaboration at the Kamioka Mine in Japan.[19] Particular advantages of this experiment are not only that it is deeper than the other two water Cherenkov experiments (it is located at 2700 mwe corresponding to $\approx 6 \times 10^6$ muons/year) but in addition the experimenters have developed, in collaboration with Hamamatsu, a 20" diameter photomultiplier tube. The 1000 photomultipliers will be mounted on the surface of the cylindrical volume, as shown in Fig. 23, and will cover $\approx 20\%$ of the surface area (as compared to $\approx 1\%$ for the IMB experiment). The total volume of the detector should be ≈ 3400 tons with a fiducial volume of 1000 tons. Excellent pulse height information should be obtained for each event, and the experimenters do not intend to use precise timing on each photomultiplier (though sufficient timing information is available to allow identification of muon decays). Fig. 24 presents for their detector a Monte Carlo calculation of a typical $e^+\pi^\circ$ event. The Cherenkov rings of the e^+ and the two photons for the π° are clearly visible. In the absence of confusing backgrounds, the pulse height information available from the photomultipliers would, in fact, be sufficient to distinguish different decay modes such as $e^+\nu$, $e^+\eta$, $e^+\pi^-$, etc., according to the Monte Carlo calculations.

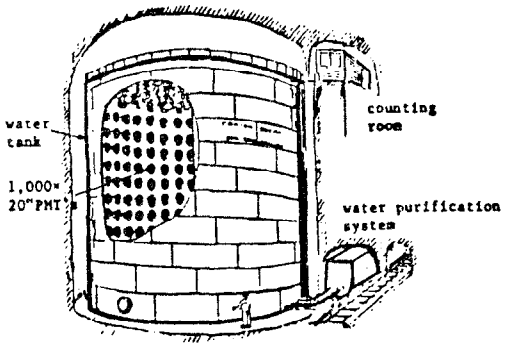


Fig. 23. Schematic of the KEK-Tokyo-Tsukuba water Cherenkov detector to be located at the Kamioka mine in Japan. The 20" diameter hemispherical photomultipliers are mounted on the surface of the cylinder and cover a full 20 per cent of the area.

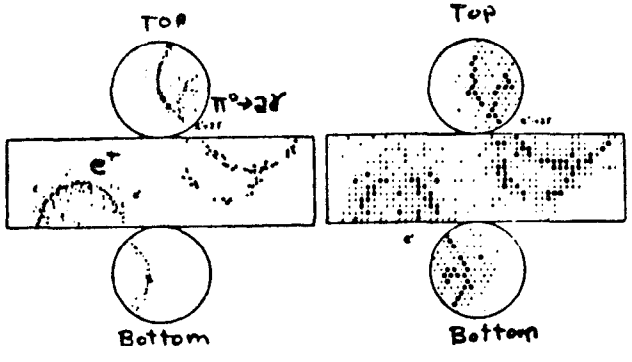


Fig. 24. Monte Carlo representation of a $p \to e^+\pi^0$ event in the Kamioka detector. (Left) A dot represents each photon; (Right) Signal observed by the photomultipliers.

Future Experiments

We now go on to talk about future experiments which have been proposed to study baryon decay. The first of these, a collaboration by Orsay, Palaiseau, Saclay, and Wuppertal to build a detector in the Frejus Tunnel between France and Italy, has been approved and is currently under construction.[20] As shown in Fig. 25, it will use flash chamber planes to measure the location of the track every 3 mm of iron. Since, however, each measurement is one dimensional, the effective tracking sensitivity will be one x-y measurement/6 mm of iron as compared to one x-y measurement/10 mm of iron for the Nusex detector. Since the flash tubes must be triggered, Geiger tubes are included at periodic intervals. The detector will be 1500 tons total with an anticipated fiducial volume of $\simeq$ 1000 tons. It will be located at a depth of 4200 mwe comparable to that of the Nusex experiment. Excavation of the hole to house the experiment is proceeding well, and it is anticipated that in approximately one year 500 tons or more of the detector will be installed. Given a tracking sensitivity similar to or possibly slightly better than that of the Nusex experiment combined with the total tonnage of more than 1000 tons, this experiment will clearly be an important element in the search for baryon decay. A Monte Carlo event for the reaction $p \to e^+\pi^0$ is shown in Fig. 26.

Another fine sampling iron plate detector has been proposed by a Argonne-Minnesota-Oxford-Rutherford collaboration.[21] This detector, nicknamed Soudan II, would be located near to where the 35 ton Soudan I prototype is currently operating. It proposes to use 5 mm

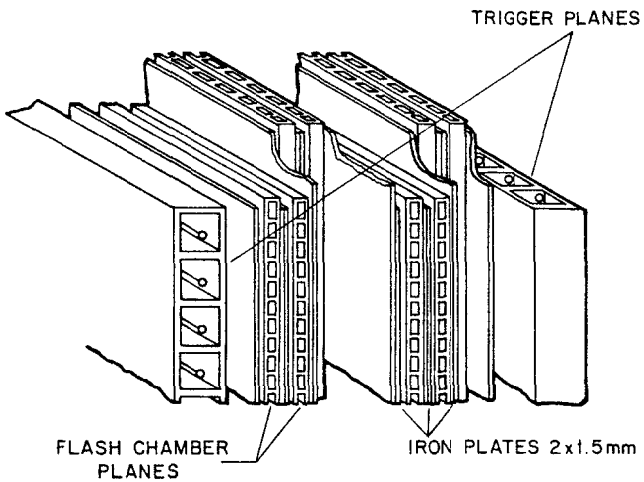


Fig. 25. Design of a fine-sampling iron plate calorimeter being constructed by an Orsay-Palaiseau-Saclay-Wuppertal collaboration in the Frejus tunnel between France and Italy.

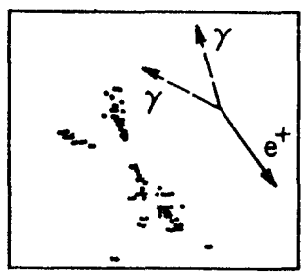


Fig. 26. An example of a $p \rightarrow e^+\pi^0$ event in the Frejus detector (Monte Carlo).

thick iron plates. Sampling would be provided by long drift distance drift chambers which would provide two dimensional readout as well as ionization information. It is anticipated that the ionization information (which is not present in either the Nusex or Frejus experiments) would significantly improve the capability to identify a particle and would also provide the possibility of identifying the track direction at least some fraction of the time. Fig. 27 shows a schematic of one possible design for the detector, although other designs are also under consideration. An illustration of the type of event topology that might be able to be identified given the existence of ionization information and knowledge of the track direction is shown in Fig. 28. Without knowledge of the track direction it would be very difficult to exclude the possibility that such a topology was produced by a neutrino interaction.

We now go on to consider two detectors which have been proposed which would use liquid scintillator as the primary target material rather than iron or other inactive material. The first of these, the simplest in design, has been proposed as a second stage by the University of Pennsylvania-Brookhaven collaboration currently operating in the Homestake Mine.[22] Shown in Fig. 29, the detector consists simply of tubes filled with liquid scintillator stacked on top of one another alternating in direction. The detector would thus be totally active, would provide good total energy measurement, and would provide some information on the topology of the event, though clearly the latter would not be as good as from the detectors designed to explicitly measure each track. It has been proposed to build

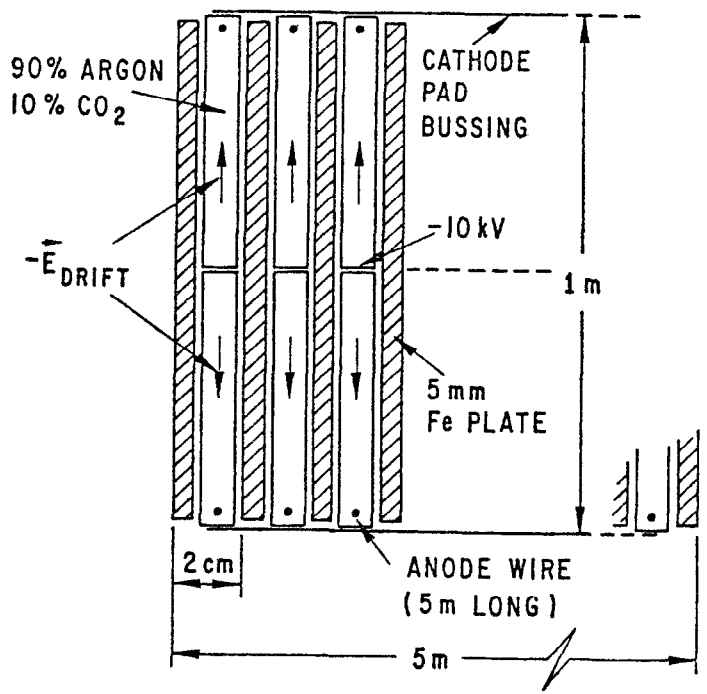
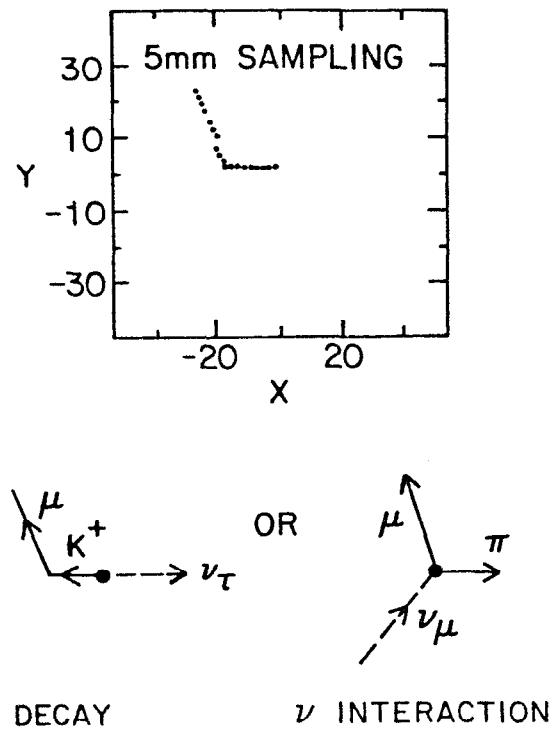


Fig. 27. Schematic representation of the proposed construction of a 50 ton Soudan II module from 5 mm thick iron plates and 5 m x 0.5 m x 1 cm planar drift chambers. Note that the horizontal and vertical scales are different. The module would contain 500 chambers and be read out by 500 anode wires and 500 cathode strips on the two external 5 m x 5 m faces. The Minnesota-ANL-Oxford-Rutherford collaboration has proposed building a 1000 ton detector in the Soudan mine.



NEED TRACK DIRECTIONAL INFORMATION

Fig. 28. Illustration of a $p \to \nu K^+$ decay in the proposed Soudan II detector. Information on the direction of the tracks, obtained statistically in this detector by an analysis of the dE/dx along the track, would be required to interpret such events.

THE HOMESTAKE TRACKING SPECTROMETER
A ONE-MILE DEEP 1400-TON
LIQUID SCINTILLATION NUCLEON DECAY DETECTOR

UNIVERSITY OF PENNSYLVANIA

BROOKHAVEN NATIONAL LABORATORY

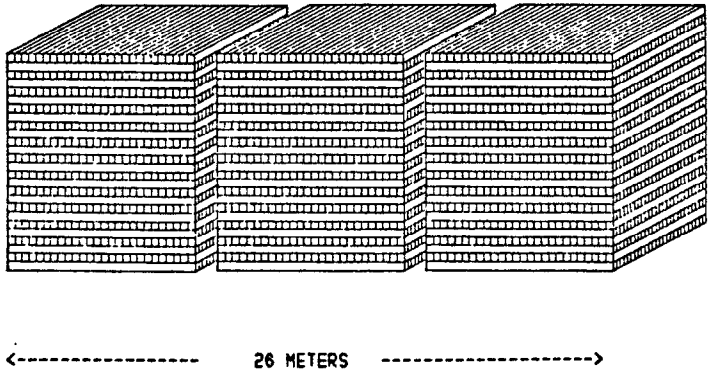


Fig. 29. Schematic representation of the Homestake II detector proposed by the Pennsylvania-BNL collaboration. Crossed rectangular cells filled with liquid scintillator would allow excellent total energy measurement and some information on dE/dx and topology.

approximately 1000 tons which would be located near to where the Homestake experiment is currently operating.

The second liquid scintillator experiment is being proposed by another University of Pennsylvania group and is based on a scale-up of a neutrino experiment currently operating at Brookhaven.[23] The detector would consist of liquid scintillator planes separated by proportional drift tubes which would measure both the x and y coordinate of the track and also provide ionization information. An overview of the experiment is shown in Fig. 30 while Fig. 31 presents a detail of the liquid scintillator cells and the proportional drift tubes (here the scale is that proposed for the baryon decay experiment). An indication of the type of sensitivity that could be obtained with such a detector is obtained from Fig. 32 which shows a real neutrino interaction in the the neutrino detector, and from Fig. 33 which shows the response of the proportional drift tubes to pions, electrons and protons. Finally, Fig. 34 shows a typical electron shower also observed in the neutrino experiment. This detector, in addition to being almost entirely active, and hence giving excellent information on the total energy of the event, has excellent tracking and dE/dx capabilities for particle identification. A final virtue not realized in most other tracking detectors is that the use of the timing information from the scintillator should allow relatively unambiguous determination of the track directions.

Finally, I should mention that there is a plan to build a very large underground international facility at the Gran Sasso Tunnel in

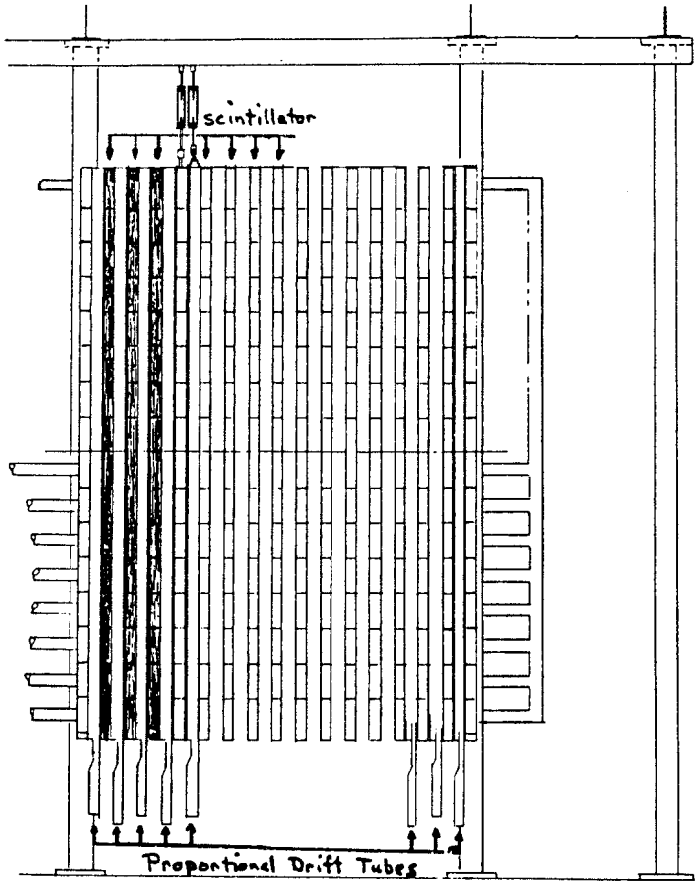


Fig. 30. Side view of the existing E734 neutrino detector built and operated by a Brown-BNL-KEK-Osaka-Pennsylvania-Stony Brook-Tokyo collaboration. Liquid scintillator planes 4 m x 4 m x 8 cm alternate with X-Y proportional drift tube planes of similar size which provide both position and pulse height information. A Pennsylvania group has proposed a baryon decay detector of similar construction and ten times the size.

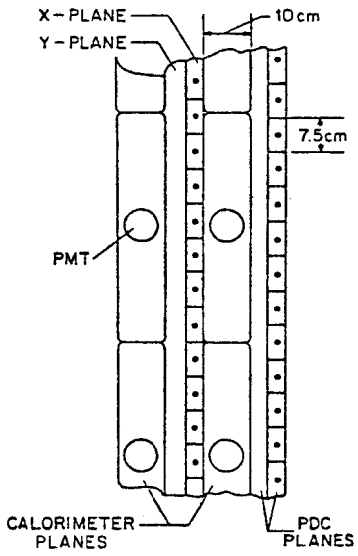


Fig. 31. Schematic outline of a double module of the Penn Nucleon Decay Detector. The ends of two 8 m long liquid scintillator calorimeter planes are shown, along with the crossed planes of proportional drift cells (PDC's).

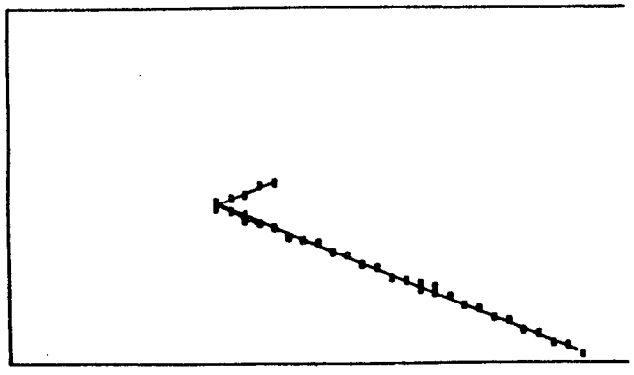


Fig. 32. A typical neutrino interaction in the BNL E734 detector. The neutrino beam enters from the left. Only the PDT hits are shown in this view.

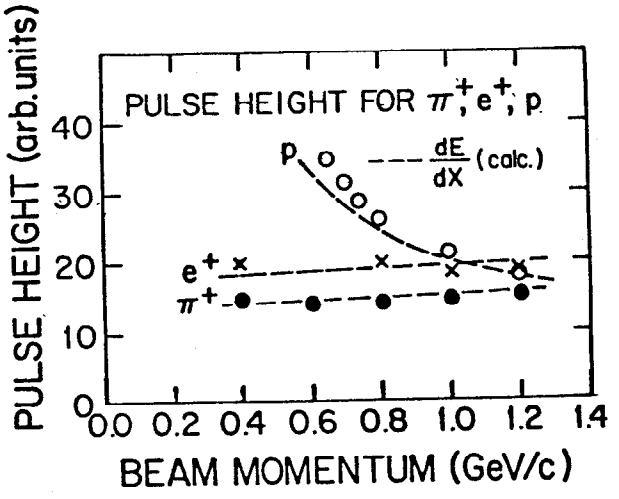


Fig. 33. The mean energy loss observed as a function of momentum for pions, protons, and electrons, in a single test plane of proportional drift tubes from the BNL E734 neutrino detector.

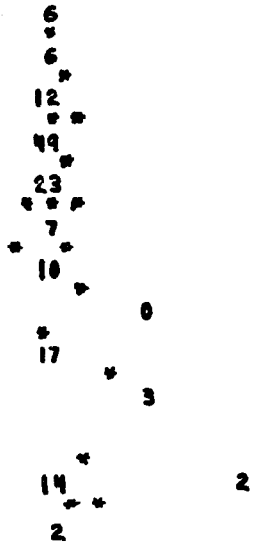


Fig. 34. A low energy electron shower observed in the BNL E734 neutrino detector. Each star indicates a PDT hit and the numbers indicate the energy deposited, in MeV in the calorimeter cells. Not shown is the energy loss measured in each of the PDT cells.

Italy which is nearing completion. The current plan is to provide three large underground halls each with a volume of $\approx 30{,}000$ cubic meters. Designs for a new baryon decay detector similar in principle to that of Nusex but using techniques which would allow more economical mass construction of a detector as large as 10,000 tons are currently under way.[24]

Neutrino Oscillations

Next we go on to talk about a mass scale which is approximately 26 orders of magnitude smaller than the one we have just been talking about, that is, a scale of a few eV where experiments attempting to measure directly the mass of the neutrino and also experiments searching for neutrino oscillation are currently sensitive.

We presently believe that electron neutrinos, muon neutrinos, and tau neutrinos are eigenstates of the weak interaction. But let us suppose that the electron neutrino or the muon neutrino is massive and let us further suppose that separate lepton number is not conserved, that is,

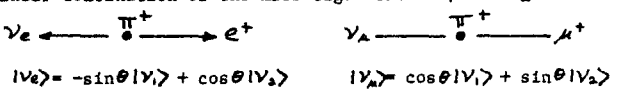
$$\langle \nu_e | H | \nu_\mu \rangle \neq 0$$

In this event, ν_e and ν_μ will in general mix and will not be mass eigenstates.[25] Note that in our present theoretical framework which assumes that only those quantum numbers which are coupled to gauge fields are rigorously conserved, the violation of electron number conservation or muon number conservation is not so outlandish as it might have been considered a few years ago.

Let the neutrinos which are mass eigenstates be denoted by ν_1 and ν_2. Then the electron and muon neutrinos may be expressed as a linear combination

$$|\nu_e\rangle = -\sin\theta|\nu_1\rangle + \cos\theta|\nu_2\rangle$$
$$|\nu_\mu\rangle = \cos\theta|\nu_1\rangle + \sin\theta|\nu_2\rangle$$

Thus, when a π^+ meson decays, for example, to $e^+\nu_e$ or $\mu^+\nu_\mu$, the ν_e or ν_μ is a linear combination of the mass eigenstates ν_1 and ν_2.



$|\nu_e\rangle = -\sin\theta|\nu_1\rangle + \cos\theta|\nu_2\rangle$ $\quad$ $|\nu_\mu\rangle = \cos\theta|\nu_1\rangle + \sin\theta|\nu_2\rangle$

This is exactly analogous to what happens when a W^- decays to $\bar{u}$ and d or $\bar{c}$ and s quarks.



$d = d\cos\theta_c + s\sin\theta_c$ $\quad$ $s = s\cos\theta_c - d\sin\theta_c$

Given a ν_μ at t=0, what is the probability of finding a ν_e at a later time t? The two mass eigenstates evolve in time according to the characteristic e^{-iEt}, which, if the particles were at rest, would be e^{-imt}; then the neutrino state at a later time is

$$\psi(t) = \cos\theta|\nu_1\rangle e^{-iE_1t} + \sin\theta|\nu_2\rangle e^{-iE_2t}$$

and the amplitude for finding a ν_e in the final state at time t is

$$\langle\nu_e|\psi(t)\rangle = [-\sin\theta\langle\nu_1| + \cos\theta\langle\nu_2|]\cos\theta|\nu_1\rangle e^{-iE_1t} + [-\sin\theta\langle\nu_1| + \cos\theta\langle\nu_2|]\sin\theta|\nu_2\rangle e^{-iE_2t}$$

The probability of observing a ν_e at time t is then

$$|\langle\nu_e|\psi(t)\rangle|^2 = \tfrac{1}{2}\sin^2 2\theta(1 - \cos(E_1 - E_2)t)$$

Now suppose that we are observing the neutrino in the lab frame and that it has a momentum $p_\nu >> m_1$ or m_2. Then we may approximate $E_1 - E_2$ by the expression

$$E_1 - E_2 = \sqrt{p_\nu^2 + m_1^2} - \sqrt{p_\nu^2 + m_2^2} \approx \frac{m_1^2 - m_2^2}{2p_\nu}$$

and hence obtain for the probability of finding a ν_e at time t, given initially a ν_μ at time 0

$$P(\nu_e, t; \nu_\mu, 0) = \sin^2 2\theta\left(1 - \cos\frac{(m_1^2 - m_2^2)}{2p_\nu}t\right)$$

Putting in $\hbar$ and c explicitly, the time for the neutrino state to oscillate through one complete cycle is

$$\tau_{osc} = \frac{4\pi p_\nu}{m_1^2 - m_2^2} = \frac{4\pi p_\nu c\hbar}{(m_1^2 - m_2^2)c^4}$$

Now it should be noted that this derivation while correct is a slight cheat in the sense that the question of whether the two eigenstates of slightly different masses really have the same momentum or not has been ignored. To understand this subtlety correctly it is necessary to do a wave packet treatment of neutrino oscillations which has been done by Boris Kayser.[26] One does indeed obtain the same expression.

If the neutrinos are traveling close to the speed of light,

which presumably they are, then the oscillation length observed in the laboratory is approximately

$$L_{osc} = \tau_{osc} c$$

If we then measure $\Delta^2 \equiv m_1^2 - m_2^2$ in eV^2, $p_\nu c$ in MeV, and x (ℓ) in meters, the probability for finding a ν_e at position x given a ν_μ at position 0 is

$$P(\nu_e, x; \nu_\mu 0) = \frac{1}{2}\sin^2 2\theta \left(1 - \cos \frac{2.54 \Delta^2 x}{p_\nu}\right)$$

To conform with the perhaps most popular notation, I will henceforth write ℓ instead of x, and use the approximate identity $E_\nu \approx p_\nu$ to obtain the standard expression

$$P(\nu_e \ell; \nu_\mu 0) = \sin^2 2\theta \sin^2 \frac{1.27 \Delta^2 \ell}{E_\nu}$$

with an oscillation length

$$L_{osc} = \frac{2\pi E_\nu}{1.27 \Delta^2}$$

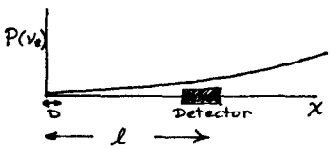
Before discussing specific experiments, it is useful to consider three different regimes of L_{osc}, the oscillation length, and ℓ, the distance of the detector from the point at which the neutrino was initially created.

1. $L_{osc} \gg \ell$; "Low Mass Limit"

In this case, the argument of the second sine function is much less than one, and we may use the small angle approximation to replace the sine by its argument. Then we obtain

$$P(\nu_e \ell; \nu_\mu 0) \approx \sin^2 2\theta \left[\frac{1.27 \Delta^2 \ell}{E_\nu}\right]^2$$

$$P(\nu_\mu \ell; \nu_\mu 0) \approx 1$$



Since the probability of observing a ν_e is very small, the probability that the initial state is still a ν_μ is approximately 1. The ratio for the probabilities of observing a ν_e or a ν_μ is then

$$R_{e\mu} \equiv \frac{\nu_e}{\nu_\mu} = \sin^2 2\theta \left[\frac{1.27 \Delta^2 \ell}{E_\nu}\right]^2$$

If we perform an experiment and are able to establish an upper limit $R_{e\mu}^{max}$ on the ratio of the number of ν_e to ν_μ, then we obtain the following limit on the mixing angle and the difference in the masses

$$\sin 2\theta \, \Delta^2 < .8 \frac{E_\nu}{\ell} \sqrt{R_{e\mu}^{max}}$$

Of course, if we were to observe a number of electron neutrinos which was inconsistent with either the expected number of ν_e in the initial beam or with the expected number of ν_μ interactions misidentified as having produced an electron, then one would claim evidence for neutrino oscillations. It should be clear that E_ν / ℓ is a good figure of merit of the sensitivity of the experiment. The smaller the value of E_ν / ℓ for a particular experiment, the smaller the value of $\sin 2\theta$ or Δ^2 to which one is sensitive. It should also be noted that for this type of experiment, the finite source length D which is inevitably present in any experiment is not very important as long

as $D << \ell$ which is usually the case. Furthermore, variations in the neutrino energy E_ν are also not very important as long as they are not too large.

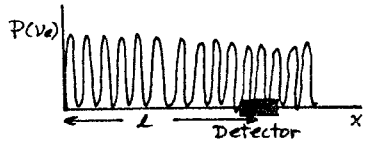
2. $L_{osc} << \ell$; High Mass Limit

In this case, if we sum over the entire length of the detector, we are simply observing the average number of neutrinos of each type.

$$\left\langle \sin^2 \frac{1.27\Delta^2 \ell}{E_\nu} \right\rangle = \frac{1}{2}$$

$$P(\nu_e \ell; \nu_\mu\ 0) = \frac{1}{2}\sin^2 2\theta$$

$$P(\nu_\mu \ell; \nu_\mu\ 0) = 1 - \frac{1}{2}\sin^2 2\theta$$



If we furthermore assume that the mixing angle is small (which in general it is since otherwise it would have already been observed), then the ratio of the number of electron neutrinos to the number of muon neutrinos is

$$R_{e\mu} = \frac{\nu_e}{\nu_\mu} \approx \frac{1}{2}\sin^2 2\theta$$

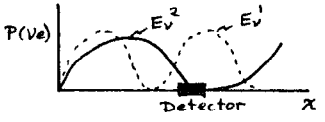
and we see that experiments searching for neutrino oscillations in the high mass limit are effectively measuring the mixing angle.

$$\sin^2 2\theta = 2R_{e\mu}$$

It should be noted that in this case the finite source length or variations in the energy of the neutrinos will prevent one from observing the individual oscillations taking place throughout the detector. Since it is in general hopeless to observe the individual oscillations, the actual size of the source or the actual magnitude of variations in E_ν are therefore not very important.

3. $L_{osc} \approx \ell$

The third case obviously corresponds to oscillation lengths approximately equal to the distance of the detector from the source of the neutrinos. In this case, very large effects can be observed depending on whether the exact values of E_ν and ℓ are such that the detector is located at the point of maximum oscillation probability, or at a 0, or at some other point. In general, experiments will thus have significant "wiggles" in the sensitivity as a function of E_ν depending on the exact energy composition of the neutrino beam and the distance ℓ from the detector.



Appearance Experiments

In addition to categorizing experiments according to their sensitivity in the high mass region or low mass region, it is useful to consider two different types of experiments. The first is the so-called appearance experiments, that is, one takes a beam of a particular type of neutrino, as pure as one can make it, and searches for a different type of neutrino not initially present in the beam. This kind of experiment is in general very sensitive to small values of Δ^2 and mixing angle because one is looking for something which is not supposed to be there. One can often use a single detector for an experiment of this kind. Let us represent by ν_e^{osc} the actual number of neutrinos oscillating from ν_μ to ν_e, by ν_e^{BEAM} the contamination of

ν_e initially in the beam, and let us represent by ν_e^{FAKE} the fraction of ν_μ which, if they interact in the detector, are incorrectly determined to be ν_e (for example, by giving a signature which may be interpreted as an electron). Then the observed ratio for the number of electron neutrinos to the number of muon neutrinos is

$$R_{e\mu}^{obs} = \frac{\nu_e^{osc} + \nu_e^{BEAM} + \nu_e^{FAKE}}{\nu_\mu} \equiv R_{e\mu} + \delta$$

where $R_{e\mu} = \nu_e^{osc}/\nu_\mu$, and δ represents the contribution from the beam contamination and the misidentification probability. δ then essentially sets the limits as to how sensitive an experiment one can perform. So one would like to make δ very small by using a very pure beam. One of the ways of doing this is to use a narrow-band beam. In addition, one would like to use a very good detector so that the probability that an apparent ν_μ event is due to a ν_e is as small as possible. Bubble chambers and fine grained electronic experiments are generally very good in this respect. In the event that $R_{e\mu}^{obs} > \delta$, then one in principle has observed oscillations. In the case, which is much more likely, that $R_{e\mu}^{obs} \approx \delta$, then one can obtain a limit on Δ^2 and $\sin 2\theta$, (though the sensitivity of the experiment can be increased by using two detectors, as discussed below). For the low mass limit, one has simply

$$\sin 2\theta\, \Delta^2 \leq .8 \frac{E_\nu}{\ell}\sqrt{\delta}$$

For $\sin 2\theta = 1$, we have the so-called "maximum mixing angle" limit for Δ^2.

$$\Delta^2 < 0.8 \frac{E_\nu}{\ell}\sqrt{\delta}$$

For the high mass limit one has simply

$$\sin^2 2\theta \leq 2\delta$$

It is convenient to represent these limits as shown in Fig. 35 where we have plotted the log of $\sin^2 2\theta$ versus the log of Δ^2. The region of sensitivity may be characterized by the high mass limit $\sin^2 2\theta \leq 2\delta$ which is independent of Δ^2, by the maximum mixing angle limit $\Delta^2 < .8 \frac{E_\nu}{\ell}\sqrt{\delta}$, and by the line which connects these two which has a slope of 1/2.

Typical values for a broad band beam of the ratio of electron neutrinos to muon neutrinos are between .5% and 1%, whereas for a narrow band beam one believes that one can obtain a ratio of ν_e to ν_μ in the energy region of interest of $< 5 \times 10^{-4}$. The ratio ν_e^{FAKE}/ν_μ might be typically 1% for a counter experiment for the case where one does not know the energy of the incident ν_μ to as good as perhaps .1% for the case where the energy of the incident ν_μ is known. Bubble chambers can do much better[27] with a misidentification probability, even for a broad band beam, of $\approx 2 \times 10^{-4}$.

Two Detector Appearance Experiments

One can also perform appearance experiments using two detectors to try to beat down the limitations of δ. In this case one compares

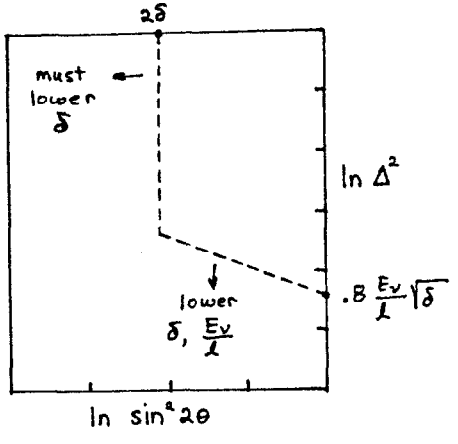


Fig. 35. Schematic of the limits from a typical neutrino oscillation experiment. The region to the upper right of the dashed lines (which are described in the text) is excluded.

the observed number of electron neutrinos in detector 1 with the observed number in detector 2 and performs a subtraction. One can then eliminate, in principle, the contribution resulting from the contamination in the beam (although in practice this is not always so simple since one must verify that the ν_e's and ν_μ's are produced in such a way that their ratio is the same in both detectors). Similarly, the first and second detectors should be as similar as possible so that the misidentification probability is the same for each measurement. In practice, one should be able to improve the sensitivity by approximately a factor of 10 in this way, although it is clear that high statistics is then required.

Disappearance or Survival Experiments

In the second type of experiment, the so-called "disappearance" or "survival" experiments, one measures the number of neutrinos of a given type at two different locations to see whether any have disappeared. This is clearly a much more difficult type of experiment. It requires, in general, either (1) an absolute knowledge of the flux, or (2) variations in the observed energy dependence of the flux, or (3) an observed departure from a $1/R^2$ falloff.

The ability to calculate a priori the absolute flux of neutrinos at accelerators is in general not sufficiently good to allow experiments of this kind utilizing a single detector. The knowledge of neutrino fluxes from reactors is perhaps better determined and results of $\bar{\nu}_e$ oscillation experiments using a single detector have been reported (see the talk by F. Boehm at this conference as well as

the discussion below). A second possibility is to measure the flux of neutrinos as a function of energy and to search for deviations from the expected energy dependence. Since uncertainties in the calculated flux as a function of energy may well be less than the uncertainty in the absolute flux, single detector experiments of this type are more feasible than those which yield no information on the energy of the neutrinos. Nonetheless, the results from such experiments are still apt to be dominated by the systematic uncertainty in the calculated flux. The third type of experiment, which is by far the most suitable for disappearance experiments, utilizes either two detectors or a movable detector to measure the flux at different distances L in a way that is as free as possible from systematic uncertainties. This type of experiment requires a careful understanding of the beam, since one must know the ratio of the fluxes expected as the function of position in the absence of any neutrino oscillations. In general, the dependence of the flux on L is more complicated than simply $1/L^2$ because of the effects of the finite source size.

Let us now consider a two detector experiment shown schematically in Fig. 36. For the case of an accelerator experiment (the principles are essentially identical for reactor experiments) we have protons hitting a target which is followed by a decay region of length D in which the pions and K mesons decay. For these experiments, the finite source size, which is in general of order, D is not negligible. We assume the first detector is located at a distance L_1 from the source and the second detector at a distance L_2. We then measure the number of ν_μ interactions at the first detector $N_\mu(L_1)$ and the number of interactions at the second detector $N_\mu(L_2)$. The ratio of the number of neutrino interactions at the two detectors after integration over the finite source size may be expressed as

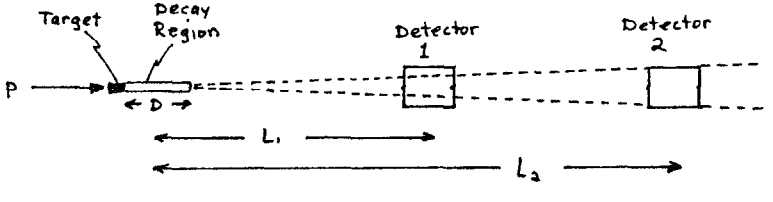


Fig. 36. Experimental layout of a typical two-detector neutrino oscillation experiment.

$$R = \frac{N_\mu(L_2)}{N_\mu(L_1)} = 1 - K(E_\nu)\sin^2 2\theta$$

where $K(E_\nu)$ is given by

$$K(E) = \frac{\sin(\pi D/L_{osc})}{\pi D/L_{osc}} \sin\left[\frac{1.27\Delta^2(L_2-L_1)}{E_\nu}\right] \sin\left[\frac{1.27\Delta^2(L_2+L_1)}{E_\nu}\right]$$

A schematic example of the behavior of $K(E_\nu)$ and hence of the ratio R is shown in Fig. 37 for the case of no oscillations and for the case

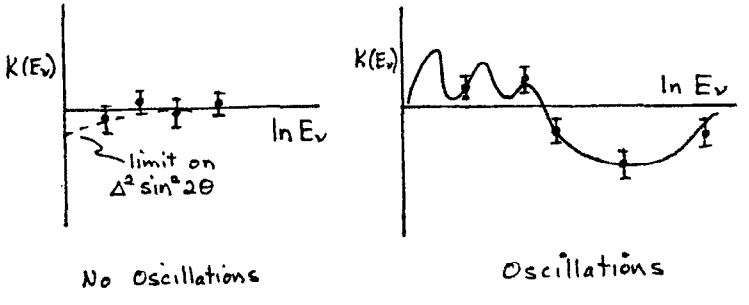


Fig. 37. Schematic illustration of the behavior of the function $K(E_\nu)$ which is related to the oscillation probability as a function of E_ν for a two-detector disappearance experiment.

assuming oscillations are present. In general one would like to measure the number of neutrinos as a function of energy either by using a detector which can reconstruct the energy of the neutrinos or by using a narrow-band beam which can be run at several different energies.

Experiments and Results

We now go on to talk about results on neutrino oscillations from existing experiments and also about experiments which are likely to take place in the relatively near future. I will make no attempt to give a comprehensive list of such experiments (such a list has been recently compiled by R. E. Lanou[28]), but will concentrate primarily on those experiments which currently give the best limits or which promise to expand our knowledge the most in the near future. An outline of these experiments, and hence of the rest of the talk is shown below.

(1) Present Results

(a) Limits on	$\nu_\mu \rightarrow \nu_e$	FNAL Bubble Chamber
(b) Limits on	$\bar{\nu}_e \rightarrow \bar{\nu}_x$	Reactor experiments (CALTEC-SIN-TUM)

(2) Future Program

CERN

CDHS	$\nu_\mu \rightarrow \nu_\mu$	
CHARM	$\nu_\mu \rightarrow \nu_\mu$	PS Beam, existing detectors
BEBC	$\nu_\mu \rightarrow \nu_e$	
JURA	$\nu_\mu \rightarrow \nu_\mu$	SPS Beam, new detector
	$\nu_\mu \rightarrow \nu_e$	(not yet approved)
	$\nu_\mu \rightarrow \nu_\tau$	

BNL

BNL-Brown-KEK-Osaka-Penn-SB-Tokyo	$\nu_\mu \rightarrow \nu_e$	NB, existing detector, small mixing angle
	$\nu_\mu \rightarrow \nu_\mu$	(not yet approved)
BNL-Col-Ill-JH-NRL	$\nu_\mu \rightarrow \nu_e$	new NB, new detector, small
	$\nu_\mu \rightarrow \nu_\mu$	(not yet approved)

FNAL

Col-FNAL-NW-Chic	$\nu_\mu \rightarrow \nu_\mu$	high Δ^2, "small mixing angle"

LAMPF

ANL-CIT-Lampf-Louisiana-Ohio St.	$\nu_e \rightarrow \nu_e$	new detector, existing stopped beam
	$\bar{\nu}_\mu \rightarrow \bar{\nu}_e$	

A very nice experiment presenting limits on the oscillation of $\bar{\nu}_e$ to any other type of neutrinos has been performed by the CALTEC-SIN-TUM collaboration at the Osgen reactor in Switzerland.[30] In this experiment they use a liquid scintillator target shown in Fig. 38 to detect the reaction $\bar{\nu}_e + p \rightarrow e^+ n$. The energy of the positron is measured and in addition the neutron, which is moderated by the scintillator, is detected in ^3He chambers. These chambers have a very large cross-section for detecting the neutron and have positional information. Hence, the signature for an event includes both a time coincidence and spatial coincidence of the positron and the neutron. The detector is heavily shielded and, as we will see below, the backgrounds have been suppressed very effectively. The figure of merit $E_\nu/L \approx .06\text{-}.2$ which is a rather small value compared to current accelerator experiments. I will not discuss the experiment in any more detail since a detailed discussion will be presented at this

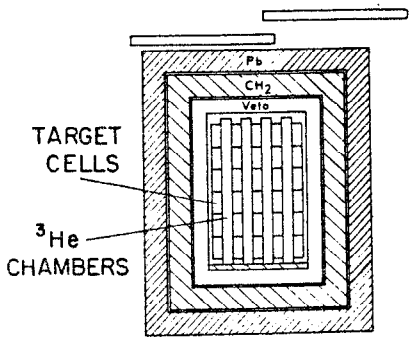


Fig. 38. Experimental arrangement for the CALTEC-SIN-TUM reactor experiment. The neutrino detector consisting of 30 liquid scintillator target counters and four ^{3}He wire chambers is at the center. Each target counter is viewed by four photomultiplier tubes. Six veto scintillation counter planes surround the detector. Four umbrella vetos help reducing the cosmic-ray background. Lead and CH_2 shieldings are shown.

conference by F. Boehm; however, I will present the results. Shown in Fig. 39a are the measurements of the positron spectrum for reactor on and reactor off; the first thing to notice is that there is a large difference between the reactor on and reactor off rates yielding a much cleaner signal than has been available in previous reactor experiments. The subtracted spectrum is shown in Fig. 39b. The game now is to take the calculated neutrino flux and to compare it with the one that is observed. While there are, of course, uncertainties in the calculated flux, knowledge of the primary fission chains within the reactor combined with measurements of the positron spectrum at much closer distances to the reactor yield a knowledge of the flux which is accurate to $\approx$5%. Shown in Fig. 40 is a bin by bin comparison as a function of energy of the positron yield observed compared to what would be expected in the absence of any oscillations. The three curves show the expected behavior for $\Delta^2 = 0$ (i.e., no oscillations) and also for two cases of neutrino oscillations with the parameter Δ^2 and $\sin^2 2\theta$ just at the limit of the sensitivity of the experiment. The forbidden domain (at 90% confidence level) of oscillation parameters Δ^2 and $\sin^2 2\theta$ lies to the right of the solid line in Fig. 41. Oscillation parameters to the left of this line are allowed. The limit $\Delta^2 < 0.16$ eV^2 at maximum mixing angle is a big improvement over the results of a year ago. In particular, previously reported results indicating the presence of $\bar{\nu}_e$ oscillations are inconsistent with the results of this experiment.[31]

Another experiment[32] searching for oscillation of muon neutrinos to electron neutrinos sets much better limits on the mixing angle in

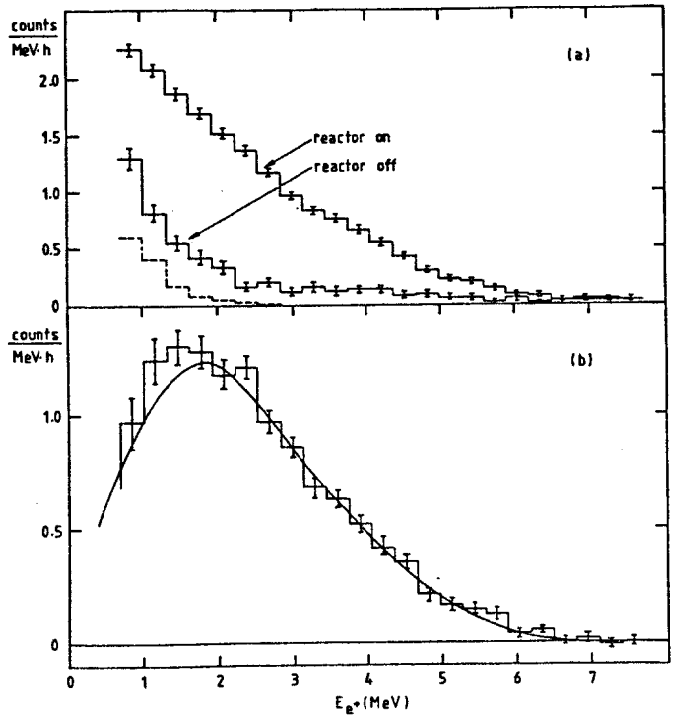


Fig. 39. Experimental results for the CALTEC-SIN-TUM experiment. (a) Reactor-on and reactor-off spectra. Bin width = 0.305 MeV. The errors shown are statistical. The contribution of the accidentals is indicated by the dashed curve. (b) Experimental positron spectrum obtained by subtracting reactor-off from reactor-on spectra. The solid curve represents the predicted positron spectrum assuming no neutrino oscillations.

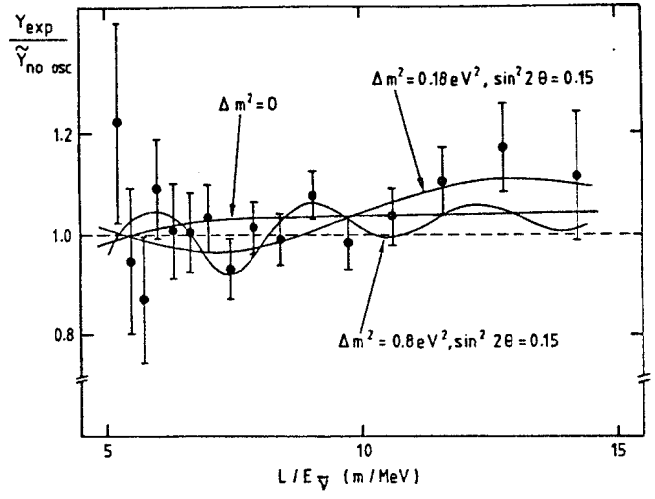


Fig. 40. Ratio of experimental to predicted (for no oscillations) positron spectra for the CALTEC-SIN-TUM experiment. The errors of the data points shown are statistical. Oscillation functions obtained from a fit (see text) are shown for various sets of oscillation parameters.

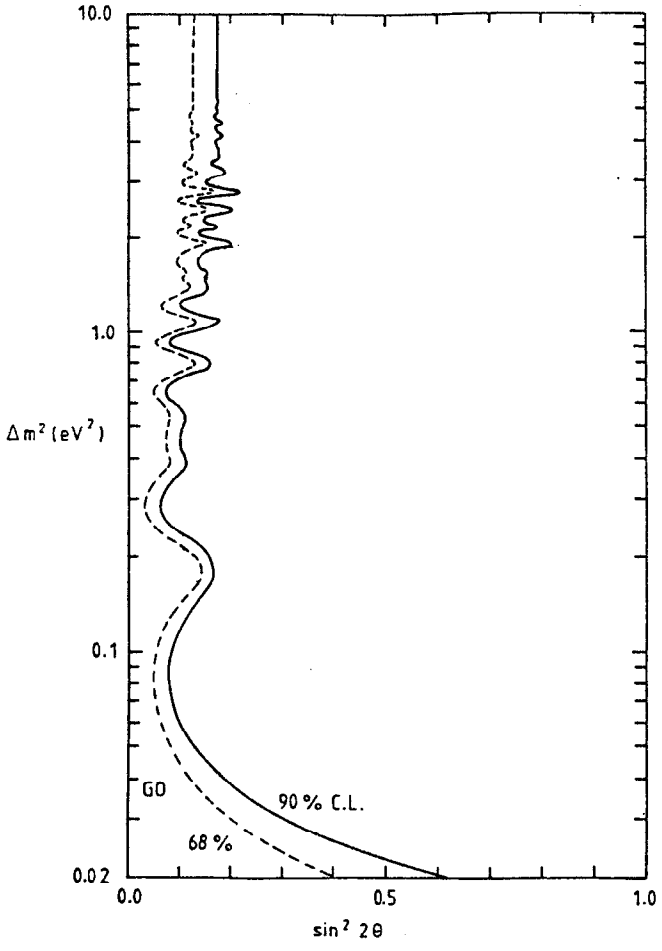


Fig. 41. Limits on the neutrino-oscillation parameters Δm^2 (Δ^2) vs. $\sin^2 2\theta$ given by the CALTEC-SIN-TUM experiment at the Gosgen reactor (labelled GO). The regions to the right of the curves are excluded at the confidence level indicated.

the higher mass region $\Delta^2 \simeq 1$ eV^2. This experiment used the 15' bubble chamber at Fermilab to search for $\nu_\mu \rightarrow \nu_e$ transitions in normal wide-band beam running. The detector was located $\simeq$ 1200 meters from the decay region as shown in Fig. 42. The bubble chamber was filled

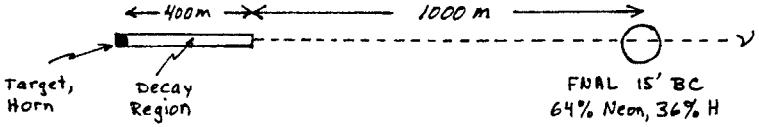


Fig. 42. Schematic layout of the neutrino beam and 15' BC at FNAL.

with a mixture of 64% neon and 36% hydrogen which has proven to be a good combination if one desires both relatively large mass but at the same time wishes to identify electrons rather cleanly. The mean value of E_ν/L for the oscillation experiment is $\simeq$ 16 MeV/m. The experiment observes 595 events with $E_e > 1$ GeV which, after corrections for scanning efficiency, etc., corresponds to an initial sample of 942 ± 82 ν_e interactions. For the same fiducial volume they obtain $68{,}500 \pm 4000$ ν_μ interactions; this together with a calculated ratio $\nu_e/\nu_\mu = 1.5 \pm .3\%$ would imply that they should observe in the absence of any neutrino oscillation 1027 ± 210 ν_e interactions. The .3% represents the experimenter's estimate of the systematic uncertainty in the calculated ratio ν_e/ν_μ. Comparison of the observed and expected rates for ν_e interactions then yields

$$R_{e\mu} < 3 \times 10^{-3} \quad \text{90\% confidence level}$$

and hence the limits

$$(\sin^2 2\theta = 1)\ \Delta^2 < 0.7\ \text{eV}^2$$

$$\sin^2 2\theta\,(\text{large}\ \Delta^2) < .006$$

Note that the sensitivity to small mixing angles is much better in this experiment than in the previously discussed reactor experiment. It is almost invariably true that appearance-type experiments are much more sensitive to small mixing angles than the disappearance or survival experiments. I will show the detailed sensitivity as a function of Δ^2 and $\sin^2 2\theta$ at the end of the talk after I have discussed each of the experiments.

The CERN program includes three approved experiments each using existing detectors. This includes the BEBC,[33] CDHS,[34] and CHARM[35] experiments which will expose their detectors to a new neutrino beam from the PS. The location of these detectors $\approx$ 900 meters from the new neutrino area (Fig. 34) combined with a mean neutrino energy of $\approx$1 GeV yields $E_\nu/L \approx 1$ MeV/m. The CHARM and CDHS experiments will install a piece of their detector at a new location $\approx$ 140 meters from the neutrino source, and by measuring the rate of ν_μ interactions at the two detectors will be sensitive to the oscillations of ν_μ into any other types of neutrinos. A bare target will be used to allow as clear an understanding of the neutrino flux as possible. Each of the experiments essentially amounts to counting the number of muons produced in the two detectors as a function of range, though some additional sensitivity is anticipated by comparing the observed number of neutral current interactions to the number of charged

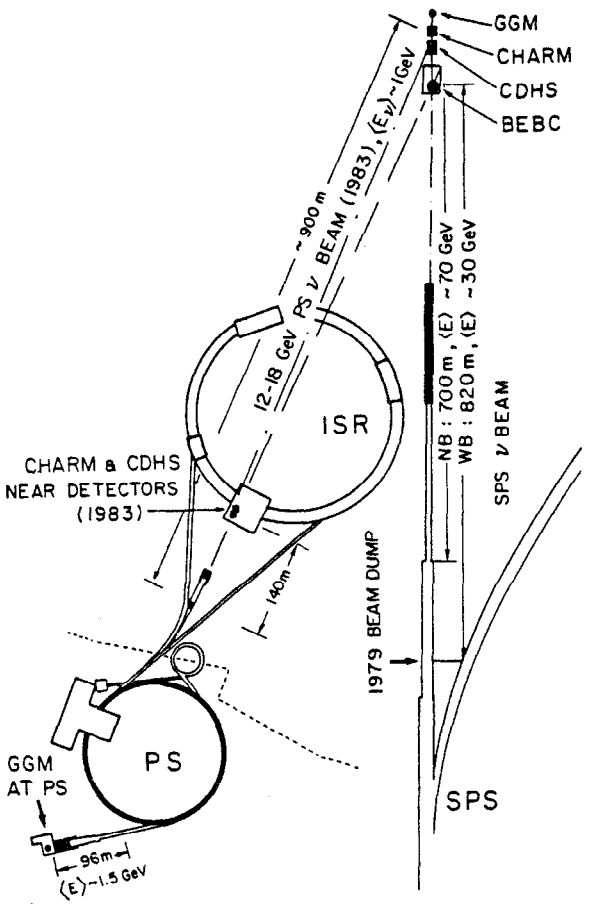


Fig. 43. Layout for the neutrino oscillation experiments at CERN showing the location of the existing detectors (labelled CHARM, CDHS and BEBC) and the site of the new neutrino beam and near detectors for CDHS and CHARM (labelled 1983).

current interactions. In addition, the CHARM experiment hopes that measurements of the hadronic energy present, although crude, will allow some determination of the energy of the neutrino which interacted. Fig. 44 is to remind you of the nature of the CDHS detector which consists of steel plates with samplings provided primarily by scintillation counters though drift chambers are also present to better define the angle and momentum of the muon. Much of the detector, which has recently been rebuilt now, has 2.5 cm iron plates to allow finer sampling. An indication of the layout of the two experiments is presented in Fig. 45 which shows a schematic of the two CHARM detectors. The CHARM detector, as you recall, consists of one radiation length thick marble plates with sampling provided by both scintillator and proportional drift tubes. An estimate of the sensitivity of the CDHS experiment is provided in Fig. 46 which presents the ratio of the number of events observed in detector 2 compared to that of detector 1 as a function of Δ^2 and $\sin^2 2\theta$. An indication of the systematic error is also present, and corresponds to a maximum mixing angle sensitivity to Δ^2 of $\approx .25$ eV^2 and a sensitivity to $\sin^2 2\theta$ in the "high mass regime" of $\simeq 0.12$. The sensitivity of the experiment is of course cut off once the oscillation length becomes short compared to the distance of the first detector from the neutrino source.

A Padova-Pisa-Athens-Wisconsin[33] collaboration will use a horn-focused beam and the excellent electron identification of the BEBC bubble chamber to improve the limits on $\nu_\mu \rightarrow \nu_e$ oscillations. They anticipate a sensitivity to Δ^2 at maximum mixing of approximately

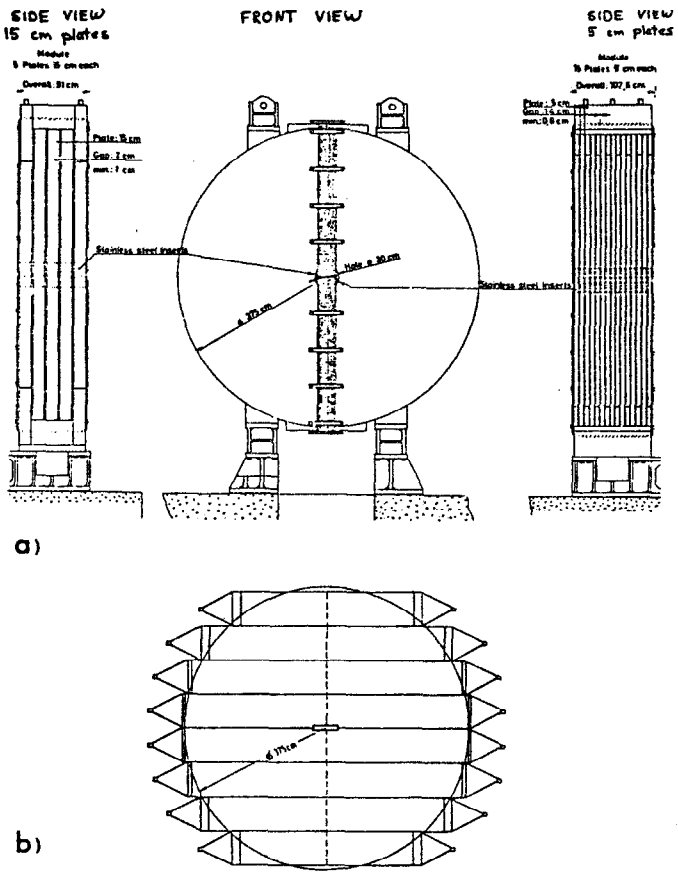


Fig. 44. Schematic of the CDHS detector. (a) Front and side views of the iron toroid modules. The near detector for the neutrino oscillation experiment will consist of two modules with 2.5 cm Fe plates, two modules with 5 cm plates, and two modules with 15 cm plates. The far detector has similar segmentations. (b) Front view illustrating the placement of the scintillation counters.

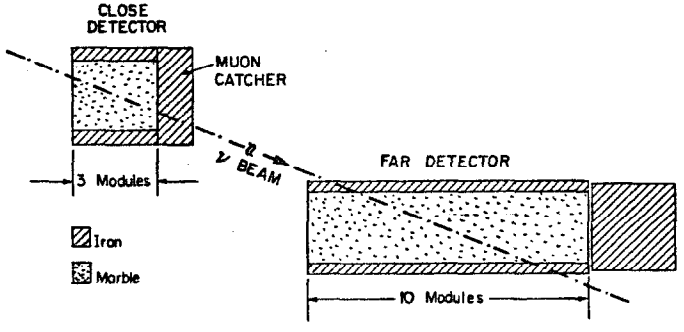


Fig. 45. Illustration of the placement of the near and far CHARM detectors relative to the neutrino beam. The orientation of the CDHS detectors is similar.

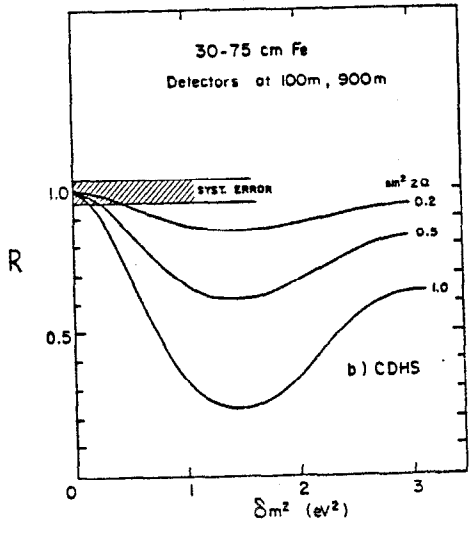


Fig. 46. Ratio of the number of ν_μ interactions at the far and near detectors for the CDHS experiment as a function of Δ^2 and $\sin^2 2\theta$.

.09 eV^2 and a sensitivity to mixing angles of $\approx .03$ in the high mass region.

Now we consider the neutrino oscillation program at Brookhaven. Two groups have proposed experiments each consisting of a phase 1 which would use a single detector to provide sensitivity to $\nu_\mu \rightarrow \nu_e$ oscillations and a phase 2 in which two detectors would be used to perform a ν_μ survival experiment very similar to the ones at CERN which we have just discussed.

The first of these, proposed by a BNL-Brown-KEK-Osaka-Pennsylvania-Stony Brook-Tokyo-UCI collaboration (E775),[37] would use the large existing detector at 110 meters (built by that group for experiment E734) and the existing narrow-band beam to try to set a limit on the mixing angle $\sin^2 2\theta$ with sensitivity of $\approx 10^{-3}$. Fig. 47 shows a schematic of this detector which has already been discussed briefly in connection with the baryon decay experiment. Fig. 48 shows the location of this detector as well as the sites for the proposed new detectors. It is hoped that the excellent sensitivity of this detector to electrons combined with an anticipated ν_e/ν_μ ratio of 5×10^{-4} will allow a sensitivity to mixing angles in the vicinity of 10^{-3}. The flux distributions from the existing narrow-band beam are presented in Fig. 49.

The second experiment is based on the proposal by a BNL-Columbia-JHU-Illinois-NRL collaboration to build a detector similar to the one described above at a distance 850 meters from the neutrino source. The scintillator would be replaced by inactive material to allow a significantly cheaper construction. The initial detector (Fig. 50) would be 175 tons, though in phase 2 it would be upgraded to ≈ 350

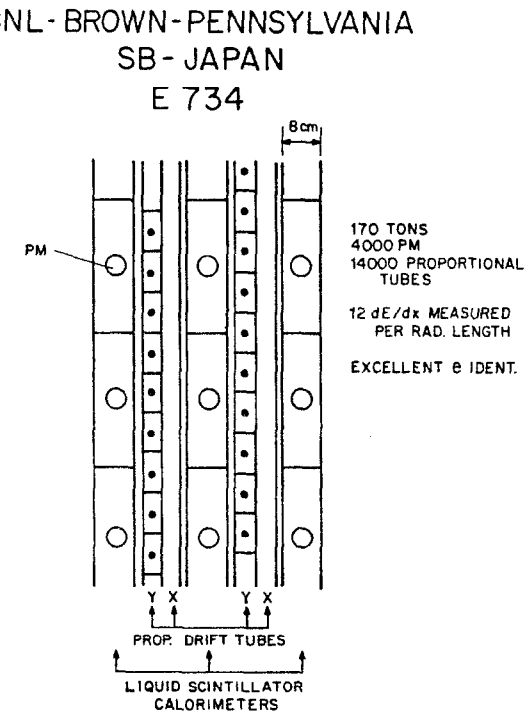


Fig. 47. Schematic of the E734 neutrino detector constructed by the BNL-Brown-KEK-Osaka-Pennsylvania-Stony Brook-Tokyo collaboration at BNL. Photomultipliers at each end of the liquid scintillator cells determine the time of the event and the energy loss in the scintillator. X and Y planes of proportional drift tubes after each scintillator determine the track positions and provide additional dE/dx information.

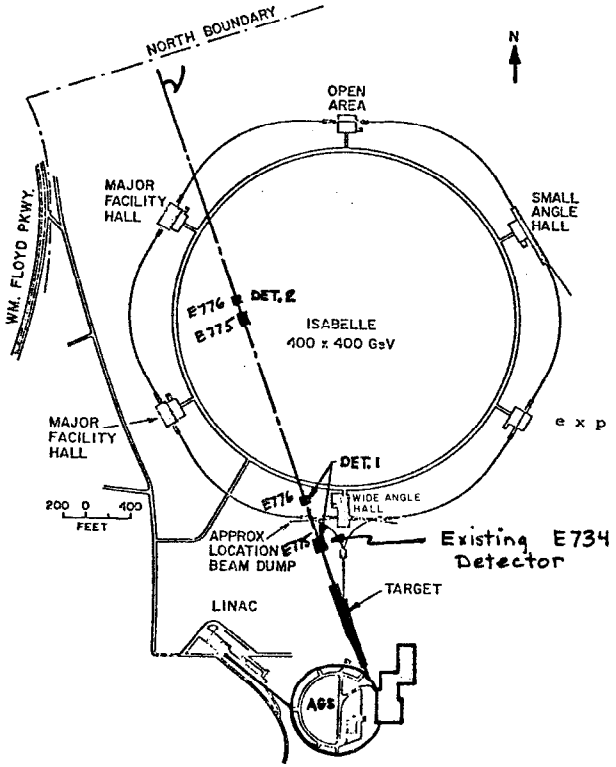


Fig. 48. Diagram showing the locations of the existing (E734) and proposed detectors at BNL.

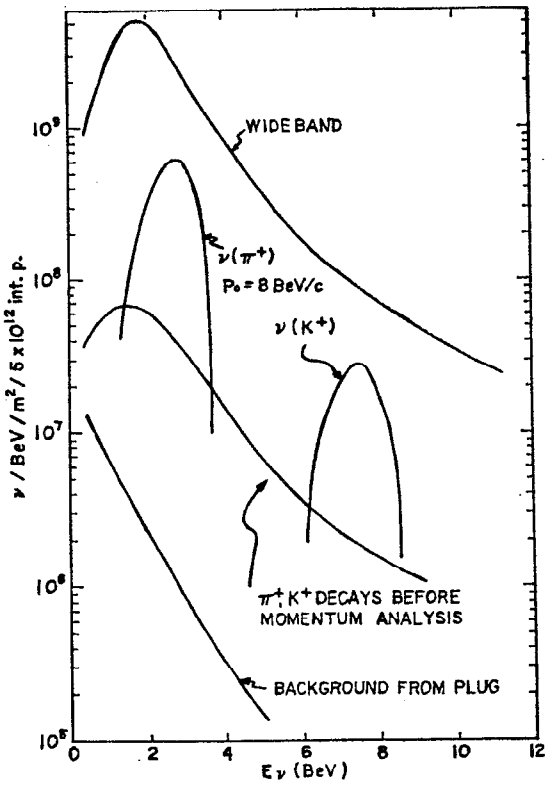


Fig. 49. Neutrino flux distribution from the existing BNL narrow-band horn-focussing system.

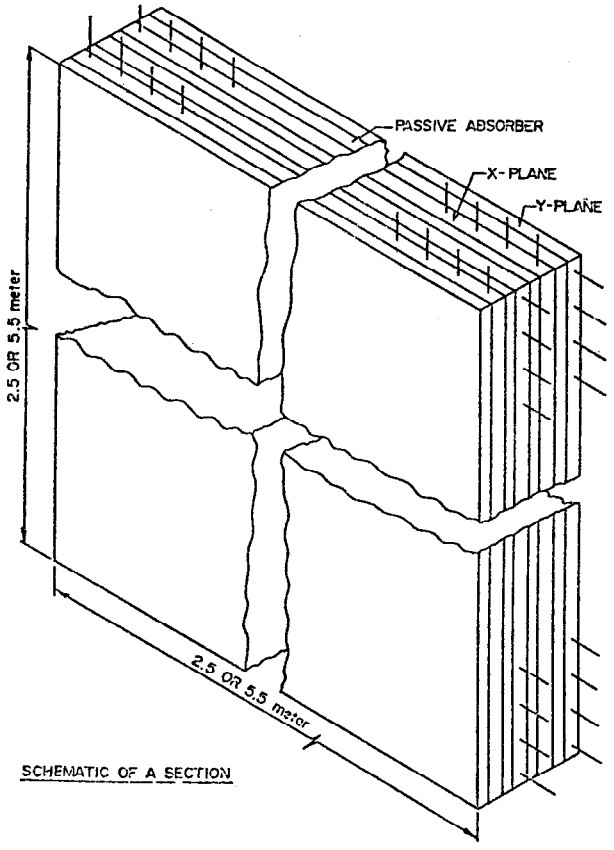


Fig. 50. Schematic of the 175 ton neutrino detector proposed by the BNL-Columbia-Illinois-Johns Hopkins-NRL collaboration. The proportional drift tubes are very similar in design to those of the E734 detector, but the liquid scintillator is replaced by inactive material.

tons. A new narrow-band beam would be constructed to try to obtain a higher neutrino flux at a lower energy (Fig. 51). The sensitivity of this experiment to Δ^2 for maximum mixing angles would not be as good as that of the reactor experiment, nor would the sensitivity to small mixing angles in the higher mass region be as sensitive as that of the other Brookhaven experiment just discussed. However, its sensitivity would be superior to both of these experiments in the regime where both Δ^2 and $\sin^2 2\theta$ are reasonably small.

In phase 2, each of the groups at Brookhaven would build a second detector and perform a two-position measurement of the ν_μ flux to obtain limits on the oscillation probability of ν_μ into other types of neutrinos. Neither of these experiments is, however, currently approved. Fig. 52 gives an indication of the sensitivity of one of these experiments, the particular selling point of which would be the ability to reconstruct the neutrino energy for quasi-elastic events and also to perform rather precise measurements of the neutral current to charged current ratio. The latter capability provides an alternative sensitivity to neutrino oscillations which is largely independent of the ability to measure either the flux as a function of energy or the absolute rate of ν_μ interactions.

I now discuss much more briefly experiments under way at two other laboratories. At Fermilab, the CIFRR collaboration[39] is currently performing a neutrino oscillation experiment with detectors located at 743 meters and at 1080 meters, using a narrow-band beam at multiple energies to search for oscillations $\nu_\mu \rightarrow \nu_\mu$ in the same manner as discussed for the CERN and Brookhaven experiments, but with

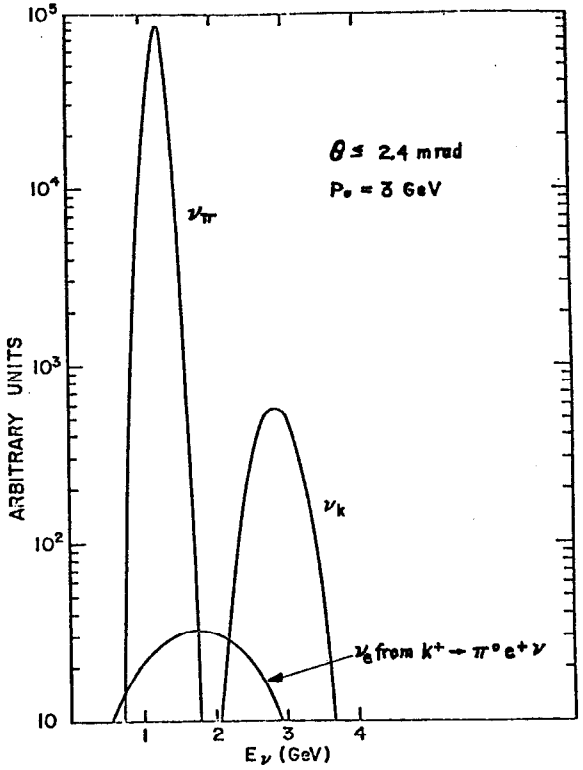


Fig. 51. Design neutrino flux for the new narrow band horn to be constructed at BNL.

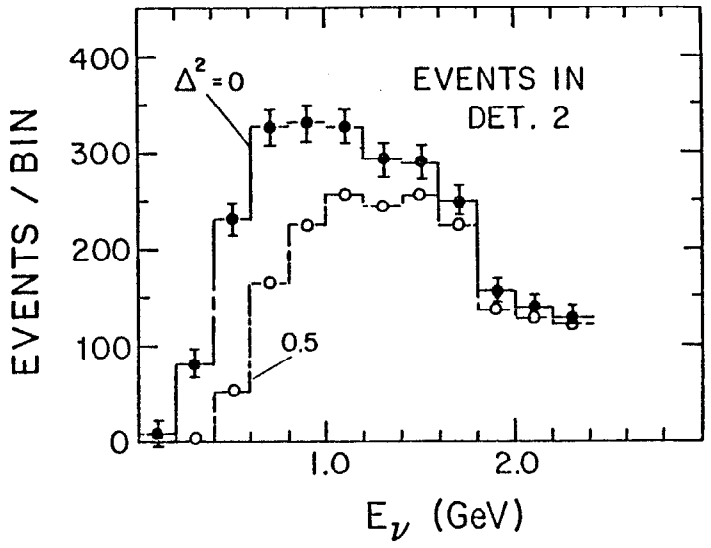


Fig. 52. Calculated ν_μ flux at the far detector of the proposed BNL-Brown-KEK-Osaka-Pennsylvania-Stony Brook-Tokyo-UCI oscillation experiment for maximum mixing angle and $\Delta^2 = 0$ or $\Delta^2 = .5$ eV^2. For larger Δ^2 (a few eV^2) very dramatic alterations of the ν spectra are obtained.

a sensitivity which is optimized for still larger values of Δ^2. It is anticipated that the experiment will be sensitive over the domain $\sin^2 2\theta \simeq 0.2$ for $20 < \Delta^2 < 900$ eV^2. Results should be available from this experiment within the next few months.

An ANL-CIT-LAMPF-Louisiana-Ohio State collaboration[40] is currently constructing a detector to search for ν_e disappearance, using the reaction $\nu_e + n \rightarrow p + e^-$, and for oscillations of the type $\bar{\nu}_\mu \rightarrow \bar{\nu}_e$ by searching for the reaction $\bar{\nu}_e + p \rightarrow e^+ + n$ at LAMPF. They accomplish this by the neat trick of using a detector very similar to the existing neutrino detector at Brookhaven, but which would use water Cherenkov counters instead of liquid scintillator as the active target (Fig. 53). In this way the detector can be filled either with heavy water or with light water depending on whether one wants neutrons and protons or only protons available as a target. At LAMPF energies interaction of the neutrinos with nucleons in heavier nuclei such as oxygen are very strongly suppressed. The detector will be mounted on wheels so that measurements may be made at multiple distances from the neutrino source.

There are at least two additional proposals for ambitious neutrino oscillation experiments which might be carried out in the more distant future. Unfortunately, I do not have time to discuss either of these other than to briefly note them. One proposes to construct a detector in the Jura Mountains at a distance of 17 km from the SPS.[41] It would concentrate on ν_μ disappearance as well as providing an explicit search for $\nu_\mu \rightarrow \nu_e$ and $\nu_\mu \rightarrow \nu_\tau$ transitions. The second experiment[42] would take advantage of a new proposed neu-

THE DETECTOR

FOR i) ν_e disappearance WANT $\nu_e + n \rightarrow p + e^-$ and movable detector

$\Rightarrow$ SO WANT Heavy WATER Cherenkov Counter ON Wheels

FOR ii) $\bar{\nu}_\mu \rightleftarrows \bar{\nu}_e$ WANT $\bar{\nu}_e + p \rightarrow e^+ + n$

$\Rightarrow$ SO WANT Light WATER Cherenkov Counter ON Wheels

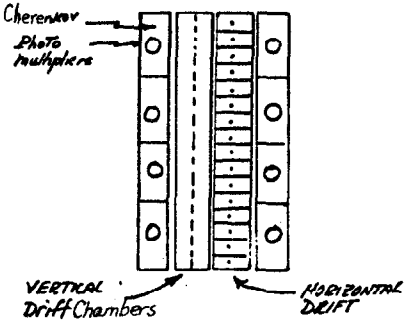


Fig. 53. Schematic of the detector for the ANL-CIT-LAMPF-Louisiana-Ohio State experiment at LAMPF. The detector may be filled with either light or heavy water, and is mounted on wheels so that measurements may be made at multiple distances from the source.

trino facility at LAMPF to obtain more precise limits on ν_μ survival as well as $\nu_\mu \rightarrow \nu_e$ transitions.

Finally, we are in a position to compare the sensitivities of the experiments we have discussed. The last two figures rely heavily on a summary prepared by R. E. Lanou at the recent Snowmass Summer Study.[28]

Shown in Fig. 54 are the sensitivities for $\nu_\mu \rightarrow \nu_e$ as well as some results for $\bar{\nu}_e$ or ν_e survival experiments. The results of the FNAL 15' bubble chamber experiment and the reactor experiment of F. Boehm et al. are shown by solid lines, while the anticipated results of experiments expected to be completed at BNL, CERN and LAMPF in the next 2-3 years are indicated by a dashed line. Also indicated are the limits of sensitivity which might be obtained towards the end of the decade in experiments utilizing new low energy facilities such as an AGS upgrade or LAMPF II combined with very large (500-1000 ton) detectors of the type currently employed at BNL. Experiments employing large detectors underground which observe the interactions of atmospheric neutrinos,[43] or experiments employing large quantities of gallium to detect the PEP neutrinos from the sun,[44] may be sensitive to very small values of Δ^2 provided that the mixing angle is reasonably large.

Finally, we show in Fig. 55 the anticipated results for survival experiments. Curve (a) shows the approximate existing limits while the dashed curve just to the left of it indicates the anticipated sensitivity of Experiment 701 currently running at Fermilab. Curve (b) presents the combined sensitivity that could be obtained by the CDHS

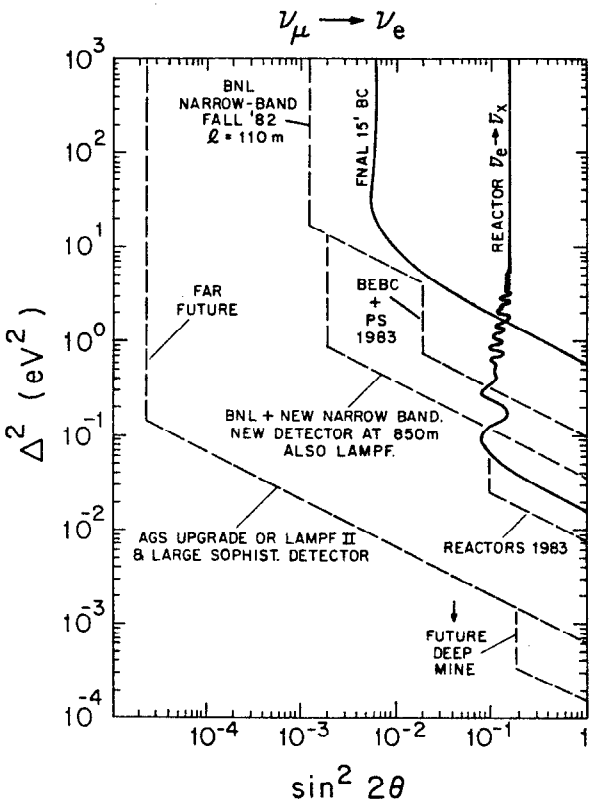


Fig. 54. Summary of the sensitivities for $\nu_\mu \rightarrow \nu_e$ and $\bar{\nu}_e \rightarrow \bar{\nu}_x$ experiments. The existing limits from the Gosgen reactor experiment and the 15' BC experiment at Fermilab are shown by the solid lines. Results from experiments to be completed at BNL, CERN, LAMPF and the Gosgen reactor in the next two years are shown by dashed lines. Also shown are possible future results from deep mine experiments (using baryon decay detectors, for example) and from ambitious experiments at upgraded low energy accelerators. The sensitivity shown for the latter is quite optimistic.

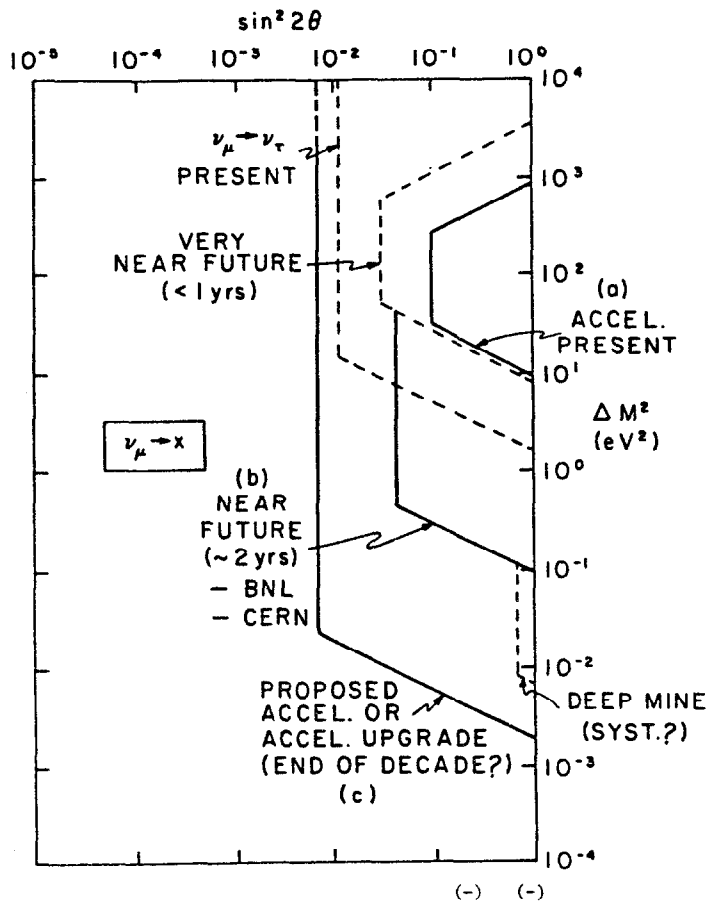


Fig. 55. Summary of sensitivities for $\nu_\mu \rightarrow \nu_x$ experiments. The present limits are shown by curve (a), while the dashed line just to the left shows the results expected from E701, which has recently finished running at Fermilab. Curve (b) is an envelope of the results expected within the next two years from CERN and BNL. An optimistic estimate of the results that might be achieved by ambitious experiments at future low energy facilities is given by curve (c). Deep mine experiments may be able to probe to small Δ^2 for relatively large mixing angles.

and CHARM experiments at CERN as well as the phase 2 experiments proposed at Brookhaven. Again, an indication of the sensitivities which might be obtained by very ambitious experiments utilizing new accelerator facilities is indicated by curve (c) and the possible contribution of deep mine experiments is also shown. It is apparent that with a sustained effort using many different facilities and types of experiments, our search for neutrino oscillations may be extended by orders of magnitude in both the sensitivity to small masses and to small mixing angles.

Acknowledgments

There are many people with whom I have had very interesting discussions concerning grand unification, proton decay, and neutrino oscillations. In particular I would like to thank J. Ellis, P. Langacker, G. Segre, W. Fischler, M. Murtagh, E. Beier, A. K. Mann, and R. E. Lanou. J. Van der Velde, D. Cline, and E. Fiorini were kind enough to provide me with information on the IBM, HPW, and NUSEX experiments respectively. M. Kuklinski did an excellent job typing the manuscript in a timely fashion. A. Mosher was terrific in organizing the Summer Institute.

Finally, I would like to especially thank David Leith, who provided the opportunity for me to speak to you, not only by inviting me, but also by being one of the strong supporters of the SLAC Summer Institute over many years.

References and Footnotes

* Alfred P. Sloan Research Fellow

(1) J. Ellis, Les Houches Summer School, Les Houches, France, Aug. 1981 and CERN preprint TH-3174.

(2) P. Langacker, Phys. Rep. 72C, 185 (1981).

(3) C. Quigg, Proceedings of the Nato Advanced Study Institute, "Techniques and Concepts of High Energy Physics," St. Croix, U.S. Virgin Islands, July 2-13, 1980; preprint FERMILAB-Conf-80/64-THY.

(4) E. L. Hill, Rev. Mod. Phys. 23, 253 (1951).

(5) C. N. Yang and R. L. Mills, Phys. Rev. 96, 191 (1954).

(6) S. L. Glashow and M. Gell-Mann, Ann. Phys. (N.Y.) 15, 437 (1961).

(7) W. J. Marciano, The Second Workshop on Grand Unification, ed. by J. P. Leveille, L. R. Sulak, and D. G. Unger, (Birkhauser, Boston), 151 (1981).

(8) S. Hawking, D. N. Page, and C. N. Pope, Phys. Lett. 86B, 175 (1979); Nucl. Phys. B170, 283 (1980).

(9) Ya. B. Zeldovich, Phys. Lett. 59A, 254 (1976).

(10) P. Langacker, talk presented at the International Conference on Baryon Nonconservation, Tata Institute of Fundamental Research, Bombay, January 11-14, 1982; University of Pennsylvania preprint, UPR-0186T.

(11) P. Langacker, Proceedings of the 1982 Summer Workshop on Proton Decay Experiments, ed. by D. S. Ayres (Argonne National Laboratory, Argonne, IL)

(12) M. L. Cherry, M. Deakyne, K. Lande, C. K. Lee, R. I. Steinberg, and B. Cleveland, Phys. Rev. Lett. 47, 1507 (1981).

(13) M. A. Shupe, The Second Workshop on Grand Unification, ed. by J. P. Leveille, L. R. Sulak, and D. G. Unger (Birkhauser, Boston), 41 (1981).

(14) M. G. K. Menon et. al., paper submitted to the XXI International Conference on High Energy Physics, Paris, July 26-31, 1982; S. Miyake and V. S. Narasimham, The Second Workshop on Grand Unification, ed. by J. P. Leveille, L. R. Sulak, and D. G. Unger (Birkhauser, Boston), 11 (1981).

(15) D. Perkins, talk presented at the XXI International Conference on High Energy Physics, Paris, July 26-31, 1982.

(16) E. Fiorini, paper submitted to the XXI International Conference on High Energy Physics, Paris, July 26-31, 1982; E. Fiorini, The Second Workshop on Grand Unification, ed. by J. P. Leveille, L. R. Sulak, and D. G. Unger (Birkhauser, Boston), 55 (1981).

(17) D. Sinclair and T. W. Jones, The Second Workshop on Grand Unification, ed. by J. P. Leveille, L. R. Sulak, and D. G. Unger (Birkhauser, Boston), 84 (1981).

(18) C. Wilson, The Second Workshop on Grand Unification, ed. by J. P. Leveille, L. R. Sulak, and D. G. Unger (Birkhauser, Boston), 80 (1981).

(19) H. Ikeda et. al., Proceedings of the 1981 International Conference on Neutrino Physics and Astrophysics, Maui, Hawaii, ed. by R. J. Cence, E. Ma, and A. Roberts, Vol. 1, 224 (1981).

(20) R. Barloutaud, The Second Workshop on Grand Unification, ed. by J. P. Leveille, L. R. Sulak and D. G. Unger (Birkhauser, Boston), 70 (1981).

(21) J. Bartelt et. al., Minnesota-Argonne-Oxford proposal submitted to U. S. Department of Energy and U. K. Science and Engineering Council. See also Ref. 13.

(22) K. Lande et. al., BNL-Pennsylvania proposal submitted to U.S. Department of Energy. See also Ref. 12.

(23) A. K. Mann, E. W. Beier, L. S. Durkin, S. M. Heagy, and H. H. Williams, University of Pennsylvania proposal submitted to the U.S. Department of Energy.

(24) A preliminary version of this proposal was described in the Workshop on Grand Underground Detectors, Ist. di Fisica, Rome, Oct., 1981.

(25) For recent treatments of neutrino oscillations, see S. Bilensky and B. Pontecorvo, Phys. Rep. 416, 225 (1978), and A. K. Mann and H. Primakoff, Phys. Rev. D15, 655 (1977). In the discussion presented in this paper I will make the simplifying assumption that only two of the neutrino flavors mix.

(26) B. Kayser, Phys. Rev. D24, 110 (1981).

(27) M. Murtagh, BNL, Upton NY, private communication.

(28) R. E. Lanou, Proceedings of the DPF Workshop on the Future of High Energy Physics and Facilities, Snowmass, CO, June-July, 1982.

(29) The discussion will be based primarily on reactor or accelerator based neutrino oscillation experiments, though an indication of the sensitivities of experiments detecting atmospheric or solar neutrinos is presented in the summary.

(30) J. L. Vuilleumier, Phys. Lett. 114B, 298 (1982).

(31) F. Reines et. al., Phys. Rev. Lett. 45, 1307 (1980).

(32) N. J. Baker et. al., Phys. Rev. Lett. 47, 1576 (1981).

(33) Padova-Pisa-Athens-Wisconsin collaboration, proposal CERN/SPSC/80-57/P146 and CERN/PSCC/80-130/P33; PSCC/80-132/P33 Add. 1.

(34) CERN-Dortmund-Heidelberg-Saclay collaboration, proposal CERN/PSCC/80-106/P30.

(35) CHARM collaboration, proposal CERN/PSCC/81-8/P37.

(36) H. Wachsmuth, Proceedings of the Neutrino '82 Conference, Balatonfured, Hungary; preprint CERN/EP 82-102.

(37) BNL proposal E775.

(38) BNL proposal E776.

(39) FNAL proposal E701.

(40) LAMPF proposal E645.

(41) Annecy-Athens-Davis-Hawaii-Imperial College-Lyon-Oxford-Paris collaboration, proposal CERN/SPSC/82-20/P178.

(42) LAMPF-New Mexico-Maryland-Temple-University of California (Riverside) collaboration; LAMPF proposal E638.

(43) For a review of the possibilities for studying neutrino oscillations using atmospheric neutrinos, see D. S. Ayres, T. K. Gaisser, A. K. Mann, R. E. Shrock, Proceedings of the DPF Workshop on the Future of High Energy Physics and Facilities, Snowmass, CO, June-July, 1982.

(44) Detection of the PEP neutrinos from the sun would in principle allow a sensitivity to $\Delta^2 \approx 10^{-11}$ eV^2 for large mixing angles. See the talk by R. Davis, Proceedings of the Neutrino Oscillation Workshop, Brookhaven National Laboratory, Jan. 30-31, 1981, BNL 51380.

SLAC-PUB-3093
April 1983
(T/E)

e^+e^- INTERACTIONS AT VERY HIGH ENERGY: SEARCHING BEYOND THE STANDARD MODEL

JONATHAN DORFAN*
Stanford Linear Accelerator Center
Stanford University, Stanford, California 94305

Lectures Presented at the
SLAC Summer Institute on Particle Physics:
Physics at Very High Energies
Stanford, California
August 16-27, 1982

* Work supported by the Department of Energy, contract DE-AC03-76SF00515.

© J. Dorfan 1982

TABLE OF CONTENTS

1. Introduction
2. The e^+e^- Machines of the Future
3. The Standard Model
4. Testing the Standard Model in e^+e^- at Energies Beyond Those Currently Available
   - 4.1. Search for the Top Quark
   - 4.2. Search for and Studying the Z^o and $W^\pm$
   - 4.3. Search for the Neutral Higgs Particle, H^o
   - 4.4. Tests of the Non-Abelian Nature of QCD
   - 4.5. Does α_s Run - and, If So, How Do We "Clock" It?
   - 4.6. Quark Confinement
5. Simple Extensions of $SU(3) \wedge SU(2) \wedge U(1)$
   - 5.1. Models with More Than One Higgs Doublet
   - 5.2. Models with Extended Electroweak Gauge Groups
6. Models Which Avoid the Gauge Hierarchy Problem
   - 6.1. Supersymmetry (SUSY)
   - 6.2. Technicolor Theories - Dynamical Symmetry
   - 6.3. Composite Models; Strong $SU(2)$
7. Summary and Conclusions

ACKNOWLEDGEMENTS

REFERENCES

1. Introduction

These lectures discuss e^+e^- interactions at very high energies with a particular emphasis on searching beyond the standard model which we take to be $SU(3)_{color} \wedge SU(2) \wedge U(1)$. The highest e^+e^- collision energy exploited to date is at PETRA where data have been taken at 38 GeV. We will consider energies above this to be the "very high energy" frontier. The lectures will begin then with a review of the collision energies which will be available in the upgraded machines of today and the machines planned for tomorrow. Without going into great detail, we will define the essential elements of the standard model. We will remind ourselves that some of these essential elements have not yet been verified and that part of the task of searching beyond the standard model will involve experiments aimed at this verification. For if we find the standard model lacking, then clearly we are forced to find an alternative. So we will investigate how the higher energy e^+e^- collisions can be used to search for the top quark, neutral Higgs scalars, provide true verification of the non-Abelian nature of QCD, etc.

Having done this we will look at tests of models involving simple extensions of the standard model. Models considered are those without a top quark, those with charged Higgs scalars, with multiple and/or composite vector bosons, with additional generations and possible alternative explanations for the PETRA three jet events which don't require gluon bremsstrahlung.

From those simple extensions of the standard model we will move to more radical alternatives, alternatives which have arisen from the unhappiness with the gauge hierarchy problem of the standard model. Technicolor, supersymmetry and composite models will be discussed. In the final chapter we will summarize what the future holds in terms of the search beyond the standard model.

We will be considering many different theoretical models in these lectures. The descriptions of the models will intentionally be brief (and non-rigorous); the main emphasis will be on the experimental implications of these models.

2. The e^+e^- Machines of the Future

The e^+e^- storage rings have been invaluable tools for the discovery and study of new thresholds. The fourth quark flavor was discovered at SPEAR as was the third lepton family. The clean environment provided by the e^+e^- storage rings SPEAR and DORIS permitted detailed study of charm spectroscopy and provided a wide variety of tests all of which pointed to the fact that the τ was in fact a universal lepton. The bottom quark was not discovered in e^+e^- interactions. However the study of bottomonium at DORIS and CESR has provided a wealth of information about the bottom quark. The PETRA and PEP storage rings were built with the hope of discovering the top quark. Alas top has not yet shown itself and the present PETRA limits indicate that the top quark is more massive than 18.5 GeV/c^2. However PETRA did bring striking confirmation of QCD as evidenced by events containing hard gluon bremsstrahlung. Also clear evidence for the electroweak interaction is apparent in the muon pair asymmetry measurements, the magnitude of the asymmetry confirming the predictions of the Weinberg-Salam model. These are only a few of the striking examples of how fruitful the investment in e^+e^- machines has been. With new thresholds to be tested, what energy ranges in e^+e^- interactions will be available to the experimenters of the future? We will concern ourselves here mainly with the parameters of the machines – the physics opportunities which go with these machines will be discussed in later sections.

In the next few years, PETRA will undergo a continuous energy upgrade[1] in search of the elusive top quark. By the end of 1982, PETRA will have doubled its complement of rf and will achieve a maximum energy of 40 GeV. This will be followed by the addition of new accelerating structures which will provide for a maximum energy of 46 GeV. The latter upgrade should be completed by April 1983. If the top quark has a mass below 43 GeV/c^2, we should have evidence of this from PETRA before the end of 1983. It will become apparent in these lectures that toponium will provide many important tests of the standard model aside from the obvious confirmation that there indeed exists a sixth flavor. This exciting prospect might not be too far off.

If toponium still eludes PETRA, DESY may choose to install superconducting rf cavities in PETRA which would give them a maximum energy of 60 GeV. Two tests[2] with two different superconducting cavities have been performed at PETRA. Both tests were most promising – a $\sim$ 9 GeV beam of electrons was stored in PETRA using a single superconducting cavity. Certainly no decision has yet been made to continue beyond 46 GeV. However, the means to achieve energies of $\sim$ 60 GeV at PETRA appear in hand. The time scale for such an upgrade is not clear, but if DESY were committed, PETRA could be operating with superconducting rf by late 1985. Estimates of the luminosity at these higher energies are uncertain at this time.

A conventional e^+e^- storage ring, TRISTAN, utilizing warm rf is presently under construction at KEK in Japan. This machine fills the KEK site and will have a maximum energy of $\sim$ 60 GeV. The design luminosity for the machine is $4 \times 10^{31}\ cm^{-2}\ sec^{-1}$. The present schedule calls for turn-on in early 1986 with at least two of the four interaction regions instrumented with general purpose particle detectors. A more complete description of the project can be found in Ref. 3. If PETRA stops its upgrade at an energy of 46 GeV, the TRISTAN machine will cover the territory up to 60 GeV with good luminosity.

The next big jump in available energy will come with the completion of the Stanford Linear Collider (SLC) at SLAC. The present schedule shows the SLC delivering colliding beams in late 1986. The design luminosity of the machine is $6 \times 10^{30}\ cm^{-2}\ sec^{-1}$ and the maximum energy at turn-on will be 100 GeV. A complete description of the SLC can be found in Ref. 4. However, since the SLC is not a conventional e^+e^- storage ring, we provide here a short description of the machine referring to Fig. 1. The existing linac will be upgraded to 50 GeV using an extension of the SLED ideas which enabled SLAC to raise the linac energy from 22 GeV to 34 GeV. An electron bunch is diverted out of the linac and collided with a target to produce positrons. These positrons are then fed back into the front end of the accelerator. Following passage through damping rings, which provide cooling for the electron and positron bunches, a bunch of positrons immediately followed in the next linac bucket by a bunch of electrons, is transported down the accelerator to the colliding arcs. The positrons and electrons are switched to different arcs and are brought into collision by an elaborate system of optics, termed the final focus. Following the collision, the beams are dumped.

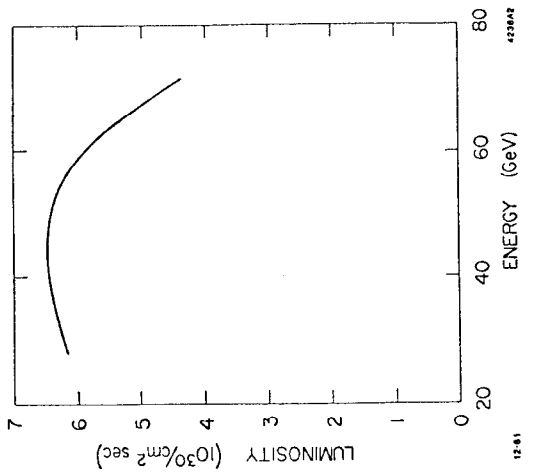


Fig. 2. Luminosity versus beam energy for the SLC.

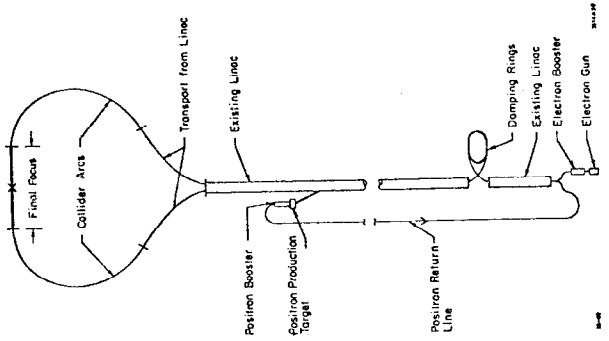


Fig. 1. Schematic layout of the SLC.

So unlike a storage ring, the SLC operates as a single pass collider. The repetition rate of the linac is 180 Hz, many orders of magnitude less than that of typical storage rings. To produce a usable luminosity, this slow collision rate must be compensated for. This will be done using an intense electron gun capable of producing 5×10^{10} electrons per bunch and by designing the final focus optics such that the transverse dimensions of the colliding beams are a few microns as opposed to conventional storage rings where these dimensions are typically a few millimeters. The expected luminosity as a function of collision energy is shown in Fig. 2. The SLC is optimized to run at the Z^0. However, the luminosity remains good down to energies of 60 GeV. If toponium should be above TRISTAN, the SLC could, in principle, be used to study it. The SLC has the distinct disadvantage of serving only one detector at a time.

The SLC project is an adventurous one to say the least. The linac must be upgraded to 50 GeV. High intensity, low emittance beams must be transmitted faithfully to the final focus which has the difficult task of focusing the beams down to micron spot sizes. It has the advantages of being cheap to build (M$ 100 for the machine) and will provide Z^0 physics in the very near future. Even at a luminosity of 10^{29} the SLC will be an interesting machine in 1987, providing $\sim$ 200 Z^0's per day. The physics goals of the SLC are clear – study the physics at the Z^0. In addition, the SLC is an important step into the future providing the first high energy test of the concept of linear colliders. The cost of a conventional storage ring goes like the square of the center of mass energy ($E_{c.m.}$), whereas the cost of a linear collider goes linearly with $E_{c.m.}$. It is entirely possible that LEP (see below), with its initial phase providing $E_{c.m.}$ = 100 GeV at a cost $\sim$ M$ 500, will be the last frontier e^+e^- storage ring which we can afford to build.

Another feature of the SLC is the promise of longitudinally polarized beams. As we will see later, longitudinally polarized beams are a powerful tool for the study of Z^0 physics.[5] Polarized electrons are produced by shining circularly polarized laser light on a galium arsinide cathode. Such an electron gun exists and has been successfully tested. Polarized electrons have already been transported down the linac and simulations of transport through the SLC arcs indicate that the transmission efficiency for the polarized electrons is $\geq 80\%$. The sign of the laser polarization can be reversed on a linac pulse by pulse basis yielding successive beam pulses of opposite spins. Hence it

appears that, with very high probability, beams with polarizations of $\geq 50\%$ will be available at the SLC.

If the linac could be raised beyond the 50 GeV beam energy, a second phase of the SLC will be possible providing maximum collision energies of $\sim$ 140 GeV.

While the U.S. high energy e^+e^- program is putting its money into the SLC, the European program for very high energies centers around the LEP project. LEP is a conventional e^+e^- storage ring which will be built at CERN. In its first incarnation – which we term LEP I – it will achieve a maximum collision energy of 100 GeV and a luminosity of 10^{31}. The project[6] is vast – requiring a tunnel with a 27 Km circumference – but the machine uses conventional storage ring technology and hence one should feel fairly confident that the design goals will be met. LEP I is slated for turn-on in about the middle of 1988 at a cost of $\sim$ M$ 500. LEP will have eight experimental halls of which four will be instrumented for LEP I.

The strength of the LEP program resides in its potential to go to $\leq$ 250 GeV collision energies. This is achieved in two different steps. By the addition of conventional rf, the machine will yield a maximum collision energy of 170 GeV (LEP II). By the application of superconducting rf the machine can go to $E_{c.m.} \leq 250$ GeV depending on the accelerating gradient which is achieved (LEP III). Gradients of 3 MeV/m corresponding to $E_{c.m.} = 220$ GeV have already been achieved in the PETRA tests.[2] The parameters of these two routes are summarized in Table 1. Time scales and costs for these upgrades are not known yet. As a guess LEP II could be available in early 1990.

Table 1. Summary of Performance With Room-Temperature rf.

	1/6 of rf installed	1/4 of rf installed	1/2 of rf installed	1 rf installed
Installed rf power (MW)	16	24	48	96
Length of rf structure (m)	271.5	407.2	814.4	1628.8
Number of experiment areas with rf	2 (partial)	2 (full)	4 (full)	8 (full)
Maximum energy (zero luminosity) (GeV)	59.0	65.5	78.0	93.0
Maximum current required (mA)	2.8	3.1	3.8	4.7
Maximum luminosity ($\Delta Q = 0.03$) ($\times 10^{31}$ cm^{-2} sec^{-1})	0.9	1.3	1.8	2.7
Energy of maximum luminosity (GeV)	51.5	58.5	70.0	85.0

Maximum Energies With Superconducting rf.

Maximum accelerating gradient (MV/m)	Two experiment areas with rf $L_c = 407.2m$	Four experiment areas with rf $L_c = 814.4m$	Eight experiment areas with rf $L_c = 1628.8m$
2.0	70.3	83.6	99.4
3.0	77.8	92.5	110.0
4.0	83.6	99.4	118.2
5.0	88.4	105.2	125.0

Beam polarization at LEP is much less certain than at SLC. A considerable amount of work is being done in this area, but there are still many hurdles to cross. These hurdles are discussed in Ref. 7. Conceptual designs for very high energy colliding linacs exist both at SLAC and NOVOSIBIRSK. The Russian VLEPP project is described in detail in Ref. 8. The motivation for linear colliders was stated earlier, namely the cost grows linearly with $E_{c.m.}$ whereas the cost of circular machines grows as $E^2_{c.m.}$. Taking into account the constants of these equations, one finds that the crossover point is roughly at $E_{c.m.} = 150$ GeV. This assumes of course, that in both cases one starts from scratch. Hence it would seem that to go beyond LEP III, one will require a colliding linac machine. The general consensus seems to be to build a first phase machine capable of 300-500 GeV collision energy followed by a second phase in the 1 TeV range. Much will depend on what is learned from the SLC. In addition luminosities of $\geq 10^{32}$ are needed to test current ideas at the $\geq$300 GeV energy scale. I include this terse discussion here to emphasize that the intellectual effort and research and development is going on in many areas so that the door to e^+e^- collisions in the 1 TeV region may be opened in the 1990's.

This section concludes with Table 2 which summarizes the machine possibilities for e^+e^- collisions for the foreseeable future.

Table 2. The e^+e^- Machine of the Future.

Where	When	$E^{max}_{c.m.}$ GeV	$\mathcal{L}^{max}_{design}$ $cm^{-2}sec^{-1}$
PETRA, DESY	October 1982	40	1.5×10^{31}
PETRA, DESY	April 1983	46	$\sim 1.5 \times 10^{31}$
PETRA, DESY	By late 1985?	60	?
TRISTAN, KEK	January 1986	60	$4 \times 10^{3}1$
SLC I	October 1986	100	6×10^{30}
SLC II	?	140	4×10^{30}
LEP I	June 1988	100	10^{31}
LEP II	?	170	3×10^{31}
LEP III	?	220-250	?
VLEPP I	1990's	300	10^{32}
VLEPP II	1990's	1000	10^{32}

3. The Standard Model

We take $SU(3)_{color} \wedge SU(2) \wedge U(1)$ as the standard model. To describe this model in detail goes way beyond the scope of these lectures. Instead we need to characterize the main features of the model so that we can catalogue those features which are still not verified. No attempt has been made here to be complete or rigorous; rather we have in mind compiling, in as brief a manner as possible, the list of essential elements which appears at the end of this section.

The class of "locally gauge invariant theories" form the theoretical framework for the standard model. Since their use is so pervasive, we will take some time to remind ourselves of the terminology. We use the $U(1)$ gauge group of electromagnetism as an example.

Consider the matter field of an electron. If we change the phase of the field by the same amount in all space we will find that the physics remains invariant. The reason for this is clear – the physics is determined by differences in phases and the global transformation discussed above will leave all phase differences fixed. We say that the electron matter field is "globally gauge invariant" with respect to phase rotations. Suppose, however, that we perform a local gauge transformation, namely we change the phase at one point in space only. Clearly this will change all relative phases and hence all physical measurables. To preserve the local symmetry we must add an additional new field, which is designed to compensate over all space for the local disturbance. As is well known to the reader, one adds to the free electron matter field a vector field whose quantum is the photon. Since compensation for the local disturbance is required over infinite distances, the photon must be massless. The order of successive local gauge transformations (successive photon emissions from an electron for instance) does not affect the physics since, in all cases, the phase change resulting from the transformations is the same. Because successive transformations commute, the theory – namely QED – is termed Abelian and the reason that QED is Abelian is that the photon does not carry the property which is conserved, that is the photon is "chargeless." To summarize, QED is a locally gauge invariant Abelian theory, and the local gauge invariance was ensured by the addition of a new field.

By direct analogy with QED, $SU(3)_{color}$ is described by a locally gauge invariant theory. The conserved quantity is color. In the standard model quarks come in six flavors – u, d, s, c, b and t – and each quark has three color degrees of freedom. Since hadrons do not exhibit color, they are color singlets. Baryons are composed of three quarks and mesons of a quark anti-quark pair. In QCD local gauge invariance is ensured by the addition of sixteen fields. The quanta of these fields are eight gluons most of which, in order to preserve the local gauge invariance, must carry color. In general, successive local gauge transformations (successive emissions of gluons from a quark for instance) will not commute because the gluons carry color. Hence QCD is a non-Abelian theory. The non-Abelian nature of QCD has some important experimental consequences.

In QED the vacuum becomes polarized by the presence of virtual e^+e^- pairs. This leads to the screening of bare electric charge. In QCD the vacuum contains both virtual quark pairs and virtual gluon pairs. This combination conspires to anti-screen bare color charge. This leads to the notion of asymptotic freedom and the accompanying features that (a) quarks and gluons are confined by the color field (i.e., we should not see free quarks) and (b) the strength of the strong (color) coupling constant, α_s, depends on the distance scale of the probe. The notion of a running coupling constant is expressed, to leading order in logs, as

$$\frac{1}{\alpha_s(Q^2)} = \frac{1}{\alpha_s(q^2)} + \frac{32 - n_f}{12\pi} \; log\left(\frac{Q^2}{q^2}\right)$$

where n_f is the number of quark flavors.

Since the gluons carry color, they can couple to themselves as well as coupling to a quark anti-quark pair. This self coupling is a consequence of the non-Abelian nature of QCD and hence any evidence for this self coupling constitutes a test of this very important feature of QCD. (Notice that there is no analog of the gluon self-coupling in QED.)

Consider Fig. 3 in which a gluon is shown emitting a gluon (a) and a quark is shown emitting a gluon (b). If the parton energies are high enough, then this perturbative picture makes sense and one finds that the probability for 3(a) is 9/4's larger than for 3(b). The fact that the gluon-gluon coupling is about twice as probable as the quark-gluon coupling implies that gluons should fragment to roughly twice as many hadrons as quark jets of the same energy. The average transverse momentum of the

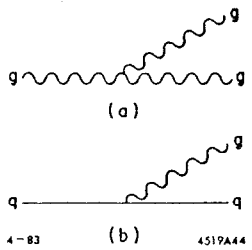


Fig. 3. The perturbative representation of the processes whereby a gluon radiates a gluon (a) and a quark radiates a gluon (b).

decay products should also be different for quark and gluon jets. This QCD prediction holds only if you believe the perturbative picture described above. In all likelihood this picture is sound and we will treat this fragmentation difference between quarks and gluons as an important prediction of QCD.

In the standard model, leptons are point-like particles which carry no color. Hence they are unaffected by the strong interaction. They couple to the gauge bosons of $SU(2)$ through their weak charge (helicity) and to the photon of $U(1)$ through their electric charge. There are six leptons – $e, \mu, \tau, \nu_e, \nu_\mu$ and ν_τ. The left-handed fermions of $SU(2)$ are arranged in flavor conserving doublets:

$$\begin{pmatrix}\nu_e\\ e\end{pmatrix}_L \qquad \begin{pmatrix}\nu_\mu\\ \mu\end{pmatrix}_L \qquad \begin{pmatrix}\nu_\tau\\ \tau\end{pmatrix}_L$$

$$\begin{pmatrix}u\\ d'\end{pmatrix}_L \qquad \begin{pmatrix}c\\ s'\end{pmatrix}_L \qquad \begin{pmatrix}t\\ b'\end{pmatrix}$$

The primes on the quarks indicate that the flavor conservation in the quark sector is not perfect. This generation mixing is summarized by the elements of the Kobayashi-Maskawa matrix, the most familiar component of this matrix being the Cabibbo angle which tells us that the d quark has a 5% strange quark admixture. The right-handed fermions occur in singlets u_R, d_R, s_R, c_R, b_R, t_R, e_R, μ_R and τ_R. In the standard model we have three generations. Associated with each charged lepton is a neutral massless lepton. Since the neutrinos have identically zero mass, there are no right-handed neutrinos.

We have now specified the particles of $SU(2) \wedge U(1)$. At this time it is a gauge invariant – with respect to weak isospin – theory with four massless bosons. This is problematical because (a) we have too many massless (long range) fields and (b) the local weak isospin symmetry implies that fermions are massless. Enter the cunning of the Higgs mechanism which is used to spontaneously break the symmetry. In this scheme, while the Lagrangian of the theory remains invariant, the vacuum (ground state) does not. The fact that the vacuum is not invariant implies that there exists stored energy in the vacuum. This stored energy is used to give mass to the bosons and the charged fermions. In the standard model the minimal scheme is used to

spontaneously break the symmetry. This is achieved using a doublet of complex fields:

$$\phi = \begin{pmatrix} \phi^+ \\ \phi^0 \end{pmatrix}$$

$$\phi^+ = \phi_1^+ + i\phi_2^+$$

$$\phi^0 = \phi_1^0 + i\phi_2^0 \quad .$$

We add a term to the Lagrangian:

$$\mathcal{L}_{Higgs} = T_{Higgs} - V_{Higgs}$$

where $V_{Higgs} = -\frac{|u^2|}{2}\ \phi^+\phi + \frac{|\lambda|}{4}\ (\phi^+\phi)^2$. If $u^2 > 0$, one finds the vacuum expectation value of ϕ is $< \phi >_0 = \begin{pmatrix} 0 \\ V \end{pmatrix}$ where $V^2 = \frac{|u^2|}{\lambda}$. When the symmetry is broken, three of the boson fields acquire mass, eliminating three of the Higgs fields. These massive bosons are the familiar $W^\pm$ and Z^0. The fourth Higgs field remains as a physical scalar particle – the Higgs particle H^0. The mass of the H^0 is given by $M_{H^0} = 2|u^2| = 2\lambda V^2$. Since the theory does not specify λ we have no prediction for the Higgs mass. However, we do get some guidance from the theorists which indicates that $7.5 \leq M_{H^0} \leq 10^3$ GeV/c^2. The lower limit comes about from considering $u^2 \equiv 0$ with the symmetry breaking arising purely from radiative corrections. A very massive H^0 is not likely when the mass scale which it is generating is $\sim$ 100 GeV/c^2. The lack of a crisp prediction for the H^0 mass, makes searching for the H^0 very difficult indeed. Fermion masses are generated by Yukawa couplings of the Higgs field. An interaction term is added to the Lagrangian:

$$\mathcal{L}_{int} = -\mathcal{G}\{\bar{R}\phi^+ L + \bar{L}\phi^+ R\} \quad .$$

In $SU(2) \wedge U(1)$ the two neutral quanta are not the physically observed particles. Rather the photon and the Z^0 are orthogonal admixtures of these neutral quanta with the relative amount of mixing specified by the Weinberg angle, θ_W. In terms of this angle, one obtains predictions for the $W^\pm$ and Z^0 masses:

$$M_W^2 = \frac{\pi\alpha}{\sqrt{2}\,\mathcal{G}_F} sin^2\theta_W \qquad (1)$$

$$M_{Z^0}^2 = M_W / cos^2\theta_W \qquad (2)$$

where α is the fine structure constant and $\mathcal{G}_F$ is the Fermi coupling constant.

The quantity $sin^2\theta_W$ has been measured in many different experiments and Kim et al[9] derive an average of 0.23 ± 0.015. One cannot use this value directly in Eqs. (1) and (2) to yield the boson masses because of the effects of radiative corrections. The bare mixing angle of the theory is given by $sin^2\theta_W^0 = \frac{e^2}{g^2}$ where e and g are the $U(1)$ and $SU(2)$ coupling strengths. The renormalized, physically measurable $sin^2\theta_W^R$ is related to $sin^2\theta_W^0$ by a radiative expansion:

$$sin^2\theta_W^0 = sin^2\theta_W^R\left(1 - \frac{\alpha}{\pi} f(sin^2\theta_W^R) + O(\alpha^2)\ldots\right) .$$

Marciano and Sirlin have studied this problem[10] and find that $sin^2\theta_W^0$ is roughly 7% larger than the measured value. Hence they predict

$$M_W = (82 \pm 2.4) GeV$$

$$M_{Z^0} = (93.0 \pm 2.0) GeV \quad .$$

Notice that a precise measurement of M_Z and an independent measurement of $sin^2\theta_W$ permit one to test the validity of the radiative correction calculations. We will see later that this can be done.

In the standard model the weak left- and right-handed fermion couplings are specified by $g_{L,R} = T_3^{L,R} - Q\ sin^2\theta_W$ where Q is the fermion charge and T_3 is the third component of the weak isospin. A more commonly used notation is

$$g = \frac{(g_R + g_L)}{2}$$

$$a = \frac{(g_R - g_a)}{2} \quad .$$

Table 3 summarizes these values for the fermions of the standard model assuming $sin^2\theta_W = 0.23$.

Table 3. Vector and Axial-Vector Fermion Couplings

Fermion	Axial Vector	Vector
ν	-0.25	0.25
e, μ, τ	0.25	$\frac{1}{4}(-1+4sin^2\theta_W) = -0.02$
u, c, t	-0.25	$\frac{1}{4}(1-\frac{8}{3}sin^2\theta_W) = 0.10$
d, s, b	0.25	$\frac{1}{4}(-1+\frac{4}{3}sin^2\theta_W) = -0.17$

The coupling of the neutral Higgs to a pair of fermions is given by

$$g_{H^0 f\bar{f}} = 2^{\frac{1}{4}}\sqrt{\mathcal{G}_F}\, M_f$$
$$\simeq 3.8\left(\frac{M_f}{M_p}\right)10^{-3}$$

where M_f and M_p are the fermion and proton masses. The important thing to notice is that the H^0 will couple to pairs of the heaviest fermions available. This fact will be used in searches for the H^0. The Higgs coupling to bosons is given by

$$g_{H^0 V\bar{V}} = 2^{\frac{5}{4}}\sqrt{\mathcal{G}_F}\, M_V^2$$
$$\simeq 7.6\left(\frac{M_V^2}{M_p}\right)10^{-3}$$

where M_V is the boson mass. So while the standard model does not predict masses for the fermions and the H^0, it does specify the couplings.

We have now covered sufficient ground to arrive at the catalogue of characteristics which we will need to discuss high energy tests of the standard model.

1. The fundamental fermions are six quarks and six leptons: u, d, s, c, b, t, and $e, \nu_e, \mu, \nu_\mu, \tau, \nu_\tau$.
2. There are nine massless bosons: eight colored gluons and the photon.
3. There are three massive vector bosons: Z^0, W^+, W^-.
4. There is one neutral scalar: H^0.
5. QCD is non-Abelian and hence: (a) particles which carry color are confined; (b) gluons couple to gluons; (c) the strong coupling constant, α_s, runs.

As we contemplate this catalogue we realize that the t quark and the ν_τ have not been seen, we should review the evidence for the existence of gluons, none of the heavy vector bosons have been seen, the H^0 has not been seen and there is no evidence for the essential feature of QCD – namely it is a non-Abelian theory.

Before we embark upon considering to remedy these untested features using high energy e^+e^- interactions, we should remember that the standard model, both QCD and the electroweak sector, is an outstanding success at low energies. There is considerable verification from all areas of experimentation and there exist no well established conflicts with any experimental data. There is no reason then, aside from aesthetics like the unhappiness surrounding procedures like the Higgs mechanism, to expect that the standard model is an incorrect description of nature. We will have the means in the next few years to make many interesting and important high energy tests. And, as usual, e^+e^- collisions will play a major role in these tests.

4. Testing the Standard Model in e^+e^- at Energies Beyond Those Currently Available

4.1 Searching for the Top Quark

The charge two-thirds top quark has not yet been seen. There is indirect evidence (see Sec. 5.3) from the absence of flavor changing neutral currents that there must be a top quark at some mass. There exists only one rather perverse "topless" model which has not been ruled out. It is then fairly certain that the top quark exists.

The present limits coming from PETRA are that the top quark mass, M_t, is below 18.7 GeV. These limits are set using either event shapes, high transverse momentum leptons arising from weak decays of heavy quarks and measurements of R the ratio of the hadronic cross section to the muon pair cross section.

In anology with the ψ and Υ systems, one expects to see several $t\bar{t}$ bound states below the threshold for open top. Energy scans have been done at PETRA to search for the $1S$ (toponium) state. Using $\sim$ 20 MeV energy steps, the energy ranges (a) 27 $< E_{c.m.} <$ 31.6 GeV and 33 $< E_{c.m.} <$ 37 GeV have been exhaustively scanned. For each scan point, R is determined. To get an upper bound on the width of a possible $t\bar{t}$ bound state, each measured point is fitted to a Gaussian plus a constant term. Radiative effects are also included in the fits and the width of the Gaussian is taken to be the machine energy resolution of 20 MeV. The resonance parameters are related to the data via

$$\int \sigma_{tot}(E_{c.m.})d\,E_{c.m.} = \frac{6\pi^2}{m^2_{t\bar{t}}}\Gamma_{ee}B_{had}$$

where $M_{t\bar{t}}$ is the assumed resonance mass, Γ_{ee} the partial width for the decay to electrons and B_{had} is the hadronic branching fraction. Fig. 4 shows the combined data from the four PETRA experiments of JADE, MARK J, CELLO and TASSO. Table 4 shows the values of $M_{t\bar{t}}$ where the fit yields a maximum $\Gamma_{ee}\,B_{had}$ for each individual experiment and for the combined data ($M_{t\bar{t}} = 33.34$ GeV) for which $\Gamma_{ee}\,B_{had} < 0.61$ keV (90% confidence limit).

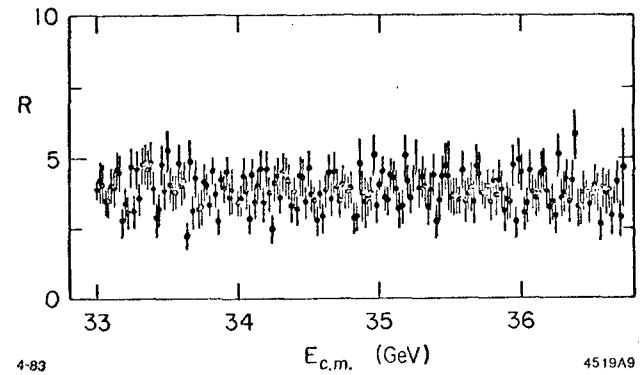


Fig. 4. $R = \sigma_{hadrons}/\sigma_{\mu\mu}$ in the region of the PETRA toponium energy scan. The data of all experiments (CELLO, JADE, MARK J and TASSO) are combined.

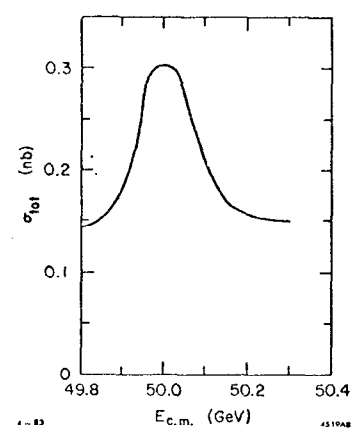


Fig. 5. The hadronic cross section in the region of 50 GeV assuming toponium is at a mass of 50 GeV.

Table 4. Results of the $t\bar{t}$-Resonance Search

Experiment	Mass of the Assumed Resonance GeV	Upper Limit of Electronic Width × BR(hadrons) keV (90% C.L.)
CELLO	33.52	1.79
JADE	33.34	1.22
MARK J	35.12	0.97
TASSO	33.34	1.33
All Experiments	33.34	< 0.61

All $q\bar{q}$ resonances ($\rho, \omega, \phi, \psi, \Upsilon$) have the common feature that $\frac{\Gamma_{ee}}{e^2} \sim 10$ keV where e is the quark charge. If we assume that this is true for the $t\bar{t}$ system and that $B_{had} \geq 0.7$ then one would expect $\Gamma_{ee}\, B_{had} > 3$ keV for toponium. Thus the PETRA data rule out the existence of toponium up to a mass range of 37 GeV/c^2.

The PETRA measurement of R has also been used to demonstrate that the open top threshold has not yet been reached.[13] In the simple quark parton model R is given by

$$R = \frac{\sigma_{had}}{\sigma_{\mu\mu}} = 3\sum_i e_i^2$$

where e_i are the quark charges and i runs over the flavors which are below threshold. For the five known flavors, $R = 3.67$ in this model. There are small modifications to the simple picture from QCD of the order of $\frac{\pi}{\alpha_s}$. The prediction[14] of QCD for five flavors is $R = 3.88$ and for the inclusion of a sixth charged two-thirds flavor $R = 5.31$. Averaging over $E_{c.m.}$ from 12 to 37.6 GeV, a value of $< R >= 3.84 \pm 0.04$ is obtained from the PETRA data. This error is statistical only and to be conservative a 10% systematic error should be assigned to $< R >$. Clearly the PETRA data rule out open top production up to 37.6 GeV.

The standard model does not calculate fermion masses and so the absence of the t quark does not imply an essential problem. Box diagrams would contribute to the $K_L - K_S$ mass difference and the decay rate for $K_L \to \mu^+\mu^-$. Buras,[11] using such an approach, consoles us with the bound that $M_t \leq 40$ GeV. What prospects exist for finding the top quark?

As we have seen, the most straightforward way of looking for top is to measure R. If one assumes one is above the top threshold then a $\delta_R = \frac{4}{3}$ should be seen. If we require a 3σ effect in R, we must measure to an accuracy $\frac{\sigma_R}{R} \simeq 8\%$. Typical PEP and PETRA experiments achieve $\leq 5\%$ for the systematic contribution to the error in the measurement of R and we will ignore these in this discussion. Allowing for statistical errors in both the luminosity measurement and the counting of hadrons, $\frac{\sigma_R}{R} = 8\%$ requires a sample of ≤ 200 hadronic events. If N is the number of days to accumulate M hadronic events in a detector, with an efficiency of ϵ, then

$$N = \frac{E_{c.m.}^2 \times 10^{33}}{86.8R < \mathcal{L} > \epsilon(3.6 \times 24 \times 10^3)}$$

where $E_{c.m.}$ is in GeV and $< \mathcal{L} >$ is the average luminosity measured in units of $cm^{-2}\ sec^{-1}$. Typically $\epsilon = 0.7$ and referring to Table 1, $< \mathcal{L} >$ can be taken as $5 \times 10^{30} cm^{-2}\ sec^{-1}$. One finds then

$E_{c.m.}$ (GeV) $(= 2M_t)$	Who, When	Number of Days for $\sim 10\%$ Measurement of R
41	PETRA, December 1982	2.5
45	PETRA, June 1982	3.0
60	TRISTAN, March 1986	5.0

Hence the measurement of R is a fast way of finding top if one is above the open top threshold. If the results of this search are negative, then one can begin scanning down in energy looking for the $1S$ state. This state will be narrower than the machine width which is 20 MeV at PETRA and projected to be 60 MeV at TRISTAN. One scans therefore in steps comparable to the machine energy. As an example of how long such a scan would take, consider Fig. 5 which is the hadronic cross section (see Ref. 3) expected at TRISTAN given that toponium is at 50 GeV. The toponium resonance has been corrected for radiative effects and the beam energy spread. Remembering that one would scan in ~ 60 MeV steps, one sees that almost independently of one's initial choice of energy for the scan, one will reach a scan point within 90% of the best possible resonant yield. The non-resonant cross section is approximately equal to

this resonant yield and therefore one would run long enough to see ~ 25 events in the continuum. The on-resonance response would then be 50 events, and one would have a significant effect with these statistics. At $< \mathcal{L} >= 5 \times 10^{30} cm^{-2}\ sec^{-1}$ it takes ten hours to accumulate 25 events at a cross section of $\sigma = .15nb$. Hence one could scan at a rate of 1 GeV/week. Having established that one was not above open top threshold first, one would then scan down from this energy, E_0. If the $1S$ state were not found within $\sim$ 4 GeV below E_0 – four weeks running – then in all probability top will be at a n energy above E_0. Clearly we have not chosen the best optimization strategy here since adjacent points in the scan can be added together. But the flavor of the discussion is correct – it would take several weeks of scanning to look for hidden top at TRISTAN given that open top was not at the maximum machine energy. For PETRA the number of events required to establish toponium is about the same. However, here the machine width is smaller and the luminosity uncertain. By the time these lectures are published, the scan rate for PETRA will have been established. I would guess that it will take about twelve hours per 20 MeV step.

If M_t >30 GeV, then the next place to look in e^+e^- collisions will be the SLC and solon thereafter LEP. A shape analysis of the hadronic events or the yield of large transverse momentum (with respect to the thrust axis) leptons will be a very clean and rapid signal for top at the Z^0. These tests are discussed fully in SLAC REPORT 247 (see Ref. 5). Figure 6 shows the yield of events as a function of the aplanarity for the t quark and separately for the five lighter quarks. A 30 GeV/c^2 mass was assumed for the t quark. The curves are normalized to a one-week run at the SLC assuming $< \mathcal{L} >= 3 \times 10^{29}\ cm^{-2}\ sec^{-1}$. The aplanarity[12] measures the amount of momentum out of the event plane as it is defined in a sphericity analysis. As the t quark mass is raised, the mean aplanarity for the t quark grows. A short run at the SLC would readily establish the presence of a t quark if M_t >30 GeV/c^2. Figure 7 shows the transverse momentum of muons, relative to the produced quark direction, for different quark parents. The top quark mass was assumed to be 25 GeV/c^2. A clear separation between top and all other species is seen. So if 30 GeV $< M_t < M_{Z^0}/2$ the SLC and/or LEP will easily find top.

How is the top quark mass measured at the Z^0? The aplanarity distribution and the lepton transverse momentum distributions are strongly dependent on M_t.

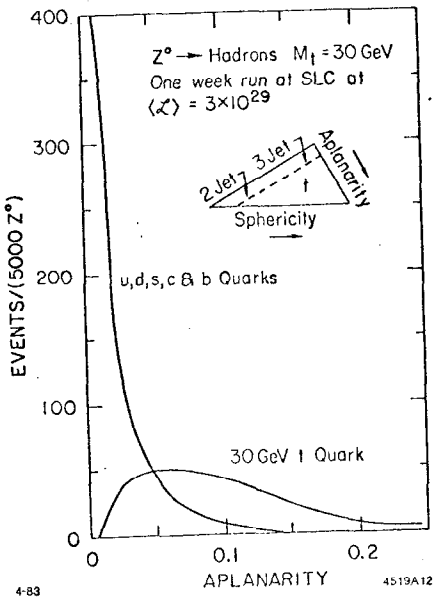


Fig. 6. The aplanarity distribution for events of the type $Z^0 \to q\bar{q}$. The distribution for $t\bar{t}(M_t = 30\ \mathrm{GeV/c^2})$ is shown separately from the lighter quarks.

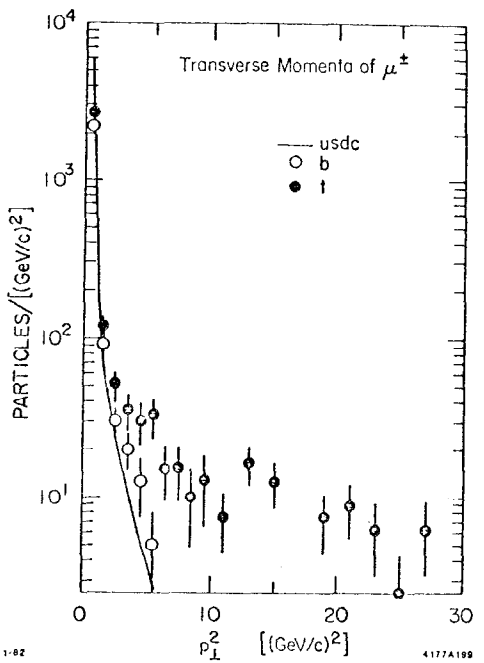


Fig. 7. The distribution of transverse momentum squared, with respect to the quark direction for all muons in the event. Contributions from the different flavors are indicated in the figure.

Certainly a rough estimate (probably $\pm$ 5 GeV/c^2) would result from such distributions but the result would depend heavily on the Monte Carlo assumptions for t quark fragmentation, etc. The jet mass does not prove to be a reliable measure of M_t. The jet mass distributions for t quark events selected by a cluster analysis[15] and aplanarity cuts appears in Fig. 8. The cluster algorithm in conjunction with an aplanarity cut $\geq$ 0.04 yielded, in this study, a $Z^0 \rightarrow t\bar{t}$ event sample with 80% purity (see Ref. 5b, pages 93-100). For M_t = 19 GeV/c^2 (Fig. 8a) the mean jet mass is about 16 GeV/c^2. For M_t = 30 GeV/c^2 (Fig. 8b) the mean jet mass increases to only 19 GeV/c^2. Thus the measured jet invariant mass is not linear in M_t; the nonlinearity becomes most marked for $M_t \geq$ 20 GeV/c^2. The reason for this behavior is that as M_t increases the events become more spherical and the assignment of the numerous soft particles to the jets becomes somewhat arbitrary: the jets are not distinct clusterings of particles. The determination of M_t from jet masses appears too dependent on Monte Carlo simulations to be of much use.

A more promising method[16] does not depend at all on the Monte Carlo simulation of the fragmentation process, but on the rate of hadron production at the Z^0. It is based on the fact that in the standard electroweak theory the partial width for $Z^0 \rightarrow t\bar{t}$ is given by

$$\Gamma_t(\beta) = 3\left(\frac{M_{Z^0}}{24\pi}\right)[g_V^2\ \beta(3-\beta^2) + 2g_A^2\ \beta^3]\ .$$

where β is the t velocity in units of the speed of light, and g_A and g_V are the t quark weak axial-vector and vector couplings, function of $sin^2\theta_W$ only. For $sin^2\theta_W = 0.23$, $g_A^2 \gg g_V^2$ and the threshold factor for $Z^0 \rightarrow t\bar{t}$ is predominantly cubic in β. Hence the rate for $Z^0 \rightarrow t\bar{t}$ is strongly modulated by the threshold factor, and the overall rate for $Z^0 \rightarrow$ *hadrons* is correspondingly reduced by the t mass effects provided $M_t < M_{Z^0}/2$. Figure 9 shows the ratio

$$\rho = \frac{\Gamma_t(\beta)}{\Gamma_u}$$

as a function of the t quark mass. Here Γ_u is the partial width for $Z^0 \rightarrow u\,\bar{u}$ (i.e., $Z^0 \rightarrow$ *massless* $Q = \frac{2}{3}$ *quarks*). With the present lower bound on M_t of 18.5 GeV, there would be 22% less hadrons from massive $t\bar{t}$ production than from massless t

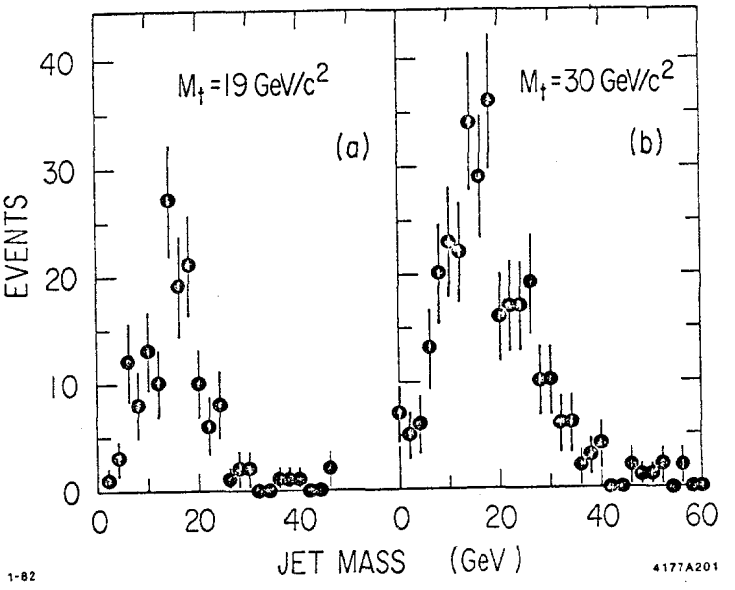


Fig. 8. The reconstructed jet masses for two-cluster events with aplanarity ≥ 0.04 for (a) top quark mass $M_t = 19$ GeV/c^2 and (b) $M_t = 30$ GeV/c^2.

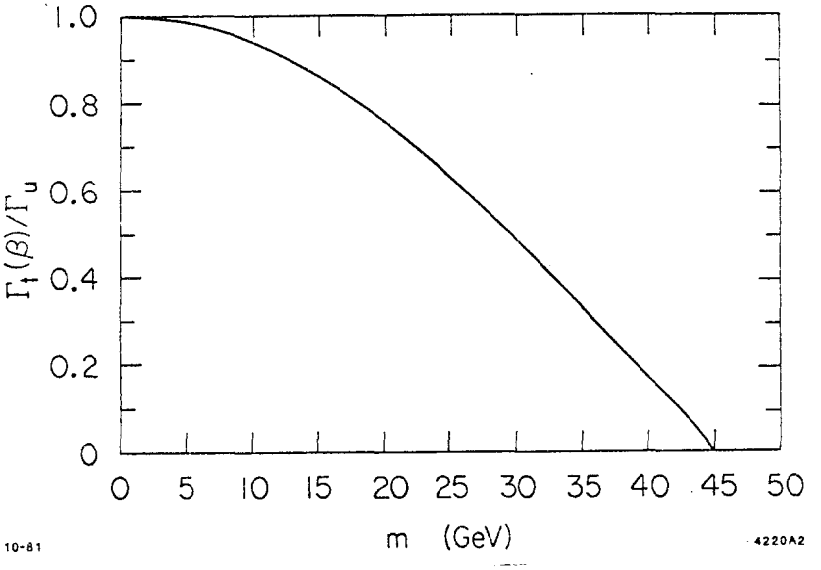


Fig. 9. The suppression factor of $t\bar{l}$ decays of the Z^0 as a function of the top quark mass for $sin^2\theta_W = 0.22$ and $M_{Z^0} = 90$ GeV/c^2.

quarks. Since 14% of $Z^0 \rightarrow$ *hadrons* is in the $u\bar{u}$ channel, an overall reduction of 3% of the hadronic rate is expected for $M_t = 19$ GeV/c^2 as compared to $M_t = 0$.

Within the standard model ρ can be expressed in terms of the ratio r of the number of hadronic events (N_h) to the number of muon pair events ($N_{\mu\mu}$) produced at the Z^0:

$$\rho = 1 + r\,\frac{\Gamma_{\mu\mu}}{\Gamma_u} - \frac{\Gamma_h}{\Gamma_u}\,,$$

where Γ_h is the hadronic width calculated for three quark generations of massless, colored weak isospin doublets, $\Gamma_{\mu\mu}$ is the calculated $\mu^+\mu^-$ partial width and Γ_u is the calculated partial width into u quarks. Hence, in principle, the experiment is simple: it consists of counting the number of hadronic and muon pair events. There is no need to measure the luminosity, and the error of the t mass estimate depends on the ability of counting hadron events and muon pairs with small systematic errors. If one assumes 10^6 Z^0's, $N_{\mu^+\mu^-} = 31{,}000$, $N_h = 730{,}000$ and $\delta(sin^2\theta_W) = 0.001$,[17] the t quark mass resolution, in the absence of any systematic error, is given in Fig. 9. The resolution is adequate and independent of t quark mass. Inevitably, there will be some systematic effects; the resolution degrades by $\sim$ 1 GeV per 1% systematic error in r. It should be pointed out that to apply this method one needs independent evidence that (a) the $t\bar{t}$ events are being produced at the Z^0 and (b) that there are no processes contributing to N_h beyond those of five known quarks. Nonetheless, this method looks very promising for estimating the t quark mass.

If $M_t > M_{Z^0}/2$, we will have to rely on LEP II, LEP III and SLC II to find the top quark. This will constitute a search in the continuum similar to that described for TRISTAN earlier in this section.

4.2 Searching for and Studying the Z^0 and $W^\pm$

It is entirely possible that the Z^0 and/or $W^\pm$ will be discovered soon at CERN in the $\bar{p}p$ collider experiments. We still need to discuss the e^+e^- option because (a) CERN might not find them and (b) the copious, background free production in e^+e^- for the Z^0, in particular, will permit tests of the standard model far more thorough and precise than offered by the $\bar{p}p$ collider.

If the Z^0 is found at $M_{z^0} = (93 \pm 2)$ GeV/e^2, this will be yet another triumph for the standard model. If a Z^0 is found either higher or lower (or both) than the

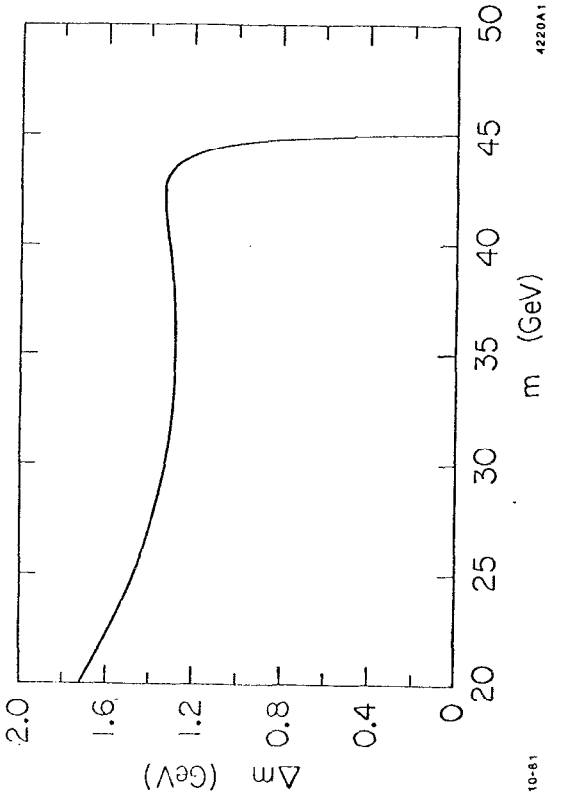


Fig. 10. The error in the determination of the top quark mass as a function of the top quark mass for a sample of 10^6 Z^0 events. No systematic errors are included in this plot.

predicted value, then probably $SU(2) \wedge U(1)$ is not the correct group. This will be discussed in Sec. 7.1.

If the Z^0 is found at its standard model mass value, then even more stringent tests can be made of the standard model by running at and near the Z^0.

A careful measurement of the Z^0 line shape will yield a precise measurement of M_{Z^0}. As noted in Sec. 3.3, this will permit a check on the radiative correction calculations for $sin^2\theta_W$. The measurement of M_{Z^0} from the Z^0 line shape is complicated by effects such as initial state radiation and beam dynamics and is by no means a simple task. However, if a precision of 300 MeV/c^2 can be obtained for M_{Z^0} this would correspond to an error of 0.0015 in $sin^2\theta_W$ (see Ref. 5a).

It will be possible at the SLC and LEP to measure all six leptonic coupling constants $v_e, a_e, v_\mu, a_\mu, v_\tau$, and a_τ and hence test $e/\mu/\tau$ universality. Since $v_f = sin^2\theta_W - \frac{1}{4}$ this will constitute another measurement of $sin^2\theta_W$. The quantities to be measured are

1. The charge asymmetry for each lepton f

$$A_{ch}^f = p_f \left[\frac{p(Z^0) + p_e}{1 + p_e p(Z^0)}\right]\left(\frac{2cos\theta}{1 + cos^2\theta}\right)$$

where p_e is the polarization of the electron beam (the positrons are assumed to be unpolarized), $p_f = \frac{2v_f a_f}{v_f^2 + a_f^2}$ is the natural polarization of the fermion f coming from unpolarized Z^0's due to the fact that $g_L \neq g_R$, $p(Z^0) = \frac{2v_e a_e}{v_e^2 + a_e^2}$ is the polarization of the Z^0 for unpolarized beams, and θ is the polar angle of the positively charged fermion.

2. The total rate

$$R_f = \frac{\sigma(f\bar{f})}{\sigma_{point}}$$

$$\propto (a_f^2 + v_f^2)(a_e^2 + v_e^2) \ .$$

If we integrate over the polar angle θ and assume that $p_e = 0$ we find

$$A_{ch}^f = \frac{3a_e\, v_e\, a_f\, v_f}{(a_e^2 + v_e^2)(a_f^2 + v_f^2)} \ .$$

Hence a measurement of A_{ch}^e and R_e will yield $|a_e|$ and $|v_e|$. If one measures the polarization of the τ (or μ in principle, but this is not practical) then from

$$\frac{A_{ch}^\tau}{P_\tau} = \frac{3}{2}\,\frac{a_e v_e}{(a_e^2 + v_e^2)}$$

one obtains also the relative sign of $|v_e|$ and $|a_e|$. Then from measurements of all R's and A_{ch}'s, the six coupling constants can be measured. The measurement of the charge asymmetry and lepton rates is not experimentally taxing and is routinely done[18] at PETRA and PEP. The measurement of p_τ has been studied extensively in the SLC workshop (see Ref. 5b, page 116). The spectrum of the π, e or μ in the decays $\tau \to \pi\nu_\tau$, $\tau \to e\nu_\tau\bar{\nu}_e$ and $\tau \to \mu\nu_\tau\bar{\nu}_\mu$ are modified by the polarization of the parent τ. In the case of $\tau \to \pi\nu_\tau$ the flat π energy spectrum obtained for an unpolarized τ becomes

$$\frac{dn}{dx_\pi} = 1 + P_\tau(2x_\pi - 1) \ ,$$

where $x_\pi = \frac{2E_\pi}{E_{c.m.}}$, when the τ has polarization P_τ. Hence a measurement of the energy spectrum of the π yields a measurement of P_τ. The details of the experimental measurement are clearly given in Ref. 5b above. Suffice it to say that with even a modest general purpose detector the measurement is readily made.

The presence of longitudinally polarized beam electrons makes things much easier. First of all we note that

$$A_{ch}^f = v_f v_e \sim v^2 \qquad \text{for } p_e = 0$$

$$\simeq v_f \qquad \text{for } p_e \approx 0.5$$

and, since the vector coupling constant is small (~ 0.02), polarized beams enhance markedly the observed charge asymmetry. Figure 11 shows the charge asymmetry as a function of $E_{c.m.}$ for the standard model with $sin^2\theta_W = 0.23$. Curves for unpolarized beams (0) and both orientations of longitudinally polarized electrons (R and L) are shown. In order to achieve a sizeable charge asymmetry with unpolarized beams requires moving off the resonance peak. This costs rate as shown by the dashed curve. However, with polarized beams the charge asymmetry is large on the resonance peak.

The use of polarized beams also alleviates the need for the τ polarization measurement. Consider the longitudinal spin flip asymmetry given by

$$A_L(\theta) = \frac{\frac{d\sigma}{d\Omega}(\theta, p_e = +) - \frac{d\sigma}{d\Omega}(\theta, p_e = -)}{\frac{d\sigma}{d\Omega}(\theta, p_e = +) + \frac{d\sigma}{d\Omega}(\theta, p_e = +)}$$

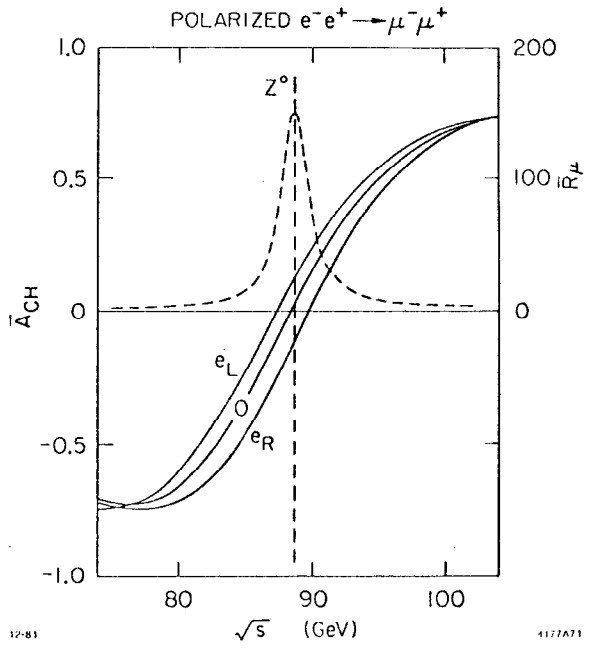


Fig. 11. The charge asymmetry as a function of $E_{c.m.}$ is shown for polarized and unpolarized beams according to the predictions of the standard model with $sin^2\theta_W = 0.23$. Also shown as a dashed curve is $R_\mu = \sigma(\mu^+\mu^-)/\sigma_{point}$.

Writing out this expression and integrating over any interval which is symmetric about $\theta = 90^o$ yields

$$A_L = p_e\left[\frac{2v_e a_e}{v_e^2 + a_e^2}\right]$$

one thus measures the relative sign of $|v_e|$ and $|a_e|$. At the Z^0 peak, A_L is large, measuring $\sim 16\%$ for $p_e = 0.5$ and $sin^2\theta_W = 0.23$.

The accuracy with which one obtains $sin^2\theta_W$ and the coupling constants is discussed in Ref. 5b, page 28. We summarize here by saying that for a sample of 10^6 Z^0 decays and a 3% branching ratio to $\mu^+\mu^-$ one obtains from the $\mu^+\mu^-$ channel

$$\left.\begin{array}{l}\delta(sin^2\theta_W) \simeq 0.002 \\ \\ \delta(v_\mu/a_\mu) \simeq 0.008\end{array}\right\} \text{ from } A_{ch}$$

and

$$\left.\begin{array}{l}\delta(sin^2\theta_W) = 0.001 \\ \\ \delta(v_\mu/a_\mu) = 0.01\end{array}\right\} \text{ from } A_L$$

It should be clear from the above discussion that measurements at the Z^0 will test the standard model very stringently. Any cracks in the armor will surely show up.

What about the $W^\pm$? Below W^+W^- threshold, we could look for the process shown in Fig. 12, namely $e^+e^- \to W^\pm e^\mp \nu_e$. However, the cross section for this process is $10^{-37} - 10^{-38}$ cm^2 and for an average luminosity of 10^{31} and a cross section of $5 \times 10^{-38} cm^2$ the rate for this process would be 5×10^{-2} events/day. Given that these events would have to be extracted from a hadronic background of ~ 10 events/day, this avenue does not look promising. So we investigate the process $e^+e^- \to W^+W^-$ which proceeds via the three graphs shown in Fig. 13 with a production cross section as shown in Fig. 14. There is some usable production cross section at 170 GeV which is chosen since it is the highest LEP II energy. At this energy $\sigma_{W^+W^-} \simeq 7 \times 10^{-36}$ cm^2

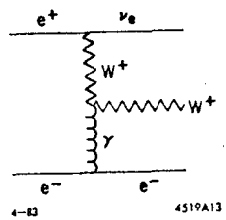


Fig. 12. $e^+e^- \to W^\pm e^\mp \nu_e$.

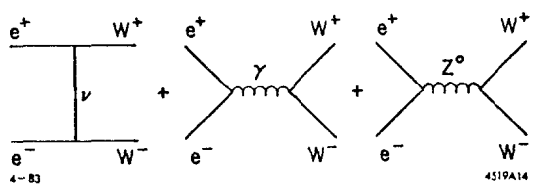


Fig. 13. The three processes which contribute to $e^+e^- \to W^+W^-$.

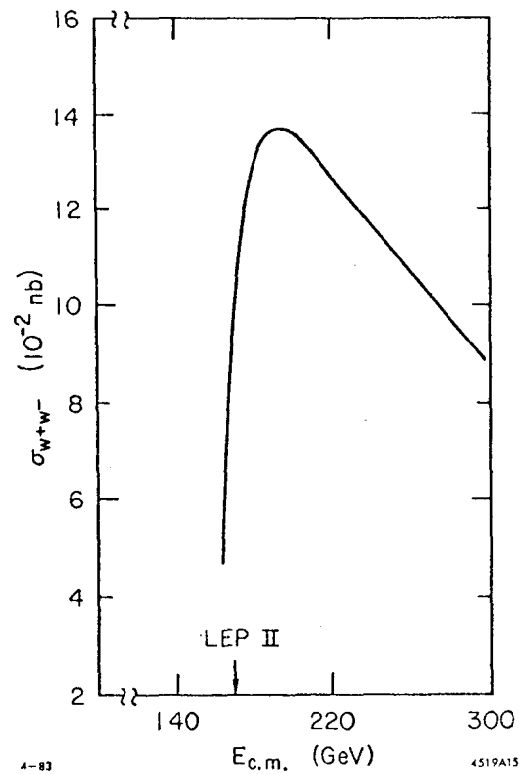


Fig. 14. The cross section for $e^+e^- \to W^+W^-$ as calculated in the standard model. The maximum LEP II energy is shown.

and for $< \mathcal{L} >= 5 \times 10^{31}\ cm^{-2}\ sec^{-1}$ one would obtain 20 W^+W^- events/day. A topology which would be readily observable would be

$$e^+e^- \to W^+ \quad W^- \qquad (3)$$
$$\qquad\qquad\quad \hookrightarrow q\bar{q}$$
$$\qquad\quad \hookrightarrow \ell^+\nu_e$$

where ℓ refers to a charged lepton. The events would have a single lepton in one hemisphere and a hadron jet in the other. Further confirmation of the process (3) would come from the measurement of the hadron jet mass which would reconstruct to the $W^{\pm}$ mass. The W coupling strength to fermions is democratic and hence for $N = 3$ generations

$$\frac{\Gamma(W \to \ell\nu)}{\Gamma(W \to ALL)} = \frac{1}{4N} = \frac{1}{12}$$

$$\frac{\Gamma(W \to q\bar{q})}{\Gamma(W \to ALL)} = \frac{3}{4N} = \frac{1}{4} \ .$$

Summing over the possible quark final states and assuming either the $e\nu_e$ or $u\nu_\mu$ possibility of the leptonic decay, the topology of (3) would yield 5 W^+W^- events/day. This signal could not be missed.

The measurement of $\sigma(e^+e^- \to W^+W^-)$ is an important test of the gauge structure of $SU(2) \wedge U(1)$. If $g_{Z^0W^+W^-}$ were zero, some of the cancellations occurring in the contributions from interference terms (see Fig. 12) would vanish, and $\sigma(e^+e^- \to W^+W^-)$ would roughly double. In this way e^+e^- interactions would offer a unique test of the standard model unavailable at the $\bar{p}p$ collider.

4.3 Searching for the Neutral Higgs Particle, H^0

The Higgs mechanism is probably the most controversial part of the standard model because it requires very precise fine tuning to work. (See the lectures of Susskind, these proceedings.) Because the mass of the H^0 is not predicted by the theory it is also one of the most difficult areas of the theory to test. The two most promising places to search for the H^0 in e^+e^- interactions is at toponium and the Z^0.

Consider the decay of a heavy $Q\bar{Q}(1^{--})$ state, V, into $H^0\gamma$ as shown in Fig. 15a. This process was first discussed by Wilczek.[19] For $M_{H^0} \ll M_V$, the decay rate for this process is given by

$$\frac{\Gamma(V \to H^0\gamma)}{\Gamma(V \to e^+e^-)} \simeq \frac{\mathcal{G}_F M_V^2}{4\sqrt{2}\,\pi\alpha}\left[1 - \frac{M_{H^0}^2}{M_V^2}\right] \ .$$

Considering then the two upcoming toponium sources, we find

	$E_{c.m.}$ GeV	$< \mathcal{L} >$ $cm^{-2}sec^{-1}$	# V per day	$\frac{\Gamma(V\to H^0\gamma)}{\Gamma(V\to ee)}$	$\Gamma(V \to ee)$ %	# $V \to H^0\gamma$ per day
PETRA	40	1.6×10^{31}	400	0.14	6	3.4
TRISTAN	60	2×10^{31}	220	0.32	6	4.2

where we have used the estimates[2c] in Fig. 16 to obtain the rates above. The production rate for toponium $\to H^0\gamma$ at both PETRA and TRISTAN is quite favorable.

What about the event shapes? The photon in the decay of toponium $\to H^0\gamma$ will be monochromatic with its energy given by

$$X_\gamma^{H^0} = 2E_\gamma/E_{c.m.} = \left(1 - \frac{M_{H^0}^2}{M_V^2}\right) \ .$$

The decay of the H^0 will be predominantly to the heaviest fermion pair available and estimates for H^0 branching fractions as a function of M_{H^0} are given in Fig. 17. The event shape will depend on M_{H^0} but in essence the events will have a monochromatic photon in one hemisphere and a hadron jet in the other hemisphere (see Fig. 15b). The main background will come from the process shown in Fig. 15c, $V \to gg\gamma$, where the symbol g is used to denote a gluon. From Fig. 16 we see that

$$\frac{\Gamma(V \to gg\gamma)}{\Gamma(V \to H^0\gamma)} \simeq 7 \quad \text{at} \quad M_V = 40\text{GeV/c}^2$$

$$\simeq 3 \quad \text{at} \quad M_V = 60\text{GeV/c}^2$$

This background is distinguishable from the signal when we use the property that the photon from the signal is monochromatic. Roughly speaking the photon spectrum

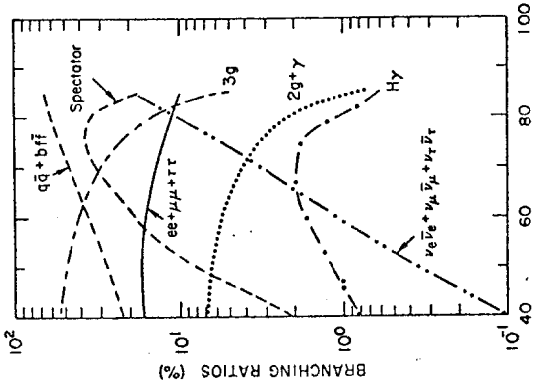


Fig. 16. The quarkonium branching fractions are shown (taken from Ref. 20) as a function of the quarkonium mass. The neutral Higgs boson mass was taken to be 10 GeV/c^2.

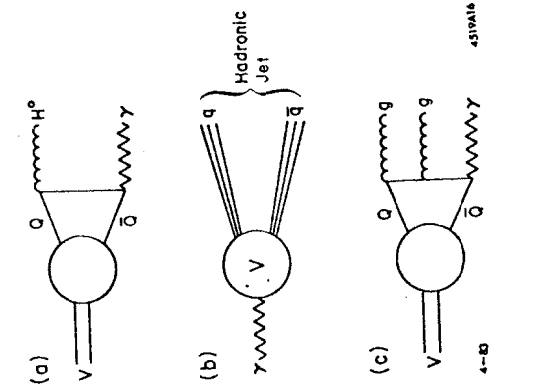


Fig. 15. The decay of heavy quarkonium $V \rightarrow H^0\gamma$ is shown in (a). In (b) h^0 decays to a quark antiquark pair and (c) shows the main background for (a) namely $V \rightarrow gg\gamma$.

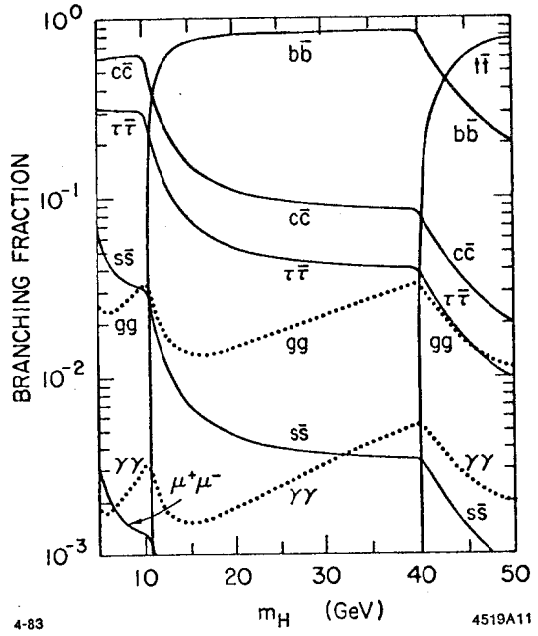


Fig. 17. Decay modes of the neutral Higgs boson as a function of its mass.

from the background is linear

$$\frac{dn}{dx_\gamma} \simeq X_\gamma \qquad \text{for} \quad V \to gg\gamma \ .$$

Assume that the photon is measured in a calorimeter whose energy resolution $\sigma_E/E = \sigma_X/X = .1/\sqrt{E}$. For $X_\gamma > 0.5$ $\sigma_{X_\gamma} \simeq 2\%$ As an example consider that $M_V = M_{t\bar{t}} = 60$ GeV/c^2 then for

$$\begin{aligned} M_{H^0} = 20\,\text{GeV}, \ \ X_\gamma^{H^0} = 0.89 \ \ \text{or} \ \ E_\gamma = 27\,\text{GeV} \\ = 10\,\text{GeV}, \ \ X_\gamma^{H^0} = 0.97 \ \ \text{or} \ \ E_\gamma = 29\,\text{GeV} \ . \end{aligned}$$

Figure 18 depicts the experimental problem, namely with a resolving width of 2% and $X_\gamma = 0.89$. Can we sort out the signal from a background which is three times as copious? The figure is drawn so that the relative areas of the Gaussian (signal) and the triangle (background) are 1 : 3 and the Gaussian has a width of 2% . One sees that indeed the signal would readily be seen. With enough data one could remove the background by requiring the $H^0 \to \tau^+\tau^-$ decay. For $M_{H^0} = 10$ GeV/c^2, $B(H^0 \to \tau^+\tau^-) = 30\%$ and one pays an acceptable price. For $M_{H^0} = 20$ GeV/c^2, $B(H^0 \to \tau^+\tau^-) = 5\%$ and a long run would be needed to establish the H^0 if one required the $H^0 \to \tau^+\tau^-$ decay mode.

Having established the signal, how well could one measure M_{H^0}? One could either measure the jet mass or obtain the mass from the measured photon energy. It is hard to estimate how well one would do using the former method because it will depend on the characteristics of the detector and on Monte Carlo corrections. For the latter method

$$X_\gamma = \left(1 - \frac{M_{H^0}^2}{M_V^2}\right) \Rightarrow \sigma_{M_{H^0}} = \frac{M_V^2}{2M_{H^0}}\sigma_{X_\gamma} \ .$$

For $\sigma_E/E = .1/\sqrt{E}$ and $M_{H^0} = 20$ GeV/c^2 and $M_v = 60$ GeV/c^2 one finds $\sigma_{M_H^0} =$ 1.8 GeV/c^2.

We can conclude that for $M_{H^0} \leq M_{t\bar{t}}/2$, toponium should yield the H^0 via the decay toponium $\to H^0\gamma$. Suppose that either $M_{H^0} > M_{t\bar{t}}/2$ or the SLC turns on at about the same time as TRISTAN. Can one search for the H^0 at the Z^0? Bjorken[21]

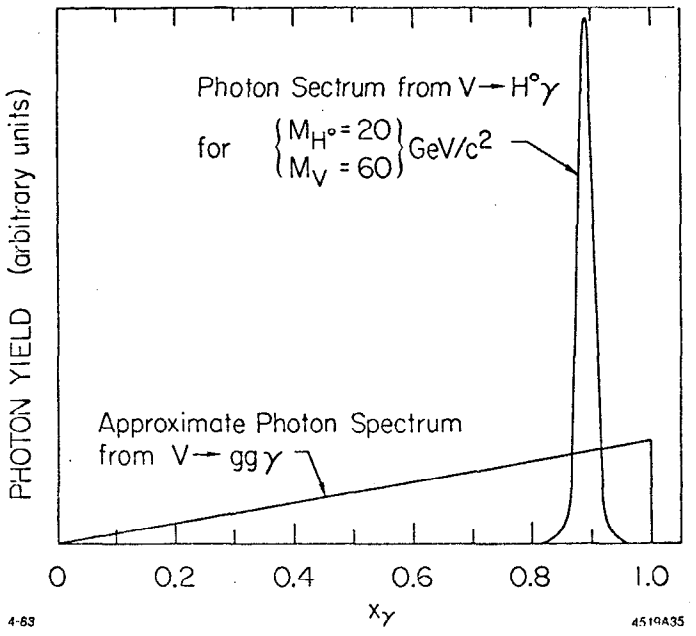


Fig. 18. The photon spectrum from $V \to H^0\gamma$ assuming $M_{H^0} = 2-$ GeV/c^2, $M_V = 60$ GeV/c^2 and $\sigma_E/E = 10\% \ / \sqrt{E}$. Also shown in an approximation to the photon spectrum for the background $V \to gg\gamma$. The relative areas of the two curves are chosen to simulate the expectations for these two processes.

pointed out that indeed one could utilize the process $Z^0 \rightarrow$ virtual $Z^0 + H^0 \rightarrow H^0 \ell^+ \ell^-$ as shown in Fig. 19. Here $\ell^\pm$ are charged leptons. The production rate[22] for this process is shown in Fig. 20. Also shown is the rate for $Z^0 \rightarrow H^0 \gamma$ which vanishes in first order because the photon and the Z^0 are "orthogonal." The $Z^0 \rightarrow H^0 \ell^+ \ell^-$ event rate is not large and will require that the SLC and LEP obtain their promised peak luminosity. For a $< \mathcal{L} >= 3 \times 10^{30}\ cm^{-2}\ sec^{-1}$ the event rates for each lepton channel are 1.2/day for $M_{H^0} = 10$ GeV/c^2, 0.4 events/day for $M_{H^0} = 20$ GeV/c^2 and 0.3 events/day for $M_{H^0} = 30$ GeV/c^2. This signal must be observed in the presence of a hadronic event rate of ~9,000 events/day. The key to extracting a signal is the event topology. The dilepton pair take most of the energy in the process, leaving the H^0 close to rest. Figure 21 shows the dilepton invariant mass spectrum for different values of M_{H^0}. The slow H^0 is assumed here to decay to a pair of quarks. What results then is an event with two quark jets which are roughly back to back and a pair of high energy leptons whose direction is not correlated to the hadronic sphericity axis. Figure 22 shows this topology schematically. There have been numerous studies of the detection of these $H^0 \ell^+ \ell^-$ events at the various Z^0 workshops; we have used the study done for the SLC workshop.[5b] Hadronic events at the Z^0 were produced using a Monte Carlo simulation program. Events were selected which had two electrons (muons will look essentially the same). Figure 23 shows the dilepton mass spectra which arise from the signal and the $Z^0 \rightarrow$ *hadrons* background. In order to reduce the background, each lepton is required to have an angle $>$ 200 mrad relative to the sphericity axis of the hadronic system. This will cause virtually no loss ($\sim 2 \times 200/2 \times \pi \times 10^3 =$ 6%) of signal events because the leptons have no correlation to the hadronic system. However, the background is substantially reduced because the main source is $Z^0 \rightarrow t\bar{t}$ where both t's decay semileptonically and in this case it is rare to get two high energy decay leptons which have in addition large transverse momentum. It appears then as if the hadronic background can be handled.

In order to establish a signal, one must look for a peak in the spectrum of the mass recoiling against the dilepton pair. This recoil mass is shown in Fig. 24 for $M_{H^0} = 10$ GeV/c^2 assuming that one detects electrons in an electromagnetic calorimeter with an energy resolution of $\sigma_E/E = 10\% / \sqrt{E}$. A clear signal is seen with a mass resolution of roughly 1 GeV/c^2. The mass resolution degrades approximately linearly

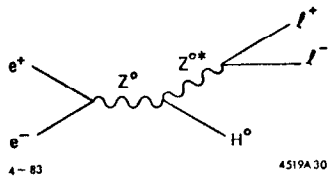


Fig. 19. The process $e^+e^- \rightarrow Z^0 \rightarrow H^0 \ell^+ \ell^-$.

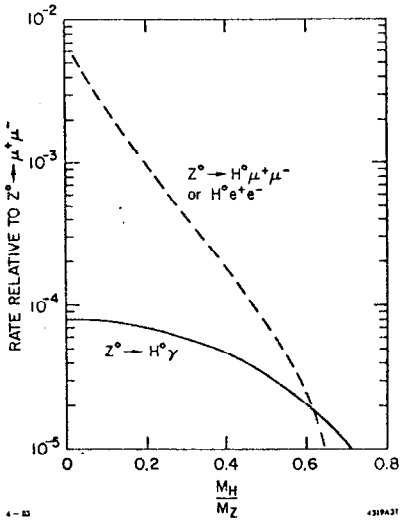


Fig. 20. The decay rate for $Z^0 \rightarrow H^0 e^+ e^-$ or $Z^0 \rightarrow H^0 \mu^+ \mu^-$ relative to $Z^0 \rightarrow \mu^+ \mu^-$ which has a branching fraction of 3% .

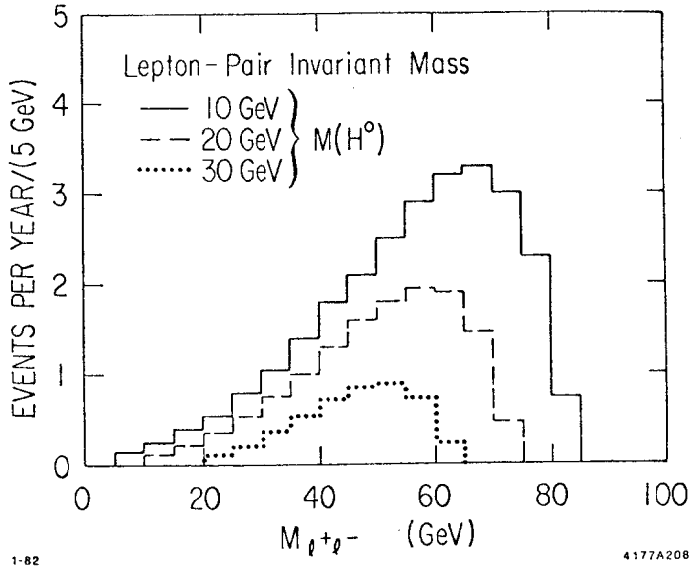


Fig. 21. Dilepton mass spectra for $Z^0 \rightarrow H^0\ell^+\ell^-$ for several choices of the Higgs mass. The normalization corresponds to 2000 hours of beam time at an average luminosity of $10^{30}\ cm^{-2}\ sec^{-1}$.

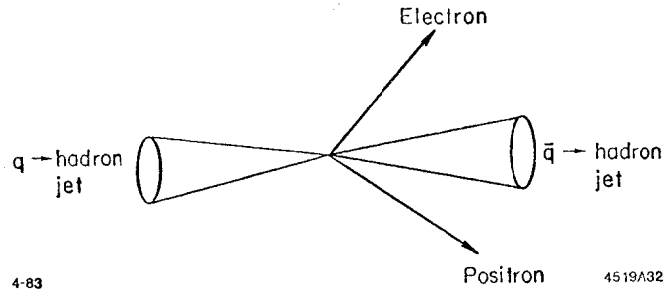


Fig. 22. A schematic representation of the topology of the $Z^0 \rightarrow H^0\ell^+\ell^-$ events.

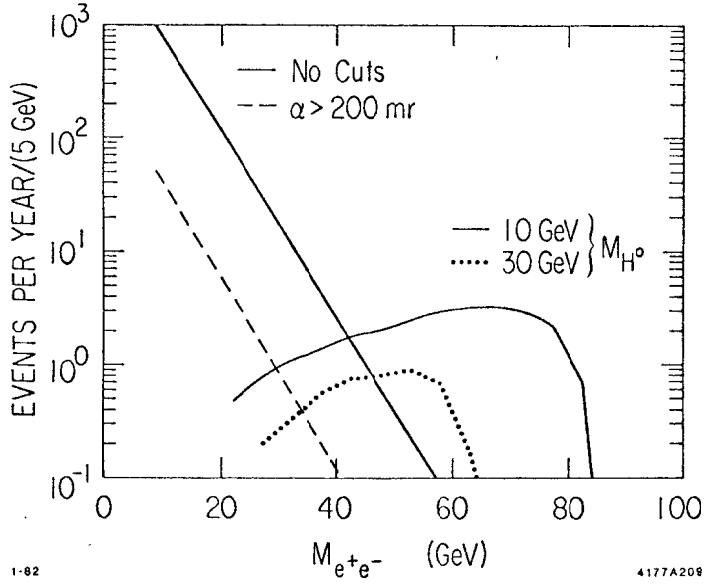


Fig. 23. The electron-positron pair mass spectra for: (a) e^+e^- pairs from jets without cuts (solid line), (b) e^+e^- pairs from jets with a 200 mrad cut described in text (dashed line), and (c) e^+e^- pairs from $Z^0 \rightarrow H^0e^+e^-$, $M_{H^0} = 10\ \mathrm{GeV/c^2}$ (solid line) and $M_H = 20\ \mathrm{GeV/c^2}$ (dashed line).

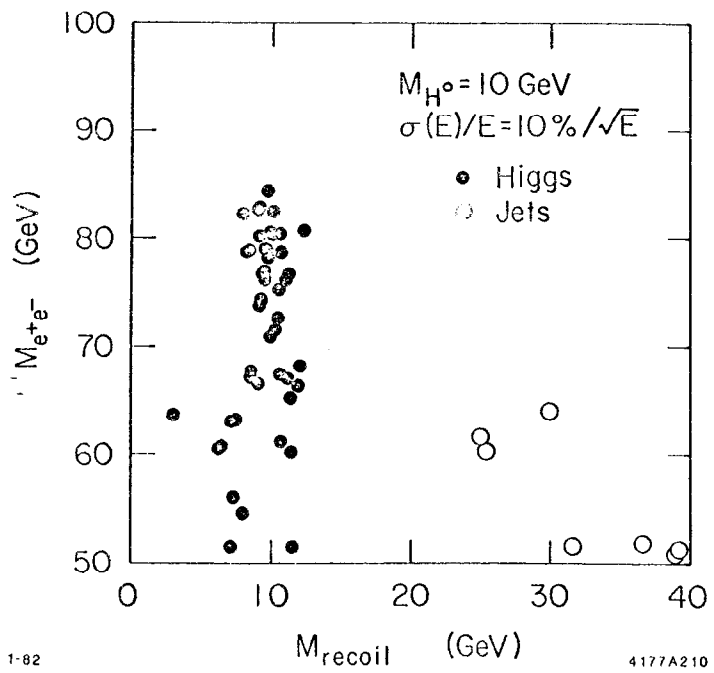


Fig. 24. Scatter plot of $M(e^+e^-)$ versus recoil mass calorimeter with resolution $\sigma_E/E = 10\%/\sqrt{E}$.

with the calorimeter resolution and, particularly for a high mass H^0, one would not want to do this measurement with a calorimeter having an energy resolution worse than $20\%/\sqrt{E}$. If the muon channel is chosen the muon momentum resolution required which corresponds to $\sigma_E/E = 20\%/\sqrt{E}$ is $\sigma_{P/P} = 0.1\% P$ assuming that the typical lepton momentum is 30 GeV/c. Because the rate is so small an optimal detector should have good solid angle coverage and be able to detect both the dielectron and dimuon modes. The requirements for lepton/hadron separation are not too taxing. A rejection of 50 : 1 would be more than adequate.

We can summarize this discussion by saying that searches for the H^0 will be possible at the SLC and LEP provided that these machines achieve their design luminosities of $\geq 5 \times 10^{30}\ cm^{-2}\ sec^{-1}$. Experiments will have sensitivity to the mass range $5 \leq M_{H^0} \leq 40$ GeV/c^2. The upper limit comes from rate and hadronic background limitations and the lower limit from backgrounds arising from two photon processes which were not discussed here.

Assume nature is unrelenting and $M_{H^0} > 40$ GeV. Searches will have to be performed at LEP II, LEP III and SLC II and possibly at the high energy colliding linacs. The H^0 can be pursued using the reaction $e^+e^- \rightarrow H^0Z^0$ where the dominant contribution to the process comes from an intermediate virtual Z^0 as shown in Fig. 25. The cross section for this process is given by[23]

$$\sigma(e^+e^- \rightarrow Z^0H^0) = \frac{\mathcal{G}_F^2 M_{Z^0}^2}{48\pi} f(S, M_{Z^0}, M_{H^0})(1 - 4sin^2\theta_W + 8sin^4\theta_W)$$

where $\sqrt{s} = E_{c.m.}$ and

$$f(s, M_{Z^0}, M_{H^0}) = \frac{1}{s}[1-A]^{\frac{1}{2}}[1-B]^{\frac{1}{2}}\left\{(1-A)(1-B) + 12\frac{M_{Z^0}^2}{s}\right\}\left[\frac{1}{(1-\frac{M_{Z^0}^2}{s})^2}\right]$$

and $A = \frac{(M_{Z^0}+M_{H^0})^2}{s}$, $B = \frac{(M_{H^0}-M_{Z^0})^2}{s}$. Figure 26 shows the ratio of $\sigma(e^+e^- \rightarrow Z^0H^0)$ to the point cross section as a function of $E_{c.m.}$ and M_{H^0}. The cross section for $e^+e^- \rightarrow Z^0H^0$ is comparable to the point cross section and therefore the event rates will be favorable. For fixed $E_{c.m.}$ the cross section remains independent of M_{H^0} until one comes close to threshold. As $E_{c.m.}$ is increased, the relative rate decreases quite rapidly.

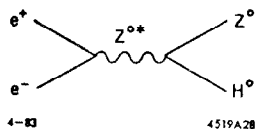


Fig. 25. The process $e^+e^- \to Z^{0*} \to Z^0H^0$.

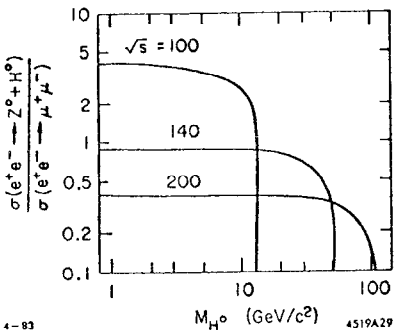


Fig. 26. The rate for the process $e^+e^- \to Z^0H^0$ is shown as a function of $E_{c.m.}$ and M_{H^0}. The rate is normalized to the point cross section which has the value $86.8/E^2_{c.m.}$ nb.

Running at the highest LEP II energy of $E_{c.m.} = 170$ GeV the event rate for a H^0 with a mass of 40 GeV/c^2 is ~ 3 events/day. This assumes a $< \mathcal{L} >= 1.6 \times 10^{31}\ cm^{-2}\ sec^{-1}$. The final state Z^0H^0 must be extracted from a hadronic background of ~ 15 events/day. In general these two processes will not easily be separated. One could guarantee separation by requiring that the $Z^0 \to e^+e^-$ or $\mu^+\mu^-$ or $\tau^+\tau^-$ or $\nu\bar{\nu}$. This constitutes 3% of the Z^0 decays per charged lepton pair plus 9% for the $\nu\bar{\nu}$ channel. In the lepton decay channels one would have an extra handle on the process by calculating the dilepton invariant mass which should be the Z^0 mass. The H^0 mass would have to be reconstructed from the H^0 decay products.

The search for the H^0 at LEP II and LEP III will be possible for H^0 masses $\leq \frac{E_{c.m.}}{2}$ provided that these machines achieve their design luminosity. For very heavy H^0's, those which would be found at the colliding linacs, a luminosity of $10^{32} - 10^{33}\ cm^{-2}\ sec^{-1}$ is needed.

4.4 Tests of the Non-Abelian Nature of QCD

We first consider the evidence which exists for gluons. Such evidence comes from e^+e^- interactions at PETRA, PEP and CESR and from deep inelastic lepton scattering. For an excellent review of this topic see Ref. 24. In all respects the data are in good agreement with the predictions of QCD and no conflicts exist. In particular, QCD predicts the presence of three jet events in e^+e^- at $E_{c.m.} \geq 10$ GeV and indeed such events are seen. Let us review the evidence for the three jet events as obtained by the PETRA groups and confirmed recently by the PEP experiments.

The first striking property of the hadronic events at PETRA is that the mean transverse momentum of particles relative to the thrust or sphericity axis grows with increasing $E_{c.m.}$. The growth of the average p_t occurs in the plane containing most of the momentum, the $< p_t >$ out of this plane is almost independent of $E_{c.m.}$. These effects are shown in Fig. 27. If one looks at the high energy hadronic events clear three jet structures are seen. A model in which $e^+e^- \to q\bar{q}$ in which the quark mean p_t in the fragmentation process is allowed to grow with $E_{c.m.}$ does not account for the growth of $< p_t >$ in the event plane. The interpretation of the data is that the growth of $< p_t >$ in the plane occurs because of the emission of a gluon(s) namely $e^+e^- \to qqg$. This process can be thought of as bremsstrahlung of a gluon off a quark (antiquark) line. The process is shown pictorially in Fig. 28a. QCD predicts, to first

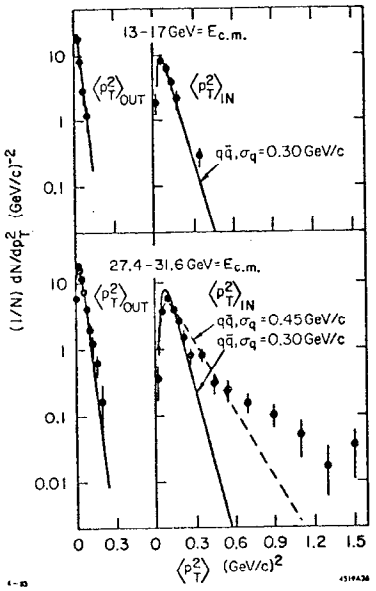


Fig. 27. The mean transverse momentum squared per event as shown both normal to the event plane ($< p_t^2 >_{out}$) and in the event plane ($< p_t^2 >_{in}$) at $E_{c.m.} = 13$, 17 and 27.4 - 31.6 GeV. These data are from the TASSO group. The predictions of the quark model ($e^+e^- \rightarrow q\bar{q}$) are shown assuming the quark fragmentation process is characterized by a $\sigma_q =$ 300 MeV/c (solid line) or = 450 MeV/c^2 (dashed line).

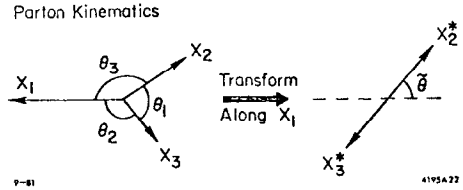


Fig. 28. (a) The kinematics for the process $e^+e^- \rightarrow qqg$ where $X_i = E_i/E_{c.m.}$ and E_i are the parton energies. (b) The defraction of the Ellis-Karliner angle, $\tilde{\theta}$.

order in α_s, the distribution of the parton momenta

$$\frac{1}{\sigma_0}\frac{d\sigma}{dx_1 dx_2} = \frac{2\alpha_s}{3\pi}\left[\frac{x_1^2+x_2^2}{(1-x_1)(1-x_2)} + \begin{matrix}(1,2,3)\\ cyclic\ \ permutations\end{matrix}\right]$$

where $x_1 = 2\frac{E_i}{E_{c.m.}}$ and E_i is the parton energy. The analyses performed at PETRA constitute tests of the above Dalitz plot distributions ($\Sigma x_i = 2$). For example the measured distribution of x_1 in clear three jet events is shown in Fig. 29 along with the prediction of the QCD Monte Carlo. These tests have been performed by all the PETRA groups[25] and the MARK II at PEP[26] and in all cases the data are well represented by the QCD Monte Carlo simulation programs. We omit here the discussion of how the three jet events are obtained. There are many methods for doing this[27] and suffice it to say that for the conclusions above all these methods are reasonable. Besides checking these Dalitz plot distributions, the spin of the assumed gluon has been measured. The method employed by the TASSO and MARK II group is that suggested by Ellis and Karliner[28] in which one transforms to the rest frame of the (x_2, x_3) system using the measured direction and velocity of the fastest parton (x_1). This is shown pictorially in Fig. 28b. $\tilde{\theta}$ is the decay angle in this (x_2, x_3) rest frame and $\frac{dN}{d\ cos\tilde{\theta}}$ can be thought of as the decay angular distribution of the gluon which will be sensitive to the spin of the gluon. If one assumes that the partons are massless

$$cos\,\tilde{\theta} = \frac{x_2 - x_3}{x_1}\ .$$

Figure 30 shows the $cos\,\tilde{\theta}$ distribution for clear three jet events as obtained by TASSO.[25] The prediction of QCD for spin 1 and spin 0 gluons is also shown. The spin 1 hypothesis reproduces the data well, the spin 0 hypothesis is a poor representation of the data. To quantify this, TASSO finds

$$< cos\,\tilde{\theta} >_{data} = 0.3391 \pm 0.0079$$

$$< cos\,\tilde{\theta} >_{data} - < cos\,\tilde{\theta} >_{QCD} = 0.0019 \pm 0.0084 \quad \text{and}$$

$$< cos\,\tilde{\theta} >_{data} - < cos\,\tilde{\theta} >_{scalar\ gluon} = 0.0411 \pm 0.0084$$

and hence the scalar gluon is ruled out at the four standard deviation level. This result is confirmed by the MARK II[29] and all the other PETRA groups.[25]

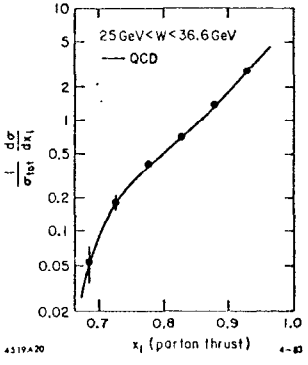


Fig. 29. The parton thrust distribution as measured by the TASSO group. The solid curve is the prediction of QCD to leading order in α_s which is taken to be 0.17.

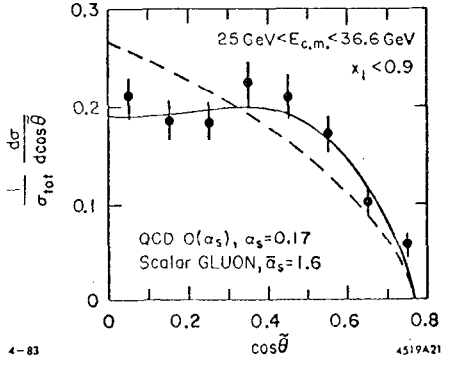


Fig. 30. The distribution of the Ellis-Karliner angle, $\tilde{\theta}$, for the three jet events with $X_1 < 0.9$ obtained by the TASSO group. The solid curve is QCD with $\alpha_s = 0.17$, the dashed curve is the prediction for a scalar gluon.

The groups running on the Υ first at DORIS[30] and more recently at CESR[31] have shown that the event shapes of the hadronic events agree very well with the QCD prediction that the Υ decays to three gluons. As an example, the data of the PLUTO group for thrust is shown in Fig. 31.

We can summarize by saying that in all these studies, the predictions of the first order QCD, as they are incorporated in Monte Carlo simulation programs, do an excellent job of accounting for the experimental data. QCD makes predictions for parton distributions and the experiments observe hadrons. The gap is bridged by models for this fragmentation process. The simulation programs have many adjustable parameters which give the experimenters some freedom when the comparisons are made. So some of the arguments become somewhat circular.

In the light of this criticism we should ask whether there are competing theories or models which can account for the observed data. We know that at energies ≤ 10 GeV, $e^+e^- \rightarrow q\bar{q}$ plus fragmentation of the quarks into hadrons account very well for the e^+e^- data. Can one make simple extensions to such models to account for the 30 GeV e^+e^- data? There are a wide variety of these extended $q\bar{q}$ models and in general one is able to arrange the parameters of the models to reproduce the $< p_t >$ distributions both in and out of the event plane. However in doing so the x_1 distributions never agree with the data. We borrow Table 5 directly from Ref. 25 to show the kinds of models which have been tried. The notation $q_\perp$ is the quark transverse momentum, σ_q is the average of this quantity and x_1 is as discussed earlier in this section. Figure 32 indicates how the first and third models in Table 5 fail to account for the data. The other models fail in a similar way.

There is a model which is not a simple extension of $e^+e^- \rightarrow q\bar{q}$ whose proponents claim accounts well for the PETRA data. The model, which goes under the name of Quantum Geometrodynamics, is due to G. Preparata and coworkers at Bari. The model has the somewhat uncomfortable feature of evolving with the evolving data and so a clear and complete reference is hard to find. However, the interested reader can start with the references given in Ref. 32.

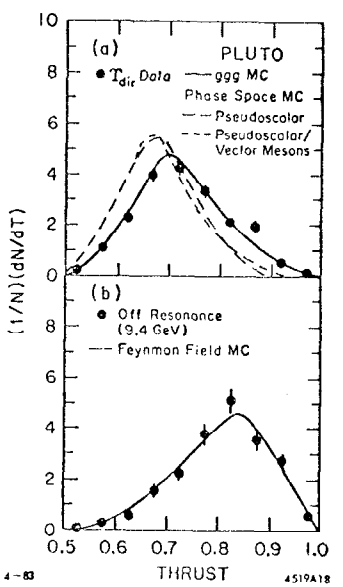


Fig. 31. The thrust distributions as measured by PLUTO for V and the continuum.

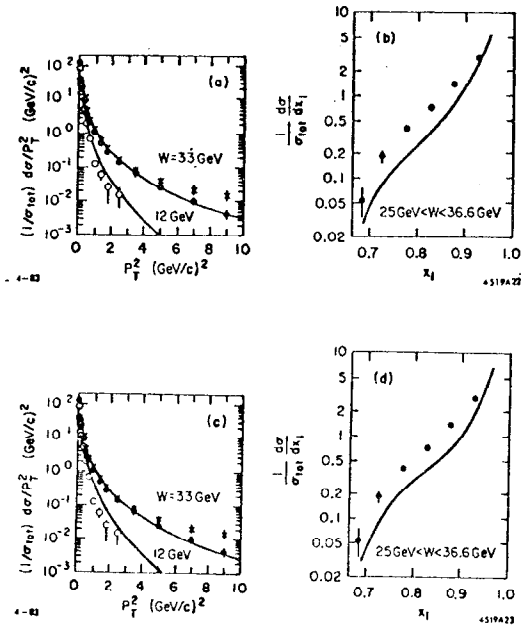


Fig. 32. The (TASSO) data in (a) and (c) are the same namely the distribution of transverse hadron momentum squared with respect to sphericity axis. For the high energy data, the parton thrust distribution is shown in (b) and (d). The fits to (a) and (c) are for the model described in column one of Table 5, and those to (b) and (d) are for the model described in column four of Table 5.

Table 5. Comparison with Two Jet Models.

Model	Result	
$\frac{d\sigma}{dq_\perp^2} \sim exp\left(\frac{-q_\perp^2}{2\sigma_q^2}\right)$	$p_\perp^2$, $< p_\perp^2 >_{in}$, $< p_\perp^2 >_{out}$	good
$\sigma_q = 320$ GeV/c for u,d,s,	x_1	too low
$\sigma_q = 800$ MeV/c for c, b	$p_\perp^2$ w.r.t. 3 axes	too broad
$\frac{d\sigma}{dq_\perp^2} \sim exp\left(\frac{-q_\perp}{a}\right)$	$p_\perp^2$, $< p_\perp^2 >_{in}$, $< p_\perp^2 >_{out}$	good
	x_1	too low
$\frac{d\sigma}{dq_\perp^2} \sim exp\left(\frac{-dq_\perp^2}{2\sigma_q^2}\right) +$	$p_\perp^2$, $< p_\perp^2 >_{in}$, $< p_\perp^2 >_{out}$	good
$a\, q_\perp^{-4}$	x_1	too low

QGD differs greatly in motivation for QCD and in its Monte Carlo formulation it has far less parameters than QCD plus fragmentation. In particular the model does not have gluons and hence, while it predicts three jet events, it also predicts that the three jets should all fragment identically. This being a leading issue, we proceed to look at this model. The model is not easy to describe but we do our best in this limited space. At the heart of the model is an object called a "fire sausage" or "fire string" which is a bag in space-time. The concept is that one starts off with geometry – simple domains in space-time which contain a $q\bar{q}$ pair – and then, using a wave function for this domain and a set of physical boundary conditions, one generates dynamics. The dynamics comprise a particle spectrum and perturbative bag interactions. The particle spectrum which evolves is a set of Regge trajectories.

Multiparticle states originate from the decay of well defined $q\bar{q}$ structures – the fire strings (FS). These FS's are tube-like structures – see Fig. 33 – which contain a coherent superposition of Regge trajectories of different orbital angular momentum. In three space you can visualize this object as containing $q\bar{q}$ waves moving freely inside a cylinder of length $R_\ell \sim mass$ and a radius $R_\perp \sim log(mass)$. There are two ways that the FS can decay and in both cases the process is specified by QGD without freedom

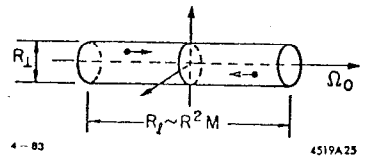


Fig. 33. A schematic representation of a fire-string (FS).

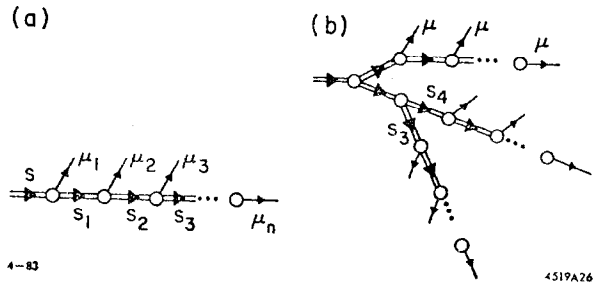


Fig. 34. The chain (a) decay and the tree (b) decay of a fire string.

of parameters. The two decay mechanisms, chain (a) and tree (b), are shown in Fig. 34. The kernels for these decays are predicted by QGD and the only parameter in the model is α which is the relative amount of chain and tree decay required by nature.

From this brief discussion it probably hasn't been clear, but the decay process outlined above is akin to hadronization plus perturbative QCD. In QGD, a FS is produced in e^+e^- with the quark content specified by the quark charge squared. The angular distribution of the axis of the FS is taken to be $1+cos^2\theta$ in the usual manner. A Monte Carlo simulation program, called EPOS, has been written incorporating the ideas outlined above. It has only one parameter α (or two if one adds in baryons as decay products of the FS). Using the TASSO data from PETRA, Preparata et al.,[32] have fit α and find it to be $\alpha = 1.05 \pm 0.3$. Having fixed this parameter, they then compare their Monte Carlo predictions with QCD and data. Figure 35 shows the comparison between QCD and QGD for the three jet kimenatics. At the parton level the agreement is good. Fig. 36 shows the comparison between QGD and the TASSO hadron inclusive spectra. QGD agrees well with the data and even predicts the correct amount of scaling violations. More comparisons are given in the references. The reason for including this model was that in the eyes of its proponents a model, quite different than QCD, does account for the observed data and hence offers an alternative to the motion of gluons. The model is also distinguishable from QCD in that it predicts that all jets should fragment identically, whereas QCD predicts that gluons should fragment differently than quarks. QGD offers an interesting straw man and it would be nice if the experimental groups could make direct comparisons between EPOS and their data.

The verification of first order QCD as discussed earlier in this section is most impressive. It is also nontrivial; we have seen only one (of many) alternative model achieve any measure of success. However to some extent the evidence in favor of QCD is circumstantial and we should have higher standards if we are to say that QCD is the "theory of the strong world." In particular we should demand more direct evidence that QCD is a non-Abelian theory.

The most natural place to look for the proof is at toponium because $t\bar{t}$ decays to hadrons via three gluons. Since toponium is heavy (> 37.5 GeV/c^2) the three gluons will show up in most cases as three well defined jets. Application of a cluster algorithm

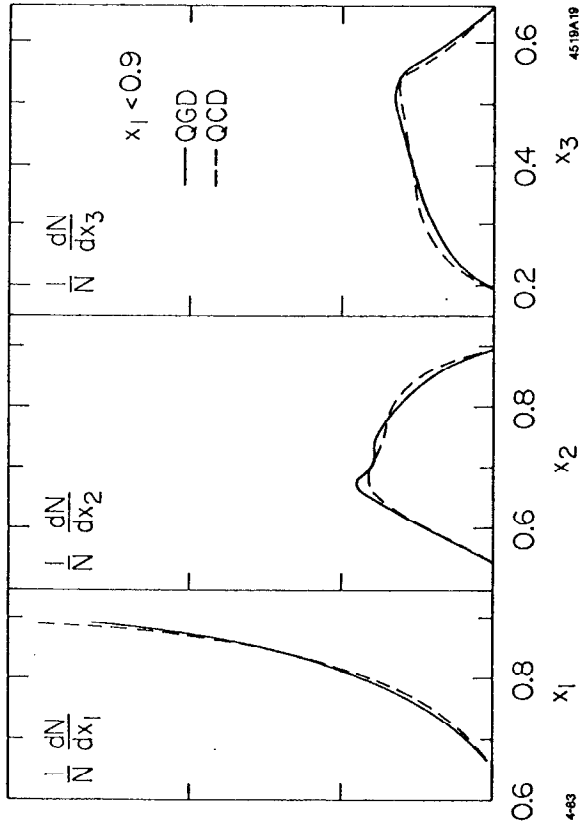


Fig. 35. A comparison between the three jet parton X distributions (see Fig. 28) for QCD and QGD.

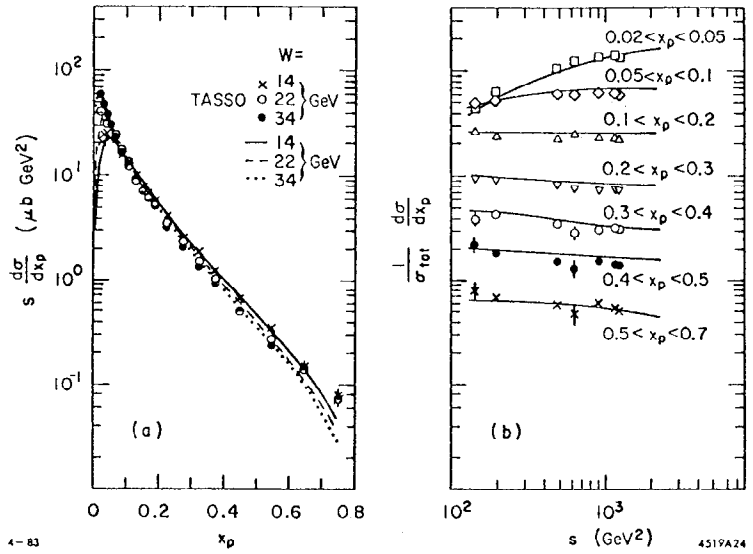


Fig. 36. Predictions of the QGD Monte Carlo simulation program EPOS are compared with the hadron inclusive spectra of TASSO (a) and with the scaling violations implied by the data (b).

will result in a large fraction of well-defined three cluster (jets) events. A study of this type was done[15] some while ago for $M_{t\bar{t}} = 30$ GeV/c^2. (The conclusions of this study are only strengthened by the fact that we know now that $M_{t\bar{t}} > 30$ GeV/c^2). Monte Carlo events were generated at 30 GeV for toponium and the continuum. We will characterize toponium as ggg and the continuum as $q\bar{q} + q\bar{q}g$, where q and g stand for quark and gluon respectively. The cluster frequency distributions obtained using the cluster algorithm are shown in Fig. 37. One sees that in the case of ggg the cluster algorithm reconstructs half the events as three jet events. It is shown in Ref. 15 that the assignment of particles to the jets by the cluster algorithm reproduces the produced jet assignments very well. Those events which are reconstructed as two jet events are those in which two of the jets overlap. In the continuum the reconstructed number of three jet events is much smaller because only about 25% of the events are $q\bar{q}g$ (i.e., have a gluon of sufficient energy to warrant calling the final state a three parton state) and many of those have a large overlap between the gluon and the quark which radiated the gluon. These will be reconstructed as two cluster events. We then propose the following procedure to test whether quarks and gluons of the same (high) energy hadronize differently. Suppose one is running at $E_{c.m.} = 40 - 60$ GeV. In this case the continuum correction is the same as the peak cross section for toponium (see Fig. 5). The first step in the test is to run at the peak of toponium and accumulate three jet events. Assuming $< \mathcal{L} > = 10^{31}\ cm^{-2}\ sec^{-2}$ and the cluster finding efficiencies from Fig. 37, one would get 18 ggg three jet events/day and 7 $q\bar{q}g$ three jet events per day; one would have a sample of three jet events in which the fastest jet had an energy of 14-18 GeV and was 70% "gluon rich." The second step is to run below toponium and accumulate three jet events. These would accumulate at 7 events/day and the fastest jet would again have 14-18 GeV and be 100% quark. One would now compare the decay properties of the fastest jet on and off the toponium resonance. The obvious variables to test are the multiplicity and the $< p_t >$ for the jet particles relative to the reconstructed jet axis. The multiplicity should be $\sim$ twice as large and $< p_t >$ should be appreciably larger for the gluon jets relative to the quark jets. One would immediately be able to tell if gluons fragment differently than quarks. The advantage of this test is that one needs no corrections, no Monte Carlo simulations – one merely compares observed distributions.

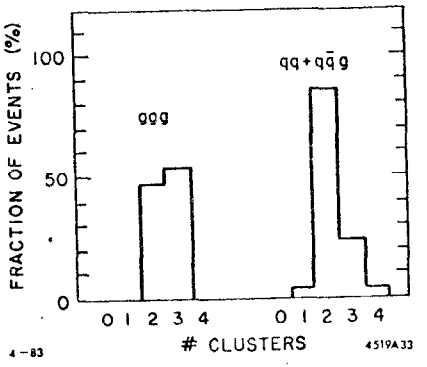


Fig. 37. The cluster frequency distributions for $e^+e^- \rightarrow ggg$ (a) and $e^+e^- \rightarrow q\bar{q} + q\bar{q}g$ (b) at $E_{c.m.} = 30$ GeV.

One could argue that a somewhat more formal test of the gluon self-coupling might be preferable. Such tests have been proposed and we choose as an example the method proposed in Ref. 33 by Koller et al. It involves looking at four jet events produced at toponium. In this case one would have dominant contributions from the two diagrams shown in Fig. 38. The authors argue that (a) is about four times more copious than (b) and hence an absence of the $g \rightarrow gg$ coupling required for (a) can be detected. We estimate that $\leq 10\%$ of the toponium hadronic decays will reconstruct as clear four cluster events. For $< \mathcal{L} >= 10^{31}\ cm^{-2}\ sec^{-1}$, this corresponds to a signal of three events/day. A one-year run under these conditions would suffice.

There are two distinct four jet topologies which result and these are shown in Fig. 39. The authors suggest focusing on the Class B events which are about twice as plentiful as Class A events. Define the two jet group which has the smallest invariant mass as the slim jet side. The choice of the slim jet favors strongly the side where the $g \rightarrow gg$ or $g \rightarrow q\bar{q}$ branching occurred. Several variables show measurably different spectra for (a) and (b) and we show in Fig. 40 the distribution of $cos\theta_{ij}$ for the two possibilities. The angle θ_{ij} is the angle of the slim jet with respect to the overall four jet thrust axis defined in the rest frame of the slim jet. One sees that the $g \rightarrow gg$ process favors $cos\theta_{ij} \rightarrow 1$ whereas the $g \rightarrow qq$ is relatively flat. If the gluon self coupling were not present one would see it both in the yield and shape of the $cos\theta_{ij}$ plot. This method would seem promising. Other proposed probes for the gluon self-coupling include tests at the Z^0 (Ref. 34) and tests in the continuum (Ref. 35).

Why not use PETRA/PEP gluon jets to study the difference between gluon and quark fragmentation? There are several problems with this approach. In general the three jet events do not have the softest jet well separated from the intermediate energy jet. This overlap of jets makes the measurement of jet energy, jet multiplicity and mean p_t very difficult. One only has a statistical assignment of the "gluon rich" jet and most of the gluons are soft. One would like to have high energy jets which were well measured with reliable particle assignments. Unfortunately, with PETRA/PEP type events one has a situation where the "gluon rich" jet is the softest and is the most poorly measured. If one asks for a high energy gluon one moves towards the configuration in which each parton carries $E_{c.m.}/3$. However, in this configuration the assignment of any jet to the gluon hypothesis is a purely statistical one, namely

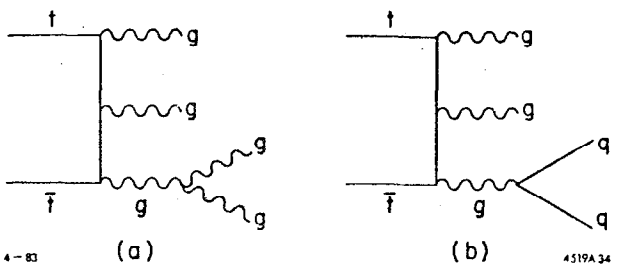


Fig. 38. The two dominant diagrams for producing four jet events at toponium.

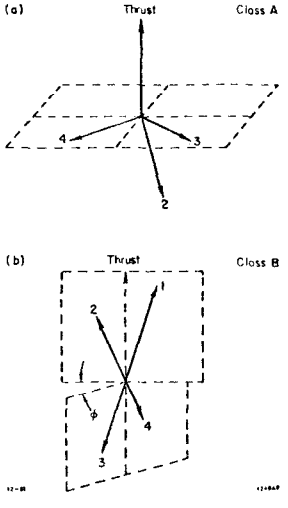


Fig. 39. Kinematic configuration for the class A and B events. In (a) the thrust axis will be along the momentum vector of one of the jets and the three other jets will be in the opposite hemisphere. In (b) there are two jets in each hemisphere.

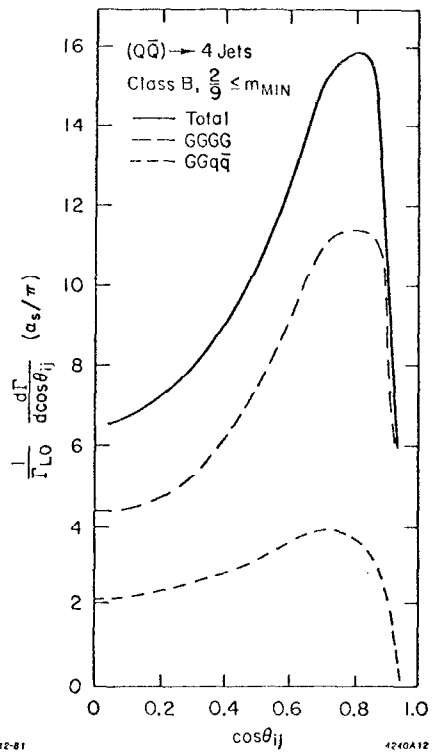


Fig. 40. Angular distribution of the two-jet system on the "slow" side of the event relative to the thrust axis. This angular distribution is evaluated as the two-jet center-of-mass.

the odds are 1/3 for any jet you choose. It is the author's opinion that it will be very difficult at the present PETRA/PEP energy range to conclusively demonstrate that gluons fragment differently than quarks. Perhaps if PETRA can get a very large ($100pb^{-1}$) data set at $\geq$ 40 GeV it can be done.

Luckily there are people who disagree with the author's personal opinion! The JADE group[36] claim that they do see differences in the mean p_t between the soft jet (gluon rich) and intermediate energy jet (quark rich). There are, however, analyses[29,37] which claim to see no effect and the JADE results require confirmation or in the words of Braunschweig (Ref. 25), "... the effect seen by the JADE group needs further study."

4.5 Does α_s Run – And, If So, How do we "Clock" It?

The question posed above seems somewhat akin to measuring the progress of a snail using a watch calibrated in femtoseconds – the point being, of course, that α_s runs very slowly. Remembering the formula given in Sec. 3 and taking $n_f = 3$ and $\alpha_s[(30\text{ GeV})^2] = 0.17$ one finds

$E_{c.m.}$ = (GeV)	$\alpha_s(Q^2)$
30	.170
93 (Z^0)	.156
140 (LEP II)	.150
300 (VLEPP I)	.140
1000 (VLEPP II)	.130

In order to understand how hard it is to see these small changes in α_s one should keep in mind that the typical errors in α_s coming from PEP/PETRA measurements are 0.02 statistical and 0.03 systematic. The present level of systematic errors is the difference in α_s at 30 and 300 GeV! So it will be very hard to measure the running coupling constant by raising $E_{c.m.}$.

Is there an alternative at present energies? Could we investigate the process whereby a quark evolves into a jet of hadrons and sample different values of Q^2 in the sense that early times $\Rightarrow$ short distances $\Rightarrow$ large Q^2? An analysis along these lines

has been performed by the MARK II group.[38] The discussion is complicated and the interested reader is encouraged to consult the reference.

4.6 Quark Confinement

Confinement was a direct consequence of the non-Abelian nature of QCD. The Fairbanks et al[39] results indicate that free quarks exist and while this result needs confirmation we cannot ignore it simply because it makes us uncomfortable. What evidence do we have from e^+e^- experiments on the existence of free quarks? None have been seen and the limits taken from Ref. 13 are shown in Fig. 41. Searches are done for quark pair production and for inclusive quark production. Figure 41 shows the limits obtained for the cross section for these processes normalized to the point cross section. As we probe still higher energies, we must always remain vigilant and ensure that the new detector designs do not preclude searching for free quarks.

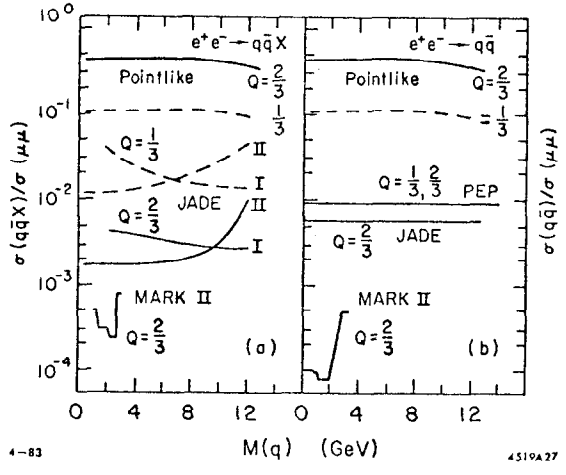


Fig. 41. Results from the e^+e^- quark search experiments is shown for the inclusive channel (a) and the exclusive channel (b). Shown are the upper limits for the production cross sections at the 90% confidence level. The two options I and II represent alternative models for obtaining corrected cross sections.

5. Simple Extensions of $SU(3) \wedge SU(2) \wedge U(1)$

5.1 Models With More Than One Higgs Doublet

The minimal version of the Weinberg-Salam model has a complex doublet of Higgs fields (Sec. 3). There are no theoretical reasons for excluding the introduction of more than one doublet of Higgs fields in the standard model. There are many instances of models which use two complex doublets. This alternative offers a possible solution to the strong CP problem, and is used in both supersymmetry models and $SU(5)$. In such models one has

$$\phi_1 = \begin{pmatrix} \phi_1^+ \\ \phi_1^0 \end{pmatrix} \ , \quad < \phi >_0 = V_1$$

$$\phi_2 = \begin{pmatrix} \phi_2^+ \\ \phi_2^0 \end{pmatrix} \ , \quad < \phi >_0 = V_2$$

where $V_1 + V_2 = V = \sqrt{2}\, g_F$. When the spontaneous symmetry breaking occurs, three of the eight fields are eaten by the $W^\pm$ and Z^0 while five remain as physical fields. These result in two neutral bosons with scalar couplings to quarks and leptons (H_1^0, H_2^0), one neutral boson with pseudoscalar couplings (h^0) and two charged scalar bosons $(H^\pm)$. In some models h^0 is associated with the axion. In order to avoid flavor changing neutral currents, it is arranged that ϕ_1 gives mass to the charge $\frac{2}{3}$ quarks and ϕ_2 gives mass to the charge $\frac{1}{3}$ quarks. The couplings, as in the minimal model, are specified:

$$g_{fH_1} = \frac{1}{V_1} M_{u,c,t} \ , \quad g_{fH_2} = \frac{1}{V_2} M_{d,s,b} \ .$$

However the ratio $X \equiv \frac{V_1}{V_2}$ is not known. Since $M_c > M_s$ and $M_t > M_b$ it is surmised, but not necessary, that $V_1 > V_2$. We will assume for discussion of searches that $X \geq 1$ and that the charged Higgs scalars like to couple to the heaviest fermion pair available. By direct analogy with the $W^\pm$ sector, Kobayashi-Maskawa type mixing can occur in the $H^\pm$ sector. We have no knowledge of how large this mixing might be but we will assume here that the mixing is small.

Why do we choose only isodoublets for the Higgs fields? There are several reasons – two are given here. Higgs fields with weak isospin $\neq \frac{1}{2}$ (triplets, etc.) cannot participate in the generation of fermion masses. They also upset the successful theoretical prediction of the standard model for the ratio of the strength of charged and neutral currents. Suppose we introduce a triplet of Higgs fields

$$\eta = \begin{pmatrix} \eta^+ \\ \eta^0 \\ \eta^- \end{pmatrix} \quad < \eta >_0 = Y \ .$$

Following the symmetry breaking one finds that $< \eta >_0$ contributes extra mass to the $W^\pm$ and

$$\rho = \frac{M_{W^\pm}^2}{M_{Z^0}^2 cos^2\theta_W} = 1 + \frac{4Y^2}{V^2} > 1 \ .$$

In the standard model $\rho = 1$ and this is well confirmed by all the data.[9]

We have no theoretical guidance for the $H^\pm$ mass. We expect that

$$\left.\begin{array}{l} H^\pm \to c\bar{s} \text{ or } c\bar{b} \\ \\ \to \tau\nu \end{array}\right\} \ M_{H^\pm} < M_t$$

$$H^\pm \to t\bar{b} \qquad\qquad M_{H^\pm} > M_t \ .$$

Pairs of charged Higgs particles will be produced in e^+e^- interactions, $e^+e^- \to H^+H^-$, with a cross section characteristic of scalars:

$$\frac{d\sigma}{d\, cos\theta} = \frac{1}{4}\, \sigma_{\mu\mu}\, \beta_H^3 sin^2\theta \tag{4}$$

$$R_{H^+H^-} = \frac{\sigma_{H^+H^-}}{\sigma_{\mu\mu}} = \frac{1}{4}\, \beta_H^3 \ . \tag{5}$$

$R_{H^+H^-}$ is too small a contribution to permit a confident discovery. The angular distribution is distinctive, but it will not be easy to see a small $(\frac{1}{16})$ admixture of $sin^2\theta$ superposed on a $cos^2\theta$ distribution. However this test should be performed by the PEP and PETRA groups. A more dramatic signature is the modification of heavy quark decay by the charged Higgs. This decay can proceed via $H^\pm$ in direct analogy with the standard $W^\pm$ diagram (see Fig. 42). The $H^\pm$ diagram dominates the $W^\pm$ for the assumption that there is small mixing in the Higgs sector. In the decays $Q \to H^\pm q$ and

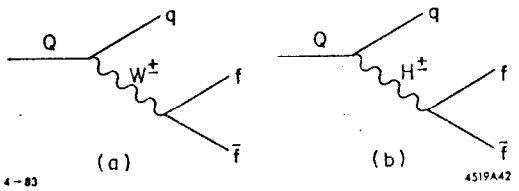


Fig. 42. The decay of a heavy quark in the standard model (a) and in the extended standard model which contains charged Higgs particles (b).

$Q \to W^{\pm} q$ the ratio $\frac{\Gamma(H^{\pm} q)}{\Gamma(W^{\pm} q)}$ ranges from 10^3 to 60 as M_Q ranges from 15 to 80 GeV/c^2. So if $M_{H^{\pm}} < M_c$, M_τ the D^0 and τ would have considerably shorter lifetimes than those measured. We may conclude then that $M_{H^{\pm}} \geq 1.8$ GeV/c^2. We can obtain a larger limit on $M_{H^{\pm}}$ from B decay. There are two possibilities (in the conventional lore considered in these lectures) for the decay of bottom via $H^{\pm}$. These are shown in Fig. 43. They offer two limiting cases: (a) $H^{\pm} \to c\bar{s}$ only in which case we will see no leptons and lots of charged energy in B decays and (b) $H^{\pm} \to \tau^{\pm}\nu$ only in which case we will see a lot of leptons and substantial missing energy in B decays. The CLEO experiment[36b] has looked for $H^{\pm}$ and shown in Fig. 44 is a plot of the observed charged energy fraction versus the lepton branching fraction. The data convincingly rule out the possibility that B decay is mediated by $H^{\pm}$. We conclude that $M_{H^{\pm}} \geq 5$ GeV/c^2. To obtain larger limits we must consider the data from PEP and PETRA.

Three event configurations are looked for. They are

$$e^+e^- \to H^+ H^- \begin{cases} \to \tau^- \nu_\tau \\ \to \tau^+ \bar{\nu}_\tau \end{cases}, \tag{6}$$

$$e^+e^- \to H^+ H^- \begin{cases} \to c\bar{s} \\ \to \tau^+ \nu_\tau \end{cases} \quad \text{and} \tag{7}$$

$$e^+e^- \to H^+ H^- \begin{cases} \to c\bar{s} + c\bar{b} \\ \to c\bar{s} + c\bar{b} \end{cases}. \tag{8}$$

These searches have been performed by many groups[40]: MARK II (6) and (7), TASSO (8), JADE (7), CELLO (6) and MARK J (6). The analyses involve choosing event topologies consistent with (6)-(8) and asking whether there exist events in excess of those resulting from conventional sources. The production rate and angular distribution is assumed to be given by (4) and (5). Monte Carlo simulations of the Higgs decays are used with variable $M_{H^{\pm}}$ to obtain limits. In the searches (6) and (7) it is assumed that the branching fractions for $H^{\pm} \to \tau\nu(B_\tau)$ and the branching fraction for $H^{\pm} \to c\bar{s}$ sum to one: $B_\tau + B_{c\bar{s}} = 1$. The analyses differ in detail; we use the MARK II analysis as an example of (6) and (7). Transverse momentum (p_t) is used as a measure

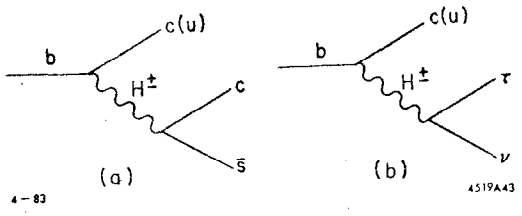


Fig. 43. If b quark decay was mediated by $H^{\pm}$, the prominent decay modes (for $M_{H^{\pm}} < M_t$) will be those shown above.

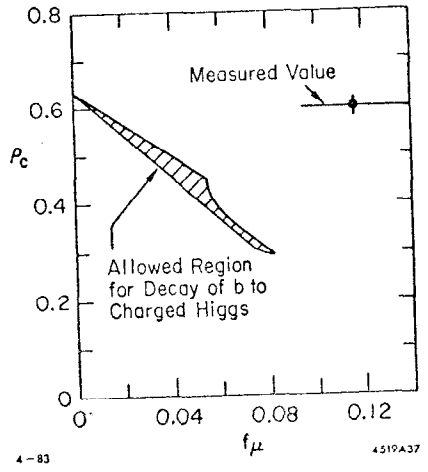


Fig. 44. Data from the CLEO experiment showing the measured charged energy fraction (p_c) versus the fraction of muons. The allowed region for the decay of b via a charged Higgs is shown along with the measured value.

of mass. We can think of the event topologies for (6) and (7) as being characterized by two hemispheres each containing the decay products of one of the parent scalars. An axis can be defined so that the p_t of both sets of decay particles is the same. This is a measure of the p_t in the parent decay. Figure 45a shows this p_t spectrum for events chosen to be representative of process (6). The conventional source for these events is $e^+e^- \rightarrow \tau^+\tau^-$ and we see that the absolutely normalized expectation for $\tau^+\tau^-$ production accounts very well for the data. There is no room for appreciable H^+H^- production. Using Monte Carlo predictions of the type shown in Fig. 45a for a 7 GeV/c^2 $H^{\pm}$, limits on $M_{H^{\pm}}$ can be obtained as a function of B_τ. These limits are shown as II in Fig. 46a. A similar analysis is done for (7), the results are shown in Fig. 45b and Fig. 46a. The results of the PETRA analysis for (6) and (7) are shown in Fig. 46b. PETRA runs at a higher $E_{c.m.}$ and hence the PETRA experiments are able to place more stringent limits on $M_{H^{\pm}}$. The study of (8) is much more difficult because the event topology will look very similar to the continuum $e^+e^- \rightarrow$ hadrons. TASSO[40] has done a four jet analysis in which they have found a kinematic separation between the scalar events and the continuum events. The results of this study are shown in Fig. 46c. Taking all the results in Fig. 46, it appears unlikely that there exists a charged scalar (with the properties described in this chapter) having a mass within the range of 5-13 GeV/c^2. Combining the τ and D^0 lifetime measurements, the CLEO, PEP and PETRA measurements it seems probable that $M_{H^{\pm}} \geq 13$ GeV/c^2. As the energy at PETRA is raised, so will the limits on $M_{H^{\pm}}$. When PETRA reaches $E_{c.m.} = 46$ GeV the experiments should have sensitivity to 21-22 GeV/c^2 in $M_{H^{\pm}}$.

Toponium is a good place to look for charged Higgs particles. If $M_{H^{\pm}} < \frac{M_{t\bar{t}}}{2}$ the diagram shown in Fig. 47 will dominate all other decay processes for toponium. This will make the toponium resonance much broader. At $M_{t\bar{t}} = 60$ GeV, Γ_{tot} is expected to be $\sim$ 10 MeV if the process in Fig. 47 is dominant. The TRISTAN machine width is predicted to be $\sim$ 60 MeV and even if charged Higgs dominate the decays of toponium, the machine resolution will dominate the measured width. The events however would be very distinctive relative to the expected decay topology $t\bar{t} \rightarrow ggg$. Firstly the events would not be planar and secondly there would be a lot of multilepton events. It would be an easy task to search for this possibility which offers the potential for achieving sensitivity up to $M_{H^{\pm}} \leq \frac{M_{t\bar{t}}}{2}$.

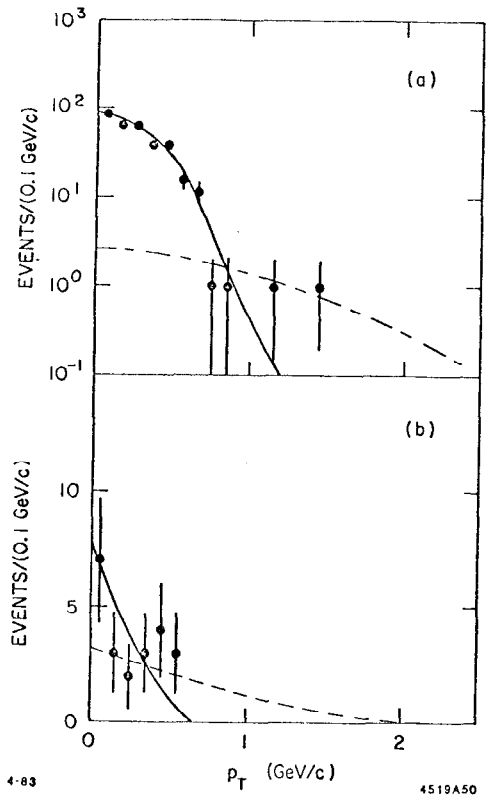


Fig. 45. (a) p_t distribution for τ-pair events. The solid curve is the expectation for normal τ-pair production. The dashed curve is the expectation for a Higgs with mass 7 GeV/c^2 and $B(H \to \tau\nu_\tau) = 0.5$.

(b) p_t distribution for events with one prong opposite a multiprong jet. The solid curve is the prediction of the hadron Monte Carlo program normalized to the data. The dashed curve is the expectation for a Higgs with mass 7 GeV/c^2 and $B(H \to hadrons) = 1 - - B(H \to \tau\nu_\tau) = 0.5$.

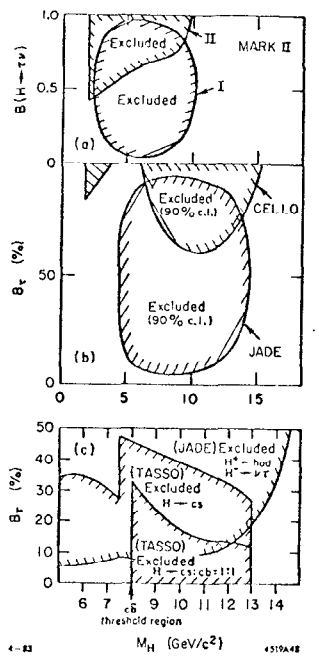


Fig. 46. Limit on $B(H^\pm \to \tau^\pm\nu)$ are shown as a function of $M_{H^\pm}$. The data come from[40] MARK II (a), JADE and CELLO (b) and TASSO (c). The models assumed in these analyses have $B(H^\pm \to \tau^\pm\nu) + B(H^\pm \to hadrons) = 1$.

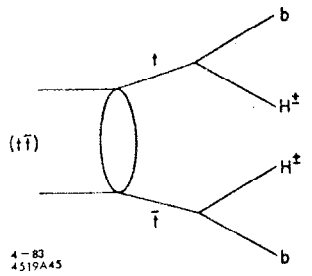


Fig. 47. The decay of toponium is the presence of a charged scalar particle.

Unfortunately the Z^0 will not be a good place to look for charged Higgs particles. The coupling of the Z^0 to charged scalars is small as shown in Fig. 48. While the hadronic cross section increases by about 10^3 at the Z^0 (relative to the e^+e^- continuum), pair production of charged Higgs particles increases by <10.

If the charged Higgs particle is more massive than $\frac{M_H}{2}$, we will have to search for it in the continuum. This will be very difficult unless there is another (new) heavy lepton which dominates the decays of the $H^{\pm}$. In the absence of the clean signature this new heavy lepton would afford, the events coming from pair production of $H^{\pm}$ will be very difficult to disentangle from the continuum jet events.

5.2 Models With Extended Electroweak Gauge Groups:

$SU(2) \wedge U(1) \wedge \mathcal{G}$.

At low Q^2, the effective Hamiltonian of the standard model for charged current interactions is given by

$$H_{cc} = \frac{4\mathcal{G}_F}{\sqrt{2}} j_\mu^+ j_\mu^-$$

and for neutral current interactions by

$$H_{NC} = -\frac{e^2}{q^2} j_{em}^2 + \frac{4\mathcal{G}_F}{\sqrt{2}} \left\{ (j^3 - sin^2\theta_W j_{em})^2 \right\}$$

where (j^+, j^-, j^3) form the weak isospin current. The success of the standard model at low energies is testament to the validity of this current-current description. Neither neutrino scattering experiments nor the *e-d* parity violation experiment probe the electromagnetic part of the weak current. Hence we can add to H_{NC}

$$H'_{NC} = -\frac{e^2}{q^2} j_{em}^2 + \frac{4\mathcal{G}_F}{\sqrt{2}} \{ (j^3 - sin^2\theta_W j_{em})^2 + C j_c^2 m \}$$

without conflicting any of the low energy experimental data. The only low energy bound for C is $C < 4$ which comes from measurements of the anomalous magnetic moment of the muon.

The lepton pair charge asymmetry measurements at PETRA and PEP probe the term $C j_{em}^2$ via the interference of the weak and electromagnetic propagators. We will return to the measurements at the end of this section. The freedom implied by the

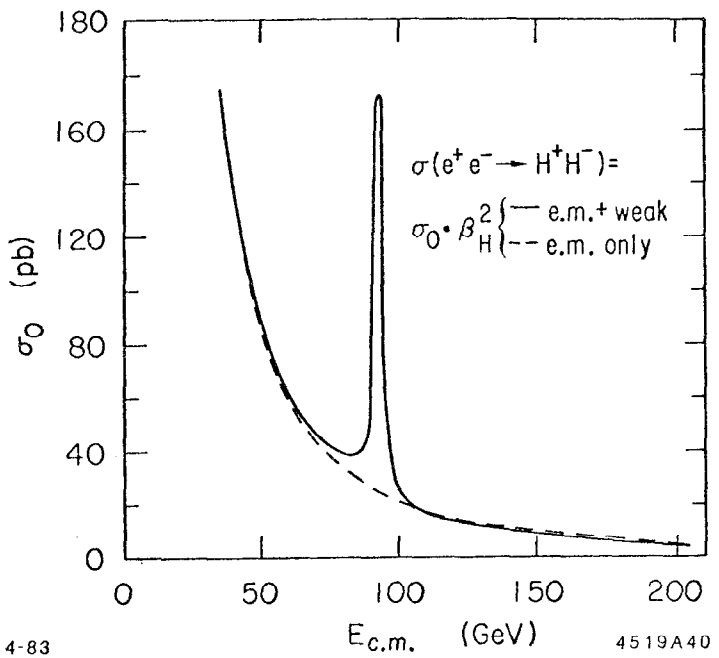


Fig. 48. The cross section for the process $e^+e^- \to H^+H^-$ as a function of $E_{c.m.}$.

addition of the term Cj^2_{em} permits models which extend the electroweak gauge group to $SU(2) \wedge U(1) \wedge \mathcal{G}$. Examples of such models are $SU(2) \wedge U(1) \wedge U(1)'$ (Ref. 41), $SU(2) \wedge U(1) \wedge SU(2)'$ (Ref. 42) and $SU(2)_L \wedge SU(2)_R \wedge U(1)$ (Ref. 43). The common feature of these models is the presence of two Z^0's with $M_{Z_1} < M_{Z^0} < M_{Z_2}$ where M_{Z^0} is the mass of the Z^0 in the standard model. The reason why one gets two energy levels is that Cj^2_{em} can be thought of as a perturbation and this perturbation splits the single energy level (M_{z^0}). We discuss briefly the models for which $\mathcal{G} = U(1)$ and $SU(2)$.

In the models in which $\mathcal{G} = U(2)$,[41] all fermions transform under $SU(2) \wedge U(1)$ in the usual manner and they are invariant under $U(1)'$. The spontaneous symmetry breaking is achieved using a pair of complex Higgs fields (see Sec. 5.1). The Higgs field ϕ_1 follows the standard model prescription. However, ϕ_2, which is invariant under $SU(2)$, has non-trivial transformations under $U(1) \wedge U(1)'$. Hence we recover the same $W^\pm$ structure as in the standard model. However ϕ_2 gives rise to an additional heavy neutral boson which can be associated with $U(1)'$. We thus obtain for $U(1)$

(e^-, ν_e) $\begin{pmatrix} V_0 & 0 \\ 0 & V_0 \end{pmatrix}$ $\begin{pmatrix} e^- \\ V_e \end{pmatrix}$

for $SU(2)$

(e^-, ν_e) $\begin{pmatrix} W^0 & W^{-1} \\ W^+ & W^0 \end{pmatrix}$ $\begin{pmatrix} e^- \\ \nu_e \end{pmatrix}$

and for $U(1)'$

(e^-, ν_e) $\begin{pmatrix} V_0' & 0 \\ 0 & V_0' \end{pmatrix}$ $\begin{pmatrix} e^- \\ \nu_e \end{pmatrix}$

<u>StandardModel</u>

$(\gamma, Z^0) = \begin{pmatrix} cos\theta & -sin\theta_W \\ sin\theta_W & cos\theta_W \end{pmatrix} \begin{pmatrix} V^0 \\ W^0 \end{pmatrix}$

one parameter $sin^2\theta_W$

<u>$SU(2) \wedge U(1) \wedge U(1)'$</u>

$(\gamma, Z_1, Z_2) = (3 \times 3) \begin{pmatrix} V_0 \\ V_o' \\ W_0 \end{pmatrix}$

three parameters .

The three parameters of $SU(2) \wedge U(1) \wedge U(1)'$ can be taken as $sin^2\theta_W$, M_1 and M_2. The parameter C is given by

$$C(\mathcal{G} = U(1)) = cos^4\theta_W \left(\frac{M_{Z^0}^2}{M_1^2} - 1\right)\left(\frac{M_{Z^0}^2}{M_1^2} - 1\right)$$

so as either $M_{1,2} \rightarrow M_{Z^0}$ we recover the standard model with $C = 0$.

In the model with $\mathcal{G} = SU(2)$[42] one goes through a similar procedure but in this instance ϕ_2 has non-trivial transformations under $SU(2) \wedge SU(2)'$. Again one obtains two neutral heavy bosons. In this model

$$C(\mathcal{G} = SU(2)) = sin^2\theta_W \left(\frac{M_{Z^0}^2}{M_1^2} - 1\right)\left(\frac{M_{Z^0}^2}{M_2^2} - 1\right)$$

and again $C = 0$ as $M_{1,2} \rightarrow M_{Z^0}$.

From PETRA we obtain limits on C via the measurements of the lepton charge asymmetries. The asymmetry data is fit using an interaction which contains the term Cj_{em}^2. The limits obtained from the PETRA groups[18] are shown in Table 6.

Table 6. Limits on C.

Group	95% C.L. for C
CELLO	< 0.031
JADE	< 0.039
MARK J	< 0.027
PLUTO	< 0.060
TASSO	< 0.030

Figure 49 shows the bounds on M_1 and M_2 obtained from the MARK J measurements. For $\mathcal{G} = U(1)$, the 95% confidence level limit requires that one of the two neutral bosons have a mass very close to M_{Z^0}. The model in which $\mathcal{G} = SU(2)$ is not as tightly constrained because $C \propto sin^4\theta_W$ as opposed to $C \propto cos^4\theta_W$ in the model with $\mathcal{G} = U(1)$.

What are the prospects of sorting out the correct electroweak gauge group as we go up in $E_{c.m.}$? We can imagine two scenarios. In the first scenario there is no Z^0 near 93 GeV/c^2. In this case we will have to move down to lower energies searching for Z_1. One would presumably benefit in such a search from the fact that there will be a substantial radiative tail for the Z_1 which will show up in a measurement of R. In the second scenario M_1 would be very close to M_{Z^0} with M_2 substantially larger

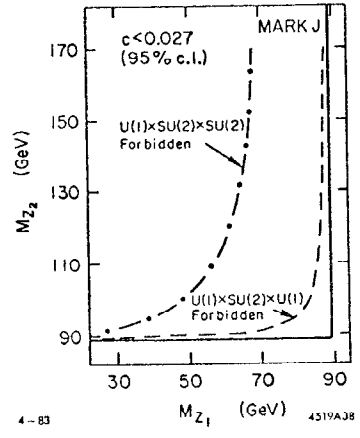


Fig. 49. Forbidden regions of the M_{Z_1}, M_{Z_2} plot are shown for the two possibilities $\mathcal{G} = U(1)$ and $\mathcal{G} = SU(2)$. The region to the left of the curves is forbidden.

than M_{Z^0}. What can be done in such a situation? This is thoroughly discussed in the SLC workshop[5b] and we borrow here liberally from this discussion (pages 44-52). The trick to sorting out the latter scenario is the longitudinal asymmetry measurement discussed in Sec. 4.2. If one looks back at the form of the modified neutral current Hamiltonian, one sees that, in essence, the addition of the term Cj^2_{em} has the effect of modifying $sin^2\theta_W$. The longitudinal asymmetry (A_L) is exceedingly sensitive to $sin^2\theta_W$ as we see in Fig. 50. Shown in Fig. 50 is A_L as a function of $E_{c.m.}$ for the standard model and for $SU(2) \wedge U(1) \wedge U(1)'$ in which $sin^2\theta_W$ is taken to be 0.22 (in agreement with the world average[9] $sin^2\theta_W = 0.230 \pm 0.015$). Running at the Z^0 pole one would easily see the deviation from the standard model. However one will have to run at a substantially higher $E_{c.m.}$ in order to get sensitivity to M_2. Although not discussed here in detail, we show the sensitivity of A_L to tests for the model $SU(2)_L \wedge SU(2)_R \wedge U(1)$.[43] Figure 51 shows A_L as a function of $E_{c.m.}$ for the standard model and the left-right symmetric model. In this case running at the nominal Z^0 mass can distinguish the extended model from the standard model and yield the mass of the second heavy boson. This is shown more explicitly in Fig. 51b. We again see how important longitudinally polarized electrons will be at the Z^0. We can conclude by saying that with the benefit of such polarized beams, considerable sensitivity to the electroweak gauge group can be obtained by running at the nominal Z^0 mass.

5.3 Models Without a Top Quark

The top quark has not been seen. This has led many people to speculate that maybe the top quark doesn't exist. Models have been constructed in which the left-handed b quark is a singlet; the four lower mass quarks retain their standard left-handed doublet assignment. These models are listed and discussed by Kane[44] and Kane and Peskin[44]. All the models discussed by Kane and Peskin have the common feature of substantial flavor changing neutral currents, which in particular lead to modifications of B decay. Kane and Peskin show that for all models there is a large rate for B's to decay to dileptons and quantitatively

$$r = \frac{\Gamma(B \to X\ell^+\ell^-)}{\Gamma(B \to X\nu\ell)} > 0.12 \ .$$

The CLEO experiment[31b] has looked for these dilepton events. They find ten such events (on 4S) where they expect twelve from conventional sources. This allows them

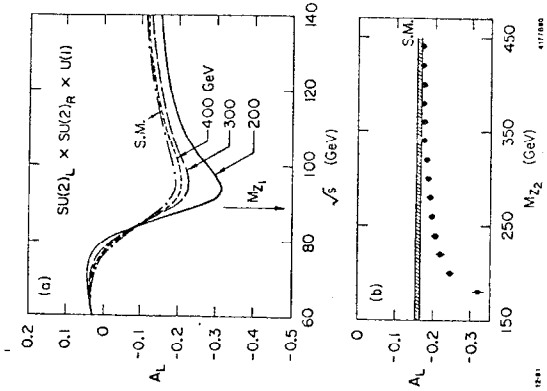


Fig. 51. (a) The longitudinal lepton charge asymmetry is shown as a function of $E_{c.m.}$ for the standard model and $SU(2)_L \wedge SU(2)_R \wedge U(1)$. Curves of different M_{Z_2} are shown for the latter model. The sensitivity to M_{Z_2} is shown on (b) when the data are accumulated at an energy of M_{Z^0}.

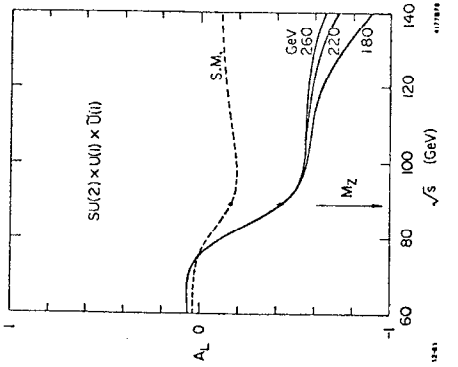


Fig. 50. The longitudinal lepton charge asymmetry is shown as a function of $E_{c.m.}$ for the standard model and $SU(2) \wedge U(1) \wedge U(1)'$. In the latter case curves for different M_{Z_2} are shown. M_{Z_1} is assumed to be at M_{Z^0} and $sin^2\theta_W = 0.22$.

to set a limit

$$R < 0.08 \quad (90\%\ C.L.)$$

This measurement rules out all these models. More recently Peskin and Tye[45] have invented a model which suppresses the flavor changing neutral currents. The model has a most unnatural assignment of quarks:

$$\begin{pmatrix} u \\ d' \end{pmatrix}_L , \begin{pmatrix} c \\ s' \end{pmatrix}_L , \begin{pmatrix} c \\ b \end{pmatrix}_R \quad u_R, d_R, s_R, b_L \ .$$

However it cannot be ruled out by the present data. Possible future avenues are (a) at the Z^0 the charm axial-vector coupling constant will be zero and (b) the B will have a substantially shorter lifetime (factor of 10) than in the standard model. To test (a) is very hard – one would have to tag charm jets and measure the charm quark asymmetry.

5.4 More Generations – The Generation Puzzle

The discovery of the τ and the b quark has led to a very beautiful symmetry between the quark and lepton sectors. Nature at present appears to have three generations of both quarks and leptons. While this symmetry is indeed attractive, we are led to an obvious question – why three generations? Why not five or ten? We readily understand the need for one generation – our very being is dependent on it. But more than one generation seems superfluous and it is interesting to speculate on why nature chose to replicate itself in this strange way.

The distinguishing generation element is mass-successive generations have higher masses. A perfectly defensible reason why we see three generations then is that the energy of our machines is not sufficient to yield the next generation(s). The prospect of higher energy machines implies more quarks and leptons. We may go to our theoretical friends and ask them where we need to look; where will the next generation appear? The answer is that none of the current theories understands the generation puzzle and no mass predictions exist. Bjorken, in 1978, contemplated the fermion mass spectrum and mused that the mass of the next charged lepton would be at $\simeq 10$ GeV/c^2 and the mass of the top quark would be $\simeq 27$ GeV/c^2. The former is violated by the PETRA and PEP limits, so we see that our guide will have to be experiment.

How do we search for new flavors? There are three obvious possibilities

1. Search for a new charged lepton, $L^{\pm}$,
2. Search for a new $Q = -\frac{1}{3}$ quark, and
3. Search for more ν's.

We do not include searches for $Q = \frac{2}{3}$ quarks because if such a quark were found, it would satisfy our need for the top quark. Consider the search for $L^{\pm}$. The $W^{\pm}$ which mediate the decays of $L^{\pm}$, is democratic with respect to fermion coupling strengths. Allowing for three quark colors we have

$$B(L^{\pm} \to \ell^{\pm}\nu\nu) = \frac{1}{12} = 8\%$$

and

$$B(L^{\pm} \to hadrons) = 74\% \quad .$$

(These numbers will be modified slightly by QCD corrections but for the argument being made here these small modifications are unimportant.) We will therefore be able to use the standard low multiplicity searches for $L^{\pm}$ which will be pair produced in e^+e^- interaction with $R = \frac{\beta_L(3-\beta_L^2)}{2}$. Backgrounds are small because the $< n >_{charge}$ is large for the hadronic events. As an example, at TRISTAN assuming $E_{c.m.} = 60$ GeV, $< L >= 10^{31}\ cm^{-2}\ sec^{-1}$ one will have 20 L^+L^- events produced/day ($\beta_L = 1$) of which five events/day would have the topology of a single lepton in one hemisphere and ≥ 3 charged hadrons in the other hemisphere. Such a signal would be hard to miss. As $E_{c.m.}$ is raised, the searches will be rate limited and a high luminosity will be required. The rate goes like $E_{c.m.}^{-2}$. However at the Z^0 there will be plenty of rate with $B(Z^0 \to L^+L^-) = 3\%$. For these searches one has sensitivity up to $\frac{E_{c.m.}}{2}$.

Searches of this kind have been done at PETRA and PEP. The limits for sequential charged heavy leptons appear in Table 7.

Table 7. Limits on Sequential Heavy Leptons

Experiment	95% C.L. Lower Limit
JADE	18.1
MARK J	16.0
PLUTO	14.5
TASSO	15.5
MAC	14.0
MARK II	13.8

By the end of 1983, PETRA will have sensitivity to $M_{L^{\pm}} \simeq 23$ GeV/c^2.

How do we search for a $Q = -\frac{1}{3}$ quark? The change in R is $\frac{1}{3}$ which is too small to see given the present accuracy of R measurements. The new quark will be heavy and so event shapes will be a useful indicator. The presence of a new quark will be signalled by the onset of spherical, low thrust events. The signal is distinctive, but the rate is still low. The searches performed at PETRA indicate how such searches are made. Figure 52 shows the thrust for hadronic events containing a muon in the MARK J detector. The muon tag is used to enhance the heavy quark decay fraction. Shown on the plot is the expected yield for the five known quarks and for the five known quarks plus a charge $-\frac{1}{3}$ quark. The mass limit for charge $-\frac{1}{3}$ quarks obtained by the PETRA groups[13] is $M_{-\frac{1}{3}} > 15$ GeV/c^2. These kinds of shape analysis searches can be continued as $E_{c.m.}$ is raised. However, it takes a considerable amount of data (the PETRA limits come from data sets of $\sim 50 pb^{-1}$) to achieve good sensitivity and hence the searches require high luminosity machines.

At the Z^0, there is plenty of rate. A shape analysis akin to that discussed in Sec. 4.1 would very quickly signal a new heavy flavor. The question would then be is it a charge $-\frac{1}{3}$ or $\frac{2}{3}$ quark? Two possibilities come to mind for deciding. Because the weak coupling contants differ (see Sec. 3) for the two quark species, the production rate at the Z^0 differs. The difference is about 20% and if there was nothing else new contributing to the Z^0 total decay rate, it would probably be possible to make an assignment of the quark charge based on the event rate of the new flavor. The other alternative would be to measure the charge or longitudinal asymmetry which is

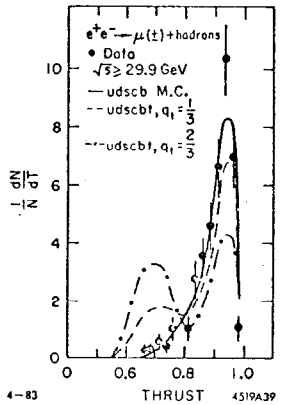


Fig. 52. The data of MARK J show the hadron thrust for hadronic events which contain a muon. Three alternative Monte Carlo options are shown. This measurement permits the MARK J to set limits on the presence of a charge $-\frac{1}{3}$ quark.

sensitive to the weak coupling constants. Running at the Z^0 provides sensitivity of $M_{-\frac{1}{3}} \leq \frac{M_{Z^0}}{2}$.

The third option for searching for new flavors involves counting the number of ν species. This can be done by measuring the width of the Z^0:

$$\Gamma_{Z^0} = \frac{\mathcal{G}_F M_{Z^0}^3}{\sqrt{2}\ 24\pi}\left\{2N_\nu + [1+(1-4\ sin^2\theta_W)^2]\,N_\ell \right.$$

$$+3\left[1+(1-\frac{8}{3}sin^2\theta_W)^2\right]N_{\frac{2}{3}}$$

$$\left.+3\left[1+(1-\frac{4}{3}sin^2\theta_W)^2\right]N_{-\frac{1}{3}}\right\}$$

where N_ℓ = number of charged leptons, N_α = number of quarks with charge α and N_ν = number of neutrino flavors. Each additional neutrino flavor contributes

$$\frac{\mathcal{G}_F M_{Z^0}^3}{\sqrt{2}\ 12\pi} \simeq 160\,\text{MeV} \quad \text{to}\,\Gamma_{Z^0}\ .$$

In the standard model, $\Gamma_{Z^0} = 2.5$ GeV. In order to observe a 3σ effect implies measuring Γ_{Z^0} to $\simeq 2\%$. This will be a very difficult task because the measured width will have to be corrected for complicated radiative effects, beam dynamics (machine energy spread, stability, etc.). G. Barbiellini et al.,[47] discuss running above the Z^0 searching for events of the type

$$e^+e^- \rightarrow \gamma Z^0 \qquad (9)$$
$$\qquad\quad \hookrightarrow \nu\bar{\nu}$$

The signature for these events would be a single hard photon. The main background comes from $e^+e^- \rightarrow e^+e^-\gamma$. However, if one can cover the solid angle with electromagnetic calorimetry down to $\sim 6^o$ of the beamline, then the γ from $e^+e^-\gamma$ must be accompanied in the detector by at least one of the $e^\pm$. The cross section for (9) is given in the standard model by

$$\frac{d^2\sigma}{dxdy} = \frac{\mathcal{G}_F^2\ \alpha\ E_{c.m.}^2(1-x)\left[(1-\frac{x}{1})^2+\frac{x^2y^2}{4}\right]}{6\pi^2\ \ x(1-y^2)}$$

$$\times\left\{\frac{N_\nu(g_V^2+g_A^2)+2(g_V+g_A)\left[1-E_{c.m.}^2(1-x)M_{Z^0}^2\right]+2}{\left[1-E_{c.m.}^2\frac{(1-x)}{M_{Z^0}^2}\right]+\Gamma_{Z^0}^2M_{Z^0}^2}\right\}$$

where $x = \frac{E_\gamma}{E_{c.m.}}$ and $y = cos\theta_\gamma$. One chooses $E_{c.m.}$ so as to optimize the signal to noise. Figure 54 is taken from Barbiellini et al., showing the photon yield resulting from a choice of $E_{c.m.} = 105$ GeV. Each additional ν flavor contributes a change of $0.01nb^{-1}$. A 60 day run at $< L >= 2\times 10^{30}\ cm^{-2}\ sec^{-1}$ will produce 300 events with E_γ within 2.5 GeV of the peak. If SLC or LEP can achieve their design luminosity, then this ν counting experiment will be a realistic possibility. It should be pointed out that in fact the experiment described above actually counts the number of neutral, weakly coupled objects some of which might not be neutrinos. An example of other possible sources are supersymmetry particles (see next section). The detector required for this experiment is one which has continuous electromagnetic coverage down to angles of 6^o. This coverage can be crude in the forward directions (small angles) since the signal photon gives adequate rate if $160^o < \theta < 20^o$. An energy resolution of $\sigma_E/E \leq 15\% / \sqrt{E}$ is required. Charged tracking is needed in the region $160^o < \theta < 20^o$ to ensure that the energy deposited in the calorimeter was that of a neutral particle. These requirements are not very stringent and it will not be difficult for the general purpose detectors at LEP and SLC to ensure that they will be able to make this important measurement.

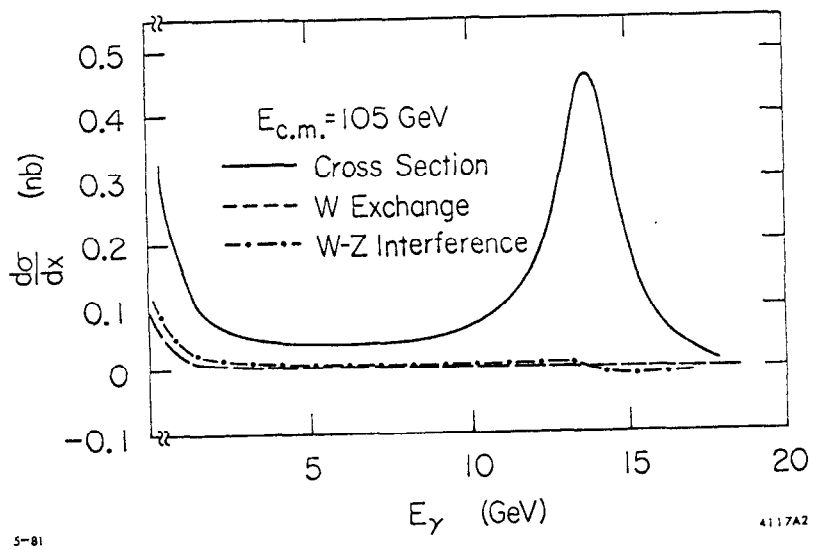


Fig. 53. The differential cross section $d\sigma/dx$ ($x = 2E_\gamma/E_{c.m.}$) is shown as a function of E_γ for the process $e^+e^- \to \gamma\nu\bar{\nu}$. The calculation assumes $E_{c.m.} = 105$ GeV.

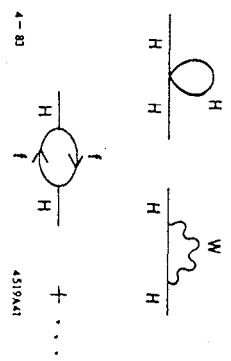


Fig. 54. Examples of loop diagrams which contribute quadratic divergence to the Higgs mass.

6. Models Which Avoid the Gauge Hierarchy Problem

There are many different ways to state the so called "gauge hierarchy problem." The Higgs mechanism sets a mass scale – the electroweak scale – in a most unnatural way because the process requires remarkably fine tuning. Stated another way, the radiative corrections to the Higgs mass, shown in Fig. 54, are quadratically divergent.

This issue is covered very elegantly in the lectures of L. Susskind in these proceedings and we will not take time here to discuss it further. We will consider three ways to avoid the unnaturalness of the Higgs mechanism:

1. Cancel each quadratically divergent diagram uniquely – supersymmetry,
2. Put in a cut-off parameter at a scale of $\sim 10^3$ GeV – technicolor, and
3. Make $SU(2)$ strong at the scale of $\sim 10^3$ GeV – composites of confined fermions.

6.1 SUPERSYMMETRY (SUSY)

In supersymmetry new particles are introduced with couplings such that the quadratic divergences are cancelled graph by graph to all orders. Such a magic cancellation implies a symmetry of nature is at work – in fact a "supersymmetry." The new symmetry is most unfamiliar to us. We are accustomed to symmetries which relate particles of the same spin; multiplets of flavor $SU(3)$, color $SU(3)$, isospin $SU(2)$, electroweak $SU(2) \wedge U(1)$ all contain particles with the same spin. Supersymmetry introduces a high level of uniformity by grouping together in multiplets particles whose spin differ by $\frac{1}{2}$ a unit. Symmetry operations transform fermions into bosons and vice versa. Hence the photon has a SUSY partner with spin $\frac{1}{2}$ called the photino, leptons and quarks have spin zero partners called sleptons and squarks etc., etc. The multiplets of SUSY are shown in Table 8.

Table 8. Supersymmetry Particle Multiplets

	Spin 1	Spin $\frac{1}{2}$	Spin 0
Massless Multiplet	Photon Gluons	Photino Gluino	
Massive Gauge Multiplet	$W^{\pm}$ Z^0, U	Wino, Zino, Goldstino	Shigges
Matter Multiplet		Leptons Quarks	Sleptons Squarks

Unless supersymmetry is broken, we will have a mass degeneracy between the familiar particles and their SUSY partners. This is clearly not the case and hence SUSY must be broken. The mildest way to do this is spontaneously and the simplest scheme was that proposed by Fayet.[48] In Fayet's scheme there is only a single generator, Q_α, which will permit transformations which change the spin by a $\frac{1}{2}$ unit:

$$Q_\alpha|Fermion>=|Boson> \qquad (\alpha = 1,2 \text{ spin index})$$

$$Q_\alpha|Boson>=|Fermion> \quad .$$

Such schemes having only one generator are called simple and we will restrict our discussion to such models. (Models having more than one generator are called extended models.) In Fayet's model the gauge group is expanded to $SU(2) \wedge U(1) \wedge U(1)'$ which results in a new massive gauge boson which is called U. The spontaneous breakdown of the symmetry is achieved using a pair of complex Higgs doublets. The result is the appearance of charged and neutral scalars (called shigges) as described in Sec. 5.1. There are many schemes for breaking SUSY and each leads to different mass splittings, and hence masses, for the SUSY particles. In Fayet's scheme one obtains bounds for the particle masses and in particular

$$M_{H^{\pm}} \leq 80 GeV/c^2$$

$$M_{H^0} \geq 30 GeV/c^2 \qquad \text{and}$$

$$M_{squarks}, M_{sleptons} \leq \frac{M_{W^{\pm}}}{2} \simeq 40 GeV/c^2 \, .$$

In this simple model, all the SUSY partners of the fermions have masses below $\frac{M_{Z^0}}{2}$. Other than spin, all members of the same multiplet have the same quantum numbers and hence their couplings to the Z^0 and photon will be the same. The production rates for sfermions are half that of the fermions. (The usual $\frac{1}{4}$ characteristic of scalars is multiplied by two because there are two scalar partners for each fermion.) These comments are modified near threshold by the usual β^3 turn-on for scalar particles.

How do sfermions decay? They decay (see Fig. 55) to their fermion partners plus a photino or goldstino (sleptons) or a photino, gluino or wino (squarks). The photino and goldstino can be thought of as neutrino-like for the purposes of interactions in any detecting device, although in general this statement is not true. This description of SUSY was not intended to be complete or rigorous. The interested reader will find the references in Ref. 49 very complete. However, the preceding discussion suffices to establish how one would search for SUSY particles.

Searches for squarks and sleptons can be pursued in the e^+e^- continuum. These scalars will be pair produced with a characteristic $sin^2\theta$ angular distribution and a production rate

$$\sigma(S_q, S_{\bar{q}}) = 3\sigma(S_\ell, S_{\bar{\ell}}) \equiv 3 \cdot \frac{2}{4} \cdot \beta^3 \sigma_{point}$$

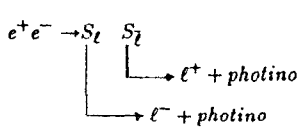
and if $\beta = 1$

$$R(S_q, S_{\bar{q}}) = \frac{1}{2} R(q, \bar{q})$$

$$R(S_\ell, S_{\bar{\ell}}) = \frac{1}{2} R(\ell, \bar{\ell})$$

where S_q and S_ℓ refer to the scalar partners of quarks and leptons. For each new squark species, $\delta R = \frac{2}{3}$ or $\frac{1}{6}$ depending on its charge. R is know at PETRA to $\pm 5\%$ (systematic error) or $\simeq 0.2$. Hence it is probable that most or all of the charge $\frac{2}{3}$ squarks have masses above 18.5 GeV/c^2.

Direct searches have been performed for the scalar leptons via the process



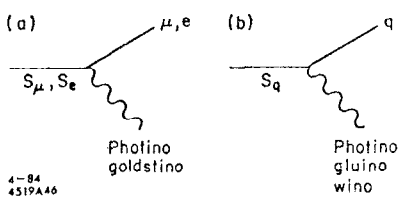


Fig. 55. The decay of sleptons (a) and squarks (b).

where $\ell = e$ or μ or τ. These searches proceed in an obvious way — one searches for ee, $\mu\mu$ and $\tau\tau$ events in excess of the QED rate. If $\beta \simeq 1$ there would be an increase above QED of $\approx 50\%$ in the yields of these events. One also expects lots of missing energy and momentum. The 95% confidence level limits obtained at PETRA are given in Table 9 which is compiled from the references in Ref. 50. In all these tests the neutral missing particle (photino or goldstino) is assumed to be stable.

Table 9. Mass Limits (95% confidence level) for S_e, S_μ, S_τ (see Ref. 50).

Experiment	Excluded Mass Range (GeV/c^2)		
	Electron	Muon	Tau
CELLO	2 - 16.8	3.3 - 16	6 - 15.3
JADE	< 16	$--$	4 - 13
MARK J	$--$	3 - 15	M_τ - 14
PLUTO	< 13	$--$	$--$

We can summarize Table 9 by saying that M_{S_e}, $M_{S_\mu} > 16$ GeV/c^2 and $M_{S_\tau} > 14$ GeV/c^2.

The searches described for sleptons involve the assumption that $M_{S_\ell} \leq \frac{E_{c.m.}}{2}$. M. K. Gaillard et al.,[51] have proposed a mechanism whereby one can obtain sensitivity beyond $\frac{E_{c.m.}}{2}$. The process involved in shown in Fig. 56, where the symbol $\tilde{\gamma}$ is used for the photino. Under the assumption that the photino is stable and has a small mass, the e^+ takes up very little transverse momentum and hence continues down the beampipe. The signature is an event with a single electron with substantial energy and large missing transverse momentum. The cross section for the process is calculated in Ref. 51. One finds that for $E_{c.m.} \simeq 40$ GeV

$$\sigma(S_e\tilde{\gamma}) = 5\%\ \sigma_{point} \qquad \text{for } M_{S_e} = 15\ GeV/c^2$$

$$= .15\%\ \sigma_{point} \qquad \text{for } M_{S_e} = 30\ GeV/c^2$$

For $< \mathcal{L} >= 10^{31}$ this would correspond to an event rate of $\sim$ 100/month and

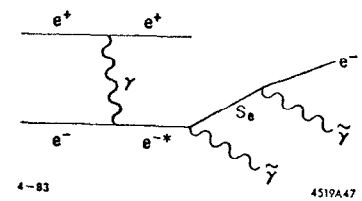


Fig. 56. The process $e^+e^- \to e^+e^-\tilde{\gamma}\tilde{\gamma}$. The e^+ will go perferentially in the forward direction leaving only the e^- in the detector.

3/month, respectively. Backgrounds will come from QED processes ($ee\gamma$) where the photon escapes through uninstrumented cracks in the detectors. Suppression of these backgrounds are aided by the fact that the signal has a roughly isotropic angular distribution for the $e^{\pm}$ and the $e^{\pm}$ is energetic. Since the observation of Ref. 51, most of the PEP and PETRA detectors have augmented their hardware so that they will trigger on a single high energy (few GeV) electron. We should expect results from these searches within six to twelve months, with expected mass sensitivity in the range of 20-30 GeV/c^2.

All the tests for charged and neutral Higgs particles given in Secs. 4.3 and 5.1 apply also for the Shiggs particles.

The Z^0 will offer a superb testing ground for SUSY. In Fayet's simple model all the sfermions will have masses below $\frac{M_{Z^0}}{2}$ and the Z^0 will be 50% wider than in the standard model. Fayet's model aside, for each new squark, the rate of Z^0 decays will go up by about 5% and for each new charged slepton it will go up by 1.5% ($\beta = 1$ is assumed). The squarks would be heavy and hence detectable using a shape analysis and the sleptons will yield to tests analogous to those described earlier in this section for continuum production. Given the high production rate for Z^0's, these events will easily be seen. The neutrals (photino, goldstino) will be observed in the process

$$e^+e^- \rightarrow \gamma Z^0 \\ \qquad\quad \hookrightarrow \tilde{\gamma}\tilde{\gamma}$$

as described in the neutrino counting experiment of Sec. 5.4.

High energy e^+e^- interactions offer a much wider range of tests than those discussed here. We have ignored the issue of the stability of the neutrals, the detection of the gluino, etc., etc. These can be found in the references or weekly on the preprint shelves. It should be remembered that the simple model of Fayet might be wrong and that the extended models do not necessarily have low lying charged fermions. Supersymmetry is a very attractive theory offering the potential for unifying gravity, QCD and electroweak interactions. Testing SUSY, however, might be very frustrating if the mass scale keeps growing.

6.2 Technicolor Theories – Dynamical Symmetry Breaking

In order to have a theory which is renormalizable, gauge bosons must acquire mass as a result of spontaneous symmetry breaking. In the standard model, this breaking is achieved using the Higgs mechanism. However, it is possible for the gauge interactions themselves to cause spontaneous symmetry breakdown. The class of theories in which this dynamical mechanism is employed is called Technicolor Theories.[52]

In these theories a new set of unbroken, non-Abelian gauge interactions are introduced which become strong at a scale $\Lambda_{TC} \sim 1$ TeV. Technicolor is therefore analogous to QCD with a spectrum of technicolor singlets with masses of ~ 1 TeV. The analogs of the QCD fermions are so called technifermions and the role of the Higgs particles of the standard model are assumed by spin zero bound states of these technifermions. In the minimal technicolor schemes all the light pseudoscalars are eaten by the gauge bosons of the weak interaction. Since we do not have Higgs particles there is no Yukawa mechanism for generating ordinary fermion masses. In technicolor this must be achieved by an additional gauge interaction which couples ordinary fermions to technifermions.

The mass generation scheme in the standard model via Yukawa couplings (a) and the four fermion type interaction in technicolor theories (b) are shown in Fig. 57. Models which include the additional gauge interaction for mass generation are called extended technicolor (ETC) models. No completely satisfactory model of ETC has emerged as discussed in Susskind's lectures in these proceedings. In the ETC schemes there are more light pseudoscalars than in the minimal model, and after the weak interaction bosons have been given mass, a spectrum of physical scalars (technipions) remain. The number of these technipions depends on the ETC model. However, independent of the model there is an irreducible minimum of four technipions with masses in the 10 GeV/c^2 range. We will call these $P^{\pm}$, P^0 and $P^{0\prime}$. These scalars are analogous to the four light hadrons, $\pi^{\pm}$, π^0 and η^0, of normal color. In addition to the technipions there is a spectrum of technihadrons with masses in the 250-1000 GeV/c^2 range.

What do we know about the masses of the technipions? There are two contributions to the technipion masses. The first arises from the electroweak interaction and can be calculated in a completely model independent way. The second contribution comes from ETC and is very model dependent. In the absence of ETC $M_{P^{\pm}} \simeq$ (5-8) GeV/c^2 and $M_{P^0} \equiv 0$. The addition of ETC generates extra mass and typically $M_{P^{\pm}} \leq$

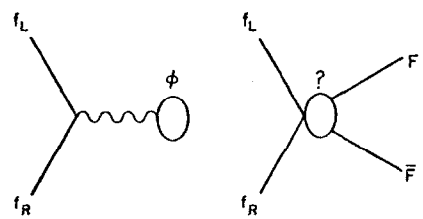


Fig. 57. The generation of fermion masses: (a) via the Higgs field ϕ in the standard model and (b) via the four Fermi type interaction in ETC.

10-15 GeV/c^2 and $M_{P^0} \leq 5$ GeV/c^2. However there are some ETC models in which $M_{P^\pm} \simeq 30$ GeV/c^2.

What about the technipion couplings? In most models the situation is similar to that of charged and neutral Higgs particles – hyperpions like to couple to the heaviest fermion pair available. Since they are scalars their production angular distribution and rate are the same as for H^0, $H^\pm$ as discussed in Sec. 4 (H^0) and 5.1 ($H^\pm$). In particular the searches for $H^\pm$ described in Sec. 5.1 (see Fig. 46) apply equally well for $P^\pm$. Hence it is very unlikely that $M_{P^\pm} \leq 15$ GeV/c^2 and this eliminates a large class of technicolor models. As PETRA raises its energy and assuming that no scalars are found, technicolor is becoming a less likely scenario. By the end of 1983, PETRA experiments will have sensitivity to $M_{P^\pm} \leq 22$ GeV/c^2.

Supposing that a charged scalar is found. Is it a technipion or a Higgs? Given the freedom in the models, it will be very difficult to distinguish these two possibilities.[53] However, if we assume that either the standard model or technicolor is correct but not both, then the neutral scalars could provide a means for separating these two options. We recall from Sec. 4 the discussion of the processes $Z^0 \to H^0 Z^{0*} \to H^0 \ell^+ \ell^-$ and $e^+e^- \to Z^{0*} \to Z^0 H^0$. These processes involved the coupling $Z^0 Z^0 H^0$ which is large in the standard model. However for technicolor the $Z^0 Z^0 P^0$ coupling is zero to first order and the analogous decays involving P^0 particles occur at an exceedingly low rate.[53] Typically one finds that the rates for the channels involving P^0's are about 10^{-4} times smaller than those involving H^0's. Hence if we observe these processes, then we confirm the standard model. If no such processes are seen but a charged scalar has been found, then the most likely scenario is that the standard model is wrong and technicolor could be correct.

The searches for technihadrons will require LEP III and the high energy colliding linac machines.

6.3 Composite Models; Strong $SU(2)$

Another solution to the gauge hierarchy problem is offered by the model of Abbott and Farhi[54] in which the weak interactions are the result of the composite nature of quarks and leptons. In this model the $SU(2)$ is strong and hence confining at the scale of the weak interactions, $\mathcal{G}_F^{-\frac{1}{2}} \simeq 300$ GeV. This procedure is analogous to

QCD in which the confining scale is at a few hundred MeV. In the same sense that QCD offers a sensible way to set a mass scale, the strong $SU(2)$ theory does too and the gauge hierarchy problem is avoided. The composite model retains the gauge structure of the standard model namely $SU(3) \wedge SU(2) \wedge U(1)$. It contains a complex doublet of Higgs fields, but the scalar potential is adjusted so that no spontaneous symmetry breaking occurs. The particle content is the same as in the standard model – left-handed doublets and right-handed singlets. Since the right-handed fermions are singlets of $SU(2)$ they are not confined and hence are the right-handed quarks and leptons. However, the left-handed fermions are confined at the scale $\mathcal{G}_F^{-\frac{1}{2}}$ and the familiar left-handed fermions must be constructed from these confined particles. The absence of spontaneous symmetry breaking implies that $U(1)$ and $SU(2)$ are not mixed and hence $U(1)$ becomes the $U(1)$ of electromagnetism.

In analogy with QCD, we expect a rich spectrum of particles, most of them with masses $\simeq$ 300 GeV. There are some bound states with light masses and these are the left-handed quarks and leptons. These particles are constructed out of bound states of the left-handed confined fermions and the scalars mentioned above. This generates particles with the correct quantum numbers but they are massless. Yukawa couplings are used to generate mass for the quarks and leptons and in this way the full quark and lepton spectrum of the standard model is recovered.

The weak interaction Lagrangian in this theory is

$$L = \frac{4\mathcal{G}_F}{\sqrt{2}}\left\{J_\mu^+ J_\mu^- + (J_\mu^3)^2\right\} + \frac{4\mathcal{G}_F}{\sqrt{2}}\ \xi\ (J_\mu^0)^2$$

where $\vec{J}_\mu = (J^+, J^-, J^3)$ is the weak isovector current and J_μ^0 is the weak isoscalar current. Since no evidence for the latter current exists, ξ is assumed, without any justification, to be <0.05. The standard model weak interaction Lagrangian is

$$L_{SM} = \frac{4\mathcal{G}_F}{\sqrt{2}}\left\{J_\mu^+ J_\mu^- + (J_\mu^3 - sin^2\theta_W J_\mu^{EM})^2\right\}\ .$$

How do we account for the difference and hence make the composite model Lagrangian consistent with the low energy data?. The solution lies in the observation that, because of the composite nature of the fermions, they possess electric (and magnetic) form factors. When one adds in the contribution from the interaction of this charge distribution and the electromagnetic interaction (γ's), one can obtain consistency with the low energy data. The parameter $sin^2\theta_W$ in this model has nothing to do with electroweak mixing. Rather it measures the strength of the mixing between a photon and one of the vector mesons of strong $SU(2)$. The data can be fit if this mixing parameter takes on a value of 0.23. This is a very large mixing when compared with the comparable QCD situation where the photon-rho mixing is 0.02. The strong $SU(2)$ theory does not explain the large mixing; the value is taken to ensure that the experimental data can be fit. Also it is odd that while the electric form factor is large the magnetic form factor must be kept small so as not to develop too large a muon magnetic moment.

Following the discussion above, this model can describe the low energy data. However, there is no narrow Z^0 in this model. If there is a narrow Z^0 in the 100 GeV/c^2 mass range then this model is wrong. If there is no Z^0, and this model becomes a candidate for the standard model, we would have to search for the particle spectrum associated with the strong scale at $\mathcal{G}_F^{-\frac{1}{2}}$ (cf hadrons of QCD). There will be particles with masses $\geq$ 250 GeV/c^2. In addition (ala π's in QCD) there will be some vector mesons with masses in the 100-200 GeV/c^2 range. They will not be easy to find because they will decay strongly and can be expected to have widths on the order of 20-30 GeV. The best signature would come from the fact that these strong $SU(2)$ decays will treat quarks and leptons democratically (aside from the 3:1 advantage from color) and hence one will see a lot of leptons in the decays. One would need to be running at LEP II and LEP III with a device which had good lepton/hadron rejection so that a clean measurement of R_e or R_μ could be made. This possibility is discussed[55] by DeRugula in a delightful article on "glints." The study of the high mass spectrum will require the colliding linac machines.

We have discussed a model in which the quarks and leptons are composite. What experimental evidence do we have for the size of fermions? Since photons couple to charge they make an excellent probe of the size of fermions. This can be done using measurements of the processes

$$e^+e^- \rightarrow f\bar{f}$$

where $f = e, u, \tau, q$. The data at PETRA have been fit assuming that the pointlike

QED cross section is modified by a form factor of the type

$$F^{\pm} = 1 \mp \frac{q^2}{q^2 - \Lambda_{\pm}^2} \ .$$

Table 10 shows the 95% confidence level lower limits for $\Lambda_{\pm}$. These results are taken from Ref. 18.

Table 10. 95% Confidence Level Lower Limits for $\Lambda_{\pm}$ (GeV)

	e		μ		τ		q	
	Λ^+	Λ^-	Λ^+	Λ^-	Λ^+	Λ^-	Λ^+	Λ^-
CELLO	83	85	–	–	139	120	–	–
JADE	112	106	142	126	111	93	–	–
MARK J	128	161	194	153	126	116	190	285
PLUTO	80	234	107	101	79	63	–	–
TASSO	140	296	127	136	104	189	–	124

We may conclude that fermions are pointlike down to $\sim 10^{-16}$ *cm*. As we go to higher energies we must continue these measurements to probe larger composite mass scales.

7. Summary and Conclusions

We have discussed how we can continue to test the standard model using e^+e^- interactions at energies beyond those presently available. We have seen that the machines which we will have available in the next ten years will permit us to make many important and decisive tests of the standard model. We have investigated how we can test theories which go beyond the standard model. Some of these theories involve minor modifications of the standard model, others were much more radical. We saw that these studies are done in the continuum, at toponium and at the Z^0. Rather than summarize the important searches in words, we have chosen to provide the reader with a reminder in the form of Table 11. The key for this table is $E \equiv E_{c.m.}$, a cross indicates that the search is not possible, a check indicates that it is, and no entry means that an entry is not applicable or not interesting.

How are we situated with respect to Table 11? Figure 58 summarizes the available energy of e^+e^- high energy machines as a function of calendar year. Toponium and the Z^0 are vital to our searches. Z^0 factories will soon exist in both the U.S.A. and Europe and by 1988 there should be five or six good detectors running at the Z^0. If $M_t < \frac{M_{Z^0}}{2}$, then toponium can be studied at one or some of PETRA or TRISTAN or SLC or LEP. The region from 100-250 GeV is covered by LEP on a time scale estimated to be the early 1990's.

But we saw lots of options for thresholds above $\mathcal{G}_F^{-\frac{1}{2}} \simeq 300$ GeV. Supersymmetry, technicolor, composite models are but a few of these options. This is clearly the new frontier and every effort must be made to accelerate the availability of the colliding linacs. If we look at Fig. 58 we find that, to very good approximation, the entries lie on a straight line. If we extrapolate this line to $E_{c.m.} = 500$ GeV (1000 GeV) we find ourselves in the year 2000 (2005). Hopefully we can prove that the present linear relationship is not a universal law of nature and that the frontier machines can be built and operated this century.

Table 11. Summary of Searches Discussed in These Lectures.

	Continuum	Z^0	Toponium
Top	$E > 38$ GeV	√	
Z^0	$E > 38$ GeV lower limit M_Z	√	
$W^\pm$	$E > 2M_W$	×	×
H^0	$E > M_{Z^0}$	√	√
Gluon	maybe, $E > 38$	maybe	√
Free quark	All E	√	√
$H^\pm$	$M_H < M_t$	×	√ $M_H < M_t$
Multiple Z's	M_Z, $E > M_{Z^0}$	√ (M_1)	
New Generations:			
$L^\pm$	√	√	√
$Q = -\frac{1}{3}$	maybe	√	
ν's	$100 < E < 110$ GeV	√	
SUSY:			
S_q	√	√	√
S_L	√	√	√
Technicolor:			
$P^\pm$	same as $H^\pm$		
P^0			√
Technihadron	$E > 200$ GeV		√
$SU(2)_{strong}$	$E > 100$ GeV $E > 250$ GeV	√	
Composites	All E	√	

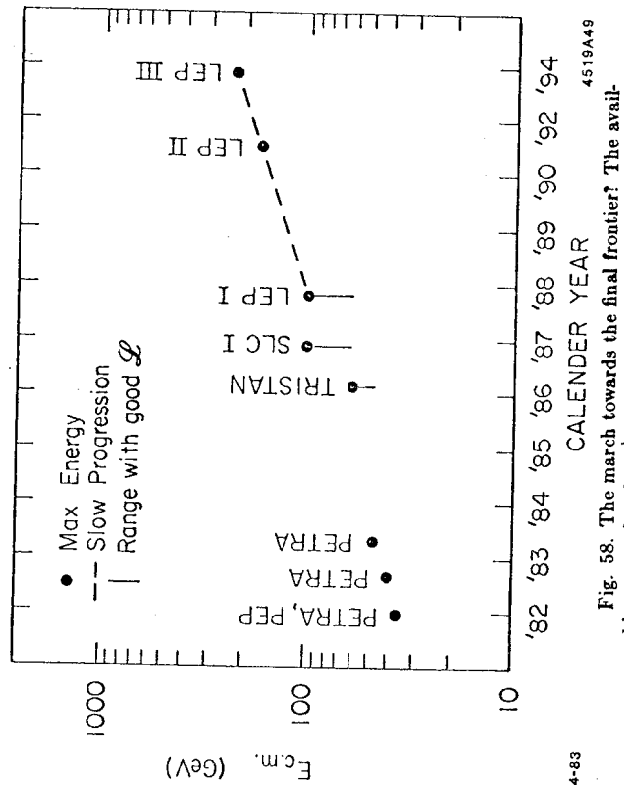


Fig. 58. The march towards the final frontier? The available energy for the e^+e^- machines as a function of calendar year. In the case of the new machines a range of expected good luminosity is shown.

We should remember that we could arrive at $\sim$ 200 GeV and the standard model might still be the best description of nature which we have. What then? The sceptics will say that there is no good reason to push further for surely only Bedouins like deserts! Well the response to those sceptics is, "What self-respecting Bedouin would resist an oasis?" The only way to demonstrate that there is nothing new happening beyond the frontier is to cross it!

e^+e^- interactions at very high energies offer the potential for wide ranging tests of current high energy theories. The next ten years should prove to be very exciting indeed.

Acknowledgements

The author would like to thank Fred Gilman for his guidance in choosing the structure and format of these lectures. The author would also like to thank Peter Zerwas for many helpful and illuminating discussions.

REFERENCES

1. G. A. Voss, Proceedings of the 1981 International Symposium on Lepton and Photon Interactions at High Energies, Bonn, 1981, p. 926.
2. CERN Courier, Vol. 22 (10), p. 411 and p. 415 (1982).
3. S. Ozaki, Proceedings of the 1981 International Symposium on Lepton and Photon Interactions at High Energies, Bonn, 1981, p. 935.
4. SLAC Linear Collider Conceptual Design Report, SLAC-299 (June 1980); B. Richter, SLAC-PUB-2854 (1981).
5. (a) C. Y. Prescott, SLAC-PUB-2854 (1981). (b) Proceedings of the SLC Workshop, SLAC-247 (March 1982).
6. See for instance ECFA 81/54 General Meeting on LEP Villars-sur-Ollon, Switzerland, June 1981 and references therein.
7. General Meeting on LEP Villars-sur-Ollon, Switzerland, June, 1981, p. 132.
8. U. Amaldi, Proceedings of the 1981 International Symposium on Lepton and Photon Interactions at High Energies, Bonn, 1981, p. 944.
9. J. Kim et al., Reviews of Modern Physics 53, 211 (1981).
10. W. Marciano and A. Sirlin, Proceedings of the Cornell Z^o Theory Workshop, February 1981, p. 40.
11. A. Buras, Phys. Rev. Lett. 46, 1354 (1981).
12. The aplanarity is defined in the sphericity tensor analyses: J. D. Bjorken and S. J. Brodsky, Phys. Rev. D 1, 1416 (1970). For the use of aplanarity as described here see for instance TASSO collaboration, Phys. Lett. 86B, 243 (1979).
13. For a review of the PETRA measurements see J. Bürger, Proceedings of the 1981 International Symposium on Lepton and Photon Interactions at High Energies, Bonn, 1981, p. 126.
14. M. Dine and J. Sapirstein, Phys. Rev. Lett. 43, 668 (1979); K. G. Chetyrkin et al., Phys. Lett. 85B, 277 (1979); W. Celmaster and R. J. Gonsalves, Phys. Rev. Lett. 44, 560 (1980).
15. J. Dorfan, Z. Phys. 17, 349 (1981).

16. G. J. Tarnopolsky, SLAC-PUB-2842 (1981).

17. The error in $sin^2\theta_W$ is assumed to be one order of magnitude smaller than its present value, since the precision will be achieved by the measurement of the Z^o mass.

18. See for instance J. G. Branson, Proceedings of the 1981 International Symposium on Lepton and Photon Interactions at High Energies, Bonn, 1981, p. 279.

19. F. Wilczek, Phys. Rev. Lett. 39, 1304 (1978).

20. J. P. Leveille, Proceedings of the Cornell Z^o Theory Workshop, February 1981, p. 242.

21. J. D. Bjorken, SLAC-198 (1976).

22. R. N. Khan et al., Phys. Lett. 82B, 117 (1979).

23. S. L. Glashow et al., Phys. Rev. D 18, 1724 (1978).

24. P. Söding, AIP Conference Proceedings, No. 81, 107 (1981).

25. W. Braunschweig, Proceedings of the 1981 International Symposium on Lepton and Photon Interactions of High Energies, Bonn, 1981, p. 68.

26. J. Dorfan, Proceedings of the SLAC Summer Institute on Particle Physics, July 1981; SLAC-PUB-2813 (1981).

27. Examples of three jet algorithms are: TRIPLICITY - S. Brandt and H. Dahmen, Z. Phys. C1, 61 (1979). TRIJETTINESS - S. L. Wu and G. Zobernig, Z. Phys. C2, 207 (1979). CLUSTER ALGORITHM - J. Dorfan, Ref. 15, ibid.

28. J. Ellis and I. Karliner, Nucl. Phys. B148, 141 (1979).

29. R. Hollebeek, Proceedings of the 1981 International Symposium on Lepton and Photon Interactions of High Energies, Bonn, 1981, p. 1.

30. J. K. Bienlien, Proceedings of the 1981 International Symposium on Lepton and Photon Interactions of High Energies, Bonn, 1981, p. 190.

31. (a) R. D. Shamberger, Proceedings of the 1981 International Symposium on Lepton and Photon Interactions of High Energies, Bonn, 1981, p. 217. (b) A. Silverman, Proceedings of the 1981 International Symposium on Lepton and Photon Interactions of High Energies, Bonn, 1981, p. 138.

32. G. Preparata et al., Phys. Rev. Lett. 47, 891 (1981); G. Preparata, Proceedings of Physics in Collision I, 1981, p. 53; G. Preparata et al., BARI/GT/81-16.

33. K. Koller et al., SLAC-PUB-2858 (1982).

34. O. Nachtman et al., HD-THEP-82-9 (1982).

35. G. Körner et al., Nucl. Phys. B185, 365 (1981).

36. JADE Collaboration: W. Bartel et al., DESY 82-086 (1982).

37. See Ref. 25, page 87, MARK J results.

38. B. Lohr et al., SLAC-PUB-2983 (1982).

39. G. S. Larue et al., Phys. Rev. Lett. 38, 1011 (1977); Phys. Rev. Lett. 42, 142 (1979); Phys. Rev. Lett. 46, 967 (1981).

40. MARK II Collaboration: C. A. Blocker et al., Phys. Rev. Lett. 49, 517 (1982). CELLO Collaboration: H. J. Behrend et al., DESY 82-021 (1982). JADE Collaboration: W. Bartel et al., Phys. Lett. 114B, 211 (1982). MARK J Collaboration: A. Adeva et al., LNS Technical Report No. 125 (1982). TASSO Collaboration: M. Althoff et al., DESY 82-069 (1982).

41. E. H. De Groot et al., Z. Phys. C5, 127 (1980). This reference discusses the general question of $SU(2) \wedge U(1) \wedge G$.

42. V. Barger et al., Phys. Rev. D 25, 1384 (1982).

43. A. De Rugula et al., Annals of Phys. 109, 242,258 (1977).

44. G. Kane, UMHE 80-18 (1980); G. Kane and M. Peskin, UMHE 81-51 (1981).

45. M. Peskin and S.-H. H. Tye, Proceedings of the Cornell Z^o Theory Workshop, CLNS-81-485 (1981).

46. J. D. Bjorken, SLAC-PUB-2195 (1978).

47. G. Barbiellini et al., Phys. Lett. 106B, 414 (1981).

48. P. Fayet, Phys. Lett. 69B, 489 (1977).

49. Review articles include: P. Fayet, "Supersymmetry, Particle Physics, and Gravitation," Proceedings of the Europhysics Study Conference on "Unification of the Fundamental Interactions," Erice, Sicily, March 17-24, 1980 and CERN

preprint TH-2864, which emphasizes theoretical aspects of spontaneously broken supersymmetry; G. R. Farrar, Proceedings of the International School of Subnuclear Physics, Erice (Italy), August 1978, which emphasizes low energy phenomenological implications; and P. Fayet and S. Ferrara, Phys. Rep. 32C, 249 (1977), which surveys the whole field of supersymmetry as it existed in 1977.

50. JADE Collaboration: D. Cords, Proceedings of the XXth International Conference on High Energy Physics, Madison, 1980. MARK J Collaboration: D. P. Barber et al., Phys. Rev. Lett. 45, 1904 (1980). PLUTO Collaboration: H. Spitzer, Proceedings of the XIth Rencontre de Moriond, ed. Tran Than Van, Les Arcs, 1980, and DESY 80-43 (1980). CELLO Collaboration: H.-J. Berend et al., DESY 82-021 (1982). New results have also been published by JADE Collaboration: W. Bartel et al., DESY 82-023 (1982). MARK J Collaboration: B. Adeva et al., MIT/LNS 125 (1982).

51. M. K. Gaillard et al., Phys. Lett. 116B, 279 (1982).

52. S. Weinberg, Phys. Rev. D 19, 1277 (1979); L. Susskind, Phys. Rev. D 20, 2619 (1979); K. Lane and M. Peskin, Proceedings of the 1980 Rencontre de Moriond, ed. J. Tran Than Van; E. Eichten, Proceedings of the 1980 Vanderbilt e^+e^- Conference; E. Farhi and L. Susskind, CERN preprint TH-2975; P. Sikivie, Varenna Lectures (1980).

53. A. Ali and M. A. B. Beg, Phys. Lett. 103, 376 (1981).

54. L. F. Abbott and E. Farhi, Phys. Lett. 101B, 69 (1981); Nucl. Phys. B189, 547 (1981).

55. A. De Rugula, Phys. Lett. 96B, 279 (1980).

THE GAUGE HIERARCHY PROBLEM,

TECHNICOLOR, SUPERSYMMETRY, AND ALL THAT

Leonard Susskind

Physics Department, Stanford University

Stanford, California 94305

© L. Susskind 1982

I. The Gauge Hierarchy Problem

The standard SU(3) x SU(2) x U(1) theory of strong, electromagnetic and weak interactions appears to correctly describe all physics down to the smallest distance scales yet probed. Most probably the Z°, $w^\pm$ and top quark will be discovered. Should this occur we will be left with the following situation: a highly accurate phenomenology of all known physics (excepting gravity) exists but no explanation is in sight for a variety of fundamental questions such as the origin of generations, the values of fundamental constants, the exact equality of the electric charge of the proton and the positron, and the role of gravitation. Clearly the standard theory must give way to some more complete theory at some small distance scale. There are well known reasons to think that such a complete fundamental synthesis can only take place somewhere between 10^{14} and 10^{19} GeV.

What if anything lies between the weak scale $\sim 10^2$ GeV and the scale of unification? The simplest answer is nothing beyond the z, w top quark and Higgs. Nothing new will be encountered below 10^{14} GeV. It is obviously of the utmost importance to know whether there are any indications, one way or another, for this "BORING DESERT" hypothesis. These lectures are about one such negative indication, namely the gauge hierarchy problem (GHP) or the problem of naturalness of the two widely separated scales. represented by the expectation value of the Higgs field $\langle\phi\rangle \sim 250$ GeV and the unification or Planck scale.

The GHP is a consequence of several assumptions which I will now list.

1) The standard SU(3) x SU(2) x U(1) theory including quark, lepton photon, Z°, $w^\pm$ and one or more Higgs scalar fields correctly describes nature up to energies $\sim$ M very much larger than the weak scale $\sim$ 250 GeV.

2) New physics of an unspecified nature occur at scale $\sim$ M possibly including SU(5), gravity, etc.

3) The behavior of the world at ordinary energies is not exceedingly sensitive to the values of fundamental parameters. In particular the very existence of a low energy world, characterized by the Higgs expectation value $\sim$ 250 GeV should not require the fundamental parameters of the microscopic world at scale $\sim$ M to be "Fine Tuned."

This last assumption, usually called "NATURALNESS" is less familiar than the others and requires some explanation. To understand its meaning we must recall that a phenomenological field theory such as the standard model must be cut off at small distances to be defined. The formal path integral is meaningless until a prescription is given for regularizing its short distance behavior. This prescription specifies a momentum k as a cutoff and a set of parameters (coupling constants g and mass parameters μ) which will generally depend on k. The cutoff theory is only useful for momenta and energies less than k.

What about the effects of quantum fluctuations involving wavelengths smaller than k^{-1}. The central point of renormalization theory is that these effects can be lumped into the values of the constants g and μ (apart from very small effects which vanish like inverse powers of k). A change in the cutoff from k to k' can be compensated by a change in g and μ. Accordingly we consider (g,μ) to be functions $[(g(k), \mu(k)]$. The important point that I want to emphasize is that the phenomenological parameters g, μ are dynamical objects which depend in a complicated way on all the physics at length scales smaller than k^{-1}.

Let us now apply this idea to some hypothetical unified theory. I will begin by supposing that the theory contains no light fields of mass $< M$ other than those of the standard model. In this case if the cutoff k is less than M the physics of low energies ($< k$) must be the standard model with gauge couplings $g_3(k)$, $g_2(k)$, $g_1(k)$, Yukawa couplings $g_y(k)$, quartic scalar couplings $\lambda(k)$ and a mass parameter $\mu^2(k)$. The last of these is the usual (negative) mass squared of the Higgs field, which has potential

$$V(\varphi) = \lambda \varphi^4 - \mu^2 \varphi^2 \tag{1}$$

These parameters summarize all the unknown physics at momenta $> k$. In particular they depend non-trivially on the structure of the unified theory at distances shorter than M^{-1}.

The mass of every ordinary particle in the standard theory is proportional to the vacuum expectation value of $<\phi>$. For example quark and lepton masses have the form

$$m_q \sim g_y \langle \varphi \rangle \tag{2}$$

The Z and W masses are proportional to

$$g_2 \langle \varphi \rangle \tag{3}$$

and the Higgs mass to

$$\sqrt{\lambda}\langle \varphi \rangle \tag{4}$$

The VeV $<\phi>$ is not a new parameter but can be calculated from $\lambda(k)$ $\mu(k)$, $g(k)$ and $g_y(k)$. For example suppose we begin by ignoring all quantum fluctuations and calculate $<\phi>$ by minimizing $V(\phi)$. This gives

$$\langle \varphi \rangle = \mu(k)/2\sqrt{\lambda(k)} \tag{5}$$

This however is not a good approximation if the cutoff k is large ($\sim M$). It is spoiled by quantum fluctuations of all modes down to wavelengths $\sim k^{-1}$. A much better approximation is to use a low energy cutoff k^1 say of order 1 TeV. For most purposes we may write $k^1 = 0$ since $k^1 \ll\ll k$).

$$\langle \varphi \rangle \approx \mu(0)/2\sqrt{\lambda(0)} \tag{6}$$

Thus $<\phi>$ may be well approximated by computing the "renormalized" mass and coupling $\mu(0)$, $\lambda(0)$.

For example consider $\mu(0)$ which is calculated by Feynman graphs

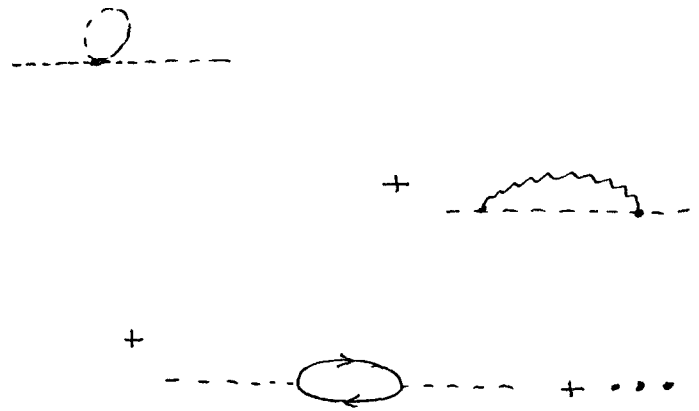


Fig (1)

Each graph in Fig. 1 is cutoff dependent and proportional to k^2. Thus $\mu^2(0)$ has the form $\mu^2(0) = \mu^2(k) + k^2(c_1\lambda + c_2 g^2 + \cdots)$ (7)

Now the point is that we believe that the values of $(g(k)\ldots\mu(k))$ are most closely related to the fundamental underlying unified theory when k is as large as possible, say of order M. Then Eq. (7) becomes

$$\mu^2(0) = \mu^2(M) + M^2(c_1\lambda(M) + \cdots) \tag{8}$$

How big is $\mu^2(0)$. From Eq. (6) we see that $\mu(0)$ should be $\sim \langle\phi\rangle \sqrt{\lambda(0)}$ and for typical $\sqrt{\lambda} \sim 1$, $\mu(0)$ is of order 10^2 GeV. Suppose the scale $M \sim 10^{15}$ GeV. Then we may write Eq. (8) as

$$\frac{\mu^2(0)}{M^2} = 10^{-26} = \frac{\mu^2(M)}{M^2} + (C_1\lambda + \cdots) \tag{9}$$

This is a very unreasonable situation. It requires the dimensionless parameter $\mu^2(M)/M^2$ to cancel the complicated series $(C_1\lambda+\ldots)$ to 26 decimal places in order that the world of ordinary particles be as light as it is. But $\mu^2(M)/M^2$ only knows about physics at small distances. To obtain such cancellation would require a miraculous conspiracy among the parameters of the unified theory. In other words, the existence of a scale $\sim 10^2$ GeV in the standard theory with a second more fundamental scale at 10^{15} GeV is unnatural. This is called the GHP.

Possible Solutions to the GHP

1) Forget it for now. Some future theory will explain the fine tuning of $\mu(M)$. The boring desert exists just like in the usual SU(5) model. No new discoveries above 250 GeV until 10^{15} GeV.

2) Technicolor. It is possible for a low energy world to emerge naturally. A familiar example is QCD with massless quarks and gluons. In this case chiral symmetry and gauge invariance insure the absence of any perturbative renormalizations of quark and gluon masses. The coupling constant $g(k)$ is renormalized and therefore depends on the cutoff scale k. The correct dependence is given by the renormalization group

$$\frac{dg(k)}{d\log k} = \beta(g(k)) = -\beta_0 g(k)^3 + \cdots \tag{10}$$

Thus if g is chosen fairly small at $k \sim M$ then at a much smaller momentum scale g will become large. This smaller scale is called λ_{QCD} and satisfies

$$\lambda_{QCD} \sim M e^{-\frac{1}{2\beta_0 g^2(M)}} \tag{11}$$

Evidently λ_{QCD}/M can be very small ($\sim 10^{-15}$) with no fine adjustment of parameters. In fact we need not even introduce a very small parameter to get $\lambda_{QCD/M}$ very small. In this case it is sufficient to make $g(M) \sim$ to get $\lambda_{QCD/M} \sim 10^{-15}$.

This brings us to a distinction between degrees of naturalness. I will consider a theory to be "seminatural" if it requires very small but not finely adjusted parameters. In these theories the smallness of the Higgs expectation value is stable but unexplained. On the other hand, theories like QCD I will call completely natural. In these theories all very small mass scales are exponentially small in terms of fundamental parameters such as g. Technicolor is an attempt to build a completely natural theory by mimicking QCD.

The important observation leading to T.C. is that the real role of the fundamental scalar ϕ is to spontaneously break the chiral gauge symmetry SU(2) x U(1). Now in QCD chiral symmetries are also broken, not by vacuum expectations of fundamental scalars but by quark bilinears

$$\langle 0|\bar{q}q|0\rangle \sim \Lambda_{QCD}^3 \tag{12}$$

In fact, if no Higgs fields were introduced into the standard SU(3) x SU(2) x U(1) theory, the ordinary QCD chiral breaking would break SU(2) x U(1) and give mass to $W^{\pm}$ and Z. The pattern of masses

$$M_W = \cos\theta_W M_Z \quad , \quad m_\gamma = 0 \tag{13}$$

would be the same as in the conventional theory because the chiral multiplet containing $\langle qq\rangle$ is isomorphic to the Higgs multiplet. In fact the massless

pion multiplet would mix with the gauge fields and become the longitudinal Z^0, $W^{\pm}$. However, because the strength of the condensate $<qq>$ is of order $(\lambda_{QCD})^3$ the resulting masses of Z, $W^{\pm}$ are

$$m_W \approx \frac{1}{2} g_2 \lambda_{QCD} \qquad (14)$$

(g_2 = SU(2) coupling). The correct formula replaces $<\phi>$ by the pion decay constant F_π. This leads to masses ~ 2000 times too small.

However suppose that a second QCD-like gauge sector (technicolor) exists. The gauge group does not have to be SU(3) but should become strong at a mass scale ~ 2000 λ_{QCD}. If this sector contains fermions (F) which carry T.C. instead of color but which form conventional weak doublets then condensates

$$<\bar{F}F>$$

will induce SU(2) x U(1) breaking. The Z and W will get masses of the correct magnitude and no very small or finely adjusted parameters are needed. The main prediction of this kind of theory is the existence of a rich spectrum of "technihadrons" with masses, widths and splittings ~ 2000 times their hadrons' counterparts.

The technicolor idea is a very elegant solution to the GHP but unfortunately runs into grave difficulties. As I have described it T.C. can explain the weak scale and masses of Z, W. What it fails to do is to provide a mechanism for ordinary fermion masses. In the conventional theory these arise from the Yukawa couplings of fermions (say quarks) to Higgs. Schematically we write

$$g_Y \bar{q} q \Phi$$

where g_y is a dimensionless coupling. When ϕ gets a vacuum value a fermion mass term

$$g_Y <\Phi> \bar{q} q$$

results.

In T.C. theory ϕ is replaced by the fermion bilinear $\bar{F}F$. To get masses for ordinary quarks an effective coupling

$$G \bar{q} q \bar{F} F$$

must exist with fermion coupling constant G (with units of m^{-2}). The light fermion mass is then

$$\sim G <\bar{F}F>$$

Where can the required 4 fermion couplings come from? Ordinary SU(3) x SU(2) x U(1) interactions do not induce couplings of the right kind. Thus we are forced to introduce yet further physics. Several possibilities have been suggested.

The first possibility called extended T.C. introduced new gauge degrees of freedom (E) which couple ordinary fermions to technifermions as in Fig. 2.

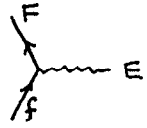


Fig 2

The required 4-Fermi couplings are generated by Fig. (3)

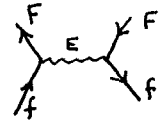


Fig 3

The coupling G is given by

$$G \sim g_E^2 / M_E^2 \qquad (15)$$

where g_E is the coupling of the E-bosons. The light fermions then have mass

$$m_f^2 \sim \frac{g_E^2}{M_E^2}\langle \bar{F}F\rangle \sim g_E^2\,\frac{\lambda_{TC}^3}{M_E^2}$$

$$= \lambda_{TC}\left(\frac{g_E^2\,\lambda_{TC}^2}{M_E^2}\right) \qquad (16)$$

Another popular idea is that quarks and leptons and technifermions are massless composites of some hypothetical preons bound by yet a third strong interaction called metacolor. The 4 fermi couplings FFqq, FFℓℓ would be due to exchange of preons as in Fig. (4)

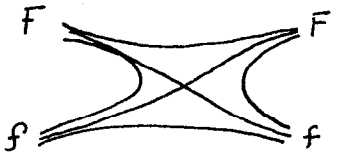


Fig 4

Unfortunately these ideas do not seem to be consistent with the observed suppression of neutral strangeness changing currents. In other words there is no known techni-Gim mechanism. For example in the ETC theory the existence of E-bosons coupling q to F through the vertex in Fig. (5)



Fig 5

would imply gauge coupling of q to q and F to F to close the nonabelian gauge algebra. Thus we will inevitably find additional 4-Fermi couplings $\bar{q}q\ \bar{q}q$ from Fig. (6)

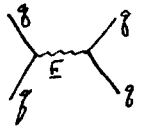


Fig 6

These couplings will generally include neutral strangeness changing interactions with strength

$$G_{NSC} \sim \frac{g_E^2}{M_E^2} \qquad (17)$$

of course if g_E^2/M_E^2 is small enough there is no danger. However, from Eq. (16) we see that

$$\frac{g_E^2}{M_E^2} \sim \frac{m_q}{\lambda_{TC}^2} \qquad (18)$$

In other words g_E^2/M_E^2 must be large enough to do the job it was designed to do, i.e., provide quark masses.

When typical quark masses are used in Eq. (18) it is found that the resulting magnitude of G_{NSC} is too large by many orders of magnitude to be consistent with known bounds on G_{NSC}. The worst disaster is the K_L-K_S mass difference which bounds G_{NSC} to be 10^6 times smaller than m_q/λ_{TC}^3.

Similar considerations apply to preon models where preon exchange will generate unacceptable NSC currents if they are made large enough to account for quark masses.

Perhaps somebody will discover a techni-Gim mechanism which can operate in a class of technicolor models. However, without such a mechanism I am forced to conclude that T.C. is very unlikely.

3) This brings us to the third possible solution. Consider the electron mass in QED. The electron mass (like the Higgs mass) gets renormalized. Offhand, if we did not know better we would expect

$$\delta m \sim \alpha k$$

where α is the fine structure constant and k the cutoff. This however, is incorrect. The reason is that if the bare mass of the electron is zero the theory has a symmetry (chiral symmetry) which prevents a mass counterterm from occurring. Therefore if m_0, the bare mass, vanishes so does δM. Accordingly δM is proportional to m_0 and the correct formula is

$$\delta_m \sim m_0 \alpha \ln \frac{k}{m_0} \tag{19}$$

Thus requiring $\delta M < m$ (naturalness) allows k to be enormous. This is many times bigger than the Planck mass.

Now suppose we could find a symmetry which was exact only if μ^2 (Higgs mass) were zero. In the same way we would argue that the quadratic divergences in the renormalization of μ^2 would cancel and

$$\delta_{\mu^2} \sim \alpha m_0^2 \log \frac{k^2}{m_0^2}$$

As long as $\log k^2/m_0^2$ is not too big the stability of a very small μ^2/k^2 or μ^2/M^2 would be insured. This kind of theory does not explain the smallness of μ^2 or m_0^2, but it does not require fine tuning of m_0. It is seminatural. A general definition of a seminatural theory is that a symmetry exists in the limit $\mu_0 \to 0$ which insures the vanishing of $\delta\mu$. Small breaking characterized by dimensionless parameters of order $\frac{\mu_0^2}{M^2}$ will then allow μ^2/M^2 to have a nonvaning small value which is stable with respect to radiative corrections.

Are there known symmetries which can protect massless scalar bosons from acquiring mass? Until the discovery of supersymmetry in the early 1970's the answer was no. Today we know that a combination of super and chiral symmetries can do the job. The rest of these lectures are about the supersymmetry solution to the GHP.

II. Supersymmetry

Supersymmetry transforms bosons into fermions and fermions into bosons. If the symmetry is unbroken it insures the equality of fermion and boson masses even after quantum radiative corrections. Now suppose that when a multiplet including a scalar a and a fermion ψ is massless, there is a chiral symmetry under which

$$\psi \to e^{i\gamma_5 a}\psi$$

The fermion mass will then remain zero to all orders in the coupling. But because supersymmetry is operative the boson mass will also remain zero.

Let us begin with a scalar complex boson field A and a 2-component left-handed spinor $\psi_\alpha (\alpha = 1,2)$ and a second boson field F. The field F will not be an independent quantum field but will be eliminated. It is called an auxiliary field and is useful in doing the bookkeeping of supersymmetry. The three fields

$$\Phi \equiv (A, \psi, F)$$

form a so-called chiral super field. A supersymmetry transformation mixes them. An infinitesimal super transformation is parametrized by a complex infinitesimal spinor parameter ε_α. The rule is

$$\left.\begin{aligned} \delta A &= i\varepsilon_\alpha \psi^\alpha \\ \delta\psi &= -i\varepsilon F + 2\bar{\varepsilon}\sigma_\mu \partial_\mu A \\ \delta F &= 2i\bar{\varepsilon}\sigma_\mu \partial_\mu \psi \end{aligned}\right\} \tag{20}$$

Several points are unusual about this transformation law. First of all if we consider ε to be an ordinary (commuting) number, then δA is a fermion field and $\delta\psi$ is a boson. We could work with such a convention but it is far more efficient to assume ε is an element of an anticommuting algebra,

i.e., that it is fermionic

$$\{\varepsilon_\alpha \varepsilon_\beta\} = \{\varepsilon_\alpha \ \varepsilon_\beta^*\} = 0$$

The second odd fact concerns dimension counting. If ϕ and ψ are canonical fields then they have dimensions m and $m^{3/2}$ respectively. This means that ε has dimensions of $m^{-1/2}$. The dimension of F is then forced to be m^2 or else Eq. (20) can not be consistent. Thus F can not be a canonical field.

To illustrate how supersymmetry works we consider a simple free field example. The Lagrangian for A is

$$\partial_\mu A^* \partial_\mu A \tag{21}$$

and for ψ

$$\bar{\psi} \not{\partial} \psi \tag{22}$$

For F the only term in L is F*F. Note that a free kinetic term for F is dimensionally inconsistent. Now it is an easy exercise to show that $\delta L=0$ under the supersymmetry transformation (20) the field F does not propagate. Its equation of motion is

$$\frac{\partial \mathcal{L}}{\partial F^*} = F = 0 \tag{23}$$

To add interactions to L, we must know how to multiply superfields. Consider two superfields Φ_1 and Φ_2

$$\Phi_1 = (A_1, \psi_1, F_1)$$

$$\Phi_2 = (A_2, \psi_2, F_2)$$

Their product $\Phi_1 \Phi_2$ is a superfield defined by

$$\Phi_1 \Phi_2 = (A_1 A_2, \ \psi_2 A_1 + \psi_1 A_2, \ A_1 F_2 + A_2 F_1 + 2\psi_1 \cdot \psi_2) \tag{24}$$

You can check that if Φ_1 and Φ_2 transform according to (20) so does $\Phi_1 \Phi_2$.

Next we see that under (20) the F-term of a superfield gets changed by a pure divergence under a supertransformation. Thus we may put it into L without destroying the SS of the action; for example we can put

$$\frac{m}{2} (\Phi\Phi)_F = (AF + \bar{\psi}\psi) m \tag{25}$$

in L. This term gives mass m to ψ and couples A to F. However, since derivatives of F do not appear in L, it may be eliminated. The Eq. of motion for F gives

$$F = -mA^* \tag{26}$$

Using $F = -mA^*$ in L then gives $m^2 A^* A$ in L so that A is also a massive field. We can also add Φ_F^3 to the Lagrangian without spoiling either supersymmetry or renormalizability

$$g \Phi_F^3 \sim g(A^2 F + i \psi \psi A) \tag{27}$$

This term evidently contains a Yukawa coupling $\psi\psi A$ between the scalar and spinor components of Φ. The A^2F term can be understood in one of two ways. Since derivatives of F do not appear in L_1 we may eliminate it. For example if no ϕ^2 term is present then F appears in the combination

$$FF^* + gA^2 F + gA^{*2} F^* \tag{28}$$

The Eq. of motion for F* is

$$F + gA^{*2} = 0$$

or

$$F = -gA^{*2}$$

Plugging this back into (28) gives

$$-g(A^*A)^2$$

in the scalar field potential.

Two things should be noted. First although we began with Φ^3 in the "superpotential" the result in the ordinary scalar Lagrangian was not A^3 but the renormalizable A^4 type coupling. Any higher powers of Φ in the superpotential inevitably lead to nonrenormalizable theories.

The second noteworthy feature is that the Yukawa coupling g and quartic coupling g^2 are linked. This link can not be broken without destroying supersymmetry. Conversely supersymmetry insures that the renormalization of the Yukawa and quartic couplings preserve the connection between them.

If in addition the supermultiplet Φ was given a mass m, then the term would also yield a cubic term

$$gm\, A^*A^2 + cc$$

Again SUSY insures that the connection between the Yukawa coupling, mass and cubic coupling is unrenormalized.

The second way to understand the auxiliary field F is to treat it like a quantum field without a kinetic term. The propagator for F is not $1/k^2$ but instead it is just 1. The F field must be included in internal lines of graphs but since it does not have poles in its propagator it never appears externally on shell.

Thus consider the coupling gA^2F. This can be interpreted as vertex shown in Fig. (7)

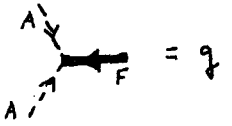


Fig 7

By exchanging F we generate diagrams with 4 external A-lines

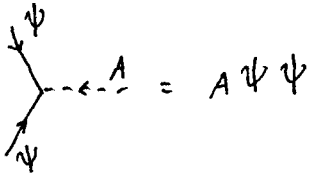


Fig 8

with amplitude g^2. This is of course just the quartic coupling induced by solving for F and eliminating it.

Individual Feynman graphs can be combined into supersymmetric combinations according to a simple rule. Do not eliminate the auxiliary fields. Draw graphs which would occur in ordinary Φ^3 theory. Then for each graph allow each internal line to be an A, ψ or F in all combinations. The vertices which are non zero are

a)



b)

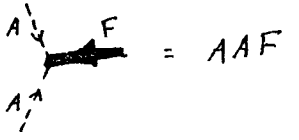


Fig (9)

(If in addition a mass term Φ^2 is present then the rules must be slightly modified--we leave it as an excercise to the reader.) Thus consider the vacuum supergraph in Fig. (10)

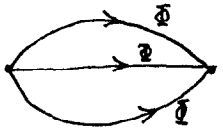


Fig 10

According to our rule this includes the following kinds of graphs Fig. (11)



Fig (11)

The graphs b are really of the form



Fig(12)

It is such supersymmetric combinations which satisfy the constraints of supersymmetry. For example, if we consider boson and fermion mass renormalization we can begin with the supergraph

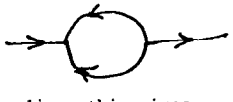


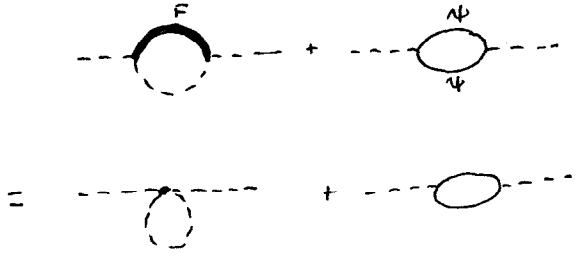
Fig 13

For external fermion lines this gives



Fig 14

while for external bosons it is



These contributions to fermion and boson masses are exactly equal. Similar considerations apply to renormalization of the coupling constants to find the combinations of graphs which preserve the connections between the quartic and Yukawa couplings.

That scalar and spinor masses and couplings renormalize in exactly the same way is remarkable in a quantum field theory but can be understood as a direct consequence of supersymmetry. A far more remarkable fact for which I know no obvious explanation is that these couplings do not renormalize at all. This is a strange result which can be proved graph by graph using the supergraph formalism of Grisaru, Rocek, and Siegel but which has no general explanation. The general statement is that no coupling of the form

$$\Phi^n + cc$$

is ever generated in the effective action by loop diagrams. Before concluding this survey of SUSY I will briefly describe another kind of supermultiplet which includes gauge bosons. This is the so-called real superfield containing components

$$R = (V_\mu, \lambda, D)$$

where V_μ is a vector field, λ a real (majorana) spinor and D a scalar auxiliary field. The three components must have identical gauge quantum numbers (electric and weak charge, color, etc.) since V_μ will be gauge bosons such as photons, $W^\pm$, Z^0, gluons and so forth. The so called gauginos λ must consist of neutral colorless photinos, zinos, charged colorless winos and an electrically neutral color octet of gluinos. If the gauge symmetry of R is nonabelian, R couples to itself through cubic and quartic couplings. The vertices include VVV Yang Mills vertices, $\lambda\lambda V$, vertices VDD. In addition, R couples to matter fields ϕ with couplings which include all the usual gauge coupling as well as $\lambda\psi A$ and DAA* coupling. In particular the AA*D couplings generate new quartic AA* AA* couplings when the auxiliary field D is eliminated.

III. Breaking SUSY

Supersymmetry requires that particles come in multiplets forming chiral ($A\psi$) or real ($V\lambda$) supermultiplets. This would require partners for all the usual particles. For example, quarks and leptons should have scalar partners, squarks and sleptons; Higgs bosons should be accompanied by Fermionic Higgsinos and gauge bosons by photinos, zinos, winos, and gluinos. Since no such particles exist at low energy we must assume SUSY is broken, and that the partners are massive enough to escape detection. As with ordinary symmetries supersymmetry can be broken either explicitly or spontaneously. We shall begin by considering explicit symmetry breaking. The context of the discussion will be a minimal supersymmetric extension of the standard SU(3) x SU(2) x U(1) + quarks + leptons + Higgs.

Let us begin by enumerating the particle content of such a theory

1) Gauge Fields

The usual massless (before Higgs) gauge fields for photons, Z's, W's and gluons are accompanied by majorana photinos, zinos, winos and gluinos. The photino and zino is electrically neutral and colorless. A linear combination of photino and zino form the neutral partner of the charged winos. Together they form an $SU(2)_{weak}$ triplet. Gluinos are electroweak singlets which form an octet under color. Since the Lagrangian mass term for gauge bosons (pre Higgs) vanishes, supersymmetry would require massless gauginos. Thus bare masses for gauginos explicitly breaks SUSY.

2) Quarks and leptons are accompanied by scalar and pseudoscalar particles. The left (right) handed fermion $SU(2)_w$ doublets (singlets) are accompanied by complex zero spin partners to form chiral supermultiplets. The "left- and right-handed" spin zero particles can be added (subtracted) to form scalar (pseudoscalar) partners. In the absence of supersymmetry breaking

these are degenerate with their fermionic partners. Furthermore if the Yukawa couplings of quarks and leptons to Higgs vanish then they must all be massless by virtue of chiral symmetry. In this limit any mass for scalar quarks (squarks) and leptons (sleptons) explicitly breaks SUSY.

3) Higgs doublets are accompanied by fermions. A simple Higgs doublet has a Weyl partner one component of which is charged and the other neutral. I will now explain why two Higgs doublets are required.

In the standard theory the Higgs field H can be used to give mass to both up and down quarks. This is because H and its complex conjugate form SU(2) doublets. Thus Yukawa couplings of the form

$$g_D Q_L H D_R^\dagger + g_u Q_L H^\dagger U_R^\dagger \qquad (29)$$

are allowed.

In a supersymmetric theory these couplings arise from cubic terms in the superpotential formed from the chiral supermultiplets of the same chirality. Now if H is an L.H.chiral supermultiplet then H* is R.H. since Q_L, $D_R^\dagger$ and $U_R^\dagger$ are L.H.. The coupling $Q_L H Q_R^\dagger$ is allowed but $Q_L H^\dagger U_R^\dagger$ is not. The remedy for this situation is to double the Higgs content by introducing a second Higgs doublet $\bar{H}$ which transforms like H* under the electroweak group but which is L.H. Eq. (29) is replaced by

$$g_D Q_L H D_R^\dagger + g_u Q_L \bar{H} U_R^\dagger \qquad (30)$$

in the superpotential.

The supersymmetric part of the Lagrangian contains all the usual interactions generalized to be supersymmetric. This means gauge couplings and Yukawa interactions. No bare masses are allowed for gauge, quark, or lepton supermultiplets. SUSY does however, allow the Higgs mass term

$$\bar{H} H$$

which produces equal (positive) masses for all Higgs bosons. In order to produce spontaneous symmetry breaking in the electroweak sector, the Higgs mass matrix must have some negative eigenvalues. This can only arise from supersymmetry breaking.

The breaking of supersymmetry should satisfy the criterion that it not lead to quadratic divergences in the scalar masses and thereby render the theory unnatural. This constrains the breaking term in the Lagrangian to the so-called soft terms. Generally these include scalar and fermion masses as well as cubic scalar interactions. However, the constraints of SU(3) x SU(2) x U(1) limit the breakings to:

1) Scalar quark and lepton masses
2) Gaugino masses
3) Higgs and Higgsino masses.
4) Trilinear squark operators

Each of these operators has a coupling constant with dimensions of a mass or mass squared. Accordingly the radiative contribution to the scalar masses arising from soft breaking will generally have a coefficient of mass squared. This means that it is no worse than logarithmically dependent on the cutoff mass.

The predictions of supersymmetry include the existence of a spectrum of superpartners. One of these superpartners must be stable. To see this, let us define a quantum number R

$$R = (-1)^{F+L+3B}$$

where F = fermion number, L = lepton number, and B = baryon number. This quantum number is 1 for all ordinary particles and -1 for their partners. Thus, to the extent that lepton and baryon number are conserved, R is a good quantum number. Accordingly, the lightest odd-R particle must be stable or almost so.

Broken supersymmetry does not predict the masses of the super-partners. However, if supersymmetry is to solve the GHP, then they must be no heavier than a few TeV and possibly much lighter. If and when these particles are discovered, they will be unmistakable because supersymmetry predicts their couplings. For example, suppose a scalar electron is discovered which can decay into a photino. Super-symmetry tells us that the coupling constant for this process is the electric charge e.

Composite Models for Quarks and Leptons *

Haim Harari

Weizmann Institute of Science, Rehovot, Israel

Abstract

We discuss the motivation for constructing composite models for quarks and leptons, the hopes we have for a successful model and the difficulties encountered, so far, in this field. This paper corresponds to the contents of lectures given at the SLAC Summer Institute (August 1982), at the DESY Workshop on "Electroweak Interactions at High Energies" (September 1982) and at the Solvay Conference at the University of Texas, Austin, Texas (November 1982).

1. Foreword.

The possibility that quarks and leptons are composite, plays a peculiar role in present-day particle physics. On one hand, it is the most natural extrapolation of the development of modern physics and the least imaginative proposition for extending our theoretical ideas beyond those of the "standard model" of electromagnetic, weak and color interactions. On the other hand, any attempt to construct an explicit composite model immediately faces serious difficulties, necessitating assumptions and ideas which are at least unusual, possibly revolutionary. Thus, we are dealing with an approach which is, paradoxically, extremely speculative and somewhat unimaginative

*Supported in part by U.S.-Israel Binational Science Foundation.

© H. Harari 1982

at the same time. In this lecture we review the present status of this field, emphasizing the hopes as well as the difficulties. We do not discuss specific models in any detail.

2. Compositeness and the Fundamental Interactions.

Every level of compositeness in the history of modern physics, led to a major revision of the list of fundamental forces. The understanding of atomic structure showed that Van-der-Waals forces are residual electromagnetic effects and are therefore not a separate fundamental interaction. The substructure of the nucleus revealed the existence of a new short-range force (the Strong or Nuclear or Hadronic Force) and led to the identification of an even shorter-range force (the Weak force). The hadron substructure uncovered the Color force and showed that the Nuclear or Hadronic forces are residual color effects. It is almost certain that a possible substructure of quarks and leptons, if found, will reveal one or more new forces. It is also possible that it may demote one or more of the existing "fundamental interactions" into the role of a "residual interaction."

New fundamental particles may be found in the future and may have escaped detection in the past in several different ways:

(i) The production of high mass free particles requires experiments at sufficiently high energies. The W and Z bosons and the toponium bound states have presumably escaped detection in such a way.

(ii) Low mass (or even massless) particles may escape detection if they interact weakly with all visible matter. That is how the neutrino eluded experiments for several decades. We may have a variety of light neutral particles, especially Goldstone or pseudo-Goldstone-bosons escaping us now in such a way.

(iii) Confined particles, even if they have small effective masses, require experimental probes with energies far exceeding their confinement energy scale. Only such probes can reach into small distances in which the confined particle can be indirectly observed. Thus, many GeV's were needed for indirect evidence for light quarks and massless gluons, where the confinement scale is $\Lambda_c \sim 100$ MeV. If there is a second confining force with a scale Λ_H, we will need energies which substantially exceed Λ_H in order to "observe" the new confined states.

In close correspondence with these three methods, there are at least three ways of discovering a new fundamental interaction:

(i) It may be a short-range interaction corresponding to distance scales and energy scales beyond those presently available. That is how the strong nuclear force remained unknown until the 1930's.

(ii) It may be an extremely weak force, not necessarily with a short range. Such a force can be uncovered only by increasing the sensitivity and accuracy of low energy experiments.

(iii) It may be a confining force, mediated by a massless boson but possessing a confinement scale beyond present energies.

Any of these possibilities may "hide" additional new interactions which could play an important role in quark and lepton compositeness. There may also be a fourth, hitherto unknown, method by which new particles and new interactions may escape detection. After all, had we discussed this subject 15 years ago, we would have listed only the first two items in the above lists of possibilities. We would not have anticipated the possiblity that an extremely strong force with massless force-carriers (Color) could have escaped detection. Today, we may be equally blind. The binding force of the constituents of quarks and leptons is perhaps eluding us in a new clever way.

3. Why Do We Wish to Go Beyond the Standard Model?

The standard model of electromagnetic, weak and color forces is based on a renormalizable local gauge theory, where $SU(3)_c \times SU(2) \times U(1)$ is the basic gauge group, and its spontaneous breaking via a Higgs mechanism leaves an unbroken $SU(3)_c \times U(1)_{EM}$ gauge group. Ignoring temporarily the Higgs sector, the model involves massless quarks, leptons, photon, gluons and weak bosons with only three independent parameters representing the coupling constants of the three interactions. The Higgs sector induces all the necessary masses, increasing the number of arbitrary parameters to twenty or more.

There are several reasons which lead us to believe that the standard model, in spite of its elegance, self-consistency and experimental success, cannot be the final answer. Every one of these reasons is, to some degree, a matter of taste. However, the emerging overall picture convinces us that there must be some new fundamental physics beyond the standard model.

Why do we wish to go beyond the standard model?

(i) Too many parameters. It is unlikely that the laws of physics contain over twenty independent parameters and that the various Cabibbo angles and quark or lepton masses are as fundamental as the fine structure constant. A theory beyond the standard model may enable us to calculate most of these parameters, starting from a small number of constants. Such a calculation will hopefully explain the peculiar mass spectrum of the observed quarks and leptons.

(ii) Generation Puzzle. The standard model contains no clues explaining the existence of several generations of quarks and leptons. There is no good reason for having three generations (or any other specific number of generations). We do not know what distinguishes the generations from each other. A new quantum number or a new property which "labels" the generations can emerge only from theories which go beyond the standard model. Any hope of calculating the mass matrices for the quarks and leptons must involve an understanding of the distinction between fermions of different generations.

(iii) Pattern within one generation. The mysterious triplication of generations enhances the significance of another puzzle, namely--the pattern observed within one generation. The standard model does not explain why quark and lepton charges are quantized in a related way. It does not explain why the color and electric charge are correlated (integer charge always comes with

color singlets, noninteger charge with color triplets). It also does not explain why the quarks and leptons possess identical SU(2) properties (left-handed doublets; right-handed singlets) and why all integer multiples of $Q=\frac{1}{3}$ between Q=-1 and Q=+1 appear but no $|Q|>1$ fermions seem to exist. All of these features would have required explanation even if we had only one generation. Since the same pattern occurs three times, there must be a particularly good reason for repeatedly having that specific pattern within the generation.

(iv) Unification. One other motivation for going beyond the standard model is the obvious hope of unifying the three interactions. We must remember that the SU(2)xU(1) gauge theory provides us with a beautiful and important connection between the electromagnetic and weak interactions,but it does not fully unify them. We still have an independent coupling constant for each interaction.

(v) Hierarchy problem and fine tuning. These may count as two problems or one problem depending on one's point of view. In any way of looking at it, we have here a mismatch between different energy scales. Assuming that there is an important energy scale beyond the standard model (be it the Planck mass or a somewhat lower energy scale of some other type of new physics), it is difficult to understand how particles with masses corresponding to the low energy scales of the standard model can survive enormous self-energy corrections. Vector bosons and fermions may be protected from such corrections by a gauge symmetry or a chiral symmetry, respectively. Scalars are not protected, in general.

The above five arguments are not compelling in any rigorous sense. However, after considering them, it is difficult to avoid the conclusion that some deeper theory must lie beyond the standard model, settling at least some of the above issues.

4. Avenues Leading Beyond the Standard Model.

We have listed five reasons to go beyond the standard model: (i) Too many parameters; (ii) Generation puzzle; (iii) Pattern within one Generation; (iv) Unification; (v) Hierarchy problem and fine tuning. At least five different classes of approaches have been proposed for handling these issues. There is no one-to-one correspondence between the five problems and the five classes of models. Let us briefly review each approach:

(a) "Horizontal Symmetries": These are alleged new symmetries[1] connecting the different generations. Such symmetries cannot settle any issue except, possibly, the generation puzzle (ii). We return to some of these ideas in section 9. No convincing horizontal symmetry scheme has been proposed, so far.

(b) "Technicolor". The fine tuning problem (v) may be resolved or at least postponed, to higher energies, by postulating that the Higgs scalars are condensates of new fundamental "technifermions" bound by a new confining "technicolor" interaction[2]. This approach does not shed any light on problems (i)-(iv). In fact, it normally leads to additional particles and additional free parameters. The technicolor idea is a limited version of compositeness, in which scalars and, consequently, the longitudinal components of massive

gauge bosons, are composite objects. Quarks, leptons, transverse gauge bosons and technifermions are all fundamental. In order to produce quark and lepton masses, technicolor schemes must be extended to include new gauge bosons which connect quarks to techniquarks[3]. Such bosons usually play a role similar to that of Horizontal gauge bosons, thus incorporating the Horizontal symmetry approach into the technicolor scheme. Here, again, no satisfactory model is presently available.

(c) Grand Unification. This approach satisfactorily settles points (iii) and (iv). The structure of one generation is beautifully accounted for in any scheme[4] based on O(10) or any of its candidate subgroups (SU(5) or SU(4)xSU(2)xSU(2)). The three interactions are clearly unified. However, the number of free parameters is increased beyond those of the standard model, no explanation is given to the generation puzzle, and the hierarchy problem remains unanswered. In addition, we must face an energy "desert" spanning twelve orders of magnitude and the controversial possibility of heavy magnetic monopoles. Proton decay is the earliest crucial test of grand unified theories.

There are ambitious attempts[5] to combine Grand unification, technicolor, and horizontal symmetries in all-encompassing schemes based on large groups such as SU(7), SO(14) etc. No convincing model has been found.

(d) Supersymmetry. Supersymmetry, besides being an attractive mathematical "toy," provides a hope for settling the hierarchy problem[5]. Unfortunately, the particle spectrum is doubled, introducing alleged supersymmetric partners for all gauge bosons, quarks, leptons, and scalars. Thus we have more particles and more parameters, without solving any of the problems (i)-(iv). Grand unification can be combined with supersymmetry, thus combining possible solutions to points (iii)(iv)(v), but the price is, again, a significantly more complicated spectrum of particles as well as additional theoretical problems.

(e) Composite Models. Here we assume that quarks, leptons, scalars, and possibly some gauge bosons are composite objects of some new fundamental constituents. Here, again, no satisfactory model is available. In the following sections (6-12) we discuss the hopes and difficulties of such models, vis-a-vis the various reasons for going beyond the standard model.

But, before we move on to our discussion of composite models, we must discuss the question of experimental tests.

5. Experiments Beyond the Standard Model.

Theories which go beyond the standard model, like all other theories in physics, must pass two types of tests: self-consistency and agreement with experiment. The requirement of theoretical self-consistency is not as simple as it sounds. We must remember that in all previous stages in the understanding of the structure of matter, from the Bohr atom to the quark model, the original version of the theory had many correct ingredients but suffered from serious theoretical inconsistencies. In all cases, experimental clues played a crucial role in the acceptance of the correct ideas. The

satisfactory theoretical self-consistency came only gradually, with modifications which were partly discovered by pure reasoning and partly through new experimental facts. Our main difficulty today is the total lack of any experimental facts which might force us to go beyond the standard model. To rely entirely on arguments of theoretical self-consistency is dangerous. It is not clear that such arguments would have allowed the quark model to be developed!

We therefore believe that experimental clues are crucial. In order to review such clues we must first discuss the relationship between the hypothetical new theory which goes beyond the standard model, and the Lagrangian of the standard model. In all cases we do not wish to discard the standard model. We would like to keep it as a good approximation of the ultimate theory, valid at energies well below the new high energy scale. Schematically, we may consider the following situation: We have a new theory at small distances and high energies. Its Lagrangian, L_{NEW}, is useful for describing high energy phenomena. It hopefully corresponds to a renormalizable theory which is fully self-consistent. At lower energies we may have an effective Lagrangian L_{EFF} which, in principle, can be derived from the fundamental high energy Lagrangian. It is presumably approximately equal to the standard-model Lagrangian L_{SM}.

$$L_{NEW} \to L_{EFF} \cong L_{SM}$$

When we search for experimental tests of the new theory, we may look for two general classes of tests:

(i) Tests of L_{NEW}. These are, necessarily, high energy tests involving future high-energy accelerators. If the energy scale of L_{NEW} is Λ_H, we may look for particles of mass Λ_H (e.g., Horizontal gauge bosons in Horizontal symmetry schemes, Monopoles in grand unified theories, Technihadrons in Technicolor models, etc.). We may also look for light particles which are confined within small confinement radii corresponding to a high energy scale Λ_H (e.g., preons in some composite models, techniquarks, etc).

(ii) Tests of the small difference between L_{EFF} and L_{SM}. The low-energy phenomenology of the new scheme is, presumably, almost identical to that of the standard model. The small differences between the two may actually provide us with the first clues for physics beyond the standard model. Such clues may come from a variety of terms in L_{EFF}. A few examples:

(a) L_{EFF} may contain high-dimension four-fermion operators such as $uude^-$ or $\bar{\mu}e\bar{e}e$. These must be preceded by a coefficient of order Λ_H^{-2}. Such terms induce transitions like $p \to e^+\pi^0$ or $\mu \to 3e$, respectively. These are low-energy processes which, if observed, would necessitate some physics beyond the standard model.

(b) L_{EFF} may show slight deviations from certain coupling-constant relations of the standard model. For instance, the coupling constants $g_{We\nu}$, $g_{W\mu\nu}$ which are identical in the standard model ("universality") may turn out to differ by terms of order m_ℓ/Λ_H as a result of some e-μ difference which is revealed only at the scale of Λ_H.

(c) L_{EFF} may contain weakly coupled light Goldstone bosons χ with Yukawa couplings such as $\frac{m_e}{\Lambda_H}\chi\bar{e}e$. Such bosons are difficult to detect. If they exist, they could provide hints for some new physics.

The above classes of experimental tests are relevant to any theory which goes beyond the standard model. They are also true for composite models of quarks and leptons. The right-hand side of figure 1 indicates the general orders of magnitude of the new energy scale, corresponding to various theoretical approaches beyond the standard model. On the left-hand side of the same figure we show some of the experimental bounds which are relevant to composite models of quarks and leptons. We now turn to a discussion of these bounds.

6. Experimental Constraints on Composite Models of Quarks and Leptons.

Any attempt to construct a composite model for quarks and leptons must take into account several experimental constraints:

(i) The anomalous magnetic moments of the electron and muon provide us with an (almost) model-independent constraint[7]. It has been argued that if a composite structure at a scale Λ_H leads to deviations from the QED predictions for g-2, and if the composite model has a chiral symmetry, we expect:

$$\delta(g-2)_\ell \sim 0\left(\frac{m_\ell}{\Lambda_H}\right)^2$$

In the case of the muon, present g-2 experiments yield $\Lambda_H > 500\text{GeV}$. If we relax the chiral-symmetry assumption, the bound is much more

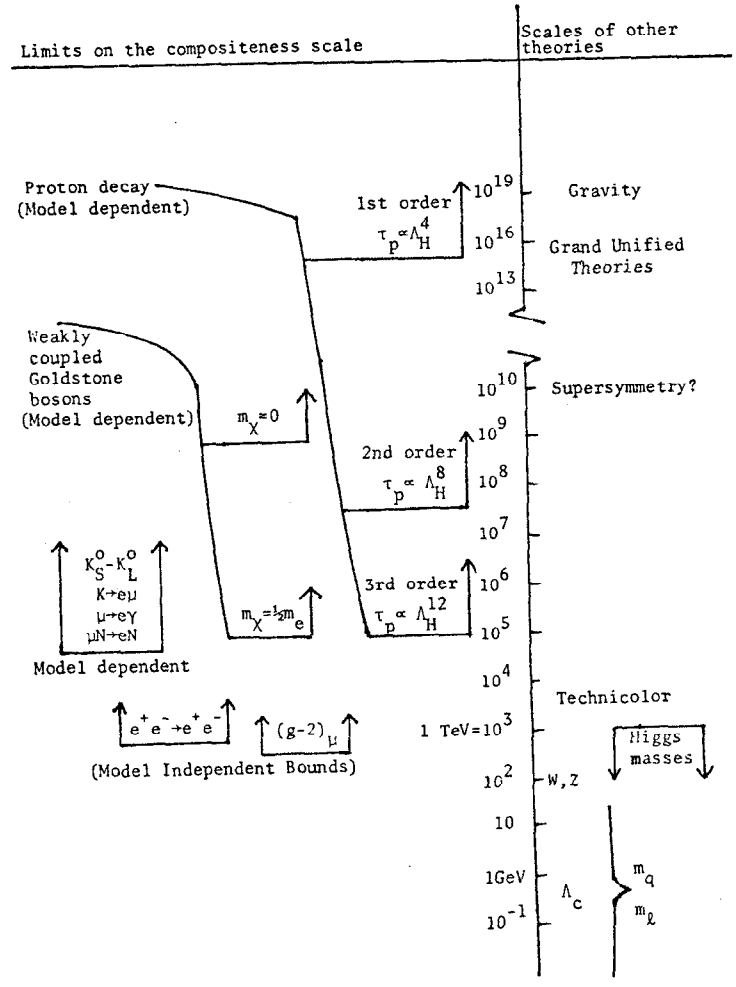


Figure 1: Experimental limits on the energy scales of theories beyond the standard model.

severe. The 500 GeV bound for the muon is essentially model-independent. However, it is only an order of magnitude estimate, and factors of π could easily change it in either direction.

(ii) If electrons are composite, we expect L_{EFF} to contain a four-fermion term of the form $\bar{e}e\bar{e}e$. Such a term would contribute to the cross-section for $e^+e^- \to e^+e^-$. The present agreement between this cross-section and QED places a new model-independent bound[8] on Λ_H. Here, again, one can only estimate the order of magnitude, obtaining $\Lambda_H > 700$GeV. Similar related estimates may be obtained for $e^+e^- \to \mu^+\mu^-$ and for neutral current neutrino reactions[8].

(iii) The absence of the decays $\mu \to e\gamma$, $\mu \to 3e$, $K \to \mu e$, $K \to \pi\mu e$ and the reaction $\mu N \to eN$ provide us with model-dependent bounds on compositeness. If the muon and the electron are prevented from transforming into each other by some selection rule or by a strong suppression-factor which depends on their detailed internal structure, no useful bounds can be derived from the present experimental limits. However, it is possible that the muon and the electron can easily convert into each other, the transition being suppressed only by the physical dimension of the composite system. In such a case we would expect L_{EFF} to include effective four-fermion terms such as $\frac{1}{\Lambda^2}\bar{\mu}e\bar{e}e$ or $\frac{1}{\Lambda^2}\bar{s}d\bar{e}\mu$. These would enable us to derive limits of the order of $\Lambda_H \sim 10\text{-}100$TeV for various processes. We emphasize, however, that this case is very different from the previous item. No selection rule can forbid an $\bar{e}e\bar{e}e$ effective interaction, but it is perfectly reasonable to expect a small suppression factor ε based on some selection rule, appearing in an expression of the form $\frac{\varepsilon}{\Lambda^2}\bar{\mu}e\bar{e}e$. If ε is sufficiently small, the bound on Λ_H may become totally useless.

(iv) A related experimental bound follows from the well-measured K_S-K_L mass difference. The observed value can be accounted for by the standard model. A composite model for quarks might allow an effective term of the form $\frac{\varepsilon}{\Lambda^2}\bar{s}d\bar{s}d$ contributing to ΔM. Here, again, the constraints are model dependent. If ε is sufficiently small, due to a selection rule based on the different internal structure of s and d, no useful bound can be deduced. If $\varepsilon \sim 0(1)$, we may obtain a very strong bound around 1000 TeV. However, it is somewhat unlikely that any composite model would allow $\varepsilon \sim 0(1)$.

(v) Many composite models[9] may involve massless Goldstone bosons or extremely light pseudo-Goldstone bosons χ, whose Yakawa couplings to ordinary quarks and leptons are of order $\frac{m_\ell}{\Lambda_H}$ or $\frac{m_q}{\Lambda_H}$. Such bosons can easily escape detection in terrestrial experiments. However, the process $\gamma + e \to \chi + e$ which must occur frequently in stars places a limit[10] on the $\chi\bar{e}e$ coupling, and through it - on the compositeness scale. From the known limit on the allowed energy loss of red giant stars, we obtain: for a massless Goldstone boson - $\Lambda_H > 10^9$GeV; for $m_\chi = \frac{1}{2}m_e$, $\Lambda > 10^5$GeV; for $m_\chi = m_e$ no useful limit is obtained in this way. Thus the constraints are extremely sensitive to the boson mass.

(vi) Proton decay provides another crucial, but model-dependent, test for the compositeness scale. If no selection rules or suppression factors exist, we find the usual result:

$$\tau_p \sim \frac{\Lambda_H^4}{m_p^5}$$

leading to $\Lambda_H > 10^{15}$GeV. However, proton decay is actually forbidden in some composite models. In other models it may proceed in second order[11] (giving $\Lambda_H > 10^7$ GeV) or in third order[12] (giving $\Lambda_H > 10^5$GeV)

The overall picture is the following: At present, there is no experimental evidence for quark or lepton compositeness. Model-independent bounds tell us that $\Lambda_H > 0.5$ TeV or $r < 4.10^{-17}$cm. Any specific model must be compared with a variety of model-dependent tests. For instance, anyone who wishes to suggest that quark and lepton compositeness will be revealed already at energies around, say, 10-1000 TeV, must provide strong suppression factors for proton decay, and the K_S-K_L mass difference, as well as avoid massless Goldstone bosons which couple to electrons and up and down quarks. Additional experimental tests which one must consider involve $\sin^2\theta_w$, the W-Z mass ratio, the W magnetic moment, the possible existence of "right-handed" weak bosons, etc.

7. Requirements from an Ideal Composite Model.

What do we hope to achieve by constructing a successful composite model of quarks and leptons?

(i) Such a model should include a few species of fundamental objects interacting with each other through few types of fundamental interactions. The total number of parameters is presumably extremely small: several coupling constants and possibly (but not necessarily) a few mass parameters. All masses of the composite quarks and leptons should, in principle, be calculable from the parameters of the fundamental theory, in the same way that all hadronic masses and coupling constants are, in principle, calculable from the QCD coupling and a few quark masses.

(ii) The pattern of quarks and leptons within one generation should be fully explained in terms of the features of the fundamental fermions. For instance, if both quarks and leptons are composites of the same set of fundamental fermions, their charge quantization must clearly be related. The peculiar relation between electric charge and color may simply emerge from the color and charge of the fermions. The restrictions on |Q| may be related to the number of constituents within a composite quark or lepton, in the same way that the limitations on the strangeness or isospin of hadrons follow from the number of valence quarks in a hadron.

(iii) The different generations may be excitations of a composite system, similar to excited atoms, nuclei or hadrons. The type of excitation in each case must be different, however.

(iv) The scalar particles, as well as the quarks and leptons, are presumably composites of the new fundamental fermions. Hopefully, no fundamental scalar particles are necessary. The fundamental fermions may be massless or may have explicit mass terms, but need not gain masses through symmetry breaking. The problem of fine tuning may thus be avoided.

(v) Other features are left open. Color, Electromagnetism and the weak interactions may all exist in the underlying theory.

Alternatively, one or more of these interactions may turn out to be a residual force, appearing only in L_{EFF}. Additional color-like or other types of forces may be needed in order to bind the new fermions inside the quarks and leptons. The underlying theory may be left-right symmetric, with Parity being spontaneously broken at the composite level. Alternatively, the fundamental theory may already include explicit parity violation.

It is not at all clear that a composite model with all the above desired features can be constructed, but it is certainly worth exploring. So far no one has come close.

Among the various problems which face model builders, we choose to discuss four in some detail:

(a) The problem of scales. Quark and lepton masses are much smaller than any possible compositeness scale. This is the most difficult problem for all composite models, and it has several interesting aspects, which we discuss in section 8.

(b) The generation puzzle. If quarks and leptons are composite, what kind of quantum number distinguishes among generations and what kind of excitation can yield a higher-generation quark or lepton? We discuss this issue in section 9.

(c) Structure within one Generation. Can we select a simple set of fundamental constituents, such that the entire pattern within one generation will be fully accounted for in a natural way? We propose an answer in section 10.

(d) Possible Compositeness of Gauge Bosons. In addition to the quarks, leptons and scalar Higgs particles some of the gauge bosons of the standard model may be composite. If they are, the corresponding interactions become residual and do not appear in the fundamental high-energy Lagrangian. Among the various gauge bosons, the most likely candidates for compositeness are the W and Z bosons. We discuss their possible composite nature in section 11.

8. The Problem of Energy Scales.

We have already explained why composite quarks and leptons must be approximately massless with respect to their compositeness scale Λ_H. Such masslessness must emerge from a symmetry principle. The simplest symmetry which may prevent a fermion from acquiring a mass is a chiral symmetry[13]. We may therefore wish to look for a composite model with a chiral symmetry.

The chiral symmetry is essentially automatic if the fundamental fermions appearing in L_{NEW} are massless. However, the existence of a chiral symmetry in the fundamental Langrangian does not necessarily guarantee its preservation at the composite level. The chiral symmetry may be broken spontaneously, leaving no reason for massless fermions at the composite level.

Thus the necessary logical sequence of assumptions is as follows:

(i) The fundamental Lagrangian contains massless fermions and therefore possesses a chiral symmetry.

(ii) The full chiral symmetry or, at least, a chiral subsymmetry remains unbroken at the composite level.

(iii) The chiral symmetry of the effective Lagrangian containing the composite fermions, prevents the latter from gaining a mass. We have composite massless fermions.

Three questions imediately arise:

(a) If the new fundamental fermions are massless, why don't we observe them?

(b) What is the interaction which binds the fundamental fermions inside the composite quarks and leptons?

(c) If both fundamental and composite fermions are massless, what provides us with the necessary "compositeness scale" Λ_H?

All three questions can be immediately answered by one postulate[13], if we assume a new color-like force ("hypercolor")with a scale parameter Λ_H. All fundamental fermions carry hypercolor. They are confined by hypercolor forces of characteristic scale Λ_H into hypercolor-singlet composite fermions with an effective radius $r \sim \Lambda_H^{-1}$. The confined fundamental fermions cannot be experimentally observed. The binding and the scale are provided by the hypercolor gauge force.

The above scenario is an attractive framework for the construction of a composite model. However, it is crucial that the chiral symmetry or at least a chiral subgroup must remain unbroken at the composite level. This is not a priori impossible,but it differs from the observed pattern of chiral symmetry breaking in QCD. No composite massless fermions emerge in QCD. The hypercolor situation must, for some reason, be different!

We now face a dilemma which stems from the following statements:

(i) We believe that in two-flavor massless QCD, the chiral symmetry is completely broken. No chiral subgroup remains intact.

(ii) If we neglect all interactions except hypercolor (all other interactions are probably much weaker at the Λ_H-scale), a hypercolor model with K fundamental massless fermions is isomorphic to K-flavor massless QCD.

(iii) In order to have massless composite fermions, some chiral symmetry should remain unbroken in the hypercolor case.

(iv) In no case do we have a full dynamical understanding of chiral symmetry and its breaking.

It is hard to reconcile statements (i), (ii), (iii), but no negative proof can be given. What are the logical possibilities?

(a) A reasonable attitude, advocated by some theorists, is simply to declare that (i), (ii) and (iii) are inconsistent. In that case one should not continue to pursue our discussion beyond this point, and the hypercolor idea should be abandoned. Perhaps this is true. Perhaps not.

(b) One way out is to consider a composite model in which left- and right-handed fermions have different transformation properties under the gauge group. Such a model is not isomorphic to QCD and statement (ii) does not apply to it. In such a model an $\bar{f}f$ condensate cannot break the chiral symmetry without breaking the original gauge symmetry. Two options are open: Either there is no condensation or the gauge symmetry breaks itself into a smaller subgroup. The first

possibility has been studied by various authors and no realistic model was found. The second possibility is the interesting "tumbling" approach[14]. Here, again, no realistic model was found. However, the left-right symmetric classification may still be the correct solution.

(c) It is possible that the pattern of chiral symmetry-breaking depends on the number of flavors K. This could happen at least in two ways. There may be a phase transition at some K-value, K>3, leading to a different pattern for QCD and for a hypercolor theory with K>3 flavors of fundamental fermions. It is also possible that the general $SU(K)_L \times SU(K)_R$ chiral symmetry always breaks, leaving a small conserved chiral subgroup which is trivial for K=2 but is nontrivial for large K. An example could be a discrete Z_K chiral group. A chiral Z_2 cannot protect any fermion from acquiring a mass. A chiral Z_4 or Z_6 can do it. There is no dynamical reason to expect any of these speculations to be true, but there are no complete arguments against them.

(d) Another possible speculation is that the presence of the color or electroweak interactions somehow influences the pattern of chiral symmetry breaking in a hypercolor scheme. This is the most obvious difference betweeen the hypercolor case and QCD. The simplest attitude would be to treat color and electroweak interactions as minor perturbations which cannot substantially change anything. However, subtle effects may occur. For instance, imagine a situation in which the chiral symmetry can break via $\bar{f}f$ or $\bar{f}\bar{f}ff$ condensates, the potential having two similar minima. A small perturbation could conceivably change the balance between the two minima, making the $\bar{f}\bar{f}ff$ condensate the likely one. At this point we may also add that the usual $N_c \to \infty$ argument for the breaking of chiral symmetry in QCD[15] does not necessarily remain valid if N_c/N_f is held fixed. In some composite models, such a fixed ratio may be a necessary requirement.

The above discussion can be summarized very simply: One can speculate about scenarios which provide the required pattern of chiral symmetry breaking for a composite model. All such scenarios are not supported by any decent dynamical arguments, but they cannot be ruled out.

Even if we succeed in producing a composite model with a chiral symmetry which is not completely broken, we still have to worry about the anomaly-matching condition[13], to which we now turn.

Let us assume that we have constructed a composite model of quarks and leptons based on an $SU(N)_H$ hypercolor gauge group and containing K fundamental massless fermions, all assigned to the N-dimensional representation of $SU(N)_H$. The underlying Lagrangian automatically possesses a global $SU(K)_L \times SU(K)_R \times U(1)$ symmetry. The U(1) factor is a vector charge counting the number of fermions. An additional axial U(1) factor is broken by instanton terms.

The model contains "flavor" triangle anomalies corresponding to products of three SU(K) currents or to products of two SU(K) currents and the U(1) current. Such anomalies are perfectly legitimate, since the $SU(K)_L \times SU(K)_R \times U(1)$ symmetry is not gauged. However, in the zero momentum limit, a given anomalous term can be exactly calculated both

from the underlying theory and from the low-energy effective theory containing three composite particles. The results must be the same, thus imposing a severe constraint on the spectrum of composite particles.

If, in the underlying level, the anomaly does not vanish, the theory must produce massless composite particles[13)16)]. We may consider three logical possibilities:

(i) The chiral symmetry is not broken at all. There are composite massless fermions. Their contribution to each anomaly must be exactly equal to that of the fundamental massless fermions. Thus a severe constraint is imposed, connecting the fundamental fermions to the composite fermions. This is the famous 't Hooft condition[13)].

(ii) The chiral symmetry is completely broken. No chiral subsymmetry remains. The only massless composite particles are Goldstone bosons. Their contribution to the anomaly is equal to that of the fundamental fermions. However, since the Goldstone bosons have unknown couplings, the anomaly constraint can only be used in order to compute these couplings, leading to equations similar to the Goldberger-Trieman relations.

(iii) The chiral symmetry is broken, but a chiral subgroup remains conserved. The chiral subgroup may be continuous or discrete. In this case, massless Goldstone bosons must exist but massless fermions may also exist. The combined contributions of the massless composite bosons and fermions must balance the anomaly of the underlying theory.

The anomaly constraint is particularly powerful in case (i). It is not very useful in case (ii), but we are interested in massless composite fermions, and they do not occur in that case. Case (iii) allows composite massless fermions, and the anomaly constraint is somewhat less powerful.

We suspect that case (iii) is the most likely candidate for a realistic composite model. In particular, we may consider the interesting possibility of a continuous chiral symmetry in the original Lagrangian, broken into a discrete chiral symmetry at the composite level. Such situations arise naturally in simple unrealistic "toy" models[17)].

In case (iii) the massless composite fermions are accompanied by massless Goldstone bosons. Such bosons appear in a wide variety of composite models. They may escape detection because their Yukawa couplings to quarks and leptons are of order m_q/Λ_H and m_ℓ/Λ_H, respectively. We have mentioned the resulting experimental constraint in section 7.

We have gone here through an elaborate maze of difficulties, all stemming from the fundamental mismatch between the compositeness scale Λ_H and the masses of the composite objects. If the chiral symmetry hypothesis, together with a new hypercolor force, will not solve the problem, what other options do we have? The most likely possibility is some new fundamental force with some new features, not resembling any of the known interactions. Various ideas in that direction have been considered, including magnetic monopoles[18)], dimensional compactification[19)], nonlocal theories[20)], and quarks and

leptons as massless supersymmetric Goldstone fermions[21]. It is difficult to believe that the correct theory can be found without some experimental hints.

9. The Generation Puzzle.

The existence of quark and lepton generations is, perhaps, the most striking experimental fact which guides us beyond the standard model. Let us first discuss the general problem, then turn to the possible description of generations within composite models of quarks and leptons.

We have three identical generations of quarks and leptons. The standard model does not contain any quantum number which distinguishes among the generations. Yet, we suspect that such a quantum number must exist. Three classes of solutions have been considered for a generation-labelling quantum number. In all cases we are looking for a symmetry which is already spontaneously broken at the stage of creating the fermion masses. The existence of Cabibbo mixing tells us that any "generation number" cannot remain exactly conserved.

The three possibilities are:

(i) A discrete generation label. A discrete symmetry is introduced, such that each generation obtains a different eingenvalue under the symmetry operation. It is necessary that, say, e, μ and τ have different eingenvalues. It is not necessary that e and u have the same eingenvalues, although it would be more elegant if they did. The scalar particles must have well-defined transformation properties under the discrete symmetry and the allowed Yukawa couplings are severely restricted by the symmetry. The mass matrix for analogous states in different generations contains matrix elements contibuted by different scalar fields. If scalar fields with a non-vanishing generation number obtain vacuum expectation values, the discrete symmetry is broken and Cabibbo mixing is introduced. There is no real theoretical difficulty in describing the generations using a discrete symmetry. The only drawback of such an approach is the fact that all such discrete symmetries appear completely arbitrary and artificial.

(ii) A Continuous Global Symmetry. A variation on the same theme would be a continuous global symmetry under which each generation obtains a different eingenvalue. Here we face a serious difficulty: If the continuous symmetry is spontaneously broken, an unwanted Goldstone boson appears. Here, again, the ad hoc nature of the symmetry is usually unattractive.

(iii) A Gauged Generation Label. A third possibility which avoids the dangerous Goldstone boson is to consider an extra "horizontal" gauge group under which different generations form a gauge multiplet. The simplest example is a U(1) gauge symmetry but larger groups can be considered. The complications are: A severe anomaly constraint; the existence of a new gauge boson (or bosons); the danger of flavor changing neutral currents associated with "horizontal" gauge bosons.

Of the three possibilities, the discrete one is the only one which leads to no great difficulties. If we could find a discrete symmetry which is "natural" in the sense that its existence is caused

or guaranteed by some other feature of the overall theory, it would be a likely candidate for a generation-labeling scheme.

Another important property of a generation-labeling quantum number is its space-time nature.

Let us consider an operator under which e^o, μ^o and τ^o possess the quantum numbers X_e, X_μ, X_τ. Here e^o is a massless electron appearing in the standard model Lagrangian. If the symmetry is vectorial, $X(e_L)=X(e_R)$ etc. If it is axial, $X(e_L) = -X(e_R)$ etc. In the first case a scalar field with X=0 can induce diagonal mass terms for e, μ and τ.

The necessary X-values for scalar fields which contribute to mass-matrix elements are:

$$\begin{pmatrix} 0 & X_e-X_\mu & X_e-X_\tau \\ X_\mu-X_e & 0 & X_\mu-X_\tau \\ X_\tau-X_e & X_\tau-X_\mu & 0 \end{pmatrix}$$

On the other hand, if X is an axial quantum number, the three diagonal mass-matrix elements must be contributed by three different scalar fields.

The necessary values are:

$$\begin{pmatrix} 2X_e & X_e+X_\mu & X_e+X_\tau \\ X_e+X_\mu & 2X_\mu & X_\mu+X_\tau \\ X_e+X_\tau & X_\mu+X_\tau & 2X_\tau \end{pmatrix}$$

In view of the different scales of the masses of different generations, we believe that the axial option is preferable[22]. In grand unified theories such as O(10) only axial quantum numbers are possible, since e_L^- and e_L^+ belong to the same multiplet and must have the same eigenvalue for a given generation-labeling operator. Consequently, e_L^- and e_R^- must have opposite eigenvalues.

We conclude that, on quite general grounds, an attractive generation-labeling symmetry would be an <u>axial discrete</u> symmetry, provided that it is not artificially concocted. In composite models we do not have an arbitrary freedom for inventing such symmetries. The fundamental Lagrangian in such models is fully specified, and all symmetries at the composite level must follow in one way or another from the properties of the theory.

Corresponding quarks and leptons in different generations must have the same $SU(3)_c \times SU(2) \times U(1)$ quantum numbers. They differ by some "generation number." All generations are approximately massless in comparison with the compositeness scale. Hence, they cannot be obtained by radial or orbital excitations of the first-generation "ground state." A possible excitation of a composite massless fermion which may lead to a different composite massless fermion is an excitation by one or more pairs of fermionic constituents. In a given composite model we should therefore investigate the possibility of constructing a system of preons and antipreons forming a scalar under the Lorentz group as well as under $SU(3)_c \times SU(2) \times U(1)$, but possessing a nonvanishing value of some "generation number." Such a system could be the difference between corresponding composite fermions in different generations.

An interesting possibility[23]: In hypercolor composite models with K massless constituent fermions, we have a global

$SU(K)_L \times SU(K)_R \times U(1)$ symmetry. An additional axial U(1) factor is broken. Hovewer, a discrete axial Z_{2K} symmetry always remains unbroken. Such a symmetry may serve as an adequate candidate for a generation number. It is an axial, discrete symmetry and it is not artificial at all. It exists in the theory, "waiting" to be used.

10. Structure Within One Generation.

Each generation of quarks and leptons contains eight types of states. We list them in table 1, arranged in descending order of their electric charges.

	Color	Q	B-L
e^+	1	1	1
u	3	$\frac{2}{3}$	$\frac{1}{3}$
$\bar{d}$	$\bar{3}$	$\frac{1}{3}$	$-\frac{1}{3}$
ν_e	1	0	-1
$\bar{\nu}_e$	1	0	1
d	3	$-\frac{1}{3}$	$\frac{1}{3}$
$\bar{u}$	$\bar{3}$	$-\frac{2}{3}$	$-\frac{1}{3}$
e^-	1	-1	-1

Table 1: Fermions and antifermions of the first generation

An inspection of the table reveals a few features which cannot be explained within the standard model:

(i) The electric charges of the quarks and the leptons are quantized in a related way. Thus $Q(u)=\frac{2}{3}Q(e^+)$ and the hydrogen atom is exactly neutral. This is not at all guaranteed if the SU(2) and U(1) gauge interactions are unrelated.

(ii) The sum of the electric charges of all fermions vanishes. This is the famous condition for the vanishing of the triangle anomaly in SU(2)xU(1). It is the only ingredient of the standard model which explicitly connects quarks and leptons and which tells us that a model with quarks and no leptons (or vice versa) is not renormalizable. A fermion (antifermion) is defined as a left-handed doublet (singlet) of the SU(2) gauge group in the standard model.

(iii) There are certain color-charge combinations which exist (and repeat themselves in higher generations). Other combinations do not exist. We have surprising correlations. For instance, 3Q (mod 3) is identical to the color triality, although no relation between charge and color is implied by the standard model.

(iv) The electric charge is limited by $|Q| \leq 1$.

The above regularities cannot be accidental. They must be explained by some theoretical structure which goes beyond the standard model, either by embedding the three different gauge groups in a larger simple group or by constructing all quarks and leptons from more fundamental constituents.

In a grand unified O(10) theory all of these regularities are beautifully accounted for by the structure of the group and its 16-dimensional spinor representation. The related charge quantization of quarks and leptons is guaranteed by the relationship between the SU(2) and U(1) couplings. The absence of anomalies is automatic in O(10). The color-charge correlations are dictated by the specific way

in which $SU(3)_c \times U(1)_{EM}$ is embedded in O(10). The $|Q| \leq 1$ limitation is a property of the 16-dimensional multiplet. In a SU(5) grand-unified theory all of these features are also explained.

In a composite model one would hope to explain the pattern within one generation by a set of simple rules based on the properties of the fundamental fermions. Such rules should presumably be analogous to the quark model rules which neatly explain the repeated appearance of decuplets, octets and singlets of the flavor-SU(3), with no other representation appearing.

A particularly satisfactory explanation of all features of one generation is given in the rishon model[24], based on a hypercolor SU(3)-group. There we postulate two types of fermions: The T-rishon in a $(3,3)_{1/3}$ of $SU(3)_H \times SU(3)_c \times U(1)_{EM}$ and the V-rishon in a $(3,\bar{3})_0$. The structure of one generation is given by the hypercolor-singlet lowest-color states of three rishons and three antirishons. These states are listed in Table 2.

All four features which we mentioned at the beginning of this section, can be neatly explained in such a model:

(i) All electric charges are due to the T-rishon or $\bar{T}$-antirishon. Hence, quark and lepton charges obey simple ratios. A Hydrogen atom contains $e+u+u+d \equiv 4T+4\bar{T}+2V+2\bar{V}$. Its neutrality is trivially understood.

(ii) The quarks and leptons in one generation are $3(u+d)+e+\nu_e \equiv 6(\bar{T}+T+\bar{V}+V)$ Hence, their sum of electric charges (or any other additive quantum number) vanishes, and the standard-model anomaly cancellation is simply understood.

	Color	Q	B-L	Rishon Combination
e^+	1	1	1	TTT
u	3	$\frac{2}{3}$	$\frac{1}{3}$	TTV
$\bar{d}$	$\bar{3}$	$\frac{1}{3}$	$-\frac{1}{3}$	TVV
ν_e	1	0	-1	VVV
$\bar{\nu}_e$	1	0	1	$\bar{V}\bar{V}\bar{V}$
d	3	$-\frac{1}{3}$	$\frac{1}{3}$	$\bar{T}\bar{V}\bar{V}$
$\bar{u}$	$\bar{3}$	$-\frac{2}{3}$	$-\frac{1}{3}$	$\bar{T}\bar{T}\bar{V}$
e^-	1	-1	-1	$\bar{T}\bar{T}\bar{T}$

Table 2: Rishon model assignments of first generation fermions and antifermions.

(iii) The color-charge correlation is automatic. Replacing a T by a V corresponds to $\Delta Q = -\frac{1}{3}, \Delta(\text{triality}) = -1$. Hence, the equality between 3Q(mod 3) and the color triality.

(iv) All quarks and leptons are three-rishon states, all combinations appear and the fundamental charge is $\frac{1}{3}$. Hence, the observed electric charges must correspond to all integer multiples of Q ranging between Q=+1 and Q=-1. $|Q|>1$ values cannot be obtained from three rishons or antirishons.

The rishon model, like all other composite models, suffers from several difficulties which we have discussed in detail elsewhere[24]. Its success in accounting for the structure within one generation is, however, impressive.

11. Composite Weak Bosons and Residual Weak Interaction.

In composite models of quarks and leptons we usually face at least four types of gauge bosons: Hypergluons, gluons, photon, and weak bosons.

Which of these bosons must be elementary? Can some of them be composite?

There is a certain confusion in discussing the possibility of composite gauge bosons. There are theories in which a certain fermion-antifermion pair of fields may appear to have some or all of the properties of a gauge boson. In some sense this is a composite gauge boson, but it appears in the same fundamental Lagrangian with the fermion fields and all other fields of the theory. Such a possibility is very interesting and some toy-models incorporating it have been constructed.

A different concept of a composite gauge boson is this: It does not appear at all in the fundamental Lagrangian of the theory (in the same way that other composite objects do not appear there). It does appear in the low-energy effective Lagrangian together with all other composite particles. Here we would like to study whether some of the gauge bosons may appear as composites in this sense.

In a hypercolor composite model, the hypergluon must clearly appear as a fundamental massless gauge field in the underlying Lagrangian. It will not appear at all in the low-energy Lagrangian. What about the gluon, photon and weak bosons? Consider first the massless gauge bosons (gluon and photon). If an exactly massless gauge boson appears in the low-energy effective Lagrangian, the Lagrangian must be exactly gauge invariant under the corresponding gauge group. This gauge invariance cannot be broken by higher dimension terms which are proportional to Λ_H^{-N} (N positive). If no small corrections of any kind are allowed to break the exact gauge invariance of the effective Lagrangian, it is essentially unavoidable that the original underlying Lagrangian also possesses the same local gauge symmetry. But in that case, it would probably contain the corresponding massless gauge bosons as fundamental fields. We therefore suspect that the gluon and the photon are not composite. They have the same status as the hypergluon in the underlying Lagrangian which must now be gauge invariant at least under $SU(N)_H \times SU(3)_c \times U(1)_{EM}$.

The above argument does not necessarily apply to the massive W and Z weak bosons. The weak gauge symmetry of the effective Lagrangian could be an approximate symmetry, broken by higher dimension terms which vanish as $\Lambda_H \to \infty$. It is conceivable that this approximate gauge symmetry is not fully present at the underlying level. In fact, the longitudinal components of W and Z are "born" from the scalar fields which are probably formed as condensates of the fundamental fermions. In some sense, at least the longitudinal W and Z must be composite in such a scheme.

The possibility of composite W and Z which do not appear in the underlying Lagrangian is extremely interesting. It leads to exciting consequences but also to serious difficulties.

Let us consider a process such as neutrino-neutrino scattering, in a model in which neutrinos are composite. The neutrino carries no

hypercolor, color or electric charge. However, it must contain objects which possess at least hypercolor, possibly even color. At short distances of order Λ_H^{-1}, the two scattered neutrinos must experience a short range residual hypercolor force. Even if the nature of the binding force of the constituents is different, and even if it is not a color-like interaction, we still expect a short-range residual interaction between two composite neutrinos. One way of parametrizing this short-range force is in terms of the exchange of the lightest bosonic bound states of the same fundamental constituents. If W and Z are such composite states, their exchange may control the longest-distance component of the residual short-range force. In that case, the conventional weak interactions are identified as a residual effect[25] of the original hypercolor force (or any other fundamental binding force inside the neutrino). The weak interactions are then eliminated from the list of fundamental interactions in the same way that hadronic interactions are residual color forces.

If the photon is fundamental but W and Z are composite, how do we understand the "unified" electroweak theory of the standard model? In the standard model, the electromagnetic and weak interactions are not fully unified. Their relative strength remains an arbitrary parameter, related to $\sin^2\theta_W$. The standard model provides us with a clear mechanism for γ-Z^o mixing which could be somewhat analogous to the γ-ρ^o, γ-ω^o and γ-ϕ^o mixing of the old "vector dominance" idea. A major difference between the two situations stems from the different order of magnitude of the ρ^o and the Z^o direct couplings. Experimentally, $g^2_{\gamma\rho}\sim 1/300$ while $g^2_{\gamma Z}\sim 1/4$. How can we explain such a difference?

Many authors have discussed this issue during the last year[26]. Their consensus in that there is no difficulty in obtaining a $g_{\gamma Z}$ of the correct order of magnitude, provided that the spacing between Z^o and any higher composite boson is of the order of a TeV or so. That sets another bound or the compositeness scale Λ_H, for the case of a composite Z.

In fact, we may consider two extreme possibilities in theories with composite W and Z bosons:

(i) The compositeness energy scale is relatively low, say, between 1 TeV and 10 TeV. In such a case we may hope to observe experimental deviations from the standard model predictions for the properties of W and Z. Such a deviation could be seen in the W/Z mass ratio, W magnetic moment, small violations of universality, etc. For $\Lambda_H\sim 1$ TeV, the effects could probably be detected within the next decade (but the model should cope with all the constraints of figure 1, a highly nontrivial requirement!)

(ii) The compositeness scale is $\Lambda_H \gg M_W$ (say, above 100 TeV). In such a case L_{EFF} should be extremely close to L_{SM} and no experimental effects can be observed in the near future. In that case, however, we must face a new puzzle: If $\Lambda_H \gg M_W$, what symmetry principle protects M_W and M_Z from obtaining higher order mass corrections which would lift them up to the order of magnitude of Λ_H? So far no one has proposed a convincing reason for a small mass of a composite W or Z boson. In the absence of such a reason, the possibility $\Lambda_H \gg M_W$ appears to be unlikely.

Needless to say, there is a continuum of possible Λ_H-values. The lower Λ_H is, the sooner we can detect deviations from the standard model . For smaller Λ_H it is easier to understand the value of M_W but it is more difficult to construct a model which survives all the tests of figure 1.

We therefore conclude that the possibility of composite W and Z bosons is interesting, but serious difficulties exist, especially for large Λ_H-values.

12. Summary and Outlook.

We conclude with four statements:

(i) At present, there is no experimental evidence for quark or lepton compositeness. Both high energy and low energy experiments should continue to search for such evidence. Experimentalists should probably ignore specific theoretical composite models and concentrate on pushing the various experimental limits until some new effects are discovered.

(ii) There is strong circumstantial evidence for the compositeness of quarks and leptons. In view of the lack of experimental clues, it is perhaps too early to demand a serious self-consistent theoretical model.

(iii) There is no satisfactory theoretical model of composite quarks and leptons. However, the models proposed so far contain many interesting new ideas. Each of these ideas should be investigated on its own merit, regardless of the detailed model which may have led to it. Several correct ingredients of the correct theory may already be with us now.

(iv) We have hardly begun to investigate the subject of compositeness. It is almost unavoidable that the next decade or two will bring new experiments, new theoretical ideas as well as new difficulties for quark and lepton compositeness. The subject will certainly stay with us for a long time. It is not at all clear whether by the end of the century (and the millenium) we will know whether the electron is composite.

Acknowledgement

I would like to thank Nathan Seiberg for a long and fruitful collaboration and for many helpful discussions.

References

1. See e.g. H.Harari, Proceedings of the Jerusalem Einstein Symposium, 1979.
2. S.Weinberg, Phys. Rev. D19,1272(1979); L.Susskind, Phys. Rev.D20,2619(1979).
3. For a review see e.g. E.Farhi and L.Susskind, Phys. Reports, 74C,277(1981).
4. H.Georgi and S.L.Glashow, Phys. Rev. Letters, 32,438(1974); J.C.Pati and A.Salam, Phys. Rev. D8,1240(1973); D10,275(1974).
5. See e.g. E.Farhi and L.Susskind, Phys. Rev. D20,3404(1979).
6. For a review see e.g. B.Zumino, to be published in Proceedings of the 1982 Solvay Conference, Austin, Texas, Nov. 1982.
7. G.L.Shaw, D.Silverman and R.Slansky, Phys. Letters 94B,57(1980); S.J.Brodsky and S.D.Drell, Phys. Rev. D22,2236(1980).

8. E.Eichten, private communication.

9. See e.g. H.Harari and N.Seiberg, Nuclear Phys. B204,141(1982).

10. See e.g. D.A.Dicus, E.W.Kolb, V.L.Teplitz and R.V.Wagoner, Phys. Rev. D18,1829(1978).

11. H.Harari, R.N.Mohapatra and N.Seiberg, Nuclear Phys. (in print).

12. J.C.Pati and A.Salam, Phys. Rev. D10, 275(1974).

13. G.'tHooft, Proceedings of the Cargese Summer Institute, 1979.

14. S.Raby, S.Dimopoulos and L.Susskind, Nuclear Phys. B173, 208(1980).

15. See e.g. S.Coleman and E.Witten, Phys. Rev. Letters 45,100(1980).

16. Y.Frishman, A.Schwimmer, T.Banks and S.Yankielowicz, Nuclear Phys. B177,157(1981).

17. H.Harari and N.Seiberg, Phys. Letters 115B,450(1982).

18. J.C.Pati, Phys. Letters, 98B,40(1981).

19. See e.g. E.Witten, to be published in Proceedings of the Banff Summer Institute, Banff, Alberta, Canada, August 1981.

20. See e.g. S.L.Adler, Phys. Rev. D21,2903(1980).

21. See e.g. W.A.Bardeen and V.Visnjic, Fermilab-Pub 81/49-THY, 1981.

22. See e.g. A.Davidson and K.C.Wali, Phys. Rev. Letters 26, 691(1981).

23. H.Harari and N.Seiberg, Phys. Letters 102B,263(1981).

24. H.Harari and N.Seiberg, Phys. Letters 98B,269(1981); Nuclear Phys. B204,141(1982).

25. H.Harari and N.Seiberg, ref.24; O.W.Greenberg and J.Sucher, Phys. Letters 99B,339(1981).

26. See e.g. J.J.Sakurai, Munich preprint MPI-PAE/TH 22/32; P.Cnen and J.J.Sakurai, Phys. Letters 110B,481(1982); R.Barbieri and R.N.Mohapatra, CCNY - HEP - 82/14; H.Fritzsch and G.Mandelbaum, Phys. Letters 109B, 224 (1982); M.Kuroda and D.Schildknecht, CERN preprint, TH-3395; H.Fritzsch, D.Schildknecht and R.Kogerler, CERN preprint TH-3264.

Electron-Proton Colliding Beams

The Physics Programme and the Machine

B.H.Wiik

II. Institut für Experimentalphysik, University of Hamburg

and

Deutsches Elektronen-Synchrotron DESY, Hamburg, Germany.

© B.H. Wiik 1982

1. Introduction
2. Electron-Proton Interactions at High Energies
3. Description of an Electron-Proton Colliding Beam Facility
4. The Transverse Motion
5. Magnet Imperfections and Resonances
6. The Synchrotron Motion
7. Effects of the Synchrotron Radiation on the Single Particle Motion
8. Polarisation
9. Current Limitations
10. Layout and Performance of HERA

1. Introduction

At present we have a simple and appealing picture of nature. At distances down to 10^{-16} cm, the smallest distances explored, experiments have shown that matter is made of two species of fundamental, pointlike fermions, quarks and leptons. The weak, electromagnetic and strong force which act between these constituents is described by gauge fields and is mediated by the exchange of gauge bosons. These forces might result from a single force; there is strong indirect evidence that the weak and the electromagnetic force coalesce into a single electroweak force at center-of-mass energies above 100 GeV, this electroweak force may be unified with the strong force at c.m. energies on the order of 10^{15} GeV.

Much of the experimental basis for our present understanding of nature results from deep inelastic lepton-hadron experiments. Examples are the discovery of quarks as physical entities, the first indirect evidence of gluons, the carriers of the strong force, and the discovery of the neutral weak current. The lepton-hadron interaction can be studied at center-of-mass energies well above the electroweak unification energy of 100 GeV by colliding electrons and protons in a two ring colliding beam facility.

The possibility of colliding electrons and protons was first considered by Hereward et al.[1] and further investigated by Goldzahl and Michaelis[2] as an option for the ISR. The discovery of pointlike constituents in deep inelastic electron proton scattering prompted joint LBL-SLAC group[3] to investigate a dedicated electron-proton colliding beam facility in more detail. The study showed that the

center-of-mass energies and expected luminosities for such a facility would be sufficient to investigate deep inelastic processes in the kinematic range where the electromagnetic and weak interaction are expected to be of similar strength. This is well outside the reach of available and proposed fixed target machines. Since then similar studies[4] have been carried out in nearly all high energy laboratories, however, they have not led to the construction of an electron-proton colliding beam facility.

At present several proposals to construct electron-proton facilities are ready for decision.

DESY has proposed to construct HERA[5], a dedicated electron-proton colliding beam facility, on a site joining the present site. HERA is designed to collide 820 GeV protons with 30 GeV electrons in four interaction regions yielding 314 GeV in the center of mass which is equivalent to the kinematical region covered by a 52 TeV fixed target machine. The maximum momentum transfer squared is 98400 GeV^2. The predicted luminosity at 314 GeV in c.m. is $6 \cdot 10^{31} cm^{-2} s^{-1}$. The project has been submitted to the German Government and recommended for construction by a review panel. The project can be completed late 1989 if authorized in 1983.

KEK plans to construct Tristan[6] designed to collide 25 GeV electrons with 300 GeV protons in three interaction regions. The maximum momentum transfer squared is $3 \cdot 10^4$ GeV^2 with an expected luminosity of $1.8 \cdot 10^{31}$ $cm^{-2} s^{-1}$. KEK has proposed to first construct an e^+e^- colliding ring capable of reaching 60 GeV in c.m. and this part of the project has been approved. A decision on the ep part is expected after first operation of the e^+e^- ring scheduled for 1985.

In addition to the dedicated facilities, a group of physicists[7] has proposed to collide 5 GeV electrons with the proton beam from FNAL Tevatron. A decision on this proposal has been postponed and will be considered at a later date. The same group has also proposed[7] an ep option for ISABELLE.

CERN has the option[8] of colliding the electrons in LEP with the protons in the SPS in one interaction region. This option yields a maximum momentum transfer squared of $5.4 \cdot 10^4$ GeV^2 and a predicted luminosity of $4 \cdot 10^{29}$ $cm^{-2} s^{-1}$ in the parasitic mode and $1.3 \cdot 10^{31}$ $cm^{-2} s^{-1}$ when both LEP and SPS are operating only for ep collisions.

In these lectures I'll first discuss the physics programme which can be carried out at a large electron - proton colliding beam facility, and from this discussion we will derive some of the constraints which physics impose on the machine parameters.

In the main part of my talk I'll review the physical principles of circular accelerators. Since this is perhaps a new topic to most of you, I have tried to be pedagogical and have borrowed freely from the excellent literature[9,10,11,12] available. A more in depth treatment including a complete set of references to the original work can be found in the literature listed above and in the references listed at the beginning of each chapter.

M.Sands[9] has given a translucent discussion of the physical principles of an e^+e^- colliding ring and J.LeDuff[13] has very ably reviewed the same subject in the previous SLAC summer school. In these lectures we will therefore put more emphasis on the behaviour of the protons and the problems associated with colliding electrons and protons.

This part of the lecture begins with an overview of an electron-proton colliding beam facility using HERA as an example. The physics of such a facility is then reviewed in more detail starting out with the transverse and longitudinal motion of a single particle in the magnetic guide field and the accelerating r.f. field. The influence of the synchrotron radiation on the single particle motion is discussed next. How to obtain transversely polarised electron and how to transform this into a longitudinally polarised electron beam in the interaction point is described in chapter 8. Limitations on the stored current caused by various kinds of instabilities are reviewed in chapter 9. HERA is discussed in more detail in the last chapter, with emphasis on the layout of the interaction region and the optimalisation of the luminosity.

2. Electron-proton Interactions at High Energies

2.1 Introduction

It has been shown experimentally that the proton contains point-like quarks confined by the strong interaction and that an electron incident on a proton interacts directly with one of these quarks in accordance with Fig. 2.1. The interaction between a lepton and a quark is mediated by a neutral or charged spacelike current. The variables and the kinematic of the process is defined in Fig. 2.1.

The physics programme[14] at an ep collider may be summarized as follows:

1. Determine the properties of the spacelike electroweak current at a mass which is large compared to the characteristic mass of the weak interaction. Measurements with electrons and positrons in well defined helicity states can be used to determine the properties of both charged and

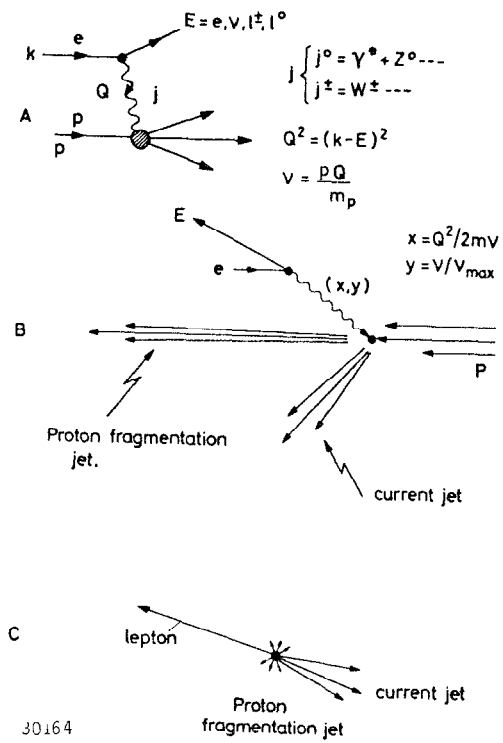


Fig. 2.1 Kinematics of deep inelastic electron proton collisions.

neutral currents in detail. For example, measurements with left handed positrons or right handed electrons are very sensitive probes for new weak currents.

2. Use the local, well defined electroweak current to explore the proton at distances down to 10^{-17} cm. Measurements of the structure functions will pose stringent tests of our present understanding of strong interaction. Such measurements may also reveal new constitu-

ents of the proton or they may show that quarks are composite objects.

3. Search for new phenomena. Examples are the search for free quarks, for supersymmetric particles, and for elementary particles with combined lepton and baryon numbers, the leptoquarks.

This programme demands a large kinematical area. The kinematical region available with HERA is equivalent to that of a 52 TeV fixed target machine and is shown in Fig. 2.2. The scale is set by the black dot in the left hand corner representing the region which can be explored using a 1 TeV muon or neutrino beam on a fixed target. Lepton beams with somewhat lower energies will become available at the Tevatron[15] in 1983. It is clear that HERA opens a new kinematical region well outside that available with present or planned fixed target machines.

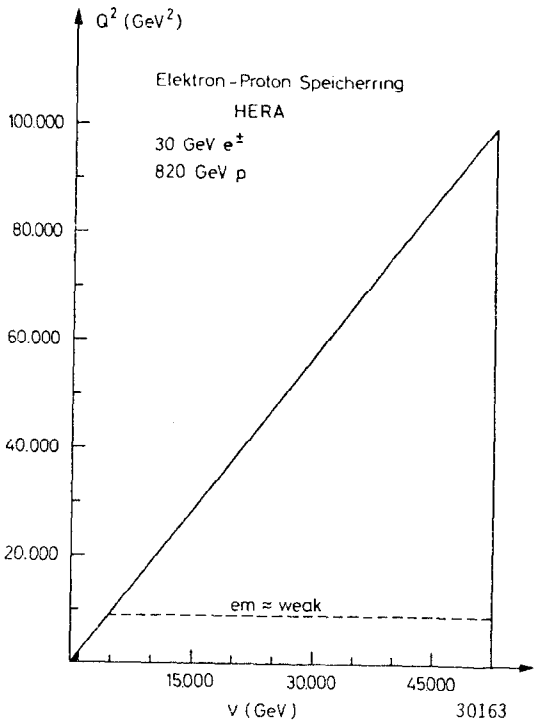


Fig. 2.2
Kinematical region in Q^2 and ν which can be explored with HERA.

The Q^2-value corresponding to the characteristic mass of the weak interaction squared is shown as the dotted line. A large kinematical region is available beyond this Q^2-value.

The final state topology in deep inelastic electron-proton interactions is striking and easy to recognize. As indicated in Fig.2.1b and 2.1c the scattered lepton appears at a large angle with respect to the beam axis and the corresponding transverse momentum is balanced by the struck quark which fragments into a jet of hadrons appearing at large angles on the opposite side of the beam axis. The remains of the proton give rise to a forward jet of hadrons focused along the proton beam axis with no net transverse momentum. Because of the imbalance between incident electron and proton momenta the particles will in general emerge in the forward hemisphere along the proton direction. The proton jet, the quark jet and the lepton defines a plane with small momenta transverse to the plane and large momenta in the plane.

The kinematic of the final lepton and of the current jet at nominal HERA energies of 30 GeV electrons on 820 GeV protons is shown in Figs.2.3a resp.2.3b. For a given Q^2 and x, the energy and the angle of the lepton, respectively, the current jet in the laboratory system is ob-

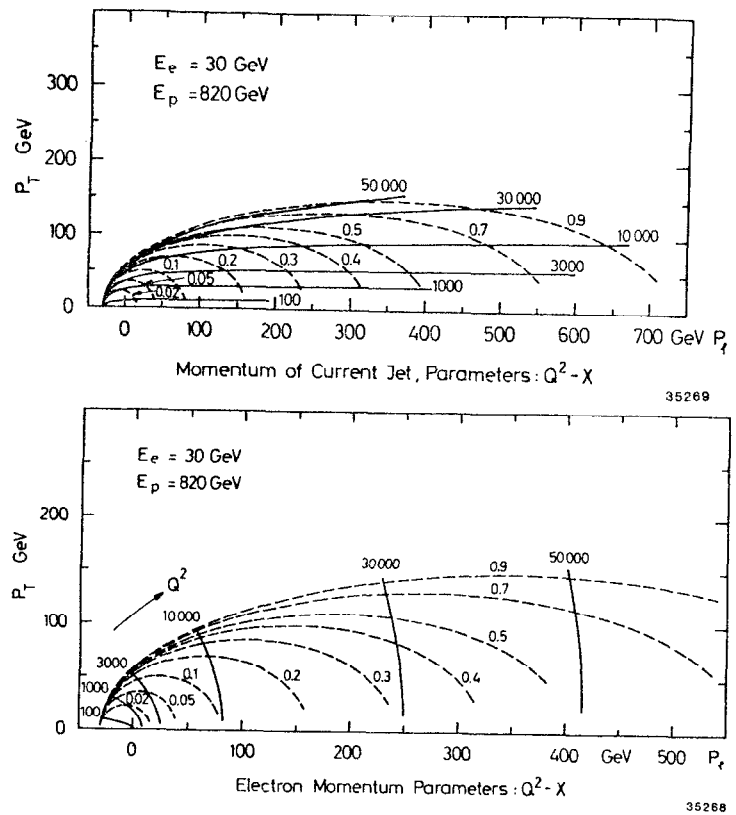


Fig. 2.3a,b - The laboratory momenta of the final lepton and the current jet with Q^2 and x as parameters. The laboratory angles and energies can be read off directly by connecting points with a given x and Q^2 with the origin.

tained by joining the relevant points with the origin. Note that the laboratory angles of the lepton and the current jet are in general large. Lowering the incident electron energy will focus the final state particles more strongly along the proton direction until particles belonging to the current jet are lost down the beam pipe. In this case Q^2 and x cannot be reconstructed from the current jet alone making it impossible to measure the form factors of the charged current.

Simply on the basis of topology it seems unlikely to confuse a deep inelastic electron-proton event with a background event such that the accessible Q^2-range appears not to be limited by the background. Note that particles from the lepton vertex and the quark vertex are kinematically well separated. In the standard model[16] only single neutrinos or electrons are allowed at the lepton vertex, such that the observation of jets emerging from the lepton vertex is a clear indication of new physics. It will therefore be possible to observe very rare exotic processes possessing this signature.

The Q^2-range which can be investigated is therefore only dependent on the rate - i.e. on the luminosity and the center-of-mass energy. In Fig. 2.4 the average luminosity needed to produce 100 charged current events a year with $Q^2 > Q_o^2$ is plotted versus Q_o^2 for various values of the center-of-mass energy. The year is assumed to have 5000 hrs and the rate is evaluated in the standard model with

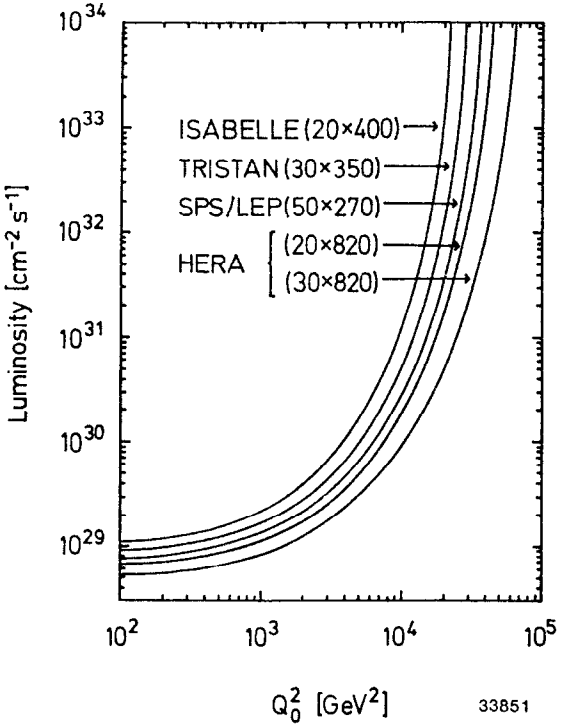


Fig. 2.4 - The average luminosity needed to produce 100 charged current events with $Q^2 > Q_0^2$ in 5000 hrs (1 year) of data taking versus Q_0^2 for various center-of-mass energies.

one charged vector boson. It is possible to explore Q^2-values up to say 3000 GeV^2 with a luminosity as low as $2 \cdot 10^{29}$ cm^{-2}s^{-1}. To produce 100 charged current events with $Q^2 > 10\,000$ GeV^2 per year requires a luminosity of $1.5 \cdot 10^{30}$ cm^{-2}s^{-1} - a factor of 40 below the HERA design luminosity. To obtain the same number of events with $Q^2 > 10\,000$ GeV^2 by colliding 20 GeV electrons with 400 GeV protons requires an average luminosity of $3 \cdot 10^{31}$ cm^{-2}s^{-1} - a factor 20 higher than the luminosity required at HERA. Note that for a luminosity of 10^{32} cm^{-2}s^{-1} we expect 100 events a year with $Q^2 \gtrsim 35\,000$ GeV^2.

2.2 Low Q^2-physics

The electron beam at HERA is equivalent to a well collimated bremsstrahlungsbeam with an endpoint energy of 52 TeV. The untagged photon-proton luminosity is typically on the order of a few percent of the electron-proton luminosity yielding some 10^7 hadronic events per day.

The photon has a dual character, it may convert into a vector meson and interact like a hadron. However, it has also a pointlike part and may induce hard processes like deep inelastic Compton scattering and the QCD analogues of Compton scattering and Bethe-Heitler processes as indicated in Fig. 2.5. Note that the QCD Bethe-Heitler process can be used to measure the gluon structure function (q = u,d,s) and to search for heavy quarks. A total of 10^5 $c\bar{c}$ pairs are expected to be produced per day at HERA via the QCD Bethe-Heitler process and some 20 $t\bar{t}$ pairs if $m_t = 50$ GeV.

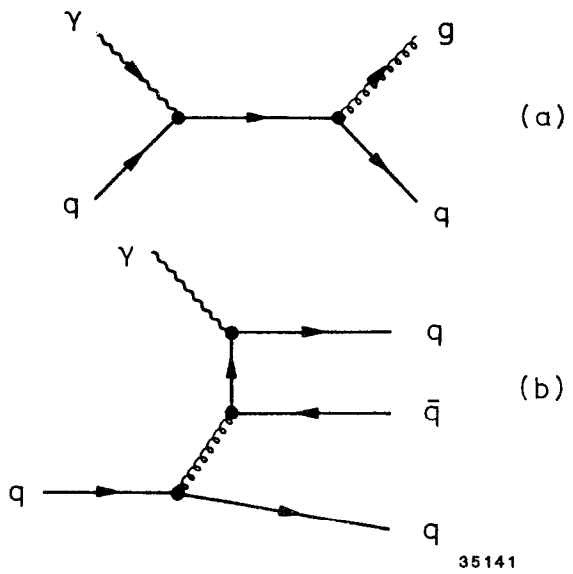


Fig. 2.5 - Hard processes induced by the pointlike part of the photon a) QCD Compton b) QCD Bethe-Heitler.

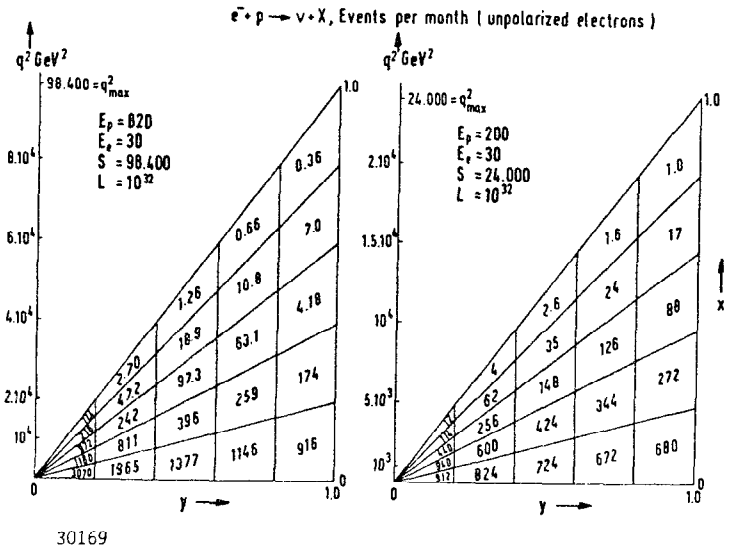
2.3 Properties of the currents

2.3.1 Charged currents

Present data are all consistent with a left handed current which is mediated by a single charged vector boson with a mass around 80 GeV. The observed simplicity of the charged current might well only reflect the static limit studied so far and a rich structure with many vector bosons, some perhaps giving rise to right handed currents, might appear at high energies. From a purely experimental point HERA has some unique features compared to present fixed target experiments.

- Very high energy.
  The beam is equivalent to a monoenergetic neutrino beam with an energy up to 52 TeV.
- Choice of helicity.
  It will presumably be possible to change the helicity of the incident lepton - i.e. the cross section for left and right handed electrons (or positrons) can be measured directly.
- Visibility.
  The target is massless and can be surrounded by fine grained detectors including particle identification.
- Favourable kinematics.
  The lepton, the current jet and the target fragmentation jet are presumably well separated in space and the event is easily recognized.

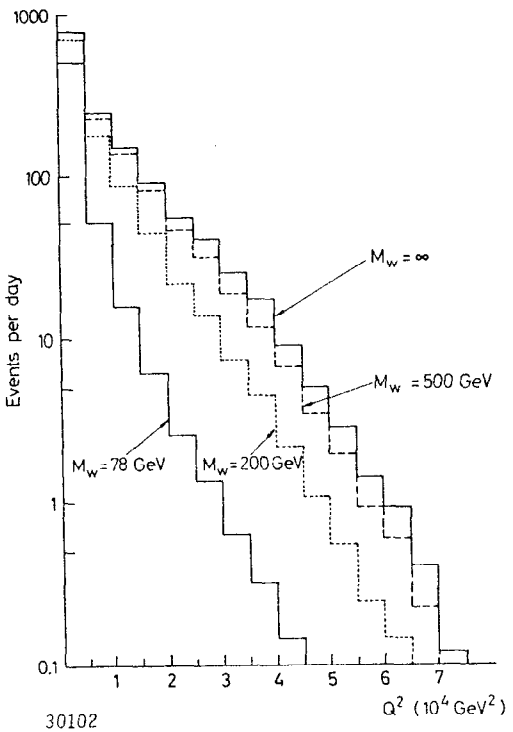
The x, y distribution of charged current events in bins of $dxdy = (0.2)^2$ expected after one month of data taking with an unpolarised 30 GeV electron beam colliding with protons of 820 GeV is shown in Fig. 2.6. The rates were estimated in the standard model[16] with m_W = 78 GeV and formfactors parametrized according to Buras and Gaemers[16] and assuming a luminosity of 10^{32} cm^{-2}s^{-1}. Given the distinct signature of charged current events it seems possible to explore nearly the entire kinematic region.



30169

Fig. 2.6 - Number of charged current events in bins of dxdy = $(0.2)^2$ produced per month of data taking assuming the standard model and a luminosity of $10^{32}cm^{-2}s^{-1}$. To obtain the number of events expected per year of data taking at the nominal HERA luminosity using left handed electrons multiply the left plot with a factor 8 and the right hand plot with a factor 5.

The expected number of events per year for the reaction $e_L^- + p \to \nu + x$, evaluated with the assumptions listed above, is plotted in Fig. 2.7 versus Q^2 for various propagator masses. It is clear that the mass of the propagator can be measured as long as it is below 500 GeV. The data can also be used to determine whether the charged current is damped by a single vector boson as presently believed or by several.



30102

Fig. 2.7

Events per day for $e^- + p \to \nu + x$ in Q^2 bins of 5000 GeV^2 with the standard assumptions.

Right handed currents do not occur in the standard model. Sensitive searches for these currents may be carried out using right handed electrons and left handed positrons. Such measurements will reveal the existence of right handed currents if the mass of the right handed propagator is less than 600 GeV and the longitudinal beam polarisation is at least 80% known to an accuracy of 1%. This mass limit is valid even if the electron is partnered with a massive neutrino in a right handed doublet.

At $x > 0.4$ only valence quarks contribute to the cross section – i.e. $e^- + u \to d + x$ and $e^+ + d \to u + x$ are the dominant processes. This makes it possible to study the fragmentation of a well defined flavour. However, in principle it also opens the possibility of measuring the Kobayashi-Maskawa mixing angles[17] directly:

$$e^- + u \to s + x \quad \text{and} \quad e^- + u \to b + x$$
$$e^+ + d \to c + x \quad \text{and} \quad e^+ + d \to t + x \,.$$

2.3.2 Neutral currents

One photon exchange and Z^0 exchange contribute coherently to $e + p \to e' + x$ and both contributions are of similar strength at HERA energies. Measurements of this process can therefore decide if indeed the electromagnetic and weak interactions are manifestations of a single force and if this unification occurs as conjectured in the standard model[16] or if a more complicated mechanism involving many Z^0's is realized in nature. The number of neutral current events produced per day in a bin $dxdy = (0.2)^2$ is plotted in Fig. 2.8. Again due to the characteristic topology of deep inelastic events HERA can extend the Q^2 range from the present few hundred GeV^2 out to some 40 000 - 50 000 GeV^2.

The presence of a weak current in the amplitude has clear signatures:

1) Parity violation

$$\sigma(e_L^- + p \to e^{-\prime} + x) \neq \sigma(e_R^- + p \to e^{-\prime} + x)$$
$$\sigma(e_L^+ + p \to e^{+\prime} + x) \neq \sigma(e_R^+ + p \to e^{+\prime} + x)$$

This effect can only be caused by a neutral weak current.

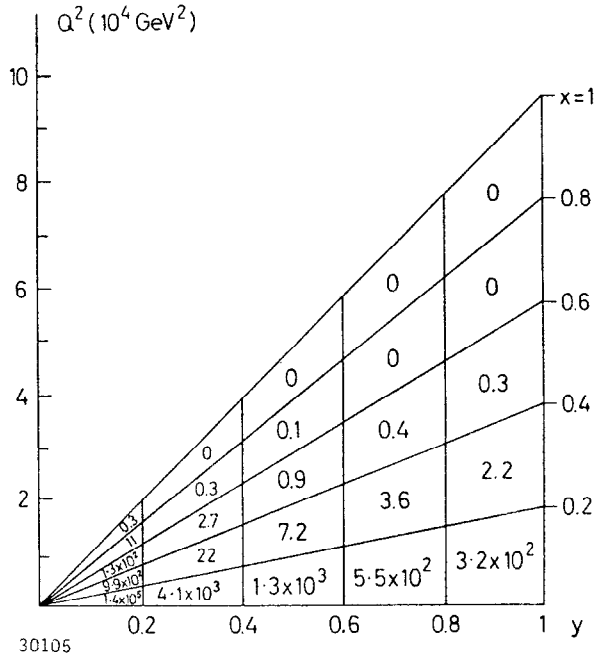


Fig. 2.8 - Number of events per day for $e^- + p \to e^- + x$ at $s = 9.6 \cdot 10^4$ GeV^2 and the standard assumptions.

2) Apparent C-violation

$$\sigma(e_L^- + p \to e^{-\prime} + x) \neq \sigma(e_L^+ + p \to e^{+\prime} + x)$$
$$\sigma(e_R^- + p \to e^{-\prime} + x) \neq \sigma(e_R^+ + p \to e^{+\prime} + x)$$

Two-photon exchange will also give rise to a charge asymmetry. This effect, however, is expected to be of order $\alpha/\pi \ln (Q^2/m^2)$ with $m \sim 300$ MeV. At large values of Q^2 this effect is small compared to the charge asymmetry caused by Z^0 exchange and it has furthermore a different Q^2 dependence.

3. The presence of a $1 - (1-y)^2$ term which is not allowed in the one photon exchange approximation. This effect cannot be caused by two photon exchange.

The size of these effects in the standard model is shown in Fig. 2.9 where the ratio

$$\frac{\sigma(\gamma + z^0)}{\sigma(\gamma)}$$

evaluated for left and right handed electrons and positrons is plotted as a solid line versus y for x = 0.25.

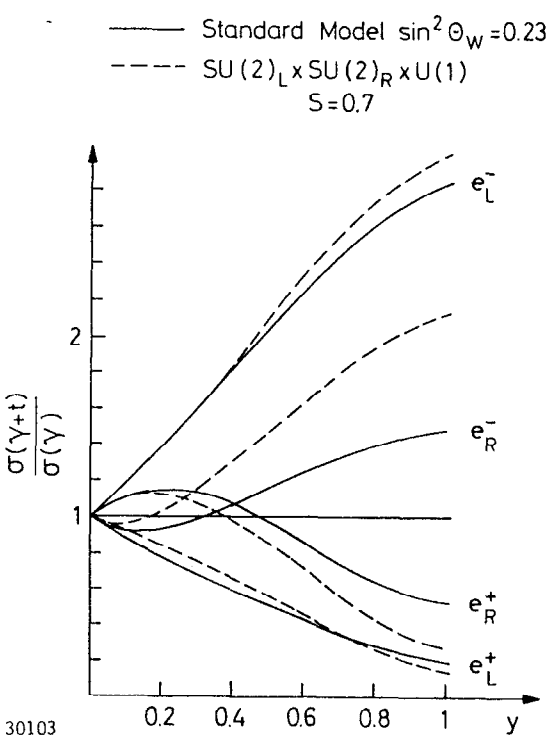


Fig. 2.9

The ratio $\sigma(\gamma+z^0)/\sigma(\gamma)$ plotted versus y for x = 0.25. The ratio is evaluated for two different weak interaction models.

The neutral current measurements at HERA are complementary to measurements at SLC and at LEP. For example it is easy to construct a scenario in which the Z^0 peak is not observed in e^+e^- annihilation but propagator effects are seen in deep inelastic $e + p \to e' + x$.

The most trivial explanation would be to assume that the Z^0 peak is washed out by a large number of $\nu\bar{\nu}$ decays. A perhaps more exciting possibility has been put forward by Abbott and Farhi[19]. Usually $g_2^2/4\pi \ll 1$, where g_2 is the SU(2) coupling constant and hence SU(2) does not confine. Abbott and Farhi suggest that perhaps $g_2^2/4\pi$ is of order one and that SU(2) indeed does confine leading to composite fermions and bosons. Since

$$\frac{G_F}{\sqrt{2}} = \frac{g_2^2}{8m_W^2}$$

this would imply that the vector bosons in such a model are much heavier than the vector bosons in the standard model.

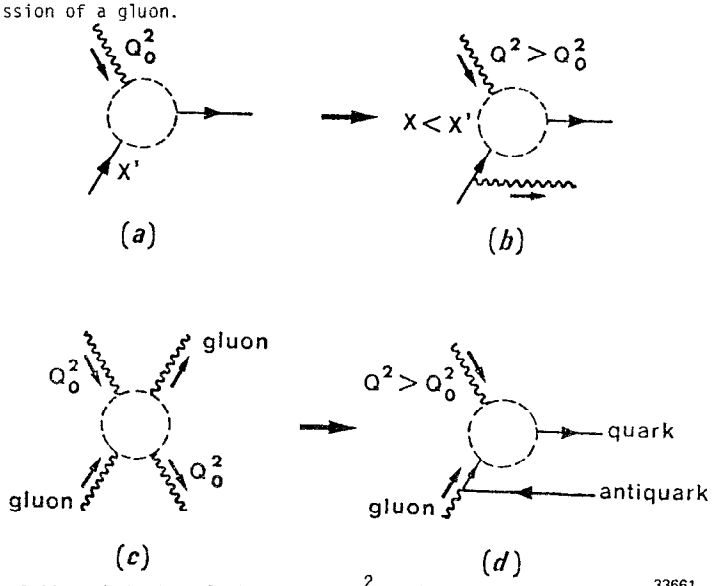
Flavour changing neutral currents like $e^- + d \to \tau^- + b$ may appear. In the example above the τ decay products will emerge on the lepton side instead of a single lepton. Such events would be spectacular and easy to observe.

2.4 Exploring the Proton

Measurements of the total electroweak cross section at values of Q^2 between a few GeV^2 and a few hundred GeV^2 have revealed[20] that the proton is made of pointlike fermions, the quarks. At short distances the quarks behave like free particles, yet the proton cannot be "ionized." The measurements further show that the quarks account for about a half of the proton momentum, the other half being car-

ried by particles with only strong charge.

Measurements[21] at increasing values of Q^2 showed that the form factors are enhanced at low and depleted at high values of x. This observation is naturally explained in any field theory of strong interactions as shown schematically in Fig. 2.10. The resolving power of a spacelike electroweak current increases with Q such that the proton may be probed at shorter and shorter distances. Thus we may "see" the quark content of the gluon, or the quark after the emission of a gluon.



33661

Fig. 2.10 - a) A virtual photon with Q_0^2 striking a quark.
b) A virtual photon of higher Q^2 resolving the quark into a quark and a gluon.
c) A virtual photon with Q_0^2 traversing a gluon without interaction.
d) A virtual photon of higher Q^2 resolving the gluon into a quark-antiquark pair.

The experimental observations led to the formulation of Quantum Chromodynamics[22]. In this theory the strong interaction is mediated by eight coloured massless vector bosons, the gluons. The strong coupling constant α_s decreases with increasing values of Q^2 as

$$\alpha_s (Q^2) = \frac{12\pi}{(33 - 2n_f) \ln Q^2/\Lambda^2}$$

where n_f is the number of flavours and Λ the characteristic mass of the strong interaction.

The Q^2-evolution of the form factors can be unambiguously computed in QCD. The result of such an computation is shown schematically in Fig. 2.11. Careful measurements of the cross section over wide range in Q^2 are needed to distinguish the logarithmic scaling violations inherent in QCD from a power series as would occur in a fixed point theory.

The correction factors needed to extract the cross section from the raw data must be small in order to determine the form factors with the required relative precision of a few percent. The results of a Monte Carlo calculations for charged current events are shown in Fig. 2.12. Plotted is the ratio between the extracted form factor and the input form factor for values of Q^2 between 6 and 40 000 GeV^2. Note that for the HERA parameters the ratio approaches one - i.e. only small corrections must be applied to the raw data. This is no longer true if the electron energy is lowered say to 5 or 10 GeV keeping the proton energy fixed at 800 GeV. In this case hadrons from the current jet are lost down the beam pipe causing large corrections.

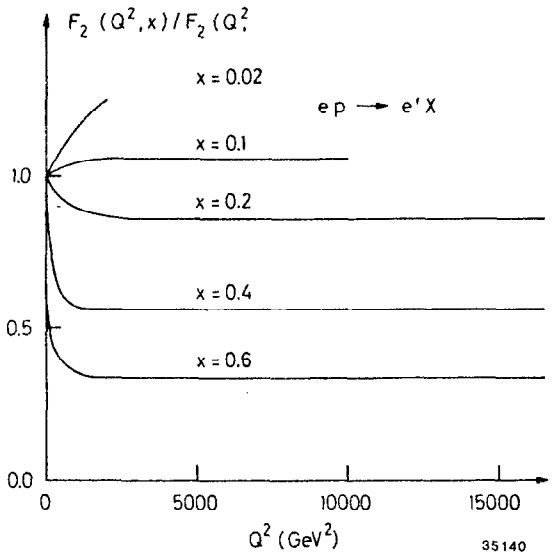


Fig. 2.11
The Q^2 dependence of the formfactors. plotted is the ratio $F_2(Q^2)/F_2(2,x)$ versus Q^2 for various values of $x = Q^2/2m\nu$.

The slow variation of the form factors with Q^2 as predicted in field theories makes it easy to search for new phenomena which may show up as scaling violations. Some possible sources of non QCD scaling violations are:

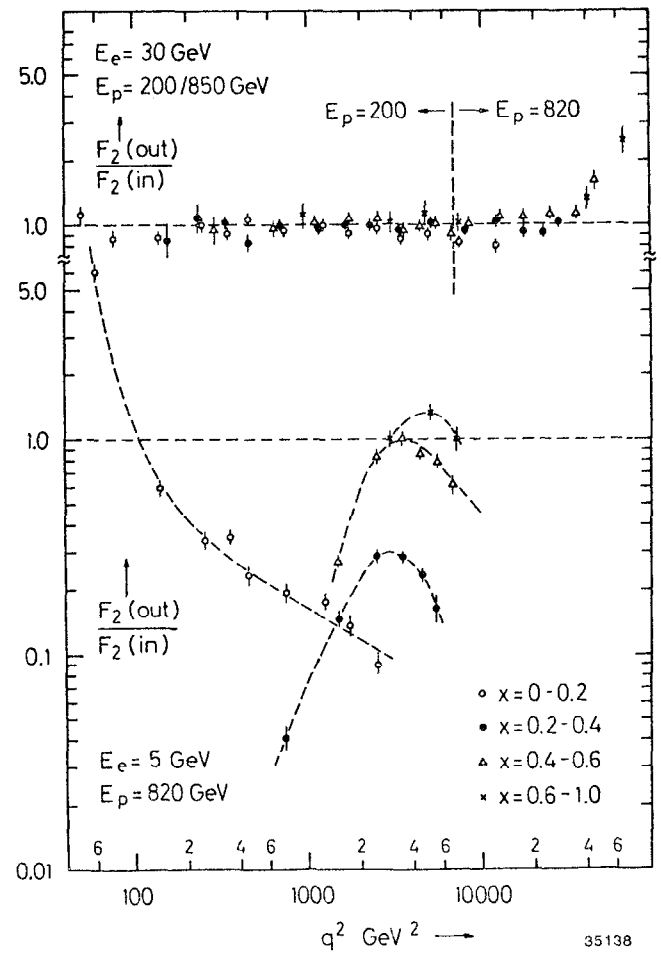


Fig. 2.12 - The correction factor which must be applied to be raw charged current data to extract the form factor $F_2(Q^2,x)$. Shown are the results of a Monte Carlo calculation of the ratio $F_2(out)/F_2(in)$ for various values of x plotted versus Q^2.

New constituents in the proton. For example in supersymmetric models[23] the protons must contain, besides the normal quarks and gluons, scalar quarks and fermion gluinos. Thus the fraction of the momentum carried by the normal quarks will decrease at large values of Q^2 since the total proton momentum is now shared amongst more constituents. Scalar quarks will also contribute to the longitudinal form factor $F_L(x, Q^2) = F_2(x,Q^2) - 2xF_1(x,Q^2)$. Again precision measurements over a wide range in Q^2 are needed to extract information on new constituents.

Quarks and leptons may have finite size. Faced with the large number of leptons and quarks many physicists find it natural that these particles are composite[24] made of new building blocks. With HERA we can probe the fermion structure down to 10^{-17} cm. If the leptons have a size we would expect to observe a leptonic form factor and ultimately the production of excited leptons. The cross section would be modified by a form factor $F(Q^2) = \frac{1}{(1 + q^2/M^2)}$ giving rise to a scaling violation which is very different from that expected in QCD. A 10% measurement at $4 \cdot 10^4$ GeV^2 would be sensitive to a mass of the order of 1 TeV.

An excited lepton could decay into $e + \gamma$, $e + Z^o$ and $e^{\mp} + W^{\pm}$ leading to peaks in the invariant spectrum. Note that the topology of such a final state with several particles emerging from the lepton vertex makes it easy to find.

The cross section would be modified in a similar manner, if the quark has a structure - i.e. again one might probe down to distances of $(1\ \text{TeV})^{-1}$. In this case the formfactors may increase or decrease depending on the charges and the weak coupling constants of the new constituents.

The colour degree of freedom of quarks may also be excited[25] at small distances, and fractionally charged quarks resolved into integrally charged quarks of different colours:

$$u \to u_r\ (e = 1),\ u_y\ (e = 1),\ u_B\ (e = 0)$$

$$d \to d_r\ (e = 0),\ d_y\ (e = 0),\ u_B\ (e = -1)$$

Thus above the threshold for colour thaw:

$$(\tfrac{2}{3})^2\, u(x) \to \tfrac{1}{3}\,(1^2 + 1^2 + 0^2)\, u(x) = \tfrac{2}{3}\, u(x)$$

$$(\tfrac{1}{3})^2\, d(x) \to \tfrac{1}{3}\,(0^2 + 0^2 + 1^2)\, d(x) = \tfrac{1}{3}\, d(x)$$

In the valence quark approximation the electroproduction cross section would rise by a factor of 1.7. This model also contains charged gluons. The photon may interact with these gluons and this would contribute to the longitudinal cross section.

2.5 New Physics

The combination of high luminosity and the opening of a large kinematical region makes HERA well suited to search for new phenomena. Three obvious examples are discussed below:

2.5.1 New Fermions

Electron-proton collisions are ideally suited to produce electron-like charged or neutral leptons and new heavy quarks which couple to the u or d quarks in the proton. Such couplings are known to be rather weak in the standard model, however, new currents may exist. Indeed if the basic fermions are not pointlike they must have excited states which couple to the ground state. The rate for producing a heavy quark from a light quark is plotted in Fig. 2.13 with the mass of the outgoing lepton as a parameter. The rates were evaluated with the assumptions listed above plus the assumption that the new current couples with the same strength as the old one.

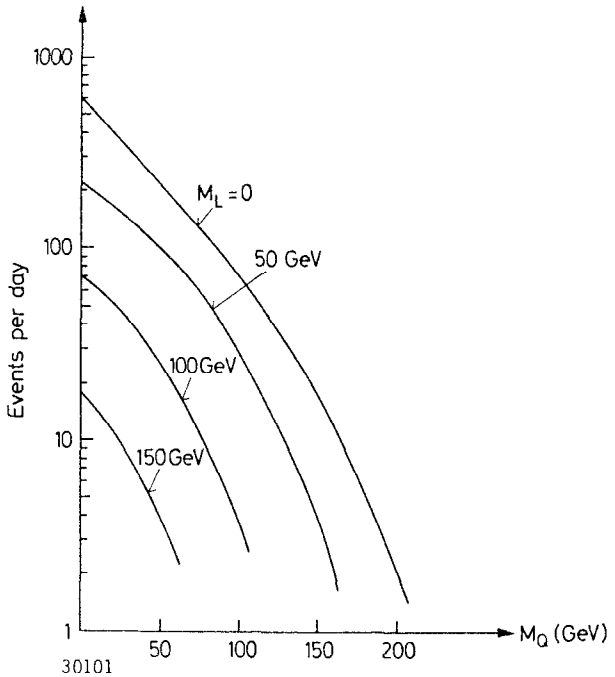


Fig. 2.13 - Number of events per day for $e^- + p \to L^- + Q + x$ at $s = 9.6 \times 10^4$ GeV^2 assuming left handed coupling, unpolarised electrons, m_{W_1} = 78 GeV, Buras-Gaemers parametrization with Λ = 0.5 GeV and a luminosity of 10^{32} cm^{-2}s^{-1}.

Leptons and quarks with masses to 150 - 200 GeV can be found in this way. The decay of these particles leads to rather spectacular signatures on the lepton side: $L^0 \to e^- Q q'$, i.e. the single lepton emerging from the lepton vertex in the standard model will be replaced by a high multiplicity jet containing leptons.

2.5.2 Leptoquarks

It is generally accepted that the gauge symmetry must be spontaneously broken to give mass to the intermediate vector bosons and to make the theory renormalizable. It has been proposed, as an alternative to the standard Higgs mechanism, that the symmetry breaking arises dynamically from the gauge interactions themselves. In this model a new set of unbroken non-Abelian gauge interactions [26] with a mass scale on the order of 1 TeV is introduced. This interaction gives rise to a complicated spectrum of technicolourless bound states with masses starting around 1 TeV. In addition, the technicolour interaction will result in leptoquarks, fundamental particles with combined lepton and baryon numbers and a mass predicted around 160 GeV.

The cross section resulting from the Feynman graphs in Fig.2.14a has been evaluated by Rudaz and Vermaseren[27] and is plotted in Fig. 2.14 versus the mass of the leptoquark. Roughly one event per day is expected for a leptoquark mass of 160 GeV and a suppression factor $\sin^2\theta_{et} \approx 0.05$. The topology of such an event is remarkable with a broad jet, resulting from the decay of the leptoquark $(LQ) \to e\ t$, emerging at the lepton side.

2.5.3 Leptoproduction of supersymmetric particles

Gauging the isospin led to the successful unification of electromagnetic and weak interactions. In supersymmetric[23] theories the same story is repeated for the spin, and this leads to a connection between fermions and bosons. Indeed the fundamental feature of supersymmetry is that it can generate fermions from bosons and vice versa. Thus for every particle with spin J there will in principle

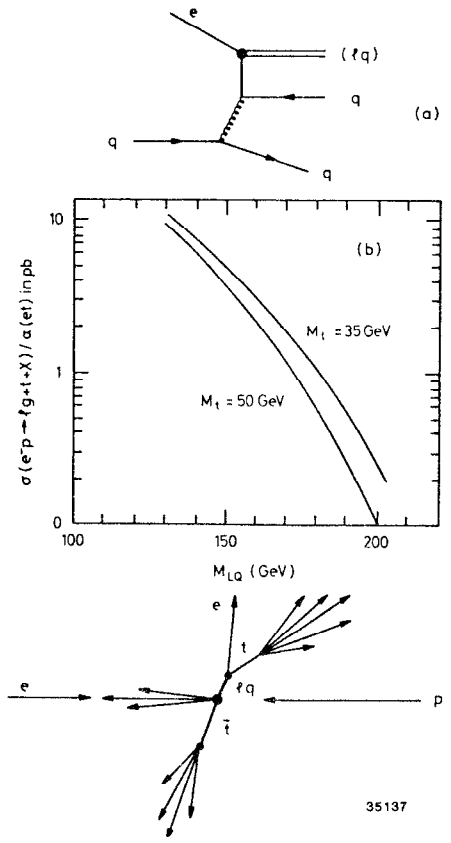


Fig. 2.14 - a) The Feynman graph for producing a leptoquark in deep inelastic ep reactions and the resulting topology.

b) The cross section for ep → (LQ) + x evaluated according to a).

be two new particles with spin J ± 1/2.

A partial list[28] of such new particles is given in Table 2.1.

Table 2.1 - Possible supersymmetric particles

Types of conventional particles	Spin 1	Spin 1/2	Spin 0
Matter		quark q	scalar quarks $\tilde{q}$
		lepton ℓ	scalar lepton $\tilde{\ell}$
Massive Gauge Bosons	$W^{\pm}$,	supersymmetric heavy lepton	Higgs scalar
	Z^0	$\tilde{W}^{\pm}$, $\tilde{Z}^0$, H	H
Massless Gauge Boson		photino $\tilde{\gamma}$	
		nuinos $\tilde{\nu}$	
	g	gluino $\tilde{g}$	

Electron-proton collisions at high energies are well suited to search for supersymmetric particles:

Above threshold scalar quark and scalar leptons can be directly produced[29]

$$e + q \to \tilde{e} + \tilde{q}$$

$$e + q \to \tilde{\nu} + \tilde{q} .$$

The observable mass range for supersymmetric particles depends on the signature. If the scalar leptons decay into a jet of scalar particles then cross sections as low as 10^{-38} cm^{-2} corresponding to 10 events a year may be observable. If the dominant decay modes are of the type $\tilde{\ell} \to \ell + G$ and $\tilde{q} \to q + G$ where G is the undetectable

Goldstino, then the background will be more severe. In standard neutral current events, however, the direction and energies of the scattered lepton and the current jet are strongly correlated. Since in a supersymmetric neutral current event the electron and current jet results from decay processes this correlation is destroyed and the background can to a large extent be eliminated by suitable cuts.

Estimates[26] show that one may probe the mass range up to 100 - 150 GeV for the existence of supersymmetric quarks and leptons.

Scalar leptons can also be searched for in the process $e + p \to e^* + p \to G^0 + e + p \to e^- + p$ + missing energy and neutrino. The signature is very clear with only an electron and a proton in a final state. One should be able to observe this process if the mass of the produced supersymmetric particles is below 100 GeV.

2.6 Summary

To explore the Q^2 region above 10^4 GeV^2 requires center-of-mass energies on the order of 300 GeV or above. In principle the relative electron and proton energies do not matter. However, the Q^2 and ν values of a charged current event must be determined from a measurement of the current jet and such a measurement can only be carried out if the electron energy is not too small. 30 GeV electrons colliding with 800 GeV protons is acceptable ; lowering the electron energy to 5 GeV keeping the proton energy constant is not.

The luminosity must approach 10^{32} cm^{-2}s^{-1} in order to be able to explore the main fraction of the available kinematic region. Note from Fig. 2.4 that the event rate depends on both luminosity and center-of-mass energy - i.e. one may trade luminosity versus center-of-mass energy.

The ability of using electrons and positrons in well defined helicity states is crucial for the determination of neutral current coupling constants and in the search for right handed currents.

3. Description of an Electron-Proton Colliding Beam Facility

In this part we give an overview of an electron-proton colliding beam facility using HERA[5] as an example. Some of the most important parameters are listed in Table 3.1. HERA consists of two circular accelerators, one for electrons (positrons) and one for protons arranged such that the counterrotating electron and proton beams collide in four points along the circumference. The accelerator has a fourfold symmetry; four 360 m long straight sections are joined by four arcs with a geometric radius of 779.2 m yielding a total circumference of 6336 m. The electrons and the protons collide in the middle of the four long straight sections. The layout of the machine is shown in Fig. 3.1.

Each of the circular accelerators is made of the following elements:

A guide field which bends the charged particles on a circular path and provides the necessary focusing to keep the particles transversely bunched over a distance of 10^{10} km. Nowadays most machines are of the separate function type - i.e. the bending by dipole fields,

Table 3.1 - Basic parameters

	p-ring	e-ring	units
Nominal energy	820	30	GeV
$s = Q^2_{max}$	98400		GeV^2
Luminosity	0.6×10^{32}		$cm^{-2}s^{-1}$
Polarization time		20	min
Number of interaction points	4		
Length of straight sections	360		m
Free space for experiments	15		m
Circumference	6336		
Bending radius	603.8	540.9	m
Magnetic field	4.53	0.1849	T
Total number of particles	6.3×10^{13}	0.76×10^{13}	
Circulating current	480	58	mA
Energy range	200 → 820	10 → 35	GeV
Emittance $(\varepsilon_x/\varepsilon_z)$	0.47/0.24	1.6/0.16	10^{-8}m
Beta function β^*_x/β^*_z	3/0.3	3/0.15	m
Dispersion function D^*_x/D^*_z	0/0	0/0	m
Beam-beam tune shift $\Delta Q_x/\Delta Q_z$	0.0006/0.0009	0.008/0.014	
Beam size at crossing σ^*_x	0.12(0.91)**	0.22	mm
Beam size at crossing σ^*_z	0.027	0.013	mm
Number of bunches	210		
Bunch length	9.5	0.93	cm
RF frequency	208.189	499.667	MHz
Maximum circumferential voltage	100***	290	MV
Total RF power	4-6	13.2	MW
Filling time	20	15	min
Injection energy	40.0	14.0	GeV
Energy loss / turn	1.4×10^{-10}	142.3	MeV
Critical energy	10^{-6}	111	keV
Heat loss at 4.3 K	13.2		kW
Lead cooling gas rate	42.5		g/s
Design refrigeration power at 4.3K	20		kW
Design lead gas rate	64		g/s

* At the interaction point
** Including the bunch length
*** 25 MV is foreseen initially corresponding to 1 - 1.5 MW.

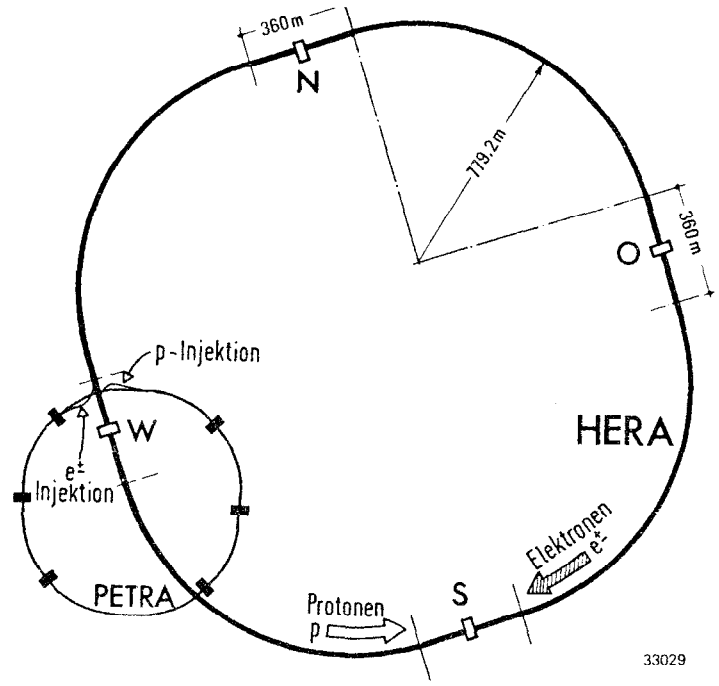


Fig. 3.1 - The layout of HERA.

the focusing by quadrupole fields and the corrections by higher multipole fields are provided by separate elements arranged in a repetitive pattern (cells).

An accelerating system made of a power source (klystron, tetrode) and resonating cavities. Energy is transferred to the particles by the longitudinal electric field oscillating in the cavities at a frequency which is an integer multiple of the particle revolution frequency. The r.f. system is used to accelerate particles from the injection energy to the final energy and - in the case of electrons - to compensate the average energy loss caused by synchrotron radiation. The r.f. system also provides longitudinal focusing of the beam.

A high vacuum system. A particle covers a distance of 10^{10} km during a typical storage time of 10 hrs such that a high vacuum system is mandatory to minimize the losses due to beam gas interactions. A pressure on the order of 10^{-11} torr is needed for the protons. The synchrotron radiation of the electron beam strikes the walls of the vacuum chamber leading to gas desorption which makes it difficult to maintain a pressure below 10^{-9} torr in the electron ring. However, this pressure is sufficient since the oscillation of electrons, excited by beam-gas interactions is damped by synchrotron radiation.

A monitor system to observe the behaviour of the particles and a sophisticated control system to supervise the operation of the accelerator and to take corrective action if needed.

An injection system capable of loading the rings with electrons and protons in a time which is very short compared to the anticipated storage time of several hours. Not only the peak energy but also the minimum usuable energy of an accelerator is limited. For a machine made of superconducting magnets this limit is probably determined by the constant field errors caused by persistent currents in the superconductor. The strength of these higher multipole fields relative to the dipole field increases with decreasing energy and they may well limit the injection energy of the protons to some 5% of the peak energy. The electron beam is rather stable due to the damping caused by the synchrotron radiation. The damping time is proportional to $1/E^3$. Thus the operating range of an electron ring, limited by instabilities at the lower end and by the available r.f. power at the higher end, is rather small compared to the range available for a proton ring. In the case of HERA, a chain consisting of linear accelerators, the DESY synchrotron and PETRA are used to boost the energy of the protons to 40 GeV and the electrons to 14 GeV respectively before injecting into HERA.

An extraction system designed to eject the stored proton beam in a single turn. This is necessary since a localized loss of 10^{-4} of the design current, or some 10^{10} protons, in a magnet at 4.5 T will destroy the superconducting state and lead to a quench. Thus the proton beam must be ejected without a loss at the onset of an instability or at the end of a run.

The interaction region is presumably the most complex part of an electron proton collider. The two beams with rather different properties must be brought into a small angle, low beta (i.e. small

beam spot) collision geometry. The electron spin, which is perpendicular to the orbit in the arcs, must be turned to be either parallel or antiparallel to the beam direction in the interaction point and then be restored to its vertical direction upon entering the arcs. Furthermore the dispersion in the lattice must be made to disappear in the interaction point, and sufficient space for r.f. cavities, injection and ejection systems must be found.

The layout favoured for HERA is shown in Fig. 3.2. The beams cross in the horizontal plane of the electron ring at an angle of ± 10 mrad in middle of the 360 m long straight section. A horizontal crossing is advantageous since the radial size of the electron beam is much larger than its vertical size. The choice of a relatively large crossing angle makes it possible to design the machines without common elements such that the electron and proton energies can be chosen and varied independently. The resulting increase in the effective horizontal beam size can be compensated by bringing the proton quadrupoles closer to the interaction point with a resulting reduction in vertical beam size. A free distance of ± 7.5 m around the interaction point is available for experiments. In this design the spin is turned into the longitudinal direction by an 80 m long rotator installed at the end of the arcs and restored to the transverse direction by a similar rotator positioned at the entrance to the next arc. The large distance between the interaction point and the last bend in the rotator minimizes the amount of synchrotron radiation which reaches the detector. In each section roughly 200 m is available for the r.f. system and the injection and

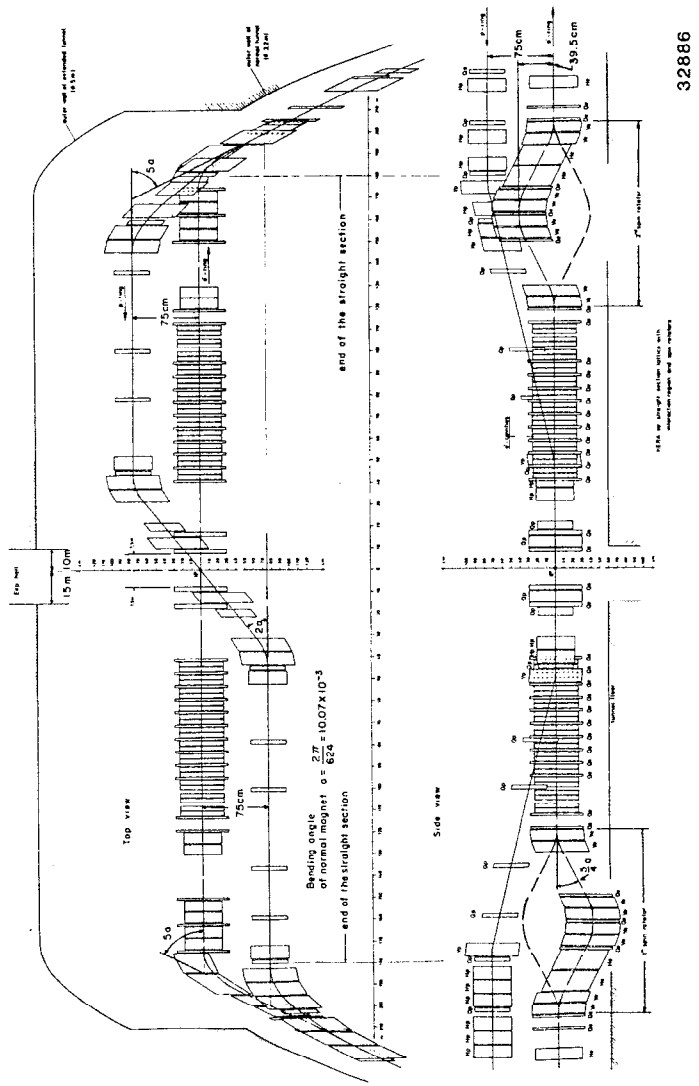


Fig. 3.2 - Layout of the interaction region.

ejection system.

Energy and luminosity are obviously two factors which determine the quality of an ep facility. The physics discussed in chapter 2 emphasized the importance of investigating the region of Q^2 greater than 10^4 GeV^2 and showed that luminosities of the order of 10^{31} cm^{-2}s^{-1} to 10^{32} cm^{-2}s^{-1} are needed to obtain a useful event rate at such large values of Q^2

The maximum momentum transfer squared Q^2_{max} which can be obtained in an ep colliding ring is given by

$$Q^2_{max} = 4\, E_e E_p \,. \qquad (3.1)$$

The maximum energy of the proton beam is determined by the product of the bending radius ρ and magnetic induction B

$$E_p\ (\text{GeV}) = \frac{B\,\rho\ (\text{T.m.})}{3.3356} \,. \qquad (3.2)$$

Thus, for a given radius, the energy is limited by the strength of the magnetic field. Due to the pioneering work at FNAL and BNL superconducting accelerator magnets can be mass produced with reproducible properties for an induction up to 5 T. The nominal induction of the superconducting dipole magnet in HERA is 4.53 T yielding a proton energy of 820 GeV.

An electron of energy E (GeV) transversing a circle of radius ρ (m) radiates an average of e U_e(keV) per turn:

$$e\,U_o(\text{keV}) = 88.5\,\frac{E^4}{\rho} \,. \qquad (3.3)$$

This energy loss must be restored by the r.f. system and to this end the cavities must be fed the power P_o. This power is the sum of the losses in the cavity and the energy radiated by the beam.

The cavity losses are given by $U^2/2R$ where U is the peak voltage in the cavity and R the total shunt impedance of the r.f. cavity system. In principle this term can be made negligibly small by using superconducting cavities; however, the second term still remains. The radiation losses are given by $i \cdot U_o$. High luminosities require a large circulating current such that the radiation term tends to dominate. The peak electron energy is therefore not limited by the magnetic field strength but rather by the available r.f. power. To reach the nominal energy of 30 GeV in HERA with a stored current of 56 mA requires 13.2 MeV of r.f. power with 4 MW needed to establish the circumferential voltage and 8 MW to compensate for the synchrotron radiation. 1.2 MW are lost in the waveguides. The dipole field is only 0.18 T.

It is important to push the electron energy for two reasons. Firstly the electron energy must be on the order of several percent of the proton energy to avoid that particles from the current jet are lost down the beampipe, making it difficult to reconstruct the final state. This point was illustrated in Fig.2.12 which shows the corrections which must be applied to the experimental data in order to determine the formfactor $F_2(x_1, Q^2)$ from charged current interactions. Whereas the corrections in the case of 30 GeV electrons colliding with 820 GeV protons (200 GeV) are small and presumably manageable they become very large and probably unreliable in the case of 5 GeV electrons colliding with 1000 GeV protons.

The synchrotron radiation in the arcs will polarise the circulating electrons transversely to the beam plane. The maximum polarisation P_o = 92.4% is approached as:

$$P(t) = P_o (1 - e^{-1/\tau_p}) \tag{3.4}$$

with a build-up-time τ_p in seconds given by:

$$\tau_p = \frac{98.7}{E^5} \rho^3 \left(\frac{R}{\rho} \right) \tag{3.5}$$

The beam energy E is in GeV and the bending radius ρ, respectively the geometric radius R in meter.

The electron energy should therefore be so large that τ_p is very short compared to the anticipated beam life time. At 30 GeV τ_p is of the order of 20 min.

The luminosity, assuming n_b bunches of protons and electrons is given by:

$$L = \left(\frac{N_e N_p}{A} \right) f_o n_b \tag{3.6}$$

Here N_e and N_p are the number of electrons respectively protons per bunch, f_o the resolution frequency and A the effective beam cross section.

The ultimate limit on the number of electrons and protons is given by the tune shift - i.e. the effect of the electron beam on the proton beam and opposite. However, the real limit may well be given by the available r.f. power for the electrons or by instabilities for the protons. - In HERA we expect a luminosity of $6 \cdot 10^{31}$ cm^{-2}s^{-1} at a c.m. energy of 314 GeV.

4. The Transverse Motion[10,30)]

The magnet system of a circular accelerator is made of deflecting and focusing elements arranged in a repetitive pattern around the ring. The reference particle sees only dipole fields and retraces its orbit on every turn. The other particle traverse the magnetic elements off axis and experiences a linear restoring force in addition to the deflecting force. An arbitrary particle executes quasi-harmonic oscillation (betatron oscillation) with respect to the closed orbit of the reference particle. In this chapter we discuss the properties of the betatron oscillation in the linear approximation.

4.1 The Equation of Motion

We will first derive the equations of motion for a charged particle travelling in a guide field made of a deflecting dipole field and a focusing quadrupole field. The particle motion is described using the coordinate system defined in Fig. 4.1. The position of the reference particle is given by the radius ρ and the distance s_o measured along the orbit from an arbitrary origin. The position of an arbitrary particle is given by the vector

$$\vec{t} = r \vec{n}_r + z \vec{n}_z \tag{4.1}$$

where $\vec{n}_r$ and $\vec{n}_z$ are unit vectors. Usually relative coordinates are used:

$$x = r - \rho \quad \text{and} \quad z. \tag{4.2}$$

We consider the motion in a time independent field. Along the reference orbit the induction $\vec{B}$ is normal to the horizontal plane i.e.

$$B_s = B_x = 0 . \tag{4.3}$$

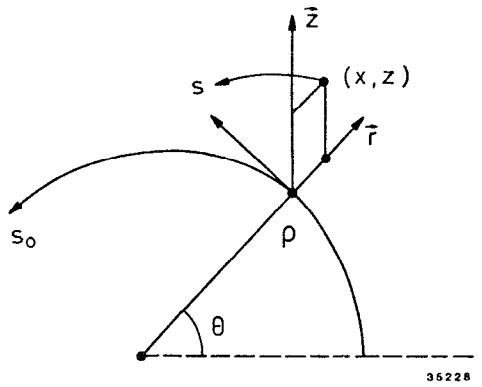


Fig. 4.1 - The coordinate system.

The magnetic induction is furthermore assumed to be symmetric with respect to the horizontal plane.

We consider particles oscillating with small amplitudes around the reference orbit. The induction can be expanded in a power series in x and z. Keeping only the first order terms yields:

$$B_z(s,x,z) = B_o(s) + \left(\frac{\partial B_z}{\partial x}\right)_o x + \ldots\ldots$$
$$B_x(s,x,z) = \left(\frac{\partial B_x}{\partial z}\right)_o z + \ldots\ldots \qquad (4.4)$$

In the median plane $\frac{1}{\mu_o}\nabla \times \vec{B} = \vec{j} = 0$ - i.e.

$$\frac{\partial B_z}{\partial x} = \frac{\partial B_x}{\partial z} \quad . \qquad (4.5)$$

It is convenient to normalize the dipole field and the gradient field to the momentum of the reference particle:

$$G(s) = \frac{1}{\rho_o} = \frac{e\,B_o}{o} \qquad (4.6)$$

$$K(s) = \frac{e}{p}\frac{\partial B}{\partial x} = \frac{1}{B\rho}\frac{\partial B_z}{\partial x} = \frac{1}{B\rho}\frac{\partial B_x}{\partial z} \qquad (4.7)$$

Note that both G(s) and K(s) are periodic functions with period L

$$G(s+L) = G(s)$$
$$K(s+L) = K(s) \qquad (4.8)$$

where L is the length of one turn.

The equation of motion of a charged particle in a magnetic field is given by the Lorentz force

$$\frac{d}{dt}(m\dot{\vec{t}}) = e(\vec{v} \times \vec{B}) \qquad (4.9)$$

We will first evaluate the left hand side. The time derivative of the position vector $\vec{t}$ is given by:

$$\dot{\vec{t}} = \dot{r}\vec{n}_r + r\dot{\vec{n}}_r + \dot{z}\vec{n}_z + z\dot{\vec{n}}_z \qquad (4.10)$$

The differentials of the unit vectors can be obtained from Fig. 4.1 by inspection.

$$d\vec{n}_r = \vec{n}_\theta d\theta \rightarrow \dot{\vec{n}}_r = \vec{n}_\theta \dot{\theta}$$
$$d\vec{n}_\theta = -\vec{n}_r\, d\theta \rightarrow \dot{\vec{n}}_\theta = -\vec{n}_r \dot{\theta} \qquad (4.11)$$
$$d\vec{n}_z = 0 \rightarrow \dot{\vec{n}}_z = 0$$

With the results of eqs. 4.10 and 4.11 the left hand side of eq. 4.9 yields:

$$\frac{d}{dt}(\dot{m}\vec{r}) = [\frac{d}{dt}(\dot{m}r) - mr\dot{\theta}^2]\vec{n}_r + [\frac{1}{r}\frac{d}{dt}(mr^2\dot{\theta})]\vec{n}_\theta + [\frac{d}{dt}(m\dot{z})\vec{n}_z] \qquad (4.12)$$

The right hand side of equation 4.9 in cylindrical coordinates is given by:

$$e(\vec{v} \times \vec{B}) = \begin{pmatrix} \vec{n}_r & \vec{n}_\theta & \vec{n}_z \\ \dot{r} & r\dot{\theta} & \dot{z} \\ B_r & B_\theta & B_z \end{pmatrix} \qquad (4.13)$$

The three components of the equation of motion can thus be written as:

$$(\ddot{r} - r\dot{\theta}^2) = (\frac{e}{m})(r\dot{\theta}B_z - \dot{z}B_\theta) \qquad (4.14a)$$

$$\frac{1}{r}\frac{d}{dt}(r^2\dot{\theta}) = (\frac{e}{m})(\dot{z}B_r - \dot{r}B_z) \qquad (4.14b)$$

$$\ddot{z} = (\frac{e}{m})(\dot{r}B_\theta - r\dot{\theta}B_r) \qquad (4.14c)$$

Equation 4.14a can be written as:

$$\frac{d^2x}{ds^2} = x'' = \frac{1}{r} + \frac{eB_o}{p}(1 + \frac{1}{B_o}\frac{\partial B_z}{\partial x}x) \qquad (4.15)$$

with the magnetic induction as defined above in eqs. 4.3 and 4.4 and the substitution:

$$\frac{d}{dt} = (r\dot{\theta})\frac{d}{ds} = v\frac{d}{ds} \qquad (4.16)$$

This can be simplified using:

$$\frac{1}{r} = \frac{1}{\rho + x} = \frac{1}{\rho}(1 - \frac{x}{\rho}), \qquad \frac{1}{p} = \frac{1}{p_o + \Delta p} = \frac{1}{p_o}(1 - \frac{\Delta p}{p}) \qquad (4.17)$$

and

$$\frac{eB_o}{p_o} = -\frac{1}{\rho_o} .$$

Neglecting second order terms and using the definitions given in eqs. 4.6 and 4.7 yields the equation of motion in the horizontal plane:

$$x'' + (G^2(s) + K(s))\,x = G(s)\frac{\Delta p}{p} \qquad (4.18)$$

Note that in general $G^2(s) + K(s) \approx K(s)$.

The equation for the motion in the vertical plane follows from eq. 4.14c. With the approximations used above

$$z'' - K(s)\,z = 0 . \qquad (4.19)$$

Evaluation of eq. 4.14b yields:

$$\Delta p = \text{const.}$$

The transverse particle motion is described by two independent linear equations. The equations are of the harmonic oscillator form except that the restoring force K(s) is a function of the azimuthal coordinate.

4.2 The Magnetic Elements

The first strong focusing machines were made of combined function elements - i.e. the bending and the focusing field were produced by a single magnet.

This has several drawbacks:

- The average induction B_0 must be low to avoid saturation of the pole tips.
- The ratio of the bending and the focusing strength is fixed by the shape of the polefaces and the machine tune can only be changed by additional independent quadrupoles.
- The emission of synchrotron radiation will cause the radial beam size to grow exponentially.

For these reasons most modern machines are designed as separate function machines. The bending and the focusing properties of the guide field are provided by independent elements arranged in a repetitive pattern of identical units - the cells. A standard FODO cell is shown in Fig. 4.2. The cell consists of a horizontal focusing quadrupole, bending magnets, a horizontal defocusing quadrupole and bending magnets. In general sextupole and octupole magnets for higher order corrections and dipole magnets to minimize closed orbit deviations are incorporated into the cell.

In a standard dipole the field shape is determined by the iron, and the induction is limited to 2T to avoid saturation. The next

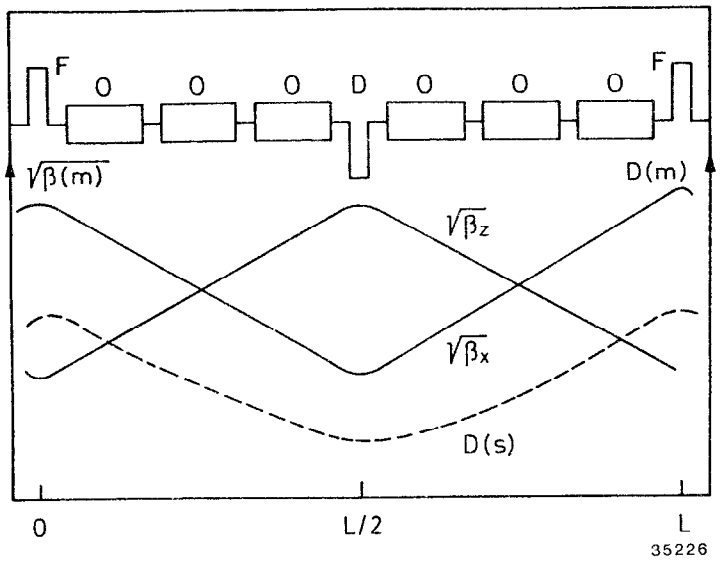


Fig. 4.2 - a) The magnet ordering in a simple FODO cell.
b) Variation of the betafunction and the dispersion over a cell.

generation of circular proton machines seeks to use superconducting coils to produce higher inductions. In this case the induction is determined by the current distribution and effects like persistent currents and production tolerances make the magnets rich in higher order multipoles. No accelerator exploiting this technology is operating although the FNAL Tevatron is nearly completed and long term tests involving strings of more than 100 magnets have been very encouraging. Indeed it seems possible to construct 5T superconducting dipole magnets of high and reproducible quality. The coils are wound using a Rutherford type helium transparent NbTi wire and magnets with an induction of 8 - 10 T seem feasible using this technology. Bending fields above 10 T require presumably a new conductor like $NbSn_3$.

The distribution of magnetic induction in a quadrupole lens is shown schematically in Fig. 4.3. The induction disappears on the axis and increases linearly with the distance from the beam axis in both the horizontal and vertical plane.

$$B_x = g\, z \qquad B_z = g\, x \tag{4.20}$$

with $g = \frac{\partial B_z}{\partial x} = \frac{\partial B_x}{\partial z}$.

A stream of parallel particles traversing a quadrupole of length l will be focused in one plane and defocused in the orthogonal plane with the same focal length f. In the focusing plane:

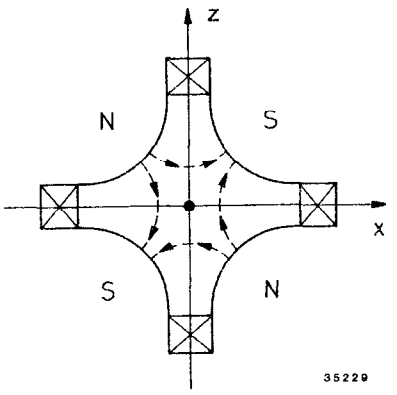


Fig. 4.3 - The magnetic induction pattern of a quadrupole lens.

$$x' = \frac{B_z\, l}{B_0\, \rho} = -\left(\frac{g\, l}{B_0 \rho}\right) x = -k\, l\, x = -\frac{x}{f} \tag{4.21}$$

f, the focal length is given by:

$$f = -\frac{1}{k\, l} \tag{4.22}$$

A charged particle beam traversing a quadrupole magnet is focused in one plane and defocused in the orthogonal plane. However, a pair of quadrupole lenses spaced at a distance L will focus the beam in both planes provided f > L. To see this consider the transfer matrix for a quadrupole doublet in the thin lens approximation (see 4.5):

$$M_x = \begin{pmatrix} 1 & 0 \\ 1/f & 1 \end{pmatrix} \begin{pmatrix} 1 & L \\ 0 & 1 \end{pmatrix} \begin{pmatrix} 1 & 0 \\ -1/f & 1 \end{pmatrix} = \begin{pmatrix} 1-L/f & L \\ -L/f^2 & L/f+1 \end{pmatrix} \tag{4.23}$$

$$M_z = \begin{pmatrix} 1 & 0 \\ -1/f & 1 \end{pmatrix} \begin{pmatrix} 1 & L \\ 0 & 1 \end{pmatrix} \begin{pmatrix} 1 & 0 \\ 1/f & 1 \end{pmatrix} = \begin{pmatrix} 1+L/f & L \\ -L/f^2 & -L/f+1 \end{pmatrix}$$

Comparing the element m_{21} for both matrices yields:

$$f_x = f_z = -L/f^2 .$$

The focal length of a lens decreases with increasing momentum as:

$$f \sim 1/p .$$

Thus a machine made of only dipole and quadrupole magnets will have a strong chromatic aberration. This can be corrected with sextupole elements as discussed in chapter 5.3.

A sextupole lens is shown schematically in Fig. 4.4. The field distribution in Cartesian coordinates x and z can be written as:

$$\begin{aligned} B_x(x, z) &= B'' \; x \; z \\ B_z(x, z) &= \frac{B''}{2}(x^2 - z^2) \end{aligned} \tag{4.24}$$

with $B'' = \dfrac{\partial^2 B_z}{\partial x^2}$.

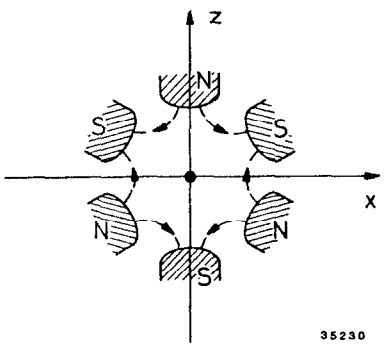


Fig. 4.4 - The magnetic induction pattern of a sextupole.

4.3 The Matrix Solution

The transverse motion in x and z for particles with $\Delta p = 0$ is described by the solutions to the linear homogenous equation

$$u''(s) + K(s)\, u(s) = 0 \tag{4.25}$$

The position u(s) and the slope u'(s) of a particle with azimuthal coordinate s can be written as a vector:

$$\vec{u}(s) = \begin{pmatrix} u \\ u' \end{pmatrix}_s \tag{4.26}$$

The value of u(s) at an arbitrary azimuth $s = s_1$ is related to its value at the origin s_o by a linear transformation

$$\vec{u}(s_1) = M(s_1 \mid s_o)\, \vec{u}(s_o) \tag{4.27}$$

$M(s_1 \mid s_o)$ is a 2 x 2 matrix and the value of the maxtrix elements can be determined from the two particular solutions C(s) and S(s) of eq. 4.25.

The particular solutions are defined by their values and derivatives at the origin $s = s_o$.

$$\begin{aligned} C(s_o) &= 1 \qquad C'(s_o) = 0 \\ S(s_o) &= 0 \qquad S'(s_o) = 1 \end{aligned} \tag{4.28}$$

The general solution of eq. 4.25 is then the sum of the particular solutions:

$$\begin{aligned} u(s) &= u(s_o)\, C(s) + u'(s_o)\, S(s) \\ u'(s) &= u(s_o)\, C'(s) + u'(s_o)\, S'(s) \end{aligned} \tag{4.29}$$

This expression can be verified for $s = s_o$ using the boundary conditions for C(s) and S(s) defined above.

The value at an arbitrary point $s = s_1$ is then given by eq. 4.27. Written in matrix form we find:

$$\begin{pmatrix} u \\ u' \end{pmatrix}_{s_1} = \begin{pmatrix} C(s_1) & S(s_1) \\ C'(s_1) & S'(s_1) \end{pmatrix} \begin{pmatrix} u \\ u' \end{pmatrix}_{s_o} \tag{4.30}$$

The transfer matrix $M(s_1 \mid s_o)$ for a particle between the azimuthal positions s_o and s_1 is determined by the values of the particular solution at $s = s_1$.

4.3.1 Transfer matrices for $\Delta p = 0$

A separate function machine is made of dipole magnets, quadrupole magnets and drift distances. We will now evaluate the transfermatrices for these elements, each of length $L = s - s_o$. The transfermatrix for a string of elements is simply the product of the transfer matrices for individual elements:

$$M(s_n \mid s_o) = M(s_n \mid s_{n-1}) \; - - - \; M(s_2 \mid s_1)\, M(s_1 \mid s_o) \tag{4.31}$$

a) Field free region

$K(s) = 0$ in a field free region and particles drift with constant slope. - The particular functions are now solutions of $u''(s) = 0$. These solutions are

$$\begin{aligned} C(s) &= 1 \qquad S(s) = s - s_o = L \\ C'(s) &= 0 \qquad S'(s) = 1 \end{aligned} \tag{4.32}$$

Thus the transfer matrix is given by

$$M(s_1 \mid s_o) = \begin{pmatrix} 1 & L \\ 0 & 1 \end{pmatrix} \tag{4.33}$$

b) Focusing element

The particle motion in a focusing element is given by

$$u''(s) + K(s)\, u(s) = 0 \tag{4.34}$$

with $K(s) > 0$.

The resulting particular solutions are:

$$C = a \cos\sqrt{K}\, L \quad \text{and} \quad S = b \sin\sqrt{K}\, L \tag{4.35}$$

with the values of a and b determined by the boundary conditions above, i.e.

$$a = 1 \qquad b = \frac{1}{\sqrt{K}}.$$

The transfermatrix for a focusing element of length L is thus given by:

$$M(s_1 \mid s_0) = \begin{pmatrix} \cos\sqrt{K}\,L & \frac{1}{\sqrt{K}}\sin\sqrt{K}\,L \\ -\sqrt{K}\cdot\sin\sqrt{K}\,L & \cos\sqrt{K}\,L \end{pmatrix} \qquad (4.36)$$

c) Defocusing element

The particle motion in a defocusing element is given by:

$$u''(s) - K(s)\,u(s) = 0 \qquad (4.37)$$

The resulting particular solutions are:

$$C = a\cosh\sqrt{K}\,L \quad \text{and} \quad S = b\sinh\sqrt{K}\,L \qquad (4.38)$$

The boundary condition yields:

$$a = 1 \quad \text{and} \quad b = \frac{1}{\sqrt{K}} \,.$$

The transfermatrix for a defocusing element of length L is thus given by:

$$M(s_1 \mid s_0) = \begin{pmatrix} \cosh\sqrt{K}\,L & (\frac{1}{\sqrt{K}})\sinh\sqrt{K}\,L \\ \sqrt{K}\cdot\sinh\sqrt{K}\,L & \cosh\sqrt{K}\,L \end{pmatrix} \qquad (4.39)$$

4.3.2 The Twiss matrix

The transfer matrix for a single cell or for a complete turn can be written in its most general form as:

$$T(s+L \mid s) = \begin{pmatrix} \cos\mu + \alpha\sin\mu & \beta\sin\mu \\ -\gamma\sin\mu & \cos\mu - \alpha\sin\mu \end{pmatrix}$$

$$= \begin{pmatrix} 1 & 0 \\ 0 & 1 \end{pmatrix}\cos\mu + \begin{pmatrix} \alpha & \beta \\ -\gamma & -\alpha \end{pmatrix}\sin\mu = I\cos\mu + \alpha\sin\mu \,. \qquad (4.40)$$

This matrix is called the Twiss matrix and the coefficients α, β and γ are periodic functions with the period L. The Twiss matrix must have unit determinand since it is the product of unit determinand matrices. This condition yields:

$$\beta\gamma - \alpha^2 = 1 \,. \qquad (4.41)$$

A particle executes stable betatron oscillation if the particular solutions C and S are bounded. The general stability condition can be conveniently expressed using the Twiss matrix.

The transfer matrix for two turns M_1M_2 is simply the product

$$M_1M_2 = (I\cos\mu_1 + J\sin\mu_1)(I\cos\mu_2 + I\sin\mu_2) \qquad (4.42)$$

Multiplying and inserting the relation $J^2 = -I$ yields:

$$M_1M_2 = I\cos(\mu_1 + \mu_2) + J\sin(\mu_1 + \mu_2) \qquad (4.43)$$

Eq. 4.43 can be easily generalized to n turns:

$$T_{n\ldots1} = I(\cos\mu_1 \cdots \cos\mu_n) + J(\sin\mu_1 \ldots\sin\mu_n) \qquad (4.44)$$

The betatron oscillations are bounded if the phase advance μ per turn is real:

$$\mathrm{Tr}\,|T| = 2\cos\mu \leq 2 \qquad (4.45)$$

4.4 The Betatron Function

The transverse motion of a charged particle ($\Delta p = 0$) in both planes with respect to the reference orbit is given by the solution to the equation

$$u''(s) + K(s)\,u(s) = 0 \,. \qquad (4.25)$$

This equation is rather famous; it was first investigated by the

astronomer Hill in conjunction with the orbitals of the moon. Below we sketch the solution[10] to this equation.

According to the theorem of Floquet, Hill's equation has two independent particular solutions of the form

$$u_k(s) = p_k(s)\, e^{\pm i\mu \cdot s/L} \tag{4.47}$$

where $p_{1,2}(s)$ are periodic functions with period L:

$$p_{1,2}(s) = p_{1,2}(s + L) \tag{4.48}$$

The solution after one complete turn can be written as:

$$u_k(s + L) = p_k(s + L)\, e^{\pm i\mu(s+L)/L} = u_k(s)\, e^{\pm i\mu} \tag{4.49}$$

and it can be related to the Twiss matrix for one complete turn:

$$u_k(s)\,(\cos\mu \pm i\sin\mu) = (\cos\mu + \alpha\sin\mu)\, u_k(s) + \beta\sin\mu\, u_k'(s) \tag{4.50}$$

This equation must be valid for all values of the phase advance μ. Equating the $\cos\mu$ terms yields a trivial identity whereas equating the $\sin\mu$ terms yields:

$$\frac{u_k'}{u_k} = \frac{\pm i - \alpha}{\beta} \tag{4.51}$$

Logarithmic differentiation leads to the expression:

$$\frac{u_k''}{u_k'} - \frac{u_k'}{u_k} = \frac{-\alpha'}{\pm i - \alpha}\,\frac{\beta'}{\beta} \tag{4.52}$$

An alternative expression for the right hand side of eq. 4.52 can be obtained by combining eq. 4.51 and Hill's equation. To multiply eq. 4.51 with K(s) and substitute $u_k'' = -Ku_k$ yields

$$\frac{u_k''}{u_k'} = -\frac{K\beta}{\pm i - \alpha} \tag{4.53}$$

Subtracting eq. 4.51 from the equation above yields:

$$\frac{u_k''}{u_k'} - \frac{u_k'}{u_k} = -\frac{\pm i - \alpha}{\beta} - \frac{K\beta}{\pm i - \alpha} \tag{4.54}$$

Equating the right hand sides of eq. 4.52 and eq. 4.54 yields:

$$(\alpha^2 + K\beta^2 + \alpha\beta' - \alpha'\beta - 1) \mp i\,(\beta' + 2\alpha) = 0 \tag{4.55}$$

The real and the imaginary part must disappear independently and this yields the relations:

$$\begin{aligned} \beta' &= -2\alpha \\ \alpha' &= K\beta - \gamma\,. \end{aligned} \tag{4.56}$$

Substituting $\alpha = -\frac{1}{2}\beta'$ in eq. 4.51 results in a relationship between u_k, β and their derivatives

$$\frac{u_k'}{u_k} = \frac{i + \frac{1}{2}\beta'}{\beta} \tag{4.57}$$

Eq. 4.57 can be logarithmically integrated:

$$\begin{aligned} u_k(s) &= a\sqrt{\beta}\, e^{\pm i\mu} \\ u_k(s) &= a\sqrt{\beta}\cos(\mu(s) + \mu_o) \end{aligned} \tag{4.58}$$

with

$$\mu(s) = \int \frac{ds}{\beta} \tag{4.59}$$

$\beta(s)$ is called the betatron function and $\mu(s)$ the betatron phase.

The solution of Hill's equation is a quasiharmonic oscillation with an instantaneous amplitude proportional to $\sqrt{\beta}$ and a reduced

wave length $\lambda = \beta(s)$. Q, the number of transverse oscillations per turn is given by eq. 4.59 integrated over one complete turn

$$Q = \frac{1}{2\pi} \oint \frac{ds}{\beta} \tag{4.60}$$

The Twiss matrix can be expressed using eqs. 4.41 and 4.56 as:

$$T = \begin{pmatrix} \cos\mu - \frac{1}{2}\beta' \sin\mu & \beta \sin\mu \\ -\frac{1 + \frac{1}{4}\beta'^2}{\beta} \sin\mu & \cos\mu + \frac{1}{2}\beta' \sin\mu \end{pmatrix} \tag{4.61}$$

The linear optic of an accelerator is completely determined by the knowledge of $\beta(s)$ and its derivative. Note that the complete magnet system contributes to the value of the betatron function at a given position s.

The betatron function resulting from a given magnet arrangement is readily determined using the matrix formalism discussed above. Let us assume that the machine is made of n elements. The transfer matrix for a complete turn is given by the product of n individual transfermatrices.

$$\begin{pmatrix} \cos\mu + \alpha\sin\mu & \beta\sin\mu \\ -\gamma\sin\mu & \cos\mu - \alpha\sin\mu \end{pmatrix} = \begin{pmatrix} C & S \\ C' & S' \end{pmatrix} = \prod_{j=0}^{n} M \begin{pmatrix} C & S \\ C' & S' \end{pmatrix}_j \tag{4.62}$$

Equating the elements m_{12} on both sides of the equation yields:

$$\beta(s + L, s) = \frac{S(s + L, s)}{\sin 2\pi Q} \quad . \tag{4.63}$$

The value of the betatron function at the position s is proportional to the value of the sine like function after one revolution. The value of sin 2π Q is given by the trace of the transfermatrix for one turn:

$$\cos 2\pi Q = \frac{1}{2} \mathrm{Tr}\,(C(s + L, s) + S'(s + L, s)). \tag{4.64}$$

4.5 Off Energy Particles

The particle energy will in general differ from the design energy. A finite energy deviation will to first order only affect the radial motion which is now described by the solution to eq. 4.18

$$\begin{aligned} x''(s) + K_x(s)\, x(s) &= G(s) \frac{\Delta p}{p} \\ K_x(s) &= G^2(s) + K(s) \end{aligned} \tag{4.18}$$

The solution to eq. 4.18 can be written as the sum of two functions

$$x(s) = x_p(s) + x_\beta(s) \tag{4.65}$$

$x_\beta(s)$ is the solution to the homogeneous equation and describes the betatron oscillations around the closed orbit given by $x_p(s) = D(s) \frac{\Delta p}{p}$, where D(s) is the unique particular solution to the inhomogeneous equation

$$D''(s) + K_x(s)\, D(s) = G(s) \tag{4.66}$$

satisfying the boundary condition

$$\begin{aligned} D(L) &= D(0) \\ D'(L) &= D'(0) \end{aligned} \tag{4.67}$$

The solution can be written as (see chapter 5.2.2 with the substitution $x_c \to D$ and $\delta G \to G$):

$$D(s) = \frac{\sqrt{\beta(s)}}{2\sin\pi\nu} \oint G(s') \sqrt{\beta(s')} \cos(\mu(s) - \mu(s')) - \pi Q) ds' \qquad (4.68)$$

Thus with the knowledge of the betatron function one can compute the off energy function. The variation of D(s) over a FODO cell is plotted in Fig. 4.2.

We can also write the solution in matrix form for the various elements which make up an accelerator.

D(s) must satisfy eq. 4.18 with constant values of K(s) and G(s). The solution shall satisfy the boundary condition

$$D(0) = D'(0) = 0 \qquad (4.69)$$

Inspection of equation 4.62 suggests the following Ansatz

$$D(s) = (a + b \cos\sqrt{K}\, L) \qquad (4.70)$$

Inserting this Ansatz into eq. 4.62 yields

$$a = \frac{1}{K\rho} \qquad (4.71)$$

and the boundary condition in eq. 4.65 yields

$$b = \frac{-1}{K\rho} \quad . \qquad (4.72)$$

The particular solution of the inhomogenous equation for a focusing element is thus given by:

$$D(s) = \frac{(1 - \cos\sqrt{K}\, L)}{K\rho} \qquad (4.73)$$

Correspondingly the particular solution of eq. 4.62 for a defocusing element is given by

$$D(s) = \frac{(1 - \cosh\sqrt{|K|}\, L)}{|K|\rho} \qquad (4.74)$$

The matrix formalism discussed in chapter 4.3 can be extended to include off momentum particles

$$\begin{pmatrix} x \\ x' \\ \frac{\Delta p}{p} \end{pmatrix}_{s_1} = M \begin{pmatrix} x \\ x' \\ \frac{\Delta p}{p} \end{pmatrix}_{s_0} \qquad (4.75)$$

with

$$M(s|s_0) = \begin{pmatrix} C & S & D \\ C' & S' & D' \\ 0 & 0 & 1 \end{pmatrix}_s$$

The values for C, S and D are given above. The values of D and D' can be computed from eq. 4.73 for a focusing element and from eq. 4.74 for a defocusing element.

4.6 The FODO Cell

The commonly used FODO cell, shown in Fig. 4.2 is made of a horizontally focusing and defocusing quadrupole doublet spaced by dipole magnets. In this chapter we will evaluate the optical properties of such a cell in the thin lens approximation. In this approximation the length of a lens l approaches zero with

$K\,l \to \frac{1}{f}$ = constant i.e. $\sqrt{K}\,l \to 0$. The transfer matrix for the FODO cell shown in Fig. 4.2 is given by the product of matrices for the individual elements. The transfer matrix at the entrance of a focusing quadrupole is given by

$$M = M_o\, M_D\, M_o\, M_F$$

$$= \begin{pmatrix} 1 & \frac{L}{2} \\ 0 & 1 \end{pmatrix} \begin{pmatrix} 1 & 0 \\ \frac{1}{f} & 1 \end{pmatrix} \begin{pmatrix} 1 & \frac{L}{2} \\ 0 & 1 \end{pmatrix} \begin{pmatrix} 1 & 0 \\ \frac{-L}{f} & 1 \end{pmatrix}$$

$$= \begin{pmatrix} 1 - \frac{L}{2f} - \frac{L^2}{4f^2} & L + \frac{L^2}{4f} \\ \frac{-L}{2f^2} & 1 + \frac{L}{2f} \end{pmatrix} \qquad (4.77)$$

f is the focal length of the lens and L the cell length. This matrix must equal the Twiss matrix T - i.e. $M_{ih} = T_{ih}$

$$T = \begin{pmatrix} \cos\mu + \alpha\sin\mu & \beta\sin\mu \\ -\gamma\sin\mu & \cos\mu - \alpha\sin\mu \end{pmatrix} \qquad (4.78)$$

The Twiss parameters can then easily be expressed in terms of the focusing strength f and the cell length L using the relationship above.

The phase advance μ across the cell is obtained from:

$$\begin{aligned} \mathrm{Tr}\, T &= \mathrm{Tr}\, M \\ 2\cos\mu &= 2 - \frac{L^2}{4f^2} \\ \sin\frac{\mu}{2} &= \frac{L}{4f} \end{aligned} \qquad (4.79)$$

The value of the β-function at a position of a focusing quadrupole is given by:

$$T_{12} = M_{12}$$

$$\beta_F \sin\mu = L\,(1 + \frac{1}{4}\frac{L}{f})$$

$$\beta_F = \frac{L}{\sin\mu}(1 + \sin\frac{\mu}{2}) = 2f\,\left(\frac{1 + \frac{1}{4}\frac{L}{f}}{1 - \frac{1}{4}\frac{L}{f}}\right)^{1/2} \qquad (4.80)$$

The β function at the position of a defocusing quadrupole is obtained by interchanging the position of M_D and M_F in eq. 4.77. This yields:

$$\begin{aligned} \beta_D &= \frac{L}{\sin\mu}\,(1 - \sin\frac{\mu}{2}) \\ \beta_D &= 2f\,\left(\frac{1 - \frac{1}{4}\frac{L}{f}}{1 + \frac{1}{4}\frac{L}{f}}\right)^2 \end{aligned} \qquad (4.81)$$

The values of the β-functions normalized to the cell length L are plotted in Fig. 4.6a versus the phase advance μ. Note that the difference:

$$\beta_F - \beta_D = 4f\,\mathrm{tg}\frac{\mu}{2} \qquad (4.82)$$

increases monotonically with the phase advance.

The value of α_F is extracted from the relation

$$T_{11} - T_{22} = M_{11} - M_{22}$$

$$\alpha_F = -\frac{1 + \sin\frac{\mu}{2}}{\cos\frac{\mu}{2}} \qquad (4.83)$$

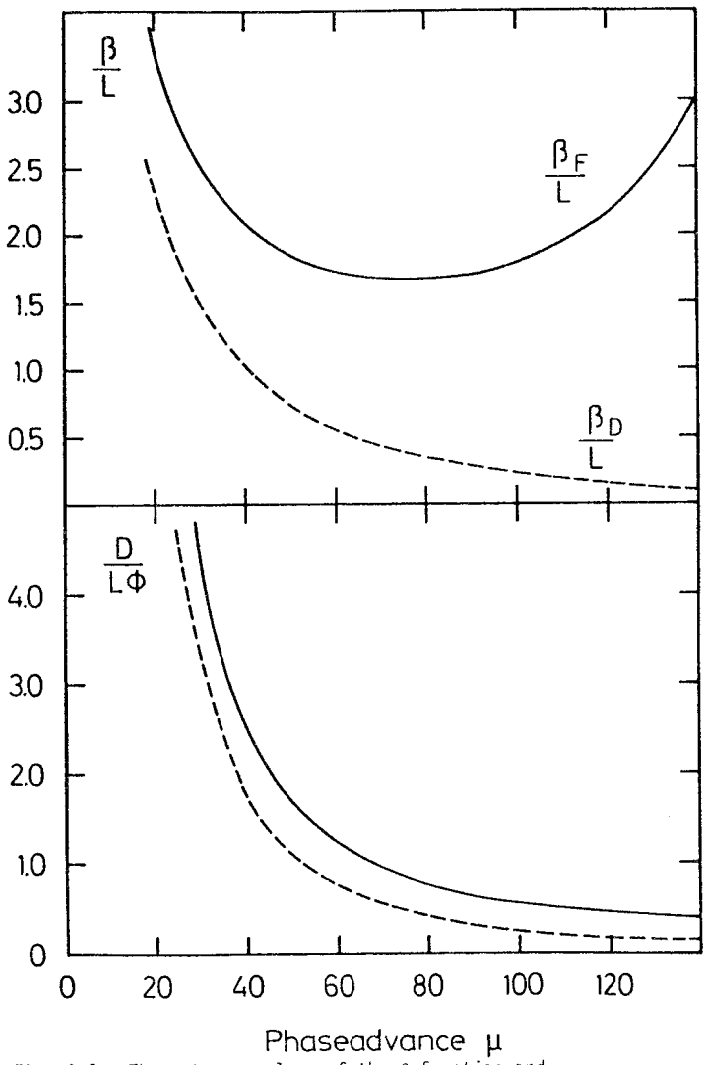


Fig. 4.6 - The extreme values of the β-function and the off energy function as a function of the phase advance μ per cell. 35223

The value of γ_F is determined from:

$$\begin{aligned} T_{21} &= M_{21} \\ -\gamma_F \sin\mu &= \frac{-L}{2f^2} \\ \gamma_F &= \frac{1}{f\cos\frac{\mu}{2}} \end{aligned} \tag{4.84}$$

The values of α_D and γ_D at the position of a defocusing quadrupole are given by interchanging M_D and M_F in eq. 4.77. This yields:

$$\alpha_D = \frac{1 - \sin(\frac{\mu}{2})}{\cos\frac{\mu}{2}} \tag{4.85}$$

$$\gamma_D = \frac{1}{f\cos\frac{\mu}{2}} \tag{4.86}$$

To determine the dispersion function D(s) we must make use of the 3 x 3 matrices defined in eq. 4.76. The computational effort can be reduced by making use of the fact that the slopes of the dispersion functions disappear in the middle of the quadrupoles:

$$\begin{pmatrix} D_D \\ 0 \\ 1 \end{pmatrix} = M \begin{pmatrix} D_F \\ 0 \\ 1 \end{pmatrix} \tag{4.87}$$

with $M = M_D(\frac{1}{2}f)\, M_o(\frac{1}{2}L) M_F(\frac{1}{2}f)$

$$\begin{pmatrix} 1 & 0 & 0 \\ \frac{1}{2}f & 1 & 0 \\ 0 & 0 & 1 \end{pmatrix} \begin{pmatrix} 1 & \frac{1}{2} & \frac{L\phi}{8} \\ 0 & 1 & \frac{\phi}{2} \\ 0 & 0 & 1 \end{pmatrix} \begin{pmatrix} 1 & 0 & 0 \\ -\frac{1}{2f} & 1 & 0 \\ 0 & 0 & 1 \end{pmatrix} \tag{4.88}$$

$$\begin{pmatrix} 1 - \frac{1}{4}\frac{L}{f} & \frac{L}{2} & \frac{L\phi}{8} \\ -\frac{L}{8f^2} & 1 + \frac{L}{4f} & (1 + \frac{L}{8f})\frac{\phi}{2} \\ 0 & 0 & 1 \end{pmatrix} \qquad (4.89)$$

L and ϕ are respectively the length and the bending angle of the cell. This yields the equations:

$$\begin{aligned} D_D &= (1 - \frac{L}{4f})\, D_F + L\frac{\phi}{8} \\ 0 &= -(\frac{L}{8f^2})\, D_F + (1 + \frac{L}{8f})\frac{\phi}{2} \end{aligned} \qquad (4.90)$$

Solving eq. 4.90 for the dispersion functions yields:

$$\begin{aligned} D_F &= \frac{1}{\sin^2\frac{\mu}{2}} \quad \frac{L\phi}{4}(1 + \tfrac{1}{2}\sin\tfrac{\mu}{2}) \\ &= (\frac{4f^2}{\rho})(1 + \frac{L}{8f}) \end{aligned} \qquad (4.91)$$

$$\begin{aligned} D_D &= \frac{1}{\sin^2(\frac{\mu}{2})} \quad \frac{L\phi}{4}(1 - \tfrac{1}{2}\sin\tfrac{\mu}{2}) \\ &= (\frac{4f^2}{\rho})(1 - \frac{L}{8f}) \end{aligned} \qquad (4.92$$

The normalized dispersions $\frac{D}{L\phi}$ are plotted in Fig. 4.6b versus phase advance.

The average value of the dispersion function is given by:

$$\langle D \rangle = \frac{4f^2}{\rho} \quad . \qquad (4.93)$$

4.7 The Courant-Snyder Invariant

The transverse motion of a charged particle in a magnetic field including synchrotron radiation (see chapter 7) is described by the solutions to the equation

$$u'' + J(s)\, u' + K(s)\, u = 0 \, . \qquad (4.94)$$

At present energies the synchrotron radiation from a proton can be neglected, i.e. J(s) = 0 and eq. 4.94 is reduced to the familiar Hill's equation.

The Wronskian determimant is defined as:

$$W(s) = \begin{pmatrix} u_1 & u_2 \\ u_1' & u_2' \end{pmatrix} \qquad (4.95)$$

u_1 and u_2 are solutions of the differential equation, i.e. they satisfy:

$$\begin{aligned} u_1'' + J(s)\, u_1' + K(s)\, u_1 &= 0 \\ u_2'' + J(s)\, u_2' + K(s)\, u_2 &= 0 \end{aligned} \qquad (4.96)$$

Multiplying the first equation with u_2, the second with u_1 and subtracting the two equations yields:

$$\frac{dW}{ds} + J\,W = 0 \qquad (4.97)$$

with $W = u_1u_2' - u_1'u_2$.

The solution of this equation is given by

$$W(s) = W_0\, e^{\int_{s_1}^{s_2} J\, ds} \, . \qquad (4.98)$$

Thus in the case of an electron the Wronskian depends on s whereas for a proton $W(s) = W_0$ is a constant of motion.

To determine the invariant W_o we take $u_1 = \sqrt{\beta}\, e^{i\mu(s)}$ and set $u_2 = u$, i.e. u_2 is an arbitrary real solution of Hill's equation,

$$W_o = (u\, u_1' - u'\, u_1) = u_1 \left(u \frac{u_1'}{u_1} - u'\right) = u_1 \left(u \frac{i - \alpha}{\beta} - u\right) \tag{4.99}$$

where eq. 4.51 has been used to substitute

$$\frac{u_1'}{u_1} = \frac{i - \alpha}{\beta}$$

$$W_o W_o^* = u_1 u_1^* \left(u \frac{i - \alpha}{\beta} - u'\right)\left(u \frac{[-i - \alpha]}{\beta} - u'\right) \tag{4.100}$$

With $u_1 u_1^* = \beta$ the equation above simplifies to:

$$WW^* = \frac{u^2 + (\alpha u + \beta u')^2}{\beta} = \frac{\varepsilon}{\pi} \quad . \tag{4.101}$$

We consider the value of WW^* at a fixed azimuth s_o, i.e. α_o and β_o are constants. On each succesive turn the particles will arrive at $s = s_o$ with different values of u and u' however the values must satisfy eq. 4.101. Thus on successive turns the particles trace an ellipse in u u' space as indicated in Fig. 4.7. The area of the ellipse is given by

$$A = \pi\, u_{max}\, u_o' \tag{4.102}$$

with u_{max} and u_o' defined in Fig. 4.7.
It follows from eq. 4.101:

$$u_{max} = \sqrt{\frac{\varepsilon\beta}{\pi}} \quad \text{and} \quad u_o = \sqrt{\frac{\varepsilon}{\pi\beta}} \tag{4.103}$$

Substituting these values into eq. 4.102 yields:

$$A = \varepsilon \ .$$

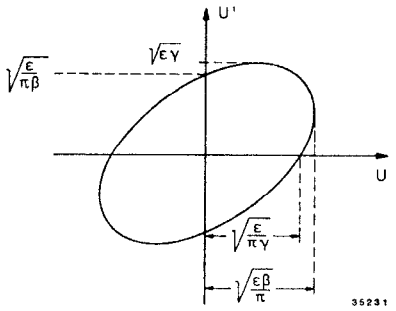


Fig. 4.7
The phase ellipse.

The quantity uu' is by definition the beam emittance - i.e. the product of beam size and angular divergence. The Wronskian can thus be identified with the beam emittance and it follows that the beam emittance is a constant of motion for a proton beam, but not for an electron beam because of the synchrotron radiation.

The betatron motion is thus completely defined

$$u = \sqrt{\frac{\varepsilon}{\pi}}\ \sqrt{\beta}\ \cos(\mu(s) - \mu_o)) \tag{4.104}$$

Note that for a proton beam the emittance ε and hence the betatron amplitude decreases with increasing energy as:

$$\varepsilon = \pi\,(u\, u') = u \frac{p_\perp}{p} = u \frac{p_\perp}{\beta\gamma} \tag{4.105}$$

where β is the normalized particle velocity $\beta = \frac{p}{E}$ and $\gamma = \frac{E}{m_o c^2}$. Usually the invariant emittance $(\varepsilon\ \beta\ \gamma)$ is quoted.

5. *Magnet Imperfections and Resonances*[10,30,31]

5.1 Introduction

In the previous discussion we assumed that the guide field is made of ideal dipole and quadrupole magnets. However, a real magnet has imperfections; magnets are not exactly reproducible and they can only be installed with a certain precision. The resulting deviations from the ideal guide field are grouped into linear and nonlinear errors.

The linear errors are caused by imperfections in the dipole and the quadrupole components of the field and these errors cause closed orbit deviations and tune changes. The magnitude of the linear effects are independent of the particle amplitude.

The nonlinear errors are caused by higher multipole fields and their effects depend on the particle amplitude. Nonlinear effects are particularly important in machines made of superconducting magnets. Superconducting magnets are rich in higher multipoles since the field is produced directly by the current distribution and not shaped by the iron yoke. An ideal $\cos\theta$ current distribution would produce a perfect dipole field. However, the $\cos\theta$ distribution in a real magnet is only approximate and it is only possible to position the wires with a certain precision. The relative strength of these errors is independent of the induction. The persistent currents, caused by flux trapped in the conductor, lead to higher multipole fields. The strength of these multipoles is independent of excitation and they are therefore particularly important at low fields - i.e. at injection.

5.2 Linear Field Errors

Dipole and quadrupole field errors raise the obvious question whether a closed orbit still exists, and if so, how are the betatron function and the tune changed in their presence. We will address these questions in this section.

5.2.1 Dipole Errors

The ideal equilibrium orbit is no longer a possible trajectory; however, in the case of small field errors we expect to find a neighbouring trajectory which will close on itself. This new orbit, depicted in Fig. 5.1 is called the disturbed closed orbit and the particles now make betatron oscillations around this orbit.

$$\Delta x = 0$$

$$\Delta x' = \Delta G \cdot \Delta s$$

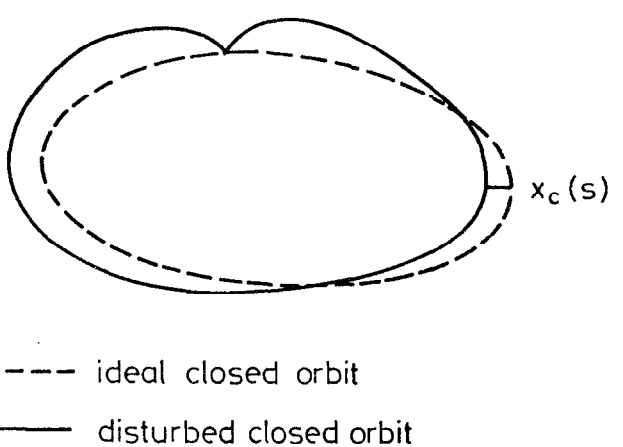


Fig. 5.1 - The change in closed orbit due to an dipole error $\Delta G \Delta s$.

The amplitude x(s) of an arbitrary particle with respect to the ideal equilibrium orbit is the sum of the disturbed closed orbit amplitude $x_c(s)$ and the betatron amplitude $x_\beta(s)$.

$$x(s) = x_c(s) + x_\beta(s) \tag{5.1}$$

Assume that there is a disturbance $\Delta B \Delta s$ located at s = 0. This disturbance will change the slope of the trajectory at this point but not its displacement.

$$\Delta x' = \frac{\Delta B \Delta s}{B\rho} \tag{5.2}$$

or $$\Delta x'' = \frac{\Delta x'}{\Delta s} = \frac{\Delta B}{B\rho} = \Delta G .$$

Thus the equation for the disturbed closed orbit is given by

$$x_c'' + K_x x_c = \Delta G \tag{5.3}$$

The general solution of eq. 5.3 can be written as:

$$x_c(s) = a \sqrt{\beta}(s) \cos(\mu(s) - \mu_o) \tag{5.4}$$

The constants a and μ_o are determined from the condition that the orbit must close on itself after one turn:

$$x_c(L) = x_c(0) \tag{5.5a}$$

$$x_c'(L) + \Delta G \, \Delta s = x_c'(0) \tag{5.5b}$$

By substituting the solution eq. 5.4 into eqs. 5.5a and 5.5b we find:

$$\mu_o = \pi Q_x \tag{5.6}$$

$$a = \frac{\Delta G \Delta s}{2 \sin \pi Q_x} \sqrt{\beta(0)} \tag{5.7}$$

The disturbed closed orbit is thus given by:

$$x_c(s) = \frac{\Delta G \Delta s \sqrt{\beta(0)}}{2 \sin \pi Q} \sqrt{\beta(s)} \cos(\mu - \pi Q_x) \tag{5.8}$$

Assuming that the dipole errors are distributed according to $\delta G(s')$ around the ring eq. 5.8 can be generalized:

$$x_c(s) = \frac{\sqrt{\beta(s)}}{2 \sin \pi Q_x} \oint \delta G(s') \sqrt{\beta(s')} \cos(\mu(s) - \mu(s') - \pi Q_x) \, ds' \tag{5.9}$$

The salient features of eq. 5.9 can be summarized as follows:

- The displacement of the closed orbit is everywhere proportional to the strength of the disturbance $\Delta B \Delta s$ and to the square root of the beta function at the position of the disturbance. It is also proportional to the square root of the beta function at the point of observation.

- In order for the closed orbit distortion to remain finite $Q_x(Q_y)$ must not be an integer. For integer Q values the particles will cross the disturbance with the same phase on every turn - i.e. the particles will receive a kick in the same direction on every turn leading to an divergent amplitude.

Correction dipole magnets are installed in all machines to minimize the closed orbit deviations. This is done by observing the beam position with monitors at say 4 positions per betatron wavelength and adjusting the correction dipoles to minimize the closed orbit amplitude. Typically disturbed closed orbit amplitudes on the order of 1 mm rms are obtained after corrections.

5.2.2 Gradient Errors

A gradient error located at s = 0 can be represented by a thin lens of focal strength $\delta = 1/f$. Such an error will obviously modify the betatron function of the undisturbed lattice and shift the tune from its undisturbed value. These effects can be evaluated using the Twiss matrix T. The Twiss matrix for a complete turn is given by the product of a quadrupole matrix Q - representing the disturbance - and the undisturbed Twiss matrix T_o

$$T = Q\,T_o \tag{5.10}$$

$$T = \begin{pmatrix} \cos\mu+\alpha\sin\mu & \beta\sin\mu \\ -\gamma\sin\mu & \cos\mu-\alpha\sin\mu \end{pmatrix} = \begin{pmatrix} 1 & 0 \\ -\delta & 1 \end{pmatrix} \begin{pmatrix} \cos\mu_o+\alpha_o\sin\mu_o & \beta_o\sin\mu_o \\ -\gamma_o\sin\mu_o & \cos\mu_o-\alpha_o\sin\mu_o \end{pmatrix}$$

The index refers to the undisturbed orbit. Multiplying the matrices on the right hand side and taking the trace yields:

$$\frac{1}{2}\,\mathrm{Tr}\,(T) = \cos\mu = \cos\mu_o - \frac{\delta\,\beta_o}{2}\sin\mu_o \tag{5.11}$$

This expression can be simplified for small tune changes - i.e. $\mu = \mu_o + \Delta\mu$:

$$\Delta\mu = -\frac{\delta\,\beta_o}{2} \tag{5.12}$$

or since $\Delta Q = 2\pi\Delta\mu$:

$$\Delta Q = -\frac{\delta\,\beta_o}{4\pi} \tag{5.13}$$

Thus the tune change ΔQ is directly proportional to the strength of the disturbance and to the value of the betatron function at the position of the disturbance.

Next we evaluate the change in the betatron function at $s = s_2$ caused by a gradient error at $s = s_1$.

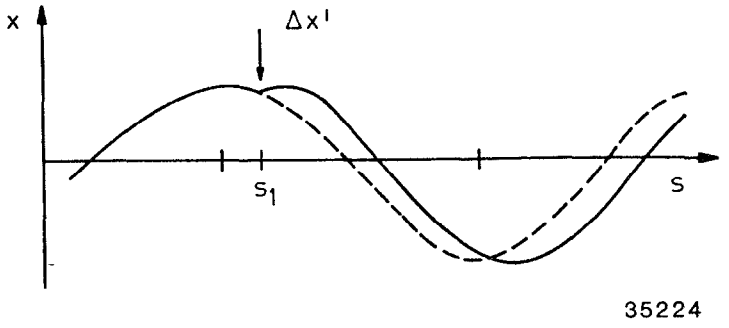


Fig. 5.2 - Change in the betatron function due to a gradient error at $s = s_1$.

The unperturbed Twiss matrix for a single turn can be written as:

$$T^o = A(s_1 \to s_2)\,B(s_2 \to s_1) = \begin{pmatrix} a_{11} & a_{12} \\ a_{22} & a_{22} \end{pmatrix} \begin{pmatrix} b_{11} & b_{12} \\ b_{21} & b_{22} \end{pmatrix} \tag{5.14}$$

Including the disturbance at $s = s_1$ yields a Twiss matrix T:

$$T = \begin{pmatrix} a_{11} & a_{12} \\ a_{21} & a_{22} \end{pmatrix} \begin{pmatrix} 1 & 0 \\ \delta & 1 \end{pmatrix} \begin{pmatrix} b_{11} & b_{12} \\ b_{21} & b_{22} \end{pmatrix} \tag{5.15}$$

Hence

$$\Delta T = T_{12} - T^o_{12} = \delta a_{12}\,b_{12} = \delta\sin(\mu_o - \mu_2 + \mu_1)\,\sin(\mu_2 - \mu_1)\beta_1\beta_2 \tag{5.16}$$

The change in T_{12} can also be expressed as a total differential:

$$T_{12} = \Delta(\beta_2 \sin\mu) = \Delta\beta_2 \sin\mu_o + \beta_2 \Delta\mu \cos\mu_o \qquad (5.17)$$

Equating eq. 5.16 and eq. 5.17 with the substitution $\Delta\mu = -\frac{\delta\beta_1}{2}$ yields the change in betatron amplitude at $s = s_2$ due to a gradient error δ at $s = s_1$:

$$\Delta\beta_2(s_2) = \frac{\delta\beta_1\beta_2 \cos[2\pi Q_x - 2(\mu_2 - \mu_1)]}{2\sin 2\pi Q_x} \qquad (5.18)$$

The change in the betatron function is directly proportional to the strength of the disturbance and the product of the betatron function at the position of the disturbance and the position of the observation.

The beam becomes unstable if the tune approaches a half integer - i.e. $Q_x \neq \frac{(2n+1)}{2}$.

The beat frequency introduced by an gradient error is twice the beat frequency caused by an dipole error.

With a gradient error k(s) distributed around the ring the tune shift and the change in betatron function can be written as:

$$\Delta Q = -\frac{1}{4\pi} \oint k(s)\, \beta(s)\, ds \qquad (5.19)$$

$$\Delta\beta(s) = \frac{\beta(s)}{2\sin 2\pi Q} \oint k(s')\, \beta(s') \cos 2[\pi Q + \mu(s') - \mu(s)] ds' \qquad (5.20)$$

5.3 Non Linear Errors

We have seen above that the betatron oscillations became unstable for integer and half integer tune values in the presence of dipole and quadrupole errors. Higher order multipole errors will drive higher order resonances[31] - i.e. the particle motion will now become unstable for fractional tune values 1/n = 1/3, 1/4, ... In general Q values satisfying the relation

$$\ell Q_x + m Q_z = s \qquad (5.21)$$

with $|\ell| + |m| = n$, and ℓ, m, s and n integers will be unstable. The ensuing resonance pattern is shown in Fig. 5.3 and the corresponding driving terms for the lowest order multipoles are listed in Table 5.1.

Table 5.1 - Resonance driving terms

Multipole	Order n	regular	skew
Quadrupole	2	$x^2 - y^2$	$2xy$
Sextupole	3	$x^3 - 3xy^2$	$y^3 - 3x^2y$
Octupole	4	$x^4 - 6x^2y^2 + y^4$	$4xy^3 - 4x^3y$
Decapole	5	$x^5 - 10x^3y^2 + 5xy^4$	$10x^2y^3 - 5x^4y - y^5$

For example a third order resonance will yield four forbidden lines in the resonance diagram shown above, namely $3Q_x = s$, $3Q_y = s$ and the coupling resonances $Q_x + 2Q_y = s$ and $2Q_x + Q_y = s$.

Indeed the order of a resonance is identical to the order of the driving term for an ideal closed orbit. However, in the presence of closed orbit errors a multipole of order n may excite lower orders.

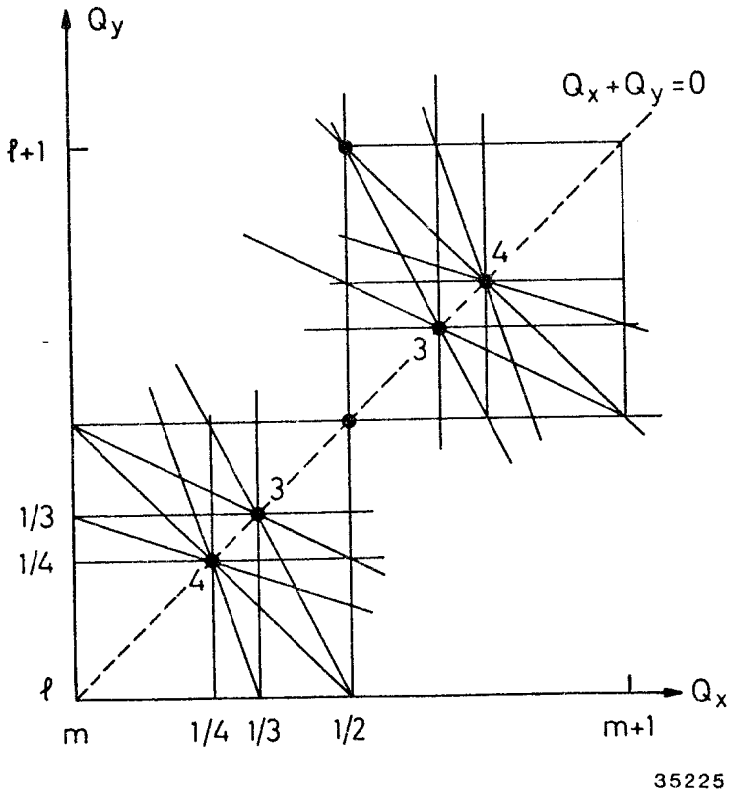


Fig. 5.3 - The pattern of forbidden tune values caused by low order resonances.

The width of resonance lines depends not only on the strength and the azimuthal distribution of the driving terms but also on the betatron amplitude in the case of non linear errors - i.e. sextupole and higher.

Multipole errors may therefore limit the practical aperture to values which are smaller than the geometric aperture given by the vacuum chamber.

5.3.1 The Resonance Mechanism

The phase space coordinates p and x of a particle can be represented in the circle diagram (Fig. 4) as:

$$\begin{aligned} p &= \beta x' = a \sin Q\theta \\ x &= x = a \cos Q\theta \end{aligned} \qquad (5.22)$$

$a = \sqrt{(\beta x')^2 + x^2}$ is the amplitude and θ the azimuthal angle of the particle in the machine - i.e. the particle makes Q turns in the phase space diagram per revolution. This representation is well suited to demonstrate the basic resonance mechanism.

A field error $\Delta B \Delta s$ change the momentum of a particle by:

$$\Delta p = \beta \frac{\Delta B \Delta s}{B\rho} \qquad (5.23)$$

The momentum kick, shown in Fig. 5.4 advances the phase by

$$\Delta\mu = \Delta p \frac{\cos Q\theta}{a} \qquad (5.24)$$

and increases the amplitude by:

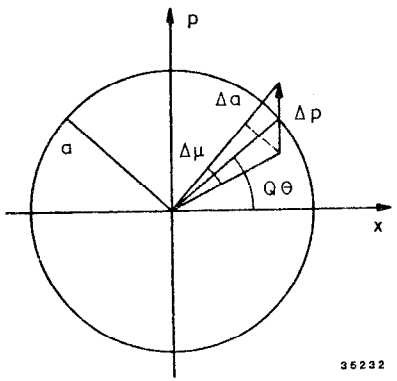


Fig. 5.4 - The circle diagram in normalized phase space.

$$\frac{\Delta a}{a} = \Delta p \frac{\sin Q\theta}{a} \tag{5.25}$$

As an example we will consider the particle motion in the plane in the presence of a sextupole of strength B'' and length l. The magnetic induction resulting from this sextupole is given by:

$$\Delta B = \frac{B''}{2} x^2 \tag{5.26}$$

The sextupole produces a momentum kick:

$$\Delta p = \beta x' = \beta\left(\frac{B'' l x^2}{2B\rho}\right) = \beta \frac{B'' l}{2B\rho} a^2 \cos^2 Q\theta \tag{5.27}$$

The resulting change in phase (eq. 5.24) and amplitude (eq. 5.25) is given by

$$\Delta\mu = \beta \frac{B'' l}{2B\rho} a \cos^2 Q\theta = \beta \frac{B'' l}{8B\rho}(3\cos Q\theta + \cos 3Q\theta) \tag{5.28}$$

$$\frac{\Delta a}{a} = \frac{\beta B'' l}{2B\rho} a \cos^2 Q\theta \sin Q\theta \tag{5.29}$$

We are now in a position to evaluate the width of the third integer stopband.

Let us assume that the radial tune Q_x is close to an 1/3 integer. In this case $\cos Q\theta$ averages to zero and we are left with the term proportional to $\cos 3Q\theta$. This term varies slowly from turn to turn modulating the unperturbed tune Q_x^o with an amplitude ΔQ_x given by:

$$\Delta Q_x = \frac{\Delta\mu}{2\pi} = \frac{\beta B'' l \cos 3Q\theta}{16\pi B\rho} \tag{5.30}$$

During the lifetime of the beam the tune will take all values within the limits:

$$Q_x^o - \frac{\beta B'' l a}{16\pi B\rho} \leq Q_x \leq Q_x^o + \frac{\beta B'' l a}{16\pi B\rho} \tag{5.31}$$

If $3\,Q_x = s$ = integer is inside this band, the perturbed value of Q_x will become equal to the integer s after several turns. From then on the particle will lock on to the resonance and advance in phase by $2\pi s$ per turn. The resonance thus appears to have a finite width given by the strength of the disturbance $B''l$, the amplitude a and the value of the betatron function β at the position of the disturbance.

The change in amplitude is given by:

$$\frac{\Delta a}{a} = \frac{\beta\, B''\, l\, a}{8\, B\, \rho} \sin 3Q\theta \qquad (5.32)$$

Thus on every turn the particle receives a kick in the same direction resulting in a monotonically growing amplitude.

It is clear from the discussion above that the motion of a particle will be stable if the amplitude a satisfies the condition:

$$a < \frac{16\pi\,(B\rho)\,\Delta Q_x}{l\,\beta\,B''} \qquad (5.33)$$

where ΔQ_x is the distance between the working point and the third integer resonance. Similar relationships can be obtained for higher resonance. Thus non linear fields may limit the machine acceptance to values less than the geometric acceptance.

Such fields may be caused by the magnets or they may be due to higher order correcting fields. For example the sextupoles needed to correct the chromaticity introduce strong non linearities.

5.4 The Chromaticity

The focal length of a lens is inversely proportional to the particle momentum causing particles of different momenta to have different tune values. A single lens of length Δs leads to tune spread ΔQ of:

$$\Delta Q = \frac{1}{4\pi}\,\beta(s)\,\Delta k(s)\,\Delta s \qquad (5.34)$$

The total tune spread is obtained by substituting $\Delta k = -k(s)\,\Delta p/p$ and integrating over one revolution. This results in an expression for the natural chromaticity

$$\xi = \left(\frac{\frac{\Delta Q}{Q}}{\frac{\Delta p}{p}}\right) = -\frac{1}{4\pi}\oint \beta(s)\,k(s)\,ds \qquad (5.35)$$

The natural chromaticity is negative and large. For example the natural chromaticity of the HERA proton ring in $\xi_x = -62$ and $\xi_y = -88$ with roughly equal contributions from the arcs and the straight section. This corresponds to a tune spread of $Q_x = \pm 0.07$ and $Q_y = \pm 0.09$ for a typical momentum spread of $\pm 10^{-3}$. Thus - if left uncorrected - the beam will cross low order resonances and be lost.

However, the chromaticity can be corrected by sextupoles located adjacent to the focusing quadrupoles. At least two families of sextupoles are needed to correct for the chromaticity in both planes. Let us consider the motion in the horizontal plane. The sextupole field is given by

$$B_z = \frac{1}{2}\left(\frac{\partial^2 B_z}{\partial x^2}\right) x^2 = \frac{1}{2}\,B''\,x^2 \qquad (5.36)$$

The sextupole field can be written as an amplitude dependent gra-

dient field with

$$k = \left(\frac{B''}{2B\rho} \right) x = mx \, . \qquad (5.37)$$

The resulting tune change is given by:

$$\begin{aligned} \Delta Q &= \frac{1}{4\pi} \oint m \, \beta(s) \, x(s) \, ds \\ &= \frac{1}{4\pi} \oint m \, \beta(s) \, (x_\beta(x) + D(s) \, \frac{\Delta p}{p}) \qquad (5.38) \\ &= \frac{1}{4\pi} \oint m \, \beta(s) \, D(s) \, \frac{\Delta p}{p} \end{aligned}$$

The total chromaticity ξ of the ring is the sum of the natural chromaticity caused by the momentum spread of the particles and chromaticity produced by the correcting sextupole magnets.

$$\xi = \left(\frac{\frac{\Delta Q}{\Delta p}}{p} \right) = - \frac{1}{4\pi} \oint \beta(s) \, (k(s) - m \, D(s)) \, ds \qquad (5.39)$$

6. The Synchrotron Motion [10,32]

6.1 Introduction

Energy is transferred to the particles by means of an accelerating system made of a power source and resonating cavities. The r.f. power P is fed to the cavity and excites a longitudinally electric field with a peak voltage $\hat{V}$ oscillating at a frequency ω. The required power is given by:

$$P = \frac{\hat{V}^2}{2R} \qquad (6.1)$$

R is the total shunt impedance of the cavities. As an example the PETRA cavities operating at a fixed frequency of 500 Mhz have a shunt impedance of $12 \frac{M\Omega}{m}$. Ferrite loaded cavities designed to work over a large range in frequencies have much lower shunt impedances.

The average energy gain per turn for the reference particle is given by:

$$e \, U = e \, \hat{V} \sin (\omega T_o + \phi_o) \qquad (6.2)$$

For the reference particle to remain in phase on sucessive turns ω must be an integral multiple h of the revolution frequency $\Omega_o = \frac{2\pi}{T_o}$

$$\omega = h \, \Omega_o \, . \qquad (6.3)$$

The harmonic number h is the maximum number of bunches which can be accelerated simultaneously. Particles with energies and r.f. phases different from those of the synchronous particles will execute oscillations in energy and phase with respect to the synchronous particle.

The relative change in revolution time $\eta(p)$ for a particle with momentum different from that of the synchronous particle is given by:

$$\eta(p) = \frac{dT}{T} = - \frac{d\Omega}{\Omega} = \left(\frac{dL}{L} - \frac{d\beta}{\beta} \right) \qquad (6.4)$$

where L denotes the machine circumference and βc the particle velocity. The first term results from the change in orbit length with momentum and the second term from the change in velocity.

The time dilatation function $\eta(p)$ is in general written as:

$$\eta(p) = \left(\frac{1}{\gamma_{tr}^2} - \frac{1}{\gamma^2} \right) \frac{dp}{p} \qquad (6.5)$$

with:

$$\frac{d\beta}{\beta} = \frac{1}{\gamma^2}\,\frac{dp}{p}$$

$$\frac{1}{\gamma_{tr}^2} = \left(\frac{dL}{L}\right)\left(\frac{dp}{p}\right)^{-1} \qquad (6.6)$$

Note that for particles with the transition energy $\gamma = \gamma_{tr}$ the revolution time is independent of momentum.

The transition energy γ_{tr} can be expressed using the optical parameters. The incremental change in orbit length for a particle travelling a distance ds with a radial amplitude x, is given by:

$$dL = (1 + G(s)\,x(s))\,ds \qquad (6.7)$$

$$L = \oint dL = \oint (1 + G(s)\,x(s))\,ds \qquad (6.8)$$

$$dL = L - L_o = \oint G(s)\,D(s)\,\frac{dp}{p}\,ds$$

The first term in eq. 6.5 is given by:

$$\frac{1}{\gamma_{tr}^2} = \alpha = \left(\frac{dL}{L}\right)\left(\frac{dp}{p}\right)^{-1} = \frac{1}{L}\oint G(s)\,D(s)\,ds \qquad (6.9)$$

The quantity α is usually called the momentum compaction. In the case of a separate function machine only the bending magnets contribute to α:

$$\alpha = \frac{G_o}{L}\oint D(s)\,ds \qquad (6.10)$$

As a rough approximation

$$\alpha = \frac{1}{Q^2} \qquad (6.11)$$

For electrons usually $\gamma >> \gamma_{tr}$ and an electron with a positive Δp has longer revolution time than the synchronous particle. This is also true for protons above the transition energy. However, below the transition energy a particle with positive ΔE has a shorter revolution time. At $\gamma = \gamma_{tr}$ the revolution time is independent of momentum and there is no phase focusing.

The synchrotron motion is illustrated in Fig. 6.1 for a particle above the transition energy. Plotted is the energy deviation ΔE versus the phase deviation $\Delta\phi$ both counted with respect to the synchronous particle. Consider a particle with positive ΔE which traverses the r.f. cavity at the synchronous phase ϕ_o. After one revolution the particle will traverse the r.f. cavity with the phase $\phi_o + \Delta\phi$. Thus it will gain less energy than the synchronous particle. The particle will continue to move away in phase until $\Delta E = 0$. It will then start to move towards ϕ_o and arrive at ϕ_o with an energy less than that of the synchronous particle. From then on it will gain more energy than the synchronous particle but continue to move away in phase until its energy equals that of the synchronous particle. As soon as the energy is higher than that of the synchronous particle it will start to move towards ϕ_o and arrive at ϕ_o with an energy higher than that of the synchronous particle. This completes one period. The aim of this chapter is to derive and solve the equations for the synchrotron oscillations and to determine the stable boundaries in $\Delta\phi$ and ΔE in terms of the r.f. parameters. The effects of the synchrotron radiation on the synchrotron motion will be discussed in chapter 7.

6.2 The Equation of Motion

The synchronous particle is accelerated at a constant radius R_o and the magnetic induction must therefore be increased proportional to the gain in momentum:

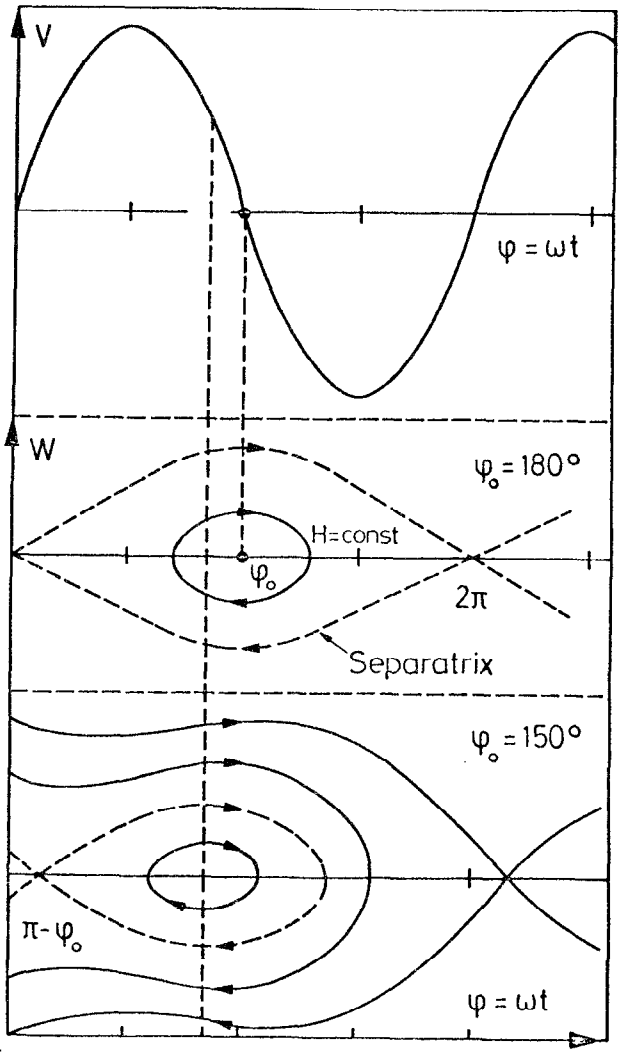


Fig. 6.1 - Longitudinal trajectories in $W = \frac{\Delta E}{\Omega_o}, \phi$ space for a stationary bucket $\phi_o = 180^o$ and a moving bucket $\phi = 150^o$.

$$dp = eR_o \frac{dB}{dt} T_o \qquad (6.12)$$

T_o is the revolution time $T_o = \frac{2\pi R_o}{\beta c}$.

The relationship between energy gain and ramping speed is given by:

$$dE_o = 2\pi e R_o^2 \frac{dB}{dt} = e \hat{V} \sin\phi_o \qquad (6.13)$$

We will now consider the synchrotron motion of particles with small energy and phase deviations with respect to the synchronous particle.

$$\Delta\phi = \phi - \phi_o , \quad dE = E - E_o \text{ and } d\Omega = \Omega - \Omega_o \qquad (6.14)$$

The change in revolution frequency for a particle with an energy deviation ΔE was derived above.

$$- \frac{d\Omega}{\Omega} = \eta \frac{dp}{p} = \eta \frac{dE}{R \Omega p} \qquad (6.15)$$

The corresponding change in phase angle is given by:

$$d\phi = - h \, d\theta = - h \Omega \, dt \qquad (6.16)$$

Combining eqs. 6.15 and 6.16 yields:

$$\frac{dE}{\Omega} = \left(\frac{p R}{h \eta \Omega} \right) \frac{d\phi}{dt} \qquad (6.17)$$

The energy gain of a particle arriving at a different phase will differ from that of the synchronous particle

$$\Delta p = \frac{\Delta E}{R\Omega} = \frac{e \hat{V}}{R \Omega} \sin\phi = \frac{T e \hat{V}}{2\pi R} \sin\phi \qquad (6.18)$$

$$\dot{p}R = \frac{e\hat{V}}{2\pi} \sin\phi \qquad (6.19)$$

The energy gain relative to that of the synchronous particle is given by:

$$\dot{Rp} - R_o\dot{p}_o = \frac{e\hat{V}}{2\pi}(\sin\phi - \sin\phi_o) \qquad (6.20)$$

Expanding R and p to first order yields:

$$\frac{d}{dt}(R_o\,\Delta p) = \frac{e\hat{V}}{2\pi}(\sin\phi - \sin\phi_o) \qquad (6.21)$$

Substituting $p = \frac{dE}{R\Omega}$ in the equation above and considering only small amplitude phase oscillation yields:

$$\frac{d}{dt}\left(\frac{\Delta E}{\Omega_o}\right) = \frac{e\hat{V}}{2\pi}(\sin\phi - \sin\phi_o) = \frac{e\hat{V}}{2\pi}\cos\phi\,\Delta\phi \qquad (6.22)$$

Combining eqs. 6.17 and 6.21 yields the equations for small amplitude phase oscillations:

$$\frac{d}{dt^2}(\Delta\phi) + \omega_s^2 = 0 \qquad (6.23a)$$

$$\omega_s = \left(\frac{-\eta_o\, h\, e\hat{V}\cos\phi_o\Omega_o}{2\pi\, p_o\, R_o}\right)^{1/2} \qquad (6.23b)$$

The solution for $\eta_o\cos\phi_o < 0$ is a sinusoidal oscillation with frequency ω_s:

$$\Delta\phi = A\sin(\omega_s t + \phi_o) \qquad (6.24)$$

We may now distinguish two cases:

Below transition energy $\eta_o < 0$ and the phase ϕ_o must be chosen between 0 and $\pi/2$ for stable acceleration and between $3/2\pi$ and 2π for stable deceleration. Above transition energy $\phi_o > 0$, and ϕ_o must be between $\pi/2$ and π for stable acceleration and between π and $3/2\pi$ for stable deceleration.

6.3 Phase Space Boundary and small Amplitude Oscillations

The limiting values in phase and energy for an assembly of particles traversing a given r.f. system can be determined using the Hamiltonian formalism.

The phase angle ϕ and the normalized energy

$$W = \frac{E}{\Omega_o} \qquad (6.25)$$

are used as conjugate variables. The Hamiltonian equations expressed in terms of these variables:

$$\frac{d\phi}{dt} = \frac{\partial H}{\partial t} = \frac{h\,\eta_o\Omega_o}{p_o\,R_o}W \qquad (6.26)$$

$$\frac{dW}{dt} = -\frac{\partial H}{\partial \phi} = \frac{e\hat{V}}{2\pi}(\sin\phi - \sin\phi_o) \qquad (6.27)$$

The equations above were obtained by inserting eqs. 6.17 and 6.22 into the Hamiltonian equations of motion.

The synchrotron motion is thus described by the following Hamiltonian:

$$H = \frac{h\,\eta_o\Omega_o}{2p_o\,R_o}W^2 + \frac{e\hat{V}}{2\pi}(\cos\phi - \cos\phi_o + (\phi-\phi_o)\sin\phi_o) \qquad (6.28)$$

The longitudinal motion of the particles is represented in the W-ϕ plane by trajectories of constant H. Note that the synchrotron motion repeats itself every 2π in phase, i.e. h times around the ring. Within each period of 2π the motion has two fixed points given by $\dot{\phi} = \dot{W} = 0$. From eqs. 6.26 and 6.27 these fixed points occur at:

$$W = 0\ ,\ \phi = \phi_o \quad \text{or} \quad \phi = \pi - \phi_o \qquad (6.29)$$

The fixed points $W=0$ and $\phi = \phi_o$ are inside the stable region and correspond to the synchronous particle. The separatrix - i.e. the limiting curve which separates the stable and the unstable region passes through the second fixed point at $W = 0$ and $\phi = \pi - \phi_o$. Note that the particle motion in ϕ and W becomes slow as particles approaches the fixed point - i.e. the synchrotron frequency ω_s slows down as the particles approach the limit of stability.

The separatrix can be evaluated by inserting the coordinates of the unstable fixed point into the Hamiltonian eq. 6.28. The maximum energy deviation is given by

$$(W)^2_{sep} = \frac{e\hat{V}p_o R_o}{\pi h \eta_o \Omega_o} \left((\pi - 2\phi_o) \sin\phi_o - 2\cos\phi_o \right) \qquad (6.30)$$

To obtain the extreme in phase we equate:

$$H = \frac{h\eta_o\Omega_o}{2p_o R_o} \tilde{W}^2_{sep} = \frac{h\eta_o\Omega_o}{2p_o R_o} W^2 + \frac{e\hat{V}}{2\pi} (\cos\phi - \cos\phi_o + (\phi-\phi_o)\sin\phi_o) \qquad (6.31)$$

Substituting $\tilde{W}^2_{sep}$ according to eq. 6.30 on the left hand side and introducing the coordinates ϕ_{max} and $W = 0$ on the right hand side of eq. 6.31 yield the following transcendental equation for the maximum phase:

$$(\pi - 2\phi_o) \sin\phi_o - 2\cos\phi_o = \cos\phi_{max} - \cos\phi_o + (\phi_{max} - \phi_o)\sin\phi_o \qquad (6.32)$$

The phase space trajectories for $\phi_o = 180^o$ and $\phi_o = 150^o$ are shown in Fig. 6.1. These trajectories correspond respectively to a stored and an accelerated beam above the transition energy.

The amplitude of the longitudinal oscillation is determined by the initial conditions of the injected particle. Let us consider a particle which is injected at the correct r.f. phase $\phi = \phi_o$ but with a normalized energy deviation $\tilde{W} = \frac{\Delta E}{\Omega_o}$. If $\tilde{W}, \phi_o$ is within the separatrix then the particle will travel on a closed trajectory in ϕ,W space with a maximum energy deviation $\tilde{W}$. The maximum excursion in phase can be evaluated from the Hamiltonian:

$$H(\phi,W) = \frac{h\eta_o\Omega_o}{2p_o R_o} \tilde{W}^2 = \frac{h\eta_o\Omega_o}{2p_o R_o} W^2 + \frac{e\hat{V}}{2\pi} (\cos\phi - \cos\phi_o + (\phi-\phi_o)\sin\phi_o) \qquad (6.33)$$

Let us consider three special cases:

a) Storage of particles with energies below the transition energy. In this case $\phi_o = 0$ and the resulting value of ϕ_{max} is obtained from eq. 6.33 for $W = 0$

$$\left(\frac{h\eta_o\Omega_o}{2p_o R_o}\right) \tilde{W}^2 = \frac{e\hat{V}}{2\pi} (\cos\phi_{max} - 1)$$

$$\phi_{max} = \pm 2 \arcsin \left(\frac{\pi h(-\eta_o)\Omega_o}{2p_o R_o e \hat{V}} \right)^{1/2} \tilde{W} \qquad (6.34)$$

b) Storage of particles with energies above the transiton energy. In this case $\phi_o = \pi$ and ϕ_{max} is again obtained from eq. 6.32 with $W = 0$.

$$\phi_{max} = \pm \arccos \left(\frac{\pi h \eta_o \Omega_o}{2p_o R_o e \hat{V}} \right)^{1/2} \tilde{W} \qquad (6.35)$$

c) A particle with $\gamma > \gamma_{tr}$ is accelerated and we consider small amplitude oscillations $\Delta\phi = \phi - \phi_o$. The Hamiltonian in eq. 6.33 can then be simplified to:

$$\frac{h\eta\Omega_o}{ep_oR_o}\,\tilde{W}^2 = \frac{h\eta_o\Omega_o}{2p_oR_o}\,W^2 - \frac{e\hat{V}}{2\pi}\left(\frac{\Delta\phi}{2}\right)^2\cos\phi_o \qquad (6.36)$$

The extreme amplitudes in phase for a particle with $W_{max} = W$ is given by

$$\Delta\phi = \pm\left[\frac{-2\pi h\,\eta\,\Omega_o}{e\,V\,p_oR_o\cos\phi_o}\right]^{1/2}\tilde{W}\,. \qquad (6.37)$$

6.4 Adiabatic Damping

The equation for the synchrotron oscillation was derived assuming time independent parameters for the synchronous particle. This is permitted since the timescale for an accelerating cycle is very long compared to the synchrotron oscillation period T_s. The change in W and ϕ during the accelerating cycle can be evaluated using the Bolzmann-Ehrenfest theorem. If a non-dissipative oscillatory system is described by the canonical variables p and q, then, according to the Bolzmann-Ehrenfest theorem, these parameters will change during the cycle such that

$$I = \oint p\,dq = \text{constant}. \qquad (6.38)$$

where the integral extends over one period of oscillation.

We now use this theorem to investigate the time behaviour of W and ϕ for small amplitude oscillations.

$$I = \oint W\,d\phi = \oint W\frac{d\phi}{dt} = \left(W\frac{d\phi}{dt}\right)\frac{2\pi}{\omega_s} \qquad (6.39)$$

Replacing $\frac{d\phi}{dt}$ according to eq. 6.26 and ω_s according to eq. 6.23b yields:

$$I = W^2\left[\frac{-(2\pi)^2\,h\,\eta_o\Omega_o}{p_oR_o\,e\,\hat{V}\cos\phi_o}\right]^{1/2} \qquad (6.40)$$

The normalized energy makes sinusoidal oscillations. Averaged over one turn $W^2 = \frac{1}{2}\tilde{W}^2$ where $\tilde{W}$ is the peak amplitude. Then adiabatically $\tilde{W}$ will change as:

$$\tilde{W} \sim \left[\frac{-p_oR_o\,\tilde{V}\cos\phi_o}{\eta_o\,\Omega_o}\right]^{1/4} \qquad (6.41)$$

i.e. $\tilde{W}$ will grow proportional to $p_o^{1/4}$.

We can write down a similar equation for the phase oscillations:

$$I = \oint \Delta\phi\,dW = (\Delta\phi\,\frac{dW}{dt})\,\frac{2\pi}{\omega_s} \qquad (6.42)$$

Replacing $\frac{dW}{dt}$ according to eq. 6.27 and ω_s according to eq. 6.28b leadsto

$$\hat{\Delta\phi} \sim \left[\frac{\eta_o\,\Omega_o}{p_oR_o\cos\phi_o}\right]^{1/4} \qquad (6.43)$$

Thus the maximum value of the phase amplitude $\hat{\Delta\phi}$ decreases with momentum as:

$$\hat{\Delta\phi} \sim p_o^{-1/4} \qquad (6.44)$$

Note that $W\,\Delta\phi$ is an invariant.

7. Effects of the Synchrotron Radiation on the Single Particle Motion [9]

7.1 Introduction

The instantaneous power P_γ radiated by a relativistic particle of energy E deflected in a magnetic field of induction B is given by:

$$P_\gamma = \frac{e^2 c^3}{2} C_\gamma E^2 B^2 \qquad (7.1)$$

where

$$C_\gamma = \frac{4}{3} \left(\frac{e^2}{mc^2} \right) \frac{1}{(mc^2)^2} .$$

The instantaneous radiated power is proportional to the product of beam energy and magnetic induction squared and inversely proportional to the fourth power of particle mass. For given values of E and B an electron will lose 10^{13} times more energy than a proton per turn. The motion of the protons is thus not influenced by synchrotron radiation at present energies and the equations discussed above remain valid. On the other hand the design of an electron machine is governed by synchrotron radiation and the single particle motion is strongly influenced by the emission of photons.

The average energy loss (eU_o) of an electron of energy E_o moving on the design orbit is obtained by integrating P_γ over one turn.

$$(e\,U_o) = \frac{1}{2} \oint P_\gamma \, ds \qquad (7.2)$$

$$(e\,U_o) = \frac{C_\gamma E_o^4}{2\pi} \oint G^2(s)\, ds$$

For a seperate function machine with $G = \frac{1}{\rho_o}$ in the dipoles and zero elsewhere:

$$(e\,U_o) = \frac{88.5 \text{ keV } E_o^4 \text{ (GeV)}}{\rho_o \text{(m)}} \qquad (7.3)$$

The synchrotron radiation is focused within a cone of opening angle $\frac{1}{2\gamma}$ along the direction of particle motion. The electrons do not radiate continuously but emit discrete quanta with an energy distribution shown schematically in Fig. 7.1. A half of the total radiated power is

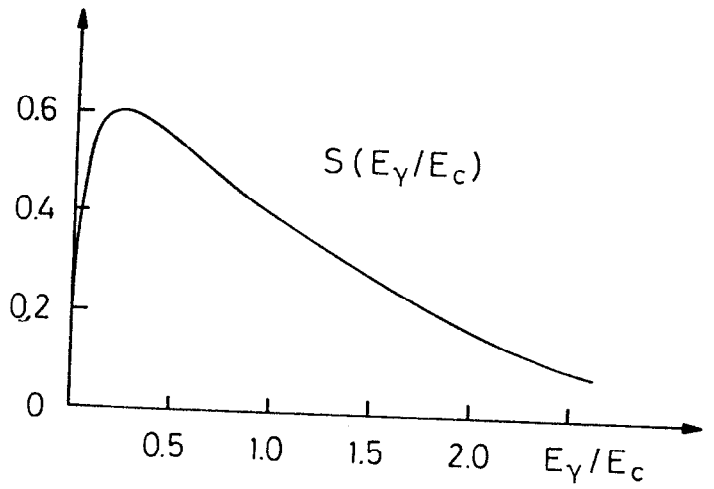


Fig. 7.1 - The energy distribution of the synchrotron radiation measured in units of the critical energy.

carried by photons with energies above the critical energy E_c:

$$E = \frac{2.23\ \text{keV}\ E_o^3\ (\text{GeV})}{\rho_o(\text{m})}$$

The mean photon energy is proportional to the critical energy

$$\langle E_\gamma \rangle = \frac{8}{15\sqrt{3}} E_c \qquad (7.5)$$

The average energy loss suffered by the electrons per turn must be replenished by the r.f. system. However, both the number and the energy of the emitted photons fluctuate from turn to turn and this represents a source of noise which excites oscillations.

Both the betatron oscillations and the synchrotron oscillation are damped by the average effects of the synchrotron radiation and excited by its quantum fluctuations. The final beam dimensions result from the equilibrium between the two effects.

The synchrotron radiation also governs the design of the technical components for HERA's electron ring.

The total power radiated by the beam is given by $P_b = (e\ U_o)\ n_e$. At 30 GeV the nominal current of 56 mA radiates a total power of 7.5 MW. This radiation will strike the outer walls of the vacuum chamber with a linear power density of max. 2.1 kW/m.

Furthermore a certain percentage of the photons will Compton scatter and to avoid radiation damage to equipment in the tunnel the majority of these photons must be confined within the vacuum chamber, respectively with the magnet system. A photon striking the wall of the vacuum chamber will lead to gas desorption. In order to achieve the vacuum needed one must use either a distributed pumping system or closely spaced discrete pumps.

Below we will discuss the effects of the synchrotron radiation on the single particle motion. This discussion will follow the excellent account given by M.Sands in reference 9.

7.2 Radiative Damping

7.2.1 The longitudinal motion

The instantaneous power radiated by an off energy electron differs from that radiated by the synchronous electron since the particles have different energies and travel through different regions of the guide field. The average energy loss per turn (eU) for an off energy particle is given by:

$$eU = e\,U_0 + 0\,\Delta E \qquad (7.6)$$

where $0 = e\left(\frac{dU}{dE}\right)_{E_0}$. The equation of synchrotron motion (eq. 6.20) must be modified to include the energy loss due to synchrotron radiation:

$$\frac{d}{dt}\left(\frac{\Delta E}{\Omega_0}\right) = \frac{e\,\tilde{V}}{2\pi}\cos\phi_0\,\Delta\phi - 0\,\Delta E \qquad (7.7)$$

Combining eq. 7.7 with eq. 6.15 yields the phase oscillation equation in the presence of synchrotron radiation.

$$\frac{d^2\Delta\phi}{dt^2} + 2\alpha_\varepsilon \frac{d\Delta\phi}{dt} + \omega_s^2 \Delta\phi = 0 \qquad (7.8)$$

with $\alpha_\varepsilon = \frac{0}{2T_o}$.

For damping times $\tau_\varepsilon = \frac{1}{\alpha_\varepsilon}$ which are long compared to the revolution time eq. 7.8 has the solution.

$$\Delta\phi = A\, e^{-\alpha_\varepsilon \cdot t} \cos(\omega_s t) \qquad (7.9)$$

Thus, neglecting quantum fluctuations, the amplitude of the longitudinal oscillation decreases exponentially with a time constant τ_ε.

α_ε can be expressed in terms of the lattice parameters. To this end we integrate the energy loss over one turn:

$$(e\,U) = \oint P_\gamma\, dt = \frac{1}{c} \oint P_\gamma \left(1 + \frac{x}{\rho}\right) ds \qquad (7.10)$$

Since we are interested in the energy loss of an off energy electron $x = D \frac{\Delta E}{E_o}$.

Differentiation of eq. 7.10 yields:

$$\left(\frac{e\, dU}{dE}\right)_{E=E_o} = \frac{1}{2} \oint \left(\frac{dP_\gamma}{dE} + \frac{D}{\rho} \frac{P_\gamma}{E_o}\right) ds \qquad (7.11)$$

The first term evaluated according to eq. 7.1 and with the substitution: $\frac{dB}{dE} = \frac{dB}{dx} \frac{dx}{dE} = \frac{D}{E_o} \frac{dB}{dx}$ yields:

$$\frac{dP_\gamma}{dE} = 2 \frac{P_\gamma}{E_o} + 2 \frac{DP_\gamma}{E_o B_o} \frac{dB}{dx} \qquad (7.12)$$

Eq. 7.11 is written as:

$$\frac{edU}{dE} = \frac{e\, U_o}{E_o} (2 + \Delta J) \qquad (7.13)$$

with

$$\Delta J = \frac{1}{c\, U_o} \oint \left(DP_\gamma \left(\frac{1}{\rho} + \frac{2}{B_o} \frac{dB}{dx}\right)\right) ds \qquad (7.14)$$

The expression for ΔJ can be simplified using eq. 7.2 and the definition $K_1(s) = \frac{1}{B\rho} \left(\frac{dB}{dx}\right)$

$$\Delta J = \frac{\oint D(s) G(s) \left(G^2(s) + 2K_1(s)\right) ds}{\oint G^2(s)\, ds} \qquad (7.15)$$

Eq. 7.15 evaluated for a separate function machine yields

$$\Delta J = \frac{1}{2\pi} G_o^2 \int_{\text{magnets}} D(s)\, ds = \frac{\alpha R}{\rho_o} \qquad (7.16)$$

where R is the average machine radius. Note that for a separate function machine ΔJ is small whereas it is large for a combined function machine, i.e. an accelerator satisfying $G(s)\, K(s) \neq 0$.

The inverse damping time α_ε - evaluated for a separate function machine - is given by:

$$\alpha_\varepsilon = \frac{e\, U_o}{2E_o T_o} \left(2 + \frac{\alpha R}{\rho_o}\right) \approx \frac{e\, U_o}{E_o T_o} \qquad (7.17)$$

The characteristic damping time for longitudinal oscillations is simply the time it takes the electron to radiate away all its energy. Evaluated for the electron ring of HERA gives $\frac{1}{\alpha_\varepsilon} = 4.5$ msec at 30 GeV. Note that the damping time is inversely proportional to E_o^3.

7.2.2 The vertical betatron oscillations

The radiative damping mechanism for the vertical betatron motion is illustrated in Fig. 7.2. The electron emits a photon along its direction of motion - i.e. the electron suffers only a loss of energy without a change of position or slope. However, in traversing the r.f. cavities the electron receives a longitudinal kick compensating the average energy loss - i.e. $\Delta E = e\,U_0$. Thus the slope of the particle is slightly reduced after traversing the cavity:

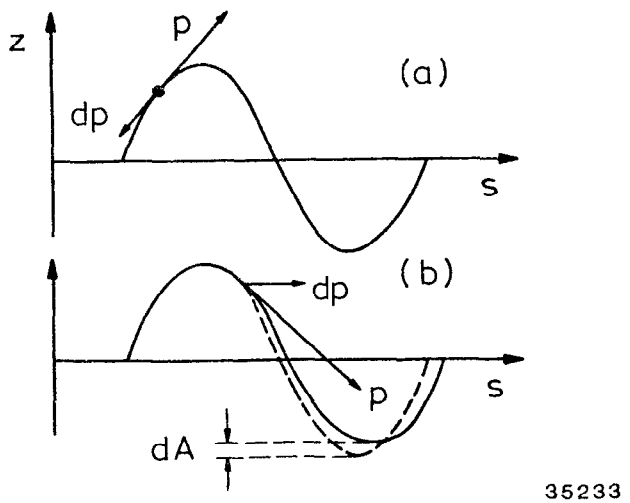


Fig. 7.2 - The vertical motion of a particle in the arcs (a) and in the r.f. cavities (b).

$$z' + dz' = \frac{p}{p_0 + \delta p} = z'\,(1 - \frac{\delta p}{p_0}) \qquad (7.18)$$

$$dz' \approx -z'\,\frac{dE}{E_0} = -z'\,(\frac{e\,U_0}{E_0})$$

The position z and the slope z' of the electron is given by

$$z = A\cos\mu \quad \text{respectively} \quad z' = \frac{A}{\beta}\sin\mu. \qquad (7.19)$$

The amplitude A can be written as:

$$A^2 = z^2 + (\beta z')^2 \qquad (7.20)$$

The change in amplitude caused by the energy loss due to synchrotron radiation and its replenishment by the r.f. cavities is given by:

$$AdA = -\beta^2 z'\,dz' \approx -(\beta z')^2\,(\frac{e\,U_0}{E_0}) \qquad (7.21)$$

The electron emits photons with equal probability along the orbit. Averaging $\beta z'$ over all phase angles μ yields:

$$\langle \beta z' \rangle^2 = \frac{A^2}{2} \qquad (7.22)$$

Inserting eq. 7.22 into eq. 7.21 and integrating over t yields

$$A = A_0\,e^{-\alpha_z t} \qquad (7.23)$$

with $\alpha_z = \dfrac{(eU_0)}{2E_0T_0}$.

The amplitude of the transverse motion is thus exponentially damped with a damping time twice the longitudinal damping time.

7.2.3 Damping of the radial betatron motion

The damping mechanism outlined above is also effective for the radial betatron motion. However, the photon is radiated in a region

with radial dispersion and this yields a term which is antidamping. The basic mechanism is outlined in Fig. 7.3. The total radial displacement is a sum of the closed orbit displacement x_ε and the betatron displacement with respect to this closed orbit

$$x = x_\beta + x_\varepsilon \tag{7.24}$$

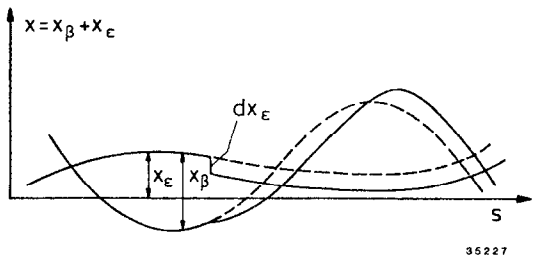


Fig. 7.3 - Radial amplitude growth due to the emission of synchrotron radiation at a position with dispersion.

When the electron radiates a photon the closed orbit will suddenly jump by $dx_\varepsilon = D \frac{dE}{E_0}$. However, the spatial position of the electron remains unchanged such that a change in the closed orbit must be compensated by a change in betatron amplitude:

$$dx_\beta = -D \frac{dE}{E_0} \tag{7.25}$$

The change in slope due to D' is neglected.

The radial position and slope of the electron can be written as:

$$x_\beta = A\cos\mu,\ x'_\beta = \frac{A}{\beta}\sin\mu\ . \tag{7.26}$$

This yields:

$$AdA = x_\beta\, dx_\beta = -D\, x_\beta \frac{dE}{E_0} \tag{7.27}$$

The energy loss in a path length $d\ell$ is given by:

$$dE = -\frac{P_\gamma}{c} d\ell = -\left(1 + \frac{x_\gamma}{\rho_0}\right) \frac{P_\gamma}{c} ds \tag{7.28}$$

The resulting change in amplitude

$$AdA = D\, x_\beta \left(1 + \frac{x_\beta}{\rho_0}\right) \frac{P_\gamma}{c} \frac{ds}{E_0} \tag{7.29}$$

The expectation value of dA is obtained by averaging eq. 7.29 over all phase angles

$$\frac{\langle dA \rangle}{A} = \frac{D}{2\rho_0} \frac{P_\gamma}{E_0} \frac{ds}{c} \tag{7.30}$$

For a separate function machine, $e\,U_0$, the total energy loss per turn, is equal to $P_\gamma \frac{ds}{c}$ summed over all the dipole magnets. The resulting change in the amplitude is

$$\frac{dA}{A} = \frac{\langle D \rangle}{2\rho_0} \frac{e\,U_0}{E_0} \tag{7.31}$$

Thus the finite dispersion leads to an exponentially growing radial amplitude with a time constant given by:

$$\frac{\langle D\rangle}{\rho_o}\ \frac{e\,U_o}{2E_o T_o} \tag{7.32}$$

The total change in amplitude is simply the sum of the dispersion effect and the r.f. acceleration effect derived in chapter 7.2.2.

$$\frac{1}{A}\ \frac{dA}{dt} = \alpha_x = -\left(1 - \frac{\langle D\rangle}{\rho_o}\right) \frac{e\,U_o}{2E_o T_o} \tag{7.33}$$

Substituting $\langle D\rangle = \alpha R$ and comparing with eq. 7.16 yields:

$$\alpha_x = -(1 - \Delta J)\ \frac{U_o}{2E_o T_o} \tag{7.34}$$

For a separate function machine ΔJ is less than one and the radial motion is damped.

7.2.4 Robinson's Theorem

We have evaluated the damping times for all three degrees of freedom. The damping coefficients can be written as:

$$\alpha_i = J_i\ \frac{\langle P_\gamma\rangle}{2E_o} = J_i\ \frac{e\,U_o}{2E_o T_o} \tag{7.35}$$

with $J_x = 1 - \Delta J$, $J_z = 1$ and $J_\varepsilon = 2 + \Delta J$.

Note that the sum of the damping partition number is a constant:

$$\Sigma\, J_i = 4 \tag{7.36}$$

This has been shown by Robinson[33] to be true on general grounds as long as effects of the fields induced by the circulating electron beams can be neglected. ΔJ is a property of the detailed layout of the ring. Note that for a separate function machine $\Delta J << 1$ leading to damping in all three degrees of freedom. In a combined function machine ΔJ will be larger than one causing the radial beam size to grow exponentially.

7.3 Radiation excitation and beam dimensions

In the preceding section we have shown that the single particle motion is damped by the interplay between the average energy loss due to synchrotron radiation and its replenishment by the r.f. system. However, the emission of synchrotron radiation is a quantum process - the radiation is emitted in discrete quanta and both the energy and the number of the photons fluctuate. These fluctuations are a source of noise and excite single particle oscillations. The final beam dimensions result from the equilibrium between the damping caused by the average energy loss and the noise introduced by its fluctuations.

The electrons in a r.f. bucket of width ΔE have a Gaußian energy distribution with a rms value of

$$\sigma_\varepsilon = \left(\frac{C_q}{\rho J_E}\right)^{1/2} \frac{E^2}{m_o c^2} \tag{7.37}$$

with $C_q = \frac{55\,\hbar}{32\sqrt{3}\ mc} = 3.84\ 10^{-13}$ cm.

This results in a rms bunch length:

$$\sigma_\ell = \left(\frac{R\,\alpha\,\Omega_o}{\omega_s}\right) \frac{\sigma_E}{E} \tag{7.38}$$

Thus the bunch length of the electron beam is rather short, the rms bunch length in HERA is of the order of a cm at 30 GeV and

scales with energy and tune as $\sigma_\ell \sim E/Q$.

The final emittance is the equilibrium between the damping caused by the r.f. system, compensating the average radiation loss and the growth caused by the quantum fluctuations.

$$\varepsilon_x = \left(\frac{J_\varepsilon}{J_x}\right)\left(\frac{\sigma_\varepsilon}{E}\right)^2 \left(\frac{\langle D_x\rangle}{\langle\beta_x\rangle}\right) \approx \left(\frac{J_\varepsilon}{J_x}\right)\left(\frac{\sigma_E}{E}\right)^2 \left(\frac{R_{arc}}{8Q_{arc}^3}\right) \frac{\mu^3}{tg\left(\frac{\mu}{2}\right)\sin^2\left(\frac{\mu}{2}\right)} \qquad (7.39)$$

R_{arc} is the average radius in the arcs and Q_{arc} is the contribution to the tune from the arcs. Note that the factor

$$\frac{\mu^3}{tg\left(\frac{\mu}{2}\right)\sin^2\left(\frac{\mu}{2}\right)}$$

is 8 at $\mu_o = 0$ and varies little with the phase advance μ for μ less than 90^o per cell.

The emittance of an electron beam is not a constant of motion but varies with the tune. Strong focusing, i.e. short cell length and large phase advance per cell will lead to a small radial emittance.

Since the vertical dispersion is rather small the vertical emittance is mainly due to the coupling of vertical and radial motion. In general the coupling may be as small as a few percent for a well aligned machine.

This results in a ribbon type beam for the electrons as compared to a round proton beam. However, it is of course in principle possible to deliberately increase the coupling between the radial and the vertical motion by installing skewed quadrupoles.

8. Polarisation [34)]

The importance of colliding electrons or positrons of well defined helicity with protons is discussed in section 2.

Beams with a high degree of polarisation have been observed[35)] at PETRA and the beams have been collided without destroying the initial polarisation. Scaling from these results it seems reasonable to expect transversely polarized $e^{\pm}$ beams in HERA.

8.1 Transverse polarisation

The spin of electrons (positrons) injected into an accelerator will align along the direction of its vertical guide field. The spin sum along the vertical direction is zero for an unpolarized beam, i.e. there is the same number of electrons with spin pointing upwards as downwards. As the electrons are deflected in the magnetic guide field they emit synchrotron radiation which in part is due to a spin flip transition. The probability of magnetic dipole emission depends on the orientation of the initial spin. These probabilities are given by:

$$\begin{aligned} W(\uparrow\downarrow) &= \frac{5\sqrt{3}}{16}\frac{e^2\gamma^5\hbar}{m^2c^2\rho^3}\left(1+\frac{8}{5\sqrt{3}}\right) \\ W(\downarrow\uparrow) &= \frac{5\sqrt{3}}{16}\frac{e^2\gamma^5\hbar}{m^2c^2\rho^3}\left(1-\frac{8}{5\sqrt{3}}\right) \end{aligned} \qquad (8.1)$$

where the arrows $(\uparrow\downarrow)$ indicate the initial and the final spin directions either parallel or antiparallel to the direction of the magnetic induction. The circulating beam will gradually become polarized with

the spins aligned antiparallel to direction of the guide field. The beam polarisation builds up exponentially:

$$P(t) = P_0 (1 - e^{-t/\tau_p}) \qquad (8.2)$$

In the absence of populations effects P_0, the maximum degree of polarisation, is given by:

$$P_0 = \frac{n(\downarrow) - n(\uparrow)}{n(\downarrow) + n(\uparrow)} \qquad (8.3)$$

where the final polarisation $n(\downarrow)$ and $n(\uparrow)$ are determined by detailed balance:

$$n(\uparrow)\, W(\uparrow\downarrow) = n(\downarrow)\, W(\downarrow\uparrow) \qquad (8.4)$$

Combining eqs. 8.3 and 8.4 yields:

$$P_0 = \frac{W(\uparrow\downarrow) - W(\downarrow\uparrow)}{W(\uparrow\downarrow) + W(\downarrow\uparrow)} = \frac{8}{5\sqrt{3}} = 0.92 \qquad (8.5)$$

τ_p, the build up time of polarisation is given by

$$\tau_p = (W(\uparrow\downarrow) + W(\downarrow\uparrow))^{-1} \qquad (8.6a)$$

Using eq. 8.1 and inserting the numerical values yields:

$$\tau_p = \frac{98(s)\ \rho^2(m)\, R(m)}{E^5(GeV)} \qquad (8.6b)$$

where ρ is the bending and R the average radius of the machine.

The requirement that τ_p must be short compared to the storage time of several hrs determines the minimum electron energy. The polarisation time for a 30 GeV electron beam in HERA is of about 20 min.

Bargman, Michel and Telegdi[36] have written down the general equation for spin motion in electric and magnetic fields. For the spin motion in a circular accelerator this expression can be simplified to:

$$\frac{d\vec{n}}{ds} = -\left(\frac{e\, B_0}{m\, c^2}\right)\left(a + \frac{1}{\gamma}\right) \vec{z} \times \vec{n}$$

The coordinate system, moves with the beam. $\vec{n}$ is the direction of the spin in space and B_0 is pointing along the vertical direction $\vec{z}$ and $a = \frac{(g-2)}{2} = 0.0011597$.

It follows immediately from eq. 8.7 that the spin component along the $\vec{z}$ direction is conserved whereas the radial spin component S_x or the spin component directed along the direction of particle motion S_s precesses an angle

$$\frac{e\, B_0}{m\, c^2}\, a\, 2\pi\, \rho = 2\pi\, \gamma a \text{ per turn} \qquad (8.8)$$

$$= (2\pi)\, \frac{E}{0.44065}$$

The electrons in a bunch have different energies corresponding to different precision frequencies γa. This destroys the polarisation along the $\vec{x}$ and the $\vec{s}$ direction.

The radiative polarisation generates a vertical spin alignment in the arcs while the experiments require a longitudinal polarisation at the interaction point, preferable with the option to change from one helicity to the other. A possible spin rotator will be discussed in chapter 10.

8.2 Depolarisation Mechanisms[34,37]

The discussion above is valid for an ideal machine. The guide field of a real machine, however, is not perfect and these imperfections may depolarize the beam.

If the beams are polarized along the vertical direction then errors in the vertical field will not affect the spin. The particles must still turn 2π and their spin precess by $2\pi a\gamma$.

A non vanishing radial field, however, will cause the electron spin to precess around the $\bar{x}$ axis leading to depolarisation. Let us assume that a quadrupole is misaligned by 1 mm in the vertical direction. Using HERA parameters this corresponds to a vertical deflection:

$$\Delta\theta = \frac{(\Delta B_x \ell)}{B\rho} = \frac{12.5\ \text{T/m}\ (10^{-3}\ \text{m})\ 1\text{m}}{3.33 \cdot 30} = 0.125\ \text{mrad}$$

equivalent to a precision angle ϕ_x:

$$\phi_x = (a\,\gamma)\,\Delta\theta = 8.6\ \text{mrad at 30 GeV.}$$

This is a rather small angle. However, if $a\gamma = n$ = integer then the precession adds on successive turns leading to complete depolarization. The depolarizing resonances $\gamma a = n$ are spaced 440 MeV apart and the beam energy must be chosen such that the spin tune does not equal an integer number. However, the electrons have a finite energy spread with a rms width σ_ε growing proportional to E^2. At 27.5 GeV at HERA the computed energy spread is 28 MeV - i.e. the spacing between adjacent resonance is 16 σ_ε and this should be sufficient. Note that this effect may make it difficult to achieve transverse polarisation in larger machines like LEP.

The spin motion is also modulated by the synchrotron and betatron motion such that the general resonance condition can be written as:

$$\gamma a \pm k_x Q_x \pm k_z Q_z \pm k_s Q_s = n. \qquad (8.9)$$

where k and n are integers and $Q_{x,z,s}$ the tune shifts.

The importance of these side band resonances will be enhanced by the synchrotron radiation. To illustrate the effect let us consider a planar machine. The electron emits a photon at a position of non-vanishing vertical dispersion. The vertical closed orbit will jump and the particle starts to make vertical oscillations which takes it through regions of space with non vanishing radial field components. The spin will thus precess around the radial axis away from the vertical spin direction. The vertical oscillations damp out after a few msec but the spin is now pointing in a different direction. The polarising mechanism will restore the original spin direction with a time constant τ_p. However, since the electron radiates some 10^{11} times during one damping time τ_p the spin will gradually diffuse away from the vertical axis leading to an unpolarized beam.

The crucial quantity which determines the spin diffusion is the so called spin diffusion coefficient or spin chromaticity:

$$\vec{d} = \gamma \left(\frac{\partial \vec{n}}{\partial \gamma} \right) \frac{\delta E}{E} \qquad (8.10)$$

The spin rotators, unless very carefully designed and matched into the lattice, will be strong sources of beam depolarisation.

In the linear approximation, prescriptions[38] exist of how to design a machine, including spin rotators, such that the spin dispersion is zero. The beam-beam interaction will also cause depolarisation and this effect is now being evaluated using spin tracking programs.

9. Current Limitations [39]

The motion of a single particle is determined by the guide field, but particles moving within an assembley of particles will experience additional forces resulting from:

- The repulsion of like sign particles moving together. In this case the electric and magnetic force subtract resulting in a space charge force which decreases inversely proportional to the energy of the particle squared. For particles moving in opposite directions the forces add and the resulting beam-beam instability is the ultimate performance limit of a colliding beam machine.

- Electric and magnetic fields associated with longitudinal and transverse oscillations of the particles interact with the surroundings (beam pipe, cavities) and induce electro-magnetic fields which in turn may act back on the beam. The resulting force can drive the beam unstable if the phase of the induced force is ahead of the oscillation and its strength is large enough to overcome the natural damping caused by the incoherence of the particle motion. If the induced fields decay rapidly then only the bunch itself is affected and we have a single bunch instability. However adjacent bunches may communicate by means of slowly decaying wake fields causing collective bunch instabilities.

In this chapter we will discuss some of the instabilities which can affect a bunched proton beam. The electron motion is in general more stable due to the strong radiative damping.

9.1. Longitudinal Instabilities

9.1.1 Introduction

As discussed below, it seems advantageous to cross the electron and the proton beam at a finite angle. The electron bunch, due to its radiative damping, is much shorter than the proton bunch and the luminosity is therefore directly proportional to the linear charge density of the protons $e\lambda(s)$ - i.e. short, intense proton bunches are needed to reach high luminosity. The longitudinal electron distribution can be approximated by a Gaußian whereas the proton line density is well represented by a parabolic function

$$\lambda(s) = \frac{6N_b}{\ell^3}\left(\frac{\ell^2}{4} - s^2\right) \qquad (9.1)$$

where ℓ is the bunch length measured at the base.

The luminosity is also directly proportional to the number of proton bunches - i.e. we would like to store a larger number of bunches in HERA.

The combination of a high line density and a large number of bunches make HERA prone to instabilities.

Let us first consider the situation shown in Fig. 9.1. A continuous particle beam of radius a moves along the $\vec{s}$ direction with velocity $\vec{\beta}c$ in the center of circular beam pipe of radius b. A varying longitudinal particle density gives rise to a longitudinal space charge force and to longitudinal wake fields produced by currents induced in the walls of the beam pipe. The sum of both

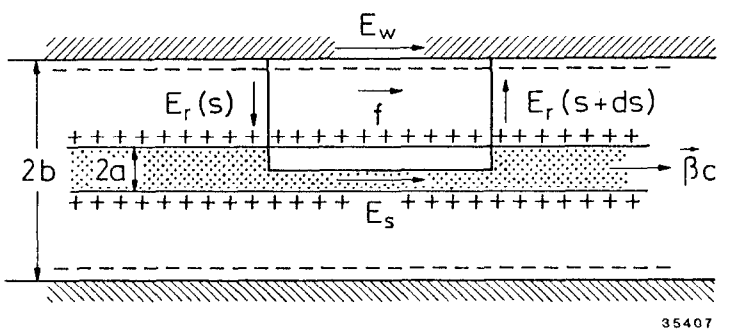


Fig. 9.1 - A uniform beam of radius a moving with β^*c along the $\vec{s}$ direction in the center of a circular beam pipe of radius b.

effects produces a longitudinal voltage which acts on the beam. We will now evaluate these effects.

The electric and the magnetic fields produced by moving charges can easily be obtained by solving Maxwell's equations.

$$\varepsilon_o \operatorname{div} \vec{E} = \rho(s) \tag{9.2a}$$

$$\frac{1}{\mu_o} \operatorname{rot} \vec{B} = \rho(s)\,(\vec{\beta}c) \tag{9.2b}$$

with $\rho = \frac{e\lambda(s)}{\pi a^2}$.

The line density $\lambda(s)$ is assumed to vary slowly as a function of s. Maxwell's equations have then the solutions:

$$E_r = \frac{e\,\lambda}{2\pi\varepsilon_o}\,\frac{r}{a^2} \quad ; \quad B_\theta = \frac{\mu_o\, e\,\lambda\,\beta c}{2\pi}\,\frac{r}{a^2} \qquad r \leq a \tag{9.3a}$$

$$E_r = \frac{e\,\lambda}{2\pi\varepsilon_o}\,\frac{1}{r} \quad ; \quad B_\theta = \frac{\mu_o\, e\,\lambda\,\beta c}{2\pi}\,\frac{1}{r} \qquad r \geq a \tag{9.3b}$$

The longitudinal field at the center of the beam can then be determined from the relationship:

$$\oint \vec{E}\,\vec{d\ell} = -\frac{\partial}{\partial t} \int \vec{B}\,\vec{dt} \tag{9.4}$$

The integration path $\vec{\ell}$ and the enclosed area $\vec{f}$ are defined in Fig. 9.1.

Inserting the fields from eqs. 9.3a, b into eq. 9.4 and evaluating the integrals gives the following relation for the longitudinal field E_s at the center of the beam:

$$E_s = \frac{e\,g_o}{4\pi\varepsilon_o}\,(1 - \beta^{*2})\,\frac{\partial\lambda}{\partial s} + E_w \tag{9.5}$$

The constant g_o is defined as $g_o = (1 + 2 \ln \frac{b}{a})$ and E_w is the electric field on the axis resulting from induced wall currents.

In general the particle density fluctuates over distances which are large compared to the diameter of the beam pipe. In this case the beam sees an inductive resistance:

$$E_w = -\frac{L}{2\pi R}\,\frac{dI_w}{dt} = \frac{e\,\beta^{+2}\,c^2\,L}{2\pi\,R}\,\frac{\partial\lambda}{\partial s} \tag{9.6}$$

L is the total inductance seen by the beam per turn.

The total axial electric field resulting from space charge and inductance is given by:

$$E_s = -e\left(\frac{g_o}{4\pi\,\varepsilon_o\,\gamma^2} - \frac{\beta^2\,c^2\,L}{2\pi\,R}\right)\frac{\partial\lambda}{\partial s} \tag{9.7}$$

The total voltage seen by the particle per turn

$$U_s = -R\left(\frac{g_o\,Z_o}{2\beta\gamma^2} - \Omega_o\,L\right)\frac{\partial\lambda}{\partial s} \tag{9.8}$$

$Z_o = \frac{\mu_o}{\varepsilon_o} = 377$ Ohms and Ω_o is the angular revolution frequency. Note that only the inductive term remains at large values of γ.

The fluctuations must be of the form:

$$\Lambda = \Lambda_o + \Lambda_1\, e^{i(n\theta - \omega t)} \tag{9.9}$$

or

$$I = I_o + I_1\, e^{i(n\theta - \omega t)}$$

for an instability to occur. Furthermore the angular frequency of the disturbance ω must be an integer multiple of the angular revolution frequency Ω_o, i.e. $\omega = n\Omega_o$. A density fluctuation of this form leads to an effective voltage per turn:

$$U_s = -i Z_i I_1 e^{i(n\theta - \omega t)} \qquad (9.10)$$

In the case considered above the resistance is purely imaginary with

$$Z_i = R \left(\frac{n g_o Z^o}{2\beta \gamma^2} - \omega L \right) \qquad (9.11)$$

In general Z_i will have both a real and an imaginary part:

$$Z = Z_r + i Z_i \qquad (9.12)$$

The interaction between the beam and the environment shifts the frequency of the disturbance by $\Delta\omega$. Note that instabilities can only occur for certain values of $\omega = n \Omega_o + \Delta\omega$. The frequency shift for a general impedance Z is complex;

$$\Delta\omega = \Delta\omega_r + i\Delta\omega_i \qquad (9.13)$$

Substitute eq. 9.13 into eq. 9.9 yields:

$$I = I_o + I_1 e^{\Delta\omega_i} e^{i(n\theta - (n\Omega_o + \Delta\omega_r) t)} \qquad (9.14)$$

An imaginary frequency shift leads to exponentially growing or decaying oscillations with a time constant $\frac{1}{\Delta\omega_i}$. Depending on initial conditions (noise, etc) one or both of these solutions may be realized - i.e. the beam is unstable.

The reactive impedance $Z = i Z_i$ considered above yields:

$$(\Delta\omega)^2 = \frac{e \eta \Omega_o^2 n I_o Z_i}{2\pi \beta^2 E} \qquad (9.15)$$

with Z_i given by eq. 9.11.

An inspection of eq. 9.7 shows that an inductive impedance drives the beam unstable at energies below the transition energy, however, the beam is stable above the transition energy. The situation is reversed for a capacitive resistance, stable particles motion below and unstable particles motion above the transition energy. A resistive impedance always drives the beam unstable.

If all the particles in the beam have the same energy, as in the case considered above, then they remain in phase and even a minute disturbance is sufficient to cause an exponentially growing amplitude. This is no longer true if the particles in the beam have a finite energy spread. In this case the particles have different revolution frequencies and only act coherently over a time interval which is inversely proportional to the spread in revolution frequencies. As long as the frequency shift of the disturbance is smaller than the spread in revolution frequencies energy can be transferred from the instability and converted into incoherent motion. Thus the unstable motion is damped and the disturbance must exceed a certain threshold before the particle motion becomes unstable. This general mechanism is called Landau damping.

In the case of a bunched beam the damping is caused by the spread in phase oscillation frequencies S resulting from non linearities in the r.f. potential. For a bunch which is somewhat smaller than the r.f. bucket:

$$S \simeq \frac{\omega_s}{16} \phi_{RF} \qquad (9.16)$$

ϕ_{RF} is the bunch length measured in RF phase angle.

The particle motion will be stable as long as:

$$S > 4\Delta\omega_i \qquad (9.17)$$

We will discuss some of the instabilities which may occur for a bunched beam in more detail.

9.1.2 The microwave instability (turbulence)

This instability involves high frequencies corresponding to wave lengths which are short compared to the bunch length and in this case the theory developed for a continuous beam may be applied. Above threshold the momentum spread and the bunch length are blown up to values which are large compared to the equilibrium values determined by the r.f. parameters and the injected bucket area.

To avoid this instability the longitudinal impedance Z divided by the mode number $n = \frac{\omega}{\Omega_o}$ must satisfy the condition

$$\left|\frac{Z}{n}\right| < \frac{3 F (m_p c^2) \gamma |\eta|}{e I_o} \left(\frac{\Delta p}{p}\right)^2 \qquad (9.18)$$

For a parabolic current distribution F $\sim$ 0.65. It is clear that the beampipe must be designed to minimize Z. At the SPS $\frac{Z}{n}$ is around 30Ω and we should be able to do better at HERA. Note that I_o is the peak current i.e. about 60 amp in HERA at 820 GeV and a parabolic current distribution. The HERA parameters demand $|\frac{Z}{n}| < 60\Omega$ at the peak energy of 820 GeV and $|\frac{Z}{n}| < 10\Omega$ at injection energy of 40 GeV to avoid this instability.

9.1.3 The inductive wall impedance

The reactive impedance seen by a bunched beam will in general be inductive for low and medium frequencies. As shown in Fig. 9.1, the induced voltage U_s, will distort the circumferential r.f. voltage seen by the particle and hence affect the particle motion within the bunch. In particular, the induced voltage U_s will shift the incoherent phase oscillation frequency and change the bunch length. The incoherent frequency shift, for a parabolic line density distribution is given by:

$$\frac{\Delta\omega_s}{\omega_s} = \frac{3 I_o (\Omega_o L)}{2\pi^2 h M V \cos\phi_o} \left(\frac{2\pi R}{\ell}\right)^3 \qquad (9.19)$$

I_o is the total current, L the inductance integrated around the ring, Ω_o the revolution frequency i.e.

$$\Omega_o L = \left(\frac{Z}{n}\right)_{ind},$$

h is the harmonic number, M is the number of bunches and R is the geometric radius.

The frequency shift will reduce the Landau damping - indeed the Landau damping disappears completely if the incoherent frequency distribution is shifted so far that this is outside the frequency of the disturbance. Note that the frequency shift is inversely proportional to the third power of the bunch length - i.e. the beam

can be stabilized by an increase in bunch length and a corresponding reduction in luminosity.

The bunch length is increased above the transition energy and decreased below. For protons

$$\frac{\Delta \ell}{\ell} = -\frac{1}{2}\,\frac{\Delta\omega_s}{\omega_s} \qquad (9.20)$$

The inductive impedance $|\frac{Z}{n}|_{ind}$ depends strongly on the detailed layout of the vacuum chamber and the cavities. At the ISR $|\frac{Z}{n}|_{ind} \simeq 20$ ohms was measured, at the SPS $|\frac{Z}{n}|_{ind} \approx 10$ ohms. At the peak energy of 820 GeV the estimated frequency shift in HERA is

$\frac{\Delta\omega_s}{\omega_s} = -0.04$ with an accelerating peak voltage of 100 MV and

$|\frac{Z}{n}|_{ind} = 10$ ohms.

Coupled bunch mode instabilities

A single bunch may execute different types of oscillations characterized by a mode number m - i.e. a dipole mode with frequency ω_s, a quadrupole mode with frequency $2\omega_s$, a sextupole mode with frequency $3\omega_s$ and so on. These modes are in general excited by narrow band, high Q resonators like the cavities. However, if several equidistant bunches are stored along the circumference of the machine, then these bunches may be coupled together by broad band, low Q resonators and execute additional coupled mode oscillations. The number of independent oscillation modes are equal to the numbers of bunches.

The strength of these instabilities are difficult to estimate, however, several methods are available to stabilize the beam.

a) Identify and damp the resonator which couples the bunches.

b) Increase the Landau damping either by a blow up of the bunch area ($S = \frac{\omega_s \phi_o^2}{16}$) or by operating a cavity at a harmonic of the r.f. frequency.

c) Decouple the bunch by using a cavity which operates on a sub-harmonic of the r.f. frequency. In this case different bunches have different synchrotron frequencies.

d) Use a feed back system.

9.2 RF Noise

The r.f. system contains a white noise spectrum. The part of the noise spectrum with frequencies around $n\,\omega_s$ - where n is an integer - will lead to a slow build up of the rms phase oscillation amplitudes - i.e. to a dilution of longitudinal phase space density. This effect has been sucessfully compensated at the SPS collider using a very low noise feed back system.

9.3 Transverse instabilities

9.3.1 Transverse space charge effects

As discussed in chapter 4 the transverse motion of a single particle in the guide field of a circular accelerator is described by the solution to Hill's equation:

$$u''(s) + K_o(s)\, u(s) = 0 \qquad (4.25)$$

This equation is valid for both the radial (x) and the vertical (z) motion provided $\Delta p = 0$.

The space charge force acting between non relativistic particles moving together will modify the focusing strength

$$K(s) = K_o(s) + \delta K \,. \qquad (9.21)$$

From eq. 5.34 a gradient change δK will lead to a spread in tune values:

$$\Delta Q = -\frac{\delta K\, \beta\, (2\pi R)}{4\pi} \qquad (5.34)$$

To avoid beam losses resulting from crossing a half integer resonance:

$$\Delta Q \lesssim 0.25 \,.$$

We will now estimate the limit on the current imposed by the space charge force. To this purpose we assume a uniform beam of radius a moving along the positive s direction with a uniform velocity $\vec{\beta c}$ as considered above.

The electric and the magnetic fields for $r \leq a$ produced by the moving charges are given by eq. 9.3a.
The resulting force on a particle travelling a distance x from the center of the beam is given by

$$F = e\,(\vec{E} + \vec{v} \times \vec{B})$$
$$F_r = \left(\frac{e\,\rho}{2\varepsilon_o}\right) \frac{r}{\gamma^2} \qquad (9.22)$$

i.e. the space charge force has only a radial component which disappears at relativistic energies.

The force is equivalent to an acceleration:

$$(m_o\gamma)\left(\frac{d^2x}{dt^2}\right) = (m_o\gamma)\,(\beta c)^2 \frac{d^2x}{ds^2} = \frac{e\,\rho}{2\varepsilon_o}\,\frac{x}{\gamma^2} \qquad (9.23)$$

The particle density $\frac{\rho}{e}$ can be expressed by the total number of particles stored along the circumference $2\pi R$ of the ring:

$$\frac{\rho}{e} = \frac{N}{(2\pi R)\,\pi a^2} \qquad (9.24)$$

This leads to the equation:

$$\delta\left(\frac{d^2x}{ds^2}\right) = r_o \frac{N}{R\pi a^2} \frac{1}{\beta^2\gamma^3}\, x \qquad (9.25)$$

From a comparison with eq. 4.25 we see that the total change in focusing power per turn is given by

$$\delta K = -\frac{r_o\, N}{\pi\, a^2 \beta^2 \gamma^3\, R} \qquad (9.26)$$

The corresponding tune shift is obtained by combining eq. 9.26 with eq. 5.34:

$$\Delta Q = -\frac{r_o\, N}{2\pi\, a^2 \beta^2 \gamma^3}\,\beta = \frac{r_o\, N}{2\pi a^2 \beta^2 \gamma^3}\,\frac{R}{Q} \qquad (9.27)$$

Thus the beam is stable if:

$$N \leq \frac{2Q|\Delta Q|(\pi a^2)\,\beta^2\gamma^3}{r_o\, R} \qquad (9.28)$$

The space charge limits the amount of current which can be stored in a machine with a aperture (πa^2). This is the basic limitation at low energies.

9.3.2 Transverse head tail instability

This instability, first observed at ADONE, was explained by Pellegrini and Sands as due to the following mechanism: The particles moving in the head of a bunch make betatron oscillations which induce strong, rapidly decaying transverse electromagnetic fields. These fields will interact with the particles in the tail of the bunch and will increase their betatron oscillations. After half a synchrotron oscillation period the particles in the head and the particles in the tail have changed place and the feed back loop is now closed if the betatron phase of the particles in the new head is ahead of the betatron phase of the particles in the new tail. This will occur if the chromaticity is negative.

To see this let us evaluate the difference in betatron phase between particles in the head and the tail of a bunch. This phase shift is obtained by integrating $\Delta\omega_\beta$ over half a synchrotron period:

$$\Delta\omega = \int_0^{T_s/2} \Delta\omega_\beta \, dt \qquad (9.29)$$

The betatron phase depends on Q and the revolution frequency Ω_o.

$$\frac{\Delta\omega_\beta}{\omega_\beta} = \left(\frac{\Delta Q}{Q} + \frac{\Delta\Omega}{\Omega} \right) \qquad (9.30)$$

The change in tune ΔQ is given by the chromaticity:

$$\Delta Q = \xi \frac{\Delta p}{p} = \frac{\xi}{\beta^2} \frac{dE}{E} \qquad (5.35)$$

The change $\Delta\Omega$ in revolution frequency is given by the time dilation factor $\eta(p)$. We consider a proton with an energy well above the transition energy

$$\frac{\Delta\Omega}{\Omega} = -\frac{\eta}{\beta^2} \frac{dE}{E} \approx -\frac{\alpha}{\beta^2} \frac{dE}{E} \qquad (6.5)$$

Combining both terms yield:

$$\Delta\omega_\beta = \frac{\omega_\beta}{\beta^2} \left(\frac{\xi}{Q} - \alpha \right) \frac{dE}{E} \qquad (9.31)$$

$$\approx \frac{\omega_\beta}{\beta^2} \frac{\xi}{Q} \frac{dE}{E} \, .$$

Substituting eq. 9.31 into the integral of eq. 9.29 yields:

$$\Delta\mu = -\frac{2}{\beta^2} \left(\frac{\omega_\beta}{\omega_s} \right) \left(\frac{\xi}{Q} \right) \frac{dE}{E} \qquad (9.32)$$

Since the uncorrected natural chromaticity is negative the betatron phase advance $\Delta\mu$ will be positive. Thus the fundamental head-tail mode is unstable.

Note that sextupoles can be used to cancel the natural chromaticity - i.e. $\xi = 0$. In this case no phase relation exists between particles in the head and in the tail of the bunch and the fundamental head-tail instability does not occur. However, it is difficult to cancel the chromaticity exactly. Furthermore higher order single bunch head tail modes can occur for positive values of the chromaticity.

If the transverse impedance has a sufficiently long memory it may also couple head tail oscillations of adjacent bunches.

Both the single and coupled head tail modes may be corrected by using an octupole magnet to induce a tune spread. However, remember that an octupole is a non linear element which drives resonance lines and may by itself limit the acceptance.

9.3.3 The beam-beam tune shift

The electric and magnetic forces between interacting bunches moving in opposite directions add, thereby resulting in a strong direct space charge force which persists at higher energies. For bunches of opposite charge the forces are attractive - i.e. one bunch acts as a focusing lens in both planes. For like sign bunches the force is repulsive and equivalent to a defocusing lens. For particles travelling close to the axis the lens will be nearly linear while it is strongly non linear for particles with a large displacement.

This interaction affects the particle motion in several ways:

- it excites coherent transverse oscillations
- it introduces a non linear coupling of vertical and horizontal motion
- it excites higher order resonances.

Although the beam-beam interaction is strongly non-linear it is commonly parametrized by the tune shift ΔQ induced by its linear part. We will here estimate the tune shift suffered by a proton of normalized energy γ traversing a bunch containing N_e electrons Gaußian distributed transversely to the beam axes with rms size σ_x and σ_z.

The focal length of such a "space charge" lens can be written as:

$$\frac{1}{f_u^p} = (k\,\ell)_u^p = \frac{2N_e}{(\sigma_{ex}^* + \sigma_{ez}^*)\,\sigma_{eu}^*}\,\frac{r_p}{\gamma_p} \qquad (9.33)$$

The stars indicate that beam sizes are evaluated at the crossing point, u = x or y.

The tune shift caused by a lens of focal strength $f = \frac{1}{k\ell}$ located at a position where the amplitude function has the value β is given by:

$$\Delta Q = \frac{\beta\, k\ell}{4\pi} \qquad (5.13)$$

Introducing the strength of the lens from eq. 9.27 yields:

$$\Delta Q_u^p = \frac{N_e}{2\pi(\sigma_{ex}^* + \sigma_{ez}^*)\sigma_{eu}^*}\,\frac{r_p}{p}\,\beta_u^*$$

To find the effect of the electron beam on the proton beam one may to first order simply replace p by e in the formulae above.

It is clear that the ultimate tune shift limit must depend on the details of the machine and the tune advance between crossings. However, it has been found experimentally at the high energy electron machines that a tune shift of $\Delta Q^e \leq 0.025$ is acceptable

for electrons. At the CERN SPS $p\bar{p}$ collider a tune shift of 0.003 has been obtained for bunched proton beams. The factor ten difference between the electron and the proton tune shift limits is presumably due to the radiative camping of the electron beam.

10. Layout and Performance of HERA

In this last chapter we briefly discuss the choice of the main parameters for HERA[5] and evaluate the luminosity.

10.1 The Lattice

The present choice of lattice for the electron and the proton ring are shown in Fig. 10.1. Both machines have a periodic FODO cell structure consisting of equidistant focusing and defocusing quadrupoles with as much as possible of the intervening space filled with bending magnets. The main lattice parameters are listed in Table 10.1. They can be derived to a good approximation using the formulas listed in chapter 4.5.

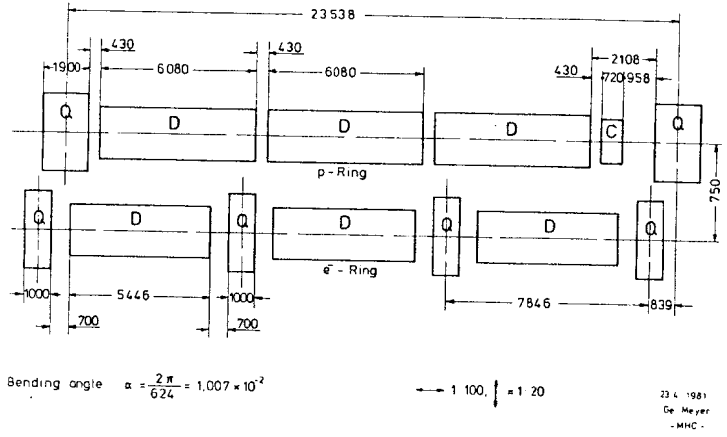


Fig. 1 HERA normal cell lattice

Fig. 10.1 - Lattice for the electron and the proton ring HERA.

Table 10.1 - HERA lattice parameters

	p-ring	e-ring
Circumference (m)	6336	
Number of superperiods	4	
Lattice	FODO	
Straight section length	360 m	
Normal cells /octant	9	34.5*
Dispersion suppressing cells/ octant	4	2
Number of dipoles / cell	6	2
Magnetic length of dipole (m)	6.08	5.446
Aperture of bending magnet (mm)	60.0 ϕ	70 x 40
Bending radius (m)	603.8	540.9
Bending angle (mrad)	10.07	
Magnetic length of quadrupole (m)	1.90	1.00
Aperture of quadrupole (mm)	60.0 ϕ	50.0 ϕ
Betatron phase advance/cell	90^o	60^o
Momentum compaction	$1.315 \cdot 10^{-3}$	$0.495 \cdot 10^{-3}$
Transition energy (GeV)	25.9	
Working point Q_x/Q_z	32.15/35.19	48.3/48.2
Cell quadrupole focal length (m)	16.6	7.8
Cell quadrupole gradient (T/m)	91.2	12.7
Amplitude function β^{max} (m)	80.4	27.2
β_{min} (m)	13.8	9.1
Dispersion D^{max}(m)	1.9	0.39
D_{min}(m)	0.92	0.24

* The horizontal bend of each spinrotator is equivalent to that of 2.5 normal cells.

Fig. 10.2 shows a cross section through the tunnel in the arcs with the proton machine installed above the electron ring.

In the e^+e^- mode of HERA the cell length is a free parameter which, for a given emittance and hence luminosity, may be chosen for minimum cost. In the ep case, the proton cell length should be an integral multiple of the electron cell length. The electron emittance and hence the focal length should be chosen such that it is possible to match the electron and the proton beam sizes at the interaction point for a given horizontal/vertical coupling of the electron beam. It can be shown that the optimum cell length is around 10 m for an aperture limited e^+e^- design luminosity of $4 \cdot 10^{31}\ m^{-2}s^{-1}$ at $2 \cdot 25$ GeV. Since the minimum is rather flat we have chosen a cell length of 15.692 m for mechanical reasons. In an octant of the electron ring there are 34 1/2 periodic cells and 2 dispersion suppressing cells in the arcs and 2 1/2 cells are incorporated into the spin rotator.

The large number of electron cells per octant reflects the need to have a dense focusing structure for the electrons. In the electron ring the beam emittance is determined by the equilibrium of synchrotron radiation and focusing strength (eq. 7.39). A dense focusing structure leads to a small beam emittance, low synchrotron frequency and a lower r.f. voltage. It is also possible to match the vertical electron beam size to that of the proton in the interaction point by varying the emittance.

The chromaticity is compensated using two families of sextupoles located adjacent to the focusing quadrupoles.

The useful aperture of the proton ring is presumably limited by non linearities rather than the geometric aperture:

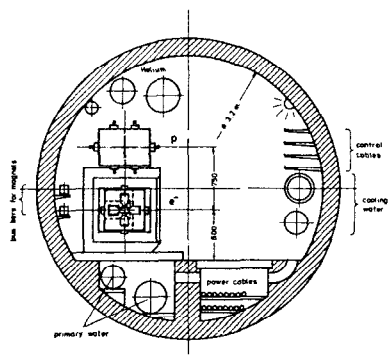
These non linearities result from:

- The sextupoles needed to compensate the natural chromaticity. At least two families are needed and their strength can be written as

$$m_F = s_F \ell_F = \frac{1}{D_F}\left(\frac{1}{f} + \frac{4\pi\,(\xi_{IR})}{N_c\,(\beta_F - \beta_D)}\right) \qquad (10.1)$$

$$m_D = \frac{D_F}{D_D} m_F$$

ξ_{IR} is the chromaticity resulting from the straight sections and N_c is the number of cells.



HERA
cross section in the arc

Fig. 10.2 - A cross section through the beam tunnel in the arcs.

- The higher field harmonics caused by the approximation to a cosθ current distribution in the dipole magnets and by positioning errors of the wires. The field can be written as a sum of the harmonic coefficients b_n for normal multipole fields and a_n for skew multipole fields. These coefficients are obtained from the Fourier expansion of the azimuthal field component.

$$B_\theta(r,\theta) = B_o \sum_{n=1}^{\infty} \left(\frac{r}{r_o}\right)^{n-1} (b_n \cos n\theta - a_n \sin n\theta) \qquad (10.2)$$

B_o is the induction on the axis and r_o = 2.5 cm is the reference radius.

The tolerances on the field components were taken to be the same as those imposed on the FNAL magnets:

Normal and skewed quadrupole: $a_2, b_2 = 2.5 \cdot 10^{-4}$

Sextupole : $b_3 = 6 \cdot 10^{-4}$

Skewed sextupole and all higher multipoles including the 18-pole $= 2 \cdot 10^{-4}$

This distribution was assumed to be a Gaußian centered at zero with a rms value a third of the tolerances listed above. A cold iron magnet has much higher values of the multipole components and their relative strength also changes with current due to iron saturation.

- Persistent currents. These currents induce mainly a constant setupole field with a strength proportional to the filament diameter. For the 10μm filaments used in the HERA cables the relative strength of the persistent current sextupole relation to the dipole field is $-2 \cdot 10^{-3}$ at the injection energy of 40 GeV. If left uncorrected these sextupoles would introduce a chromaticity of $\xi_H = -181$ and $\xi_V = 143$. We assume that the mean value of the persistent current sextupoles are compensated by a bucking field such that only the $\pm$ 10% fluctuations must be included in the computations must be included in the computations.

The resulting nonlinear aperture was investigated using a fast tracking programme[40]. The particles, with a given initial amplitude are tracked around the ring and their amplitude checked after each sextupole. If at least one particle is found outside the goemetric aperture then the amplitude is unstable, if all particles (in general 16) survived 100 turns then the amplitude was called stable.

The stable amplitude for the cell depicted in Fig. 10.1 is plotted versus momentum in Fig. 10.3. The computation was done at the injection energy of 40 GeV for a phase advance of 60^0 and 40^0 per cell.

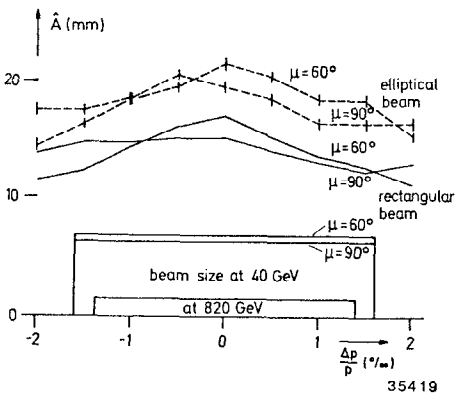


Fig. 10.3 - The stable amplitude limits at the injection energy of 40 GeV are plotted versus momentum for a phase advance of 60^0 corresponding to Q_x/Q_z = 33.15 / 35.18 and a phase advance of 90^0 yielding Q_x/Q_z = 25.16 / 29.23 The limits are evaluated for a rectangular and an elliptical phase space distribution. The maximum horizontal beam size ($2.2\sigma_x$) at 40 GeV and 820 GeV is shown for comparison.

Within the accuracy of the computation the non linear aperture is the same for 60^0 and 90^0 phase advance. For a rectangular beam phase space and $\varepsilon_x = \varepsilon_z$ the non linear aperture is on the order of 14 mm. It might be more realistic to assume an elliptical phase space and in this case the aperture is around 18 mm. The aperture at 820 GeV is slightly larger since persistent current effects can be neglected

at high energies. The values should be compared to the geometric aperture of $\pm$ 28 mm. Measurements at the ISR found a beam lifetime on the order of 18.5 hours with the vertical collimators set at 2.2σ. This aperture is indicated at the injection energy of 40 GeV and at 820 GeV. This aperture, even at 40 GeV, is comfortably smaller than the non linear aperture determined by the tracking programme. The emittance growth due to beam-gas and intra beam scattering has been evaluated and found to be negligible for injection times on the order of half an hour.

At present the computation time is about 5000 times longer than the natural revolution time such that only short storage times may be investigated. We are now building a dedicated computer which will enable us to investigate storage times on the order of several hours.

10.2 The r.f. System

The r.f. system for the electron ring is based on the 500 Mhz system used in PETRA. Indeed r.f. equipment like klystrons, cavities, waveguides and other components will be transferred from PETRA to HERA.

At the nominal energy of 30 GeV each particle loses 142.3 MeV per turn in synchrotron radiation. For a phase advance of 60^{o} the peak voltage must be 166.7 MV per turn to ensure a beam life of 24 hours due to quantum fluctuations. The stable r.f. phase is 58.6^{o}. The number of synchrotron oscillation per turn is 0.038 and the r.m.s. bunch length is 9.3 mm.

The injection system for the protons is designed to fill HERA with 210 bunches of protons with $3 \cdot 10^{11}$ protons per bunch using the following sequency of accelerators:

Proton Linac (50 MeV) → DESY (7.6 GeV) → PETRA (40 GeV) → HERA

The bunches with the final number of particles per bunch are formed in DESY such that a complicated stacking procedure, which may lead to an emittance growth, is avoided. To reach the highest luminosity the proton r.f. system must be designed not only to accelerate but also to produce a short proton bunch with a high line density. The stable bunch length shrinks from about 100 m at low energies to a fraction of 1 m at the peak energy of HERA. Some of the shrinkage is provided by the natural evolution of the bunch length during acceleration but in addition the frequency is increased twice during the acceleration sequence.

These frequency changes are done at transfer. The first step is from 2.8 MHz in DESY to 10.37 MHz in PETRA as the beam is transferred. The second step from 10.4 MHz to 208 MHz occurs between PETRA and HERA. In order for the PETRA bunch to fit into the much shorter HERA bucket a bunch rotation is applied to the bunch before transfer.

We now give some of the parameters for the r.f. systems as presently planned. We assume that adiabatic capture works with an efficiency of 70% and that 10% of the protons are lost during each transfer. To reach the design value of $3 \cdot 10^{11}$ protons/bunch a total of $1.6 \cdot 10^{3}$ protons are injected from the Linac in a single turn

into DESY. At DESY the protons are captured into three 100 m long bunches. The momentum spread is $1.2 \cdot 10^{-3}$ corresponding to a bunch area of 0.005 rad. A peak voltage of 1.43 kV at a frequency of 0.891MHz (h=3) is needed at injection.The protons are accelerated through transition (γ_{tr} = 5.680) and transferred bunch by bunch into PETRA. Note that the protons are injected at 7.6 GeV which is above the the transition energy (γ_{tr}=6.0) in PETRA. The frequency at injection is 2.817 MHz and the peak voltage is 11.22 kV. Such a system can easily be realized using ferrite loaded cavities. Longitudinal instabilities do not appear to be a problem - the Laslett Q shift is -0.103 at injection and (Z/n) must be less than 40Ω to avoid the microwave instability.

PETRA is loaded with 18 out of 20 possible bunches spaced 384 ns apart. PETRA will then accelerate the protons to 40 GeV, limited by the saturation of the dipole magnets. At injection the r.f. frequency is 10.33 MHz with a peak voltage of 19.8 kV. At the end of the accelerating cycle the r.f. frequency is 10.41 MHz and a peak voltage of 8.35 kV. The Laslet Q shift is only -0.040 at injection and (Z/n) must be less than 14.4 Ohm at 40 GeV.

Since the required frequency swing is only 0.6% cheap reentrant r.f. cavities can be used instead of ferrite loaded cavities. At 40 GeV the bunches can be made short without creating a large Q-shift and it is therefore possible to go directly to the final r.f. frequency of 208 MHz in HERA. At 40 GeV in PETRA the bunch is 10 m long. Clearly the bunches must be compressed to about 1.3 m before they are transferred to HERA. The simplest way to do this is to perform a one quarter bunch rotation in an abruptly increased bucket. This requires much less voltage than adiabatic compression of the bunch and the voltage is only required during the short time of one quarter synchrotron oscillation. The bunches must then be transferred between PETRA and HERA in one go and this is possible since the ratio of the circumference is 80 to 220. The bunch rotation can be done by simply pulsing the accelerating cavities to some 500 kV for about a msec.

The PETRA cycle is repeated 12 times until HERA is loaded with 210 bunches spaced uniformly by 96 ns except for a notch 1 μs long. The notch is needed for the risetime of the beam abort kickers.

There are several reasons for choosing a rather low r.f. frequency in HERA.

Firstly we have seen that a low frequency makes the final bunch compression in PETRA easier.

The inductive wall impedance shifts the coherent synchrotron frequency according to eq. 9.19. Landau damping breaks down if this shift exceeds the incoherent frequency spread of the particles in the bunch. The voltage required to prevent this (eq. 9.19) is proportional to $\omega_{r.f.}^2$ for a given ratio of bunch length to bucket length. Even for a (Z/n) as low as 5 Ω the r.f. peak voltage must be 100 MV for a r.f. frequency of 208 MHz and a bunch length of 38 cm. Lower frequency r.f. cavities are difficult to fit into the ring due to their larger diameter.

10.3 Interaction Region

The interaction region in an electron-proton collider is complex. It must bring the two different beams into a small angle low beta

collision geometry and it must turn the electron spin to be either parallel or antiparallel to the beam direction at the interaction point. Furthermore, the dispersion in the lattice must be made to disappear in the straight section, and sufficient space for r.f. cavities, injection and ejection system must be found.

In the design we must first decide whether to use a head on collision geometry, or to opt for a crossing angle. Since luminosity and beam-beam tune shift vary in the same manner with crossing angle, a larger angle would simply achieve the same conditions as a head on collision but requires more protons and electrons. To optimize the luminosity, the interaction region must be designed to produce a small value of the betatron function at the interaction point. The minimum value of the betatron function is presumably limited by the maximum chromaticity introduced by the vertically focusing quadrupoles. The vertical chromaticity introduced by the eight vertically focusing quadrupoles is given by:

$$\xi_y^{IP} = -\frac{8}{4\pi}\frac{f}{\beta^*} \qquad (10.3)$$

f is the focal length and β^* the value of the betatron function at the interaction point. The quadrupoles must thus be positioned as close as possible to the interaction point. To set the scale, the arcs contribute $\xi_y^a = 30$ to the vertical chromaticity. The arbitrary assumption that the interaction region should make a smaller contribution yield the inequality $\xi < 45\beta^*$.

Rather strong quadrupole fields are needed to focus the proton beam and it therefore seems advisable not to pass the electrons through the field of the proton quadrupoles.

In the head on collision geometry the electron and the proton beam must be separated by a dipole magnet. In order not to flood the interaction region with synchrotron radiation this bend must be rather gentle and the vertically focusing proton quadrupole will therefore be located rather far from the interaction point.

In the present layout (Fig. 3.2) we have chosen to cross the beams at an angle of $\pm$ 10 mrad in the horizontal plane. A horizontal crossing is advantageous since the width of the electron beam is much larger than its height. The large crossing angle makes it possible to install the proton quadrupoles directly following the electron quadrupole. In the present layout the front face of the vertically focusing quadrupoles is positioned at $\pm$ 7.5 m and at $\pm$ 10 m with respect to the IP for electrons and protons respectively. It is possible to detect particles down to 13 (32) mrad. This is more than sufficient (Fig. 2.12) to measure the formfactors with high precision at values of Q^2 which overlap with present data. Note that the two machines are totally independent. It is thus possible to inject into one ring while leaving the other at high energy. It is also possible to vary the center of mass energy by changing the proton energy and keeping the electron fixed at 27.5 GeV where polarisation is expected to occur.

The next problem is to incorporate the spin rotators. Several possible designs exist. The solution presently adopted is shown schematically in Fig. 10.4.

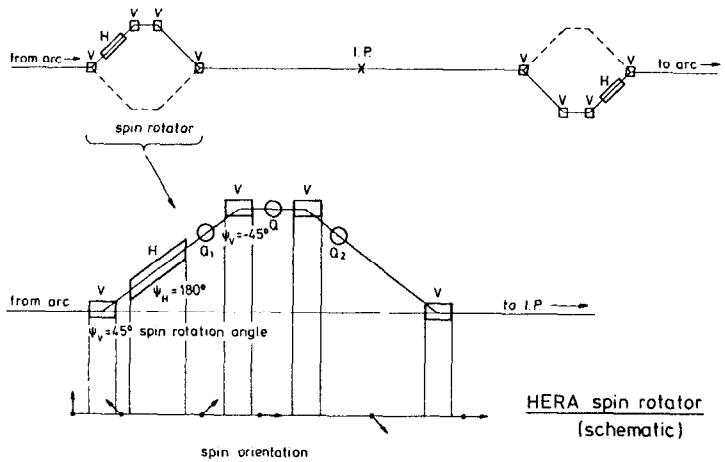


Fig. 10.4 - Principal layout of the spin rotators.

The essential part of the rotator is a horizontal bending magnet which causes the spin to precess by π around the vertical axis and is surrounded by two vertical bending magnets of opposite sign that generate a spin rotation of $\pm \pi/4$ about the radial axis. A pair of vertical bending magnets restores the original beam direction without changing the spin direction. There is again one such rotator at each end of the straight section; the first makes the polarisation longitudinal and the second restores the transverse polarisation. For opposite helicity at the interaction point, all vertical bends are inverted, while the horizontal bends remain unchanged. Since these horizontal bends are rather strong, they are designed to be a part of the normal bending in the arc. In the HERA design each horizontal rotator magnet replaces exactly 5 of the 78 normal cell bending magnets per octant.

The horizontal bending magnets must thus deflect the particles through a well defined angle. α = 50.32 mrad and precess the spin around the vertical direction by $\phi_y = \pi$. Since $\phi_y = (\gamma a)\,\alpha$, both conditions can only be satisfied for a single energy E_0 = 27.8 GeV corresponding to a spin tune $\nu = (\gamma a)$ = 62.4 GeV.

To operate the rotator at a different energy requires two correction bends to feed the beam band into its nominal position in the arcs. With such correctors it is possible to properly operate the rotators in an energy range of, say 0.5 GeV around E_0 and explore the optimum between depolarising resonances.

The final layout of the interaction regions is shown in Fig. 3.2. The spin rotators are located at the ends of the $\pm$ 180 m long straight sections. With the expections of the vertical spin rotator bends the electron ring stays in the plane. Note that the 1st bending magnet is located nearly 120 m from the IP. Detailed calculations show that it is possible to position detector elements

within a few cm of the beam without being swamped by synchrotron radiation.

10.4 Luminosity

The luminosity of an electron - proton colliding beam machine with the beams crossing in the horizontal plane at an angle 2ϕ is given by:

$$L = \frac{f_o\, n_b\, N_e\, N_p}{2\pi(\sigma^2_{xp,eff} + \sigma^2_{xe})^{1/2}\,(\sigma^2_{zp} + \sigma^2_{ze})^{1/2}}$$

In this formula f_o is the revolution frequency, n_b the number of bunches in the ring, N_e and N_p the number of electrons and protons per bunch respectively, $\sigma_{xp,eff} = (\sigma^2_{sp} + (\sigma_{sp}\,\phi)^2)^{1/2}$ with σ_{sp} denoting the proton bunch length, σ_{xe} is the width of the electron beam and σ_{zp} and σ_{ze} the heights of the proton and the electron beam respectively. The beam sizes are all defined in the interaction point and are calculated from the beam emittances and the values of the amplitude function at the interaction point. The emittance of the proton beam is determined by the injectors, whereas the emittance of the electron beam is given by the electron energy and the phase advance per cell.

We will now discuss the choice of the various parameters which enter the luminosity computation.

The ultimate limit to the luminosity is given by the maximum allowed value of the beam-beam tune shifts. The tune shifts, derived in chapter 9, can be expressed for the vertical direction as:

$$\Delta Q_{ze} = \frac{\beta^*_{ze}\, r_e\, N_p}{2\pi\gamma_e(\sigma^*_{xp,eff} + \sigma^*_{zp})\,\sigma^*_{zp}}$$

$$\Delta Q_{zp} = \frac{\beta^*_{zp}\, r_p\, N_e}{2\pi\gamma_p(\sigma^*_{xe} + \sigma^*_{ze})\,\sigma^*_{ze}}$$

Here γ_e and γ_p are respectively the electron and the proton energy measured in units of the rest energy and β^*_e and β^*_p are the values of the amplitude function at the origin. ΔQ is quoted per interaction region.

For head-on collisions a tune shift limit of 0.025 has been observed at high energy e^+e^- colliders compared to approximately 0.003 observed at the CERN $p\bar{p}$ collider. We will use $\Delta Q_e = 0.025$ and $\Delta Q_p = 0.0025$ as the limiting values also in the case of a finite crossing angle.

The luminosity was evaluated with $\beta^*_{ze} = 0.15$ m, $\beta^*_{xe} = 3.0$ m, $\beta^*_{zp} = 0.30$ m and $\beta^*_{xp} = 3.0$ m. The vertical chromaticities evaluated according to eq. 10.3 yield:

$$\xi^{IP}_{ze} = 31.8 \qquad \xi^{IP}_{zp} = 21.2\ .$$

The effective horizontal beam size is determined by the crossing angle and the length of the proton bunch. With the 100 MV r.f. system as proposed the bunch is 9.5 m long (σ_s) at 820 GeV.

The vertical emittance for the electron beam is determined by the vertical and horizontal coupling. Couplings as small as 1% have been observed at PETRA. The spinrotator will increase the vertical coupling and with the present rotator we find a value of 10%. This can be reduced and we assume a coupling of 4% for the calculations here. To maximize the luminosity the phase advance per cell is adjusted in discrete steps of 30^0, 45^0, 60^0 and 90^0.

The luminosity is also proportional to the number of bunches per beam. In the case of a crossing geometry the number of bunches is a free parameter. In the present design we have limited the number of bunches to 210 corresponding to a spacing of 28.8 m between adjacent bunches.

The electron current at high energy is limited by the available r.f. power. At HERA we assume that at most 12 MW is available at the r.f. cavities. It takes about 4.0 MW to establish the required circumferential voltage of 166.7 MV at 30 GeV. With an average energy loss of 142.3 MeV per turn the remaining 8 MW is sufficient to accelerate a current of 56 mA.

For the protons we assume a limit of $3 \cdot 10^{11}$ protons per bunch. As a comparison 10^{11} protons per bunch have been stored at the SPS collider. The hope for increase in protons is based on a very smooth beam pipe with a low (Z/n), a high r.f. peak voltage to produce a

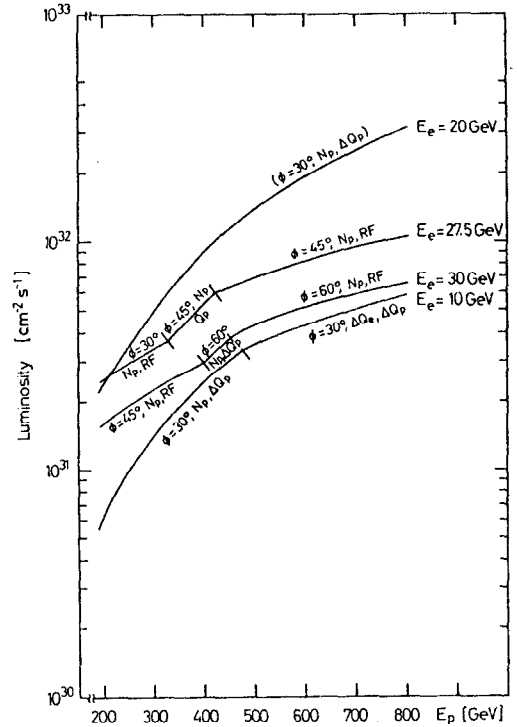


Fig. 10.5 - Luminosity as a function of proton energy for various electron energies. The luminosity limiting parameters are indicated.

high line density and the use of octupoles and feed back systems to stabilize the beam.

The luminosity is plotted in Fig. 10.5 versus the proton energy for electron energies of 10, 20, 27.5 and 30 GeV. Listed in the brackets is the phase advance per cell in the electron beam which with the parameter in the proton respectively in the electron beam which limits the luminosity. Note that at 30 GeV the luminosity is limited by the available currents - i.e. the luminosity can be increased by either storing a higher current or by moving the quadrupoles closer and lower the vertical β function. Indeed at 30 GeV and 820 GeV the tune shifts are rather low Q_{xe}/Q_{ze} = 0.008/0.014 and Q_{xp}/Q_{zp} = 0.0006/0.0009.

At E_e = 20 GeV sufficient electron current can be stored to reach the proton tune shift limit. In this case a peak luminosity of $3 \cdot 10^{32}$ $cm^{-2}s^{-1}$ is realistic.

With the luminosity predicted at HERA we should thus be able to explore the kinematical region $Q^2 > 10000$ GeV^2 where surprises are expected to occur. With some luck this may happen before the end of the decade.

References

1) H.G.Hereward, K.Johnsen, A.Schoch and C.J. Zilverschon, Proc. 3rd Internat.Conf. on High Energy Accelerators, Brookhaven, 1961.

2) L.Goldzahl and E.G.Michaelis, CERN 66-12 (1966).

3) C.Pellegrini, J.Rees, B.Richter, M.Schwartz, D.Möhl and A.Sessler, Proc. 8th Internat.Conf. on High Energy Accelerators, CERN, 1971, p. 153.

4) H.Gerke, H.Wiedemann, B.H.Wiik and G.Wolf, DESY H-72/22 (1972)

R.Chasman and G.A.Voss, IEEE Trans.Nucl.Sci. NS-20, No.3 (777) 1973

EPIC Machine Design Study Group, 9th Intern.Conf. on High Energy Accelerators, Stanford, 1974.

T.L.Collins, P.A.Edwards, J.Ingebretsen, D.E.Johnson, S.Ohnuma, A.G.Ruggiero and L.C.Teng IEEE Trans.Nucl.-Sci. NS-22, No. 3 (1911) 1975

5) Report of the Electron-Proton Working Group of ECFA, Study of the Proton-Electron Storage Ring Project HERA ECFA 80/42, DESY HERA 80/01 - 1980 HERA - A Proposal for a large Electron-Proton Colliding Beam Facility at DESY - DESY HERA 81/10

6) T.Nishikawa, Proc. of 9th Int.Conf. on High Energy Accelerators, May 1974, Stanford, California, Report of the TRISTAN ep ($e\bar{e}$) Working Group UTPN-165 / UT-345 July 1980

7) Electron-Proton Interaction Experiment, Fermilab Proposal 659, Spokesman: W.Y.Lee, R.R.Wilson. A more ambitious proposal was put forward by a group of Canadian Physicists but terminated due to lack of funds.

CHEER - A feasibility Study for an Electron Ring at a High Energy Proton Accelerator.

8) P.E.Faugeras, CERN / SPS / DI-MST 81-16 and LEP Note 303.

9) M.Sands - The Physics of Electron Storage Rings - SLAC-121

10) H.Bruck, Accelerators Circulaire des Particules Press Universitaires de France, Paris, 1966

11) Theoretical Aspects of the Behaviour of Beams in Accelerators and Storage Rings. - Proceedings of the First Course of the International School of Particle Accelerators, Erice 10-22 Nov. 1976 - CERN 77-13

12) Physics of High Energy Particle Accelerators, edited by: R.A.Carrigan, F.R.Huson and M.Month, American Institute of Physics - 1982

13) J. Le Duff: Stanford Summer Institute 1981

14) The various proposals listed above contain a discussion of the physics which can be carried out with a large electron-proton colliding ring - for an early complete discussion see: C.H.Llewellyn-Smith and B.H.Wiik, DESY 77/38 (1977) CHEEP-An ep facility in the SPS: J.Ellis, B.H.Wiik and K.Hübner CERN 78-02.
Most figures and rules shown below are taken from this work and from reference 5.

15) Superconducting Accelerator Design Report - Fermi National Accelerator Laboratory (1979)

16) S.L.Glashow, Nucl.Phys. 22, 579 (1961)

S.Weinberg, Phys.Rev.Lett. 19, 1267 (1967)

A.Salam, Proc. 8th Nobel Symposium, Stockholm, Almquist and Wiksells, Stockholm 1968 p. 363

17) A.J.Buras and K.J.F.Gaemers, Nucl.Phys. B 132, 249 (1978)

18) M.Kobayashi and T.Maskawa, Proc. Theor.Phys. 49, 652 (1973)

19) L.F.Abbott and E.Farhi, Nucl.Phys. B 189, 547 (1981)

20) For an early account on the observation of pointlike constituents see: W.K.H.Panofsky, Proceedings of the XIV International Conference on High Energy Physics, Vienna, Austria, 1968

21) For an early report on Scaling Violation see: R.E.Taylor in Proc. of the Int.Symposium on Lepton and Phtoton Interactions at High Energies, Stanford 1975 and J.Drees, Proc. of the Int. Neutrino Conference, Aachen 1976.

22) H.Fritzsch, M.Gell-Mann and H.Leutwyler, Phys.Lett. 47B. 365 (1973) D.J.Gross and F.Wilczek, Phys.Rev.Lett.30, 1343 (1973) H.D.Politzer, Phys.Rev.Lett. 30, 1346 (1973) S.Weinberg, Phys.Rev.Lett. 31, 31 (1973)

23) Yu. A.Gal'fand and E.P.Likthman, JEPT Lett. 13, 323 (1971) P.V.Volkov and V.P.Akalov, Phys.Lett. 46B, 109 (1973) J.Wess and B.Zumino, Nucl.Phys. B70, 39 (1974)

24) For a recent review and a complete set of references see: M.E.Peskin, 1981 International Symposium on Lepton and Photon Interactions at High Energies, Bonn, August 1981

25) J.C.Pati and A.Salam, Phys.Rev. D8, 1240 (1973) and Phys.Rev.D10, 275 (1974)

26) J.Schwinger, Phys.Rev.125, 397, 2286 (1973)

R.Jackiew and K.Johnson, Phys.Rev. D8, 2286 (1973)

J.M.Cornwall and R.E.Norton, Phys.Rev.D8, 3338 (1973)

M.A.Beg and A.Sirlin, Ann.Rev.Nucl.Sci 24, 379 (1974)

S.Weinberg, Phys.Rev. D13, 979 (1976) and Phys.Rev. D19, 1277 (1979)

L.Susskind, Phys.Rev.D20, 2619 (1979)

27) S.Rudaz and J.Vermaseren, CERN Preprint TH-2961 (1981).

28) G.Barbiellini et al., ECFA/LEP Specialized Study Group 9, DESY Report 79/67.

29) S.K.Jones and C.H.Llewellyn-Smith, University of Oxford Preprint 73/82.

30) E.D. Courant and H.S.Snyder; Ann. Physics 3, 1 (1958)

K.G.Steffen in Proc. Int. School "Enrico Fermi," Course XLVI, Physics with Intersecting Storage Rings, Academic Press (1971)

E.Keil in ref. 11.

31) A.Schock, CERN Report 57-1 (1978)
G.Guignard, CERN 78-11 (1978)
E.J.N.Wilson in ref. 11.

32) B.W.Montague in ref. 11.

33) K.Robinson, Phys.Rev. 111, 373 (1958)

34) I.M.Ternov, Yu.M.Loskutov and L.I.Korvina, Sov.Phys. JETP, 14, 921 (1962)

A.A.Sokolov and I.M.Ternov, Sov.Phys.Dokl. 8, 1203 (1961)

A.W.Chao in ref. 12 - Talks given at the Polarized Electron Acceleration and Storage Workshop Hamburg, March 22-27, 1982 DESY M-82/09.

35) H.D.Bremer et al., DESY 80/76 and DESY 82/26.

36) V.Bargman, L.Michel and V.L.Telegdi, Phys.Rev.Lett. 2, 435 (1959)

37) V.N.Baier and Yu. F.Orlov, Sov.Phys.Dokl. 10, 1145 (1966)

Ya. S. Derbenev and A.M.Kondratenko, Sov. Phys. JETP 37, 968 (1973)

38) A.W.Chao and K.Yokoya, KEK-81-7;

K.Steffen, Internal Report CBN 81-29, Newman Lab. Cornell - November 1981.

39) For a review on instabilities including references see: A.Hofmann, B.Zotter and F.Sacherer in ref. 11.

40) A.Wrulich - DESY HERA 82/07.

Evidence for Jets from a Transverse Energy Triggered Calorimeter Experiment at Fermilab

Michael Arenton
(for the E-609 Collaboration*)

Argonne National Laboratory

Talk Presented at the 10th SLAC Summer
Institute on Particle Physics, August 1982

*the members of the E-609 collaboration are:
R. Ditzler, T. Fields - Argonne National Laboratory, M. Dris - NRC Democritos, M. Harrison - Fermilab, A. Kanofsky - Lehigh University, R. Gustafson - University of Michigan, L. Cormell, J. Fleischman, E. Gardella, C. Hitzman, W. Kononenko, B. Robinson, W. Selove, G. Theodosiou, B. Yost - University of Pennsylvania, M. Corcoran, K. Johns, H. E. Miettinen, C. Naudet, J. Rice, J. Roberts - Rice University, H. Chen, A. Erwin, A. Hasan, C. Kuehn, K. Nelson, M. Thompson - University of Wisconsin.

© M. Arenton 1982

Abstract

We have recently completed the first part of running for experiment E-609 at Fermilab. The E-609 hadron jet experiment uses a 132-segment 8-steradian full azimuth calorimeter with tower structure. Additional parts of the apparatus are described in the paper. A novel triggering system allowed us to take data with many different kinds of triggers simultaneously. We give a preliminary report on data obtained in 400 GeV pp collisions, concentrating on data from two triggers, both of which have no special geometrical requirement for the form of the transverse energy deposition. One of these was a global total E-transverse trigger; the other was a "2-high" trigger, which required that 2 or more calorimeter segments (any 2) each give a signal larger than about 1.0 GeV/c. We present details of an analysis of the planarity distributions of the data. A method of randomizing the data is presented that allows us to determine the extent to which the data can be explained by simple random fluctuations. This analysis shows that there is a few percent of jetlike events in the global trigger data. The "2-high" trigger, however, shows a clear excess of high planarity, jetlike events, on the order of 20% of the sample, over what is expected from random fluctuations of isotopic events.

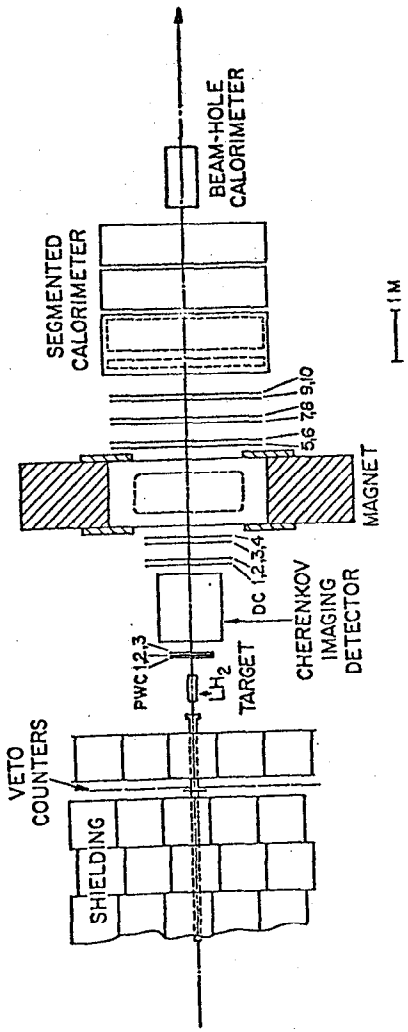
I. INTRODUCTION

We have recently completed the first part of running for experiment E-609 at Fermilab. The E-609 hadron jet search experiment uses a full azimuth calorimeter with unique well-proven design features. The flexibility of the E-609 detector system allowed us to take data with simultaneous use of approximately two hundred different trigger conditions. In this note, we give a preliminary report on data which we obtained using transverse energy triggers and related triggers which have no special geometrical requirement for the transverse energy deposit.

Interest in understanding the effects of using such triggers has increased since the NA5 experiment at CERN reported an absence of clear jet structure in 300 GeV hadron collision events having large transverse energy.[1] This absence, as observed by NA5 in the first hadron calorimeter experiment with full coverage in azimuthal angle, has stimulated several calculations and models[2] concerning the origins of large E_T events and has also raised questions concerning hadron jet phenomena which had been previously observed at Fermilab and the ISR.[3]

II. EXPERIMENTAL SETUP

Our detector system, shown in Fig. 1, is located in the M6E beam line at Fermilab. The results described in this note were obtained using a 400 GeV proton beam. The heart of the detector system is a segmented sampling scintillation calorimeter, consisting of 132 towers of four longitudinal sections



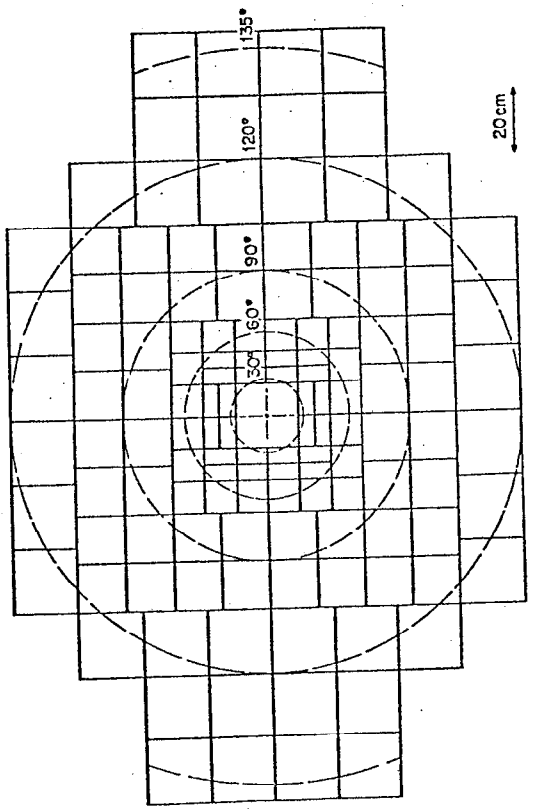
TOP VIEW OF E-609 APPARATUS

Fig. 1

each. These towers point at the liquid hydrogen target, so that the cascade shower crosstalk between adjacent towers is minimized. The front face of the calorimeter is shown in Fig. 2. The calorimeter has several special features which prevent spurious responses such as high pulse height tails and hot spots.[4] Transverse momentum in each calorimeter segment is the product of sin theta-lab and the deposited energy. Calorimeter module signals were balanced against each other by steering a muon beam through each module and adjusting the high voltage to achieve the required pulse height. The calorimeter response was then determined using hadron beams of various momenta. The analysis of the calibration data is still in progress, and the P_T scale of the data reported here is uncertain to 10-15 percent.

The detector system also incorporates a magnetic spectrometer using 12 planes of drift chambers, 3 PWC planes, and a magnet with a small transverse momentum kick of $\sim$ 0.1 GeV/c. This small value was used to avoid large systematic shifts in trigger thresholds, which are determined by the geometry of the calorimeter and based on straight line trajectories. Another special feature of our detector system is the imaging Cerenkov counter[5] for secondary particle identification.

Data were taken using many types of triggers concurrently. Most of these triggers summed the transverse energy in the calorimeter in particular geometric regions (e.g., "two-arm" triggers or "one-arm" triggers). However, the results presented in this note are based only upon triggers for which no special geometric requirements were imposed, as described in the next section.



FRONT VIEW OF CALORIMETER ARRAY AT 400 GeV/c

Fig. 2

III. PLANARITY ANALYSIS

Our analysis effort to date has focussed on the question of whether events observed using as a trigger the total transverse energy (called the "global" trigger) show evidence for clustering of the secondary hadrons, i.e., "jet," behavior. We have studied "planarity" distributions, as used in the CERN NA5 analysis,[1] as well as azimuthal distributions, which have been used in the E-557 Fermilab analysis.[6]

The experimental planarity distribution which we obtained for global trigger events with E_T > 11 GeV into the angular region 17 < theta-lab < 122 mrad (i.e., 30 degrees < theta c.m. < 120 degress) is given in Fig. 3. Note that the side "wings" of our calorimeter array as shown in Fig. 2 were not used in our planarity analysis. The planarity distribution in Fig. 3 is similar to those reported by the NA5 and E-557 experiments. (The agreement concerning the absolute cross section for E_T (global) triggers among the three experiments has not yet been studied thoroughly.)

The central physics question concerning Fig. 3 is whether the rather non-planar average character of the events is due to all events having little or no jet structure, or whether, to the contrary, Fig. 3 contains some number of jet-like events (e.g., with planarity > $\sim$ 0.8) which are not merely statistical fluctuations of the average (non-planar) events. To answer this question requires knowledge of the planarity distribution to be expected in the absence of jet behavior. We have estimated the uncorrelated particle planarity distribution by taking the events and destroying any dynamical correlation by randomizing the azimuthal angles of the particles in the

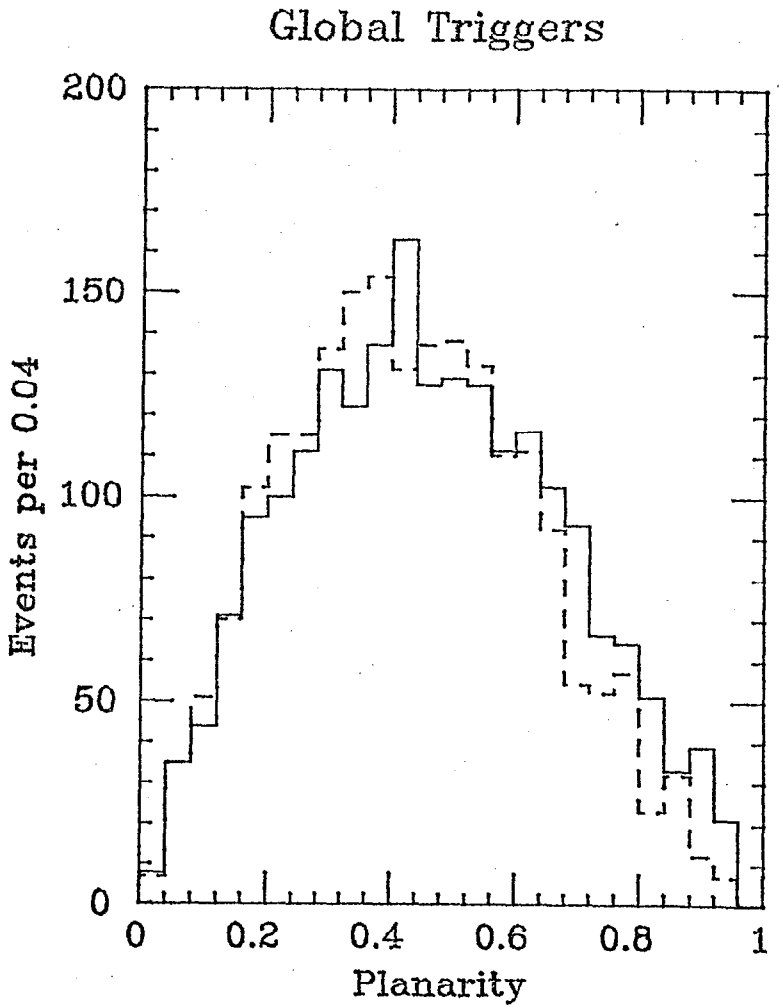


Figure 3. Distribution in planarity of events satisfying the global trigger with E_T > 11 GeV. The data are shown by the solid histogram. The dashed histogram shows the distribution of the data after randomization of particle azimuths by the procedure described in the text.

event. We retained the effects of momentum conservation, however, by requiring that the randomized event have approximately the same degree of transverse momentum unbalance as the original event. In detail the vector difference between the original and final transverse momentum unbalances was required to be less than 0.5 GeV in magnitude. Preliminary studies show the results to be insensitive to the exact value of this cut. This restriction was applied by the brute force technique of redoing the randomization until the cut was satisfied. A somewhat subtle point in this analysis is the fact that we want to randomize actual particle momenta while what is measured is energy deposition in calorimeter segments. We have used a simple algorithum to combine calorimeter segment energy into clusters. The clusters are then the quantities randomized. The algorithum is conservative in the sense that it tends to some extent to overestimate the planarity after randomization.

The randomized planarity distribution for the global trigger events is shown as the dashed line in Fig. 3. The randomized distribution fails to account for the frequency of events at high planarity, say greater than 0.8. However, it appears that at most a few percent of the events are in the excess above $\sim$ 0.8. Clearly what is needed is some additional, but still geometrically unbiased, trigger requirement to enrich these events in the sample. We have tried to achieve this by considering only events in which any two to more calorimeter segments each detected a p_T of greater than, say, 1 GeV/c. This minimum value is high enough to be improbable in the low p_T (e^{-6p_T})

single particle distribution, and yet low enough to be very probable in the fragmentation of partons having a few GeV/c of transverse momentum. Our "two-high" trigger had the sole requirement that any two calorimeter segments each have E_T > 1 GeV, and produced events whose planarity distribution is shown in Fig. 4. For direct comparison with Fig. 3, this figure shows only events having global E_T > 11 GeV. It is evident that these events are substantially more planar than those in Fig. 3. The possibility that statistical fluctuations of non-correlated particles led to the observed planarity distribution of Fig. 4 was estimated using the same randomization method described above, and the results are again shown by the dashed line. Our conclusion is that the event sample with planarity > 0.8 from the "two-high" trigger contains a significant fraction of events (probably > 50 percent) having dynamical momentum clustering (rather than being statistical fluctuations of events having no real jet structure).

We have also examined this "two-high" trigger as a function of the total global E_T deposited in the calorimeter. Figure 5 shows the data and randomized planarity distributions for "two-high" trigger events for global E_T bins of 2 to 5 GeV, 5 to 8 GeV and 8 to 11 GeV. There is still substantial evidence for an excess of high planarity events in the 8 to 11 GeV sample, but little below 8 GeV. Note in particular the 2 to 5 GeV data that are very planar but show little excess over the randomized distribution; presumably the high planarity is the result of momentum conservation.

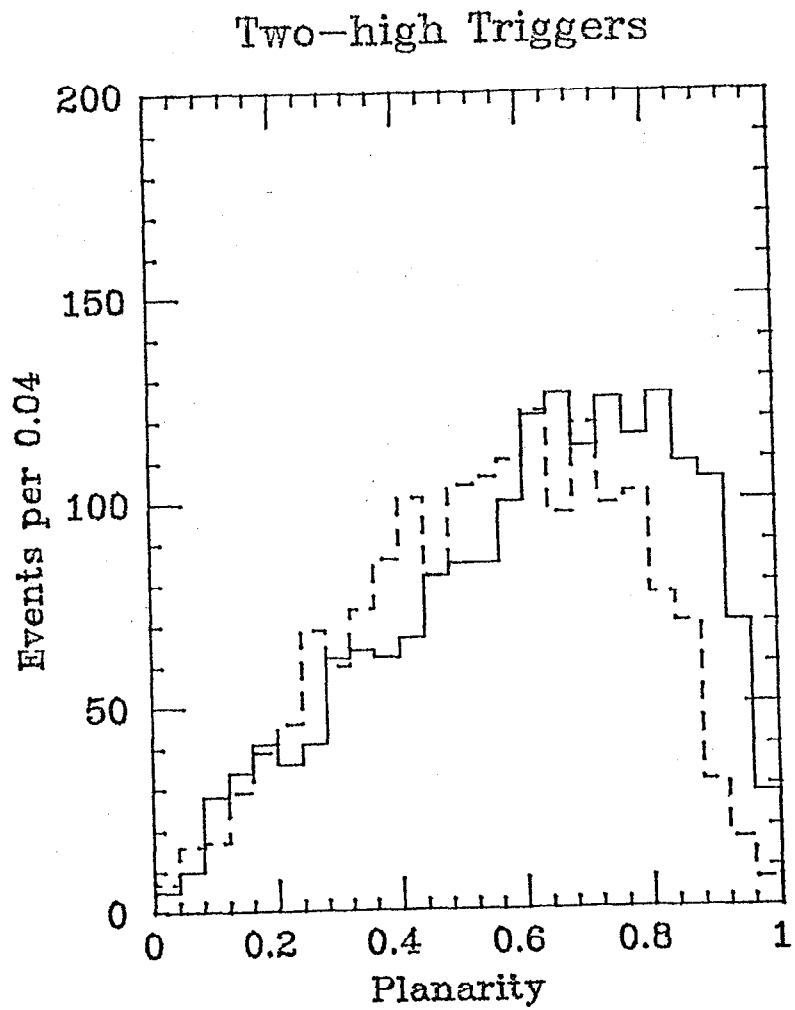


Figure 4. Distribution in planarity of events satisfying a trigger requiring any two calorimeter segments to each have p_T greater than 1 GeV/c. The events in this plot also have global E_T > 11 GeV. The data are the solid histogram and the dashed histogram shows the data after randomization of particle azimuths.

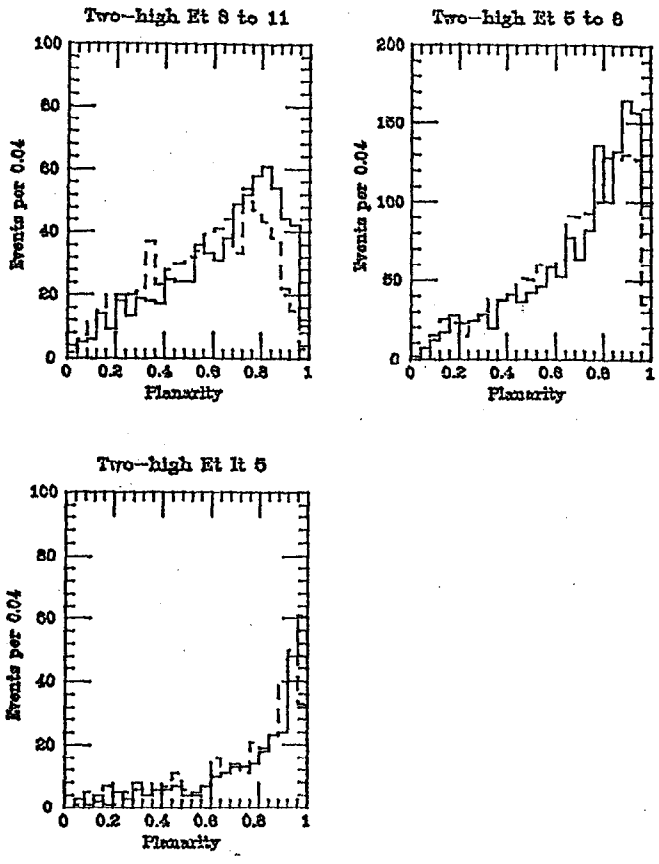


Figure 5. Planarity distributions of two-high triggers for three ranges of global E_T. The data are the solid histograms and the dashed histograms show the distribution after randomization of particle aximuths.

We have also examined the planarity distributions from a simple Monte Carlo program that generated events whose single hadron p_T distributions and multiplicity distributions agree with experiment and which are constrained to satisfy transverse momentum conservation. The planarity distribution from the Monte Carlo cannot account for the numbers of events with planarity greater than 0.8 seen in the data.

IV. CONCLUSIONS

From data recently obtained in E-609 on 400 GeV/c pp interactions we have presented results using two geometrically unbiased triggers. We find that while only a few percent of the "global trigger" events show di-jet characteristics at large E_T, there is a substantial excess of jetlike events over that expected from random distributions of particles in events selected by the "two-high" trigger. Further studies of the properties of these events are in progress.[7] Finally, we note that the "two-high" events are also present in the "global trigger" sample but are masked by other events lacking a clear di-jet structure that satisfy the global trigger with about an order of magnitude greater cross section.

This experiment could not have been carried out without the efforts of many people at Fermilab. We would particularly like to thank Dr. H. Haggerty and his group for their efforts with the superconducting beam line.

This work was supported by the U. S. Department of Energy.

References

(1) C. DeMarzo et al., Phys. Lett. 112B, 173 (1982).

(2) Some examples are described in:

R. Singer et al., Phys. Rev. D25, 2451 (1982);
G. C. Fox and R. L. Kelly, LBL-13985 (1982);
F. W. Bopp and P. Aurenche, Z. Phys. C 13, 205 (1982).
R. Odorico, IFUB 82/16 (1982).
H. Bengtsson and T. Akesson, LUND preprint (1982).

(3) For a recent review, see P. Darriulat, Ann. Rev. Nucl. Sci. 30, 159 (1981).

(4) L. Cormell et al., Performance of a Segmented Hadron Calorimeter, IEEE Trans. Nucl. Sci. NS29, 307 (1982).

(5) B. Robinson, to be published.

(6) B. Brown et al., Phys. Rev. Lett. 49, 711 (1982).

(7) Some preliminary results on event properties are presented in a paper submitted to the XXI International Conference on High Energy, Paris, July 1982.

A Search for Neutrino Oscillations with $\Delta m^2 > 20$ eV^2

Wesley H. Smith
Columbia University,
New York, NY 10027

Abstract

The status of an experiment by the CCFR collaboration[1] to search for neutrino oscillations is reported. The experiment uses two similar detectors at two different locations in the Fermilab dichromatic neutrino beam. The measurement is made with a flux of 3.4×10^{18} protons on target and is sensitive to neutrino oscillations with $20\ \text{eV}^2 < \Delta m^2 < 800\ \text{eV}^2$ and $\sin^2(2\alpha) > 0.05$.

1. Introduction

There are many theoretical suggestions[2] that a neutrino of one type such as a ν_μ may oscillate into a neutrino of a different type such as ν_e, ν_τ, $\bar{\nu}_\mu$, or some presently unknown additional type. If there are two neutrino eigenstates of the weak interaction, $|\nu_\mu\rangle$ and $|\nu_x\rangle$, with different masses, and which are quantum mechanical mixtures of the neutrino mass eigenstates, $|\nu_1\rangle$ and $|\nu_2\rangle$, with masses M_1 and M_2 :

$$|\nu_\mu\rangle = \cos\alpha|\nu_1\rangle + \sin\alpha|\nu_2\rangle \ ,$$

$$|\nu_x\rangle = -\sin\alpha|\nu_1\rangle + \cos\alpha|\nu_2\rangle \ ;$$

where α is the mixing angle which characterizes the contribution of the mass eigenstates to the weak interaction eigenstates. In order for oscillations to occur, the mass difference, $\Delta m^2 = M_1^2 - M_2^2$, must be non-zero, so at least one of the neutrinos must have a non-zero mass. In addition, a coupling must exist between the two neutrino types so that lepton

© W. Smith 1982

number is not exactly conserved. If this is the case, then the probability P of the appearance of a neutrino of type ν_x at a distance L from the source where a ν_μ was initially created is:

$$P(\nu_\mu \rightarrow \nu_x) = \sin^2(2\alpha)\sin^2(1.27\Delta m^2 L/E_\nu) \qquad (1)$$

where the mass difference is in eV^2, L is the distance from the source in kilometers and E_ν is the energy of the neutrino in GeV.

There are two classes of experimental searches for neutrino oscillations. Firstly, there are exclusive searches, which look for specific oscillations, such as $\nu_\mu \rightarrow \nu_e$ or $\nu_\mu \rightarrow \nu_\tau$; and secondly, there are inclusive searches, which look for a decrease in the apparent cross section caused by a specific type of neutrino oscillating into another state. A positive signal in an exclusive search in a ν_μ beam would indicate the probability of ν_μ going into another neutrino is non-zero, whereas in an inclusive experiment a positive signal indicates that the probability of ν_μ to remain a ν_μ is not one. Exclusive searches for ν_e interactions in a ν_μ beam are sensitive to ν_μ oscillations into either ν_e or ν_τ and are limited by the ν_e contamination in the ν_μ beam. This type of experiment is not sensitive to $\nu_\mu \rightarrow \nu_x$ if ν_x does not interact and give a charged lepton. A summary of the present status of neutrino oscillation experiments may be found in the article by H. H. Williams in these proceedings.

The advantage of an inclusive experiment may be demonstrated by considering some possible cases. Suppose there is a fourth flavor of charged lepton h, with a high enough mass to prevent its observation by PEP or PETRA experiments. While the cross section for $\nu_h N \rightarrow h^- x$ would be highly suppressed by phase space at Fermilab energies, oscillations of the type $\nu_\mu \rightarrow \nu_h$ would be no less likely than other neutrino oscillations. However, the $\nu_\mu \rightarrow \nu_h$ oscillation would reduce the apparent charged current cross section and would therefore be observable in an inclusive experiment. Another case where an inclusive experiment provides a unique probe of oscillations is the mixing of a muon neutrino with a non-interacting type of neutrino. An example of such a sterile neutrino would be a left-handed muon antineutrino, or a Majorana neutrino. If right-handed leptonic couplings exist, then oscillations of the type $\nu_\mu \rightarrow \bar{\nu}_\mu$ would also cause an apparent reduction in the charged current cross section.

The neutrino oscillation Experiment 701 at Fermilab is unique in two ways. First, the range of neutrino energies between 50 and 250 GeV, the distance from source to detector of 500 to 1000 meters and the length of the neutrino source of 342 meters are optimal for observing oscillations in the mass range of 10 to 1000 eV^2. Lower energy experiments at reactors, LAMPF, BNL or the CERN PS cannot reach Δm^2 values greater than 10 eV^2. Second, the cross section for neutrino interactions at Fermilab is larger than that found at lower energy machines. The statistics of this experiment of 450,000 charged current events in both detectors far exceed those possible at these other machines. The sensitivity of an inclusive experiment to small mixing angles is directly related to the size of the event sample. This experiment is sensitive to values of $\sin^2(2\alpha)$ below 0.05.

Inclusive searches for oscillations are difficult because they must either compare measurements of $\sigma^{\text{total}}_{\nu_\mu}$ at different energies or at different distances from the neutrino source. The comparison of different energies

is severely limited by systematic uncertainties in the calculated neutrino flux as a function of both energy and time. These uncertainties ultimately limit the accuracy of total cross section measurements. At present, there are two high statistics measurements of the neutrino and anti-neutrino total cross section, CFRR at Fermilab[3] and CDHS at CERN.[4] These experiments quote systematic flux errors of 5-10% which limit the observation of changes of the cross section with energy. Even though the two experiments are at two different distances from their neutrino sources, any comparison between them to measure oscillations is rendered useless by the errors in their relative flux normalization.

These problems of flux normalization cause the only reliable method of performing an inclusive oscillation search to be simultaneously measuring the interaction rate in two similar detectors located at two different distances from the neutrino source (decay pipe). Since the two detectors are exposed to the same neutrino beam at the same time, the systematic uncertainties are minimized. For the CCFR two-detector experiment at Fermilab, the systematic errors are below 1% and do not limit the ultimate sensitivity of the experiment.

2. Apparatus

The two detectors used in the CCFR experiment consist of the Lab E 1000 ton CFRR detector used previously in Fermilab Experiment 616,[3] and a totally new 200-ton detector constructed in the Wonder Building. Both detectors sit on the Fermilab dichromatic neutrino beam line as shown in Fig. 1.

The Lab E detector is shown in Fig. 2. It consists of a calorimeter target followed by an iron toroid muon magnetic spectrometer. The target calorimeter contains

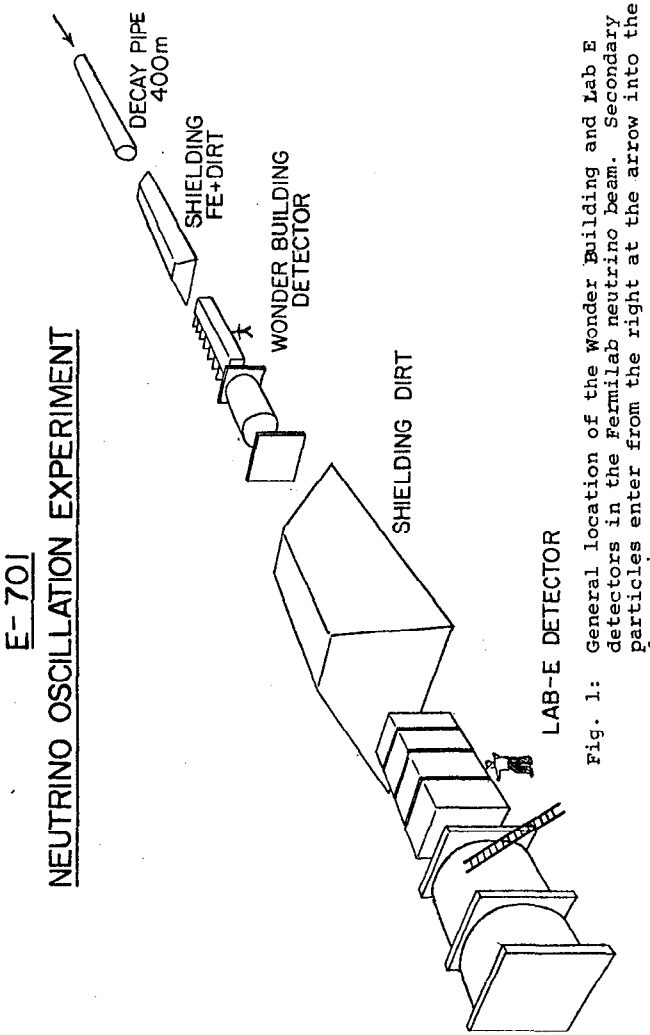


Fig. 1: General location of the Wonder Building and Lab E detectors in the Fermilab neutrino beam. Secondary particles enter from the right at the arrow into the decay pipe.

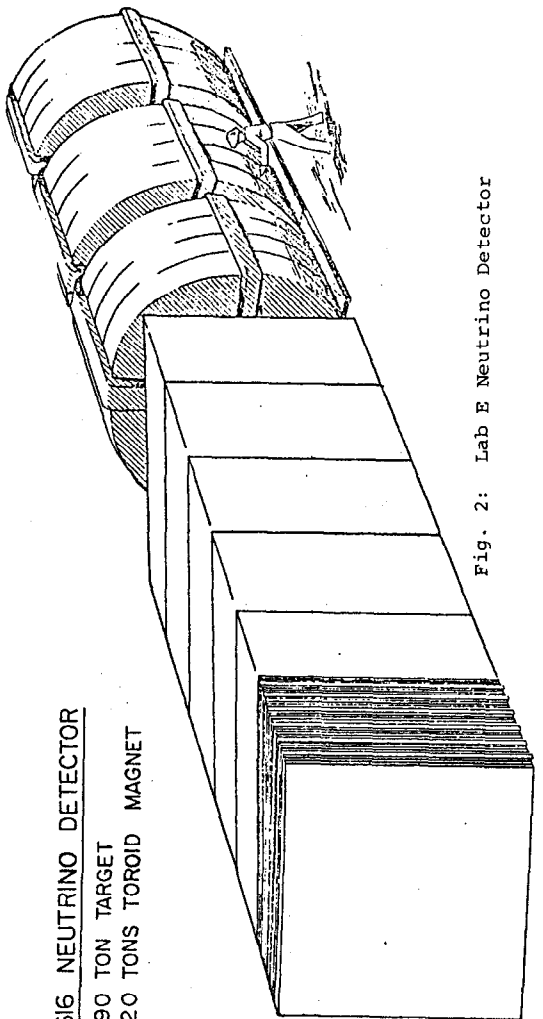


Fig. 2: Lab E Neutrino Detector

690 tons of square steel plates (10 ft x 10 ft x 2 in.) interspersed with spark chambers (every 20 cm of steel) and liquid scintillation counters (every 10 cm of steel). The target is divided into six modules of equal size of which the downstream four modules were used for E-701 data taking. The muon spectrometer is made up of three toroidal iron magnets. Each toroid has a radius of 5 ft 11 in. and a central hole for the excitation coils of 5 in. in radius. There are eight planes of doped acrylic scintillation counters (every 20 cm of steel) in each toroid. In addition, each toroid is followed by five spark chambers. The measured resolution of the calorimeter is:

$$\frac{\Delta E_H}{E_H} = \frac{0.89}{\sqrt{E_H(\text{GeV})}} \quad .$$

The total P_t kick of the toroids is 2.4 GeV/c and the momentum resolution for muons is 11%.

The Wonder Building detector, shown in Fig. 3, is similar to the Lab E detector. The detector target is 5 ft x 5 ft in transverse dimension because neutrinos which traverse near the 5 ft edge in the Wonder Building end up near the 10 ft edge of the target in Lab E. Fiducial cuts are made in both detectors in order to compare regions of the target for which identical fluxes are subtended. The target is made up of fifty-six 5 ft x 5 ft x 4 in. steel plates, seventeen 5 ft x 10 ft spark chambers and forty-six 5 ft x 5 ft x 1 in. doped acrylic scintillation counters.

The muon spectrometer in the Wonder Building needs to be of similar size to the Lab E spectrometer because the kinematics of the muon angle in neutrino interactions do not change between the two detectors. There is one toroid that is 10 ft in diameter, 96 in. in length, and

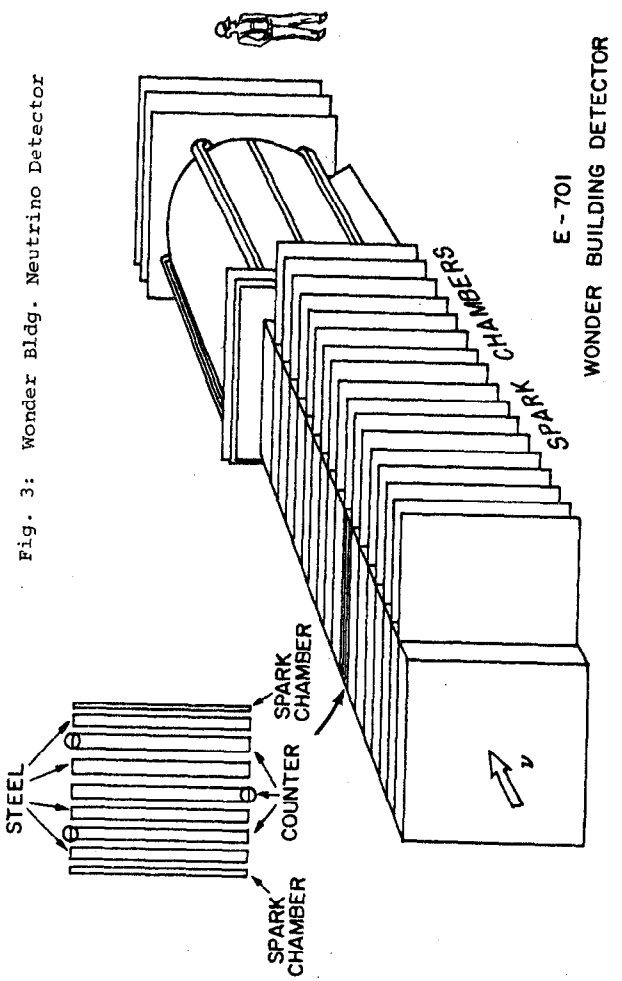


Fig. 3: Wonder Bldg. Neutrino Detector

has a hole for the excitation coils that is 10 in. in diameter. There are twenty 5 ft x 10 ft spark chambers placed before and after the toroid. The hadron energy resolution of the calorimeter is $90\%/\sqrt{E_{Had}}$. The total P_t kick of the toroid is 1.2 GeV/c and the momentum resolution for muons is 16%.

3. Methods

The two detectors sit in the Fermilab dichromatic neutrino beam which produces neutrinos through the decay of roughly monochromatic pions and kaons.[5] The 400 GeV/c protons from the main ring strike a 12-in. long BeO target. Charged secondaries (pions, kaons, and protons) produced in the forward direction ($\theta <$ 1.6 mrad) of a selected sign and momentum ($\Delta P/P$ = 9.4%) are transported through a specially designed point to parallel beam channel and travel through a 340 m long evacuated pipe where some of them decay into neutrinos and muons. The surviving secondary hadrons and decay muons are then stopped by a beam dump followed by a 600 m long earth shield. The neutrinos travel 743 m from the midpoint of the decay pipe to the midpoint of the Wonder Building detector. They then traverse another 310 m of earth shielding before they reach the midpoint of the Lab E apparatus, which lies 1080 m from the midpoint of the decay pipe. The general layout is shown in Fig. 4. The neutrinos travel with negligible attenuation through the shielding, and some of them interact in the Wonder Building while others interact in Lab E.

The two triggers used to identify charged current events were the same in both detectors. The muon trigger required a particle to penetrate the downstream part of the calorimeter and to go past one iron toroid. Such events satisfy the kinematic requirements of $\theta_\mu <$

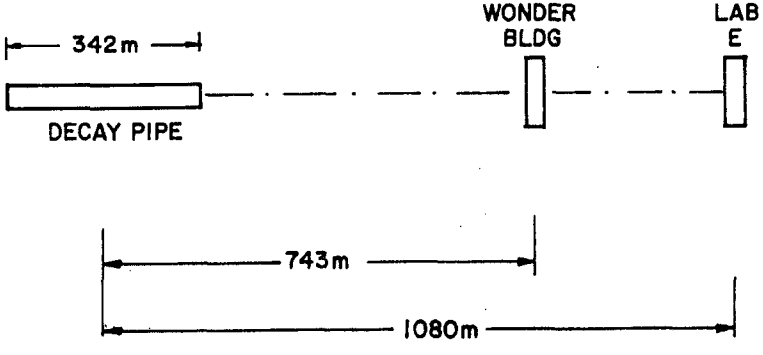


Fig. 4: Experimental setup.

100 mrad and $P_\mu > 10$ GeV/c. These events can be fully reconstructed since both hadron energy and muon momentum are measured. The penetration trigger required 4 GeV of energy in the target calorimeter and a particle penetrating through at least 1.6 m of steel. Additional software requirements of $E_H > 10$ GeV and $\theta_\mu < 370$ mrad were imposed. Events satisfying this trigger include charged current events where the muon is produced at a large angle, leaving the target calorimeter at the side and never reaching the spectrometer. The penetration requirement implies that $P_\mu > 2.9$ GeV/c. In order to eliminate spurious triggers due to muons originating in the earth shield in front of each apparatus, the signal from a large scintillator in front of each detector was required in anti-coincidence with all triggers.

Given the distances from the decay pipe midpoint to the Wonder Building detector of 743 m and to the Lab E detector of 1080 m, Eq. (1) predicts the event ratio for the two detectors shown in Fig. 5. The first significant maximum in the ratio occurs where the argument for the sin term is $3\pi/2$ (not $\pi/2$); the first minimum occurs at π. This behavior is a consequence of the distance ratio of the two detectors from the neutrino source being 0.70.

In a real experiment, the neutrino energy, E_ν, is known with some precision and the distance from the neutrino source, L, is known to the length of the detector and the length of the source, which in this case is the decay pipe. These errors in E_ν and L tend to reduce the changes in rate expected from Eq. (1). For example, if two monoenergetic neutrino beams have energies that differ by 20%, then after three oscillation lengths the lower energy has a maximum when the

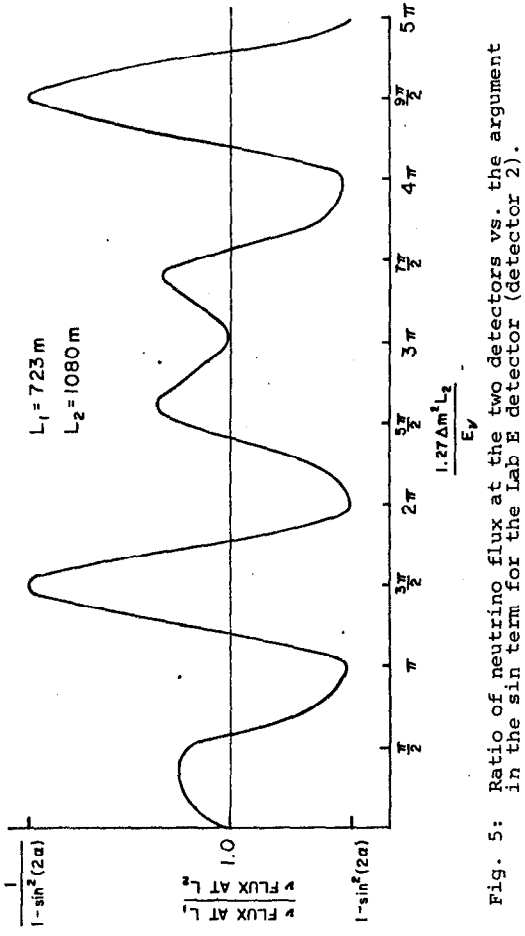


Fig. 5: Ratio of neutrino flux at the two detectors vs. the argument in the sin term for the Lab E detector (detector 2).

higher has a minimum as shown in Fig. 6. To keep the smearing of the oscillating behavior less than 0.2 oscillation lengths, the energy resolution must be:

$$\Delta E_\nu / E_\nu < 0.2\ N_L \quad , \tag{2}$$

where N_L is the number of oscillation lengths to the detector. For an experiment with 10% energy resolution, Eq. (2) implies that the detectors are sensitive to rate changes in the one to three oscillation length region. This consideration translates into an upper limit on this experiment's sensitive region in Δm^2 of 910 eV^2.

The finite length of the decay pipe also reduces the measured flux differences between the two detectors, especially when the oscillation length is comparable with the decay pipe length. The oscillation length defined as the distance in which the argument of the sin term in Eq. (1) changes by π is given by:

$$L_{osc}(\text{meters}) = 2.47 \times 10^3 * E_\nu(\text{GeV})/\Delta m^2(\text{eV})^2 \quad .$$

For an experiment using 400 GeV protons incident on the secondary production target, the maximum neutrino energy is about 240 GeV and, thus, the maximum Δm^2 probed is 1300 eV^2.

The lower mass limit to the sensitive region for detecting oscillations is due to the experimental errors. From Eq. (1), it can be seen that the ratio of events in the two detectors is approximately equal to $1.27(\Delta m^2/E_\nu)\cdot(L_2-L_1)$, which must be greater than the experimental error. The experimental error is composed of the statistical and systematic error. If, as will be shown below, the systematic error is less than 1%, a statistical error of approximately 1% or more would affect the sensitive region. A straight-

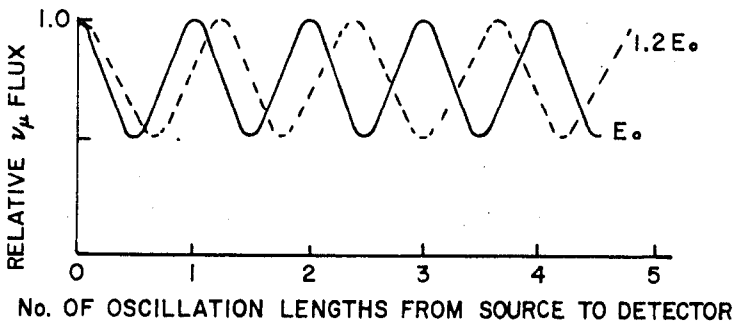


Fig. 6: Example of oscillations for two energies that differ by 20%.

forward calculation of the lower mass bound on this region assuming 1% systematic error and the present experimental statistics yields:

$$\Delta m^2 > 10 \text{ eV}^2 .$$

There are two methods employed in comparing the event rates in the two detectors. In the first method, events are separated into bins of measured energy and a ratio is computed for each bin. In the second, each detector is divided into radial bins around the beam center, and event yields in corresponding bins are compared. The size of the event bins in the Wonder Building is scaled down with respect to those in Lab E by the ratio of the distance between Wonder Building and the decay pipe to the distance between Lab E and the decay pipe. These two methods are somewhat complementary, although each has certain advantages and systematic shortcomings.

For the radial bin method, the neutrino energy and its spread in a given bin is inferred from the energy distribution of pions and kaons in the decay pipe. From the kinematics of the parent pion/kaon decay for a particular neutrino angle, i.e., for a particular interaction radius, it is expected that there should be neutrinos of two distinct energies arising from the decay of either pions or kaons. Neutrinos from kaon decay should have energies near the hadron beam energy, and neutrinos from pion decay should cover a range below 0.43 of the beam energy setting. For events satisfying the muon trigger, the measured energy is the sum of the total hadron energy measured in the calorimeter and the muon energy measured in the spectrometer. This should be the total neutrino energy. Figure 7 is a scatter plot of the total energy

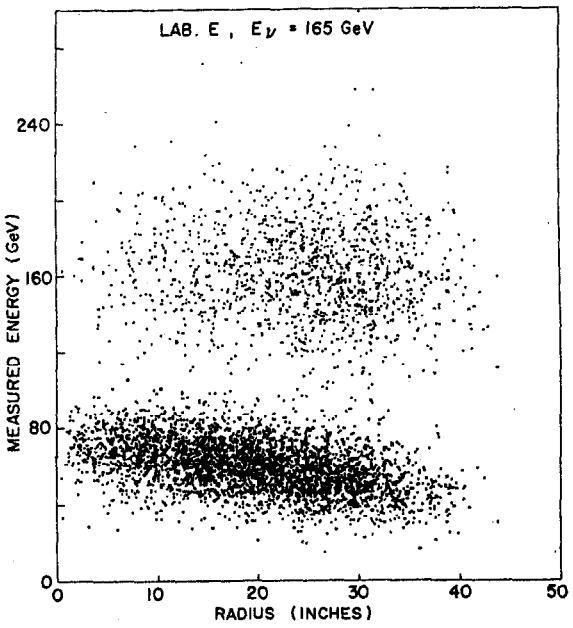


Fig. 7: Scatter plot of event energy vs. interaction vertex radius for the Lab E detector.

and radius of interaction for such events in the Lab E detector at a neutrino beam energy setting of +165 GeV. Figure 8 shows the total measured energy of events in the Lab E detector. Figure 9 shows the radius-energy plot for the Wonder Bldg. detector. The radius of interaction has been scaled by the ratio of the Lab E decay pipe distance to the Wonder Building decay pipe distance so that Figs. 9 and 7 should be directly comparable. Figure 10 shows the total measured energy of events in the Wonder Building detector. These figures show that the separation into two energy bands is clear.

In the case of events satisfying the penetration trigger, which are events with a muon for which only hadron energy was measured, the neutrino energy is not directly measurable. However, a substantial fraction of the kaon neutrino events of this type have a hadron energy which is larger than E_π, the maximum energy possible for a pion neutrino interaction. If the hadronic energy is lower than E_π and greater than 10 GeV, the muon trigger has a very high acceptance for events due to kaon neutrinos. The small fraction of events not satisfying the muon trigger is determined from the kaon neutrino events satisfying the trigger by a geometrical correction. The remaining events in this hadronic energy band are then due to pion neutrinos. Finally, for events with a hadron energy less than 10 GeV, the muon trigger acceptance is 100%, because the muon production angle is constrained by kinematics to be very small. Since for these events the muon is always analyzed, the total neutrino energy is measured, and they can always be identified as due to pion or kaon neutrino interactions.

The energy resolution or spread in a certain radial

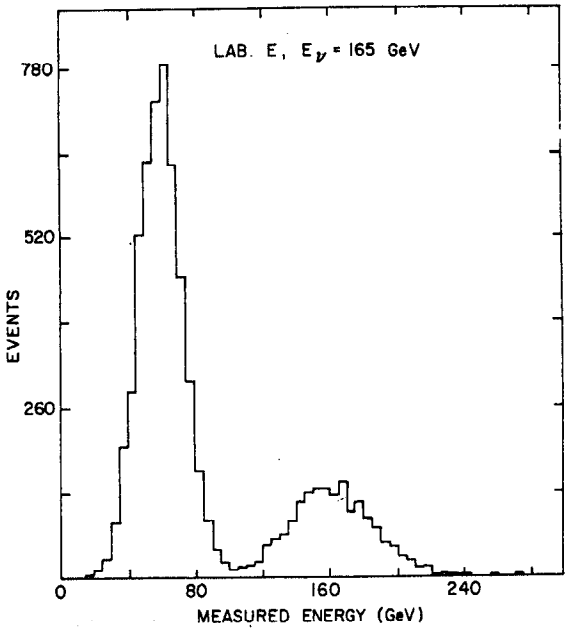


Fig. 8: Total measured energy of events in the Lab E detector.

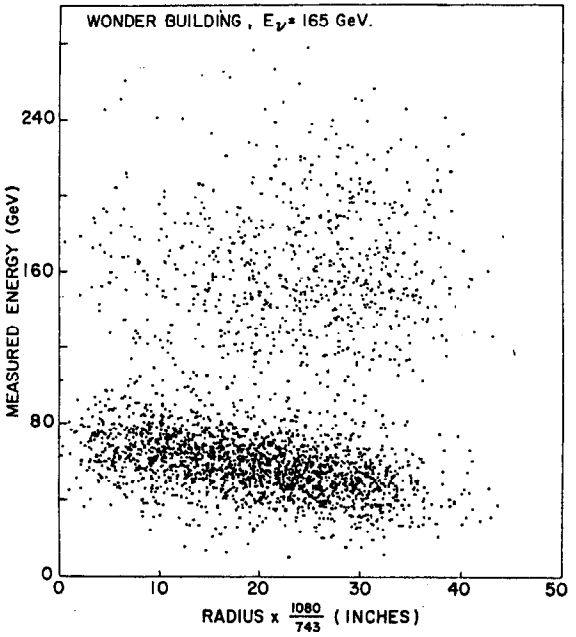


Fig. 9: Scatter plot of event energy vs. scaled interaction vertex radius for the Wonder Bldg. detector.

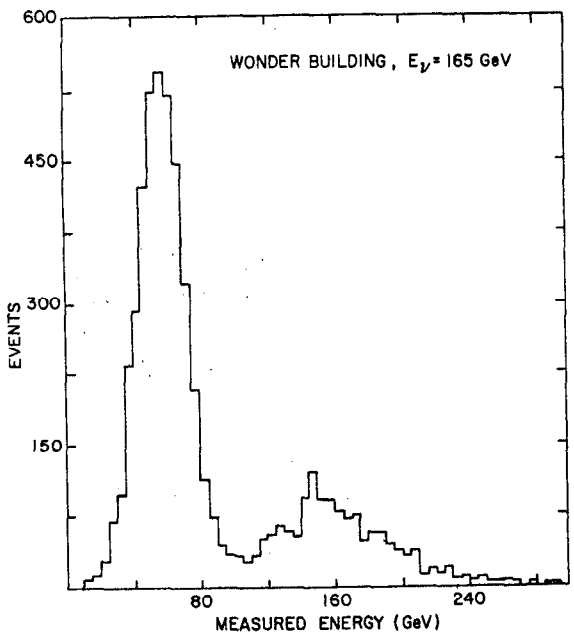


Fig. 10: Total measured energy of events in the Wonder Building detector.

bin depends on the width in energy of the secondary pion/kaon beam, the angular divergence and transverse size of this secondary beam and the size of the radial bin. For kaon neutrinos the energy spread in a radial bin is dominated by the spread in secondary energy, which is approximately 9%. Since pion neutrino energy spread has sizable contributions from both beam divergence and radial bin size, it is somewhat larger than 10%. For this reason, the energy binning method in which the detector resolution is 10% is more accurate for pion neutrinos. For kaon neutrino events, there are small corrections to the raw event rate due to the secondary beam shape coupled with the finite decay pipe length, errors in the beam center at each detector and errors in the relative position of the decay pipe with respect to the detectors. Figure 11 shows an estimate of the error introduced by these three effects. This estimate assumes a secondary beam with σ_θ = 0.14 mrad and σ_x = 2.5 in., an error in the relative beam centers of 1 in. and an error in the decay pipe position of 1 m. The beam center in each detector is determined to about 1/2 in. by fitting the spatial distribution of pion neutrino events. As shown in Fig. 11, the errors introduced by these effects are small and with corrections can be reduced to below 1%.

When using the energy binning method, the energy spread within a bin is related to the measurement errors in muon momentum and hadronic energy, E_H, discussed previously. At small $y = E_H/E_\nu$, the neutrino energy resolution is about 10% for Lab E and 13% for the Wonder Building. For pion neutrino events, this resolution is substantially smaller than the radial binning method. In addition, the number of events within a given energy bin is independent of the

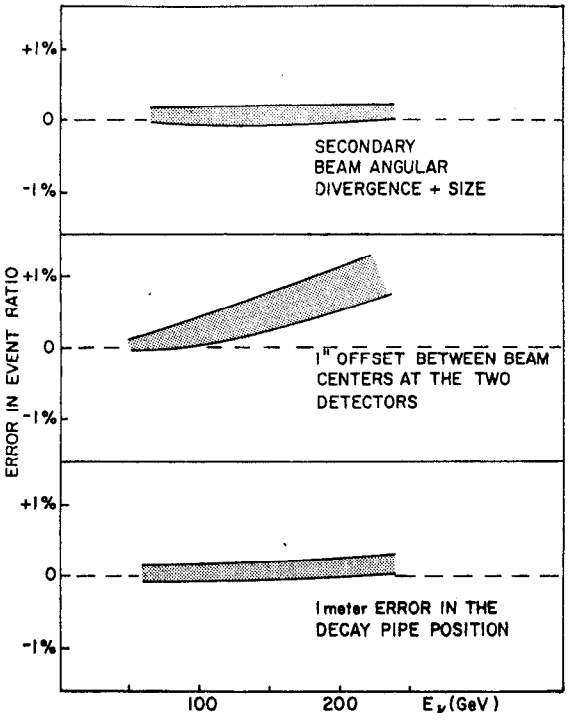


Fig. 11: Systematic errors introduced by three sources to the ratio of events observed in corresponding radial bins of the two detectors.

secondary beam size and divergence. However, the comparison of the detectors is dependent on their relative energy calibration. This relative calibration is determined directly from the data by comparing the mean energy in corresponding radial bins in the two detectors for kaon neutrino events. The 10% energy spread in a typical bin allows this cross calibration to be made to better than 2%. With the energy binning method, the sample of pion neutrino events is reduced by 25% since only those events for which the muon momentum is measured can be included.

It is evident that a combination of the radial binning and energy binning methods can be used to measure the event ratio between the two detectors over the full energy range covered by pion and kaon neutrinos. The systematic errors introduced by the geometrical setup and the detector resolutions are less than 1%. An example of how a theoretical data sample similar to the present one would look with $\Delta m^2 = 380\ eV^2$ and $\sin^2(2\alpha) = 0.2$ after the analysis described above is shown in Fig. 12. A fit to this simulated data yields measurements of $\Delta m^2 = 380 \pm 11\ eV^2$ and $\sin^2(2\alpha) = 0.20 \pm 0.02$. The results of this fit are displayed in Fig. 13. A fit assuming zero mixing yields a confidence level below 10^{-8}.

4. Data Analysis

Neutrino data from 3.4×10^{18} protons on target were recorded at five secondary energies (250, 200, 165, 140, and 100 GeV) from January through June 1982. The total sample of muon trigger events with a momentum analyzed muon included 257,000 events observed in the Lab E detector and 192,000 events in the Wonder Building detector. From these events, a sample is selected that passes severe fiducial and

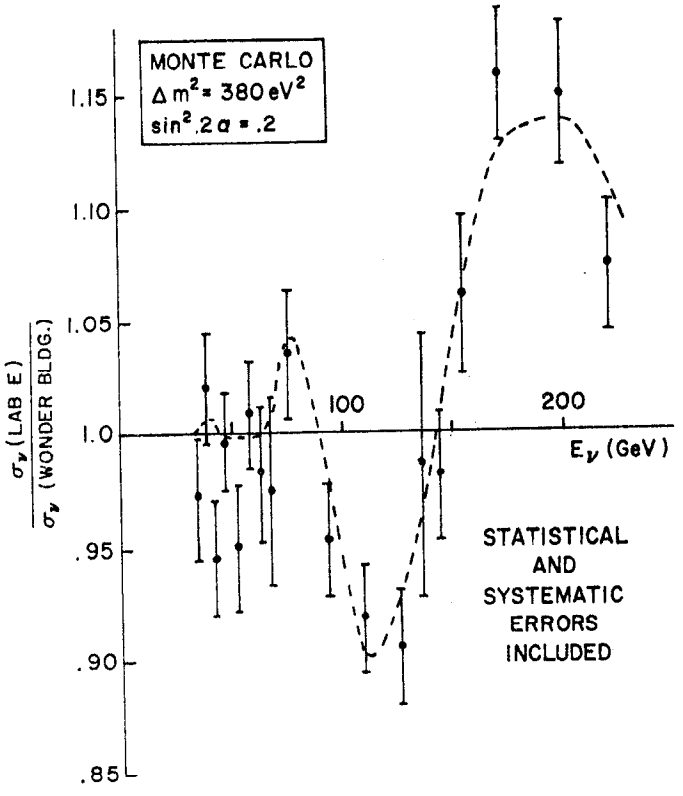


Fig. 12: Monte Carlo "fake" data for the hypothesis $\Delta m^2 = 380\ eV^2$ and $\sin^2(2\alpha) = 0.2$ for a data sample approximately equal to E-701 statistics.

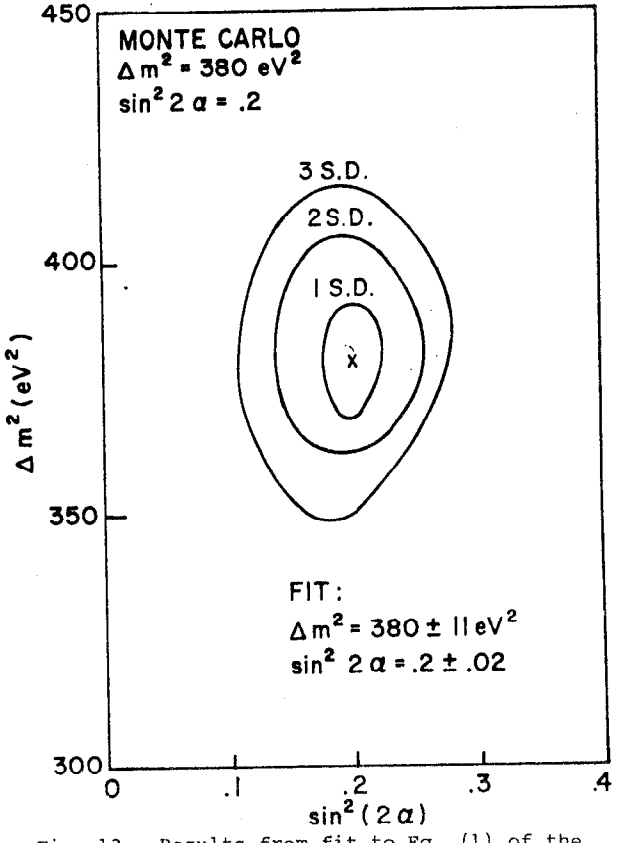


Fig. 13: Results from fit to Eq. (1) of the data in Fig. 12. Contours are 1, 2, and 3 standard deviations.

reconstruction cuts, which ensure that all events occur in regions of good acceptance and small background in the detector in which they were observed and in the region in which they would occur in the other detector. After these cuts, 65,000 events remain in the Lab E sample and 61,000 events remain in the Wonder Building sample. These events constitute the basis for the measurement of neutrino oscillations.

The cuts applied to the data include good secondary beam centering, requiring the event vertex within a 40 in. x 40 in. area in the Wonder Building and the corresponding 62 in. x 62 in. area in Lab E, restricting further the fiducial region in the beam direction to establish definitively a muon track in the target, and requiring all muon tracks to have less than a 150 mrad angle with the incident beam direction, and to be reconstructed with a momentum greater than 7.5 GeV and a χ^2 per degree of freedom less than 5. Moreover, each event is required to pass an additional series of geometrical cuts demanding a reconstruction of the muon track that passes through the trigger counters contributing to a muon trigger and through the steel of the toroids. Finally, each event is projected and scaled to the detector in which it did not occur and is required to pass these same geometrical cuts. This last series of cuts ensures that events used for comparison of rates between the two detectors would, in fact, have been observed in both detectors. This enables rate comparisons independent of any physics assumptions including the physics of the primary interaction, multiple scattering or muon energy loss. Thus the comparison of the flux in the two targets is made unambiguously even though the targets are slightly different. The effect of the small apparatus differences is to reduce slightly the number of events to be used in the comparison.

The analysis of the muon triggers is at present incomplete. Therefore, Fig. 14 shows a calculation of the ratio of events in the Lab E detector to events in the Wonder Building detector vs. neutrino energy without the presence of neutrino oscillations, based on the event statistics. The estimated statistical error of each point is displayed, but its value is set to 1. This figure demonstrates the statistical power of the E-701 data. These data can be translated into the display of the region of sensitivity of this experiment in the mixing angle, α, and mass difference, Δm^2, shown in Fig. 15. This shows good sensitivity for 20 $eV^2 < \Delta m^2 < 800$ eV^2 with $\sin^2(2\alpha)$ as low as 0.05 and always less than 0.15. As previously mentioned, the sensitivity will improve with the inclusion of penetration trigger events. The event sample will increase by 50% at the lowest beam energy settings to 20% at the highest with the inclusion of these triggers.

References

1. This talk is presented on behalf of the CCFR collaboration: P. Auchincloss, C. Haber, M. Ruiz, F. Sciulli, M. Shaevitz, W. Smith, R. Zhu, Columbia; D. Garfinkle, F. Merrit, M. Oreglia, P. Reutens, U of Chicago; R. Coleman, E. Fisk, B. Jin, D. Levinthal, B. Marsh, P. Rapidis, D. Jovanovic, H. White, Fermilab; A. Bodek, F. Borcherding, N. Giokaris, K. Lang, I. Stockdale, U of Rochester.

2. B. Pontecorvo, JETP Sov. Fiz. 53, 1717 (1967); S. Gribov, B. Pontecorvo, Phys. Lett. 28B, 493 (1963); S.M. Bilenky, B. Pontecorvo, Phys. Reports 41, 2251 (1978).

3. M. Shaevitz, in Neutrino-81, Proceedings of the International Conference on Neutrino Physics and Astrophysics, edited by R.J. Cence, E. Ma, A. Roberts (Maui, Hawaii, 1981), p. 311.

4. F. Eisele, Ibid., p. 297.

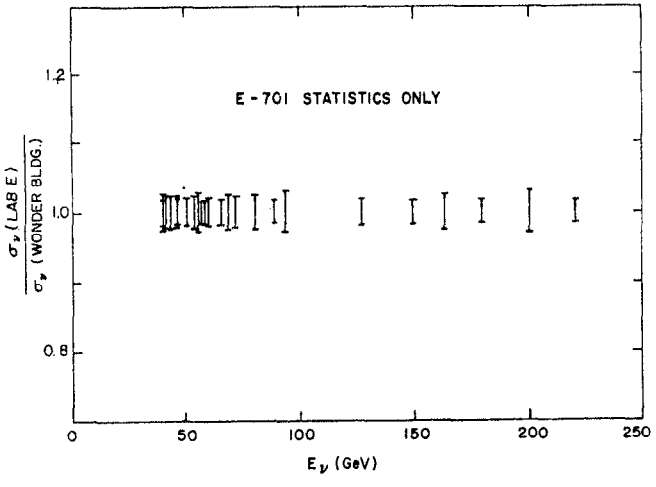


Fig. 14: The ratio of events in the Lab E detector to those in the Wonder Bldg. detector. The true errors are shown, but the values of the points are set to 1. This shows how the data sample would look if there were no oscillations. This demonstrates the statistical power of the data.

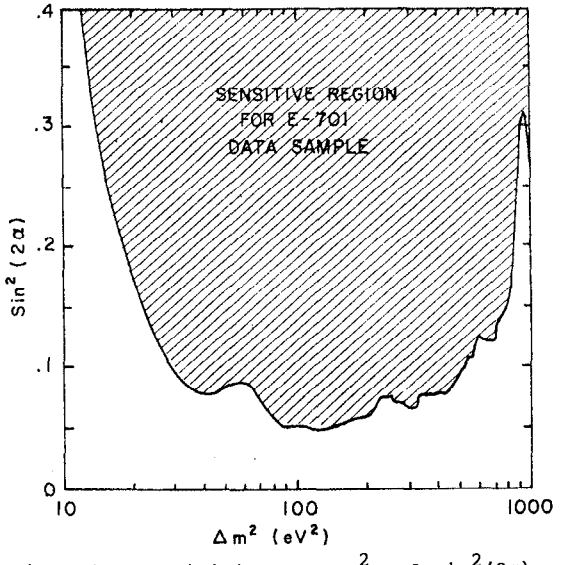


Fig. 15: Sensitivity vs. Δm^2 and $\sin^2(2\alpha)$ for the E-701 data sample.

5. A detailed description of the beam line and its monitoring may be found in P.A. Rapidis in Proceedings of the Summer Institute on Particle Physics, SLAC, 1981, edited by Anne Mosher (SLAC, Stanford, 1982).

This research was supported in part by the National Science Foundation.

RESULTS FROM EXPERIMENT UA1 AT THE CERN $p\bar{p}$ COLLIDER

Aachen-Annecy (LAPP)-Birmingham-CERN-Helsinki-
London (QMC)-Paris (Coll. de France)-Riverside-Rome-Rutherford
Appleton Lab.-Saclay (CEN)-Vienna Collaboration

Presented by
D. DiBitonto
CERN, Geneva, Switzerland

ABSTRACT

Proton-antiproton collisions at $\sqrt{s}$ = 540 GeV are currently being investigated by experiment UA1 at the CERN Collider. Topics presented in this talk include the latest results on multiplicity distributions, inclusive transverse momentum spectra for charged and neutral particles, correlations between high-p_T charged particles, jet studies with preliminary information on yield and the fragmentation function, transverse energy distributions, a search for Centauro-like events, and elastic $p\bar{p}$ scattering.

INTRODUCTION

The UA1 detector[1] is a large solid-angle device with charged-particle tracking and electromagnetic/hadronic separation capability, and has been described elsewhere[2]. Briefly, it consists of a cylindrical Central Detector drift chamber with image read-out (x,y,z), surrounded by barrel and end-cap electromagnetic (e.m.) calorimeters of 26 and 27 radiation lengths thickness, respectively, all of which is located in a dipole magnetic field of 0.7 T. The outer hadron calorimetry is realized by the laminated return yoke of the magnet instrumented with scintillator slabs and is 4.9 and 7.1 absorption lengths thick in the barrel and end-cap regions, respectively. Muon drift chambers complete the apparatus by surrounding the hadron calorimeters on all six sides, as shown in Fig. 1.

© D. DiBitonto 1982

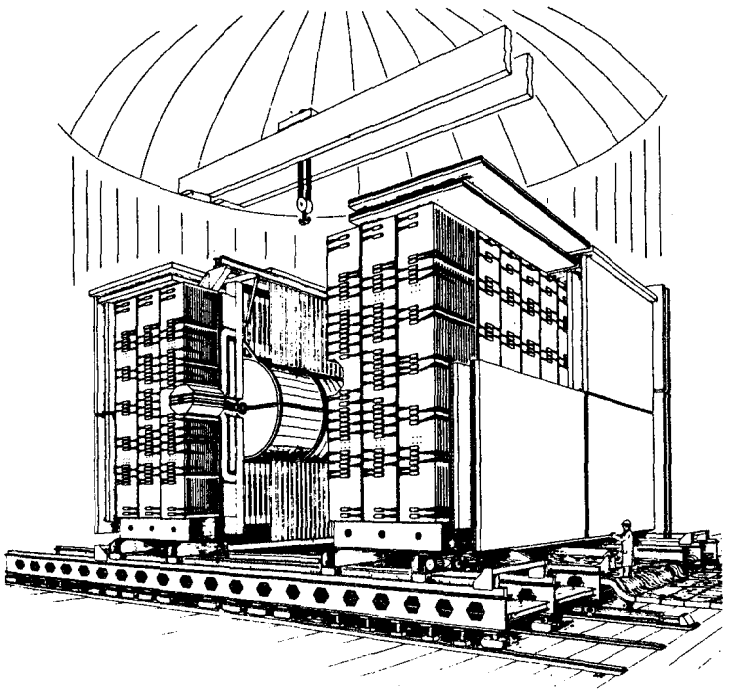
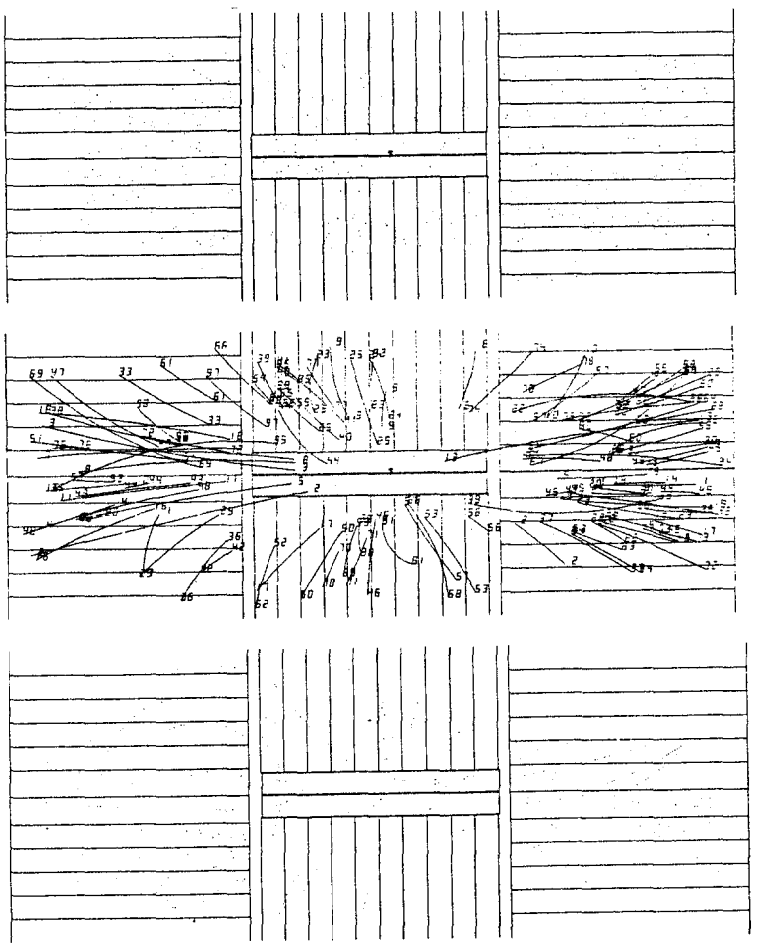


Fig. 1 Schematic view of the UA1 experimental set-up, showing access to the central detector, outer calorimeters, and muon chambers.

All results presented here are confined to the central region $5° < \theta < 175°$ (rapidity interval $|y| \lesssim 3$). The data sample was taken in November and December of 1981 and corresponds to a total integrated luminosity of 180 $(\mu b)^{-1}$. The mean luminosity for these runs was $\sim 3 \times 10^{26}$ cm^{-2} s^{-1}.

All events recorded were obtained from a so-called minimum- or low-bias trigger, defined by the "or" of two hodoscopes, each of which demands at least one charged particle in both sides of the detector. The angular range in θ subtended by these hodoscopes is 12-56 mrad and $\sim$ 56-300 mrad; single diffraction events are therefore specifically excluded by this trigger. The inelastic cross-section for the low-bias trigger corresponds to $\sim$ 40 mb, with an uncertainty dominated by the luminosity (±30%). Examples of a few such events are shown in Fig. 2.



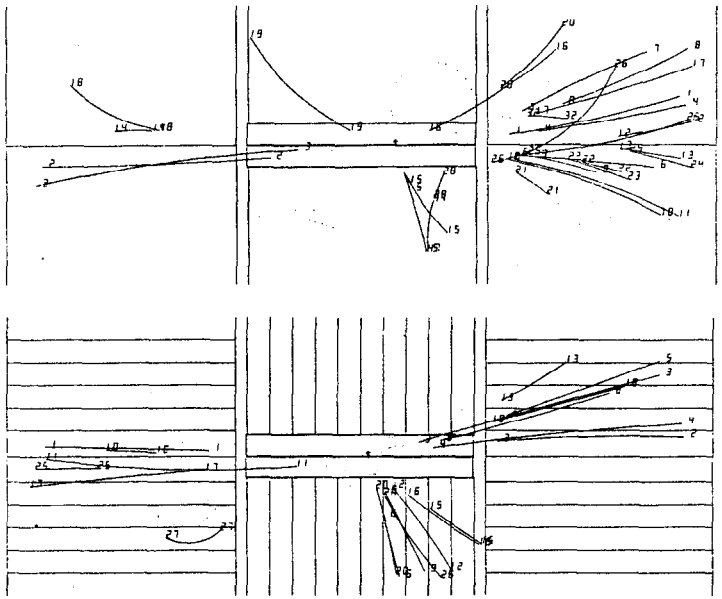


Fig. 2 Sample of events recorded in the central detector image chambers from the data sample presented in this talk

CHARGED-PARTICLE MULTIPLICITY[3]

The data sample here consists of 8000 events recorded in the central detector with zero magnetic field, with a track reconstruction efficiency $\varepsilon \gtrsim 96\%$. Corrections for secondary tracks include γ conversions, with the γ/π ratio taken from UA5, neutral strange particle decays, and nuclear interactions. The acceptance was determined assuming azimuthal Φ symmetry and by Monte Carlo tracks generated and reconstructed by program.

The charged-particle multiplicity distribution is shown in Fig. 3, as a function of the pseudorapidity variable $\eta = \log \tan \theta/2$, and is consistent with a flat distribution in rapidity; the dip at $\eta = 0$ is a result of Jacobian transformation from rapidity to pseudorapidity.

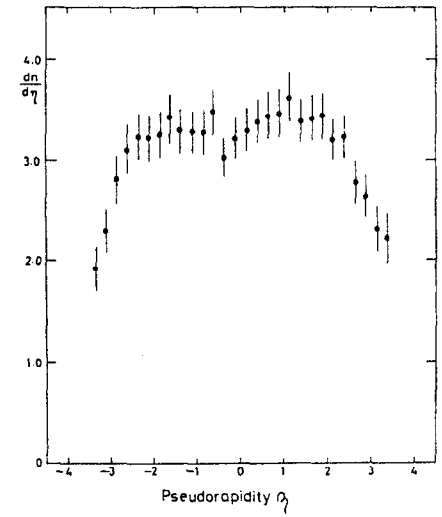


Fig. 3 Pseudorapidity density distribution for all charged multiplicities corrected for acceptance and background

The height of the pseudorapidity plateau at $\eta = 0$ is:

$$\frac{dN}{d\eta} = 3.3 \pm 0.2 \quad (\eta = 0) \qquad (1)$$

to be compared with our previously published value[4] of 3.6 ± 0.3, for which no correction for K^0 and Λ^0 was included. This value at the collider represents an 80% increase from Intersecting Storage Rings (ISR) energies ($\sqrt{s}$ = 63 GeV); the shape of this distribution exhibits a narrowing of the plateau with respect to the ISR, i.e., a wider fragmentation region, since the plateau has increased only 2 units of y out of the 4.6 units available. Preliminary measurements of $dN/d\eta$ at $\langle\eta\rangle = 5.6$ suggest a multiplicity-independent value of $dN/d\eta \to 1.0$ at large η. The pseudorapidity density for various multiplicities is shown in Fig. 4, and compares well in shape to similar distributions measured at the ISR by Thomé et al.[5].

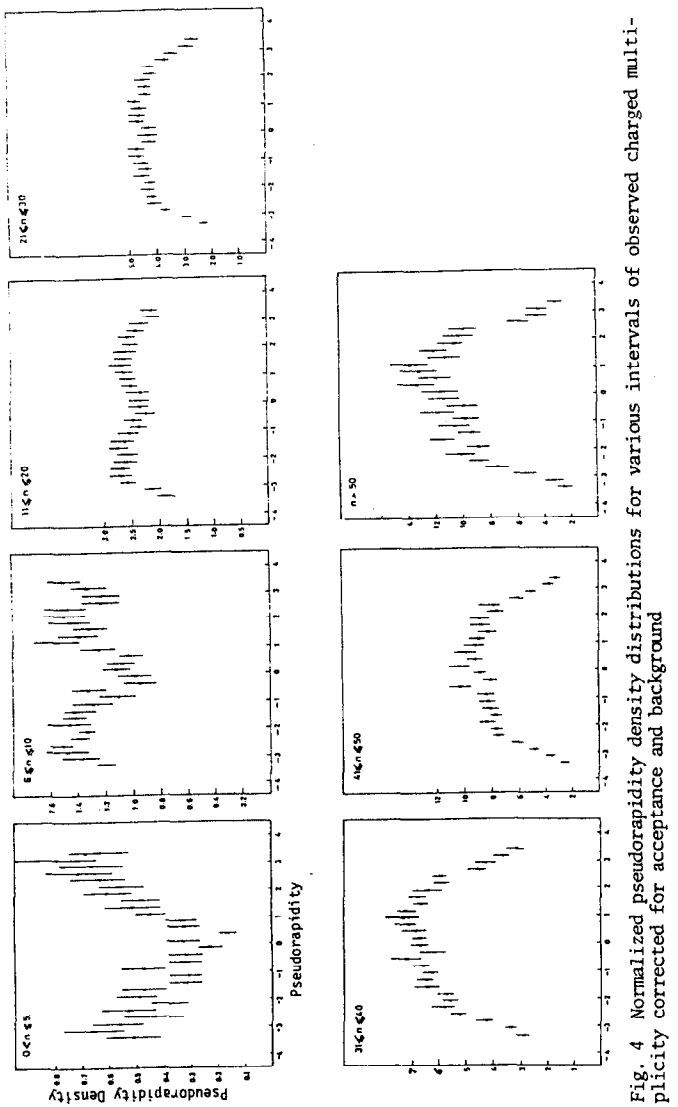


Fig. 4 Normalized pseudorapidity density distributions for various intervals of observed charged multiplicity corrected for acceptance and background

Consider now the same charged-particle multiplicities, but plotted as a function of the KNO variable $z = n^{\pm}/\langle n^{\pm}\rangle$. According to the KNO scaling hypothesis[6], multiplicity distributions assume an energy-independent shape when plotted as a function of z:

$$\text{KNO:} \quad \langle n\rangle P_n \underset{s\to\infty}{\to} \psi\left(\frac{n}{\langle n\rangle}\right) = \psi(z) \ , \qquad (2)$$

where $P_n = \sigma_n/\sigma_{ine}$, is the probability of observing an event with multiplicity n. These distributions are plotted in Fig. 5 for two

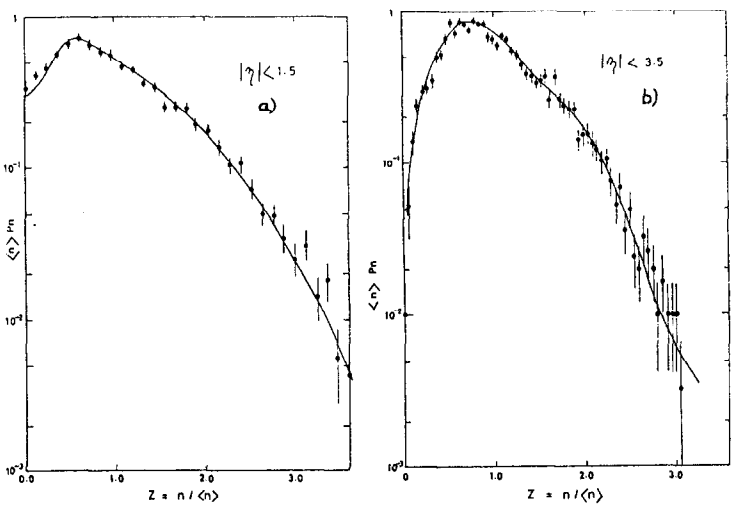


Fig. 5 Observed multiplicity distributions for (a) $|\eta| < 1.5$ and (b) $|\eta| < 3.5$ plotted in KNO variables

rapidity intervals, $|\eta| < 1.5$ and $|\eta| < 3.5$. Note that although the shapes of these distributions are both different for the two intervals, they are nearly the same over the FNAL and ISR energy regions when confined to the same η interval.

In order to compare more conveniently the shapes of these distributions, we define the following moments:

$$\frac{\langle n\rangle}{D} = \frac{\langle n\rangle}{\left[\langle n(n-1)\rangle - \langle n\rangle^2\right]^{\frac{1}{2}}}$$

$$\gamma_2 = \frac{\langle (n-\langle n\rangle)^2\rangle}{\langle n\rangle^2}$$

$$\gamma_3 = \frac{\langle (n-\langle n\rangle)^3\rangle}{\langle n\rangle^3} \qquad (3)$$

$$\gamma_4 = \frac{\langle (n-\langle n\rangle)^4 - 3\langle (n-\langle n\rangle)^2\rangle^2\rangle}{\langle n\rangle^4}$$

These moments are plotted in Fig. 6 over a wide range in $\sqrt{s}$ and show very weak energy dependence, if any, thus supporting the KNO scaling hypothesis over the full η interval.

Various fits to the collider data used for low-energy data are shown in Fig. 7. Shown are a Slattery parametrization[7] from FNAL data, a de Groot formula[8] based on a derivation from an uncorrelated cluster model, and finally a fit by Kaidalov and Ter Martirosyan[9] based on a quark-gluon string Pomeron model specifically not satisfying KNO scaling.

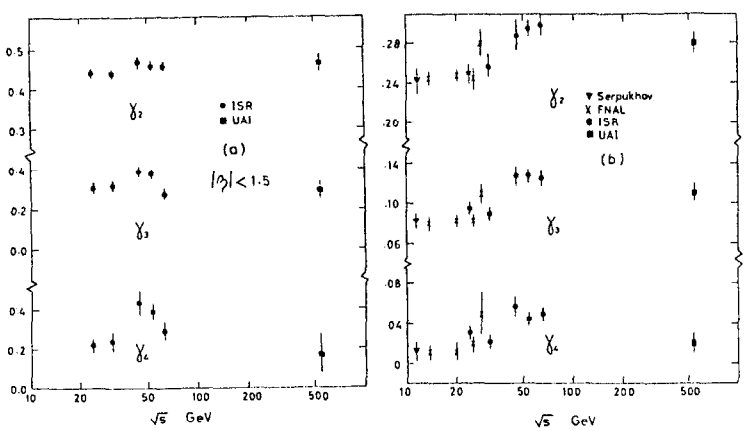


Fig. 6 The moments γ_2, γ_3, and γ_4 as a function of $\sqrt{s}$ for (a) $|\eta| < 1.5$ and (b) all η for all other data, $|\eta| < 3.5$ for this experiment

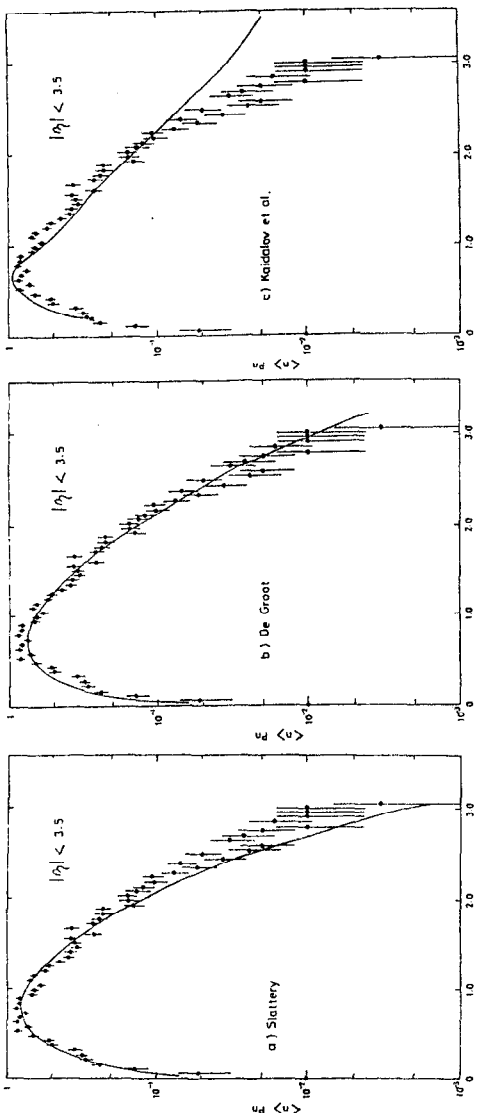


Fig. 7 Comparison of the multiplicity distribution for $|\eta| < 3.5$ with (a) the Slattery parametrization, (b) the de Groot formula, and (c) the calculation of Kaidalov and Ter Martirosyan

INCLUSIVE p_T SPECTRUM FOR CHARGED PARTICLES[10]

The data sample here consists of charged tracks measured in the central detector at 0.56 T and 0.28 T magnetic field, and was taken with a low-bias trigger with hodoscopes located between 12 and 56 mrad of the beams. The total integrated luminosity for these data is $\int L\, dt = (1 \pm 0.25)\ (\mu b)^{-1}$ and is dead-time corrected.

Pattern-recognition and track-reconstruction programs were all checked by physicists scanning the events, and were estimated to be 92 (±2)% over the full detector and 97 (±1)% in three quadrants with the best acceptance. The over-all spatial resolution of the detector was determined to be ∿ 280 μm in the drift direction and ∿ 2.3% of the wire length in the charge division coordinate with a drift angle $\theta = 22.5\ (\pm 0.1)°$. Wire positions were determined by survey during construction and after installation, with an over-all positioning $\sigma \lesssim 0.3$ mm.

Acceptance was determined by Monte Carlo calculation assuming flat physical distributions in Φ and in rapidity. Regions with less than 50% acceptance were excluded from the spectrum and compensated for by geometrical factors, while accepted tracks were weighted according to charge, p_T, y, and Φ. Corrections to the final p_T spectrum include a flattening of the spectrum due to the experimental resolution $\Delta p_T/p_T \simeq 0.02\ p_T$, particle decays (Lorentz boost of secondaries), and bad track reconstruction. All tracks above $p_T = 5$ GeV/c were scanned, with the result that for tracks with transverse momentum between 3 and 5 GeV/c, 3% were considered doubtful, while for $p_T \geq$ ≥ 5 GeV/c, 17 (±7)% of the tracks were considered doubtful.

The invariant cross-section for charged tracks is shown in Fig. 8 in the rapidity interval $|y| < 2.5$ for $0.3 \leq p_T \leq 10$ GeV/c. The total inelastic cross-section used for normalization is estimated to be ∿ 40 mb. Also shown are data from the ISR for nearly the same kinematic interval. In comparison with ISR results, the inclusive p_T cross-section at collider energies has increased by three orders of magnitude at $p_T = 10$ GeV/c, and the spectrum shows considerable flattening at low p_T. The QCD fit to the UA1 data shown is by Odorico[11] and it includes

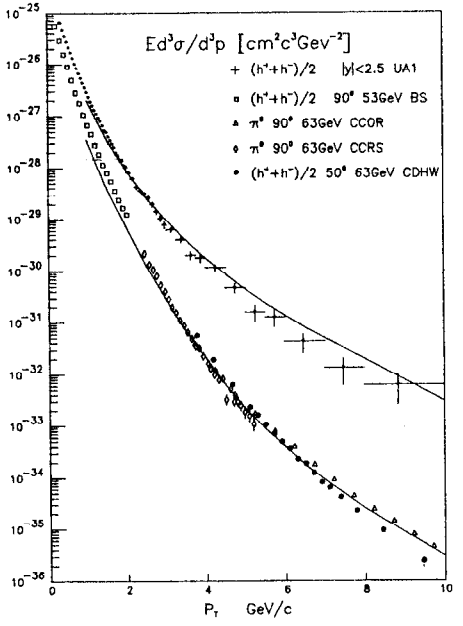


Fig. 8 The invariant cross-sections as a function of transverse momentum for: (a) UA1 data at $\sqrt{s} = 540$ GeV for charged hadrons in the rapidity interval $|y| < 2.5$, (b) ISR data at $\sqrt{s} = 63$ GeV for π^0 at 90° and charged hadrons at 90° and 50°, (c) QCD predictions at $\sqrt{s} = 540$ GeV and $\sqrt{s} = 63$ GeV for π^0 at 90°.

the effects of gluon bremsstrahlung. An empirical parametrization to the data is given by the formula

$$E\frac{d^3\sigma}{d^3p} = A\frac{p_{T_0}^n}{(p_{T_0} + p_T)^n} \qquad (4)$$

where

$$A = 0.46 \pm 0.1\ cm^2\ c^3\ GeV^{-2}$$
$$p_{T_0} = 1.30 \pm 0.18\ GeV/c$$
$$n = 9.14 \pm 0.77\ ,$$

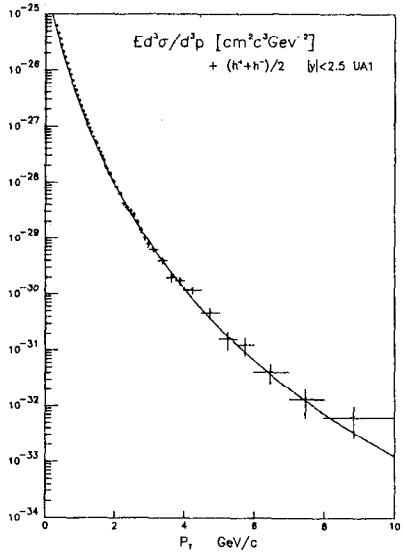


Fig. 9 The invariant cross-sections as a function of transverse momentum for hadrons ($\sqrt{s}$ = 540 GeV) compared with a fitted curve of the form $Ed^3\sigma/d^3p = Ap_{T_0}^n/(p_t + p_{T_0})^n$

and is shown in Fig. 9. Note that the mean p_T at collider energies is now

$$\langle p_T \rangle = 424 \text{ GeV/c} \qquad (5)$$

to be compared with the ISR value of 357 MeV/c.

The same spectrum is shown in Fig. 10 for different multiplicity densities and thus gives evidence for strong correlations between multiplicity dN/dy and p_T. This correlation is most dramatically shown when the mean transverse momentum, as determined from the invariant cross-section, is plotted as a function of the number of charged particles per unit of rapidity, as shown in Fig. 11. The accompanying data from FNAL and ISR suggest that $\langle p_T \rangle$ depends strongly on dN/dy and perhaps less so on $\sqrt{s}$.

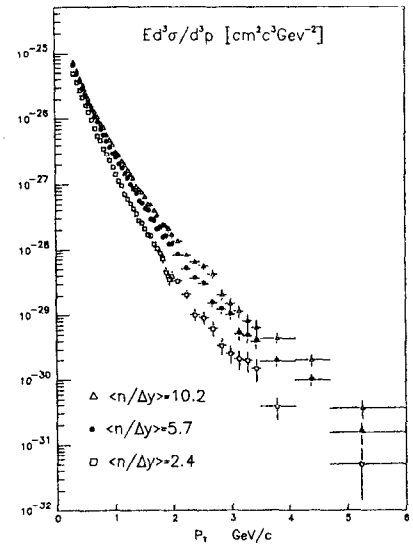


Fig. 10 The invariant cross-sections as a function of transverse momentum for charged hadrons ($\sqrt{s}$ = = 540 GeV) for three bands of charged track multiplicity in the interval $|y| < 2.5$ (normalized to the full cross-section at p_T = 0 GeV/c)

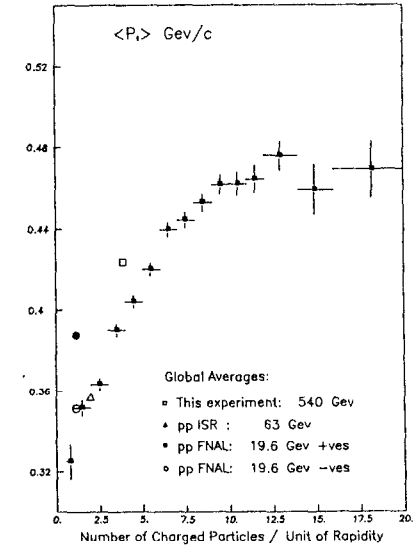


Fig. 11 The mean transverse momentum of charged hadrons ($\sqrt{s}$ = 540 GeV) as a function of charged track multiplicity in the rapidity interval $|y| < 2.5$. (Error bars are purely statistical. Systematic effects from acceptance and fitting procedures could alter the $\langle p_T \rangle$ scale up to 10 MeV/c. Points without error bars give the global average of p_T as a function of the mean number of charged particles per unit of rapidity at FNAL, ISR, and collider energies.)

INCLUSIVE p_T SPECTRUM FOR NEUTRAL ELECTROMAGNETIC PARTICLES[12]

Neutral e.m. showers in this data sample were measured in the end-cap e.m. calorimeters, located in the angular interval $5° < \theta < 25°$ symmetrically about both beams. The trigger requirement was a local deposition of transverse energy in two adjacent azimuthal cells, in addition to the basic low-bias trigger. A total of 5000 events were recorded with $E_T > 4$ GeV and $E_T > 6$ GeV for a total integrated luminosity of 1.95 $(\mu b)^{-1}$ and 5.77 $(\mu b)^{-1}$, respectively.

All 32 azimuthal calorimeter cells were calibrated relative to one another to within ±3% with a 4 Ci ^{60}Co source; the absolute calibration was obtained from the calorimeter response to a test electron beam and the same ^{60}Co source. The absolute energy scale is ±5%, with a resolution in transverse energy of $\sigma E_T/E_T = 12\%/\sqrt{E_T}$.

The event selection requirements were (i) that a primary vertex be reconstructed in the central detector, with no charged track pointing to either triggering cell, (ii) that energy deposition in four

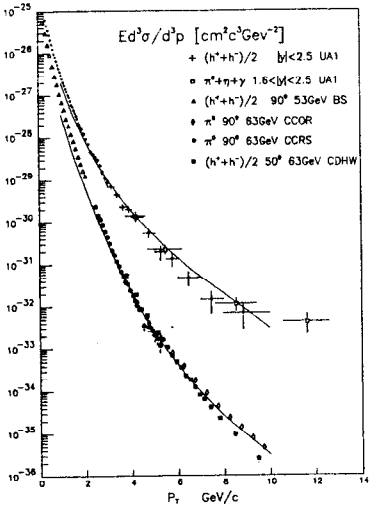


Fig. 12 Single-particle invariant cross-section as a function of p_T measured at the proton-antiproton collider and at the ISR

longitudinal segments of the triggering cells be compatible with an e.m. shower profile and (iii) that there be only one cluster in the accompanying multiwire proportional chamber (MWPC) position detector for two triggering cells with a total charge deposited on the wires compatible with E_T. After these cuts, there remained a total of 77 neutral e.m. showers with $E_T > 3.8$ GeV.

Acceptance was determined by a Monte Carlo calculation assuming a 2/3 π^0 + 1/3 η mixture, with a p_T distribution taken from the charged particle data measured in the central detector. No direct γ's were assumed. Above $p_T \sim 10$ GeV/c the acceptance is ∼ 100% since both γ's merge into one unresolved cluster, and drops to 34% at $\langle p_T \rangle \sim 4$ GeV/c.

The invariant cross-section for neutral e.m. particles is shown in Fig. 12 and agrees well with the charged-particle data as measured in the central detector. The highest p_T event recorded in these data occurs at 12 GeV/c in the forward region $1.6 < |y| < 2.5$.

CORRELATIONS BETWEEN HIGH-p_T CHARGED PARTICLES[13]

The theoretical framework[14] for this topic is parton scattering and subsequent fragmentation. Correlations have indeed been observed at lower ISR energies[15], although the hard scattered parton appearing as a high-p_T particle is usually obscured by the forward-going fragmenting "debris" accompanying the interaction. At the collider, however, this forward fragmentation is very much transformed forward, thus allowing the original hard-scattering processes to stand out more clearly. The relevant kinematic variable here is Feynman x_T, which at collider energies, is quite small (see Fig. 13):

$$x_T = \frac{2p_T}{\sqrt{s}} < 0.04 \ . \qquad (6)$$

The data sample consists of 48,000 low-bias events recorded in the central detector (B = 0.56 T) and another 39,000 events with the additional trigger requirement of at least 30 GeV transverse energy in the electromagnetic and hadronic calorimeters. After a software trigger requirement of $(p_T)_{max} > 4$ GeV in the central detector, 0.5%

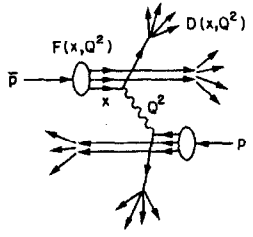


Fig. 13 Hard scattering process in hadron-hadron collisions. Partons located in the incoming nucleons with structure functions $F(x,Q^2)$ are scattered out of the nucleus and subsequently hadronize as jets of particles described by the fragmentation function $D(x,Q^2)$. Remaining partons form very forward going jets.

events remained of the low-bias events, and 2.1% of those events with E_T > 30 GeV. The factor of ∿ × 4 increase in yield from the high E_T data sample is due to the increased track multiplicity (∿ × 2) and yield from the invariant cross-section (∿ × 2.5). As a consistency check, 85% of low-bias events selected with $(p_T)_{max}$ > 4 GeV satisfy E_T > 30 GeV.

In Fig. 14 the rapidity difference between secondaries and a trigger p_T particle greater than 4 GeV/c is shown for secondaries with p_T > 0, 1, and 2 GeV/c in the hemisphere towards the triggering particle, along with the azimuthal angle difference for the same events. Note that the very sharp correlation for p_T secondaries > 2 GeV/c near $\Delta y = 0$ and $\Delta\Phi = 0, 180°$ is absent when a randomly triggering particle is chosen (Fig. 15). The correlations both in rapidity and azimuthal angle are best shown by the scatter plot in Fig. 16 with the same p_T cuts on secondary particles around the triggering particle. The clustering of secondary particles around the high-p_T triggering particle leads naturally to a local increase in multiplicity around the triggering particle, which is demonstrated by the invariant cross-section in Fig. 17 for the triggering cone $|\Delta y| < 0.5$ and $|\Delta\Phi| < 30°$. Finally, the rapidity difference between the highest p_T particle in the opposite hemisphere from the triggering particle and other secondaries in the

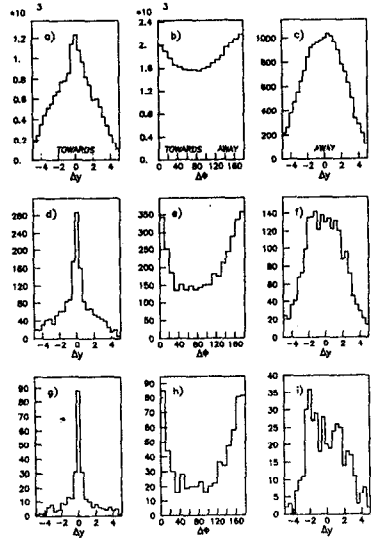


Fig. 14 (a) Rapidity difference between secondaries in the towards hemisphere and the trigger particle of p_T > 4 GeV/c; (b) azimuthal angle difference between all secondaries and the trigger particle of p_T > > 4 GeV/c; (c) rapidity difference between secondaries in the away hemisphere and the trigger particle of p_T > 4 GeV/c; (d) to (f) as for (a) to (c) but for secondaries with p_T > > 1 GeV/c; (g) to (i) as for (a) to (c) but for secondaries with p_T > 2 GeV/c.

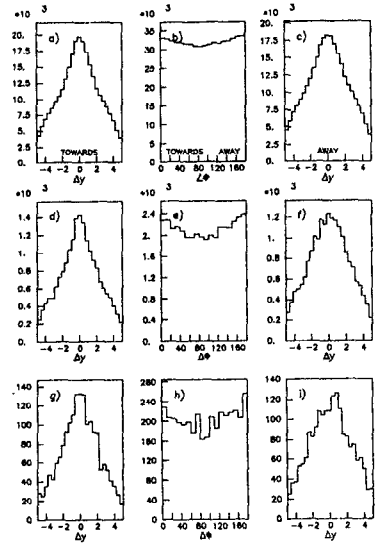


Fig. 15 (a) to (i) Same cuts as in Fig. 14 but for a randomly chosen trigger particle

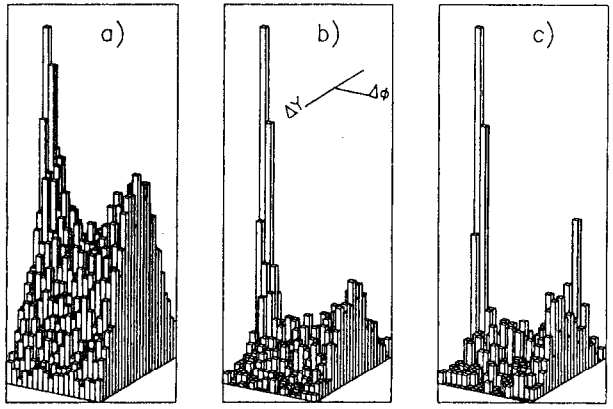


Fig. 16 Correlation between rapidity difference and azimuthal angle difference of secondaries with respect to the trigger particle of p_T > 4 GeV/c; a) for all secondaries; b) for secondaries with p_T > > 1 GeV/c; c) for secondaries with p_T > 2 GeV/c.

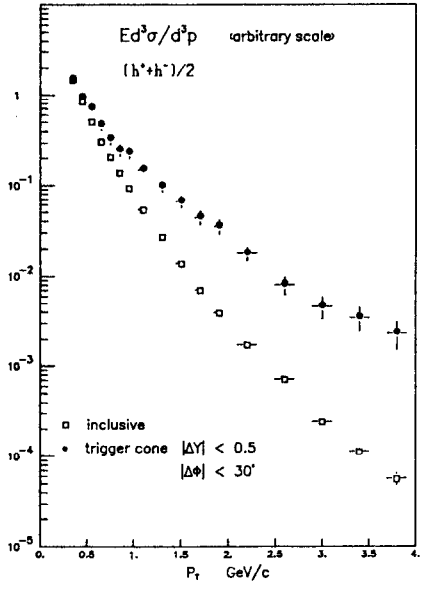


Fig. 17 p_T spectrum of towards secondaries within $\Delta y = \pm 0.5$ and $\Delta\phi = \pm 30°$ of the trigger particle in rapidity and azimuthal angle, compared with the minimum bias inclusive p_T spectrum

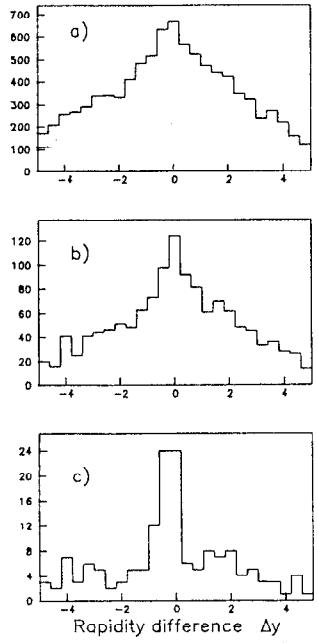


Fig. 18 Rapidity difference between the highest p_T particle in the away hemisphere and other secondaries in the away hemisphere; a) for all such secondaries; b) for secondaries with p_T > 0.8 GeV/c; c) for secondaries with p_T > 1.5 GeV/c.

same opposite hemisphere is shown in Fig. 18. The clustering near $\Delta y = 0$ is evidence for back-to-back scattering of partons within the nucleons.

JET STUDIES

Jets or clusters of particles have been demonstrated by correlations in Δy and $\Delta\Phi$ with respect to a high-p_T track. Another method[16] currently being investigated by our group is to search for clusters with low relative p_T^2. The algorithm begins by first calculating the relative p_T^2 between every pair of tracks, combining pairs with the lowest value of relative p_T into a cluster, and then looking for a *break* in the ordered

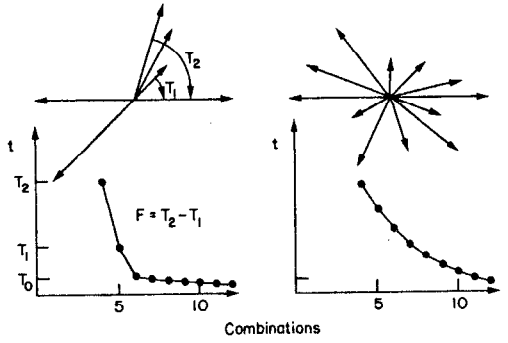


Fig. 19 Ordered p_T^2 distribution of all combinations of pairs of tracks for jet-like events with a local clustering of particles and softer, more isotropic particles

t distribution (see Fig. 19). Three main parameters characterizing the t distribution are the gradient ($F = T_i - T_{i-1}$), threshold T_0, and curvature. One main advantage of this method is topological: one is able to deal with a much larger category of "jetty" events not necessarily having a high-p_T particle, or which may be soft and not at all jet-like as a result of bremsstrahlung effects.

One example of an event found by the algorithm is shown in Fig. 20. The total energy for this event as measured in the calorimeters is 91 GeV, with an invariant mass of $\sim$ 90 GeV/c^2.

To test the algorithm sensitivity to the various parameters defining the gradient, curvature, and threshold, the invariant differential cross-section for clusters found by the algorithm has been measured for various values of the gradient F (Fig. 21). Above 5 GeV/c transverse momentum of the jet cluster, the cross-section converges on values independent of F. For future analysis a cut is made on the jet $p_T > 5$ GeV/c.

Results of the jet studies with this algorithm are summarized in Table I. The mean charged particle multiplicity of the clusters found is $\sim$ 12 tracks, with a mean relative $\langle p_T^2 \rangle$ per track around the cluster axis of $\sim$ 0.24 (GeV/c)^2. The percentage yield of clusters found is a lower limit with respect to the actual number produced, owing to rather

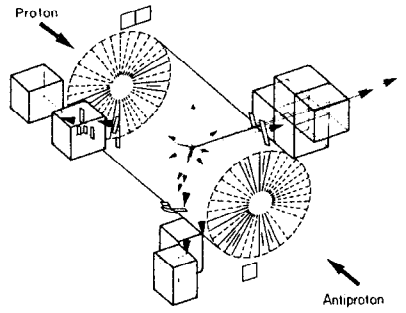


Fig. 20 Three-jet event recorded in the central detector with matching calorimetry. The total energy of this event is 91 GeV, with an invariant mass of 90 GeV/c^2.

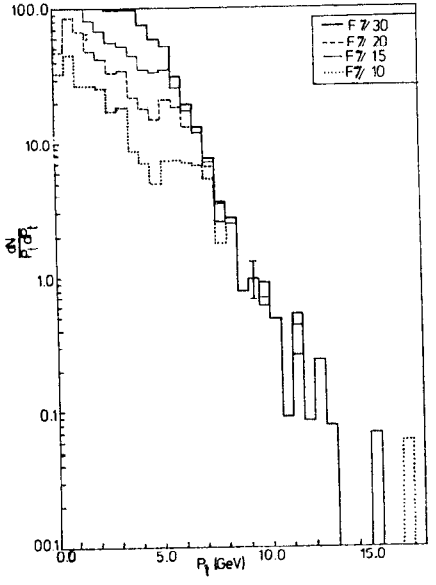


Fig. 21 Inclusive p_T distribution of clusters found by the algorithm described in the text

Table I

Characteristics of clusters found in the central detector

Trigger	Events	% yield[a)]	No.	⟨multiplicity⟩	$\langle p_T^2 \rangle$	Max. p_T of jet
Low bias	10,230	0.75 ± 0.09	77	11.1	0.22	12.8
	44,876	0.97 ± 0.04	433	11.0	0.23	12.8
High E_T (E_T > 30 GeV)	36,303	5.83 ± 0.13	2115	11.5	0.23	22.0
E_T > 60 GeV Δy = 3	560	23.6 ± 2.1	132	12.3	0.25	15.6

a) % yield: percentage of events in which there is at least one jet which has N ≥ 2, $\langle p_T^2 \rangle$ < 0.5, p_T jet ≥ 5 GeV/c, 25° < θ < 155°.

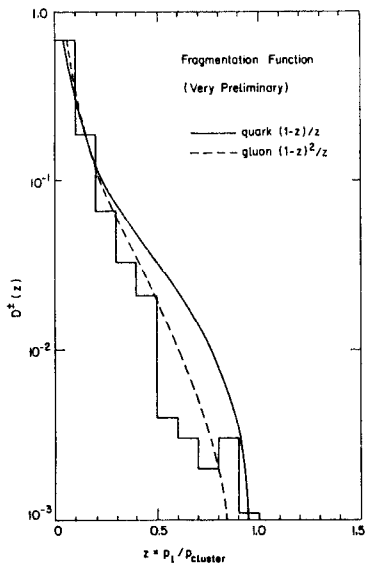


Fig. 22 Fragmentation function D(z), z = p_ℓ/p cluster, for clusters found

restrictive cuts to better enhance the jet signal, although this clearly indicates that as the transverse energy of the event increases, the corresponding jet yield also increases, and at a much higher rate. Preliminary data from the calorimeters (not presented in this talk) show that this yield tends to 100% for $E_T \gtrsim 80$ GeV.

As a first attempt to sort out the nature of the partons involved in the hard-scattering processes leading to jets, a preliminary plot of the fragmentation function of the clusters found is shown in Fig. 22. The phenomenological curves shown are for a parton assumption of both quarks and gluons; the latter spectrum may be expected to be softer with respect to a hard-scattered valence quark. These data favour a predominantly gluon parton component, according to this naïve description, which may be reasonable considering the very low values of x_T we are dealing with.

TRANSVERSE ENERGY DISTRIBUTION IN THE CENTRAL CALORIMETERS[17]

Working outward from the central detector we next encounter the e.m. and hadronic calorimeters, shown in Fig. 23 and summarized in Table II. The resolution, response, and absolute energy scale of these calorimeters was determined in test beams; all of this was monitored during actual data taking by a 4 Ci ^{60}Co source (∿ 184,000 GeV/s) for the e.m. part, and by a β source (where possible), cosmic-ray muons (absolute scale), and a laser system using fibre optics for the hadronic part.

The data sample consists of ∿ 28,000 low-bias events taken with zero magnetic field. After a vertex requirement and timing cuts, there remained ∿ 20,000 beam-beam candidates. The cross-section $d\sigma/dE_T$ as a function of transverse energy E_T is shown in Fig. 24. Note that the bulk of transverse energy seen in the apparatus is nearly uniformly distributed, since the mean transverse energy scales linearly with acceptance cuts in pseudorapidity. When the same data (full acceptance) are plotted as a function of a KNO-like variable $z = E_T/\langle E_T \rangle$, the calorimetry spectrum matches well with the charged-particle multiplicity distribution measured in the central detector (Fig. 25) when the effects of $\langle p_T \rangle$ correlation with multiplicity and smearing are included.

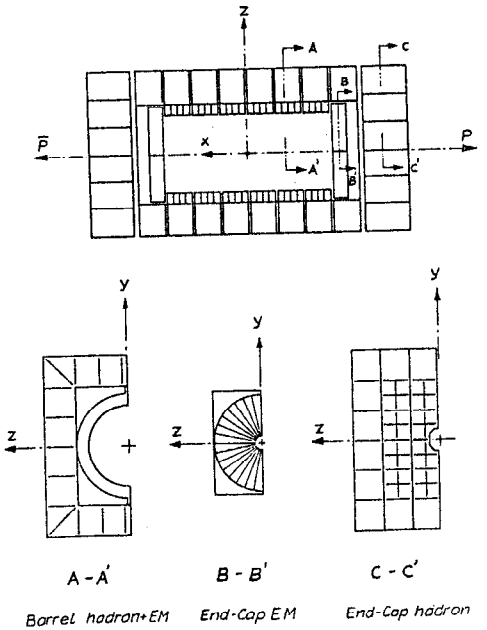


Fig. 23 The UA1 central calorimeters

Table II

Central calorimeter characteristics

Calorimeter	Sampling step	Thickness[a]	Depth segments in read-out[a]	Solid angle coverage	Cell size	Resolution
e.m. barrel	1.2 mm lead 1.5 mm scintillator	26 X_0	3.3:6.6:9.9:6.6 X_0	$25° \leq \theta \leq 155°$ $\phi \sim 2\pi$	$\Delta\theta \sim 5°$ $\Delta\phi \sim \pi$	$0.15/\sqrt{E}$
e.m. end-cap	4.0 mm lead 6.0 mm scintillator	27 X_0	4:7:9:7 X_0	$5° \leq \theta \leq 25°$ $\phi \sim 2\pi$	$\Delta\theta \sim 20°$ $\Delta\phi \sim 11°$	$0.12/\sqrt{E_T}$
Hadron barrel	5 m iron 1 cm scintillator	4.9 X	2.5:2.5 X	$25° \leq \theta \leq 155°$ $\phi \sim 2\pi$		$0.8/\sqrt{E}$
Hadron end-cap	5 m iron 1 cm scintillator	7.1 X	3.5:3.5 X	$5° \leq \theta \leq 25°$ $\phi \sim 2\pi$		$0.8/\sqrt{E}$

a) X_0 = radiation length, X = absorption length.

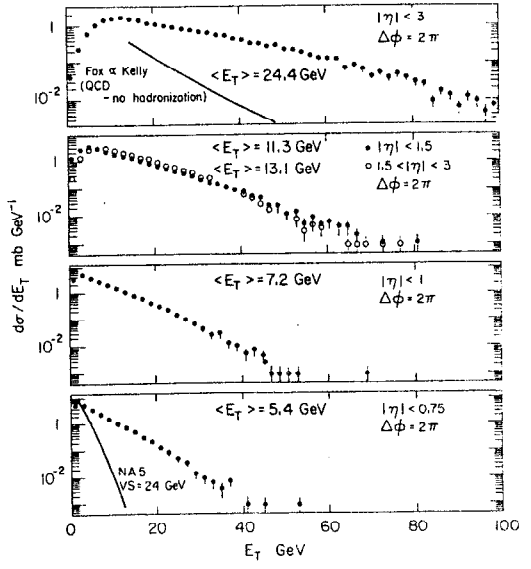


Fig. 24 $d\sigma/dE_T$ spectra for various acceptances as shown on the figures

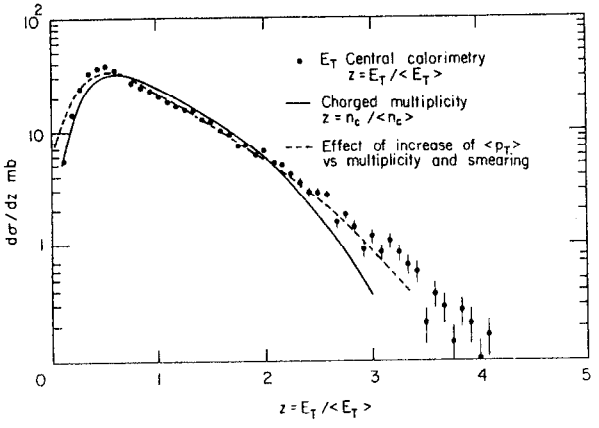


Fig. 25 E_T distribution for $|\eta| \leq 3$ in the KNO-type variable $z = E_T/\langle E_T \rangle$

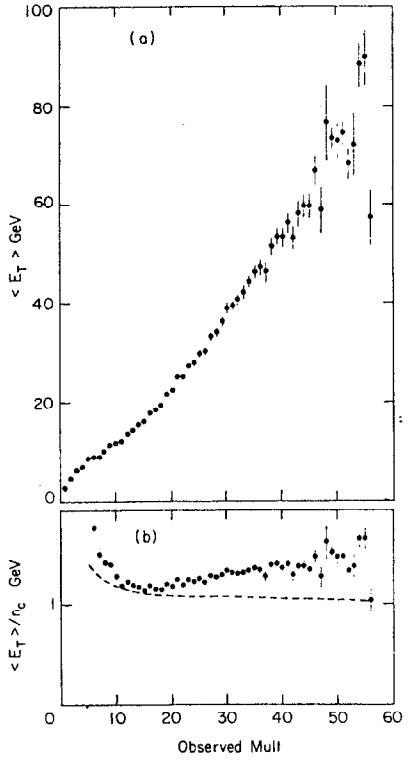


Fig. 26 a) Average E_T versus observed charged multiplicities; b) average E_T per observed charged particle versus the observed multiplicity

The mean transverse energy measured in the calorimeters is plotted as a function of the observed charged particle multiplicity in the central detector in Fig. 26. The strong correlation between $\langle E_T \rangle$ and multiplicity indicates that the bulk of large E_T events are built up of a large number of particles with relatively low E_T, as shown in Fig. 26 where the mean E_T per particle is $\sim$ 1 GeV. The upward trend of these plots reflects the strong correlation between $\langle p_T \rangle$ and multiplicity.

SEARCH FOR CENTAURO-LIKE EVENTS[18]

We close our discussion on calorimetry with a search for events with abnormal e.m. and hadronic behaviour. These so-called Centauro events are six cosmic-ray events reported in the literature[19] with (i) high hadron multiplicity, (ii) e.m. multiplicity consistent with zero and (iii) $\langle p_T \rangle$ per track of at least 1 GeV/c (as measured from 2 events). Correlations between (i) and (iii) are to be expected, based on the strong correlation between $\langle p_T \rangle$ and $\langle n_{ch} \rangle$ which has already been observed by UA1. Point (ii), however, remains an anomaly when considered in terms of conventional isospin conservation in hadronic interactions.

There are problems with energy scale however, in interpreting these cosmic-ray events. The emulsion chambers used in these experiments detect *hadronic* energy via secondary e.m. cascades. The total hadronic energy is therefore proportional to the visible e.m. energy, with a constant of proportionality K_γ^{-1} a function of the incoming particle composition, $K_\gamma \approx 0.2$ for nucleons and ≈ 0.3 for pions. For the typical visible e.m. energies of 330-370 TeV observed, the total energy of the Centauro events (lab. frame) is enormous:

$$E_{tot} = \frac{330 - 370}{K_\gamma} \text{ TeV} \approx 1700 \text{ TeV} \quad (K_\gamma = 0.2 \text{ pions}). \tag{7}$$

This energy should be compared with the equivalent laboratory energy of the collider,

$$(E_{tot})_{\bar{p}p} = 155 \text{ TeV} . \tag{8}$$

Despite the large discrepancy in energy scale, a search for these events at the collider is nonetheless reasonable, given the high luminosity attainable when compared to the very low cosmic-ray rates ($< 1 \text{ m}^{-2} \text{ d}^{-1}$ for $E_{tot} > 100$ TeV).

To see what the signature for Centauro events in the c.m. system would be, the energies and angles of the best measured Centauro event were Lorentz transformed under two different hypotheses[20]: (i) a collision hypothesis in which a fast proton strikes an air nucleon, producing a Centauro which then decays either into mixed hadrons (K_γ = 0.3) or nucleon-antinucleon pairs (K_γ = 0.2) and (ii) a decay hypothesis in which a Centauro is produced from a decaying "fireball" with the kinematic constraint that $\Sigma p_\ell^* = 0$ in the fireball rest frame. In hypothesis (i), most particles are transformed into the forward region of the apparatus, while in the second hypothesis these particles appear more in the central region, since there is no target particle and the Lorentz factors are $\sim \times 10$ larger.

To distinguish between e.m. and hadronic interactions, a photon was defined by energy deposited in the first sample of the e.m. calorimeters ($\sim 4\ X_0$), while hadronic energy was defined by energy deposited in the last two samples of the e.m. calorimeter ($\sim 14\ X_0$) and the ~ 5 absorption lengths of the hadron calorimeters. The second e.m. sample has been excluded, since photons and hadrons both deposit significant energy there. The response of the calorimeters to e.m. and hadronic energy is shown in Fig. 27. Near 0.2 GeV/c this separation is

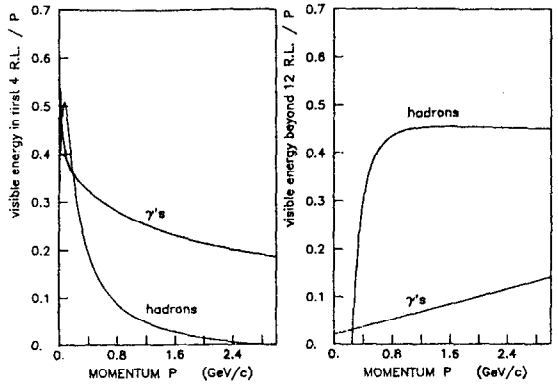


Fig. 27 Calorimeter response to photons and hadrons in the first four radiation lengths/p and beyond 12 radiation lengths/p

poor, although above about 0.3 GeV/c, where the majority of particles are found, the separation is reasonably clear.

A total of 48,000 low-bias events were analysed with the Centauro selection criterion. Scatter plots of the raw uncut e.m. versus hadronic energy are shown in Fig. 28, along with the $\langle p_T \rangle$ as a function of multiplicity for the different angular regions (Fig. 29).

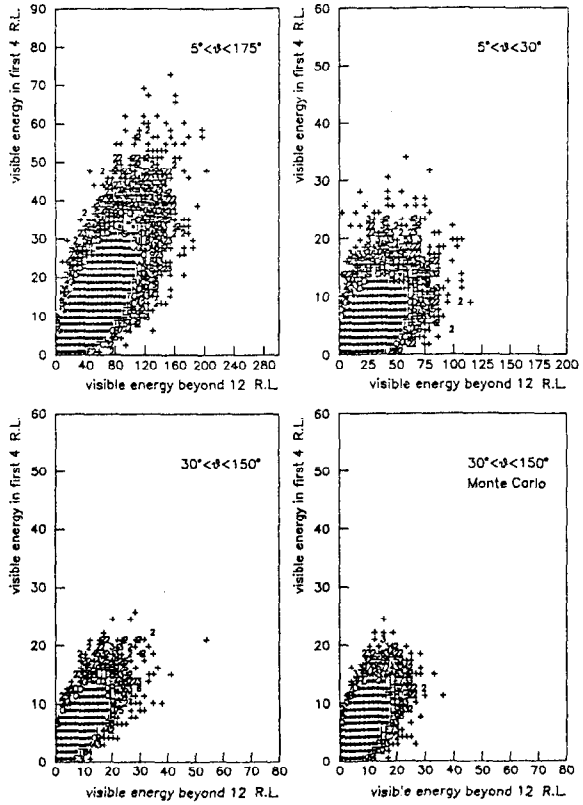


Fig. 28 Visible energy in the first four radiation lengths versus the visible energy beyond 12 radiation lengths in various angular regions of the detector, no cuts applied to the data

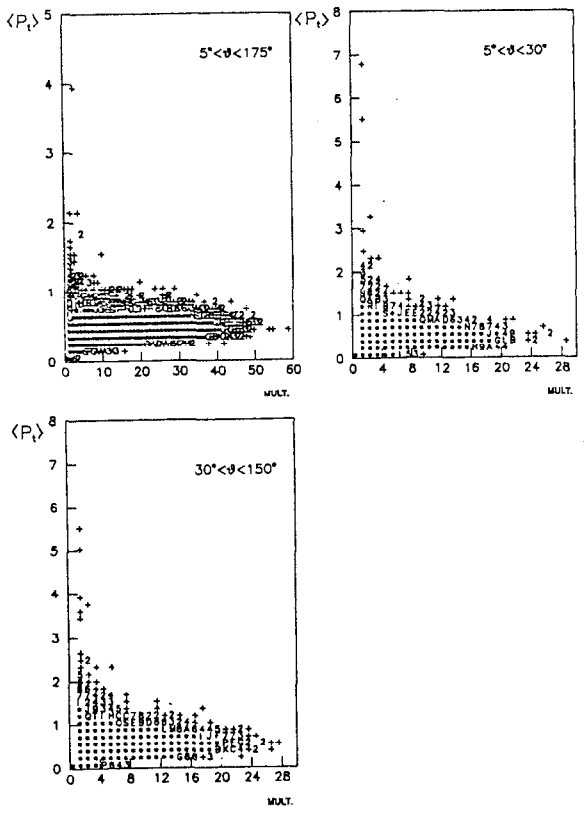


Fig. 29 Mean transverse momentum versus charged-particle multiplicity for all events

The events remaining with $n_{ch} > 10$ tracks and $p_T > 1$ GeV/c are shown in Fig. 30, along with the Lorentz transformed Centauro events for the collision (1 + 2) and decay (3 + 4) hypotheses.

No such anomalous events were seen, setting an upper limit for Centauro production at the collider of

$$\sigma \lesssim 1\ \mu b\ . \qquad (9)$$

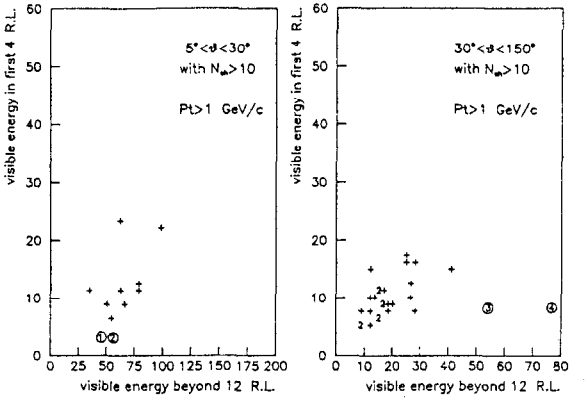


Fig. 30 Visible energy in the first four radiation lengths versus the visible energy beyond 12 radiation lengths, with the additional requirement of at least 11 charged tracks per event with $p_T >$ > 1 GeV/c. Circled numbers refer to transformed Centauro events into the UA1 apparatus as described in the text.

Considerations that one must bear in mind for this negative result are threefold: the analysis assumes that Centauro events are vertex associated (i.e., that they be within $\sim$ 1 mm of the primary vertex), that we have assumed that Centauro events are *not* accompanied by spectator "debris" with normal e.m. behaviour, and perhaps most importantly, the difference in energy threshold between collider and Centauro events.

One possible interpretation of Centauro events may lie in a thermodynamic model. In a sufficiently high energy regime with very high energy density ($dE_T/dy \approx 100$ GeV/unit of rapidity), particle production may follow a thermodynamic behaviour, producing many particles abundantly (e.g.,pions, kaons, nucleons, Λ's, etc.) to the extent that the e.m. component, π^0, is overwhelmed by the accompanying hadronic component.

SMALL-ANGLE ELASTIC SCATTERING[21]

Luminosity monitors located in Roman pots at ±23 m from the main interaction point in UA1 are currently being used to study small-angle elastic scattering. The kinematic range accessible is $0.14 < |t| <$

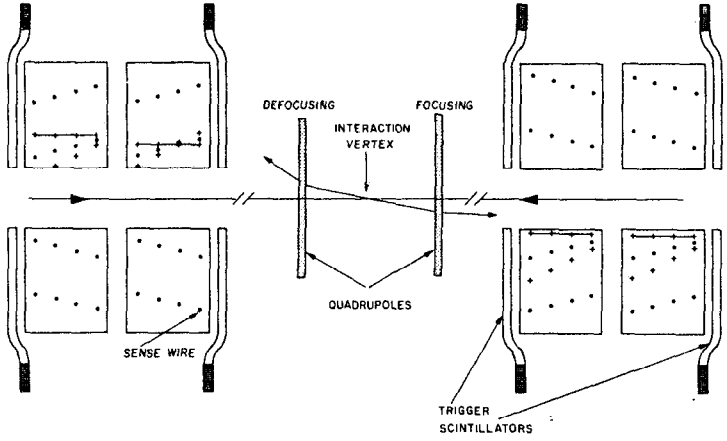
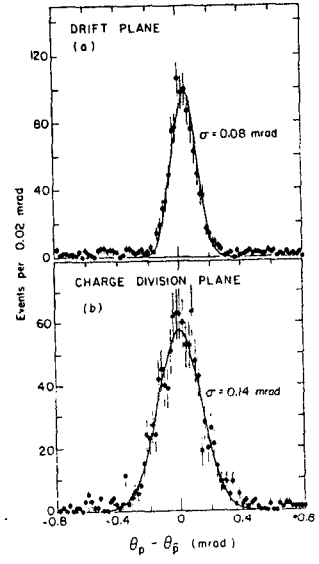


Fig. 31 Arrangements of the 4 drift-chamber telescopes (vertical plane). The elastic-scattering event slows the asymmetry induced by the machine quadrupoles.

< 0.2 GeV^2, corresponding to $1.1 < \theta < 2$ mrad. The experimental set-up is shown in Fig. 31 and consists of drift chambers with drift-time measurement in the vertical coordinate and charge division in the horizontal coordinate.

The data sample consists of 5437 events collected at a mean luminosity of $\sim 10^{26}$ cm^{-2} s^{-1} in a 7.5 h period. From the standard up-down event trigger for elastic candidates, the event topology consisted of $\sim$ 20% clean elastic events, $\sim$ 30% inelastic events and the remaining 50% beam-gas and beam-vacuum events.

The collinearity distributions for both drift plane and charge division plane projections are shown in Fig. 32 for elastic events. The resolution in the drift projection is dominated by the vertical spread of the beams (0.06 mrad) and by the beam angular divergence (0.03 mrad), while the charge division projection error is dominated by the electronics accuracy of $\sim$ 1% ($\Delta z/z$). Elastic event candidates were accepted with $|\theta_p - \theta_{\bar{p}}| < 0.3$ mrad in both projections, and $|\Phi| \equiv \tan^{-1}(\theta_H/\theta_V) < 20°$.



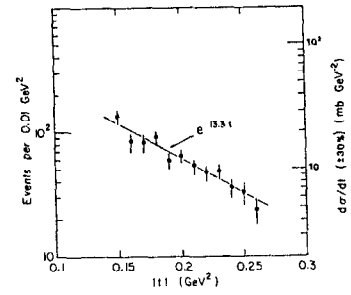


Fig. 32 Collinearity plot on (a) the vertical and (b) horizontal planes for candidate elastic scattering events

Fig. 33 Number of elastic events (545 total) versus $|t|$. The right-hand ordinate shows $d\sigma/dt$ with systematic uncertainty ±30%.

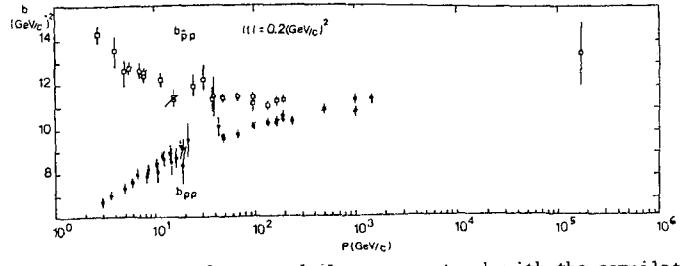


Fig. 34 Comparison of measured slope parameter b with the compilation of Burq et al., for $\langle t \rangle = -0.2$ GeV^2

The differential elastic cross-section $d\sigma/dt$ is shown in Fig. 33. The slope parameter b obtained from a fit $e^{-b|t|}$ is $b = 13.3 \pm 1.5$ GeV^{-2}. The large error in $d\sigma/dt$ (±30%) is due to the uncertainty in the luminosity. A compilation by Burq et al.[22] of the slope parameter for different energies in $p\bar{p}$ and pp elastic scattering is shown in Fig. 34 for the t range near 0.2 GeV^{+2}, and is compatible with a log s^2 dependence of b when extrapolated to the UA1 point.

CONCLUSIONS

- The inclusive charged particle spectrum has been measured up to p_T = 10 GeV/c, $|y| < 2.5$.
- The invariant cross-section rises by $\times 10^3$ from ISR to collider energies at p_T = 10 GeV/c.
- Correlations between p_T and charged multiplicity have been observed.
- $\langle p_T \rangle_{p\bar{p}}$ is compatible with $\langle p_T \rangle_{ISR}$ for the same multiplicity per unit of rapidity.
- The inclusive neutral particle spectrum ($\pi^0 + \eta^0 + \gamma$) has been measured up to 12 GeV/c, $1.6 < |y| < 2.5$.
- We report the first observation of strong correlations between high-p_T charged particles in both y and Φ.
- Coplanar production of two clusters in opposite hemispheres observed suggests hard scattering and fragmentation of partons.
- Preliminary studies on jet production indicate very high yields in events with transverse energy $\gtrsim$ 50 GeV.
- The central pseudorapidity charged particle density is $dN/d\eta|_{\eta=0} = 3.3 \pm 0.2$.
- The shape of $dN/d\eta$ is narrower with respect to an extrapolation from ISR energies.
- The full multiplicity distribution $|\eta| < 3.5$ exhibits KNO scaling, with a departure from KNO for $|\eta| < 1.5$ as observed at the ISR.
- The scaled E_T distribution in $z = E_T/\langle E_T \rangle$ reflects KNO scaling.
- The mean transverse energy per particle increases with charged multiplicity.
- An upper limit of $\sigma < 1$ μb at $\sqrt{s}$ = 540 GeV has been set for Centauro-like events.
- The elastic differential cross-section $d\sigma/dt$ has been measured in the t range $0.14 < |t| < 0.26$ GeV^2 and can be parametrized as $e^{-b|t|}$ with $b = 13.3 \pm 1.5$ GeV^{-2}.

FUTURE PHYSICS

The purpose of this experiment is the observation of the intermediate vector bosons $W^{\pm}$ and Z^0, produced with $\sim$ 2 nb and $\sim$ 1 nb cross-section respectively, in our apparatus. The most direct experimental signature for the W is expected in its leptonic decay mode $W^{\pm} \to \ell^{\pm}\nu$, owing to the enormous Q value given to the leptons from two-body decay. For an 8% leptonic branching ratio for the W, and a 3% branching ratio into e^+e^- for the Z^0, the signals for W and Z^0 are then

$$\begin{aligned} W^{\pm}&: \ \sigma(BR \to e^{\pm}\nu) = 160 \text{ pb} \\ Z^0&: \ \sigma(BR \to e^+e^-) = 30 \text{ pb} \ . \end{aligned} \tag{10}$$

For the forthcoming $p\bar{p}$ runs, the mean luminosity is expected to be $\sim 10^{28}$ cm^{-2} s^{-1}, with a total integrated luminosity for 1982 of $\sim$ 100 (nb)$^{-1}$. This would then correspond roughly to 16 W and 3 Z^0 candidates by the end of this year.

Other high-priority items on the physics agenda include searches for the top quark, Higgs particle, and Wγ events. The large available e.m. energy at the collider of $\sqrt{s}$ = 540 GeV makes searches for the top quark[23] with masses in excess of 18.5 GeV/c^2 (the current upper limit from PETRA) immediately possible. In particular, searches for open top hadron seem promising in the light of possibly quite large diffractive cross-sections for new heavy flavours. Perturbative QCD calculations[24] suggest an m_q^{-2} scaling law, which together with the large charm cross-section observed at the ISR of $\sim$ 1 mb [25] could well produce open top cross-sections of $\sim$ 5(1) μb for m_{top} = 20(50) GeV/c^2. Signals from high-p_T leptons through the semi-leptonic decay of the top quark[26] may well be a way to identify this quark experimentally. Observation of the Higgs particle is a crucial step in further verifying the standard model, although its experimental signature is not yet clear. One may well have to isolate a clean W event sample for this purpose, with an expected cross-section smaller than that of the W. Finally events in which a W is accompanied by a photon provide an important test of the gauge nature of the electroweak theory[27], although here, the expected cross-section for this reaction is < 1 pb.

Acknowledgements

This work was made possible by the organizers of the SLAC Summer Institute, and I wish to thank them for their very generous support and hospitality during my stay there. This experiment and its impressive results are due to the combined effort of many people, and I warmly thank my colleagues of UA1 for giving me this opportunity to speak on their behalf.

REFERENCES

1) Aachen-Annecy (LAPP)-Birmingham-CERN-London (QMC)-Paris (Collège de France)-Riverside-Rutherford-Saclay (CEN)-Vienna Collaboration, A 4π solid-angle detector for the SPS used as a proton-antiproton collider at a centre-of-mass energy of 540 GeV. Proposal CERN/SPSC/78-06/P92 (1978).
M. Barranco Luque et al., Nucl. Instrum. Methods 176, 175 (1980).
M. Calvetti et al., Nucl. Instrum. Methods 176, 255 (1980).
K. Eggert et al., Nucl. Instrum. Methods 176, 217 and 223 (1980).
A. Astbury, Phys. Scr. 23, 397 (1981).

2) M. Calvetti, The UA1 central detector, Talk given at the Int. Conf. on Instrumentation for Colliding Beam Physics, SLAC, Stanford, 17-23 February 1982, CERN-EP/82-44.
S. Cittolin, The UA1 data acquisition system, Talk given at the Int. Conf. on Instrumentation for Colliding Beam Physics, SLAC, Stanford, 17-23 February 1982.
UA1 Collaboration, First results from the UA1 detector at the SPS Collider, presented by B. Sadoulet at the 17th Rencontre de Moriond, Les Arcs, 20-26 March 1982.
UA1 Collaboration, The CERN proton-antiproton collider programme, presented by P.I.P. Kalmus at the Int. Workshop on Very High Energy Interactions in Cosmic Rays, University of Pennsylvania, 22-24 April 1982, CERN-EP/82-58.

3) G. Arnison et al., Charged particle multiplicity distributions in proton-antiproton collisions at 540 GeV centre-of-mass-energy, presented by M. Corden at the 21st Int. Conf. on High Energy Physics, Paris, 26-31 July 1982, CERN-EP/82-134.

4) G. Arnison et al., Phys. Lett. 107B, 320 (1981).

5) W. Thomé et al., Nucl. Phys. B129, 365 (1977).

6) Z. Koba, H.B. Nielsen and P. Olesen, Nucl. Phys. B40, 317 (1972).

7) P. Slattery, Phys. Rev. Lett. 29, 1624 (1972).

8) E.H. de Groot, Phys. Lett. 57B, 159 (1975).

9) A.B. Kaidalov and K.A. Ter Martirosyan, ITEP-51 (1982).

10) G. Arnison et al., Transverse momentum spectrum for charged particles of the CERN proton antiproton collider, presented by A. Norton at the 21st Int. Conf. on High Energy Physics, Paris, 26-31 July 1982, CERN-EP/82-125, submitted for publication in Phys. Lett.

11) R. Odorico et al., Does a transverse energy trigger actually trigger on large p_T jets?, presented by R. Odorico at the 21st Int. Conf. on High Energy Physics, Paris, 26-31 July 1982.

12) G. Arnison et al., Inclusive p_T spectrum for neutral electromagnetic particles, presented by A. Norton at the 21st Int. Conf. on High Energy Physics, Paris, 26-31 July 1982, CERN-EP/82-120.

13) G. Arnison et al., First observation of correlations between high transverse momentum charged particles in events from the CERN proton antiproton collider, presented by A. Norton at the 21st Int. Conf. on High Energy Physics, Paris 26-31 July 1982, CERN-EP/82-124, submitted for publication in Phys. Lett.

14) R.P. Feynman, Phys. Rev. Lett. 23, 1415 (1969).
R.P. Feynman, Photon-hadron interactions (W.A. Benjamin, NY, 1972).
J.D. Bjorken, Phys. Rev. 179, 1547 (1969).
J.D. Bjorken and E.A. Paschos, Phys. Rev. 185, 1975 (1969).

15) P. Darriulat et al., Nucl. Phys. B107, 429 (1976).
A.G. Clark et al., Nucl. Phys. B160, 397 (1979).
CERN-Dortmund-Heidelberg-Warsaw Collaboration, Study of deep inelastic proton-proton interactions at the ISR, presented by P. Hanke at the 17th Rencontre de Moriond, Les Arcs, 20-26 March 1982.
W. Geist, talk at this conference.
R. Schindler, talk at this conference.

16) G. Thompson, Jet search in the central detector, Report presented at the UA1 Workshop on Physics Analysis, Vienna, 1-3 July 1982, EP/UA1/Pub#/M 82-24.

17) G. Arnison et al., Transverse energy distributions in the central calorimeters, presented by M. Corden at the 21st Int. Conf. on High Energy Physics, Paris, 26-31 July 1982, CERN-EP/82-122.

18) G. Arnison et al., Search for Centauro-like events at the CERN proton antiproton collider, presented by M. Spiro at the 21st Int. Conf. on High Energy Physics, Paris, 26-31 July 1982, CERN-EP/82-121.

19) C.M.G. Lattes et al., Phys. Rep. 65, No. 3 (1980).

20) R. Kinnunen and C. Rubbia, Proc. 17th Int. Cosmic Ray Conference, Paris, 1981 (CEA, Saclay, 1981), Vol. 11.

21) G. Arnison et al., Small angle elastic scattering at the CERN proton antiproton collider, presented by A. Astbury at the 21st Int. Conf. on High Energy Physics, Paris, 26-31 July 1982, CERN-EP/82-123.

22) J.P. Burq et al., Phys. Lett. 109B, 124 (1982).

23) D.M. Scott, Proc. 2nd Topical Conf. on Forward Collider Physics, Madison (1981) (eds. V. Barger, D. Cline and F. Halzen) (Amer. Inst. Phys., New York, 1981), p. 151.

24) S.J. Brodsky et al., SLAC PUB 2660 (1981).

25) D. DiBitonto, Proc. 2nd Topical Conf. on Forward Collider Physics, Madison (1981) (eds. V. Barger, D. Cline and F. Halzen) (Amer. Inst. Phys., New York, 1981), p. 26.

26) D. DiBitonto, CERN-EP/82-22 (1982).

27) R.W. Brown, Proc. 2nd Topical Conf. on Forward Collider Physics, Madison (1981) (eds. V. Barger, D. Cline and F. Halzen) (Amer. Inst. Phys., New York, 1981), p. 251.

RESULTS FROM THE UA2 EXPERIMENT AT THE CERN SPS COLLIDER

Presented by : T. Himel
CERN, Geneva

The UA2 Collaboration
(Univ. Bern, CERN, NBI Copenhagen, LAL Orsay,
Univ. and INFN Pavia, CEN Saclay)

ABSTRACT

We present results on inclusive cross section of π^0, π^+ and π^- production and particle ratios K/π, $p+\bar{p}/\pi$. A simple search for quarks has shown no positive results.

High total transverse energy final states have been observed and show clear evidence for high energy jets.

INTRODUCTION

The CERN SPS $\bar{p}p$ collider, with a $\sqrt{s}$ = 540 GeV, opened a new area of physics with its first run in the fall of 1981. The UA2 Experiment has a well segmented large solid angle total absorption calorimeter and a charged particle spectrometer. Results obtained range from the production of identified charged particles in the central region of relatively low transverse momentum ($\sim$ 1 GeV/c) and high cross section, to the production of high transverse momentum ($\sim$ 50 GeV/c) hadronic jets with a much lower cross section ($\sim$ nb).

© T. Himel 1982

APPARATUS

A cross section of the UA2 detector is shown in Figure 1. At the center of the apparatus a vertex detector consisting of cylindrical proportional and drift chambers measures particle trajectories in a region without magnetic field. For the results presented here it will be used to separate events due to $\bar{p}p$ collisions from background and to determine the interaction point with a precision of ±1 mm along the beam line.

The vertex detector is surrounded by a highly segmented electromagnetic and hadronic calorimeter (the central calorimeter) which covers the pseudorapidity interval $-1 < \eta < 1$ (polar angle $40^\circ < \theta < 140^\circ$) and an azimuthal range of 300°. In the present stage of the experiment the remaining azimuth ($\pm 14^\circ$ around the horizontal plane) is covered by a single arm spectrometer to measure charged and neutral particle production ($|\eta| < 0.85$).

The forward and backward regions ($20^\circ < \theta < 37.5^\circ$ and $142.5^\circ < \theta < 160^\circ$, respectively), are each instrumented by twelve toroidal magnet sectors followed by drift chambers, multitube proportional chambers and electromagnetic calorimeters.

The single arm spectrometer (Fig. 2) has a magnetic field integral of 1.1 T.m. Charged particle trajectories are measured in a set of 12 drift chamber planes. This information, together with a measurement of the interaction point, allows the momentum to be measured with a resolution of $\Delta p/p = \sqrt{(0.5)^2 + (0.5p)^2}$ % (p in GeV/c). Time-of-flight information comes from hodoscopes behind the drift chambers. It is used together with the interaction time to measure the TOF over 2.5 m with a resolution of 0.48 ns.

The spectrometer is also used to measure π^0, η^0 and γ production by measuring photon energy and position. The TOF hodoscope is part of a scintillator-iron-scintillator sandwich that is also used for photon identification. The counters after the 2 cm thick iron plate act as a preshower counter for a lead-glass wall. The wall contains 2 arrays of lead-glass blocks, each having a cross section of 15 × 15 cm^2, and a depth of 14.5 radiation lengths. The two arrays are

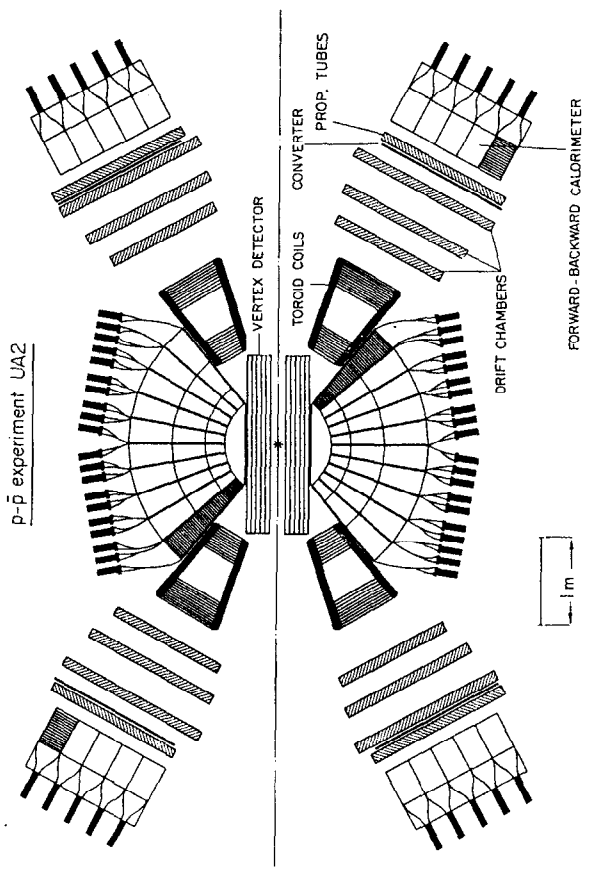


Fig. 1
Cross section of the UA2 detector.

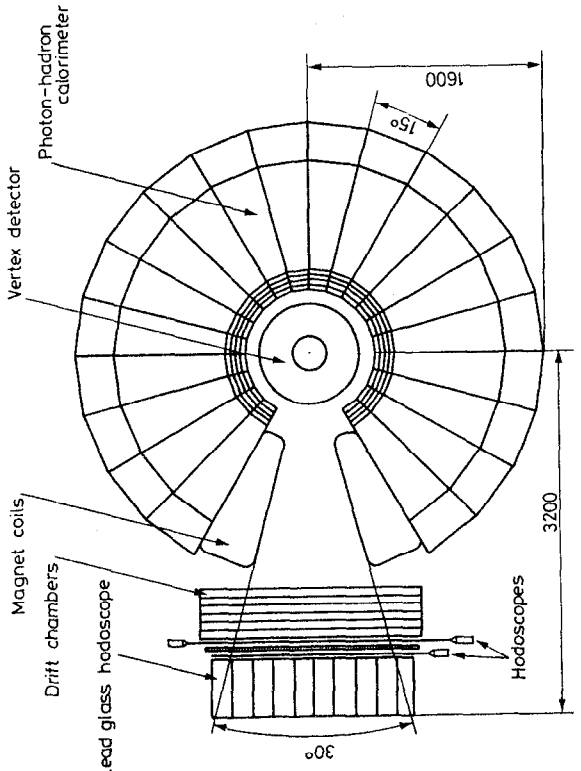


Fig. 2
End view of the UA2 detector.

separated by 30 cm in about the middle where a dE/dx counter has been installed. The energy resolution of the lead-glass wall has been measured to be $\sigma_E/E = (11.6 + 32.5/E)^{\frac{1}{2}}$ % (E in GeV). Each block has been calibrated using 10 GeV electrons, and is monitored with a Xe light flasher system. The calibration remained stable to within ±2% during the $\bar{p}p$ running period.

The dE/dx counter mentioned above is used to search for fractionally charged particles (quarks). It consists of 5 scintillator plates. Each plate is 4 cm thick and is viewed by two 5" PM's whose light guides are covered by additional scintillators used as veto counters. This dE/dx counter has also been calibrated at the CERN PS, and its response to minimum ionizing particles (MIP) has been studied as a function of the impact point.

The central calorimeter is segmented into 200 cells, each covering 15° in ϕ and 10° in θ and built in a tower structure pointing to the centre of the interaction region. The cells are segmented longitudinally into a 17 radiation length thick electromagnetic compartment (lead-scintillator) followed by two hadronic compartments (iron-scintillator) of two absorption lengths each giving a total of 4.5 absorption lengths. The light from each compartment is collected by two BBQ-doped light guide plates on opposite sides of the cell.

All calorimeters, including the forward-backward modules, have been calibrated in a 10 GeV/c beam from the CERN PS using incident electrons and muons. The calibration has since been tracked with a Xe light flasher system. In addition, the response of the electromagnetic compartments is checked regularly by accurately positioning a Co^{60} source in front of each cell and measuring the direct current from each photomultiplier. The systematic uncertainty in the energy calibration for the data discussed here is less than ±2% for the electromagnetic calorimeter and less than ±3% for the hadronic one.

The response of the calorimeter to electrons, single hadrons and multi-hadrons (produced in a target located in front of the calorimeter) has been measured at the CERN PS and SPS machines using beams from 1 to 70 GeV. In particular, we have studied the longitudinal and transverse shower development and the effect of particles

impinging near the cell boundaries.

The energy resolution for electrons is measured to be $\sigma_E/E = 0.14/\sqrt{E}$ (E in GeV). In the case of hadrons, σ_E/E varies from 32% at 1 GeV to 11% at 70 GeV. The resolution for multi-hadron systems of more than 20 GeV is similar to that of single hadrons.

Two scintillator arrays, with a total of 24 counters, surround the beam pipe at ±10.3 m from the interaction point. These counter arrays cover 1.1 units of rapidity around $\eta = \pm 4.7$. A coincidence of a signal from each side is required in the trigger, for the data presented in this talk, to suppress backgrounds from non beam-beam collisions. The same counters are used to evaluate the integrated luminosity for the cross section normalization.

The total integrated luminosity for which we present results is 79 μb^{-1}, calculated under the assumption that the non-diffractive $\bar{p}p$ cross section at $\sqrt{s} = 540$ GeV is 38 mb. The systematic error in the luminosity measurement has been estimated to be ±17%.

RESULTS FROM THE SINGLE ARM SPECTROMETER

π^0 inclusive cross-section[1]

The photons emitted in the acceptance of the large angle magnetic spectometer are observed in the lead-glass array. The energy deposited in the lead-glass cells is reduced to clusters, two photons can be resolved into separated clusters provided their separation exceeds ∿ 25 cm. From the energy and the centroid position of the clusters a two-photon mass is calculated. This mass spectrum is shown in Fig. 3. A clear π^0 peak appears over a combinatorial background of 20 to 30% depending on the transverse momentum. A signal due to the $\eta \to 2\gamma$ decay is observed when stricter cuts better suited to this decay mode are applied to the data. This is shown in the inset of Fig. 3. The amount of observed η is compatible with the ratio η/π^0 of 0.55 observed at the ISR.

From the π^0 signal we extract the inclusive cross section from 1.5 to 4.5 GeV/c transverse momentum averaged over ±0.7 units of

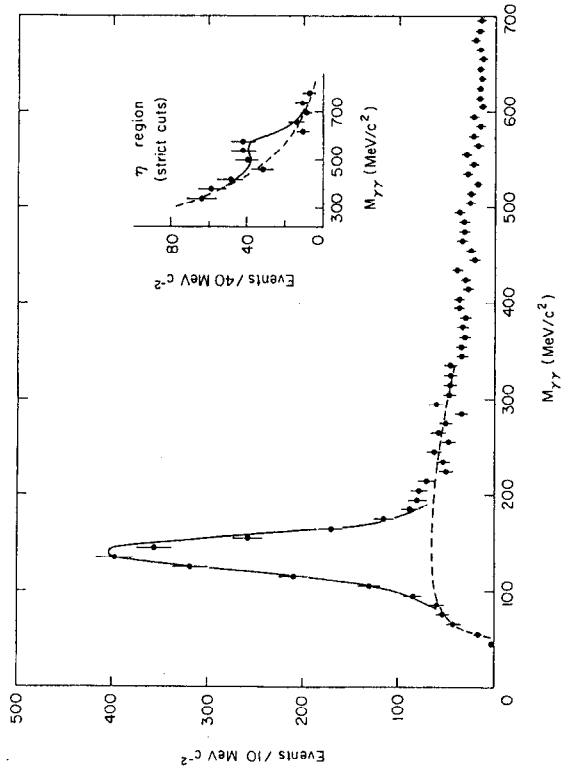


Fig. 3
Invariant mass distributions for two-photons sample.

rapidity. It is shown in Fig. 4. The solid line shows the π^0 cross-section measured at the ISR at $\sqrt{s}$ = 53 GeV. The dashed line shows the ISR data extrapolated to $\sqrt{s}$ = 540 GeV with p_T^{-n} $(1 - X_T)^q$. At high transverse momentum we observe a large increase of the π^0 cross-section when the energy rises from 53 to 540 GeV.

π^+ and π^- inclusive cross-section[2]

The charged particle spectrum is obtained by measuring the momentum of charged tracks in the magnetic spectrometer. From the time of flight measurement pions are separated from kaons up to 1.1 GeV/c and protons from pions and kaons up to 1.4 GeV/c transverse momentum.

The measured π^+ and π^- cross sections are consistent and the average value of the two is displayed in Fig. 5 for a rapidity range of ±0.7 units.

In Fig. 6 we present a fit to the $(\pi^+ + \pi^-)/2$ and π^0 cross section of the empirical form

$$E\, d^3\sigma/dp^3 \propto 1/(1 + p_T)^n$$

giving $n = 8.3 \pm 0.2$.

K/π and $p,\bar{p}/\pi$ particle ratios[2]

The charged particle identification gives the possibility to measure separately the charged kaon spectrum from 0.4 to 1 GeV/c transverse momentum and the proton-antiproton spectrum form 0.4 to 1.8 GeV/c.

Cross-sections for particle production are found to be equal to those for the corresponding antiparticle and their average values are compared to the pion cross-section : the result is shown in Fig. 7 for K/π and $p(\bar{p})/\pi$ as a function of the transverse mass $M_T = \sqrt{M^2 + p_T^2}$.

The average value for K/π is 0.39 ± 0.04 to be compared to 0.23 at ISR energies. The average value for p/π is 1.02 ± 0.07 similar to ISR energies.

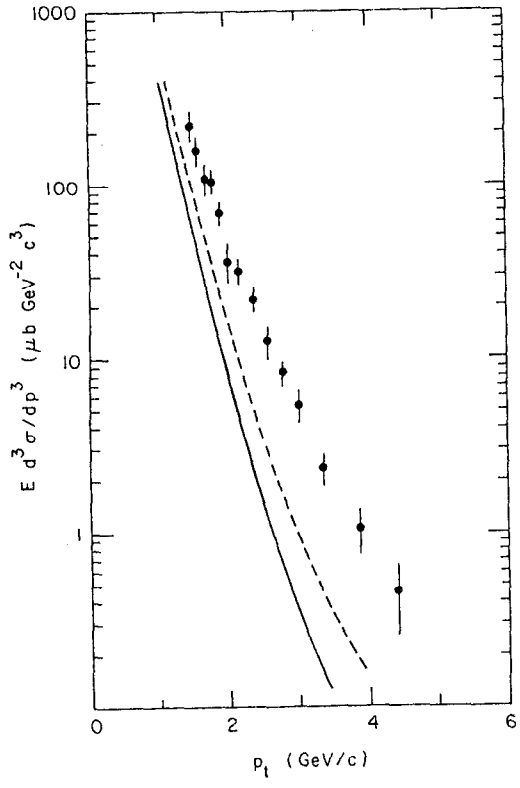


Fig. 4

Invariant cross section for π^0 production.

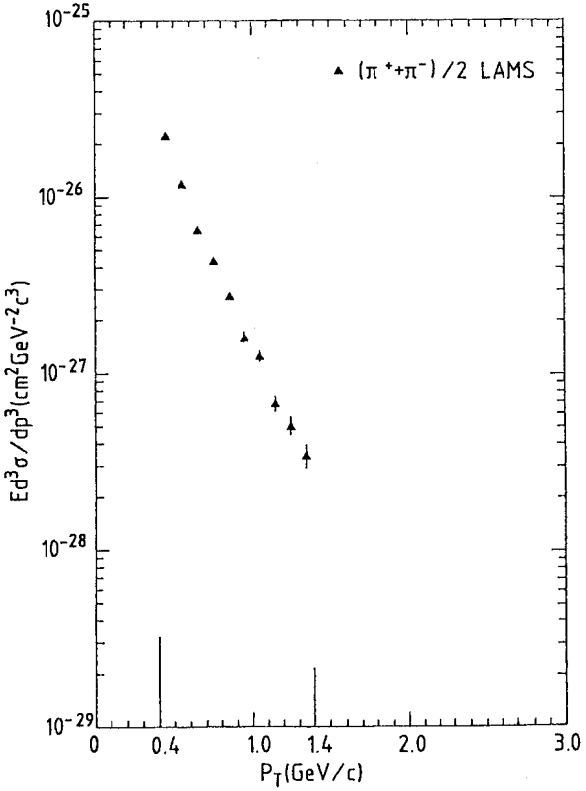


Fig. 5

Invariant cross section for charged pion production.

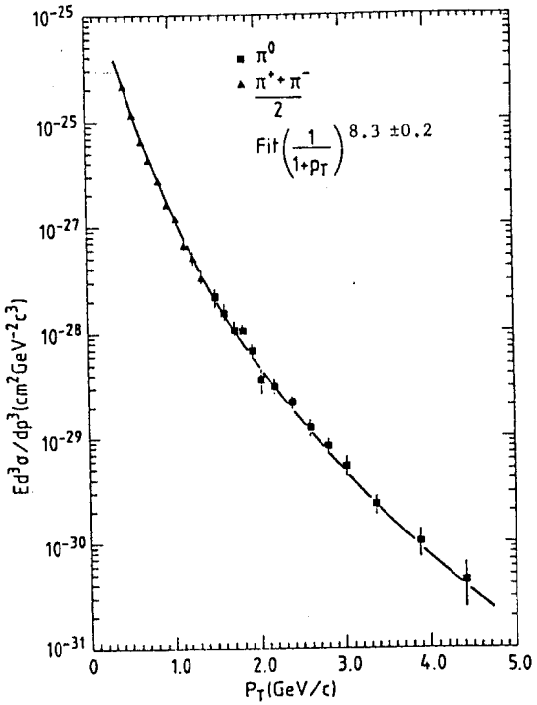


Fig. 6

Invariant cross section for all pion production.

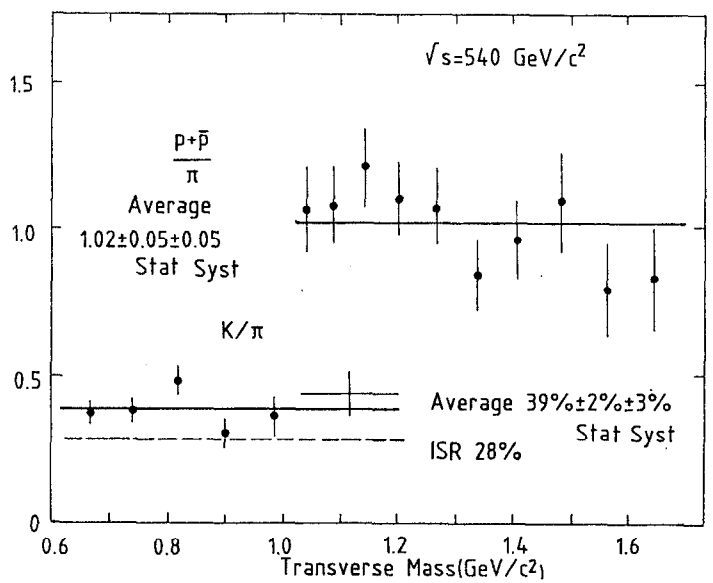


Fig. 7

K/π and p/π cross section ratios.

Search for fractionally charged particles[3]

The dE/dx counter is used to get 5 measurements of the ionization produced by any particle that produces 5% of MIP in at least 3 of the 5 scintillators. After analysis there are no candidates for fractionally charged particles in a sample of ∿ 6000 charged particles. This null result can be expressed as a 90% confidence level upper limit of 4×10^{-4} for the ratio of quark yield ($m_Q < 0.5$ GeV) to that of particles with unit electric charge. This limit is based on the assumptions that quarks are produced with the same p_T distribution as pions and that they aren't absorbed in the material of the detector.

OBSERVATION OF LARGE TRANSVERSE MOMENTUM JETS[4]

Data have been taken with a trigger on total transverse hadronic energy in the central calorimeter. The sample contains backgrounds from beam halo particles which are eliminated by requiring that the pattern of hits in the vertex chambers and the pattern of energy deposition in the calorimeters are consistent with that expected for particles emerging from a $\bar{p}p$ collision. After these cuts there are < 10% background events left in the data sample and no more than 15% of the good events could have been lost.

The distribution of events as a function of the transverse energy ΣE_T in the interval $-1 < \eta < +1$, $30^\circ < \phi < 330^\circ$ is presented in Fig. 8; it is observed to fall off exponentially as has been observed in experiments with a similar solid angle coverage at the SPS and at Fermilab ($\sqrt{s} = 24$ GeV). There are 10 events having $\Sigma E_T > 60$ GeV.

We estimate that the uncertainty in the energy scale due to systematic effects (150 MeV minimum cell energy, variation in response of the electromagnetic compartment for charged and neutral pions, and calibration errors) to be ±5%. In the lower energy experiments, events with large ΣE_T (the largest accessible value is approximately 20 GeV) have predominantly high multiplicity, cylindrically symmetrical configurations. It is however commonly expected that at the

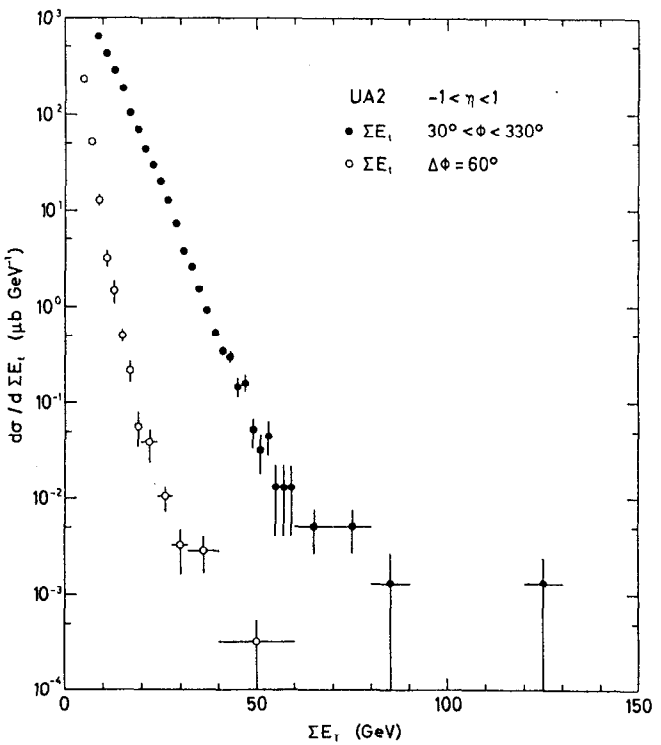


Fig. 8

Observed transverse energy distributions.

present collider energy, $\sqrt{s}$ = 540 GeV, sufficiently large values of ΣE_T can be reached that two-jet configurations resulting from hard scattering will dominate. An indication of this is already provided by the fact that the two highest energy points in Fig. 8 lie significantly above the exponential.

A more sensitive test is provided by studying the ΣE_T distribution into a solid angle which is substantially smaller though still sufficiently large to contain most of the energy for hadron jets in the E_T region of interest (E_T > 15 GeV). The $d\sigma/d\Sigma E_T$ distribution for $-1 < \eta < 1$, $\Delta\phi = 60^\circ$ is shown in Fig. 8 ; it demonstrates a clear departure from an exponential. Figure 8 illustrates that regions of high energy density are confined to within a small solid angle.

A rather spectacular illustration of this is shown in Fig. 9. This event is the one with the largest $\Sigma E_T \simeq 129$ GeV that we have seen.

It exhibits striking features : energy is concentrated within two small regions separated in azimuth by $\Delta\phi \simeq 180^\circ$ and towards which several collimated tracks are observed to point. In addition the transverse energies of the two clusters are approximately equal (57 and 60 GeV).

The jet like characteristics of this event are by no means unique as will now be shown. We put into a "cluster" all cells which share a common side and contain an energy $E_{cell} > E_{cell}^{min}$; E_{cell}^{min} is normally chosen to be 400 MeV, though the results obtained are relatively insensitive to the exact value chosen. Clusters having two or more local maxima separated by a valley deeper than 2 GeV are then split. On the average, for ΣE_T > 30 GeV, we obtain $\simeq$ 4.4 clusters having E_T > 2 GeV per event, each cluster consisting of typically 4 cells.

The cluster (resp. the two clusters) with the largest transverse energy in an event accounts for a fraction h_1 (resp. h_2) of the total transverse energy ΣE_T measured in the central calorimeter. The dependence upon ΣE_T of h_1 and h_2 is illustrated in Fig. 10. In particular all events with ΣE_T in excess of 60 GeV have an average of 67% of the transverse energy contained in only two clusters.

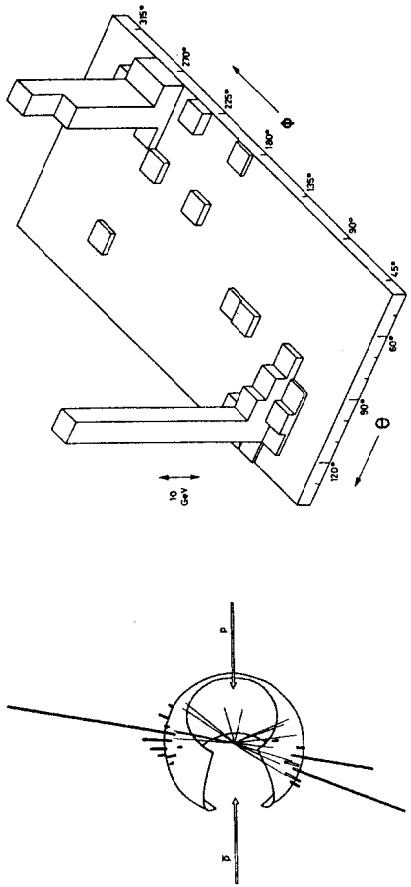


Fig. 9

The highest energy event, ΣE_T = 129 GeV, M = 140 MeV.

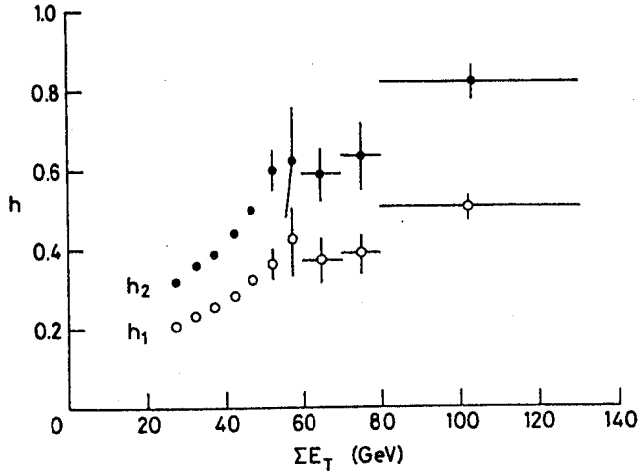


Fig. 10

Fraction of total transverse energy (ΣE_T) contained in the highest and two highest clusters as a function of ΣE_T.

Furthermore, as is shown in Fig. 11, as ΣE_T increases, $r_{2,1} = E^2/E^1$ increases showing that the two largest jets tend to balance each other and $r_{3,2} = E^3/E^2$ decreases showing the dominance of two jet systems as opposed to multi jet. When there are two high energy clusters in the central calorimeter Fig. 12 shows that they have a strong azimuthal back to back correlation. The average transverse momentum of the pairs ($E_T^{1,2} > 10$ GeV) is 6 GeV/c of which at least 3 GeV/c is of instrumental nature. Futhermore, in those events having $E_T^1 > 10$ GeV and $E_T^2/E_T^1 < 0.4$, 6% of them have at least 5 GeV transverse energy in the forward/backward electromagnetic calorimeters (which are not used in the trigger). The azimuthal distribution for those events is shown in Fig. 13 and again a strong back-to-back correlation is seen.

We do not see any significant cluster-cluster rapidity correlation.

INCLUSIVE JET PRODUCTION CROSS SECTION

There are 59 events containing at least one cluster with $E_T >$ 20 GeV. The evaluation of the inclusive jet production cross section from these events requires the knowledge of the detector acceptance and luminosity.

The detector acceptance is obtained from a Monte Carlo simulation that generates jets with the model of Horgan and Jacob, superimposed on a system of soft hadrons accounting for the remaining fraction of $\sqrt{s}$. The jets fragment into hadrons (assumed to be charged and neutral pions only) which are then followed into the calorimeters to generate a pattern of energy depositions.

The data generated by the Monte Carlo simulation undergo the same analysis chain as the real data. In particular, we find that the distribution of cluster sizes in the Monte Carlo data is very similar to that of the real data, indicating that both hadronic fragmentation and shower developments are correctly described in the simulation program.

The comparison of the E_T-distribution of the Monte Carlo data with that used as an input provides the correction function $\alpha(E_T)$ by

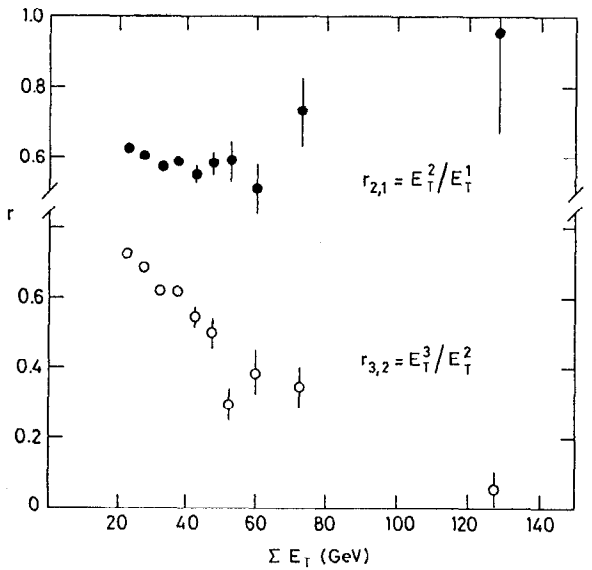


Fig. 11

Average ratio of energy in second highest cluster to first and third to second as a function of ΣE_T.

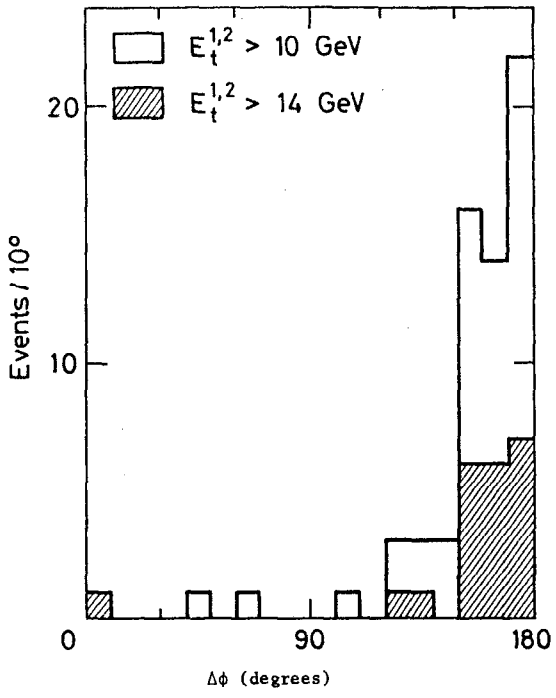


Fig. 12

Azimuthal separation of two highest energy clusters.

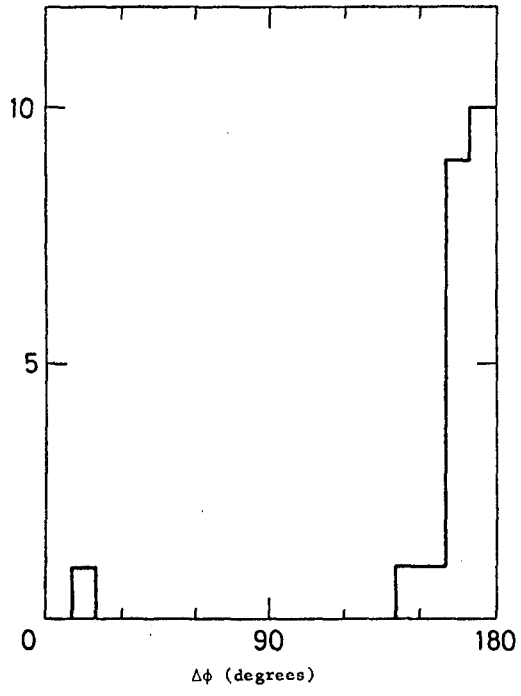


Fig. 13

Azimuthal separation of central calorimeter clusters and forward/backward electromagnetic clusters when there is no second high E_T cluster in the central calorimeter.

which the observed cross section must be divided to obtain the jet inclusive cross section.

Fig. 14 shows the cross-section for inclusive jet production as a function of the jet transverse energy E_T. The errors shown are only statistical. There is an overall uncertainty of ±20% in the vertical scale reflecting the uncertainties in the knowledge of the total luminosity and in the Monte Carlo calculated acceptance. An uncertainty of ±2.5% in the E_T-scale, reflecting the calorimeter energy calibration uncertainties, results in an additional vertical uncertainty of ±20%. Another uncertainty results from the fact that, as already mentioned, the trigger to record large-E_T events required a coincidence with a pair of small angle charged secondaries. This requirement introduces a bias which may affect both the absolute magnitude of the cross-section and its E_T-dependence. We finally note that the possible merging of two high E_T clusters produced with a small angular separation may increase the measured cluster energy by as much as 2 GeV on the average.

Our measured cross is at a level comparable with the QCD calculation of Horgan and Jacob[5], which is also shown in Fig. 14. In the framework of this model, inclusive jet production is dominated by gluon-gluon scattering in the kinematical region of this experiment. The ISAJET Monte Carlo (which has been used to fit the ISR data presented at this conference) also gives very good agreement with our data although it has different structure and fragmentation functions.

ACKNOWLEDGEMENTS

We deeply acknowledge the help of the technical staffs of the Institutes collaborating in UA2.

Financial support from the Danish Natural Science Research Council to the Niels Bohr Institute group and from the Schweizerischer National-fonds zur Förderung der wissenschaftlichen Forschung to the Bern group are acknowledged.

The author would also like to thank the organizers for an enjoyable conference.

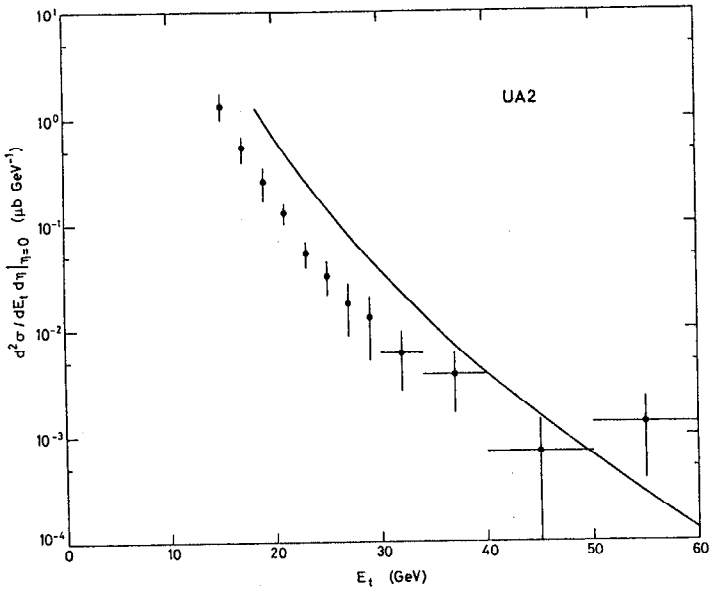


Fig. 14

Inclusive jet production cross section.

REFERENCES

[1] Inclusive π^0 Production at the CERN $p\bar{p}$ Collider. The UA2 Collaboration. Physics Letters 115B (1982) 59.

[2] Inclusive Charged Particle Production at the CERN $\bar{p}p$ Collider. The UA2 Collaboration (submitted to Physics Letters).

[3] A search for Relativistic Particles with Fractional Electric Charge at the CERN $\bar{p}p$ Collider. The UA2 Collaboration. (to be published in Physics Letters).

[4] Observation of Very Large Transverse Momentum Jets at the CERN $\bar{p}p$ Collider. The UA2 Collaboration. (to be published in Physics Letters).

[5] R. Horgan and Jacob, Nucl. Phys. B179 (1981) 441.

CALT-68-950
DOE RESEARCH AND
DEVELOPMENT REPORT

The Emergence of Jet Structure in Events Triggered on Large Transverse Energy at $\sqrt{s}$ = 63 GeV*

Rafe H. Schindler

California Institute of Technology, Pasadena, CA 91125

Talk presented at the 1982 SLAC Summer School for the Axial Field Spectrometer Collaboration[1] CERN-Tel Aviv-Brookhaven National Laboratory - Niels Bohr Institute-Rutherford Appleton Laboratory-Univ. of Pennsylvania-Univ. of Lund.

ABSTRACT

We present data obtained from a 1.7 sr uranium-copper hadron calorimeter, triggered on transverse energy (E_T) in pp collisions at $\sqrt{s}$ = 63 GeV at the CERN-ISR. From the observed change in energy flow within the calorimeter we extract a hard scattering cross section from $p_\perp$ = 6 to 14 GeV, at y = 0. This "jet" cross section is found to agree well with a QCD motivated Monte Carlo model, both in slope and normalization. Properties of charged particles over the full azimuth in the central detector provide a consistent picture that an increasing fraction of events are produced with limited transverse momentum to the energy flow axis, as E_T is increased.

* Work supported in part by the US Department of Energy under Contract No. DE-AC03-81-ER40050
September 23, 1982

© R. Schindler 1982

Problems of Jet Studies in Hadron Collisions

The goal of this experiment was to search for jet structure in hadron-hadron collisions using an "unbiased" trigger. Should a clear jet signal emerge in these events, then one has available a unique laboratory for studying their properties. In contrast to jets produced in e^+e^- machines, one expects a large fraction of events to emerge from gluon-gluon and quark-gluon scattering in the protons. Since only the harder collisions are expected to arise from quark-quark scattering, one can in principle connect up smoothly to the e^+e^- jets by simply raising the $p_\perp$. Early experiments using single particle high $p_\perp$ triggers have observed events consistent with the expectations of hard scattering of partons, and their final fragmentation. These experiments suffer however, from the effects of "trigger-bias," in that they only select a very small subset of all scatterings which lead to large $p_\perp$ fragments. In doing so, the shape of the event on the trigger-side is itself distorted. On the away-side, the recoil jet direction in space is indeterminate since the scatterings in pp collisions do not have a well-defined center-of-mass (CMS), and primordial $k_\perp$ destroys the $p_\perp$ conservation which provides some angular correlation.

These problems are largely resolved by use of a calorimeter which is triggered on transverse energy (E_T)[2]. The criteria essential to an unbiased measurement can be specified:

[i] The device should collect the energy of hadrons and leptons over a region large compared to the size of the jet.

[ii] The response of the device should be equal for electromagnetic and hadronic energy.

[iii] The device should be immune on an event by event basis, to the contamination of spectator fragments, since it must operate in a 4-jet environment.

A number of large E_T calorimeter experiments have been performed at FNAL and the CERN-SPS[3]. Figure 1 shows, for example, the planarity distributions from NA5 (C. de Marzo et al, ref. 3) at $\sqrt{s}$ = 24 *GeV*. Here, no evidence was seen for a change in structure when the E_T in their 2π azimuth, $-.86 < y < .67$, calorimeter was raised as high as 18 GeV. Similar results at $\sqrt{s}$ = 29 *GeV* in a 2π calorimeter triggered on E_T, have been reported (B. Brown et al., ref. 3).

The lack of a clear jet structure in events triggered on large E_T has been analyzed theoretically by several authors[4]. Bengtsson et al. present a phenomenological argument showing that the competition between "soft" and "hard" scattering processes which contribute to an E_T trigger never reaches a cross-over point (see Fig. 2), at lower $\sqrt{s}$. Field et al. argue from a QCD standpoint that soft gluon bremsstrahlung, both from the high $p_\perp$ jets and the spectator jets creates an E_T trigger bias, masking event structure at low $\sqrt{s}$.

In the rest of this paper we will endeavor to prove that at $\sqrt{s}$ = 63 *GeV*, our data triggered on a 1.7 sr hadron calorimeter well satisfy the three criteria for an "unbiased" trigger, and that a well-resolved jet-structure dominates the events for triggers with sufficiently high E_T.

Apparatus

Fig. 3 shows a view of the calorimeter[5] and drift chamber. The central chamber is immersed in a 5.6 KG magnetic field supplied by the open axial field magnet (Fig. 4). In the final configuration of the experiment, the calorimeter will fully enclose the drift chamber by the addition of two vertical walls of calorimeter. For this analysis, only the roof stacks are used in the trigger, and the floor stacks are recorded. The roof is formed of 32 stacks each containing 6

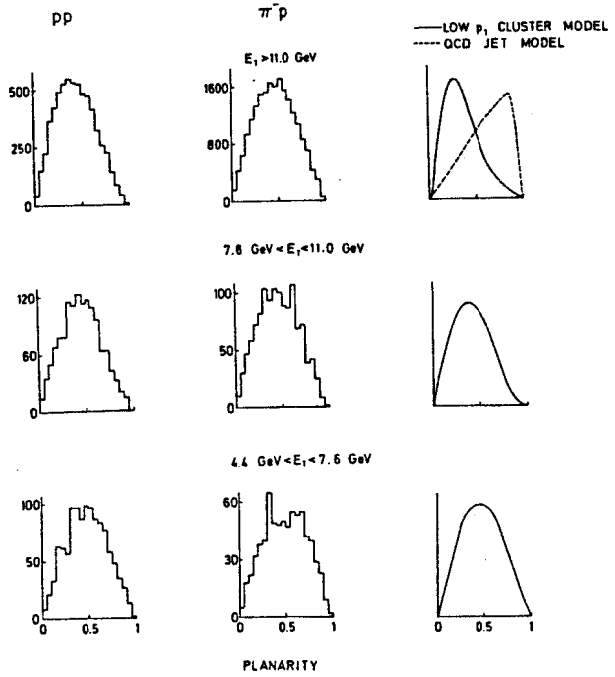


Fig. 1

The planarity distributions from experiment NA5 (Ref.3)

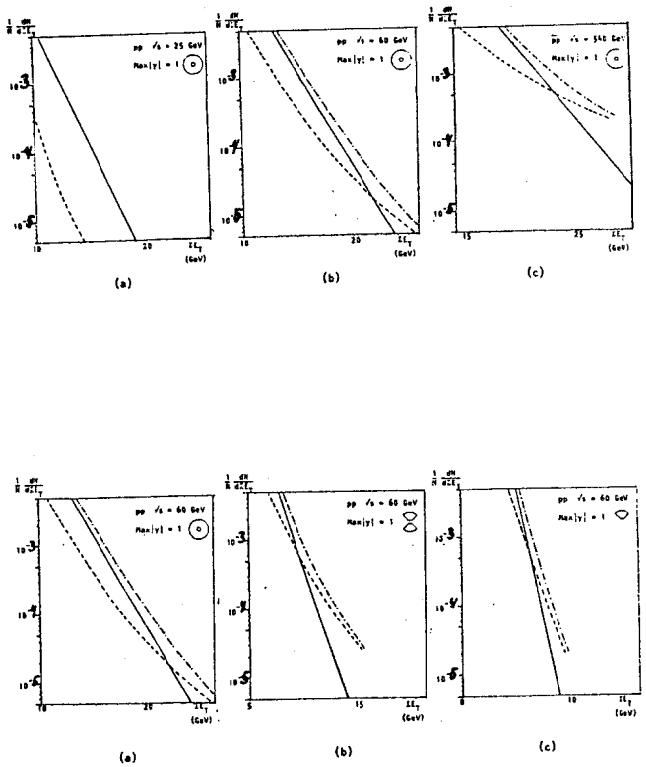


Fig. 2

The expectations for crossover at various $\sqrt{s}$ and various calorimeter geometries (Ref.4).

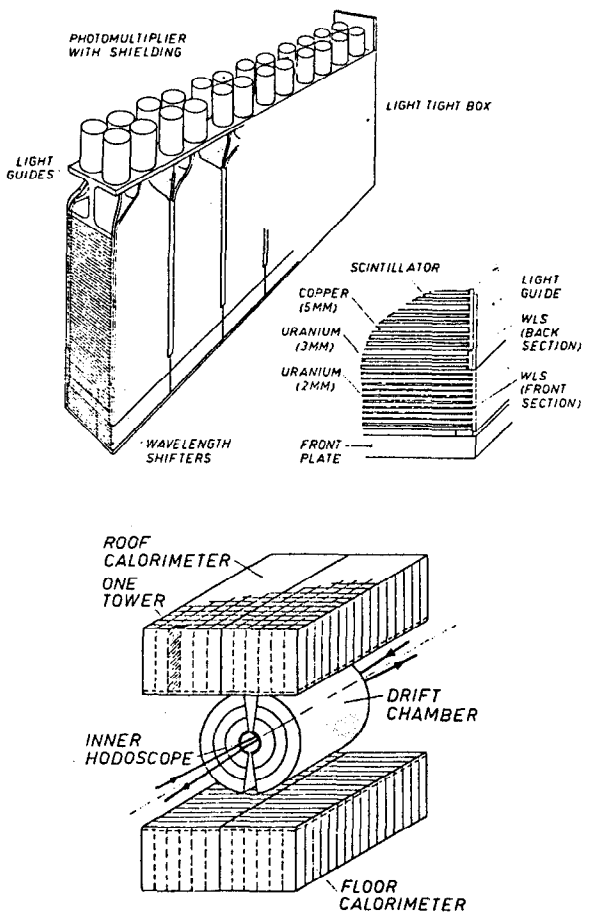


Fig. 3

View of the calorimeter and central drift chamber. Details of a calorimeter stack.

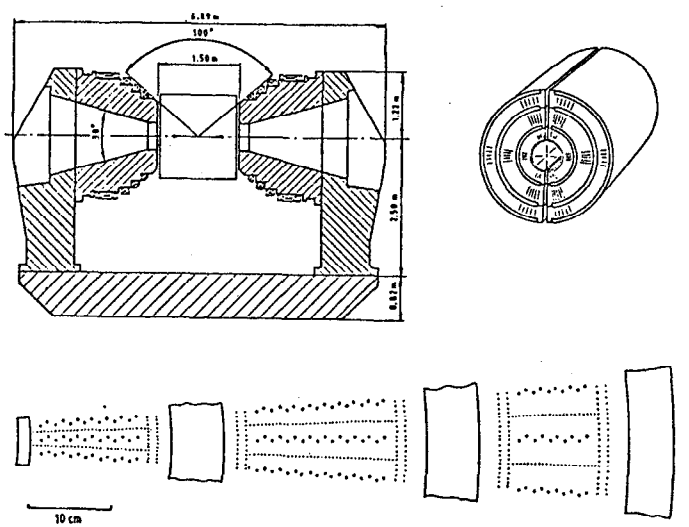


Fig. 4

Details of the drift chamber and axial-field magnet.

towers (see Fig. 3). The face of each tower is $20 \times 21.6\ cm^2$ and is located in a plane $\sim 118\ cm$ from the beam crossing. Each tower has 4-fold wavelength shifter (WLS) readout: right and left at two depths (the first 6 *r.l.* and the second ~ 3.6 absorption lengths).

The front section (EM) has 2mm uranium metal plates ($\sim 0.5\ r.l.$) interspersed with 2.5 mm scintillators. The rear section is composed of 3mm uranium and 5mm copper plates (in 2:1 proportion), again interspersed with 2.5 mm scintillators. Test beam measurements have shown that above $\sim 1\ GeV$ the resolution for hadrons is $\sim 37\%/\sqrt{E}$ and for electrons about $16\%/\sqrt{E}$. At 4 *GeV* the ratio of response to electromagnetic versus hadronic energy is about 1.14. These three numbers should be contrasted with 50%, 15%, and 1.5 for the same calorimeter made entirely of 5 mm copper plates. The very similar response to hadrons and electrons in the uranium calorimeter results from fission compensation (see C. W. Fabjan et al., Ref. 5). This in turn accounts for the significant improvement in resolution over the uncompensated calorimeter. This property makes the calorimeter unique in reducing the event to event fluctuations in response which trouble all conventional calorimeters. Fig. 5 shows, for example, how gaussian the upper end of the response is to 4 GeV hadrons. No evidence for a charge-exchange shoulder is observed.

While the calorimeter is found to be linear to about 1% to electrons and hadrons above $\sim 1.5\ GeV$, it deviates significantly from linearity for hadrons below this value. This is presumably a result of the tradeoff of energy loss to dedx versus an hadronic interaction. Dedx loss is more efficient at depositing energy (by ~ 25% relative to electrons), hence as a larger fraction of energy is lost in this way, the calorimeter becomes nonlinear. At the same time, the fluctuations in loss diminish, leading one to obtain an improvement in resolution at low momenta. Our measurements are summarized in Fig. 6. The details of

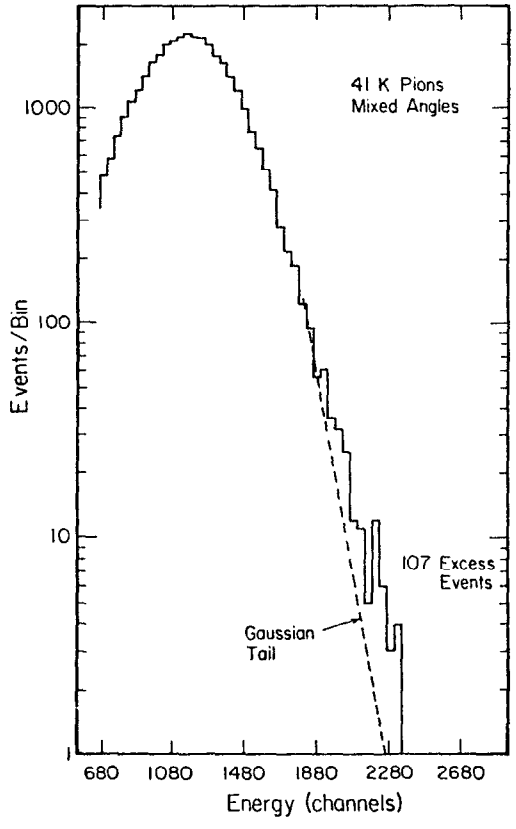


Fig. 5

Pulse height for 41K π- at 4 GeV, with a Gaussian superimposed.

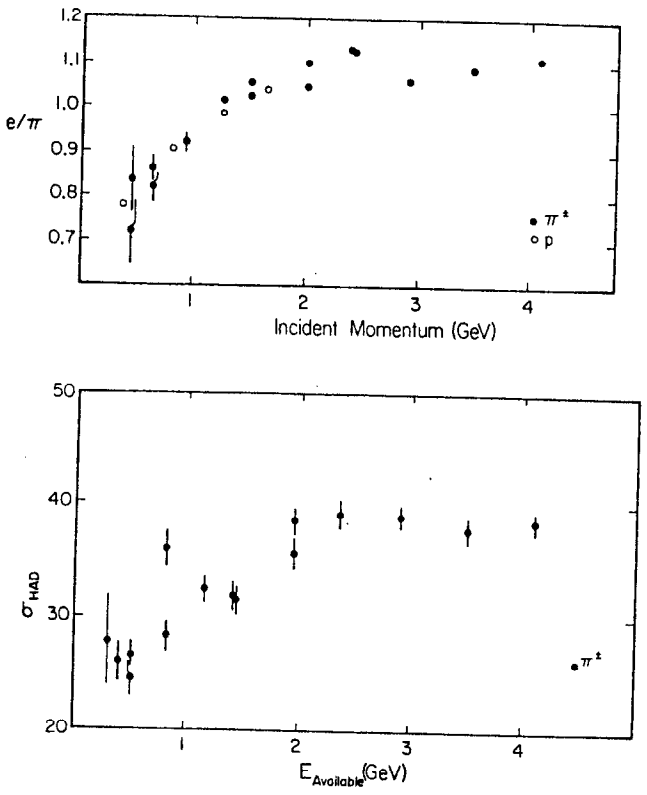


Fig. 6

Ratio of electromagnetic to hadronic response of the calorimeter versus momentum. The change in resolution of hadrons versus available energy.

these effects are all important in determining the proper energy scale, as the bulk of the particles measured at the ISR are relatively soft (< 2 GeV).

The calorimeter calibration is maintained by frequently monitoring the uranium activity over a 10 μ sec. gate. This provides a $\pm$ 2.5% inter-tower calibration. Calibration and pedestal stability varies from about 3 to 2% over the E_T range 6 - 14 GeV. The uncertainty in E_T is larger and will be discussed below.

Position resolution on the calorimeter varies from 0.85 to 2 cm for EM showers above 0.5 GeV, independent of incidence angle. For hadrons the resolution varies from about 3 to 12 cm because of the large parallax. Combinations of WLS information within a tower and the ~ 25 cm attenuation length scintillator which optically couples the towers within a stack, allow this precision. The fiducial region of the roof calorimeter subtends 1.93 (1.69) sr for em (hadronic) showers. In the CMS this corresponds to a $\Delta\varphi = 72°\,(66°)$ and $|\cos\vartheta| < 0.70(0.68)$ for electromagnetic (hadronic) showers.

The E_T trigger is formed by a weighted sum over the phototube dynodes of the roof. This transforms pulse-height in the laboratory to transverse energy in the CMS. The E_T signal derived is discriminated and placed in coincidence with a minimum multiplicity of ≥ 2 hits in the 44 element scintillation counter array (IH) surrounding the beam (see Fig. 3). A "minimum bias" trigger was formed from upstream and downstream counters (BB) covering $2° < \vartheta < 6°$, OR'ed with IH. This non-calorimeter trigger recorded > 95% of the inelastic cross section, and thus provided a means of checking the calorimeter trigger. In addition, the BB counters were used as our luminosity monitor.

The data consisted of 10^6 triggers recorded at an average luminosity of $1.43 \times 10^{31}\ cm^{-2}\,sec^{-1}$ for a livetime of ~ 7 hours. Five distinct trigger thresholds were used, in addition to minimum bias triggers [Fig. 7]. E_T is calculated by first clustering energy in the wall, using the WLS information to determine

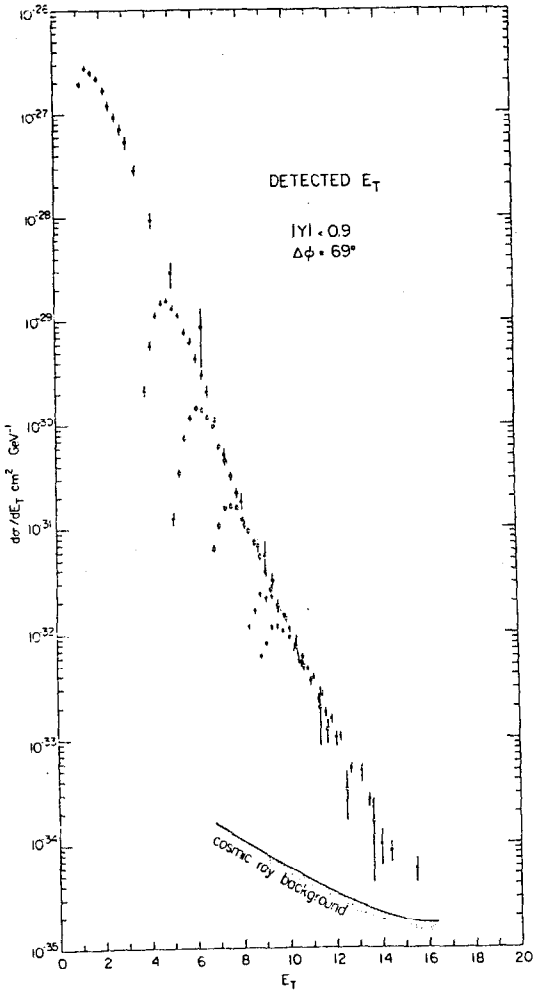


Fig. 7

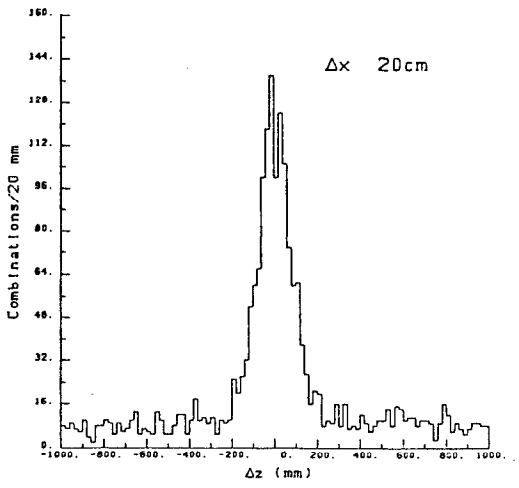
$d\sigma/dE_T$ uncorrected; error bars are statistical only. Solid circles are from minimum bias triggers. The other symbols refer to data sets taken at different thresholds. The upper limit for the background from cosmic rays is indicated.

centroids and to correct for WLS response ($\lesssim$ 4% of E_T). Clusters are normally 3 × 3 towers, and are allowed to expand along a stack to account for light sharing. While the maximum cluster is 3 × 6 towers, the average is 3 × 3. Fig. 8 shows the match of low $p_\perp$ (~ 500 MeV/c) charged tracks in low multiplicity events, to the found clusters, in two views, cutting alternately on the other view. The width for these momenta is consistent with our beam test results. While clustering helps reduce the summed r.m.s. noise and aids in energy localization, it is not useful in correcting for the small difference in e/π response remaining in the calorimeter. Lacking this knowledge, the data are presented uncorrected at this point in the analysis. Events with more than 15% of their E_T in clusters on the edge of the calorimeter are removed, to reduce the effects of energy leakage. Additionally we required the vector sum of the clusters' directions to point within ± 25° in azimuth and $|y| < 0.5$ of the wall center, in the laboratory.

Triggers were also required to satisfy a set of timing and vertex cuts:

[1] The event time calculated from the IH elements was required to lie within ± 15ns of the nominal event time, to reduce the accidentals within the longer 60 ns trigger gate. [- 4.50%].

[2] Pileup protection using timing on the IH and BB elements rejected second events within ± 150ns of the nominal time. This discrimination could be employed to within ± 12ns of the nominal time, reducing the accidental rate to $\lesssim$ 1.3%. Even this low accidental rate can lead to a trigger bias in E_T, which we estimate to be at most 9 (21%) at 6 (14) GeV. This type of background would tend to obscure any event structure. [-20%].



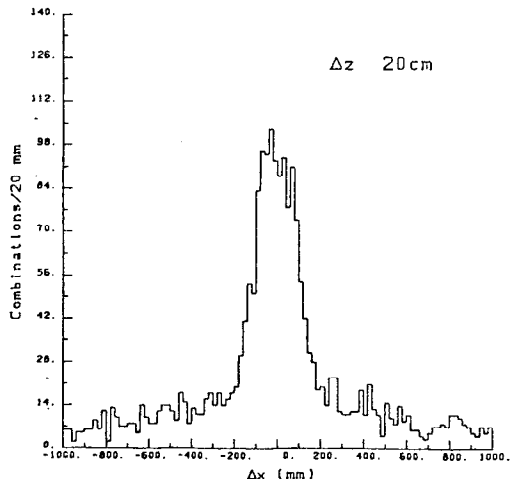


Fig. 8

Match of clusters to charged tracks with $p_\perp > .5$GeV at the calorimeter face. Two views are shown, with each view alternately cut on 20 cm in the other view.

[3] All events are required to have a charged track vertex within a fiducial volume around the beam-interaction region. This suppresses any cosmic-ray or beam-gas background which satisfies the E_T requirement and crosses IH to satisfy the multiplicity requirement. [-8%].

These cuts remove about 30% of the triggers before calorimeter information is used. The loss of 0 and 1 prong events is negligible since the mean charged multiplicity for $E_T > 6$ GeV is $\gtrsim 10$. The loss of events from non-uniformities in the calorimeter (+ 14%) has been corrected for in Fig. 7.

Two backgrounds not explicitly rejected by these cuts are residual beam-gas and cosmic rays in time with an inelastic event. Runs without beams imply that while the cosmic ray spectrum is quite flat relative to E_T, the contribution to the 12-14 GeV bin in E_T is $\lesssim 5\%$ (see Fig. 7). Beam gas is harder to estimate, but single beam runs suggest that "self-triggering" beam gas events are $\lesssim 14\%$ for $12 < E_T < 14$ before any vertex or timing cuts. The high degree of vertexed charged track-calorimeter correlation rules out a significant fraction of upstream beam gas events supplying E_T, in time with an inelastic event supplying the multiplicity requirement but little E_T. All the data in Fig. 7 were normalized using the BB counters. This leads to a 7% normalization uncertainty. The E_T from 7.7 K events taken with a minimum bias trigger are shown also in Fig. 7. These have been corrected for the loss of 0 and 1 prongs (+ 6.8%). An extrapolation to the lowest calorimeter trigger threshold shows excellent agreement in both slope and normalization, indicating the stability of our procedure. The excellent agreement between calorimeter thresholds also indicates our ability to control systematic effects and backgrounds which may vary with the trigger level.

The Structure of Events

As pointed out in the previous sections, $d\sigma/dE_T$ in itself is not the jet cross section. Furthermore, with many contributing processes to E_T, and our incomplete spectrometer coverage, it is not possible to correct the energy scale without a complicated model of our E_T triggers. Our goal is first to prove that our triggers contain jets, and then to measure the jet cross section. The former is not highly sensitive to energy scale errors which only dilute the structure. The latter is highly sensitive, but fortunately it provides us with a definite model by which to correct the energy.

To study event structure the data were divided into 8 E_T bins. In each bin, the clusters with $p_\perp > 25\ MeV$ were ordered in E_T, and those making up 80% of E_T were summed vectorally to calculate the axis E' of energy flow. This axis was also required to point towards the calorimeter center ($\Delta\vartheta = 50°$ and $|y| < 0.5$).

Using all clusters in the wall, ($p_\perp > 25\ MeV$) and the $\vec{E}'$ direction we formed the quantity analogous to thrust (T):

$$T = \sum_i |\vec{E}' \cdot \vec{P}_i| / \sum |\vec{P}_i| \qquad (1)$$

with sums carried out over clusters, and $\hat{E}'$ being a unit vector along $\vec{E}'$. Because of geometry, T takes on values between ≈ 0.7 and 1.0. A pencil-like event has $T \approx 1$; a high multiplicity isotropic event has $T \approx 0.86$, and the T = 0.7 event, would be two particles opened as widely as possible in the calorimeter.

Fig. 9 shows the thrust distributions in bins of observed E_T. The striking feature is the constancy of the distribution until $E_T \approx 7.5$ and then gradual peaking of the distribution as E_T is raised within the calorimeter wall. While the cuts applied above are somewhat arbitrary, we have varied the cutoff energies to as high as 250 MeV; the fraction defining E' from 70% to 90%; and the fiducial cut to $\Delta y = 0.30$ $\Delta\varphi = 20°$; all without changing the general feature of the rise with E_T.

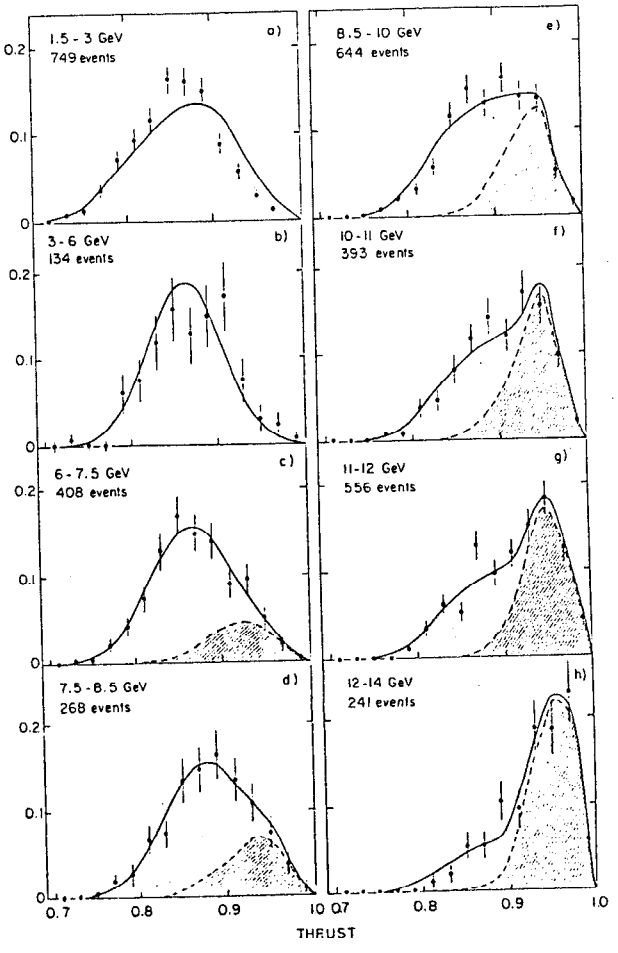


Fig. 9

Fraction of events per 0.02 units of thrust for the 8 bins of E_T. The shaded area is the hard scattering component to the fit; the solid curve is the total fit.

To test that the triggers were not backgrounds we required, in addition to the roof trigger, that the floor should record > 3 *GeV*, or that the vertex multiplicity exceed the mean detected multiplicity ($n \sim 8$ for $|y| < 0.5$). These cuts would highly suppress backgrounds from both beam gas and cosmic rays which required in-time inelastic events, and themselves put few tracks in the central region of the calorimeter. In neither case was a change in the T distribution observed.

While the distribution of T appears to join smoothly from low E_T (where the calorimeter was not used to trigger) to high E_T (where it was used), we would like to prove that increasing multiplicity alone coupled to our pattern recognition cannot produce increasing thrust. We would also like to quantify our results for the T distribution for jet-like events. To accomplish these goals we have generated two classes of events; those *without* an explicit hard scattering component ("minimum-bias") and those *with* one. All events were passed through a full simulation of the calorimeter response, and then processed through our normal calorimeter pattern recognition and analysis chain[6].

ISAJET[7] is used to generate these minimum-bias events. Fig. 9a shows the excellent agreement in shape of these events for detected $E_T < 3$ *GeV*. The spectrum of E_T from ISAJET was checked against data to 6 GeV and also found in reasonable agreement. To get to higher E_T with reasonable statistics we generated minimum-bias events forcing higher multiplicity[7]. Fig. 9b shows the data and Monte Carlo for these events from 3 to 6 GeV. Again good agreement in shape is seen. From 6 to 8 GeV (not shown), the value of $< T >$ was found unchanged for the Monte Carlo, but as expected, the width diminished, reflecting the increase in multiplicity. This latter effect is visible already in the data and Monte Carlo of Fig. 9a,b. We conclude that our procedure appears insensitive to simple increases in multiplicity, and that the calorimeter trigger itself is not a bias to the thrust measurement.

To study the shape of jet-like events as detected in the calorimeter and to extract the hard-scattering component in our E_T triggers, we rely on the second set of Monte Carlo data. ISAJET was used to produce a spectrum of events containing two large $p_\perp$ jets and two spectator jets[8]. Since these events are produced with the theoretical cross section, our selection of them in bins of *observed* E_T will have all the effects of resolution smearing on the $p_\perp$ spectrum as well as detector and algorithm biases. In addition they have the contamination of the beam jets (typically 800 MeV), and the opposing jet (typically 100 MeV). The shaded regions of Fig. 9c-h show the shape of these events for each detected E_T bin from 6 to 14 GeV. One sees that the detector appears sensitive to small changes in thrust with E_T.

To quantify our results we have fit by maximum likelihood with Poisson statistics the two contributions to the thrust distribution: a signal from the hard scattering model, and a background from minimum-bias-like events. Note that this latter component produces a shape which is consistent with *any* source of a random deposition of energy in the calorimeter. It is largely independent of E_T. To reduce model dependence of the result, we have allowed the fitting function from each component to slide by up to 1 bin (0.02) in thrust. This corresponds to a small variation in the multiplicity and/or width of the fragmentation model. The average shifts are all less than 0.5 bins, and do not alter the results above 7.5 GeV. Only the first bin appeared sensitive to the exact form of the minimum-bias used, and the allowance for a shift in the fit. An additional systematic error has been included for this data point.

The shape of T in the hard scattering model is insensitive to Λ and the exact form of the fragmentation and structure functions used. The advantage of this technique in extracting the jet component is that it is largely geometric, and the

sizes of jets are comparatively well known.

The results of the fits show that a fraction of four jet events rises approximately linearly from $\lesssim$ 20% to ~ 75% as E_T varies rom 6 to 14 GeV. This significant a change in the jet fraction with rising E_T has not been previously seen.

Once the event fraction from hard scattering has been extracted, in this manner, the model can be used to correct in each *detected* E_T bin for geometrical acceptance, beam-jet contamination, the energy scale and resolution; to obtain the $p_\perp$ spectrum of the original constituent. These corrections increase the cross section by *only* about a factor of 4, going from 6 to 14 GeV. Fig. 10 shows the resultant invariant cross section for inclusive jet production at y = 0. The dashed curve is the input into the correction procedure showing that a proper slope is used to correct for resolution smearing. It is therefore not necessary to iterate the procedure. The inner errors on the points are statistical, reflecting the data, fit, and the correction procedure. The outer errors are systematic, from three main sources; luminosity (± 7%), the Monte Carlo procedure (3.5 to 2%) and the energy scale uncertainty (5% to 3.5%). Smaller systematic errors from the calorimeter response, and the fit procedure are also included on some points.

We find the cross section to be well represented by an exponential $e^{-bp_\perp}$ with slope b = 1.02 ± 0.09 GeV^{-1}. The cross section predicted using the Baier et al.[8], and the Owens and Reya[9] structure functions is shown in Fig.10. The latter, having a softer gluon component, predict a lower cross section at higher $p_\perp$, but with similar slopes.

Fig. 10 also shows the inclusive π^o cross section at $\sqrt{s}$ = 63 GeV[10]. We see that over our $p_\perp$ range of 6 to 14 GeV, the ratio of single π^o to jet varies from ~ 200 to ~ 1500. This is not inconsistent with previous techniques (Bromberg et

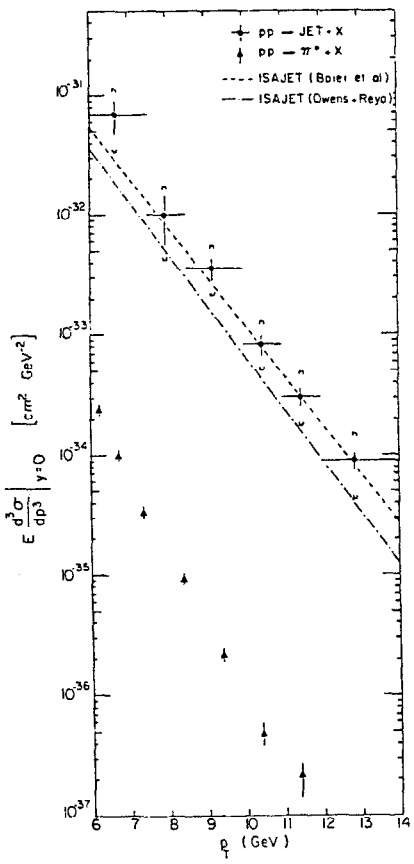


Fig. 10

Invariant cross-section at y = 0 for inclusive jet production in pp collisions at $\sqrt{s}$ = 63 GeV. Also shown is the invariant cross-section for π^o production at $\sqrt{s}$ = 63 GeV, y=0 (Ref.10). Lines are theoretical predictions (see text).

al., Ref. 3), since in our procedure $\lesssim$ 20% of the events at low E_T are attributed to jets.

Analysis in the Central Chamber

While the calorimeter provides an excellent trigger on high E_T events, it does not have the spacial granularity and momentum resolution necessary to study the events in detail. To compliment our calorimetric analysis we have looked at the classical parameters such as q_T, $\vec{P}_{out}$, and $<p_\perp>$ (see Fig. 11a) using only charged tracks in the central drift chamber. It is described in detail elsewhere[11]. Briefly, the cylindrical drift chamber is 1.4 m long extending radially from 0.2 to 0.8 m from the beam intersection. It is azimuthally segmented in 4° wedges, each containing 42 sense wires yielding time and pulse height information. The latter gives z position as well as a particle identification by dedx measurement. The spacial resolution is ~ 230 μm in azimuth and 1.5 cm longitudinally. With a 5.6 KG axial magnetic field, a momentum resolution of about 2.5% at 1 GeV is obtained for tracks with $45° < \vartheta < 135°$. Two azimuthal regions of ±4°, at 90° and 270° are excluded for beam-pipe supports.

In our analysis, only tracks with $p_\perp > 0.075$ GeV and $p_\perp < 10.0$ GeV were used. All tracks were required to have $|y| < 0.8$ but tight cuts on track and geometry give rise to a decreasing acceptance from $|y| = 0.6$ to $|y| = 0.8$.Our results are not sensitive to these cuts.

Tracks are classified as same side or away side depending on their space angle relative to the trigger direction E' in the calorimeter. In Fig. 11b we show the $<q_T>$ to the E' axis versus E_T. A value of 400 MeV on the same side is found, almost constant with E_T. These results are similar to those found in e^+e^- jets, and those measured using a single particle trigger in pp collisions[12]. On the away side $<q_T>$ rises slightly as expected, since in the overall CMS the

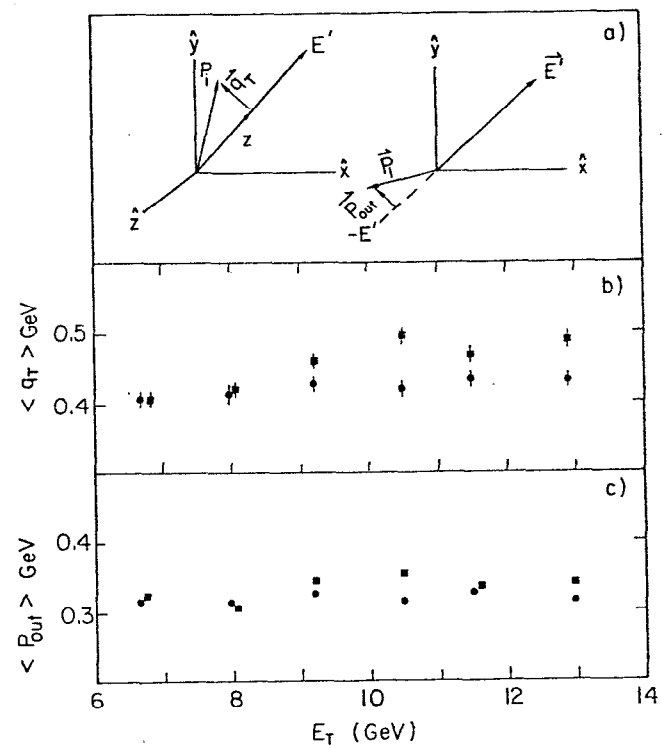


Fig. 11

a) Definition of the variables q_T, and P_{out}. $\hat{z}$ is in the direction of the beams.
b) $\langle q_T \rangle$ for the same side (circles) and away side (squares), versus E_T.
c) $\langle P_{out} \rangle$ for the same side (circles) and away side (squares), versus E_T.

constituents are not expected to be back-to-back. If we work only in the transverse plane (see Fig. 11c), then the variation with E_T is seen to be largely removed on the away side.

Fig. 12 shows the $\langle p_\perp \rangle$ of tracks with $\Delta\varphi < 50°$, $50 < \Delta\varphi < 130$, and $\Delta\varphi > 130°$, where $\Delta\varphi$ is the azimuthal angular difference from $\vec{E}'$. Note the nearly linear rise with E_T on both sides of the event, and the nearly constant level of $\sim 400\ MeV$ at 90° to the trigger. The difference in $\langle p_\perp \rangle$ on same and away sides may be attributable in part to primordial $k_\perp$, and perhaps more likely, to the small difference in rapidity acceptance on the two sides, because of the calorimeter trigger.

Fig. 13 shows the flow of transverse energy versus $\Delta\varphi$. This quantity is formed summing E_T in $\Delta\varphi$ bins, and normalizing the result to unity. Dedx information from the drift chamber is used whenever possible to make mass assignments, and only tracks with $p_\perp > 0.250\ GeV$ are used. An acceptance correction for geometrical losses is applied, but not for loss due to overlap of tracks in the 4° sectors. The general features follow those observed in $\pi^o\pi^o$ correlation[13]: very strong forward and backward peaks, which *narrow* with rising E_T. We note that the width on the trigger side is seen to decrease to about 10°; considerably smaller than the calorimeter acceptance.

Finally, we have done a shape analysis of the distribution of charged tracks, in an attempt to extract the fraction of jet-like events, just as was done with the calorimeter. We formed the quantity C' (semi-circularity) from the eigenvalues A and B, obtained by diagonalization of the transverse momentum tensor in each event:

$$C' = 1 - (A-B)/(A+B) \qquad (2)$$

where (A < B).

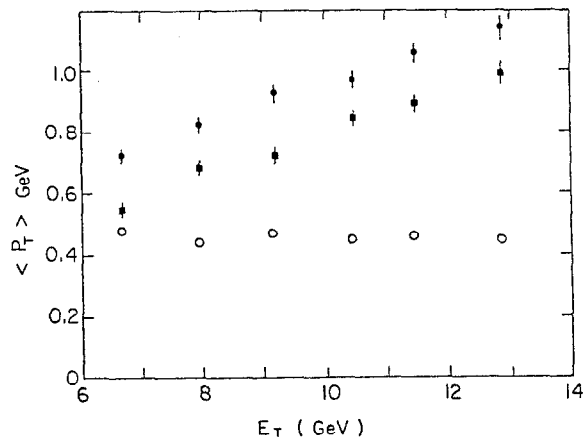


Fig. 12

$\langle p_\perp \rangle$ in c.m.s. for the tracks with $\Delta\varphi$ relative to $\vec{E}'$ for $\Delta\varphi \leq 50^o$ (circles) $50^o \leq \Delta\varphi \leq 130^o$ (open circles), $\Delta\varphi > 130^o$ (squares) versus E_T.

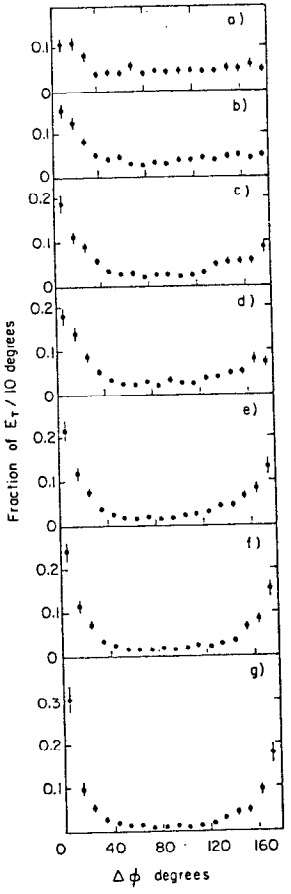


Fig. 13

Fraction of visible energy flow for the tracks for $\Delta\varphi$ bins of 10^{o} for E_T bins of: a) 1.5-3GeV; b) 6-7.5 GeV; c) 7.5-8.5 GeV; d) 8.5-10 GeV; e) 10-11 GeV; f) 11-12 GeV; and g) 12-14 GeV.

If the whole event is employed, then circularity (C) is related to planarity (P) by C = 1 - P. Small values of C or C' correspond to collimated events, while $C \approx 0.5$ is typical of isotropic events. Again by fitting, using ISAJET shapes, we obtain a fraction 30 ± 15% at 6-8.5 GeV and 60 ± 10% at 11-14 GeV. Fig. 14 shows the data and the results. This is in excellent agreement with the calorimeter result.

Conclusions

We have observed a significant change in event shape when triggering on increasing E_T collected over a large solid angle. The fraction of triggers which we associate with hard-scattering structure increases from $\lesssim$ 20% to about 75% as E_T rises from 6 to 14 GeV. The cross section relative to single high $p_\perp$ π^o production changes from ~ 200 to ~ 1500 over this range of $P_\perp$. The detailed structure of events in the drift chamber also yield a consistent fraction of hard scattering events, at each E_T. The event structure exhibits *limited* transverse momentum to the jet axis; *no* away side rapidity correlation; an *increase* of $\langle p_\perp \rangle$, and an angular extent of energy flow which is *much* smaller than the calorimeter size.

The emergence of a clear jet signature in pp collisions now opens up the door to unbiased studies of quark and gluon fragmentation, with rates comparable or exceeding those available in e^+e^- machines.

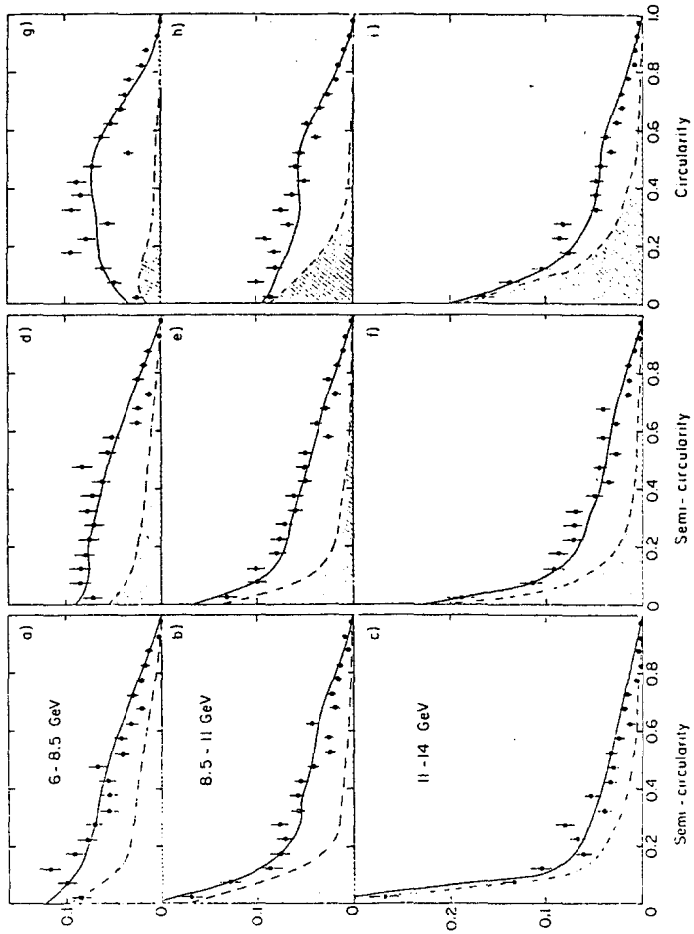


Fig. 14

Circularity (or semi-circularity) for tracks calculated for the different E_T bins: a),d), and g) 6-8.5 GeV;b), e) and h) 8.5-11 GeV; and c), f), and i) 11-14 GeV. The semi-circularity for same side tracks in (a), (b), and (c); the semi-circularity for away side tracks in (d), (e), and (f); and the circularity for the full event in (g), (h), and (i). The curves are the result of a fit to the ISAJET Monte Carlo; shaded regions are two-jet calculations.

References

1. T. Åkesson, M. G. Albrow, S. Almehed, R. Batley, O. Benary, H. Bøggild, O. Botner, H. Brody, V. Burkert, A. Di Ciaccio, D. Cockerill, S. Dagan, E. Dahl-Jensen, I. Dahl-Jensen, G. Damgaard, W. M. Evans, C. W. Fabjan, P. Frandsen, S. Frankel, W. Frati, H. Gordon, A. Hallgren, K. H. Hansen, B. Heck, H. J. Hilke, J. E. Hooper, G. Jarlskog, P. Jeffreys, T. Jensen, G. Kesseler, T. Killian, J. v.d. Lans, D. Lissauer, B. Lörstad, T. Ludlam, N. A. McCubbin, U. Mjörnmark, R. Møller, W. Molzon, B. S. Nielsen, A. Nilsson, L. H. Olsen, Y. Oren, L. Rosselet, E. Rosso, R. H. Schindler, B. Schistad, I. Stumer, E. Vella, W. J. Willis, M. Winik, W. Witzeling, and C. Woody.
2. J. D. Bjorken, Phys. Rev. D8 (1973) 4098; W. Ochs and L. Stodolsky, Phys. Lett. 69B (1977) 225; J. H. Cobb et al., Phys. Rev. Lett. 40 (1978) 1420; W. Ochs, Physica Scripta 19 (1979) 127.
3. See for example: C. Bromberg et al., Phys. Rev. Lett. 38 (1977) 1447; M. Corcoran et al., Phys. Rev. D21 (1980) 641; B. Brown et al., Fermilab-Conf. 82/34-exp.; C. de Marzo et al., Phys. Lett. 112B (1982) 173.
4. H. U. Bengtsson and T. Åkesson, contributed paper to the 21st International Conference on High Energy Physics, Paris (1982). R. D. Field, G. C. Fox, R. L. Kelly, preprint CALT 68-927 (1982).
5. O. Botner et al., Nucl. Instrum. Methods 196 (1982) 315; O. Botner et al., IEEE Trans Nucl. Science, Vol. NS-28 No. 1 (1981) 510; C. W. Fabjan et al., Nuclear Instrum. Methods 141 (1977) 61.
6. A computer model [O. Benary et al., BNL Internal Report 0G-613 (1981) and CERN Internal Report R607/313] was used to simulate the energy deposition of different species of particles. For both electromagnetic and hadronic showers, we have used the mean longitudinal parametrization suggested by R. Bock et al. [CERN EP/80-206 (1980)]. Since this originated from a

coarser calorimeter, special precautions were taken to ensure linearity for hadrons below 3 GeV and photons below 0.5 GeV. Each hadronic shower is divided into two components, pure electromagnetic and pure hadronic. For the lateral development of the showers we have used a two-dimensional Gaussian form where the variance was taken as one half of one "equivalent absorption (radiation) length" for hadrons (photons). This is 24 cm and 1.2 cm, respectively. The hadronic width is allowed to increase with depth. The magnetic field, minimum-ionization energy loss of charged particles, depth of interaction point, particle decays, WLS readout, light-coupling between towers, and the electromagnetic to hadronic energy response and resolutions were incorporated. These parameters were compared with beam test results and adjusted accordingly.

7. F. E. Paige and S. D. Protopropescue, ISAJET: A Monte Carlo Generator for pp and $\bar{p}p$ interactions, BNL 29777 (1980). Jet production cross-sections are calculated using standard QCD perturbation theory in the leading log appoximation. The jet production and fragmentation are decoupled. The coupling constant used is

$$\alpha_s(Q^2) = 1/B \ln(Q^2/\Lambda^2)$$

$$B = (33 - 2f)/12$$

where f is the number of quark flavors with $M_q < Q$ and $\Lambda = 0.1 GeV$. The effective Q, which must be of the order of the transverse momentum involved, was chosen as [R. Feynman, R. Field, G. Fox, Phys. Rev. D18 (1978) 3320]: $Q^2 = 2\hat{s}\hat{t}\hat{u}/(\hat{s}^2 + \hat{t}^2 + \hat{u}^2)$, where $\hat{s}$, $\hat{t}$, $\hat{u}$ are the standard invariants of the elementary scattering process. The partons are u, d, s, and g. The structure functions of Baier et al. [Z. Phys. C2 (1979) 265] are used. The program produces two high $p_\perp$ jets and two spectator jets. In this analysis, the partons are given primordial k_T of 0.88 GeV (FWHM). In the fragmentation process, high $p_\perp$ partons may emit hard gluons. The value of $\sigma(q_T)$ = 0.35 GeV was chosen both for the high $p_\perp$ and spectator jets. The light-quark jets reproduce properly the data observed in jet production in e^+e^- interactions at PEP/PETRA.

8. By "minimum-bias" event we refer to any inelastic strong interaction leading to multi-particle production at low transverse momentum. ISAJET is also used to generate these events with no explicit high $p_\perp$ fragmentation component. The program uses a simplified version of the cut-reggeon field theory of Abramovskii, Kanchelli, and Gribov [Sov. J. Nucl. Phys. 18 (1974) 308]. A leading baryon is generated and the remaining energy is divided among several "cut pomerons," which fragment into hadrons using the modified Field-Feynman [Nucl. Phys. B136 (1978) 1] ansatz. Short range rapidity correlations are introduced through resonances. The multi-pomeron technique approximates well KNO Scaling and is tuned to reproduce the observed multiplicities at the ISR and SPS-collider. Higher multiplicities can be forced by selecting a large number of cut pomerons.

9. J. F. Owens and E. Reya, Phys. Rev. D17 (1978) 3003.

10. C. Kourkoumelis et al., Z. Phys. C5 (1980) 95.

11. H. Gordon et al., Nucl. Instrum. Methods 196 (1982) 303; D. Cockerill et al., Nucl. Instrum. Methods 176 (1980) 159.

12. A. L. S. Angelis et al., Phys. Scripta 19 (1979) 116; C. Kourkoumelis et al., Nucl. Phys. B158 (1979) 39; For example G. Wolf et al., Proceedings of the 1979 International Symposium on Lepton and Photon Interactions at High Energies (Fermilab, 1979) p. 34.

13. For example, J. H. Cobb et al., Phys. Rev. Lett. 40 (1978) 1420; C. Bromberg et al., Phys. Rev. Lett. 38 (1977) 1447.

QUARK AND GLUON JETS FROM THE SPLIT FIELD MAGNET DETECTOR AT THE ISR

CERN-Dortmund-Heidelberg-Warsaw Collaboration(*)
presented by W.M. Geist

ABSTRACT

Events are analyzed in which a single identified hadron ($\pi^{\pm}$, $K^{\pm}$) with high transverse momentum is produced at a polar angle of about 50°. These events show a prominent, coplanar 4-jet structure. Detailed measurements of the momentum and quantum number structure of the jets and of correlations among them are presented. The data allow the determination in a model independent way of the quark or gluon origin of both sideways jets. When confronting the data with predictions from lowest order QCD remarkable agreement is found, e.g., scalar gluons are ruled out. It turns out that experiments of this type can contribute significantly to an experimental study of the triple gluon vertex.

The experiment was performed at $\sqrt{s}$ = 62 GeV and 44 GeV using the Split Field Magnet detector.

Invited Talk presented at the Summer Institute on Particle Physics
Stanford 1982

(*) Members of the CDHW Collaboration are: C.D. Buchanan, K. Doroba, D. Drijard, A. Firestone, H.G. Fischer, H. Frehse, W. Geist, R. Gokieli, P. Hanke, M. Heiden, W. Herr, W. Hofmann, P.G. Innocenti, E.E. Kluge, J.W. Lamsa, T. Lohse, W.T. Meyer, T. Nakada, M. Panter, A. Putzer, K. Rauschnabel, R. Sosnowski, J. Spahn, J. Spengler, O. Ullaland and D. Wegener.

© W.M. Geist 1982

1. INTRODUCTION

Experiments dealing with high transverse momentum phenomena in hadron-hadron collisions aim at a measurement of parton-parton scattering. Recently it has become clear that events triggered by a single identified meson with high transverse momentum provide the cleanest testing ground for these ideas on a quantitative level [1].

The experiment presented here is based upon this concept. It makes use of a single hadron trigger at the Split Field Magnet detector (SFM). Fig. 1 shows the top view of the upgraded SFM, a spectrometer consisting of many multiwire chambers [2] which measure momenta of charged particles in almost the full solid angle. The shaded areas (at polar angles θ of about 50° relative to the beams) indicate the geometrical acceptance of the three-level trigger scheme [3] for single hadrons (T) of transverse momenta $p_T^T \gtrsim 3.5$ GeV/c(*). Atmospheric Cerenkov counters covering the trigger region separate pions from heavier particles (65% K^+/35% p and 90% K^-/10% $\bar{p}$ for the two charges). The detector is surrounded by a time-of-flight system (TOF) for particle identification, a liquid argon calorimeter (LAR) for π^0 detection at $\theta \gtrsim 270°$ [4] completes the set-up. At an energy of $\sqrt{s}$ = 62 (44) GeV a total of 10^7 ($3 * 10^6$) triggers were taken; so far about $110 * 10^3$ ($20 * 10^3$) events with $p_T^T \geq 4$ GeV are fully reconstructed.

The data and all model predictions shown are preliminary; the data are, however, acceptance corrected if the acceptance was smaller than about 85%. If not explicitly stated otherwise only events with $p_T^T \geq 4$ GeV/c taken at $\sqrt{s}$ = 62 GeV are studied.

2. FOUR-JET STRUCTURE

It goes without saying that, given a detector with good acceptance for the full phase space, event topologies can be well measured. Fig. 2 displays, for high p_T^T events at $\sqrt{s}$ = 62 GeV, the

(*) The superscript T is dropped for inclusive distributions.

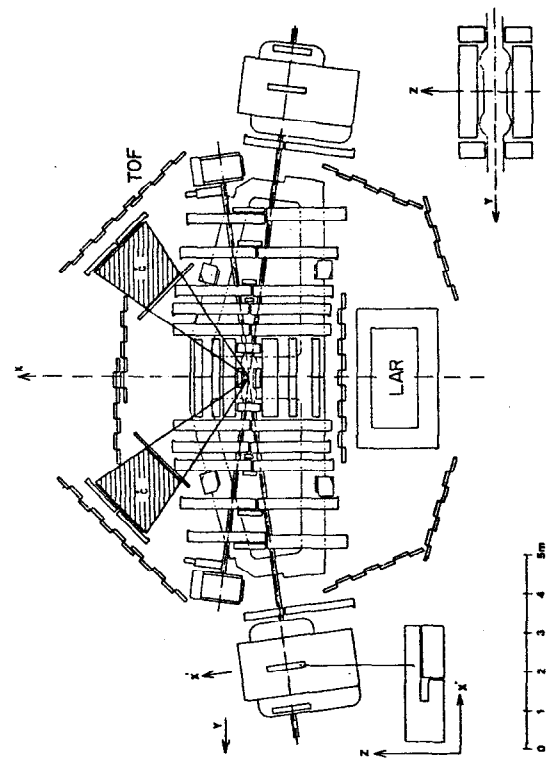


Fig. 1 Top view of the Split Field Magnet Detector.

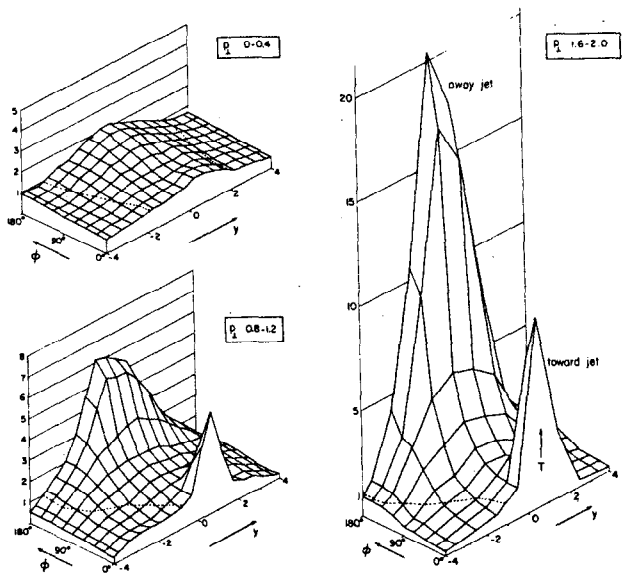


Fig. 2 Density of particles in high transverse momentum events (p_T^T > 4 GeV/c, $\sqrt{s}$ = 62 GeV) relative to density from normal inelastic collisions for three intervals of the secondaries' transverse momenta p_T.

density of charged secondaries (excluding the non-identified trigger) relative to the particle density from normal inelastic collisions at the same energy. The ratio is shown as function of the c.m.s. rapidity y and of the azimuthal angle ϕ about the beam axis for three intervals of the secondaries' transverse momentum PT. For p_T > 0.4 GeV/c one observes two maxima at $\phi \lesssim 0°$ and $\phi \lesssim 180°$ reflecting abundant production of secondaries collimated around a common axis, i.e., of particle jets. The "toward jet" is lined up with the trigger at $\phi = 0°$ and the wider "away jet" recoils in a coplanar configuration at $\phi \lesssim 180°$. The relative particle yield in both jets increases strongly with P_T indicating a substantial "hard" component in these jets.

The rapidity distributions for secondaries with P_T > 1 GeV/c emitted into the "toward" azimuthal wedge ($\phi = 0° \pm 25°$) and into the "away" wedge ($\phi = 180° \pm 25°$) are shown in fig. 3(a) for non-identified triggers at different values of p_T^T. In the toward region one finds the marked correlation pattern of the toward jet. The particle density in the wider away jets increases strongly with P_T^T and becomes more asymmetric around y = 0. The latter trends are not only a consequence of "just kinematics." This is proven by fig. 3(b) which shows, for the away wedge, a non-zero difference between particle densities associated with π^+ and K^- triggers. Since energy-momentum conservation should be independent of the trigger's flavour the observed difference must reflect dynamics (see also sect. 5).

Whereas the production of sideways jets is convincingly demonstrated by figs 2 and 3 the existence of jets along the beam direction is not obvious from these data. To visualize the 4-jet structure of the events analyzed here a scaled momentum flow F(θ) is introduced: $F(\theta) = Q(\theta)/\langle q(\theta)\rangle^{IN}$, $q(\theta)$ is the momentum

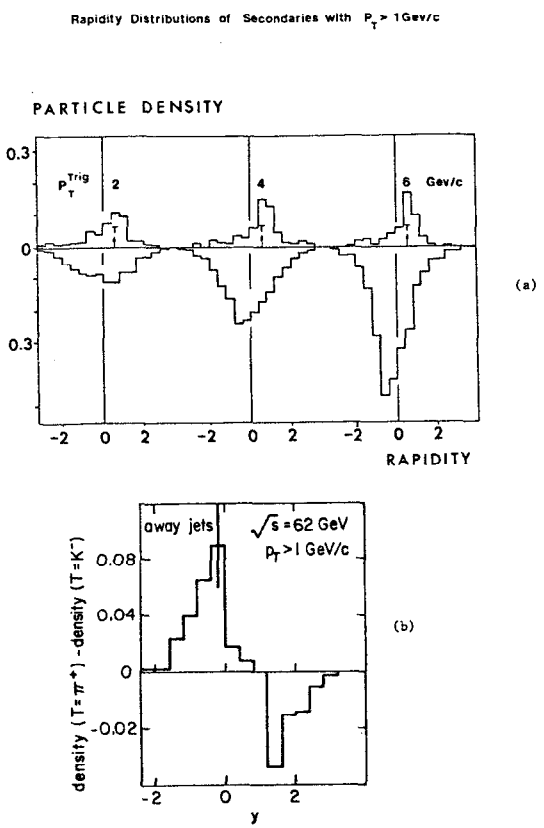


Fig. 3 (a) Rapidity distribution for toward and away wedges as function of p_T^T for secondaries with $p_T > 1$ GeV/c. The rapidity of the trigger is indicated by an arrow.

(b) Difference between π^+ and K^- triggers of rapidity distributions in the away wedge.

projected onto the scattering plane(*) of a single particle produced at θ and $Q(\theta)$ is the sum over $q(\theta)$ in a given bin of θ excluding the trigger. The factor $\langle q(\theta)\rangle^{IN}$, the average of $q(\theta)$ over all inelastic events, was chosen in order to remove the effect of two different momentum scales - transverse and longitudinal - encountered in hadronic interactions. The pattern of $F(\theta)$ is displayed in arbitrary units in fig. 4(a) for events triggered by non-identified hadrons with $p_T^T \geq 6$ GeV/c and in fig. 4(b) for normal inelastic events. Fig. 4(a) shows (a) clustering around the trigger direction, i.e., the toward jet, (b) two "spectator" jets along the beam direction (at $\theta = 0° \pm 15°$ and $\theta = 180° \pm 15°$) similar to those in fig. 4(b), and (c) a prominent structure between $\theta \gtrsim 200°$ and $\theta \lesssim 340°$ due to away jets. It is common to figs 2, 3(a) and 4(a) that the distribution of particles produced at $\phi \gtrsim 180°$ (or $\theta > 180°$) is much wider in terms of y (or θ) than the narrow toward jet. This asymmetric behaviour is explained on the basis of figs 4(c,d) where scaled momentum flows are shown for events with $p_T^T \geq 4$ GeV/c and with a secondary trigger particle with transverse momentum larger than 2 GeV/c (excluded from $F(\theta)$) at either $\theta \gtrsim 245°$ or $\theta \lesssim 295°$. In both cases one now finds in addition narrow jets along the secondary trigger. Hence the wide enhancement in fig. 4(a) is a superposition of narrow jets emitted at varying polar angles [5].

Independent evidence for a 4-jet topology is derived from the dependence of the charged multiplicity of the full event on p_T^T. Fig. 5 shows that the measured multiplicity of charged hadrons, corrected for decays of neutral particles and for losses, increases strongly with p_T^T up to about 3.0 GeV/c with little change at larger p_T^T. This can qualitatively be understood as follows: the multiplicity of the sideways jets is expected to increase with p_T^T (i.e., with jet energy) similarly to jets from e^+e^- collisions. On the other hand the multiplicity of the spectator jets decreases due to the reduced energy available - as it has been found in Drell-Yan

(*) The scattering plane is defined by the direction of the trigger and the beam axis.

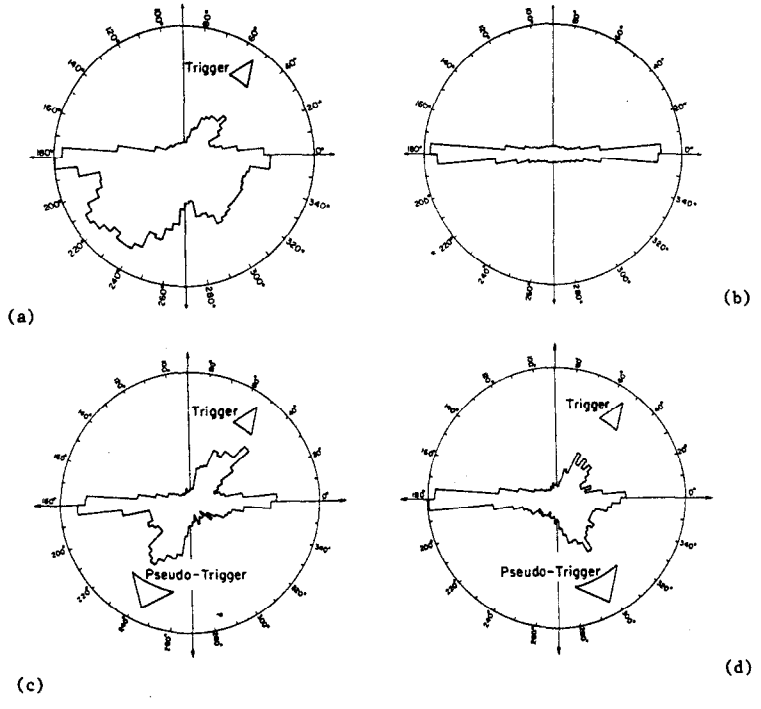


Fig. 4 (a) Scaled momentum flow as function of polar angle for events with $p_T^T > 6$ GeV/c.

(b) Same as (a) but for normal inelastic events.

(c) Same as (a) but for $p_T^T > 4$ GeV/c and a back-to-back pseudotrigger with $p_T > 2$ GeV/c.

(d) Same as (c) but for a back-to-antiback pseudotrigger.

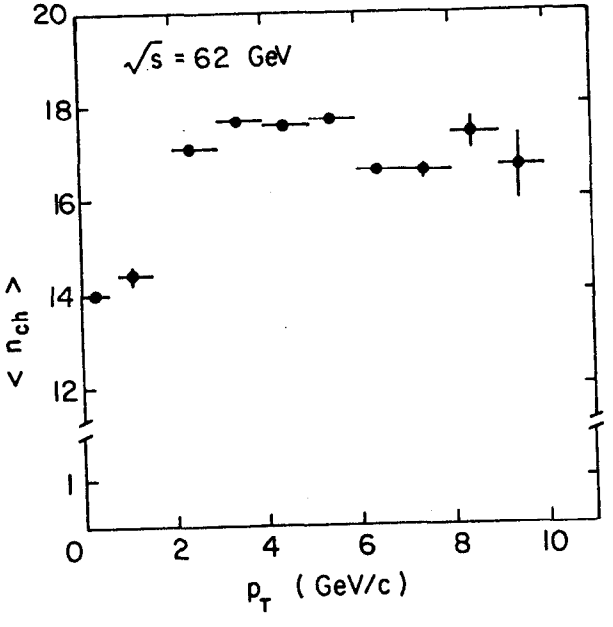


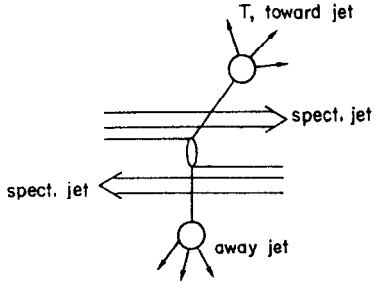
Fig. 5 Corrected charged multiplicity $\langle n_{ch} \rangle$ as function of p_T^T (trigger not identified); the systematic error of ∿ 0.6 is not shown.

processes [6] - such that the total multiplicity becomes approximately independent of p_T^T. More detailed calculations confirm this interpretation [7,8].

3. THEORETICAL FRAMEWORK

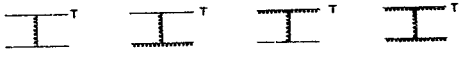
3.1 Hard scattering and QCD

Rather large cross sections for meson production at high transverse momentum in hadron-hadron collisions are expected from hard scattering of partons. Fragmentation of the scattered partons gives rise to the toward jet including the trigger particle and to the away jet as shown in the diagram below:



While the direction of the toward jet is determined to a large extent by the trigger T, the angular dependence of away jet production reflects the shape of the matrix element for parton-parton scattering.

The non-interacting hadron constituents fragment into jets preserving the beam direction (spectator jets). Thus the 4-jet structure presented in the previous section is explained and turns out to be a consequence of the compositeness of hadrons. The manifold pattern renders the interpretation of measurements more difficult as compared to e.g. e^+e^- collisions. This drawback is, however, overcompensated by the fact that only hadron collisions are a laboratory for gluon scattering: in the diagrams below the most important QCD subprocesses for hard scattering of quarks (——) and gluons (∿∿) are given:



One realizes the unique situation that gluons show up in the Born term via the triple gluon vertex as a consequence of the non-abelian nature of QCD.

A Monte Carlo program was set up [9] to compare the data with detailed predictions based upon lowest order QCD. Its basic ingredients are outlined in the Appendix; more details are given in ref. [9]. To illustrate more global predictions the calculated inclusive cross section for $\pi^{\pm}$ production at $\sqrt{s}$ = 62 GeV and 44 GeV are shown in fig. 6 (solid lines) together with the measurements [3,10]. There is remarkable agreement within a factor of $\lesssim 3$ for $p_T^T \gtrsim 4$ GeV/c and nearly perfect agreement for $p_T^T \geq 6$ GeV/c. However, better precision on the input to the simulation program is needed before drawing safe conclusions. It is nevertheless interesting to point out that these QCD calculations contain a large contribution from gluons in addition to quarks (dashed line) - mainly via the triple gluon vertex. Very good agreement is also obtained for the inclusive particle ratios [3] at $\sqrt{s}$ = 62 GeV/c as exemplified by the dependence on p_T^T of the fraction of π^- among negative particles in fig. 6(c).

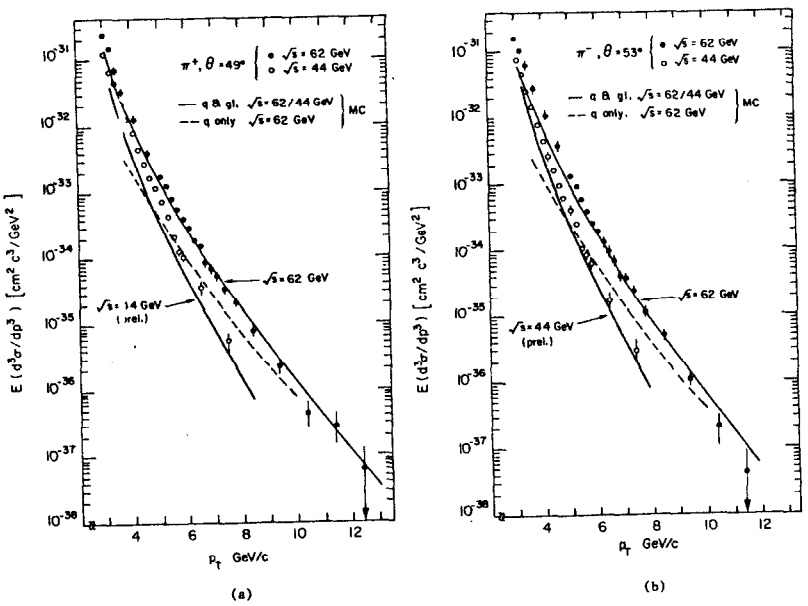


Fig. 6 Invariant cross section for inclusive π^+ (a) and π^- (b) production at $\sqrt{s}$ = 62 (●) and 44 GeV (○). The solid lines are QCD predictions and the dashed line shows the contribution of quarks alone.

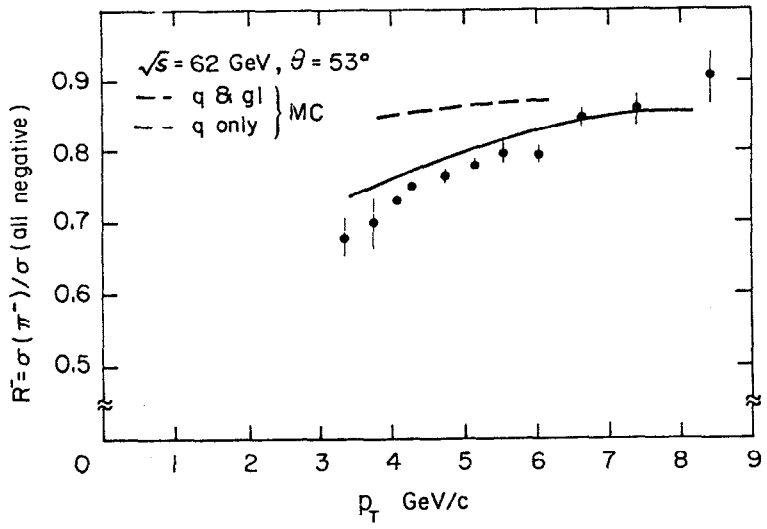
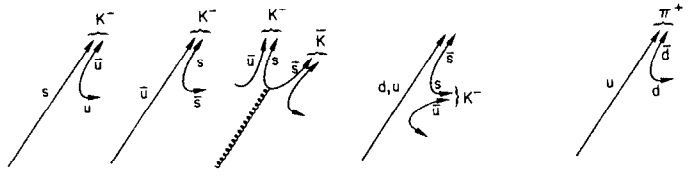


Fig. 6(c) Fraction of π^- among negative secondaries.

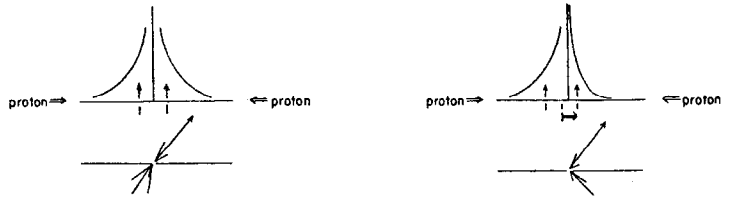
3.2 The origin of mesons with high transverse momentum

One may anticipate that the triggering particle carries most of the energy of the scattered parton and therefore reflects its identity to a certain degree. In the following the most plausible sources for triggering π^+ (= $u\bar{d}$) and K^- (= $s\bar{u}$) are discussed: obviously mesons at high p_T^T could be due to scattered sea quarks; two examples for K^- production are sketched below. Positive pions can furthermore be produced as leading particles from u-quark fragmentation à la Field-Feynman [11] (see below), whereas K^- triggers do not contain any valence quark of the proton, such that they may only be second generation hadrons from valence quark fragmentation. Both K^- and π^+ can, finally, be produced by gluon fragmentation. This implies a short range compensation of quantum numbers, e.g., of charge or strangeness as indicated below for K^- production:



3.3 Kinematics and the away jet

The influence of parton-parton kinematics on the configuration of sideways jets is outlined in the diagram below:



Colliding quarks have approximately equal and opposite momenta in the proton-proton rest system before and after the interaction. A trigger particle at $\theta \neq 90°$ therefore forces the momentum of the away jet to line up with the trigger direction ("back-to-back" configuration). In the case of quark scattering off a parton with a "softer" structure function, e.g., like a gluon, the parton-parton rest system moves relative to the overall c.m.s. system such that both the toward and the away jet populate more often the same longitudinal hemisphere in the proton-proton c.m.s. ("back-to-antiback" configuration). Hence triggering off 90° offers a way to enrich away jets of a certain type on kinematical grounds.

Away jets due to gluons are neutral objects. From gluon exchange one expects that the average away jet due to valence quarks carries net positive charge since the gluon couples equally to u and d quarks such that for away jets u : d $\approx$ 2 : 1 as in the incident proton.

4. TOWARD JETS: STRUCTURE AND ORIGIN

In sect. 2 jet-like clustering of secondaries about the trigger direction was found. It is of interest to compare these jets to the ones obtained from e^+e^- collisions. In order to do so the distribution of the secondaries' transverse momenta p_{TJ} relative to their average direction was measured for the toward jet [12]. The distribution is of exponential shape with $\langle p_{TJ} \rangle \approx 0.45$ GeV/c (not shown) as in e^+e^- reactions [13]. This quantity determines, of course, the width of the toward rapidity distribution in fig. 3(a).

For a more detailed study of toward jets a fragmentation variable z_F is defined by $z_F = \vec{p}^s \cdot \vec{p}^T/|\vec{p}^T|$, where $\vec{p}^s$ and $\vec{p}^T$ are the momenta of a secondary in the toward jet and of the trigger particle. Fig. 7(a) shows the normalized distribution in z_F of

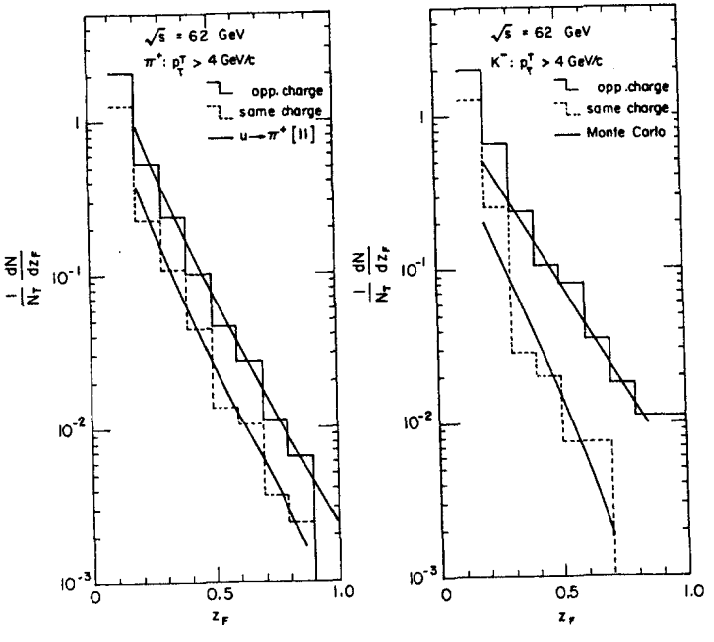


Fig. 7 (a) Normalized toward z_F distribution for negative and positive secondaries accompanying a π^+ trigger. The solid lines come from a fit of a model of u-quark fragmentation.

(b) Normalized toward z_F distributions for positive and negative secondaries accompanying a K^- trigger. The solid lines are QCD predictions.

secondaries with positive and negative charges for π^+ triggers. In order to minimize contributions from a background due to the fragments from the nearby spectator jet only secondaries with $\theta > \bar{\theta}_s$ were entered; $\bar{\theta}_s$ is the polar angle of the average total momentum of toward secondaries with $z_F \gtrsim .2$ [12]. A correction factor of 2 was applied since the jets are supposed to be symmetric about their axis. The remaining background is negligible for $z_F > 0.2$. The particle density in fig. 7(a) decreases strongly with z_F, but there is still a substantial number of secondaries with $z_F > 0.5$. This implies that p_T^T is often much smaller than the toward jet momentum as expected from parton models [7]. For all values of z_F there are more negative ("opposite charge") than positive ("same charge") secondaries compensating the trigger charge (R(opp./same) $\gtrsim$ 2.3 for $z_F > 0.3$). These data are now used to test a fragmentation model [11] in some detail: the upper solid line in fig. 7(a) reproduces the result from a fit of the model for u-quark fragmentation to the distribution of negative secondaries. The only free parameter of the fit is the average jet energy E. With E thus determined the distribution of positives can be predicted (lower solid line). Since the model fits the data well the value of E obtained is probably a reliable estimate of the jet energy. From E and p_T^T one calculates $\langle z_{TR} \rangle = \langle p_T^T/E \rangle$, the average fraction of the jet energy transferred to the triggering hadron. The dependence of $\langle z_{TR} \rangle$ on $x_T = 2 \cdot p_T^T/\sqrt{s}$ is given in fig. 8 for $\sqrt{s}$ = 62 GeV and 44 GeV averaged over all trigger flavours [14]: $\langle z_{TR} \rangle$ scales and rises from about 0.73 at $x_T \gtrsim 0.1$ to 0.82 at $x_T \gtrsim 0.3$ in reasonable agreement with our QCD prediction (solid line). A determination of $\langle z_{TR} \rangle$ for individual trigger flavours and from a measurement of E using all toward jet tracks yields comparable results within the systematic error of 0.05.

For these values of $\langle z_{TR} \rangle$ the triggering particle should "remember" the flavour of the parent parton.

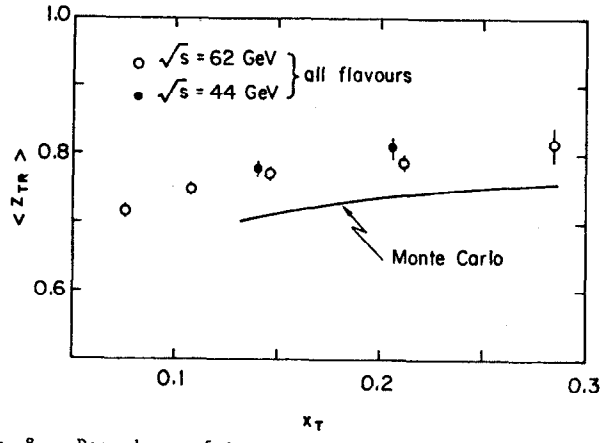


Fig. 8 Dependence of $\langle z_{TR} \rangle$ on x_T for data obtained at $\sqrt{s}$ = 62 GeV and 44 GeV and a QCD prediction.

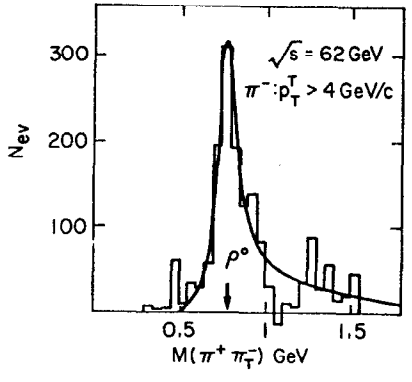


Fig. 9 Effective mass distribution (background subtracted) for $\pi^+\pi^-$-pairs, where π^- is the trigger particle with $p_T^T > 4$ GeV/c. A Breit-Wigner function is superimposed.

This is only true, however, if there is no abundant resonance production which may give rise to e.g. π^+ production at high p_T^T via the process $d \to \rho^0 \to \pi^+$. To resolve this problem a background subtracted effective mass distribution for $\pi^-\pi^+$ pairs including the π^- trigger is shown in fig. 9, a Breit-Wigner function (solid line) is superimposed and reproduces the data well. From the measured ρ^0 signal one estimates that only about 5% of all pion triggers come from ρ decays. This is consistent with $d\sigma(\rho^0)/d\sigma(\pi^-) \approx 1.3$ at $p_T \gtrsim 4$ GeV/c since only a few very asymmetric ρ^0 decays yield a pion with rather high transverse momentum. Measurements on resonance production at high transverse momentum will [1(b)] give valuable information on parton fragmentation into leading resonances.

So far the data suggest that π^+ (π^-, data [1(b)] not shown) production at high p_T^T is dominated by u (d)-quark fragmentation. This is finally confirmed by fig. 10 which shows the relative density of positive and negative particles from spectator jets for π^+ and π^- triggers as function of the Feynman variable x_F. For $x_F < 0$ there is no dependence on the trigger flavour, as expected from gluon exchange. On the other hand there is an excess for $x_F > 0$ of positive particles accompanying π^- triggers and of negatives associated with π^+ triggers. This is a long range correlation, not the familiar short range ($\Delta x \approx 0.1$) compensation of charge. It excludes large contributions from sea-quarks and/or gluons to both π^+ and π^- production, for which all ratios should be unity (except for short range charge conservation). This conclusion is also supported by the measured inclusive π^+/π^- ratio [3] which is significantly different from unity and reflects the relative shape of u- and d-quark structure functions.

The origin of π^+ triggers being established these data are used as a reference for an analysis of K^- production. Fig. 7(b) shows the normalized z_F distributions for K^- triggers in analogy to fig. 7(a): for K^- triggers the ratio R(opp./same) (≈ 8.6 for

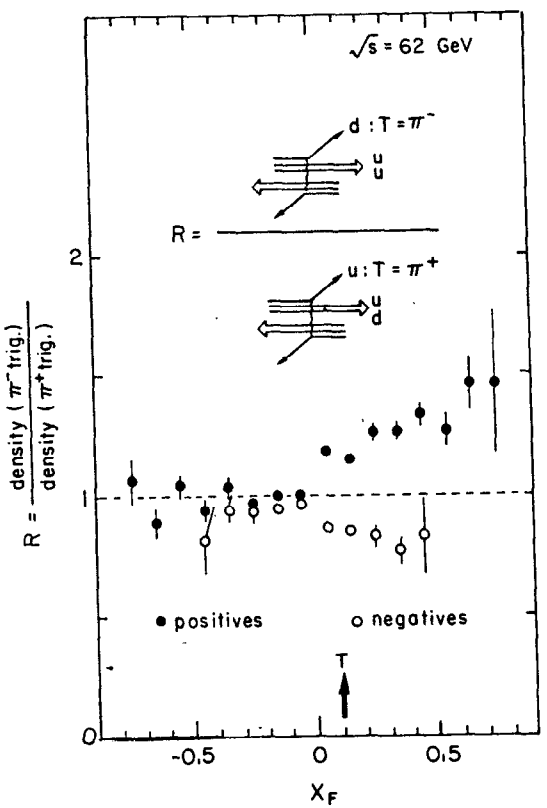


Fig. 10 Relative densities of positive and negative secondaries associated with π^- and π^+ trigger with $p_T^T > 4$ GeV/c as function of x_F.

$z_F > 0.3$) is much larger than for π^+ triggers proving that there is a stronger compensation of the trigger charge, or, in other words, the triggering K^- and its associated toward jet come from a more neutral parton. The same trend is, however, predicted for valence quarks fragmenting into second generation K^- [11]. The solid lines in fig. 7(b) show QCD predictions for the charge structure of toward jets associated with triggering K^-. The data are well reproduced by the model in which gluons dominate K^- production. The differences found in fig. 7 for π^+ and K^- triggers rule out K^- as fragments of $\bar{u}$-quarks for which $R(\text{opp./same})_{K^-} = R(\text{opp./same})_{\pi^+}$ should hold.

A measurement of K^0_s production in toward jets gives a much bigger yield (factor 2) for K triggers than for pion triggers (not shown, [15]). This corresponds to strong local compensation of strangeness for K^- triggers. Jets due to s^-quarks do carry strangeness, therefore also this potential source of K^- production can be discarded.

The data presented in this section imply that pions at high p_T^T are predominantly leading fragments of valence quarks. K^- triggers turn out not to be leading fragments of s^- and $\bar{u}$-quarks. Other sea-quarks should even contribute less to K^- production since they cannot fragment into leading K^-. Hence the only remaining partons that could dominate K^- production at high p_T^T are, so far, valence quarks and partons without net charge and without net strangeness.

5. AWAY JETS: STRUCTURE AND ORIGIN

A measurement of the longitudinal structure of away jets is displayed in fig. 11 for π^+ triggers: the normalized distribution of charged particles in the away wedge is given as function of a scaling variable $x_E = p_T/p_T^T$. The knowledge of $\langle z_{TR} \rangle$ (sect. 4) makes it possible to also show the dependence on $x_E' = x_E \cdot \langle z_{TR} \rangle$; for an exact balance of the transverse momenta of both sideways jets, x_E'

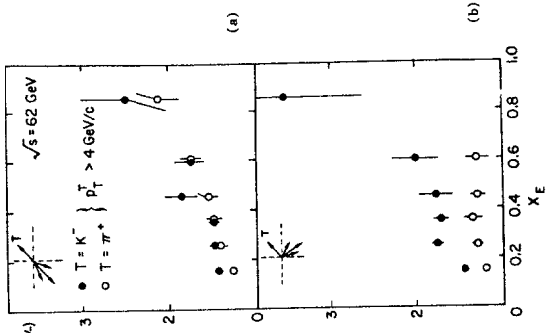


Fig. 12

(a) Ratio of positve to negative away secondaries as function of x_E for the back-to-back configuration for K^- (●) and π^+ (○) triggers.
(b) Sames as (a) but for the back-to-antiback configuration.

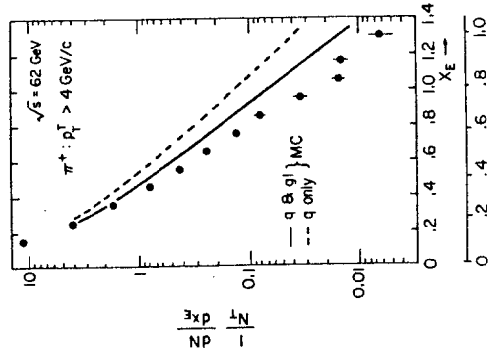


Fig. 11

Normalized away x_E (x_E') distribution for π^+ triggers with $p_T^T > 4$ GeV/c. The solid line is a QCD prediction, the dashed line neglects the gluon contributions.

approximates the fraction of the away jet's energy transferred to a single particle. The data presented in fig. 11 cover three orders of magnitude up to $x_E' \gtrsim 1.0$. The shape of the distribution is similar to the fragmentation function derived from e^+e^- collisions. Reasonable agreement is found with predictions from leading order QCD (solid line): the dashed line emphasizes the need for gluons in the framework of this model as in the case of inclusive spectra (fig. 6).

The measured charge composition in away jets is given in fig. 12 as function of x_E for secondaries with $y < 0$ (back-to-back, see sect. 3.3) and $y > 0$ (back-to-antiback).

The relative production rate of positive and negative secondaries (charge ratio R(+/-)) is significantly different from unity for the back-to-back configuration (fig. 12(a)) both for π^+ and K^- triggers. Above $x_E \gtrsim 0.5$, where the particles reflect the flavour of the parent parton, $R(+/-) \gtrsim 1.5$ is consistent with what one expects from valence quark fragmentation due to more abundant u-quarks.

For π^+ triggers which were shown to come from valence quarks as well (sect. 4), the back-to-back configuration corresponds therefore to the "classical" quark-quark scattering.

The data in fig. 12(b) for the back-to-antiback configuration reveal significant differences between π^+ and K^- triggers. From gluon exchange (sect. 4, fig. 10) one expects, however, identical away jets for all triggers which come from quark fragmentation. Hence a quark origin of K^- triggers is ruled out. The value of the charge ratio in fig. 12(b) for K^- triggers suggests furthermore (see above) that the away jets are due to valence quarks. Dominant contributions from valence quarks in the back-to-antiback configuration indicate, on a kinematical basis (sect. 3.3), that the parton yielding the trigger has a softer structure function than quarks. So the final conclusion is that only soft (relative to quarks) partons that carry neither charge nor strangeness are

left as the dominating source for K^- production at $p_T^T \gtrsim 4$ GeV/c. This also explains the finding that a back-to-antiback configuration occurs more often for K^- than for π^+ triggers (fig. 3(b)). With d-quarks and gluons as the parent partons of π^- and K^- at high p_T^T, respectively, the inclusive ratio of π^- and negative particles ($\gtrsim \pi^- + K^-$) in fig. (8c) is a measure of the relative production rate of d-quarks and gluons. Hence fig. 8(c) shows that gluons are produced at about the predicted relative rate, which is mainly due to diagrams including the triple gluon vertex.

The charge ratio for away jets in the back-to-antiback configuration for π^+ triggers is smaller than that of fig. 12(a) and is consistent with a contribution from fragmenting soft neutral partons.

All measurements presented so far support simple parton ideas or are even in rather remarkable agreement with QCD predictions. This encourages more subtle investigations making explicit use of Monte Carlo calculations. As an example a determination of the gluon spin is described in the following: as mentioned in sect. 3.1 the angular distribution of away jet axes is related to the shape of the matrix element for hard scattering, i.e., the gluon spin [16]. Experimentally, away jet particles with more than about 40% of the away jet momentum ($x_E \geq 0.5$ or $x_E' \gtrsim 0.4$) are used as an approximation of the jet axis. Fig. 13 shows the normalized distribution in rapidity for these particles for π^+ triggers with 4 GeV/c $\leq p_T^T \leq$ 6 GeV/c. The normalization was done such that a comparison with simulations is independent of the predicted rate. The smooth curves are the results of Monte Carlo calculations [16] for scalar and vector gluon exchange. Evidently, scalar gluons are at variance with the data. Reasonable modifications of the ingredients of the Monte Carlo program are, if anything, in favour of vector gluons. The more symmetric rapidity distribution from scalar gluons corresponds to little angular dependence of the

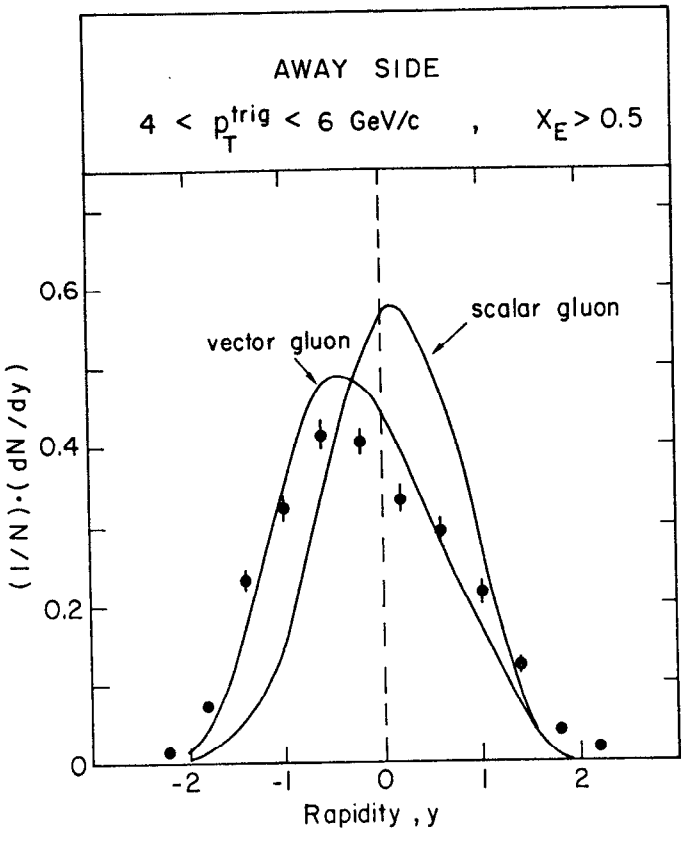


Fig. 13 Rapidity distribution for away secondaries with $x_E > 0.5$ associated with π triggers. The solid lines correspond to predictions for vector and scalar gluons.

matrix elements compared to the Moller-type scattering for vector gluons. Since triple gluon vertices should not exist for scalar gluons, also the measured cross section for K^- production may be taken as evidence against scalar gluons.

6. CONCLUSIONS

A few selected measurements of hard scattering processes in hadronic collisions were presented; they come from a second generation experiment at the Split Field Magnet. The apparatus was triggered by single identified hadrons produced with high transverse momentum at a polar angle of 50°; the events were recorded and reconstructed in almost full solid angle.

The following results were obtained:

(a) The events show a prominent, coplanar four-jet structure: the toward jet associated with the trigger, the recoiling away jet and the two spectator jets along the beam direction. These features are a manifestation of dynamics, not only a simple consequence of momentum conservation.

(b) A measurement of quantum number correlations and of the fraction of the jet energy transferred to the trigger particle shows that $\pi^+(\pi^-)$ triggers are leading fragments of u-(d)-quarks. The data provide detailed tests of fragmentation models.

(c) The correlations between trigger flavours and properties of spectator jets confirm the above interpretation of $\pi^\pm$ production and suggest that there is no flavour exchange in hard processes.

(d) The charge stucture of away jets is different for π^+ and K^- triggers. Together with correlations measured in the toward jet (a) this rules out a quark origin of K^- triggers, but indicates that they are leading fragments of soft flavourless partons.

These conclusions do not depend on any detailed model; in particular, they are independent of Monte Carlo calculations.

(e) Predictions from leading order QCD are in surprising agreement with inclusive and correlation data. In this framework gluons dominate K^- production. A model dependent analysis of away jets shows that gluons have non-zero spin. For vector gluons the triple gluon vertex is expected to give the largest contribution to K^- production and the predicted cross section agrees well with the data.

More details will be obtained from a study of π^0, strange particle and (anti-)baryon production in the sideways jets and from a measurement of dependencies on trigger angle, transverse momentum and primary energy.

The correspondence between the flavour of the trigger (the leading particle in the jet) and the flavour of the parent parton allows for a tagging of various subprocesses on an event-by-event basis by an appropriate choice of the trigger particle, e.g., K^- triggers at moderate transverse momenta enhance toward jets from gluons.

Thus it turns out that experiments using single particle triggers provide a sensitive test for the parton origin of jets. They allow setting experimental bounds on the cross section for parton-parton scattering and on the triple gluon vertex. Especially the ISR is a valuable tool for studies of gluon scattering at high luminosity.

APPENDIX

A Monte Carlo program to predict leading order QCD effects in deep inelastic hadron-hadron scattering:

(a) The incoming partons (quarks and gluons) are described by scaling violating structure functions as derived in [17]; the distribution of the partons' transverse momenta k_T inside the protons is assumed to factorize from the structure function and is given by an exponential distribution in k_T^2 with $\langle k_T \rangle = .85$ GeV/c.

(b) The parton-parton cross sections of [18] were taken; $\alpha_s(Q^2) = \frac{12\pi}{25} [\ln(Q^2/\Lambda^2)]^{-1}$ with $\Lambda = 0.3$ GeV was used and the scale Q^2 was calculated from the Mandelstam variables s, t, u on the parton level: $Q^2 = \frac{2stu}{s^2 + t^2 + u^2}$. Partons are massless.

(c) Parton fragmentation functions D(z) are assumed to factorize from the structure functions. Gluons split [19] into a quark and an antiquark which fragment independently. Scaling violations are predicted by QCD and are introduced into the scheme of [11] by an Q^2 dependent exponent $b(Q^2, Q_0^2)$ [19]:

$$D(z, Q^2) \to (1 - z)^{b(Q^2, Q_0^2)} \quad \text{for } z \to 1,$$

where $Q_0^2 = 4$ GeV^2 and z is the fraction of the parton energy carried by one fragment; $b(Q^2, Q_0^2)$ is different for gluon and quark fragmentation. Transverse momenta q_T of fragments have an exponential distribution in q_T^2 with an average of 323 MeV/c.

More details can be found in [9].

REFERENCES

[1] (a) R.D. Field, G.C. Fox and R.L. Kelly, CALT-68-927;
(b) H.G. Fischer, Rapporteur's talk, Int. Conf. on High Energy Physics, Lisbon, 9-15 July 1981, CERN/EF 81-12.

[2] W. Bell et al., Nucl. Instr. & Meth. 156 (1978) 156.

[3] D. Drijard et al., CERN/EP 82-70, to be published in Nucl. Phys. B.

[4] M. Panter, Ph.D. Thesis, University of Dortmund (1982).

[5] D. Drijard et al., The jet structure of large transverse momentum events in pp interactions, to be published.

[6] D. Antreasyan et al., CERN/EP 81-116.

[7] S.D. Ellis and M.B. Kislinger, Phys. Rev. D9 (1974) 2027.

[8] C. De Marzo et al., MPI-PAE/EXP.EL 105.

[9] T. Lohse, Diploma Thesis, University of Dortmund (1982).

[10] J. Spahn, Ph.D. Thesis, UCLA, 1982.

[11] R.P. Feynman and R.D. Field, Nucl. Phys. B136 (1978) 1.

[12] D. Drijard et al., High p_T hadrons as leading particles in jets: I. Momentum distributions of secondaries in the trigger jet, to be published.

[13] See e.g. P. Duinker, DESY 81-012.

[14] C.D. Buchanan, Comparison of single particle trigger, high p_T results in proton-proton collisions at $\sqrt{s}$ = 45 and 63 GeV, presented at the XVIIth Rencontre de Moriond, Les Arcs, 20-26 March 1982;
D. Drijard et al., High p_T hadrons as leading particles in jets (II), to be published.

[15] K. Rauschnabel, Ph.D. Thesis, Univ. of Dortmund (1982).

[16] D. Drijard et al., Experimental study of parton-parton scattering amplitudes and the spin of the gluon, submitted to the XXI Int. Conf on High Energy Physics, 26-31 July 1982, Paris.

[17] H. Abramowicz et al., Z. Phys. C12 (1982) 289.

[18] B.L. Combridge et al., Phys. Lett. 70B (1977) 234.

[19] G. Altarelli and G. Parisi, Nucl. Phys. B126 (1977) 298.

CU-TP-249

SOFT HADRON PRODUCTION IN QCD JETS

A.H. Mueller

Department of Physics
Columbia University
N.Y.,N.Y. 10027

This research was supported in part by the U.S. Dept. of Energy.

Talk given at the topical conference of the 10th SLAC Summer Institute on Particle Physics, August 1982.

© A. Mueller 1982

Abstract

Soft hadron production, the small x region, in QCD jets is reviewed. The most striking prediction is that there should be no central plateau in the dominant two jet events in e^+e^- annihilation. The $e^{c\sqrt{\ell n Q^2}}$ growth of the average multiplicity is shown not to be affected by the first higher order corrections.

I. Introduction

The most striking success of QCD has been the existence of jets of hadrons. These jets were definitively seen first in e^+e^- collisions and now clean two jet events have appeared from the $\bar{p}p$ collider at CERN. Detailed quantitative predictions of QCD jets are much less certain. It now appears that hadronization effects are both necessary and quite model dependent.[1] All tests of QCD in jet analyses have concentrated on hard hadrons, the soft hadrons furnishing the uncertainties appearing in the various models of hadronization.

In fact it has never been clear whether QCD would be able to make predictions for the slow particles emerging from jets. The issue is, perhaps, still not clear. The leading logarithms for soft particle production have now been completely calculated in the past year,[2,3] and they show a most remarkable result. If one plots $x\frac{d\sigma}{dx}$ versus $\ell n\, 1/x$ as indicated in Fig.1, this cross-section is predicted to peak[4] at $\ell n\, 1/x \approx 1/4\, \ell n\, Q^2/\mu^2$ with a broad dip going down to $\ell n\, 1/x \approx 1/2\, \ell n\, Q^2/\mu^2$. This is a most unexpected result. In hadronic physics we are all familiar with a broad central plateau which slowly rises with energy. The prediction for soft particles coming from genuine QCD jets is that this central plateau becomes a central dip with the typical particle being rather energetic compared to its kinematic limitations.

Unfortunately, there is as yet no systematic procedure for correcting and improving this leading logarithmic result. Ultimately, such a procedure is crucial. However, the first corrections to this leading logarithmic calculation have recently been done[5] and are found not to change the qualitative picture described above. In fact, these corrections are vanishing small at large Q^2.

I think the emergence of this dip at small x in $x\frac{d\sigma}{dx}$ would be a major qualitative success of perturbative QCD. (The quantitative predictions suffer from the usual uncertainties of higher order corrections and hadronization effects.) It is not completely

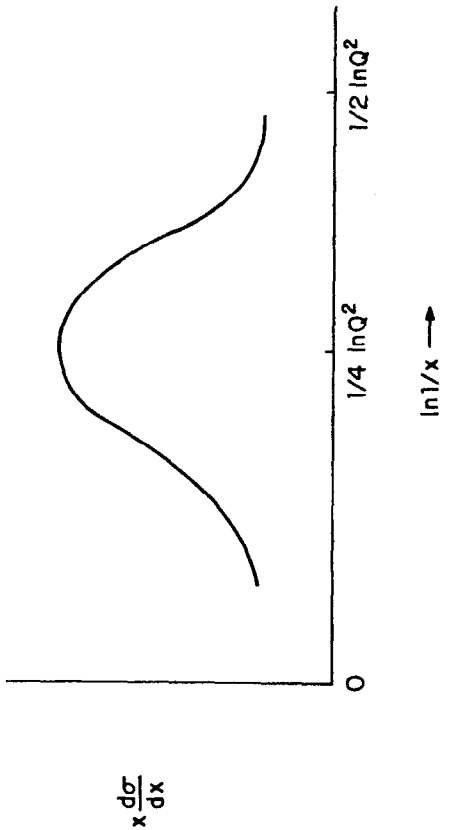


Fig. 1

clear at what energies this dip should appear. It could appear at the highest PETRA and PEP energies. If the dip does not appear at these energies it could be found, perhaps, at the $p\bar{p}$ CERN collider in those events which have clear two jets transverse to the beam directions. It should be clearly visible at the Fermilab collider and at the Stanford single pass collider.

II. The Leading Logarithms

Some years ago there was an intense effort directed at proving factorization for various processes in QCD.[5-9] In the case of e^+e^- annihilation into a hadron carrying a fraction x of its maximum possible momentum, one defines an inclusive cross-section $\frac{d\sigma}{dx}$. Factorization then takes the form

$$Q^2 \int_0^1 \frac{d\sigma}{dx} x^{n-1}\, dx \xrightarrow[Q^2 \to \infty]{} A_n\, E_n(Q^2) \qquad (1)$$

where A_n depends on the details of the produced particle and on non-perturbative effects in general. $E_n(Q^2)$ is calculable from the renormalization group and perturbation theory as

$$E_n(Q^2) = C_n(\alpha(Q^2)) e^{\int_{\mu^2}^{Q^2} \frac{d\lambda^2}{\lambda^2} \gamma_n[g^2(\lambda^2)]} . \qquad (2)$$

After determining γ_n and C_n to some order of perturbation theory, one can attempt to calculate soft particle production in the following manner. A_n reflects the conversion of gluons (We shall suppose that only the small x region is of concern, in which case gluons play the dominant role. In this region the quark distributions simply follow the gluon distributions.) into hadrons. This is a conversion which is not calculable in perturbation theory, however, since only masses of order μ are involved, A_n is regular in n and cannot significantly affect the x distribution of $\frac{d\sigma}{dx}$ at very large Q^2. Thus, we may consider the

problem of the x distribution of gluons of mass μ. For this cross-section we may write

$$x\frac{d\sigma}{dx} = \frac{1}{Q^2}\int_{L-i\infty}^{L+i\infty}\frac{dn}{2\pi i}\, x^{-n+1}\, E_n(Q^2). \qquad (3)$$

When x is small the $x^{-n+1} = e^{-(n-1)\ell n\, 1/x}$ factor in (3) suggests that one distort the contour to the left toward the line $\mathrm{Re}\, n = 1$. However, E_n, as calculated from (2) is singular at the point $n = 1$ in perturbation theory, and for this reason it is not clear whether (3) can be used to obtain the small x region from perturbative QCD calculations.

In order to calculate the small x behavior, a necessary task is to determine the behavior of $\gamma_n(g^2)$ for small g^2 and small n-1. The structure of $\gamma_n(g^2)$ is

$$\gamma_n(g^2) = \sum_{r=1}^{\infty}\alpha^r\sum_{s=1}^{2r} c_{rs}\,\frac{1}{(n-1)^{2r-s}}\,. \qquad (4)$$

All those terms involving $s=1$ we call the leading series. They have the maximum number of powers of $\ell n\, 1/x$ for a given order of α. Those terms with $s = 2$ are called the next to leading series. At the moment we are discussing the leading series, the leading logarithmic approximation. In Section III we shall briefly discuss the next to leading series, which has been calculated. We know of no systematic procedure to calculate c_{rs} for $s \geq 3$.

The pioneering discussions of the small x behavior of $x\frac{d\sigma}{dx}$ were given by Bassetto, Ciafaloni and Marchesini,[10] by Furmanski, Petronzio and Pokorski[11] and by Konishi.[12] These authors evaluated the leading terms for gluon ladders. They found the remarkable result that

$$\gamma_n = \frac{1}{2}\left[-(n-1) + \sqrt{(n-1)^2 + \frac{4\alpha C_A}{\pi}}\,\right]. \qquad (5)$$

That is, the singularities at n-1 have gone away and in their stead γ_n is non-analytic in α at $n=1$.

Although (5) is a correct evaluation of the ladder graphs, it turned out that non-ladder graphs give contributions to the leading logarithms also. These contributions were evaluated explicitly through three loops[13] where the form

$$\gamma_n = \frac{1}{4}\left[-(n-1) + \sqrt{(n-1)^2 + \frac{8\alpha C_A}{\pi}}\,\right] \qquad (6)$$

was suggested. This equation for γ_n was later proved[2] to sum correctly all the leading terms for an arbitrary number of loops. The remarkable feature which arises from this analysis is that it is possible to obtain the correct answer, Eq.6, for the leading terms if one considers only ladder graphs but with a restriction on the regions of phase space[2,13] allowed for the produced gluons. This is a restriction which does not follow from any analysis of the ladder graphs by themselves. The restriction is easy to state. Referring to Fig.2 the restriction is simply that

$$p \ll k_1 \ll k_2 \ldots \ll k_n = Q/2$$

$$\theta(\vec{p},\vec{k}_1) \ll \theta(\vec{k}_1,\vec{k}_2) \ll \theta(\vec{k}_2,\vec{k}_3) \ldots \ll \theta(\vec{k}_{n-1},\vec{k}_n) \qquad (7)$$

in, say the center of mass frame where $q=(Q,0,0,0)$. Thus, the leading logarithms correspond to a branching process where later emissions occur with smaller angles than earlier emissions. The angular ordering given in Eq.7 was found independently by Ermolaev and Fadin.[14]

We may determine the small x behavior for the production of gluons of mass μ in e^+e^- annihilation by substituting (6) into (2) and (3). (It turns out that C_n is finite in the region in question.) One finds that

$$Q^2 x\frac{d\sigma}{dx} = \frac{\mathrm{const}\;\bar{n}(Q^2)\; e^{-3\sqrt{\frac{8C_A}{\pi b}}\;\frac{(\ell n\, 1/x - 1/4\;\ell n\, Q^2/\mu^2)^2}{\ell n^{3/2}\, Q^2/\Lambda^2 - \ell n^{3/2}\,\mu^2/\Lambda^2}}}{\left[\ell n^{3/2}\, Q^2/\Lambda^2 - \ell n^{3/2}\,\mu^2/\Lambda^2\right]^{1/2}} \qquad (8)$$

with

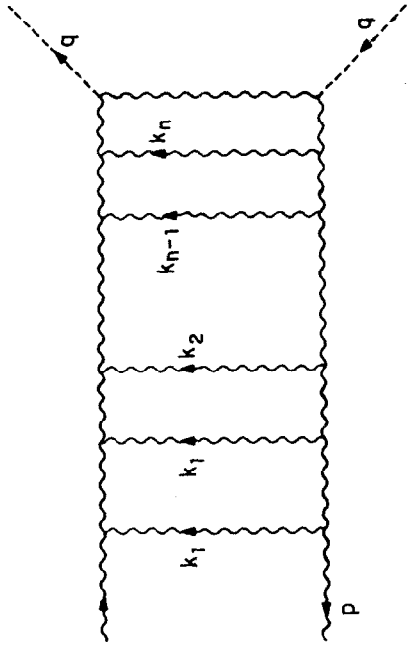


Fig. 2

$$\bar{n}(Q^2) = \text{const. } e^{\sqrt{\frac{2C_A}{\pi b}}\left(\sqrt{\ln Q^2/\Lambda^2} - \sqrt{\ln \mu^2/\Lambda^2}\right)} \quad . \quad (9)$$

The peaking of $x\frac{d\sigma}{dx}$ at $\ln 1/x \approx 1/4 \ln Q^2/\mu^2$ is clearly exhibited by (8). Except for a factor of $1/\sqrt{2}$, (9) is the result found in Refs.10-12. This peaking at $\ln 1/x = 1/4 \ln Q^2/\mu^2$ and the dip for x values much smaller than that value follows from (6) but not from (5). If we had used Eq.5 we would have found a broad maximum centered about $\ln 1/x = 1/2 \ln Q^2$. That is the behavior of a rising central plateau. The behavior exhibited in Eq.8 is thus not a kinematic effect, but rather an effect which occurs only in gauge theories and follows from the emission of soft vector particles from a conserved vector current.

III. Corrections to the Leading Terms

A result for which corrections cannot be computed must be taken with some caution. Ideally, one would like to have a guarantee that (8) and (9) are asymptotic behaviors in QCD for which subdominant terms could be systematically calculated. So far no such procedure has been found, although I think it is likely that a relevant formalism will in time, be found. Lacking a systematic procedure, the next best thing is a brute force calculation of the next to leading terms in (4). This has been done.[5] The resulting anomalous dimension has the form

$$\gamma_n = \gamma_n^{(o)}\left[1 + \frac{c_1\alpha}{\sqrt{(n-1)^2 + \frac{8\alpha C_A}{\pi}}} + \frac{c_2\,\alpha(n-1)}{(n-1)^2 + \frac{8\alpha C_A}{\pi}}\right] + c_3\alpha \ , \quad (10)$$

with $\gamma_n^{(o)}$ being the γ of Eq.6. For α and $(n-1)$ small the corrections are indeed small compared to the leading logarithmic terms. The main effects are a $\ln \ln Q^2/\Lambda^2$ term added to the exponential in (9) and a shift of the peak in the x distribution to

smaller values of x. The explicit form of this shift is given in Ref.5.

IV. Conclusions

The distribution and multiplicity of soft particles produced in QCD jets appears to be very different from that emerging in a hadron-hadron collision without hard scatterings. The most striking effect is the suppression of soft particle production relative to those particles having intermediate energies, $p = 0(\sqrt{Q})$. This suppression follows from the requirement that particles emitted later in the branching process have smaller angles. However, when a particle is almost at rest it requires a large emission angle in order to have a reasonable phase space for production. The only resolution to the simultaneous requirements of both a large and a small emission angle for very soft particles is a suppression of their production. We thus expect the lack of a central plateau to be a very general feature of gauge theories for soft particles emerging from jets. We also strongly feel that soft particle production in non jet events in hadron-hadron collisions is completely different than soft particle production from hard jets. However, once a hard jet is produced the distribution of produced hadrons should not depend on how that jet was produced. Thus $p-\bar{p}$ colliders should be a good place to study jet properties.

We have not at all addressed the question of whether non-perturbative effects might destroy the analysis described above. Presumably, non-perturbative effects should not affect the far off-shell evolution of gluons which leads to (8) and (9), but the situation is not entirely clear. The gluon and quark evolution necessary to get (8) and (9)takes place over a very long time during which color separation might occur. However, color separation is not required to occur since the quark-anti-quark pair initially produced in the e^+e^- annihilation does not play a significant part in the evolution leading to (8) and (9). It has been suggested[15,16] that perturbation theory might already shield the parton evolutions from forming large color fluctuations without the necessity of non-perturbative effects. It is important to extend and clarify this idea. Recent critiques of the purely perturbative approach are given in Refs. 17 and 18.

References

1) See the talk of S.L. Wu at this conference.

2) A. Bassetto, M. Ciafaloni, G. Marchesini and A.H. Mueller (to be published in Nuclear Physics).

3) Yu. L. Dokshitzer, V.S. Fadin and V.A. Khoze, Leningrad preprint (March 1982).

4) A.H. Mueller, in Proceedings of the International Symposium on Lepton and Photon Interactions, Bonn (1981).

5) A.H. Mueller, Columbia University preprint CU-TP-247.

6) R.K. Ellis, H. Georgi, M. Machacek, H.D. Politzer and G.G. Ross, Nucl. Phys. B152 (1979) 285.

7) G. Sterman and S. Libby, Phys. Rev. D18 (1978) 3252.

8) D. Amati, R. Petronzio and G. Veneziano, Nucl. Phys. B140 (1978) 54; B146 (1978) 29.

9) A.H. Mueller, Phys. Rev. D18 (1978) 3705.

10) A. Bassetto, M. Ciafaloni and G. Marchesini, Nucl. Phys. B163 (1980) 477.

11) W. Furmanski, R. Petronzio and S. Pokorski, Nucl. Phys. B155 (1979) 253.

12) K. Konishi, Rutherford Report RL79-035 (1979).

13) A.H. Mueller, Phys. Letters 104B (1981) 161.

14) B.I. Ermolaev and V.S. Fadin, JETP Letters 33 (1981) 269.

15) D. Amati and G. Veneziano, Phys. Letters 83B (1979) 87.

16) Yu. L. Dokshitzer, D.I. Dyakonov and S.I. Troyan, Phys. Reports 58C (1980) 269.

17) S. Gupta and H. Quinn, Phys. Rev. D25 (1982) 838.

18) J.D. Bjorken, Fermilab preprint.

NEUTRINO MASS LIMITS FROM OSCILLATION AND DOUBLE BETA DECAY EXPERIMENTS

F. Boehm

California Institute of Technology, Pasadena, CA 91125

INTRODUCTION

In the framework of grand unified theories the weak interaction states describing physical neutrinos are predicted to be mixed states[1]. If, in addition, finite rest mass is associated with these states, several new phenomena are predicted to occur. Neutrino mixing, including light and heavy neutrinos, can lead to observable effects in weak decays, such as new monochromatic lepton lines. Another consequence is the well known neutrino oscillation process, i.e., the transition from one neutrino type to another. I would like to first review the static aspect of neutrino mixing, its experimental consequences and current results, and then turn to the dynamics of a mixed neutrino system discussing our present knowledge of neutrino oscillations. Finally, I shall discuss the neutrinoless double beta decay, an old field which has reappeared as a powerful and sensitive way of testing lepton non-conservation and neutrino mass.

1. STATIC NEUTRINO MIXING AND HEAVY NEUTRINOS

Following general practice[1] we write the weak-interaction neutrino state $\nu_\ell (\ell = e,\mu,\tau)$ as a superposition of mass-eigenstate neutrinos ν_i $(i = 1,2,3)$,

$$\nu_\ell = \sum_i U_{\ell i} \nu_i . \qquad (1)$$

© F. Boehm 1982

The expansion coefficients $U_{\ell i}$ which are the elements of a unitary matrix represent the mixing amplitudes.

It may be argued that the state ν_ℓ is predominantly composed of a light neutrino ν_1, with small admixtures of one or two heavy neutrinos ν_2 and ν_3, restricting $|U_{\ell_{2,3}}|^2 \ll 1$. As a consequence, there will be a branch proceeding via the heavy neutrino, with branching ratio $B_{\ell i} \approx |U_{\ell i}|^2$. Shrock[2] has pointed out that the two-body decays, K-μν, π-μν, π-eν offer sensitive tests in a search for these branchings. What would be expected is a monochromatic lepton line, due to the decay of the heavy neutrino, at some energy below the regular lepton peak. For example, in the decay $K^+ \to \mu^+\nu$ the muon momentum range between 100 MeV/c and 220 MeV/c was explored[3] with good momentum resolution, and stringent limits could be set for heavy neutrino masses. Figure 1, taken from a recent paper by Yamasaki[3], shows the data from this search. In a similar fashion the decays $\pi \to \mu\nu$[4] and $\pi \to e\nu$[5] were explored spectroscopically. No evidence for heavy neutrinos was seen, and the resulting limits of the branching ratios $B_{\ell i}$ are depicted in Fig. 2.

In nuclear beta decay a heavy neutrino may give rise to a discontinuity or "kink" in the beta spectrum. Shrock[2] has analyzed the existing spectroscopic data finding no evidence for kinks. These results are also shown in Fig. 2. In a similar fashion, by analyzing the ^3H decay spectrum, Simpson[6] finds branching ratios of less than 10^{-3} to 10^{-1} for $m_{\nu\ \text{heavy}}$ of 0.1 to 10 keV.

Another relationship capable of supplying information on branching ratios into heavy neutrinos can be taken from double-beta

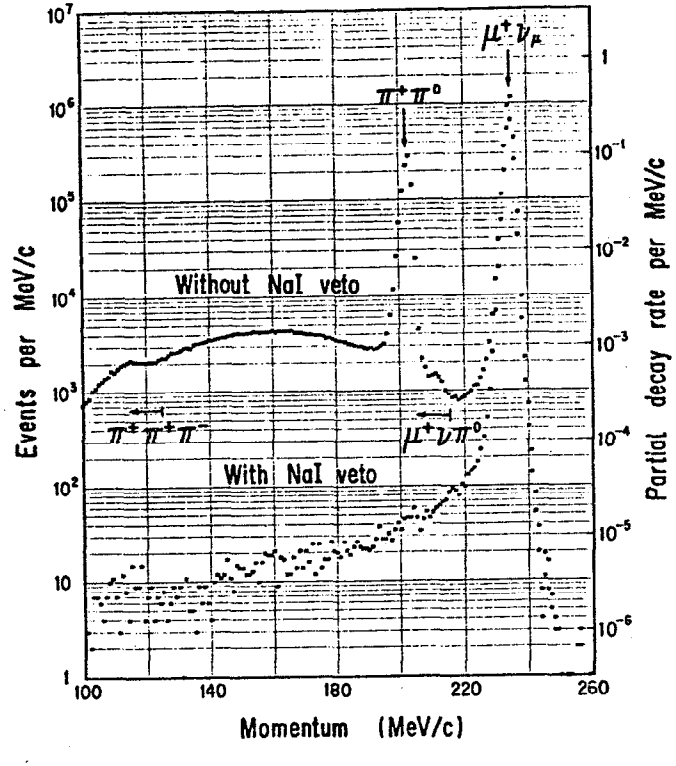


Fig. 1

Momentum spectrum of charged particles from K^+ decay (taken from Ref.3).

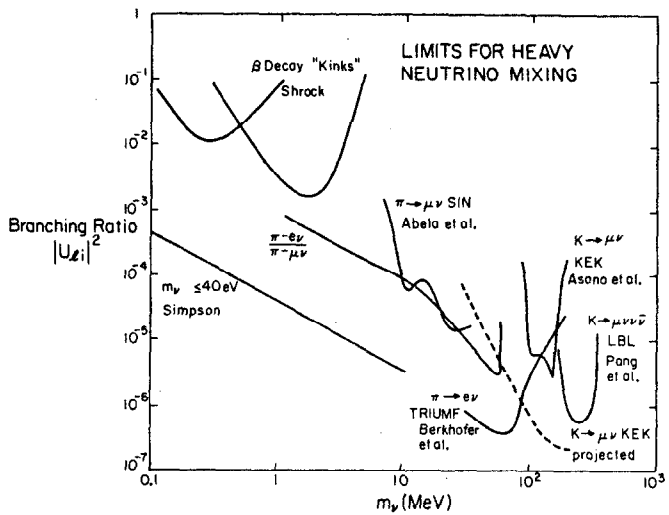


Fig. 2

Limits for branching ratios into heavy neutrino decay as a function of heavy neutrino mass as established from various experiments.

decay. Simpson[7] argues that the mass limit from double-beta decay which is about 10-40 eV (see part 3 of this talk) can be interpreted as an average Majorana mass which for small mixing is given by

$$m_\nu = m_{\nu\,\text{light}} \cos^2\theta + m_{\nu\,\text{heavy}} \sin^2\theta \leq 40 \text{ eV}.$$

With $m_{\nu\,\text{light}} \ll m_{\nu\,\text{heavy}}$ it follows that

$$\sin^2\theta \leq 4 \times 10^{-5}/m_{\nu\,\text{heavy}}\,(\text{MeV}),$$

an argument which holds for $m_\nu < p_\nu$. The resulting limit is also shown in Fig. 2.

Other limitations shown in Fig. 2 were derived from branching ratios and are quoted in Refs. 2 and 8. We conclude that there is no evidence for heavy neutrinos that have masses between 10^{-1} and 10^3 MeV, with branching ratios larger than 10^{-4} to 10^{-6}.

2. DYNAMIC NEUTRINO MIXING - NEUTRINO OSCILLATIONS

The dynamics of a mixed neutrino state follows from Eq. 1 by considering the evolution in time of a mass eigenstate $\nu_i(t)$,

$$\nu_i(t) \sim e^{-iE_i t}; \quad E_i = \sqrt{p^2 + m_i^2}\,.$$

Assuming that at least one of the masses m_i of the pure states ν_i is non-zero, neutrino oscillations will occur.

For the simplified case of 2 neutrinos, ν_{ℓ_1} and ν_{ℓ_2}, the matrix $U_{\ell i}$ contains only one independent parameter, the mixing angle θ. The probability for appearance of a new state ℓ_2 in a

detector a distance L (m) away from the source emitting neutrinos in the state ℓ_1 is given by

$$P(\nu_{\ell_1} \to \nu_{\ell_2}) \sim \frac{\sin^2 2\theta}{2} \left[1 - \cos(2.53\ \Delta m^2 (L/E_\nu))\right]. \qquad (2)$$

The quantities $\sin^2 2\theta$ and $\Delta m^2 \equiv |m_1^2 - m_2^2|\,(eV^2)$ are the two parameters characterizing neutrino oscillation in this 2 neutrino model; E_ν (MeV) is the neutrino energy. Similarly, the probability of disappearance of a state ℓ_1 is given by

$$P(\nu_{\ell_1} \to X) \sim 1 - P(\nu_{\ell_1} \to \nu_{\ell_2}). \qquad (3)$$

The oscillations are characterized by an oscillation length $\Lambda\ (m) = 2.48E\ (MeV)/\Delta m^2\ (eV^2)$.

For illustration, the values of L/E_ν to be explored by various experiments are shown in Fig. 3.

We now review the experimental results on oscillations in the appearance channels $\nu_\mu \to \nu_e$ and $\nu_\mu \to \nu_\tau$. No evidence for oscillations has been reported, and the current best upper limits of the parameters Δm^2 and $\sin^2 2\theta$ are shown by the solid lines in Fig. 4. The curves which are 90% confidence limit contour lines have been composed from the data referred to by the label. A detailed list of references is contained in the recent review by Baltay[8] in Neutrino 81. The regions to the right of the curves are excluded.

As for forthcoming results, several experiments have been proposed with the aim of exploring the region of smaller Δm^2 and $\sin^2 2\theta$. The sensitivities expected to be reached in these experiments

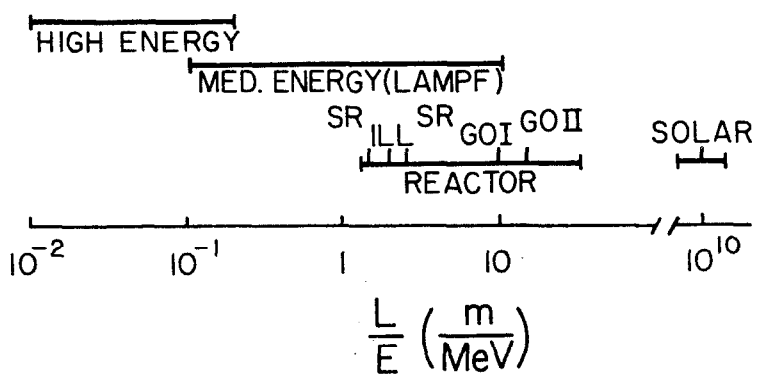


Fig. 3

Illustration of the L/E_ν value for various oscillation experiments.

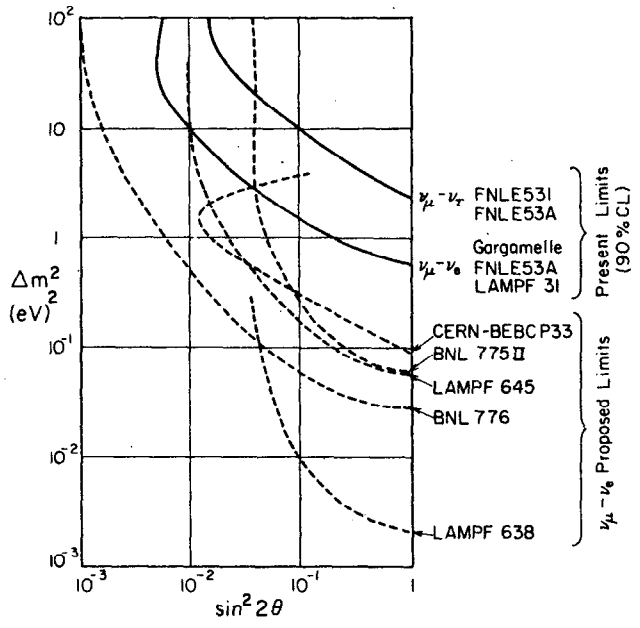


Fig. 4

Limits for neutrino oscillations $\nu_\mu \rightarrow \nu_e$ and $\nu_\mu \rightarrow \nu_\tau$. The solid curves represent current experimental limits at 90% c.ℓ. The dashed curves illustrate forthcoming experimental limits.

are shown in Fig. 4 by dashed lines (the experiments are identified by Laboratory and proposal number[9]). It appears that an improvement in sensitivity of more than an order of magnitude should be attainable in the next 2-3 years.

Disappearance experiments have been conducted at high energy accelerators as well as with the help of fission reactors. Their results, in terms of the two parameters Δm^2 and $\sin^2 2\theta$ are summarized in Fig. 5. By far the most stringent limits come from a recent $\bar{\nu}_e \rightarrow$ X experiment[10] at the Gösgen power reactor. Since this work has not yet appeared in publication, I shall briefly describe it here.

The Caltech-Munich-SIN group[10] has just completed a measurement of the neutrino spectrum at a distance of 38 m from the core of the 2800 MW reactor at Gösgen, Switzerland. The set up of the experiment is sketched in Fig. 6. The neutrinos were detected by the reaction $\bar{\nu}_e$ p-e^+n using a composite liquid scintillation detector and ^{3}He-multiwire proportional chambers[11]. A time correlated e^+, n event constituted a valid signature. Compared to our earlier experiment at Grenoble[11] the signal-to-noise was markedly improved by enforcing position-correlation cuts for the time-correlated events in the scintillation cells and the ^{3}He chamber. Cosmic ray related fast neutron background was effectively reduced by means of pulse-shape discrimination. Events from charged cosmic-ray particles were eliminated with a tight liquid scintillator-veto.

About 11,000 neutrino induced events were recorded in a six-months reactor-on period. Background was recorded during a one-month reactor-off period. Figure 7 (a) depicts the time correlated

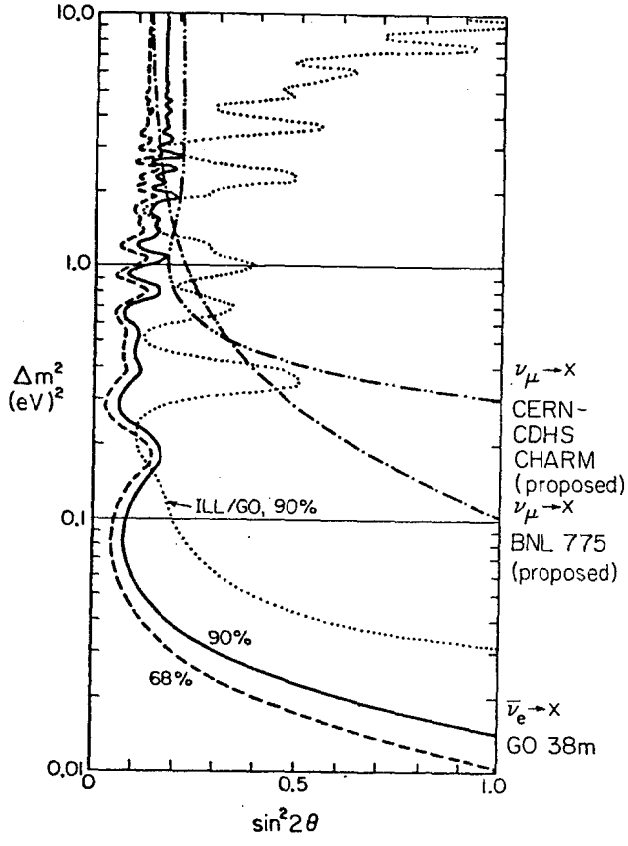


Fig.5

Limits for neutrino oscillations $\nu_\mu \to X$ and $\nu_e \to X$. The solid curve represents current experimental limits at 90% c.l. from the Gösgen reactor experiment. Limits obtained from the ratio of the ILL (8.7 m) and Gösgen (L = 38 m) data are shown by the dotted curved labelled ILL/GO. Forthcoming experimental limits are shown by broken lines.

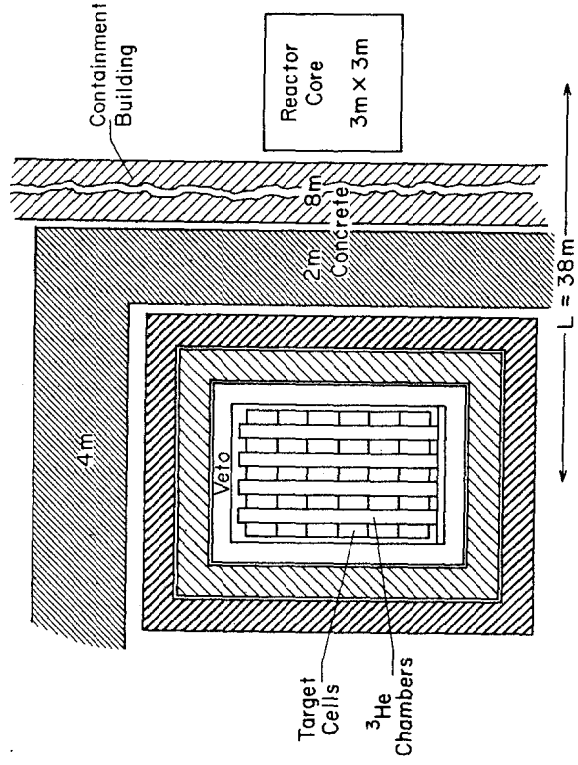


Fig. 6

Arrangement for Gösgen experiment. (Drawing is not to scale.)

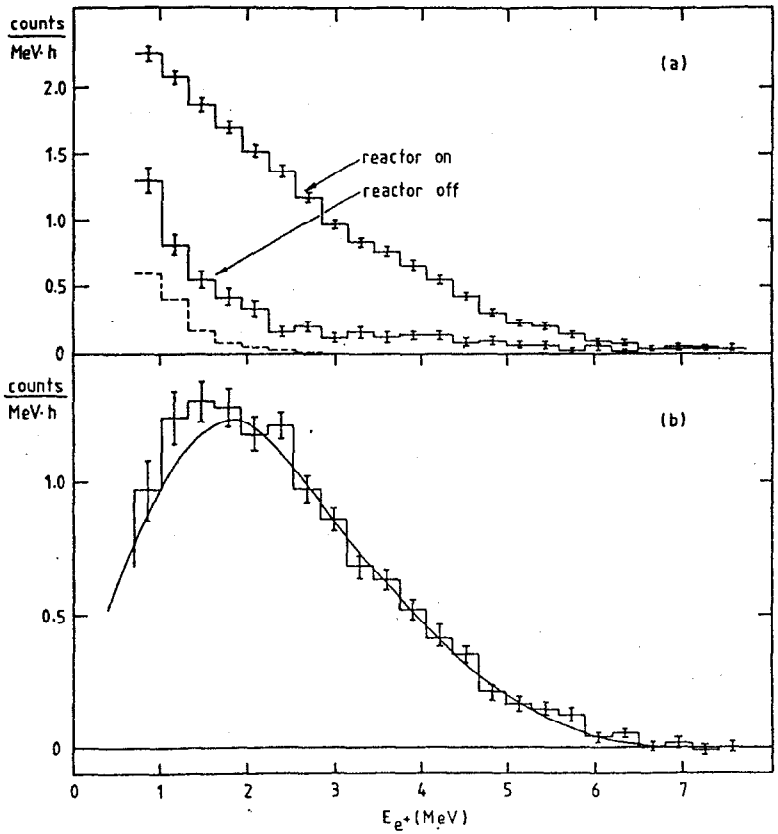


Fig. 7

(a) Reactor-on and reactor-off spectra. Bin width = 0.305 MeV. The errors shown are statistical. The contribution of the accidentals is indicated by the dashed curve. (b) Experimental positron spectrum obtained by subtracting reactor-off from reactor-on spectra. The solid curve represents the predicted positron spectrum assuming no neutrino oscillations ($Y_{\text{no osc}}$).

positron spectrum. Figure 7 (b) shows the difference spectrum reactor-on minus reactor-off together with a curve representing the expected spectrum for no oscillations. The latter was obtained from the on-line beta spectroscopic measurements at the Laue-Langevin reactor by Schreckenbach *et al*[12] studying ^{235}U and ^{239}Pu fission targets. These two isotopes account for about 89% of the total fission energy at the Gösgen reactor. The remaining 11% are due to fission of ^{238}U and ^{241}Pu. The calculations of Ref. 13 were used to evaluate the contribution to the beta spectra from ^{238}U and ^{241}Pu. The variation in time of the contributions of each fissioning isotope is well known and was taken into account.

In the data analysis cuts were made for the time correlation of e^+ and n signals, for the positron correlation, and for the pulse shape in the scintillator. The latter makes it possible to eliminate signals from proton recoil following a neutron collision. The calculated spectra to which the experimental spectrum was compared were obtained by multiplying the no-oscillation spectrum with the oscillation functions $P(E_\nu, L, \Delta m^2, \theta)$ and integrating over detector and core dimensions.

Figure 8 shows the ratio of the observed yield to the yield expected for the no-oscillation case, as a function of $L/E_{\bar{\nu}}$, together with the best fit for $\Delta m^2 = 0$ and for two possible $\Delta m^2 \neq 0$ solutions. A systematic χ^2 test to all possible values of Δm^2 and $\sin^2 2\theta$, including those shown in Fig. 8, followed by a maximum likelihood ratio test resulted in the 68% and 90% confidence limit contour lines displayed in Fig. 5. The same procedure was also

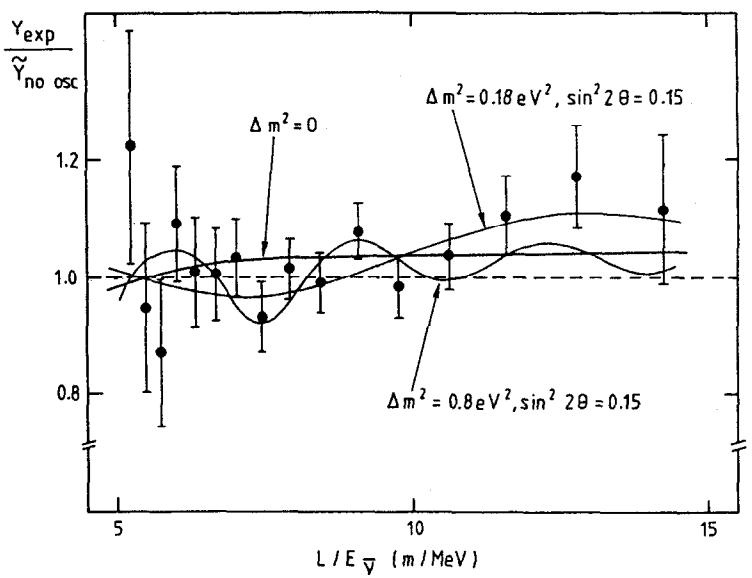


Fig. 8

Ratio of experimental to predicted (for no oscillations) positron spectra. The errors of the data points shown are statistical. Oscillation functions consistent with the data are shown for various sets of oscillation parameters.

applied to the ratio of the data of Ref. 11 taken at L = 8.7m to the present data (L = 38m), and the resulting contour lines are also shown in Fig. 5. This ratio test is somewhat less restrictive because of the moderate statistical accuracy of the data of Ref. 11.

It must be concluded from this experiment that there are no neutrino oscillations with parameters larger than those given by the curves GÖ in Fig. 5. For large mass parameters it is found that $\sin^2 2\theta \leq 0.17$ (90% c.ℓ.), and for maximum mixing the limit is $\Delta m^2 < 0.016$ eV^2 (90% c.ℓ.). The results are in clear disagreement with those by Reines *et al.*[14] For the integral yield it is found that the experimental value divided by the predicted no-oscillation value is 1.05 ± 0.05 (68% c.ℓ.).

A brief summary of present and future reactor experiments is contained in Table I.

The limits for ν_μ disappearance are not very restrictive at present, the constraint on Δm^2 for full mixing being about 7 eV^2 [8], but several experiments have now been proposed to search for oscillations in the $\nu_\mu \to X$ channel. As an example the curves in Fig. 5 illustrate the expected sensitivity limit (90% c.ℓ.) for the CDHS and CHARM experiments[9] at CERN and for a Brookhaven experiment[9]. These experiments will be able to provide an almost 2 order of magnitude improvement in sensitivity to Δm^2. Another experiment at Los Alamos[9] may further improve that limit.

Recent searches[17] for particle-antiparticle transitions $\nu_\mu \to \bar{\nu}_e$ and $\nu_e \to \bar{\nu}_e$ revealed no evidence having oscillation parameters Δm^2 (full mixing) larger than 0.7 eV^2 and 7 eV^2, respectively.

Table I. Status of Reactor $\bar{\nu}_e \rightarrow$ X Oscillation Experiments

Reactor, Collaboration	L(m)	$\Delta m(\theta = \pi/2)$	Status
ILL (Grenoble), Caltech-Munich-ISN[11]	7.8 m	$< 0.15\ eV^2$	completed
Gösgen I, Caltech-Munich-SIN[10]	38 m	$< 0.016\ eV^2$	completed
Gösgen II, Caltech-Munich-SIN[10]	48 m	$< 0.01\ eV^2$	in progress
Savannah River, UC Irvine[15]	15-50 m		in progress
Bugey, Annecy-ISN[16]	13.5 m, 18.5 m		in progress

3. NEUTRINOLESS DOUBLE-BETA DECAY

Double-beta decay, a second-order semileptonic process accompanying a transition from a nucleus Z to Z + 2, may be observable if the transition from Z to Z + 1 is energetically forbidden. The process is known to proceed in two ways, (1) via standard second-order beta decay $Z \rightarrow (Z+2) + e_1 + \nu_1 + e_2 + \nu_2$, known as the 2ν-double-beta decay, and (2) by the no-neutrino process $Z \rightarrow (Z+2) + e_1 + e_2$. This second process violates lepton number and, if observed, would signal that neutrinos have a finite Majorana mass, or that there are right handed currents, or both[18]. It should be noted that other mechanisms not involving neutrino exchange have also been discussed[19]. It is this second process which is receiving much attention today, but I shall have to include the first process in the discussion as well, since it is of help to elucidate the nuclear parameters.

Inasmuch as double-beta decay is somewhat outside the general interest of particle physics, I would like to be more explicit in the discussion that follows.

For the 2ν $\beta\beta$-process the situation is illustrated in Fig. 9. The transition from Z to Z + 2 proceeds via a set of giant Gamow-Teller states in Z + 1. Its strength, as far as the nuclear physics is concerned, is given by a second-order perturbation matrix-element between initial state i, intermediate state m, and final state f,

$$\sum_m \frac{\langle f|H_w|m\rangle\langle m|H_w|i\rangle}{E_m - E_i} .$$

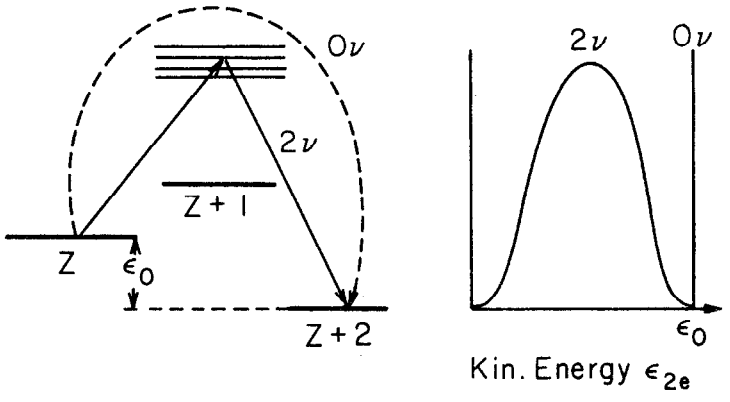


Fig. 9

Energy levels and energy spectra in double-beta decay.

The decay energy is shared by four leptons, which results in a distributon of the energy of both electrons sketches in the figure.

The 0ν decay, on the other hand, may proceed by virtual neutrino exchange, as illustrated in Fig. 10. The neutron n_1 emits an electron e_1 and a neutrino. The latter is absorbed by the neutron n_2 which then emits an electron e_2. The decay energy is shared by the electrons. A detector measuring the total electron energy thus will exhibit a monochromatic peak at energy ϵ_0 as illustrated in Fig. 10. If the neutrino is a Dirac particle emitted as a right-handed $\bar{\nu}_R$ it cannot be absorbed without breaking helicity and charge conjugation. In order for the process to go, it will be required that (a) the neutrino be a Majorana particle ($\nu^M \equiv \bar{\nu}^M$), (b) there will be a helicity flip ($\nu_R^M \to \nu_L^M$). Two mechanisms have been identified[20,21] which can give rise to a helicity flip:

1. The lepton wave function has an explicit right helicity admixture with the lepton current given by

$$\ell_\lambda \approx \frac{m_\nu p_\nu}{m_\nu^2 + p_\nu^2} e\gamma_\lambda(1+\gamma_5)\,\nu^M.$$

We assume here that the hadronic current is purely left-handed.

2. There is a neutrino mass term in the standard left current of the form

$$\ell_\lambda \approx e\gamma_\lambda[(1+\gamma_5) + \eta(1-\gamma_5)]\,\nu^M.$$

The Majorana neutrino thus violates lepton number by two units.

Let us now consider the rates for both, the 2ν and the 0ν processes, as based on the work by Rosen[20]. The rate for the 2ν

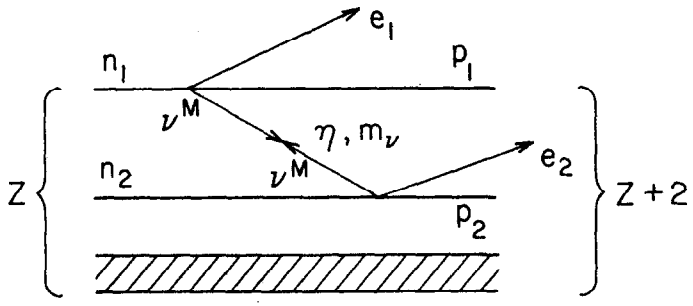


Fig. 10

Illustration of neutrinoless double-beta decay.

process can be written as follows:

$$\Gamma^{2\nu} = \frac{\ln 2}{T_{\frac{1}{2}}^{2\nu}} = 3 \times 10^{-21} \, F_{2\nu}(\varepsilon_0) \, C(\varepsilon_0 Z) \, \frac{|M_{GT}|^2}{<\Delta E_N + \varepsilon_0/2 + 1>^2} \; (\text{year}^{-1})$$

where $F_{2\nu}(\varepsilon_0) \sim \varepsilon_0^{11} + 22\varepsilon_0^{10} + \ldots$ is the 4-fermion phase-space factor, $C(\varepsilon_0 Z)$ is the Coulomb function, M_{GT} is the second-order Gamow-Teller matrix-element describing the transitions via states in Z + 1 (see Fig. 9) and ΔE_N is the average nuclear energy difference between these states and the initial state. With a lepton energy ε_0 of about $5\,m_e$, the energy denominator is roughly $25\,m_e$. The main uncertainty in this decay rate stems from the nuclear matrix element $|M_{GT}|^2$ and may be as large as a factor of $10^{\pm 2}$.

A rough estimate for the 2ν half-life yields $T_{\frac{1}{2}}^{2\nu} \simeq 10^{22 \pm 2}$ years.

In the element tellurium (Z = 52) double-beta decay has been experimentally studied for two isotopes, $^{128}\text{Te} \rightarrow {}^{128}\text{Xe}$ and $^{130}\text{Te} \rightarrow {}^{130}\text{Xe}$. By forming the ratio of the half lifes, the matrix elements, assumed to be the same in both decays, can be eliminated. Thus one has

$$\frac{T_{\frac{1}{2}}^{2\nu\ 128}}{T_{\frac{1}{2}}^{2\nu\ 130}} \simeq \frac{F_{2\nu}^{130}}{F_{2\nu}^{128}} = 5600.$$

A similar estimate for the 0ν process can be made. Both right-hand current (RHC) and mass mechanisms have been included[20,21]. For a transition between groundstates ($0^+ - 0^+$) this rate is given by

$$\Gamma^{0\nu} = \frac{\ln 2}{T^{0\nu}_{1/2}} = 5 \times 10^{-16}\, F_{0\nu}(\varepsilon_0)\, C(\varepsilon_0 Z) \left| \frac{M_{GT}}{\langle r_{ij} \rangle m_p} \right|^2 \text{(year}^{-1}\text{)}.$$

The quantity $F_{0\nu}(\varepsilon_0)$ is the 2-fermion phase-space factor. It has terms in mass (m in units m_e) and RHC (η) in the following form,

$$F_{0\nu}(\varepsilon_0) = m^2 f_m(\varepsilon_0) + m\eta f_{m\eta}(\varepsilon_0) + \eta^2 f_\eta(\varepsilon_0).$$

$f_m \sim \varepsilon_0^5 + 10\,\varepsilon_0^4 + \ldots$ has the same energy dependence as in allowed beta decay (s-wave) and $f_\eta \sim \varepsilon_0^7 + \ldots$ has higher powers in enegy reflecting the content of orbital angular momentum (p-wave) in the RHC process. The quantity $|\ |^2$ represents the Gamow-Teller matrix-element divided by an average nucleon separation distance (~ 0.5 nuclear radius), m_p being the proton mass.

Again, a rough estimate gives $T^{0\nu}_{1/2} \simeq 10^{15\pm2}\ \eta^{-2}$ (or m^{-2})(years).

We note that the 0ν decay is 10^7 times faster than the 2ν decay, if $\eta = 1$ or $m = 1$. The reason for this is twofold: the matrix-elements are larger and the phase space factor is larger, the latter having to do with the fact that the virtual neutrino is constrained to the nucleus and thus can have a momentum given by $p_\nu = \hbar c/R \simeq 35$ MeV/c.

As before we can form the half-life ratio for the tellurium isotopes and find[20],

$$\frac{T^{2\nu}_{1/2}\ 128}{T^{0\nu}_{1/2}\ 130} = \begin{cases} 320\ (m = 0) \\ 31\ (\eta = 0) \\ 80\ (m = \eta) \end{cases}$$

Let us have a closer look at the tellurium results. Geochemical lifetime measurements have been conducted over a long period of time. The results are shown in Fig. 11. The data points arranged in chronological order are labelled by author and provenance of the ore. Clearly the lifetime values scatter considerably in excess of the error limits given by the authors. This seems to point to the fact that there are unresolved difficulties in our understanding of the xenon abundance in tellurium ore.

Until recently the only ^{128}Te measurement was that by Hennecke[22] giving a half-life ratio $R = T^{128}_{1/2}/T^{130}_{1/2} = 1600 \pm 50$. This ratio can not be explained by 2ν decay alone, and has therefore inspired several researchers[20,21,23] to invoke the presence of 0ν decay. A recent measurement by Kirsten *et al.*[24] however gives a ratio of $R = 10{,}000^{+\infty}_{-5000}$ invalidating that claim.

What is measured are the numbers of ^{128}Xe and ^{130}Xe atoms assumed to be formed by double-beta decay in Te ore. From these numbers the half-life ratio:

$$R = \frac{T^{128}_{1/2}}{T^{130}_{1/2}} = \frac{\Gamma^{130}_{2\nu} + \Gamma^{130}_{0\nu}}{\Gamma^{128}_{2\nu} + \Gamma^{128}_{0\nu}} = \frac{\Gamma^{130}_{2\nu}}{\Gamma^{128}_{2\nu}} \left(\frac{1 + (\Gamma^{130}_{0\nu} / \Gamma^{130}_{2\nu})}{1 + (\Gamma^{128}_{0\nu} / \Gamma^{128}_{2\nu})} \right)$$

is obtained. This ratio involves (besides the 2ν ratio) the ratio of the matrix-elements

$$\rho \equiv \frac{|M_{GT}|}{\left|\frac{M_{GT}}{\langle r \rangle}\right|} \frac{m_p}{\left\langle \Delta E_N + \frac{\varepsilon_0}{2}\ 1 \right\rangle} = \begin{cases} 1.2\ \text{Rosen}^{20} \\ 0.5\ \text{Haxton}^{23} \end{cases}.$$

The two quoted calculations show that ρ is not very sensitive to details of the evaluation. The neutrino mass then is approximately

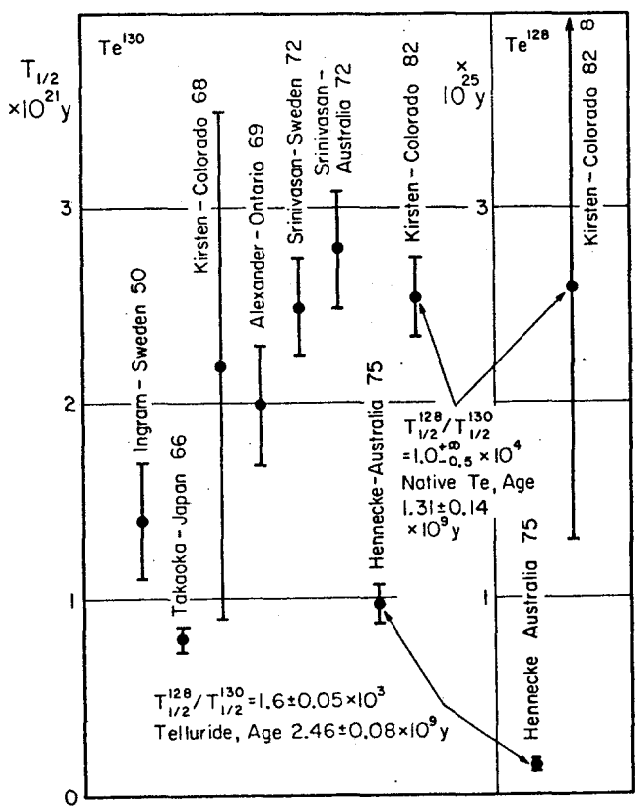


Fig. 11

Overview of the geochemical life-time data for ^{128}Te and ^{130}Te arranged in chronological order. The references are M.G. Inghram and J.H. Reynolds, Phys. Rev. 78, 822 (1950); N. Takaoka and K. Ogata, Z. Naturf. 219, 84 (1966); T. Kirsten *et al.*, Phys. Rev. Lett. 20, 1300 (1968); E. Alexander *et al.*, Earth Planet Sci. Lett. 5, 478 (1969); B. Srinivasan *et al.*, J. Inorg. Nucl. Chem. 34, 2381 (1972); E.W. Hennecke, Ref. 22; T. Kirsten Ref. 24.

given by[20]

$$m_\nu \simeq \frac{\rho}{10^4}\sqrt{\frac{6{,}600-R}{21.5\,R}}\,; \quad \eta = 2.3\, m_\nu .$$

With the R value of Kirsten[24] and $\rho = 0.5$ one obtains the following limits

$$m_\nu < 3.1 \text{ eV}; \quad \eta < 1.4 \times 10^{-5}.$$

In contrast, the best limit for η from beta-decay experiments is $\eta < 0.1$. Figure 12 shows the allowed values for m and η from the experiments by Kirsten[24] and Hennecke[22]. The scales correspond to the evaluations of Haxton[23], Rosen[20], and Doi[21].

I shall briefly mention several other $\beta\beta$ results, notably those in ^{82}Se and ^{76}Ge. No ratio argument is possible in these cases, and the calculations have a larger uncertainty stemming from the uncertainty in the matrix elements.

In ^{82}Se geochemical lifetimes $T^{0\nu+2\nu}$ of $1.45 \pm 0.15 \times 10^{20}$ y[25] and $2.8 \pm 0.9 \times 10^{20}$ y[26] have been reported. Laboratory experiments[27] give a much shorter life-time of $T^{2\nu} = 1.0 \pm 0.4 \times 10^{19}$ y, while $T^{0\nu} > 3.1 \times 10^{21}$ y has been reported[28]. The calculation[29] gives $T^{2\nu} = 1.7 \times 10^{19}$ in agreement with the laboratory experiment, but not with the geochemical results. Based on the calculated $T^{2\nu}$ it follows that $T^{0\nu} = 1.6 \times 10^{12}/m_\nu^2$ or $m_\nu < 12$ eV. If instead the matrix element is taken from the geochemical life-time, then $m_\nu < 52$ eV.

In the case of ^{76}Ge there is an excellent laboratory limit by Fiorini *et al.*[30] of $T^{0\nu} > 5 \times 10^{21}$. Based on Haxton's

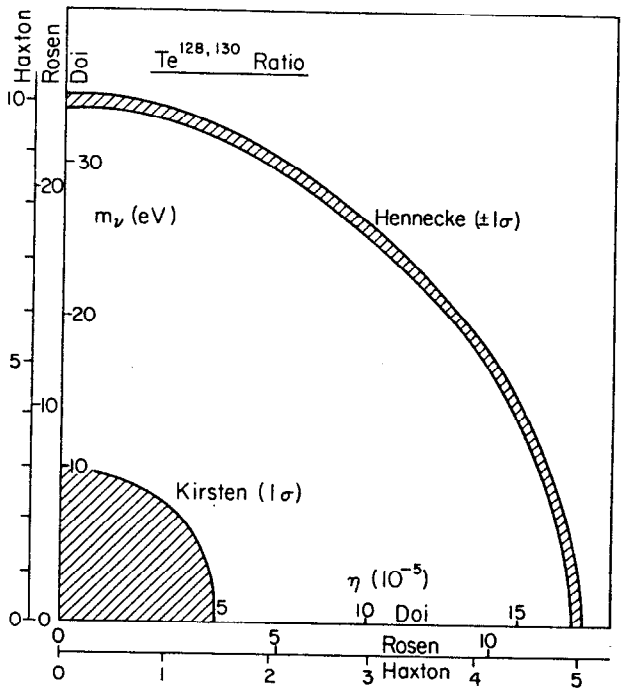


Fig. 12

Values of m_ν and η from double-beta decay life-times of ^{128}Te and ^{130}Te. The three axes correspond to the calculations of Ref. 20, 21, and 23.

calculation[31] the mass limit is $m_\nu < 15$ eV. The results for Se and Ge are summarized in Fig. 13.

The results[31] in ^{48}Ca of $T^{0\nu} > 1.6 \times 10^{21}$ y and $T^{2\nu} > 3.6 \times 10^{19}$ y are more difficult to interpret in terms of neutrino mass limit. Recent work by Belotti *et al.*[32] gives limits for $T^{0\nu}$ of $10^{18} - 10^{19}$ years for the cases of ^{58}Ni, ^{92}Mo, ^{100}Mo, ^{148}Nd, and ^{150}Nd.

Before concluding this section, I would like to mention several further considerations. First, It should be noted[20] that in addition to the upper mass limit presented here, the ββ experiments also provide for a lower limit of the neutrino mass. Since the mass term is proportional to $m_\nu p_\mu/(m_\nu^2 + p_\nu^2)$ which for $m_\nu >> p_\nu$ approaches p_ν/m_ν, we have for $p_\nu \approx 35$ MeV/c a mass limit of $m_\nu >$ few GeV.

Next, it is important to be able to distinguish between RHC and mass terms. According to Rosen[20] and Doi *et al.*[21] the selection rules for the mass term are: $\Delta J = 0^+$; $0^+ \to 0^+$ only. While for the RHC term (where there are momentum dependent terms in the matrix elements) $\Delta J = 0^+, 1^+, 2^+$; $0^+ \to 0^+, 1^+, 2^+$. The effects of these selection rules are summarized in Fig. 14. Thus if a ββ branch to the 2+ state is observed, it would constitute evidence for right-hand currents.

In a more esoteric vain, it was pointed out by Rosen[20] that the angular correlation between the two electrons is different for RHC and mass mechanisms. Preferential opposite emission is predicted in the latter case since $\Delta J = 0$ is required, while a

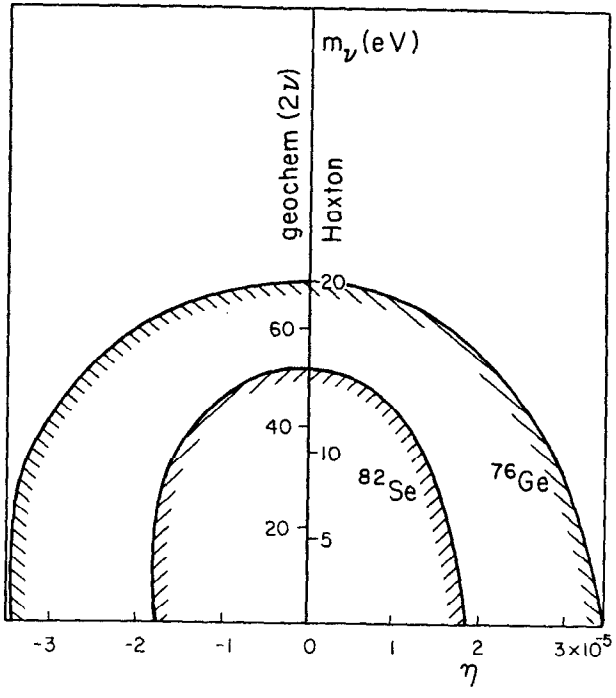


Fig. 13

Values of m_ν and η from double-beta decay life-times of ^{82}Se and ^{76}Ge. The axes correspond to the calculations of Ref. 29.

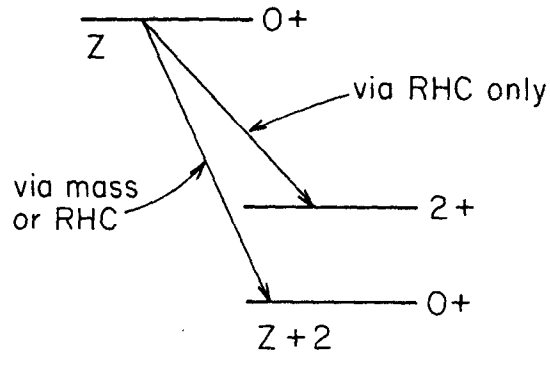


Fig. 14

Selection rules for double-beta decay to 0^+ and 2^+ states.

deviation from this will occur for right-handed particles.

As to the outlook, there are several experiments with ^{76}Ge in progress now, including one at Milano[33], at Caltech[34], and Battelle[35], using large high resolution Ge detectors and improved background suppression. It can safely be predicted that an order of magnitude improvement of the present sensitivity will be achieved soon, leading to a more stringent limit of the neutrino mass, as illustrated in Fig. 15. Work is in progress on a new ^{82}Se measurement by the Irvine group[27]. An experiment on ^{136}Xe is in preparation[36] using a liquid Xe TPC. Compared to the geochemical experiment, clearly these laboratory experiments are more decisive if evidence for the important neutrinoless $\beta\beta$ process should be established, and should be pursued vigorously. If neutrinos are of the Majorana type, present evidence points to the fact that their masses cannot exceed 3 or 10 eV. This result appears at variance with the findings in the ^{3}H decays.

If taken literally, these experiments could lead to the conclusion that electron antineutrinos are not Majorana but rather Dirac particles.

This and other developments of the evidence for neutrino mass are summarized in Table II. Much of the claims for finite mass of 1980 have proved to be invalid, except fot the ^{3}H spectrum, an experiment which is waiting to be challenged.

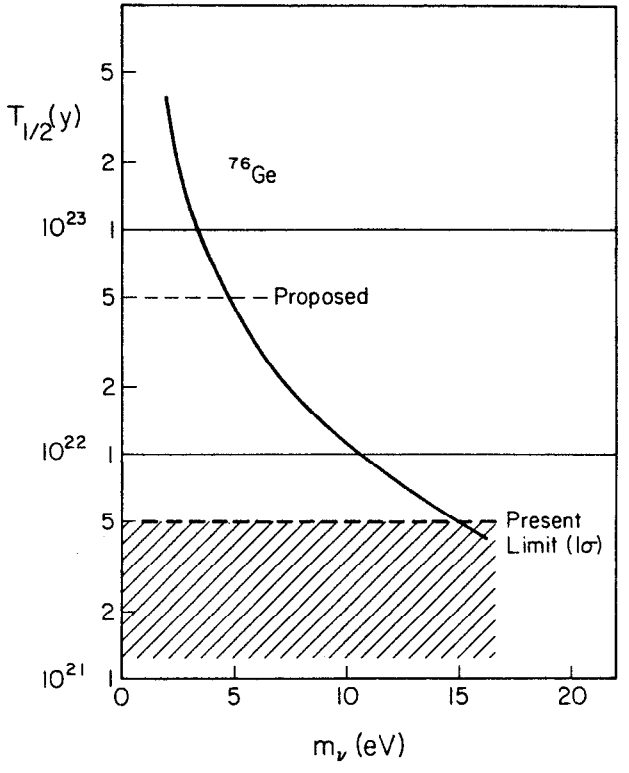


Fig. 15

Illustration of neutrino mass limits which can be achieved from life-time measurements in ^{76}Ge.

Table II Evidence for Neutrino Mass

Experiment	Claim, 1980	Present Status, 1982
$\bar{\nu}_e \rightarrow X$ (Reines)	Oscillations $\Delta m^2 \sim 1eV^2$	No Evidence, $\Delta m^2 < 0.016eV^2$
^3H Spectrum (ITEP)	$14 < m_\nu < 46eV$	Unchallenged
Solar ν Puzzle (Davis)	Supporting Oscillations	Possible Support
$\nu_\mu \rightarrow X$ Beam Dump (CERN)	Osc. large Δm^2	No Evidence
0_ν -$\beta\beta$ $Te^{128,130}$ (Hennecke)	$m_\nu^M \sim 10eV$	No Evidence, $m_\nu^M < 3eV$

REFERENCES

1. P.H. Frampton and P. Vogel, Physics Report 82, 342 (1982).
2. R.E. Shrock, Phys. Lett. 96B, 159 (1980), and Phys. Rev. D 24, 1232 and 1275 (1981).
3. Y. Asano et al., Phys. Lett. 104B, 84 (1981), T. Yamasaki, Neutrino 82, 1982.
4. R. Abela et al., Phys. Lett. 105B, 263 (1981).
5. D. Berkhofer et al., Neutrino 81, Vol. II, p. 67, Univ. Hawaii, 1982.
6. J.J. Simpson, Phys. Rev. D 24, 2971 (1981).
7. J.J. Simpson, Phys. Lett. 102B, 35 (1981).
8. C. Baltay, Neutrino 81, Vol. II, p. 295, Univ. Hawaii, 1982.
9. For CERN Proposals, see A.L. Grant, Neutrino 81, Vol. II, p. 214; M. Murtagh et al., Brookhaven Proposal E775; A. Pevsner et al., Brookhaven Proposal E776; T. Romanowsky et al., LAMPF Proposal 645; T. Dombeck et al., Los Alamos Proposal 638.
10. Caltech-Munich-SIN Collaboration, J.-L.Vuilleumier et al., Phys. Lett. B, to be published.
11. H. Kwon et al., Phys. Rev. D 24, 1097 (1981).
12. K. Schreckenbach et al., Phys. Lett. 99B, 251 (1981).
13. P. Vogel et al., Phys. Rev. C 24, 1543 (1981).
14. F. Reines, H.W. Sobel, and E. Pasierb, Phys. Rev. Lett. 45, 1307 (1980).
15. M. Mandelkern, Neutrino 81, Vol. II. p.203 (1981).
16. J.F. Cavaignac et al., Raport Annuel 1980, ISN 81.01, p. 71.
17. A.M. Cooper et al., Phys. Lett. B 112, 97 (1982).
18. Detailed references are contained in the recent reviews of ref. 20, and in Yu. G. Zdesenko, Sov. J. Part. Nucl. 11 (6), 582 (1981); D. Bryman and C. Picciotto, Revs. Mod. Phys. 50, 11 (1978).
19. R.M. Mohapatra and J.D. Vergados, Phys. Rev. Lett. 47, 1713 (1981).
20. S.P. Rosen, Neutrino 81, Vol. II, p. 76, Univ. Hawaii, 1982, and Workshop on Low Energy Tests on High Energy Physics, I.T.P., Santa Barbara, Jan. 1982. See also, H. Primakoff and S.P. Rosen, Phys. Rev. 184, 1925 (1969); Halprin et al., Phys. Rev. D 13, 2567 (1976).

21. M. Doi, T. Kotani, H. Hishiura, K. Okuda, and E. Takasugi, Phys. Rev. 103B, 219 (1981).

22. E. Hennecke, O. Manuel, and D. Sabu, Phys. Rev. C11, 1378 (1975).

23. W.C. Haxton, G.J. Stephenson and D. Strottman, Los Alamos preprint LA-UR-81-3454, Phys. Rev. D., to be published.

24. T. Kirsten, E. Jessberger, E. Pernicka, and H. Richter, to be published (1982), presented at Workshop on Low Energy Tests of High Energy Physics, I.T.P., Santa Barbara, Jan. 1982.

25. T. Kirsten and H. Muller, Earth and Plan. Sci. Lett. 6, 271 (1969).

26. B. Srinivasan et al., Econ. Geol. 68, 252 (1973).

27. M. Moe and D. Lowenthal, Phys. Rev. C22, 2186 (1980).

28. B. Cleveland et al., Phys. Rev. Lett. 35, 737 (1975).

29. W.C. Haxton, G.J. Stephenson, and D. Strottman, Phys. Rev. Lett. 47, 153 (1981).

30. E. Fiorini et al., Nuovo Cim. A13, 747 (1973).

31. R. Bardin et al., Phys. Lett. 26B (1967), Nucl. Phys. A158, 337 (1970).

32. E. Bellotti, E. Fiorini, C. Liguori, A. Pullia, A. Sarracino, and L. Zanotti, preprint, Milano 1981.

33. E. Bellotti, Workshop, I.T.P., Santa Barbara, Jan. 1982.

34. F. Boehm, Workshop, I.T.P., Santa Barbara, Jan. 1982.

35. F. Avignone, Workshop, I.T.P., Santa Barbara, Jan. 1982.

36. H. Chen, private communication.

PRODUCTION OF PROMPT NEUTRINOS IN 400 GEV PROTON INTERACTIONS*

Sam Childress

Fermi National Accelerator Laboratory

Batavia, Illinois 60510

Results of Fermilab Experiment 613. Presented at the 1982 SLAC Summer Institute on Particle Physics by:

R. J. Loveless

University of Wisconsin

Madison, Wisconsin 53706

© S. Childress 1982

INTRODUCTION

Evidence for the existence of neutrino sources other than the decays of relatively long-lived particles ($\pi,\kappa,\Lambda,\Sigma$) was first seen in 400 GeV proton beam dump experiments carried out at the CERN SPS.[1-3] Such experiments provide a technique for studying the production of short-lived particles produced in proton-nucleus interactions which decay into states containing neutrinos.

Considerable suppression of conventional ν sources is achieved by interacting a primary proton beam in a large high density target. Only very short decay paths for π and κ mesons then exist, as determined by their absorption lengths in the target material. The use of targets of different effective density enables separation of the prompt ν from conventional, or non-prompt, ν fluxes by an extrapolation to infinite target density.

The prompt neutrino flux extracted is expected to be predominately due to the production and subsequent semileptonic decay of charmed particles. Results of the second CERN beam dump run[4-6] indicate several possible anomalies with this interpretation. But it must be emphasized that the experiments are difficult, with large potential backgrounds and, at present, very low statistics.

This paper reports preliminary results of the first beam dump neutrino experiment at Fermilab, E613. Design goals of the experiment were to measure cross sections, energy and angular dependence separately for prompt ν_u, $\bar{\nu}_u$ and ν_e ($\bar{\nu}_e$) events, along with the A dependence of prompt neutrino production using different materials. Refinements over the CERN experiments included:

1. Large increase in solid angle acceptance of the detector.
2. Decrease of non-prompt target associated backgrounds relative to prompt signals.
3. Different target materials for A dependence determination. (Tungsten target data only are reported here).
4. Extensive study and measurement of potential upstream background sources.

Experimental Setup

A plan view of the experiment is shown in Fig. 1. The calorimeter detector is located only 56 meters downstream of the target, rather than ~800 meters as in previous CERN experiments. This enables measurement of neutrino events from 0-37 mr.

The very close target-detector distance was made possible by use of the "active" beam dump shown in the figure. A magnetized iron shield 11 meters in length deflected muons vertically above and below the detector. This was followed by 11 meters of passive iron, which shielded the detector from low momentum muons deflected by magnet return yokes and scattered back toward the detector. The residual muon flux at the face of the detector was $\sim 1.2 \times 10^5$ per 10^{12} protons, or a reduction factor of approximately 10^4. Typical beam intensities were from $1 - 4 \times 10^{12}$ protons/pulse, with a 1.0 second slow extracted beam spill.

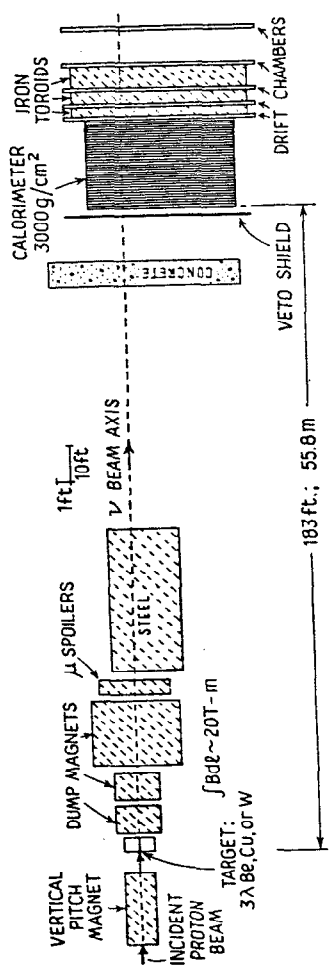


Figure 1

Most data accumulation during the initial experimental run was with tungsten targets of either full or one-third effective density.

The detector, shown schematically in Fig. 2, consists of a 150 metric ton calorimeter made up of 30 modules. Each module has twelve 6.4 mm Pb plates separated by 6.4 mm gaps of liquid scintillator for a total of 14.4 radiation lengths, 0.5 absorption length and 105 gm/cm^2 per module. The modules are separated vertically into five horizontal cells, each viewed on opposite sides by a photomultiplier tube. Energy response of the calorimeter is linear, with a measured resolution $\sigma/E = .55/\sqrt{E}$ for hadrons and $.27/\sqrt{E}$ for electrons. The use of lead plates in the calorimeter provided good separation of charged current electron neutrino from neutral current events.

Between each calorimeter module are two PWC planes of horizontal and vertical wires on 2.54 cm centers. These are operated in a proportional mode with analog pulse height readouts. Fiducial mass of the detector is 80 metric tons, with a sensitive region of transverse dimensions 3 x 1.5 m^2. Beam axis is centered vertically on the detector and 0.75 m from one side, as illustrated in Fig. 1. This horizontal asymmetry allows measurement of neutrino interactions at larger production angles.

The calorimeter is followed by a muon spectrometer consisting of drift chambers and solid iron magnets. A trigger was initiated by energy deposition of sufficient amplitude within one of 24

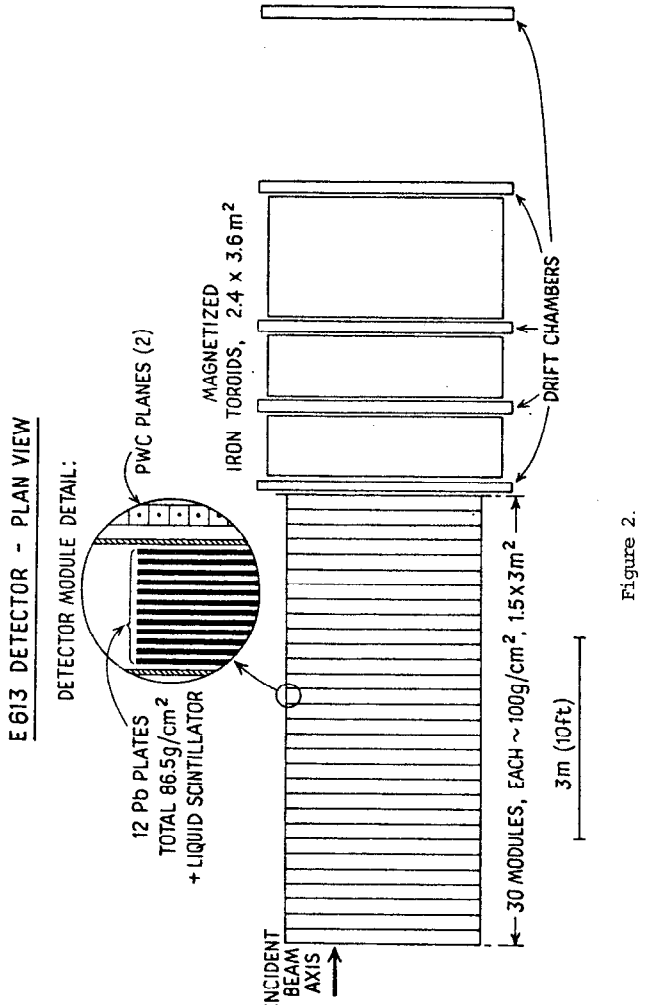


Figure 2.

overlapping groups of 16 calorimeter cells, coupled with a null signal from the triple wall of veto counters in front of the detector. The trigger threshold varied between 5 and 12 GeV (equivalent hadronic energy) for most of the detector.

Data Collection

For the 1981 run, data were collected with 1.3 x 10^{17} protons incident on a full density tungsten target and 0.3 x 10^{17} on a segmented target with effective density one-third that of tungsten. Live time for data accumulation averaged 70%. The total beam exposure after correction for live time and bad spills was 1.0 x 10^{17} protons.

Because of significant cosmic ray trigger background during the 1 sec spill length, triggers were also accumulated during a beam off gate of equal length to monitor this flux. The beam on trigger rate averaged 30 per pulse, of which 0.2 were neutrino induced interactions, 12 were cosmic rays, and the remainder were largely due to showers from muon interactions in material above and below the detector.

Background

Control of beam line backgrounds is of critical importance in a prompt neutrino experiment. Very small amounts of scraping of the proton beam upstream of the dump could significantly increase the muon neutrino flux due to long secondary decay paths. These additional events would then be seen as a false prompt signal after the extrapolation to infinite target density.

Beam backgrounds were measured by more than 30 monitors positioned along the evacuated pipe through which the beam is transmitted. These monitors had measurement sensitivity for the interaction of 10^{-7} of the proton beam. Monitors were calibrated by inserting foils of known thickness into the path of the beam, and additionally changing the beam pipe vacuum by measured amounts.

Monitor readings were recorded on tape for each beam pulse, and data cuts made for readings above selected values. No evidence for a change in neutrino rates was seen for test runs in which beam line changes produced monitor rates different by more than an order of magnitude from normal values.

For the downstream 130 meters of the beam line, which was at 0^0 with the detector, the average measured background represented an interaction of 3 parts in 10^6 of the beam. Approximately half of this background was due to beam gas interactions for beam line gas pressure $\sim 10^{-2}$ Torr. The neutrino background produced was determined to be 0.3% of the prompt signal for the full density tungsten target.

A significant non-prompt component to the neutrino signal seen in the detector is expected due to finite target density. This background is especially large for charged current muon neutrino events, and is considerably reduced by use of tungsten targets in this experiment. A comparison of prompt signal to full density target background for different experiments is given in the following table. Included is the Fermilab muon beam dump E595.[7]

TABLE I

Experiment	Prompt Signal/Background	Target
CDHS, CHARM (1-μ events)	0.4	Cu
E595 (μ beam dump)	0.1	Fe
E613 (1-μ events)	1.1	W
E613 (0-μ events)	4.6	W

Extrapolation to infinite target density using data on both full and partial density targets allows extraction of a prompt signal in each experiment, but large target backgrounds significantly affect the measurement error of the prompt component. For the prompt single muon measurement of E595 high statistics compensate for the poor prompt signal to background ratio.

The beam exposure for each target must also be carefully measured to avoid large biases in extracting the prompt signal. Data collection for E613 alternated between full and partial density targets to reduce the effect of possible time dependent changes of the SEM intensity monitor. A system of large acceptance ionization chambers and scintillation counters downstream of the target directly monitored the beam intensity on target for each pulse. For the complete run these monitors agreed with the SEM on a pulse by pulse basis to better than 1.5%.

Approximately 0.2% of the beam interacted in the SEM and target SWIC just upstream of the target. This produced a significant, but calculable, background of 8.3% of the non-prompt neutrinos from the full density W target. A correction was applied in the target extrapolation for this upstream background. In addition, a correction was made for hadrons punching through the tungsten targets into the iron dump immediately downstream. The net effect of these corrections on the extrapolation is to reduce the effective density ratio of the two targets from 3 to ~2.7.

Event Selection

The raw trigger rate of 225000/10^{16} protons was reduced to 1000/10^{16} by computer analysis which rejected non-neutrino events and imposed fiducial volume cuts and an energy cut of $E_{Vis} > 20$ GeV. Remaining event candidates were visually double scanned for:

i) 1-μ events (ν_u^{CC} interactions)

ii) 0-μ events ($\nu_u^{NC} + \nu_e^{NC} + \nu_e^{CC}$ interactions)

Fig. 3 illustrates typical events in each of these classes.

For the 1-μ events, the presence of the secondary muon provided an unambiguous signature in the detector. The major systematic effect to be resolved was the acceptance of the downstream muon spectrometer. A study of the 0-μ event candidates produced a sample of ν_u^{CC} (miss) consistent with Monte Carlo expectations for the number of ν_u^{CC} events having the muon outside the spectrometer acceptance. An independent computer selection was

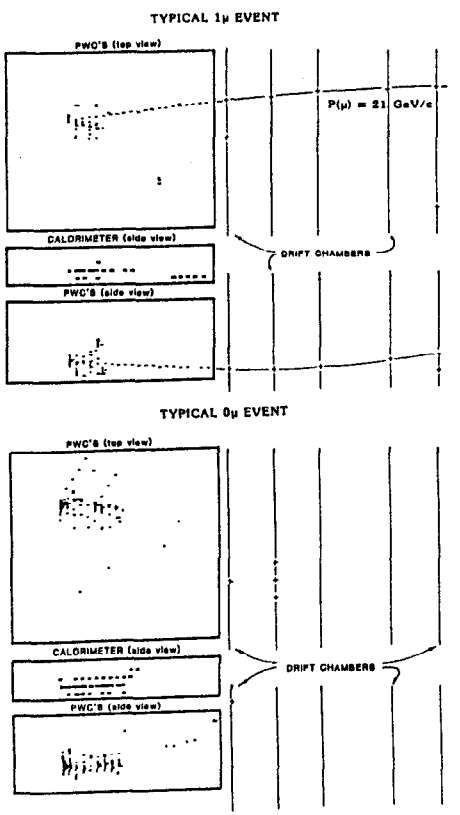


Figure 3

also performed for 1-μ events, which required the muon pass through at least 2 drift chamber superplanes. Results were in good agreement with those from the visual scan.

Separation of ν_e and NC events in the 0-μ sample was achieved using their longitudinal shower development in the calorimeter. Because of the Pb plates a typical electron shower was contained within one module, but a hadron shower extended ~5-6 modules.

Having determined the Z origin of an event within a given module, observed module energies were shifted so the event occurred at the front of a "shifted module."

The scaling variable Y_s is then defined as:

$$Y_s = \frac{E_{had}}{E_\nu} \simeq \frac{2\,E_{2n}}{E_{TOT}}$$

where E_{2n} is the observed hadronic energy in modules 2 through n and E_{TOT} is the total energy in all modules. For neutral current events, Y_s should be ~1.0 with a spread determined by π^0 production. For incoming electrons however, Y_s should peak near 0.0, since $E_{2n} \simeq 0$ for a purely electromagnetic shower. These effects are shown in Fig. 4.

A ν_e^{CC} interaction is a linear combination of the two curves, but NC events strongly approximate the solid curve of Fig. 4.

This enables a bin by bin subtraction of the ν_u^{NC} interactions normalized to the ν_u^{CC} data, with a resulting distribution in Y_s containing only ν_e, $\bar{\nu}_e$ and NC ($\nu_e + \bar{\nu}_e$) events, as seen in Fig. 5.

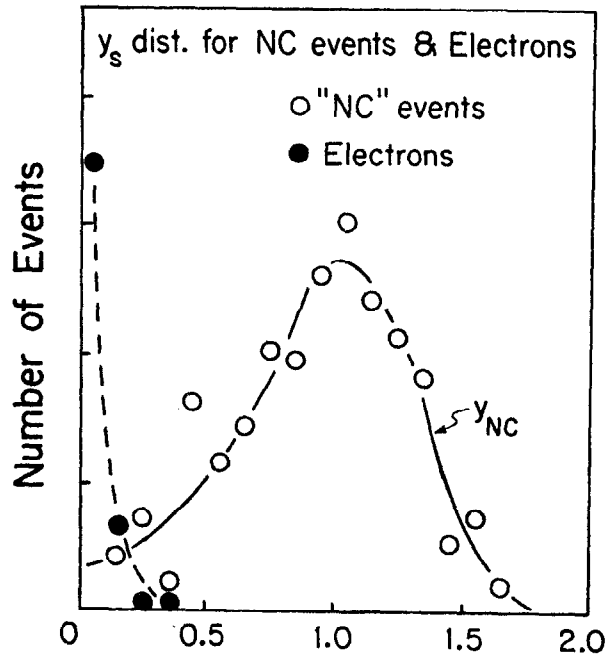


Figure 4

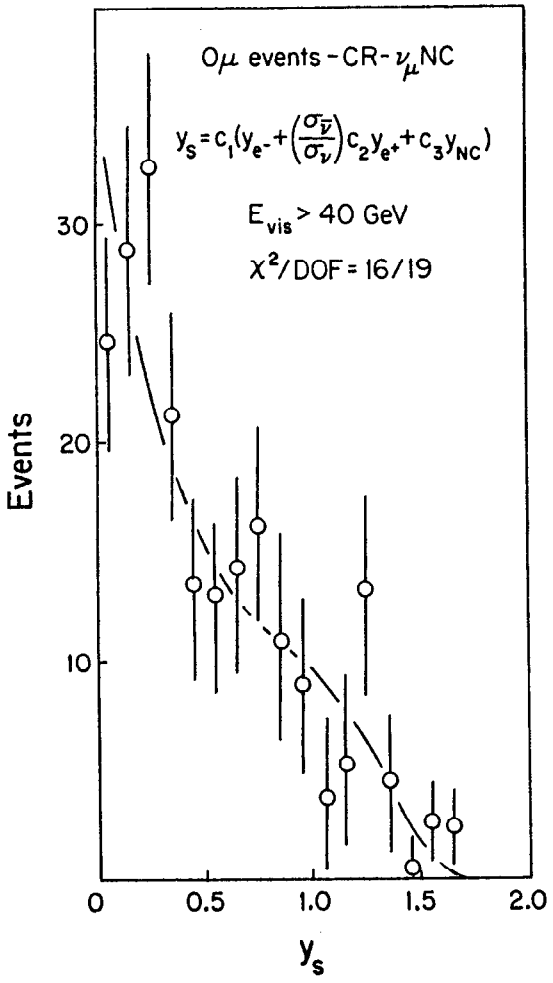


Figure 5

The data in the figure were fitted to a linear combination of the expected Y_s distribution for ν_e^{CC}, $\bar{\nu}_e^{CC}$ and NC ($\nu_e + \bar{\nu}_e$) events.

A second method of extracting the ν_e^{CC} events is obtained if we assume no anomalies. Then,

$$\sigma_{\nu_e} = \sigma_{\nu_u} \text{ and } \frac{NC}{CC}(\nu_e) = \frac{NC}{CC}(\nu_u)$$

and all neutral current events can be subtracted from the 0-μ data. The ν_e rate obtained in this manner is consistent with that obtained using the longitudinal shower development to separate ν_e and NC events.

Target Extrapolation

The prompt neutrino signal is obtained by extrapolation to infinite target density, as shown in Fig. 6. The extrapolation is much flatter for ν_e events than for ν_u events, as is expected.

In order to determine prompt neutrino yields as a function of energy and angle, the infinite density extrapolation was done on a bin by bin basis.

ν_u^{CC} Results

Table II shows raw data, corrected results, and the extrapolated prompt signal for ν_u and $\bar{\nu}_u$.

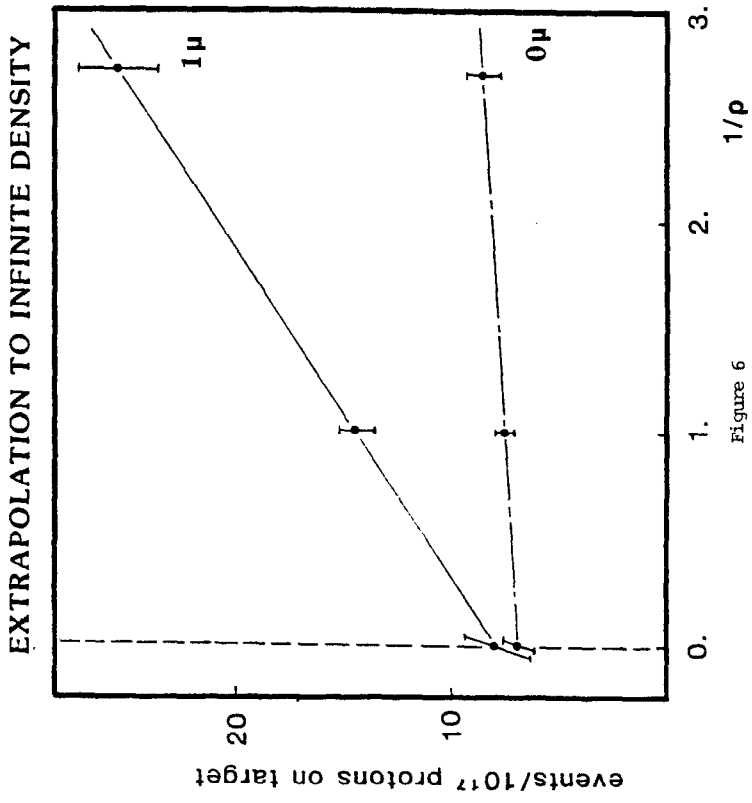


Figure 6

TABLE II

1-μ Results

	1/ρ	Protons (10^{16})	Raw Events	Corrected Events/10^{16} Protons
	2.7	2.1	197	208 ± 15
ν_u	1.0	7.9	415	116 ± 6
Prompt				62 ± 14
	2.7	2.1	93	80 ± 9
$\bar{\nu}_u$	1.0	7.9	145	42 ± 4
Prompt				19 ± 7

A statistically significant prompt signal is obtained for both ν and $\bar{\nu}$. Most charm production models predict equal ν and $\bar{\nu}$ fluxes. From the prompt rates obtained in Table II we find the flux ratio

$$\bar{\nu}_u/\nu_u = 0.64 \pm .3 \quad \text{FOR } E_\nu > 20 \text{ GeV}$$

If it is assumed that the major contribution to prompt neutrinos is central production of $D\bar{D}$, a charm production cross section can be extracted.

Additional production model assumptions are:

i) Excitation function of $\sigma(D\bar{D}) \sim S^{1.3}$

ii) Proton elasticity ~0.3

iii) A^1 dependence

iv) BR $(D \to \nu) = 16.4 \pm 2.4\%$ as obtained from e^+e^- data

v) $E\frac{d^3\sigma}{dp^3} \propto (1-|X|)^n e^{-br_\perp}$

where $X \frac{2P_L}{\sqrt{s}}$ and $r_\perp = P_\perp$ or $M_\perp \equiv (P_\perp^2 + M_D^2)^{1/2}$

For the choice of parameters

$$n = 3,\ b = 2,\ r_\perp = P_\perp$$

the total $D\bar{D}$ production cross section is then determined to be:

$$\sigma_{D\bar{D}} = 16_{\mu b} \pm 3 \text{ (statistical)} \pm 3 \text{ (systematic)}$$

Charm production cross sections reported by other beam dump experiments have included slightly different model parameters. For comparison, we have translated their results to this model as shown in Table III.

TABLE III

COMPARISON OF BEAM DUMP PROMPT CROSS SECTIONS

WITH IDENTICAL MODEL

Experiment	Flavor	$\sigma(D\bar{D})$ μb
BEBC (0-2 mr)	ν_u	45 ± 15
	ν_e	26 ± 15
CHARM (0-2 mr)	ν_u	14 ± 5
E595 (0-40 mr 350 GeV)	u	15 ± 5
E613 (0-37 mr)	ν_u	16 ± 4

The degree of model dependence of the charm production cross section was further examined by fitting the data with a model proposed by J. Leveille,[8] in which n = 5 and b = 3.45 with $m_\perp = (P_\perp + M_D)^{0.5}$ substituted for $P_\perp$. For the Leveille model we obtain a cross section of 28 ± 6 μb.

The dependence of the prompt 1-μ events on neutrino energy and transverse momentum is shown in Fig. 7 and 8. The dashed lines are predictions of the $n = 3,\ b = 2,\ r_\perp = P_\perp$ model, and the solid lines those of the $n = 5,\ b = 3.45,\ r_\perp = m_\perp$ model. A reasonable agreement with the E_ν and $P_\perp$ distributions is obtained for either model.

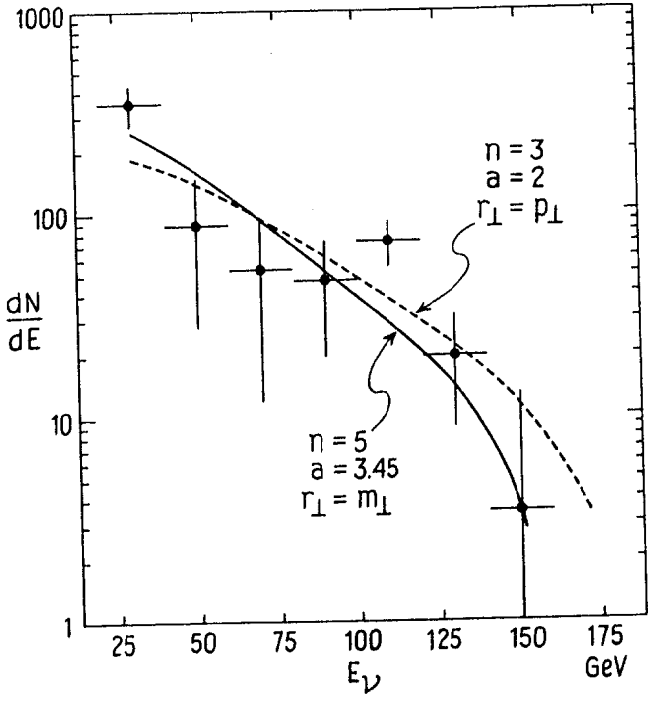


Figure 7

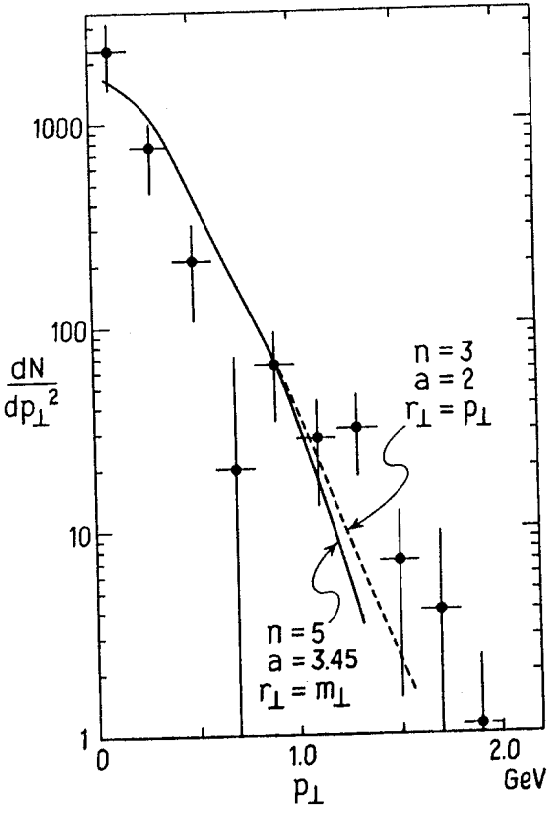


Figure 8

0-μ Results

For those events without a final state muon (0-μ events) the extrapolation to infinite target density produces a prompt neutrino sample consisting of electron neutrino and ν_μ neutral current events.

Table IV shows raw data, beam off date, corrected results and the prompt 0-μ signal from the target extrapolation.

TABLE IV

0-μ Results

1/ρ	Protons (10^{16})	Raw Events	Beam Off	Corrected Events/10^{16}
2.7	1.9	198	12	125 ± 9
1.0	7.6	563	26	96 ± 8
Prompt				79 ± 8

As for the 1-μ results, we consider models for charm production in the form

$$E\frac{d^3\sigma}{dp^3} \propto (1-|X|)^n e^{-br_\perp}$$

where X is Feynman X of the charmed particle and $r_\perp = P_\perp$ or $m_\perp \equiv (P_\perp^2 + m_D^2)^{1/2}$. For central production of $D\bar{D}$, where the charmed quarks share the energy of the incoming protons, n is expected[8,9] to be in the range of 3-5. For diffractive production of $\Lambda_c\bar{D}$, however, the Λ_c distribution is expected to have n = 1 or less.[10,11]

Figure 9 and 10 show the dependence of the prompt 0-μ events on neutrino energy and transverse momentum. As for the 1-μ data, the dashed lines are predictions of the n = 3, b = 2, $r_\perp = P_\perp$ model, and the solid lines those of the n = 5, b = 3.45, $r_\perp = m_\perp$ model. Again, reasonable agreement is obtained using either model.

Systematic data biases are expected to be smaller for 0-μ events than for 1-μ, due to the lack of muon acceptance corrections. Hence, for these data we have investigated the model dependence further. The dotted line in Fig. 9 and 10 shows the prediction for a diffractive model of charm production with n = 1, b = 2, $r_\perp = P_\perp$. The data clearly favor central production over diffractive production.

To obtain a limit on the $\Lambda_c\bar{D}$ diffractive production, we first normalize the n = 5, b = 3.45 $m_\perp$ model to the data in the 20-120 GeV range. The data are then examined for evidence of an n = 1 term in the 120-200 GeV range. Assuming a mixture of the n = 1 and n = 5 models, we find that less than 5.3% (90% confidence level) of the prompt events on tungsten come from diffractive production after correcting for the different acceptance of the apparatus for central and diffractive events. Assuming diffractive production ~ $A^{0.7}$, central production ~ $A^{1.0}$, and BR $(\Lambda_c^+ e) = 4.5 \pm 1.7\%$, this gives a limit of $\sigma(\Lambda_c^+ \bar{D}) < 13$ μb.

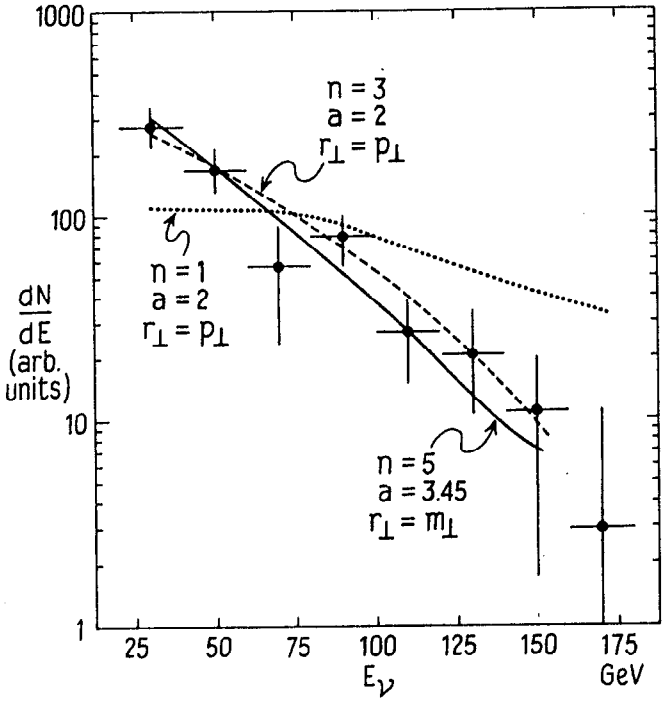


Figure 9

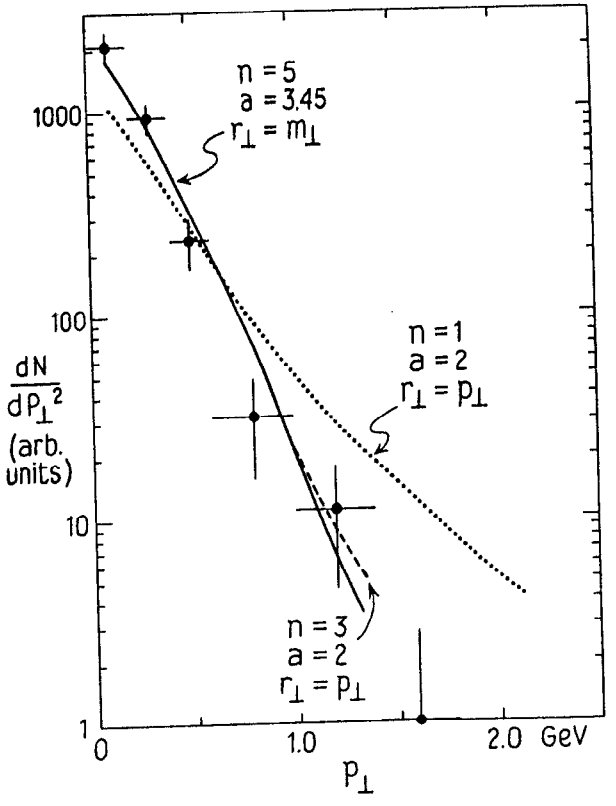


Figure 10

This result is substantially lower than recent estimates of 150 μb[12]. In their original form, "hidden charm"diffractive models seem not able to explain the apparent large difference between the observed charm production cross sections at 400 GeV and at ISR energies.

Neutral current events can be extracted from the 0-μ data to obtain a prompt $(\nu_e + \bar{\nu}_e)^{CC}$ signal, as described in a previous section. When this is done, we find

$$R \equiv \frac{(\nu_e + \bar{\nu}_e)^{CC}}{(\nu_u + \bar{\nu}_u)^{CC}} = 0.78 \pm .19 \quad (E_{VIS} > 20 \text{ GeV})$$

When R is plotted as a function of neutrino energy as shown in Fig. 11, an apparent energy dependence is seen. Error bars shown are statistical only, however, and most systematic effects are largest at the low energy limit. As an example, for $20 < E_\nu < 30$ GeV the acceptance for ν_u^{CC} events is .27, whereas it rises rapidly to .77 above 60 GeV. For all events above 30 GeV we find

$$R = 1.0 \pm 0.3$$

Values of R, as determined by different experiments, are shown in Table V.

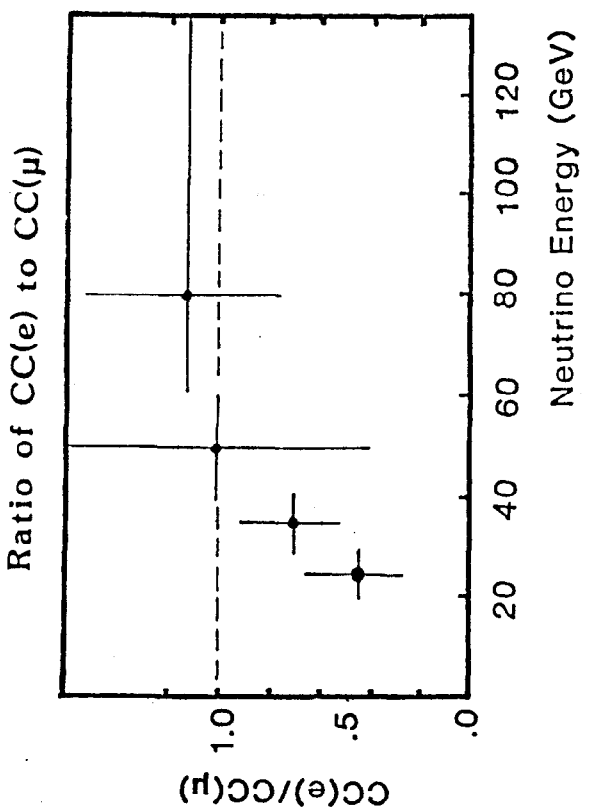


Figure 11

TABLE V

RATIO OF ν_e^{CC} TO ν_u^{CC} FOR DIFFERENT EXPERIMENTS

Experiment	$R = (\nu_e/\nu_u)^{CC}$ E_ν >20 GeV
BEBC	$0.59 \pm {}^{.35}_{.21}$
CHARM	$0.48 \pm .16$
CDHS	$0.64 \pm {}^{.22}_{.15}$
E613	$0.78 \pm .19$

The consensus of the CERN experiments is that R ~0.6 ± .1, while the result of this experiment can not as yet either confirm the CERN results or the expected value of 1.0. For the second E613 experimental run, recently completed, a muon charged current trigger has reduced low energy acceptance problems considerably, and enabled a significant increase in statistics. A definitive answer as to the existence of this apparent ν_e, ν_u universality breaking is expected in the near future.

Supersymmetry Limit

The results of this experiment have also been analyzed to set limits on the mass and decays of supersymmetric particles.[14] No anomalous signal is seen above the visible energy cutoff of 20 GeV. But stringent new limits can be set using three pieces of experimental data.

i) $(\nu_e/\nu_u)^{CC} = 1.09 \pm 36$ for $E_\nu > 40$ GeV. 90% CL upper limit for anomalous events is 0.56 of the ν_u^{CC} events.

ii) Anomalous pure electromagnetic events are $<40/10^{17}$ protons. This is a 90% limit; none are observed.

iii) Limit of 7 0-μ events with visible $P_\perp$ >1.5 GeV/c in a sample with 573 ν_u^{CC} events.

The calculation used for production of gluinos ($\tilde{g}$) is that of Kane and Leveille.[15] Photino ($\tilde{\gamma}$) and goldstino ($\tilde{G}$) cross sections were first calculated by Fayet.[16]

We obtain limits for the following types of interactions.

I. Gluino decays into a long lived photino, which interacts in the calorimeter, the interaction occurring through a scalar quark ϕ.

From the $P_\perp$ distribution, we obtain limits on $M_{\tilde{g}}$ as a function of m_ϕ/m_z, as shown in Fig. 12. The photino interaction cross section used is $\sigma_{\tilde{\gamma}} = \tilde{C}\, E \times 10^{-38}$ cm^2, where $\tilde{C} \propto (m_z/m_\phi)^4$.

II. Gluino decays into a short lived photino, which then decays into a goldstino and photon.[17] The cross section for goldstino interactions is $\sigma = C_{\tilde{G}}\, E \times 10^{-38}$ cm^2, where $C_{\tilde{G}}$ =

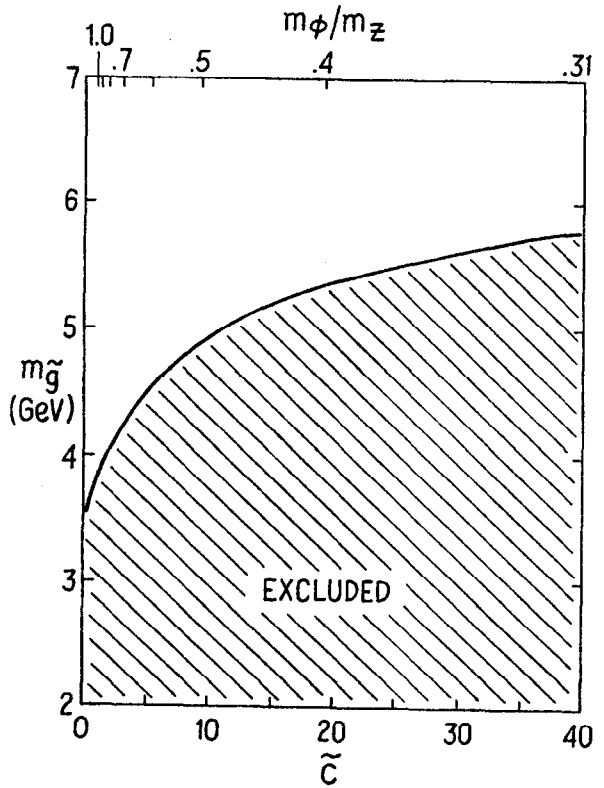


Figure 12

$0.015/(\Lambda_{ss}\ (\text{TeV}))^4$, Λ_{ss} is the supersymmetry breaking parameter. Limits are obtained using the $P_\perp$ distribution and the overall limit for anomalous events/ν_u^{CC} events. Results are shown in Table VI.

III. Gluino decays into a photino with intermediate lifetime, the photon from $\tilde{\gamma} \to \gamma\tilde{G}$ being seen in the calorimeter. From the limit on anomalous pure EM events we determine limits on the ratio of photino lifetime to photino mass. These are shown in Table VII.

IV. Gluino decays into a goldstino and a gluon, with the goldstino interaction cross section as in II. Again limits are obtained using the $P_\perp$ distribution. Results are shown in Table VI.

TABLE VI

LOWER LIMITS FOR Λ_{ss} (TeV) FOR CASE II, $(\tilde{g} \to \tilde{\gamma}\, q\bar{q}$ AND $\tilde{\gamma} \to \tilde{G}\,\gamma)$ AND CASE IV, $(\tilde{g} \to \tilde{G}\, g)$

$m_{\tilde{g}}$ (GeV)	Λ_{ss} (TeV) 90% CL Limit	
	Case II	Case IV
3	.36	.69
4	.20	.41
5	.13	.23
6	.09	.14

TABLE VII

EXCLUDED REGIONS OF PHOTINO LIFETIME FOR CASE III

($\tilde{g} \to \tilde{\gamma}\, q\bar{q}$; $\tilde{\gamma} \to \tilde{G}\ \gamma$; γ SEEN IN CALORIMETER)

$M_{\tilde{g}}$ (GeV)	Excluded $\tau_{\tilde{\gamma}}/M_{\tilde{q}}$ (sec/GeV) 90% CL
3	8.0×10^{-11} - 7.6
4	8.3×10^{-11} - 0.63
5	1×10^{-10} - 6.8×10^{-2}
6	1×10^{-10} - 7.8×10^{-3}

Conclusions

Results from the initial run of the Fermilab neutrino beam dump experiment E613 confirm the existence of prompt ν_e and ν_u production first seen by the pioneering CERN experiments, and provide significant evidence toward understanding this production.

Cross sections, energy and transverse momentum distributions are in good agreement with expectations that the dominant signal seen is due to the hadronic production and subsequent semileptonic decay of charm. Model dependent charm production cross sections $\sigma(D\bar{D})$ are determined to be ~15-30 μb, predominantly from central production. No positive evidence is seen for diffractive Λ_c production, with stringent limits found for $(1-X)^1$ production. No evidence is seen for anomalous events of the type predicted by supersymmetry models.

Two outstanding questions remain to be resolved in future runs. The present measurement of $R = (\nu_e/\nu_u)^{CC}$, while consistent with one, does not rule out the possibility of a significant deviation from one, as seen in the CERN experiments. A decisive measurement of this ratio is of utmost importance, as the CERN results defy any simple explanation using standard theoretical models.

Additionally, the large difference in cross sections and the amount of diffractive production seen by this experiment ($\sqrt{s}$ ~27.4) and at the ISR ($\sqrt{s}$ ~65) are not readily resolved. The ISR experiments find diffractive production of Λ_c to be dominant, but this type of production should have only a small energy dependence. It is hoped that this question can be resolved during initial runs at the Fermilab Tevatron.

Acknowledgements

The author owes a special debt of gratitude to Dr. R.J. Loveless of the University of Wisconsin, who, with very little prior notice, represented E613 at the SLAC Summer Institute and presented these results when an injury made it impossible for me (S. Childress) to attend.

This work is supported in part by the National Science Foundation and the Department of Energy.

FOOTNOTES AND REFERENCES

*The members of Experiment 613 are:

C. Castoldi, G. Conforto; University of Florence and R.C. Ball, C.T. Coffin, H.R. Gustafson, L.W. Jones, M.J. Longo, T.J. Roberts, B.P. Roe; University of Michigan, and M.B. Crisler, J.S. Hoftun T.Y. Ling, T.A. Romanowski, J.T. Volk; Ohio State University and M.E. Duffy, G.K. Fanourakis, R.J. Loveless, D.D. Reeder, D.L. Schumann, E.S. Smith; University of Wisconsin and S. Childress; Fermilab (formerly at University of Washington).

1. P. Alibran et al., Phys. Lett. 74B, 134 (1978).
2. T. Hansl et al., Phys, Lett. 74B, 139 (1978).
3. P.C. Bosetti et al., Phys. Lett. 74B, 143 (1978).
4. P. Fritze et al., Phys. Lett. 96B, 427 (1980).
5. M. Jonker et al., Phys. Lett. 96B, 435 (1980).
6. H. Abramowicz et al., CERN preprint EP 82-17.
7. J.L. Ritchie et al., Phys. Lett. 44, 230 (1980).
8. J. Leveille, U. Michigan preprint UM HE 82-20.
9. C. Michel, Proceedings of the XIV Rencontre de Moriond, Les Arcs (Savoie), FRANCE, March 1979, Vol. I., edited by J. Tran Than Van.
10. S.J. Brodsky et al., Phys. Rev. D23, 2745 (1981).
11. V. Barger et al., Phys. Rev. D25, 112 (1982).
12. S. Brodsky and C. Peterson, SLAC preprint PUB-2888.
13. F. Muller, Proceedings of the IV Warsaw Symposium on Elementary Particle Physics, 14 (1981).
14. P. Fayet, Phys. Lett. 78B, 417 (1978).
15. G.L. Kane and J.P. Leveille, Phys. Lett. 112B, 227 (1982).
16. P. Fayet, Phys. Lett. 86B, 272 (1979).
17. N. Cabibbo, G.R. Farrar, L. Maiani, Phys. Lett. 105B, 155 (1981).

RECENT RESULTS FROM CLEO AT CESR

Carl Rosenfeld

Department of Physics and Astronomy

University of Rochester, Rochester, NY 14627

I. *Introduction.*

In the period August–December, 1981, both the Cornell Electron Storage Ring (CESR) and the CLEO detector[1] benefitted from major upgrades. 1) The interaction region quadrupoles were removed and reinstalled in a mini-β configuration. As a result the luminosity increased by a factor of seven to 350 nb^{-1} per day. 2) The conventional CLEO solenoid was replaced by a superconducting solenoid. The new coil enables operation at 1.0 T compared with the old value of 0.4 T. 3) Four dE/dx modules replaced the remaining Čerenkov modules. All of the eight particle identification modules are now of the dE/dx type. In the 7.5 months since completion of the upgrade CLEO has acquired an integrated luminosity of 10 pb^{-1} at the $\Upsilon(3S)$, 30 pb^{-1} at the $\Upsilon(4S)$, and 2 pb^{-1} at the Υ.

In Section II we report our observation of continuum D^* production, and in Section III we present branching fractions for some decay modes of the Υ family. The topic of Section IV is the viability of nonstandard models of b quark decay.

© Carl Rosenfeld 1982

Section V discusses b decay phenomenology in the standard model and the experimental constraints on the weak mixing angles. In Section VI we consider possibilities for B meson reconstruction, and we present upper limits on the branching fractions of some favorable decay modes. In Section VII we summarize our major results.

II. Continuum D^* production.

This topic nicely illustrates the benefits of improved luminosity and resolution. The data come from 23 pb^{-1} of recent running at the $\Upsilon(4S)$ and the nearby continuum. We consider the process

$$e^+e^- \to c\bar{c} \to D^{*+}X$$
$$\hookrightarrow D^0\pi^+$$
$$\hookrightarrow K^-\pi^+.$$

For this analysis[2] we treat every charged track observed in the central drift chamber both as a π and as a K. For all assignments $K^-\pi_1^+\pi_2^+$ and the charge conjugates we calculate $M(K\pi_1)$ and $\Delta \equiv M(K\pi_1\pi_2) - M(K\pi_1)$. When the $K\pi\pi$ system is a D^*, the resolution (σ) of Δ is only 1.0 MeV because measurement errors approximately cancel. Figure 1 shows the distribution of Δ when

$$|M(K\pi) - M(D)| < 45 \text{ MeV}, \tag{1}$$

and Fig. 2 shows the distribution of $M(K\pi)$ when

$$\left|\Delta - \left(M(D^{*\pm}) - M(D^0)\right)\right| < 1.5 \text{ MeV}. \tag{2}$$

In both figures the D^* signal stands well above the background. All the particle combinations entered in these distributions satisfy the requirement that the D^* energy be at least 70% of the beam energy which reduces the background and ensures that the D^* is not the decay product of a B meson. For further analysis we accept as a

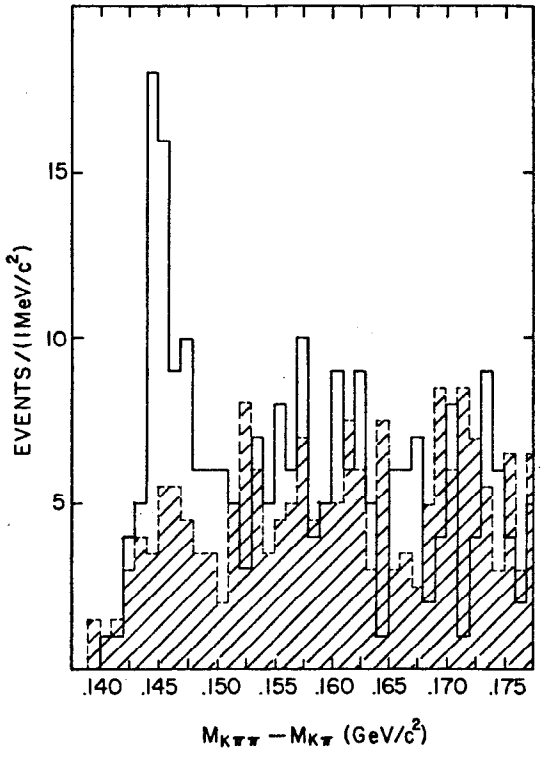


Fig. 1. Distribution of $\Delta \equiv M(K^\pm\pi^\mp\pi^\mp) - M(K^\pm\pi^\mp)$ for all track combinations meeting requirement (1) and having $z > 0.7$. The shaded histogram is for events in sidebands around the D^0 mass, $115 < |M(K\pi) - M(D)| < 205$ MeV.

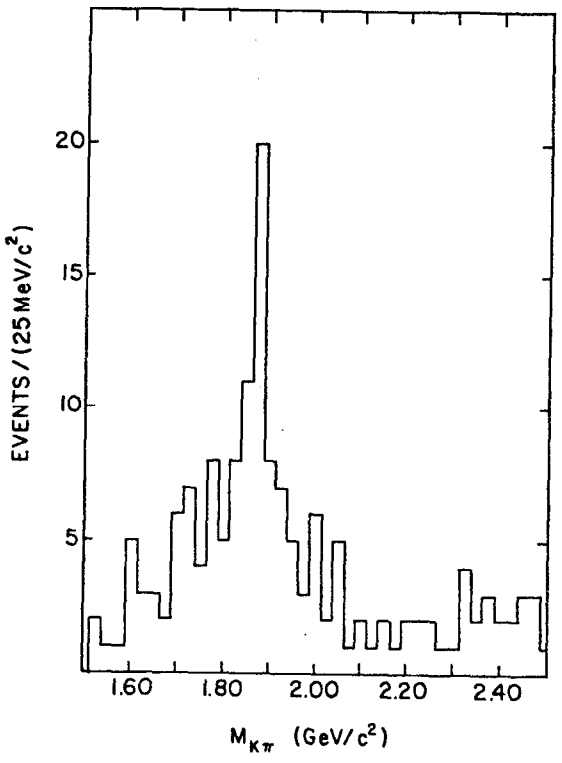


Fig. 2. Distribution of $M(K^{\pm}\pi^{\mp})$ for track combinations meeting requirement (2) and having $z > 0.7$.

D^* those particle combinations which satisfy both of the requirements (1) and (2). In Fig. 3 we show the fragmentation function $W^2\, d\sigma/dz$ where $z \equiv 2E(D^*)/W$ and W is the center-of-mass energy. Also shown in the figure is a Mark II measurement[3] of this function at 29 GeV as well as measurements of the corresponding functions for $D^{\pm}$ and D° at lower energies.[4] At the crude level of comparison permitted by the available statistical precision, the CLEO result appears consistent with most of the other measurements. For the cross section we find $\sigma(D^{*+}, z > .7) = 0.6 \pm 0.1 \pm 0.2$ nb. Isospin invariance implies equality for the charged and neutral D^* cross sections, and we conclude that $\sigma(D^{*+} + D^{*\circ}, z > .7)$ accounts for $40 \pm 7 \pm 13\%$ of produced c quarks.

III. A potpourri of Υ spectroscopy.

The branching fraction $Br(\Upsilon \to \tau^+\tau^-)$. The Υ is sufficiently heavy that the rate for the QED process $\Upsilon \to \gamma \to \tau^+\tau^-$ is nearly the same as the rate for the corresponding decay to $\mu^+\mu^-$. CLEO has measured the rate for the $\tau^+\tau^-$ decay mode and obtained the expected result. We select τ pairs which decay in the "1 vs 3" charged track topology. Two recent measurements[5] of the branching fraction for this configuration are both $25 \pm 3\%$. Figure 4 shows the visible cross section for $e^+e^- \to \tau^+\tau^-$ as a function of the center-of-mass energy W. The points at the right, taken at the $\Upsilon(3S)$, the $\Upsilon(4S)$, and several continuum energies, establish the level of the pure QED process. The curve indicates the W^{-2} projection of this level to the Υ energy. The measurement at the Υ stands about 3.5 σ above the QED cross section. The final result is $Br(\Upsilon \to \tau^+\tau^-) = 3.0 \pm 1.0 \pm 1.0\%$ which may be compared with the $\mu^+\mu^-$ branching fraction of $3.2 \pm 0.7\%$ as given in the *Review of Particle Properties*.[6]

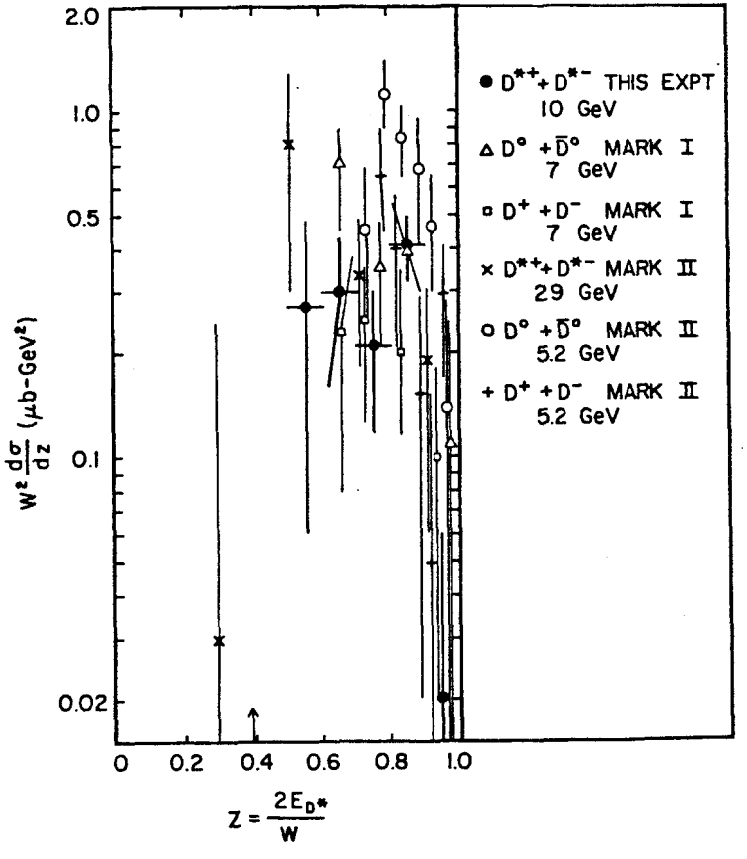


Fig. 3. Differential cross section for charged D^* mesons at 10.2 to 10.6 GeV from CLEO, and at 29 GeV from Mark II.[3] Also shown are the cross sections for charged and neutral D mesons at lower energies.[4]

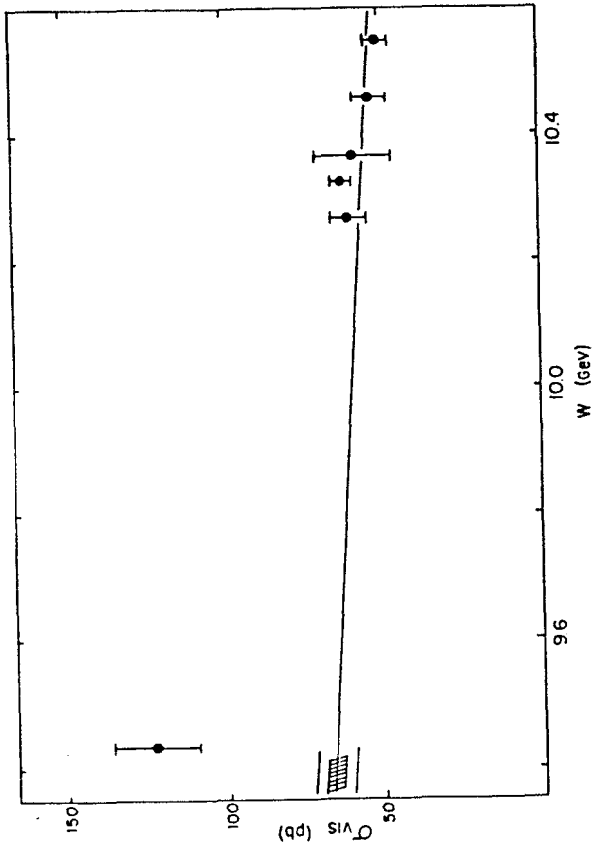


Fig. 4. The visible cross section for $e^+e^- \to \tau^+\tau^-$ vs center-of-mass energy. The lowest energy data point is at the Υ. The curve is the W^{-2} projection of the QED cross section from the measurements near 10.4 GeV to the Υ energy.

The branching fraction $Br(\Upsilon(3S)) \to \mu^+\mu^-$. In Fig. 5 we show the rate for $e^+e^- \to \mu^+\mu^-$ as a function of W. Using these data in the same way as we used the data of the preceding figure we can obtain $Br(\Upsilon \to \mu^+\mu^-) = 2.9 \pm 0.7\%$ which agrees well with the value quoted above. We wish to focus attention, however, on the data point at $W = 10.33$ Gev, the mass of the $\Upsilon(3S)$. This point is also significantly above the level of the QED process, and we obtain $Br(\Upsilon(3S) \to \mu^+\mu^-) = 3.2 \pm 1.6\%$. Potential models[7,8] predict approximately 2% for this branching fraction. Using the relation $\Gamma_{TOT} = \Gamma_{ee}/B_{\mu\mu}$ and the measured value[9] of Γ_{ee} we obtain $\Gamma_{TOT}(\Upsilon(3S)) = 13 \pm 6$ KeV.

The branching fraction $Br(\Upsilon(3S) \to \pi^+\pi^-\Upsilon)$. This measurement is another good illustration of the utility of the recently upgraded luminosity and magnetic field in the detector. The analysis[10] is based on 10 pb^{-1} of integrated luminosity at the peak of the $\Upsilon(3S)$. Of the events under the peak, 55% are resonance decays. In Fig. 6 we histogram the mass recoiling against every pair of oppositely charged tracks treating them as pions. The enhancement at the Υ mass, though small compared to the background, is statistically significant. Twenty-two of the events from this data sample have been identified as examples of

$$\Upsilon(3S) \to \pi^+\pi^-\Upsilon \to \pi^+\pi^-\ell^+\ell^-.$$

For these events we show the histogram of the mass recoiling against the pions (which was not used in the selection) in Fig. 7. Clearly this sample is nearly free of background.

We have two independent methods for estimating the branching fraction. In Method A we fit the distribution of Fig. 6 to the sum of a Gaussian and a smooth background. In Method B we use the rate for the $\pi^+\pi^-\ell^+\ell^-$ events in conjunction with the measured value of $Br(\Upsilon \to \mu^+\mu^-)$. Method A has the disadvantage of high

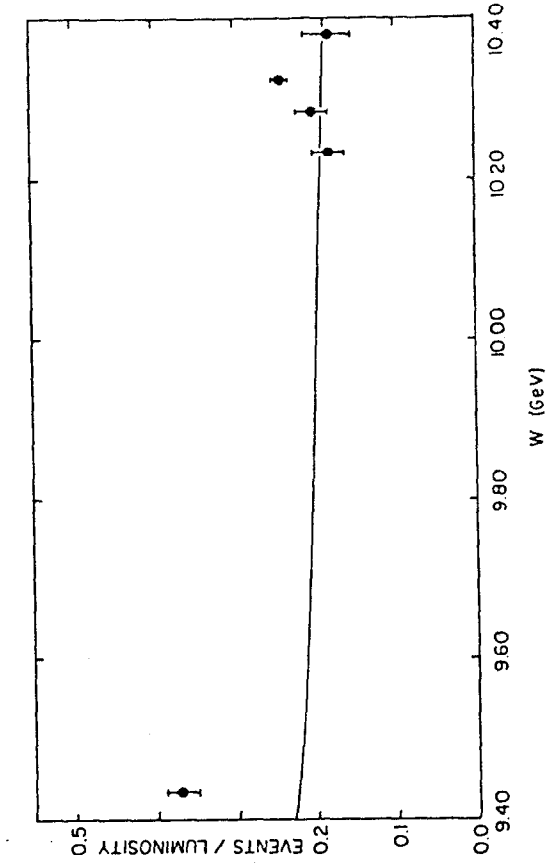


Fig. 5. The visible cross section for $e^+e^- \to \mu^+\mu^-$. From the enhancement at $W = 10.33$ GeV we determine $B_{\mu\mu}(\Upsilon(3S))$.

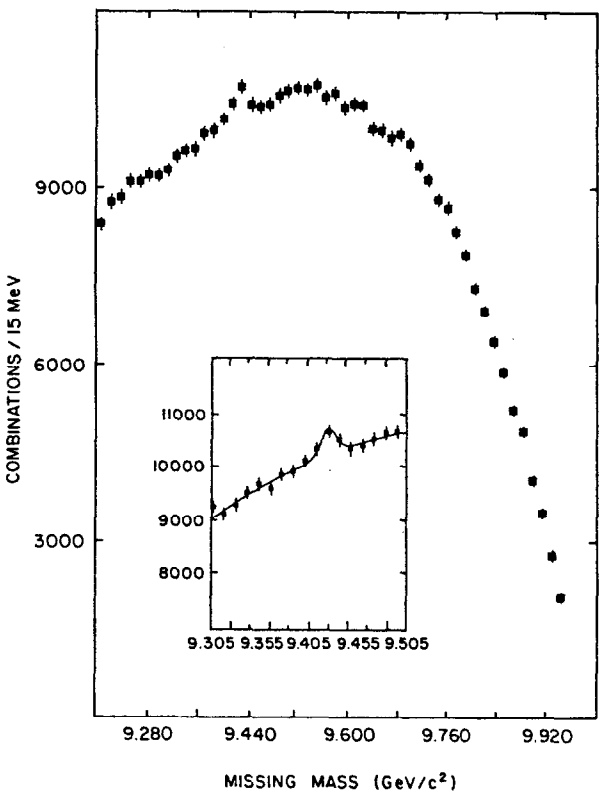


Fig. 6. Distribution of the mass recoiling against every pair of oppositely charged tracks for $\Upsilon(3S)$ events. The inset shows the fitted distribution used to calculate the branching fraction $Br(\Upsilon(3S) \to \pi^+\pi^-\Upsilon)$.

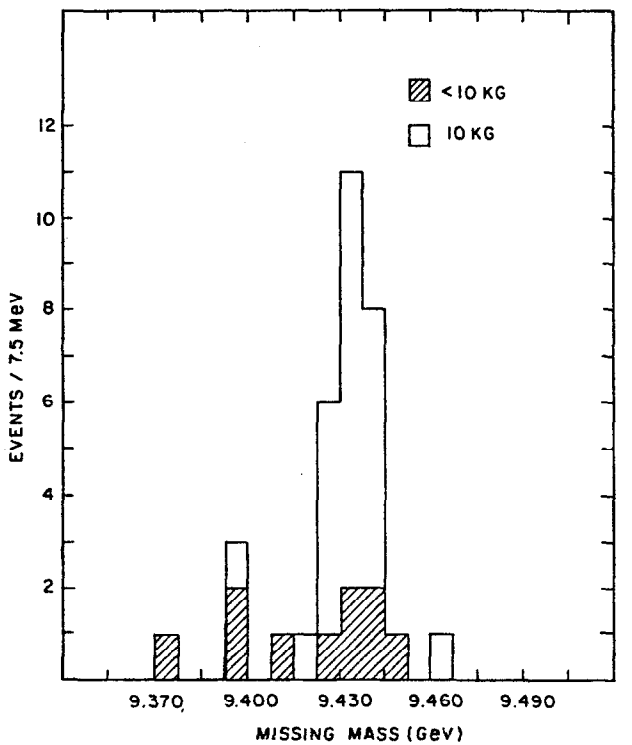


Fig. 7. Histogram of the mass recoiling from the pions in $\Upsilon(3S) \to \pi^+\pi^-\ell^+\ell^-$ events.

background while Method B has the disadvantage of small sample size. We give the results in the following table.

	Method A	Method B
No. of $\Upsilon(3S)$ decays	29000	35000
Acceptance	0.58	0.21
$Br(\Upsilon \to \mu^+\mu^-)$	—	0.033
No. of events observed	$911 \pm 220 \pm 66$	22 ± 5
$Br(\Upsilon(3S) \to \pi^+\pi^-\Upsilon)$	$5.4 \pm 1.3 \pm 0.5\%$	$4.4 \pm 1.2 \pm 0.5\%$

Average $Br = 4.9 \pm 0.9 \pm 0.5\%$

The model of Kuang and Yan[11] predicts 1.3–3.4% for this branching fraction. Although phase space favors $\Upsilon(3S) \to \pi\pi\Upsilon$ by a factor of six over $\Upsilon(2S) \to \pi\pi\Upsilon$, the model predicts $\Gamma(3S)/\Gamma(2S) \approx 0.1$ because of cancellations in the matrix element. We have to give the model high marks for this result.

IV. b quark decay—ruling out nonstandard models.

We investigate b quark decay using data taken at the $\Upsilon(4S)$. We believe that this resonance decays to a pair of b-flavored mesons for two reasons. 1) The width is greater than the beam energy spread, and we measure[12] $\Gamma(4S) = 20 \pm 6$ MeV. This width is about 500 times the width of the Υ. 2) The yield of electrons and muons from the resonance is most easily explained as coming from the weak decay of a quark[13] having a mass near 5.0 GeV. Possibly $\Upsilon(4S) \to B^*\bar{B} \to \gamma B\bar{B}$, but this alternative is equivalent to the $B\bar{B}$ decay for the purposes of the following discussion.

Most of the interesting possibilities for how a b quark might decay fit somewhere in Fig. 8. We consider in turn these various alternatives. The definitive demonstration that the b is not stable is just the observation of the $\Upsilon(4S)$ by CLEO and CUSB. We can be certain on the one hand that b-flavored particles are produced and on the

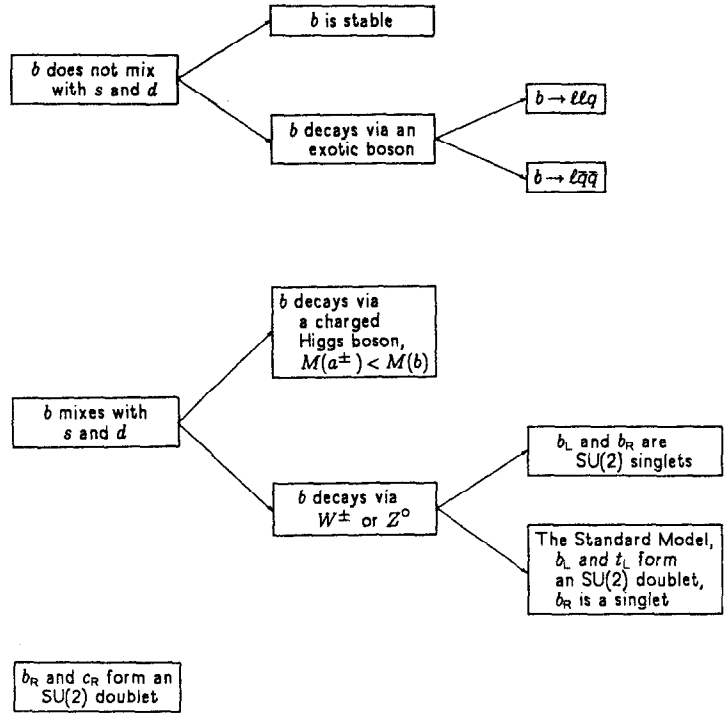


Fig. 8. A classification of models of b quark decay.

other that they decay well within the beam pipe. The lifetime limit from an early CLEO analysis[14] is $\tau_B < 10^{-10}$ s.

The light charged Higgs models. In one class of variations on the standard model the b is heavier than a charged spin-zero boson $a^{\pm}$ which may be an elementary Higgs particle[15] or a hyperpion.[16] We use the term "Higgs model" to cover both cases. The decay $b \to qa^-$ is semiweak (the decay amplitude has only one weak vertex), so the rate handily outstrips the rate for the usual weak decay modes. Models for which $M(a^-) < M(\tau)$ are already ruled out by data on τ decay.[6,15] If $M(a^-) < 2.4$ GeV, the a^- decays to $\mu^-\bar{\nu}_\mu$ and $\tau^-\bar{\nu}_\tau$ with the latter mode predominant above 1.9 GeV. For 2.4 GeV $< M(a^-) < M(b)$ the a^- can decay to $s\bar{c}$ as well as $\tau^-\bar{\nu}_\tau$, but theory offers no unambiguous guidance as to the branching fraction. Our strategy for ruling out these models is the following. If $Br(a^- \to s\bar{c}) \approx 100\%$, then we would have a negligible yield of electrons and muons. If $Br(a^- \to \tau^-\bar{\nu}_\tau) \approx 100\%$, the leptonic τ decays produce barely enough electrons and muons. In this case, however, the energy appearing in charged particles is too low because of the neutrinos, on average 2.4 per B decay. We have measured[17,18] the following inclusive properties of the $\Upsilon(4S)$.

1) The charged energy fraction,

$$\rho_c \equiv \left\langle \sum_i \left(|\vec{p}_i|^2 + m_\pi^2 \right)^{1/2} \right\rangle \Big/ M(\Upsilon(4S)),$$

where the average is over events and the sum is over charged particles resulting directly from B decay or from the decay of short-lived daughters including K_S^0 and Λ. We treat all particles as pions because the identity of most is undetermined and because most are in fact pions.[19]

2) $e/B \equiv$ the rate for a B decay to produce an electron of energy greater than 1.0 GeV. One GeV is the minimum required for electron identification in CLEO.

3) $\mu/B \equiv$ the rate for a B decay to produce a muon which penetrates the CLEO iron absorber and traverses the muon detector. On account of the variable thickness of the iron the muon acceptance rises from zero at 1.0 GeV to 80% at 2.2 GeV. We have incorporated this dependence in the model calculations of μ/B.

For these quantities we find $\rho_c = 0.60 \pm 0.03$, $e/B = 0.090 \pm 0.014$, and $\mu/B = 0.033 \pm 0.005$. We have calculated the corresponding predictions of the models by Monte Carlo. The simulations cover the full range of possibilities for the Higgs mass and branching fractions, the proportion of $b \to ua^-$ vs $b \to ca^-$, and the production ratio of B^+B^- to $B^0\bar{B}^0$. Figure 9 summarizes these results. The models populate the region below and to the left of the boundary curves. The best fitting model is ruled out at a confidence level of 99.5%. JADE, CELLO, and MARK II[20] have searched for $e^+e^- \to a^+a^-$ and have shown that the $a^{\pm}$ does not exist in a region of $M(a^{\pm})$ vs $Br(a^- \to \tau^-\bar{\nu}_\tau)$ which partially overlaps the sensitive region of the CLEO analysis.

Exotic models which forbid mixing of b with the light quarks. These models generally call for some enlargement of $SU(2) \otimes U(1)$, and the b decays via its coupling either to a gauge boson or to a Higgs boson of the enlarged group. In Table 1 we give a sampling of the models in this category. We note that not all of these models are t-less, and the merit of testing them would not be reduced by discovery of the t quark.

We would prefer not to confront models one-by-one but instead to seek some commonality which will permit us to test them in large groups. These models, as well as the standard model, conform to the following assumptions. 1) The b decays to three fermions from the menagerie of "established" quarks and leptons augmented only by extra neutrinos or neutrino-like leptons. 2) The decay conserves charge and color. These assumptions imply that b decay final states belong to one of three classes: a) $q_1q_2\bar{q}_3$, b) $\ell_1\ell_2q$, c) $\ell\bar{q}_1\bar{q}_2$ where q is a u, d, s, or c quark and ℓ is a lepton

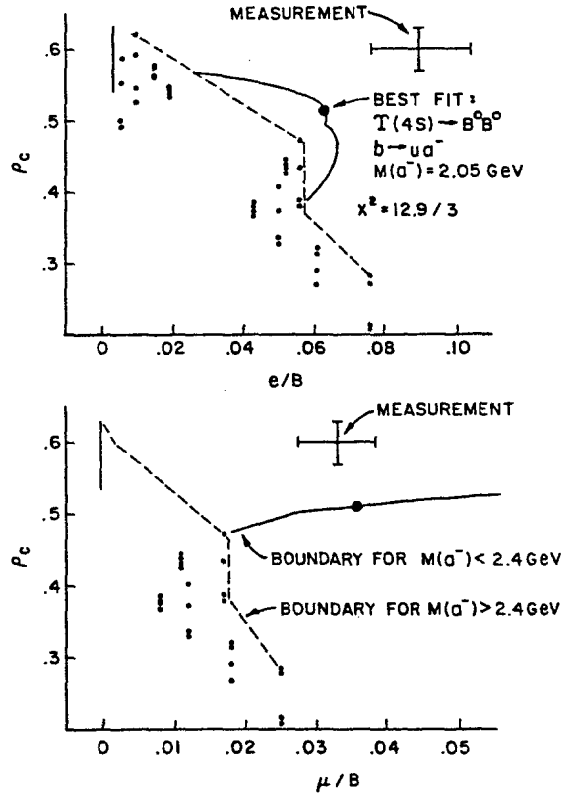


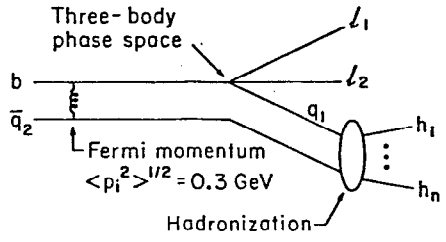
Fig. 9. Charged energy fraction ρ_c vs lepton yields e/B and μ/B as measured by CLEO and as calculated for the light charged Higgs models.

TABLE 1. Examples of models of b decay which forbid mixing with the light quarks.

Reference	Symmetry	b decay final states: $q_u \equiv u$ or c, $q_d \equiv d$ or s	
Derman[21]	$S(3) \otimes SU(2)_L \otimes U(1)$	$e^{\pm}\ell^{\mp}q_d$, $e^-\bar{\nu}_e q_u$, $\bar{\nu}_e \ell^- q_u$,	$\ell \equiv \mu$ or τ
Mohapatra[22]	$SU(2)_L \otimes SU(2)_R \otimes U(1)$	$\mu^-\bar{\nu}_M u$, $e^-\bar{\nu}_\tau u$, $\tau^-\bar{\nu}_e u$,	$M^- \equiv$ a heavy lepton
Georgi and Machacek[23]	$SU(4) \otimes SU(2)_L \otimes U(1)$	$\tau^+\bar{u}u$, $\tau^0\bar{u}\bar{d}$,	$\tau^0 \equiv$ a massless lepton
Georgi and Glashow[24]	E_6	$\tau^+\ell^- q_d$, $\bar{\nu}_\tau \nu q_d$,	$\ell \equiv e$ or μ

or antilepton (including neutrinos). Standard model final states are in both classes a) and b). In our examples of exotic models the final states are either in class b) exclusively or in class c) exclusively. Our objective then will be to rule out models in which the b decays exclusively to $\ell\ell q$ or to $\ell\bar{q}\bar{q}$.

The strategy for dealing with the $b \to \ell\ell q$ models depends on the three inclusive measurements described above. If all the primary leptons were electrons or muons, e/B or μ/B or both would be grossly too high. If instead all the primary leptons were taus or neutrinos, then ρ_c would be much too low. It is possible to fabricate a model which matches two of the three measurements, but we can demonstrate systematically that no model can match all three. For this purpose we use a Monte Carlo which simulates b decay in a spectator picture as shown schematically in the following figure.



$M(b) = 4.9$ Gev
$M(c) = 1.5$ GeV
$M(s) = 0.15$ GeV
$M(u) = M(d) = 0$

For the hadronization we use the Lund algorithm.[25] There are 40 ways to choose the flavors of the fermions which are represented by the following "factored" list.

$$\begin{bmatrix} \Upsilon(4S) \to B^+B^- \\ \Upsilon(4S) \to B^\circ \bar{B}^\circ \end{bmatrix} \times \left[b \to \begin{bmatrix} ee \\ \mu\mu \\ e\mu \\ e\tau \\ \mu\tau \\ \tau\tau \\ \nu\nu \end{bmatrix} \times \begin{bmatrix} d \\ s \end{bmatrix} \right.$$
$$\left. \begin{bmatrix} e\nu \\ \mu\nu \\ \tau\nu \end{bmatrix} \times \begin{bmatrix} u \\ c \end{bmatrix} \right]$$

We have calculated $(\rho_c)_i$, $(e/B)_i$, and $(\mu/B)_i$, $i = 1, \ldots, 40$. None of these 40 cases fits the measurements, but we must also consider mixtures. We specify a mixture by a vector of branching fractions $\vec{a} \equiv a_i$, $i = 1, \ldots, 40$ where $a_i > 0$ and $\sum_i a_i = 1$. Then

$$\rho_c = \sum_i a_i (\rho_c)_i \,, \qquad e/B = \sum_i a_i (e/B)_i \,, \qquad \mu/B = \sum_i a_i (\mu/B)_i \,.$$

We construct a χ^2 for the model in the usual way,

$$\begin{aligned} \chi^2(\vec{a}) = \; & [\rho_c(\vec{a}) - \rho_c(\text{meas})]^2/\sigma_\rho^2 \\ & + [e/B(\vec{a}) - e/B(\text{meas})]^2/\sigma_e^2 \\ & + [\mu/B(\vec{a}) - \mu/B(\text{meas})]^2/\sigma_\mu^2 \,, \end{aligned}$$

and we use the computer code MINUIT to search $\vec{a}$ space for the minimum χ^2. Table 2 describes the best fitting model. This model is ruled out at a confidence level of 99.7%.

The general method just described is also effective for the $b \to \ell\bar{q}\bar{q}$ class of models. In this case every B decay produces a baryon. The ρ_c, e/B, and μ/B are not sufficient to invalidate these models because, by judicious choice of quark flavors, a model can be engineered to compensate the loss of charged energy via neutrinos by an overabundance of protons. By including the proton and lambda yields in the comparison of the models with the data we foreclose this possibility. CLEO has measured[26] $p/B \equiv$ the rate for a B decay to produce a proton in the momentum interval $0.7 < p < 1.5$ GeV and $\Lambda/B \equiv$ the rate for a B decay to produce an identifiable Λ. The lambda acceptance ranges from 4% to 8% over the momentum interval $0.6 < p < 2.2$ GeV. The results are 0.06 ± 0.04 for p/B and $0. \pm 0.003$ for Λ/B. The baryons are now in a dilemma like the leptons—if they are protons, they tend to make p/B too high, and if they are neutrons, they tend to make ρ_c too low. The best fitting model in this class, which we describe in Table 3, is ruled out at the 99.99% confidence level.

Table 2. Minimum χ^2 solution for the $b \to \ell\ell q$ models.

$Br(\Upsilon(4S) \to B^+B^-) = 1$		$\chi^2/\text{DoF} = 13.8/3$		
b final state	Branching fraction	ρ_c	e/B	μ/B
$e^+\tau^-s + e^-\tau^+s$	4%	.64	.73	.012
$\mu^+\tau^-s + \mu^-\tau^+s$	12	.64	.056	.23
$\tau^+\tau^-s$	84	.46	.073	.008
average		.49	.097	.036
$(\text{residual}/\sigma)^2$		13.3	0.2	0.3

Table 3. Minimum χ^2 solution for the $b \to \ell\bar{q}q$ models.

$Br(\Upsilon(4S) \to B^0\bar{B}^0) = 1$			$\chi^2/\text{DoF} = 26.3/5$			
b final state	Branching fraction	ρ_c	e/B	μ/B	p/B	Λ/B
$e^+\bar{u}u$	7%	.71	.84	—	.27	—
$\mu^+\bar{u}u$	5	.71	—	.44	.27	—
$\mu^+\bar{c}c$	17	.59	.004	.042	.18	.04
$\tau^+\bar{u}u$	25	.49	.058	.012	.31	—
$\tau^-\bar{d}d$	46	.37	.056	.012	.02	—
average		.48	.099	.036	.15	.006
$(\text{residual}/\sigma)^2$		17.0	0.4	0.2	5.0	3.7

Exotic models with b-d, b-s mixing. In these models the b decays via its coupling to the $W^\pm$ and Z^0, but the SU(2) representation for the b is nonstandard. An example is a model proposed by Georgi and Pais[27] based on SU(3)⊗U(1). In this model the b quark decay modes are the following.

$b \to qq\bar{q}$	63%	
$e^-\bar{\nu}_e u, \mu^-\bar{\nu}_\mu u$	12	each
$\nu\bar{\nu}d$	7	
$e^+e^-d, \mu^+\mu^-d$	2	each

The neutral current decays are a feature of all models in this category because the GIM mechanism is not applicable when b_L is not in an SU(2) doublet. Kane and Peskin[28] have demonstrated a lower bound on the neutral current decay rate:

$$r \equiv \frac{Br(b \to \ell^+\ell^- q)}{Br(b \to \ell^-\bar{\nu}q)} > 0.12 .$$

Our strategy for eliminating these models is to show that the rate for $b \to \ell^+\ell^- q$ is below this bound.

The major backgrounds to the neutral current events are the following.

1) Parallel decays:

$$\Upsilon(4S) \to B\bar{B} \begin{cases} \to \ell_1^- \bar{\nu} X_1 \\ \to \ell_2^+ \nu X_2 . \end{cases}$$

This background creates only unlike-sign dileptons. If the electron and muon efficiencies are equal, $N_{ee} = N_{\mu\mu} = \frac{1}{2}N_{e\mu}$.

2) Fakes. Occasionally a hadron masquerades as a lepton. The rate of double fake events is negligible, but the rate of events with one real lepton and one fake is significant. The real-fake events are equally likely to be like sign or unlike sign.

Supposing again that the (real) electron and muon efficiencies are equal, we expect

$$N[e^{\pm}(fake)e^{\mp}(real)] = N[e^{\pm}(fake)\mu^{\mp}(real)],$$
$$N[\mu^{\pm}(real)\mu^{\mp}(fake)] = N[e^{\pm}(real)\mu^{\mp}(fake)].$$

Another potential background is cascade decays,

$$\Upsilon(4S) \to B\bar{B}$$
$$\quad \hookrightarrow \ell_1^- \bar{\nu} D X_1$$
$$\quad\quad \hookrightarrow \ell_2^+ \nu X_2 .$$

CLEO identifies electrons and muons only if their momentum exceeds 1.0 GeV, and less than 2% of D decays produce such energetic leptons. Consequently the cascade decay background is less than 7% of the rate from parallel decays. The background from continuum $D\bar{D}$ production is negligible for the same reason.

In the following table we give the dilepton tallies[29] from 11.2 pb^{-1} at the $\Upsilon(4S)$ peak and 4.7 pb^{-1} below the peak.

	N_{ee}	$N_{\mu\mu}$	$N_{e\mu}$
Like sign, on $\Upsilon(4S)$	2	2	5
Like sign, below $\Upsilon(4S)$	0	1	0
Unlike sign, on $\Upsilon(4S)$	8	10	16
Unlike sign, below $\Upsilon(4S)$	0	1	2

Of the 34 unlike-sign on-peak events approximately 10 are real-fake background and the balance are parallel decays. To suppress systematic error in our estimate of the number of neutral current decays we consider

$$S \equiv N_{ee} + N_{\mu\mu} - N_{e\mu}$$

for the unlike-sign events. The CLEO electron and muon efficiencies, 0.160 and 0.167 respectively, are nearly equal, and therefore the expectation value of S is close to zero for both parallel decays and real-fake events. From the table above we obtain $S = 2 \pm 6$. The corresponding upper limit for the ratio of the neutral current to the charged current semileptonic decays is $r < 0.12$ at the 94% confidence level and $r < 0.09$ at the 90% confidence level. The future of the singlet b_L models does not look promising.

The $(c,b)_R$ model. Of the classes of nonstandard models listed in Fig. 8 we have considered and rejected all but this one contender. In this model, proposed by Peskin and Tye, the virtual process $b \to cW^-$ proceeds with no suppression from weak mixing angles. The b lifetime is considerably shorter than in the standard model, but most other aspects of b phenomenology are much the same.[30] Confronting this model will be a difficult experimental challenge.

V. b quark decay—measuring parameters of the standard model.

Three properties of b decay comprise most of the standard model phenomenology: the b lifetime, the semileptonic branching fractions, and the ratio

$$\Gamma(b \to uW^-)/\Gamma(b \to cW^-).$$

The theoretical expectation for the lifetime is $c\tau \ll 300$ μm, and at the $\Upsilon(4S)$ the $\beta\gamma$ of a B meson is less than 0.1. A lifetime measurement clearly requires a better spatial resolution than CLEO will be able to achieve in the foreseeable future.

The semileptonic branching fractions. The prediction of a spectator model[31] which includes the QCD nonleptonic enhancement is

$$B_e = B_\mu = 0.147 - \frac{0.042w}{1+2.5w},$$

where $w \equiv \Gamma(b\to u)/\Gamma(b\to c)$. A better model,[31] which includes nonspectator contributions, predicts

$$Br(B^{\pm}\to e\nu X) = 0.147 - \frac{0.137w}{1+3.15w},$$
$$Br(B^{\circ}\to e\nu X) = 0.091 + \frac{0.011w}{1+2.1w}.$$

We do not know the proportions f and $1-f$ of $\Upsilon(4S)$ decay to charged and neutral B mesons, so CLEO can measure only the average

$$\overline{Br} \equiv f\,Br(B^{\pm}\to \ell\nu X)+(1-f)Br(B^{\circ}\to \ell\nu X).$$

The results,[18]

$$\overline{Br}(e\nu X) = 0.127\pm 0.017\pm 0.013,$$
$$\overline{Br}(\mu\nu X) = 0.122\pm 0.017\pm 0.031,$$

are in excellent agreement with the model.

Options for measuring $\Gamma(b\to u)/\Gamma(b\to c)$. The most obvious approach would be to measure $Br(B\to DX)$ by observing the D mesons. We have looked for D's at the $\Upsilon(4S)$, and we have found modest signals in the two-body decay channels as we show in Figures 10 and 11. The signal in $K^{\pm}\pi^{\mp}$ corresponds to $3\pm 1\pm 1$ D°'s per B decay. Despite this "success," the general approach founders because only the $D\to K\pi$ channels are visible above the combinatoric background, our K identification efficiency is only about 6%, the branching fractions for these channels are small, and they have not been measured with sufficient precision.

A more promising technique takes advantage of the dominance of the $c\to s$ transition. We infer the rate for $b\to c$ from the inclusive kaon rates. The following table gives our kaon results.[32]

	$B\bar{B}$	Continuum
$K^{\pm}$/event	1.58 ± 0.13	0.90 ± 0.04
K°/event	1.24 ± 0.21	0.89 ± 0.04

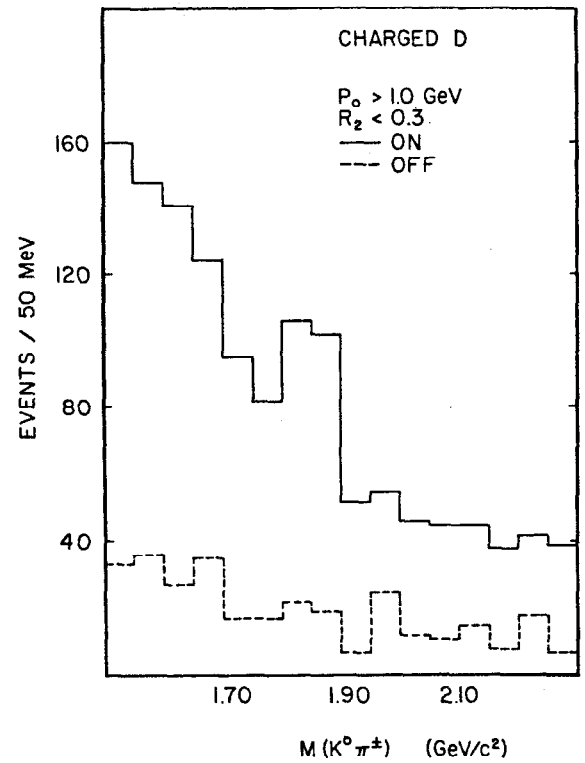


Fig. 10. Distribution of $M(K^{\circ}\pi^{\pm})$ for events at the $\Upsilon(4S)$ energy (solid) and below (dashed).

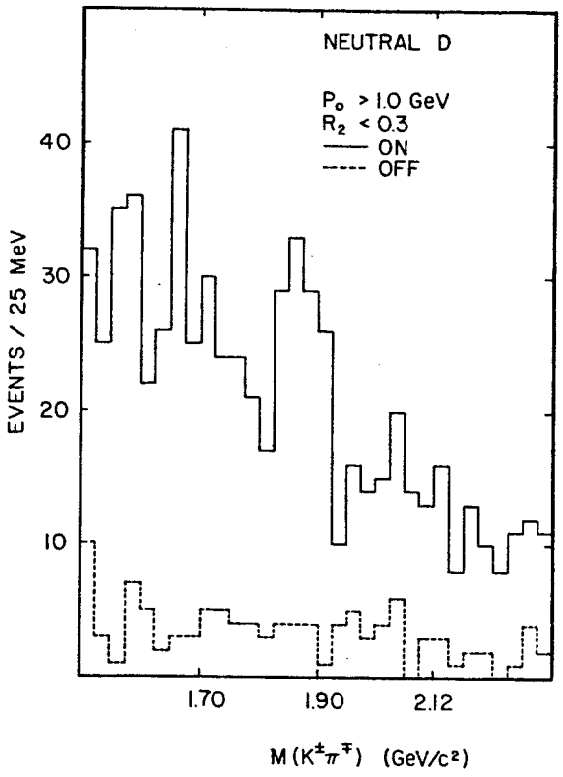


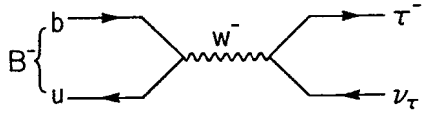
Fig. 11. Distribution of $M(K^{\pm}\pi^{\mp})$ for events at the $\Upsilon(4S)$ energy (solid) and below (dashed). The kaons are identified by time of flight.

We can reduce the systematic error by considering the ratios

$$\rho \equiv \frac{K/(B\bar{B}\text{ event})}{K/(\text{continuum event})},$$
$$\bar{\rho} \equiv (\rho^{\pm} + \rho^{\circ})/2$$
$$= 1.58 \pm 0.15.$$

Our B decay Monte Carlo predicts $\bar{\rho} = 1.8 \pm 0.1$ for $b \to c$ and $\bar{\rho} = 0.95 \pm 0.10$ for $b \to u$. The net result is $\Gamma(b \to u)/\Gamma(b \to c) < 0.8$ at the 90% confidence level—an improvement on our first effort, no doubt, but still not a precision measurement.

A third possibility is to measure $Br(B^- \to \tau^- \bar{\nu}_\tau)$.



$$\Gamma \propto f_B^2 |V_{ub}|^2$$

A virtue of this approach is that this branching fraction is proportional to the smaller $b \to u$ rate. The liabilities, however, are formidable: we do not know f_B^2 with any precision, the branching fraction is expected to be less than 2%, and the channel has no good signature. Once V_{ub} has been measured by other means, this branching fraction might shed some light on f_B. For the present we should pursue the more promising alternatives.

Our final option for a determination of $\Gamma(b \to u)/\Gamma(b \to c)$ is the lepton spectrum from semileptonic decays.[33] Because the c quark is much heavier than the u, $b \to \ell\nu c$ produces a softer spectrum than does $b \to \ell\nu u$. In Figures 12 and 13 we show the measured electron and muon spectra. Superimposed on the data are Monte Carlo generated curves for several models distinguished by the hadronic system X in the

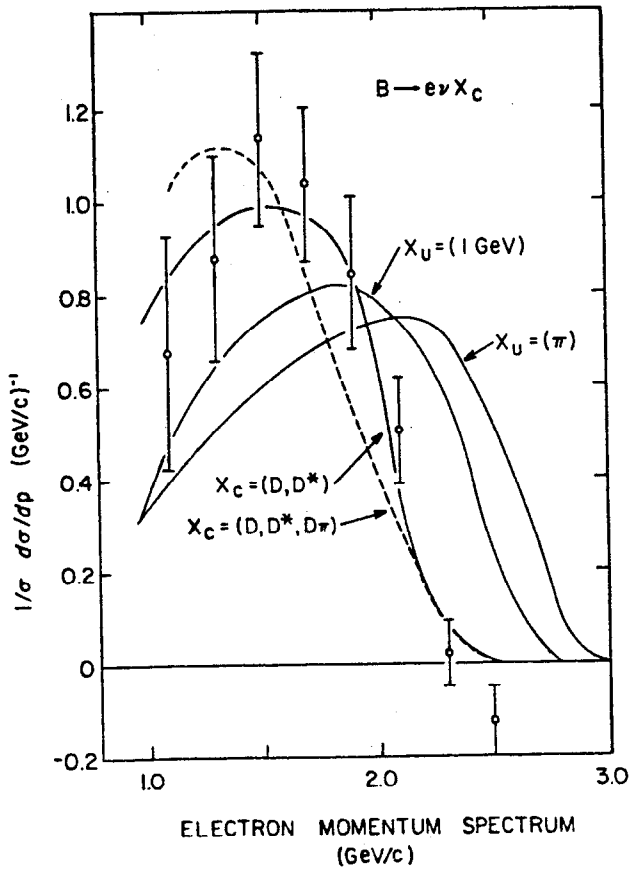


Fig. 12. Measured electron spectrum from the $\Upsilon(4S)$ and the predicted spectra for $B \to e\nu X$ using four alternatives for X.

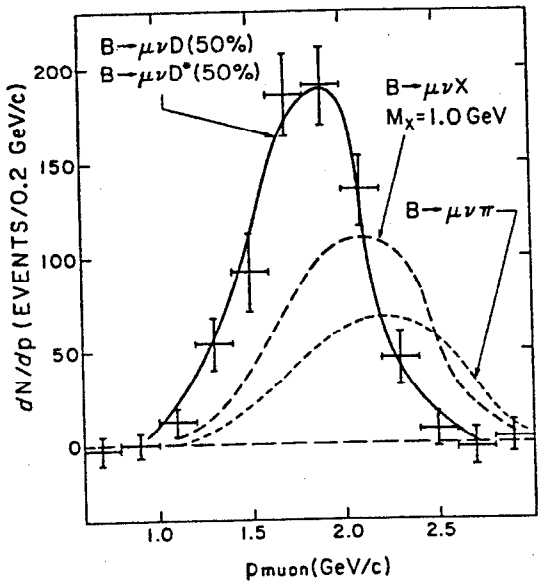
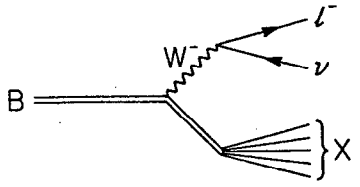


Fig. 13. Measured muon spectrum from the $\Upsilon(4S)$ and the predicted spectra for $B \to \mu\nu X$ using three alternatives for X.

following diagram.



For computing the $V-A$ matrix element, X is treated as elementary. Clearly choosing X to be 50% D and 50% D^* gives an excellent fit, and no $b\to u$ at all is required. If we simulate models with successively higher proportions of $b\to u$ for fixed $M(X_u)$, eventually the χ^2 deteriorates. In this fashion we obtain an upper limit on $b\to u$ as a function of $M(X_u)$, and we show this result in Fig. 14. Just how to garner from this exercise an overall upper limit is not altogether obvious, but we suggest $\Gamma(b\to u)/\Gamma(b\to c)<0.2$ as not too far off the mark. The lepton spectrum approach to the determination of this ratio is evidently the most successful.

Constraints on the K-M angles. We next want to show what additional constraints our upper limit on $(b\to u)/(b\to c)$ places on the weak mixing angles of the standard model. In this discussion we follow the Particle Data Group conventions and notation,[6]

$$\begin{pmatrix} d' \\ s' \\ b' \end{pmatrix} = V(\theta_1,\theta_2,\theta_3,e^{i\delta})\begin{pmatrix} d \\ s \\ b \end{pmatrix}.$$

With no loss of generality the quark states may be chosen so that $0\le\theta_i\le\pi/2$ and $0\le\delta\le\pi$. Analyses by Barger *et al.*[34] and Pakvasa *et al.*[35] constrain the angles as follows. 1) The comparison of nuclear β decay with μ decay determines $V_{ud}\equiv c_1$ with the result $s_1=0.23$. 2) Strange particle decays determine $V_{us}\equiv s_1c_3$ with the result $c_3>0.87$, $s_3<0.5$. 3) The K_L^0-K_S^0 mass difference and CP violation imply that $c_\delta\simeq\pm1$ and that $(c_\delta s_3, s_2)$ is somewhere inside the unshaded region of Fig. 15.

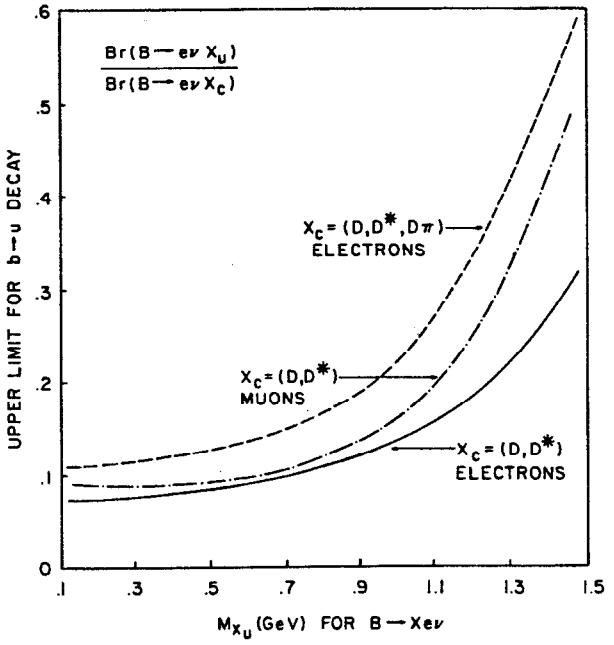


Fig. 14. Upper limit for $\Gamma(b\to u)/\Gamma(b\to c)$ as a function of $M(X_u)$, the mass of the hadronic system resulting from $b\to e\nu u$.

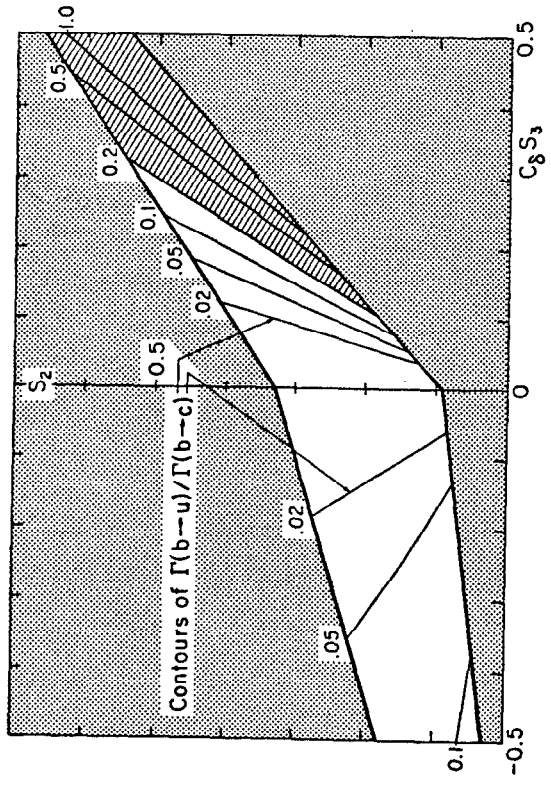


Fig. 15. Constraints on the weak mixing angles θ_2 and θ_3. From measurements of d and s quark decay all but the unshaded region can be ruled out. The hatched region can be ruled out using the CLEO measurement of $\Gamma(b\to u)/\Gamma(b\to c)$.

Within this region we show the contours of constant $\Gamma(b\to u)/\Gamma(b\to c)$. The hatched area to the right of the 0.2 contour is ruled out by the CLEO measurement.

VI. B meson decay.

What we know so far about the B meson mass is the following. Let $\Delta M \equiv M(\Upsilon(4S))/2 - M(B)$. Since the $\Upsilon(3S)$ is below threshold for $B\bar{B}$ decay, $\Delta M < 112$ MeV. Theoretical predictions[8] for the width of the $\Upsilon(4S)$ depend on ΔM, and the measured width implies $\Delta M < 50$ MeV. If the $\Upsilon(4S)$ were above threshold for decay to $B^*\bar{B}$, then the CUSB experiment would expect to see the γ from the $B^* \to \gamma B$ transition, and they do not.[36] The theoretical expectation[8] for $M(B^*) - M(B)$ is 50 MeV from which we infer that $\Delta M < 25$ MeV.

Whether a precise determination of $M(B)$ is of scientific importance in its own right is unclear, but as an adjunct to some other measurements its utility is clear-cut. In particular knowing the mass would help us to know the ratio

$$Br(\Upsilon(4S)\to B^0\bar{B}^0)/Br(\Upsilon(4S)\to B^+B^-),$$

and knowing this ratio is crucial to separating $Br(B^\pm \to \ell\nu X)$ from $Br(B^0 \to \ell\nu X)$ and to measuring B^0-$\bar{B}^0$ mixing. A better determination of $\Gamma(b\to u)/\Gamma(b\to c)$ would also benefit from a precise value for $M(B)$.

Reconstruction of a B would yield a mass value with greatly improved precision and is a worthy goal. In $\Upsilon(4S)\to B\bar{B}$ events, however, the average charged multiplicity is 12 and the average γ multiplicity is 12. Our efficiency for detecting all the debris from a typical B decay is low, and the combinatoric background is overwhelming. A brute force approach has not worked.

Instead we should try finesse. In this context finesse means a low multiplicity final state with a high branching fraction and a clear signature, for example,

$$B \to \psi K \qquad \text{and} \qquad B \to \psi K \pi.$$

Some predictions[37] for $Br(B \to \psi X)$ are as high as 3%. We have searched for these decay modes[38] and for the inclusive ψ signal with the following results:

$$Br(B \to \psi X) < 1.9\% \text{ using single muons,}$$

$$Br(B \to \psi X) < 1.4\% \text{ using dimuons,}$$

$$Br(B^{\pm} \to \psi K^{\pm}) < 1\%,$$

$$Br(B^{0} \to \psi K^{\pm} \pi^{\mp}) < 2.5\%.$$

All of the above limits are at the 90% confidence level. Evidently finesse has not worked either, at least not yet.

VII. Summary and acknowledgements.

The highlights of this presentation have been the following.

1) CLEO has observed D^* production from the continuum. The D^*'s with $z > 0.7$ account for $40 \pm 7 \pm 13\%$ of produced c quarks.

2) We have observed additional Υ family transitions, and in particular

$$Br(\Upsilon \to \tau^+\tau^-) = 3.0 \pm 1.0 \pm 1.0\%,$$

$$Br(\Upsilon(3S) \to \mu^+\mu^-) = 3.2 \pm 1.6\%,$$

$$Br(\Upsilon(3S) \to \pi^+\pi^-\Upsilon) = 4.9 \pm 0.9 \pm 0.5\%.$$

3) Most nonstandard models of b quark decay have been ruled out.

4) $\Gamma(b \to u)/\Gamma(b \to c) < 0.2$.

5) $Br(B \to \psi X) < 1.4\%$.

Looking ahead, we anticipate further substantial improvement in the CESR luminosity within the next year. If our past experience is a true guide to the future, the higher luminosity will propel us toward further advances in our investigation of b quark physics.

The CESR staff has worked tirelessly to improve the accelerator, and we are much indebted to them for their success. Funding for this research came from the National Science Foundation and the U. S. Department of Energy.

References

[1]D. Andrews *et al.*, CLEO 82-04 (1982), and Nucl. Instrum. Methods (to be published). The members of the CLEO collaboration are K. Chadwick, J. Chauveau, P. Ganci, T. Gentile, Joan A. Guida, R. Kass, A. C. Melissinos S. L. Olsen, G. Parkhurst, R. Poling, C. Rosenfeld, G. Rucinski, and E. H. Thorndike, *University of Rochester*; J. Green, R. G. Hicks, F. Sannes, P. Skubic, A. Snyder, and R. Stone, *Rutgers University*; A. Chen, M. Goldberg, N. Horwitz, A. Jawahery, M. Jibaly, P. Lipari, G. C. Moneti, and H. Van Hecke, *Syracuse University*; M. S. Alam, S. E. Csorna, M. Mestayer, and R. S. Panvini, *Vanderbilt University*; D. Andrews, P. Avery, K. Berkelman, D. G. Cassel, J. W. DeWire, R. Ehrlich, T. Ferguson, R. Galik, M. G. D. Gilchriese, B. Gittelman, D. L. Hartill, D. Herrup, S. Holzner, M. Ito, J. Kandaswamy, V. Kistiakowsky, D. L. Kreinick, Y. Kubota, N. B. Mistry, F. Morrow, E. Nordberg, M. Ogg, R. Perchonok, R. Plunkett, A. Silverman, P. C. Stein, S. Stone, D. Weber, and R. Wilcke, *Cornell University*; A. J. Sadoff, *Ithaca College*; C. Bebek, J. Hassard, M. Hempstead, J. M. Izen, W. W. MacKay, F. M. Pipkin, J. Rohlf, and Richard Wilson, *Harvard University*; H. Kagan, *Ohio State University*.

[2]C. Bebek *et al.* (CLEO Collaboration), Phys. Rev. Lett. 49, 610 (1982).

[3]J. M. Yelton *et al.* (Mark II Collaboration), Phys. Rev. Lett. 49, 430 (1982).

[4]P. A. Rapidis *et al.* (Mark I Collaboration), Phys. Lett. 84B, 507 (1979); M. W. Coles *et al.* (Mark II Collaboration), Phys. Rev. D 26, 2190 (1982).

[5]CELLO Collaboration, Phys. Lett. 114B, 282 (1982); C. A. Blocker *et al.* (Mark II Collaboration), Phys. Rev. Lett. 49, 1369 (1982).

[6]Particle Data Group, Phys. Lett. 111B, i (1982).

[7]M. Krammer and H. Kraesmann, Phys. Lett. 73B, 581 (1978).

[8]E. Eichten *et al.*, Phys. Rev. D 21, 203 (1980).

[9]D. Andrews *et al.*, CLEO 81/06, p. 134 (1981).

[10]J. Green *et al.* (CLEO Collaboration), Phys. Rev. Lett. 49, 617 (1982).

[11]Y.-P. Kuang and T.-M. Yan, Phys. Rev. D 24, 2874 (1981).

[12]D. Andrews *et al.* (CLEO Collaboration), Phys. Rev. Lett. 45, 219 (1980); G. Finocchiaro *et al.* (CUSB Collaboration), *ibid.* 45, 222 (1980);

[13]C. Bebek *et al.* (CLEO Collaboration), Phys. Rev. Lett. 46, 84 (1981); K. Chadwick *et al.* (CLEO Collaboration), *ibid.* 46, 88 (1981); L. J. Spencer *et al.* (CUSB Collaboration), *ibid.* 47, 771 (1981).

[14]E. H. Thorndike, in *High Energy Physics—1980*, edited by L. Durand and L. G. Pondrom (American Institute of Physics, New York, 1981), p. 705.

[15]E. Golowich and T. C. Yang, Phys. Lett. 80B, 245 (1979); L. N. Chang and J. E. Kim, *ibid.* 81B, 233 (1979); C. H. Albright, J. Smith, and S.-H. H. Tye, Phys. Rev. D 21, 711 (1980); D. R. T. Jones, G. L. Kane, and J. P. Leveille, *ibid.* 24, 2990 (1981).

[16]M. A. B. Bég, H. D. Politzer, and P. Ramond, Phys. Rev. Lett. 43, 1701 (1979); E. Eichten and K. Lane, Phys. Lett. 90B, 125 (1980); J. Ellis, M. K. Gaillard, D. V. Nanopoulos, and P. Sikivie, Nucl. Phys. B182, 529 (1981).

[17]K. Chadwick *et al.*, CLEO 81-06, p. 3 (1981); G. Rucinski, Ph.D. thesis, University of Rochester, 1982 (unpublished).

[18]K. Chadwick *et al.*, CLEO 82-05 (1982), and Phys. Rev. D. (to be published).

[19]A. Brody *et al.* (CLEO Collaboration), Phys. Rev. Lett. 48, 1070 (1982); M. S. Alam *et al.* (CLEO Collaboration), *ibid.* 49, 357 (1982).

[20]CELLO Collaboration, Phys. Lett. 114B, 287 (1982); JADE Collaboration, *ibid.* 114B, 211 (1982); C. A. Blocker *et al.* (Mark II Collaboration), Phys. Rev. Lett. 49, 517 (1982).

[21]E. Derman, Phys. Rev. D 19, 317 (1979).

[22]R. N. Mohapatra, Phys. Lett 82B, 101 (1979).

[23]H. Georgi and M. Machacek, Phys. Rev. Lett. 43, 1639 (1979).

[24]H. Georgi and S. L. Glashow, Nucl. Phys. B167, 173 (1980).

[25]T. Sjöstrand, University of Lund Report No. LU TP 80-03, 1980 (unpublished). We use the algorithms for the decay of low mass $q\bar{q}$ pairs, and we have adapted these to accommodate baryonic systems as well. We do not use any procedures which produce jets.

[26]A. Brody *et al.*, CLEO 81-06, p. 80, 1981.

[27]H. Georgi and A. Pais, Phys. Rev. D 19, 2746 (1979).

[28]G. L. Kane and M. E. Peskin, Nucl. Phys. B195, 29 (1982).

[29]J. Green *et al.*, CLEO 82-06, p. 23 (1982).

[30]V. Barger *et al.*, Phys. Rev. D 24, 1328 (1981).

[31]J. P. Leveille, University of Michigan, UMHE 81-18 (1981).

[32]C. Bebek *et al.*, CLEO 82-06, p. 31 (1982).

[33]D. Andrews *et al.*, CLEO 82-06, p. 14 (1982).

[34]V. Barger *et al.*, Phys. Rev. Lett. 42, 1585 (1979).

[35]S. Pakvasa *et al.*, Phys. Rev. D 23, 2799 (1981).

[36]R. D. Schamberger *et al.* (CUSB Collaboration), Phys. Rev. D 26, 720 (1982).

[37]H. Fritzsch, Phys. Lett. 86B, 164 (1979); H. Fritzsch, *ibid.* 86B, 343 (1979); T. DeGrand and D. Toussaint, *ibid.* 89B, 256 (1979).

[38]D. Andrews *et al.*, CLEO 82-06, p. 3 (1982).

WHAT HAVE WE LEARNED FROM THE UPSILONS?

Juliet Lee-Franzini

SUNY at Stony Brook, Stony Brook, New York, 11794

INTRODUCTION

The Upsilon family holds a special place in present day particle physics because it offers several arenas for the confrontation between theory and experiment. In the area of strong interactions the T system had established the validity of the potential model approach through the properties of its triplet S states. The recent measurements of its P-wave levels yielded further proof of the flavor independence of the color interquark forces. They indicate also, that potential models' predictions are favored over those resulting from QCD Sum Rule computations. Furthermore, a study of the fine structure splitting allows us to choose amongst the various ansatz proposed for the Lorentz structure of the potential to describe the spin dependence of the color forces. New measurements of the hadronic transitions between the radially excited states and the ground state confirm the general correctness of the QCD multipole expansion description, but suggest modifications of its detailed formulation. Finally, the measured leptonic branching fraction of the T can yield the most precise value of $\Lambda_{\overline{MS}}$, once the theoretical uncertainty for the latter's extraction is solved.

In the weak interaction sector T"' decays supply us with b-flavored mesons, almost at rest, whose decay properties elucidate the nature of the b quark couplings, and extend our knowledge of the quark mixing matrix. Finally, in the Higgs sector, by virtue of its large

© Lee-Franzini 1982

mass, the b-quark coupling to the Higgs field is larger than for all other fermions. We are therefore able to put stringent limits on the existence of the axion by combining two heavy quarkonia searches.

In this paper I discuss in detail the Upsilon contributions to the three areas, using data taken by the CUSB Collaboration [1], primarily after the installation of mini-β insertions in CESR in late 1981. During that down period the CUSB detector was also reconfigured with substitution of cathode readout proportional chambers in place of drift chambers for innner tracking, and the addition of scintillation counters surrounding the central detector to allow for muon triggers. Figure 1a is a partially exploded (end caps are pulled away from their running position) cut away isometric view of the CUSB detector and fig. 1b shows two sections of the detector along and perpendicular to the beam. Figure 2a shows $R_{visible}$ measured by CUSB as a function of total c. of m. energy, with the four bound states prominently featured. Figure 2b shows schematically the level diagram. The various transitions which were studied by CUSB in this recent period are indicated by arrows.

I. T and Reflections on QCD.

A. The Search for Other Narrow States and the Measurement of ΔR.

We have searched for new narrow resonances in e^+e^-→ hadrons in addition to the four $^3S_1$ states , in the c. of m. region from 10.24 GeV to 11.6 GeV. It is expected that one of the next higher radial excitations, n=5 [2] or n=6 [3], could have as narrow a natural width as 4 $^3S_1$. Below the flavor threshold, either vibrational states and/or D states made visible in e^+e^- annihilation through S-D mixing, will appear as narrow resonances whose widths are identical to the beam

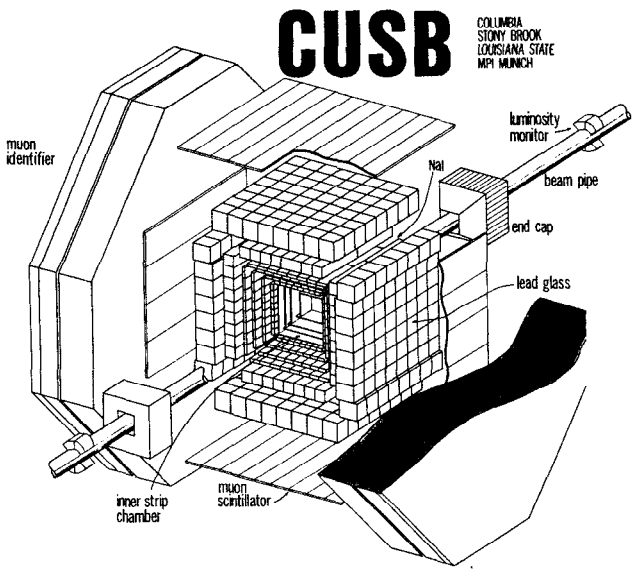


Fig 1a) A partially exploded cut away view of the CUSB detector.

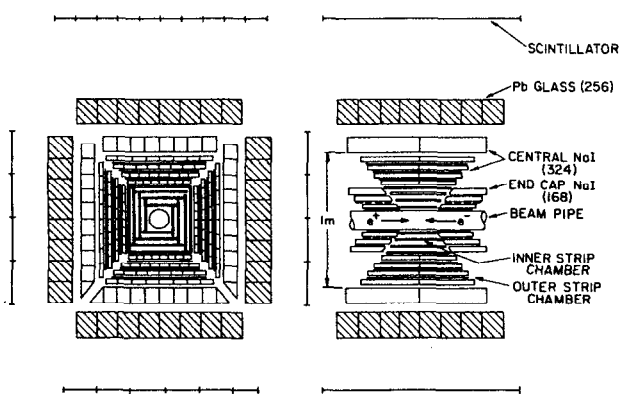


Fig 1b) Cut away end and side views of the CUSB detector.

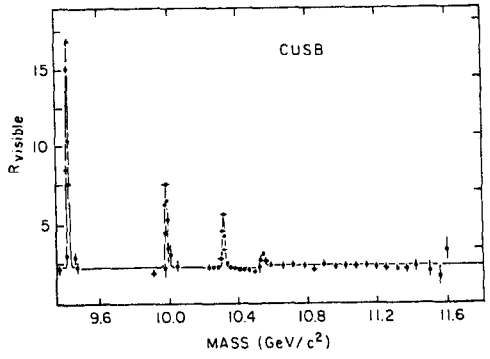


Fig 2a) $R_{visible}$ vs center of mass energy from CUSB.

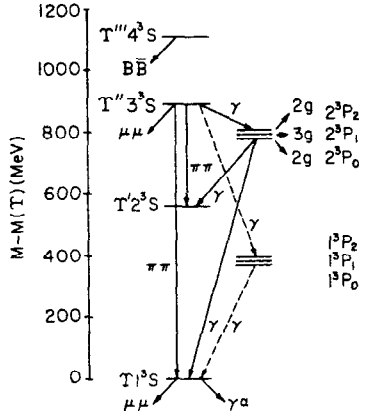


Fig 2b) Level diagram for the T system. Arrows indicate transitions discussed in the paper.

energy spread. In the three regions which we have searched, we found no positive signal; figure 3a shows the result of our most recent scan. We use a maximum likelihood method to establish the 90% c.l. limits:[4,5]

(i) $\Gamma_{ee} \leq 0.3$ KeV for a resonance of width ≃ 40 MeV, $10.6<\sqrt{s}<11.6$ GeV,

(ii) $\Gamma_{ee} \leq 20$ eV, in the region $10.34<\sqrt{s}<10.52$ GeV, and

(iii) $\Gamma_{ee} \leq 20$ eV, in the region $10.24<\sqrt{s}<10.31$ GeV. The limit established for region (ii) where string vibrational states are expected to exist is ≃ a factor of 4 below theoretical estimates.[6]

The level of $R_{visible}$, however, changes from 2.29 ± 0.029 below the T''' to 2.54 ± 0.040 above the T''', see figure 3b. Since this change is abrupt across the flavor threshold, it is reasonable to suppose that this increase is due to the production of B mesons and their excited states. Therefore, using the appropriate efficiencies computed for CUSB for continuum events and for $B\bar{B}$ events we obtain that R below T''' is 3.54 ± 0.05, above the T''' is 3.85 ± 0.05 and $\Delta R = 0.31 \pm 0.06$.[4] All errors quoted are statistical only; systematic uncertainties are of the order of 10% and cancel out in the evaluation of ΔR. This increase in R of 0.31 is remarkably close to the expected contribution from having passed the threshold for the production of charge 1/3 quark. As a side remark we note that the R value above the T''' is very close to those measured at PETRA and PEP; therefore it is not likely that we have crossed the production threshold for supersymmetric quarks (R = 1/2), or even for technipions (ΔR = 1/4) in the intervening region between CESR and PETRA energies.

B. Dynamics of T Decays.

The fact that quarkonia ground states decay into three gluons as postulated by Appelquist and Politzer[7] did not receive direct confir-

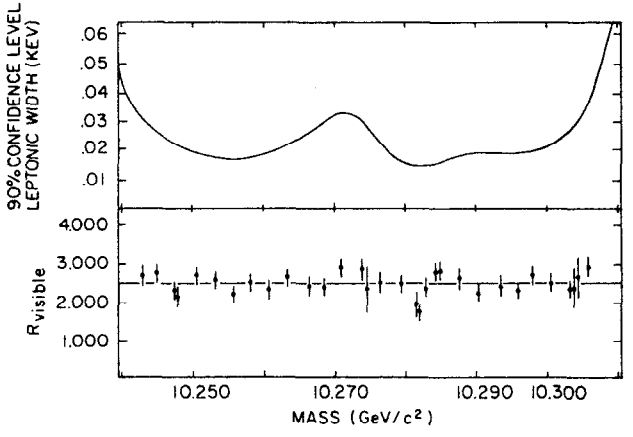


Fig 3a) 90% confidence level upper limit on Γ_{ee} vs center of mass energy from 10.24 to 10.31 GeV.

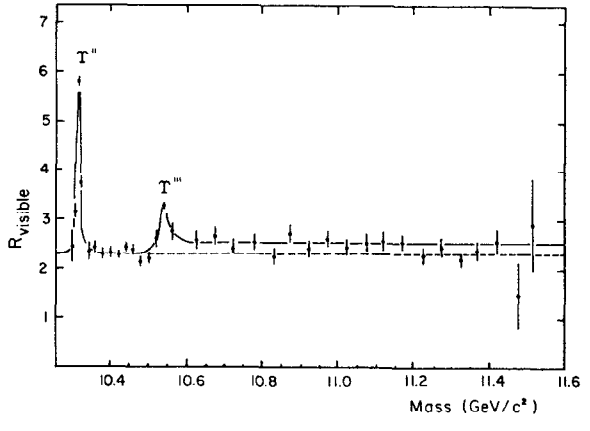


Fig 3b) $R_{visible}$ across the free flavor threshold, showing the change in $R_{visible}$.

mation until the existence of the T system because the J/ψ system did not have sufficient energy available to make the three jet nature of the decay apparent. In our detector we measure the fractions of 2 jet and 3 jet final states by the use of a thrust-like variable T' based on energy measurement. In figure 4a our thrust distributions for the T ground state and the continuum are shown; they are clearly widely separated.[8] The ability of CUSB to sense small amounts of admixture of two jet events in the three jet populations gave us the first indications that there were possible $^3S \rightarrow {}^3P$ transitions from the first two excited radial states. Figure 4c catalogues schematically the 2 jet and 3 jet contributions from such a state. In this way we have found for the T" a 20% ± 4% excess of 2 jet final states which we interpreted as evidence for $T'' \rightarrow \gamma\, {}^3P$, ${}^3P \rightarrow gg$. Figure 4b shows the measured thrust distribution from the T", which is visibly more "thrusty" than the 3 jet ground state (dashed line) distribution. Similarly, the excess 2 jet fraction measured on the T' was 7% ± 3%. However, in this case the excess obtained from thrust measurement is only a lower limit of the possible ${}^3P \rightarrow 2g$ because of the presence of a large fraction (see next section) of soft pions resulting from hadronic cascade transitions which lower the thrust and result in a lower apparent value of the 2 jet excess.[8]

C. Hadronic Cascades.

Hadronic transitions from the first radial excited state to the ground state in the Upsilon system has been observed by several groups including CUSB [9]. It was the comparison of the rate $T' \rightarrow T\pi\pi$ with that for $\psi' \rightarrow \psi\pi\pi$ which gave an independent proof of the vector nature of the gluon. From the 3^3S_1 (T") state hadronic transitions can

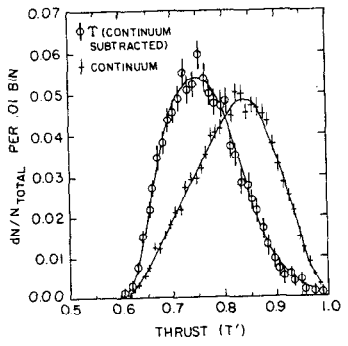


Fig 4a) Thrust distributions for T and continuum data.

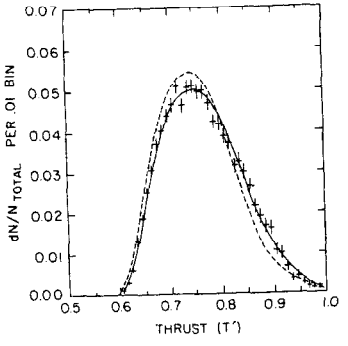


Fig 4b) Thrust distribution for T " data; dashed line is expected thrust for T", solid line is best fit for variable amounts of T and continuum thrust.

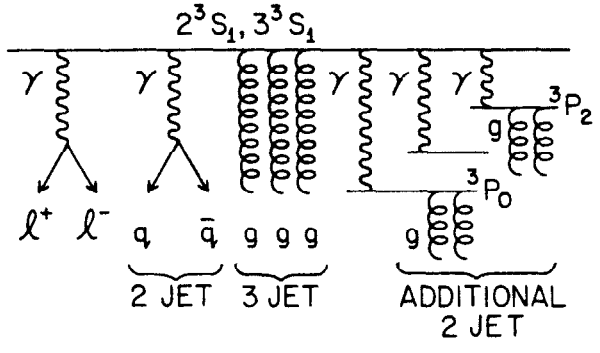


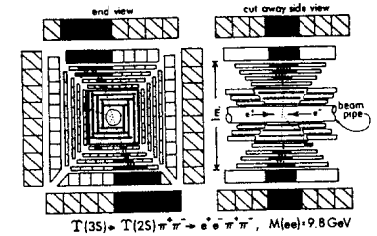
Fig 4c) Schematic representation of 2^3S_1 and 3^3S_1 decays, showing excess 2 jet contribution.

occur to both the first radial excitation and to the ground state. In CUSB we detect these transitions by looking for events with two pions accompanied by a dielectron or dimuon pair resulting from the final T or T' decay. Figure 5a shows a typical $T(3S) \rightarrow T(2s)\pi^+\pi^- \rightarrow e^+e^-\pi^+\pi^-$ event in CUSB, together with the selection criteria and efficiencies for such events. Figure 5b shows a scatter plot of the total energy deposited by the pion tracks versus the dilepton mass. The two clusterings correspond to $T'' \rightarrow T'\pi^+\pi^-$ and $T'' \rightarrow T\pi^+\pi^-$ transitions. CUSB has also observed these hadronic cascades with two π^0 emissions: the signature in CUSB for them is four showers consistent with 2 π^0's accompanied by a high energy lepton pair. In figure 6a we see the corresponding scatter plot of total energy deposited by the showers versus the dilepton mass; again two clusters are clearly visible. In the following we show a comparison of the CUSB measured rates with those predicted by Kuan and Yan using a multipole expansion of the gluon field.

$T' \rightarrow T\pi^+\pi^-$	$T'' \rightarrow T'\pi^+\pi^-$	$T'' \rightarrow T\pi^+\pi^-$	
18% ± 6%	3.1% ± 2.0%	3.9% ± 1.3%	CUSB[10]
16.7% to 18%	1.5% to 2.3%	1.4% to 3.4%	K & Y[11]

The agreement between the measured and predicted rates are excellent. However, the original theory also predicted a peaking towards high mass values for the mass spectrum, in agreement with experiment for the T' (see fig. 6b). The mass spectrum from $T'' \rightarrow T\pi\pi$ agrees instead with phase space (see figure 6b). Finally, while the mass spectrum from $T'' \rightarrow T'\pi\pi$ suffers badly from lack of statistics, it is not inconsistent with peaking at high mass. Clearly both this theory and experiment need some refinement. The data are inconsistent with the predictions of a theory assuming scalar—meson dominance.[12]

Fig 5a) Typical $\Upsilon'' \to \Upsilon'\pi^+\pi^- \to e^+e^-\pi^+\pi^-$ event in CUSB, with selection criteria.



$\Upsilon(3S) \to \Upsilon(2S)\pi^+\pi^- \to e^+e^-\pi^+\pi^-$, M(ee)=9.8 GeV

SELECTION CRITERIA

"Bhabha like" events with extra tracks. (C.L. ≥1% for fit 2C)

e e : > 5° from edges in central detector.
M(ee) > 6 GeV.
Acollinearity ee < 20°.
2 ISC tracks < 14° from shower centroid.
z vertex < 2.5 cm.

$\pi\pi$:	$3S \to 2S$ Q=50 MeV	$3S \to 1S$ Q=610 MeV
	Track ≥ 20° from e	Track ≥ 20° from e
	≥ 1 track ISC	2 track ISC
	≥ 1 plane NaI	≥ 2 planes NaI
	Heavy ionization	Minimum ionization
Efficiency:	11%	30.5%

Fig 5b) CUSB scatter plot of observed pion energy vs dilepton mass; open circles are e^+e^- and solid triangles are $\mu^+\mu^-$ events.

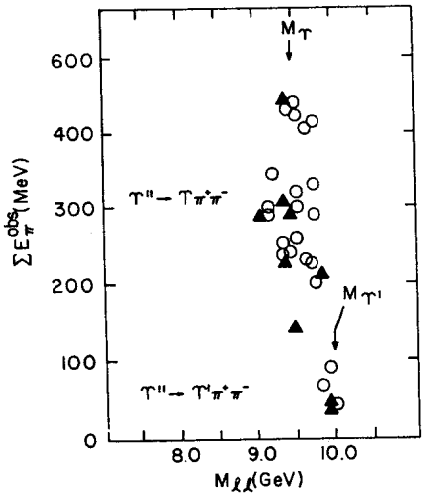


Fig 6a) CUSB scatter plot of observed photon energy from $\Upsilon'' \to \pi^0\pi^0\Upsilon, \Upsilon'$; open circles are e^+e^- and solid triangles are $\mu^+\mu^-$ events.

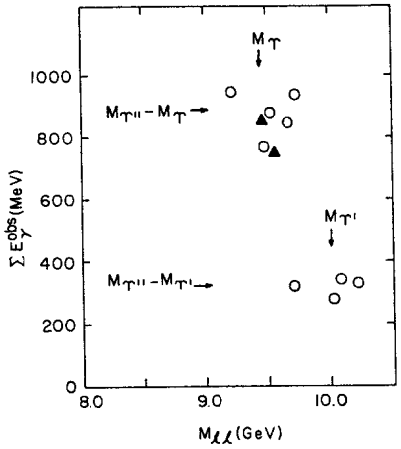
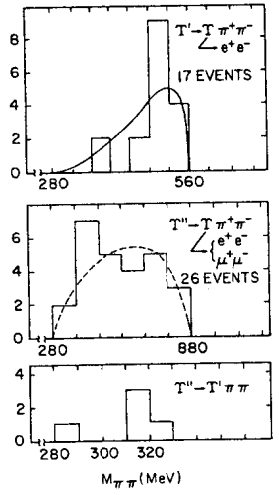


Fig 6b) Dipion mass spectra for $\Upsilon' \to \Upsilon\pi^+\pi^-$ (top), $\Upsilon'' \to \Upsilon\pi^+\pi^-$ (middle), and $\Upsilon'' \to \Upsilon'\pi^+\pi^-$ (bottom).



D. Photonic Transitions.

1. Inclusive spectrum.

The CUSB inclusive γ spectrum obtained at the T" peak from 64,689 hadronic events is shown in figure 7a; some structure is visible at about 100 MeV. When the spectrum is fitted with a polynomial, a χ^2 of 148 is obtained for 86 d.o.f. (c.l. < 1/16000). The curve shown is a fit obtained excluding 13 bins around the signal region which gave a χ^2 of 77 for 73 d.o.f. The excess over the curve contains 2150 γ's (over ≃ 37,000 γ's); it is a 10σ signal. γ spectra from 31,486 continuum hadronic events and 40,491 T region hadronic events are shown in figures 7b and 7c respectively. The curves are polynomial fits to the data, they gave χ^2's of 107 (fig. 7b) and 80 (fig.7c) for 86 d.o.f.

An alternate way to obtain the background curve is to predict it absolutely using properties of thrust distributions (see section I B). The thrust distribution at the T" is a linear combination of that from the continuum (41.6%) and that from the T (58.4%). Applying these coefficients to the spectra from 7b and 7c after they have been appropriately scaled by the number of hadronic events (64,869/31,386 for 7b; 64,869/40,491 for 7c), we obtain a background curve which is essentially indistinguishable from the one in figure 7a in the region of interest hence which yields the same excess in the 100 MeV region.

The subtracted spectrum is shown in figure 8a. The measured center of gravity of the signal is 97.7 MeV. Using our efficiency for 100 MeV photons of ≃ 17%, we obtain a branching ratio for T" → (100±20 MeV) γ's + X of 34%, with 3% statistical uncertainty. Both the position and the high rate of this signal make it highly likely that X is the $2^3P_{2,1,0}$ levels (also called χ_b''s) and that the bump consists of three

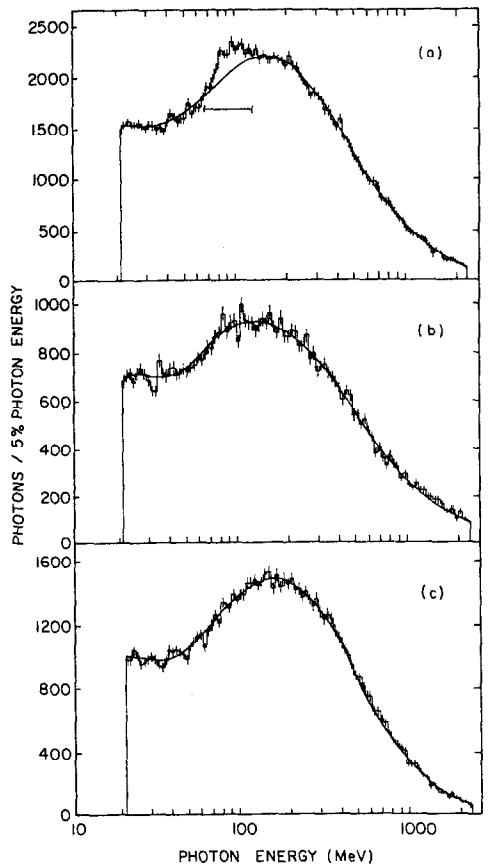


Fig 7) The observed inclusive photon spectrum from (a) the T" region, (b) the continuum, and (c) the T region. The bin size is 5% in ΔE/E. The excluded region in the polynomial fit is indicated by the horizontal bar in (a). The solid lines are polynomial fits (see text).

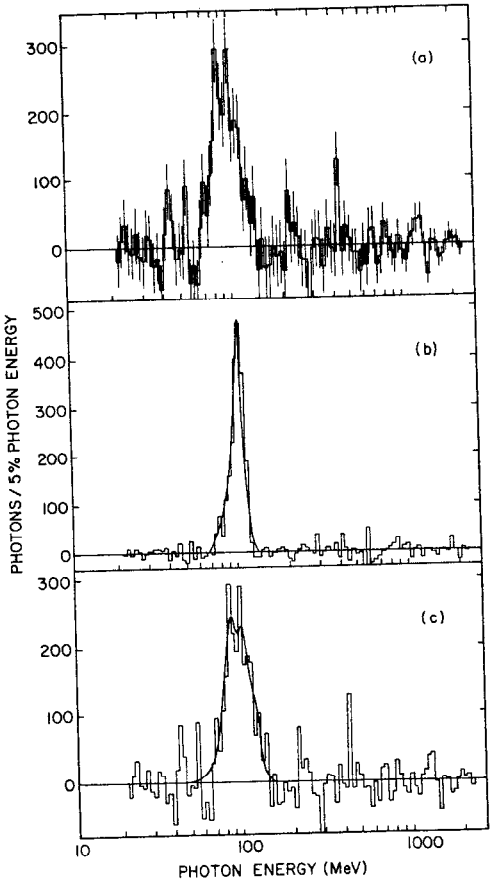


Fig 8) (a)The subtracted photon signal for $T'' \to \chi_b' + \gamma$ (see text). (b)The experimental photon energy resolution function. The solid line is a fit to two gaussians of width 6.7 and 12.5% of the peak position, the wider one displaced down by 10% and contributing 35% of the total area. (c)Fit of three lines to the subtracted photon spectrum.

E1 transition photon lines.[13]

The resolution function of the detector and γ search code combined is determined by Monte Carlo methods and is checked by reconstructing π^0's. Figure 8b gives the resolution function at 100 MeV, $\sigma \simeq 8\%$. It is far narrower than the signal peak in figure 8a. A fit with 3 such lines with arbitrary intensities and locations yields a χ^2 of 16.0 for 14 d.o.f., for 2 lines a χ^2 of 22 for 16 d.o.f. and for 1 line a χ^2 of 58.3 for 18 d.o.f. (c.l. $< 10^{-5}$). The intensities of the three lines, whose envelope is shown in figure 8c, divided by the $k^3(2J+1)$ factor (where k is the momentum of the γ and J is the presumed angular momentum of the state) and arbitrarily normalized to 1 for the middle line, are 0.95 ± 0.3, 1, 1.1 ± 0.4, consistent with the expectation that all three should be identical for 4π solid angle acceptance for γ's from E1 transitions. The center of gravity for the three fitted lines, excluding the kinematic k^3 factor, is 93 ± 1 (± 4) MeV.

2. Search for E1 transitions in exclusive channels.

We also searched for two photon transitions corresponding to

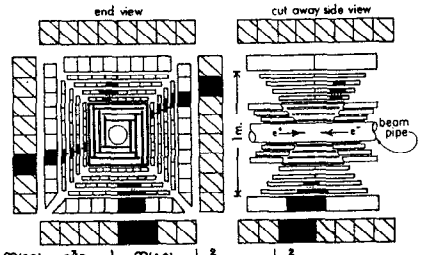
(i) $3^3S \to 2^3P_J + \gamma_1$, $2^3P_J \to 2^3S + \gamma_2$

(ii) $3^3S \to 2^3P_J + \gamma_1$, $2^3P_J \to 1^3S + \gamma_2$

(iii) $3^3S \to 1^3P_J + \gamma_1$, $1^3P_J \to 1^3S + \gamma_2$

followed by T or $T' \to \mu\mu$ or ee. Events of this kind have a characteristic signature of two almost collinear μ's or e's of about 5 GeV, plus two γ's whose energies add up to the T"-T' or T"-T mass difference. Since we cannot distinguish γ_1 from γ_2 we shall call γ_1 the lower energy γ and γ_2 the higher energy one in each event. Figures 9a and 9b show a typical event and the selection criteria for the dimuon and

Fig 9a) Typical event and the selection criteria for $T'' \rightarrow 2^3P + \gamma \rightarrow T\gamma\gamma \rightarrow \mu\mu\gamma\gamma$.



$T(3S) \rightarrow 2^3P + \gamma' \rightarrow T(1S) + \gamma'\gamma'^2 \rightarrow \mu\mu\gamma'\gamma'^2$

$E\gamma' = 90$ MeV, $E\gamma'^2 = 755$ MeV

SELECTION CRITERIA

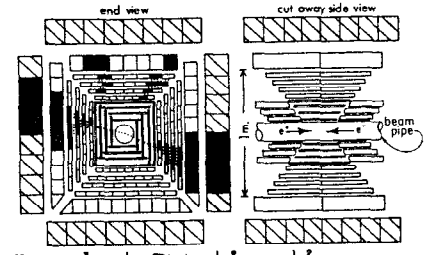
μ trigger with 2 neutral clusters.

$\mu\mu$: >5° from edges in central detector.
μ track is minimum ionizing.
Acollinearity < 15°.

$\gamma\gamma$: >5° from edges in central detector.
$E\gamma > 50$ MeV, $E\gamma' + E\gamma'^2 \geq 150$ MeV
γ centroid > 10° from μ
≤1 beam pipe conversion.

Efficiency: 12%

Fig 9b) Typical event and the selection criteria for $T'' \rightarrow 2^3P + \gamma \rightarrow T\gamma\gamma \rightarrow ee\gamma\gamma$.



$T(3S) \rightarrow 2^3P + \gamma' \rightarrow T(1S) + \gamma'\gamma'^2 \rightarrow ee\gamma'\gamma'^2$

M(ee) = 9.32 GeV, $E\gamma' = 91$ MeV, $E\gamma'^2 = 702$ MeV

SELECTION CRITERIA

"Bhabha like" with 2 neutral showers.

ee : >5° from edges in central detector.
M(ee) > 5 GeV.
Acollinearity ee < 17°.
2 ISC tracks < 14° from shower centroid.
z vertex < 2.5 cm.

$\gamma\gamma$: >5° from edges in central detector.
$E\gamma > 50$ MeV, $E\gamma' + E\gamma'^2 \geq 150$ MeV
γ centroid ≥ 45° from e.
≤1 beam pipe conversion.

Efficiency: 17%

ee final states. Figure 10a shows the scatter plot of the two γs for 18 $\mu\mu\gamma\gamma$ events, note that they show clean clusterings corresponding to reactions (i) and (ii). There are three candidates for reaction (iii), although two are on the 2σ boundary line. The dimuon events are virtually background free. A similar scatter plot, figure 10b, is shown for 50 ee$\gamma\gamma$ candidates. The invariant e^+e^- mass for these events are shown in figure 10c. They include background from double Bremsstrahlung, the magnitude of which is shown by the dotted line in figure 10c and the amount of which is estimated by studying the population outside the $\pm 2\sigma$ band, the yield from continuum running, and by modelling from superimposing two single Bremsstrahlungs. All three methods agree. The sum of the two photon energies for the candidates inside the $\pm 2\sigma$ band are shown in figure 11a, and they obviously correspond to the mass differences between the T" and T', or T" and T. It is reasonable to assume that these double photon events arise from reactions (i) through (iii). The product branching ratios obtained by CUSB for these reactions are[14]:

$\Sigma_{i=1}^{3}$ [BR($T'' \rightarrow \gamma_i \chi'_{bi}$) * BR($\chi'_{bi} \rightarrow \gamma T'$)] = (5.9 ± 2.1)% 3.3%

$\Sigma_{i=1}^{3}$ [BR($T'' \rightarrow \gamma_i \chi'_{bi}$) * BR($\chi'_{bi} \rightarrow \gamma T$)] = (3.6 ± 1.2)% 2.8%

$\Sigma_{i=1}^{3}$ [BR($T'' \rightarrow \gamma_i \chi_{bi}$) * BR($\chi_{bi} \rightarrow \gamma T$)] < 3%, 90% c.l. 1.1% .

The last column are theoretical expectations for these product ratios obtained using the E1 rates given by Eichten et al[15], the hadronic rates given by Barbieri et al[16] and the measured T" total width.[17]

It is expected that the 2^3P_0 level has a small E1 BR for transitions to the T ground state, hence most of the double γ transitions are from the $2^3P_{2,1}$ levels. Their position can be found by making a two line fit to the major portion of the γ_1 distribution. Such a fit

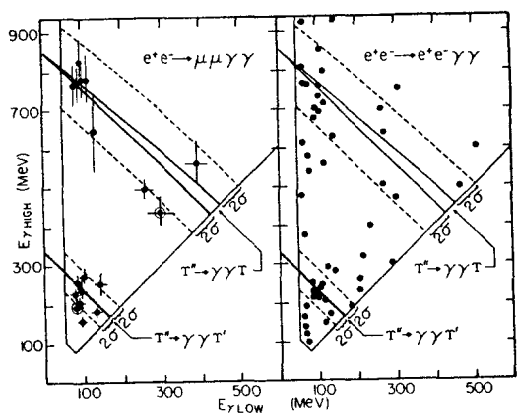


Fig 10a,b) Scatter plot of E_{lo} vs E_{hi} with selection boundary (solid line) and 2σ bands (dashed line) indicated for (a) $e^+e^- \to \mu\mu\gamma\gamma$ events, and (b) $e^+e^- \to ee\gamma\gamma$ events.

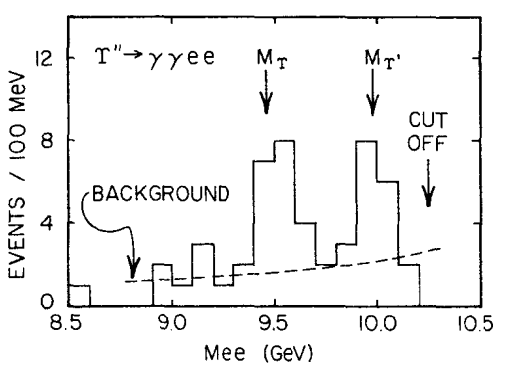


Fig 10c) Invariant dielectron mass for $T'' \to ee\gamma\gamma$ events, with background indicated (see text).

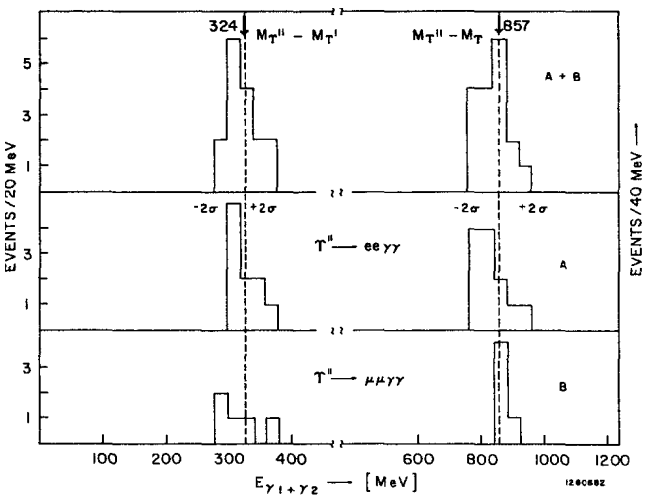


Fig 11a) Sum of two photon energies for all candidates inside ±2σ band.

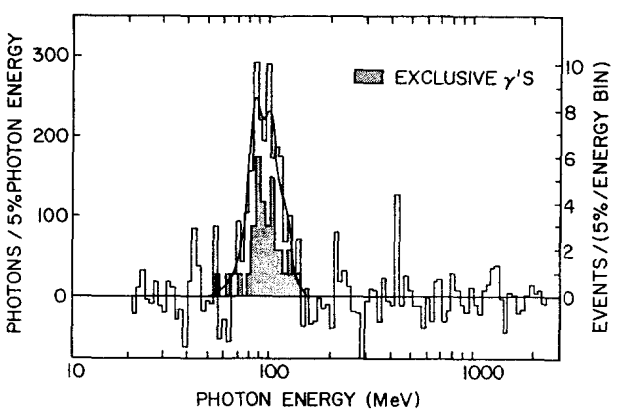


Fig 11b) Superimposition of the inclusive Υ spectrum (histogram and solid curve) with the spectrum of the lower energy photons from the exclusive decays (shaded histogram).

has a confidence level of 45%, whereas the probability that the observed signal is due to a single line is less than 3%. The three events whose γ_1 are larger than 114 MeV are used to obtain the position of the third line. The γ_1 distribution from the exclusive events are shown in figure 11b, plotted superimposed on the inclusive γ spectrum. In the following table we list the photon energies resulting from fitting the inclusive and exclusive data as described in the previous and present section.

	CUSB E1 Transition Photon Energies†	
	Inclusive Spectrum[13]	Exclusive Spectrum[14]
$3^3S_1 \to 2^3P_2 + \gamma$	84.5 ± 2.0 ± 4 MeV	84 ± 3 ± [5 MeV]
$2^3P_1 + \gamma$	99.5 ± 3.2 ± 4 MeV	99 ± 2 ± [5 MeV]
$2^3P_0 + \gamma$	117.2 ± 5.0 ± 4 MeV	[119 ± 5 ± 5 MeV]

†The first error is the diagonal element of the error matrix; the second is a generous estimate of the systematic uncertainty by the author.

The agreement between these two entirely independent analyses is gratifying. The center of gravity of the three fitted lines is 93 MeV, and this value will be used hereafter in comparison with theoretical models. The branching fraction of 34% as quoted in section I.D.1., when combined with the values of the T" leptonic width, $B_{\mu\mu}$ and the hadronic branching ratio [10] yield

$\Gamma(E1) = 6.5 \pm 0.8 \pm 0.6$ keV where the first error is statistical and the second is the estimated systematic uncertainty.

E. $2^3P_{2,1,0}$ Levels and Potential Models.

There has always been a discrepancy between the DORIS and CESR energy scales of 0.027%.[17] In order to facilitate comparison between CESR measurements and theoretical predictions I have adopted the DORIS energy scale because recent absolute measurements of the T mass at VEPP-4[18] agree with the DORIS value. Taking into account the 1/2 MeV recoil during γ emission we obtain 2^3P(c.o.g.) = 10.255 ±0.004 GeV. Potential models inspired by QCD and those built empirically by fitting to a power law, on the whole predict the 2P level position and the E1 transition rate which are close to the experimental value (see the following table). A major exception is the new heavy $Q\bar{Q}$ bag model approach of Baacke et al.[26] whose predicted position is off by ≃ 60 MeV and whose predicted rate is down by over an order of magnitude.

Measurement and Predictions of the 2^3P level Properties

Author	c.o.g. [GeV]	$\Gamma(E1)$* keV	$r=\frac{M(J=2)-M(J=1)}{M(J=1)-M(J=0)}$
CUSB[13]	10.255 ± 0.0004	6.5 ± 0.8	0.83 ± 0.32
Beavis et al.[19]	10.246	---	1.00
Eichten et al.(K&Y)[11]	10.27	6.11	----
Eichten & Feinberg[20]	10.271	---	1.00
Martin[21]	10.242	---	---
Quigg & Rosner[22]	10.245	7.24	---
Kraseman & Ono[23]	10.271	10.24†	0.67
Khare[24]	----	----	0.50
Buchmuller & Tye[25]	10.25	6.15	---
Baacke et al.[26]	10.312	0.41¶ (5.2)	0.77
Buchmuller[27]	10.250	6.8	0.67
Byers & McCrary[28]	10.250	7.6	0.48

* wherever appropriate the k factor in the $\Gamma(E1)$ expression has been adjusted to the measured value of 93 MeV.
¶ not scaled by k^3.
† this value is obtained by Kraseman using dipole sum rules, whereas the c.o.g. value and the r value are obtained from a potential model.

F. Fine Structure of the 2^3P Levels.

Potential models require additional assumptions about spin dependent interactions to predict the fine structure of the P-levels. Different authors therefore obtain different results. A convenient way of comparing theory and experiment is the ratio of the two splittings (J=2 to J=1 and J=1 to J=0). This ratio is given in the last column of of the previous table. The CUSB result cannot at present distinguish between various calculations. We expect to install a high resolution quadrant in the coming year such that the three lines will be resolved in order to measure r with high accuracy.

G. 2^3P (c.o.g.) and Flavor Independence.

Quigg and Rosner[29] had first shown evidence for the flavor independence of the color forces by noting the value of [E(3S)-E(2S)]/[E(2S)-E(1S)] for the J/ψ family is approximately equal to the value for the T family. This implied that the power ν which characterizes the power law potential of the form $V(r) = \lambda r^{\nu}$ for both systems is the same, independent of the flavor of the quark. Its value is approximately 0.

While this result is encouraging, it could be fortuitous. Q&R pointed out that further tests of flavor independence can be obtained by comparing the levels splittings [E(2S)-E(1P)]/[E(2S)-E(1S)] of the J/ψ family which yields a value of $\nu \simeq .15$ to the corresponding one from the T family. We have measured instead the c.o.g. of the 2P in the T system, which, amusingly, lies at the same radius (see figure 12a) as the χ_c state in the potential. Using a plot of C. Quigg[30], figure 12b, which displays the relation between the value of the power ν and the ratio [E(3S)-E(2P)/ E(3S)-E(2S)] we obtain $\nu = -0.15$.

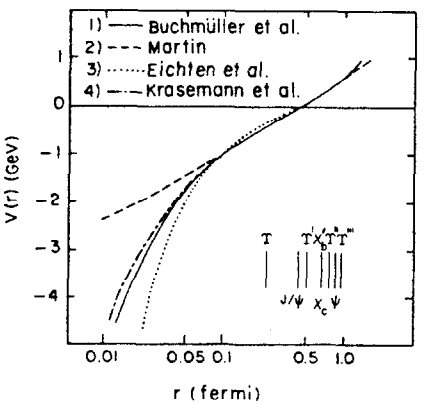


Fig 12a) Potentials as a function of the radius. The radii for various T and J/ψ states are indicated.

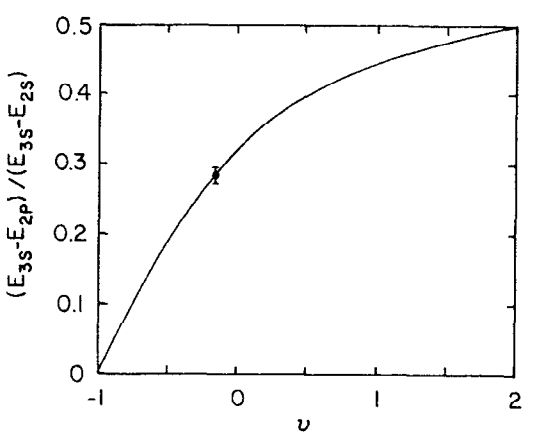


Fig 12b) Prediction (Ref. 30) for the ratio $\Delta E(3S-2P)/\Delta E(3S-2S)$ vs the power of the potential (ν). The data point is the CUSB measured value.

This is a remarkable agreement considering the large difference in velocities and the neglect of relativistic effects, and is another proof of the flavor independence of the color forces.

H. 1^3P Level and QCD Sum Rules.

Theorists who adopt the QCD Sum Rules approach claim to be free of the vagaries associated with the phenomenology of potential model approaches. One of their firm predictions is the position of the 1^3P level in the T system.

I. 1^3P (c.o.g.) = 9.835 ± 0.03 GeV.[31]

Using an alternate computational method of exponential moments, Bertlmann[32] predicts that the J=2 to J=0 splitting is 20 MeV and that

II. 1^3P (c.o.g.) = 9.803 ± 0.01 GeV.

These positions are lower by 30 to 90 MeV relative to potential model predictions. Typical models of the latter group (for ex. ref.22 and ref. 25) predict the 1^3P El partial rate to be ≃ 6 keV with a c.o.g. of 9.86 GeV, which corresponds to a branching ratio of ≃ 18%. If one is allowed to scale by the k^3 factor, the QCD Sum Rule results imply BR's of the order of 44% (I) to 50% (II).

The 1980 CUSB T' sample of 10^4 resonance events is consistent with results of potential model predictions. We also set a 90% c.l. limit on the BR for El transitions for k ≃ 190 MeV (J=2 - J=0 of 46 MeV) of 10%, and for k = 220 MeV (J=2 - J=0 of 20 MeV) of 7%. Therefore we have preliminary evidence in favor of potential model predictions versus QCD Sum Rule calculations.

II. T and Higgs Fields.

In the Standard Model the Higgs couples to the Fermion mass, i.e.,

$$\text{Lagrangian}_{\text{interaction}} = 2^{1/4} G_F^{1/2} m_H (q\bar{q} \text{ or } \ell\bar{\ell}), \quad [33]$$

hence heavy quarkonia are good hunting ground for Higgs related phenomena. Wilczek [34] and others proposed a natural solution to the CP violation problem by postulating the existence of an "axion" (an instanton solution of the Higgs fields) which is a light neutral pseudoscalar particle. The $T \to \gamma a$ rate is given by

$$\frac{\Gamma(T \to \gamma a)}{\Gamma(T \to \mu\mu)} = \frac{G_F m_b^2}{\sqrt{2}\pi\alpha\, x^2} \quad \text{where } x = \frac{\langle\phi_2\rangle}{\langle\phi_1\rangle} \text{ is the ratio}$$

of the vacuum expectation of the Higgs fields. A similar expression holds for $J/\psi \to \gamma a$, except the x^2 factor occurs in the numerator. Combining the two expressions one obtains a model independent prediction that $B(T\to\gamma a) * B(J/\psi\to\gamma a) = B_{\mu\mu}(T) B_{\mu\mu}(J/\psi) \frac{G_F^2 m_c^2 m_b^2}{2\pi^2\alpha^2} = (1.6\pm0.3)\times10^{-8}$

for m_c = 1.5 GeV, m_b = 4.9 GeV, $B_{\mu\mu}^T$ = 3.3% and $B_{\mu\mu}^{J/\psi}$ = 6.9%.

We searched in CUSB for these standard axions. [35] The signature for $T\to\gamma a$ (see figure 13a) is the presence of just a photon with $E=\frac{M(T)}{2}$ since the axion is relatively long lived and interacts weakly, leaving no trace in the detector. We find zero such events. Figure 13a shows a possible decay but with too little energy. It is kinematically consistent with being a radiative Bhabha event. Figure 13b show the spectra of such single photons found at the T(1S), T(3S) and from the continuum, note the absence of photons with energy close to the beam energy. These three spectra are equal, proving that the observed photons are from QED processes. We obtain 90% c.l. limits of $B(T\to\gamma a) < 3.5\times10^{-4}$ from the T(1S) sample, and $<1.2\times10^{-4}$ from the T(3S) sample. The combined 90% c.l. limit for $B(T\to\gamma a)$ is $<3.8\times10^{-5}$.

Our result together with the one from the Crystal Ball[36]

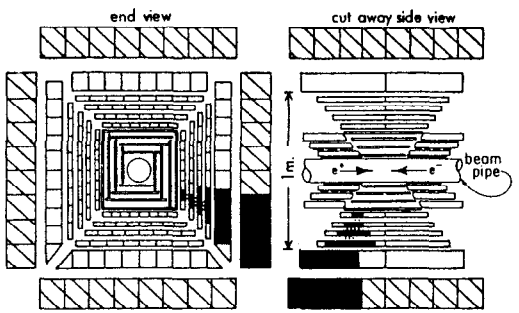


Fig 13a) Single photon candidate (rejected as axion event because E_{obs} = 1.6 GeV is too low) and selection criteria.

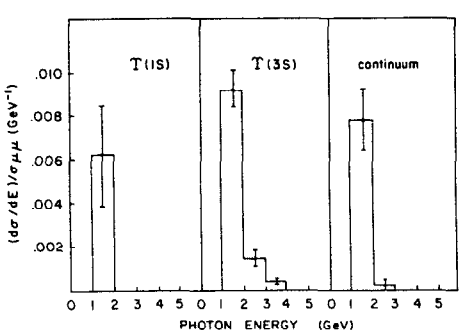


Fig 13b) Single photon spectra for T (left), T" (middle), and continuum (right), with no axion candidates.

$B(J/\psi \to \gamma a) < 1.4\times10^{-5}$ gives

$B(T\to\gamma a)*B(J/\psi\to\gamma a) < 0.6\times10^{-9}$ 90% c.l. limit, a factor of 26 less than the prediction. So we can safely say the "standard axion" is dead, long live the "invisible axion"!

III. T"" and the Weak Interactions

A. T"" and the B Meson Mass.

CUSB has searched for the presence of B^*'s in T"" decays.[37] The lack of signal for their production also yields the best bounds at present on the B-meson mass, which is important to the calculation of the end point of the electron spectrum and its smearing of the β-decay of the B's. The fact that $M_{T''} < 2M_B < M_{T''''}$[38] implies that B-mesons could be produced in T"" decay with a laboratory momentum of $0 < p < 1100$ MeV/c, resulting in a laboratory Doppler smearing of the electron spectrum end point of 0 to 40% (f.w.) in addition to a small uncertainty of the end point itself in the B rest frame (< 2.2%). A large Q value for $T'''' \to BB$ would imply , however as in the D case, large production of B^*'s which are quite reliably predicted to decay as $B^* \to B + \gamma$ with $M_{B^*} - M_B \simeq$ 50 MeV. We have searched for 50 MeV γ's from T"" decays in our detector and obtained a null result. Our 90% confidence level upper limit is B.R. $(T''' \to B^*B) < 9\%$. Figure 14a shows the observed inclusive γ spectrum from T"' after background subtraction and the expected signal for B.R. equal to 1. Combining the B.R. limit and the measured T"' width with the potential model calculations by Eichten [2] we derive limits for the lab K.E. of the B mesons from T"" of $10 < T_B < 25$ MeV, with $T \simeq 15$ MeV favored. Bigi and Ono [39] have obtained $T = 4.5^{+6}_{-3}$ MeV. We find their central value inconsistent with the shape of the resonance.

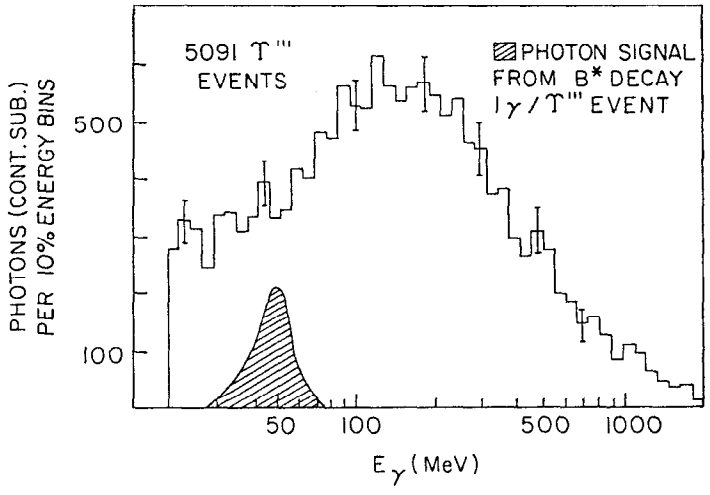


Fig 14a) Inclusive photon spectrum on the T'''. The shaded curve is the expected photon signal for one photon from B^* decay per T''' event.

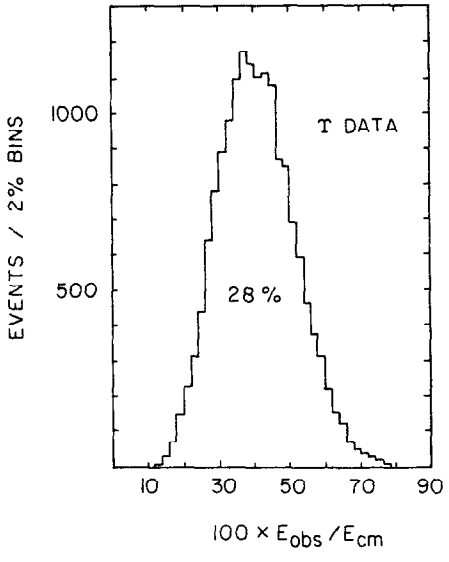


Fig 14b) The fraction of the center of mass energy observed in CUSB for T hadronic events. The rms spread is 28%.

We shall use T = 15 MeV in section IIIC, corresponding to a Doppler smearing of 15%. This corresponds to M_B = 5.274 GeV.

B. T ''' and Exotic Models.[40]

In the standard model the couplings of W to quarks and leptons lead to $b \to q\ell\bar{\nu}$ and $b \to qq\bar{q}$ with well defined ratios; in particular, the decay $b \to q\ell\bar{\nu}$ ($\ell = e,\mu$) accounts for about 26% of all decays with experiments and theory in good agreement. For these decays the average ν energy is 1.35 GeV, and for the T'''' the total energy in ν's is on the average 6.4% of the c. m. energy. Models have been proposed for the b decay without coupling to W, such as I) $b \to \ell\ell q$ and II) $b \to \ell qq$ where 33% and 17% respectively of the energy would be carried away by ν's. In addition, in model II baryons could appear in the quark evolution leading to an additional apparent missing energy. CUSB is an excellent and extremely stable calorimeter which measures all the elctromagnetic (π^0) energy, and about half of the charged particle energy over 60% of 4π. Thus we expect to measure 40% of the beam energy. Figure 14b shows the fraction of the c. of m. energy observed in CUSB for T hadronic events.[41]

Figure 15a shows the fraction of the total energy observed at the four resonances and continuum. Note the extreme similarity of the first four values which average to 40.94% ± 0.06%. The Monte Carlo result is 42%, which we renormalize to the observed value. For the T'''', assuming 100% $B\bar{B}$ decay, standard b-decay and using the measured B.R.'s, we obtain that 38% of the energy should be observed, which compares quite well with the measurements of 38.44% ± 0.35%. For model I we compute 29%, 29σ away from the measurement, and for model II, less than 34%, i.e., more than 14σ away. Alternatively, model I could account for only

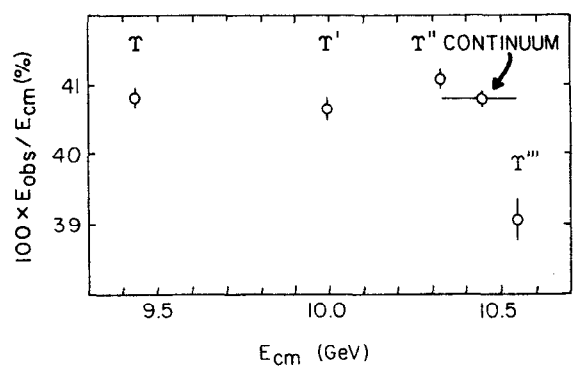


Fig 15a) The average fraction of the total energy observed in CUSB for the four resonances and the continuum. Note the suppressed vertical scale.

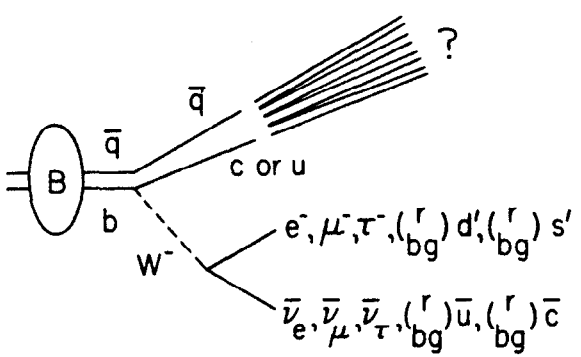


Fig 15b) Schematic representation of B meson decay in the spectator model.

3.3% of b-decays, and model II for less than 7.5%. Finally, we wish to point out that if models I and II were correct, our detection efficiency for Υ'''' decays would be decreased by a factor of about three, implying that its leptonic width is ≃ 0.9 KeV, *in strong contradiction* with potential models and any naive expectations.

C. B Decay Leptonic Spectrum and Mixing Matrix Parameters.

In the standard model the b semileptonic decay is given, ignoring the Fermi constant, by an effective coupling $(e\nu)_\alpha (V_{bu}(bu)_\alpha + V_{bc}(bc)_\alpha)$ where $(ab)_\alpha = \bar{u}_a \gamma_\alpha (1-\gamma_5) u_b$ etc. and V_{bu}, V_{bc} are the relevant elements of the quark mixing matrix. [42] The question is what can we learn about V_{bu}/V_{bc} from the B semileptonic decay ($B \to e\nu X$) which has been discovered some time ago.[43] QCD evolution of quarks is a somewhat mysterious process and the question is, what is X for $b \to u$ and $b \to c$? On the other hand, the spectator model for computing the B.R.'s is expected to be reliable for theoretical reasons and is so far experimentally confirmed. Sometime ago Cabibbo, Corbo and Maiani[44] had calculated the D beta decay spectrum in the spirit of the spectator model by assuming that the bound c-quark moves with a Fermi motion in the D meson. They also folded in the D motion in the lab and computed QCD radiative corrections which are not critical for $D \to e\nu X$ where the e spectrum vanishes at the kinematic limit. The agreement with the D data is excellent. Encouraged by this, we applied the method to B decay into $X_{c=0}$ and $X_{c\neq 0}$ using the same Fermi motion and the above mentioned B motion. We ignored radiative corrections, waiting for Altarelli et al. [45] to complete their computations. Their new results are in excellent agreement with our simple calculations which are shown as the curves in figure 17b. There are clear differences in the $b \to u$ and $b \to c$ spectra and in the end

points. Calculations by Bigi and Evertz[46] include resonance effects, and the authors conclude that they steepen the spectra but do not alter the end points. Figure 15b shows the amplitudes for B decay.

In the CUSB detector we can obtain a very clean electron signal for energy above 1 GeV. Figure 16 shows a typical electron candidate on the T"", with a partial list of the selection criteria. The histogram indicates the overlap background as measured from the difference in the shower centroid polar angle and the track polar angle. At ≈ 2.2 GeV, the end point for $B \to e\nu X_c$, our resolution is approximately 3%. Our energy scale is also similarly accurate, by using 5 GeV e^+e^- Bhabha scattering as calibration. These uncertainties are small compared to the ≈ 17% difference in the computed endpoints. In other words resolution unfolding is a minor effect; Doppler smearing is in fact dominant. The main complication comes from the fact that the T"" is only ≈30% of σ(hadron) and the large continuum does give some high energy electrons from decays of fast D's. Figure 17a gives the raw electron spectrum at the T"" and the measured continuum contribution to it. As expected, the continuum fades away at the end of the spectrum , thus the results are quite independent from the subtraction. The subtracted spectrum has been compared with the outlined calculation, using the masses given by A. Martin[47]: m_b = 5.2 GeV and m_c= 1.8 GeV, curve B in figure 17b. If we use m_b = 5.2 GeV and let m_c free, we obtain m_c= 2.0 GeV as a best fit; we are fully consistent with m_c=1.8 GeV and are 10σ's away from m_q<500 MeV. Curve A is obtained for m_q=0 and does not vary much up to m_q=700 meV. Curve C is the contribution from secondary (D's from B'decays) D decays, which should be added to

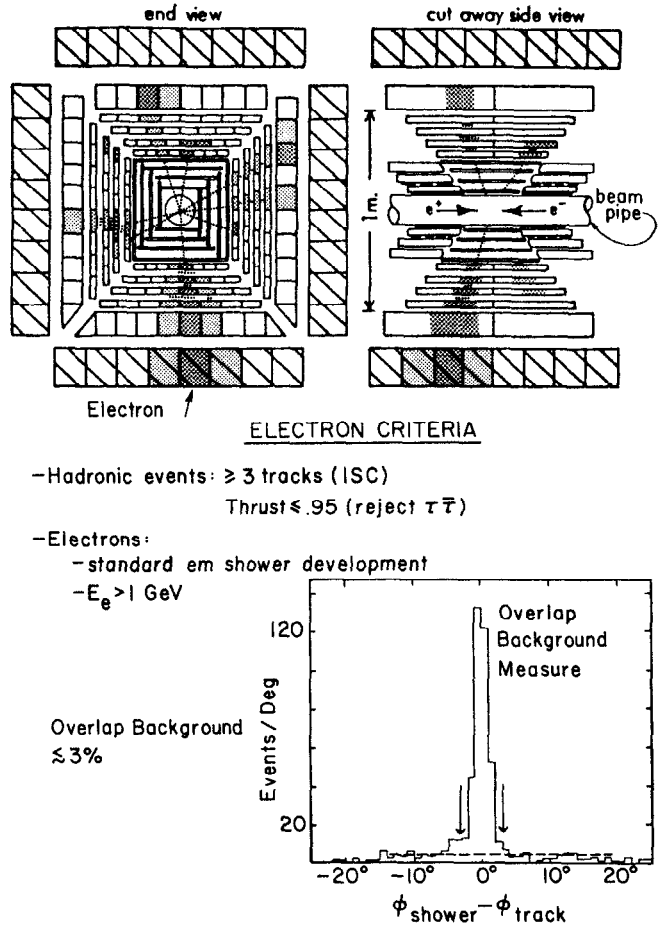


Fig 16) Typical electron candidate on the T"", with partial list of the selection criteria. The histogram indicates the overlap background as measured from the difference in Φ_{shower} and Φ_{track}.

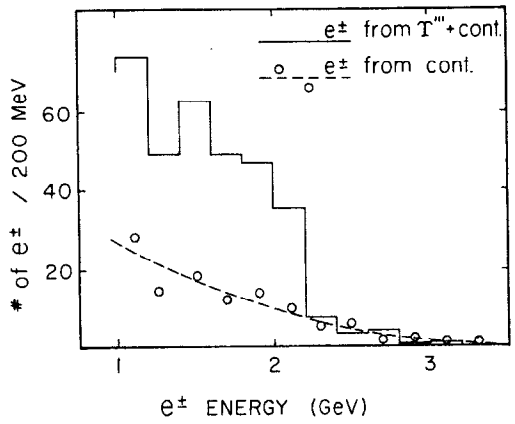


Fig 17a) The histogram represents the raw electron spectrum for T''' events, the dashed line is a fit to the continuum electron spectrum.

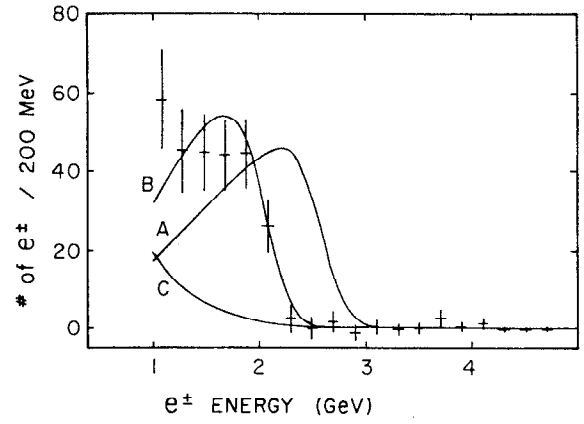


Fig 17b) The background subtracted electron spectrum on the T'''. For explanation of curves, see text.

curve B when comparing with the data.

The experimentally measured spectrum is consistent with zero contribution from b→u, curve A. On the basis of our results and the spectra in figure 17b, justified by the complete calculations of ref. 45, we obtain a 90% c.l. upper limit of

$BR(B \to e\nu X_u)/BR(B \to e\nu X_c) < 9.3\%$.[48] Using the factor from integrating over available phase space for b→u and b→c from ref. 45, the above limit corresponds to:

$$|V_{ub}/V_{bc}|^2 < 0.04 \text{ or } |V_{bu}|/|V_{bc}| < 0.20.$$

In the Maiani notation this imposes a bound $\sin\beta/\sin\gamma < 0.20$ which represents a significant improvement on our knowledge of the K-M matrix even as recently summarized.[49] The CUSB contribution to the bounds on the mixing matrix angles is shown on a figure (#18) which Maiani had presented at the Paris Conference.[50]

Finally, from the same data we obtain an improved result for the B semileptonic branching ratio of $BR(B \to e\nu X) = 0.131 \pm 0.012$, in good agreement with calculations in the standard model with corrections for strong interaction effects.[51]

IV. Conclusions

The various branching ratios which have been measured at CESR by CUSB and CLEO are summarized in figure 19.[52] We have certainly made excellent progress in adding to our understanding of strong inteactions, Higgs related phenomena, and weak interactions, by studying the T system. Some of the highlights are:

A. The discovery of the first P-wave $b\bar{b}$ state and its properties confirm the flavor independent potential approach. Measurement of their

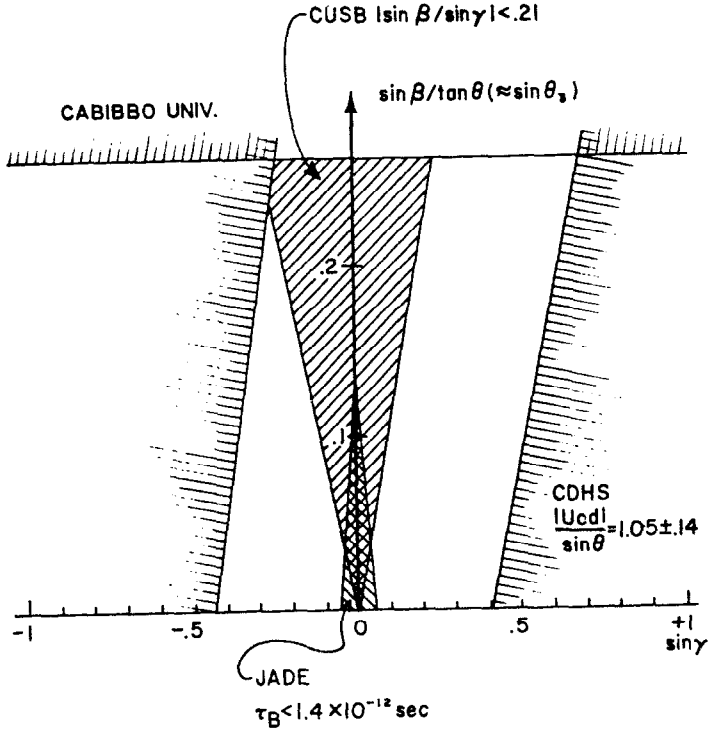


Fig 18) Experimental bounds on mixing matrix angles.

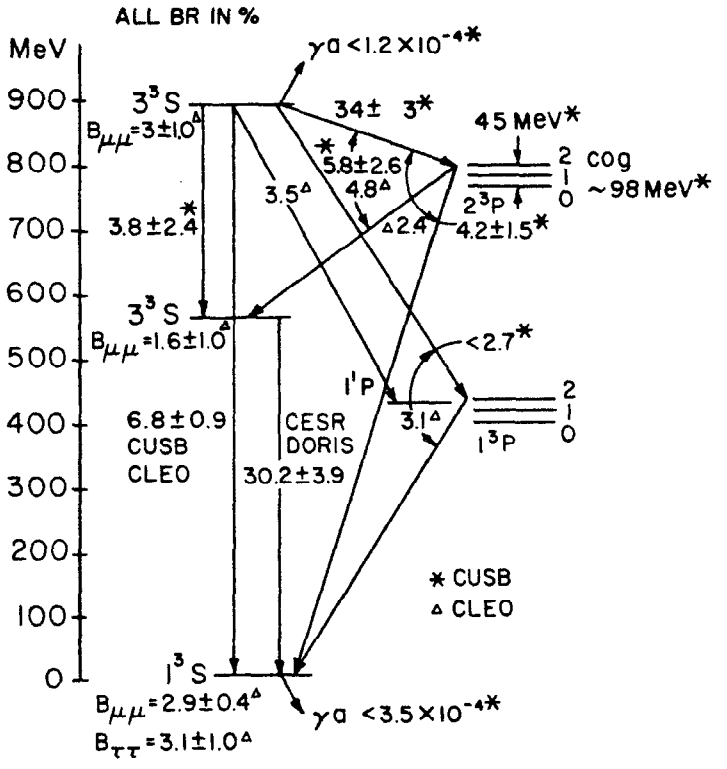


Fig 19) Observed transitions in the T system with CLEO and CUSB experimental values indicated.

fine structure will determine the effective spin dependence of the color forces.

B. $\Upsilon'' \rightarrow \pi\pi\Upsilon$ and Υ' are both observed. Their branching ratios are in reasonable agreement with those predicted using a multipole expansion in the color field. The unexpected difference in the pion spectra in the decay of Υ'' and Υ' to Υ suggest that refinements of the theory are necessary.

C. R and ΔR are fine to lowest order in QCD, $\Lambda_{\overline{MS}} \simeq 125$ MeV. No string vibrational states have been observed at the expected level.

D. The standard axion is dead.

E. $\Upsilon''' \not\rightarrow B^{*}B$, therefore the Υ''' is barely above threshold. The B-meson mass is most likely 5.274 GeV.

F. The "standard model" of weak interactions is confirmed once more (there are no exotic b couplings). In particular the semileptonic B.R. agrees with expectations, and the first significant limit on V_{bu}/V_{bc} helps to set more stringent bounds on the elements of the mixing matrix.

Our immediate and more long range plans are:

A. Measure this winter the c.o.g. of the 1^3P state to confirm our preliminary evidence of favoring potential model predictions over QCD Sum Rule predictions.

B. Resolve the three lines in the 2^3P peak with a partial detector with higher resolution in the next year, to measure the fine splitting accurately.

C. Complete the high resolution detector and go after the η_b to study the Υ hyperfine splitting at some further future.

Acknowledgements

The author happily acknowledges all members of the CUSB Collaboration. In addition, she thanks P. Franzini for innumerable discussions. Finally, she thanks P. Franzini, R. D. Schamberger, Jr. and P. M. Tuts for help in the preparation of this manuscript.

REFERENCES

1. The members of the CUSB Collaboration circa 1980-81 include: T. Bohringer, P. Franzini, K. Han, G. Mageras, D. Peterson, E. Rice, J. K. Yoh (Columbia University); G. Finocchiaro, J. Horstkotte, C. Klopfenstein, J. Lee-Franzini, R. D. Schamberger, M. Sivertz, L. J. Spencer, P. M. Tuts (SUNY at Stony Brook); R. Imlay, G. Levman, W. Metcalf, V. Sreedhar (Louisiana S.U.); G. Blanar, H. Dietl, G. Eigen, E. Lorenz, F. Pauss, H. Vogel (MPI, Munich); S. W. Herb (Cornell U.).

2. E. Eichten, Phys. Rev. D22, 1819 (1980).

3. S. Ono, Phys. Rev. D23, 1118 (1981).

4. E. Rice et al., Phys. Rev. Lett. 48, 906 (1982).

5. E. Rice et al., contribution #187, to the XXIth Int. Conf. on High Energy Physics, Paris (1982), hereafter referred to as Paris Conf.

6. W. Buchmuller and S.-H. H. Tye, Phys. Rev. Lett. 44, 850 (1980).

7. T. Appelquist and H. D. Politzer, Phys. Rev. Lett. 34, 43 (1975).

8. D. Peterson et al., Phys. Lett. 114B, 277 (1982).

9. G. Mageras et al., Phys. Rev. Lett. 46, 1115 (1981).

10. G. Mageras et al., contribution #189, Paris. Conf. (1982).

11. Y. P. Kuang and T. M. Yan, Phys. Rev. D24, 2874 (1981).

12. G. W. Intemann, Phys. Rev. D26, 611 (1982).

13. K. Han et al., contribution #191, Paris Conf. (1982).

14. G. Eigen et al., contribution #190, Paris Conf. (1982).

15. E. Eichten et al., Phys. Rev. D21, 203 (1980).

16. R. Barbieri, R. Gatto, and R. Kogeler, Phys. Lett. 60B, 183 (1976); R. Barbieri, R. Gatto, and E. Remiddi, ibid. 61B., 465 (1976).

17. P. Franzini and J. Lee-Franzini, Phys. Rep. 81, 239 (1982).

18. A. S. Artamonov et al., Inst. of Nuc. Phys. Preprint 82-94 (1982).

19. D. Beavis et al., Phys. Rev. D20, 2345 (1979).

20. E. Eichten and F. Feinberg, Phys. Rev. D21, 203 (1980).

21. A. Martin, Phys. Lett. 93B, 338 (1980); ibid 100B, 511 (1981).

22. C. Quigg and J. Rosner, Phys. Rev. D23, 2625 (1981).

23. H. Krasemann and S. Ono, Nucl. Phys. B154,283 (1979);
H. Krasemann, TH-3036 CERN Preprint (1981).

24. K. Khare, Phys. Lett. 93B, 385 (1981).

25. W. Buchmuller and S.-H.H. Tye, Phys. Rev. D24, 132 (1981).

26. J. Baacke et al., Dortmund Preprint DO-TH 81/10 (1981).

27. W. Buchmuller, MPI-PAE/PTh 12/82 (1982).

28. R. McClary and N. Byers, UCLA Preprint UCLA/82/TEP/12 (1982).

29. C. Quigg and J. Rosner, Phys. Rep. 56, 169 (1979).

30. C. Quigg, private communication.

31. M. Voloshin et al., ITEP-21 (1980);
M. Voloshin and V. Zakha, Internal Report DESY F15-80/03 (1980).

32. R. A. Bertlmann, CERN Preprint TH 3192 (1981).

33. F. Wilczek, Phys. Rev. Lett. 39, 1309 (1977).

34. F. Wilczek, Phys. Rev. Lett. 40,279 (1978).

35. M. Sivertz et al. Phys. Rev. D26,717 (1982).

36. C. Edwards et al. Phys. Rev. Lett. 48, 903 (1982).

37. R. D. Schamberger, Jr. et al., Phys. Rev. D26,720 (1982).

38. G. Finocchiaro et al., Phys. Rev. Lett. 45, 222 (1980);
D. Andrews et al., ibid. 219 (1980).

39. I.I. Bigi and S. Ono, Nucl. Phys. B189, 93 (1979).

40. See for example: E. Derman, Phys. Rev. D19, 317 (1979);
H. Georgi and S. Glashow, Nucl. Phys. B167, 173 (1980).

41. P. M. Tuts et al., contribution #180, Paris Conf. (1982).

42. L. Maiani, Proc. of the 1977 Symp. on Leptons and Photons, ed. by F. Gutbrod, Hamburg.

43. C. Bebek et al., Phys. Rev. Lett. 46, 84 (1981);
L. J. Spencer et al. ibid. 47,771 (1981).

44. N. Cabibbo, G. Corbo, and L. Maiani, Nucl. Phys. B155, 93 (1979).

45. G. Altarelli et al., Univ. of Rome Preprint 302 (1982).
contribution to the Paris Conf. (1982).

46. I.I. Bigi and H.G. Evertz, Preprint PITHA 82/08 (1982).

47. A. Martin, Phys. Lett. 103B, 55, (1981).

48. C. Klopfenstein et al., contribution #185, Paris Conf. (1982).

49. S. Pakvasa, in Proceedings of Paris. Conf. (1982).

50. L. Maiani, in Proceedings of Paris Conf. (1982).

51. J. Leveille, in Proc. of Moriond Workshop on Heavy Flavours, 1982.

52. J. Lee-Franzini, in Proceedings of Paris. Conf. (1982).

SLAC-PUB-2943
June 1982

Heavy Quark Fragmentation from e^+e^- Annihilation and νN Scattering Experiments.

D. Schlatter, SLAC

Talk at the Topical Conference of the SLAC Summer Institute 1982

1) Introduction.

The fragmentation of heavy quarks is both of theoretical and practical interest, but so far little is known about it. Most properties of the D meson have been determined within the first years of its discovery[1]. However, the fragmentation function of the D meson, or more generally that of charmed hadrons, has not been measured over a wide momentum range. At SPEAR energies the threshold was too high; D mesons could only be produced at the upper end of the spectrum[2]. Recently, several e^+e^- experiments have reported D* production around 30 GeV[3-6]. There was already indirect evidence from measurements of the lepton spectrum in opposite side dilepton events in ν N scattering[7,8], indicating that charmed quarks fragment differently from light quarks. Substantially more neutrino scattering data are now available making it possible to extract a charm fragmentation function from $\mu^+\mu^-$ events[9]. Another neutrino experiment using emulsions[10] has observed several events with charmed hadrons, and they have also measured the charm spectrum. Thus far, no one has been able to reconstruct a bottom meson, and all new

*. Work supported in part by the Department of Energy, contracts DE-AC03-76SF00515, W-7405-ENG-48, and DE-AC02-76ER03064.

© D. Schlatter 1982

information on the bottom quark is indirect. Inclusive lepton spectra in e^+e^- annihilation allow one to determine semi-leptonic branching ratios[6,11-13] and the fragmentation function of the b-quark[14]. The heavy quark fragmentation functions, among other things, matter in understanding the inclusive hadron spectra and their energy dependence in e^+e^- annihilation. For a quantitative analysis and comparison to, e.g.,QCD, one needs to know the heavy quark fragmentation functions.

2) Early Results.

In deep inelastic νN scattering charmed quarks are produced via the GIM mechanism[15]:

$$\nu + d\ (s) \rightarrow \mu^- + c$$

The second lepton, of opposite charge, originates from the semileptonic decay of the charmed particle:

$$c \rightarrow s + l^+ + \nu$$

The CDHS collaboration was the first to study the charm fragmentation function[7] from this reaction. They observed about 315 $\mu^+\mu^-$ events in an exposure of the 200 GeV neutrino narrow band beam at CERN. The result of the normalized μ^+ spectrum is shown in fig. 1 as well as the expectations from different models. The only conclusion that could be drawn at the time was that charmed quarks fragment harder than light quarks.

The production of D-mesons in e^+e^- annihilation provides a particularly clean way to study the charmed quark fragmentation, since the initial quarks are "known" in this case. However, early measurements did not have enough energy in the center of mass to be well above the theshold for D production. The MARK I collaboration at SPEAR[2] could only

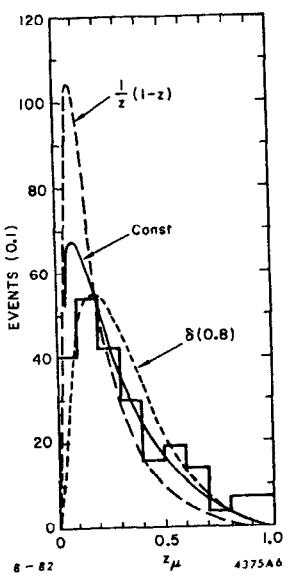


Fig. 1

Muon spectrum, $z=E_\mu/(E_\mu + E_{had})$, from early CDHS $\nu N \rightarrow \mu^-\mu^+ + h$ scattering.

observe D-mesons with $z=2E_D/E_{cm} > 0.6$ (the threshold is at z=0.51 at that energy). The result is shown in fig. 2.

Higher energy (for e^+e^-) and more statistics (for νN scattering) were needed to get better measurements.

3) Recent Results from νN Scattering Experiments.

In 1981 the CDHS collaboration has analysed 10380 $\mu^-\mu^+$ events in deep inelastic νN scattering[9] in the 400 GeV neutrino wide band beam at CERN. The large statistics allows the determination of the charm fragmentation function from a fit in bins of $z=E_D/E_c$ of the μ^+ spectrum, $z_\mu=p_\mu/(p_\mu+E_{hadron})$, and the hadron spectrum, $y_h=E_{hadron}/E_{tot}$. The result is shown in fig.3. The fragmentation function shows a peak around z≈0.7 with a very small contribution below 0.4. Since the data points are correlated, the detailed shape cannot be obtained reliably. A simple delta function, $\delta(z-0.68)$, also gives an adequate fit to the data. However the average z is well determined and is $\langle z\rangle=0.68\pm0.08$ including systematic errors. Since the energy of the D meson is not measured in this experiment, a Monte Carlo model has been used to determine E_D. Also, one should remember, that this is a measure of the c quark fragmentation into any charmed hadron. D-mesons are only the dominant contribution.

A second neutrino scattering experiment, E531 at Fermilab, has used a different technique. The neutrino interaction took place in an emulsion and the outgoing particles were then measured in a downstream spectrometer[10]. A sketch of this experiment is shown in fig. 4a. All charm candidates were scanned and fully reconstructed. In a preliminary analysis (≈50% of their data) they obtained 42 charmed hadrons, unambiguously

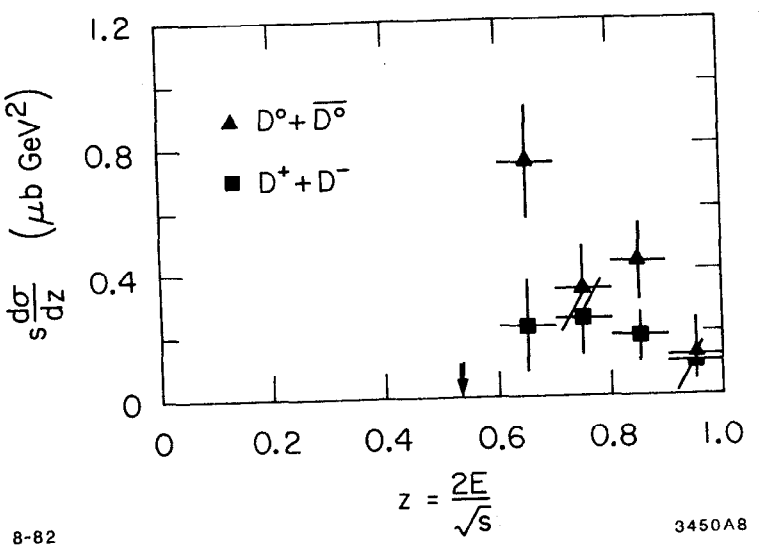


Fig. 2

D spectrum from MARK I at SPEAR.

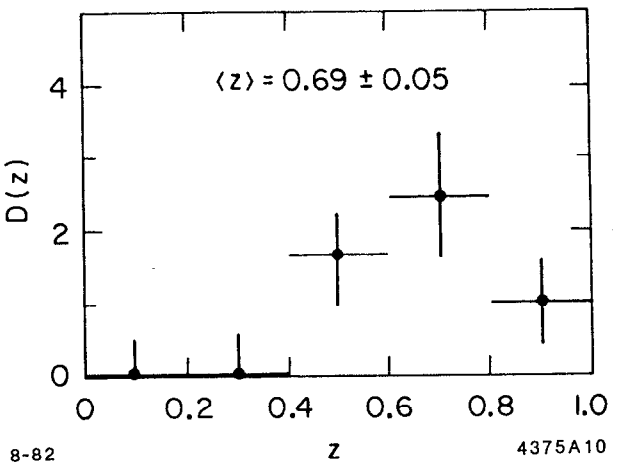
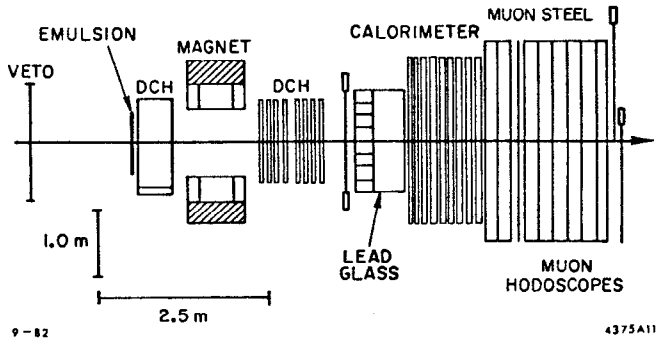
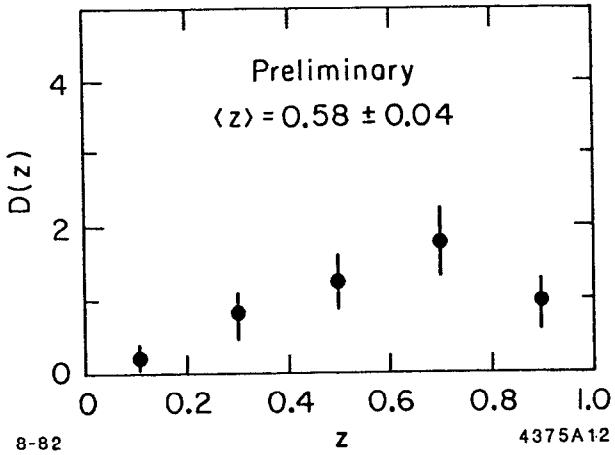


Fig. 3

Charm fragmentation from the CDHS νN experiment.



a) E531 ν-emulsion experiment at FNAL.



b) Charm fragmentation from E531 ν-emulsion experiment.

Fig. 4

reconstructed. The resulting fragmentation function[16] is shown in fig. 4b, very similar to the one obtained by the CDHS group. Its average z value is $\langle z \rangle = 0.58 \pm 0.04$ (statistical error only).

4) Charm production in e^+e^- at high energies.

The observation of charmed mesons produced in high energy e^+e^- annihilation is more difficult compared with D production at SPEAR. The high multiplicity yields a large combinatorial background. Other means are necessary to reduce this background. In the reaction

$$D^* \rightarrow D\,\pi, \quad D \rightarrow K\pi$$

the kinematic constraint from the $D^* \rightarrow D$ decay with $\Delta M = 145$ MeV suppresses the background very efficiently. The first observation of D^*'s at high energies has been published by the MARK II collaboration at the PEP storage ring[3]. They have searched for the channels where the D^* is charged and the D is neutral. No positive particle identification has been used, the time-of-flight measurement was only required to be consistent with a pion or kaon assumption. Despite the good momentum resolution of $(\delta p/p)^2 = 0.015^2 + (0.006p)^2$, the combinatorial background does not allow one to observe the D-meson in the $K\pi$ spectrum. However, if the $K\pi$ mass is within ±70 MeV of the D mass, a clear D^* signal is observed when fast ($z > 0.4$) $D\pi$ candidates are selected (see fig. 5a). The corrected D^* spectrum is shown in fig. 5b for $z > 0.2$ (threshold is at 0.13 GeV). Again a similar shape as seen in the neutrino experiments is observed with an average $\langle z \rangle = 0.59 \pm 0.05$.

A second experiment at PEP, DELCO, has reported the observation of the D^* meson[5]. This detector is not particularly suited to reconstruct resonances in jet events. But the particular kinematics of the $D^* \rightarrow D\pi$

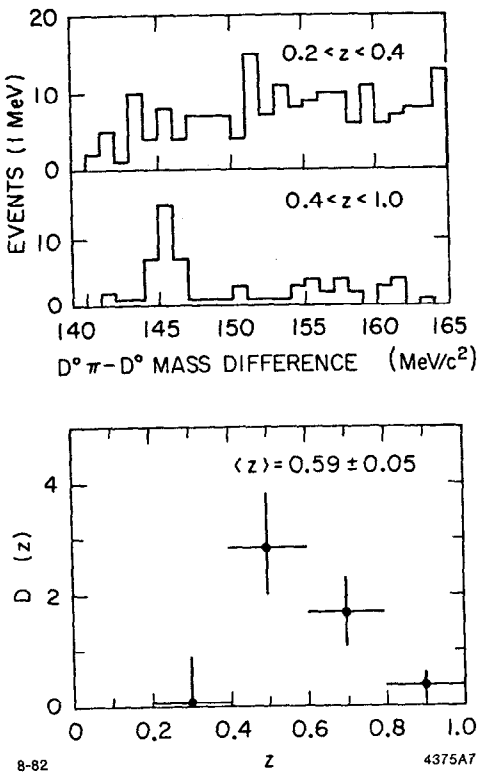


Fig. 5

D^* results from MARK II at PEP.

a) $D^0\pi - D^0$ mass difference.

b) D^* fragmentation function.

decay together with the particle identification capabilities of the DELCO detector make this analysis possible. The background in the spectrum of the mass difference $K\pi\pi - K\pi$ is reduced considerably by kaon and pion identification, thus compensating the poor mass resolution of 5 MeV. Fig. 6a shows a D* peak above a small background, in particular for $z>0.4$. The fragmentation function is more flat than the ones obtained in the other experiments. Given the large errors at small z values there is good agreement with the MARK II result. One should also have in mind that the acceptance for D* in the DELCO detector is rising from the threshold to its maximum in the second bin whereas it is constant for the MARK II detector for $z>0.2$.

The largest sample of D* events has been collected by the CLEO group[5] at the CESR storage ring at 10 GeV center of mass. They found 83 D* events showing a clear signal in the $K\pi\pi - K\pi$ mass difference (see fig. 7a). But the fragmentation function is only measured above $z>0.5$ (threshold is at 0.37). Therefore, not much can be concluded about the shape of the fragmentation function. The TASSO group at PETRA has reported D* production as well[6] but only for $z>0.5$. In Fig. 8 the mass differences of all 5 e^+e^- experiments are summarized.

5) Theoretical expectation.

Simple kinematical considerations[1,7] for a heavy quark fragmenting into a hadron containing Q (as sketched in fig. 9) lead to a different shape than the one from light quark fragmentation. The inertia of the heavy quark Q is retained by the $(Q\bar{q})$-meson, resulting in a harder fragmentation than if the quark masses can be neglected. Following these

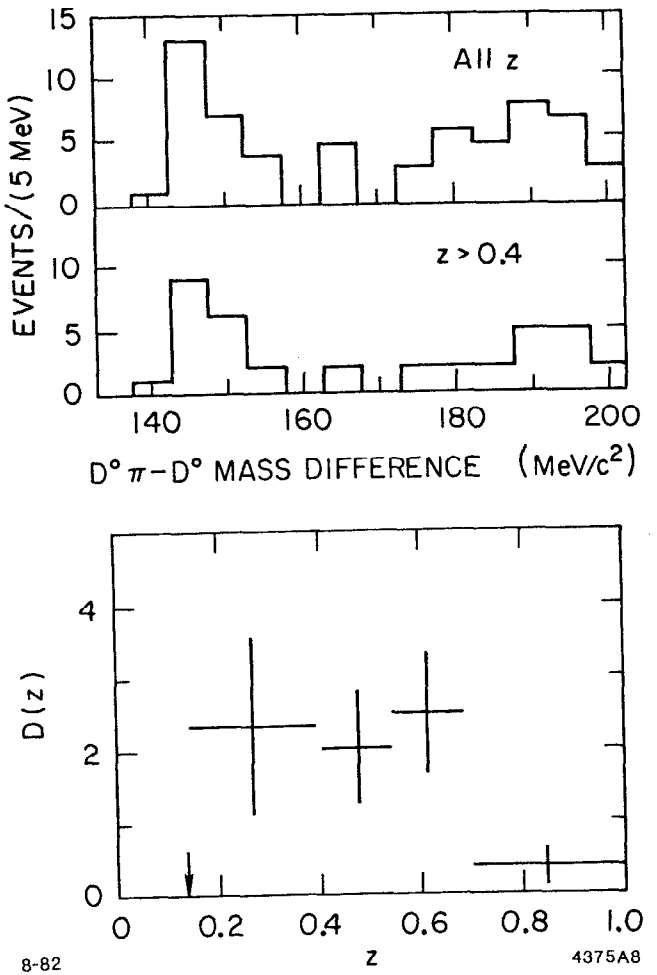


Fig. 6

D* results from DELCO at PEP.

a) $D^0\pi$-D^0 mass difference.

b) D* fragmentation function.

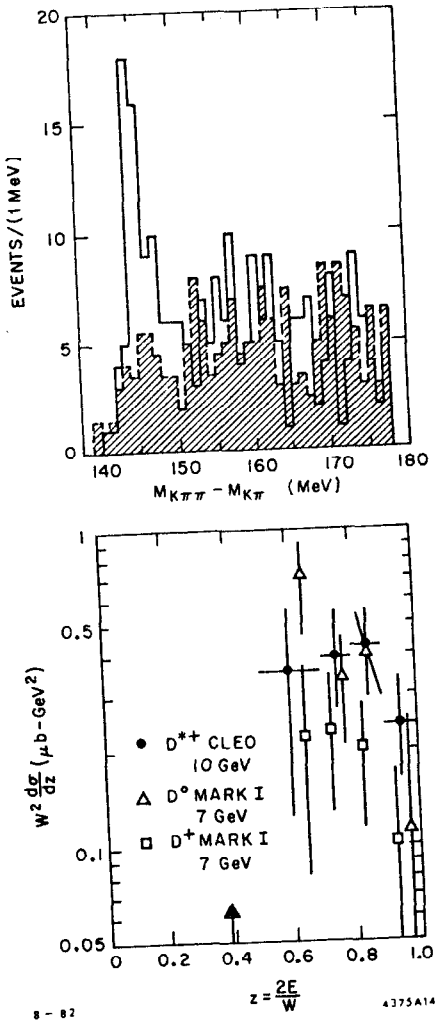


Fig. 7

D* results from CLEO at CESR.

a) $D^0\pi$-D^0 mass difference.

b) D* fragmentation function.

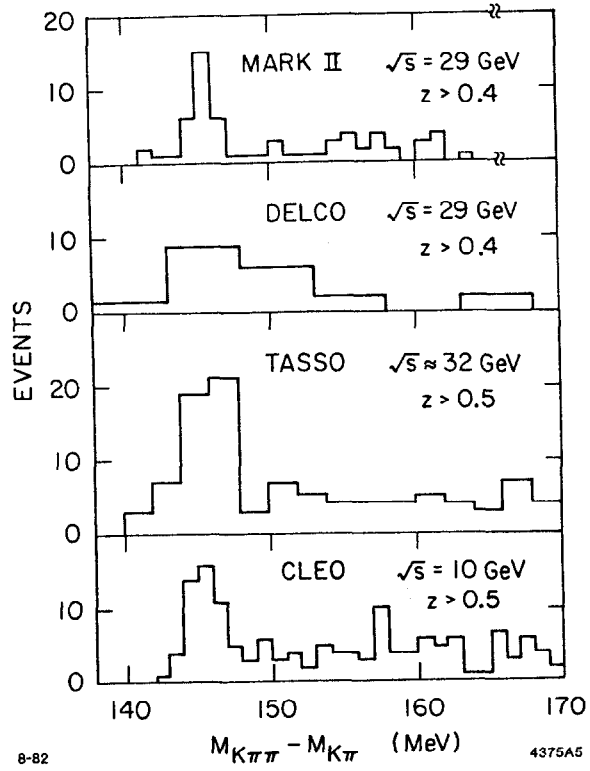


Fig. 8

$D^0\pi$-D^0 mass difference from 4 different e^+e^- experiments.

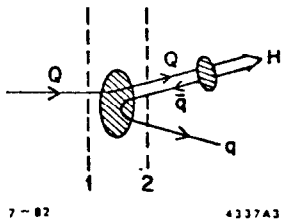


Fig. 9

The fragmentation of a heavy quark Q into a meson ($Q\bar{q}$).

ideas and calculating the quantum mechanical transition probability for the process as shown in fig. 9, one gets the following fragmentation function[18]:

$$D_Q(z) = \frac{N}{z\,(\,1 - 1/z - \epsilon_Q\,(1-z)\,)^2} \qquad (5.1)$$

where N is a normalization factor. The parameter ϵ_Q scales inversely with the square of the quark mass, $\propto 1/m_Q^2$. In fig. 10 this function is drawn for $\epsilon_Q = 0.25$ on top of the four measurements from νN and e^+e^- experiments. The agreement is remarkably good, given the systematically very different experiments and processes involved.

6) D* Cross-section in e^+e^- Annihilation.

Besides the shape of the fragmentation function, the D* cross section has been measured by several experiments. Two branching ratios ($B(D^*\to D)$ and $B(D\to K\pi)$) which are not measured very precisely enter into the total D* cross section. The $D\to K\pi$ branching was taken to be $(3\pm0.6)\%$[19] by all groups while there have been two values used for the $D^*\to D$ branching, $(44\pm10)\%$[20] and $(64\pm10)\%$[21]. In Fig. 11 the D* cross section from all experiments has been plotted (assuming $B(D^*\to D)=64\%$). There is rather satisfactory agreement given the small data samples of each experiment. The total D* cross section from MARK II, DELCO and CLEO are displayed in table I. All results have a relatively large cross section ($\approx$ 50% of the total $c\bar{c}$ production), but the error due to the branching ratios is big ($\geq$ 25%).

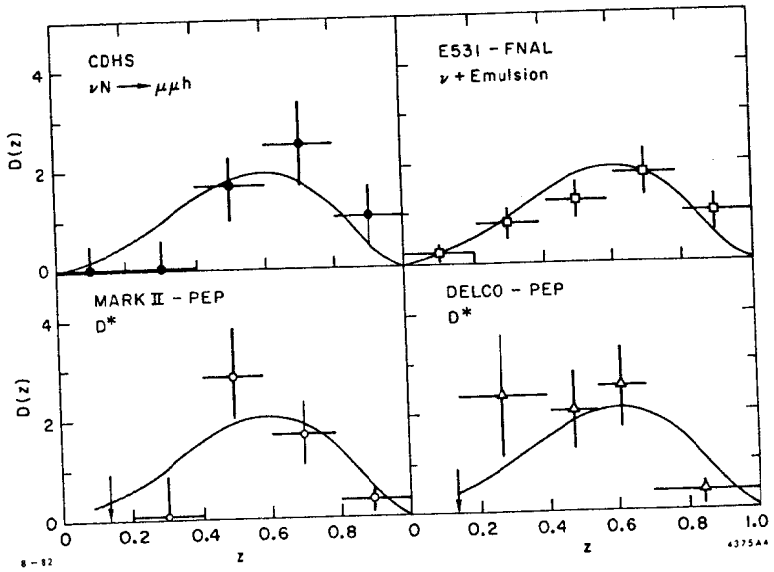


Fig. 10

Charm fragmentation function from νN and e^+e^- experiments. The curve is eq. 5.1 with $\epsilon_Q = 0.25$.

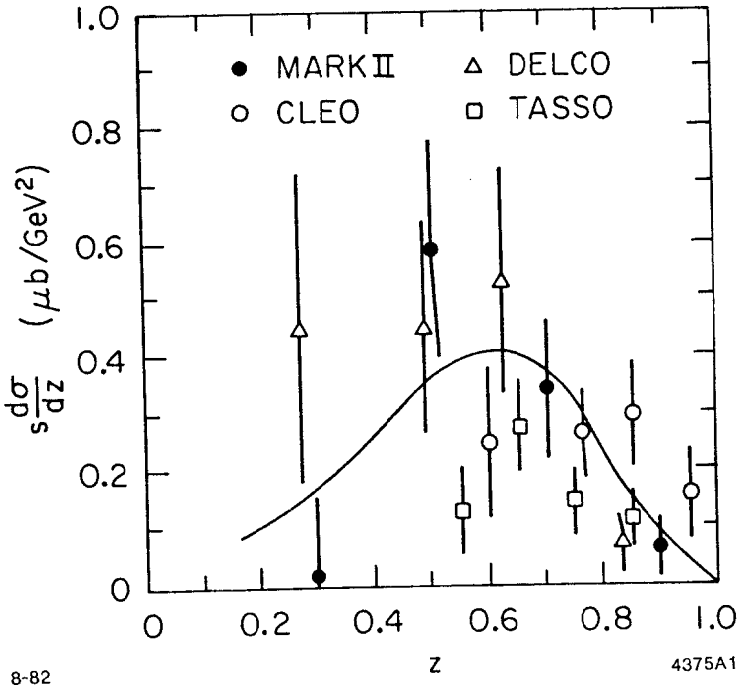


Fig. 11

D* cross section in e^+e^- with $B(D^* \to D)=0.64$ and $B(D \to K\pi)=0.03$.

Table I.

D* cross section, $\sigma(D^{*+}+D^{*-})$ in nb, for two different values of $B(D^{*}\to D)$. The underlined values are the published ones.

Experiment	$B(D^{*}-D)=44\%$	$B(D^{*}-D)=64\%$	$c\bar{c}$	$b\bar{b}$
MARK II[22]	0.25±0.13	0.17±0.09	0.30	0.10
DELCO[5]		0.20±.06±.07	0.30	0.10
CLEO[9]	1.6±.04±.04	1.1±.03±.03	3.0	

7) Inclusive Electrons in Hadronic e^+e^- Events.

In the same way as the lepton spectrum from opposite-side dilepton events in deep inelastic neutrino scattering provides information on the charm fragmentation, the inclusive lepton spectrum in hadronic events in e^+e^- annihilation at high energies allows a determination of the charm and bottom fragmentation function. In particular, at large transverse momentum of the lepton with respect to the jet axis, the bottom contribution becomes significant. Several experiments have used this signature to measure semileptonic branching ratios[6,11-19]. Table II summarizes these results.

Table II.

Semileptonic branching ratios (in %) from inclusive leptons in e^+e^-.

MARK J [11]	$B(c\to\mu)$ =	9.8±1.1±2.0
MARK II[19]	$B(c\to e)$ =	7 ± 2 ± 2
CUSB[12]	$B(b\to e)$ =	13.1±2.5±3.0
CLEO[13]	$B(b\to e)$ =	12.7±1.7±1.3
CLEO[13]	$B(b\to\mu)$ =	12.4±1.7±3.1
MARK J[11]	$B(b\to\mu)$ =	9.3±2.9±2.0
TASSO[6]	$B(b\to e)$ =	13.6±4.9±4.0
TASSO[6]	$B(b\to\mu)$ =	15.0±3.5±3.5
MARK II[19]	$B(b\to e)$ =	11.0±3.0±2.0

The Mark II collaboration has tried to determine the bottom fragmentation function simultaneously with the branching ratios since these quantities are correlated. This analysis selects electron candidates by requirement of a sufficient energy deposit (>50% of momentum) of a track in the first 8 radiation lengths of the liquid argon electromagnetic calorimeter. From 10691 e^+e^- hadron events in the MARK II detector at PEP, 1013 electron candidates were found, with substantial back-

ground. Misidentified hadrons give 425 events, and there are 200 electrons from known sources other than charm and bottom. The data were plotted in bins of p and $p_\perp$ of the electron ($p_\perp$ with respect to the thrust axis) which are shown in fig. 12. A fit of a sum over 4 processes ($c \to e^-$, $b \to e^-$, $b \to c \to e^-$ and background) in four bins of z, the relative momentum in the fragmentation process, was performed. The charm fragmentation function was taken from the D* analysis (actually the formula 5.1 with ϵ_c=0.30 was used). Since there were not enough data to determine several bins of the bottom fragmentation function, the same shape of equation 5.1, but ϵ_b as free parameter, was assumed. The result for the three parameters is B(c→e)=0.07±0.02±0.02, B(b→e)=0.11±0.03±0.02 and ϵ_b=0.04(-0.025+0.035) with a χ^2=13.6 for 18 degrees of freedom. Data points were not used in the fit where the background is dominant (p < 4 GeV - $2p_\perp$(GeV)). The fit result is a very good description of the data (see fig. 12) even in the area excluded from the fit. Fig. 13 shows the decomposition of the electron spectrum for two different $p_\perp$ intervals. There is a dominance of the electronic bottom decay fot $p_\perp$ > 1GEV and p > 3 GeV.

The result of the bottom quark fragmentation function is displayed in fig. 14. It exhibits a much harder spectrum for bottom quarks than for charm quarks. For curiosity one can scale the parameter ϵ_c=0.3 with m_c^2/m_b^2 and gets ϵ_b=0.03 compared to the measured 0.04.

8) Inclusive Hadron Spectra and Scale Breaking in e^+e^- Annihilation.

The observation of scaling violations in the nucleon structure functions from deep inelastic lepton-nucleon scattering experiments has

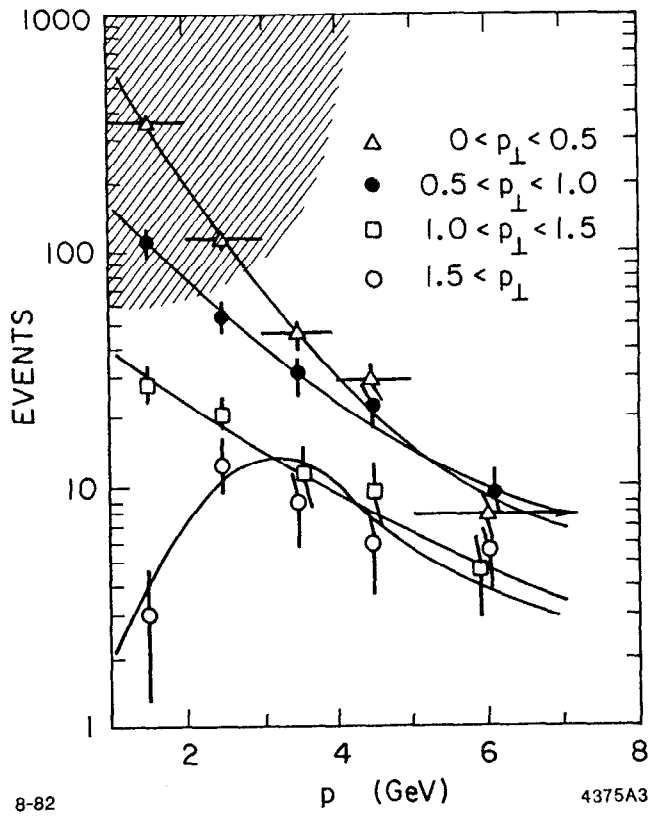


Fig. 12

Inclusive electron spectrum from MARK II for different transverse momentum. The full line is the result of a fit of $c \to e^-$, $b \to e^-$, $b \to c \to e^-$ and background. The hatched area was excluded in the fit.

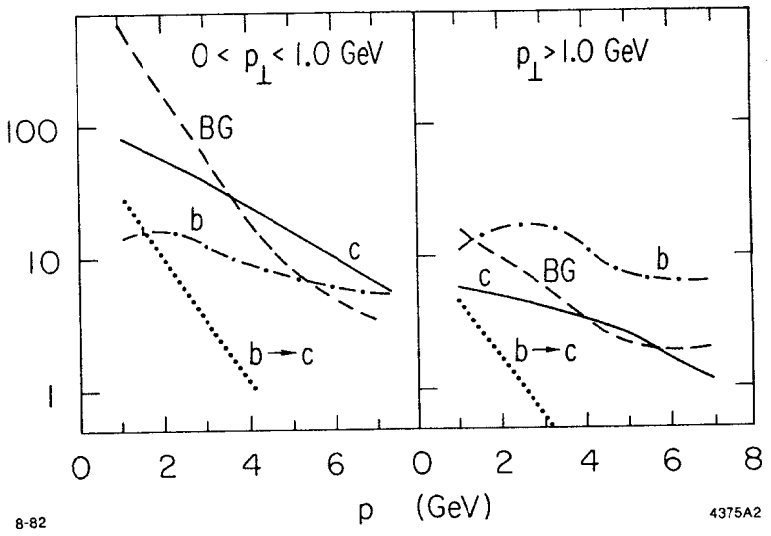


Fig. 13

Components of the electron spectrum from a fit to the MARK II data.

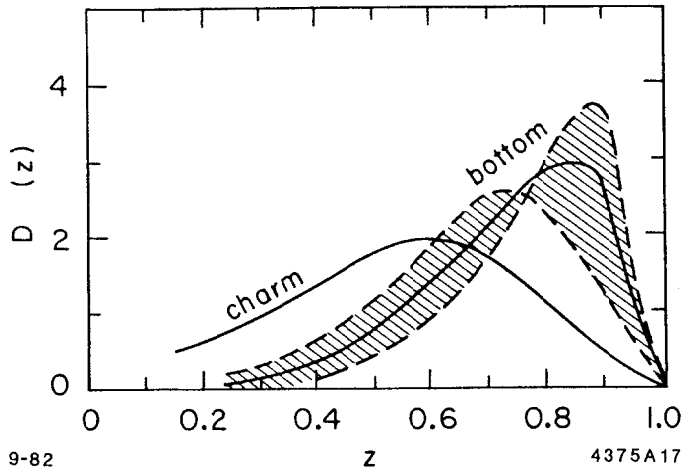


Fig. 14

Heavy quark fragmentation functions, normalized to 1. The bottom quark function is a fit result of equ. 5.1 to the MARK II data. The hatched area indicates the 1σ limits.

significantly supported the notion of QCD and gluon bremsstrahlung. Similar patterns of scale breaking are expected in the energy dependence of fragmentation functions[23]. Therefore, much attention has been paid to the measurements of the inclusive charged particle cross section in hadronic events in e^+e^- interactions. The differential cross section, $s d\sigma/dx$ (or $1/\sigma d\sigma/dx$), with x the fractional energy of the particle, has been measured by several groups. The systematic limitations in comparing measurements from different detectors at different energies at first did not allow one to observe the scaling violation effects. Only when the same detector had measured $s d\sigma/dx$ at different energies[24] was the expected scale breaking pattern observed. Recently, there have been more measurements from different groups[25,26] in good agreement with each other in the energy interval of 5 GeV to 35 GeV. In Fig. 15 the quantity $1/\sigma d\sigma/dx$ is displayed for $x>0.1$ from the TASSO and MARK II experiments. The relative uncertainty between the two experiments is 10%. At large values of x a strong decrease of the cross section with energy is observed (a factor 2 from 5 GeV to 35 GeV). The same was found by the PLUTO group[6] (fig.16). One can use the following parameterisation for the energy dependence:

$$s d\sigma/dx = b \left(1 + c_1 \ln s(\text{GeV}) \right)$$

The coefficient c_1, a measure of the strength of the scaling violation, is given in fig. 17 in good agreement from all three experiments.

The interpretation of these results is however difficult[27]. In a purely perturbative frame of QCD, scaling violation emerges only from gluon bremsstrahlung off the quarks, and non-perturbative effects from masses and transverse momenta in the subsequent fragmentation into

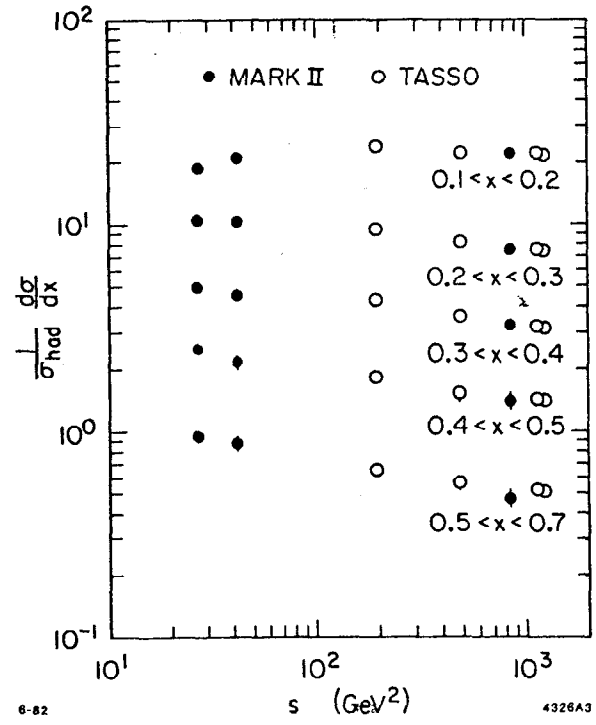


Fig. 15

Inclusive hadron spectrum from TASSO and MARK II.

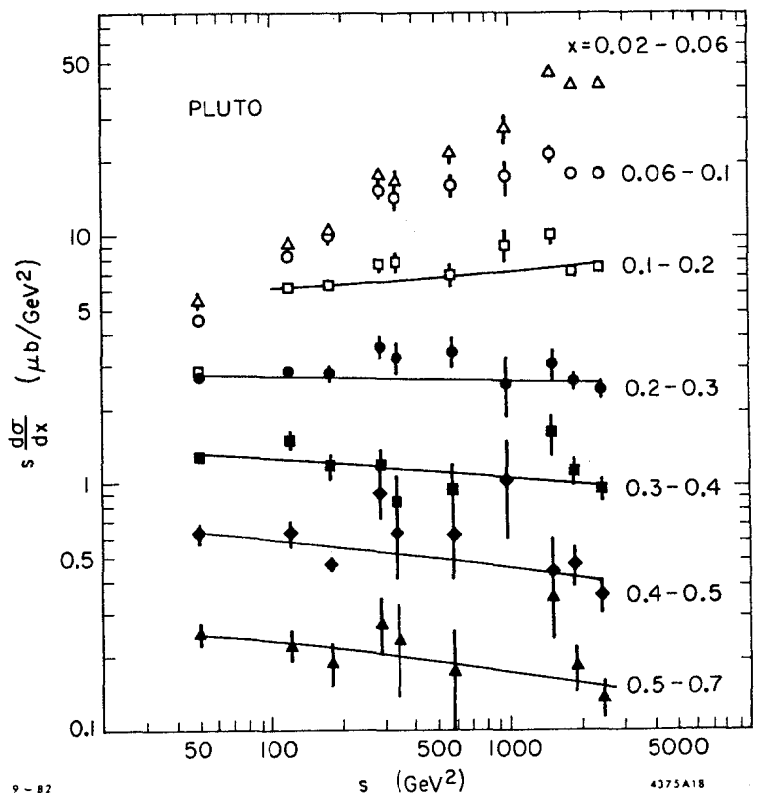


Fig. 16

Inclusive hadron spectrum from PLUTO.

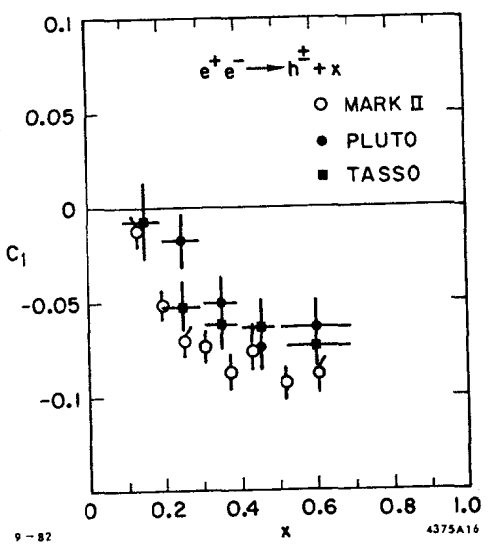


Fig. 17

Strength of the scaling violations from TASSO and PLUTO, $s d\sigma/dx \propto 1 + C_1 \ln s$(GeV).

hadrons are ignored. Indeed, such a picture[28] is able to account for the observed scaling violations with a QCD parameter $\Lambda \simeq 200$ MeV[18]. The other extreme considers only the non-perturbative contributions. A Monte Carlo simulation[29] of the fragmentation of the u,d and s quark only, yields most of the observed scale breaking (dotted line in fig. 18). The addition of the heavy charm quark, with its different fragmentation function, as discussed above, seems to be important, in particular at high energies. Finally the radiation of a hard gluon brings this model in good agreement with the data[30] (see full line in fig. 18).

In conclusion deciphering fragmentation functions seems to be difficult. Mass effects and heavy quark fragmentation are important unless much higher energies are reached.

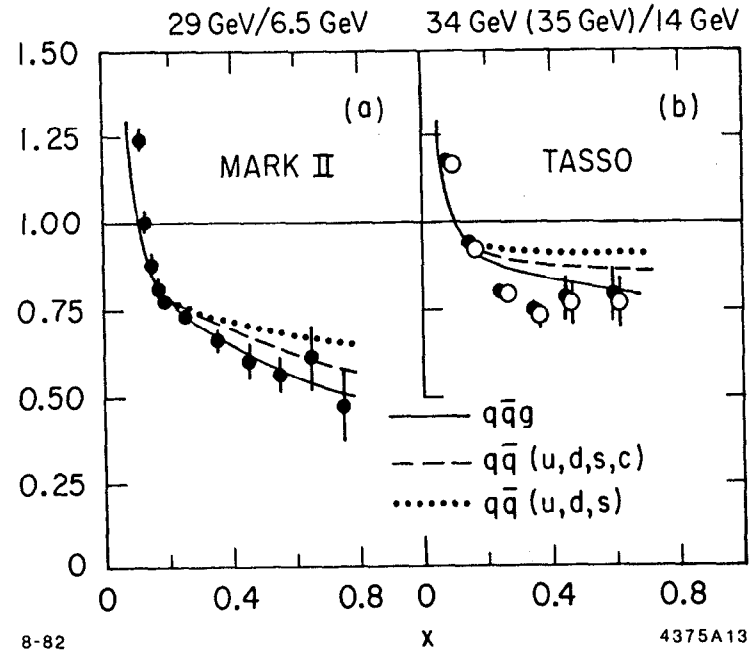


Fig. 18

Ratio of $s d\sigma/dx$ at two different energies. The dotted line is a Monte Carlo simulation with u,d and s quarks only. The dashed lines include c quarks. The full line includes hard gluon emission. a) MARK II data. b) TASSO data.

References and Footnotes.

1. G. Goldhaber et al., Phys.Rev.Lett. 37(1976) 255.
2. P. A. Rapidis et al., Phys.Lett.84B (1979) 507.
3. J.M. Yelton et al., Phys.Rev.Lett.49(1982),430
4. C. Bebek et al., Phys.Rev.Lett.49(1982) 610.
5. W.B. Atwood,SLAC-PUB 2980 (1982).
6. D. Lüke, Proc. XXI Intern. Conf. on High Energy Physics,Paris (1982).
7. M. Holder et al.,Phys.Lett.69B (1977) 377.
8. N. Armenise et al.,Phys.Lett.86B(1979)115.
9. H. Abramovicz et al., CERN-EP/82-77 (1982)
10. N. Ushida et al.,Phys.Rev.Lett.45(1980)1049.
11. J.D. Berger,Proc. XXI Intern. Conf. on High Energy Physics,Paris (1982).
12. L.J. Spencer et al.,Phys.Rev.Lett.47(1981) 771.
13. C. Bebek et al,Phys.Rev.Lett. 46(1981) 84,
    K. Chadwick et al.,Phys.Rev.Lett. 46(1981) 88.
    and K. Chadwick et al.,CLNS 82/546(1982) preprint.
14. G.H. Trilling,Proc. XXI Inter. Conf. on High Energy Physics,Paris (1982).
15. S. L. Glashow, J. Iliopoulos, L. Maiani, Phys.Rev. D2 (1970) 1285.
16. S.M. Errede,Rx-966(Ohio-State)1981,Ph.D.Thesis unpublished and private communication.
17. J. D. Bjorken, Phys.Rev.D17(1978) 171
    and M. Suzuki, Phys.Lett.71B(1977) 189
18. C. Peterson et al. SLAC-PUB-2912 (1982).
19. G. J. Feldman et al.,Phys.Rev.Lett.38(1977) 1313.
20. M. W. Coles et al.,SLAC-PUB-2916 (1982).
21. G. Goldhaber et al.,Phys.Lett.69B(1977) 503.
22. This cross section is smaller than the published value[3] which was obtained from a smaller data sample.
23. J. Owens,Phys.Lett.76B(1978)85
    T. Uematasu,Phys.Lett.79B(1978)97.
24. R. Hollebeek,Proc. 1981 Intern. Symposium on Lepton and Photon Interactions at High Energies, Bonn,p1.
25. R. Brandelik et al.,DESY 82-13 (1982).
26. J. Patrick et al.,SLAC-PUB-2936 (1982).
27. A detailed discussion can be found in ref. 18.
28. E.G. Floratos et al.,Nucl.Phys.B192(1981)417.
29. The LUND Monte Carlo program was used.
    T. Sjostrand, LU TP 80-3 and LU tp 82-3.
30. In the comparison of fig. 18 the Monte Carlo parameters have been adjusted to the MARK II data. This may account for the poorer fit of the TASSO data.

WEAK NEUTRAL CURRENTS IN e^+e^- EXPERIMENTS

Albrecht Böhm

Deutsches Elektronen Synchrotron DESY
D2000 Hamburg 52 Fed. Rep. Germany

and

III. Physikalisches Institut, RWTH Aachen
D5100 Aachen, Fed. Rep. Germany

(Presented at the SLAC Summer Institute on Particle Physics,
Stanford, California, August 1982)

© A. Böhm 1982

ABSTRACT

Results on weak neutral currents in e^+e^- reactions at PETRA and PEP are reviewed. A study of the leptonic reactions $e^+e^- \to \ell^+\ell^-$ leads to the conclusion that the electron, muon and tau lepton interact as if pointlike with cross sections, which are in agreement with the standard electro-weak theory of Glashow, Salam and Weinberg. A very significant forward-backward asymmetry of the reaction $e^+e^- \to \mu^+\mu^-$ is measured by three PETRA experiments JADE, MARK-J and TASSO. Their combined value is $A_{\mu\mu} = (-\ 10.4 \pm 1.4)\%$ in good agreement with the standard model which predicts -9.3%. PETRA experiments also measure a significant asymmetry, $A_{\tau\tau} = (-7.9 \pm 2.2)\%$, in the reaction $e^+e^- \to \tau^+\tau^-$ in accord with the GSW model and e,μ,τ universality. A fit to the cross sections of ee → ee and ee → μμ at $s = 1200\ GeV^2$ gives $\sin^2\theta_w = 0.27 \pm 0.07$ and tests the standard model at very high energies. Finally, first attempts have been made to extend these studies to hadronic reactions $e^+e^- \to q\bar{q}$ with the aim of measuring the weak neutral current couplings of heavy quarks.

I. INTRODUCTION

Weak neutral currents have been extensively studied in neutrino reactions[1,2] and electron-deuteron scattering[3]. The results give strong support to the standard $SU(2)_L \times U(1)$ theory (WS-GIM model)[4]. One therefore may ask what we learn by measurements of e^+e^- reactions at PETRA and PEP, where the c.m. energy $\sqrt{s}$ is below the Z^0 mass. A simple answer is that it is always necessary to check a theory over the whole range of interactions where it makes predictions. A quantitative answer is that one tests the theory at q^2 and s which are much higher in the e^+e^- reaction than in other fields. In addition, the reactions $e^+e^- \to \ell^+\ell^-(\ell=e,\mu,\tau)$ are purely leptonic reactions and are free from the complications due to strong interactions appearing in neutrino-nucleon scattering. They should therefore be compared to neutrino-electron scattering and, as we will see later, the data have now reached the precision of the ν-e measurements[5]. It should also be added that the measurements of $e^+e^- \to \ell^+\ell^-$ test the e-μ-τ universality. Similar arguments can be made for the reaction $e^+e^- \to q\bar{q} \to$ hadrons, where we hope to measure the weak coupling constants of the heavy quarks c, b and the as yet undiscovered top quark. Last but not least the PETRA and PEP storage rings operate at energies where for the first time we might be able to observe a deviation from the point-like four-fermion coupling. Clearly, such a deviation would either show the compositeness of leptons or, as expected, indicate the existence of the Z^0 boson. This would be an important step in our understanding of weak interactions.

There is one difficulty when we try to study weak neutral currents with charged leptons: the cross sections are dominated by the electromagnetic interaction due to their charges and the purely weak interaction is negligibly small. However,the cross section also contains an interference term between the γ and Z^0 exchange, which rises linearly with s relative to the pure QED cross section and

becomes measurable at c.m. energies of 30 to 40 GeV.

Finally it should be noted that there have been extensive searches for new particles in high energy e^+e^- reactions[6]. Many results are relevant to the theory of weak interaction. Although these searches cannot be discussed thoroughly in this talk owing to the limited time, the most relevant results should be mentioned. No leptons more massive than the tau, nor quarks heavier than the bottom have been found up to c.m. energies of 36 GeV. It would also be very exciting to find scalar or pseudoscalar particles which test our ideas about gauge symmetry breaking. Neutral Higgs particles can only be detected at the toponium and at the Z^0 peak or above. However, extensive searches for charged Higgs particles and technipions have been performed at PETRA, PEP and CESR. The result is that their existence is excluded for masses between the tau mass and 13,5 GeV independently of their decay branching ratios into $\tau\nu$, $c\bar{s}$ or $c\bar{b}$.

In the following chapters we will discuss the results of the individual leptonic reactions. The central point will be the measurements of the forward-backward asymmetry in the reaction $ee \to \mu\mu$ and $ee \to \tau\tau$. We will also combine all data on leptonic e^+e^- reactions and compare them with neutrino-electron scattering. In the last chapter we will report on first attempts to extend these measurements to the hadronic reaction $ee \to qq$ with the aim of determining the neutral current couplings of heavy quarks.

II. NEUTRAL CURRENT COUPLINGS OF LEPTONS

The reaction $e^+e^- \to \ell^+\ell^-$ is described in a model-independent way by three parameters. Following Hung and Sakurai[7] we call them h_{VV}, h_{VA} and h_{AA}. Clearly, if we use the same parameters for electron, muon and tau lepton, we assume lepton universality of the weak neutral currents. At high energies we have to introduce the Z^0 masses as additional parameters. If we only discuss models with a single Z^0, we can relate the parameters h_{VV}, h_{VA} and h_{AA} to the vector and axial vector couplings g_V, g_A, measured in neutrino-electron scattering (factorization). If the coupling constant of the neutrino to the Z^0 is given by $c_\nu/2$, we then have the following relations

$$h_{VV} = g_V^2/c_\nu^2 \qquad h_{AA} = g_A^2/c_\nu^2 \qquad h_{VA}^2 = h_{VV} \cdot h_{AA} = g_V^2 g_A^2/c_\nu^4 \tag{1}$$

Thus in theories with a single Z^0, the reactions $e^+e^- \to \ell^+\ell^-$ are described by three parameters, the two coupling constants h_{VV}, h_{AA} and the mass of the Z^0 boson.

In SU(2) x U(1) models these parameters are expressible in terms of the weak mixing angle $\sin^2\theta_w$ and of the weak isospin components of left handed and right handed leptons.

$$h_{VV} = \rho(T_{3L} + T_{3R} + 2\sin^2\theta_w)^2$$

$$h_{AA} = \rho(T_{3L} - T_{3R})^2 \qquad (2)$$

$$m_Z^2 = \frac{1}{\rho} \frac{\pi\alpha}{\sqrt{2}\, G_F} \frac{1}{\sin^2\theta_w \cos^2\theta_w}$$

The parameter ρ measures the strength of the weak neutral current interaction relative to the weak charged current interaction. We can also rewrite the third relation of (2) as

$$\rho = \frac{m_W^2}{m_Z^2 \cos^2\theta_w} \qquad (3)$$

where m_W is the mass of the charged vector boson. A combined fit to neutrino electron and electron deuteron measurements leads to[2]

$$\rho = 1.002 \pm 0.015 \quad \text{and} \quad \sin^2\theta_w = 0.234 \pm 0.013$$

Assuming $\rho = 1$ expressions (2) become

$$h_{VV} = (T_{3L} + T_{3R} + 2\sin^2\theta_w)^2$$

$$h_{AA} = (T_{3L} - T_{3R})^2 \qquad (4)$$

In the standard $SU(2)_L \times U(1)$ theory of GSW[4] the left-handed lepton fields are arranged in weak iso-doublets, the right-handed lepton fields in weak iso-singlets. Since this theory also predicts $\rho = 1$, we get

$$h_{VV} = g_V^2 = \frac{1}{4}(1-4\sin^2\theta_w)^2$$
$$h_{AA} = g_A^2 = \frac{1}{4} \qquad (5)$$

Using $\sin^2\theta_w = 0.23$, we find that $g_V^2 = 0.002$, $g_A^2 = 0.25$ and $m_Z \tilde{} 90$ GeV. The leptonic cross sections in e^+e^- reactions depend on the square of the vector or axial-vector coupling constant, but we cannot detect an effect due to the vector coupling, because it vanishes. However, the reverse argument is also valid: if we see no effect due to g_V^2, the *weak mixing angle $\sin^2\theta_w$ has to be very near to 0.25, in order to give* $g_V \tilde{} 0$. The parameters h_{VV} and h_{AA} are often called g_V^2 and g_A^2 in e^+e^- experiments and we follow that usage. However, be warned that the symbols g_V and g_A are usually reserved for the coupling constants of ν-e scattering. It should be noted that the vector and axial vector couplings in e^+e^- experiments are determined independently of assumptions about c_ν the coupling of the Z° to neutrinos. The parameter c_ν and expression (1) should be employed if the vector and axial-vector coupling constants measured in e^+e^- experiments are compared with those measured in neutrino-electron experiments.

As an example of the dependence of a cross section on these parameters, we will discuss the cross section for the reaction $ee \to \mu\mu$ or $ee \to \tau\tau$. If we define θ as the polar angle of the μ^- with respect to the outgoing e^- beam, then the μ^- angular distribution has the following form:

$$\frac{d\sigma}{d\cos\theta} = \frac{\pi\alpha^2}{2s}\left[R_{\mu\mu}(1+\cos^2\theta) + B\cos\theta\right] \qquad (6)$$

where

$$R_{\mu\mu} = \sigma_{\mu\mu} \Big/ \frac{4\pi\alpha^2}{3s} = 1 + 2g_V^2\chi + (g_V^2+g_A^2)^2\chi^2 \qquad (7)$$

and

$$\chi = \frac{G_F}{2\sqrt{2}\pi\alpha} \frac{s \cdot m_Z^2}{s - m_Z^2} \tilde{} -0.26 \text{ for } \sqrt{s} = 35 \text{ GeV}, \; m_Z = 90 \text{ GeV}.$$

The factor

$$B = 4\, g_A^2 \chi + 8 g_V^2 g_A^2 \chi^2 \qquad (8)$$

depends mainly on the axial vector coupling and it determines the forward-backward asymmetry which is given by

$$A_{\mu\mu} = \frac{N(\theta<90^o) - N(\theta>90^o)}{N(\theta<90^o) + N(\theta>90^o)} = \frac{3}{8}\,\frac{B}{R_{\mu\mu}} \qquad (9)$$

$N(\theta<90^o)$ is the number of events, where the μ^- is in the forward hemisphere, defined by the outgoing e^- beam.

This asymmetry depends on g_A^2 and is practically independent of the value of g_V^2

$$A_{\mu\mu} = \frac{3}{8}\,\frac{B}{R_{\mu\mu}} = \frac{3 g_A^2 \chi (1+2 g_V^2 \chi)}{2(1 + 2 g_V^2 \chi + \ldots)} \simeq \frac{3}{2} g_A^2 \chi \qquad (10)$$

Lepton universality is assumed in expressions (6) to (10), otherwise one should replace g_A^2 by $g_A^e \cdot g_A^\ell$ and g_V^2 by $g_V^e \cdot g_V^\ell$, where ℓ is the lepton produced in the final state. The asymmetry is negative and its absolute value increases with s. At $\sqrt{s} = 35$ GeV we calculate a value of $A_{\mu\mu} = -9.7\%$ for $g_A^2 = 1/4$ and $m_Z = 90$ GeV. The asymmetry depends weakly on the Z^o mass owing to the propagator term included in the variable χ. If we set the Z^o mass to infinity, we expect an asymmetry of -8.2%. Clearly asymmetries of this size are measurable, but it will be very hard to prove that the Z^o mass is finite with a value around 90 GeV. However, this question may be answered in the near future by the new measurements at PETRA at the end of 1982 when the energy is to be raised to $\sqrt{s} = 40$ GeV. The corresponding values for the asymmetry at $\sqrt{s} = 40$ GeV are -13.5% or -10.8%, for a Z^o mass of 90 GeV or infinitely large, respectively.

III. MEASUREMENT OF LEPTONIC REACTIONS

We will now discuss the measurements of the leptonic reactions. Table I lists the basic experimental conditions for the experiments at PEP and PETRA.

STORAGE RING	EXPERIMENTS	ENERGY	Ldt
PEP	MAC, MARK II	$\sqrt{s} = 29$ GeV	20-30 pb^{-1}
PETRA	CELLO, JADE, MARK-J, PLUTO, TASSO	$\langle\sqrt{s}\rangle = 34.5$ GeV	50-70 pb^{-1}

TABLE I Experiments and Their Basic Running Conditions at PEP and PETRA

The experiments at DESY have had the advantage that the PETRA storage ring has operated at a higher energy and has delivered a higher integrated luminosity.

In the framework of this talk it is not possible to describe the experiments and the details of the event selection. The reader is referred to publications of the individual experiments[8-14]. Leptonic events are easily recognized as two collinear back-to-back leptons, whose momenta are approximately equal to the beam momentum.

For selection one typically requires the acollinearity angle ξ to be smaller than 10^{o} and the lepton momentum to be larger than half the beam momentum. The radiative corrections to order α^3 are calculated for these cuts by the Monte Carlo program of Berends and Kleiss[15].

IV. RESULTS ON $e^+e^- \to e^+e^-$

We begin our discussion of individual leptonic reactions with Bhabha scattering, $e^+e^- \to e^+e^-$. Its measurement fulfills a twofold purpose: small angle Bhabha scattering serves as a luminosity monitor, while the angular distribution at large angles is sensitive to the weak interaction. The theoretical cross section[16] shows a rather complicated dependence on g_V^2 and g_A^2 because there are space-like and time-like exchanges of the virtual photon and the Z^o. As an example of the sensitivity of Bhabha scattering to the weak interaction Fig.1 indicates the deviation from QED for two values of the vector coupling, $g_V^2 = 0$ or $g_V^2 = 1/4$, while the other parameters are $g_A^2 = 1/4$ and $m_Z = 90$ GeV. The shape of the angular distribution of Bhabha scattering depends mainly on the vector coupling. This behaviour is opposite to that the the angular distribution of the reaction $ee \to \mu\mu$ in which the axial vector coupling g_A is dominant. We note that the weak interaction modifies Bhabha scattering only a few percent. Therefore, we do not present the results from Bhabha scattering alone, but determine the vector and axial vector couplings from a combined fit of all leptonic reactions. Since this is done in chapter IX, we only show here examples of the existing data. Fig. 2 displays the angular

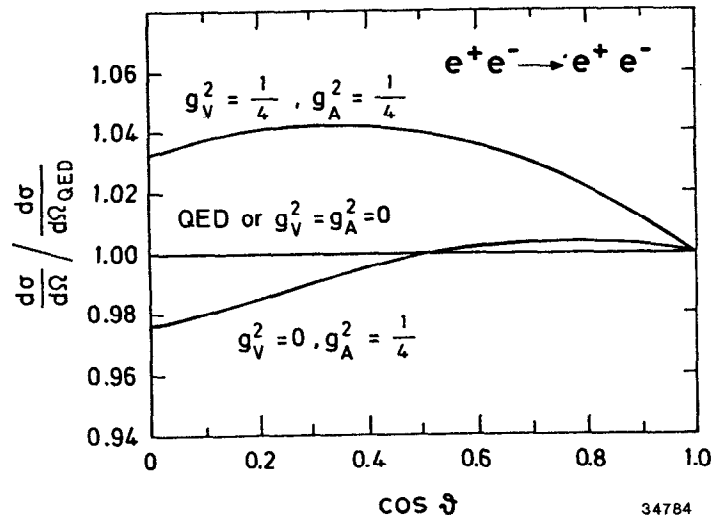


Fig. 1 Examples of how the weak interaction affects the differential cross section for Bhabha scattering, which is normalized by the QED cross section $\frac{d\sigma_{QED}}{d\Omega}$. The predictions for different values of the vector and axial vector couplings are shown. The Z^o mass is 90 GeV. The angular distribution is folded around $\theta = 90^o$, as would be the case for experiments which do not measure the charge of the electron.

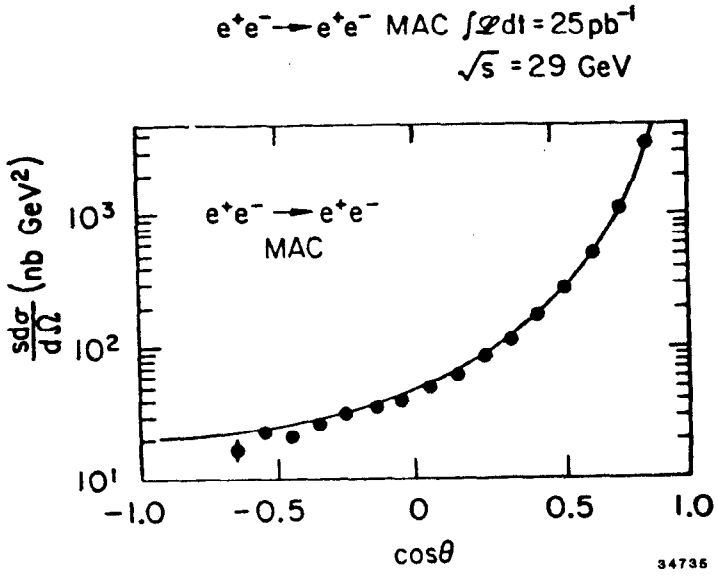


Fig. 2 Differential cross section of Bhabha scattering measured by the MAC group[13] at PEP.

distribution of Bhabha scattering measured by the MAC experiment[13] at PEP. The results of the PETRA experiments are shown in Fig. 3, where the ratio of the measured cross section to the calculated QED cross section is plotted. In this way deviations from QED are more visible. The errors indicated in Fig. 3 are only statistical. In addition, there are systematic errors on the overall normalization of 3 to 5% and point-to-point errors of 1 to 3% for the different experiments. Because the vector coupling g_V is expected to be negligibly small and the axial vector coupling modifies the cross section by less than 3%, we can not prove the existence of weak interaction in Bhabha scattering. However, we can use the measurements in a combined fit of all leptonic data to determine a limit on the vector coupling constant.

V. CROSS SECTION OF $e^+e^- \to \mu\mu$

The results on the reaction ee → μμ can be divided into two parts, the total cross section $\sigma_{\mu\mu}$ and the forward-backward asymmetry $A_{\mu\mu}$. We first consider the cross section, where we present the results in terms of $R_{\mu\mu}$, the cross section normalized to the point-like cross section. The systematic error on $R_{\mu\mu}$ is dominated by an overall normalization error due to luminosity and acceptance, which ranges between 3% and 5% for different experiments. The statistical error at the highest energies of $\sqrt{s} \simeq 34.5$ GeV is about 2% as typically 3000 muon pairs are observed.

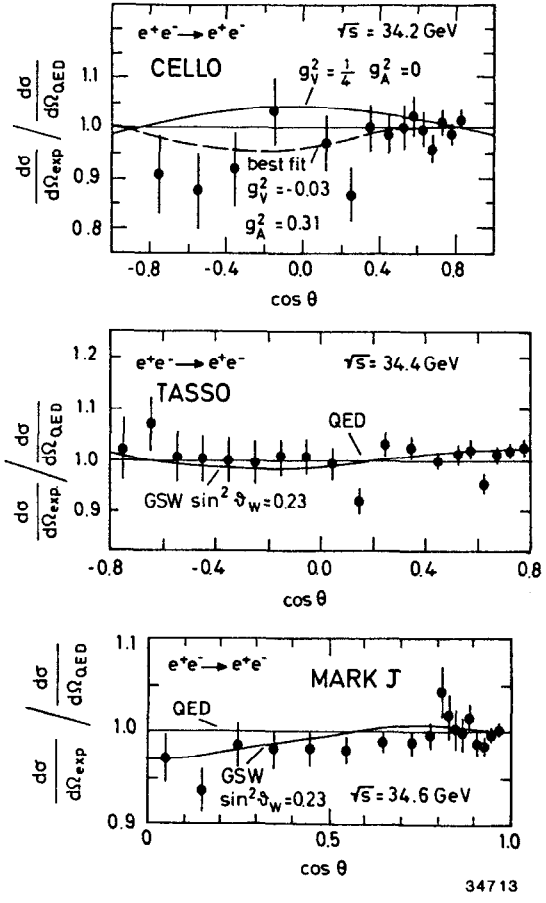


Fig. 3 Measurements of Bhabha scattering by the PETRA experiments CELLO, TASSO and MARK-J. The measured cross section is divided by the theoretical QED cross section and compared to the predictions of the electroweak theory.

The effect of the weak interaction on the cross section depends mainly on the vector coupling of the electron and the muon. From (7) we read off the approximation for the deviation $\Delta R_{\mu\mu}$ from the QED cross section $R_{\mu\mu} = 1$.

$$\Delta R_{\mu\mu} \simeq 2\chi g_V^e g_V^\mu \qquad (11)$$

Therefore no deviation from QED can be observed, if the vector coupling of the muon or the electron vanishes. This would be the case for $\sin^2\theta_w = 0.25$. In the other extreme case of $g_V^2 = 1/4$ we should observe a decrease of the cross section by 13%. The cross sections measured at PETRA at the three energies, $\sqrt{s}$ = 14, 22 and 34.5 GeV are shown in Fig. 4. The measurements agree with the pure QED prediction within the statistical and systematical errors. This result can be interpreted in two ways: first, if we assume the validity of QED, we find that the vector coupling g_V is very small and $\sin^2\theta_w$ is near 0.25. Detailed numbers will be given later for the combined fit to all leptonic reactions; second, if we neglect the weak interaction, which would in any case be unmeasurable for $\sin^2\theta_w = 0.23$, we can test QED. This is usually done in terms of a form factor writing

$$\sigma_{\mu\mu} = \sigma_{QED} \cdot F^2(s), \text{ where } F(s) = 1 \mp \frac{s}{s-\Lambda^2} \qquad (12)$$

The agreement of the cross section with the QED prediction can then be expressed by a lower limit (95% C.L.) of the cut-off parameter Λ, which ranges between 150 and 200 GeV for different experiments. This value indicates, using the Heisenberg Uncertainty Principle, that muons (and electrons) behave as point-like particles down to a distance 10^{-16}cm.

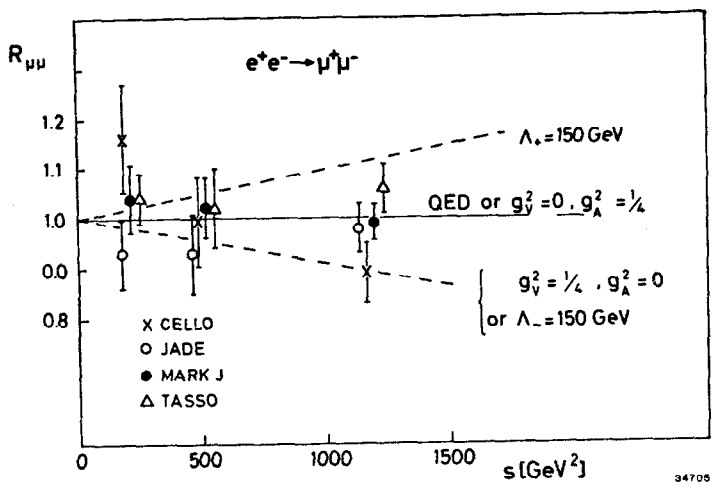


Fig. 4

Results on $R_{\mu\mu}$, which is the cross section of ee → μμ divided by the point-like cross section. The solid line shows the QED prediction, which coincides with the electro-weak prediction for $g_V^2 = 0$. The dashed lines indicate deviations from QED to be expected if the cut-off parameters $\Lambda_\pm$ are 150 GeV. The curve for Λ_- coincides with the electroweak prediction for $g_V^2 = \frac{1}{4}$, $g_A^2 = 0$.

VI. ASYMMETRY OF $e^+e^- \to \mu^+\mu^-$

The measurement of the forward-backward asymmetry is one of the central experimental tasks at high energy e^+e^- experiments. The asymmetry arises from the interference between the electromagnetic and weak interaction and depends on the weak axial-vector coupling of the electron and muon

$$A_{\mu\mu} = \frac{3}{2}\chi g_A^e\, g_A^\mu \qquad (13)$$

The GSW-model predicts a negative asymmetry because g_A^e is equal to g_A^μ and χ is negative. This means that there are more $\mu^+\mu^-$ events with the μ^- in the backward hemisphere than events with the μ^- in the forward hemisphere.

To measure the asymmetry one needs to determine the direction and the charge of the muons. The asymmetry can be measured very precisely because it is a relative measurement, independent of the luminosity measurement. It is insensitive to errors in the acceptance and reconstruction efficiency as long as the acceptance is the same for positive and negative muons. For this reason, the experiments are able to limit the systematic error of the asymmetry to $\leq 1\%$. In addition, MARK-J and MAC took equal amounts of data with positive and negative magnet polarity. The addition of both data sets effectively cancels all systematic errors, which relate to the charge measurement, and leaves no doubt that the systematic error is much smaller than 1%.

Figure 5 shows the angular distribution measured by the MARK II

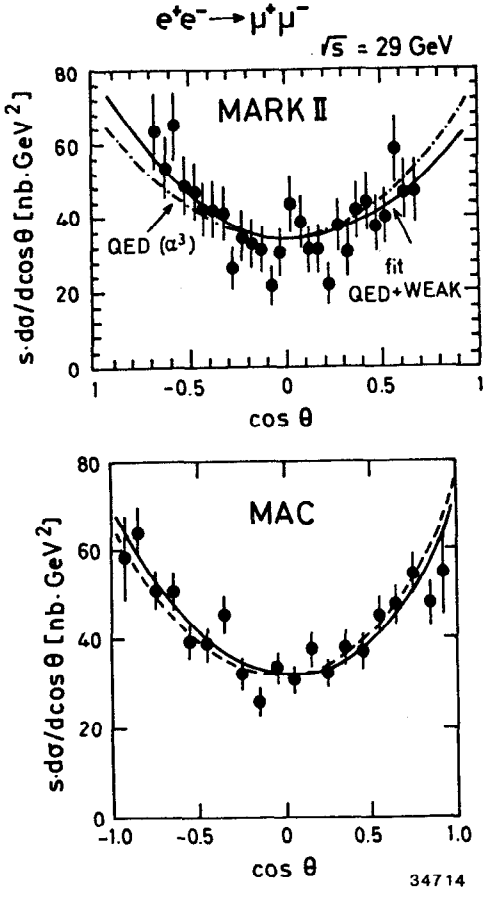
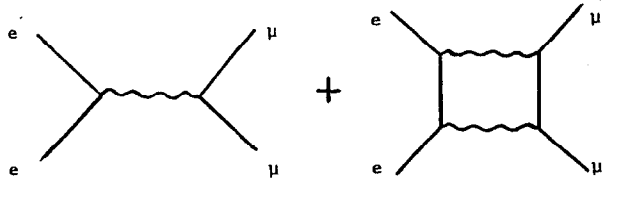


Fig. 5
Angular distribution of the reaction $e^+e^- \to \mu^+\mu^-$ measured by the MAC and MARK II experiments at PEP. The dashed line is the prediction of QED. The solid line is the best fit to the electro-weak cross section. Both curves include QED radiative corrections to order α^3.

and MAC detector at PEP. These measurements are not corrected for QED radiative effects and thus are compared with the QED prediction including corrections to order α^3. The weak interaction should increase the cross section in the backward hemisphere (negative $\cos\theta$) and decrease the cross section in the forward hemisphere. We cannot detect a statistically significant asymmetry in these measurements at 29 GeV. Turning to the measurements at PETRA at $\sqrt{s} \simeq 34.5$ GeV (Fig. 6), we see a clear and very significant negative asymmetry in the angular distribution measured by JADE, MARK-J and TASSO. This is mainly due to the higher c.m. energy, which increases the asymmetry by a factor 1.5, and due to the higher integrated luminosity reached by the PETRA storage ring. The measured values in Fig. 6 are corrected for QED radiative effects to order α^3. Therefore, the data are compared to a $1 + \cos^2\theta$ distribution, predicted from lowest order QED (dashed line) and to a fit which includes an additional $\cos\theta$ terms as predicted by the weak interaction.

Before we discuss the significance of these measurements, we should be more explicit about radiative corrections. Pure QED also produces a forward backward asymmetry, for example, through the interference of the one and two photon exchange graphs.



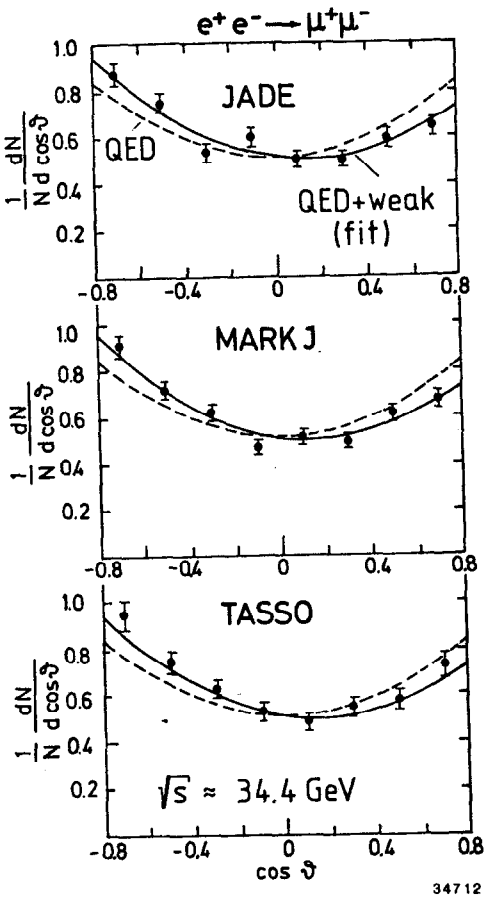


Fig. 6

Angular distribution of the reaction $e^+e^- \mu^+\mu^-$ measured by the PETRA experiments JADE, MARK-J and TASSO. The data are corrected for QED radiative effects up to order α^3. The dashed line indicates the lowest order QED prediction of $(1+\cos^2\theta)$. The solid line is a fit to the data using the electroweak cross section, given by(6).

The QED asymmetry is calculated by a Monte Carlo program from Berend and Kleiss[15]. It is found to be +1.5% for $|\cos\theta| \leq 0.8$ if one applies an acollinearity cut of $\xi < 10^\circ$ and a cut on the muon momentum of $p_\mu > 1/2\ p_{beam}$. In order to compare the measurements with the lowest order electroweak formula (10) one usually subtracts the QED asymmetry from the observed asymmetry

$$A_{weak} = A_{observed} - A_{QED} \qquad (14)$$

This correction to the asymmetry is incomplete, because we should apply radiative corrections for QED and weak interactions. A Monte Carlo program[17] which includes first order QED corrections and a large part of the weak corrections, gives an asymmetry of $A_{weak} = (-8.6\pm0.2)\%$ at $\sqrt{s} = 34.5$ GeV. Since this value includes the correction from (14) it should be compared to the lowest order electroweak asymmetry of -9.4%, obtained from (6). Whether the difference between both values shows the presence of weak radiative corrections is unclear. A simpler explanation could be that the c.m. energy squared is reduced by initital state bremsstrahlung, which creates a corresponding reduction of the asymmetry, because the asymmetry is approximately proportional to s. However, until we find a clear explanation for this difference we use formula (6) to calculate the expected asymmetry and neglect the results of the Monte Carlo calculation. A better understanding of electroweak radiative corrections is urgently needed. Otherwise we will soon have the situation that the error on the theoretical prediction is of the same size as the error on the measured asymmetry.

Table II summarizes the high energy measurements of the asymmetry. Only statistical errors are given with the measured asymmetries. The systematic errors are estimated to be smaller than 1% and are included in the combined results. The asymmetries in Table II are obtained from a fit of (6) to the measured angular distribution after it is corrected for radiative effects of QED to order α^3. The parameters of the fit are $R_{\mu\mu}$ and the coefficient B of the $\cos\theta$ term of expression (6). The asymmetry is calculated from the ratio of B to $R_{\mu\mu}$.

$$A_{\mu\mu} = \frac{3}{8} \frac{B}{R_{\mu\mu}} \qquad (15)$$

In this way one effectively extrapolates the angular distribution to $\cos\theta = 1$ and has the possibility of comparing the measured asymmetries directly to values calculated from the lowest order electroweak prediction (10).

TABLE II

RESULTS FROM PEP AND PETRA ON THE ASYMMETRY OF $e^+e^- \to \mu^+\mu^-$

Experiment	$\sqrt{s}$ (GeV)	Measured $A_{\mu\mu}$ in %	Expected in GSW for $\sin^2\theta_w$=0.23 in %
MAC	29	-4.4 ± 2.4	-6.3
MARK II	29	-9.6 ± 4.5	-6.3
PEP Results combined		-5.6 ± 2.3	-6.3
CELLO	34.2	-6.4 ± 6.4	-9.1
JADE	34.2	-10.8 ± 2.2	-9.2
MARK-J	34.6	-10.4 ± 2.1	-9.4
TASSO	34.4	-10.4 ± 2.3	-9.3
PETRA Results combined	34.4	-10.4 ± 1.4	-9.3 for m_Z=90GeV -7.9 for $m_Z = \infty$

All measurements agree well with the prediction of the GWS-theory for $\sin^2\theta_w \simeq 0.23$ which gives $g_A^\mu = g_A^e = -1/2$, $g_V \simeq 0$ and $m_Z \simeq 90$ GeV.

The asymmetry depends mainly on the product $g_A^e \cdot g_A^\mu$ and the Z^o mass. If we include a systematic error of 1% on the asymmetry of each experiment, we can draw the following conclusion from Table II.

1) If we set $m_Z = 90$ GeV, we find

$$g_A^e \cdot g_A^\mu = 0.274 \pm 0.035$$

If we insert $g_A^e = -0.530 \pm 0.035$ from νe-scattering, we determine the axial-vector coupling of the muon

$$g_A^\mu = T_{3L} - T_{3R} = -0.52 \pm 0.10$$

The value is in perfect agreement with the assumption that the left-handed muon is the lower member of a weak iso-doublet and that the right-handed muon is in a weak iso-singlet. If we assume $T_{3L} = -1/2$, then we obtain $T_{3R} = 0.02 \pm 0.10$. Comparing g_A^e with g_A^μ we get an impressive confirmation of the μ-e universality in the weak interaction.

2) Alternatively, we can determine the Z^o mass, $m_Z = 72\ ^{+36}_{-10}$ GeV, if we assume e-μ universality and $g_A^2 = 1/4$ and $g_V^2 \simeq 0$. The one standard deviation error is somewhat misleading, because the upper 95% confidence limit extends to an infinite mass. However, a firm lower limit can be put on the Z^o mass, which is 56 GeV with 95% confidence.

Figure 7 summarizes all existing measurements on this asymmetry. The low energy points are from PETRA and from SPEAR[18]. We observe a clear dependence on the c.m. energy s as predicted for an electro-weak interference. The effect of a Z^o propagator with a Z^o mass of

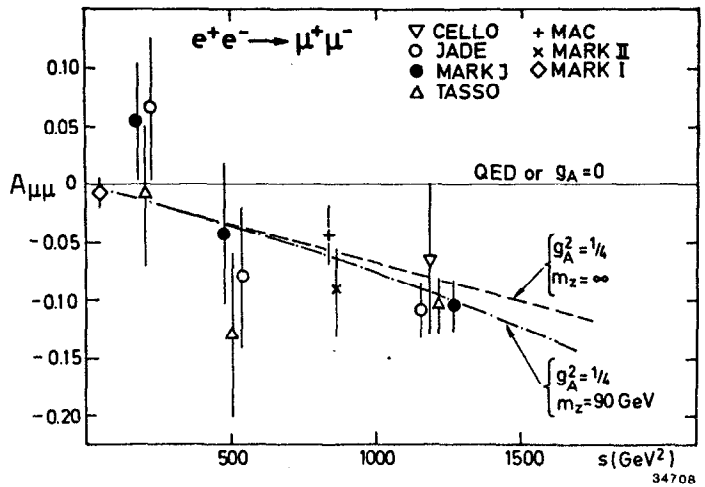


Fig. 7 Measurements of the forward backward asymmetry of the reaction $e^+e^- \rightarrow \mu^+\mu^-$ as a function of the c.m. energy squared. The data are compared to the predictions of the electroweak theory with $g_A^2 = 1/4$ for a pointlike four-fermion coupling, i.e., $m_Z = \infty$ (dashed line) and for $m_Z = 90$ GeV (dashed-dotted line). Since the measurements are corrected for radiative effects, pure QED or an electroweak theory with $g_A = 0$ predicts no asymmetry.

90 GeV cannot yet be distinguished from that of a point-like four fermion coupling ($m_Z = \infty$). However, at the end of 1982 PETRA will begin operating at an energy of 40 GeV ($s=1600$ GeV^2), where the effects of the Z^o propagator are about twice that at $s=1200$ GeV^2. With an equal amount of data at 40 GeV, we should be able to give an interesting lower and upper bound for the Z^o mass.

VII. $e^+e^- \rightarrow \tau^+\tau^-$: CROSS SECTION AND BRANCHING RATIOS

We first discuss the measurement of the cross section $\sigma_{\tau\tau}$. Tau leptons are recognized by their characteristic decays, either into lepton and neutrinos or into hadrons (low multiplicity) and a neutrino. The branching fractions of tau-leptons which are accepted by a given detector range between 28% for MARK-J and TASSO to 94% for CELLO and MAC, because the experiments use different decay modes to select tau events. The systematic error on the cross section is generally larger than for $\sigma_{\mu\mu}$ and ranges between 10% and 20%, if one includes the errors of the branching ratios. The reader is referred to the original publications for a detailed description of the selection and measurement of tau events[10-13),(19,20)]

The measured cross sections are corrected for acceptance and for QED radiative effects to order α^3 so that they can be compared directly to the lowest order QED cross section. If we plot the ratio $R_{\tau\tau}$ of the tau cross section divided by the pointlike cross section we remove the $1/s$ dependence of the cross section and simplify the comparison of the measurements to the QED prediction, which is $R_{\tau\tau}=1$.

Figure 8 shows the measured values for $R_{\tau\tau}$ as a function of s, which agree well with QED within the statistical and systematic errors. The effect of the weak interaction on $R_{\tau\tau}$ can still be neglected within measurement errors because it is proportional to $g_V^e g_V^\tau$, where at least the vector coupling of the electron is close to zero. Thus, from Fig. 8 we can draw the following conclusions.

1) The agreement of the tau cross section with the QED prediction leads to an upper limit for the cut-off parameter of $\Lambda \simeq 120$ GeV with 95% confidence level. We conclude that the tau interacts as a pointlike lepton down to distances as small as 2.10^{-16}cm.

2) Alternatively, we assume the validity of QED and determine the branching ratios of tau decay modes which were used for the selection of $ee \to \tau\tau$. MAC[13], MARK-J[21], and PLUTO[22] measure the branching ratio of $\tau \to \mu\nu\nu$. Their results are listed in Table III together with a result from MARK II at SPEAR[22].

TABLE III

RESULTS ON THE BRANCHING RATIO FOR $\tau \to \mu\nu\nu$

Experiment	B ($\tau \to \mu\nu\nu$) in %
MAC	17.6 ± 1.5 ± 1.0
MARK-J	16.3 ± 1.6
PLUTO	17.8 ± 2.0 ± 1.0
MARK II (SPEAR)	17.1 ± 0.6 ± 1.0
AVERAGE	17.1 ± 0.8

Tau leptons can also be recognized by their decay into charged hadrons of low multiplicity. Denote by B_1, B_3 and B_5 the branching

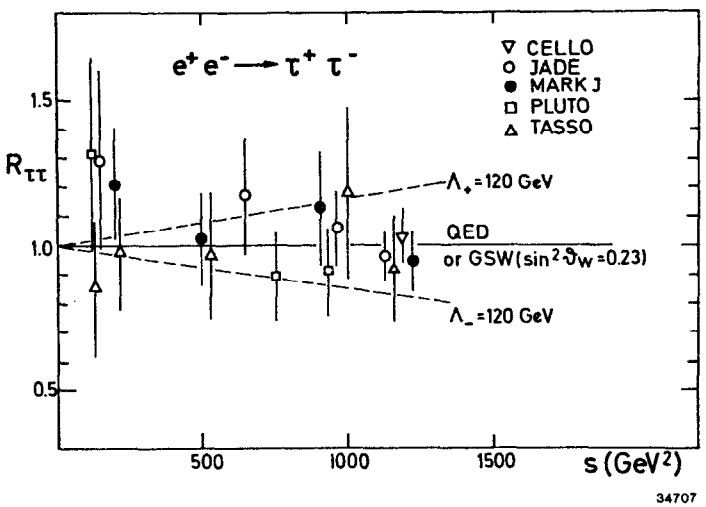


Fig. 8 Measurements of $R_{\tau\tau}$ at different c.m. energies squared. The solid line shows the prediction of pure QED which coincides with the prediction of the GSW-theory for $\sin^2\theta_W = 0.23$. Also indicated are the deviations expected if the cut-off parameter $\Lambda_\pm$ would be 120 GeV.

ratios of taus into one, three and five charged particles and additional neutral particles. Table IV shows the branching ratios which have been measured by CELLO[19], MAC[13], MARK II[20], and TASSO[23]. The branching ratios are constrained by requiring $B_1 + B_3 + B_5 = 1$, since there must be at least one charged particle in the decay of a tau lepton.

TABLE IV

BRANCHING RATIOS B_n OF THE TAU LEPTON INTO n = 1,3 and 5 CHARGED PARTICLES AND ADDITIONAL NEUTRALS

Experiment	B_1 in %	B_3 in %	B_5 in %
CELLO	84.0±2.0	15.0±2.0	1.0±0.4
MAC	84.6±0.7±1.0	15.3±0.7±1.0	< 0.7%
MARK II	86.0±3.0±1.0	14.0±3.0±1.0	< 0.7% 95%
TASSO	76.0±6.0	24.0±6.0	< 6%
Average	84.3±1.0	15.3±1.0	

VIII. $e^+e^- \to \tau^+\tau^-$: ASYMMETRY

The angular distribution of tau leptons should show a forward backward asymmetry proportional to $g_A^e \cdot g_A^\tau$ analogous to the reaction ee → μμ. If $g_A^e = g_A^\tau = -1/2$ we expect an asymmetry of -9.7% at 35 GeV. This means that negative taus go more frequently in the direction of the positron beam and positive taus tend to follow the electron beam. The charge of the tau lepton is easily determined from the sum of the charges of its decay products. Most of the experiments do not detect all decay modes and have therefore a smaller number of events than in the reaction ee → μμ, with attendant larger statistical errors.

Figure 9 shows the angular distribution measured by MAC and MARK II at $\sqrt{s}$ = 29 GeV. The prediction from QED including α^3 QED correction coincides with the best fit, which includes the weak interaction. This means that, within measurement errors a weak interaction asymmetry is not observed. However, we should not forget that the expected asymmetry at $\sqrt{s}$ = 29 GeV is small, only -6.3%. The angular distributions measured by PETRA experiments at $\sqrt{s} \simeq 34.4$ GeV are plotted in Fig. 10. The angular distributions are corrected for radiative effects of order α^3 and should therefore be compared with the lowest order QED or electroweak prediction. All four measurements depart slightly from the symmetric $(1+\cos^2\theta)$ distribution predicted by pure QED and prefer a small negative asymmetry. The angular distributions of Fig. 9 and Fig. 10 are fitted with the electroweak prediction in the form of expression (6) by varying $R_{\tau\tau}$ and B the coefficient of the asymmetric term of the cross section. The forward backward asymmetry of taus is calculated by

$$A_{\tau\tau} = \frac{3}{8}\frac{B}{R_{\tau\tau}} \qquad (16)$$

which can be compared to the electroweak prediction

$$A_{\tau\tau} = \frac{3}{2}\chi g_A^e\, g_A^\tau \qquad (17)$$

The tau asymmetries measured at PEP and PETRA are listed in Table V. The measurements have a systematic error of 1% to 2% in addition to the statistical error given in Table V.

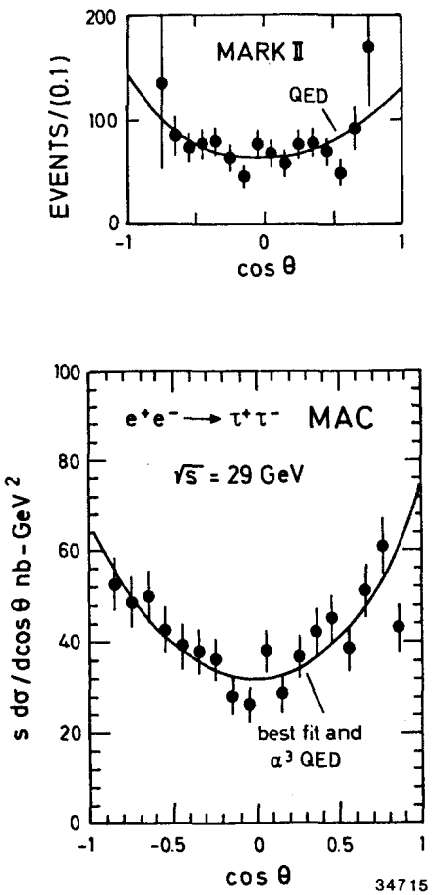


Fig. 9

Angular distribution of $e^+e^- \to \tau^+\tau^-$ measured by MAC and MARK II at PEP. The solid curve indicates the QED prediction including radiative corrections to order α^3.

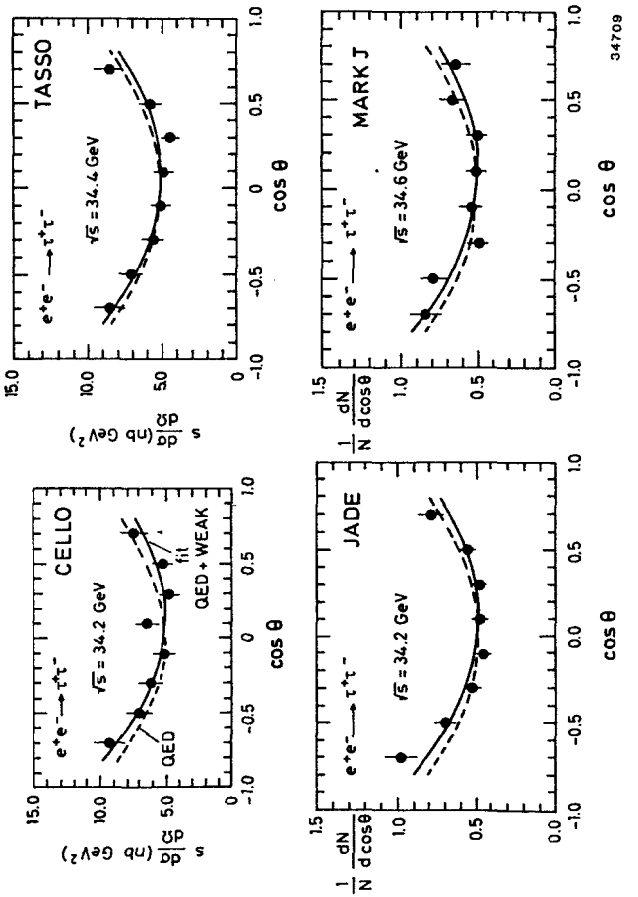


Fig. 10

Angular distribution of $e^+e^- \to \tau^+\tau^-$ measured by CELLO, TASSO, JADE and MARK-J at PETRA. The data are corrected for QED radiative effects to order α^3. The dashed line is the lowest order QED prediction of the form $(1+\cos^2\theta)$. The solid line is a fit to the data, which includes weak interaction in the form of expression (6).

TABLE V

RESULTS FROM PEP AND PETRA ON THE ASYMMETRY IN THE REACTION $e^+e^- \to \tau^+\tau^-$

Experiment	$\sqrt{s}$ GeV	$A_{\tau\tau}$ in %	Expected in GSW for $\sin^2\theta_w = 0.23$
MAC	29	-1.3±2.9	-6.3
MARK II	29	-3.2±5.0	-5.0 ($\|\cos\theta\|<0.7$)
PEP Combined	29	-1.7±2.5	-6.0
CELLO	34.2	-10.3±5.2	-9.2
JADE(prelim)	34.2	- 7.9±3.9	-9.2
MARK-J	34.6	- 8.4±4.4	-9.4
TASSO	34.4	- 5.4±4.5	-9.3
PETRA Combined	34.4	- 7.9±2.2	-9.3

The experiments at PETRA find a negative asymmetry with a typical significance of two standard deviations. Their combined value of (-7.9±2.2)% is the first significant observation of an electroweak interference associated with tau leptons. It agrees well with the expected value of -9.3% and e-μ-τ universality in weak interactions.

The asymmetry of ee → ττ measures the product $g_A^e \cdot g_A^\tau$. By combining all PEP and PETRA measurements we find (for m_Z = 90 GeV)

$$g_A^e \cdot g_A^\tau = 0.18\pm0.05.$$

If we insert $g_A^e = 0.530\pm0.035$ from νe-scattering we determine the axial vector coupling of the tau lepton

$$g_A^\tau = T_{3L} - T_{3R} = -0.34\pm0.12.$$

This value is consistent with the assumption that the left-handed tau is the lower member of a weak iso-doublet and the right-handed tau is in a weak iso-singlet.

IX. COMBINED RESULTS FROM LEPTONIC REACTIONS

We now assume e-μ-τ universality and attempt a combined fit to the leptonic reactions $e^+e^- \to \ell^+\ell^-$, where ℓ is an electron, muon or tau lepton. We can either assume the validity of the GSW theory and determine $\sin^2\theta_w$ or allow an independent variation of the vector and axial-vector coupling. In the second case, we should also vary the Z^o mass, but the data are not yet accurate enough to determine the Z^o mass. We therefore give the results of g_V^2 and g_A^2 for a Z^o mass of 90 GeV. Table VI lists the results from different experiments. Both statistical and systematic errors are included.

TABLE VI

RESULTS OF A COMBINED FIT TO LEPTONIC REACTIONS. THE THEORETICAL PREDICTION OF THE GSW-THEORY ARE OBTAINED WITH $\sin^2\theta_w$=0.23±0.01 AS MEASURED BY νN and ed SCATTERING EXPERIMENTS

Experiment	Reaction Used	g_V^2	g_A^2	$\sin^2\theta_w$
MAC	ee, μμ, ττ	<0.11(95%C.L.)	$0.16^{+0.08}_{-0.06}$	0.24±0.10
MARK II	ee,μμ	0.05±0.10	0.24±0.16	
CELLO	ee, μμ, ττ	-0.03±0.08	0.31±0.12	$0.21^{+0.14}_{-0.09}$
JADE	μμ	0.05±0.08	0.29±0.06	
MARK-J	ee, μμ, ττ	-0.02±0.05	0.28±0.06	0.26±0.09
TASSO	ee, μμ, ττ	-0.04±0.06	0.26±0.07	0.27±0.07
Combined Data on ee, μμ From JADE,MARK-J, TASSO		0.01±0.03	0.28±0.04	0.27±0.07
νe-Scattering		$0.00^{+0.01}_{-0}$	0.28±0.04	0.27±0.03
GSW Theory		0.04	0.25	0.23±0.01

The data of JADE, MARK-J and TASSO on the reactions ee → ee and ee → μμ are also combined in a fit, which includes the normalization error and the systematic error of each experiment. All results given in Table VI agree very well with the predictions of the GSW-theory for $\sin^2\theta_w = 0.23 \pm 0.01$, as measured by νN and ed scattering[2] and so confirms the validity of the GSW-theory at high q^2 and s up to 1200 GeV^2. Fig. 11 displays the values for $\sin^2\theta_w$ measured in different reactions and indicates the typical momentum transfer. It is very impressive to see that one parameter, $\sin^2\theta_w \simeq 0.23$, describes all of these reactions.

It should also be noted that the results of Table VI are obtained from purely leptonic e^+e^- reactions and can therefore be compared to measurements of neutrino electron scattering. The results from both types of experiments have a similar precision and show an excellent agreement. A comparison with the neutrino electron experiments can also be done in more detail, if one displays the results in the (g_V, g_A)-plane (Fig. 12). The allowed region for g_V and g_A has a four-fold symmetry because e^+e^- experiments measure the square of the coupling constants. Neutrino scattering alone limits the values to two regions, a vector-like and a axial-vector-like solution. To resolve this ambiguity one previously had to consider lepton-hadron scattering with the inherent complications of hadronic targets. Now a unique solution can be determined from purely leptonic reactions. To come to this conclusion we have assumed in expression (1) that $h_{VV} = g_V^2$ and $h_{AA} = g_A^2$ or equivalently $c_\nu = 1$. Sakurai has proposed to compare the ratios h_{VV}/h_{AA} and g_V^2/g_A^2 which are independent of the

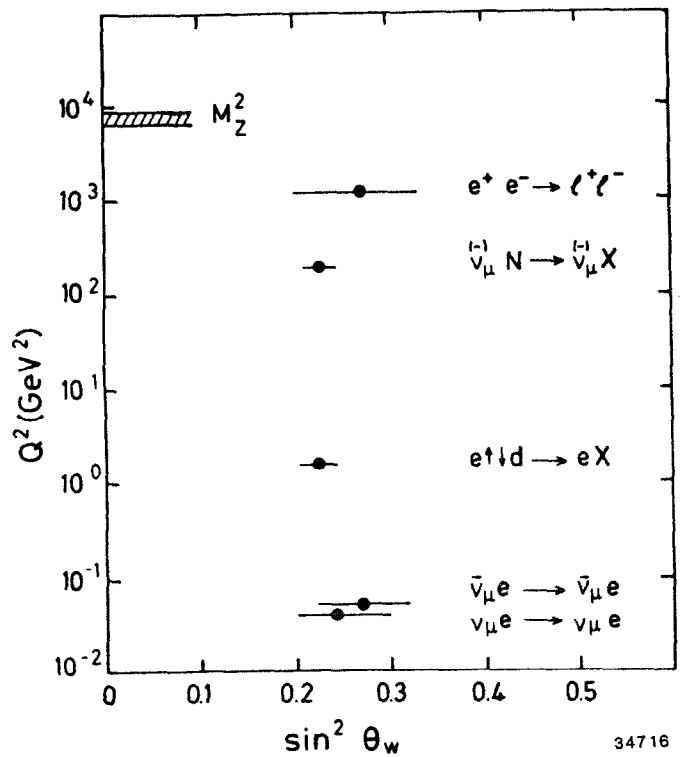


Fig. 11 The measurements of $\sin^2\theta_w$ from different reactions are plotted as a function of the momentum transfer squared. Note that the Q^2 is mainly time-like in $e^+e^- \rightarrow \ell^+\ell^-$, in contrast to the other reactions.

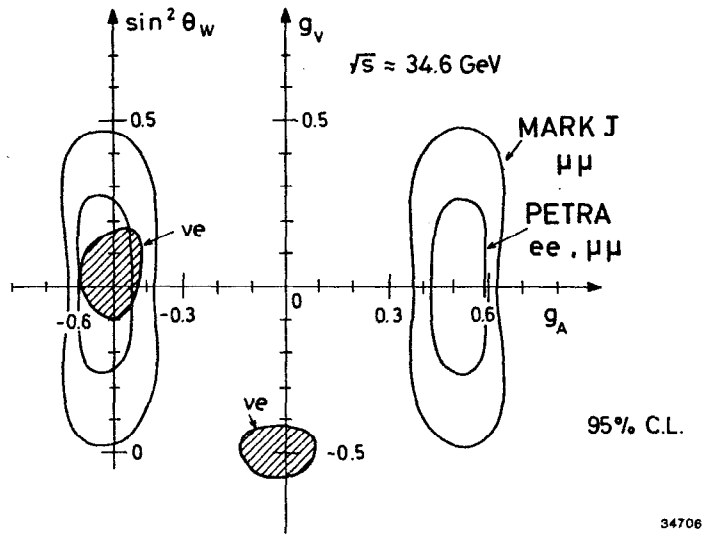


Fig. 12 Allowed regions (95% C.L.) for the vector and axial vector coupling of leptons determined by neutrino electron scattering (shaded area) and by e^+e^- experiments (unshaded regions). The contour of the MARK-J experiment results only on the measurement of $e^+e^- \to \mu^+\mu^-$, while the contour of the PETRA experiments is obtained from a combined fit of the reactions $e^+e^- \to e^+e^-$ and $e^+e^- \to \mu^+\mu^-$. The vector-like solution from νe scattering is clearly excluded, while the axial vector-like solution predicted by the GSW theory for $\sin^2\theta_w = 0.23$ is in very good agreement with the measurements of $e^+e^- \to \ell^+\ell^-$.

value of c_ν, to exclude one solution[24]. From the results of e^+e^- experiments listed in Table IV we find

$$\frac{g_V^2}{g_A^2} = \frac{h_{VV}}{h_{AA}} < 0.27 \text{ with 95\% confidence.}$$

This limit clearly excludes the vector-like solution of the neutrino electron scattering data on a more general ground, namely in the framework of models with a single Z^o.

X. MULTI-BOSON MODELS

Now we abandon the restriction of one neutral gauge boson and consider the gauge groups SU(2) x U(1) x G. These models[25, 26] have an effective neutral current lagrangian, which becomes in the low q^2 limit

$$L_{eff}^{NC} = -\frac{4G_F}{\sqrt{2}}\left[\left(J_\mu^3 - \sin^2\theta_w J_\mu^{em}\right)^2 + C\,(J_\mu^{em})^2\right] \qquad (18)$$

It differs from SU(2)xU(1) by a term proportional to the square of the electromagnetic current which is parity conserving and which is therefore invisible in the neutrino experiments and in polarized electron-deuteron scattering. However, it modifies the vector coupling and h_{VV}, previously given by (5), becomes

$$h_{VV} = \frac{1}{4}(1-4\sin^2\theta_w)^2 + 4C \qquad (19)$$

To reproduce the low energy neutrino and electron-deuteron results we

use $\sin^2\theta_w = 0.23$ and determine a limit on C. Experiments at PETRA find the upper limits (95% C.L. listed in Table VII).

TABLE VII

UPPER LIMITS FOR THE PARAMETER C WITH 95% CONFIDENCE

CELLO	0.031
JADE	0.039
MARK-J	0.021
TASSO	0.018
Combined	0.015

The parameter C is positive and a function of the couplings and masses of the Z^o bosons. The mass limits for models with two neutral bosons, where G is a U(1) or a SU(2) group[26], are shown in Fig. 13. We see that the neutral boson masses are limited to a small region, where one of the Z^o's has a mass near to 90 GeV as predicted by the standard $SU(2)_L \times U(1)$ theory.

XI. HADRON PRODUCTION $e^+e^- \to q\bar{q}$

Hadronic production in e^+e^- annihilation is well described by the pair production of spin $\frac{1}{2}$ quarks, which subsequently fragment into jets of hadrons. The cross section for the production of a quark-antiquark pair of flavor f can be obtained from formula (6) by replacing the electric and weak charges of the muon by Q_f and g_V^f, g_A^f, respectively, and multiplying the result by a factor three for the color degrees of freedom. The relative cross section R_f is then given by[27]

$$R_f = 3\{Q_f^2 - 2Q_f \chi g_V^e g_V^f + \chi^2 \left[(g_V^e)^2 + (g_A^e)^2\right] \left[(g_V^f)^2 + (g_A^f)^2\right]\} \qquad (20)$$

The vector and axial vector couplings of the quark are determined in the standard $SU(2)_L \times U(1)$ model by the third component of the weak isospin and by the weak mixing angle.

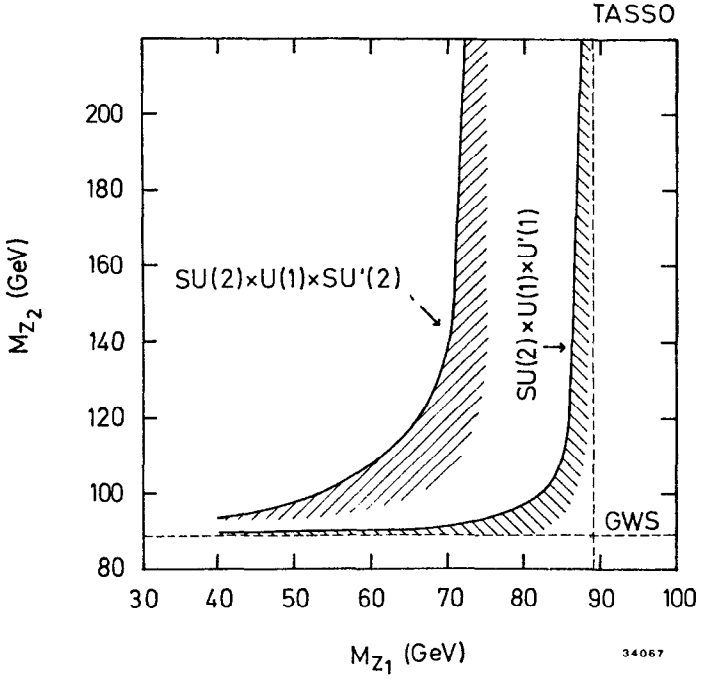


Fig. 13 Limits on the Z^o masses for models with two Z^o bosons. The allowed masses of Z_1 and Z_2 are confined to the region (partially shaded) between the solid curve and the dashed lines.

$$g_V = T_{3L} - 2Q_f \sin^2\theta_w \qquad g_A = T_{3L} \qquad (21)$$

If we arrange the left-handed quarks in weak iso-doublets $\binom{u}{d}$, $\binom{c}{s}$, $\binom{t}{b}$, we assign $T_{3L} = +\frac{1}{2}$ to the quarks u, c and t, and $T_{3L} = -\frac{1}{2}$ to the quarks d, s and b.

The total hadronic cross section is the sum of R_f over the five quark flavors u, d, s, c, b multiplied by a QCD correction

$$R = \sum_f R_f \left(1 + \frac{\alpha_s}{\pi} + \ldots\right) \qquad (22)$$

The variation of R with $\sin^2\theta_w$ is shown in Fig. 14. At first one might think that the effect is too small to be observed, but the hadronic cross section increases by 11%, if $\sin^2\theta_w$ changes from 0.10 to 0.30. This increase is still rather small in view of the systematic errors which range between 3% and 6% for different experiments. The largest contribution to the systematic error comes from an uncertainty in the absolute normalization of the cross section. If there is a systematic error, it should be independent of the c.m. energy, whereas the contribution of the weak interaction to the hadronic cross section increases with the square of the c.m. energy. Thus, by measuring the energy dependence of R a determination of $\sin^2\theta_w$ can be made. Measurements of R between 12 and 36 GeV have been obtained at PETRA (Fig. 15). The data have been fitted using equation (22) but allowing the overall normalization to vary within the errors. The strong coupling constant was taken as $\alpha_s = 0.17$ by MARK-J and TASSO and as 0.18 by JADE. The values of $\sin^2\theta_w$ are insensitive to the value of α_s, because they are determined from the energy dependence of R, not from its magnitude. Table VII summarizes

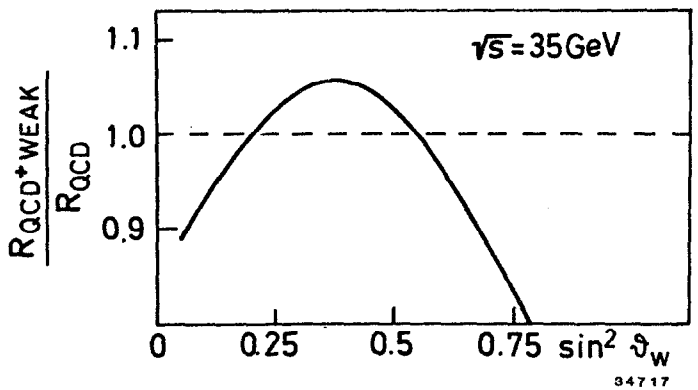


Fig. 14 Dependence of the hadronic cross section on $\sin^2\theta_w$. $R_{QCD+WEAK}$ is calculated with formula (22) including the weak interaction, while R_{QCD} is calculated without the weak interaction, i.e., with $g_V = g_A = 0$.

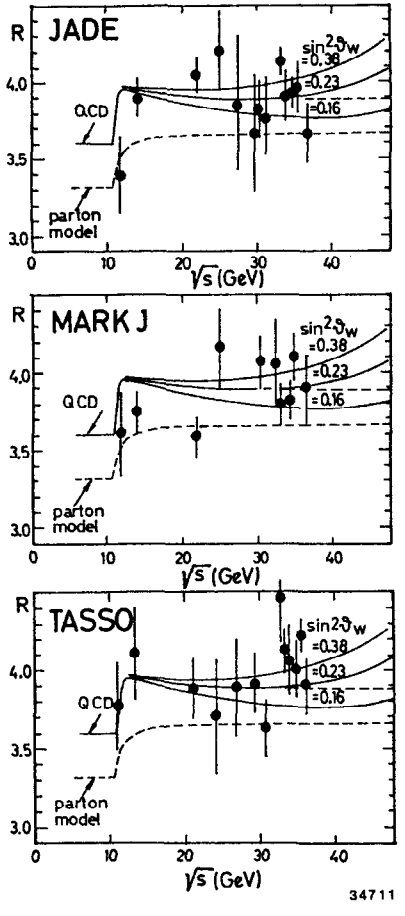


Fig. 15

Measurements of R as a function of the c.m. energy. The data from JADE[28], MARK-J[19] and TASSO[29] are compared to the prediction of the parton model and of QCD, where the weak interaction is included with different values of $\sin^2\theta_w$.

the values[19, 28, 29] of $\sin^2\theta_w$ and that of <R>, which is averaged over the energy range between 14 GeV and 36 GeV.

TABLE VII

VALUES OF $\sin^2\theta_w$ AND OF <R>

Experiment	<R>	$\sin^2\theta_w$ from $e^+e^- \to q\bar{q}$	$\sin^2\theta_w$ from $e^+e^- \to q\bar{q}$ and $e^+e^- \to \ell\bar{\ell}$
JADE	3.93±0.03±0.09	0.25±0.05	-
MARK-J	3.84±0.05±0.22	$0.44^{+0.11}_{-0.19}$	0.30±0.06
TASSO	4.01±0.03±0.20	0.40±0.15±0.02	-

The large spread of values of $\sin^2\theta_w$ and its error is explained by the fact that the χ^2 curves of the fits are rather flat for $0.25 < \sin^2\theta_w < 0.55$. Figure 14 shows that the contribution of the weak interaction is symmetric around $\sin^2\theta_w \simeq 0.38$, with generally two solutions for $\sin^2\theta_w$. Additional measurements are needed to exclude one of these. Because the hadronic cross section depends on the product of the quark and electron couplings, the MARK-J group prefers to quote $\sin^2\theta_w$ determined from a combined fit of hadronic and leptonic reactions. This value is also given in Table VII. Clearly, the precision of these measurements of $\sin^2\theta_w$ cannot compete with the neutrino-nucleon and electron-deuteron measurements, but the results give support to the validity of the GSW-theory and its applicability in the region of time-like q^2 up to 1200 GeV^2.

XII. FORWARD-BACKWARD ASYMMETRY IN $e^+e^- \to q\bar{q}$

The measurement of the angular distribution of jets in the reaction $e^+e^- \to q\bar{q}$ offers the possibility of observing the forward backward asymmetry of quarks and of determining the axial vector coupling of quarks on the condition that we find a method of distinguishing quark jets from antiquark jets. The situation is completely analogous to that of the muon asymmetry, where we must distinguish a μ^- from its antiparticle, μ^+. The methods of separating quarks from antiquarks will be described later in this chapter. For the moment we assume that we are able to do so and discuss the angular distribution and asymmetry of quarks. The main terms of the angular distribution of a quark of flavor f can be written

$$\frac{2s}{\pi\alpha^2}\ \frac{d\sigma}{d\cos\theta} \simeq 3Q_f^2\ (1+\cos^2\theta) - 12Q_f\chi g_A^e g_A^f \cos\theta + \ldots \qquad (23)$$

where θ is the angle of the quark, not the antiquark, with respect to the electron beam direction. We see from (23) that the QED contribution to the cross section is proportional to Q_f^2, while the electroweak interference term is proportional to Q_f. Because the asymmetry depends mainly on the ratio of the interference term to the QED term, it is increased by a factor $1/Q_f$ and we find

$$A_f \simeq -\frac{3}{2}\,\chi\,\frac{1}{Q_f}\ g_A^e\, g_A^f \qquad (24)$$

The asymmetry A_f measures the axial-vector coupling of a quark divided by its charge. The axial-vector coupling depends on the third component of the weak isospin of left-handed and of right-handed quark fields.

$$g_A^f = T_{3L} - T_{3R} \qquad (25)$$

Thus the asymmetry is sensitive to the multiplet structure of weak isospin. If we assume only left handed iso-doublets and right handed iso-singlet and arrange the left handed quarks in the following doublet structure

$$\binom{u}{d}\ \binom{c}{s}\ \binom{t}{b?}$$

we obtain

$$g_A = +\frac{1}{2} \text{ for u, c, and } g_A = -\frac{1}{2} \text{ for d, s, b.}$$

Since the ratio g_A^f/Q in expression (24) is always positive and χ and g_A^e are negative, we should observe a negative asymmetry for all quark flavors. In addition, we find that the absolute value of the asymmetry is increased by a factor $1/Q_f$ compared to the muon asymmetry. If we include a correction due to the quark mass[30], we expect $A_c \approx -14\%$ and $A_b = -25\%$ at 34 GeV. At first sight, these high values appear easy to measure, but an analysis of the μ-inclusive events shows that the observed asymmetries are in fact very much smaller. This results from background and an incomplete separation of c- and b-quarks which we now explain in more detail.

The forward backward asymmetry of a quark flavor can only be measured when we are able to distinguish quarks from antiquarks. This means that we have to determine the quark flavor and the quark charge. In principle this can be achieved with a study of hadronic events which contain a "prompt" lepton (μ- or e-inclusive events)[31]

$$e^+e^- \rightarrow q\bar{q} \rightarrow \begin{cases} e + \text{hadrons} \\ \mu + \text{hadrons} \end{cases}$$

We call a lepton "prompt" when it appears to come from the interaction point where it originates from a semileptonic decay of a heavy quark produced in the e^+e^- reaction. More precisely, the heavy quark fragments into a short lived hadron of the same flavor whose decay is described in the spectator model as the decay of the heavy quark. The sign of the prompt lepton charge indicates the sign of the charge of the parent quark. Examples are

$$b \rightarrow \mu^- X \qquad\qquad c \rightarrow \mu^+ X$$

The cascade decay $b \rightarrow c \rightarrow \mu^+ X$ creates some charge confusion but the lepton spectrum is softer and so a cut on the lepton momentum should in principle eliminate a large number of these events. If we neglect this problem for a moment, we find that positive muons select c-quarks and b-antiquarks; negative muons select c-antiquarks and b-quarks. If we are not able to separate the quark flavors b and c, their asymmetry will partially cancel, because we add particle and antiparticle asymmetries. Therefore a good flavor separation is of major importance for this measurement.

Quark flavors can be selected with variables, which are sensitive to the quark mass. In our present understanding, we believe that b-quarks fragment into broader jets than c-quarks of the same momentum. Since thrust measures the width of a jet, it is a good candidate for a variable to separate bottom from charm. Other variables are the transverse momentum p_T of the prompt lepton with respect of the thrust axis or the angle δ between the lepton direction and the thrust axis. MARK-J uses a cut $\cos\delta < 0.925$ and TASSO uses a cut $p_T > 1$ GeV to select b-decays[19, 32]. A Monte Carlo calculation simulating these cuts predicts that 35% of the selected events are b-quarks. The remainder is background from c-decays, π- and K-decay and from hadrons which penetrate the muon filter and are misidentified as muons (punch-through). Charm decays are selected with complementary cuts. Half of the events in this sample are c-decays, the remainder is again K- and π-decay and punch through. The quark asymmetries computed from these samples are listed in Table VIII.

TABLE VIII

RESULTS OF FIRST ATTEMPTS TO MEASURE THE FORWARD-BACKWARD ASYMMETRY OF BOTTOM AND CHARM QUARKS AT 35 GeV. THE MEASURED AND EXPECTED VALUES INCLUDE THE EFFECTS OF BACKGROUNDS AND INCOMPLETE FLAVOR SELECTION

Experiment	Measured	Expected
MARK-J	$A_b = -(17\pm10)\%$	- 5%
TASSO	$A_b = -(20\pm10)\%$	- 8%
MARK-J	$A_c = -(7\pm5)\%$	- 4%

The results in Table VIII are very preliminary and only give an indication of the status of the analysis. Incomplete flavor separation and background strongly decrease the inititally expected large asymmetries. We see from Table VIII that the expected bottom asymmetry is -5% to -8% instead of -25% which one calculates for a pure bottom sample. Clearly, the discrimination between bottom, charm, and the background level will need to be improved if significant

results are to be obtained. The statistical accuracy cannot be improved easily because these results are already based on a large amount of data. For example, the initial data sample of the MARK-J group contains 15,500 hadronic events from which 352 candidates of charm decays and 89 candidates of bottom decays are selected.

A different method for flavor tagging has been employed by TASSO[32]. Charged D^* mesons are reconstructed from the decay modes $D^{*+} \to D^0\pi^+ \to K^-\pi^+\pi^+$ and $D^{*-} \to K^+\pi^-\pi^-$. The D^* mesons are selected from the large number of $K\pi\pi$ combinations by a cut on the mass difference ΔM between the D^* mass and the D^0 mass. The events fulfilling the cut $142 < \Delta M < 148$ MeV show a D^0 peak with 47 events. The background is estimated to be 11 events so that a signal of 36 charged D^* mesons is detected. With these events the TASSO group finds a forward backward asymmetry of $A_c = -(35\pm14)\%$, where one expects -11% in the GSW model. Again, the number of events is too small to measure a statistically significant asymmetry. The hope is that with better mass resolution and with higher acceptance the statistical significance of this measurement will improve in the future.

XIII. FLAVOR CHANGING NEUTRAL CURRENTS

If the top quark does not exist and/or if the bottom quark is in a weak SU(2) singlet, flavor changing neutral currents would be expected in the b-decay. A good signature for this process is the decay $b \to \mu^+\mu^- X$. Theoretical calculations give a lower limit for its branching ratio[33]

$$B(\mu^+\mu^- X) \geq 1\%$$

A search for this decay mode of the bottom quark has been made by CLEO at CESR and recently by MARK-J at PETRA. Here we will describe the analysis of the MARK-J group. Hadronic events with a $\mu^+\mu^-$ pair in one jet are selected as illustrated in Fig. 16. If the muon pair originates from the decay of a b-quark, the angle between the two muons should be rather large due to the high mass of the b-quark. A cut of $> 15^\circ$ is chosen for this angle. One candidate has been found in a sample of 28,400 hadronic events which contains 2,570 $b\bar{b}$ events. However, one background event is also expected. The acceptance for this decay mode was calculated by a Monte Carlo program and found to be 7.1% which leads to a lower limit on the branching ratio determined by MARK-J.

$$B(b \to \mu^+\mu^- X) < 0.6\% \text{ with } 90\% \text{ C.L.}$$

The CLEO group at CESR in similar analysis finds[34]

$$B(b \to \mu^+\mu^- X) < 0.9\% \text{ with } 90\% \text{ C.L.}$$

We conclude from these results that the b-quark is a member of a weak iso-doublet and we should not give up searching for the top quark. It might turn out that we discover the existence of a top quark at PETRA in the year 1983 when energies up to 42 GeV become available.

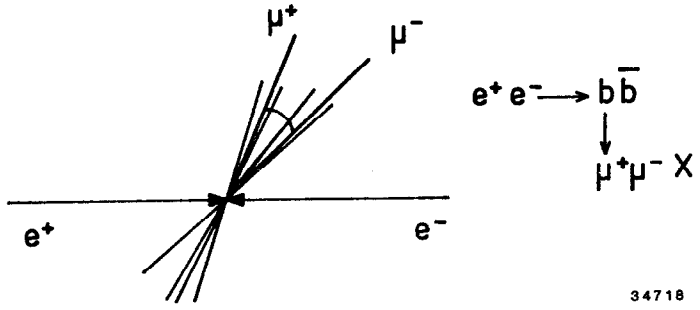


Fig. 16 Illustration of the signature of an event where one bottom quark decays via a flavor changing neutral current. A cut on the angle between the two muons eliminates background.

CONCLUSIONS

1) In $e^+e^- \to \mu^+\mu^-$, JADE, MARK-J and TASSO have observed a statistically significant forward backward asymmetry
$A_{\mu\mu} = (-10.8\pm2.2)\%$, $(-10.4\pm2.1)\%$, $(-10.4\pm2.3)\%$ respectively.
These values are in good agreement with the expectation of -9.3% from the GSW-model.

2) Leptonic reactions in e^+e^- experiments test the electroweak theories up to $s = 1200\ \text{GeV}^2$ and $q^2 \simeq 1000\ \text{GeV}^2$. We find impressive agreement with the GSW model and determine $\sin^2\theta_w = 0.27\pm0.07$.

3) In a study of $e^+e^- \to$ hadrons first attempts have been made to measure the weak neutral current couplings of heavy quarks, but a lower background from light quarks and a better separation of bottom and charm quarks is necessary in order to achieve significant results.

4) No flavor changing neutral currents have been observed

$$B\ (b \to \mu^+\mu^- X) < 0.6\% \quad (90\%\ \text{C.L.})$$

5) Charged Higgs particles and technipions are excluded for masses between the tau mass and 13 GeV[19, 34, 35].

ACKNOWLEDGEMENTS

I wish to thank the members of the CELLO, JADE, MAC, MARK II, PLUTO, and TASSO collaborations and my colleagues from the MARK-J group for discussion and for providing me with unpublished data. In particular I am very grateful to H.-U. Martyn and B. Naroska for helpful comments and to D.P. Barber and R.R. Rau for critical reading of the manuscript. Finally, many thanks to the organizers of the 1982 SLAC Summer Institute on Particle Physics for their warm hospitality.

REFERENCES

(1) For review see
L.M. Sehgal, Aachen Report PITHA 80/17;
P.Q. Hung and J.J. Sakurai, Ann. Rev. Nucl. Sci. 31, 375 (1981);
F.W. Büsser, Proc. of the Int. Conf. on Neutrino Physics and Astrophysics, Wailea, Hawaii, 1981;
G. Barbiellini, Proc. of the 1982 Int. Symp. on Lepton and Photon Interactions at High Energies, ed. W. Pfeil, Bonn 1981, p. 623;
F. Niebergall, Proc. of Neutrino '82, Balatonfüred 1982, to be published, and CERN preprint CERN-EP/82-105 (1981).

(2) Y.E. Kim et al., Rev. Mod. Phys. 53, 211 (1981).

(3) C.Y. Prescott et al., Phys. Lett. 77B, 347 (1978) and Phys. Lett. 84B, 524 (1979).

(4) S.L. Glashow, Nucl. Phys. 22, 579 (1961);
S. Weinberg, Phys. Rev. Lett. 19, 1264 (1967) and Phys. Rev. D5, 1412 (1972);
A. Salam, in Elementary Particle Theory, ed. N. Svartholm, Stockholm 1968, p. 361;
S.L. Glashow, J. Iliopoulos and L. Maiani, Phys. Rev. D2, 1285 (1970).

(5) H. Faissner, New Phenomena in Lepton-Hadron Physics (1979), ed. D.E. Fries and J. Wess (Plenum Publishing Corp., New York), p. 371;
H. Reithler, Phys. Blätter 35, 630 (1979);
F.W. Bullock, Proc. of Neutrino 79, Bergen 1979, p. 398;
R.H. Heisterberg et al., Phys. Rev. Lett. 44, 635 (1980);
M. Jonker et al., Phys. Lett. 105B, 242 (1981) and Phys. Lett. 117B, 272 (1982).

(6) J. Bürger, Proc. of the 1981 Int. Symp. on Lepton and Photon Interactions at High Energies, ed. W. Pfeil, Bonn 1981, p. 115;
A. Böhm, Proc. of the XVII Rencontre de Moriond, ed. J. Tran Tanh Van, Les Arcs 1982, p. 159, and DESY Report, DESY 82-027 (1982).

(7) P. Q. Hung and J.J. Sakurai, Phys. Lett. 69B, 323 (1977).

(8) CELLO Collaboration:
H.J. Behrends et al., Phys. Lett. 103B, 148 (1981); Z. Phys. 14, 283 (1982), and DESY Report, DESY 82-063 (1982).

(9) JADE Collaboration:
W. Bartel et al., Phys. Lett. 88B, 171 (1979); Phys. Lett. 92B, 206 (1980); Phys. Lett. 99B 281 (1981); Phys. Lett. 108B, 140 (1982).

(10) MARK-J Collaboration:
D.P. Barber et al., Phys. Reports 63, 337 (1980); Phys. Rev. Lett. 42, 1110 (1979); Phys. Rev. Lett. 43, 1915 (1979); Phys. Lett. 95B, 149 (1980); Phys. Lett. 99B 495 (1981); Phys. Rev. Lett. 48, 1701 (1982).

(11) PLUTO Collaboration:
Ch. Berger et al., Z. Phys. C4, 269 (1980); Z. Phys. C1, 343 (1979); Z. Phys. C7, 289 (1981); Phys. Lett. 94B,87 (1980); Phys. Lett. 99B, 489 (1981).

(12) TASSO Collaboration:
R. Brandelik et al., Phys. Lett. 83B, 261 (1979); Phys. Lett. 92B, 199 (1980); Phys. Lett. 94B, 259 (1980); Phys. Lett. 110B, 173 (1982); Phys. Lett. 117B, 365 (1982).

(13) MAC Collaboration:
J.G. Smith, Proc. of the XVII Rencontre de Moriond, ed. Tran Tanh Van, Les Arcs 1982, p. 131;
D.M. Ritson, Talk at the XXI Int. Conf. on High Energy Physics, July 1982, to be published in the Proceedings.

(14) MARK II Collaboration:
R. Hollebeek, 1981 Int. Symp. on Lepton and Photon Interaction at High Energies, Bonn 1981, p. 1;
J. Strait, Proc. of the XVII Rencontre de Moriond, ed. Tran Tanh Van, Les Arcs 1982, p. 145.

(15) F.A. Berends and R. Kleiss, Nucl. Phys. B177, 237 (1981).

(16) R. Budny, Phys. Lett. 55B, 227 (1975)

(17) F.A. Berends, R. Kleiss and S. Jadach, Leiden preprint.

(18) T. Himel et al., Phys. Rev. Lett. 41, 449 (1978).

(19) CELLO Collaboration:
H.J. Behrend et al., Phys. Lett. 114B, 282 (1982).

(20) MARK II Collaboration:
C.A. Blocker et al., Phys. Lett. 49, 1369 (1982).

(21) MARK-J Collaboration:
J. Burger, Talk at the XXI Int. Conf on High Energy Physics, July 1982, to be published in the Proceedings.

(22) C.A. Blocker et al., Phys. Lett. 109B, 119 (1982).

(23) TASSO Collaboration: Phys. Lett. 92B, 199 (1980).

(24) J.J. Sakurai, Proc. of the XVII Rencontre de Moriond, ed. Y. Tran Tanh Van, Les Arcs 1982, p. 241.

(25) H. Georgi and S. Weinberg, Phys. Rev. D17, 275 (1978).

(26) E.H. de Groot, G.J. Gounaris and D. Schildknecht, Phys. Lett. 85B, 399 (1979); Phys. Lett. 90B, 427 (1980) and Z. Phys. C5, 127 (1980);
V. Barber, M. Keung, and E. Ma, Phys. Rev. Lett, 44, 1169 (1980); Phys. Lett. 94B, 377 (1980); Phys. Rev. D22, 727 (1980).

(27) J. Ellis and M.K. Gaillard, CERN-Report CERN 76-18 (1976), p.21.

(28) JADE Collaboration:
G. Heinzelmann, Talk at the XXI Int. Conf. on High Energy Physics, July 1982, to be published in the Proceedings.

(29) TASSO Collaboration:
R. Brandelik et al., Phys. Lett. 113B, 499 (1982).

(30) J. Jersak, E. Laermann and P.M. Zerwas, Phys. Lett. 98B, 363 (1981).

(31) A. Ali, Z. Physik, C1, 25 (1979);
M.J. Puhala et al., Phys. Rev. D25, 95 (1982) and Phys. Rev. D25, 695 (1982).

(32) TASSO Collaboration:
D. Lüke, Talk at the XXI Int. Conf. on High Energy Physics, July 1982, to be published in the Proceedings.

(33) G.L. Kane and M.E. Peskin, Nucl. Phys. B195, 29 (1982).

(34) B. Gittelmann, Talk at the XXI Int. Conf. on High Energy Physics, July 1982, to be published in the Proceedings.

(35) CELLO Collaboration:
H.J. Berend et al., DESY 82-021 (1982).

JADE Collaboration:
W. Bartel et al., Phys. Lett. 114B, 211 (1982).

MARK II Collaboration:
A. Blocker et al., SLAC-PUB-2923 (1982).

MARK-J Collaboration:
A. Adeva et al., Phys. Lett. 115B, 345 (1982).

TASSO Collaboration:
M. Althoff et al., DESY 82-69 (1982).

TWO-PHOTON INTERACTIONS*

Dieter Cords

DESY, Hamburg

Abstract

Recent spectroscopic results on f, A_2, and f' are reviewed, and the suppression of the glueball candidate state θ in the two-photon channel is discussed. A newly observed signal in the $\pi^+\pi^+\pi^-\pi^-$ invariant mass spectrum at 2.1 GeV is reported. Measurements on deep inelastic $e\gamma$ scattering show the expected pointlike photon structure and allow testing the photon structure function F_2 for parton and QCD models. The observation of high P_T jets from hard scattering processes is presented.

---

* Talk presented at the 1982 SLAC Summer Institute on Particle Physics.

© D. Cords 1982

Introduction

Two-photon interactions are obtained at high energy electron positron storage rings. The cross section for the process, illustrated by diagram 1, can be factorized in the equivalent photon approximation[1,2] into a flux factor and into the actual two-photon cross section:

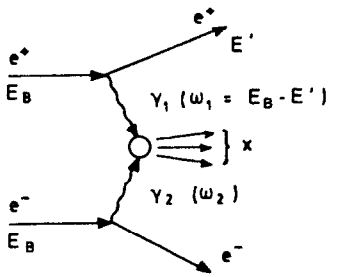


Diagram 1

$$d\sigma(e^+e^- \to e^+e^-\gamma_1\gamma_2 \to e^+e^-X) \approx dN_{\gamma_1}\, dN_{\gamma_2}\, \sigma(\gamma_1\gamma_2 \to X)$$

where dN_γ gives the number of photons in the energy interval between ω and $\omega+d\omega$. The flux factor can be used to relate the e^+e^- annihilation luminosity to the two-photon luminosity[3]:

$$dL_{\gamma\gamma} = dN_{\gamma_1}\, dN_{\gamma_2}\, L_{e^+e^-}$$

$$\approx \left(\frac{2\alpha}{\pi} \ln \frac{E_B}{m_e}\right)^2 \frac{d\omega_1}{\omega_1} \frac{d\omega_2}{\omega_2} L_{e^+e^-}$$

$$\sim \frac{1}{400} \frac{d\omega_1}{\omega_1} \frac{d\omega_2}{\omega_2} L_{e^+e^-} \quad \text{for } E_B = 15 \text{ GeV}.$$

The suppression of the two-photon luminosity by a factor of about 400 at present beam energies is compensated by the fact that the approximate[4] two-photon cross section $\sigma(\gamma\gamma \to \text{hadrons}) \approx 300 + \frac{600}{W(\text{GeV})}$ nb is much larger than the annihilation cross section $\sigma(e^+e^- \to \text{hadrons}) \approx 0.5$ nb. Therefore, the event rate for two-photon interactions is expected to be larger than the rate for e^+e^- annihilation processes at PEP and PETRA energies. However, since most of the two-photon events are produced at low invariant masses, they may not produce sufficient transverse energy to trigger the detector and therefore suffer from acceptance problems. If in addition the electron or positron is required to be tagged[5] in a typical angular range from 25 to 70 mrad with respect to the beam line, the event rate decreases further by about a factor of 10.

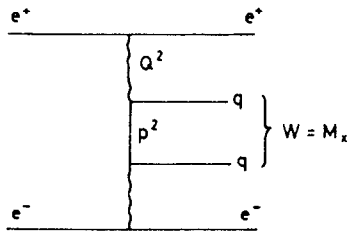


Diagram 2

If - in analogy to e^+e^- annihilation - the hadron production is represented by quark lines, one can use the four-momentum transfers Q^2 and P^2, indicated in diagram 2, to classify the various possible processes according to different kinematic regions.

kinematic region	physics of interest	experimental method
Q^2 and P^2 soft (~ 0 and ~ 1 GeV^2)	SPECTROSCOPY & 2-BODY PRODUCTION	exclusive final states with transverse momentum balance $\Sigma P_T^i \approx 0$
Q^2 hard ($\gtrsim 10$ GeV^2)	DEEP INELASTIC $e\gamma$ SCATTERING	tagged electrons with $Q^2 = 4E_B E' \sin^2\frac{\theta}{2}$ & W measurement
P^2 hard ($\gtrsim 10$ GeV^2)	HARD SCATTERING PHENOMENA	Jet analysis for the hadronic system $P^2 \sim p^2_{q,T} + (\frac{W}{2} - P_{q,L})^2 \lesssim \frac{W^2}{2}$

For the last process a minimum invariant mass W of about 5 GeV is required. The higher the W values for the selected events, the more likely it is to obtain background events from e^+e^- annihilation where one or both of the electrons radiated off a real photon in the initial state. The decreasing two-photon event rate and the increasing annihilation background reach about the same order of magnitude at a W of approximately half the total available energy.

The processes outlined above will be discussed in the following chapters.

Spectroscopy

The prime objective for analysing resonances in two-photon interactions is to obtain the radiative width $\Gamma_{R\gamma\gamma}$ via the production cross sections:

$$\frac{d\sigma(e^+e^- \to e^+e^-R)}{dM} = L_{\gamma\gamma}\left(\frac{M}{2E_B}\right)\ \frac{\sigma_{\gamma\gamma \to R}(M)}{2E_B}$$

$$\text{with}\quad \sigma_{R \to \gamma\gamma} = 8\pi(2J+1)\ \frac{\Gamma_{R\gamma\gamma}\ \Gamma}{(M^2-M_R^2)^2 + M_R^2\,\Gamma^2}$$

where M is the invariant mass of the two-photon system, J the spin, and $L_{\gamma\gamma}$ the luminosity function[6]. The well defined initial state restricts the resonance quantum numbers to:

$$I_3 = 0,\ J^{PC} = 0^{-+},\ 0^{++},\ 2^{-+},\ 2^{++},\ \ldots$$

where spin 1 states are excluded for nearly real photons. In this way one can investigate the isoscalar components of scalar and tensor meson nonets. The questions of interest are whether these resonances are pure quark bound states or have some gluonium admixture, and at what level do we expect glueball states to be produced if these states exist at all. It would also be interesting to look for even C-parity charmonium states, e.g., η_c, χ_o, χ_2, but there are no measurements yet.

In recent years many nice results on two-photon resonances have been obtained and surveys were presented at various conferences[7,8].

In this report I shall discuss the neutral members f, A_2^0, and f' of the 2^{++} meson nonet. The measured radiative widths for various decay modes are summarized in Fig. 1. As shown by the squares linked by dashed lines, SU(3) for ideal mixing and without phase space corrections predicts ratios (not absolute values) of radiative widths which are in fair agreement with the averaged measurements.

An example for the f decay into two charged pions[9] is given in Fig. 2a showing the TASSO invariant mass spectrum for two charged tracks. Since electrons, muons, and pions cannot be separated at low momenta, the QED contribution (dotted line) has to be subtracted. The QED subtracted invariant mass distribution in Fig. 2b shows in addition to the f signal at 1.27 GeV a strong enhancement near threshold. This can be contrasted with the $\pi^0\pi^0$ spectrum[10] in Fig. 3 obtained by the JADE collaboration which shows an f signal over a very small background. An example for a final state with charged and neutral particles is the A_2^0 decay[11] which is illustrated in Fig. 4. The hatched area indicates the dominant decay mode into $\rho^\pm\pi^\mp$. The f' signal[12] has been seen by the TASSO collaboration at 1.52 GeV in the K^+K^- and $K_S^0K_S^0$ final states (Fig. 5). Whereas one observes the expected constructive interference of the f' with f and A_2 as a strong enhancement below the f' mass for charged kaons, this is neither expected nor seen for neutral kaons.

It is well known that the radiative decays of the J/ψ resonance allow the formation of two-gluon states[13] of even C-parity and

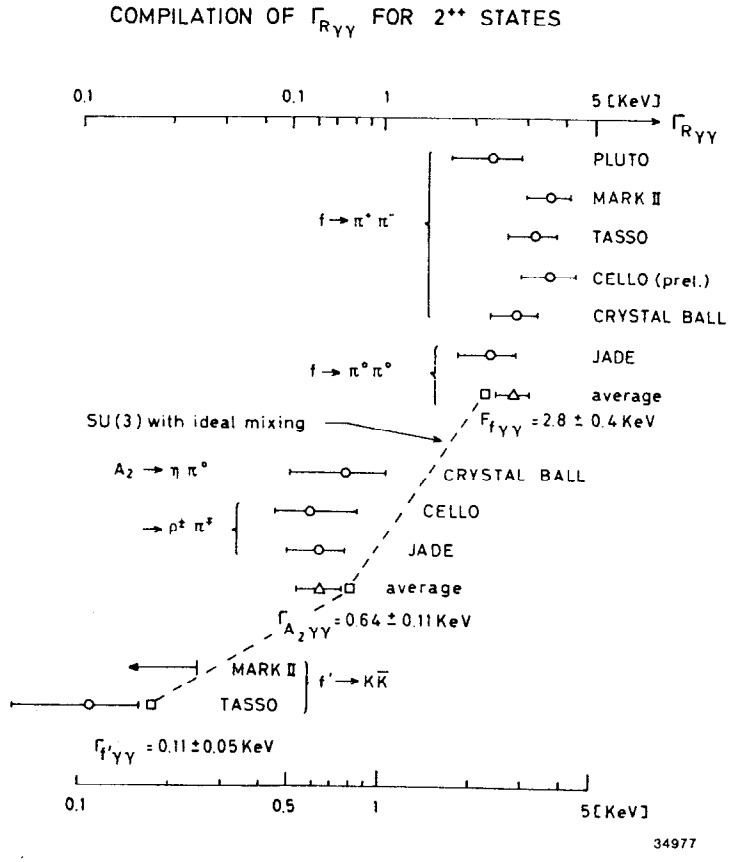


Fig. 1 : Compilation of radiative widths for the f, A_2, and f' resonances. For references see J. Olsson[8] and ref. 12. The average values are given numerically. SU(3) for ideal mixing - fixing the ratios but not the absolute values - is indicated by the dashed lines.

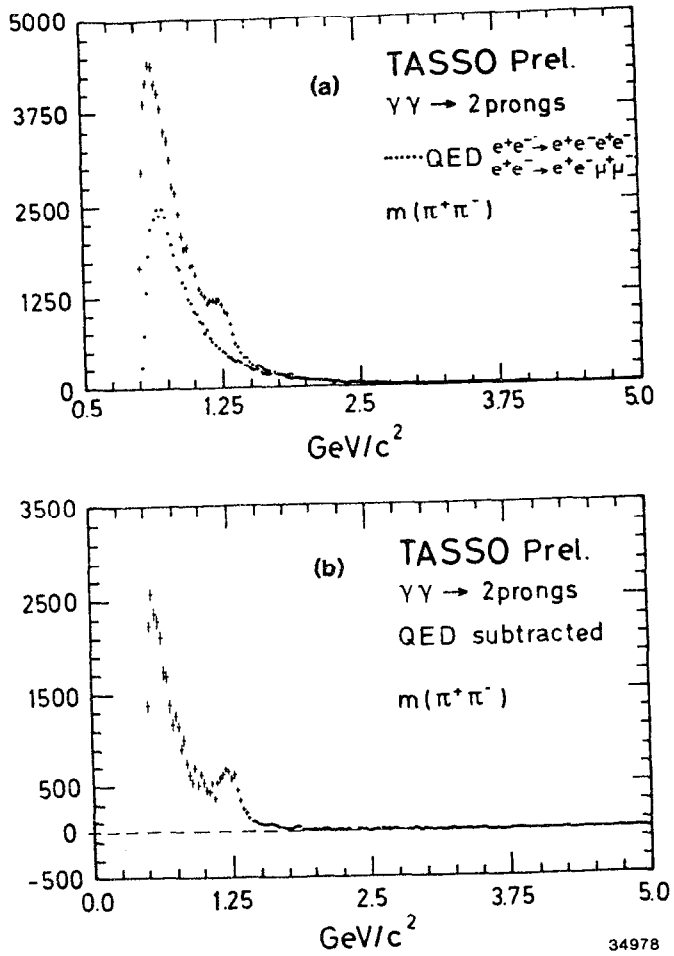


Fig. 2 : Invariant $\pi^+\pi^-$ mass from TASSO (a) for all events with 2 charged tracks and (b) after QED - i.e. $\mu^+\mu^-$ and e^+e^- - subtraction.

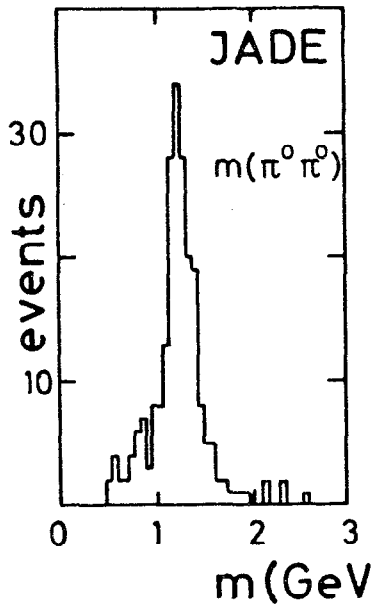
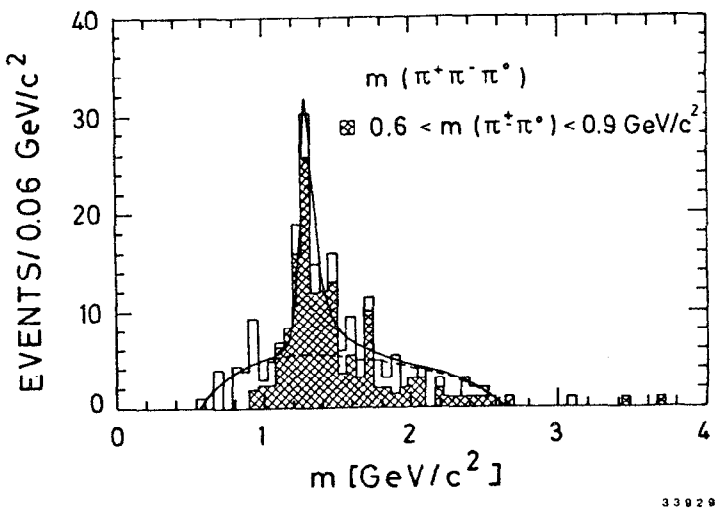


Fig. 3 : Invariant $\pi^0\pi^0$ mass from JADE.

Fig. 4 : Invariant $\pi^+\pi^-\pi^0$ mass from JADE. The cross-hatched histogram presents the dominant $\rho^{\pm}\pi^{\mp}$ decay mode of the A_2.



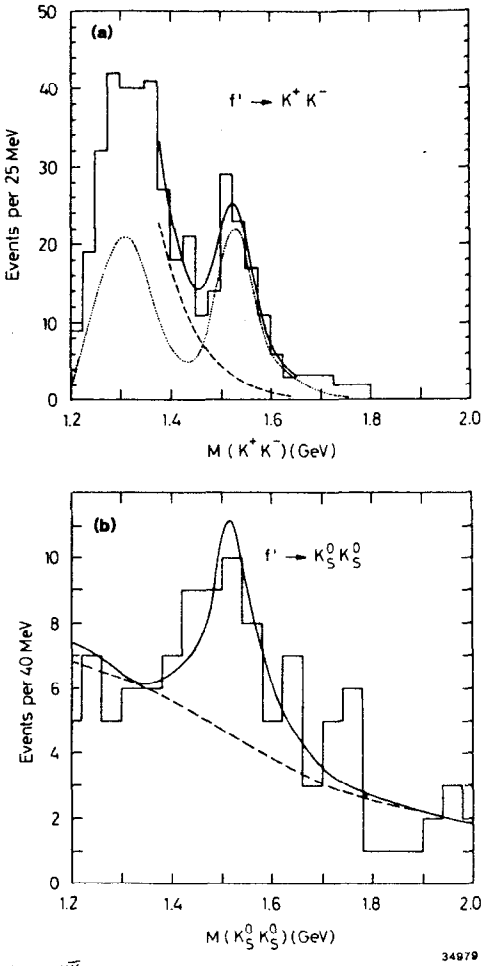


Fig. 5 : Invariant $K\bar{K}$ mass from TASSO:
(a) $M(K^+K^-)$ distribution. The dotted curve is the contribution from the interferring f, A_2, and f' resonances. The background is given by the dashed line. The full curve is the sum of both contributions.
(b) $M(K^0_S K^0_S)$ distribution. The full curve is the result of a fit to a background (dashed line) plus a Breit-Wigner shaped f'.

therefore are called "glueball-favoured." On the other hand the production of even C-parity states via two photons is called "glueball-disfavoured" because one has to insert an extra quark loop as shown by diagram 3. One may guess that the suppression factor in the two-photon case is the square root of the Okubo-Zweig-Iisuka-factor[14] which involves two quark loops and is about 1/100. Applying this to the glueball candidate state θ, observed[15] at 1.64 GeV in various decay channels, one can obtain its two-photon width from the corresponding value for the f:

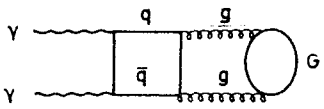


Diagram 3

$$\frac{\Gamma(\theta \to \gamma\gamma)}{\Gamma(f \to \gamma\gamma)} \approx \left[\frac{M_\theta}{M_f}\right]^3 \cdot \sqrt{OZI} \approx 0.2$$

Using the radiative f width of Fig. 1, this results in $\Gamma(\theta \to \gamma\gamma) \sim$ 600 eV. Mark II[16] has recently measured the branching fraction $BR(J/\psi \to \gamma\theta) \cdot BR(\theta \to K^+K^-) = (6.2 \pm 2.7) \cdot 10^{-4}$. According to gluonic duality arguments Koller and Walsh[17] estimated the branching ratio $BR(J/\psi \to \gamma\theta) \approx 2\%$, and therefore one expects $BR(\theta \to K^+K^-) \approx 3\%$. Using the last value together with the estimated radiative θ width one expects the following signal in the two-photon case:

$$\Gamma(\theta \to \gamma\gamma) \cdot BR(\theta \to K^+K^-) \sim 20 \text{ eV}$$

Since θ is three times as wide as the f', one is looking for an enhancement in the K^+K^- invariant mass spectrum (Fig. 5) which is less than 1/10 of the f' peak. In fact the TASSO upper limit[12] is 0.5 KeV (95% c.l.). Similar results apply to the ρρ decay of the θ. Therefore,

in addition to not being firmly established as glueball states, the θ as well as the ι are below the level of detection for present two-photon experiments.

An interesting conjecture of Schnitzer[18] and Rosner[19] implies that glueballs are not pure gluonium but contain some admixture of quarkonium states. This means that glueballs might mix with the isoscalar nonet members and as a consequence their coupling to the two-photon channel might be quite different from the estimate given above. However, at this preliminary stage I shall not pursue the question further.

A new enhancement[20] has been observed by the TASSO collaboration in the final state of 4 charged pions. Fig. 6 shows the invariant mass spectrum of the reaction $\gamma\gamma \to \pi^+\pi^+\pi^-\pi^-$ for an accumulated luminosity of 70 pb^{-1}. A signal of about 5 standard deviations can be seen at 2.1 GeV. A fit of a Gaussian distribution over a smooth background is shown in the lower histogram and results in a mass of 2.10 ± 0.01 GeV and a full width at half maximum of 94 ± 21 MeV. The mass resolution is estimated to be 60 MeV, and therefore the actual width is much less than measured. The two-photon coupling times the branching ratio of this state X of unknown spin J is given as:

$$\Gamma(X \to \gamma\gamma) \cdot BR(X \to \pi^+\pi^+\pi^-\pi^-) \cdot (2J + 1) = 1.6 \pm 0.4 \text{ KeV}$$

Since the spin and parity of this object are not determined, one cannot discuss any multiplet assignment. However, one may speculate whether this enhancement is related to a strong signal near the

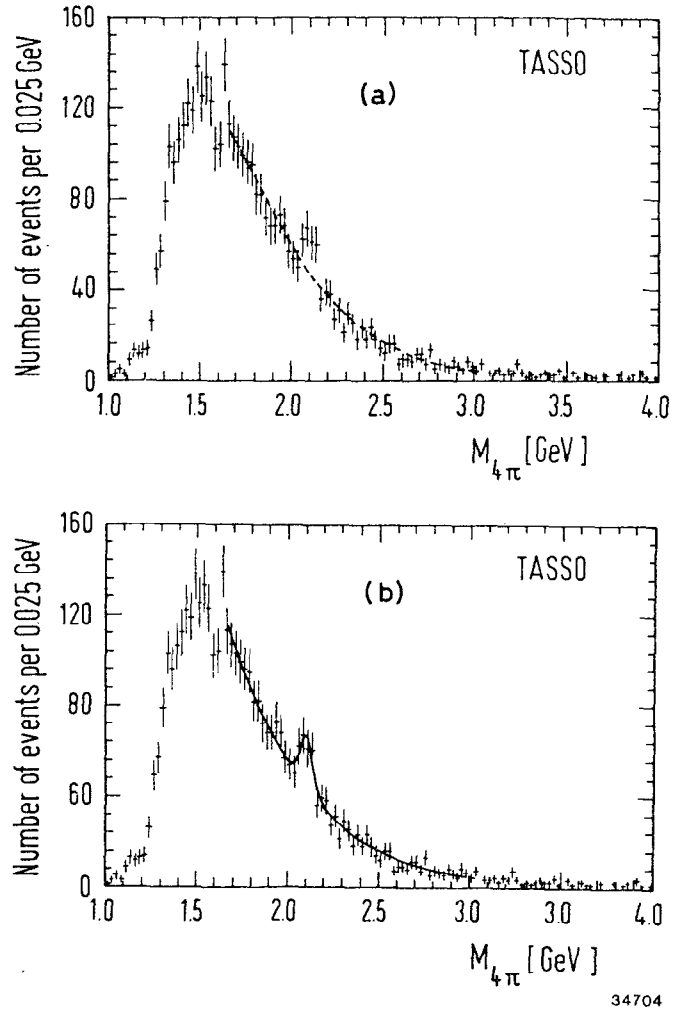


Fig. 6 : Invariant $\pi^+\pi^+\pi^-\pi^-$ mass from TASSO. The curve in (b) represents the fit of a Gaussian superimposed on a smooth background.

threshold of the $\phi\phi$ invariant mass spectrum[21] shown in Fig. 7 for the reaction π^-Be $\rightarrow \phi\phi$+... at 175 and 100 GeV/c. Recently the observation of two $\phi\phi$ resonances[22] in the reaction $\pi^- p \rightarrow \phi\phi n$ was reported at the Paris conference. The quantum numbers are quoted as $I^G = 0^+$ and $J^{PC} = 2^{++}$ for both states and the lower mass state has $M = 2.16 \pm 0.04$ GeV and $\Gamma = 315 \pm 62$ MeV. Compared to the enhancement in the two-photon case it is very wide. The special interest in $\phi\phi$ states arises from the idea that the production of these strange quark states is mediated by two gluons and can be enhanced only if the gluons form a resonance or glueball. For further details the reader is referred to Scharre's report on glueballs[23].

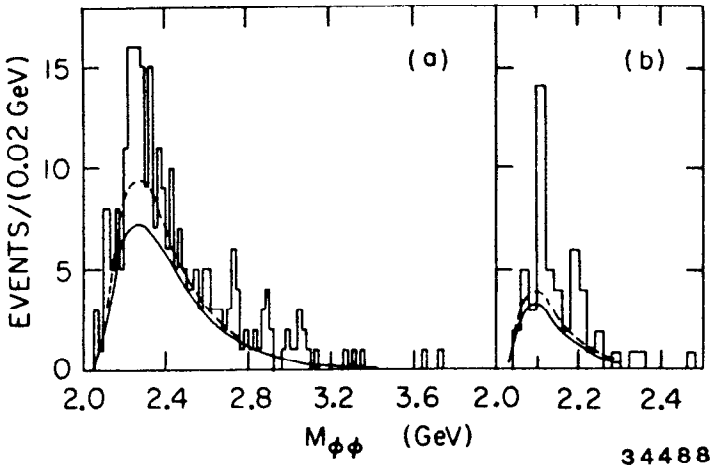


Fig. 7 : Invariant $\phi\phi$ mass from ACCMOR for π^-Be $\rightarrow \phi\phi$ + X at (a) 175 GeV and (b) 100 GeV/c. The solid curves show the expected backgrounds from ϕK^+K^- and $K^+K^-K^+K^-$ events. The dashed curves represent the total backgrounds including the estimated contributions from uncorrelated $\phi\phi$ production.

Two-Body Final States

Results on two-body final states have been reported before[7,8] and therefore I shall be very brief. It is well known that the four charged pion final state up to an invariant mass of 2 GeV is dominated by $\rho^0\rho^0$ production. Recently TASSO[24] has performed an angular correlation analysis for the $\rho^0\rho^0$ channel and found that $J^P = 0^-$ and 2^- states can be excluded within experimental accuracy. The contributions mainly come from $J^P = 0^+$ below an invariant mass of 1.7 GeV and from $J^P = 2^+$ above. The cross section somewhat depends on the assumptions put into the fitting procedure. As shown in Fig.8, it is substantially higher if the ρ's are assumed to be produced and to decay isotropically.

The production of proton antiproton pairs[8,25] has been observed by JADE and TASSO, and the cross section near the threshold is found to be smaller than the Born term expectation and larger than the vector dominance model contributions. Recent QCD calculations[26] roughly agree with the data although they come out slightly too small very close to threshold.

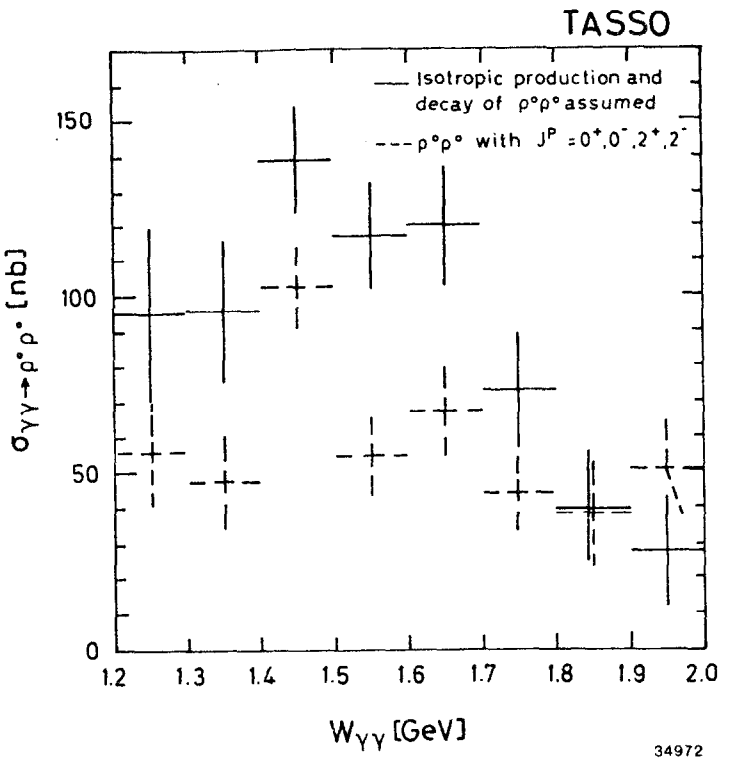
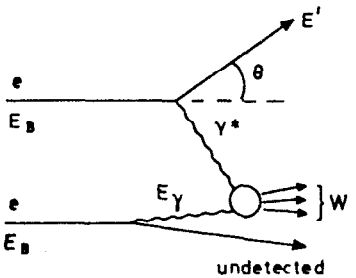


Fig. 8 : Cross section for $\gamma\gamma \to \rho^0\rho^0$ from TASSO. For the full crosses the efficiency is calculated assuming isotropic $\rho^0\rho^0$ production and decay. The dashed crosses represent the sum of different contributions from a spin parity analysis.

Deep Inelastic eγ Scattering

If one of the photons in diagram 4 is highly virtual and the other is close to mass shell, the process can be seen as deep inelastic electron scattering off a real photon[27].



$$Q^2 = 4E_B E' \sin^2 \frac{\theta}{2}$$

$$x = \frac{Q^2}{Q^2+W^2}$$

$$y = 1 - \frac{E'}{E_B} \cos^2 \frac{\theta}{2}$$

Diagram 4

The two-photon centre-of-mass energy W is measured via the final state products. Q^2 being the spacelike four-momentum-squared of the virtual photon and x,y the standard scaling variables, the differential cross section can be expressed in terms of structure functions[1,28]:

$$\frac{d^2\sigma}{dxdy} = \frac{16\pi\alpha^2}{Q^4} E_B E_\gamma \{(1-y)F_2(x,Q^2) + xy^2 F_1(x,Q^2)\}$$

In general the cross section depends on three structure functions. However, F_3 drops out if the azimuthal dependence is integrated over (the second electron is not detected). For tagging angles of present experiments, y^2 is a small number - in the range of 0.01 to 0.1 - and as a result the F_1 term can be neglected as well. Therefore, the present objective for studying deep inelastic eγ scattering is to test model predictions by means of the structure function F_2.

The simplest model for F_2 is the Born term model[28,29] which applies for lepton pair production and is illustrated by the dash-dotted curve in diagram 5. The characteristic pointlike behaviour in this case is manifested by the large values of F_2^{BORN} for large x.

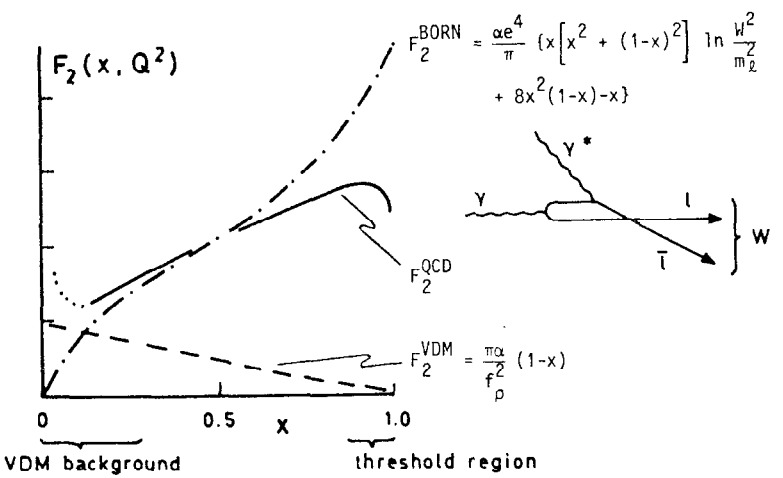


Diagram 5

On the other hand, as shown by the dashed line for hadron production in the concept of the vector dominance model[28], F_2^{VDM} drops off steadily to zero. The question of interest is: Do the hadron production data display a pointlike behaviour in addition to the vector dominance contribution? If that is so, the quark-parton model may be applied. The structure function in the quark-parton model is

obtained from the above Born term by replacing e^4 by the sum of the quark charges to the fourth power and m_ℓ by the quark mass. Therefore, the expected F_2 is very similar in shape to the dash dotted curve. In fact, the theory to be tested is QCD, in which case the structure function is written as:

$$F_2^\gamma(x,Q^2) = F_2^{QCD} = \frac{3\alpha\Sigma e_i^4}{\pi} \; f^{QCD}(x) \; \ln \frac{Q^2}{\Lambda^2}$$

+ higher order corrections

where e_i are the quark charges, f^{QCD} resembles the x dependence[30] of the Born term, and the scale parameter Λ replaces the quark mass. A typical QCD behaviour is shown by the solid curve in diagram 5. It has to be pointed out that the higher order QCD corrections[31,32] show the largest variations in the small x and large x regions. As indicated in diagram 5, the small x region is also the region where the VDM contribution is largest. At large x one enters a threshold region of small W values. Therefore, QCD is best tested in the x range from 0.3 to 0.9. The salient feature of QCD is that it retains the pointlike behaviour of the quark-parton model, i.e., $F_2^\gamma(x,Q^2) \to$ const. as $x \to 1$ at fixed Q^2. On the contrary, the proton structure function tends to zero in this case[33]: $F_2^p(x,Q^2) \sim (1-x)^n \to 0$.

The Born approximation can be tested for two-photon production of μ-pairs, and a comparison done in Fig. 9 by the CELLO collaboration[34] shows excellent agreement with the data. The structure function for hadron production has first been obtained by PLUTO[35] as shown in Fig. 10 for an integrated luminosity of 2500 nb^{-1}. The leading order

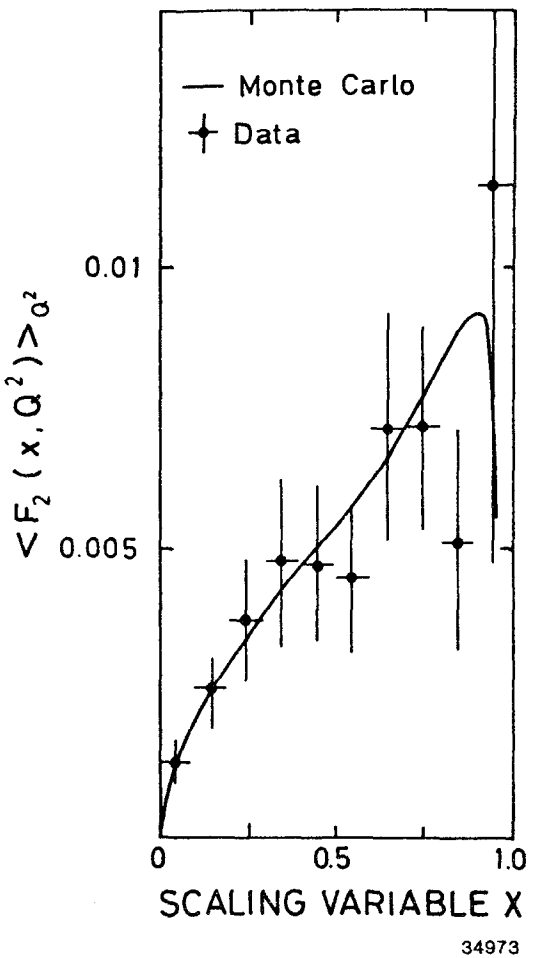


Fig. 9 : Comparison of F_2^{BORN} for $e\gamma \to e\mu^+\mu^-$ with CELLO data (absolute normalization). The F_2 values have been averaged over the Q^2 distribution of the CELLO tagging acceptance.

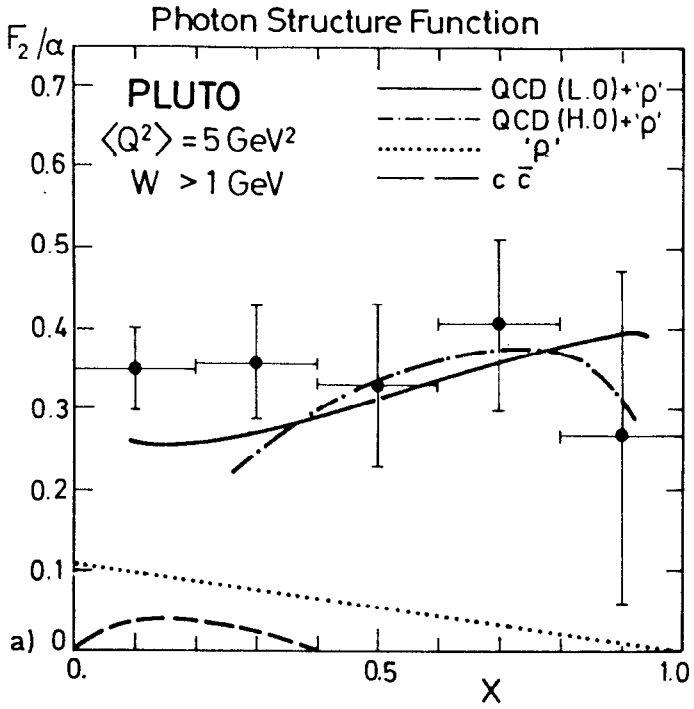


Fig. 10: Photon structure function $F_2(x)/\alpha$ from PLUTO. The various curves correspond to F_2^{QCD} with Λ = 0.2 GeV, F_2^{VDM} for 'ρ', and F_2^{BORN} for $c\bar{c}$ with M_c = 1.5 GeV.

and higher order QCD calculations both agree well with the data and the charm contribution is shown to be small. The data points in Fig. 10 are model dependent because the true x is obtained from the experimentally visible x and this already implies a knowledge of the contributing processes. The average Q^2 in the case of PLUTO is rather low. It mainly depends on the angular range used for tagging one of the electrons and is shown for the three relevant experiments in the following table:

Experiment	Angular range (m rad)	Q^2 range (GeV^2)	$\langle Q^2 \rangle$ (GeV^2)
PLUTO	Large Angle Tagger 100 - 250	1 - 15	5
CELLO	Endcap Liquid Argon 140 - 400	2 - 30	9
JADE	Endcap Lead Glass 265 - 428	10 - 52	23

Unfolding the visible x to obtain the true x - for a direct comparison of the data with the functional dependence of F_2 - already implies a knowledge of F_2. In order to avoid a simultaneous parameter dependence of the data points and of the models, the data for CELLO and JADE are plotted as a function of the visible x. As a result, the curves for the various models do not exhibit the original x dependence but are folded with the detector acceptance. Fig. 11 shows a comparison of the parton model and two versions of QCD calculations with the CELLO data[34] for an integrated luminosity of 11.2 pb^{-1}. Charm quark contributions are included, since

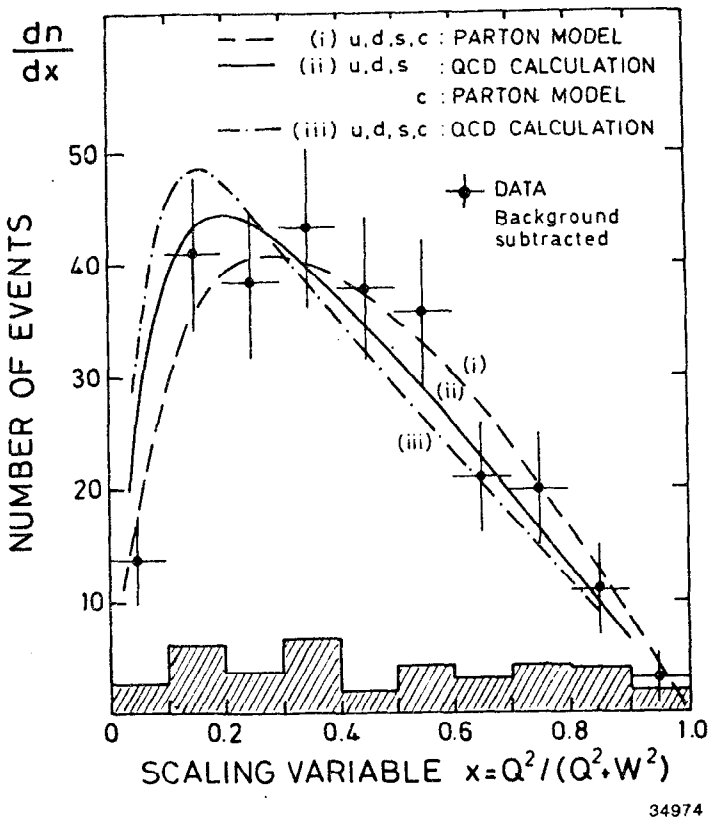


Fig. 11: Visible x distribution from CELLO. The data are compared to three different Monte Carlo simulations for F_2. The shaded area shows the background which has been subtracted from the data.

the invariant mass values W extend well above charm threshold. The curves in Fig. 11 are not very different in shape, and at the present level of experimental accuracy it is impossible to distinguish between the parton model and QCD calculations on the basis of the contour of the x distribution. Both models describe the data rather well.

How about the normalization of the structure functions? Considering only the leading order or logarithmic term of F_2^{QCD} above, the normalization depends on the number of quarks included in the charge factor and on the scale parameter Λ. Varying these parameters, a comparison has been done in Fig. 12 to the JADE data[36] for an integrated luminosity of 20.2 pb^{-1}. If the u,d,s, and c quarks are included in the leading order QCD term, the full curve in Fig. 12 shows that the scale parameter has to be adjusted to 0.3 GeV to fit the data. This situation roughly corresponds to the parton model with an assumed quark mass of 300 MeV in which case not only the shape but also the normalization seems reasonable. Omission of the charm quark from the leading order QCD term has to be compensated by larger values of $\ln \frac{Q^2}{\Lambda^2}$. As shown by the dashed curve, Λ has to drop in this case to 0.07 GeV. A proper comparison with QCD calculations has to include the charm quark because of the high W values involved, and it also has to take higher order QCD corrections into account. In fact, the dotted curve in Fig. 12 includes the next to leading order QCD term[32] in the $\overline{MS}$ scheme[37]. By varying the scale parameter in the x range above 0.4, where the VDM contribution is smallest, one obtains for the JADE data[36] a best fit of

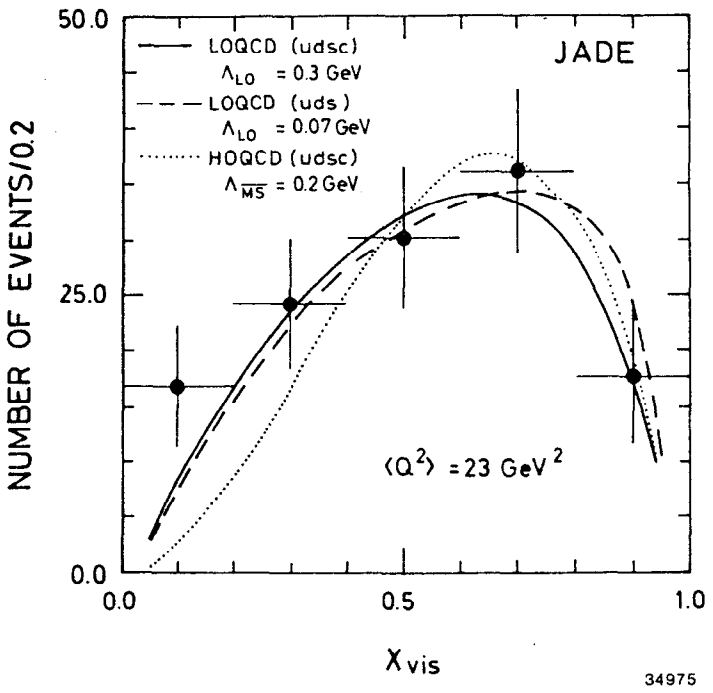


Fig. 12: Visible x distribution from JADE. The curves represent various QCD predictions (see text).

$$\Lambda_{\overline{MS}} = 0.22 \,^{+0.10}_{-0.07} \text{ GeV}.$$

The Q^2 dependence of the structure function is very smooth and given in leading order by $\ln \frac{Q^2}{\Lambda^2}$. In order not to introduce any artificial Q^2 dependence due to detector acceptance, a comparison with the data has to be restricted to that x range where $\langle Q^2 \rangle$ is constant. In Fig. 13 the expected agreement can be observed for PLUTO data[35] ($0.2 < x_{vis} < 0.8$) up to Q^2 values of 15 GeV^2 and for JADE data[36] ($0.3 < x_{vis}$) up to Q^2 values of 45 GeV^2.

Since structure functions are an important issue of two-photon physics, let me repeat the relevant points:

- The test of QCD is connected to the dominance of the pointlike term.
- The determination of the QCD scale parameter is done via the normalization of F_2^γ, but one can adjust the average quark mass such that also the parton model fits the data.
- An experimental problem consists in unfolding the visible W or visible x, because this implies a knowledge of the contributing processes and therefore is model dependent.
- There are several problems[38] connected to the QCD calculations: The effect of quark masses - in particular for the c quark - has not yet been taken into account. It is an open question, how fast - if at all - the perturbative series of higher order corrections does converge. In this context it is not clear, whether the argument of the logarithm is just Q^2 or whether it contains some additional x dependence.

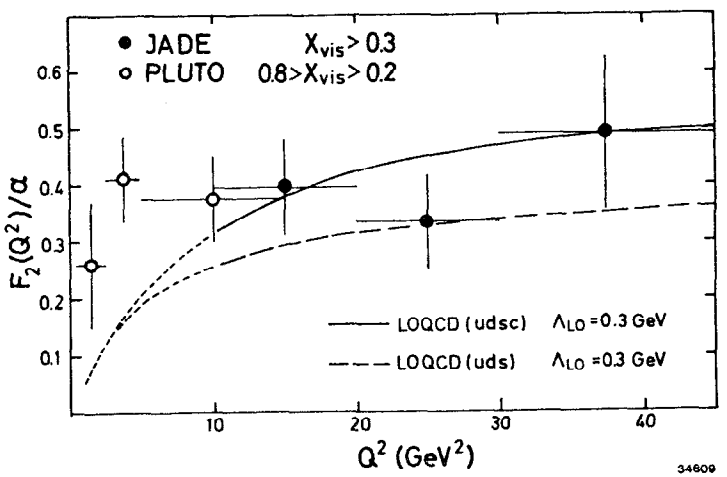


Fig. 13: Photon structure function $F_2(Q^2)/\alpha$ averaged over $x_{VIS} > 0.3$ for JADE and over $0.2 < x_{VIS} < 0.8$ for PLUTO.

Hard scattering processes[39] are characterized by the fact that a number of particles are produced at high transverse momenta with respect to the line of collision of the initial photons. One can think of several competing processes, like two or more jet events, higher twist terms, and vector dominance contributions. They are illustrated by the following diagrams:

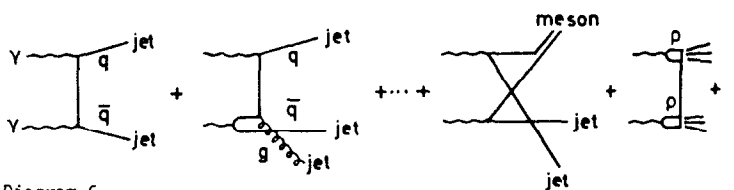


Diagram 6

For all but the first of these diagrams, part of the available energy is emitted along the initial photon directions close to the beam line. Only the 2-jet events may transfer all the energy to transversely produced jets and therefore can be expected to dominate at large transverse momenta with respect to the line of collision of the initial photons. As in e^+e^- annihilation, the cross section of this quark exchange scattering process may be normalized to μ-pair production:

$$R_{\gamma\gamma} = \frac{\sigma(\gamma\gamma \to q\bar{q})}{\sigma(\gamma\gamma \to \mu^+\mu^-)} = 3 \sum_{i=u,d,s,c} e_i^4 = \frac{34}{27}$$

The question of interest is: does the experimental 2-jet cross section approach this number? and if so, can we learn something about the quark charges, the quark propagator, and the QCD behaviour?

The 2-jet cross section depends on the minimum transverse momentum required for jets. For the above value of $R_{\gamma\gamma}$ the inclusive jet cross section has been estimated[39] to be:

$$\sigma(e^+e^- \to e^+e^- + \text{JET} + X)$$

$$\propto R_{\gamma\gamma} \frac{32\pi\alpha^2}{3(P_{T,MIN}^{JET})^2} \left(\frac{\alpha}{2\pi} \ln \frac{E_B}{m_e}\right)^2 \ln \frac{E_B}{P_{T,MIN}^{JET}}$$

$$\sim \frac{0.5\text{nb GeV}^2}{(P_{T,MIN}^{JET})^2} \sim 0.1 \text{ nb for } P_T^{JET} \geq 2 \text{ GeV at } E_B = 15 \text{ GeV}.$$

Typical 2-jet events are not back-to-back but kinked as shown in Fig. 14 for an event with a tagged electron in the JADE detector. Charged tracks (solid lines) are seen by the inner drift chambers and photons (dotted lines) - mostly from π^0 decays - are obtained from clusters in the lead glass shower counters.

For a proper analysis of hard scattering processes one has to employ jet search methods similar to those used in e^+e^- annihilation. The TASSO collaboration[40] has analysed single tag events by applying the twoplicity method to the charged hadrons in the final state. The twoplicity method, which maximizes the momentum sums along two independent directions, forces all particles into two separate groups. If the transverse momenta of these groups exceed 2 GeV, they are used to experimentally define jets and these data are plotted in Fig. 15. As one can see, the vector dominance model calculation falls short of the data points, but the quark exchange contribution involving

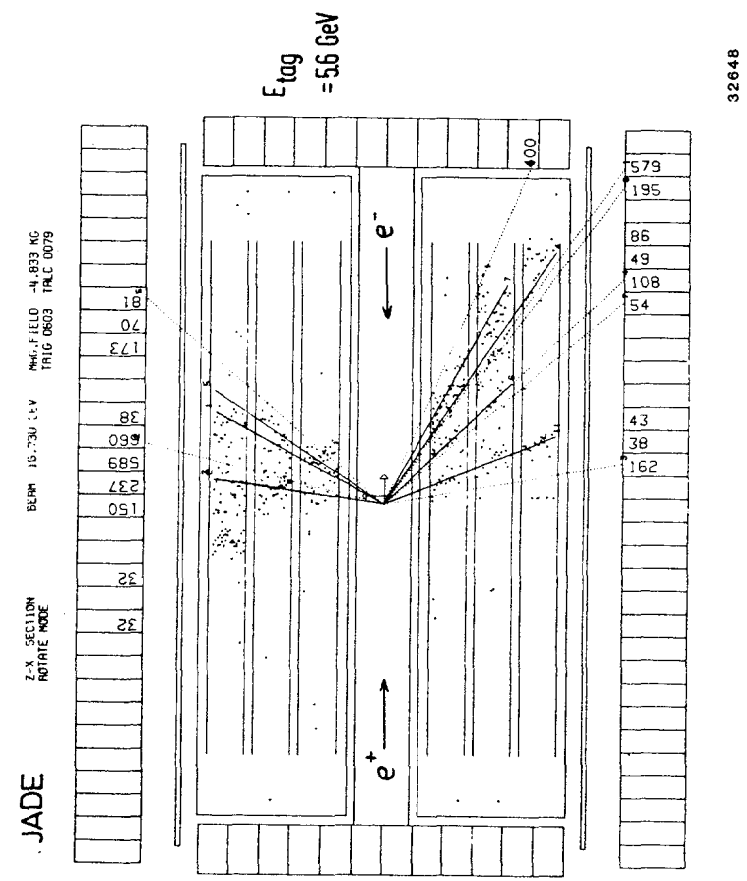


Fig. 14:
2-jet event with a tagged electron of 5.6 GeV seen in the JADE detector. Full lines are charged particles and dotted lines are photons.

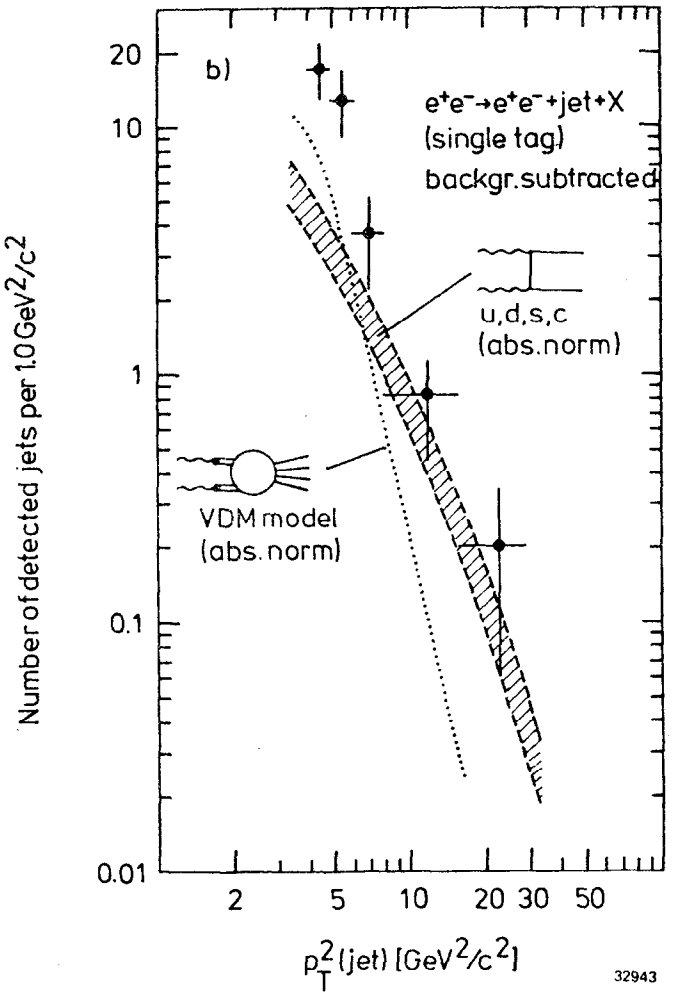


Fig. 15: P_T^2(JET) distribution from TASSO for $e^+e^- \to e^+e^-$ + jet + x compared to a $e^+e^- \to e^+e^-$ + $q\bar{q}$ model with four different types of normalization (shaded area) and to VDM (dotted line).

u,d,s, and c quarks is approached by the data for high transverse momenta.

For the JADE experiment[41] single tag events were analysed and the charged particles and photons in the final state were grouped according to a cluster search method[42]. The cluster search collects particles in well defined cones and has been extensively tested for e^+e^- annihilation events. This method allows for an arbitrary number of clusters and for single stray particles not assigned to any cluster. In order to qualify as jets the clusters have to have momenta of at least 2 GeV. For the 2-jet events obtained in this way, the jet transverse momenta exceeding 2 GeV are plotted in Fig. 16. The detector acceptance has been unfolded in order to obtain cross section values. The curve, representing the pointlike cross section normalized via the u,d,s, and c quark charges, displays the expected P_T^{-4} dependence and is approached by the data from above as the transverse momentum increases.

From the above discussion it is evident that the experimentally determined $R_{\gamma\gamma}$ is a function of the cut-off transverse momentum $P_{T,MIN}^{JET}$. Whereas JADE and TASSO tag electrons with Q^2 values of the order 0.3 GeV^2, the MAC experiment detects electrons over a wide angular range. Without requiring any cut-off in the jet momentum, the MAC group[43] plots the ratio of observed hadronic to μ-pair events as function of Q^2 in Fig. 17 and obtains a surprisingly good agreement with the quark model prediction.

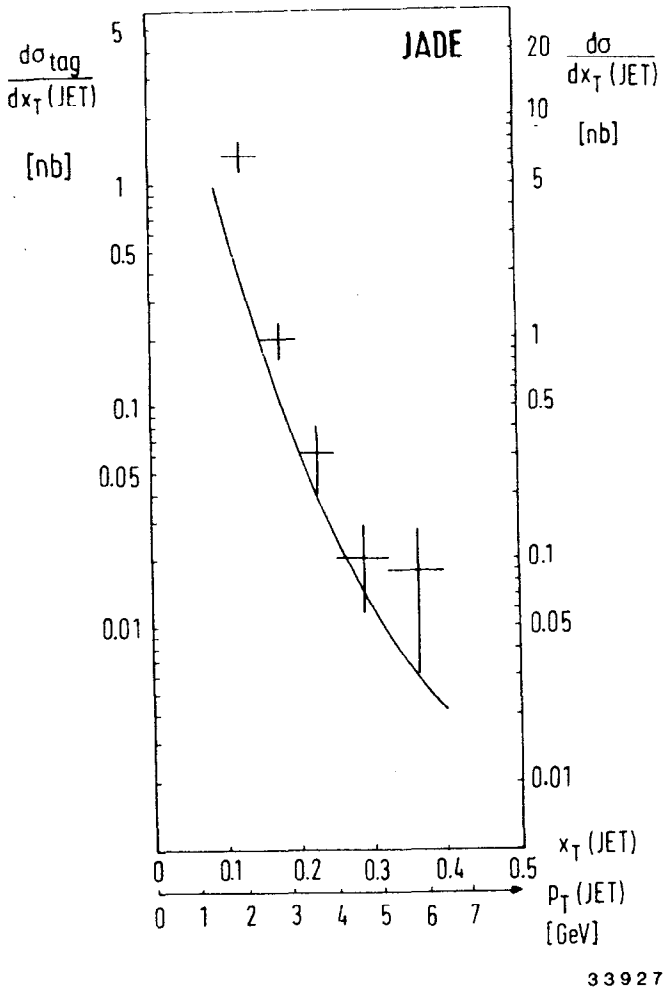


Fig. 16: Differential cross section for 2-jet events from JADE.
$x_T(JET) = P_T(JET)/E_B$.

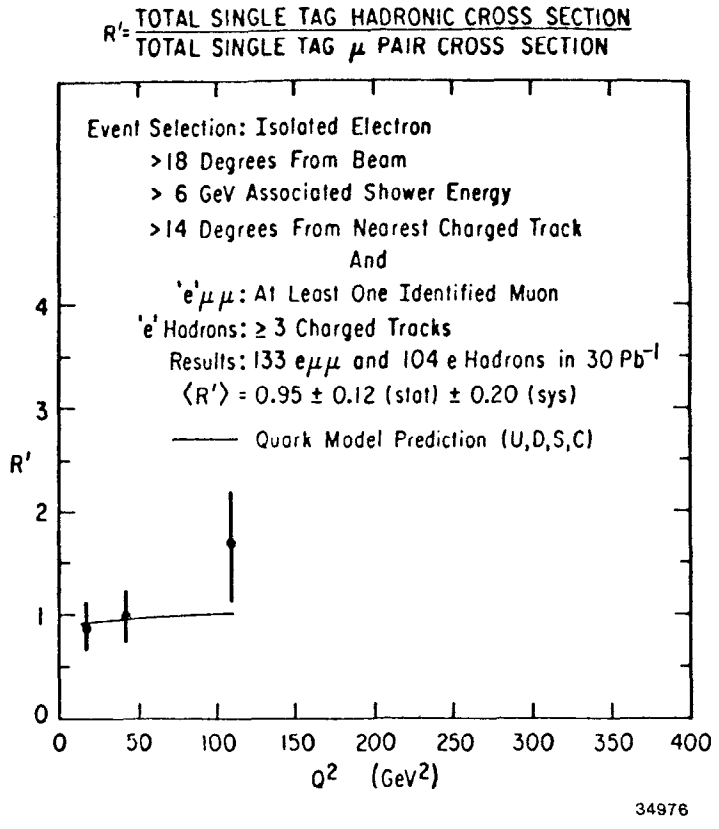


Fig. 17: Ratio of hadronic to μ-pair single tag events from MAC.

Early results on two-photon events of high invariant mass (W above 5 GeV) point at hard scattering processes. However, the data are too preliminary to allow any detailed comparison with QCD predictions or to test the quark propagator. It is an interesting feature that the $R_{\gamma\gamma}$ value of $\frac{34}{27}$ refers to fractional charged Gell-Mann-Zweig quarks[44] and has to be changed to $\frac{10}{3}$ for integer charged Han-Nambu quarks[45]. Consequently, for integer charged quarks the curve of Fig. 16 has to be scaled up by a factor of 2.65, with the data points at high P_T starting to fall below this curve. This seems to rule out the scheme of Han-Nambu quarks, but it has been pointed out recently[46] that for photons off mass-shell ($Q^2 \sim 0.3$ GeV^2 for tagged electrons at JADE) the charges may be screened and the effect reduced.

Summary

The present situation in two-photon physics may be summarized as follows:

- There are many new and nice results on resonances but no surprises. The glueballs, if they exist at all, seem to be below the level of detection efficiency of present experiments.
- The two-body final states $\pi^+\pi^-$, $\rho^0\rho^0$, $p\bar{p}$ show large cross sections near threshold.
- In deep inelastic $e\gamma$ scattering the photon structure function looks pointlike at modest Q^2 values.
- The observation of high P_T 2-jet events points at quark exchange scattering.

Acknowledgement

I have to thank my colleagues H. Kolanoski, T. Nozaki, J. Olsson, and T. Walsh for useful discussions.

References

1) H. Terazawa, Rev. Mod. Phys. 45 (1973) 615.
V.M. Budnev et al., Phys. Rep. 15C (1975) 182.

2) S.J. Brodsky et al., Phys. Rev. D4 (1971) 1532.
C. Carimalo et al., Phys. Rev. D20 (1979) 1057.

3) G. Barbiellini et al., PEP 1975 Summer Study (PEP 178) p. 159.

4) PLUTO Collaboration, Ch. Berger et al., Phys. Lett. 89B (1979) 120.
E. Hilger, DESY Report 80/75.
PLUTO Collaboration, Ch. Berger et al., Phys. Lett. 99B (1980) 287.
Ch. Berger, Proceed. 4th Intern. Coll. on $\gamma\gamma$ Interactions 1981, (Paris) p. 75.

5) C. Carimalo et al., Phys. Rev. D21 (1980) 669, and Proceed. Workshop on $\gamma\gamma$ Collisions (Amiens, 1980) p. 181.

6) G. Bonneau et al., Nucl. Phys. B54 (1973) 573.
J.H. Field, Nucl. Phys. B168 (1980) 477 and erratum B176 (1980) 545.
Ch. Berger and J.H. Field, Nucl. Phys. B187 (1981) 585.

7) D.L. Burke, Proceed. 4th Intern. Coll. on $\gamma\gamma$ Interactions 1981, (Paris) p. 123.
E. Hilger, Proceed. 4th Intern. Coll. on $\gamma\gamma$ Interactions 1981, (Paris) p. 149.

8) R.J. Wedemeyer, Proceed. 1981 Intern. Symp. on Lepton and Photon Interactions at High Energies (Bonn) p. 410.
J. Olsson, Proceed. XVIIth Rencontre de Moriond 1982, (Les Arcs, Savoie) p. 13.

9) TASSO Collaboration, private communication.

10) JADE Collaboration, Contribution to XXIst Intern. Conf. on High Energy Physics 1982 (Paris).

11) JADE Collaboration, private communication.

12) TASSO Collaboration, M. Althoff et al., DESY 82-071, to be published.

13) J.D. Bjorken, Proceed. Intern. Conf. on High Energy Physics 1979 (Geneva) p. 245.
S. Meshkov, Proceed. Orbis Scientiae 1980 (Coral Gables) p. 43.
M. Chanowitz, SLAC Summer Institute 1981 (SLAC-245) p. 41.

14) S. Okubo, Phys. Lett. 5 (1963) 105.
G. Zweig, CERN Report 8182/TH.401 (1964).
J. Iizuka et al., Progr. Theor. Phys. 35 (1966) 1061.

15) Crystal Ball Collaboration, C. Edwards et al., Phys. Rev. Lett. 48 (1982) 458.
MARK II Collaboration, D.L. Burke et al., Phys. Rev. Lett. 49 (1982) 632.

16) Mark II Collaboration, Contribution to XXIst Intern. Conf. on High Energy Physics 1982 (Paris).

17) K. Koller and T.F. Walsh, Nucl. Phys. B140 (1978) 449.
T. Walsh, Proceed. Intern. Symp. on High Energy e^+e^- Interactions, Vanderbilt 1980 (Nashville, AIP No. 62) p. 14.

18) H.J. Schnitzer, Nucl. Phys. B207 (1982) 131.

19) J.L. Rosner, Phys. Rev. D24 (1981) 1347, and "Quark content of neutral mesons" (preprint, 1982).

20) TASSO Collaboration, Contribution to XXIst Intern. Conf. on High Energy Physics 1982 (Paris), and DESY 82-073.

21) ACCMOR Collaboration, C. Daum et al., Phys. Lett. 104B (1981) 246.

22) A. Etkin et al., Contribution to XXIst Intern. Conf. on High Energy Physics 1982 (Paris), and Phys. Rev. Lett. 49 (1982) 1620.

23) D.L. Scharre, Proceed. Orbis Scientiae 1982 (Coral Gables), and SLAC-PUB-2880.

24) TASSO Collaboration, M. Althoff et al., DESY 82-062, to be published.

25) TASSO Collaboration, R. Brandelik et al., Phys. Lett. 108B (1982) 67.

26) P.H. Damgaard, preprint CLNS-81/519 (Cornell Univ., 1981).

27) T.F. Walsh, Phys. Lett. 36B (1971) 121.

28) C. Peterson et al., Nucl. Phys. B174 (1980) 424.

29) T.F. Walsh and P. Zerwas, Phys. Lett. 44B (1973) 195.

30) E. Witten, Nucl. Phys. B120 (1977) 189.
C.H. Llewellyn Smith, Phys. Lett. 79B (1978) 83.
C.T. Hill et al., Nucl. Phys. B148 (1979) 373.
R.J. DeWitt et al., Phys. Rev. D19 (1979) 2046.
W.R. Frazer and J.F. Gunion, Phys. Rev. D20 (1979) 147.

31) W.A. Bardeen and A.J. Buras, Phys. Rev. D20 (1979) 166.
D.W. Duke and J.F. Owens, Phys. Rev. D22 (1981) 2280.
T.Uematsu and T.F. Walsh, Phys. Lett. 101B (1981) 263.

32. T. Uematsu and T.F. Walsh, Nucl. Phys. B199 (1982) 93.

33. E. Bloom et al., Phys. Rev. D5 (1972) 528.
M. Breidenbach and J. Kuti, Phys. Lett. 41B (1972) 234.
W.B. Atwood et al., Phys. Lett. 64B (1976) 479.
A. Bodek et al., Phys. Rev. D20 (1979) 1471.

34) CELLO Collaboration, Contribution to XXIst Intern. Conf. on High Energy Physics 1982 (Paris).

35) PLUTO Collaboration, Ch. Berger et al., Phys. Lett. 107B (1981) 168.

36) JADE Collaboration, W. Bartel et al., DESY 82-064, to be published.

37) W.A. Bardeen et al., Phys. Rev. D18 (1978) 3998.

38) W.R. Frazer, Proceed. 4th Intern. Coll. on $\gamma\gamma$ Interactions 1981 (Paris) p. 101.
W.A. Bardeen, Proceed. 1981 Intern. Symp. on Lepton and Photon Interactions at High Energies (Bonn) p. 432.

39) S. Brodsky et al., Phys. Lett. 41 (1978) 672, and Phys. Rev. D19 (1979) 1418.
K. Kajantie, Phys. Scr. 29 (1979) 230, and Acta Phys. Austriaca, Suppl. XXI (1979) 663.
K. Kajantie and R. Raitio, Nucl. Phys. B159 (1979) 528.

40) TASSO Collaboration, R. Brandelik et al., Phys. Lett. 107B (1981) 290.

41) JADE Collaboration, W. Bartel et al., Phys. Lett. 107B (1981) 163.

42) H.J. Daum et al., Zeitschr. Phys. C8 (1981) 167.

43) MAC Collaboration, private communication.

44) M. Gell-Mann, Phys. Lett. 8 (1964) 214.
G. Zweig, CERN Report 8419/TH. 412 (1964).

45) M.Y. Han and Y. Nambu, Phys. Rev. 139B (1965) 1006.
Y. Nambu and M.Y. Han, Phys. Rev. D10 (1974) 674.
J.C. Pati, Proceed. Intern. Summer Institute on Theor. Particle Physics (Hamburg, 1975) p. 384.
H.K. Lee, preprint IC/78/95 (Trieste, 1978).

46) T. Jayaraman et al., preprint MUTP-82/3 (Madras, 1982).

QCD AND HADRON JETS -- NEW RESULTS FROM PEP AND PETRA *

by

Sau Lan Wu

Department of Physics, University of Wisconsin, Madison, Wisconsin, USA†

and

Deutsches Elektronen-Synchrotron DESY, Hamburg, Germany

* Rapporteur talk at the Topical Conference of the 1982 SLAC Summer Institute on Particle Physics, August 16 - 27, 1982, SLAC, Stanford, California, USA.

† Supported by the US Department of Energy Contract EY-76-C-02-0881.

© Sau Lan Wu 1982

Abstract

Recent experimental data related to hadron jets and QCD are reviewed from the ten detectors at PEP and PETRA. The many interesting new results include the measurements of the quark-gluon coupling constant α_s, the total hadronic cross section, and the gluon spin with high statistics, a possible difference between the quark and gluon jets, particle identification in jets, and a search for charged Higgs and technipions from four-jet events. The fragmentation functions for the heavy quarks (charm and bottom) are discussed in this Conference by Schlatter of SLAC.

1. INTRODUCTION

The most important problems of particle physics can be stated as the "gauge problem" and the "mass problem." Gauge theory describes successfully both the strong interactions and the electroweak interactions[1]. High-energy e^+e^- colliding beam accelerators have contributed greatly to our knowledge of the gauge particles: first evidence three years ago of the gluon for strong interactions from the three-jet events[2], and more recently a first, preliminary determination of the Z^0 mass from the asymmetry in $e^+e^- \to \mu^+\mu^-$[3]. Theorists have quite precise ideas about the properties of both the Z^0 and the $W^\pm$, which may soon be observed directly at the CERN $p\bar{p}$ Collider.

Unfortunately, we know much less about the mass problem than the gauge problem, especially for particles other than the gauge bosons. An example of this ignorance is our inability to foretell even roughly the mass of the top quark. With this very much in mind, PETRA plans to increase the energy three times in the coming year, first to a center-of-mass energy $W = 39$ GeV, then to about 41 GeV in early 1983, and finally to 45 GeV next fall. While this mass problem, including the search for Higgs particles[4], will undoubtedly be one of the central concerns of both LEP and SLC, attempts have recently been made to take a first look. These attempts will be discussed in Sec. 7 below.

There are at present the following detectors at PEP and PETRA:

PEP:	DELCO	PETRA:	CELLO
	HRS		JADE
	MAC		MARK J
	MARK II		PLUTO
	TPC		TASSO

At PETRA, CELLO took the place of PLUTO in summer 1982, and PLUTO probably will not be moved into the beam again.

The topics to be covered in this report are:

1. Status of α_s Determination,
2. Precise Measurement of R - TASSO, JADE, MARK J, MARK II, MAC,
3. Measurement of Gluon Spin with High Statistics - TASSO, MARK J,
4. Is Gluon Jet Different from Quark Jet? - JADE, TASSO
5. Particle Identification in Jets,

and 6. Search for Charged Higgs and Technipions from 4-Jet Events - TASSO.

2. STATUS OF α_s DETERMINATION

A. Experimental results

Seven collaborations at PEP and PETRA have determined experimentally the values of the quark-gluon strong coupling constant α_s. Their most recent results are listed in Table 1.

Roughly speaking, α_s is determined by comparing the number of three-jet events with that of two-jet events. As seen from Table 1, however, the situation is more complicated: different values of α_s are obtained when different assumptions are made in analyzing the data. This uncertainty comes mainly from two sources, first whether higher-order corrections in QCD are taken into account, and secondly what assumptions are used in treating the fragmentation of quarks and gluons into hadrons. Except for two recent determinations of α_s by the TASSO and JADE Collaborations to be discussed in Sec. D below, the second-order corrections are not taken into account. The method of energy-energy correlation[12] used by MARK II and MAC is discussed in Sec. B, while the comparison between the independent fragmentation of Hoyer et al.[13] and the Lund fragmentation[14] by CELLO is in Sec. C.

Table 1 - Measured values of the quark-gluon coupling constant α_s at PEP and PETRA

Collaboration	First order in α_s		Energy-energy Correlation	Second order in α_s
	Hoyer et al.	Lund		
CELLO[5]	0.15-0.20	0.235-0.28		
JADE[6]	0.20±0.015±0.03			0.16±0.015±0.03
MAC[7]			0.20±0.01±0.02	
MARK II[8]			0.19±0.02±0.03	
MARK J[9]			0.16±0.01	
PLUTO[10]	0.15±0.02±0.03			
TASSO[11]	0.194±0.005±0.03			0.168±0.003±0.03

B. Comments on energy-energy correlation - MARK II, MAC

The energy-energy correlation[12] function is defined by

$$\frac{1}{\sigma_{tot}} \frac{d\Sigma}{d\Omega d\Omega'} = \frac{1}{N} \frac{1}{\Delta\Omega} \frac{1}{\Delta\Omega'} \sum \sum \frac{EE'}{s} \qquad (1)$$

where σ_{tot} is the total hadronic cross section, $s = W^2$, and E and E' are the energies of the particles in the solid angles $\Delta\Omega$ and $\Delta\Omega'$ respectively. The first sum is over all N events, and the second sum is over all pairs of particles in $\Delta\Omega$ and $\Delta\Omega'$. For the purpose of determining α_s, all angles are further summed over except the angle χ between $\Delta\Omega$ and $\Delta\Omega'$, as shown in Fig. 1. The resulting cross section is

$$\frac{1}{\sigma_{tot}} \frac{d\Sigma}{d\cos\chi} = \frac{1}{N} \frac{1}{\Delta \cos\chi} \sum \sum \frac{EE'}{s} \qquad (2)$$

Even as recent as a year ago at the Bonn conference[15], the hope was expressed that this energy-energy correlation function is insensitive to fragmentation, and gives a precise test of QCD. The argument consists essentially of saying that the contributions from quark fragmentation and lepton decay are symmetric under the exchange $\chi \to \pi - \chi$, while the QCD contributions are asymmetric under this exchange.

Recent results from MARK II[8] and MAC[7] show that this independence of fragmentation is not realized. They fitted the energy-energy correlation function of eq. (2) as follows:

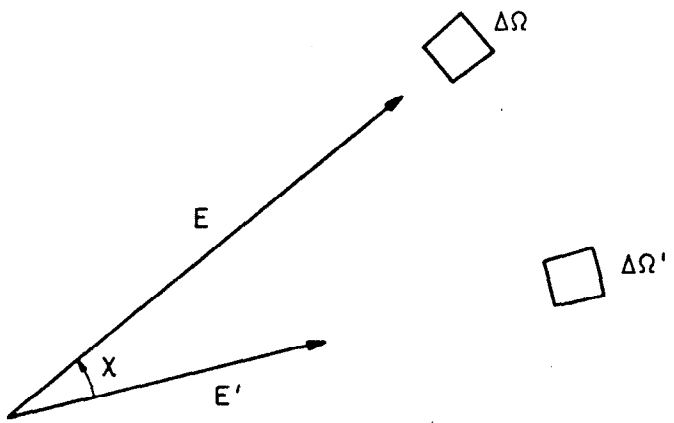


Fig. 1 - Variables for the energy-energy correlation function.

$$\alpha_s F_{QCD}(\chi) + \underbrace{\frac{A_0}{\sqrt{s}}\frac{1}{\sin^3\chi}}_{(q\bar{q}_{frag.})} + \underbrace{\frac{\alpha_s A_1}{\sqrt{s}}}_{(q\bar{q}g_{frag.})} \begin{cases} (\sin\chi)^{-3} & \chi \leq \frac{\pi}{2} \\ 1 + \cos\chi \;\}\text{(MARK II)} & \chi \geq \frac{\pi}{2} \\ \sin\chi \;\}\text{(MAC)} & \end{cases} \quad (3)$$

where the first term is given by QCD. While the first correction term due to fragmentation is symmetrical under the exchange $\chi \to \pi - \chi$, the second is not. The MARK II result is shown in Fig. 2, while the one from MAC is in Fig. 3. The fitted results for MARK II are $\alpha_s = 0.19 \pm 0.02$, $A_0 = (0.7 \pm 0.2)$ GeV and $A_1 = (2.6 \pm 0.5)$ GeV, while for MAC $\alpha_s = 0.20 \pm 0.01 \pm 0.02$, $A_0 = (1.2 \pm 0.08 \pm 0.15)$ GeV and $A_1 = (2.5 \pm 0.2 \pm 0.4)$ Gev. For the MARK II analysis, if the asymmetric correction term A_1 due to fragmentation is omitted, then the value of α_s changes from 0.19 to 0.14.

C. Lund vs independent fragmentation - CELLO

To the first order in α_s, there are two diagrams for $e^+e^- \to q\bar{q}g$, as shown in Fig. 4. These QCD diagrams are easy to compute, and give the distributions of the quark, the anti-quark, and the gluon[16]. Unfortunately, neither quark nor gluon is directly observable; instead they are fragmented into hadrons. Therefore, in order to compare the QCD predictions with the experimental data, a model is needed for this complicated fragmentation process.

Fragmentation was first studied by Field and Feynman[17] in the context of two-jet events $e^+e^- \to q\bar{q}$, and the generalization to the

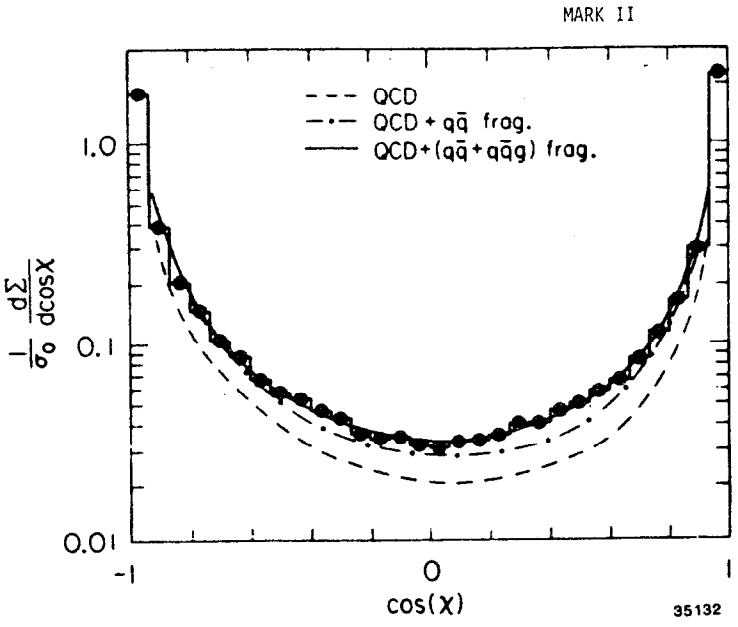


Fig. 2 - $(1/\sigma_0)d\Sigma/d\cos\chi$ as a function of $\cos\chi$. The size of the dots corresponds to the statistical errors. The dashed line is the QCD prediction. The dash-dotted line is the QCD result plus the $q\bar{q}$ fragmentation term. The solid line is the sum of the QCD predictions and the two nonperturbative contributions - MARK II.

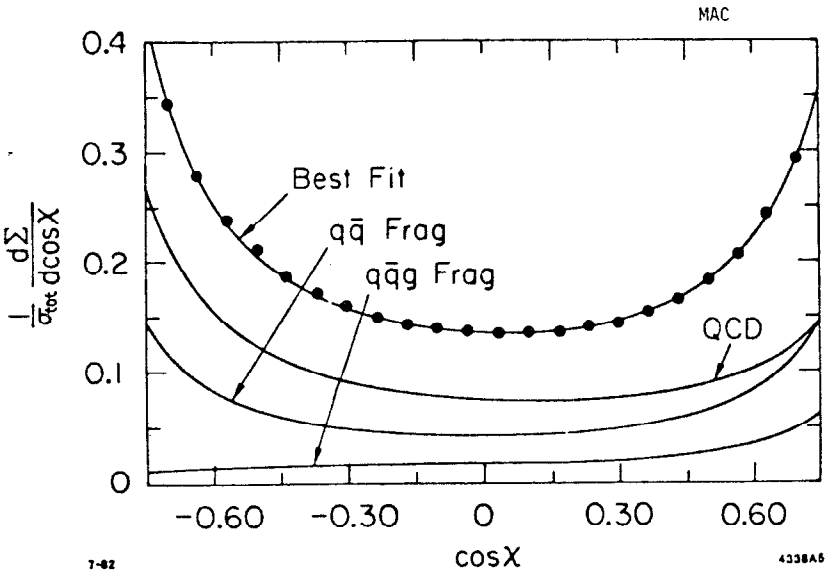


Fig. 3 - The full experimental energy-energy correlation as a function of $\cos\chi$, the correlation angle. Also shown are the fitted contributions from QCD, the $q\bar{q}$ and the $q\bar{q}g$ fragmentation terms - MAC.

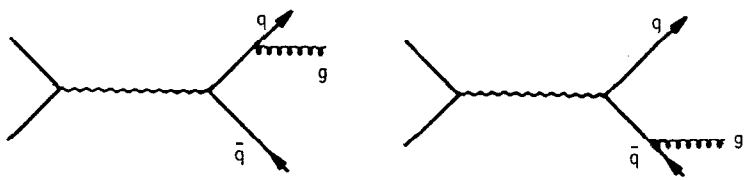


Fig. 4 - Diagrams for $e^+e^- \to q\bar{q}g$ to order α_s.

three-jet events through $e^+e^- \to q\bar{q}g$ was first carried out by Hoyer, Osland, Sander, Walsh and Zerwas[13]. In both of these Monte Carlos, the jets fragment independently, as schematically shown in Fig. 5(a). The Lund group of Andersson, Gustafson, and Sjoestrand[14] had the idea of combining fragmentation with the concept of the color string, which is stretched from the quark via the gluon to the anti-quark. This color string is envisaged to break first to produce a hadron carrying a sizable fraction of the gluon energy. The remainder of the gluon energy is then shared between the two pieces of the broken string, which are fragmented independently in their respective center-of-mass systems[14]. This Lund fragmentation process is shown schematically in Fig. 5(b).

There is no compelling argument to prefer one of these two fragmentation models over the other. While the use of the color string has its appeal, it must be emphasized that there are many more parameters in the Lund model than in the model of Hoyer et al. Under this circumstance, it is of importance to ascertain whether there is significant dependence of the α_s determination on the fragmentation model.

This problem has been studied by both the CELLO[5] and the JADE[6] Collaborations. Their results contradict each other. JADE used both fragmentation models[13,14] to determine the corrected x_1 and x_T distributions, where $x_T = x_2 \sin\theta_{12}$. They found that "the corrections are, within the errors, independent of the fragmentation scheme used." On the other hand, CELLO found that, depending on the distribution used, the Lund model gives α_s

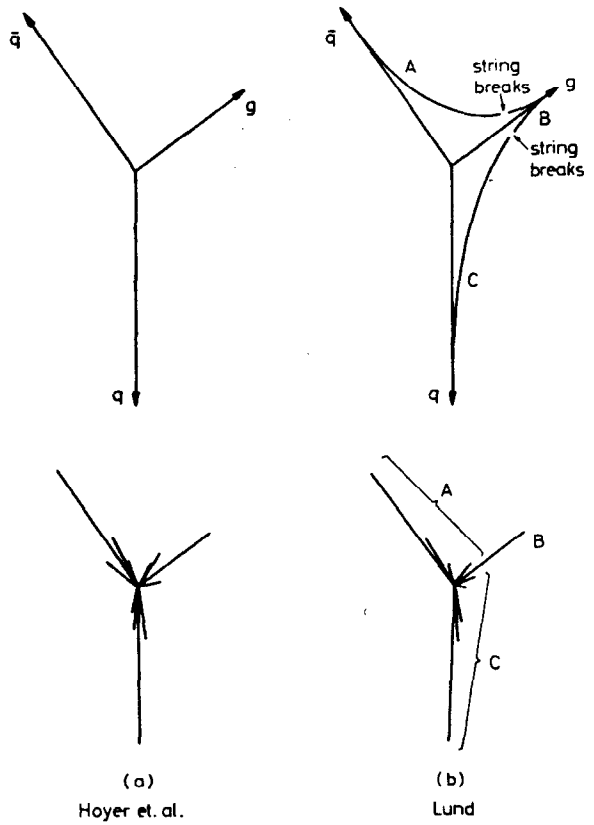


Fig. 5 - Schematic representation of fragmentation models.

between 28% to 67% higher than the model of Hoyer et al. The two extreme cases are:

Smallest difference: three-jet fraction from events with oblateness larger than 0.3

Lund $\alpha_s = 0.255 \pm 0.050$

Hoyer $\alpha_s = 0.200 \pm 0.035$ ratio = 1.28

Largest difference: energy-energy correlation function

Lund $\alpha_s = 0.25 \pm 0.04$

Hoyer $\alpha_s = 0.15 \pm 0.02$ ratio = 1.67

In particular, this result from CELLO implies that, contrary to the earlier hope as described in Sec. B, the energy-energy correlation function is sensitive to fragmentation.

In order to have a better understanding of this rather significant dependence on fragmentation, CELLO has attempted various modifications and combinations of the Monte Carlo programs. The result is shown in Fig. 6. It is seen that about two thirds of the difference is due to the different fragmentation schemes used (quark, gluon independent fragmentation scheme as in Hoyer et al. model versus the string fragmentation scheme as in the Lund model).

D. α_s determination in second order - TASSO, JADE

As shown in Table 1, the determination of α_s has been carried out in both first order and second order. In first order, the only QCD diagrams taken into account for $e^+e^- \to q\bar{q}g$ are the two shown in Fig. 4. In second order, it is necessary to consider in addition not only the

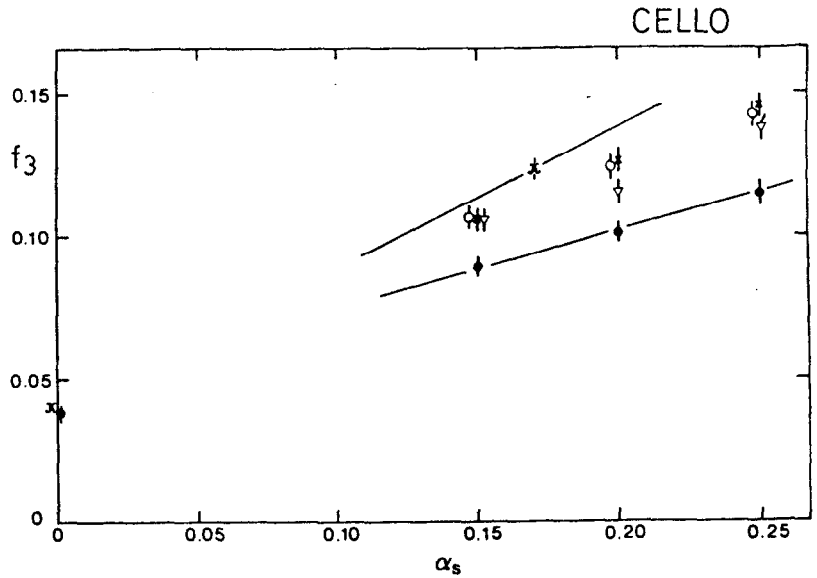


Fig. 6 - CELLO Monte Carlo study of the three-jet fraction f_3 versus α_s for different fragmentation conditions (S>0.25, A<0.10):
- ● Lund Model σ_q = 0.30 GeV/c V/(P+V) = 0.5
- x Lund program with FF fragmentation and gluon as a quark $a_g = a_f = 0.77$
- o idem but $a_g = 1$
- ▽ Lund program FF fragmentation but gluon as in LM
- x Hoyer Model with σ_q = 0.30 GeV/c.

diagrams of Fig. 7 for $e^+e^- \to q\bar{q}g$ but also those in Fig. 8 for $e^+e^- \to q\bar{q}gg$ and $e^+e^- \to q\bar{q}q\bar{q}$. This theoretical analysis was carried out by three groups: R. K. Ellis et al.[18], Fabricius et al. (FKSS)[19], and Vermaseren et al.[20]. Although all three groups studied the same diagrams, and used the same renormalization scheme, their results were in apparent conflict. FKSS has found the α_s^2 corrections to be of reasonably small size, but the other two groups have concluded that the α_s^2 corrections are comparable to the α_s terms, making it necessary to study α_s^3 corrections (which is virtually hopeless because of the large number of diagrams involved). Fortunately, this discrepancy has been understood[21] as due to different definitions of thrust and hence the three-jet events. With this understanding, it is now possible to carry out second-order determination of α_s provided that the FKSS result, rather than those of the other two groups, is used. This has been accomplished by the TASSO and JADE Collaborations.

The method used by TASSO[11] is as follows. The FKSS formulas are built in the event generator, and independent Field-Feynman (FF) fragmentation is used. The TASSO data from ρ^0 production[22] are used to fix one of the Field-Feynman parameters on the ratio of pseudoscalar to vector mesons P/V. With this ratio fixed, the second-order α_s together with the other two Field-Feynman parameters are found by fitting simultaneously the experimental data. Four distributions are used, namely those in the average transverse momentum out of the event plane $\langle p_{T\,out}^2 \rangle$, in sphericity S, in planarity, and in the momentum fraction $x = P_h/E_{beam}$ for $x > 0.3$. In terms of the normalized eigenvalues Q_1, Q_2 and Q_3 of

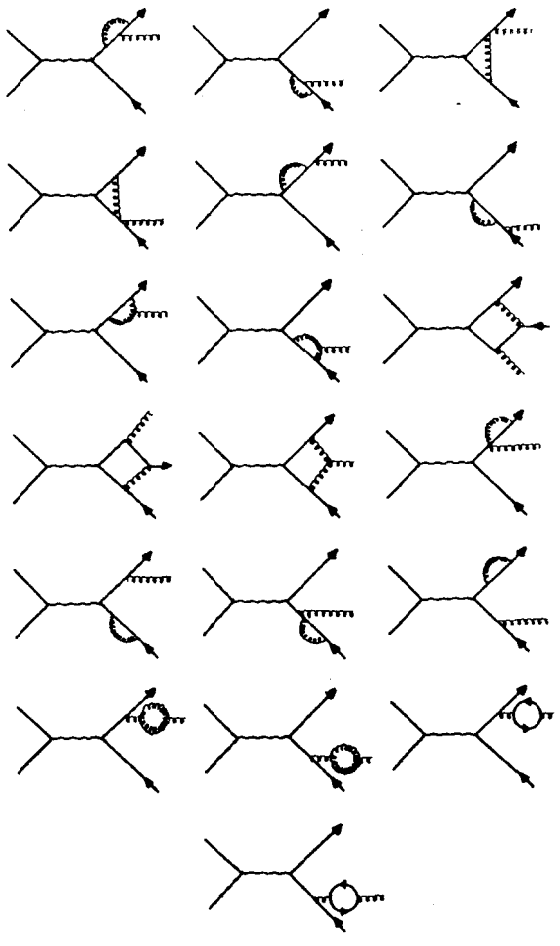


Fig. 7 - Diagrams for $e^+e^- \to q\bar{q}g$ to order α_s^2.

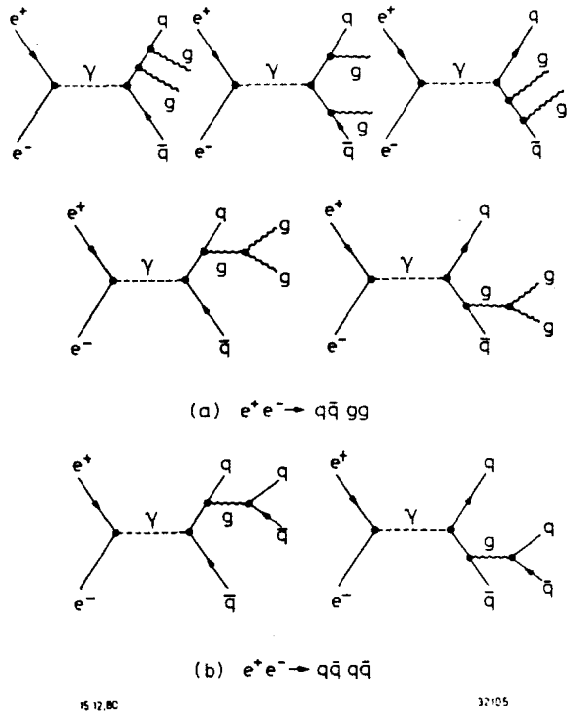


Fig. 8 - Diagrams for $e^+e^- \to q\bar{q}gg$ and $q\bar{q}q\bar{q}$ to order α_s^2 (lowest order).

the momentum tensor[11], the sphericity $S = \frac{3}{2}(Q_1 + Q_2)$ and the planarity $= Q_2 - Q_1$. The resulting second-order α_s, as already given in Table 1, and the three Field-Feynman parameters are.

$\alpha_s = 0.168 \pm 0.003$ (stat.) ± 0.03 (sys.)

$\sigma_q = (0.350 \pm 0.003 \pm 0.02)$ GeV/c

$a_F = 0.70 \pm 0.01 \pm 0.10$

and $\frac{P}{P+V} = 0.42$ from ρ^0 production, (see Sec. 6 below)

where σ_q describes the transverse momentum distribution and a_F the longitudinal momentum distribution for quark fragmentation. The systematic errors are valid only in the context of the Field-Feynman fragmentation model.

If the same procedure is applied to determinate the first order α_s, the corresponding results are

$\alpha_s = 0.194 \pm 0.005$ (stat.) ± 0.03 (sys.)

$\sigma_q = (0.358 \pm 0.003 \pm 0.02)$ GeV/c

$a_F = 0.70 \pm 0.02 \pm 0.10$

The comparison of the two fits with the TASSO experimental data is shown in Figs. 9 - 12. It is seen that these event shape distributions are well fitted by either first order or second order in α_s. The resulting values of α_s are of course not the same, the second-order result being 13% lower. It is important that the analysis is carried out with simultaneous fits. Obviously, if the second-order value for α_s were used in a first-order fit, or vice versa, the resulting fits would be very poor. In order to establish the need of second-order in α_s, the above parameters should be used for the purpose of comparing some other distribution, preferably one related to four-jet events.

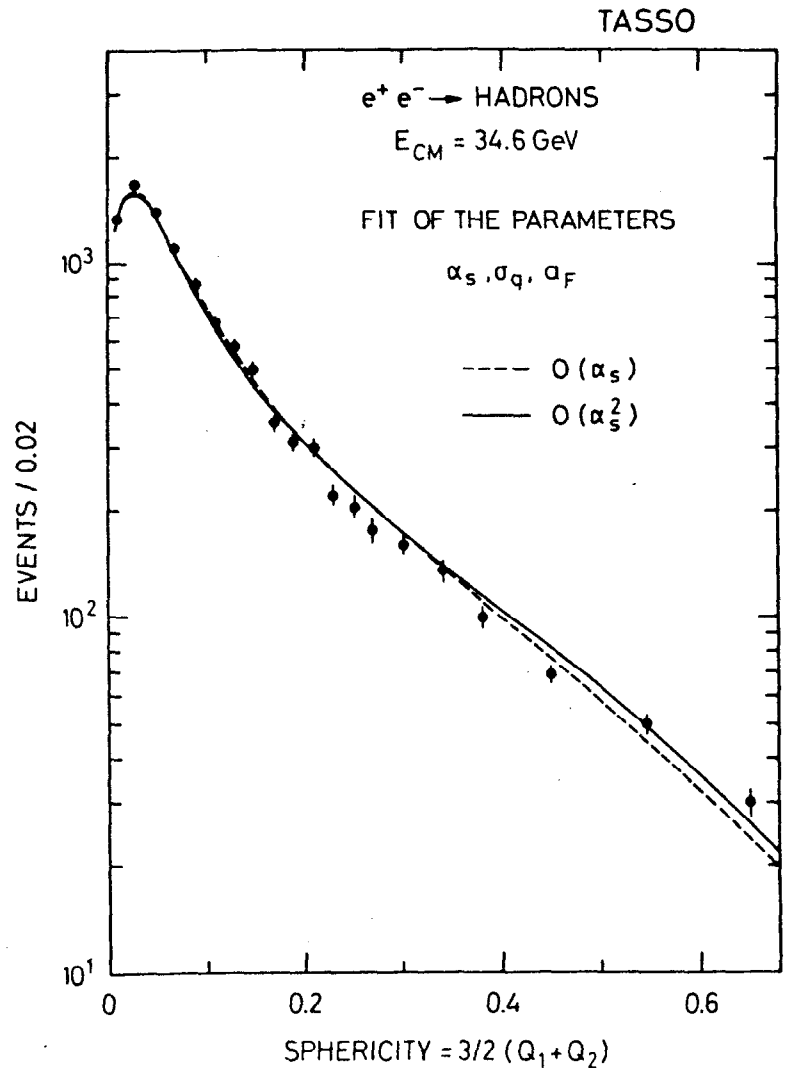


Fig. 9 - Sphericity distribution from TASSO. The dashed line and the solid line are respectively the results of the simultaneous fits in first-order and second-order QCD with Field-Feynman fragmentation.

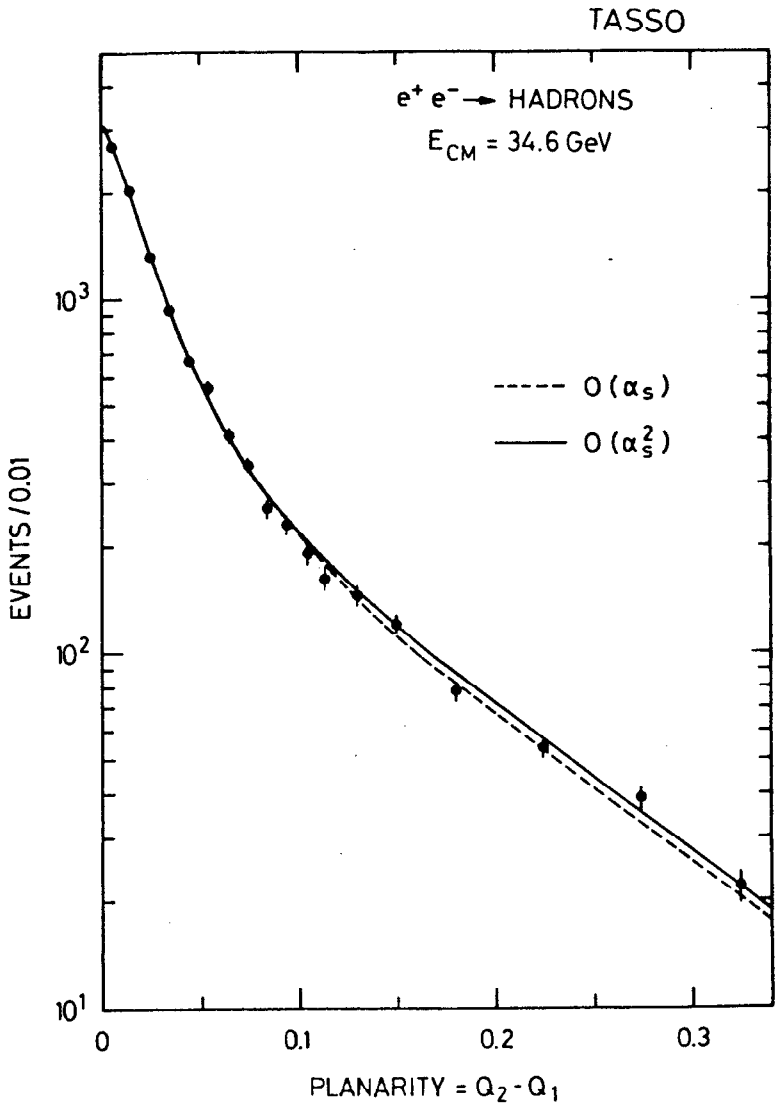


Fig. 10 - Planarity distribution from TASSO. The dashed line and the solid line are respectively the results of the simultaneous fits in first-order and second-order QCD with Field-Feynman fragmentation.

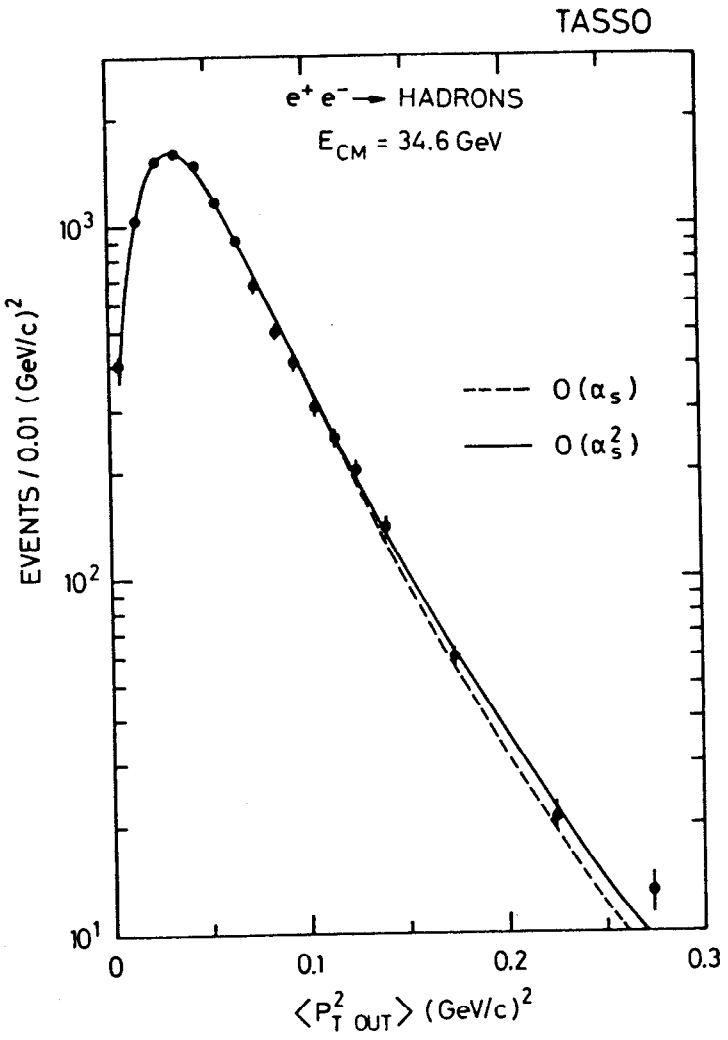


Fig. 11 - TASSO distribution in $\langle P_{T\ out}^2 \rangle$, the average transverse momentum out of the event plane. The dashed line and the solid line are respectively the results of the simultaneous fits in first-order and second-order QCD with Field-Feynman fragmentation.

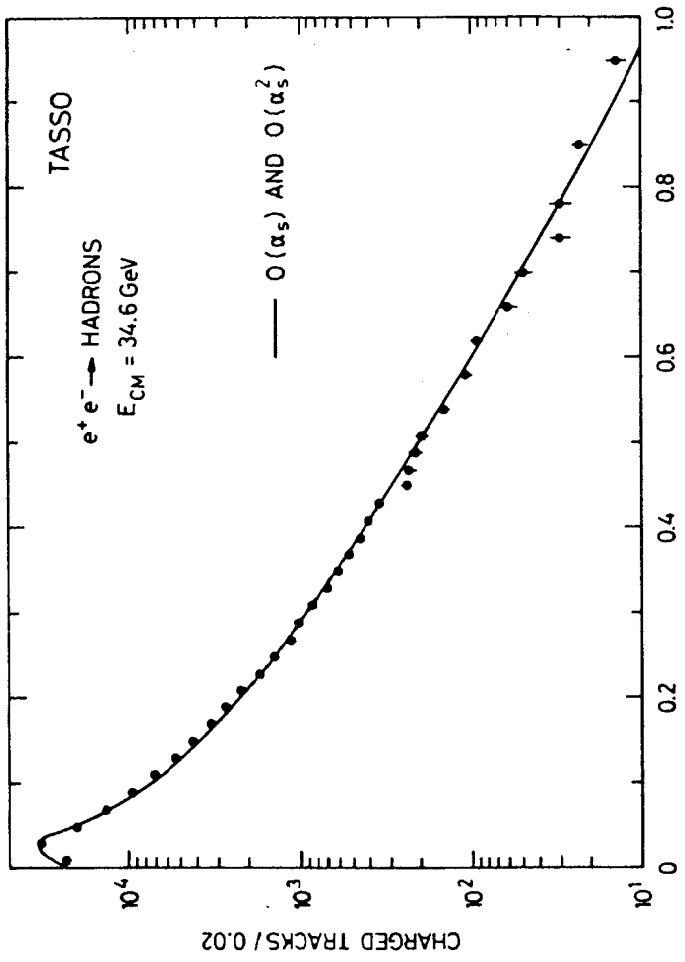


Fig. 12 - TASSO inclusive distribution in x, the momentum fraction of the charged hadrons, from TASSO. In this case the first-order and second-order results are indistinguishable.

The method used by JADE[6] is similar but not identical. The distribution in the parton thrust x_1 is shown in Fig. 13. Both independent fragmentation via Hoyer et al. and Lund fragmentation are used, and the value given in Table 1 is the average of these two fragmentation models.

A comparison of the second-order values of α_s from TASSO and JADE with the corresponding first-order results shows that there is a reduction of 13% to 20% in going from first order to second order.

3. PRECISE MEASUREMENT OF R - TASSO, JADE, MARK J, MARK II, MAC

R for the total hadronic cross section is defined as the ratio

$$R = \frac{\text{total cross section for } e^+e^- \rightarrow \text{hadrons}}{\text{total cross section for } e^+e^- \rightarrow \mu^+\mu^-} \qquad (4)$$

at the same energy. More precisely, the denominator is not the actual total cross section for $e^+e^- \rightarrow \mu^+\mu^-$, but rather the theoretical total cross section in the lowest-order QED without weak interactions. Therefore

$$R = \frac{s \text{ in GeV}^2}{86.856} \text{ (total cross section for } e^+e^- \rightarrow \text{hadrons in nb)}. \qquad (5)$$

The precise determination therefore involves the careful identification of hadronic events, subtraction of backgrounds, calculation of acceptance, measurement of luminosity, etc., but not any experimental determination of the total cross section for μ pair production.

The results of the recent measurements of R by various collaborations are listed in Table 2. So far, only the TASSO[23] value is published. The two values given by MAC[7] differ only in the method of analysis. Figure 14 gives an overall view [26] of the measured values of R from low energies to the highest available energy.

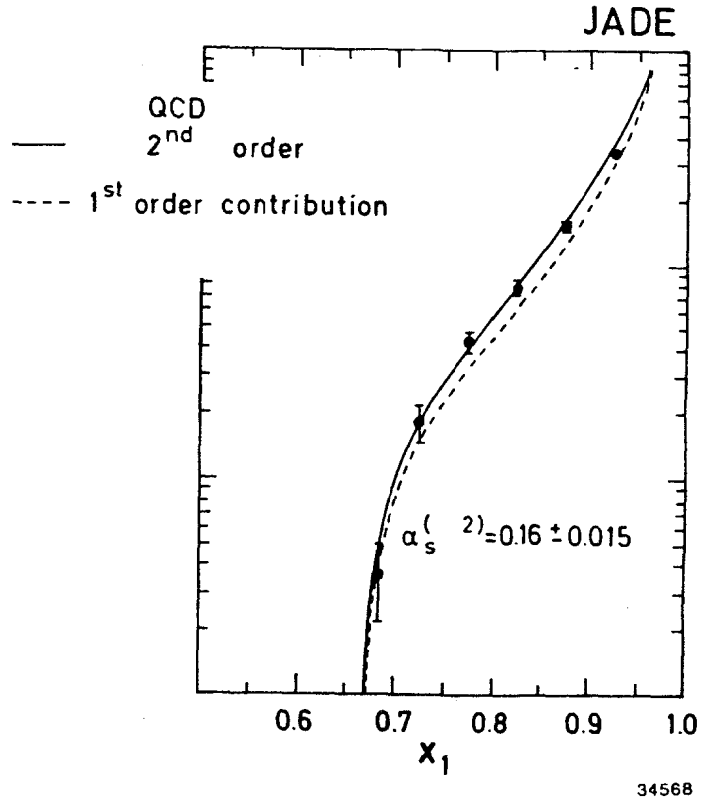


Fig. 13 - The corrected x_1 distribution together with the second-order QCD best fit. The first-order contribution of this fit is indicated by the broken curve. The fit did not include data above $x_1 = 0.85$ - JADE.

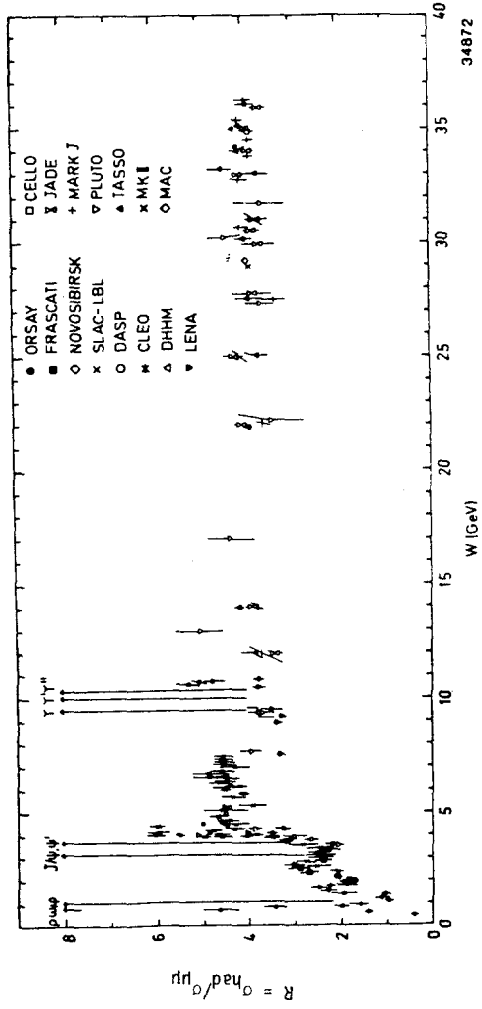


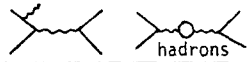
Fig. 14 - Overall view of the measured values of R for hadronic total cross sections from low energies to the highest available energy.

Table 2 - Measured values of R for total hadronic cross section at PEP and PETRA.

Collaboration	Range of center-of-mass energy in GeV	$R \pm \Delta R_{stat} \pm \Delta R_{sys}$
TASSO[23]	14.0 - 36.7	4.01 ± 0.03 ± 0.20
JADE[24]	14.0 - 36.7	3.93 ± 0.03 ± 0.09
MARK J[9,24]	12.0 - 36.7	3.84 ± 0.05 ± 0.22
MARK II[25]	29.0	3.90 ± 0.05 ± 0.25
MAC[7]	29.0	3.93 ± 0.04 ± 0.12 3.87 ± 0.04 ± 0.10

Since the JADE[24] value is the most accurate one in the energy range of PEP and PETRA, it is described in this section. The various contributions to the systematic error of JADE are shown in Table 3. When added in quadrature, the total is 3%. In Fig. 15 (a) and (b), the measured distributions in the number of charged prongs and the momentum balance along the beam direction are compared with the Monte Carlo simulation. In Fig. 15 (c), the distribution of the vertex along the beam direction is given. In all three cases, the cuts used are also shown and are quite far in the tails of the distributions.

Table 3 - Contributions to the systematic error of the JADE precise measurement of R for total hadronic cross section.

	Systematic error (ΔR) E_{cm} 22 - 36.7 GeV
Background: $N_{\tau\tau}$ (2.4% ± 1.4%) low E_{cm} $N_{\gamma\gamma}$ (0.5 ± 0.5%) high E_{cm} $N_{\gamma\gamma}$ (0.7 ± 0.5%) Σ	± 1.6%
Acceptance (85% w/o rad corr.)	± 1.5%
Luminosity (barrel Bhabhas)	± 1.8%
Radiative correction (α^3) 	± 0.8%
Higher order radiative corr.	No error for higher order corr. included
Total Σ	± 3.0%

In order to remove the background from two-photon processes

$$e^+e^- \rightarrow e^+e^- \text{ hadrons}$$

with the e^+ and the e^- in the final state going near the beam directions and hence not detected, a cut is introduced in the total visible energy, where the total visible energy is the sum of energies carried by the charged tracks and the photons. As functions of the ratio of the total visible energy to the beam energy, the observed distributions, the Monte Carlo simulation, and the cuts used are all shown in Fig. 16. The peak

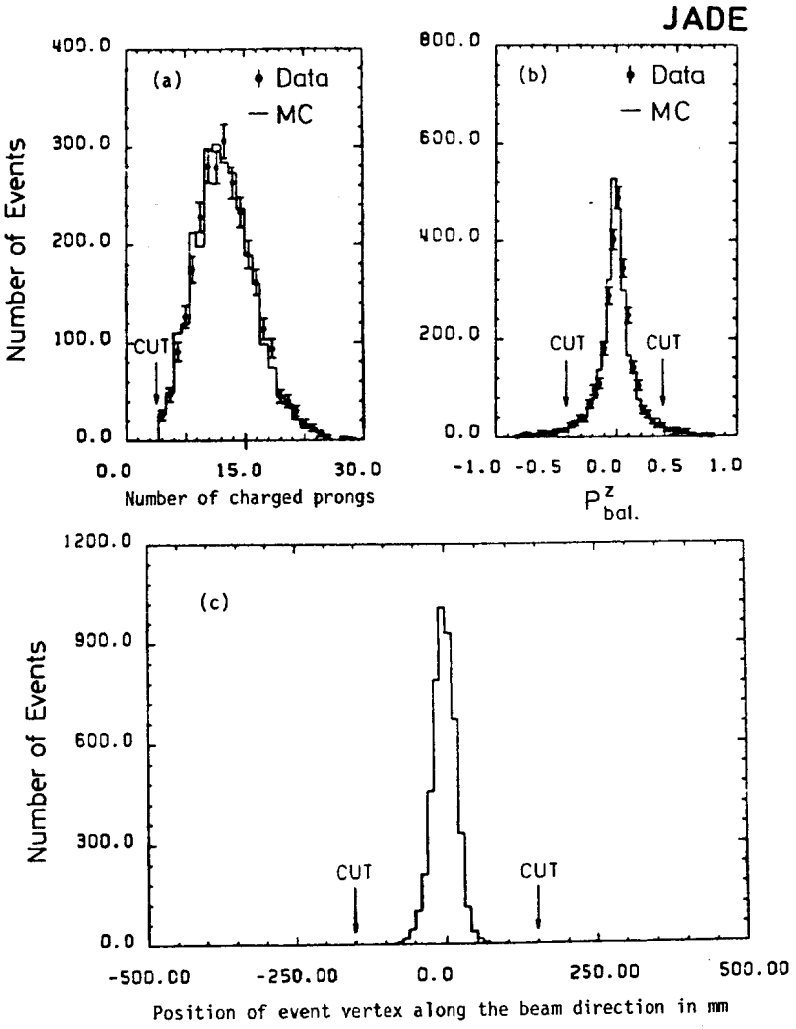


Fig. 15 - Some JADE acceptance cuts for hadronic events.

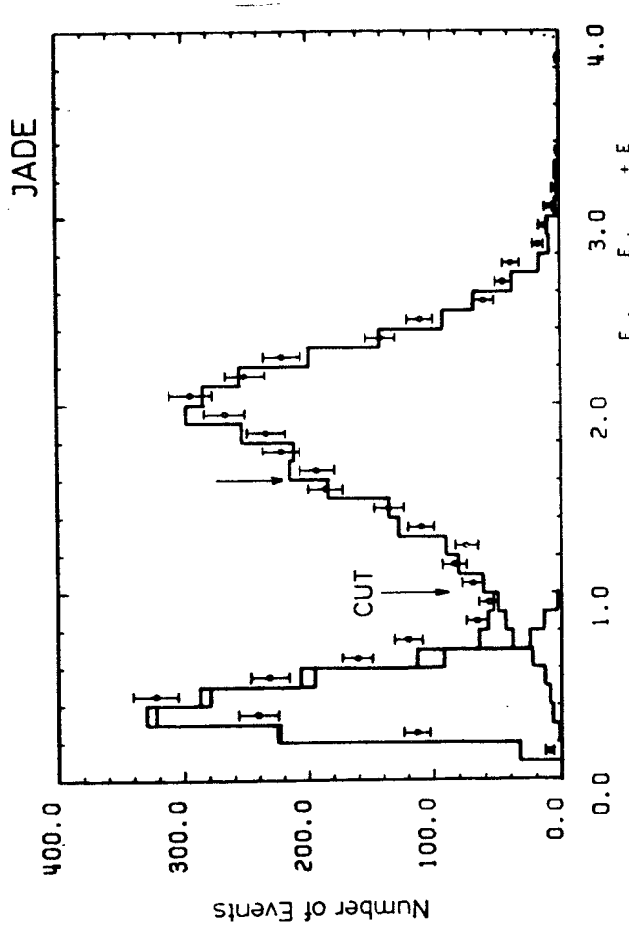


Fig. 16 - JADE acceptance cut in the ratio of the visible energy to the beam energy.

on the right is due to the hadronic events of interest, while that on the left is due to two-photon processes. Because of the good agreement between the experimental data and the Monte Carlo simulation, changing the position of the cut has relatively little effect on the value of R. For example, even with the rather extreme cuts at 1.0 and 1.6, as shown in Fig. 16, R changes by less than one per cent.

JADE has an accurate measurement of the luminosity. This is accomplished not by the small-angle luminosity monitors, but by the observation of Bhabha events in the barrel shower counters. The data, the Monte Carlo, and the cut used are shown in Fig. 17.

As functions of energy, the TASSO[23] and JADE[24] results on R are shown in Fig. 18 and Fig. 19 respectively.

One of the main motivations for the precise measurement of R for hadronic total cross section is that R as a function of the center-of-mass energy gives unambiguous determination, independent of fragmentation, of the quark-gluon coupling constant α_s and the Weinberg angle Θ_W for electroweak interaction. This extraction of these two fundamental constants from the data on R is carried out differently by the TASSO and JADE Collaborations. TASSO performed a simultaneous fit to the data by varying α_s and Θ_W, and obtained[23]

$$\alpha_s = 0.18 \pm 0.03 \pm 0.14 \quad \text{for} \quad s = 1000\ \text{GeV}^2$$

and $$\sin^2\Theta_W = 0.40 \pm 0.16 \pm 0.02.$$

The resulting R with these parameters are shown as the solid line in Fig. 18. On the other hand, JADE fitted each parameter separately with the other one held fixed. The results are[24]

If $\sin^2\Theta_W = 0.228$ is assumed, then $\alpha_s = 0.14 \pm 0.08$ at $s = 900\ \text{GeV}^2$;

if $\alpha_s = 0.18$ is assumed at $s = 900\ \text{GeV}^2$, then $\sin^2\Theta_W = 0.25 \pm 0.05$.

In both cases, systematic errors are included.

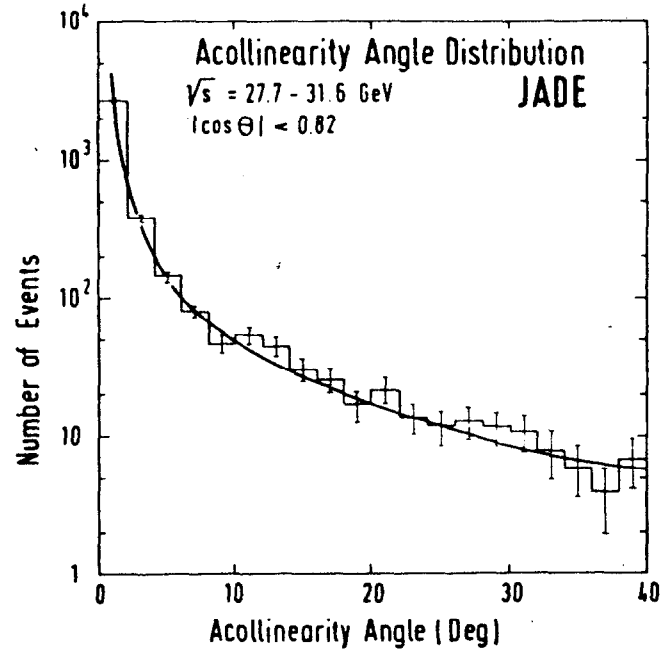


Fig. 17 - JADE luminosity measurement from Bhabha scattering.

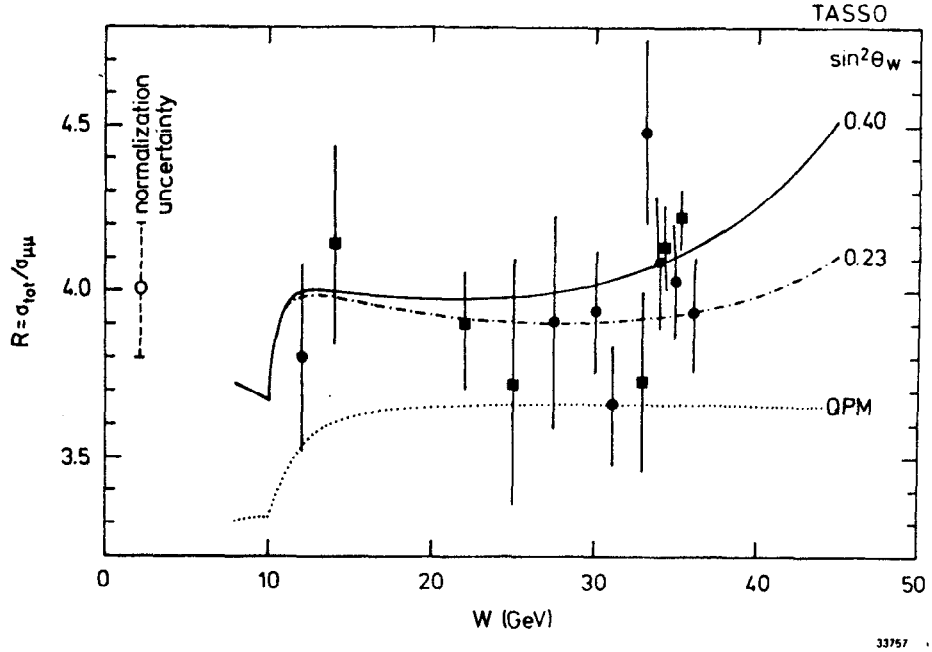


Fig. 18 - TASSO results on R for total hadronic cross section. The points marked by a circle are from the runs in 1979 and 1980, while those marked by a square from 1981. The errors shown include the statistical and point-to-point systematic uncertainty, while the overall normalization uncertainty is indicated separately on the left. The dotted line shows the expectation from the quark parton model (QPM). The full line represents the best fit including weak contributions, while the dashed-dotted line was computed with $\alpha_s(s = 1000\ GeV^2) = 0.18$ and $\sin^2\theta_W = 0.23$

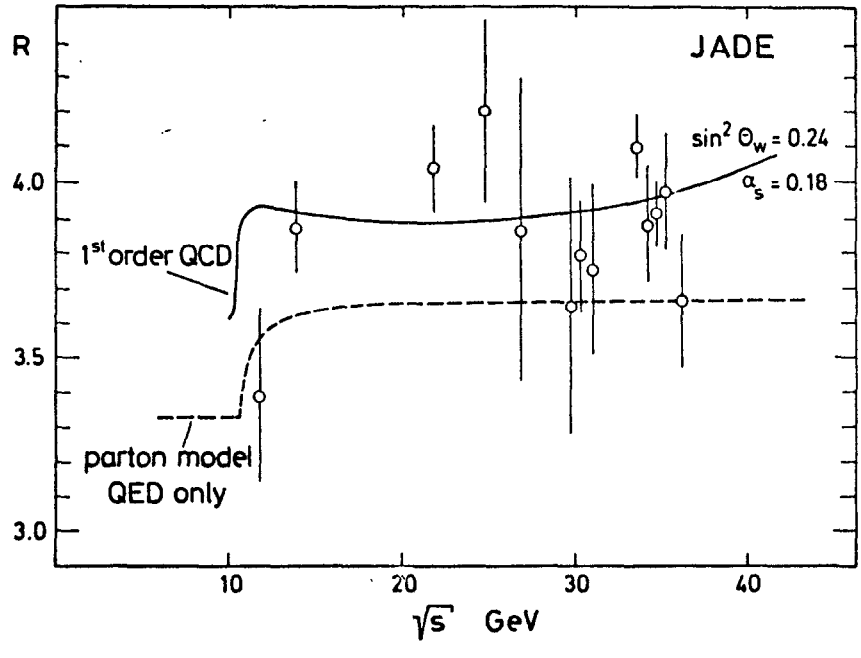


Fig. 19 - JADE results on R for total cross section. The dashed line shows the expectation from the quark parton model, while the solid line is computed with $\alpha_s = 0.18$ and $\sin^2\theta_W = 0.24$.

4. MEASUREMENT OF GLUON SPIN WITH HIGH STATISTICS - TASSO, MARK J

Since QCD is a gauge theory, its gluon must have spin 1. Experimentally, the gluon spin being 1 was first verified by TASSO[27] in 1980, and similar conclusions have been reached also by PLUTO[28] and CELLO[29]. With the high statistics available now, TASSO[30] and MARK J[9] have recently repeated the measurement of the gluon spin.

During my talk here last year, the method used by TASSO was described in some detail[31]. Exactly the same method is used with the high statistics. Briefly, let

$$x_j = E_j/E_{beam},$$

where E_j is the energy of jet j, j = 1, 2, 3. With the three x's arranged in the order

$$x_3 < x_2 < x_1,$$

the Ellis-Karliner angle is given by[32]

$$|\cos\tilde{\theta}| = \frac{x_2 - x_3}{x_1} . \qquad (6)$$

TASSO applied three-jet analysis to 16,000 hadronic events, and computed the x's from the angles between the jet directions. 1600 events survive after a cut of $x_1 < 0.9$, which implies a minimum angle of 70° between the jets. In Fig. 20, these events are plotted as a function of the Ellis-Karliner angle, and compared with the Monte Carlo predictions under the two assumptions of spin 1 and spin 0. Spin 0 is clearly ruled out.

Instead of $|\cos\tilde{\theta}|$, the ratio $x_3^2/(x_1^2 + x_2^2)$ was used by MARK J[9]. Their result is shown in Fig. 21, and, for 9 degrees of freedom, the χ^2 is 10.5 for spin 1 and 98.1 for spin 0.

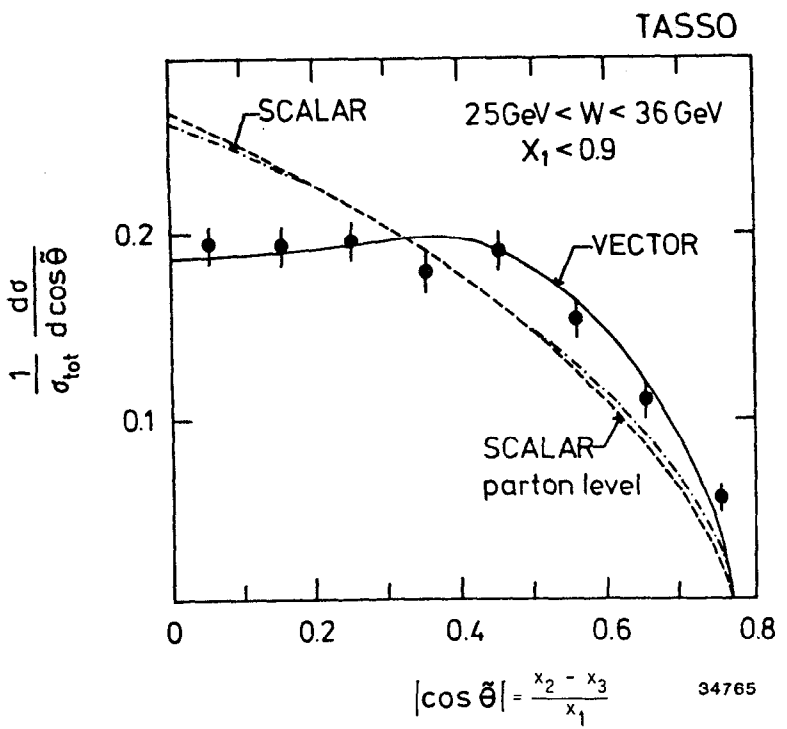


Fig. 20 - Observed distribution of the TASSO data in the region $x_1 < 0.9$ as a function of the Ellis Karliner angle $\tilde{\theta}$. The solid line shows the QCD Monte Carlo prediction, dashed line the prediction for the scalar gluons (– – – for Monte Carlo scalar model; —·—· for scalar model of parton level). All curves are normalized to the number of observed events.

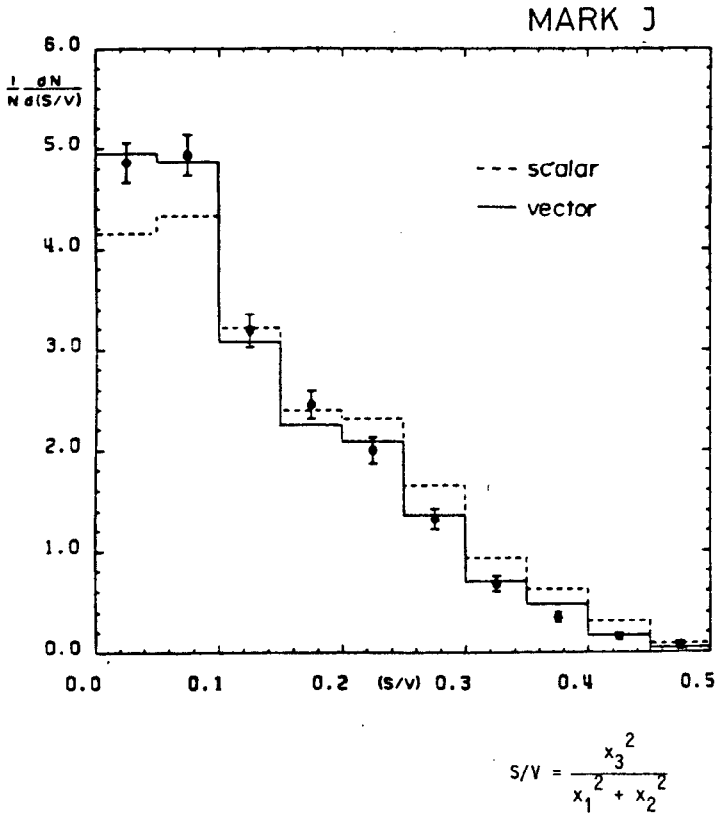


Fig. 21 - Observed distribution of the MARK J data as a function of the variable $x_3^2/(x_1^2 + x_2^2)$. The solid line shows the QCD Monte Carlo prediction, and the dotted line the prediction for scalar gluons.

5. IS GLUON JET DIFFERENT FROM QUARK JET? - JADE, TASSO

A. Average transverse momentum - JADE

A year ago at this Topical Conference, I reported[31] the preliminary result from JADE showing differences between quark and gluon jets. Briefly, their result at that time was as follows. Take the three-jet events and arrange the jets according to energy as described in the preceding section. By Monte Carlo calculation using the Lund model[14], it is found that for W = 33 GeV in 51% of the events jet 3 is the gluon jet; 22% jet 2 is the gluon jet; 12% jet 1 is the gluon jet; and 15% the event is actually a two-jet event without a gluon jet. The JADE experimental result is that, for the same visible energy, the average transverse momentum $\langle p_T \rangle$ is larger for jet 3 than for jets 1 and 2. The question was raised whether this effect was due to the use of the visible jet energy as the variable.

JADE has now carried out this analysis[24,33] using instead the jet energies calculated from the angles between the jets. Fig. 22 shows, on the basis of model calculations at W = 33 GeV, the probability n_j for jet j being closest to the gluon direction as a function of the jet energy. Note that

$$W/3 \leq E_1 < W/2$$

$$W/4 \leq E_2 < W/2$$

and

$$E_3 \leq W/3 .$$

Therefore, for any given W, the overlap between E_1 and E_2 is from W/3 to W/2, that between E_2 and E_3 from W/4 to W/3, but E_1 and E_3 never overlap.

On the basis of 2048 planar 3-jet events (out of 18424 hadronic

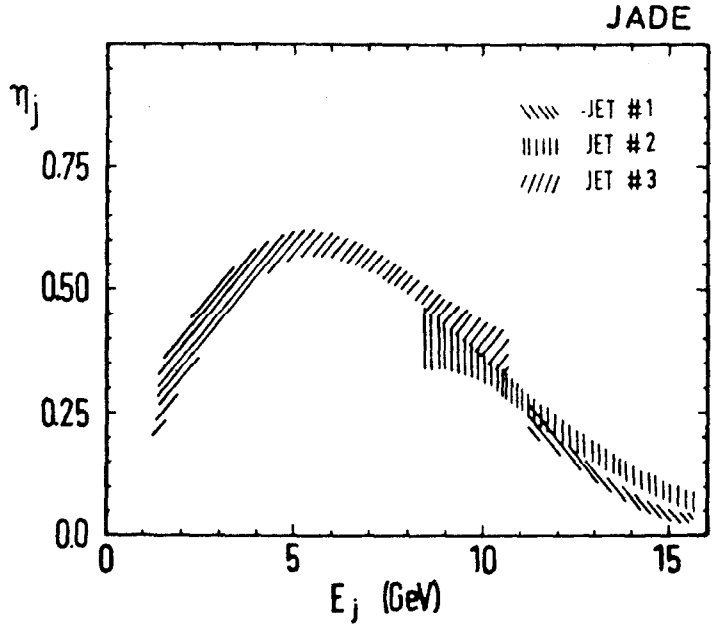


Fig. 22 - The probability η_j for jet j being closest to the gluon direction as a function of the reconstructed jet energy E_j obtained from model calculations at a fixed c.m. energy of 33 GeV. The widths of the shaded areas indicate the statistical errors.

events) at W between 29 and 36.4 GeV and 307 planar 3-jet events (out of 1945 hadronic events) at W = 22 GeV, the JADE result for the average transverse momenta of a jet is shown in Fig. 23(a). The g = q model calculation using Hoyer et al.[13] shown in Fig. 23(b) does not indicate any larger transverse momentum for jet 3, indicating that there is no significant bias in the selection of events. The experimentally observed larger transverse momentum for jet 3 can be reproduced by increasing the σ_q for the gluon from 330 MeV/c to 500 MeV/c (independent of energy), or by using the Lund model[14]. In this Fig. 23, the overlaps of the energy ranges for the three jets are much more than those kinematically allowed for any given W, as discussed in the preceding paragraph and Fig. 22. The reason is of course that the value of W range from 22 GeV to 36.4 GeV. In particular, the five data points indicated by arrows in Fig. 23(a) are from W = 22 GeV. Accordingly, as emphasized by the JADE Collaboration, the comparison is made between jet 3 at W = 29 to 36.4 GeV and jet 2 at W = 22 GeV. For this comparison, jet 3 has significantly larger average transverse momentum than jet 2 for the same jet energy.

In this comparison, it is assumed that, at the relatively low energy of W = 22 GeV, three-jet analysis is capable of identifying correctly the hadrons in the three jets. Note that a higher percentage of hadronic events at W = 22 GeV (307/1945 = 16%) is classified as three-jet events than at W = 29 - 36.4 GeV (2048/18424 = 11%). To avoid this assumption, JADE has carried out an alternative analysis[24,34] comparing jet 3 at the higher W with the quark jets from the two-jet events at W = 14 GeV. For the purpose of this comparison, the trans-

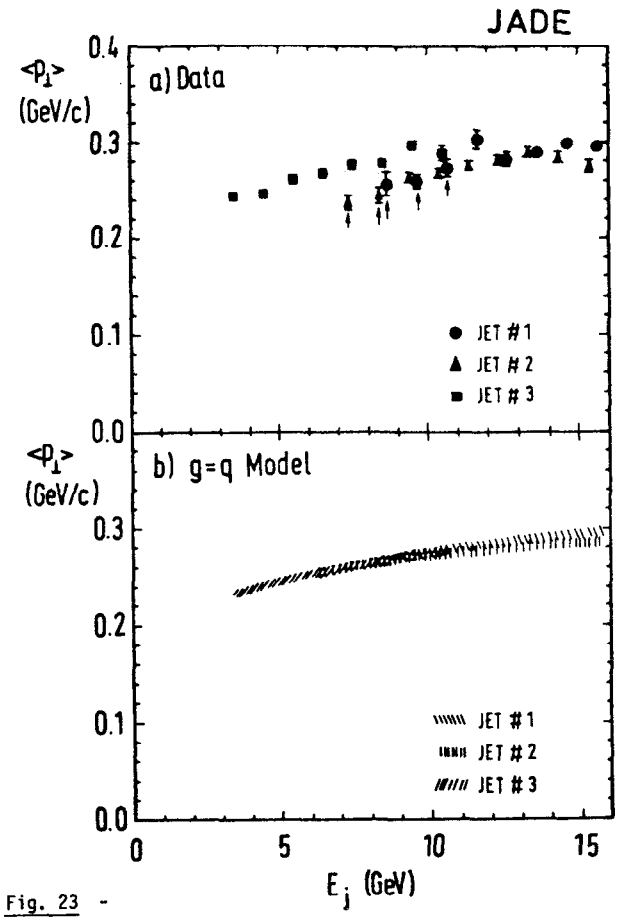


Fig. 23 - Average p_T distribution from JADE for the highest energy jets(E_1), medium energy jets (E_2), and lowest energy jets (E_3) as a function of the jet energy E_j calculated from the angles between the three jets. The center-of-mass energy is between 22 and 36.7 GeV. Fig. 20(a) is from the experimental data, where the arrows indicate the data points at W = 22 GeV. Fig. 20(b) is the prediction of the q = g Monte Carlo model.

verse momentum is calculated using only particles produced within 50° of the reconstructed jet axes, as shown in Fig. 24. The result of this comparison is shown in Fig. 25, both for the result of the Monte Carlo of Hoyer, Osland, Walsh, and Zerwas[13], and for the JADE experimental data. The conclusion is again that the gluon jet is broader than the quark jet.

B. Λ, $\bar{\Lambda}$ yield - TASSO (Preliminary)

A natural question to ask is: are there more or less baryons in gluon jets compared with quark jets of the same energy? To investigate this problem, TASSO has studied the yield of Λ and $\bar{\Lambda}$ in the jets with jet energy around 7 GeV from three-jet events at W = 34 GeV, and compared the result with the corresponding yield from two-jet events at W = 14 GeV[35]. The three-jet analysis of Wu and Zobernig[36] was applied to the 20,014 hadronic events at W around 34 GeV, and 1402 events survived as three-jet candidates after the following cuts:

(a) $x_1 < 0.9$, where x_1 is defined in Sec. 4;

(b) for each of the three jets as determined by the three-jet analysis, the sum of the absolute values of the momenta of the charged particles is required to be larger than 1.5 GeV/c; and

(c) the angle between the normal to the events plane and the beam axis is required to be less than 70°.

The TASSO results on the yields of Λ and $\bar{\Lambda}$, after correction for acceptance, are tabulated in Table 4 for W = 14 GeV, 22 GeV, and around 34 GeV (separately for all events and for the three-jet candidates). Note that at 34 GeV the yield is significantly higher for the three-jet candidates than for all events:

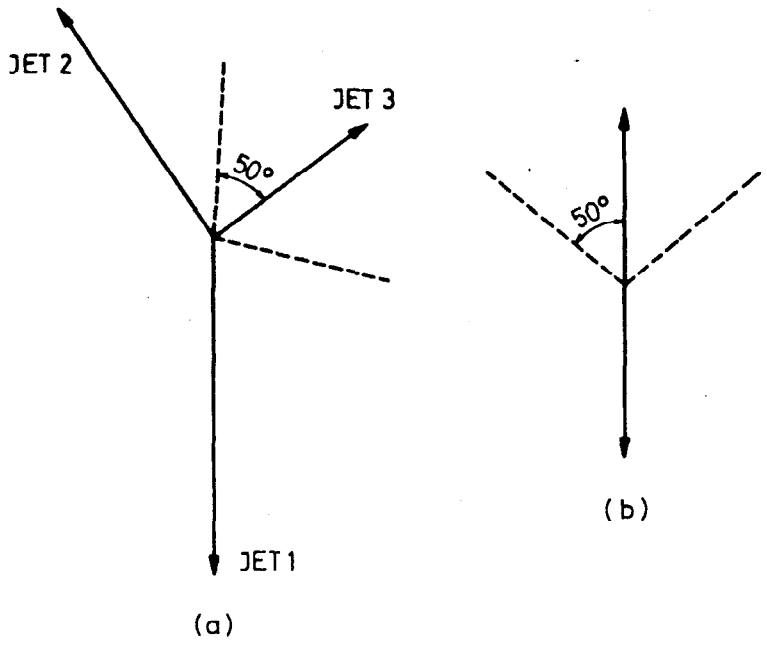


Fig. 24 - Kinematics for the JADE comparison of the p_T-distribution of (a) jet 3 (mostly gluon jet) at the center-of-mass energy of 33 GeV and of (b) two-jet events at 14 GeV. The p_T is calculated on the basis of the particles within a 50° cone of the jet axis.

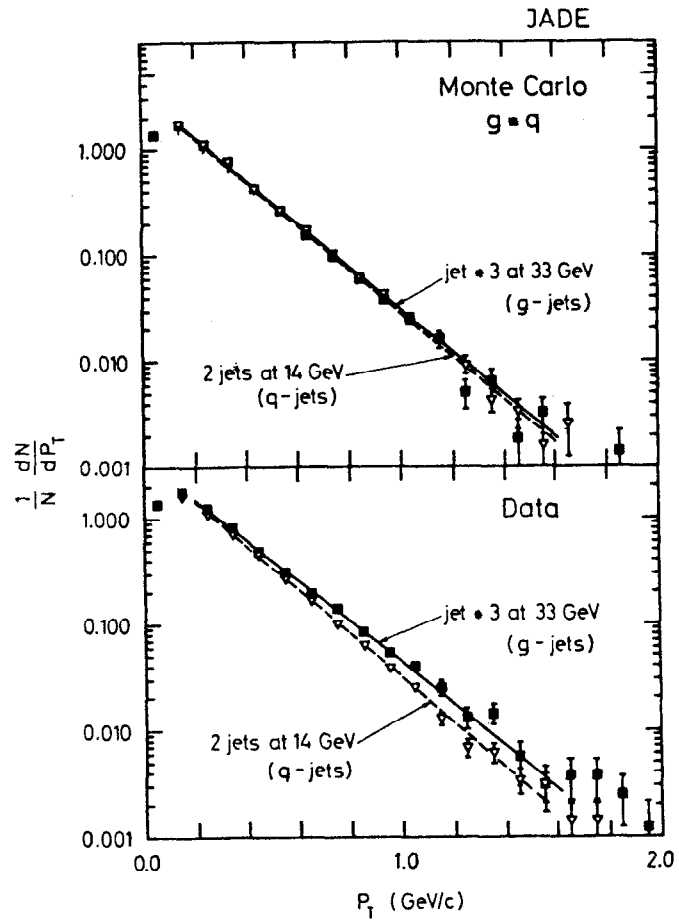


Fig. 25 - JADE comparison of the p_T-distribution of jet 3 (mostly gluon jet) at the center-of-mass energy of 33 GeV (upper straight lines) and of two-jet events at 14 GeV (lower straight lines). The upper figure is from the Monte Carlo of Hoyer et al., and the lower one from the experimental data.

$$\frac{\Lambda, \bar{\Lambda} \text{ yield for three-jet candidates}}{\Lambda, \bar{\Lambda} \text{ yield for all events}} = 2.0 \pm 0.5 ,$$

while the ratio of charged multiplicity is close to 1

$$\frac{\text{charged multiplicity for three-jet candidates}}{\text{charged multiplicity for all events}} = \frac{13.5}{11.8} .$$

Table 4 - Λ, $\bar{\Lambda}$ yield from TASSO data (preliminary).

W(GeV)	type of events	corrected Λ, $\bar{\Lambda}$ yield per event
34	all events	0.30 ± 0.04
34	3-jet events	0.59 ± 0.12
22	all events	0.22 ± 0.04
14	all events	0.13 ± 0.04

The jets from the three-jet candidates from W = 34 GeV are separated into three bins according to the jet energy: 4-9 GeV, 9-13 GeV, and >13 GeV. The Λ, $\bar{\Lambda}$ yields per jet for these three bins are shown in Fig. 26 together with those for all events at W = 14, 22, and 34 GeV

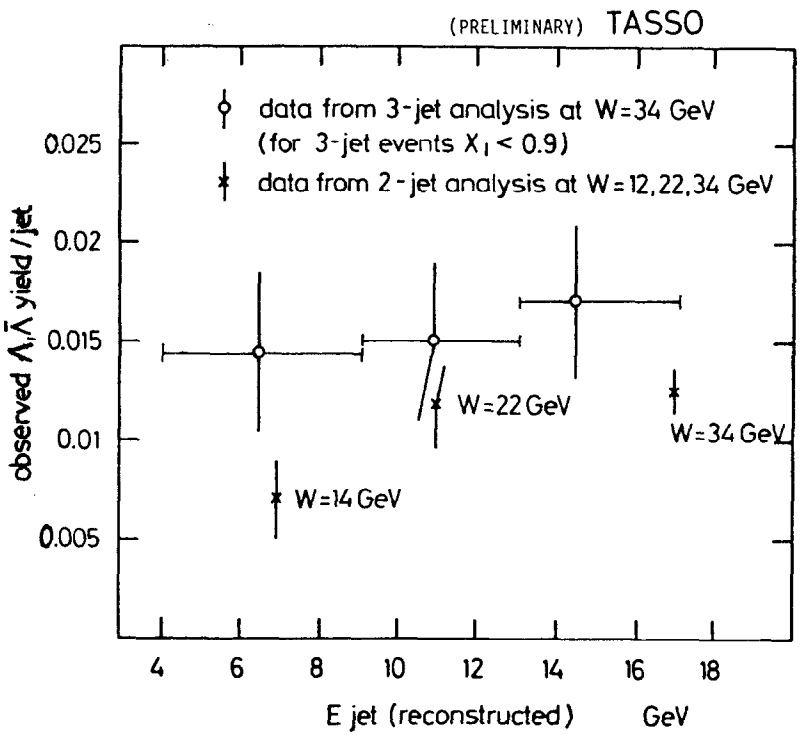


Fig. 26 - Observed Λ, $\bar{\Lambda}$ yields per jet from the three-jet candidates at W = 34 GeV, compared with those at W = 14, 22, and 34 GeV analyzed as two-jet events - TASSO.

analyzed as two-jet events. It is seen that the yield for the low energy jet, between 4 and 9 GeV, is higher than that for the 7 GeV jet from the two-jet events at W = 14 GeV. Since these low-energy jets at W = 34 GeV have about 50% gluon content, the results of FIG. 26 make it plausible that the yield of Λ and $\bar{\Lambda}$ is higher for gluon jet than for quark jet.

Related evidence has been obtained by the CLEO Collaboration at CESR[37]. They have found 0.25 ± 0.03 Λ, $\bar{\Lambda}$ per event at the resonance Υ(1S) but only 0.08 ± 0.01 at the nearby continuum. Since Υ (1S) decays predominantly into three gluons, this result is also interpreted to mean that there are more baryons in a gluon jet than in a quark jet.

6. PARTICLE IDENTIFICATION IN JETS

The knowledge of particle composition of the final state in e^+e^- annihilation is important for understanding of the fragmentation of quarks and gluons into hadrons. The following types of particles have been identified in jets and their inclusive cross sections measured:

$\pi^{\pm}$: TASSO, DELCO

π^0 : TASSO, CELLO

$K^{\pm}$: TASSO

K_S : TASSO, PLUTO, JADE, MARK II

$p, \bar{p}$: TASSO, JADE, MARK II

Λ $\bar{\Lambda}$: JADE, TASSO, MARK II

ρ^0 : TASSO

D* : MARK II, DELCO, TASSO (and CLEO at CESR)

At PETRA and PEP, TASSO, DELCO and HRS are the only detectors equipped with Cerenkov counters. The momentum ranges where charged particle separation has been achieved at TASSO[38] are listed in Table 5. Recently, the separation of charged particles by dE/dx measurements has been accomplished at TPC[39] of PEP, and is shown in Fig. 27. In this section, we concentrate mostly on the recent results on inclusive particle spectra from TASSO.

Table 5 - Momentum ranges for $\pi^{\pm}/K^{\pm}/p,\bar{p}$ separation for the various systems in the TASSO detector.

	Momentum range in GeV/c for	
	$\pi^{\pm}/K^{\pm}$ separation	$K^{\pm}/p,\bar{p}$ separation
Inner time-of-flight system	0.3 - 1.0	0.4 - 1.4
Hadron arm time-of-flight system	0.5 - 1.5	1.0 - 2.0
Cerenkov counter system	above 0.8	3 - 6 and above 10
Combined	above 0.3	0.4 - 2.0, 3 - 6, and above 10

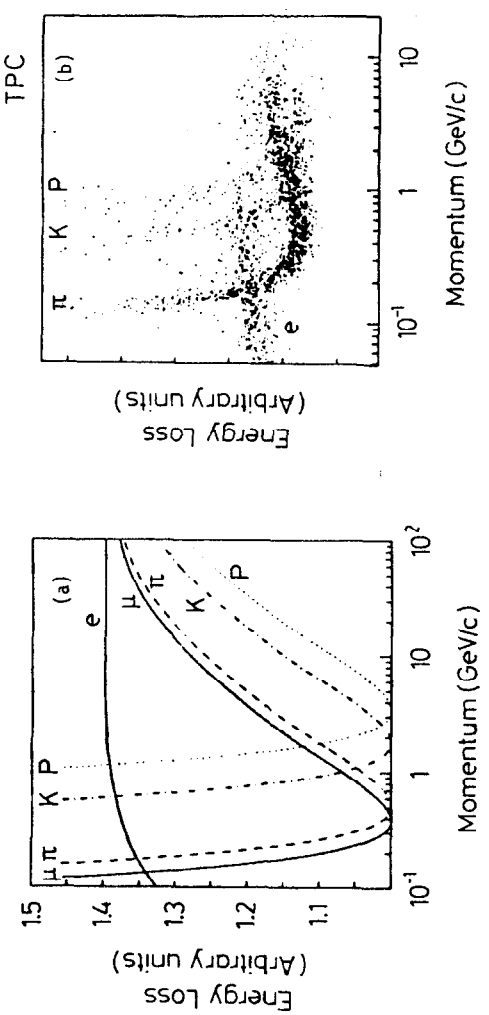


Fig. 27 - Particle separation by ionization loss in the relativistic rise region for the TPC detector at PEP: (a) the most probable energy loss vs. momentum, and (b) dE/dx vs. momentum for tracks in a sample of 1000 multihadron events at W = 29 GeV.

In Fig. 28 the differential cross sections $d\sigma/dp$ are given[26] for $\pi^{\pm}$, $K^{\pm}$, p, $\bar{p}$, Λ, and $\bar{\Lambda}$. The curves are drawn merely to guide the eye. As seen from this figure, the $\pi^{\pm}$ yield dominates for momenta below about 1 GeV/c. For example, the ratios $\pi^{\pm} : K^{\pm} : p, \bar{p}$ is approximately 100 : 10 : 1 at 0.5 GeV/c, but decrease to about 4 : 2 : 1 at 6 GeV/c. Because of phase space, all differential cross section $d\sigma/dp$ must approach zero as $p \to 0$, and hence must have maxima before dropping off. Furthermore, since the theoretically expected top quark has not yet been discovered experimentally, the total hadronic cross section is approximately proportional to s^{-1} from above the upsilon region to the highest PETRA energy. It is therefore useful to remove most of the phase-space effect and the energy dependence by considering the scaled cross sections

$$\frac{s}{\beta}\frac{d\sigma}{dx},$$

where $\beta = p/E$ is the velocity of the particle, and $x = E/E_{beam}$. The scaled inclusive cross sections for $(\pi^+ + \pi^-)$, $(K^+ + K^-)$, $(p + \bar{p})$, and $(\Lambda + \bar{\Lambda})$, as determined by TASSO, are shown in Fig. 29. Note that the cross section for $(K^+ + K^-)$, for example, is defined to be the sum of the cross section for K^+ and the cross section for K^-, not the cross section for the production of both a K^+ and a K^- in the same event. It is seen from Fig. 29 that the scaled cross sections for the various particles are rather similar in shape as functions of x.

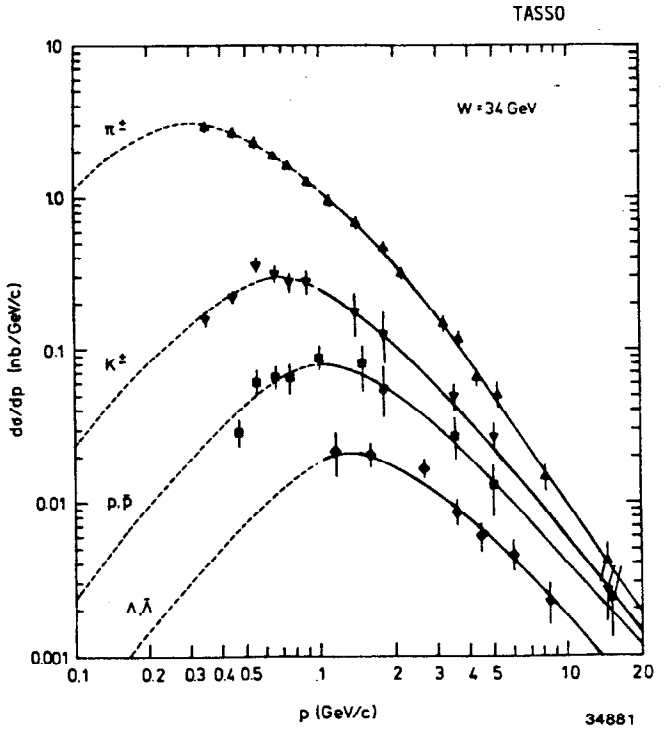


Fig. 28 - The differential cross sections for the inclusive production of $(\pi^+ + \pi^-)$, $(K^+ + K^-)$, $(p + \bar{p})$, and $(\Lambda + \bar{\Lambda})$ from TASSO at W = 34 GeV. The dashed curves are of the form $E/p^2\ d\sigma/dp \sim \exp(-bE)$ and the solid curves are drawn to guide the eye.

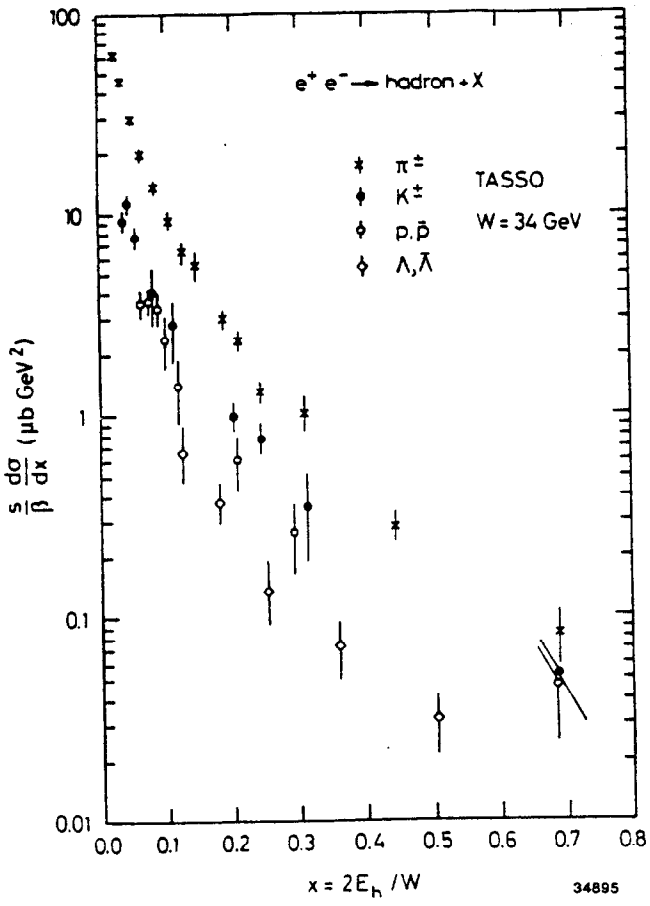


Fig. 29 - The TASSO scaled cross sections at 34 GeV for the inclusive production of $(\pi^+ + \pi^-)$, $(K^+ + K^-)$, $(p + \bar{p})$, and $(\Lambda + \bar{\Lambda})$.

The corresponding inclusive cross section for ρ^0 was recently obtained[22] at high energies and the result is shown in Fig. 30(a) for center-of-mass energy 34 GeV. Comparison with Field-Feynman Monte Carlo leads to the following value for the fraction of producing pseudo-scalar mesons:

$$\frac{P}{P+V} = 0.42 \pm 0.08 \pm 0.15.$$

This value has already been used in connection with the α_s determination in second order discussed in Sec. 2D.

The average number of hadrons per event $\langle n_i \rangle$ is calculated according to

$$\langle n_i \rangle = \frac{\int_0^{p_{max}} \left(\frac{d\sigma}{dp} \right)_i dp}{\sigma_{tot}} , \qquad (7)$$

where σ_{tot} is the total hadronic cross section. The extrapolation of $(d\sigma/dp)_i$ to zero momentum, as well as the interpolation over the momentum intervals for which particles were not identified, was done by parametrizing the invariant cross sections in the form

$$(E_i/4\pi\, p_i^2)\, (d\sigma/dp)_i = \sum_m A_{im} \exp(-B_{im} E_i) \qquad (8)$$

The average particle multiplicities for hadronic events at 34 GeV are tabulated in Table 6. The majority of the $\pi^\pm$, $K^\pm$, ... presumably result from the decay of heavier mass particles. Thus about 35% of the protons and anti-protons come from the decays of Λ and $\bar{\Lambda}$. In the case of ρ^0, integration over the measure range of $0.1 < x < 0.7$ gives $0.41 \pm 0.04 \pm 0.08$ ρ^0 per event, and extrapolation to all x yields the value given in Table 6.

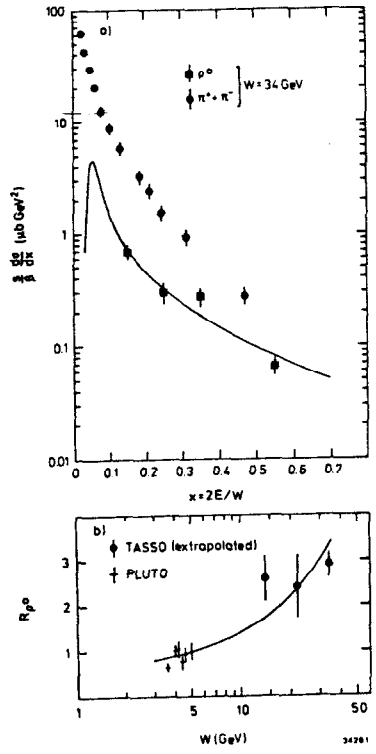


Fig. 30 TASSO data on the inclusive ρ^0 production. (a) The scaled cross section at the center-of-mass energy W = 34 GeV. Also shown is the cross section for $\pi^+ + \pi^-$ production at this energy. The smooth curve is the Field-Feynman Monte Carlo prediction for ρ^0 production assuming $P/(P+V) = 0.42$. (b) R_{ρ^0} for $e^+e^- \to \rho^0 +$ hadrons as a function of W (errors shown are statistical only). The curve shows a fit to the TASSO charged particle multiplicity in e^+e^- → hadrons normalized to R_{ρ^0}.

Since $\rho^0 \to \pi^+ + \pi^-$, there are 0.73 π^+ and 0.73 π^- per event from ρ^0 decay alone. If the productions of ρ^+, ρ^0, and ρ^- are assumed to be equal, then the decay of ρ gives 1.46 π^+, 1.46 π^0, and 1.46 π^- per event. In other words, approximately 30% of the π's come from ρ decay.

Table 6 - The average number of various particles contained in a hadronic event at 34 GeV. The number of $\pi^\pm$ contains those from the decay of ρ^0, and that for $p + \bar{p}$ contain those from the decay of $\Lambda + \bar{\Lambda}$. The data are from TASSO.

Particle	$\langle n_i \rangle$
$\pi^\pm$	10.3 ± 0.4 [38]
π^0	6.1 ± 2.0 [40]
$K^\pm$	2.0 ± 0.2 [38]
$K^0 + \bar{K}^0$	1.6 ± 0.1 [41]
ρ^0	0.73 ± 0.06 [22]
$p + \bar{p}$	0.8 ± 0.1 [38]
$\Lambda + \bar{\Lambda}$	0.28 ± 0.04 [35]

The average particle multiplicities are compared with lower-energy data for ρ^0 in Fig. 30(b)[22], and for $\pi^\pm$, $K^\pm$, and $p,\bar{p}$ in Fig. 31[38]. In all cases, the increase is roughly proportional to that of the total multiplicity.

Another way to present the data is to show the particle fractions as functions of the hadron momentum. The recent TASSO data[38] are shown in Fig. 32. For low momenta, most of the particles are pions, as already discussed. At W = 34 GeV, the ratios $\pi^\pm : K^\pm : p,\bar{p}$ are 0.55 : 0.30 : 0.15 at 5 GeV/c, and are 0.45 : 0.30 : 0.25 above 10 GeV/c. The DELCO[42] and TPC[43] data, shown in Figs. 33 and 34 are consistent with those of TASSO.

7. SEARCH FOR CHARGED HIGGS AND TECHNIPIONS FROM 4-JET EVENTS - TASSO

In current theories of weak interactions, spin-zero particles are needed in order to generate masses for the intermediate vector bosons W and Z^0. In the original Higgs mechanism[4] used in the Weinberg-Salam theory[1], the spin-zero particle is elementary and has no charged partner. If there are charged partners, these charged Higgs[44] can be pair produced in e^+e^- annihilation and, similar to the neutral Higgs, decay predominantly into the heaviest quarks and leptons that are kinematically allowed. If, in contrast to the standard model, these spin-zero particles arise from dynamical symmetry breaking, then they are composite. While the concept of dynamical symmetry breaking is

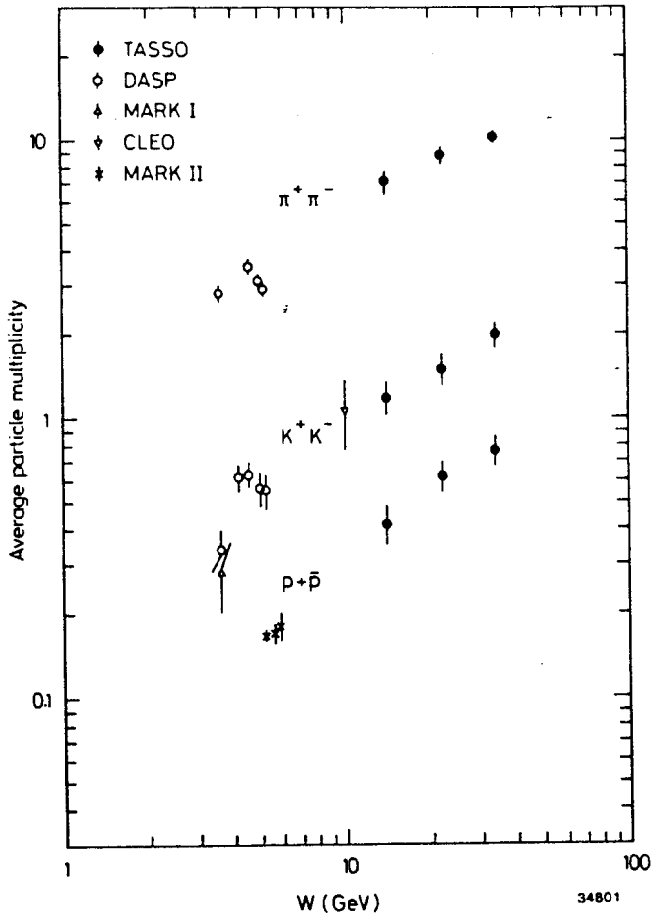


Fig. 31 - Average particle multiplicities for $\pi^{\pm}$, $K^{\pm}$, and $p,\bar{p}$ as functions of the center-of-mass energy W.

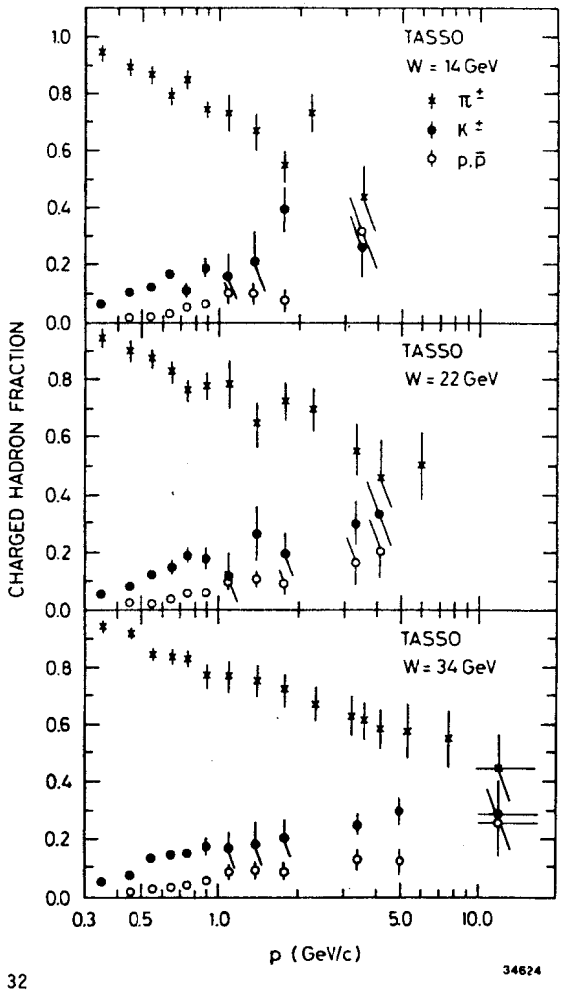


Fig. 32

Fractions of $\pi^{\pm}$, $K^{\pm}$, and $p,\bar{p}$ as functions of particle momentum at center-of-mass energy W = 14, 22, and 34 GeV. These data are from TASSO.

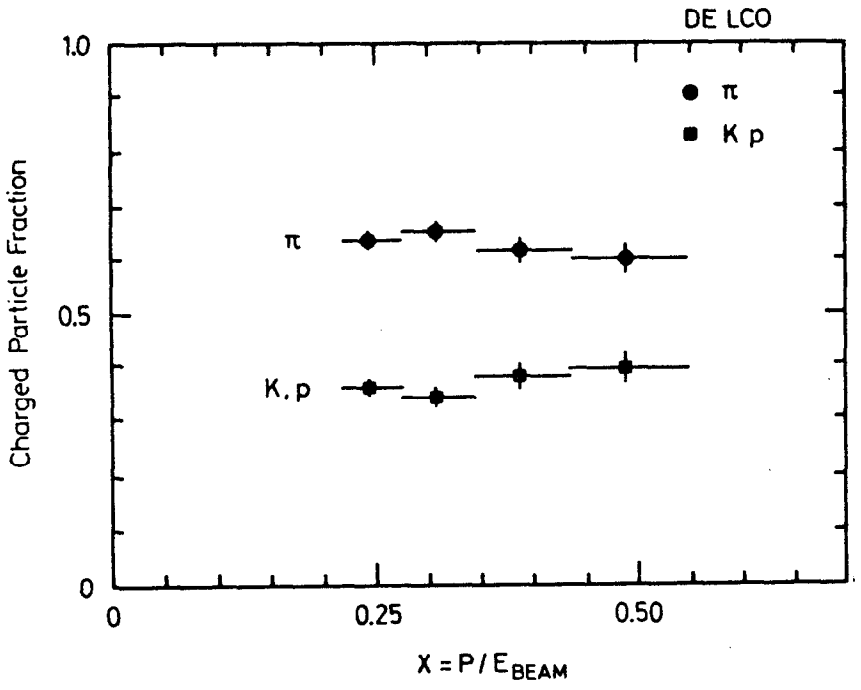


Fig. 33 - Fractions of $\pi^{\pm}$ and $K^{\pm}$ + $p,\bar{p}$ at W = 29 GeV from DELCO. The sum is of course equal to 1. The vertical error bars do not include an estimated systematic error of 0.1 on each point.

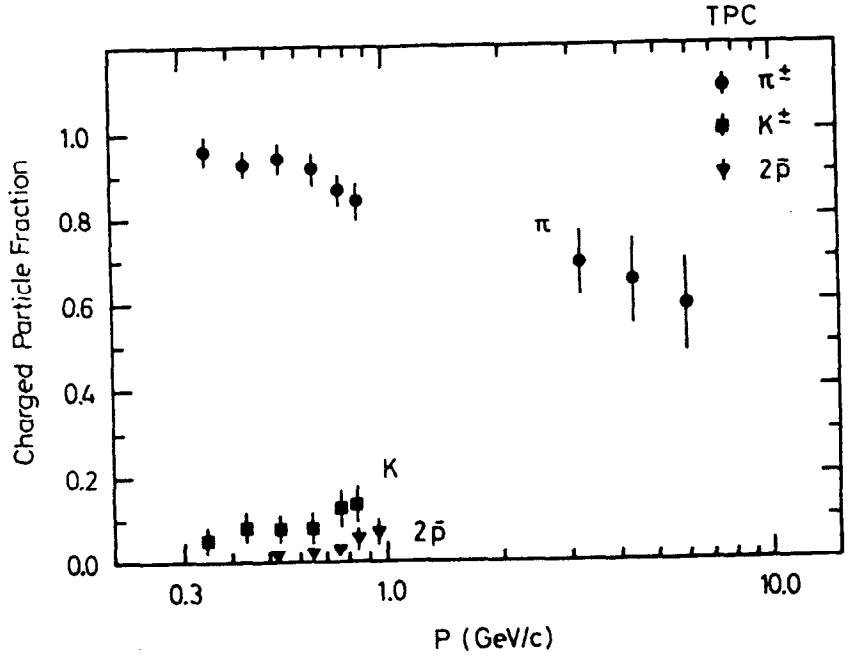


Fig. 34 - Fractions of $\pi^{\pm}$, $K^{\pm}$, and $2\bar{p}$ as functions of particle momentum at W = 29 GeV. These data are from TPC.

very attractive, specific additional assumptions are needed before concrete theoretical predictions can be obtained. At the present time, the most popular theory of this type is based on technicolor[45] and predicts the existence of spin-zero bosons of relatively low masses, called technipions. The mass of the charged technipions has been predicted to be in the range of 5 to 14 GeV[46]. Because of this low mass, this technicolor scheme, if correct, makes it possible to take a first look at the "mass problem" discussed in the Introduction. The decays into the heaviest kinematically allowed quarks and leptons are favored. The ratio of the leptonic and hadronic decay rates can be substantial or very small depending on the specific assumptions used[47]. If the leptonic decay mode is substantial, then the search for such spin-zero particles can be accomplished by studying the processes

$$e^+e^- \to H^+H^- \to (\tau\,\nu)\ (\text{hadrons}) \text{ and } (\tau^-\,\bar{\nu})\ (\tau^+\,\nu), \qquad (9)$$

where the symbol $H^\pm$ is used for both charged Higgs and technipions. In order to avoid any assumption about the size of the leptonic branching ratio, it is necessary to study also

$$e^+e^- \to H^+H^- \to \text{hadrons}. \qquad (10)$$

This process is shown schematically in Fig. 35, with the $H^\pm$ decaying into $c\bar{s}$ and $\bar{c}s$ before fragmentation into hadrons, giving rise to four jets.

The leptonic and semi-leptonic processes (9) have been studied by JADE[48], CELLO[49], MARK J[50], MARK II[51] and MAC[7]. The conclusion is that, with 95% confidence level, the hadronic branching ratio must be at least 80%.

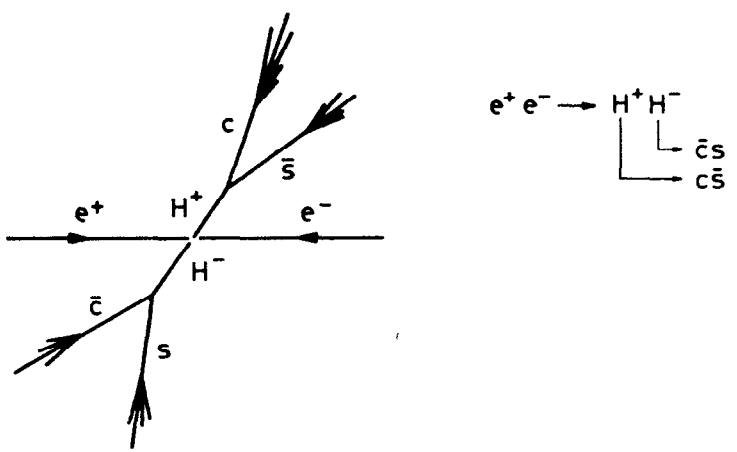


Fig. 35 - Schematic picture for the production and hadronic decay of $H^\pm$, leading to a four-jet final state.

With this knowledge, TASSO[52] undertook to study the process (10). The search for this process is not entirely straightforward since it has a small production cross section[53],

$$\frac{d\sigma}{d\Omega} = \frac{\alpha^2}{8s}\beta^3 \sin^2\theta_H$$

and

$$R_{H^+H^-} = \frac{\sigma(e^+e^- \to H^+H^-)}{\sigma(e^+e^- \to \mu^+\mu^-)} = \frac{1}{4}\beta^3 \qquad (11)$$

where β is the velocity of $H^\pm$ in the c.m. system and θ_H is the production angle with respect to the beam axis.

The final state from the process (10) consists of four hadronic jets, as shown in Fig. 35. Therefore the fast four-jet analysis[54], involving the repeated application of the three-jet analysis[36] based on generalized sphericity, can be used. However, the jet masses cannot be neglected in this case because they may be comparable to the masses of $H^\pm$. This generalization of including the non-zero jet masses in the four-jet analysis is straightforward, if the true jet velocity is approximated by the observed jet velocity[52].

The four-jet analysis is applied to both the experimental data and the Monte Carlo event simulation. Two decay processes were studied:

Case (A) $e^+e^- \to H^+H^-$, $H^+ \to \bar{c}\,s$, $H^- \to c\,\bar{s}$

i.e. $H^\pm$ decay exclusively into $c\,\bar{s}$ quarks;

Case (B) $e^+e^- \to H^+H^-$, $H^+ \to \bar{c}\,s$ or $\bar{c}\,b$, $H^- \to c\,\bar{s}$ or $c\,\bar{b}$

with $H^\pm$ decaying equally into $c\,\bar{s}$ and $c\,\bar{b}$.

The data were subjected to a number of cuts in order to maximize the signal of $e^+e^- \to H^+H^-$ over the background contribution from QCD processes. First, good four-jet candidates are selected by applying cuts in the total visible energy of the event, the minimum observed jet energy, the minimum reconstructed jet energy, and the opening angle between the jets from the same $H^\pm$ decay. After these cuts, each event is described in terms of the three variables $\Delta E = E_1 + E_2 - E_{beam}$, $m_{av} = \frac{1}{2}(m_{12} + m_{34})$, and $\theta_{av} = \frac{1}{2}(\theta_{12} + \theta_{34})$, where the various variables are shown in Fig. 36. Fig. 37 shows the two-dimensional plots in pairs of these three variables for Monte Carlo event with $m_H = 10$ GeV. It is seen that, roughly speaking, the events fill an ellipsoid whose size and orientation depends on m_H.

By a linear transformation on the three variables, the tilted ellipsoid is transformed into a sphere. The distributions of the experimental data and the Monte Carlo simulation are shown in Fig. 38 versus $(R/R_{rms})^3$, where R is the radius of the sphere and R_{rms} is the rms average of R over the Monte Carlo events for $e^+e^- \to H^+H^-$. It is seen that the two distributions are very different. In Fig. 39, the Monte Carlo distributions, one for $e^+e^- \to H^+H^-$ and the other for the QCD background, are compared with each other, and are found also to be quite different. The cut

$$R < R_{rms}$$

is therefore introduced to suppress the QCD background.

The analysis is repeated in steps of 100 MeV for m_H between 5 GeV and 14.5 GeV. With the cuts described above, the experimental data are compared with the Monte Carlo expectation in Fig. 40. The surviving

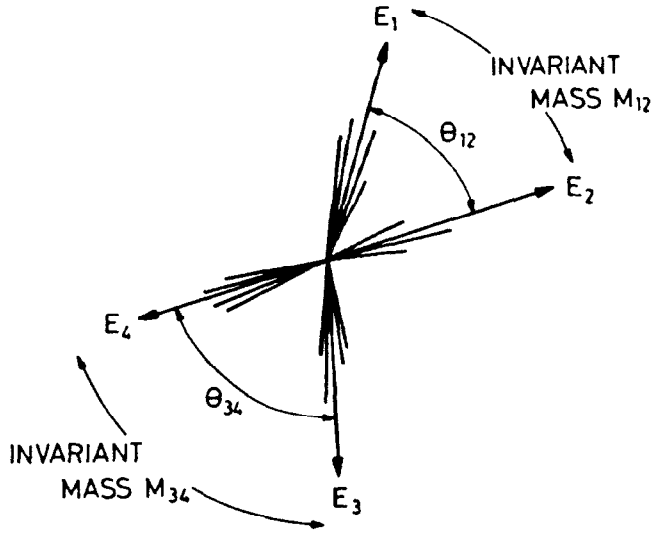


Fig. 36 - Some of the kinematic variables for a four-jet event from the pair production of $H^{\pm}$. The jets 1 and 2 are from the decay of one H, and jets 3 and 4 are from the other H.

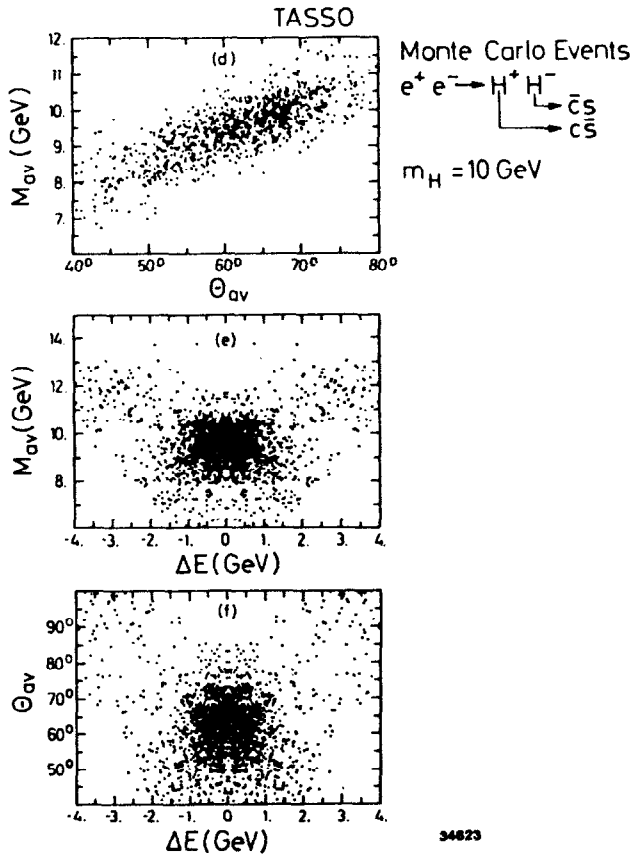


Fig. 37

Two-dimensional Monte Carlo event distributions of pairs of the three variables, the average reconstructed mass m_{av}, the average reconstructed opening angle θ_{av}, and the difference ΔE between the beam energy and the sum of the reconstructed energies of jet 1 and jet 2.

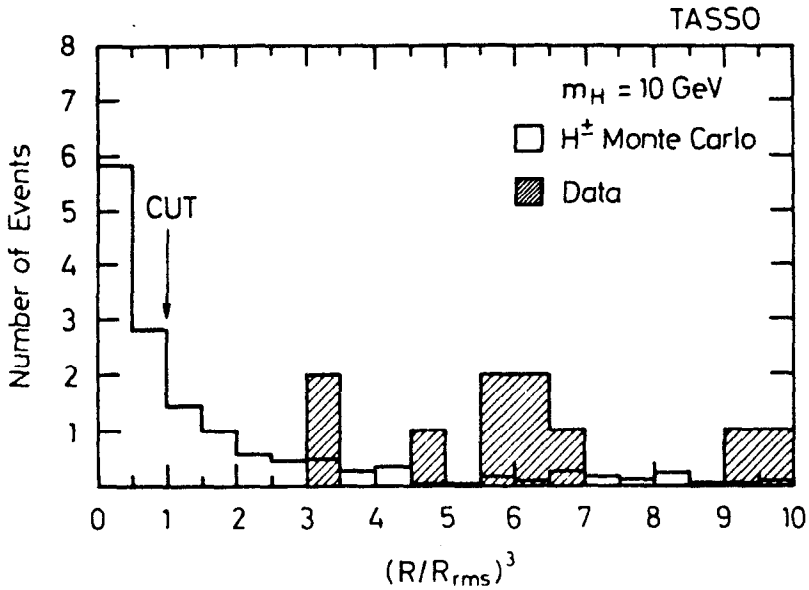


Fig. 38 - Monte Carlo and data (shaded) distributions of the one-dimensional variable $(R/R_{rms})^3$ analyzed at m_H = 10 GeV. The Monte Carlo distribution is normalized to the same total luminosity as the data. The position of cut $R = R_{rms}$ is indicated.

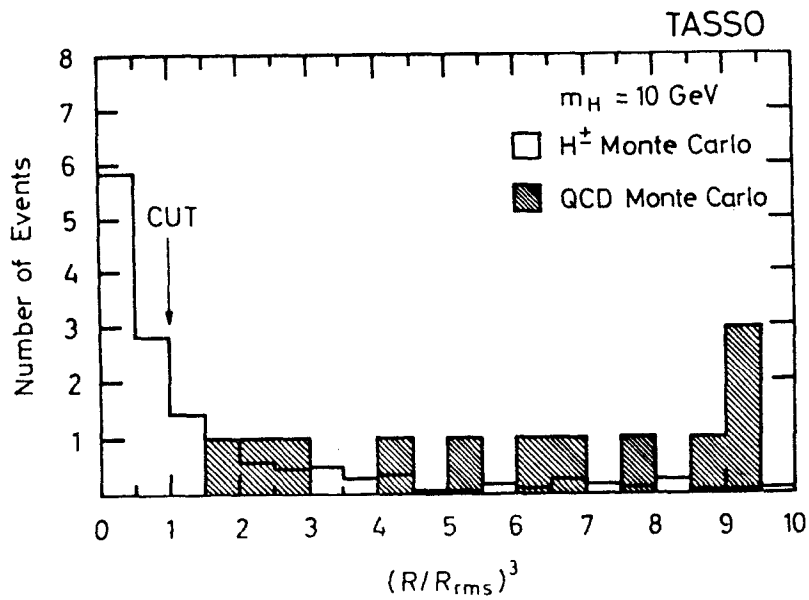


Fig. 39 - Comparison, at m_H = 10 GeV, of the $H^\pm$ and QCD Monte Carlo distributions of the one-dimensional variable $(R/R_{rms})^3$. The cut at $R = R_{rms}$ is also shown.

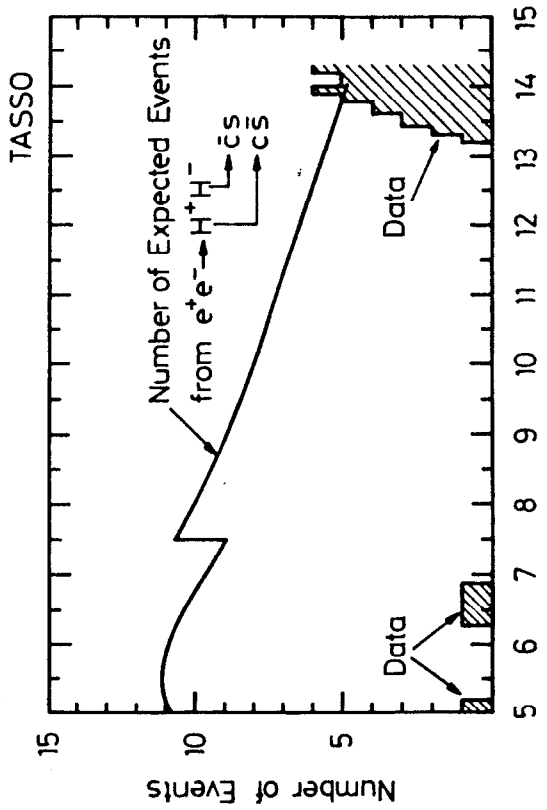


Fig. 40 - Number of expected events after all the cuts as a function of m_H for $e^+e^- \to H^+H^-$ with $H^+ \to c\bar{s}$, $H^- \to \bar{c}s$. Also shown is the number of events observed by TASSO as a function of m_H.

events above 13 GeV are consistent with QCD expectation. Note that Fig. 40 is really a compilation of many similar but independent analyses, each corresponding to a different value of m_H. In particular, the surviving event in the range of m_H between 6.3 GeV and 6.9 GeV is the same event. Finally, the region of hadronic branching ratio excluded by this TASSO result is shown in Fig. 41. Combined with the previous JADE result[48], at the 95% confidence level there is no point-like spin-zero charged particle in the mass range of 5 to 13 GeV. In particular, if the theoretical mass prediction does not change, the standard technicolor scheme is essentially ruled out.

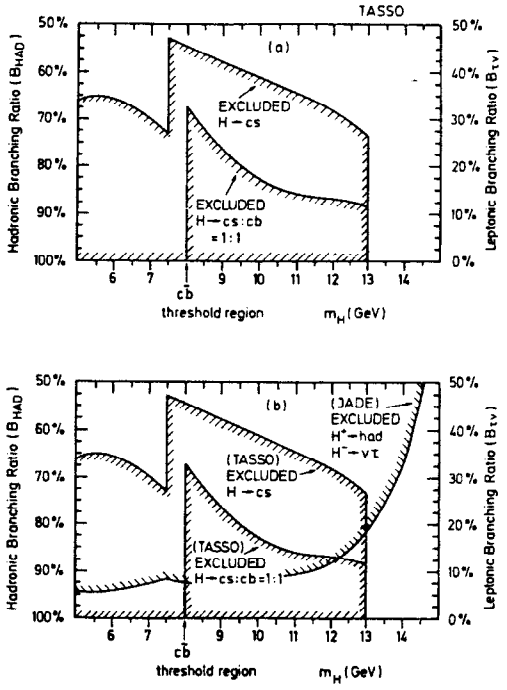


Fig. 41 (a): Limits on the hadronic branching ratio (B_{had}) as a function of $H^{\pm}$ mass from this experiment

for case (A) $e^+e^- \to H^+H^-$ with $H^+ \to c\bar{s}$, $H^- \to \bar{c}s$ and

for case (B) $e^+e^- \to H^+H^-$ with $(H \to cs)$: $(H \to cb) = 1 : 1$

The shaded area is excluded at the 95% confidence level.

The vertical scale on the right hand side of the figure indicates the corresponding leptonic branching ratio ($B_{\tau\nu}$) if the sum of $B_{had} + B_{\tau\nu} = 1$.

(b): Limits on the leptonic branching ratio from JADE for $H^+ \to \tau^+\nu$, $H^- \to \tau^-\bar{\nu}$ or $H^+ \to \tau^+\nu$, $H^- \to$ hadrons superimposed on Fig. 41(a).

Acknowledgements

I wish to thank Professors G.Feldman, F.Gilman and D.W.G.S.Leith for their hospitality at the 1982 SLAC Summer Institute on Particle Physics. I also wish to thank the many colleagues who provided me with their data. I am grateful to P.J.Dornan, A.Petersen, G.Rudolph, J. Sedgbeer, P.Söding, B.H.Wiik and G.Wolf for helpful and stimulating discussions.

REFERENCES

1) S.L. Glashow, Nucl. Phys. 22, 579 (1961)
S.Weinberg, Phys.Rev.Lett. 19, 1264 (1967)
A.Salam, Proceedings of the Eighth Nobel Symposium, May 1968, ed.: N.Svartholm (Wiley, 1968), p.367

2) B.H. Wiik, Proc. Intern. Neutrino Conf. (Bergen, Norway, 1979) p. 113
P.Söding, Proc. EPS Intern. Conf. on High energy physics (Geneva, Switzerland, 1979) p. 271
TASSO Collab., R.Brandelik et al., Phys. Lett. 86B (1979) 243
MARK-J Collab., D.P. Barber et al., Phys.Rev.Lett. 43 (1979) 830
PLUTO Collab., Ch.Berger et al., Phys.Lett. 86B (1979) 418
JADE Collab., W.Bartel et al., Phys.Lett. 91B (1980) 142

3) JADE Collaboration, W.Bartel et al., Phys.Lett. 108B (1982) 140
CELLO Collaboration, H.J.Behrend et al., DESY 82-019 (1982)
TASSO Collaboration, R.Brandelik et al., Phys.Lett. 110B (1982) 173
MARK J Collaboration, B.Adeva et al., Phys.Rev.Lett. 48 (1982) 1701
M.Davier, Rapporteur's talk, Proceedings of the 21st International Conference on High Energy Physics, Paris, 26-31 July 1982 and LAL (Orsay) Report 82/39 October 1982

4) P.W.Higgs, Phys.Rev.Lett. 12 (1964) 132; 13 (1964) 508
P.W.Higgs, Phys.Rev. 145 (1966) 1156
F.Englert, and R. Brout, Phys.Rev.Lett. 13 (1964) 321
G.S.Guralnik, C.R.Hagen, and T.W.B.Kibble, Phys.Rev.Lett. 13 (1964) 585
T.W.B.Kibble, Phys.Rev. 155 (1967) 1554

5) CELLO Collaboration, H.J.Behrend et al., DESY 82-061 (1982)

6) JADE Collaboration, W.Bartel et al., DESY 82-060 (1982)

7) MAC Collaboration (presented by D.Ritson), Proceedings of the21st International Conference on High Energy Physics, Paris, 26-31 July 1982

8) MARK II Collaboration, D.Schlatter et al., Phys.Rev.Lett. 49 (1982) 521

9) MARK J Collaboration (presented by J.Burger), Proceedings of the 21st International Conference on High Energy Physics, Paris, 26-31 July 1982

10) PLUTO Collaboration, Ch.Berger et al., Phys.Lett. 97B (1980) 459

11) TASSO Collaboration, R.Brandelik et al., Phys.Lett. 94B (1980) 437 and to be published

12) C.Basham, L.Brown, S.Ellis, and S.Love, Phys.Rev. D 19, (1979) 2018, and 24, (1981) 2383

13) P.Hoyer, P.Osland, H.E.Sander, T.F.Walsh and P.M.Zerwas, Nucl.Phys. B161, (1979) 349
A.Ali, E.Pietarinen, G.Kramer and J.Willrodt, Phys.Lett. 93B, (1980) 155

14) B.Andersson, G.Gustafson, and T.Sjöstrand, Z.Phys. C6 (1980) 235
T.Sjöstrand, Lund Preprint, LU TP 80-3(1980), LU TP 82-3(1982)
B.Andersson, G.Gustafson, and T.Sjöstrand, Nucl.Phys. B197 (1982) 45

15) MARK II Collaboration (presented by R.J.Hollebeek), Proceedings of 1981 International Symposium on Lepton and Photon Interactions at High Energies, Bonn, August 24-29, 1981

16) J.Ellis, M.K.Gaillard and G.G.Ross, Nucl.Phys. B111 (1976) 253
T.A.DeGrand, Y.J.Ng and S.-H.Tye, Phys.Rev. D16 (1977) 3251

17) R.D.Field and R.P.Feynman, Nucl.Phys. B136 (1978) 1

18) R.K.Ellis, D.A.Ross, A.E.Terrano, Phys.Lett. 45 (1980) 1226

19) K.Fabricius, G.Kramer, G.Schierholz, I.Schmitt, Z. Phys. C11 (1982) 315;

A.Ali, J.G.Körner, G.Kramer, Z.Kunszt, E.Pietarinen, G.Schierholz, and J.Willrodt, Phys.Lett. 82B (1979) 285, and Nucl.Phys. B167 (1980) 454

20) K.J.F.Gaemers and J.A.M.Vermaseren, Z.Physik C7 (1980) 81

21) T.Gottschalk, Phys.Lett. 109B (1982) 331, showed that the results of Fabricius et al. are consistent with those of R.K.Ellis et al. in the limit where the two different definitions of "thrust" are identical. See also G.Kramer, DESY 82-029 (1982)

22) TASSO Collaboration, R.Brandelik et al., DESY 82-046 (1982)

23) TASSO Collaboration, R.Brandelik et al., Phys.Lett. 113B (1982) 499

24) JADE Collaboration (presented by G.Heinzelmann), Proceedings of the 21st International Conference on High Energy Physics, Paris, 26-31 July, 1982

25) MARK II Collaboration (presented by G.Trilling), Proceedings of the 21st International Conference on High Energy Physics, Paris, 26-31 July, 1982

26) G.Wolf, Rapporteur's talk, Proceedings of the 21st International Conference on High Energy Physics, Paris, 26-31 July, 1982

27) TASSO Collaboration, R.Brandelik et al., Phys.Lett. 94B (1980) 437

28) PLUTO Collaboration, Ch.Berger et al., Phys.Lett. 97B (1980) 459

29) CELLO Collaboration, H.J.Behrend et al., Phys.Lett. 110B (1982) 329

30) TASSO Collaboration (presented by D.Lüke), Proceedings of the 21st International Conference on High Energy Physics, Paris, 26-31 July, 1982

31) Sau Lan Wu, Rapporteur talk, Proceedings of the 1981 SLAC Summer Institute on Particle Physics, July 27 - August 7, 1981, SLAC, Stanford, California, USA

32) J.Ellis and I.Karliner, Nucl.Phys. B148 (1979) 141

33) JADE Collaboration, W.Bartel et al., DESY 82-086 (1982)

34) JADE Collaboration, to be published

35) TASSO Collaboration, R.Brandelik et al., Phys.Lett. 105B (1981) 75 and to be published

36) Sau Lan Wu and Georg Zobernig, Z.Phys. C - Particles and Fields 2, (1979) 107

37) CLEO Collaboration (presented by F.M.Pipkin) Proceedings of the 21st International Conference on High Energy Physics, Paris, 26-31 July, 1982

38) TASSO Collaboration, M.Althoff et al., DESY 82-070 (1982)

39) TPC Collaboration (presented by B.Cabioud at IEEE Meeting, Washington, D.C., October 1982), TPC-LBL-82-76

40) TASSO Collaboration, R.Brandelik et al., Phys.Lett. 108B (1982) 71

41) TASSO Collaboration, R.Brandelik et al., Phys.Lett. 94B (1980) 91 and to be published

42) DELCO Collaboration (presented by J.Kirkby),Proceedings of the 21st International Conference on High Energy Physics, Paris, 26-31 July, 1982

43) TPC Collaboration, to be published

44) E.Golowich and T.C.Yang, Phys.Lett. 80B, 245 (1979)
L.N.Chang and J.E.Kim, Phys.Lett. 81B, 233 (1979)
H.E.Haber, G.L.Kane and T.Sterling, Nucl.Phys. B161, 493 (1979)
G.Barbiellini et al., DESY 79-027 (1979), and references therein

45) S.Weinberg, Phys.Rev. D13, 974 (1976); D19, 1277 (1979)
L.Susskind, Phys.Rev. D20, 2619 (1979)
S.Dimopoulos and L.Susskind, Nucl.Phys. B155, 237 (1979)
E.Eichten and K.D.Lane, Phys.Lett. 90B, 125 (1980)
M.A.B.Beg, H.D.Politzer and P.Ramond, Phys.Rev.Lett. 43, 1701 (1979)
S.Dimopoulos, Nucl.Phys. B168, 69 (1980)
M.E.Peskin, Nucl.Phys. B175, 197 (1980)
S.Dimopoulos, S.Raby and P.Sikivie, Nucl.Phys. B176, 449 (1980)
S.Dimopoulos, S.Raby and G.L.Kane, Nucl.Phys. B182, 77 (1981)
E.Fahri and L. Susskind, Phys.Rep. 74, 277 (1981)
A.Ali, DESY 81-032 (1981)
G.Barbiellini et al., DESY 81-064, and references therein

46) S.Dimopoulos, Nucl.Phys. B168, 69 (1980)
M.E.Peskin, Nucl.Phys. B175, 197 (1980)
J.Preskill, Nucl.Phys. B177, 21 (1981)
S.Chadha and M.E.Peskin, Nucl.Phys. B185, 61(1981) and B187, 541(1981)

47) J.Ellis, M.K.Gaillard, D.V.Nanopoulos and P.Sikivie, Nucl.Phys. B182, 529 (1981)

48) JADE Collaboration, W.Bartel et al., Phys.Lett. 114B, 211(1982)

49) CELLO Collaboration, H.J.Behrend et al., DESY 82-021 (1982)

50) MARK J Collaboration, A.Adeva et al., LNS Technical Report Number 125 (1982)

51) MARK II Collaboration, C.A.Blocker et al.,SLAC-PUB-2923 (1982)

52) TASSO Collaboration, M.Althoff et al., DESY 82-069 (1982)

53) N.Cabibbo and R.Gatto, Phys.Rev. 124, 1577 (1961)

54) Sau Lan Wu, Z.Phys. C - Particles and Fields 9, 329 (1981)

c, b, AND τ LIFETIME MEASUREMENTS IN e^+e^- INTERACTIONS

John A. Jaros

Stanford Linear Accelerator Center

INTRODUCTION

Measurements of the lifetimes of weakly decaying particles let us infer the strength of the interaction responsible for their decay. Two features of these interactions have emerged from studies of the lighter quarks and leptons. First, the interactions have universal strength; and second, the weak interaction mixes the physical quark states. By measuring the lifetimes of the charmed particles, the tau lepton, and hadrons containing the bottom quark, we are testing universality in a new domain and investigating new examples of mixing.

e^+e^- annihilations are a suitable laboratory for these studies. The heavy flavors are produced in sufficient numbers for lifetime determinations and are relatively easy to identify against the light flavor background. At PEP/PETRA energies, lifetimes in the 10^{-13} to 10^{-12} s range result in average decay lengths between 100 and 1000 μ. The techniques which have been successful at measuring decay lengths in this range, notably high resolution bubble chambers and nuclear emulsion, are not easily adaptable to the e^+e^- storage ring environment, with its megahertz repetition rates, occasional beam loss, and no-trespassing zone imposed by the beam pipe. However during the past two years, several of the PEP and PETRA experiments have begun

© J. Jaros 1982

to probe sub-millimeter decay lengths with drift chamber techniques, and just one year ago the Mark II collaboration at PEP installed a high precision drift chamber especially tailored for lifetime studies.

These electronic measurements at e^+e^- storage rings differ markedly from the optical techniques which have provided most of our present knowledge of charmed particle lifetimes. In the first place, they generally have much lower resolution. The optical experiments generally reconstruct the decay vertex position with an uncertainty which is small compared to the average decay length being measured, so the decay length error is purely statistical, $\Delta\lambda \approx \lambda/\sqrt{n}$. In most of the e^+e^- experiments reported so far, the decay vertex resolution (σ) is five to ten times larger than the expected lifetime. What is measured, instead of an exponential decay distribution, is the shift of the mean of an essentially Gaussian distribution to positive decay lengths. Of course, the statistical power of the method is diluted by the large errors, $\Delta\lambda = \sigma/\sqrt{n}$ where $\sigma >> \lambda$. The second difference between the techniques comes from their very distinct systematic errors. The optical techniques have been used in high background environments where events must have finite decay lengths to be recognized as charm candidates and the efficiency for detecting decay vertices varies with decay length. In the e^+e^- experiments, it has been possible (and necessary!) to select events without reference to decay lengths. However, systematic biases may be introduced when the vertex resolution is much larger than the average decay length.

This paper will focus on measurements of the τ and D^o lifetimes made with the Mark II vertex detector. This device, which is described below, has achieved a decay vertex resolution comparable to, instead of five to ten times greater than, the decay lengths being measured. Consequently, its statistical precision is only $\sim \sqrt{2}$ worse than the statistical limit, and the systematic errors are considerably reduced. The paper concludes with a description of lepton impact parameter measurements made by the JADE and MAC experiments which have been used to set upper limits to the B lifetime.

MARK II VERTEX DETECTOR

The Mark II vertex detector[1], Fig. 1, has been designed to optimize vertex resolution in the e^+e^- environment. It is a relatively short cylindrical drift chamber, 1.2 m long, with seven axial layers of drift cells. Four are about 11 cm from the beam line, and three at about 30 cm. It has 825 drift cells in all; the drift cell radius throughout the array is 0.53 cm. To keep multiple scattering to a minimum the chamber has been built directly outside a beryllium beam pipe 0.6% of a radiation length thick. The beam pipe serves as the inner gas seal for the chamber. The average resolution per layer in hadronic events is about 100 μ. When tracks are extrapolated to the vicinity of the interaction point, their accuracy is given by

$$\sigma(\mu) = \left(100^2 + \left(\frac{100}{P(\mathrm{GeV}/c)}\right)^2\right)^{1/2} ,$$

where the first term is the extrapolation error, and the second term

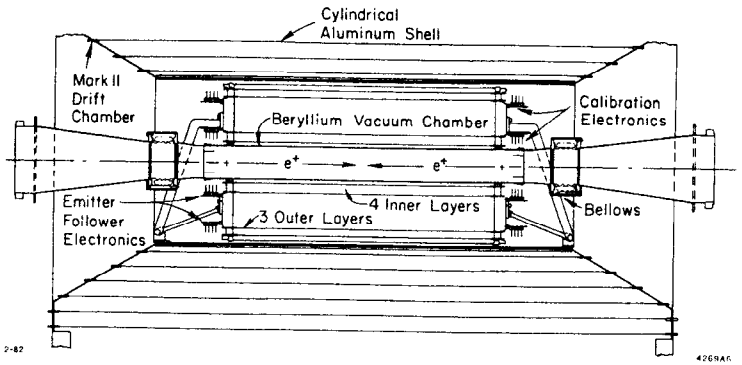


Fig. 1 Cross-section of the vertex detector as installed in the Mark II detector.

is due to multiple coulomb scattering in the beam pipe and chamber. Figure 2 shows the measured distance between the two tracks in Bhabha events after extrapolation to the origin, and it demonstrates that $\sigma_t \simeq 100\ \mu$. The chamber was installed at PEP during September, 1981 and began taking data in December, 1981. During the 1981-82 running period at PEP, an integrated luminosity of 21 pb^{-1} was accumulated at 29 GeV center-of-mass energy. Most of this data sample was used for the τ lifetime and D^0 lifetime analyses presented below.

τ LIFETIME

1. Motivation. The τ lifetime provides a sensitive check of the standard model of weak interactions. The key assumption is that tau decay proceeds in direct analogy with muon decay; i.e., that the charged weak current mediating the decay has the universal Fermi strength and V-A structure, and that the tau neutrino is massless. With these assumptions, the tau lifetime can be related to the muon lifetime with two factors, one which accounts for the greatly increased phase space in the decay, and the other for additional decay channels:

$$\tau_\tau = \tau_\mu \cdot \left(\frac{m_\mu}{m_\tau}\right)^5 \cdot B\ (\tau \to e\nu\bar{\nu})$$

Experimentally[2] $B(\tau \to e\nu\bar{\nu}) = 17.6 \pm 1.1\%$, so $\tau_\tau = 2.8 \pm 0.2 \times 10^{-13}$ s, where the error reflects the uncertainty in the electronic branching ratio.

How might this prediction fail? The most fundamental failure would be that the tau coupling strength is not universal. This

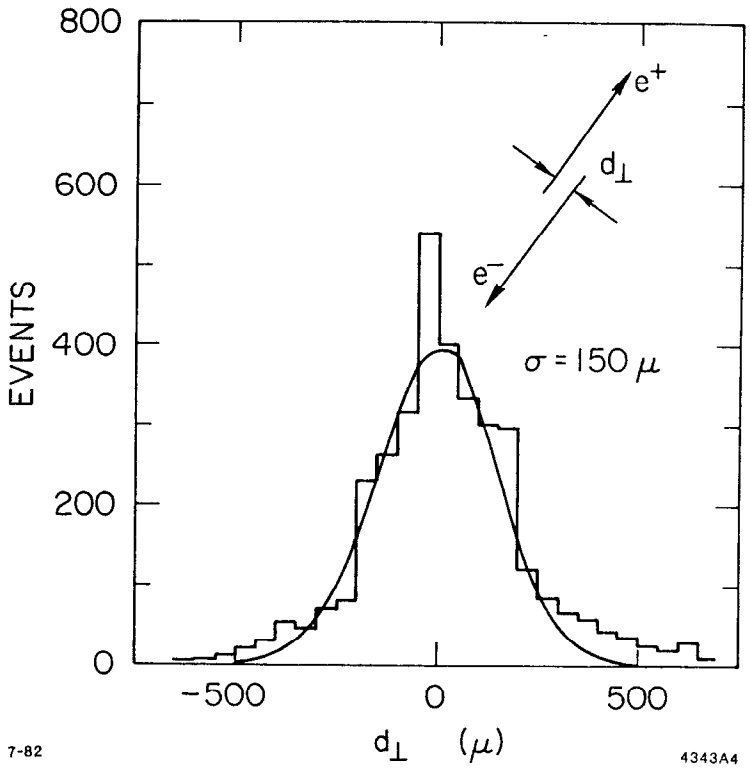


Fig. 2 Distance between tracks in Bhabha events, measured at the interaction point.

occurs, for example, in a model of Li and Ma[3] in which each lepton generation is associated with a unique gauge group -- hence unique weak bosons and couplings. The model predicts an increased τ lifetime, a proliferation of gauge bosons, and observable B^o-$\bar{B}^o$ mixing. Mixing among the quark generations in hadron decays leads to the apparent violation of universality, and of course mixing among the lepton generations would have the same effect. For example, if the tau neutrino mixed with a fourth generation neutral lepton whose mass was greater than the tau mass, the decay rate would be suppressed[4]. More trivially the tau lifetime would be extended if the tau neutrino were massive enough to limit significantly the phase space of the decay. There are other mechanisms that would alter the lifetime prediction. A charged Higgs with rather artificial couplings could increase the decay rate slightly[5]. If the tau were spin 3/2, its decay rate need not be canonical[6]. In contrast to predictions for the hadron lifetimes, where strong-interaction effects, quark mass uncertainties, and quark mixing complicate the situation, the τ lifetime prediction depends on only a few, fundamental assumptions about the weak interactions. If it is wrong, some interesting new physics is indicated.

2. Method. Tau leptons are pair-produced in e^+e^- annihilations, so each tau has the known beam energy. Thus we can measure the lifetime by determining the average decay length of the taus. At PEP energies, E_{cm} = 29 GeV, it is expected to be about 700 μ.

The decay length can be measured when the tau decays in the three-charged-prong topology. It is simply the distance between the production point, i.e., the beam position, and the position of the decay vertex. This same technique has been exploited by several PEP and PETRA experiments[7-10].

3. Event Selection. Tau production at PEP/PETRA energies is distinctive: low multiplicity, low mass, back-to-back jets are produced, which are easily distinguished from higher multiplicity hadron production. We select events in which at least one of the taus has decayed in the three-charged prong topology and the total charge of the prongs is zero. We require the three particle invariant mass to be in the range $0.7 < m_{3\pi} < 1.5$ GeV/c^2, and, to reject tau pairs produced by two-photon process, we further demand that the total energy in the event be at least one fourth the center-of-mass energy and the three-pion energy exceed 3 GeV. All three tracks must be well-measured in both the main drift chamber and the vertex detector. Figure 3a shows such an event in the Mark II detector. Figure 3b gives an enlarged view of the vertex detector for this event, and Fig. 3c shows a much enlarged view of the decay vertex in the vicinity of the interaction point.

4. Decay Length. The decay length is determined once we have measured the beam position, the decay vertex position, and the tau direction.

The rms beam size at PEP is 500 μ horizontally and about 50 μ vertically. The average beam position is remarkably stable from

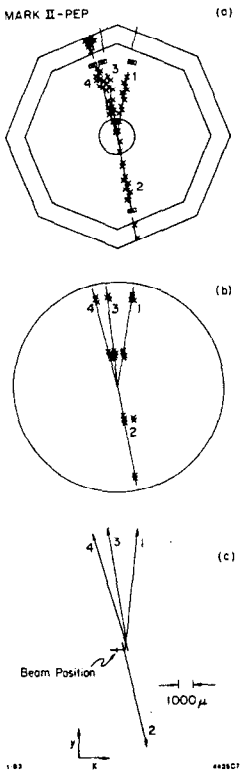


Fig. 3 (a) $e^+e^- \to \tau^+\tau^-$ as seen in the Mark II detector at PEP;
(b) closeup of the same event in the vertex detector;
(c) extreme closeup of the same event showing particle trajectories extrapolated to the vicinity of the interaction point.

one fill to the next. Over the course of the entire experiment the horizontal beam position varied less than 2 mm and the vertical beam position, 0.5 mm. We measured it by finding the average intersection point for an ensemble of well-measured tracks. As a cross check, we have compared this determination of the beam position to the vertex position measured in hadronic events. Figure 4 shows that these methods agree. The width of the Δx distribution is consistent with the known beam size, and the width of the Δy distribution is consistent with our vertex resolution. This demonstrates that the beams are stable.

The decay vertex position and its error ellipse are determined from the three pion trajectories and their associated errors with a chi-square minimization procedure. We exclude events with a vertex chi-squared per degree of freedom greater than 6. The best estimate for the projected decay length is then given in terms of the decay vertex position relative to the beam position (x_v, y_v), the sum of the beam and vertex error matrices (σ_{ij}), and the τ direction cosines (t_x, t_y) by the following expression:

$$\ell_p = \frac{x_v\sigma_{yy}t_x + y_v\sigma_{xx}t_y - \sigma_{xy}\left(x_v t_y - y_v t_x\right)}{\sigma_{yy}t_x^2 + \sigma_{xx}t_y^2 - 2\sigma_{xy}t_x t_y} \ .$$

The tau direction is accurately approximated by the direction of the 3π system. Then the decay length is

$$\ell = \frac{|\bar{p}_{3\pi}|}{p_{3\pi}^z}\,\ell_p \ ,$$

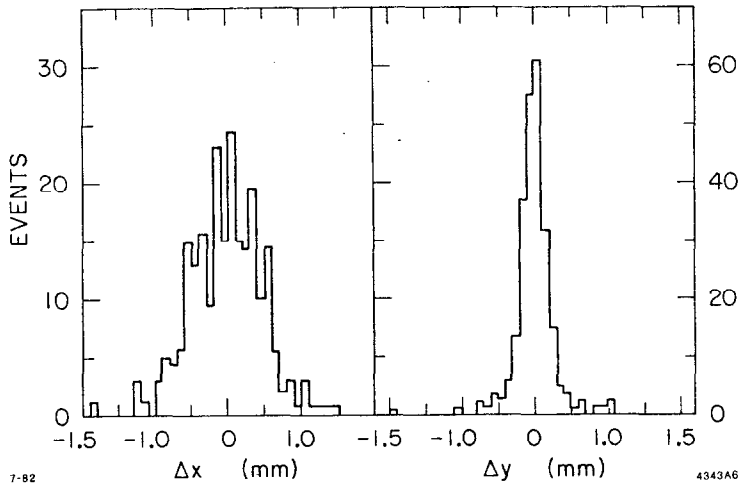


Fig. 4 Horizontal and vertical hadronic vertex positions relative to the beam position. Only those runs with tau decays are shown.

where $\vec{p}_{3\pi}$ is the total momentum of the three pion system.

Figure 5 shows the calculated error in the decay length, which depends on the opening angles and orientation of the decay, the tracking errors, and the beam size. In contrast to previous experiments, the average uncertainty in the decay length is comparable to, not five to ten times greater than, the expected decay length. Consequently, the statistical power of the experiment is improved by roughly this same factor, and the measurement bias is significantly reduced.

The measured decay lengths are shown in Fig. 6, where we have included only those events with decay length errors less than 1.5 mm. The mean of the distribution is obviously positive and its shape is asymmetric. We fit the distribution with a maximum likelihood technique which takes the decay length error into account event-by-event. The fitting function is the convolution of the Gaussian decay length error with an exponential decay distribution. We find that the average decay length is 710 ± 120 μ.

5. Checks and Corrections. We have checked our tracking, vertexing, and fitting programs with simulated data generated by Monte Carlo techniques. Roughly 1000 decays were generated for each of three lifetimes, $\tau_\tau = 0$, $\tau_\tau = 2.8 \times 10^{-13}$ s, and $\tau_\tau = 5.6 \times 10^{-13}$ s; they were then analyzed with the same programs used for actual data analysis. The simulated data are shown in Fig. 7. The zero-lifetime distribution is quite symmetric and centered near zero decay length. The nominal lifetime distribution

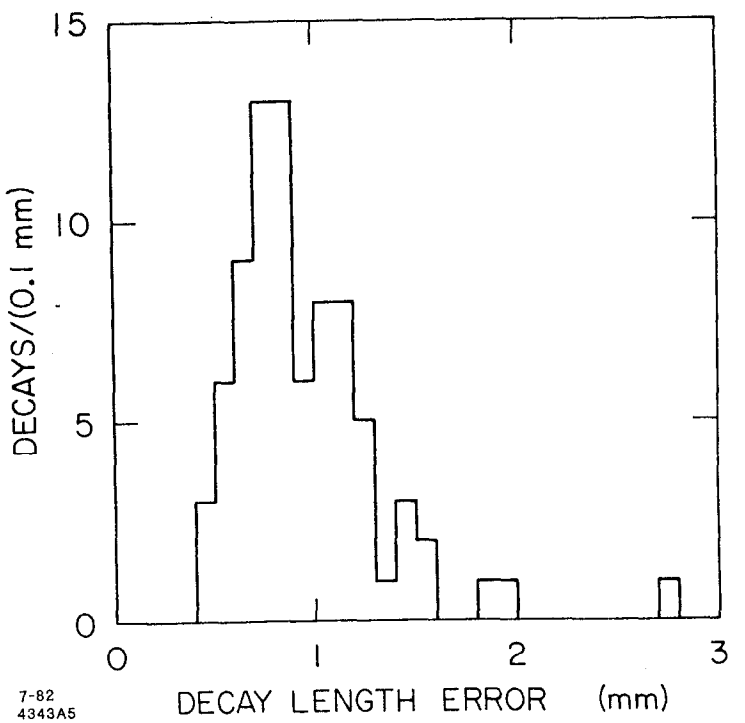


Fig. 5 Calculated error in the decay length.

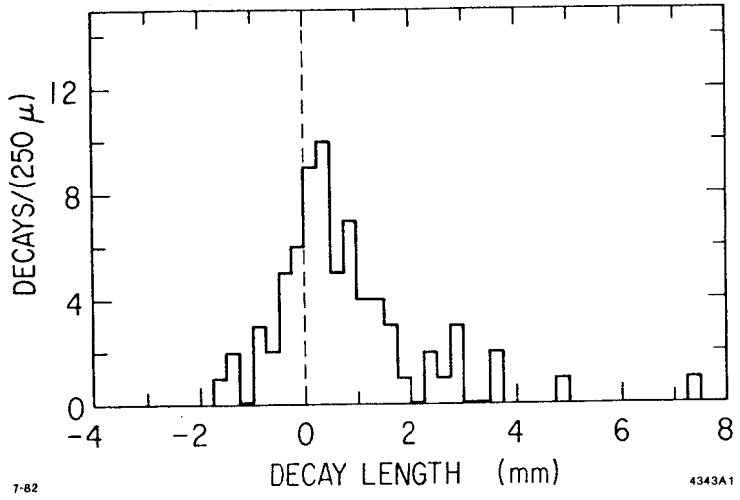


Fig. 6 Measured decay lengths.

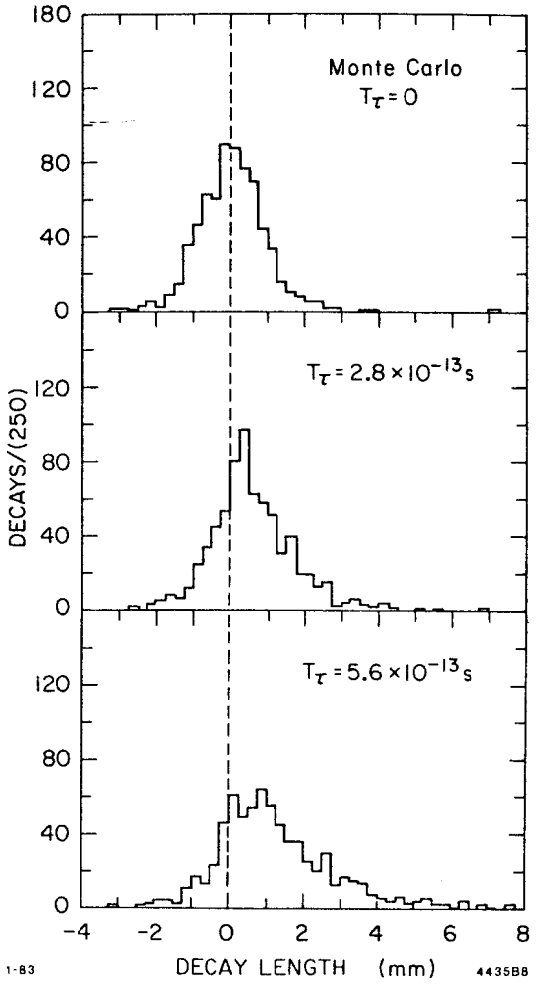


Fig. 7 Monte Carlo simulated decay length distributions for τ_τ = 0, 2.8 x 10^{-13} s, and 5.6 x 10^{-13} x.

nearly fits the data and is clearly shifted to positive decay lengths. The two-times nominal lifetime distribution shows an unmistakable exponential tail. Table I summarizes the average decay lengths generated for each of the three lifetimes, and the decay length determined by fitting the simulated data. This checks that our analysis procedure is reliable to the 50 μ level of accuracy.

Table I
Monte Carlo Simulation

Lifetime (10^{-13} s)	Average Decay Length Generated (μ)	Average Decay Length Fit (μ)
0	0	45 ± 25
2.8	644	605 ± 35
5.6	1338	1240 ± 50

We performed an additional check by analyzing pseudo-tau decays in hadronic events. Three-particle combinations were chosen in hadronic events to mimic the properties of the three-pion tau decays as accurately as possible. The average "decay length" for these combinations was 250 ± 40 μ; our hadron Monte Carlo events gave a decay length of 275 ± 50 μ. The presence of charm decays explains the finite decay length, and the Monte Carlo correctly simulates the data.

We studied systematic effects by re-analyzing the data with different assumptions about the beam position, beam width, resolution, and fitting function. The observed variations lead us to assign a systematic error of ± 150 μ to the decay length.

Using a Monte Carlo calculation, we estimate that 10% of our tau candidates are hadrons. This leads to a + 50 μ correction in the average decay length. Initial state radiation lowers the average tau energy from its nominal 14.5 GeV to 13.8 GeV.

6. Results and Conclusions. After correcting for hadron contamination and initial state radiation, we find $\tau_\tau = 3.31 \pm 0.57 \pm 0.60 \times 10^{-13}$ s, where the first error is the statistical error and the second is the systematic. Our measurement is compared to the other measurements which have appeared in the literature or were presented to the XXI International Conference of High Energy Physics, Paris, France in Table II. The number of decays studied and the average decay length error are also shown for comparison.

Table II

Experiment	Number of Decays	Average Decay Length Error (mm)	τ_τ (10^{-13} s)
TASSO[7]	599	10	0.8 ± 2.2
MARK II[8]	126	4	4.6 ± 1.9
MAC[9]	280	4	$4.1 \pm 1.2 \pm 1.1$
CELLO[10]	78	6	$4.7 \pm \frac{3.9}{2.9}$
MARK II Vertex Detector	71	0.9	$3.31 \pm .57 \pm .60$

All of the measurements are consistent with the expected lifetime. The present experiment confirms that the tau couples to the charged weak current with universal strength within the present statistical and systematic errors,

$$g_\tau/g_e = 0.92 \pm 0.086 \pm 0.090 \ .$$

If we assume that the coupling has the universal strength, we can set a limit on the mass of the tau neutrino. Figure 8 shows how the lifetime varies as a function of the tau neutrino mass[11] along with the 90% confidence level upper limit set by this measurement. We find $m_{\nu_\tau} < 0.49$ GeV/c^2, which is compatible with the .25 GeV/c^2 limit deduced from the shape of the decay lepton spectrum[12]. There is obviously little sensitivity to neutrino masses below about 150 MeV/c^2 with this method. We can also set a limit on how much the tau neutrino mixes with a heavy neutral lepton (N_o) whose mass exceeds the tau mass. The mixing angle ε is defined by the relation

$$\nu_\tau \equiv \nu'_\tau \cos\varepsilon + N_o \sin\varepsilon \quad ,$$

where ν_τ and N_o are the mass eigenstates and we've assumed there is only mixing with this heavier generation. At the 90% confidence limit $\sin\varepsilon < 0.65$. Clearly the present data do not exclude significant mixing with other lepton generations.

The prospects for improved precision and accuracy in measurements of the τ lifetime are good. An integrated luminosity of 100 pb^{-1} at PEP/PETRA energies would allow a statistical precision in the 5 to 10% range. Holding and believing the systematic errors to that level will be challenging until the vertex resolution is significantly smaller than the decay length. The Z^o should be a prolific source of $\tau\bar{\tau}$ pairs, so high statistics determinations of the τ lifetime will await LEP and the SLC. The SLC, with its micron-sized beam, is an especially interesting τ source.

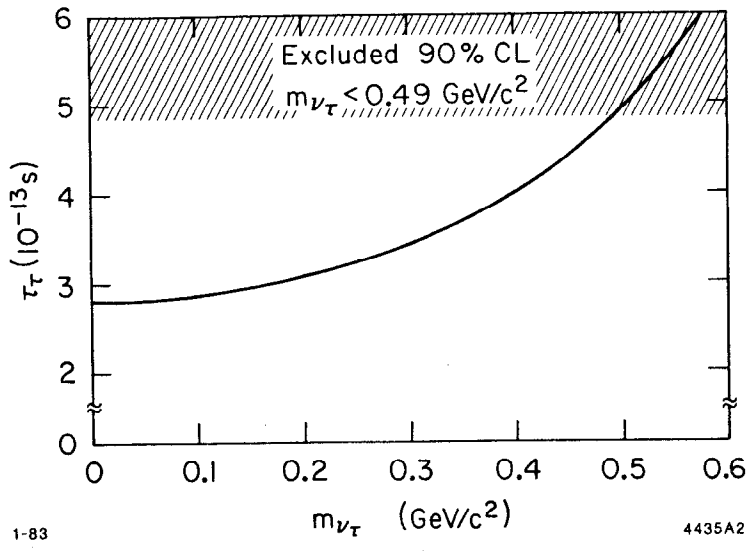


Fig. 8 Variation of the τ lifetime with the mass of the τ neutrino.

D^0 LIFETIME

There has been a flurry of experimental activity, and considerable experimental as well as theoretical confusion concerning charmed particle lifetimes in the past few years. As Kalmus[13] reported to the Paris conference, the situation seems to be stabilizing as follows: The D^0 lifetime is about 4×10^{-13} s, about half the D^+ lifetime of 9×10^{-13} s. As Fig. 9 shows, however, the experimental situation for the D^0 lifetime measurements is still a little rocky. All the experiments suffer from low statistics and possible systematic biases.

In the standard model, charmed hadron decays are expected to be unsuppressed (i.e., mixing with the heavier flavors is presumed to be small), so the decay rate is fixed by the quark mass. Although this idea predicts the correct magnitude for the charmed lifetimes, it does not account for the observed lifetime differences, indicating that free quark decay is not the sole decay mechanism. The pattern of charmed hadron lifetimes will help elucidate these decay mechanisms and hopefully serve as a guide to the decays of heavier flavors.

We have measured the D^0 lifetime with the Mark II vertex detector using a sample of D^0's which had been cleanly identified by the main tracking chamber. The measurement differs significantly from previous measurements which used optical techniques in that (i) events are selected independently of the observed decay length, and (ii) the vertex resolution is comparable to, not significantly

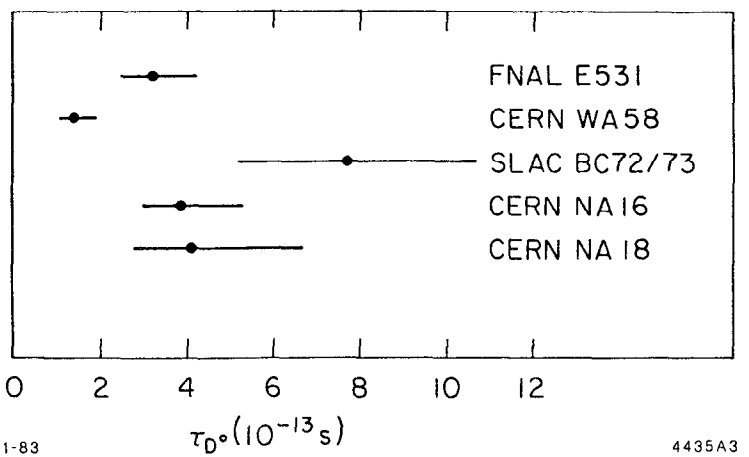


Fig. 9 World data on D^0 lifetime measurements taken from ref. 13.

smaller than, the average decay lengths. Like the others, our measurement suffers from low statistics. An integrated luminosity of 17 pb^{-1} gave seven well-measured D^o decays.

1. Event Selection. The clean event sample comes about by selecting D^o's from D^* decays. The technique is as follows. We first construct a two-particle invariant mass, arbitrarily assigning one particle the pion mass and the other the kaon mass. We select neutral combinations with $1.76 < m_{K\pi} < 1.96$ GeV/c^2 as D^o candidates, and consider the possible three-particle combinations, $m_{K\pi\pi}$. Figure 10 shows the mass difference, $m_{K\pi\pi} - m_{K\pi}$, displayed with two different cuts on the fractional energy of the three-particle combination, $z = E_{D^*}/E_{beam}$. When $z > 0.4$, one sees a clustering at .145 GeV/c^2 in the mass difference, which corresponds to $m_{D^{*+}} - m_{D^o}$. For the lifetime analysis below, we select events with $z > 0.6$. They seem to be free of background and so provide an ideal sample for study. This high momentum cut also makes it unlikely that these D^*'s have originated from B decays[14].

2. Lifetime Measurement. The decay vertex is determined by vertexing the K and π from the D^o. The decay length is then determined with the same technique used in the tau analysis above. The projected decay length is corrected using the measured D^o direction to find the actual decay length. It, in turn, is converted to the proper time using the measured D^o momentum. The average decay length is about 500 μ, and the average vertex error about 700 μ. Figure 11

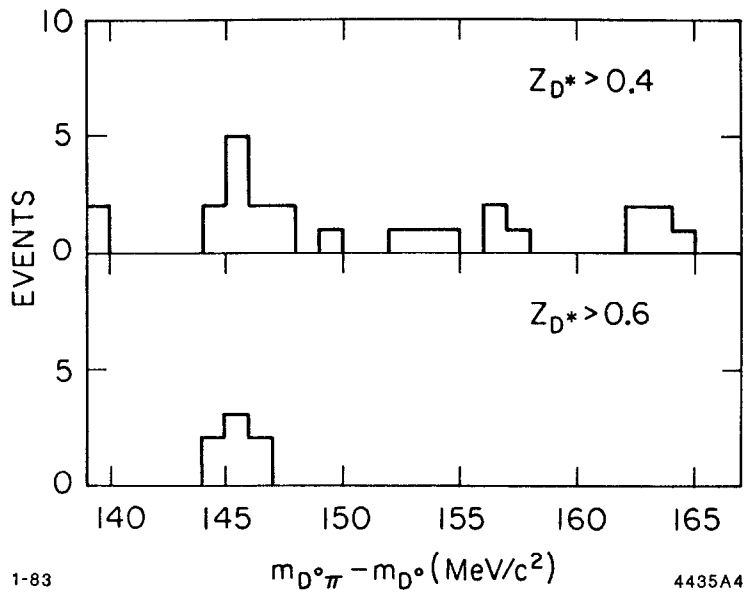


Fig. 10 $D^o\pi^\pm$ - D^o mass difference for D^o candidates decaying into $K\pi$.

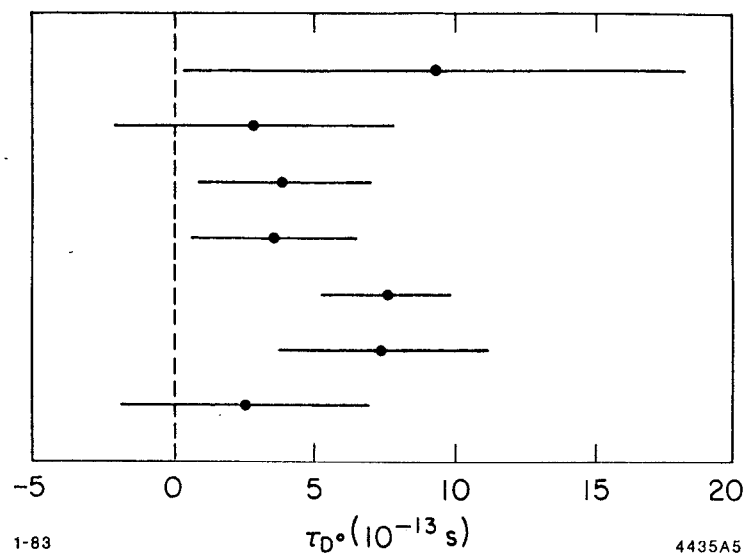


Fig. 11 Measured proper times for the seven D^0 events.

shows each of the 7 measurements with its error. As in the τ measurement, we perform a maximum likelihood fit using the convolution of a Gaussian resolution function with an exponential decay distribution as a fitting function. We have checked the analysis procedure on Monte Carlo data and considered its sensitivity to errors in the beam position, the resolution function, etc. We find the D^0 lifetime to be $\tau_{D^0} = 3.7 \pm \frac{2.5}{1.5} \pm 1.0 \times 10^{-13}$ s, where the first error is statistical and the second systematic. This result is in agreement with the current world average. The experiment is continuing, so we hope to increase the statistical significance of this measurement.

LIMITS ON THE B MESON LIFETIME

If their decays were not suppressed, the hadrons containing the b quark would be expected to decay with a lifetime

$$\tau^0_B \sim \tau_\mu \cdot \left(\frac{m_\mu}{m_b}\right)^5 \cdot \frac{1}{9} = 10^{-15}\ \text{s} .$$

The (qualitative) factor 9 comes from the number of available final states. The B meson lifetime is expected to be longer, however, since the decay is suppressed by the presumably small mixing between the second and third quark generations. The B meson lifetime thus gives a measure of the quark mixing, at least if one assumes universal weak coupling strength. Several authors[15] have related the B lifetime to the quark mixing angles. Gaillard and Maiani express the lifetime in terms of the unsuppressed lifetime as

$$\tau_B = \left[\frac{9\tau_B^o}{2.75\ \sin^2\gamma + 7.69\ \sin^2\beta - 5.75\ \sin^2\beta\ \sin^2\gamma - .25\ \sin^4\gamma}\right]$$

In this parameterization, the relevant elements of the mixing matrix are $U_{ub} \equiv \sin\beta$ and $U_{cb} \equiv \sin\gamma\cos\beta\, e^{i\delta}$, with δ a phase factor. The numerical factors account for the variations in phase space among the various decay channels. Using constraints on the mixing parameters from β decay and the K_L^o/K_S^o mass difference, the same authors predict

$$\tau_B \geq 0.3 \times 10^{-13}\ \text{s}\ ,$$

which would imply decay lengths at PEP/PETRA energies $\geq 10\ \mu$.

1. Lepton Impact Parameter. Two experiments have obtained upper limits for the B lifetime by measuring the average impact parameter of energetic muons. Events are selected which have high mass jets and an identified high-momentum muon. These events are almost entirely due to charm and beauty production. Using the thrust axis as an estimate of the B meson direction, a signed impact parameter is determined from the lepton trajectory and the known beam position as shown in Fig. 12. In the limit where the parent hadron velocity and the velocity of the muon in both the parent frame and the lab frame are relativistic, the distribution of impact parameters becomes Lorentz invariant and is a measure of the lifetime of the parent. Let the impact parameter be Δ. Then the unprojected distribution is given[16] by

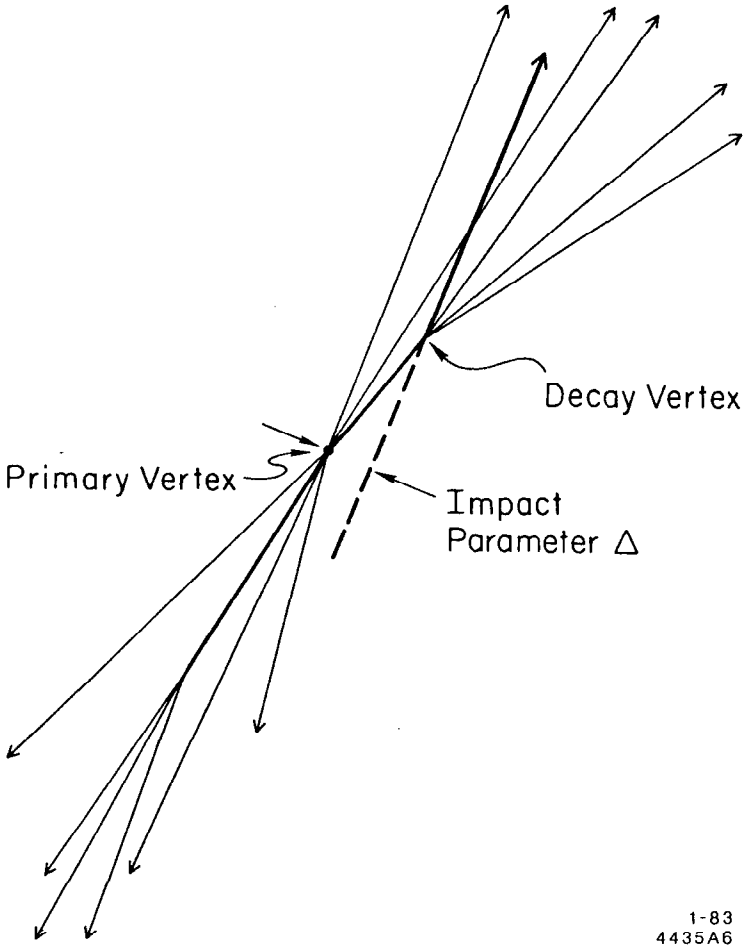


Fig. 12 Lepton impact parameter.

$$\frac{dn}{dy} = \int_0^\infty \frac{2yz^2\, e^{-z}\, dz}{(z^2+y^2)^2} \quad ,$$

where $y = \Delta/c\tau$. The distribution, which is graphed in Fig. 13, has a mean value $\bar{y} = \pi/2$. In practice, the projected distribution is measured, and its shape is somewhat distorted by event selection and particle identification cuts. The JADE group finds for their event cuts that

$$\bar{\Delta} = 200\ \mu \times \left(\frac{\tau_B}{10^{-12}\ s}\right) .$$

In addition to this procedure, the MAC experiment also measures the average displacement of the jet vertex from the beam position in a B-enriched sample of events.

2. Results and Comments. The upper limits obtained are as follows. The JADE experiment finds $\tau_B < 1.4 \times 10^{-12}$ s and the MAC experiment finds $\tau_B < 3.7 \times 10^{-12}$ s, both limits at the 95% confidence level. Thus there is as yet no evidence for a finite B lifetime, let alone Cabibbo suppression in B decays.

Several complications enter these analyses. The selection of events is model and Monte Carlo dependent, the ratio of leptons from charm to those from bottom is imperfectly known, and the estimation of the primary vertex in an event which presumably has secondary and tertiary vertices is problematical. What is measured in such studies is, of course, a mix of lifetimes from charged and neutral, charmed and beautiful mesons and baryons. Even so, the technique shows promise. As knowledge of bottom and charm production and

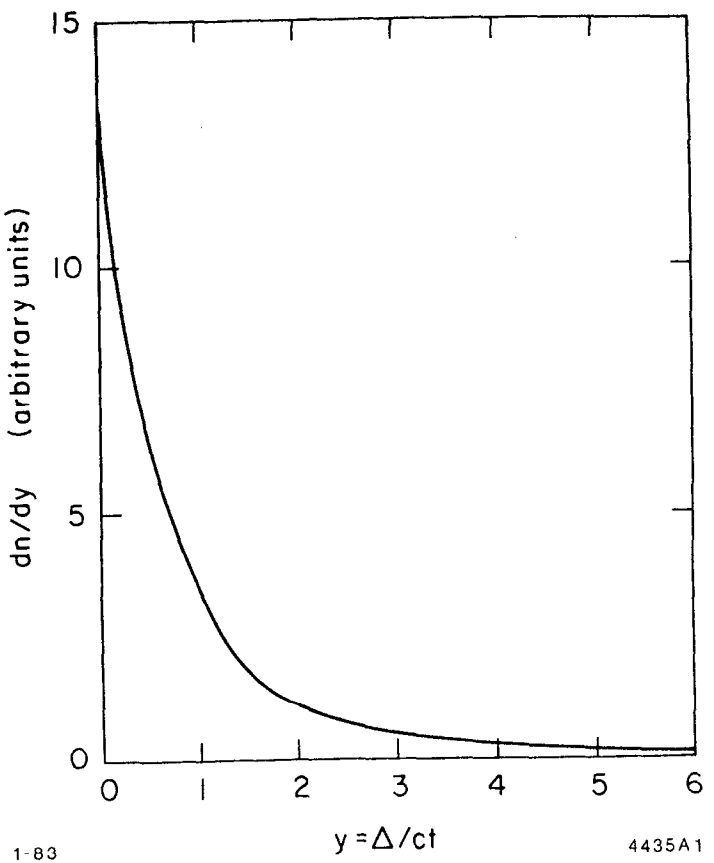


Fig. 13 Unprojected distribution of impact parameters from ref. 16.

semi-leptonic decay is refined, the results will lose their model dependence. Higher resolution devices will permit better estimates of the primary vertex, and more complicated analyses can separate charm and beauty effects.

CONCLUSIONS

Experiments at e^+e^- storage rings have successfully measured the τ and D^0 lifetimes and set interesting limits on the B lifetime. So far, the conventional wisdom has prevailed. The τ lifetime is consistent with prediction; there is no sign (but little sensitivity) of a violation of universality. The charmed particle lifetimes are roughly as expected, but richer in their phenomenology than anticipated. The B lifetime is still unknown.

The experimental art is developing rapidly. Several experiments have by now installed vertex detectors. Measurements of charmed particle lifetimes from e^+e^- experiments will complement the work that has been done at fixed target machines. Measurements of τ and B lifetimes may be the exclusive province of e^+e^- experiments for the next few years. Significant improvements in these measurements await higher resolution tracking devices, positioned closer to the interaction point, and larger data samples.

ACKNOWLEDGEMENTS

My colleagues in the Mark II collaboration collected and processed the data reported here in record time. Special mention must go to Dan Amidei, Nigel Lockyer, and George Trilling for their efforts in bringing the vertex detector into operation and their help with the τ lifetime analyses. The D^0 analysis was done by Larry Gladney, Gerson Goldhaber, and John Yelton.

REFERENCES

1. J. A. Jaros, in Proceedings of the International Conference on Instrumentation for Colliding Beam Physics, SLAC-Report 250, Stanford, California, (1982).

2. C. A. Blocker, et al., Phys. Lett. 109B, 119 (1982).

3. X. Li and E. Ma, Phys. Rev. Lett. 47, 1788 (1981).

4. D. Miller, Phys. Rev. D23, 1158 (1981).

5. G. L. Kane, SLAC-PUB-2326 (1979).

6. D. Miller, SLAC-PUB-2713 (1981).

7. R. Brandelik, et al., Phys. Lett. 92B, 199 (1980) and report to XXI International Conference on High Energy Physics, Paris, France (1982).

8. G. J. Feldman, et al., Phys. Rev. Lett. 48, 66 (1982).

9. D. Ritson, in Proceedings of the XXI International Conference on High Energy Physics, Paris, France, 1981 (to be published).

10. H. J. Behrend, et al., DESY 92/056 (1982).

11. S. Narison, CNRS 78/P.997 (1978).

12. W. Bacino, et al., Phys. Rev. Lett. 42, 749 (1979).

13. G. Kalmus, Rapporteur's talk at XXI International Conference on High Energy Physics, Paris, 1982 (to be published).

14. We estimate that 5% of the D^*'s are from B decays. See also C. Peterson, et al., SLAC-PUB-2912 (1982).

15. H. Harari, SLAC-PUB-2234 (1978); M. Gaillard and L. Maiani, LAPP-TH-09 (1979).

16. S. Petrara and G. Romano, Nucl. Inst. Meth. 174, 61 (1980).

PARTICLE SEARCHES IN e^+e^- EXPERIMENTS*

AT PEP AND PETRA

Kwong H. Lau

Stanford Linear Accelerator Center

Stanford University, Stanford, California 94305

INTRODUCTION

This talk reviews recent results in new particle searches performed by experiments at the high energy e^+e^- storage rings PEP and PETRA. I will concentrate on recent searches for :

a) hadrons with a new quark flavor,

b) spin-1/2 charged heavy leptons,

c) spin-0 charged leptons,

d) spin-0 point-like scalars or pseudoscalars, and

e) neutral heavy leptons.

Earlier results are summarized in review papers in Refs. 1-5.

---

*Work supported under contract No. DE-AC03-76SF00515.

© K. Lau 1982

SEARCH FOR A NEW QUARK FLAVOR

A search for a new quark production threshold has been made at PETRA up to a center of mass energy (E_{cm}) of 36.7 GeV by measuring the total multihadron production cross section, $\sigma(e^+e^- \rightarrow \text{hadrons})$.[6] In the naive quark-parton model, multihadron production proceeds via primary production of quark antiquark pairs which then fragment to hadrons. The multihadron production cross section, expressed in units of the muon pair production cross section , $\sigma(e^+e^- \rightarrow \mu^+\mu^-)$, is then given by :

$$R = 3 \Sigma e_q^2 \left(1 + \alpha_s/\pi \right)$$

where the sum is over accessible quark flavors. The factor of 3 comes from 3 color degrees of freedom for the quarks. The factor $(1 + \alpha_s/\pi)$ includes the QCD corrections due to the final state interactions of the quarks. The strong coupling constant α_s has a value of about 0.16. A new hadronic threshold is therefore indicated by a step increase in R. Naively, $R \sim 11/3$ for the five known flavors u, d, s, c, and b with 3 colors, and $R \sim 5$ for an additional quark of charge 2/3, such as the t quark.

The R measurements can also be used to test supersymmetry theories[7], which are attempts to unify particles with integral and half integral spin by "gauging" the spin of particles. Such theories predict the existence of spin-0 partners for the known leptons and quarks. These particles differ by a quantum number which does not affect the pair production cross section via e^+e^- annihilation. If the supersymmetric partners of the quarks (called the squarks) exist in the present energy range, multihadron production will have an additional contribution to R of

$$\Delta R = 3 \Sigma e_{sq}^2 \; 1/4 \; \beta^3 \qquad (1)$$

where the sum is over squarks which can be pair produced. The factor $1/4\ \beta^3$ comes from the fact that squarks are spin-0 particles.

The measurements of R from experiments at PEP and PETRA are summarized in Fig.1. The data are consistent with the constant value of R predicted by the quark-parton model including QCD corrections (solid line), and a new quark threshold for charge 2/3 is ruled out for center of mass energies below 36.7 GeV. The data further exclude production of an additional squark of charge 2/3 with $\beta \sim 1$.

Recently precision measurements of R have been made by the TASSO[8], MAC[9], and JADE[10] collaborations at E_{cm} of 12.0-36.7 and 29 GeV respectively,

$R = 4.01 \pm 0.03$ (stat) $\pm$ 0.20 (syst) (TASSO).

$R = 3.90 \pm 0.04$ (stat) $\pm$ 0.12 (syst) (MAC).

$R = 3.93 \pm 0.03$ (stat) $\pm$ 0.09 (syst) (JADE).

These results are both in excellent agreement with the previous combined measurements and with the quark model prediction for five flavors, 3 colors and including QCD corrections up to order α_s ($R = 3.85$ for an assumed value of 0.16 for α_s).

Measurements of the fraction of multihadron events accompanied by prompt muons provide another means of detecting new quark flavor production. Mesons with new naked flavor will decay through strong interactions to the lightest meson carrying the same flavor and then will further decay only via the weak interactions. The semimuonic branching ratio (BR) for the weak decays is estimated to be ~10%. The fraction of multihadron events accompanied by a muon with a momentum

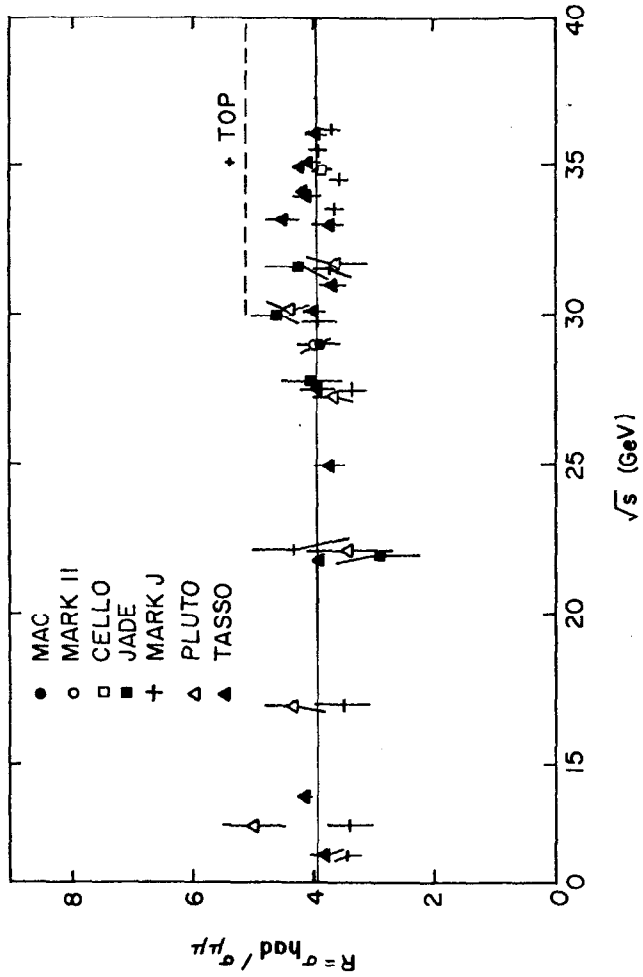


Fig. 1. Measurements of R from experiments at PEP and PETRA. The solid line is the quark model prediction for 5 flavors, 3 colors, and including QCD corrections. The dotted line is the prediction for an additional top quark of charge 2/3.

greater than 2 GeV/c has been measured by the MAC[9], PLUTO[11], MARKJ[12], and JADE[13] collaborations. The results are shown in Fig.2 where the shaded bands are predictions of the quark-parton model. Again, the results clearly exclude production of an additional quark of charge 2/3.

To rule out the existence of an additional quark of charge 1/3 is substantially more difficult. The TASSO, JADE, and CELLO collaborations have studied the topological distributions for their multihadron event samples.[14] Their results are in good agreement with the predictions of the standard quark-parton model with only five flavors and gluon emission. They rule out the existence of an additional quark of charge 1/3 or 2/3 up to a mass of about 16 GeV/c^2. The MARKJ collaboration[15] has performed similar studies using multihadron events accompanied by muons and arrives at the same conclusion. A recent analysis procedure used by the MAC collaboration provides a very sensitive method for detecting heavy particle production.[9] A multihadron event containing a muon is divided into two jets by the plane perpendicular to the thrust axis. The jet mass of the group of particles recoiling against the jet containing the muon is defined by :

$$M_{jet} = E_{beam} (1 - T_{1/2}^2)^{1/2}$$

where $T_{1/2}$ is the thrust of the recoiling particles. This jet mass will correlate with the mass of the parent quark. Fig.3 shows the recoiling jet mass distribution for a sample of 54 multihadron events containing a muon with momentum > 2 GeV/c and transverse momentum > 1 GeV/c relative to the thrust axis. The data are consistent with the predicted Monte Carlo result for c and b quark semimuonic decays assuming a 10% BR and constant fragmentation function, and rule out additional production of a heavy quark of charge 1/3 of a mass less than 13.5 GeV/c^2 at a 95%

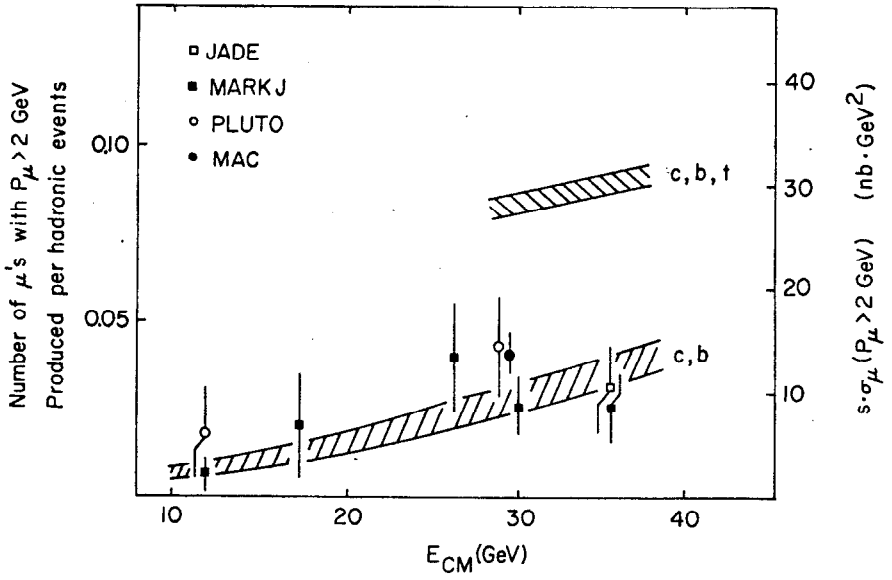


Fig. 2 Measurements of the rate of production of muons with momentum > 2 GeV/c for multihadron events. The lower shaded band is the quark-parton model prediction with a 10% semimuonic BR and different fragmentation functions for c and b quarks. The upper band includes an additional quark of charge 2/3.

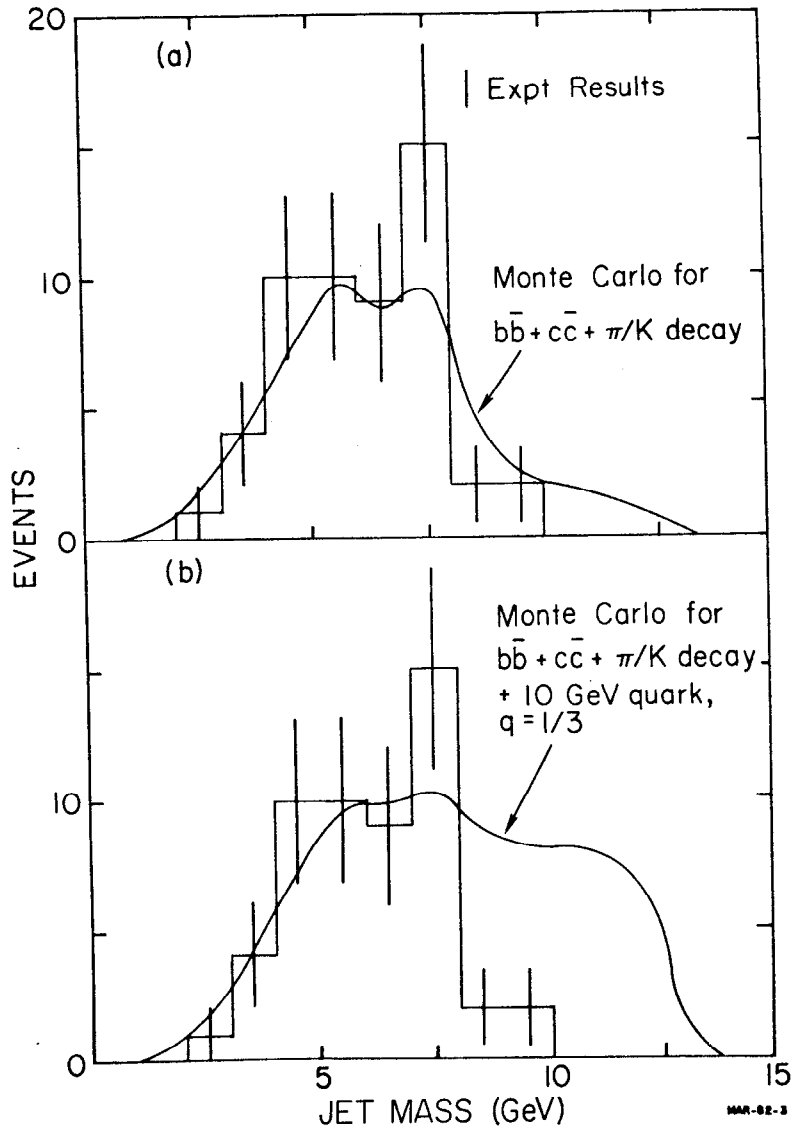


Fig. 3. Distribution of mass of hadron jet opposite to a muon with momentum > 2 GeV/c and p_t > 1 GeV/c where p_t is measured relative to the thrust axis.

confidence level (CL).

SEARCH FOR SPIN-1/2 CHARGED HEAVY LEPTONS

New spin-1/2 charged heavy lepton should fall into the following mutually exclusive categories:[2]

a) stable,

b) sequential,

c) sharing the e, μ, or τ lepton number (paralepton), or

d) an excited e, μ, or τ (ortholepton).

A charged spin-1/2 heavy lepton should be pair produced via e^+e^- annihilation (see Fig.4) with a cross section:

$$\sigma(e^+e^- \to L^+L^-) = \sigma_{\mu\mu}\, \beta(3-\beta^2)/2 \qquad (2)$$

where $\sigma_{\mu\mu}$ is the point-like cross section for pair producing light spin-1/2 fermions and $\beta(3-\beta^2)/2$ is the threshold factor for heavy spin-1/2 fermions. Experiments at PEP and PETRA have searched for all the above possibilities.

A) Search for long lifetime or stable leptons

The MARKJ[16] and JADE[17] collaborations have looked for heavy leptons which do not decay in their detectors corresponding to a flight-time > 4 ns in the laboratory frame. These events are similar to the QED process $e^+e^- \to \mu^+\mu^-$ except for a slightly different momentum spectrum due to the mass difference. These events would be categorized as muon pair events and would give an additional contribution to the muon pair cross section. No surplus of events has been observed. The existence of long

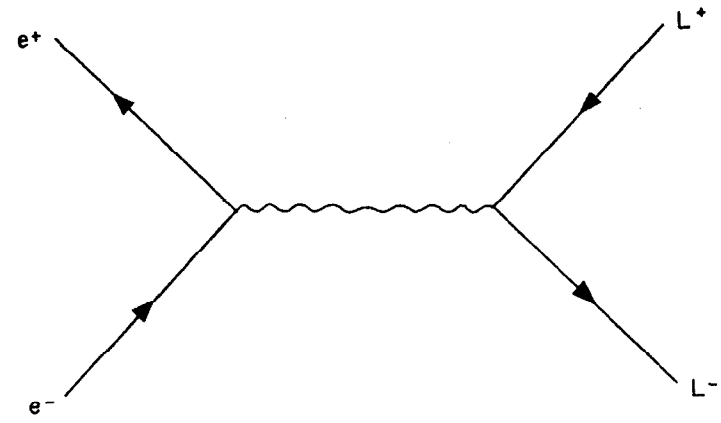


Fig. 4. Feynman diagram for the reaction $e^+e^- \to L^+L^-$.

lifetime or stable leptons up to a mass of 14 GeV/c^2 is excluded at a 95% CL. The JADE collaboration, using combined momentum and dE/dx measurements, has also looked for charged particles with a mass different from the masses of the known charged particles. Again, there is no evidence for stable charged heavy particles. The lower mass limit from JADE is 12 GeV/c^2.

B) Search for sequential leptons

Charged sequential leptons have their own lepton number and associated neutrinos. The tau lepton τ is a good example. Charged sequential leptons can be pair produced via e^+e^- annihilation with a cross section given by Eqn. 2. Sequential leptons with a mass less than 4 GeV/c^2 would be expected to have decay modes similar to those of the tau lepton and would show up as an excess to the tau pair production events. The good agreement of the tau pair production cross section with the QED prediction has excluded a possible light sequential lepton. The branching ratios of a heavier sequential lepton have been calculated[17]. It agrees quite well with the prediction of the final state counting rule which says the BR's to the possible final states $\nu_L e \nu_e$, $\nu_L \mu \nu_\mu$, $\nu_L \tau \nu_\tau$, $\nu_L u\bar{d}$, and $\nu_L c\bar{s}$ are in the ratio 1:1:1:3:3 where the factor of 3 for the hadronic final states comes from 3 color degrees of freedom. This predicts:

a) ~ 2% BR to $\mu^\pm e^\mp$ + missing momentum,

b) ~ 14% BR to $\mu^\pm$ ($e^\pm$) recoiling against a hadron jet, and

c) ~ 49% BR to two acoplanar jets of hadrons.

Searches based on these final states have been performed extensively at PEP and PETRA. No charged sequential lepton has been found. The methods used and lower mass limits obtained are given in Table I.

TABLE I LOWER MASS LIMITS ON SEQUENTIAL LEPTONS

EXPERIMENT	SIGNATURE	LOWER MASS LIMIT (95 % CL) (in GeV/c^2)	REFERENCE
JADE	Two acollinear jets	18.1	4
MARKJ	μ + hadrons	16.0	19
PLUTO	μ + hadrons	14.5	20
TASSO	Isolated charged particle + hadrons	15.5	21
MAC	Acollinear μe and μ + hadrons	14.0	9
MARKII	Acollinear μe	13.8	22

C) Search for paraleptons

A negatively charged paralepton is defined to have the same lepton number as the known positively charged e, μ, or τ.[2] For example, a negatively charged paraelectron (E^-) has the same lepton number as e^+. The radiative decay is forbidden. The weak decays of E^- are very similar to those of sequential leptons. However, due to the identity of the two final state neutrinos in the $\nu_e e \nu_e$ channel, the final state counting rule now predicts the BR's to $\nu_e e \nu_e$, $\nu_e \mu \nu_\mu$, $\nu_e \tau \nu_\tau$, $\nu_e u\bar{d}$, and

$\nu_e c\bar{s}$ to be in the ratio 2: 1 : 1 : 3 : 3. A similar argument applies to the muon and tau-associated paraleptons.

Since the BR's of a paralepton to the leptonic final states are in general larger than those of a sequential lepton of the same mass, the searches for sequential leptons are also sensitive to these paraleptons. Therefore, the mass limits in Table I apply to paraleptons as well.

D) Search for ortholeptons

Ortholeptons are excited states of the known leptons. For example, a negatively charged orthoelectron (e^{*-}) has the same lepton number as e^-. The dominant decay mode is :

$$e^{*\pm} \rightarrow e^{\pm} + \gamma$$

If e* is sufficiently light, they can be pair produced in e^+e^- interactions and detected. There has been no explicit search for $e^{*+}e^{*-}$ pair production at PEP and PETRA. However, a heavy electron can manifest itself by giving an additional contribution to the QED process:

$$e^+e^- \rightarrow \gamma\gamma$$

by a coupling of the e*, e, and γ[23], represented by the following Lagrangian :

$$L = \lambda \bar{\psi}_{e^*} \sigma_{\mu\nu} \psi_e f_{\mu\nu} + h.c. \qquad (3)$$

where λ is a measure of the strength of the $ee^*\gamma$ coupling. The $e^+e^- \rightarrow \gamma\gamma$ cross sections measured by PEP and PETRA experiments[24] are shown in Fig.5, and are in good agreement with the QED prediction. The results of the MAC collaboration used the Bhabha cross section measured with identical cuts to provide a luminosity calibration and are substantially free of systematic errors. If one assumes that e* behaves like a heavy

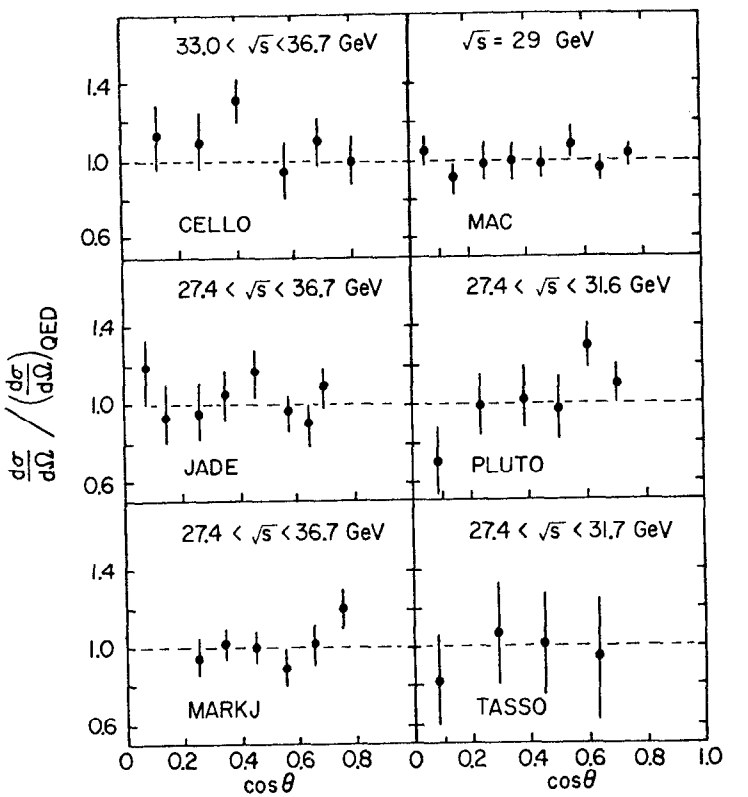


Fig. 5. Measurements of the reaction $e^+e^- \rightarrow \gamma\gamma$ from experiments at PEP and PETRA. The results are normalized to the QED prediction.

electron in the e*eγ coupling, (i.e., $\lambda = e/M_{e^*}$ where M_{e^*} is the mass of the heavy electron), the 95% CL lower mass limits obtained by PEP and PETRA experiments are given in Table II. A typical lower mass limit is 40 GeV/c^2.

TABLE II LOWER MASS LIMIT ON HEAVY ELECTRONS

EXPERIMENT	LOWER MASS LIMIT (95% CL) (in GeV/c^2)	REFERENCE
MAC	55	9
MARKJ	58	16
MARKII	50	22
JADE	47	25
PLUTO	46	26
CELLO	43	27
TASSO	34	28

The search for an orthomuon, or an excited muon, has been performed by the MAC[9], JADE[18], MARKJ[16], and MARKII[22] collaborations. Excited muon pairs can be produced via e^+e^- annihilation which then decay to $\mu\mu\gamma\gamma$ final state. The presence of an excited muon is indicated by events not accountable by higher order QED radiative processes where two muons and two photons are produced. The $\mu\gamma$ invariant mass should also peak at the μ^* mass. For example, 17 $\mu\mu\gamma\gamma$ events with at least one identified muon and both photons having energy greater than 1 GeV have been observed by the MAC detector in an integrated luminosity of 30 pb^{-1}.[9] The correlation of the two $\mu\gamma$ invariant masses for each event is shown in Fig. 6. (Note that there are two entries for each event.) For $\mu^*\mu^*$ production, the events are expected to populate around a point inside the dotted band which is a 2 standard deviations limit of the mass resolution of the MAC detector. No surplus of events in this region has been found. This excludes an excited muon up to a mass of 14 GeV/c^2. Similar results obtained by other experiments are listed in Table III.

TABLE III LOWER MASS LIMITS ON EXCITED MUONS

EXPERIMENT	LOWER MASS LIMIT (95% CL) (in GeV/c^2)	REFERENCE
MAC	14	9
MARKJ	10	16
MARKII	14	22

The search for a higher mass μ^* can rely on a $\mu\mu^*\gamma$ coupling[19] as given by Eqn. 3 with e* replaced by μ^*. This allows the production of

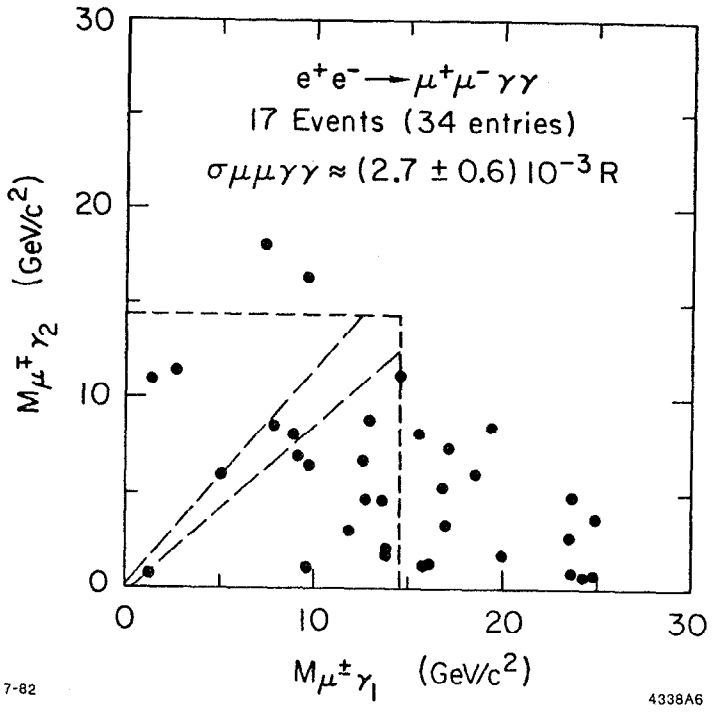


Fig. 6. Correlation of the invariant mass of the two μγ combinations for μμγγ events observed by the MAC detector. Events from μ*μ* production are expected to populate between the dotted lines. (See text for details.)

a single μ* via

$$e^+e^- \rightarrow \mu\mu^*$$

These events will be mixed with the radiative muon pair production process, $e^+e^- \rightarrow \mu^+\mu^-\gamma$. The MAC[9], MARKJ[16], MARK II[22], and JADE[19] collaborations have studied the μμγ final state and found good agreement with the QED prediction for radiative muon pair production. The limit on the mass of μ* depends on the value of λ. In most cases, a large region of the λ-M_{μ^*} plane is excluded.

In conclusion, there are no anomalous μμγ or μμγγ events which can be attributed to production of excited muons in the center of mass energies covered by PEP and PETRA.

There has been no explicit search for an excited tau. An analogous search would be to look for anomalous eμγ and and eμγγ events.

SEARCH FOR SPIN-0 LEPTONS

As mentioned earlier, supersymmetric theories predict two spin-0 partners for the known charged leptons.[7] If these particles are light, they can be pair produced via e^+e^- annihilations. The production cross section for the supersymmetric partners of the muon and tau, denoted by s_μ and s_τ respectively, is given by Eqn. 1. The production cross section for s_e is slightly more complicated.[7]

These leptons are expected to decay rapidly back to their partners by the emission of a photino which presumably is only weakly

interacting. Their signatures therefore are e^+e^-, $\mu^+\mu^-$, $\tau^+\tau^-$ final states with substantial missing momentum. These final states are distinguishable from the QED reactions : $e^+e^- \to e^+e^-$, $\mu^+\mu^-$, $\tau^+\tau^-$ by having missing momentum transverse to the beam direction. This is indicated by a large angle between the plane containing the leptons and the beam axis (called the acoplanarity angle). Fig.7 is the acoplanarity angle distribution of e^+e^- final state events seen by the TASSO detector.[29] The results are clearly in agreement with Monte Carlo predictions for e^+e^- Bhabha scattering. Expectations of an additional 4 GeV/c^2 and a 12 GeV/c^2 s_e are also indicated in the figure and are clearly ruled out. This analysis excludes a s_e up to a mass of 16.6 GeV/c^2 at a 95% CL. The MAC collaboration has searched for supersymmetric muons by analysing muon pairs with acollinearity angle greater than 10 degrees. To reduce background from the two photon process $e^+e^- \to e^+e^-\mu^+\mu^-$, at least one muon is required to have greater than 3 GeV/c momentum transverse to the beam. This results in 31 events in an integrated luminosity of 14 pb^{-1}. The acoplanarity angle distribution of these muon pairs is shown in Fig. 8. Plotted along with the data are the Monte Carlo predictions for a 10 GeV/c^2 s_μ. From this analysis, the existence of a heavy supersymmetric muon in the mass range 3-13 GeV/c^2 is ruled out at a 95% CL.

Because of their similarity in final state configurations, the searches for charged sequential leptons are also sensitive to supersymmetric taus. For example, the MAC collaboration has studied events with an isolated muon recoiling against three or more charged particles. If these events arise from s_τ pair production, the muon and the hadron jet are expected to be acoplanar. This can be measured by the

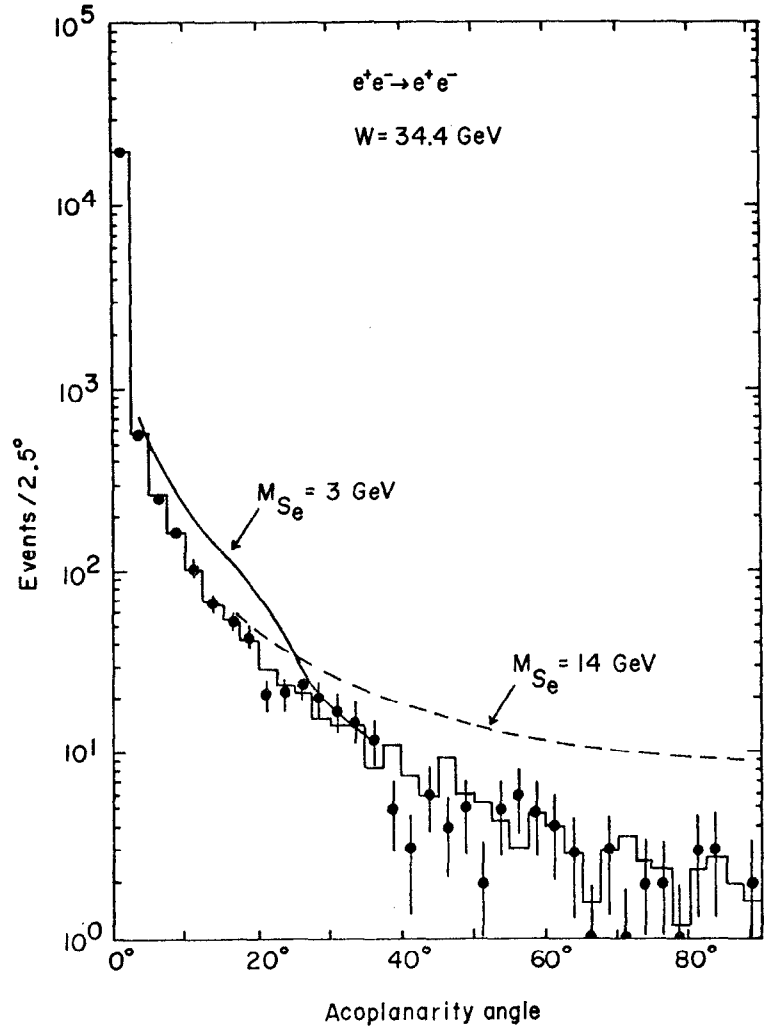


Fig. 7. The acoplanarity angle distribution of e^+e^- final state events seen by the TASSO detector.

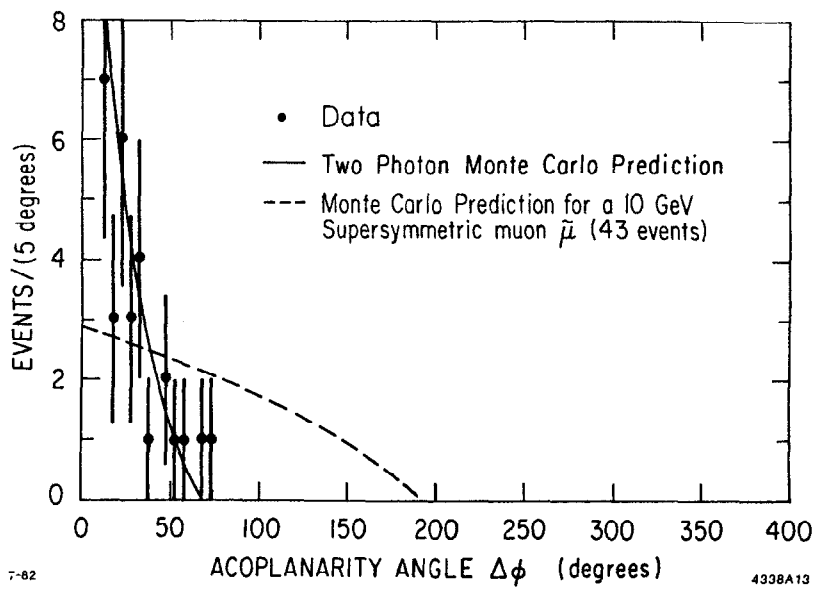


Fig. 8. The acoplanarity angle distribution of $\mu^+\mu^-$ final state events seen by the MAC detector.

momentum of the muon relative to the thrust axis of the hadron jet in a plane perpendicular to the beam. Fig.9 is a plot of this unbalanced transverse momentum for a sample of 60 tau-like events with at least 1 muon. The distribution is clearly in agreement with tau pair production and disagrees with the presence of an additional10 GeV/c^2 heavy supersymmetric tau. This analysis excludes the existence of heavy supersymmetric taus in the mass range 3-13 GeV/c^2 at a 95% CL.

In conclusion, no spin-0 supersymmetric partners of the e, μ, and τ have been found. The mass limits from PEP and PETRA experiments are given in Table IV.

The MARKII and MAC collaborations have investigated the possibility of a scalar lepton unrelated to supersymmetry which can decay to eν and μν final states.[36] This will result in μe events with missing momentum. The μe events observed by the MAC and MARKII collaborations are totally accounted for by tau pair production.[22] This establishes an upper limit on the product of the eν and μν BR's $(B_eB_\mu)^{1/2}$, which depends moderately on the assumed mass of the spin-0 lepton. The MarkII analysis essentially excludes a spin-0 scalar lepton with $(B_eB_\mu)^{1/2} >$ about 20% in the mass range 2-12 GeV/c^2.

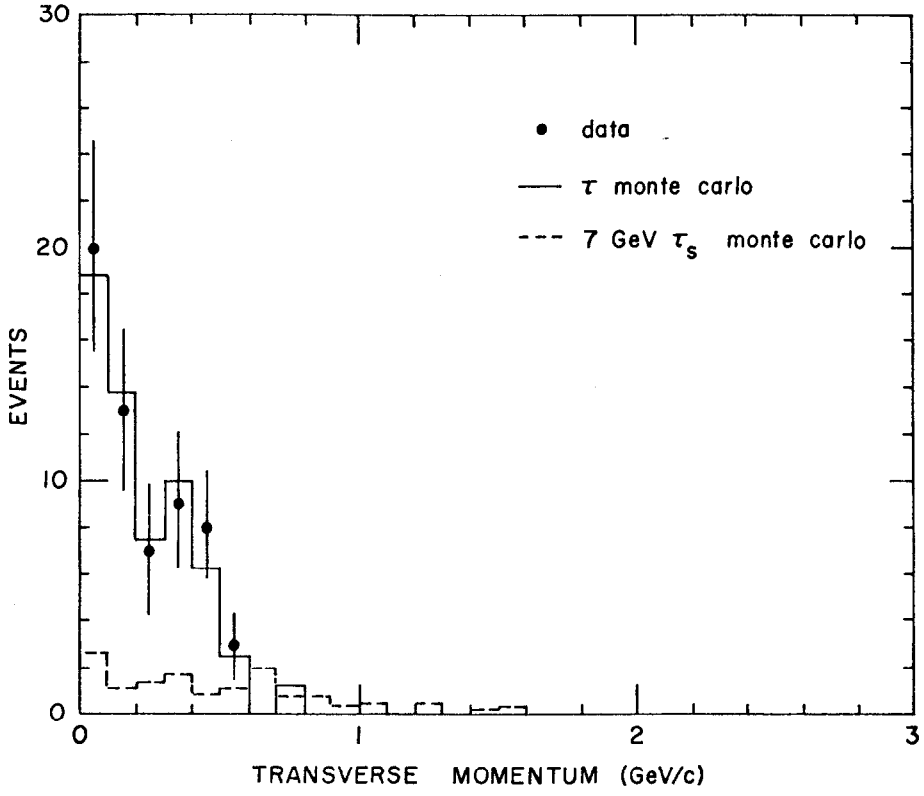


Fig. 9. The muon p_t distribution for tau-like events. p_t is measured relative to the thrust axis on a plane perpendicular to the beam direction.

TABLE IV MASS LIMITS ON SUPERSYMMETRIC LEPTONS

EXPERIMENT	PARTICLES	MASS LIMITS (95% CL) (in GeV/c^2)	REFERENCE
MAC	s_μ	3-13	
	s_τ	3-13	9
TASSO	s_e	< 16.6	
	s_μ	< 16.4	29
JADE	s_τ	4-13	30
MARKJ	s_μ	3-15	31
	s_τ	< 14	32
PLUTO	s_e	< 13	33
CELLO	s_e	2-16.8	
	s_μ	3.3-16	34
	s_τ	1.8-3.8,6-15.3	
MARK II	s_τ	1.8-9.9	35

SEARCH FOR SPIN-0 SCALARS AND PSEUDOSCALARS

The standard gauge theory uses a spin-0 neutral Higgs field to break the vacuum symmetry. Current theoretical sentiment regards this as dissatisfying. Technicolor is a simple theoretical attempt to generate the spontaneous symmetry breaking dynamically.[36] In general, these models predict Goldstone bosons called technipions π' which can be as light as a few GeV/c. Light charged Higgs particles ($H^{\pm}$) are also predicted in some extensions of the standard model.[38] These light particles can be pair produced in e^+e^- annihilation with a cross section typical of spin-0 charged particles (see Eqn. 1).

In these models, the technipions and Higgs particles have a coupling proportional to the mass of the final state particles. Therefore, they are expected to decay leptonically to $\tau\nu_\tau$, and hadronically via the heavier $c\bar{s}$ or $c\bar{b}$ system. A priori, the leptonic BR to τ (B_τ) is unknown. However, the combined searches at PEP and PETRA[39] have exhausted all possibilities : (because of their similarities in production and decay, the following results apply to π' and $H^{\pm}$,)

a) $B_\tau \sim 50\%$. There is a substantial BR to the final state where one of the π' decays to tau and the other decays hadronically. This will result in events with an isolated muon recoiling against 5 or more charged tracks. The MAC collaboration has searched for these event types and found only two candidates in 30 pb^{-1}.[9] In one of the events, two of the tracks are consistent with photon conversion in the beam pipe. After taking detection efficiency into account, this is far below the expected number from pair production of π'. A large region on the B_τ-$M_{\pi'}$ plane is therefore excluded. (See Fig.10a.) Results of similar

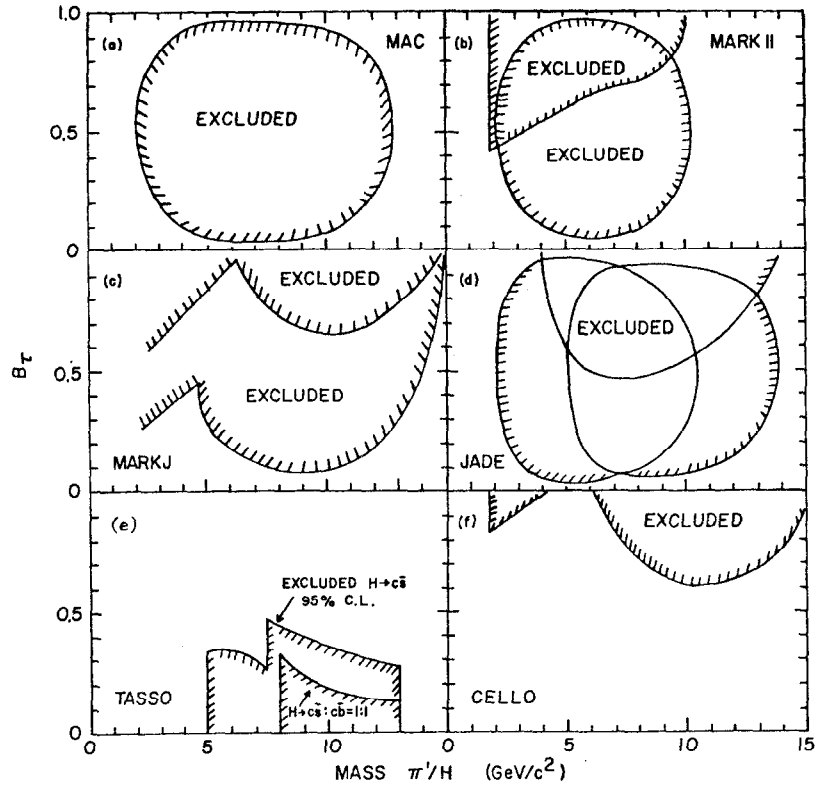


Fig. 10. Regions on the B_τ - $M\pi'$ plane excluded by experiments at PEP and PETRA.

analyses from other experiments at PEP and PETRA[39] are also shown in the same figure.

b) $B_\tau \sim 100\%$. The final state is similar to that of supersymmetric tau pair production with the tau neutrino playing the role of the photino. As explained earlier, there is no evidence for supersymmetric taus. The excluded regions are shown in Fig.10.

c) $B_\tau \sim 0\%$. The technipions would decay hadronically most of the time. Two characteristics distinguish these events from normal multihadron events : 1) These events are accompanied frequently by a prompt muon from c and b quark decay and the jet mass of the recoiling hadrons should be correlated with the mass of the technipion. Events arising from heavy technipion pair production should populate the high mass region. This signal is especially pronounced if technipions decay preferentially via $c\bar{b}$. 2) Multihadron events from technipion pair production should look like 4-jet events because there are four quarks in the final state. This is more evident if π' decays via the lighter $c\bar{s}$ system.

Searches based on 1 and 2 have been performed by the MAC[9] and TASSO[10] collaborations respectively. The observed jet mass distribution is inconsistent with the existence of a heavy π' in the mass range 7-13 GeV/c^2 decaying 100% to $c\bar{b}$. The method of 4-jet analysis was described in S. Wu's talk in this conference. No evidence for π' has been found. The excluded region is shown in Fig. 10e.

In summary, charged technipions or Higgs particles are excluded up to a mass of about 13 GeV/c^2 at a 95% CL limit independent of their BR's to $\tau\nu_\tau$, $c\bar{s}$, and $c\bar{b}$.

SEARCH FOR NEUTRAL HEAVY LEPTONS

Some models contain neutral heavy leptons. For example, a simple extension of the standard SU(2)XU(1) model proposed by Lee and Weinberg[40] predicts a rich spectrum of charged leptons accompanied by massive neutral partners. In general, it is conceivable to have a neutral heavy lepton which has either its own lepton number or the e, μ, or τ lepton number.

A search for a general neutral heavy lepton can be performed in e^+e^- interactions. Neutral heavy leptons can be pair produced in e^+e^- annihilation via the Z_0

$$e^+e^- \rightarrow Z_0 \rightarrow L_0\bar{L}_0 \ .$$

The production cross section is given by[2]

$$\sigma(e^+e^-\rightarrow L_0\bar{L}_0) = \frac{G^2\, E_{cm}^2 (v_e^2+a_e^2)(v_L^2+a_L^2)T}{96\,\pi} \qquad (4)$$

where v_L and a_L are the vector and axial vector coupling constants of L to Z_0, and T is the threshold factor. The coupling constants v_L and a_L are in general model-dependent and of order 1. For rough estimates, I have assumed ($v_L^2 + a_L^2$) = 1, and T = 1 in the following. The cross section (Eqn. 4) is small, ~ 0.2 pb at 30 GeV center of mass energy, compared with about 100 pb for charged particle pair production. Given typical integrated luminosities of 50-70 pb^{-1} at PETRA and 25-30 pb^{-1} at PEP, there would be only 5-20 events /experiment at best. Furthermore,

it is generally difficult to isolate these events.

It is relatively easy to detect events arising from pair production of e or μ-associated neutral heavy leptons because they result in events with 2e's and 2μ's in the final state respectively. These signatures are unlikely to be confused by normal multihadron events or higher order QED reactions. A meaningful search is possible in the near future. The search for e-associated neutral heavy leptons is feasible even at the present luminosity because these E_0's can be produced singly in e^+e^- interaction via W exchange (see Fig.11) which has a cross section about 10 times larger than given by Eqn. 4.[11] For a light E_0, the final state appears as an unbalanced jet containing an electron. The JADE collaboration has searched for these events and found no events satisfying these criteria.[5] The lower mass limit is 18-20 GeV/c^2 depending on details of the assumed model. There has been no explicit search for μ-associated neutral heavy leptons at PEP and PETRA.

CONCLUSIONS

Experiments at PEP and PETRA have searched for production of quarks with new flavors, heavy charged sequential, para and excited leptons, supersymmetric spin-0 charged leptons, spin-0 charged Higgs particles and technipions, and e-associated neutral heavy leptons. None of these particles has been found up to a center of mass energy of 36.7 GeV/c^2. Basically all possible proposed charged states have been searched for and their production is excluded at a 95% CL limit, or better, over most

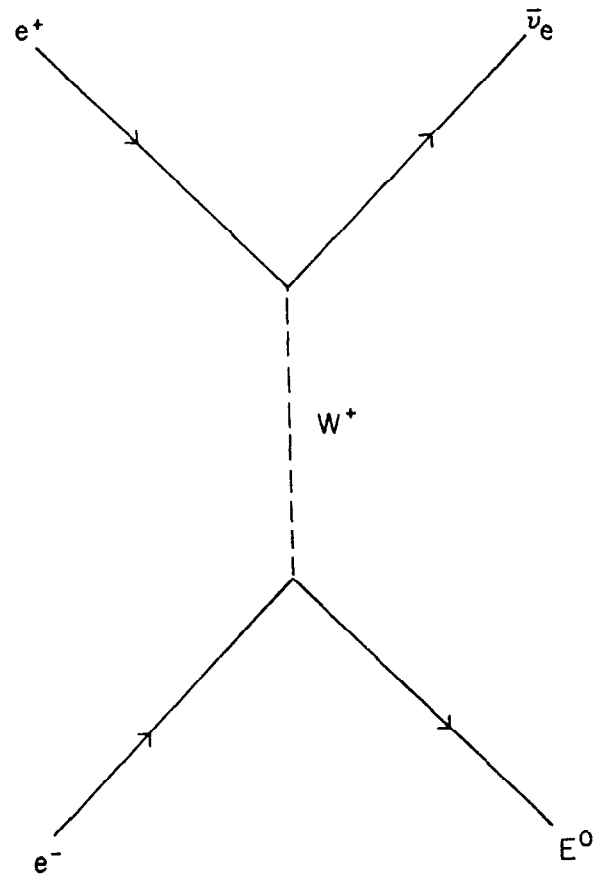


Fig. 11. Feynman diagram for $e^+e^- \to \nu E^0$ via W exchange.

of the accessible range of masses. The lower mass limits are given below:

a) By measuring R and inclusive muon production in multihadrons, the existence of a new quark of charge 2/3 or 1/3 is excluded up to a mass of 18 GeV/c^2 at a 95% CL.

b) All possible decay modes of charged sequential and para leptons have been searched for and such leptons are excluded up to a mass of 18 GeV/c^2 at a 95% CL.

c) Pair production of excited electrons and muons have not been observed up to a center of mass energy of 36.7 GeV. The existence of an excited muon is excluded up to a mass of 14 GeV/c^2 at a 95 % CL. Single production of excited muons is also not observed.

d) Charged spin-0 supersymmetric partners of e, μ, and τ have been searched for and are excluded up to a mass of about 14 GeV/c^2 at a 95% CL.

e) Charged Higgs particles and technipions have been searched for in all possible decay modes. No such particles have been observed and are excluded up to a mass of about 14 GeV/c^2 at a 95% CL.

f) The special class of e-associated neutral heavy leptons have been searched for. No such particle has been found. The lower mass limit assuming standard coupling is 18-20 GeV/c^2 at a 95% CL.

ACKNOWLEDGEMENTS

I would like to thank my colleagues of the MAC collaboration for discussing their results. I would also like to thank D. Ritson for discussions and assistance in preparing this manuscript.

REFERENCES

1. D. Cords, XX International Conference on High Energy Physics, University of Wisconsin, Madison, Wisconsin, July 1980, and DESY 80/92, 1980.

2. M. L. Perl, Physics In Collision Conference, Virginia Polytechnic Institute and State University, May 1981, and SLAC-PUB-2752, 1981.

3. P. Duinker, EPS International Conference on High Energy Physics, Lisbon, 1981.

4. A. Böhm, DESY 82/027, 1982.

5. K. H. Mess and B. H. Wiik, DESY 82/011, March 1982

6. R. Felst, International Symposium on Lepton and Photon Interactions at High Energies, Bonn, August 1981.

7. See, e.g., G. Farrar and P. Fayet, Phys. Lett. 389B, 191(1980).

8. R. Brandelik et al., Phys. Lett. 113B, 499(1982).

9. D. Ritson, XXI International Conference on High Energy Physics, Paris, June 1982.

10. S. Wu, this Proceeding.

11. Ch. Berger et al., Phys. Rev. Lett. 45, 1533(1980).

12. D. P. Barber et al., Phys. Lett. 44B, 1722(1980).

13. W. Bartel et al., Phys. Lett. 99B, 277(1981).

14. J. Bürger, Proceedings of the 1981 International Symposium on Lepton and Photon Interactions at High Energies, edited by W. Pfeil, Bonn 1981, p.115. See also Ref. 4.

15. See, e.g., Ref. 2.

16. B. Adeva et al., Phys. Rev. Lett. 48B, 967(1982).

17. W. Bartel et.al., Z. Physik C6, 295(1980).

18. Y. S. Tsai, SLAC-PUB-2450, December 1979.

19. D. P. Barber, et al., Phys. Rev. Lett. 45, 1904(1980).

20. Ch. Berger et al., Phys. Lett. 99B, 489(1981).

21. R. Brandelik et al., Phys. Lett. 99B, 163(1981).

22. R. Hollebeek, International Symposium on Lepton and Photon Interactions at High Energies, Bonn, August 1981, and SLAC-PUB-2829, October, 1981.

23. F.E. Low, Phys. Rev. Lett. 14, 238(1965).

24. P. Dittmann and V. Hepp, Z. Physik C10, 283(1981).

25. W. Bartel et. al., Phys. Lett. 192B, 206(1980); Phys. Lett. 99B, 281(1981).

26. Ch. Berger et al., Z. Physik C1, 343(1979).

27. H. J. Behrend et al., Phys. Lett. 103B, 148(1981).

28. R. Brandelik et al., Phys. Lett. 92B, 199(1980).

29. R. Brandelik et al., DESY 82-032. (Submitted to Phys. Lett..)

30. W. Bartel et al., Phys. Lett. 114B, 211(1982).

31. D. P. Barber et al., Phys. Rev. Lett. 45, 1904(1980).

32. B. Adeva et al., MIT report LNS 125. (Unpublished).

33. H. Spitzer, Proceedings of XI Rencontre de Moriond on Elementary Particle Physics, Les Arcs, 1980.

34. H. J. Behrend et al., Phys. Lett. 114B, 287(1982)

35. C. A. Blocker et al., Phys. Rev. Lett. 49, 517(1982).

36. J. Dorfan, SLAC Summer Institute on Particle Physics, Stanford, CA, August 1981, and SLAC-PUB-2813, September 1981.

37. L . Susskind, Phys. Rev. D20 2619 (1979); S. Weinberbg, Phys Rev. D19, 1277(1979).

38. E. Golowich and T. C. Yang, Phys. Lett. 80B, 245(1979); L. N. Chang and J. E. Kim, Phys. Lett. 81B, 233(1979); H. E. Haber, G. L. Kane, and T. Sterling, Nucl. Phys. B161, 493(1979).

39. See, e.g., W. Bartel, DESY 82-023, 1982; H. J. Behrend et al., DESY 82-021; B. Adeva et al., MIT report LNS 125; S. Wu, this Proceeding; D. Ritson, Ref. 9; C. A. Blocker et al., Ref. 35.

40. B. W. Lee and S. Weinberg, Phys. Rev. Lett. 38, 1237(1977).

41. J. D. Bjorken and C. Llewellyn-Smith, Phys. Rev. D7, 887(1973).

SUPERCONDUCTIVE MONOPOLE DETECTORS

Blas Cabrera

Physics Department, Stanford University

Stanford, California 94305

ABSTRACT

The theoretical basis for detection of magnetic charges using superconductive devices is summarized. Three generations of such detectors are described. They have been designed to search for a cosmic ray flux of supermassive magnetically charged particles. An upper limit for such a particle flux of 1.2×10^{-10} cm^{-2} s^{-1} sr^{-1} has been set based on 382 days operation with the original single axis detector and 61 days with a new three loop detector. No new candidate events have been seen.

I. INTRODUCTION

The theoretical similarities between flux quantization in *superconductors and Dirac's magnetic monopoles make superconductive* systems natural detectors for these elusive particles. More recently, grand unification theories have been shown to predict the existence of stable supermassive magnetically charged particles possessing the Dirac unit of magnetic charge. These particles would be non-relativistic, weakly ionizing, and extremely penetrating; and thus may have eluded previous searches. In this paper we describe three generations of superconductive detectors designed to look for a cosmic ray flux of such particles.

Superconductive technlogies primarily developed at Stanford University over the last decade have led naturally to very sensitive

© B. Cabrera 1982

detectors for magnetically charged particles. Much of the work utilizes ultra low magnetic field regions achieved using expandable superconducting shields. Application of this ultra low field technology has allowed full utilization of modern SQUID (Superconducting QUantum Interference Device) sensitivities. In Section II we describe the ultra low field technology. In Section III a simple derivation for flux quantization is presented and experimental data clearly demonstrating flux quantization in a five centimeter diameter superconducting ring are shown. The theoretical similarity between flux quantization and Dirac magnetic charges is shown in Section IV, and the exact coupling of a magnetic charge to a superconducting ring is computed in Section V. In Section VI the design and operation of the original single axis detector with its 10 cm^2 isotropic sensing area is summarized, and in Section VII the initial operation of our new three loop detector with a seven times greater loop sensing area is presented. In closing Section VIII describes our design for the next generation of larger superconductive detectors with sensing areas approaching 1 m^2.

II. ULTRA LOW MAGNETIC FIELDS

Ultra low magnetic field regions[1] are made using expandable superconducting shields. Cylinders made of pure 0.007 cm thick lead foil are tightly folded in accordion fashion as shown in Fig. 1. These are slowly cooled through their superconducting transition temperature and trap the ambient magnetic field. In an ideal superconductor one would expect the Missner effect to spontaneously exclude all magnetic fields; however, in practice one finds that

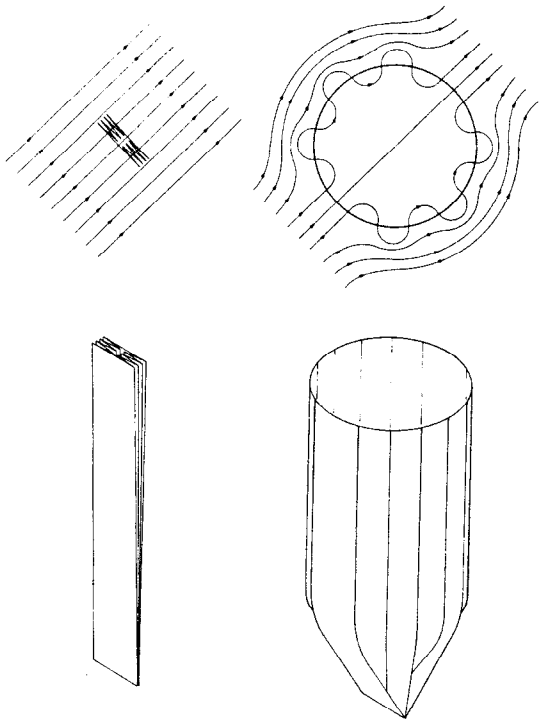


Fig. 1. Schematic representation of magnetic field before and after the expansion of a lead shield.

for thin foils pinning forces prevent the trapped flux vortices from moving. A more correct picture is thus of magnetic flux lines pinned strongly to their original locations at the moment when the shield was cooled through its transition temperature. Once superconducting any subsequent changes in the external magnetic field will be exactly cancelled by supercurrents on the outer surface of the shields. Therefore, by mechanically expanding these tightly folded cylinders while maintaining them superconducting, one obtains a region of lower magnetic field, as shown schematically in Fig. 1. To obtain the lowest magnetic fields a bootstrap technique is used. New tightly folded shields are carefully cooled inside of previously expanded ones, and after three or four cycles field levels below 10^{-7} gauss are obtained routinely.

An experimentally measured magnetic field profile is shown in Fig. 2 for a completed shield measuring 20 cm in diameter and 100 cm in length. The three field components along the cylinder axis are scanned using a 5 cm diameter sensing loop coupled to a SQUID. In addition to the magnetic charge detectors described here, these shields have been applied to three other experiments at Stanford: the relativity gyroscope experiment[2] - superconducting gyroscopes placed in earth orbit to measure small inertial frame precessions predicted by general relativity; the He^3 electric dipole moment experiment[3] - an alternate approach to the neutron measurements looking for a direct violation of time reversal invariance; and the h/m_e experiment[4] - a determination of Planck's constant over the electron mass at the several ppm level using a rotational super-

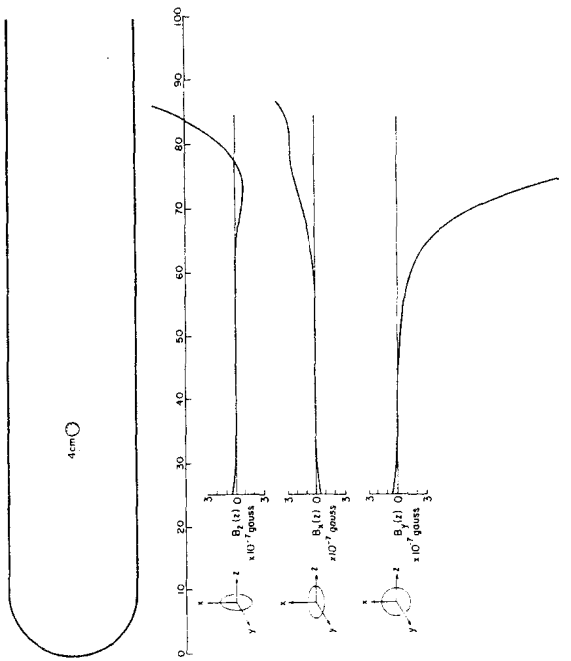


Fig. 2. Three mutually perpendicular magnetic field component profiles along the axis of 20 cm diameter superconducting shield.

conducting ring.

Constructing magnetometers capable of measuring ultra low magnetic fields has been the most difficult part of the ultra low magnetic field work. It has been relatively straightforward to obtain lower magnetic fields by simple modifications of the expansion technique; however, it has proven much more difficult to make instruments with sufficiently low background magnetic contamination levels to observe the residual fields in the shields rather than the field associated with the instrument itself. The instrument used for measuring the shield magnetic field profiles of Fig. 2 is capable of measuring absolute fields at the 10^{-9} gauss level. It is a flip coil assembly made almost entirely out of fused quartz and housed in an aluminum vacuum can. Rotation is achieved using a dacron string wrapped around a quartz pulley, and the tension in the string is maintained with a fused quartz spring. Four turns of 0.005 cm diameter niobium wire are wound inside of the 2 nm diameter quartz tubing formed into a 5 cm diameter circular coil form. The twisted pair niobium leads come out through the axis and go up to a SQUID sensor some 35 cm above the coil. We shall return to this instrument later, where we describe its use as the first magnetic charge detector to search for a cosmic ray flux of monopoles.

III. FLUX QUANTIZATION

In this section a simple theoretical derivation for flux quantization is presented. It includes all that we need in the next section for understanding the coupling of a hypothetical Dirac magnetic charge to a superconducting ring. In 1957 Gorkov[5] demonstrated theoretically that the Ginzburg-Landau (GL) equations for superconductivity are an exact consequence of the Bardeen-Schreiffer-Cooper[6] (BCS) theory in the limit of the temperature T approaching the transition temperature T_c of the superconductor. Global properties such as flux quantization are straightforward consequences of the GL equations but often become impossibly difficult to derive from the full microscopic BCS theory. It has been theoretically shown that the global properties derived from GL are valid even well below T_c, as observed experimentally.

The GL supercurrent density equation

$$\vec{j} = \frac{\hbar e^*}{2im^*}(\psi^*\vec{\nabla}\psi - \psi\vec{\nabla}\psi^*) - \frac{e^{*2}}{m^*c}\psi^*\psi\vec{A} \quad , \tag{2}$$

looks identical with the nonrelativistic single particle Schrödinger equation, however, the interpretation is somewhat different. The particles participating in the supercurrent are the Cooper pairs and have twice the mass $m^* = 2m$ and charge $e^* = 2e$ of the electron. In addition, ψ, called the order parameter, now represents a coherent many-body state of Cooper pairs with $\psi^*\psi = \frac{1}{2} n_s$ representing the local pair density, thus half the superelectron density n_s. Writing $\psi = |\psi| e^{i\phi}$ we find

$$\psi^*\vec{\nabla}\psi - \psi\vec{\nabla}\psi^* = 2\psi^*\psi\vec{\nabla}\phi \, . \tag{3}$$

A line integral of $\vec{\nabla}\phi$ will depend only on the end points. Thus upon integrating around a closed path the phase change $\Delta\phi$ must equal $n(2\pi)$, where n is an integer, in order to obtain a single-valued function ψ along any path as required physically. This requirement is exactly the origin of flux quantization and is

experimentally observable whenever the coherence of the order parameter extends around a closed path entirely within the superconductor.

Making these substitutions into Equ. 2 we obtain

$$\vec{j} = \frac{\hbar e n_s}{2m} \vec{\nabla}\phi - \frac{e^2 n_s}{mc} \vec{A} \quad . \tag{4}$$

Before taking the line integral around a closed path it can easily be shown that the current density $\vec{j}$ vanishes inside of a thick superconductor by taking the curl of both sides twice (note that n_s remains constant to a high degree throughout the superconductor)

$$\vec{\nabla} \times (\vec{\nabla} \times \vec{j}) = - \frac{e^2 n_s}{mc} \vec{\nabla} \times \vec{B} \, . \tag{5}$$

Using Maxwell's equation $\vec{\nabla} \times \vec{B} = 4\pi/c \, \vec{j}$ and taking $\vec{\nabla} \times \vec{j}$ zero for a time independent current

$$\nabla^2 \vec{j} - \frac{1}{\lambda^2} \vec{j} = 0 \quad , \tag{6}$$

where

$$\lambda = \sqrt{\frac{mc^2}{4\pi e^2 n_s}} \quad , \tag{7}$$

is the London penetration depth, typically 300-500 angstroms. Solutions for the supercurrent density $\vec{j}$ in Equ. 6 fall exponentially to zero over a characteristic length λ into the superconductor.

Now integrating Equ. 4 around a closed path Γ we obtain

$$\frac{4\pi\lambda^2}{c} \oint_\Gamma \vec{j} \cdot d\vec{\ell} = n\left(\frac{hc}{2e}\right) - \int_{S_\Gamma} \vec{B} \cdot d\vec{s} \quad , \tag{8}$$

where S_Γ is the area bounded by the path Γ. Then for a superconducting ring thick compared to λ we can always find a path Γ along which $\vec{j}$ vanishes. Thus the magnetic flux through the ring must be an integer number of

$$\phi_o = \frac{hc}{2e} = 2.07 \times 10^{-7} \text{ gauss cm}^2 \quad , \tag{9}$$

the flux quantum of superconductivity.

Flux quantization was first observed in 1961, at Stanford by Fairbank and Deaver[7] and independently in Germany by Doll and Nabauer. Using the ultra low field technology and modern SQUID sensitivities, S. Felch, J. T. Anderson and I[4] have recently demonstrated flux quantization in a single turn 5 cm diameter ring made of 0.005 cm diameter niobium wire. The data shown in Fig. 3 were taken with the h/m_e apparatus and show the ring biased within several millikelvin of its superconducting transition temperature T_c. The magnetic flux was measured with a second superconducting loop of higher transition temperature closely coupled to the ring and connected to a SQUID sensor. The potential barriers separating the various flux quantum states are reduced in height as the temperature approaches T_c until finally the kT thermal energy associated with the normal electrons is sufficient to occasionally kick the ring from one quantum state to the next. If the temperature is too low, e.g., far left of the figure, no transitions are seen; whereas if the temperature is too close to T_c the transitions between states occur too rapidly to follow with the 1 Hz bandwidth used. There is a regime, 2 to 3 millikelvin below T_c, where the transition rate is slow enough so that each of the quantum states is clearly shown. The kT thermal excitations carry the ring through no more than 6 or 7 quantum states because the energy associated with one flux quantum $\phi_o^2/2L$ is smaller than kT by a factor of nearly 10. Our measurements on this 5 cm diameter ring are the first in this regime and represent the largest area for which

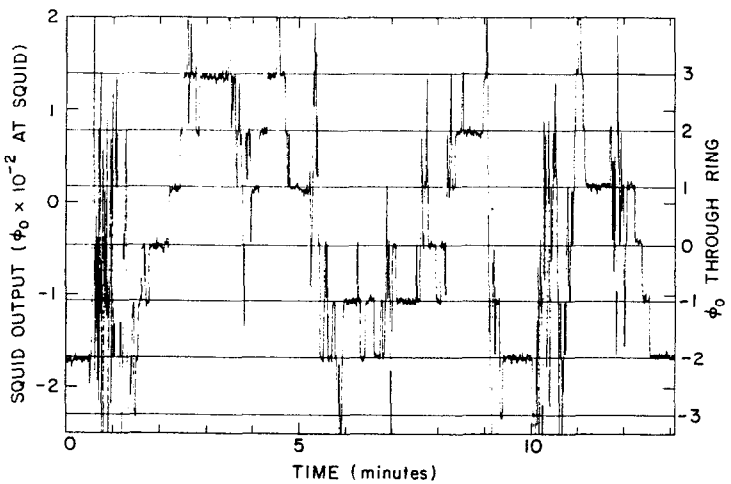


Fig. 3. Thermally induced transitions between quantum states; clearly demonstrating flux quantization. The passage of a single Dirac charge through this 5 cm. superconducting ring would induce a current change corresponding to two flux quanta change.

flux quantization has been directly observed.

As discussed in the next section the coupling of a Dirac magnetic charge to this ring would change the quantum state by 2. Thus direct observation of flux quantization in a superconducting ring necessarily demonstrates sufficient resolution for the detection of monopoles in that system.

IV. THEORETICAL BASIS FOR MAGNETIC MONOPOLES

Before calculating the coupling of a magnetically charged particle to a superconductor let us briefly consider the theory for magnetic monopoles.[8] We begin by considering the generalized Maxwell equations

$$\begin{aligned} \vec{\nabla} \times \vec{B} - \frac{1}{c}\frac{\partial \vec{E}}{\partial t} &= \frac{4\pi}{c}\vec{j}_e \\ \vec{\nabla} \cdot \vec{E} &= 4\pi \rho_e \\ \vec{\nabla} \times \vec{E} + \frac{1}{c}\frac{\partial \vec{B}}{\partial t} &= -\frac{4\pi}{c}\vec{j}_m \\ \vec{\nabla} \cdot \vec{B} &= 4\pi \rho_m \, . \end{aligned} \tag{10}$$

The magnetic charge density ρ_m and the magnetic current density $\vec{j}_m$ are normally set to zero from lack of experimental evidence for magnetically charged particles. The minus sign in the $\vec{j}_m$ term insures that the continuity equation for magnetic charges and currents has the same form as for electric charges and currents. The symmetrization of Maxwell's equations in this way is not a strong reason for believing in the possible existence of magnetic charges. One can define new electric and magnetic fields as linear combinations of the present electric and magnetic fields

$$\vec{E}' = \vec{E}\cos\theta + \vec{B}\sin\theta$$
$$\vec{B}' = -\vec{E}\sin\theta + \vec{B}\cos\theta \ , \qquad (11)$$

where θ is an arbitrary angle and then

$$\rho'_e = \rho_e \cos\theta$$
$$\rho'_m = -\rho_e \sin\theta \ . \qquad (12)$$

Thus every charged particle would carry both electric and magnetic charge in a universal ratio $\rho'_m/\rho'_e = -\tan\theta$. If we pick $\theta = \pi/4$, Maxwell's equations became symmetric but no new physics has been added. We must thus find a more fundamental reason for suggesting the existence of magnetic charges.

In 1931, Dirac[9] found such a reason by asking whether the existence of magnetically charged particles could be made consistent with quantum mechanics. Dirac considered a single electron in the field of a magnetic charge and found that for the electron wavefunction to remain single-valued a quantization condition must exist between the elementary electric and magnetic charges

$$eg = \frac{1}{2}hc \ . \qquad (13)$$

Thus if magnetic charges existed they would explain the experimentally observed quantization of all electric charges. At that time no other theoretical explanation for this observed quantization existed.

We can understand the Dirac quantization using a similar argument to the flux quantization derivation by considering the Schrödinger current density for a single electron in the field of a magnetic charge

$$\vec{j} = \frac{\hbar e}{2im}(\psi^*\vec{\nabla}\psi - \psi\vec{\nabla}\psi^*) - \frac{e^2}{mc}\psi^*\psi\vec{A} \ . \qquad (14)$$

Then for any closed path Γ not through the monopole

$$\frac{mc}{e^2}\oint \frac{\vec{j}\cdot d\vec{\ell}}{\psi^*\psi} = n\frac{hc}{e} - \int_{S_\Gamma} \vec{B}\cdot d\vec{s} \ . \qquad (15)$$

Flux quantization is not obtained because atomic distances are much smaller than the London penetration depth and thus $\vec{j}$ cannot be set to zero. In fact the term containing $\vec{j}$ in Equ. 15 is typically 10^5 larger than the flux term. However, if we take two surfaces S_Γ and S'_Γ each bounded by the path Γ and with the two together enclosing the monopole, then the current density term is identical for both. Subtracting the two equations we obtain

$$k\frac{hc}{e} = \oint_{S_\Gamma - S_\Gamma'} \vec{B}\cdot d\vec{s} = 4\pi g \ , \qquad (16)$$

where k is an integer and the closed surface integral equals to the total flux emanating from the pole. Thus Equ. 13 is obtained.

For k not zero we have introduced a discontinuity in the vector potential which produces an ambiguity in the phase change of ψ around the path Γ. The phase change obtained when considering the surface S_Γ differs by exactly $k(2\pi)$ from that obtained considering S'_Γ. But as Dirac stressed, only phase changes modulo 2π are physically observable. Thus only magnetic charges possessing an integer Dirac charge are consistent with all physical observables in quantum mechanics remaining unambiguous.

The Dirac condition does not symmetrize electric and magnetic charges because the elementary magnetic charge is predicted to be much stronger than the elementary electric charge. From Equ. 13

$$g = e/2\alpha \quad , \tag{17}$$

137/2 times greater than the electric charge e. Therefore, two magnetic charges a certain distance apart feel a force which is $(137/2)^2$ greater than that between two electric charges the same distance apart. The coupling constant, $g^2/\hbar c = \alpha(\frac{g}{e})^2 \approx 34$, would thus be stronger than that of any known force.

Note also from Equ. 16 that the flux emanating from a Dirac charge is

$$4\pi g = \frac{hc}{e} = 2\,\phi_o \quad , \tag{18}$$

exactly twice the flux quantum of superconductivity! This should not be surprising, for Dirac imposed the same single-valuedness condition on a single electron wavefunction in the magnetic field of a pole as we used in deriving flux quantization from the coherent many-body Cooper pair order parameter. The Cooper pairs possess twice the electron charge, accounting for the factor of two in Equ. 15. Thus the observation of flux quantization in a superconductive system automatically demonstrates sufficient resolution for detecting Dirac magnetic charges.

The Dirac suggestion motivated many experimental searches for particles possessing magnetic charge, but no convincing candidates were found.[10]

Over the last decade work on unification theories has unexpectedly yielded strong renewed interest in monopoles. In 1974 't Hooft and independently Polyakov[11] showed that in true unification theories (those based on simple compact groups) magnetically charged particles are necessarily present. These include the standard SU(5) Grand Unification Model. The modern theory predicts the same long range field as the Dirac solution, however, now the near field is also specified leading to a calculable mass. The Dirac theory was not able to predict a mass. The standard SU(5) model predicts a monopole mass of 10^{16} GeV/c^2, horrendously heavier than had been considered in previous searches. A detailed discussion of these theories can be found elsewhere in this volume in excellent papers by expert authors.

These supermassive magnetically charged particles would possess qualitatively different properties.[12] These include necessarily nonrelativistic velocities from which follow weak ionization and extreme penetration through matter. Thus such particles would have escaped detection in previous searches. To understand why a superconducting ring makes a natural detector[13] for such slow monopoles we next compute the coupling of a magnetic charge to a superconducting ring.

V. MONOPOLE COUPLING TO SUPERCONDUCTING RING

Rather than presenting a detailed calculation[14], here we obtain the correct result for the current change induced by the passage of a magnetic charge through a superconducting ring using a simple magnetic field line picture. Consider a magnetic charge g moving along the symmetry axis of a superconducting ring made with wire many λ in diameter. From Sec. III we know that the magnetic field inside the wire is always negligibly small. Thus no magnetic field lines may pass through the wire, and as the charge passes through the ring the field lines are brushed back. However, as the

particle proceeds to infinity after passing through the ring all of the magnetic field lines emanating from the charge cannot return through the ring. The resolution of this apparent dilemma is shown schematically in Fig. 4. Each flux line is continuously deformed as the charge g approaches the wire and each separates into two disjoint lines, one left surrounding the wire and the other remaining connected to the charge. At the point where the cross-over occurs the magnetic field is zero.

For a trajectory along the ring's symmetry axis, the magnetic field lines can be easily calculated analytically. They always lie along the surface of tubes of constant flux which are now figures of rotation about the z axis. Thus for the charge g a distance z' away from the plane of the ring with radius b, the flux $\phi(r,z)$ through a circle of radius r a distance z away from the ring is given by

$$\phi(r,z) = \phi_o\left[1 + \frac{z'-z}{\sqrt{(z'-z)^2+r^2}}\right] - \phi_o \frac{M}{L}\left[1 + \frac{z'}{\sqrt{z'^2+b^2}}\right] \qquad (19)$$

where L is the self inductance of the ring and M the mutual inductance between the ring and the circle. The first term on the right hand side is the flux from the monopole and the second the flux from the induced supercurrent in the ring. M (in henries) can be expressed in terms of the elliptic integrals E and K as

$$M = \mu_o \sqrt{rb}\left[\left(\frac{2}{k} - k\right)K(k) - \left(\frac{2}{k}\right)E(k)\right] \qquad (20)$$

where

$$k^2 = \frac{4rb}{(r+b)^2+z^2}$$

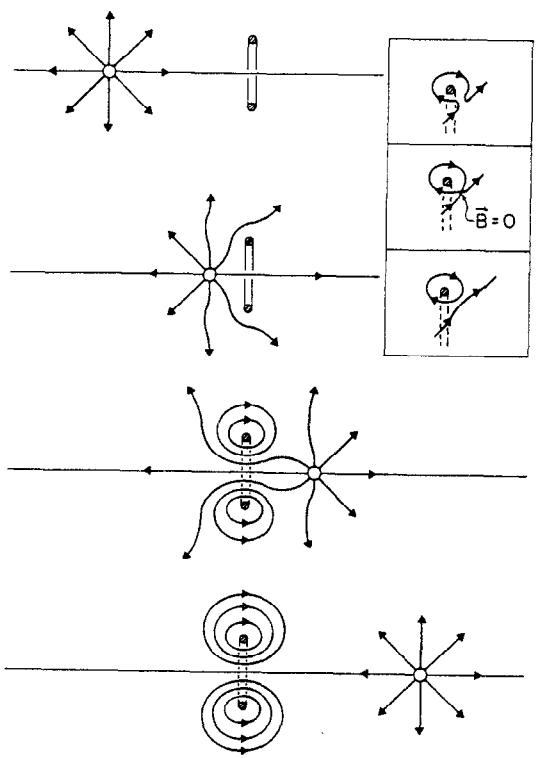


Fig. 4. Schematic representation of magnetic field lines as monopole passes through superconducting ring.

Using these equations a video simulation of the changing field lines as a monopole passes through a superconducting ring has been made by Gordon Smith at Stanford.

Returning to Fig. 4 it is clear that every field line emanating from the pole must have left a closed loop around the ring wire as the particle moved through, Thus the net change of flux through the ring must exactly equal the total flux from the pole - two ϕ_o for a monopole of unit Dirac charge. The same result is obtained for all particle trajectories which pass through the ring, whereas no net flux change results from trajectories which miss the ring. To illustrate, in Fig. 5 the induced supercurrent resulting from each of four different trajectories has been computed. Note that the rise times are similar and are of order the ring radius divided by the particle velocity. For trajectories which miss the ring only transient currents are obtained with a maximum peak to peak excursion of one ϕ_o.

Thus if a magnetic charge g passes through the ring, the number of flux quanta threading the ring will change by two; whereas, if the particle does not pass through, the flux will remain unchanged. Finally, if the magnetic charge passes through the bulk superconductor, such as the wire of the ring, it would leave a trapped doubly quantized vortex, and some intermediate total current would persist.

A superconductive system based on these properties is sensitive only to magnetic charges and thus makes a natural detector. The passage of any known particle possessing electric charge or a magnetic dipole would cause very small transient signals but no dc shifts.

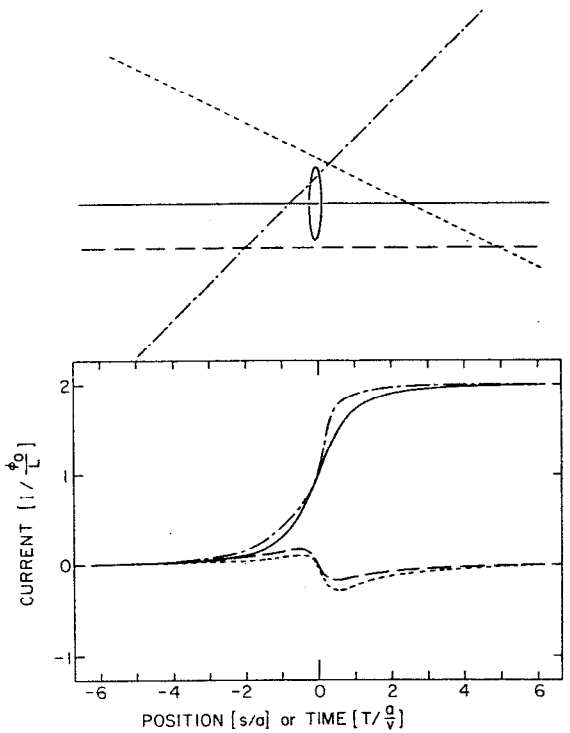


Fig. 5. The induced current in a superconducting ring for each of four different trajectories.

A cosmic flux of magnetically charged particles such as the predicted supermassive GUT monopoles can be detected by monitoring the current in a superconducting loop or scanning the surface of a superconducting sheet for spontaneously appearing doubly quantized vortices. Below several such devices are described.

VI. PROTOTYPE SINGLE LOOP DETECTOR

To test the feasibility of such devices the magnetometer built for measurements of the ultra low field superconducting shields was used in a prototype search for a particle flux of supermassive monopoles.[14] This instrument, described in Section II, has been operated as a monopole detector for a total of 382 days. It consists of a four turn 5 cm diameter loop made of 0.005 cm diameter niobium wire. The flip coil is positioned with its axis vertical and is connected to the superconducting input coil of a SQUID. The passage of a single Dirac charge through the loop would result in an 8 ϕ_o change in the flux through the superconducting circuit, comprised of the detection loop and the SQUID input coil (2 ϕ_o couple to each of the four turns). As shown in Fig. 6, the SQUID and the loop are mounted inside an ultra low field shield in an ambient field of 5×10^{-8} gauss.

The presence of the superconducting shield complicates the expected detector response. Now in addition to the trajectory coupling directly to the loop, doubly quantized supercurrent vortices appear in the walls of the shield at the points where the particle enters and exits (see Fig. 6). A field change is produced in the shield which also couples to the loop even if the trajectory misses the loop. Thus the possible values for the total current induced in the loop are no longer sharp.

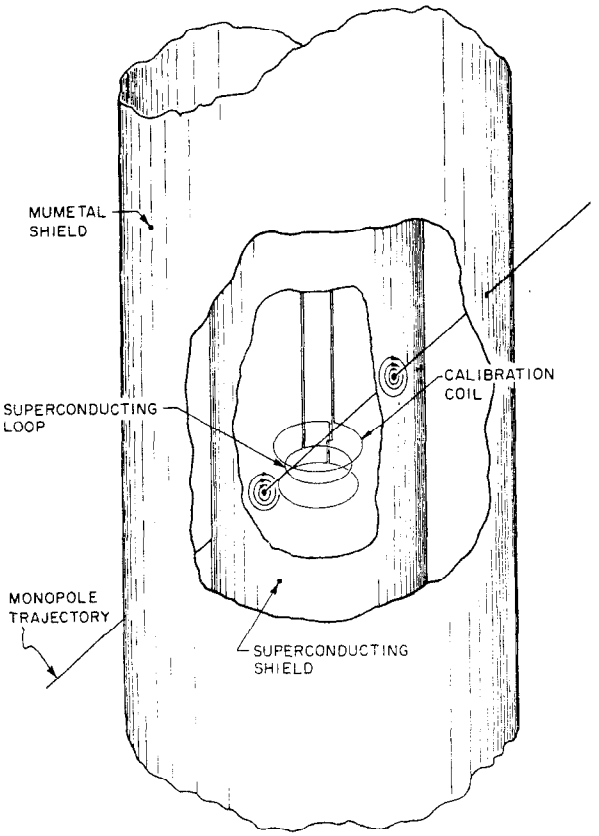


Fig. 6. Schematic of prototype monopole detector.

The distribution of all possible total induced current values for an isotropic distribution of straight line particle trajectories is shown in Fig. 8a. The density of sensing area $\mathcal{D}_\sigma$ (averaged over 4π solid angle) is plotted as a function of the total induced current. All of those trajectories which intersect the loop induce current changes between 7.5 ϕ_o and 8 ϕ_o and the integral of that portion of the distribution is 10.1 cm^2. This area corresponds exactly to the cross section of a 5.08 cm diameter loop averaged over 4π solid angle (1/2 of the loop area). In addition, for those trajectories which intersect the shield but not the loop, induced currents between 0 and 0.5 ϕ_o would be seen. The integral under this portion is infinite, but the noise level of the detector sets a natural lower cutoff. For our prototype with its noise level of 0.2 ϕ_o we obtain an additional sensing area of 145 cm^2. Thus for every event between 7.5 and 8 ϕ_o one would expect 14 events between 0.2 and 0.5 ϕ_o.

Several intervals throughout a continuous one month time period are shown in Fig. 7a, where no adjustments of the dc level have been made. Typical disturbances caused by daily liquid nitrogen and weekly liquid helium transfers are evident. A single large event was recorded (Fig. 7b). It is consistent in magnitude with the passage of a single Dirac charge within a combined uncertainty of $\pm$ 5% (resulting from the calibration uncertainty and the distribution $\mathcal{D}_\sigma$ in Fig. 8a). It is the largest event of any kind in the record.

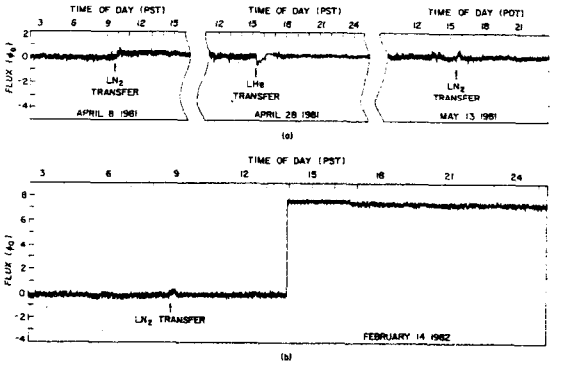


Fig. 7. (a) Typical stability during one month
(b) The candidate event

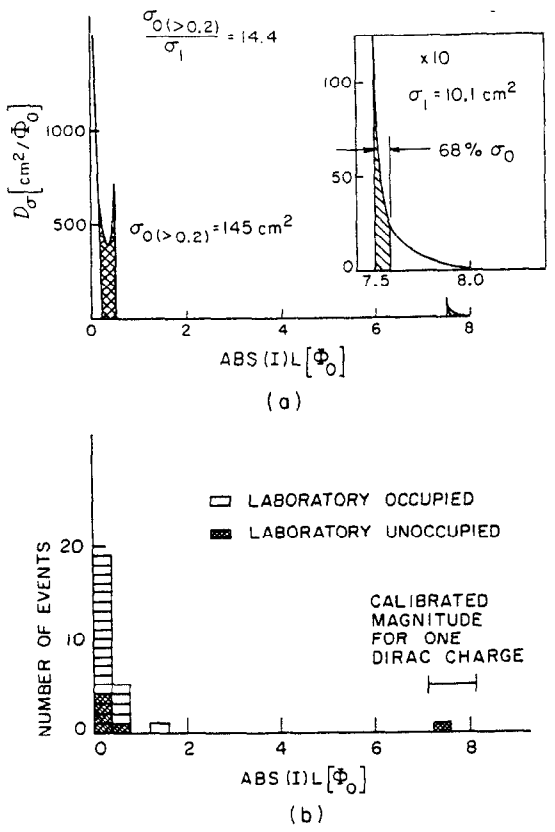


Fig. 8. (a) Density of sensing area function
(b) Histogram of all spontaneous events during first 151 days

Several histograms have been obtained from a detailed analysis of the first 151 days (the detailed analysis of the remaining 231 days is not complete, however, no large events were seen). In Fig. 8b are plotted the 27 spontaneous events exceeding a threshold of 0.2 ϕ_o which remain after excluding known disturbances (Fig. 9a) such as transfers of liquid helium and nitrogen. An event is defined as an offset with stable levels for at least one hour before and after. Only six events were recorded during the 70% of the running time when the laboratory was unoccupied. Since many more small events were seen during working hours it is clear that the detector is sensitive to disturbances. As we shall discuss below, this is consistent with its known sensitivity to mechanical disturbances. However, even if we assume that the five small events and the large event occurring during nonwork hours are real, the absence of an additional 9 small events suggests that the actual rate of large events should be three times lower. Thus a better upper bound on the particle flux is obtained by considering the lack of small events.

The most likely sources for spurious signals are associated with the mechanical sensitivity of the apparatus. Mechanically induced offsets have been intentionally generated. These could be caused by shifts of the four turn loop wire geometry, which would produce inductance changes and inversely proportional current changes (IL = flux is constant). Alternatively, trapped supercurrent vortices in or near the SQUID could move from mechanically induced local heating. In any case, sharp raps with a screwdriver handle against the detector assembly cause offsets. The magnitude distribution of 31 such induced events is shown in Fig. 9b.

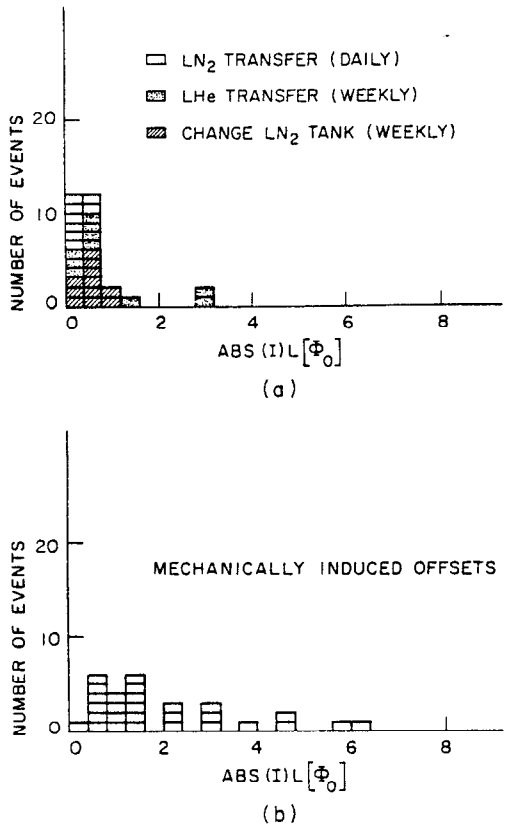


Fig. 9. Histograms (a) of all events during first 151 days directly correlated with dewar maintenance and (b) of magnitudes from all mechanically induced events from test raps.

Although we have not been able to produce such events which appear as clean as the candidate event, magnitudes close to the candidate event magnitude have been generated. If we further assume that mechanical stresses frozen into the detector upon initial cooling from room temperature could spontaneously release or be triggered by a small external disturbance, it would be possible to imagine a large spurious signal. The difficulty with easily accepting this scenario as a plausible explanation for the candidate event is that the data from this detector have been accumulated over five separate runs, each commencing with a cooldown of the apparatus from room temperature, and no other such signals were ever seen. Nevertheless, we feel IT IS NOT POSSIBLE TO RULE OUT A SPURIOUS CAUSE FOR THE FEBRUARY CANDIDATE EVENT. We are planning a series of tests on this detector aimed at reducing the uncertainty in our calibration and further clarifying the origin of the mechanically induced offsets. These tests will include repeated thermal cycling of the apparatus.

Our recent primary effort has gone into building a new detector with a larger sensing area and with sufficient cross checks to rule out spurious causes for any new events. It is described in the next section.

VII. PROGRESS ON NEW THREE LOOP DETECTOR

In the spring of 1982 a group including M. Taber, J. Bourg, S. Felch, R. Gardner, R. King and me began work on a larger detector. We have completed construction of a new three loop detector. This new detector is based on the same principles as the prototype system described in Sec. VI but has improved mechanical stability, a greater

sensing area and much better spurious signal discrimination. As shown schematically in Fig. 10, it consists of three mutually orthogonal superconducting loops, each 10.2 cm in diameter (twice that of the original device). In addition to a sevenfold increase (71 cm^2) in direct average isotropic sensing area for trajectories passing through at least one loop, 57% of those trajectories also intersect at least two loops, providing valuable coincidence information. The sensitivity of this new instrument to near miss trajectories which traverse the shield but do not intersect the three loops provides an additional effective sensing area for single Dirac charges 53 times greater (540 cm^2) than that of the prototype detector for signals of magnitude 0.1 ϕ_o or larger. Because of the smaller signal levels, this near miss sensitivity can provide lower flux bounds if no candidate events are seen, however, such a near miss candidate would not be as definitive as one corresponding to a trajectory passing through at least one loop.

We are completing a detailed analysis of the distribution functions for this new detector. These functions are plotted in a three dimensional phase space in which the axes correspond to the signal sizes seen by an event in each loop. Thus each point in this space corresponds to a three loop event. Preliminary results indicate that the volume of this phase space occupied by all possible monopole trajectories passing through at least one detector loop is about 1% of the volume of a sphere with radius just equal to that of the largest allowed event magnitude (about 6.5 ϕ_o). The magnitude is defined as the square root of the sum of the squares of each loop signal. Thus for a candidate event to be consistent with a possible

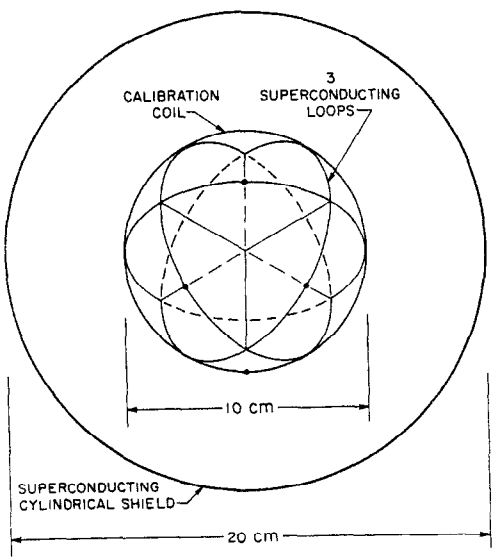


Fig. 10. Schematic of three loop monopole detector.

monopole trajectory it must lie within the allowed volume. This requirement is particularly stringent for trajectories that intersect at least one loop, but does not effectively discriminate near miss trajectories.

In addition, two known sources of spurious signals lie within well defined planes in this phase space. These are magnetic field changes at the three loops caused either by leakage fields in through the top of the superconducting shield or by the pendulum motion of the loop assembly in the shield field gradient. These planes can be experimentally determined to better than 1% resolution. Thus the most convincing candidate event would correspond to a trajectory intersecting at least one loop and lying away from these planes in the phase space. Data from an external fluxgate magnetometer and an accelerometer, both mounted on the outside of the detector, will remove most if not all signals from the planes of confusion produced by the leakage fields and the shield magnetic gradient.

To monitor the detector, we have designed a computer based data acquisition system. The output signals from the fluxgate and the accelerometer together with the outputs from the three independent SQUID loop current sensors are continuously sampled at 200 readings per second per channel. These data are temporarily stored onto a computer ring buffer (about 30 seconds long) and digitally filtered to 0.1 Hz bandwidth (one point every 5 seconds) in real time. The filtered readings are then stored on the disc to form a permanent continuous record. In addition, these filtered data are constantly compared to detect changes in the SQUID sensor levels above 0.1 ϕ_o. Such an event then triggers in software the permanent storage of the ring buffer contents around the time of the event. The high bandwidth information allows convincing discrimination against mechanically induced spurious events of any kind. However, our 10 millisecond resolution is NOT capable of observing current rise times of order 0.1 to 1 microsecond expected from the passage through a loop of a Dirac charge with velocity between 10^{-3} and 10^{-4} the speed of light. This data acquisition system is assembled and is expected to become fully operational by early 1983.

As a backup to the computer the detector is also continuously monitored on a six channel strip chart recorder at 0.1 Hz bandwidth. As of October we have operated the system for nearly three months. We have accumulated 61 days of data, primarily on the strip chart recorder with SQUID noise levels of 1 ϕ_o or better. The signal from any Dirac magnetic charge passing through at least one loop would have been detectable. NO SUCH SIGNAL HAS YET BEEN SEEN. The present noise level does not allow clear detection of near miss signals. However, using only the direct loop sensing area the dominant contribution to our experimental particle flux bound now comes from our new three axis detector.

As of October 16, 1982, the limit on the particle flux of magnetic charges passing through the earth's surface at any velocity and of any mass is less than 1.2×10^{-10} cm^{-2} s^{-1} sr^{-1}. This limit is derived combining 382 days of data from the prototype detector with its 10.1 cm^2 of average loop sensing area and 61 days from the new three axis detector with its 70.9 cm^2 loop area.

Astrophysical arguments lead to several other limits. Here to obtain representative numbers we assume a particle mass of 10^{16} GeV/c^2. Then an absolute upper bound for the galactic monopole particle flux of 4×10^{-10} cm^{-2} s^{-1} sr^{-1} is obtained from the limits on the local galactic dark mass[14]. A much smaller upper bound of 10^{-15} cm^{-2} s^{-1} sr^{-1} is obtained assuming an isotropic flux from arguments based on the existence of the 3 microgauss galactic magnetic fields.[15] However, possible models incorporating monopole plasma oscillations[16] require densities above a critical value and lead to a LOWER bound of about 10^{-13} cm^{-2} s^{-1} sr^{-1}. All of the above bounds suggest particle velocities near 10^{-3} c.

An enhanced monopole density gravitationally bound to our own solar system[17] would allow much smaller average galactic flux levels and lead to smaller particle velocities near 10^{-4} c.

Perhaps the most important experimental question is, can conventional ionization devices with their much larger sensing area detect the passage of single Dirac charges with velocities of order 10^{-4} to 10^{-3} c?[18] New calculations based on fundamental quantum mechanical arguments suggest that helium gas devices would provide such a resolution.[19]

Finally, it has been shown that the supermassive monopoles arising from grand unification theories will catalyze nucleon decay processes.[20] If the cross section for such events is of order the hadron cross section, as has been suggested,[21] then all attempts at direct detection of these monopoles may be doomed to failure. Arguments based on x-ray flux limits from galactic neutron stars[22] and assuming a strong cross section lead to an upper bound for a magnetic particle flux of about 10^{-22} cm^{-2} s^{-1} sr^{-1} - about one per year through the entire land area of Rhode Island!

VIII. LARGER SENSING AREA SUPERCONDUCTIVE DETECTORS

Superconductive devices at present are the only known velocity independent monopole detectors and directly measure the magnetic charge. Thus an important question is how large can the sensing area of such devices be made using existing technologies?

First with respect to our new three axis system, we are now working to reduce the detector noise levels below 0.1 ϕ_o and have obtained short periods of such operation. The ability to reliably detect near miss events will increase the sensing area from 70.9 cm^2 to over 600 cm^2. However, as discussed in Sec. VII, candidates in the near miss category are less convincing. Larger diameter loops with their larger self inductances provide ever decreasing signal to noise ratios and for diameters larger than about 10 cm cannot be effectively used as monopole detectors.

To overcome this limitation we are designing a new generation of superconductive detector which will use up to several square meters of a thin superconducting sheet in the form of a cylinder for recording magnetically charged particle tracks. It is analogous to a photographic emulsion which records electrically charged particle tracks. A magnetic charge, traversing the cylinder, twice in most cases, would record signatures consisting of doubly quantized trapped flux vortices in the walls (Fig.11). As long as the sheet remains superconducting, the strong flux pinning due to lattice and surface defects will prevent any motion. The ambient trapped

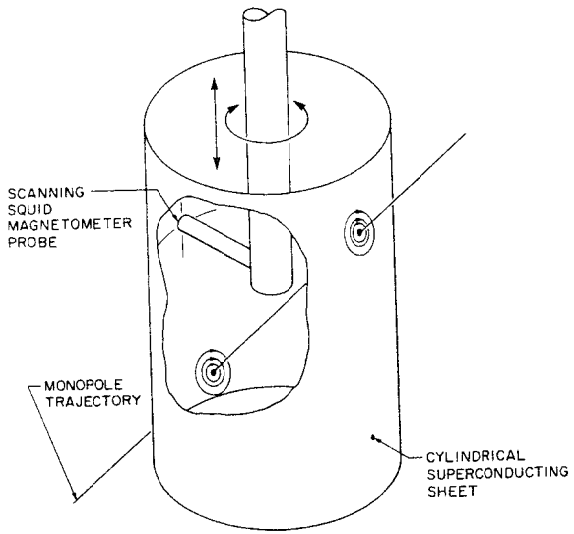


Fig. 11. Schematic of large area scanning detector.

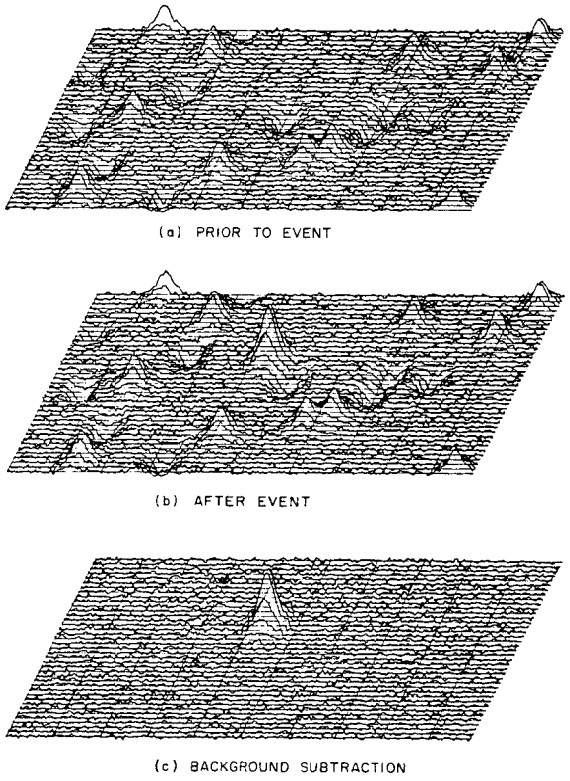


Fig. 12. Simulated data from scanning detector.

flux pattern, about one quantized vortex per cm^2 in a 10^{-7} gauss field, will be periodically recorded using a small scanning coil coupled to a SQUID. Two simulated scans, over a 10 cm by 10 cm area, are shown in Fig. 12(a) and (b). A typical SQUID noise level has been included. In (b) a new doubly quantized vortex has appeared and is most clearly seen when (a) is subtracted from (b) as shown in (c).

With our new three loop detector, or latter with the larger sensing area scanning detectors, either we will begin to see more events which would be very convincing, or we will set an upper limit approaching 10^{-12} cm^{-2} s^{-1} sr^{-1} on a magnetic particle flux - 100 times smaller than our present value. Either way, this is a very exciting time for our group.

The work described in this paper has been funded in part by NSF Grant DMR 80-26007 and DOE Contract DE-AM03-76SF00-326.

IX. REFERENCES

1. B. Cabrera, Ph.D. Thesis, Stanford University, 1975; B. Cabrera and F. van Kann, Acta Astronautica 5, 125 (1978).
2. C.W.F. Everitt, Experimental Gravitation, ed. B. Bertotti (Academic Press, New York, 1973), p. 331; J. A. Lipa, Proceedings of the International School of General Relativity Effects in Physics and Astrophysics: Experiments and Theory (3rd Course), 1977, p. 129.
3. M. A. Taber, Ph.D. Thesis, Stanford University, 1978; M. A. Taber, J. Physique C6, 192 (1978).
4. B. Cabrera and G. J. Siddall, Precision Engineering, 3, 125 (1981); B. Cabrera, S. Felch and J. T. Anderson, Physica 107B, 19 (1981); B. Cabrera, H. Gutfreund and W. A. Little, Phys. Rev. B1, June (1982).
5. L. P. Gorkov, Sov. Phys.-JETP 9, 1364 (1959).
6. See for example: A. L. Fetter and J. D. Walecka, Quantum Theory of Many-Particle Systems (McGraw-Hill, San Francisco, 1971), Chap. 13.
7. B. S. Deaver and W. M. Fairbank, Phys. Rev. Lett. 7, 43 (1961); R. Doll and M. Nabauer; ibid. 7, 51 (1961).
8. For review see: P. Goddard and D. I. Olive, Rep. Prog. Phys. 41, 1357 (1978).
9. P.A.M. Dirac, Proc. Rog. Soc., A133, 60 (1931); Phys. Rev. 74, 817 (1948).
10. For review see: A. S. Goldhaber and J. Smith, Rep. Prog. Phys. 38, 731 (1975).
11. G. 't Hooft, Nucl. Phys. 79B, 276 (1974) and Nucl. Phys. 105B, 538 (1976); A. M. Polyakov, JETP Letts. 20, 194 (1974).
12. J. P. Preskill, Phys. Rev. Lett. 19, 1365 (1979); G. Lazarides, Q. Shafi and T. F. Walsh, Phys. Lett. 100B, 21 (1981).
13. See also works on superconductive detectors for static matter searches: L. W. Alvarez, Lawrence Radiation Laboratory, Physics Note 470, 1963 (unpublished); P. Eberhard, ibid, Physics Note 506, 1964 (unpublished); L. J. Tassie, Nuovo Cimento 38, 1935 (1965); L. Vant-Hull, Phys. Rev. 173, 1412 (1968); P. Eberhard, D. Ross, L. Alvarez and R. Watt, Phys. Rev. D4, 3260 (1971).

14. B. Cabrera, Phys. Rev. Lett. 48, 1378 (1982).

15. M. S. Turner, E. N. Parker and T. J. Boydan, Enrico Fermi Institute Preprint No. 82-18.

16. E. E. Salpeter, S. L. Shapiro, and I. Wasserman, Phys. Rev. Lett. 49, 1114 (1982).

17. S. Dimopoulos, S. L. Glashow, E. M. Purcell and F. Wilczek, Nature 298, 824 (1982).

18. S. P. Ahlen and K. Kinoshita, Phys. Rev. D26, 2347 (1982).

19. S. D. Drell, N. M. Kroll, M. T. Mueller, S. J. Parke and M. A. Ruderman, SLAC Publication 3012.

20. F. Wilczek, Phys. Rev. Lett. 48, 1146 (1982).

21. V. Rubakov, JETP Lett. 33, 644 (1981); Nucl. Phys. B203, 311 (1982); C. Callan, Phys. Rev. D26, 2058 (1982)

22. E. W. Kolb, S. Colgate and J. A. Harvey, Phys. Rev. Lett. 49, 1373 (1982); S. Dimopoulos, J. Preskill and F. Wilczek, Phys. Lett. (1982), in press.

THE EARLY UNIVERSE - THE ULTIMATE ACCELERATOR

Gary Steigman

Bartol Research Foundation

Abstract

The Early Universe was a hot, dense soup of all elementary particles - a high energy physicist's dream. The high temperature and density correspond to high flux and to collisions with high center-of-mass energy - the Early Universe was the *Ultimate Accelerator*. *To convince you that cosmology provides* a valuable probe of high energy physics and that high energy physics has a significant impact on cosmology, I will begin by emphasizing the successes of the standard model in describing primordial nucleosynthesis. After a general consideration of the survival of relics from the hot big bang, I will illustrate the results with the examples of relic nucleons and relic neutrinos. Relic nucleons are the remnants of a universal baryon asymmetry which GUTs plus cosmology can account for. Relic neutrinos may, if they have a small rest mass ($\approx$ tens of eV), dominate the universal mass density.

© G. Steigman 1982

THE COSMIC CONNECTION

The organizers of this conference have asked me to talk of the impact on cosmology of recent developments in high energy physics. Indeed, developments in high energy physics - both theory and experiment - have had a considerable impact on astrophysics in general and cosmology in particular in recent years. New proposals in Unified, Grand Unified and Superunified Theories, as well as discoveries at accelerators and in more conventional laboratories, have suggested solutions to some long standing cosmological puzzles. It would be remiss, however, to fail to admit that as a dialogue between particle physicists and astrophysicists was established, the path between these two specialties at the frontier of physics has become a heavily travelled, two-way street. It has been clear to most cosmologists that to build the best models of the evolution of the Universe requires the incorporation of the very best physics - high energy physics included. With a few notable exceptions, it took the particle physics community longer to appreciate that significant constraints to models of particle physics were forthcoming from astrophysical and cosmological investigations. By now, that has changed; these days, the "compleat" high energy physicist is also a cosmologist. Today the study of the Universe is a truly interdisciplinary field.

The salient reason for the intimate connection between particle physics and cosmology is that the early Universe was very hot and very dense. High temperature and high density correspond to high center-of-mass energy and high flux. From the perspective of the particle physicist, the early Universe was the Ultimate Accelerator. Unfortunately, (or perhaps fortunately; it all depends on your point of view) adiabatic cooling forced the shutdown of this accelerator some 10-20 billion years ago. To probe particle physics at CIAC (Cosmic Isotropic Accelerator Center) requires that we be clever and careful. The general approach is briefly described as follows: The "best" high energy physics is a significant part of the microphysical input to the construction of a cosmological model to describe, in particular, the early evolution of the Universe. The Universe evolves according to the model cosmology, and comparisons are made between theoretical predictions and observational data. Agreements between theory and observation provide us with some confidence that the model - the cosmology plus the high energy physics - may be correct, or at least on the right track. Should contradictions arise, they would provide clues to flaws in the cosmology, the particle physics, or both. By this iterative symbiotic process, both the cosmology and the high energy physics advance.

To describe the heavily trafficked road between particle physics and cosmology would require an entire conference. Indeed, there have been several such conferences in recent years (for example, see the review by Kolb and Turner, 1981). I have, of necessity, adopted a much more modest goal. In pointing out some of the more interesting vistas along the way, I hope to

provide my audience with a feeling for the possibilities that exist and the sense of accomplishments already achieved by travelling this road. This talk does not pretend to either depth or breadth; those whose interest has been piqued must consult the literature, some of which will be listed below.

PRIMORDIAL NUCLEOSYNTHESIS

I've chosen to begin the journey along the road connecting particle physics and cosmology with a discussion of primordial nucleosynthesis. Why? The answer is simple and crucial: Primordial Nucleosynthesis provides us with the only probe of the Early Universe! To choose our direction for further progress - indeed, to be at all confident we're on the right road - we need to know the answers to several questions.

First and foremost, "Does the 'standard' hot big bang model (i.e.: the simplest one with the fewest arbitrary adjustable parameters) agree with observations?" If the answer to this question is in the affirmative (it will be!), we may travel further and pose more detailed questions. For example, "How many neutrino - or other 'ino' - flavors are permitted (or required) by the consistency of the standard model?" As for a question of more direct relevance to cosmology, "What is the universal density of nucleons?"

Before considering the answers to these questions, let us briefly review the requirements imposed on the cosmology by the observational data. The so-called "heavy" elements ($A \geq 12$) are believed to be cooked in stars in the course of normal stellar and galactic evolution. The abundances of the "intermediate" elements (Li, Be, B) can be understood on the basis of a cosmic ray spallation origin - in collisions between cosmic ray nuclei and the nuclei of interstellar gas atoms, heavier elements (C,N,O) are broken down to (among other products) Li, Be, B (Reeves et al. 1970). This mechanism fails, however, to account for the observed abundance of ^{7}Li. With the possible exception of ^{7}Li, then, a cosmological origin is not required for the intermediate and heavy nuclei. ^{7}Li may, however, be produced in stars (Cameron and Fowler 1971; Scalo 1976; Starrfield et al. 1978). The situation is dramatically different for the "light" elements D, ^{3}He and ^{4}He. Deuterium, being very weakly bound, is very easily destroyed. It is, therefore, very difficult to find an astrophysical site for the production of D in its observed abundance. Indeed, to date it has proved impossible to synthesize D without overproducing other elements (Epstein et al. 1976). A cosmological origin for deuterium is strongly suggested - perhaps required. ^{3}He can be produced in stars, particularly those cool, low mass stars which fail to burn helium to ^{4}He (Iben 1967). It seems likely that production in such stars in the course of galactic evolution enhances any primordial ^{3}He (Rood, Steigman and Tinsley 1976). A primordial origin for the (poorly known) present abundance of ^{3}He is not required; conversely, the big bang should not "overproduce" ^{3}He. Next to hydrogen, ^{4}He is the most abundant element in the Universe.

Stars, in the course of galactic evolution, produce ^{4}He. Stellar production, by all accounts, is insufficient to account for the observed abundance of ^{4}He. A big bang origin is required for most of the ^{4}He observed today. To recapitulate then, we require (or desire) that primordial nucleosynthesis produce all the observed D and most of the ^{4}He. It may well be that a significant fraction of the observed ^{3}He and ^{7}Li also have a primordial origin. None of the other elements requires a big bang origin. Finally, it should be mentioned that since D and ^{7}Li are easily destroyed, overproduction in the big bang is not necessarily a problem; the observed abundance may be reconciled with the primordial abundance when account is taken of astration in the course of galactic evolution. In contrast, it is difficult to destroy the more tightly bound ^{3}He – indeed, estimates suggest a net production (Rood, Steigman and Tinsley 1976). Since stars do synthesize ^{4}He, and since the observed abundance greatly exceeds the abundance of all other elements (the helium abundance by mass $Y \gtrsim 0.2$ whereas the heavy element abundance $Z \gtrsim 0.02$), the Universe must take care to not overproduce ^{4}He primordially.

Observations

In a forthcoming paper (Yang et al. 1982 - hereafter YTS^{2}O), my colleagues and I have re-examined the current observational data pertinent to determining the present abundances of the light elements. The reader is referred to that paper (and references therein) for a more detailed discussion; here I simply summarize the data and the conclusions drawn from the observations.

Deuterium is only well studied in our local neighborhood. Comparisons of D- and H-Lyman series absorption by interstellar gas in front of nearby, hot, young stars leads to an abundance (by number) within a factor two of $D/H \approx 2\times10^{-5}$ (10^5 D/H ≈ 1-4). Since primordial deuterium may be astrated, a conservative conclusion from the data is: $(D/H)_{BB} \geq 1\times10^{-5}$.

The abundance of ^{3}He is poorly known. The "solar system" abundance which is within a factor two of $^3He/H \approx 2\times10^{-5}$ may be taken as an upper limit to the present abundance. Some of the observed ^{3}He may have resulted from the burning of primordial D. The upper limits to the present abundances of D and ^{3}He $[(D/H)_{MAX} \approx (^3He/H)_{MAX} \leq 4\times10^{-5}]$ may be used to derive (YTS^{2}O) an upper limit to the sum of the primordial abundances of those elements; given the uncertainties, $[(D+^3He)/H]_{BB} \approx (12\text{-}20)\times10^{-5}$.

Because of its large and universal abundance, ^{4}He is perhaps the most important of the light elements from the point of view of cosmology. Crudely speaking, observations suggest an abundance today which ranges from $Y \approx 0.2$ to $Y \approx 0.3$. Some of the presently observed ^{4}He is surely stellar in origin. To infer a primordial abundance from current data entails uncertainties. The present situation is reviewed by YTS^{2}O who derive from the data an upper limit to the big bang abundance of $Y_{BB} \leq 0.25\text{-}0.26$. It is much more difficult (and the result

more uncertain) to set a lower limit; YTS[2]O find $Y_{BB} \gtrsim$ 0.22–0.23. Although we would hope to more narrowly constrain the primordial abundance of ^{4}He, it must be emphasized that with $0.22\text{–}0.23 \lesssim Y_{BB} \lesssim 0.25\text{–}0.26$, the helium abundance is, by far, the most accurately known of all the abundances.

Theory

The first, and most important, question confronting primordial nucleosynthesis was whether the standard model could account for the observed abundances -- in particular, those of D and ^{4}He. The observed abundances of D and ^{4}He differ by some 3–4 orders of magnitude. It is a signal success of the standard model that it correctly predicts this difference. In Figure 1, taken from YTS[2]O, the big bang abundance of ^{4}He is plotted as a function of the big bang abundance of D+^{3}He for several values of the number of two-component neutrino species. It is clear from Figure 1 that for $2 \lesssim N_\nu \lesssim 4$, consistency between theory and observation for D, ^{3}He and ^{4}He is obtained. Although we've not discussed it here, it should be mentioned that recent observations by Spite and Spite (1982) of ^{7}Li in old stars suggest that the standard model may also account for a significant fraction of the observed ^{7}Li. Our first question is thus - at present - answered affirmatively. This encourages us to embark on a more detailed comparison between theory and observation.

In Figure 2, taken from YTS[2]O, the big bang abundances of D and ^{3}He (and their sum) are shown as a function of the nucleon

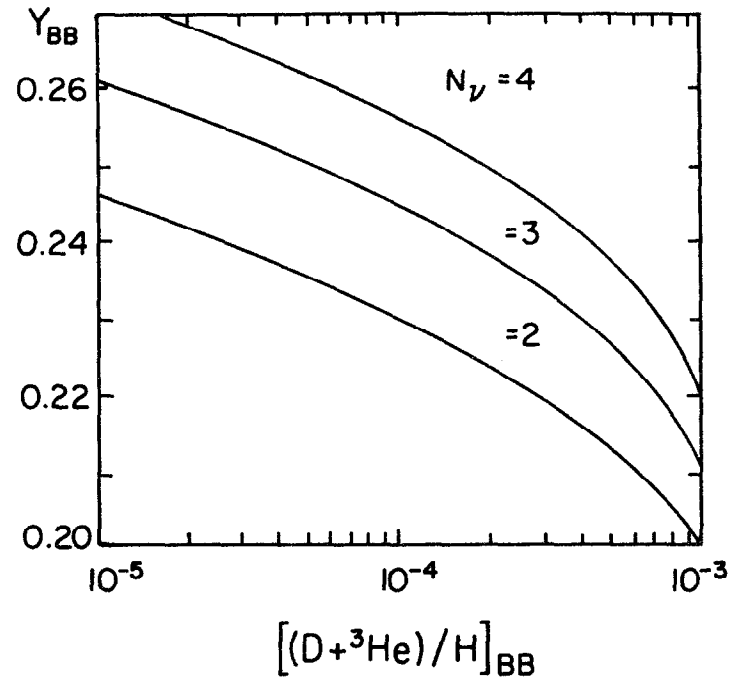


Figure 1. The predicted big bang abundance of ^{4}He (by mass, Y_{BB}) versus the predicted big bang abundance (by number relative to H) of D plus ^{3}He.

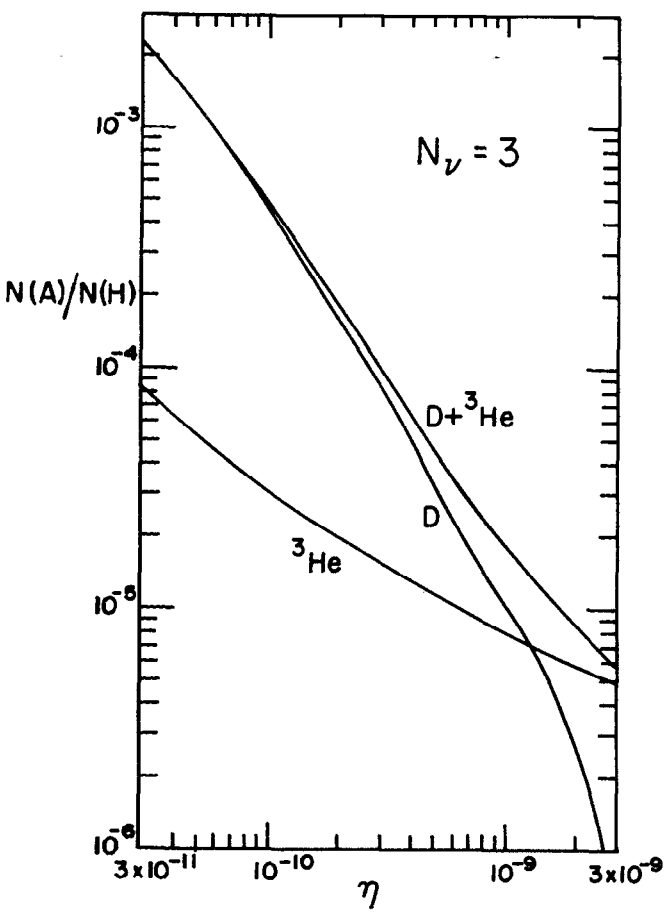


Figure 2. The predicted big bang abundances (by number relative to H) of D, ^{3}He and D+^{3}He versus the universal ratio of nucleons to photons η.

abundance η -the ratio of nucleons to photons. The higher the nucleon abundance the more rapidly is D (and, to a lesser extent ^{3}He) burned to ^{4}He; higher η corresponds to smaller yields of D and ^{3}He. If we require that primordial nucleosynthesis account for at least the minimum observed abundance of D ($D/H \gtrsim 1\times10^{-5}$), then we constrain η to be smaller than $\eta \lesssim 10\times10^{-10}$. On the other hand, a very small value of η would lead to a large primordial abundance of D. To avoid too much D+^{3}He ($[(D+^3He)/H]_{BB} \lesssim 12\text{-}20\times10^{-5}$) leads to a lower limit to η, $\eta \gtrsim (2\text{-}3)\times10^{-10}$. With these constraints on η ($2\text{-}3 \lesssim 10^{10}\eta \lesssim 10$), let us return to ^{4}He for a more detailed comparison.

In Figure 3, adapted from YTS[2]0, the ^{4}He abundance is shown as a function of η for three values of N_ν - the number of species of two-component neutrinos. Although N_ν=4 is a possibility, this value is only allowed (for $\eta \gtrsim 2\times10^{-10}$) if $Y_{BB} \gtrsim 0.25$. That the primordial abundance of ^{4}He is this large cannot be excluded although the data do suggest smaller values. Note that, if indeed N_ν=4, then the constraint $Y_{BB} \lesssim 0.26$ leads to a small value for η ($\lesssim 5\times10^{-10}$). Although the current data may be consistent with Y_{BB} as high as 0.26, future observations may reduce this upper limit. If we could infer that $Y_{BB} \lesssim 0.25$ then, for $N_\nu \geq 3$ (ν_e, ν_μ, ν_τ) we would obtain a new upper limit on η: $\eta \lesssim 8\times10^{-10}$. A further reduction in the estimated upper limit to $Y_{BB} \lesssim 0.23$ would begin to cause trouble with the standard model. The combined constraints of

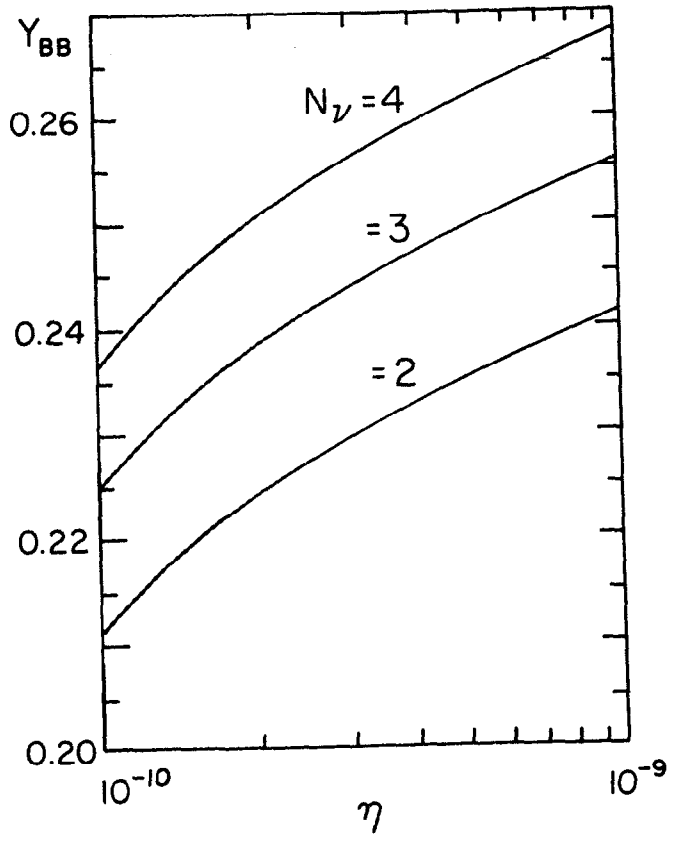


Figure 3. The predicted big bang abundance (by mass) of ^{4}He as a function of the nucleon abundance for three values of the number of species of light, two component neutrinos.

$[(D+^3He)/H]_{BB} \leq (12\text{-}20)\times10^{-5}$ (which corresponds to $\eta \geq (2\text{-}3)\times10^{-10}$) and $Y_{BB} \leq 0.23$ can only be consistent if $N_\nu < 3$. In the standard (particle physics) model, ν_τ is expected to be a light ($m\nu_\tau << 1$ MeV) neutrino similar to ν_e and ν_μ. Experimentally, however, all that is known is that $m\nu_\tau \lesssim 250$ MeV; if $m\nu_\tau \gtrsim 25$ MeV (Kolb and Sherrer 1982) then $N\nu < 3$ is possible. A true incompatibility of the standard model with the data would be obtained if observations ever led - convincingly - to the limit $Y_{BB} < 0.22$.

Nucleon Mass Density

Before moving on from this discussion of primordial nucleosynthesis, it is worthwhile (and interesting) to consider the implications for cosmology of the constraints derived from the data. In particular, we've learned that the nucleon abundance (the ratio of nucleons to photons) is constrained to lie in the range: $2\text{-}3 \lesssim \eta_{10} \lesssim 10$; $\eta_{10} = 10^{10}\eta$. Knowing the nucleon abundance we may calculate the universal mass density in nucleons.

$$\rho_N = m_N n n_\gamma;\ n_\gamma \simeq 4\times10^2 \left(\frac{T_o}{2.7}\right)^3 cm^{-3}. \qquad (1)$$

In (1), m_N is the nucleon rest mass and n_γ the density of black body photons; the range of estimates of the present temperature of the microwave background is $2.7 \leq T_o \leq 3.0$ K. It is useful to compare the nucleon mass density to the critical density ρ_c which separates those low density ($\rho_o < \rho_c$) universes which will expand forever, from the high density ($\rho_o > \rho_c$) universes whose expansion will eventually stop, to be

followed by collapse.

$$\rho_c = 3H_o^2 (8\pi G)^{-1} \simeq 2\times10^{-29} h_o^2 (gcm^{-3}). \quad (2)$$

In (2), G is Newton's gravitational constant and H_o is the Hubble parameter describing the present expansion rate of the Universe.

$$H_o = 100\ h_o\ (kms^{-1}Mpc^{-1});\ 1/2 \leq h_o \leq 1. \quad (3)$$

As an aside to which we'll return later, the inverse of the Hubble parameter has the dimension of time. The Hubble time, H_o^{-1}, provides, within the context of the standard model, an upper limit to the age of the Universe.

$$H_o^{-1} \simeq 10 h_o^{-1} \times 10^9 yr \Rightarrow t_o \leq (10\text{-}20)\times10^9 yr. \quad (4)$$

Returning to the nucleon density and comparing it to the critical density, we find

$$\Omega_N = \frac{\rho_N}{\rho_c} = 0.0035 h_o^{-2} \left(\frac{T_o}{2.7}\right)^3 n_{10}. \quad (5)$$

Since both h_o and T_o are imprecisely known, Ω_N would be uncertain even if the nucleon abundance were known to high accuracy; for $2.7 \leq T_o \leq 3.0$ K and $1/2 \leq h_o \leq 1$, $0.0035 n_{10} \leq \Omega_N \leq 0.019 n_{10}$. Combining all the uncertainties we find that: $0.01 \leq \Omega_N \leq 0.2$. The important conclusion which follows from this comparison is that: Nucleons Fail To Close The Universe By At Least A Factor Of Five.

It is instructive to compare the mass density in nucleons constrained by primordial nucleosynthesis to the estimates of the total universal mass density from dynamical considerations. The most straightforward - but impractical - approach to estimating the universal mass density is to add up all the mass in a volume large enough to provide a fair sample of the representative "stuff" of the Universe. Instead, the light emitted in such a volume is summed to provide an estimate of the universal luminosity density, $\mathcal{L}_{obs}$. Then the mass on various scales is determined dynamically (i.e.: from Newton's Laws) and compared to the light emitted on the same scale to obtain the (scale dependent) average mass-to-light ratio, $\langle M/L \rangle$. If the mass and the light were similarly distributed, then

$$\rho_{Dyn} = \langle M/L \rangle \mathcal{L}_{obs}, \quad (6)$$

would provide a fair estimate of the total, average mass density. Unfortunately, as the entries in Table 1 demonstrate, the mass and the light are not similarly distributed. Virtually all of the light comes from the inner 10-20 kpc ($\simeq 30\text{-}60\times10^3$ lyr) of galaxies, whereas the mass is much more broadly distributed. The so-called missing mass problem is really a missing light problem: on larger and larger scales there is more and more mass but not more and more light. It is therefore difficult to decide which scale provides the best estimate of the average stuff of the Universe. A natural choice would be to concentrate on the largest scales, but one must be alert to the possibility of invidious selection effects. For example, although the mass-to-light ratio is largest on the scale of Rich Clusters of Galaxies, the galaxies which contribute most of the light to $\mathcal{L}_{obs}$ do not find themselves in Rich Clusters. Perhaps

Table 1

Dynamical Estimates of the Universal Mass Density*

Region Surveyed	$\langle M/L\rangle(M_\odot/L_\odot)$	Ω_{Dyn}
Solar Neighborhood	2–3	$> 0.002\ h_o^{-1}$
Galaxies	$(10\text{–}20)h_o$	0.008–0.017
Binaries & Small Groups	$(60\text{–}180)h_o$	0.05 – 0.15
Rich Clusters	$(200\text{–}600)h_o$	0.17 – 0.50
Intracluster Gas	$[M_{HG} \simeq 0.1\ M_{Dyn}]$	0.02 – 0.05

*The entries in this table are based on the $\langle M/L\rangle$ values in Faber and Gallagher (1979).

the high observed mass-to-light ratios for Rich Clusters is less a measure of the universal mass density than of the initial conditions at the formation of the Cluster or its subsequent dynamical evolution. Because of such caveats, the entries in the last column of Table 1 should be regarded with great caution.

The quantity Ω_{Dyn} is defined as follows. From the observed luminosity density we may infer a critical mass-to-light ratio which corresponds to $\rho_{Dyn}=\rho_c$. For the recent observations of Kirshner et al. (1982 - KOSS),

$$\mathcal{L}_{obs}\ (KOSS) \rightleftharpoons \langle M/L\rangle_c \simeq 1200\ h_o\ (M_\odot/L_\odot). \qquad (7)$$

Then, Ω_{Dyn} is defined by

$$\Omega_{Dyn} \equiv \rho_{Dyn}/\rho_c \equiv \frac{\langle M/L\rangle}{1200\ h_o} \quad . \qquad (8)$$

Notice that the nucleon density as constrained by primordial nucleosynthesis ($0.01 \lesssim \Omega_N \lesssim 0.2$) is consistent with the estimate of the total mass determined dynamically on all scales except that of the Rich Clusters. It is worth noting that a lower limit to the mass in nucleons on the scale of Rich Clusters follows from the intensity of x-ray emission, via bremsstrahlung radiation, from the hot, intracluster gas. This estimate, as well as that for the inner, luminous parts of galaxies, suggests that $\Omega_N \gtrsim 0.01\text{–}0.02$ provides a reasonable lower limit to the universal nucleon density. Unless more convincing evidence in support of $\Omega_o > 0.2$ emerges, nucleons may well (but need not) dominate the universal mass density.

RELICS FROM THE EARLY UNIVERSE

Our brief discussion of the success of the standard, hot big bang model in correctly describing primordial nucleosynthesis gives us confidence that an extrapolation of the evolution of the Universe to much earlier times may not be unreasonable. During most of the evolution of the Universe all wavelengths scale with the scale factor: $\lambda \propto R$ where the scale factor R describes the universal expansion. Since interparticle separations scale with R, the number density (with an important exception to be described below) varies as $n \propto R^{-3}$. For relativistic particles (e.g., photons) the temperature (average energy per particle) and the wavelength are inversely related so that $T \propto \lambda^{-1} \propto R^{-1}$. As a result, if we go to earlier times when R was smaller, n and T

increase: The Early Universe Was Very Hot And Very Dense. For most reactions, the reaction rate becomes very fast compared to the expansion rate.

$$\Gamma \propto n\sigma \propto T^3\,\sigma(T), \tag{9a}$$

$$t^{-1} \propto \rho_{TOT}^{1/2} \propto T^2 \tag{9b}$$

$$\Gamma t \propto T\,\sigma(T) >> 1 \tag{9c}$$

As an aside, it is worth noting that for gauge interactions (2↠2), $\Gamma t \lesssim 1$ for $T \gtrsim T_{GUT}$; above the GUT temperature, gauge interactions are incapable of establishing equilibrium - the regime between the Planck temperature ($T_p \simeq 10^{19}$ GeV) and the GUT temperature ($T_{GUT} \simeq 10^{14}$ GeV) is a no-man's (or woman's!) land.

As a result of the rapid reaction rate (9c), all particles - those already discovered as well as those not yet discovered because their mass is too high or their interactions too weak to have been produced or detected at current accelerators - will be produced in abundance during the early evolution of the universe: The Early Universe Was A Hot, Dense Soup Of All Elementary Particles! The important question is, what survives?

We approach the question of the survival of relics from the early Universe as follows. Consider a comoving volume V - a volume which expands along with the general universal expansion - which is large enough to provide a representative sample of the Universe. Count the number of particles of various types in V.

$$N_i = n_i V \propto R^3 n_i \propto T^{-3} n_i(T). \tag{10}$$

In equilibrium, when the collision rate greatly exceeds the expansion rate, the particle densities are given by their *equilibrium distributions*.

$$\text{ER}(m<<T):\ n_{ER} \propto T^3 \Rightarrow N_{ER} = \text{constant}, \tag{11a}$$

$$\text{NR}(T<<m):\ n_{NR} \propto T^3[x^{3/2}e^{-x}],\ x=m/T, \tag{11b}$$

$$\Rightarrow N_{NR} \propto x^{3/2}e^{-x} \to 0. \tag{11c}$$

The results in (11) are easily understood. In equilibrium, pairs of ER particles are easily produced, and since the production rate and the annihilation rate are equal (detailed balance), the total number of ER particles in V is conserved. The situation is very different for pairs of NR particles. With masses much in excess of the temperature, it is very difficult to find a collision with enough center-of-mass energy to produce a massive pair. Only those very rare collisions, out in the exponential tail of the distribution, have enough energy to produce a massive pair. The abundance of NR particles is thus suppressed, exponentially, *compared to that of ER particles*.

Eventually, as the Universe expands and cools and the density drops, equilibrium can no longer be maintained - the reaction rate becomes smaller than the expansion rate. At that stage, no new pairs are produced and no old pairs (already present in the volume V) annihilate. Subsequently, therefore, the number of all kinds of particles in V (NR as well as ER) is conserved. The most weakly interacting, massive particles (e.g., neutral leptons) will decouple first, before their abundance becomes very small. The more strongly interacting particles (e.g., charged leptons, hadrons) remain in equilibrium longer, to a lower temperature and

a lower abundance before they too drop out of equilibrium and their number in V is conserved. Massless particles, or those which decouple while they still are extremely relativistic, are conserved at their original large abundance. For a description of the detailed calculations of the surviving abundances of relics from the big bang, see Steigman (1979) and references therein. For A-$\bar{A}$ pairs with mass m_A and annihilation cross section $\sigma_{A\bar{A}}$, the surviving abundance (relative to photons) is

$$\frac{N_A + N_{\bar{A}}}{N_\gamma} \simeq 10^{-18} \left(\frac{m_N}{m_A}\right) \frac{(\sigma v)_{N\bar{N}}}{(\sigma v)_{A\bar{A}}} \qquad (12)$$

In equation (12) m_N is the nuclear mass and $(\sigma V)_{N\bar{N}} \simeq 10^{-15} cm^3 s^{-1}$ is the N-$\bar{N}$ annihilation rate for $v \lesssim c$.

Before proceeding to a comparison between the standard theory and observations, several aspects relating to the interpretation of (12) should be elucidated. As already mentioned, (12) applies to those particles which are NR ($m > T$) when they decouple; for ER particles $N_{ER} \simeq N_\gamma$. The particles A must be stable at least on the timescale at which the result is (12) is applied; for current observations $\tau \gtrsim t_0 \gtrsim 10 \times 10^9$ yr. Finally, and most important, the foregoing discussion and the result in (12) apply to symmetric pairs $N_A = N_{\bar{A}}$; that is, to particles with a conserved charge so that they may only be produced and annihilated in pairs.

Relic Nucleons

If Baryon Number were conserved, a Baryon Symmetric Universe would be anticipated: $\Delta B = B - \bar{B} = 0$. Were that in fact the case, equation (12) would apply to the survival of relic nucleons (A=N) and we would expect $N_{\bar{N}} = N_N \lesssim 10^{-18} N_\gamma$. Actually what is observed (see Steigman 1976) is an Asymmetric Universe with $N_{\bar{N}} \ll N_N = \eta N_\gamma$, $\eta \gtrsim 10^{-10}$. For some time there were those who considered this result ($N_{\bar{N}} \neq N_N$) a cosmological puzzle. However, it was known that in the absence of a zero mass gauge boson coupled to baryon charge - the analog of the photon and electric charge - baryon number was not necessarily conserved. Grand Unified Theories have completely laid this puzzle to rest; in most GUTs Baryon Number is not conserved. In this case the present nucleon density is recognized as the relic of an earlier baryon asymmetry: $N_N = \Delta B$ (Sakharov 1967, Yoshimura 1978; Ellis et al. 1978; Dimopoulos and Susskind 1979; Toussaint et al. 1979; Weinberg 1979). For details of how to generate a universal baryon asymmetry, the reader is referred to the preceding references as well as the more extensive studies of Fry et al. (1980a,b,c) and Kolb and Wolfram (1980a,b).

For the purpose of illustration, I will outline one mechanism - the out-of-equilibrium decay scenario - for generating a net baryon number. The main ingredients necessary for generating a universal asymmmetry are exposed in this example.

Assume there is a superheavy boson (Gauge or Higgs) $S(\bar{S})$ whose decay rate is "slow." In this context, slow means that when the temperature drops to m_S, the decay rate of S is slow compared to the universal expansion rate. In this case, when T

drops below m_S, the $S(\bar{S})$ haven't decayed and $N_{\bar{S}} \simeq N_S \simeq N_\gamma$. When they finally do decay at $T_{DS} \ll m_S$ there is a non-equilibrium distribution of S and $\bar{S}$. There are three ingredients required of the S-decays to guarantee the generation of a net baryon asymmetry.

(i) Baryon Nonconservation. Suppose there are two baryon violating decay channels such as

$$S \xrightarrow{r} \bar{q}\bar{q}(B=-2/3); \quad \bar{S} \xrightarrow{\bar{r}} qq(B=+2/3)$$
$$S \xrightarrow{1-r} q\,\ell(B=+1/3); \quad \bar{S} \xrightarrow{1-\bar{r}} q\,\bar{\ell}(B=-1/3). \tag{13}$$

In (13), r and $\bar{r}$ are the branching ratios for the particular channel. In this case, the decay of each S-$\bar{S}$ pair generates a net baryon number $\varepsilon=r-\bar{r}$.

(ii) C and CP Violation. If C and CP were conserved, $r=\bar{r}$ and $\varepsilon=0$. To generate a baryon asymmetry requires C and CP violation; ε is a measure of the amount of C and CP violation.

(iii) Out-of-Equilibrium. If the S bosons were in equilibrium when they decayed, then decays would be balanced by inverse decays and $\Delta B=0$. However, we have arranged for the S-$\bar{S}$ pairs to decay when $T_{DS} \ll m_S$ when their distributions are far from equilibrium. Since $T_{DS} \ll m_S$, inverse decays cannot compete with decays so that

$$\left(\frac{\Delta B}{N_\gamma}\right)_{DS} \simeq \varepsilon\left(\frac{N_S}{N_\gamma}\right) \simeq \varepsilon \tag{14}$$

The resulting nucleon abundance at present is

$$\eta = \left(\frac{N_N}{N_\gamma}\right)_0 = \left(\frac{\Delta B}{N_\gamma}\right)_0 = \left(\frac{\Delta B}{N_\gamma}\right)_{DS}\left(\frac{N_{\gamma DS}}{N_{\gamma 0}}\right) \tag{15}$$

The last term in (15) accounts for the dilution of the nucleon abundance due to the "extra" photons produced by the decays and annihilations which occur for $T < T_{DS}$. This dilution may be estimated (see, for example, Steigman 1979) by counting the number of degrees of freedom present at T_{DS}, $N_{\gamma 0} \sim g_{DS} N_{\gamma DS}$, so that

$$\eta \simeq \varepsilon g_{DS}^{-1} \sim 10^{-2}\varepsilon. \tag{16}$$

Since we are aiming for $\eta \gtrsim 10^{-10}$, we only require a weak C and CP violation $\varepsilon \gtrsim 10^{-8}$. Although the required ε appears to be small, it is not so easy to guarantee that $\varepsilon \gtrsim 10^{-8}$ in the simplest GUTs. With minor modifications though, a variety of GUTs appear capable of accounting for the observed nucleon abundance. More important than the quantitative success however is the fundamental contribution of particle physics - GUTs - to the solution of a cosmological problem. The cosmology predicts the early Universe was hot and dense enough to produce S-$\bar{S}$ pairs copiously. The expansion of the Universe provides the possibility of non-equilibrium processes; the GUTs provide the required Baryon number, C and CP violations naturally.

Relic Neutrino

As a final example of the survival of debris from the CIAC let us consider relic neutrinos. Unified theories predict that neutrinos participate in neutral current weak interactions such

as

$$e^+ + e^- \leftrightarrow \nu_i + \bar{\nu}_i \quad (i=e,\ \mu,\ \tau\ldots?) \tag{16}$$

For temperatures greater than a few MeV, reactions (16) are in equilibrium ($\Gamma_{\nu\bar{\nu}} t >> 1$) for "light" reactions ($m_\nu << T$). In equilibrium neutrinos are roughly as abundant as photons.

$$\text{Equilibrium: } \frac{n_\nu}{n_\gamma} = \frac{3}{4} N_\nu;\ N_\nu = \sum_i \frac{1}{2} g_{\nu_i} \tag{17}$$

When e^+-e^-pairs annihilate they heat the relic photons but not the already decoupled relic neutrinos.

$$\text{Today: } \left(\frac{n_\nu}{n_\gamma}\right)_o = \frac{3}{4} N_\nu \left(\frac{T_\nu}{T_\gamma}\right)_o^3 = \frac{3}{11} N_\nu, \tag{18a}$$

$$\text{where: } (T_\nu/T_\gamma)_o^3 = 4/11 \tag{18b}$$

It is thus a predicted consequence of cosmology plus particle physics that there exists, in addition to the background of microwave photons, a background of relic, microwave neutrinos.

Relic neutrinos are as abundant as relic photons and, therefore, much more common than relic nucleons.

$$\frac{n_\nu}{n_N} \simeq \frac{3\times10^9 N_\nu}{\eta_{10}} \geq 3\times10^8 N_\nu. \tag{19}$$

If neutrinos should have a small rest mass, they may compete favorably with nucleons in contributing to the total universal mass density.

$$\frac{\Omega_\nu}{\Omega_N} \simeq \frac{3m_\nu(\text{eV})}{\eta_{10}} \geq \frac{m_\nu}{3\text{eV}}, \tag{20a}$$

$$\text{where: } m_\nu = \sum_i \frac{1}{2} g_{\nu i} m_{\nu i} \tag{20b}$$

If $m_\nu \geq$ 3eV, ours is a Neutrino Dominated Universe. The estimate of Ω_ν, itself is more uncertain since it depends on H_o and T_o.

$$\Omega_\nu h_o^2 \simeq \frac{m_\nu}{100\text{eV}} \left(\frac{T_0}{2.7}\right)^3 \gtrsim \frac{m_\nu}{100\text{eV}} \tag{21}$$

If, indeed, we live in a neutrino dominated Universe, massive relic neutrinos would have played a significant role in the growth of perturbations leading to the development of structure in the Universe (Peebles 1973, Bond, Efstathiou and Silk 1980, Wasserman 1981). Decoupled neutrinos would stream freely from regions of high density to regions of low density thus mixing up such regions and damping any perturbations which may have been present (provided, of course, that neutrinos dominate the mass density: $m_\nu \geq$ 3eV). The lighter the neutrinos are, the faster they move and the larger the scale on which neutrino damping is effective.

$$M_{D\nu} \simeq 4\times10^{18} m_\nu^{-2} M_\odot \tag{22}$$

Massive, relic neutrinos are, in many ways, very attractive (Schramm and Steigman 1980a). Since relic neutrinos are expected to be at least a billion times as abundant as relic nucleons, neutrinos with a small mass may dominate the mass of the Universe. If, indeed, the Universe is neutrino dominated - that is, if $m_\nu \geq$ 3eV - they may provide a solution to the puzzle of the missing light. Decoupled neutrinos are nondissipative and would cluster gravitationally more easily on large scales than small scales. This might explain why there is more dark mass on

large scales.

There are some cosmological constraints on the mass of such neutrinos. If neutrinos were too heavy there would be discrepancies with observations - there would be too much of a good thing! For example, since neutrinos don't shine, too massive a neutrino(s) would contribute too much dark mass. For clusters of galaxies (see Table 1),

$$\frac{M_\nu}{M_N} \lesssim \frac{M_{DARK}}{M_{LUM}} \lesssim 10\text{-}30. \qquad (23)$$

From equations (20a) and (23) then, $m_\nu \lesssim 30\text{-}100$ eV.

A similar constraint follows from a lower limit to the age of the Universe. The higher the present density Ω_0, the faster the Universe will have expanded and the younger it will be today. From the ages of globular clusters (Schramm and Steigman 1980b),

$$t_0(10^9) \gtrsim 10\text{-}13 \Rightarrow \Omega_0 h_0^2 \lesssim 1/4\text{-}3/4 \qquad (24)$$

Since $\Omega_0 > \Omega_\nu$, a comparison of equations (21) and (24) leads to the constraint $m_\nu \lesssim 25\text{-}75$ eV.

For neutrinos with $m_\nu \gtrsim 3$ eV - so that the Universe is neutrino dominated - a lower limit to m_ν follows from the requirement that neutrino damping not erase all structure in the Universe. If we insist that perturbations survive on scales of superclusters or smaller, we find

$$M_{D\nu} \lesssim M_{SC} \lesssim 10^{16} M_\odot \Rightarrow m_\nu \gtrsim 20 \text{ eV}. \qquad (25)$$

SUMMARY

In this talk I've limited myself to some sightseeing along the road connecting particle physics and cosmology. The highlights I've chosen illustrate the symbiotic relation between particle physics and cosmology. From primordial nucleosynthesis we gain some confidence that it is not unreasonable to trust the standard model in extrapolating the cosmology to earlier times and the particle physics to higher energies. We learn that there are no more than four, two-component, light neutrinos ($N_\nu \lesssim 4$) and that the nucleon abundance is small: $\eta \lesssim 10^{-9}$, $\Omega_N < 0.2$. The standard model (including GUTs) has shown why the Universe may be asymmetric ($\Delta B \neq 0$) and provided a formalism for a quantitative calculation of the nucleon abundance ($\eta \propto \varepsilon g_D^{-1}$). Finally, we've seen that the standard model predicts a background of microwave neutrinos of large abundance. Such neutrinos may, if they have a finite rest mass ($m_\nu \gtrsim 3$ eV), dominate the universal mass density. If ours is a neutrino dominated Universe, then neutrinos may provide the solution to the cosmological puzzle of the missing light. The sum of the masses of such neutrinos must not exceed 25-100 eV; the heaviest of these massive neutrinos should be at least 20 eV.

The future in this interdisciplinary area of research seems bright. There is still much each can give to the other. The width of the Z^0 will constrain N_ν. Searches for ν_τ decays may help us decide if ν_τ is light or heavy. Constraints on the existence of exotic particles will help to delimit new theories

of particle physics. The road connecting particle physics and cosmology promises to become even more congested.

ACKNOWLEDGEMENTS

The results of primordial nucleosynthesis described here derive almost entirely from work I've done with my colleagues Keith Olive, Dave Schramm, Mike Turner and Jongmann Yang. I want to thank them for permission to cite our work prior to publication and for valuable discussions in the course of our fruitful collaborations.

REFERENCES

Bond, J.R., Efstathiou, G. and Silk, J.I., Phys. Rev. Lett. 45, 1980 (1980).

Cameron, A.G.W. and Fowler, W.A., Ap. J. 164, 111 (1971).

Dimopoulos, S. and Susskind, L., Phys. Rev. D18, 4500 (1979).

Ellis, J., Gaillard, M.K. and Nanopoulos, D.V., Phys. Lett. 80B, 360 (1978).

Epstein, R., Lattimer, J. and Schramm, D.N., Nature 263, 198, (1976).

Faber, S.M. and Gallagher, J.S., Ann. Rev. Astron. a Astrophys. 17, 135 (1979).

Fry, J.N., Olive, K.A. and Turner, M.S., Phys. Rev. D22, 2953 a 2977; Phys. Rev. Lett. 45, 2074 (1980a,b,c).

Iben, I., Ap. J. 147, 624 a 650 (1967).

Kirshner, R.P., Oemler, A., Jr., Schechter, P.L. and Schectman, S.A., In Preparation (1982).

Kolb, E.W. and Wolfram, S., Phys. Lett. 91B, 217 (1980a); Nucl. Phys. B172, 224 (1980b).

Kolb, E.W., and Turner, M.S., Nature 294, 521 (1981).

Kolb, E.W. and Scherrer, R.J., Phys. Rev. D25, 1481 (1982).

Peebles, P.J.E., Ap. J. 180, 1 (1973).

Reeves, H., Fowler, W.A. and Hoyle, F., Nature 226, 727 (1970).

Rood, R.T., Steigman, G. and Tinsley, B.M., Ap. J. (Lett.) 207, L57 (1976).

Sakharov, A., JETP Lett. 5, 24 (1967).

Scalo, J.M., Ap. J. 206, 795 (1976).

Schramm, D.N. and Steigman, G., GRG 13, 101 (1981a); Ap. J. 243, 1 (1981b).

Spite, M. and Spite, F., Nature 297, 483 (1982).

Starrfield, S., Truran, J.W., Sparks, W.M. and Arnould, M., Ap. J. 222, 600 (1978).

Steigman, G., Ann. Rev. Astron. Astrophys. 14, 339 (1976).

Steigman, G., Ann. Rev. Nucl. Part. Sci. 29, 313 (1979).

Toussaint, D., Treiman, S.B., Wilczek, F. and Zee, A., Phys. Rev. D19, 1036 (1979).

Yang, J., Turner, M.S., Steigman, G., Schramm, D.N. and Olive, K.A., In Preparation (1982).

PARTICIPANTS

A:

Ramsey Ali
SLAC, Bin 81
Stanford University
Stanford, California 94305

D. Amidei
Lawrence Berkeley Laboratory
One Cyclotron Road
Berkeley, California 94720

Dikran Antreasyan
Department of Physics
Harvard University
Cambridge, Massachusetts 02138

Hideaki Aoyama
SLAC, Bin 81
Stanford University
Stanford, California 94305

Michael Arenton
Argonne National Laboratory
9700 South Cass Avenue
Argonne, Illinois 60439

R. Arnold
Department of Physics
American University
Washington, D.C. 20016

William Ash
SLAC, Bin 94
Stanford University
Stanford, California 94305

David Aston
SLAC, Bin 62
Stanford University
Stanford, California 94305

William Atwood
SLAC, Bin 96
Stanford University
Stanford, California 94305

Paul Avery
Wilson Laboratories
Cornell University
Ithaca, New York 14853

Naoki Awaji
Department of Physics
University of Nagoya
Nagoya 464
JAPAN

B:

John F. Babson
Department of Physics and Astronomy
University of Hawaii at Manoa
2505 Correa Road
Honolulu, Hawaii 96822

Andrew Baden
Lawrence Berkeley Laboratory
One Cyclotron Road
Berkeley, California 94720

Howard A. Baer
Department of Physics
University of Wisconsin
Madison, Wisconsin 53706

Joseph Ballam
SLAC, Bin 78
Stanford University
Stanford, California 94305

Rosemary Baltrusaitis
Department of Physics
California Institute of Technology
Pasadena, California 91109

Henry Band
Department of Physics
Northeastern University
Boston, Massachusetts 02115

Guido Barbiellini
CERN
CH-1211, Geneva 23
SWITZERLAND

Timothy Barklow
Department of Physics
University of Wisconsin
Madison, Wisconsin 53706

Michael Barnett
SLAC, Bin 81
Stanford University
Stanford, California 94305

Philip Barringer
Department of Physics
Indiana University
Bloomington, Indiana 47401

J. Becker
Department of Physics
University of Illinois
Urbana, Illinois 61801

Ivano Beltrami
Department of Physics
Yale University
New Haven, Connecticut 06520

Shahar Ben-Menahem
SLAC, Bin 81
Stanford University
Stanford, California 94305

David Bennett
SLAC, Bin 81
Stanford University
Stanford, California 94305

Alain Benzaken
Department of Physics
Yale University
New Haven, Connecticut 06520

Marc Bernstein
Department of Physics
University of Washington
Seattle, Washington 98195

Didier Besset
Department of Physics
Stanford University
Stanford, California 94305

Sampa Bhadra
Department of Physics
University of Colorado
Boulder, Colorado 80309

Vinod Bharadwaj
Department of Physics
University of California
Santa Barbara, California 93106

Cynthia Bilchak
Department of Physics
Case Western Reserve University
Cleveland, Ohio 44106

Guy Blaylock
Department of Physics
University of Illinois
Urbana, Illinois 61801

David Blockus
Department of Physics
Indiana University
Bloomington, Indiana 47401

Geoffrey Bodwin
SLAC, Bin 81
Stanford University
Stanford, California 94305

Felix Boehm
Lauritsen Laboratory
California Institute of Technology
Pasadena, California 91125

Albrecht Böhm
DESY
Notkestrasse 85
D-2000, Hamburg 52
WEST GERMANY

Gerard Bonneaud
SLAC, Bin 96
Stanford University
Stanford, California 94305

Maurice Bourquin
Department of Physics
Nucleaire et Corpusculaire
University of Geneva
CH-1211, Geneva 4
SWITZERLAND

Kersten Braune
SLAC, Bin 78
Stanford University
Stanford, California 94305

M. Breidenbach
SLAC, Bin 95
Stanford University
Stanford, California 94305

Stanley Brodsky
SLAC, Bin 81
Stanford University
Stanford, California 94305

Alan Bross
Lawrence Berkeley Laboratory
One Cyclotron Road
Berkeley, California 94720

Karl Brown
SLAC, Bin 94
Stanford University
Stanford, California 94305

T. Brown
Department of Physics and Astronomy
University of Hawaii at Manoa
2505 Correa Road
Honolulu, Hawaii 96822

Charles D. Buchanan
Department of Physics
University of California
Los Angeles, California 90024

Adriaan Buijs
NIKHEF
P.O. Box 41882
1009 DB Amsterdam
NETHERLANDS

Fatin Bulos
SLAC, Bin 98
Stanford University
Stanford, California 94305

Kirk Bunnell
SLAC, Bin 65
Stanford University
Stanford, California 94305

Patricia Burchat
SLAC, Bin 61
Stanford University
Stanford, California 94305

David Burke
SLAC, Bin 61
Stanford University
Stanford, California 94305

T. H. Burnett
Department of Physics
University of Washington
Seattle, Washington 98195

R. A. Burnstein
Department of Physics
Illinois Institute of Technology
Chicago, Illinois 60616

John Butler
SLAC, Bin 78
Stanford University
Stanford, California 94305

C:

Blas Cabrera
Department of Physics
Stanford University
Stanford, California 94305

Robert N. Cahn
Lawrence Berkeley Laboratory
One Cyclotron Road
Berkeley, California 94720

Michael Cain
Department of Physics
University of California
Davis, California 95616

David J. E. Callaway
Argonne National Laboratory
9700 South Cass Avenue
Argonne, Illinois 60439

Alan Campbell
Imperial College
Prince Consort Road
London SW7 2AZ
UNITED KINGDOM

J. Carlson
Lawrence Berkeley Laboratory
One Cyclotron Road
Berkeley, California 94720

Mark Carter
SLAC, Bin 81
Stanford University
Stanford, California 94305

Ronald Cassel
Department of Physics
University of Illinois
Urbana, Illinois 61801

Matteo Cavalli-Sforza
Department of Physics
Princeton University
Princeton, New Jersey 08540

George Chadwick
SLAC, Bin 94
Stanford University
Stanford, California 94305

C. C. Chang
Department of Physics
American University
Washington, D.C. 20016

Shen-Chang Chao
Institute of Theoretical Science
University of Oregon
Eugene, Oregon 97403

Jacques Chauveau
Rochester Group
Newman Laboratory of Nuclear Studies
Cornell University
Ithaca, New York 14853

Pisin Chen
SLAC, Bin 81
Stanford University
Stanford, California 94305

Tuan W. Chen
Department of Physics
New Mexico State University
Las Cruces, New Mexico 88003

S. Childress
Fermilab
P.O. Box 500
Batavia, Illinois 60510

Louis J. Clavelli
Argonne National Laboratory
9700 South Cass Avenue
Argonne, Illinois 60439

D. Coffman
Department of Physics
California Institute of Technology
Pasadena, California 91109

Joanne Cohn
Mather 432
Harvard University
Cambridge, Massachusetts 02138

Dieter Cords
DESY
Notkestrasse 85
2000-D Hamburg 52
WEST GERMANY

Paul Coteus
Department of Physics
University of Colorado
Boulder, Colorado 80302

R. F. Cowan
Department of Physics
Princeton University
Princeton, New Jersey 08540

David Coward
SLAC, Bin 65
Stanford University
Stanford, California 94305

Michael Crisler
Department of Physics
Ohio State University
Columbus, Ohio 43210

D:

Farhad Daghighian
Department of Physics
University of California
Irvine, California 92717

D. Dahl
SLAC, Bin 81
Stanford University
Stanford, California 94305

John D'Amore
Department of Physics
University of Cincinnati
Cincinnati, Ohio 45221

Christian De la Vaissiere
Lawrence Berkeley Laboratory
One Cyclotron Road
Berkeley, California 94720

Malcolm Derrick
Argonne National Laboratory
9700 South Cass Avenue
Argonne, Illinois 60439

Herbert DeStaebler
SLAC, Bin 96
Stanford University
Stanford, California 94305

Alberto Devoto
High Energy Physics
Florida State University
Tallahassee, Florida 32306

Daryl DiBitonto
CERN
CH-1211, Geneva 23
SWITZERLAND

Robert Diebold
Argonne National Laboratory
9700 South Cass Avenue
Argonne, Illinois 60439

William Dieterle
Lawrence Berkeley Laboratory
One Cyclotron Road
Berkeley, California 94720

Christine Di'Lieto
SLAC, Bin 81
Stanford University
Stanford, California 94305

Jonathan Dorfan
SLAC, Bin 95
Stanford University
Stanford, California 94305

John Dowd
Department of Physics
Southeastern Massachusetts University
North Dartmouth, Massachusetts 02747

Sidney Drell
SLAC, Bin 80
Stanford University
Stanford, California 94305

Richard Dubois
SLAC, Bin 96
Stanford University
Stanford, California 94305

Ehud Duchovni
Department of Nuclear Physics
The Weizmann Institute of Science
76100 Rehovot
ISRAEL

Craig Dukes
Randall Laboratory
University of Michigan
Ann Arbor, Michigan 48109

William Dunwoodie
SLAC, Bin 62
Stanford University
Stanford, California 94305

Marsha Duro
SLAC, Bin 63
Stanford University
Stanford, California 94305

E:

Stanley Ecklund
SLAC, Bin 60
Stanford University
Stanford, California 94305

Richard Edelstein
Department of Physics
Carnegie-Mellon University
Pittsburgh, Pennsylvania 15213

Kevin Einsweiler
SLAC, Bin 65
Stanford University
Stanford, California 94305

A. Eisner
Department of Physics
University of California
San Diego, California 92037

Roger Erickson
SLAC, Bin 78
Stanford University
Stanford, California 94305

F:

Svjetlana Fajfer
Institut za Fiziku
7100 Sarajevo
YUGOSLAVIA

Gary Feldman
SLAC, Bin 61
Stanford University
Stanford, California 94305

Enrique Fernandez
Argonne National Laboratory
9700 South Cass Avenue
Argonne, Illinois 60439

Clive Field
SLAC, Bin 78
Stanford University
Stanford, California 94305

Geoffrey Forden
Department of Physics
Indiana University
Bloomington, Indiana 47401

Melissa Franklin
SLAC, Bin 61
Stanford University
Stanford, California 94305

Paolo Franzini
Department of Physics
Columbia University
New York, New York 10027

René Fries
Department of Physics
Indiana University
Bloomington, Indiana 47401

David Fryberger
SLAC, Bin 20
Stanford University
Stanford, California 94305

Keisuke Fujii
Department of Physics
University of Nagoya
Nagoya 464
JAPAN

G:

John Gaiser
SLAC, Bin 98
Stanford University
Stanford, California 94305

K. K. Gan
Department of Physics
Purdue University
Lafayette, Indiana 47907

Roger A. Gearhart
SLAC, Bin 20
Stanford University
Stanford, California 94305

Walter Geist
CERN
CH-1211, Geneva 23
SWITZERLAND

Frederick J. Gilman
SLAC, Bin 81
Stanford University
Stanford, California 94305

Larry Gladney
SLAC, Bin 95
Stanford University
Stanford, California 94305

Gary Godfrey
SLAC, Bin 98
Stanford University
Stanford, California 94305

Michael Gold
Lawrence Berkeley Laboratory
One Cyclotron Road
Berkeley, California 94720

Laurence Golding
Lawrence Berkeley Laboratory
One Cyclotron Road
Berkeley, California 94720

Javier Gomez
Department of Physics
American University
Washington, D.C. 20016

Stephen Gray
Department of Physics
Indiana University
Bloomington, Indiana 47401

James Green
Department of Physics and Astronomy
Rutgers University
Piscataway, New Jersey 08854

H:

Gail Hanson
SLAC, Bin 61
Stanford University
Stanford, California 94305

Haim Harari
Department of Physics
Weizmann Institute of Science
76100 Rehovot
ISRAEL

John Hassard
Department of Physics
Harvard University
Cambridge, Massachusetts 02138

Jay Hauser
Department of Physics
California Institute of Technology
Pasadena, California 91109

Hisaki Hayashii
Department of Physics
University of Nagoya
Nagoya 464
JAPAN

B. Heltsley
Department of Physics
University of Wisconsin
Madison, Wisconsin 53706

Franz Herzog
Department of Physics
University of Wisconsin
Madison, Wisconsin 53706

Rolf-Dieter Heuer
Physikalisches Institut
Universitat Heidelberg
D-6900 Heidelberg 1
WEST GERMANY

Thomas Himel
CERN
CH-1211, Geneva 23
SWITZERLAND

David Hitlin
Department of Physics
California Institute of Technology
Pasadena, California 91109

Robert Hollebeek
SLAC, Bin 95
Stanford University
Stanford, California 94305

Richard Holman
National Aeronautics and Space Admin.
Goddard Space Flight Center
Greenbelt, Maryland 20771

R. Horisberger
Hansen Laboratories of Physics
Stanford University
Stanford, California 94305

George Hou
Department of Physics
University of California
Los Angeles, California 90024

Roger Hurst
Department of Physics
Northeastern University
Boston, Massachusetts 02115

David Hutchinson
SLAC, Bin 65
Stanford University
Stanford, California 94305

Miaogy Hwang
Department of Physics and Astronomy
Northwestern University
Evanston, Illinois 60201

Bernard Hyams
CERN
CH-1211, Geneva 23
SWITZERLAND

I:

Hirokazu Ikeda
KEK National Laboratory
for High Energy Physics
Ibaraki 305
JAPAN

Walter Innes
SLAC, Bin 61
Stanford University
Stanford, California 94305

Joachim Irion
Department of Physics
Harvard University
Cambridge, Massachusetts 02138

George Irwin
SLAC, Bin 63
Stanford University
Stanford, California 94305

J:

John Jaros
SLAC, Bin 61
Stanford University
Stanford, California 94305

Chueng Ryong Ji
SLAC, Bin 81
Stanford University
Stanford, California 94305

J. Johnson
Department of Physics
University of Wisconsin
Madison, Wisconsin 53706

Robert Johnson
SLAC, Bin 96
Stanford University
Stanford, California 94305

Robert Johnson
Institute of Theoretical Science
University of Oregon
Eugene, Oregon 97403

William B. Johnson
SLAC, Bin 62
Stanford University
Stanford, California 94305

Dennis Judd
Fermilab
P.O. Box 500
Batavia, Illinois 60510

K:

John Kadyk
Lawrence Berkeley Laboratory
One Cyclotron Road
Berkeley, California 94720

Young-Chuan Kao
Lawrence Berkeley Laboratory
One Cyclotron Road
Berkeley, California 94720

Lewis P. Keller
SLAC, Bin 20
Stanford University
Stanford, California 94305

Eun Joo Kim
SLAC, Bin 62
Stanford University
Stanford, California 94305

Jasper Kirkby
SLAC, Bin 63
Stanford University
Stanford, California 94305

Spencer Klein
SLAC, Bin 61
Stanford University
Stanford, California 94305

Daniel E. Klem
SLAC, Bin 96
Stanford University
Stanford, California 94305

Eike-Erik Kluge
Institute for Hochenergiephysik
Universitat Heidelberg
D-6900 Heidelberg 1
WEST GERMANY

David Koltick
Department of Physics
Purdue University
Lafayette, Indiana 47907

Paul Kooijman
Argonne National Laboratory
9700 South Cass Avenue
Argonne, Illinois 60439

Dale Koop
Department of Physics
California Institute of Technology
Pasadena, California 91109

Rudiger Kopp
CERN
CH-1211, Geneva 23
SWITZERLAND

Eve Kovacs
SLAC, Bin 81
Stanford University
Stanford, California 94305

Paul Kunz
SLAC, Bin 62
Stanford University
Stanford, California 94305

L:

Willie Langeveld
NIKHEF
P.O. Box 41882
1009 DB Amsterdam
NETHERLANDS

Andrew Lankford
SLAC, Bin 95
Stanford University
Stanford, California 94305

Rudy Larsen
SLAC, Bin 95
Stanford University
Stanford, California 94305

Tomas I. Larsson
Department of Theoretical Physics
Royal Institute of Technology
S-10044 Stockholm
SWEDEN

Kwong Lau
SLAC, Bin 94
Stanford University
Stanford, California 94305

Joseph LeBritton
Department of Physics
University of Arizona
Tucson, Arizona 85712

Bruce LeClaire
SLAC, Bin 95
Stanford University
Stanford, California 94305

Hoyun Lee
Department of Physics
University of Utah
Salt Lake City, Utah 84112

I-Hsiu Lee
Lawrence Berkeley Laboratory
One Cyclotron Road
Berkeley, California 94720

Juliet Lee-Franzini
Department of Physics
State University of New York
Stony Brook, New York 11790

David W. G. S. Leith
SLAC, Bin 62
Stanford University
Stanford, California 94305

Michael Levi
Department of Physics
Harvard University
Cambridge, Massachusetts 02138

Lorne Levinson
SLAC, Bin 62
Stanford University
Stanford, California 94305

David Levinthal
Fermilab
P.O. Box 500
Batavia, Illinois 60510

Shi Ping Li
Department of Physics
University of Washington
Seattle, Washington 98195

Holger Lierl
Max-Planck Institute
Föhringer Ring 6
D-8 Munchen 40
WEST GERMANY

Nigel Lockyer
SLAC, Bin 95
Stanford University
Stanford, California 94305

Stephen Lowe
SLAC, Bin 98
Stanford University
Stanford, California 94305

Vera Luth
SLAC, Bin 95
Stanford University
Stanford, California 94305

Richard Loveless
Department of Physics
University of Wisconsin
Madison, Wisconsin 53706

M:

Ronald Madaras
Lawrence Berkeley Laboratory
One Cyclotron Road
Berkeley, California 94720

Kaori Maeshima
Department of Physics
University of California
Davis, California 95616

Bimal P. Mahapatra
Department of Physics
Syracuse University
Syracuse, New York 13210

P. K. Malhotra
Tata Institute of Fundamental Research
Homi Bhabha Road
Bombay-40 00 05
INDIA

Usha Mallik
Laboratoire de l'Accélérateur Linéaire
Centre d'Orsay
F-91405 Orsay
FRANCE

W. Anthony Mann
Department of Physics
Tufts University
Medford, Massachusetts 02155

Alexander Markevich
SLAC, Bin 81
Stanford University
Stanford, California 94305

T. Maruyama
Department of Physics
University of Wisconsin
Madison, Wisconsin 53706

Takayuki Matsui
Hansen Laboratories of Physics
Stanford University
Stanford, California 94305

Clara Matteuzzi
SLAC, Bin 61
Stanford University
Stanford, California 94305

Thomas Mattison
SLAC, Bin 95
Stanford University
Stanford, Califonria 94305

Douglas McKay
Department of Physics and Astronomy
University of Kansas
Lawrence, Kansas 66045

Andrew C. McPherson
Herzberg Laboratories
Carleton University
Ottawa, Ontario K1S 5B6
CANADA

Robert Messner
SLAC, Bin 94
Stanford University
Stanford, California 94305

Olivia Meyer
Department of Physics
Northeastern University
Boston, Massachusetts 02115

Luca Mezincescu
SLAC, Bin 81
Stanford University
Stanford, California 94305

Geoffrey Mills
Department of Physics
California Institute of Technology
Pasadena, California 91109

Akiya Miyamoto
Department of Physics
University of Nagoya
Nagoya 464
JAPAN

Michiko Miyamoto
Kobe College
JAPAN

Kenneth Moffeit
SLAC, Bin 78
Stanford University
Stanford, California 94305

Ajaya K. Mohanty
Department of Physics
University of Maryland
College Park, Maryland 20742

Leonard Moss
SLAC, Bin 65
Stanford University
Stanford, California 94305

Robert Mozley
SLAC, Bin 65
Stanford University
Stanford, California 94305

A. Mueller
Department of Physics
Columbia University
New York, New York 10027

James Mueller
SLAC, Bin 78
Stanford University
Stanford, California 94305

Mark Mueller
Department of Physics
Stanford University
Stanford, California 94305

N:

A. K. Nandi
Rutherford Appleton Laboratory
Chilton, Didcot
Oxfordshire OX11 0QX
UNITED KINGDOM

Paolo Nason
SLAC, Bin 81
Stanford University
Stanford, California 94305

Adolfo Nemirovsky
Department of Physics and Astronomy
University of Kansas
Lawrence, Kansas 66045

Chi-Wai Ray Ng
Department of Physics
Purdue University
Lafayette, Indiana 47907

Yee Jack Ng
SLAC, Bin 81
Stanford University
Stanford, California 94305

O:

Allen Odian
SLAC, Bin 65
Stanford University
Stanford, California 94305

Arthur Ogawa
SLAC, Bin 96
Stanford University
Stanford, California 94305

Michael Ogg
Newman Laboratory of Nuclear Studies
Cornell University
Ithaca, New York 14853

Katsuhiko Ohya
Fukuyama City Junior College
for Women
Hiroshima-ken 720
JAPAN

Chong Leong Ong
SLAC, Bin 81
Stanford University
Stanford, California 94305

Piu Piu Ong
Department of Physics
Purdue University
Lafayette, Indiana 47907

Rene Ong
SLAC, Bin 61
Stanford University
Stanford, California 94305

Richard Oppenheim
Department of Physics
Yale University
New Haven, Connecticut 06520

Risto Orava
Fermilab
P.O. Box 500
Batavia, Illinois 60510

Mark Oreglia
Enrico Fermi Institute
University of Chicago
Chicago, Illinois 60637

Marius Orlowski
SLAC, Bin 81
Stanford University
Stanford, California 94305

A. Osterheld
Hansen Laboratories of Physics
Stanford University
Stanford, California 94305

Hitoshi Ozaki
Department of Physics
University of Nagoya
Nagoya 464
JAPAN

P:

Sandro Palestini
Department of Physics
Princeton University
Princeton, New Jersey 08544

Douglas Palmer
Department of Physics
University of California
San Diego, California 92037

Wolfgang K. H. Panofsky
SLAC, Bin 80
Stanford University
Stanford, California 94305

Sherwood Parker
Department of Physics
University of Hawaii
Honolulu, Hawaii 96822

Hossein Partovi
SLAC, Bin 81
Stanford University
Stanford, California 94305

Richard Partridge
Department of Physics
California Institute of Technology
Pasadena, California 91109

George Pastrana
SLAC, Bin 81
Stanford University
Stanford, California 94305

Martin Perl
SLAC, Bin 61
Stanford University
Stanford, California 94305

Ida Peruzzi
Laboratori Nazionali di Frascati
I-00044 Frascati (Roma)
ITALY

Marcello Piccolo
Laboratori Nazionali Frascati
I-00044 Frascati (Roma)
ITALY

James Pinfold
Fermilab
P.O. Box 500
Batavia, Illinois 60510

Bernard Pire
SLAC, Bin 81
Stanford University
Stanford, California 94305

Rainer Pitthan
SLAC, Bin 96
Stanford University
Stanford, California 94305

Robert Plaag
Department of Physics
University of Washington
Seattle, Washington 98195

Scott Plaetzer
Department of Physics
University of Illinois
Urbana, Illinois 61801

David Pollard
SLAC, Bin 63
Stanford University
Stanford, California 94305

B. Pollock
Hansen Laboratories of Physics
Stanford University
Stanford, California 94305

R. Prepost
Department of Physics
University of Wisconsin
Madison, Wisconsin 53706

Charles Y. Prescott
SLAC, Bin 96
Stanford University
Stanford, California 94305

John Price
SLAC, Bin 61
Stanford University
Stanford, California 94305

Q:

Helen Quinn
SLAC, Bin 81
Stanford University
Stanford, California 94305

R:

Christian Rad
Fermilab
P.O. Box 500
Batavia, Illinois 60510

Rajendran Raja
Fermilab
P.O. Box 500
Batavia, Illinois 60510

L. Kasturi Rangan
Department of Physics
Purdue University
Lafayette, Indiana 47907

Peter Rassmann
Department of Physics
Virginia Polytechnic Institute
and State University
Blacksburg, Virginia 24061

Blair Ratcliff
SLAC, Bin 62
Stanford University
Stanford, California 94305

Peter Ratoff
Department of Physics
California Institute of Technology
Pasadena, California 91109

Zbigniew Rek
SLAC, Bin 81
Stanford University
Stanford, California 94305

Patrick Reutens
Department of Physics
University of Chicago
Chicago, Illinois 60637

Sun Hong Rhie
SLAC, Bin 78
Stanford University
Stanford, California 94305

J. Richman
Department of Physics
California Institute of Technology
Pasadena, California 91109

Burton Richter
SLAC, Bin 95
Stanford University
Stanford, California 94305

David Ritson
Department of Physics
Stanford University
Stanford, California 94305

Leon S. Rochester
SLAC, Bin 96
Stanford University
Stanford, California 94305

S. Rock
Department of Physics
American University
Washington, D.C. 20016

Natalie Roe
SLAC, Bin 62
Stanford University
Stanford, California 94305

Jimmy Roehrig
SLAC, Bin 65
Stanford University
Stanford, California 94305

Leslie Rosenberg
SLAC, Bin 94
Stanford University
Stanford, California 94305

Carl Rosenfeld
Department of Physics
University of Rochester
Rochester, New York 14627

Marc C. Ross
Department of Physics
Northwestern University
Evanston, Illinois 60201

Forest Rouse
Lawrence Berkeley Laboratory
One Cyclotron Road
Berkeley, California 94720

Peter Rowson
Lawrence Berkeley Laboratory
One Cyclotron Road
Berkeley, California 94720

J. J. Russell
Department of Physics
California Institute of Technology
Pasadena, California 91109

S:

Makoto Sakuda
Department of Physics
California Institute of Technology
Pasadena, California 91109

Bruce Sawhill
SLAC, Bin 81
Stanford University
Stanford, California 94305

Theo Schaad
Department of Physics
Harvard University
Cambridge, Massachusetts 02138

Terry Schalk
Santa Cruz Institute for
Particle Physics
Santa Cruz, California 95060

Rafe Schindler
CERN
CH-1211, Geneva 23
SWITZERLAND

Dieter Schlatter
SLAC, Bin 95
Stanford University
Stanford, California 94305

Christoph Schmid
SLAC, Bin 81
Stanford University
Stanford, California 94305

William Schmidke
Fermilab
P.O. Box 500
Batavia, Illinois 60510

Kent Schwitkis
Department of Physics
University of California
Santa Barbara, California 93106

David Seckel
Department of Physics
University of Washington
Seattle, Washington 98195

Michael Seely
Department of Physics
Yale University
New Haven, Connecticut 06520

Abraham Seiden
Santa Cruz Institute for
Particle Physics
Santa Cruz, California 95060

David Shambroom
Department of Physics
Northeastern University
Boston, Massachusetts 02115

Stephen Shapiro
SLAC, Bin 62
Stanford University
Stanford, California 94305

Paul Sheldon
Lawrence Berkeley Laboratory
One Cyclotron Road
Berkeley, California 94305

David J. Sherden
SLAC, Bin 60
Stanford University
Stanford, California 94305

Toshiro Shimomura
Department of Physics
University of Nagoya
Nagoya 464
JAPAN

Juha-Pekka Sinervo
SLAC, Bin 62
Stanford University
Stanford, California 94305

William E. Slater
Department of Physics
University of California
Los Angeles, California 90024

John Sleeman
Department of Physics
University of Washington
Seattle, Washington 98195

K. Sliwa
Fermilab
P.O. Box 500
Batavia, Illinois 60510

John R. Smith
Department of Physics
University of California
Davis, California 95616

Wesley Smith
Nevis Laboratories
Columbia University
New York, New York 10027

Amarjit Soni
Department of Physics
University of California
Los Angeles, California 90024

Hidenori Sonoda
Department of Physics
California Institute of Technology
Pasadena, California 91109

Davison Soper
Institute of Theoretical Science
University of Oregon
Eugene, Oregon 97403

Tony Spadafora
Department of Physics
University of Illinois
Urbana, Illinois 61801

B. J. Stacey
Department of Physics
University of Toronto
Toronto Ontario M5S 1A7
CANADA

Gary Steigman
Bartol Research Foundation
University of Delaware
Newark, Delaware 19711

Rae Stiening
SLAC, Bin 95
Stanford University
Stanford, California 94305

Zdravko Stipcevic
Institut za Fiziku
7100 Sarajevo
YUGOSLAVIA

Ian Stockdale
Department of Physics
University of Rochester
Rochester, New York 14627

Mark Strovink
Lawrence Berkeley Laboratory
One Cyclotron Road
Berkeley, California 94720

Ryszard Stroynowski
Department of Physics
California Institute of Technology
Pasadena, California 91109

Karlheinz Stupperich
DESY
Notkestrasse 85
D-2000 Hamburg 52
WEST GERMANY

Ryuhei Sugahara
SLAC, Bin 96
Stanford University
Stanford, California 94305

Katsuhito Sugano
Fermilab
P.O. Box 500
Batavia, Illinois 60510

Akira Sugiyama
Department of Physics
University of Nagoya
Nagoya 464
JAPAN

Michael Sullivan
Department of Physics
University of California
San Diego, California 92037

Stanley Sunderwirth
Department of Physics
Yale University
New Haven, Connecticut 06520

Leonard Susskind
Department of Physics
Stanford University
Stanford, California 94305

Shiro Suzuki
SLAC, Bin 62
Stanford University
Stanford, California 94305

Zen Szalata
Department of Physics
American University
Washington, D.C. 20016

T:

Giora Tarnopolsky
SLAC, Bin 62
Stanford University
Stanford, California 94305

Shuji Tatsumi
Brookhaven National Laboratory
Upton, New York 11973

Susumu Terada
Brookhaven National Laboratory
Upton, New York 11973

Takayuki Teshima
Department of Physics and Astronomy
University of Maryland
College Park, Maryland 20742

Nobu Toge
Lawrence Berkeley Laboratory
One Cyclotron Road
Berkeley, California 94720

Walter Toki
SLAC, Bin 65
Stanford University
Stanford, California 94305

John Tompkins
Hansen Laboratories of Physics
Stanford University
Stanford, California 94305

Minh Tran
Brookhaven National Laboratory
Upton, New York 11973

Luca Trentadue
Instituto di Fisica
Universita di Parma
43100 Parma
ITALY

George Trilling
Lawrence Berkeley Laboratory
One Cyclotron Road
Berkeley, California 94720

Thomas Trinko
Argonne National Laboratory
9700 South Cass Avenue
Argonne, Illinois 60439

T. Trippe
Lawrence Berkeley Laboratory
One Cyclotron Road
Berkeley, California 94720

Yung-Su Tsai
SLAC, Bin 81
Stanford University
Stanford, California 94305

Gary B. Tupper
Department of Physics
Oklahoma State University
Stillwater, Oklahoma 74078

V:

Francesco Villa
SLAC, Bin 65
Stanford University
Stanford, California 94305

W:

Klaus Wacker
SLAC, Bin 98
Stanford University
Stanford, California 94305

David E. Wagoner
Fermilab
P.O. Box 500
Batavia, Illinois 60510

Anthony Waite
SLAC, Bin 62
Stanford University
Stanford, California 94305

Edward Wang
Department of Physics
University of Michigan
Ann Arbor, Michigan 48109

Kebin Wang
SLAC, Bin 61
Stanford University
Stanford, California 94305

Alan Weinstein
Department of Physics
Harvard University
Cambridge, Massachusetts 02138

Marvin Weinstein
SLAC, Bin 81
Stanford University
Stanford, California 94305

Roy Weinstein
Department of Physics
Northeastern University
Boston, Massachusetts 02115

J. Weiss
Argonne National Laboratory
9700 South Cass Avenue
Argonne, Illinois 60439

Bjorn Wiik
DESY
Notkestrasse 85
D-2000 Hamburg 52
WEST GERMANY

Walter Wilcox
Department of Physics
Oklahoma State University
Stillwater, Oklahoma 74078

F. Wilczek
Department of Physics
University of California
Santa Barbara, California 93106

Crispin Williams
Department of Physics
University of California
Davis, California 95616

H. H. Williams
Department of Physics
University of Pennsylvania
Philadelphia, Pennsylvania 19104

Stephen Williams
SLAC, Bin 62
Stanford University
Stanford, California 94305

Robert J. Wilson
Department of Physics
Purdue University
Lafayette, Indiana 47907

William Wisniewski
Department of Physics
University of Illinois
Urbana, Illinois 61801

Stanley Wojcicki
Department of Physics
Stanford University
Stanford, California 94305

Douglas E. Wood
Department of Physics
Purdue University
Lafayette, Indiana 47907

Nigel Wright
Argonne National Laboratory
9700 South Cass Avenue
Argonne, Illinois 60439

Sau-Lan Wu
Department of Physics
University of Wisconsin
Madison, Wisconsin 53706

Y:

Hitoshi Yamamoto
Department of Physics
California Institute of Technology
Pasadena, California 91109

Richard Yamamoto
Department of Physics
Massachusetts Institute of Technology
Cambridge, Massachusetts 02139

Wu-Guang Yan
SLAC, Bin 63
Stanford University
Stanford, California 94305

John Yelton
SLAC, Bin 95
Stanford University
Stanford, California 94305

Bing-Lin Young
Department of Physics
Iowa State University
Ames, Iowa 50011

Charles C. Young
SLAC, Bin 96
Stanford University
Stanford, California 94305

Z:

Carl Zaiser
SLAC, Bin 61
Stanford University
Stanford, California 94305

Pierre Zakarauskas
Department of Physics
University of British Columbia
Vancouver, B.C. V6T 2A3
CANADA

Peter Zerwas
SLAC, Bin 81
Stanford University
Stanford, California 94305

R. E. Zielinski
Department of Physics
University of Rochester
Rochester, New York 14627











